文部科学省・ハイテク・リサーチセンター整備事業
(平成 17 年度～平成 21 年度)

工学院大学総合研究所

ナノ表面・界面研究センター

Nano Stuctured Surfaces and Interfaces Research Center

NASIC 研究成果報告会

平成 21 年 3 月

工学院大学総合研究所

はじめに

ナノ表面・界面研究センター長
環境化学工学科 教授　長本 英俊

本研究開発プロジェクト「ナノ表面・界面の創製と応用」は平成１７年度の文部科学省のハイテク・リサーチ・センター整備事業に採択された、平成17年度から平成21年度に亘る学内外の研究者総勢57名参加の研究プロジェクトである。

プロジェクト研究の中心となるナノ表面・界面研究センター（略称 NASIC）は、先の“ハイテク・リサーチ・センター整備事業”で、継続のプロジェクト「持続型社会を支える高機能材料の創製およびリサイクルシステムの構築」も含め平成９年度から平成１６年度で建設、活用されてきた１３号館（通称、Advanced Materials Center）に施設をもっている。光電子分光装置(XPS)や透過型電子顕微鏡(TEM)などの分析装置に加え、新たにフーリエ変換核磁気共鳴装置(FT-NMR)、走査型電子顕微鏡(TEM)などを最新鋭の分析装置備えている。

原子･分子の大きさのものを取り扱うナノテクノロジーは素材、IT (情報技術)、バイオなど広範な産業の基盤に関わるもので、今や 21 世紀の最重要の技術と捉えられているが、この技術を現実に有効なものとするためには、いくつか障害がある。“原子や分子の配列をナノスケールで自在に制御する技術”の開発は様々なところで行われているが、これが可能であっても、“望む性質を持つ材料、望む機能を発現するデバイスを実現するための原子・分子の配列に関する知識の蓄積”を行って、“欲しい内容およびその目標”を明確化して実現化に結び付けることは非常に困難である。ここでは、この目標に向かって一つの実現化した例を生み出すことを目標とする。

このプロジェクト研究では「ナノ表面とナノ界面」のテーマの下、生物化学から電子デバイスまでの研究者が各々の研究について、３年間の基礎研究期間で得られた知見をまとめる、後の２年間で“望む性質や機能の発現”との関連性を検討することによって、“欲しい内容およびその目標の実現化”に結びつける応用研究を行うことを目的としている。研究課題は、４つの大課題、１．生体機能とナノテクノロジー、２．ナノ薄膜、３．ナノ界面とナノ粒子４．デバイスへの応用、及び大課題の下の小課題から成り立っている。これまでの各研究課題の状況を後に示すが、これらの先端的研究はそれぞれの研究テーマを深化するだけでなく、各テーマ間の情報の交換や他大学および研究機関の研究者と連携し、より大きな成果を生み出すように努力している。同時に、次世代を担うことになる学生たちがプロジェクトに積極的に参加して、独創的な研究や技術を開拓する能力を育むことができることを期待している。

大課題の進行状況

大課題１．生体機能とナノテクノロジー

糖質、タンパク質、脂質を組み合わせた生体分子を用い、機能性材料の開発と有用物質生産を目指したものである。小テーマ間の関連は図１で表される。

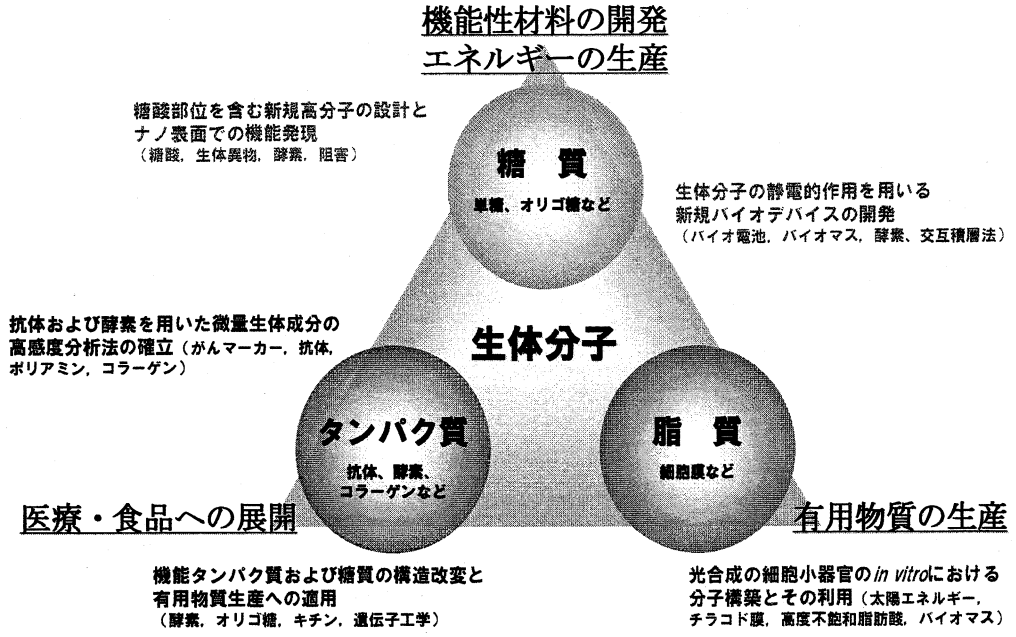

図１．大課題１における各研究テーマの関連図
（　）内は研究のキーワード

＜各研究テーマの位置づけと内容について＞

糖質関連：「機能性材料の開発」・「エネルギーの生産」

・糖酸部位を含む新規高分子の設計とナノ表面での機能発現・・・酵素（β－グルクロニダーゼ）の分子構造，特にその表面構造をナノレベルで精密解析して，その機能を効率よく阻害する糖酸部位を導入した高分子材料（合成高分子，天然多糖）を開発し，生体異物排出機能を発現させる。

・生体分子の静電的作用を用いる新規バイオデバイスの開発・・・タンパク質分子などの静電的作用を利用した分子積層型バイオデバイスを作製し，バイオマス（天然多糖，アルコール）を燃料とするバイオ太陽電池の開発を目的とする。

タンパク質関連：「医療・食料への展開」

・抗体および酵素を用いた微量生体成分の高感度分析法の確立・・・ヒト尿中に含まれるジアセチルスペルミン，ジアセチルスペルミジンの簡便かつ高精度の測定法を，抗体および酵素を用いて開発し，汎用性の腫瘍マーカーとしての臨床検査への実用化を図る。

・機能タンパク質および糖質の構造改変と有用物質生産への適用・・・タンパク質工学的分子改変による基質特異性，耐熱性，化学薬品耐性の変化などについて検討し，その成果の有用物質生産への応用展開を図る。また，天然多糖（デンプン，キチン，キトサン）分解物の特性解析，化学的改変による付加価値の付与について検討する。

脂質関連：「有用物質の生産」

・光合成の細胞小器官の *in vitro* における分子構築とその利用・・・光合成生物細胞中の細胞小器官を用いて光エネルギーから化学エネルギーへの変換システムを構築し，それを用いたバイオリアクターを作成し，そのバイオリアクターにより人間生活に有用な高機能化学物質を生成することを目的とする。

大課題２．ナノ薄膜

材料の表面の制御や制御された表面に薄膜を付与することによって、材料は新しい機能を生み出す。本研究グループでは、様々な角度から材料表面や薄膜のナノ領域にアプローチし、新しい材料の創製と評価を行うことを目的としている。

各テーマの位置付けを分かりやすくするために、テーマごとに分類用のキーワード a)大分類　b)目的・応用　を付したものを以下に示す。

テーマ間連携―手法および技術の連携も含む

１．超臨界流体を用いた有機薄膜作成技術の開発と発光素子への応用のための膜質制御と評価に関する研究
　a)機能性薄膜の開発（デバイス）
　b)ディスプレイなどへの応用を目的とした有機薄膜の合成

２．各種生分解性樹脂へのイオンビームミキシング法等による薄膜付与による機能化
　a)機能性基板の開発（ナノ構造）
　b)生分解性プラスチック表面改質による電子部品への応用

３．イオンビーム照射によるナノレベルでの表面モルフォロジー制御
　a)機能性基板の開発（ナノ構造）
　b)高分子材料の表面加工による撥水・親水性制御などへの応用

４．ポーラス構造を持つ薄膜材料を用いた新規ナノデバイスの開発
　a)酸化物薄膜の開発（ナノ構造・デバイス）
　b)チタン、ニオブのナノ構造制御によるエネルギーデバイスの開発

５．超音速フリージェット PVD によるナノ組織・ナノコンポジット膜の形成
　a)機能性薄膜の開発（ナノ構造）
　b)チタン合金薄膜の生体材料への応用

６．可視光応答型透明薄膜太陽電池の開発
　a)機能性薄膜の開発（デバイス）
　b)酸化チタンによる新規太陽電池の開発

上記のキーワードに従い、イメージを図に示すと以下のようになる。有機材料、無機材料をターゲットとして基板となる材料の開発、その基板上に創生する各種薄膜デバイスの開発を行う。双方は連携を密にして両者の特徴を生かした総合的な材料創製を目指す。

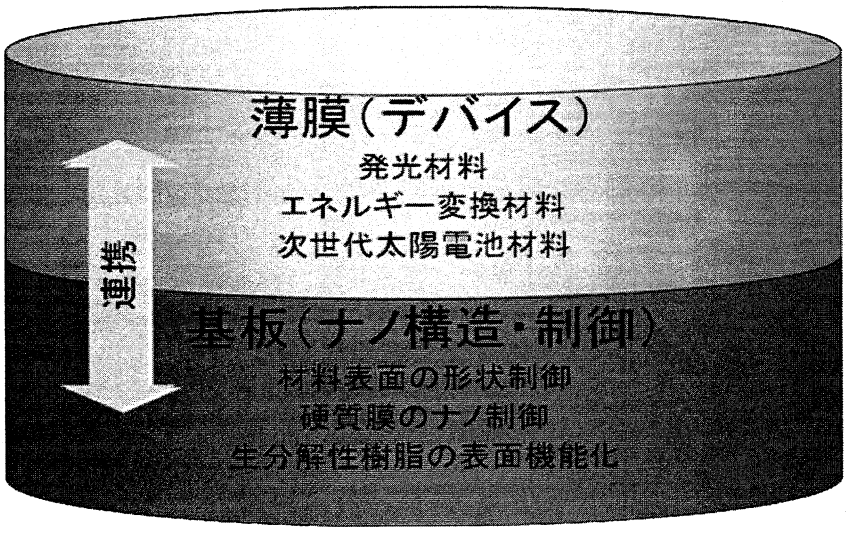

図２．大課題２での連携

大課題３．ナノ界面とナノ粒子

大課題３は、ナノサイズの粒子の合成、機能発現、およびナノ粒子の接合界面による機能発現の機構を研究し、応用分野としてナノ（触媒）粒子調製、機能性薄膜調製、界面改質を狙ったものである。

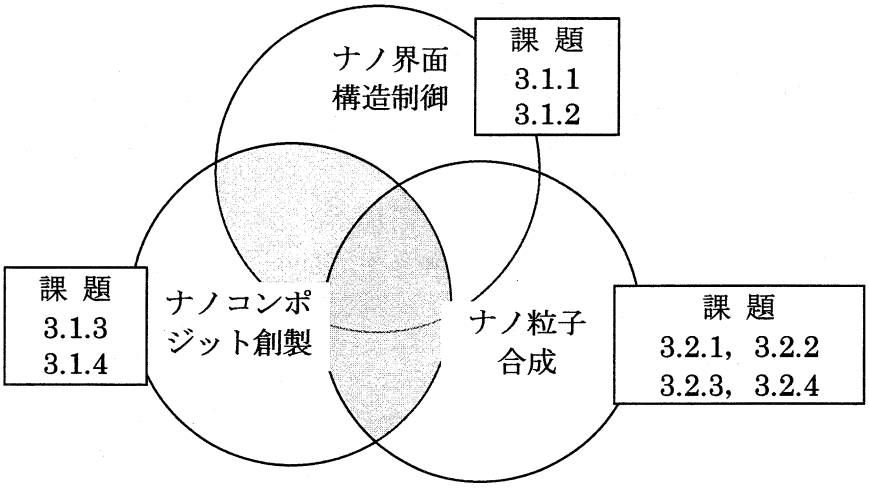

図３．大課題３での連携関係

即ち、ナノ界面構造制御およびコンポジット創製では、界面間付着性能に優れたナノ表面の創製（3.1.1）、燃料電池の固体電解質材料のナノ粒子焼結体の合成と構造制御（3.1.2）、異種ポリマーのナノコンポジットの創製（3.1.3）およびナノブロック共重合体のナノ構造制御（3.1.4）から合成法と機能発現を研究した。

ナノ粒子の合成では、ナノ粒子調製における超音波照射の有用性の検証（3.2.1）、燃料電池における燃料水素の高性能ナノ粒子触媒の創製（3.2.2）、金属錯体を利用したナノコロイドの合成と触媒活性の検証（3.2.3）およびナノ空孔調製と空孔内への有害金属イオンの閉じこめセラミックスの合成について追究した。

研究者は化学系が主体なので、NASIC の研究会の他に、種々の会合で情報交換することができた。

表１．大課題３に属する小テーマ

3.1.1	ナノ機能表面を有する生物規範型ロボットの開発研究
3.1.2	作動温度低温化を目指した固体酸化物形燃料電池の電極・電解質材料開発と界面構造の制御
3.1.3	ナノコンポジットの結晶化挙動に及ぼす充填材の影響について
3.1.4	コポリマーブラシを用いたナノ相分離構造薄膜の創製
3.2.1	溶液からの核発生および結晶粒径分布の制御
3.2.2	ナノ表面制御による白金族触媒の白金族使用量の低減または代替
3.2.3	触媒活性を有する遷移金属ナノクラスターの合成と応用
3.2.4	高分散性セラミックナノ粒子・ナノポア構造体の創製とキャラクタリゼーション

大課題４．デバイスへの応用

大テ課題４は、固体と固体の界面（半導体ヘテロ接合界面、金属と合金の界面)、および固体と液晶の界面を微視的な視点から考究し、それをデバイスに応用することを共通の基盤としており、三つの小テーマから構成されており、それらの関連は下図で表される。

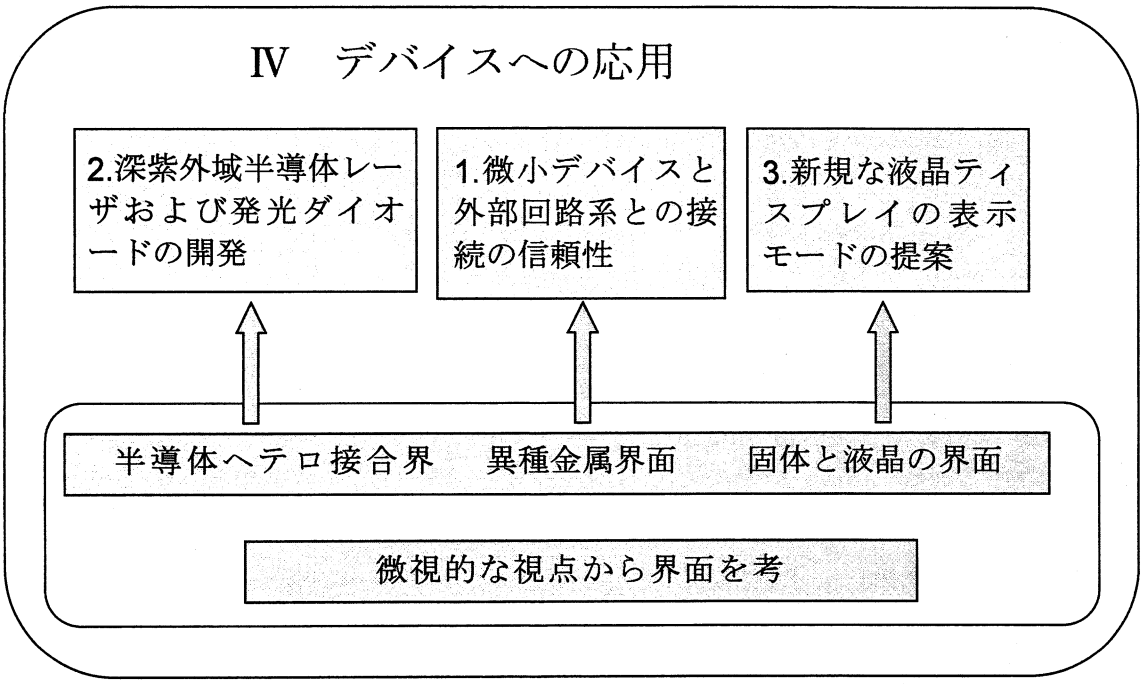

①のテーマでは、金属と合金の界面を微視的な視点から考究し、微小なデバイスと外部回路への接続における信頼性を高めることを目標としている。
②のテーマでは、半導体ヘテロ接合界面を原子層レベルで制御し、欠陥の少ない半導体ヘテロ接合を形成することによって、深紫外域で発信する半導体レーザや、低損失の半導体デバイスの実現を目指している。
③のテーマでは、固体と液晶の界面を微視的な視点から考究し、液晶の配向を制御し、新規なＬＣＤモードの提案、あるは既存モードの特性改善を図ることを目標としている。

これらのテーマは、界面をミクロな視点から考究することを共通の基盤としているが、その応用の方向は全く異なっていることから、直接的な共同研究の形態を取らず、互いの独自性を尊重しつつ研究を推進してきた。

一つのデバイスを作成するためには、様々な領域での基礎研究の成果をそれに集約しなければ目的を達成出来ないのが一般的である。大課題４の各小テーマは、大課題２「ナノ薄膜」や大課題３「ナノ界面・粒子」の研究者と研究成果を共有し、デバイスを開発するための基盤技術や評価技術を構築する方向を目指す。

目次

1. 生体分子のナノ表面

１．１　抗体および酵素を用いた微量生体成分の高感度分析法の確立

工学院大学工学部応用化学科　川喜田 正夫
工学院大学工学部応用化学科　今村 保忠
東京都臨床医学総合研究所がん治療プロジェクト　平松 恭子
都立駒込病院外科　高橋 慶一

Development of sensitive and accurate analytical systems for analysis of biomaterials utilizing the specificity of enzymes and antibodies

Masao Kawakita (Department of Applied Chemistry, Faculty of Engineering, Kogakuin University)
Yasutada Imamura (Department of Applied Chemistry, Faculty of Engineering, Kogakuin University)
Kyoko Hiramatsu (Tumor Therapy Project, Tokyo Metropolitan Institute of Medical Sciences)
Kei-ichi Takahashi (Department of Surgery, Tokyo Metropolitan Komagome Hospital)

N^1,N^{12}-Diacetylspermine (DiAcSpm), a minor component of urinary polyamines, was found to be elevated frequently in patients with various types of cancers. We developed an ELISA procedure using highly specific antibodies against DiAcSpm for more convenient measurement of DiAcSpm, and showed that it is highly sensitive in detecting early stage colorectal cancer. To establish urinary DiAcSpm test as an item for clinical diagnostic test a reagent kit for urinary DiAcSpm determination utilizing aggregation of colloidal gold nanoparticles coated by anti-DiAcSpm antibody was developed. We also began an attempt to construct an immunochromatography strip to detect urinary DiAcSpm for personal monitoring purpose.

【研究の背景】

ポリアミンは、複数のアミノ基をもつ一群のアルキルアミンである。これらは細胞増殖およびその制御に重要な役割を果たす物質の一つであり、活発に増殖する組織に多量に含まれ、またそのような組織で活発に代謝される [1]。その一部はアセチル体として尿中に排泄されるため、がん組織のような活発に増殖する組織が体内にあると、ポリアミンの尿中排泄量は増加する。1971 年に Russell がこの事実に注目し、尿中ポリアミンが腫瘍マーカーとして利用できる可能性があることを報告 [2]して以来、多くの研究が行われたが、「尿中総ポリアミン」は感度、がん特異度のいずれの面から見ても腫瘍マーカーとしては性能が不十分であると考えられるようになった [3]。しかし我々は、1990 年代に、HPLC による尿中ポリアミン成分の新たな分画分析法を開発し、新規の微量尿中ポリアミン成分 N^1,N^{12}-ジアセチルスペルミン（DiAcSpm）が存在することを見出した [4]。そして、既知のポリアミン成分とは異なり、その尿中レベルが種々の悪性腫瘍において患者の病勢をよく反映した動きを示すことを明らかにして [5]、DiAcSpm が新規腫瘍マーカーとして有用である可能性を指摘した。我々はさらに、DiAcSpm 検査を臨床検査項目の一つとして実用化することを目的として、HPLC の短所である検体処理能力の低さを克服できる、より簡便な測定法として DiAcSpm 特異的抗体を用いた免疫学的測定系の開発に取り組み、酵素

免疫測定法（ELISA 法）による DiAcSpm の高感度測定系の開発に成功した（Fig. 1）[6]。

【研究の経過および成果】

ELISA 法による測定系を利用して多数のがん患者の尿中 DiAcSpm レベルの測定を進めた。都立駒込病院で手術を受けた大腸がん患者 248 例について術前 DiAcSpm 値を測定し、カットオフ値を 0.25μmol/g creatinine（健常者 53 名についての平均+2S.D.）として陽性率を検討したところ、DiAcSpm は既存の腫瘍マーカーCEA の約 2 倍の高い陽性率を示し、特に、stage 0 および stage I の早期癌に対して CEA の 6 倍（62%）の検出感度を示した[i]。近年のがん治療法の進歩により、特に大腸がんに関しては stage 0 および stage I の段階で発見された早期がんに対しては 100%に近い５年生存率が得られるようになっている。したがって、早期がん発見のための手段を提供することは、がんを治癒可能な病気に変える上で大きな貢献をすることになる。

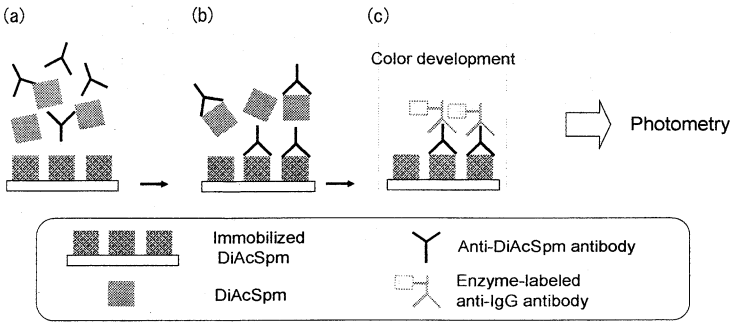

Fig. 1　An ELISA system for determination of DiAcSpm using antibodies highly specific for DiAcSpm

このように DiAcSpm の早期がんマーカーとしての性能が明らかになり、がん検診への適用も視野に入れた実用化が期待されるようになったため、我々は、従来の ELISA 法よりさらに迅速、高精度の測定系として、金コロイド凝集法を用いた DiAcSpm 測定系の開発を行った。金コロイドの表面に抗 DiAcSpm 抗体を吸着させ、ウシ血清アルブミン（BSA）に多数の DiAcSpm 分子を化学修飾によって結合させた BSA-DiAcSpm 複合体を加えると、金コロイド粒子が凝集し、色調が wine-red から灰色に変化する。この反応液中に検体を添加すると、検体中の DiAcSpm が抗体に結合し、濃度依存的に BSA-DiAcSpm 複合体の結合を妨害して金コロイド粒子の凝集を妨げ、色調の変化を抑制する。従って、この色調変化の大きさに基づいて、DiAcSpm 濃度を判定することができる（Fig. 3）。2008 年度には金コロイド凝集法による測定試薬の開発をさらに進め、臨床検査の場で実際に使用されている生化学自動分析機に搭載可能な試薬のキット化に成功し、このキットを「Auto DiAcSpm」と命名し、研究用試薬として発売した。測定の同時再現性（C.V.=1.1-2.5%）、日差再現性（C.V.=1.1-5.3%）、添加回収試験の成績（回収率 94-115%）はいずれも満足すべき性能を示す数値であり、また DiAcSpm の検出感度 5.4nM は、入院加療中に点滴の処置を受けている患者の希薄尿中の DiAcSpm 測定にも十分に対応できる水準の

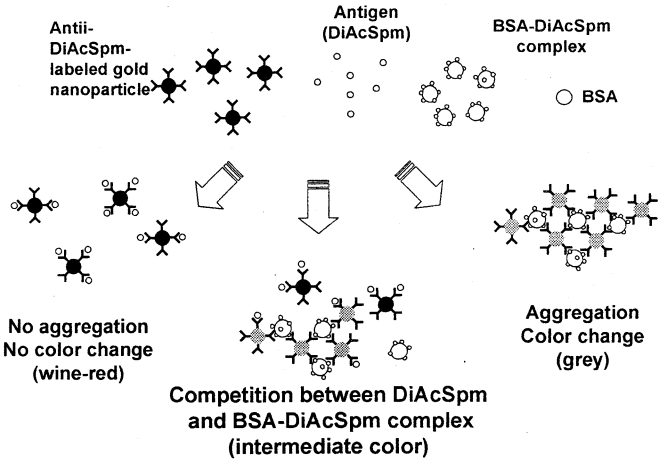

Fig. 2. Measurement of DiAcSpm utilizing aggregation of colloidal gold nanoparticles coated with anti-DiAcSpm antibody

ものである[ix,x]。この試薬を用いれば１検体を１０分間で処理することができるため、従来よりもさらに大量の検体を迅速に処理し、正確な測定値を短時間で得ることが可能になった。今後さらに、臨床治験を経て厚生労働省に対して体外診断薬としての製造承認申請を行い、実用化に向けた努力を継続する。

上記のような病院、検査機関における高精度、迅速測定用の試薬とは別に、DiAcSpm の早期がん検出性能を最大限に活用するためには、一般人が自己管理の目的で自宅で利用できる簡易・迅速測定法を開発し、早期受診の機会を増やすことが重要である。そのような簡易 DiAcSpm 検出法として、2008 年度には新たにイムノクロマト法の開発に着手した。

BSA-DiAcSpm 複合体をニトロセルロースフィルター上に固定化し、抗体標識金コロイドを毛細管現象により浸透させると、抗原抗体反応により、金コロイドがフィルター上の BSA-DiAcSpm 複合体に捕捉され、呈色する。抗体標識金コロイドが尿中の DiAcSpm と接触した後にフィルターに浸透した場合には、抗体が DiAcSpm で飽和しているために、フィルター上の BSA-DiAcSpm 複合体は金コロイドを捕捉することができず、呈色ラインは出現しない。この方法によれば、イムノクロマトストリップの上に尿を一滴垂らすだけで、約 10 分後には目視によって、ジアセチルスペルミンが一定濃度以下であるか、以上であるかを判定することができる。2008 年度には、部材の検討、使用抗体の検討、固定化の条件などの基礎検討を行った。さらに詳細な条件検討を進め、精密測定法を補完する方法として確立したいと考えている。

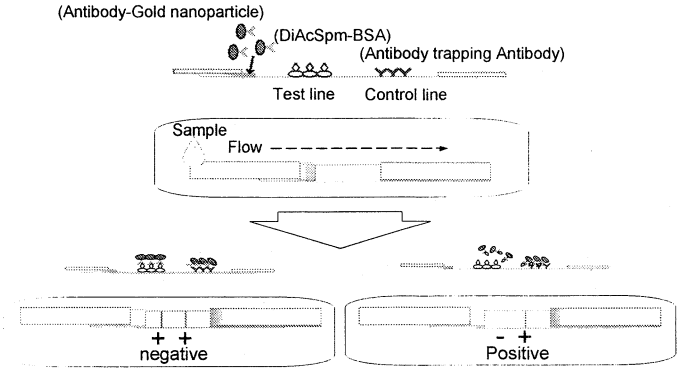

Fig. 3 Detection of DiAcSpm on immunochromatography strips

本報告においては、狭義の研究課題に沿って、DiAcSpm の分析法を中心に研究成果を述べた。種々の分析法は腫瘍マーカーとしての臨床的意義の裏付けを得てはじめて意味を持つものである。このような観点から我々は、上述の分析法を活用し、学外共同研究者と連携してがん患者の尿中 DiAcSpm の測定を進めている。その結果、尿中 DiAcSpm の上昇は癌の種類に大きく依存しない傾向があり、DiAcSpm は汎用の早期がん検出マーカーとして、がんの検診に広く適用できる可能性が示されている。このことは乳がんにおいてすでに一部明らかになり[i]、膵臓がんに関しても最近このことを示唆する結果が得られつつある。

このような早期がんマーカーとしての利用価値だけでなく、DiAcSpm はがん患者の経過観察の過程における病勢判定の指標としても優れた特性をもつ。すなわち、大腸がん手術後 6 ヶ月の時点において尿中 DiAcSpm 値がカットオフ値の３倍を超えていた患者の予後はきわめて不良である一方、カットオフ値未満であった患者の大部分は長期寛解状態にあることが明らかになった。従って、この検査の普及を図ることにより、がんによる死亡率の低下、がん患者の QOL（quality of life）の向上に大きく寄与できる可能性があり、それを実現することが今後の課題である。本研究において開発する各種の測定系は、汎用腫瘍マーカーとしての観点から DiAcSpm の臨床的意義をさらに明らかにしその実用化を図るうえで大きな寄与をすることが期待される。

【参考文献】

1. Tabor CW, Tabor H. Polyamines. Ann Rev Biochem 1984; 53: 749-90.
2. Russell DH. Increased polyamine concentrations in the urine of human cancer patients. Nature New Biol 1971; 233: 144-5.
3. Bachrach U. Polyamines as markers of malignancy. Prog Drug Res 1992;39: 9-33.
4. Hiramatsu K, Sugimoto M, Kamei S, Hoshino M, Kinoshita K, Iwasaki K et al. Determination of amounts of polyamines excreted in urine: demonstration of N^1,N^8-diacetylspermidine and N^1,N^{12}-diacetylspermine as components commonly occurring in normal human urine. J Biochem 1995; 117: 107-12.
5. Sugimoto M, Hiramatsu K, Kamei S, Kinoshita K, Hoshino M, Iwasaki K et al. Significance of urinary N^1,N^8-diacetylspermidine and N^1,N^{12}-diacetylspermine as indicators of neoplastic diseases. J Cancer Res Clin Oncol 1995; 121: 317-9.
6. Hiramatsu K, Miura H, Kamei S, Iwasaki K, Kawakita M. Development of a sensitive and accurate enzyme-linked immunosorbent assay (ELISA) system that can replace HPLC analysis for the determination of N^1,N^{12}-diacetylspermine in human urine. J Biochem 1998; 124: 231-6.

【研究業績】

i) Hiramatsu K, Takahashi K, Yamaguchi T, Matsumoto H, Miyamoto H, Tanaka S, Tanaka C, Tamamori Y, Imajo M, Kawaguchi M, Toi M, Mori T and Kawakita M. (2005) N^1,N^{12}-Diacetylspermine as a Sensitive and Specific Novel Marker for Early- and Late-Stage Colorectal and Breast Cancers. Clin Cancer Res, 11, 2986-2990

ii) Miki T, Hiramatsu K and Kawakita M. (2005) Interaction of N^1,N^{12}-Diacetylspermine with polyamine transport systems of polarized porcine renal cell line LLC-PK_1. J Biochem, 138, 479-484

iii) Yamaguchi, K., Nakamura, M., Shirahane, K., Konomi, H., Torata, N., Hamasaki, N., Kawakita, M. Tanaka, M. (2005) Urine diacetylspermine as a novel tumor marker for pancreatobiliary caracinomas. Digest Liver Dis, 37, 190-194

iv) Kawakita M and Hiramatsu K. (2006) Diacetylated Derivatives of Spermine and Spermidine as Novel Promising Tumor Markers. J Biochem, 139, 315-322

v) Muraoka, M., Miki, T., Ishida, N., Hara, T. and Kawakita, M. (2007) Variety of nucleotide sugar transporters with respect to the interaction wtih nucleoside mono- and diphosphates. J. Biol. Chem., 282, 24615-24622

vi) T. Watanabe, Y. Imamura, et al. (2007) Graded arrangement of collagen fibrils in the equine superficial digital flexor tendon. Connective Tissue Research, 48, 332-337

vii) T. Kihara, Y. Imamura, et al. (2008) Intercellular accumulation of type V collagen fibrils in accordance with cell aggregation. Journal of Biochemistry, 144, 625-633

viii) 藤江奈々、小俣一行、平松恭子、坂口政吉、川喜田正夫 (2008) スポット尿による尿中ジアセチルスペルミン量の測定の妥当性の検討. 日本分子腫瘍マーカー研究会誌, 23, 42-43

ix) 柳谷真理、土居洋介、小坂美恵子、榎本昌泰、平松恭子、高橋慶一、川喜田正夫 (2008) 金コロイド凝集法を測定原理とする尿中ジアセチルスペルミン試薬の開発. 日本分子腫瘍マーカー研究会誌, 23, 44-45

x) 川喜田正夫、平松恭子、高橋慶一、柳谷真理、土居洋介、小坂美恵子、田渕明子、森武生 (2008) 尿中腫瘍マーカーN^1,N^{12}-ジアセチルスペルミンの特性とその測定. 日本臨床検査自動化学会誌, 33, 141-144

xi) 川喜田正夫、平松恭子 (2008) 大腸がん腫瘍マーカーとしての尿中 N^1,N^{12}-ジアセチルスペルミン. 検査と技術, 36, 457-459

１．２　海洋性微細藻類による高度不飽和脂肪酸の生産

Poly unsaturated fatty acids production by marine microalgae

平野盛雄　（工学部応用化学科）

Morio Hirano　(Department of Applied Chemistry, Faculty of Engineering Kogakuin University)

Marine microalgae has been recognized as one of the most promising eicosapentaenoic acid (EPA) and docosahexaenoic acid (DHA) producers. We have already found that marine microalga KUNK9431 produced both EPA and DHA. In the present study, optimal culture conditions were investigated for production of EPA and DHA by marine microalga KUNK9431. Concentration of nitrogen and phosphorus in medium had significant effects in culture of KUNK9431. Their optimal values were determined 2.0 mM KNO_3 and 0.5 mM K_2HPO_4. A highest contents of EPA and DHA in KUNK9431 were 20.0 mg / g d.w.c. and 10.1 mg / g d.w.c., respectively.

１．はじめに

微細藻類の光合成機能の利用研究を進める上で、高い光合成活性、有益で利用価値の高い微細藻類の探索、発見は不可欠である。本研究は、医学、薬学、あるいは栄養学分野における利用、応用価値の高い微細藻類の探索、およびその大量培養条件の確立をめざして行ったものである。

エイコサペンタエン酸(EPA・C20:5)、ドコサヘキサエン酸(DHA・C22:6)などの高度不飽和脂肪酸の多くは、様々な優れた生理活性を有することが確認され、現在も新たな生理活性が次々と発見されている。それらの中には、すでに医薬品および健康食品として製品化されているものも多い。 EPA および DHA の生理機能には共通点が多く、その生理活性に由来する薬理効果として抗血栓効果、抗動脈硬化作用、高脂血症改善効果、心血管系疾患予防効果、抗アレルギー作用、認知機能改善効果、抗癌作用などが挙げられる。

ところで、今日の EPA および DHA の供給源は主に魚油であるが、魚油による供給には、特有の匂い、味による製品化分野の限定、環境汚染に伴う品質の低下、低い酸化安定性、需要増加に伴う供給量不足などの問題点が多い。これらの問題の解決策として、EPA あるいは DHA を含有する新規微細藻類の発見、およびその人工大量培養条件に関する研究が急務である。

本研究においては、EPA および DHA の新たな供給源として、EPA、DHA の両者を含有する海洋性微細藻類 KUNK9431 による高度不飽和脂肪酸合成のための人工培養条件について検討を行った。

2．実験

本研究においては、鹿児島県硫黄島近海から採取したプラシノ藻 KUNK9431 を用いた。KUNK9431 の培養は、基本培地として栄養添加人工海水培地に Soil Extract を添加した Ese 培地を用い、培地の pH は 0.1M HCl および（あるいは）0.1M NaOH を用いて調製した。また、培養器には 100m L の大型試験管を用いて、通気培養を行った。光源には白色蛍光灯を用いた。培地中の藻体密度は分光光度計を用い、750nm の吸光度より算出した。藻体中の脂肪酸分析は、脂肪酸を 5% HCl －MeOH によってメチルエステル化した後、ガスクロマトグラフィーによって定量分析した。内部標準物質としてヘプタデカン酸を用いた。

3．結果および考察

KUNK9431 の EPA および DHA 生産性向上のために、藻類培養の重要な制御因子である培地中の窒素源およびリン源濃度の制御を行った際の、KUNK9431 の生育および脂肪酸生産への影響について検討を行った。本検討に用いた窒素源およびリン源には、KNO_3 および K_2HPO_4 を用い、それらの濃度は KNO_3 を 0.25~2.5mM、K_2HPO_4 を 0.025~0.35mM とした。その結果、KUNK9431 の培養において、KNO_3 を 1.0 mM、K_2HPO_4 を 0.25 mM 含む培地を用いた場合、その EPA および DHA 生産性は最も高い値を示し、それぞれ 1.7 および 0.86 mg / L·day であった。そこで、さらに最適な KNO_3 および K_2HPO_4 濃度を求めることを目的として、培地中の KNO_3 および K_2HPO_4 濃度のモル比を４：１として、異なる KNO_3 および K_2HPO_4 濃度の培地を用いて培養を行った際の、KUNK9431 の生育および脂肪酸組成について検討を行った。その結果、KUNK9431 の培養に KNO_3 を 2.0 mM、
K_2HPO_4 を 0.5 mM 含む培地を用いた場合、KUNK9431 の最大生育量は最も高い値を示し、0.33 g cell / L であった。また、最大増殖速度は 0.085 g / L·day に達し、KUNK9431 は、他の海洋性微細藻類に比較して高い塩濃度を好む傾向にあることが分かった。また、EPA 含有量は、KUNK9431 の培養を KNO_3 を 2.0 mM、K_2HPO_4 を 0.5 mM 含む培地を用いた場合に高い値を示し、その値は 20.0 mg / g d.w.c. となり、DHA 含有量は 10.1 mg / g d.w.c. であった。ところで、この場合の藻体中の EPA および DHA 含有率は、いずれの培養条件においても大きな差異は確認されず、EPA および DHA 含有量の増減は、総高級脂肪酸量の増減に依存していた。このことから、KUNK9431 においては比較的高い塩濃度の海水中において、高級脂肪酸合成経路の活性化が促進されるものと考えられた。また、EPA および DHA の生産性においても、KNO_3 を 2.0 mM、K_2HPO_4 を 0.5 mM 含む培地を用いた場合、最も高い値を示し、それぞれ、1.7 および 0.86 mg / L·day となり、これらの結果より、KUNK9431 による EPA および DHA の生産には、窒素源およびリン源濃度の制御を行い、それぞれ、2.0、0.50mM にすべきであるとの結論に達した。

ところで、新宿から八王子への実験室移転に伴い、KUNK9431 の EPA および DHA 合成能が失活するという予期せぬ事態が発生した。そこで、その原因探索のための検討を行った。その原因について、様々な角度から予備検討した結果、唯一、両実験室における維持培養環境の違いが明確になった。一般的には、藻体の維持培養条件は厳密さを要求されないが、今回、維持培養環境の相違点である温度および光強度に焦点を当て、それらの因子に関する詳細な検討を行った。すなわち、EPA および DHA が全く検出されなくなった KUNK9431 の維持培養を、温度を 30±3℃（新宿校舎実験室に準じた温度）として、また、光強度は 27～107 μE / m² ・ s の範囲において、EPA および DHA の合成能再活性化を試みた。その結果、光強度を 27 μE / m²・s として継代培養を繰り返すことによって、KUNK9431 の EPA および DHA 含有量は次第に増加し、継代培養を 5 回行った後の KUNK9431 の EPA および DHA 含有量はそれぞれ 13.6 mg / g d.w.c.および 1.7 mg / g d.w.c.となり、EPA および DHA の合成能はそれぞれ 77 %および 25 %にまで復活した。この結果より、これまで安易に考えられてきた KUNK9431 の維持培養条件においても、厳密な温度および光強度が要求されることが分かった。

ところで、本検討を進めていく過程において、藻体の色と EPA および DHA の合成能の間に関連があることが認められた。すなわち、EPA および DHA 合成能を持つ藻体は合成能を失った藻体に比べて、明らかに黄色が目立った。今後、その黄色色素の同定を進める必要があると考えている。

4．おわりに

近年話題となっているメタボリック症候群（内臓脂肪型肥満）は血中脂質における中性脂肪、コレステロールの増加によって起こる。EPA や DHA は細胞の核内レセプターを刺激することによって、体内における過剰の中性脂肪やコレステロールを排出させるための指令を発し、それらの分解酵素を誘導する。さらに栄養学的な研究によって、メタボリック症候群改善あるいは健康維持に n-3 系高度不飽和脂肪酸の摂取が不可欠であることが明らかにされた[1)]。

そこで筆者らは微細藻類による高度不飽和脂肪酸の生産を目的として、n-3 系高度不飽和脂肪酸である EPA あるいは DHA 等の高度不飽和脂肪酸を含有する微細藻類を、日本近海から採取した微細藻類のスクリーニングによって探索し、EPA、DHA をともに含有する海洋性微細藻類 KUNK9431 を発見した。そして、それの人工培養条件の確立を行い、KUNK9431 による EPA および DHA の生産には、培地成分条件として高塩濃度の海水が適していること、また、KUNK9431 の維持培養には厳密な温度および光強度の管理が必要であることを明らかにした。

引用文献

1）Sutsmal, et al.,*Appl Microbiol Biotechnol.*, 64, 146-153 (2004)

研究業績

国際会議：

K. Abe, E. Takahashi, M. Hirano, Development of water purification system with biofilter of the aerial microalga, *Tretepohlia aurea*, 2005 環太平洋国際会議(ホノルル).

Morio Hirano, Takahiro Miyazaki, Docosahexaenoic acid and eicosapentaenoic acid production by marine microalga, 5-th International Symposium on Advanced Technology, (2006) 台南

Yuji Ohnishi, Takahiro Miyazaki, Kenjiro Sugiyama, and Morio Hirano, Optimization of culture condition for production of eicosapentaenoic acid and docosahexaenoic acid by marine microalga KUNK9431, 7-th International Symposium on Advanced Technology, (2008) **北京**

関連論文：

K. Abe, H. Hattori, M. Hirano 2007 Accumulation and antioxidant acivity of secondary carotenoids in the aerial microalga *Coelastrella striolata var. multistriata*, *Food Chemistry*, **100**, 656-661.

K. Abe, E. Takahashi, M. Hirano, 2007, Development of laboratory-scale photobioreactor for water purification by use of a biofilter composed of the aerial microalga Tretepohlia aurea, *J. Appl. Phycol.*, in press (2007).

1．3　糖酸部位を含む新規高分子の設計とナノ表面での機能発現

マテリアル科学科　橋本 和彦、大川 春樹

Design of Novel Polymers Bearing Saccharic Moieties and Their Function on the Enzymatic Surface

Kazuhiko Hashimoto and Haruki Okawa
(Department of Materials Sciences & Technology, Faculty of Engineering, Kogakuin University)

Abstract: New styryl-type glycopolymers having D,L-xylaric, L-tartaric, and D-manaric pendants were synthesized by the copolymerization of the glycomonomers with acrylamide. The resulting glycopolymers were found to inhibit the β-glucuronidase activity much more effectively than not only the corresponding saccharic acids but also the glycomonomers. Therefore they can be candidates of polymeric devices for effective excretion of xenobiotics. The inhibition mechanism of the glycopolymers was found to depend upon the structure of their saccharic units. On the other hand, the chitosan derivatives bearing D-glucaric pendants and polystyrene-type microspheres with saccharic units on the surface were also prepared and their inhibition was estimated by the hydrolysis .

1．はじめに

研究担当者らは、石油資源由来高分子材料に代わり、これまでほとんど用いられていなかった再生可能な植物資源、主としてウロン酸や糖酸、からの高分子合成を研究してきたが[1)]、それら糖誘導体の生理活性にも注目し、その特異な機能を合成高分子に挿入することを試みている。D－グルカル酸のような糖酸およびそのラクトン類が、小腸に多量に存在するβ－グルクロニダーゼ活性を阻害することが知られている。生体異物（毒物）は肝臓でグルクロン酸抱合され、小腸を経て排出されるので、糖酸誘導体を効率よく腸に送り込むことができれば、抱合体を分解するβ－グルクロニダーゼの活性を阻害し、生体異物の排出を促進できると考えられる。そこで、研究担当者らはD－グルカル酸部位を側鎖にもつ高分子（1）を設計合成したところ、得られた高分子が確かにβ－グルクロニダーゼ活性を阻害した[2)]。

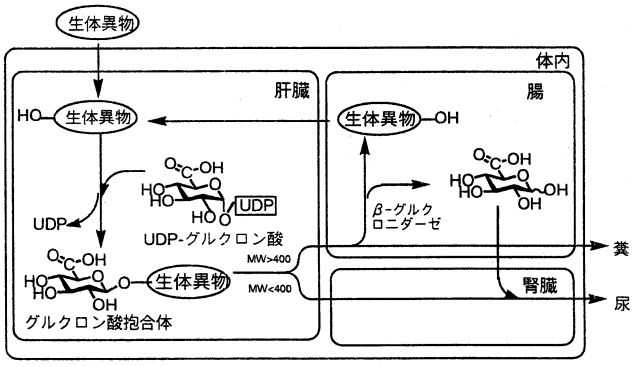

Fig.1 Metabolic Pathway & Enterohepatic Circulation of Xenobiotics

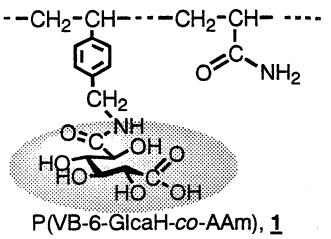

P(VB-6-GlcaH-*co*-AAm), 1

本プロジェクト研究では、炭素数の異なる各種糖酸を側鎖にもつ高分子（2，3）、および1とは炭素数は同じであるが、2位のヒドロキシ基の立体配置のみが異なる糖酸を側鎖にもつ高分子（4）を合成し、それらの酵素阻害機能を、それらのモノマーおよび糖酸自身の酵素阻害能とも比較考察して、阻害機構を調査した。また自然界から得られる多糖（キトサン）を糖酸の Polymeric Carrier　に用いたり、高分子ミクロスフェアの表面へ糖酸部位を導入する試みも行った。

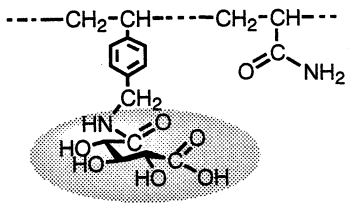

P(VB-D,L-XylaH-*co*-AAm) , 2

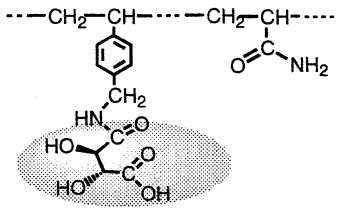

P(VB-L-TartaH-*co*-AAm), 3

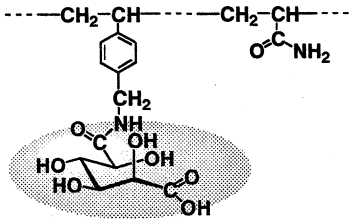

P(VB-D-ManaH-co-AAm), 4

２．炭素数の異なる糖酸部位を側鎖にもつ新規糖鎖高分子の酵素阻害能

キシラル酸および酒石酸部位を側鎖にもつ高分子（2，3）存在下、基質に *p*－ニトロフェニル β－グルクロニドを用い、β－グルクロニダーゼによる加水分解を３７℃で行い、生成した *p*－ニトロフェノールの濃度の経時変比を分光学的に追跡し、分解速度を算出した。高分子無添加の場合の分解速度を基準として分解速度を算出し、阻害率を算出した。

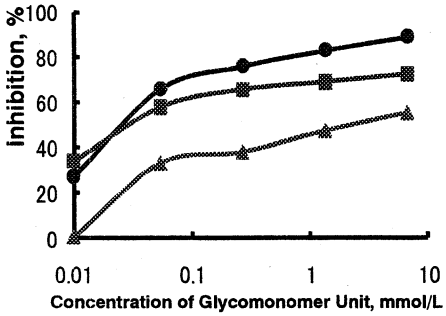

Fig. 2. Inhibition of β-glucuronidase activity by different glycopolymers at 37℃ .
●, P(VB-6-D-GlucaH-*co*-AAm) 1, 27%,;
■, P(VB-D,L-XylarH-*co*-AAm) 2, 22%;
◆, P(VB-L-TartaH-*co*-AAm) 3, 23%.

2，3は、*p*－ニトロフェニル β－グルクロニドのβ－グルクロニダーゼによる加水分解を、グルカル酸を側鎖にもつ高分子1と同様に、阻害することがわかったが、糖酸部位の炭素数が減少するにつれて、その阻害率が低下した（図２）。

高分子1の糖酸部位であるグルカル酸が、高分子2，3の糖酸部位のキシラル酸、酒石酸よりも、基質Ｄ－グルクロン酸抱合体のＤ－グルクロン酸部位と似たコンホメーションをとり得るためと思われる。

対応する糖酸部位を側鎖にもつスチレン型モノマー、および糖酸誘導体存在下での、β－グルクロニダーゼ活性に対する阻害率は、図３および図４にまとめたようにいずれの高分子阻害剤の場合も特に低濃度領域において、元の糖酸やモノマーよりも高い阻害能をもつことがわかった。酵素β－グルクロニダーゼが分子量約７５０００の４つのサブユニットからなることが知られていることを考慮すれば、この実験結果は糖酸部位が高分子鎖に沿って存在することによるクラスター効果が発現したものと推測する。

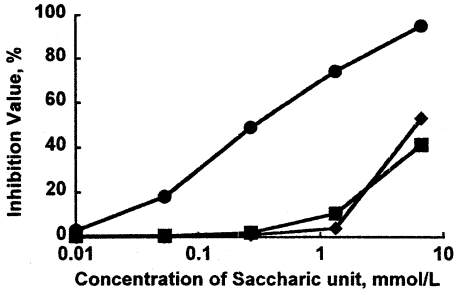

Fig. 3. Inhibition of β-glucuronidase activity by different glycomonomers at 37℃. .

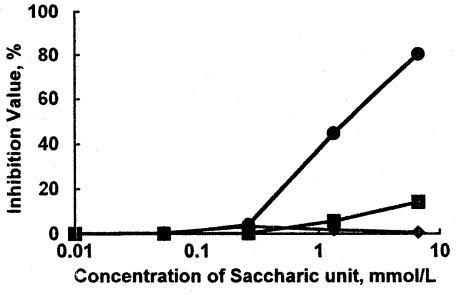

Fig. 4. Inhibition of β-glucuronidase activity by different saccharic derivatives at 37℃.

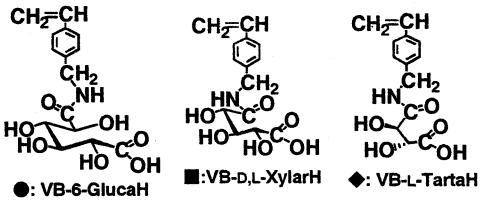

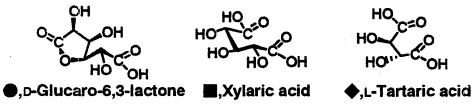

キシラル酸および酒石酸部位を側鎖にもつスチレン型モノマーが高濃度ではかなりの阻害能をもつこと、およびＤ－グルカル酸部位を側鎖にもつスチレン型モノマーも元のＤ－グルカル酸より阻害能が高いことは、疎水性の高いｐ－ビニルベンジル基も阻害能に何らかの寄与があることを示唆する。

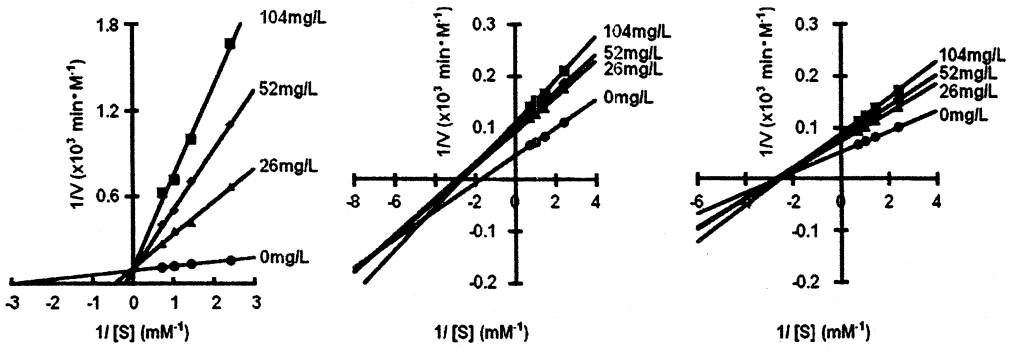

1, 30% M_n=1.04x10⁴　　2, 41% M_n=1.32x10⁴　　3, 23% M_n=0.88x10⁴

Fig. 5 Lineweaver-Burk plot for kinetic data on the hydrolysis of p-nitrophenyl β-D-glucuronide in the presence of different glycopolymers at 37℃.

図５のLineweaver-Burkプロットは、高分子1は拮抗阻害型相互作用に近いことを示したが、高分子3では阻害機構が異なり、どちらかと言えば非拮抗阻害型に見えることがわかった。

３．D－マンナル酸を側鎖にもつ新規糖鎖高分子の合成とその酵素阻害機能

D－マンナル酸を側鎖にもつ新規スチレン誘導体は、D－マンニトールの酸化と分子内縮合により得られるジラクトンへのp－ビニルベンジルアミンの開環付加を経て合成した（スキーム１）。得られたモノマーをアクリルアミドとラジカル共重合することにより、D－マンナル酸を側鎖にもつ新規糖鎖高分子（4）を得た（表１）。

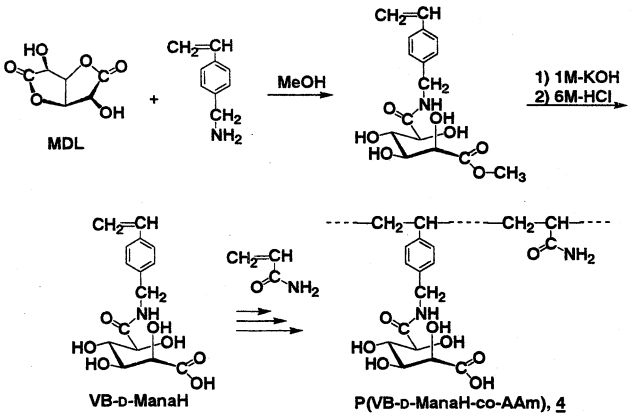

Scheme 1 Synthesis of Glycopolymers Bearing D-Mannaric Moieties

既に報告されているように、D－マンナル酸及びそのジラクトンは、β－グルクロニダーゼを阻害しないにも関わらず、得られた高分子4及びそのモノマーは酵素阻害能をもつことは興味が持たれる（図６）。

また高分子4は、上記の高分子1，2，3と同様に低濃度での阻害能が対応するモノマーより高く、やはりクラスター効果が発現した。

高分子4に関するLineweaver-Burkプロットは、阻害機構が、単なる拮抗型や非拮抗型では表現できないことを示唆する（図７）。

Table 1 Synthesis of P(VB-D-ManaH-*co*-AAM) (4)

Expt. No.	VB-D-ManaH mg(mmol)	AAm mg(mmol)	$[M]_0$ mol/L	AIBN Mol%	Time h	Copolymer mg	Copolymer Mole fraction of M_1	M_n $\times 10^{-4}$	M_w/M_n
1	195 (0.6)	170 (2.4)	1.5	1.00	24	184	0.34	1.4	1.9
2	195 (0.6)	170 (2.4)	3.0	0.25	24	168	0.34	3.1	3.5
3	292 (0.9)	362 (3.1)	3.0	0.05	36	208	0.30	6.4	2.0

[a] Mole fraction of M_1 in feed, 2.0; Solvent, Me_2SO; Temp., 60°C.

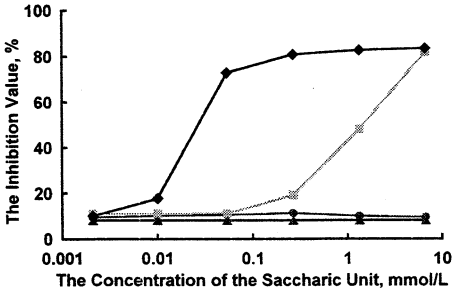

Fig. 6 The Inhibition of the β-Glucuronidase Activity by D-Mannaric Series Inhibitors at 37°C
◆, P(VB-ManaH-*co*-AAM) (4); ■, VB-ManaH; ●, MDL.

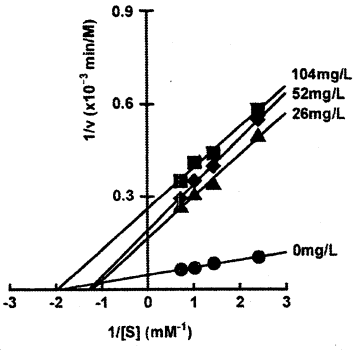

Fig. 7 Lineweaver-Burk plot for kinetic data on the hydrolysis of p-nitrophenyl β-D-glucuronide in the presence of glycopolymer(4) at 37°C.

４．キトサンへの糖酸部位の導入

糖酸部位を運搬する高分子として合成高分子の代わりに、安全性の高い天然多糖から得られるキトサンを用いて、その側鎖を化学変換し、に糖酸部位を導入した（5）。

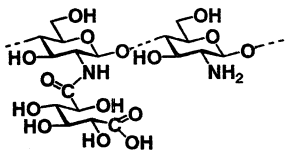

5

図８に示したように、得られたキトサン誘導体5もポリスチレン型阻害剤（1，2，3，4）と同様に酵素β－グルクロニダーゼの活性を阻害し、実用上有効であることがわかった。

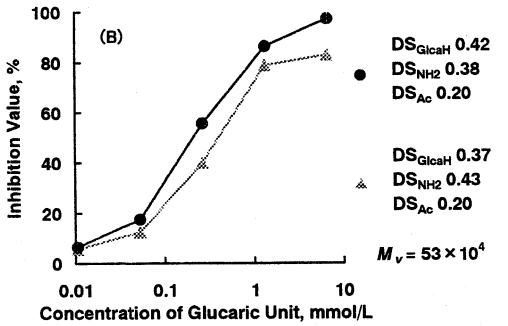

Fig. 8 Inhibition of β-glucuronidase activity by citosan derivative (5) with different amonuts of glucaric moiety at 37°C.

5．糖酸部位を表面にもつポリスチレン型ミクロスフェア

前述の水溶性高分子阻害剤を、水不溶のミクロスフェア（微粒子）に変換することを試みた。ポリスチレンのミクロスフェア調整法を参考に、エタノールと２－メトキシエタノールとの混合溶媒中、ヒドロキシプロピルセルロースを加えて、各種糖酸を側鎖にもつスチレン誘導体とスチレンとの分散共重合を行った（表２）。

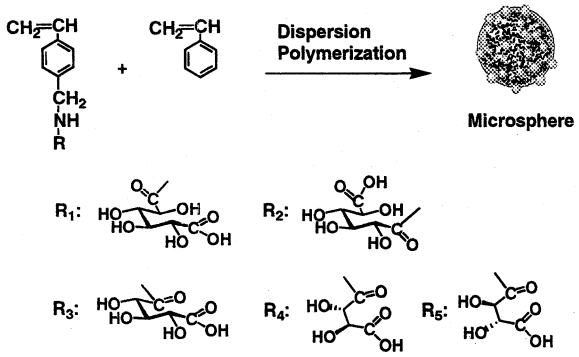

Table 2 Preparation of Polystrene-type Microsphere Containing D-Glucaric Unit

Expt. No.	R_1 monomer g (mmol)	Styrene g (mmol)	mol % of R_1 in feed	rpm[b]	Polymer Yield g	Polymer Yield mol% of R_1[d]	ϕ[c] μm
1	0.32 (1.0)	0.94 (9.0)	10	200	0.26	7	2.4
2	0.32 (1.0)	0.94 (9.0)	10	300	0.43	7	1.9
3	0.32 (1.0)	0.94 (9.0)	10	500	0.37	8	1.3

[a] Temp., 75°C; Time, 24 h. [b] Rate of Stirring.
[c] Average Diameter of Microsphere. [d] Determined by Elemental Analysis.

図９および表２に示したように、撹拌速度により得られるミクロスフェアの平均粒径が変化した。粒径分布を狭くするには、装置の改良が必要と思われる。

元素分析により算出した共重合体中の糖酸部位の含有量は、仕込みモノマー量より低かったが、その一部はミクロスフェアの表面に存在すると仮定し、調製したミクロスフェア存在下での、β－グルクロニダーゼによる加水分解試験を行った。

ミクロスフェアの平均粒径が小さい方が、阻害能が高かった。この結果は、β－グルクロニダーゼと相互作用するＤ－グルカル酸部位がミクロスフェアの表面に存在するが、その濃度が低いことを意味する。

同様にして、Ｄ－キシラル酸、および酒石酸部位を表面にポリスチレン型ミクロスフェアも調製した。

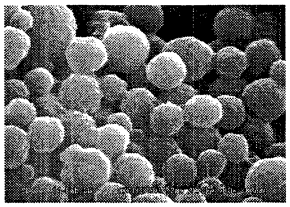

Fig. 9. SEM Image of Microsphere. mole% of R_1 monomer unit, 7%. ϕ_m; 1.4 μm

6．総括

合成高分子のみならず、天然多糖の側鎖に糖酸部位を導入しても、酵素β－グルクロニダーゼの活性を阻害するデバイスになり得ること、またミクロスフェアにしてもその阻害活性を発現することがわかった。酵素表面の活性部位と高分子鎖との距離を考慮して、スペーサーの効果を検討中である。また、高分子表面への酵素の吸着をＡＦＭで直接観察する試みも行っている。

研究業績　(雑誌論文)

1) "Synthesis of New Hydroxy-Bearing Polyurethanes. Polyaddition of D-Glucose-Derived Diols with Diisocyanates",
K.. Hashimoto, K. Yanagida, S. Nara, H. Okawa, *Polymer J.*, 37(5), 384-390 (May, 2005).

2) "Effect of Anomeric Linkage on the Sialylation of Glycosides by Cells".
M. C. Z. Kasuya, M. Ikeda, K. Hashimoto, T. Sato, K. Hatanaka, *J. Carbohydr. Chem.*, 24, 705-715 (2005).

3) "Glycopolymeric Inhibitors of β–Glucuronidase. III. Configurationnal Effects of Hydroxy Groups in Pendant Glyco-Units in Polymers upon Inhibition of β-Glucuronidase",
K. Hashimoto, H. Satito, R. Ohsawa, *J. Polym. Sci.: Part A: Polym. Chem.*, 44 (16), 4895- 4893 (Aug. 2006).

4) "The Synthesis of the Glycopolymers Containing Pendant D,L-Xylaric and L-Tartaric Moieties and Their Inhibition Behavior on the ß-Glucuronidase Activity,"
A. W. Kawagichi, T. Kaida, H. Okawa, K. Hashimoto, *Polymer J.*, 40(10), 944-952 (Oct., 2008).

5) "Synthesis of Glycopolymers Bearing Mannaric Pendants As Inhibitors on the ß-Glucuronidase Activity. The Inhibition Mechanisms of Mannaric- and Glucaric-Compounds."
A. W. Kawaguchi, H. Okawa, K. Hashimoto, *J. Polym. Sci.: Part A: Polym. Chem.*, 47(8), 2032-2042 (Apr., 2008) *in press.*

研究業績　(国際学会発表および国内学会での発表)　省略

1．4 静電的相互作用を用いる分子積層型バイオ太陽電池の開発

Development of bio-solar fuel cell using layer-by-layer deposited multilayer films containing enzymes

工学部応用化学科　阿部　克也、小野　擴邦

Katsuya Abe and Hirokuni Ono, Department of Applied Chemistry, Faculty of Engineering

Abstract: We are promising both dye-sensitized photoelectrochemical solar cells and biofuel cells such as candidates for production of renewable energy. In this study, the photoanode consists of an ITO electrode coated with organic sensitizer dye and enzymes was fabricated by means of alternate electrostatic layer-by-layer assembly. Key to the operation of the cell is the coupling of the oxidation of biological fuels such as alcohols by NADH/ NAD^+ and $FADH_2/FAD^+$ carriers in the enzyme multilayer films. The hybrid cell has several potential advantages over either the photoelectrochemical cell or the biofuel cell operating individually.

【1】研究背景

現在、二酸化炭素排出による地球温暖化や化石資源の枯渇という環境問題に直面している。これらの問題を解決する方法として注目を集めているのがクリーンかつ無尽蔵な再生可能なエネルギーであり、温室効果ガスの排出量を長期的に削減するための施策の一つとして太陽光発電の導入量の増大が掲げられている。したがって、化石資源への依存を少しでも減らす努力の一方で、太陽電池への期待が非常に高まっており、様々なタイプの太陽電池が開発されている。さらに、脱結晶シリコン化の流れの中で、製法が簡単で生産コストが低くでき、着色性や柔軟性などの特徴をもつ有機系太陽電池が期待されている。一方、上述した環境保全や資源循環の実現に向けて、カーボンニュートラルという特性を持つ生物資源（バイオマス）への関心が最近ますます高まってきている。例えば、多種多様なバイオマス燃料（糖やアルコール類など）を直接利用できるバイオ電池は、新規な電源として注目を集めるだけでなく、環境問題の解決策への一つのアプローチとなると期待されている。バイオ電池は、広義にはバイオデバイスと呼ばれ、電極触媒として酵素や微生物を用いるために電極不活性な糖やアルコール類などを燃料とすることができる。また、非常に穏和な条件下で作動でき、環境負荷が比較的少なく安全性が高いといった特徴をもっている。この様なバイオ電池は、電極・電子メディエータ・酵素タンパク質から構成されたシンプルな電池であるが、これら物質間のスムーズな電子移動や酵素タンパク質の特徴が電池の性能に大きく反映する欠点を持っている。このためには電極上に目的分子を上手にかつ穏やかに配列させることが重要である。

生体分子などを基板上に薄膜として固定化する代表的な手法に、Langmuir-Blodgett 膜法、自己組織化単分子膜法、脂質二分子膜法や交互積層膜法などがある。これらのうち交互積層膜法は、操作が非常に簡単であることが利点の一つとして挙げられる[1-4]。この方法は、静電的相互作用を利用して分子（例えば、酵素タンパク質や色素）の層を薄く作ることが可能であり、得られた薄膜は分子同士が近くに配置されるためスムーズな電子移動が得られるものと考えられ、バイオデバイスの研究開発を行う上で有効な手段であると言える。

本研究では、生体分子の静電的相互作用を用いる新規バイオデバイスの開発の一環として、ク

リーンな太陽エネルギーとバイオマスからのエネルギー源を利用する酵素分子の電子伝達系および分子積層型バイオデバイスの開発を目的としている。

本研究のバイオデバイスは、太陽電池部分に有機色素の分子層を、バイオ電池部分に酵素タンパク質の分子層を組み合わせたものから構成される。Fig.1 に分子積層型バイオ太陽電池の模式図を示す。この電池の特徴として、①種々の酵素タンパク質からなる積層膜（補酵素の固定化も含む）の電子伝達サイクルによるアルコールの 2 段階酸化反応、②積層膜の電子サイクルを介したスムーズな電子移動、③有機色素からなる分子積層膜の光励起反応が挙げられる。

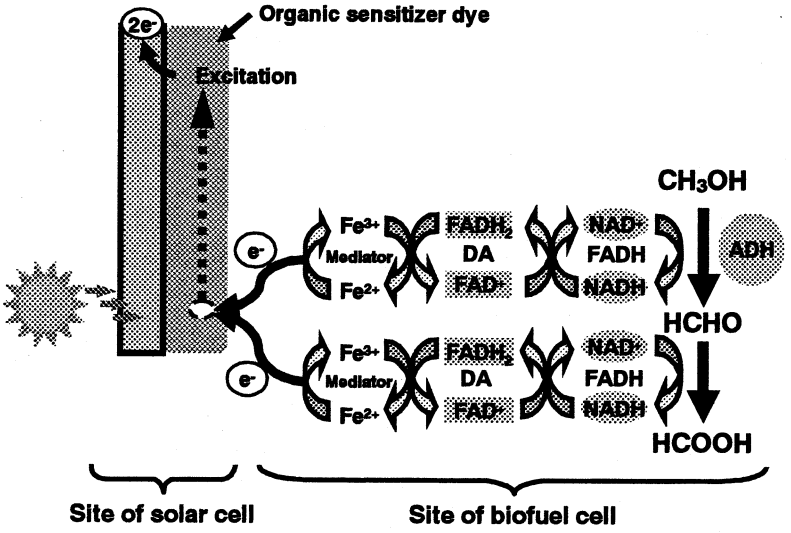

DA: Diaphorase.
FADH: Formaldehyde dehydrogenase.
ADH: Alcohol dehydrogenase.
Mediator: Ferrocene-modified PEI (Fc-PEI).

Fig. 1 Schematic diagram of bio-solar fuel cell using layer-by-layer deposited multilayer films containing enzymes.

【2】研究成果

色素分子積層膜の作製および光電流測定：分子積層膜は、水溶液中で正電荷をもつフェロセン修飾ポリエチレンイミン(Fc-PEI)と負電荷をもつ有機色素あるいは酵素タンパク質を用い、静電的相互作用によって水晶振動子の Au 電極あるいは ITO 電極（透明ガラス電極）上に作製した。通常、これらの電極表面は負電荷をもった状態にある。今回、有機色素には銅フタロシアニン（CuPc、λ_{max} = 612 nm）とコンゴーレッド（CR、λ_{max} = 510 nm）を用いた。

Fig.2 に太陽電池部分の CuPc および CR 色素積層膜の作製結果を示す。$(CuPc/Fc\text{-}PEI)_n$ および $(CR/Fc\text{-}PEI)_n$ 積層膜（n=積層回数）は、pH 1.5 に調整した CuPc 水溶液と中性の CR 水溶液を用いてそれぞれ作製し、膜形成過程は QCM 測定により監視した。この結果、CuPc は 1 回の積層で 1000～2000 Hz の振動数変化が観察され、1 層あたり厚さ 25 nm程度の薄膜が Au 電極上に形成したことが分かった。なお、溶液の pH は CuPc 分子の基板表面への吸着に対して強く影響することが分かっているが、現在のところその原因はよく分かっていない。

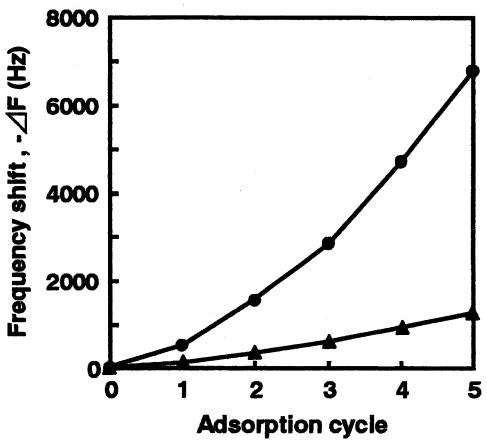

Fig. 2 Frequency shift in alternate adsorption of (CuPc/Fc-PEI)n (●) and (CR/Fc-PEI)n (▲) (n = number of bilayer) on Au electrode.

また、CR については 1 回の積層で 100～200 Hz の振動数変化が観察され、1 層あたり厚さ 2.5nm 程度の薄膜が Au 電極上に形成したことが分かった。一方、基板を ITO 電極に変えたときの$(CuPc/ Fc\text{-}PEI)_5$および$(CR/ Fc\text{-}PEI)_5$積層膜の可視吸収スペクトルの測定を行った。その結果を Fig.3 に示す。CR は CuPc の 1/7 以下の膜厚であったが、λ_{max} の吸光度が CuPc のそれより約 2 倍高いことが示された。このことは、各色素分子のモル吸光係数（CuPc:ε = 7000、CR:ε = 45000）の差異に基づくものと考えられるが、これ以外に基板上の分子の配向性も関係していると推察される。

次に、ITO 電極上に作製した色素分子積層膜の Fc-PEI のフェロセン（$Fe^{2+} \Leftrightarrow Fe^{3+}$）の酸化還元能をサイクリックボルタメトリー(CV 法)によって評価した。Fig.4 に色素分子の積層回数に対するFe^{2+}の酸化反応に伴う電流値を示す。この結果、両方の色素において積層回数が増すにしたがって電流値は増加し、積層膜内の鉄イオンが酸化還元能を示すことが分かった。このことは Fc-PEI が膜内で電子授受の役割を十分に果たしていることを意味しているが、積層回数 7 層目では共に電流値の減少が観察された。その現象はおそらく膜抵抗によるものと思われるが、太陽電池部分を作製する際に積層回数は重要なファクターであることを示している。したがって、色素分子積層膜は 5 層でとした。

本研究では、静電的相互作用で作製した CuPc あるいは CR からなる積層膜電極〔$(CuPc/PEI)_5$/ITO および$(CR/PEI)_5$/ITO 電極〕に関する光電流発生の検討を行った。測定は 3 電極方式を用い、ウォータージャケット付き電気化学セル内で行った。また、光源にはハロゲンランプ(150 W)を用いた。Fig.5 に代表的な色素分子積層膜の光電流測定結果を示す。CR の色素積層膜電極に対して光照射したとき、その ON-OFF に伴う光電流発生がより明確に観察され、この色素分子積層膜が太陽電池としての機能を持っていることが分かった。$(CuPc/PEI)_5$/ITO 電極については、基板上の分子の配向性などが起因したために高い光電流発生が見られなかったと思われる。以上の結果から、本研究では分子積層型バイオ太陽電池の太陽電池部分に CR からなる色素積層膜を使用することにした。

分子積層型バイオ太陽電池の作製：まず、Fig.1 に示す

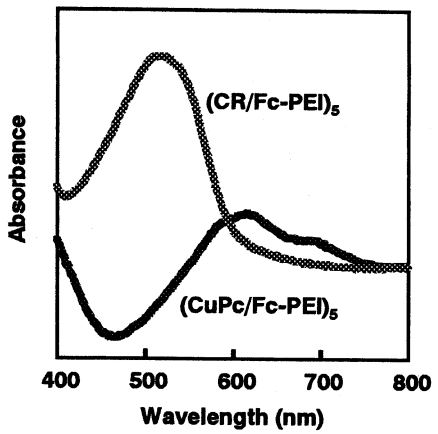

Fig. 3 Absorption spectra for (CuPc/Fc-PEI)5 and (CR/Fc-PEI)5 films deposited on ITO electrodes.

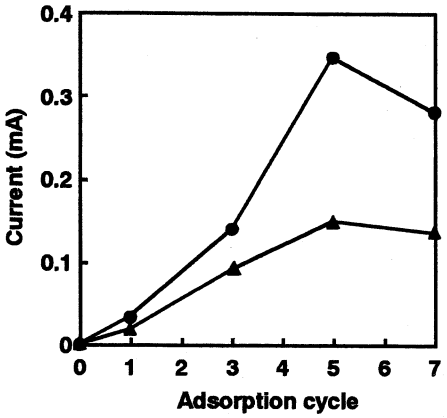

Fig. 4 Relationship between current and number of bilayers in (CuPc/Fc-PEI)n (●) and (CR/Fc-PEI)n (▲) films deposited on ITO electrodes.

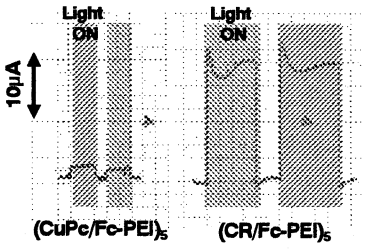

Fig. 5 Current responses to illumination of (CuPc/Fc-PEI)5 and (CR/Fc-PEI)5/ITO electrodes.

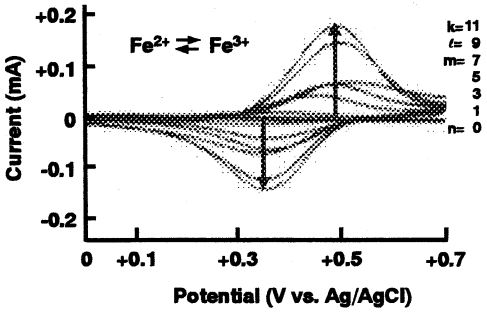

Fig.6 Cyclic voltammograms of (CR/FC-PEI)n/(DA/Fc-PEI)m/(FADH/Fc-PEI)l/(ADH/Fc-PEI)k/ITO electrodes.

CR 色素分子積層膜上への酵素タンパク質（DA、FADH、および ADH）の積層膜の作製について検討した。複合タンパク質からなる積層膜の形成は CV 法により評価した（Fig.6)。この結果、積層回数が増すにしたがって電流値は増加することから、$(CR/Fc\text{-}PEI)_5$ 積層膜上に各タンパク質は電子メディエータ分子(Fc-PEI)と静電的に交互吸着することが分かった。今回は、ITO 電極上に$(CR/PEI)_n(DA/Fc\text{-}PEI)_m(FADH/\ Fc\text{-}PEI)_l(ADH/PEI)_k$（n=5、m, *l*, and k=2）の積層膜を作製し、この分子積層型電極をバイオ太陽電池とした。

次に、作製したバイオ太陽電極に対して光照射したときに、積層膜内の電子伝達サイクルの駆動(Fig.1)によるメタノールからギ酸までの 2 段階酸化反応を定性的に検討した。第 1 段階目の反応は ADH と FADH の補酵素を利用するホルムアルデヒドまでの酸化反応であり、第 2 段階目は FADH によるギ酸までの酸化反応である。その結果、60 分間の光照射において、メタノール添加後に光電流の増加・減少が観察され、ギ酸の生成が HPLC 分析により最終的に確認された。測定系に DA、FADH、および ADH を溶解させて同様な実験を行った場合にはギ酸の生成は見られなかった。おそらく、電極上に種々の酵素タンパク質分子が上手く配置されたことで電子移動が容易に行える環境が生まれた結果、電子伝達サイクルが駆動したものと考えられる。今後、アルコールの消費量、ギ酸の生成量、および発生する光電流を経時的に測定することによってマテリアルバランスを明確化し、バイオマスを燃料とする新規バイオデバイスの開発が期待される。

引用文献

1) Y. M. Lvov, G. N. Kamau, De-Ling Zhou, J. F. Rusling 2000 Assembly of Electroactive ordered multilayer films of cobalt phthalocyanine teterasulfonate and polycations. *J. Colloid Interface Sci.* **212**, 570-575.

2) E.J. Calvo, C. Danilowicz, C.M. Lagier, J. Manrique, M. Otero 2004 Characterization of self-assembled redox polymer and antibody molecules on thiolated gold electrodes. *Biosensors and Bioelectronics* **19**, 1219-1228.

3) S. Suye, T. Matsuura, T. Kimura, H. Zheng, T. Hori, Y. Amano, H. Katayama 2005 Amperometric DNA sensor using gold electrode modified with polymerized mediator by layer-by-layer adsorption. *Microelectronic Engineering* **81**, 441-447.

4) K. Abe, A. Ishii, M. Hirano, J. F. Rusling 2005 Photoactivity characteristics of a biodevice using primary photosynthetic reaction centers. *Electroanalysis* **17**, 2266-2272.

研究業績

口頭発表：

1. 阿部克也、北原裕己、小野擴邦、第 60 回日本生物工学会大会(2008).
2. 阿部克也、古川和弥、小野擴邦、第 60 回日本生物工学会大会(2008).
3. Katsuya Abe, Yusuke Kobayashi, Hirokuni Ono, IUMS2008, XII. International congress of bacteriology and applied microbiology (2008).

論文発表（査読付）：

1. Katsuya Abe, Emi Takahashi, Morio Hirano, 2008 Development of laboratory-scale photobioreactor for water purification by use of a biofilter composed of the aerial microalga *Trentepohlia aurea* (Chlorophyta). *J. Appl. Phycol.*, **20**, 283-288.

1．5 機能タンパク質および糖質の構造改変と有用物質生産への適用

菅原康里　坂口政吉
（工学部　応用化学科）

Structural Modification of Functional Protein and Sugar, and its Application to Production of Useful Materials

Yasusato Sugahara and Masayoshi Sakaguchi
Department of Applied Chemistry, Kogakuin University

Economical hydrolysis of chitin was studied to obtain chitin oligosaccharides. Chitin was hydrolyzed with concentrated hydrochloric acid at 40°C for 40 min. The degraded chitin was precipitated in large amount of acetone and washed with acetone until acid free. The precipitate was extracted by acetone water solution changing their ratios. Chitin oligosaccharides were fractionated effectively by solution composition. The increase of water recovered the longer chained oligosaccharides. The mixture of chitin oligosaccharides can be separated by fractional dissolution.

In case of study of glucoamylase with comparing the characteristics of glucodextranase, conserved region 4 comprising their active site may discriminate substrates.

1. 緒言

キチンオリゴ糖に種々の生理活性が見出され、簡便な調製法に関心がもたれている。一般に、これらオリゴ糖を得るには、キチンを濃塩酸で加水分解し、中和後反応液を活性炭カラムに吸着させ、エタノールで溶出、あるいは、加水分解後、中和溶液からの塩類の除去をイオン交換膜電気透析装置で行なっている。このような煩雑な操作が、キチンオリゴ糖の価格を高めている。また、酸加水分解はキチン分子のグルコシド結合をランダムに切断するためサイズの異なるキチンオリゴ糖が混在して回収され、単一のサイズごとに精製しにくい事も原因の一つにあげられる。本研究では、キチンオリゴ糖を大容量かつ簡便にサイズごとに分画する方法として、分別溶解法を用いて、特に生理活性の高いと言われる、キチン6量体の分画について検討した。

また、糖質分解酵素において、よく似た立体構造および高い一次配列相同性を示すにもかかわらず、その分解する基質が異なる酵素が知られ、その基質特異性に関与するアミノ酸へ興味が持たれている。その中で、本研究では細菌由来のグルコアミラーゼ(CGA)[1,2]とグルコデキストラナーゼ(GDase)[3]を取り上げ、二つの酵素を組み合わせたキメラ酵素を構築し、その基質特異性に関与するアミノ酸またはアミノ酸群の同定を試みた。

2. 実験

2.1 キチンの加水分解および分別溶解

東京化成工業製キチンをウイリーミルで60meshに粉砕したキチン(分子量:320,000、脱アセチル化度:3.2%) 0.2 gに濃塩酸8mLを加え、40°Cで所定時間加水分解を行った。反応後、加水分解物はアセトン200mL中に投入して、4°Cで24時間静置した。沈殿物は吸着した酸を除去するために、ろ過、アセトン洗浄を繰り返した(第一段階)。加水分解後の残渣は、再度、同様の条件で加水分解を行って、オリゴ糖を抽出した(第二段階)。さらに、加水分解後、アセトン沈殿を行い、アセ

トン-H_2O溶液5mlを試料に加え、分別溶解を試みた。マグネチックスターラーで攪拌しながら20℃で1日放置した後、遠心分離によって上清と沈殿に分けた。沈殿はアセトン-H_2Oの割合を変化させ、分別溶解を繰り返した。いずれも、得られたオリゴ糖はGPCカラム(GS220HQ、Shodex)で分析し、定量した。

2.2　キメラ酵素の特性解析

CGAの活性部位を構成する保存領域をGDaseにおいて対応する保存領域へ遺伝子工学的に変換したキメラ酵素を構築し、大腸菌内で発現させ、精製を行い、その精製酵素を用いてその特性を調べた。

3.　結果と考察

3.1　キチンの加水分解反応

3.1.1　第一段階加水分解　キチンを濃塩酸で反応時間を変え、加水分解を行い、加水分解後のアセトン沈殿量とアセトン沈殿物を水抽出した後の残渣量におよぼす加水解時間の影響について検討を行った。加水分解時間30分までは、回収率がほぼ100%であったが、30分を経過すると、直線的に減少した。水抽出後の残渣量もアセトン沈殿量と同様に30分を経過すると減少した。アセトン沈殿量と残渣量の差(水抽出量)はオリゴ糖量と考えられるが、反応時間に関わらず、ほぼ一定であった。

Fig.1 は第一段階加水分解の水抽出分中のオリゴ糖分析結果について示したものである。加水分解時間が長くなるにしたがって、オリゴ糖量は増加しているが、75分になるとやや減少している。これは、長時間の加水分解により、反応が進行しすぎたためと考えられる。加水分解の進行に伴って、4〜6量体の生成量が多くなっている事が分かる。

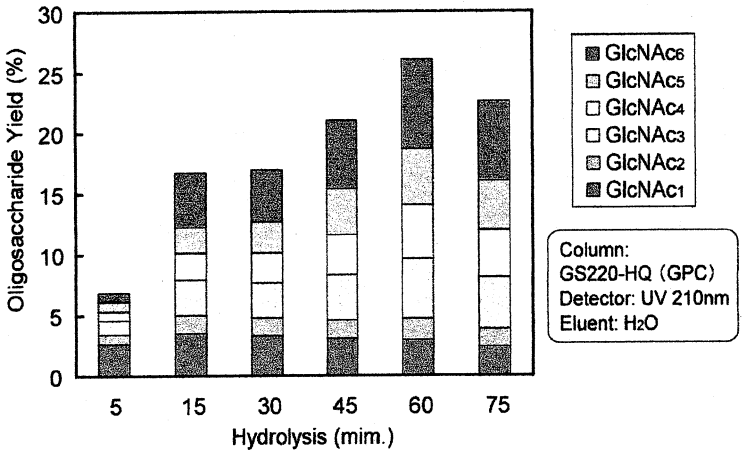

Fig.1　Oligosaccharides obtained in 1st step hydrolysis.

3.1.2　第二段階加水分解

40℃で15、30、45、60分加水分解した後、水抽出した第一段階加水分解残渣を再度、40℃で15分加水分解し、再びオリゴ糖を水抽出した。第一段階での加水分解と同様の重量減が見られた。また、第二段階加水分解のアセトン沈殿量は全ての試料において減少したが、その減少量は少なかった。第一段階加水分解で得られた試料には加水分解されにくい部

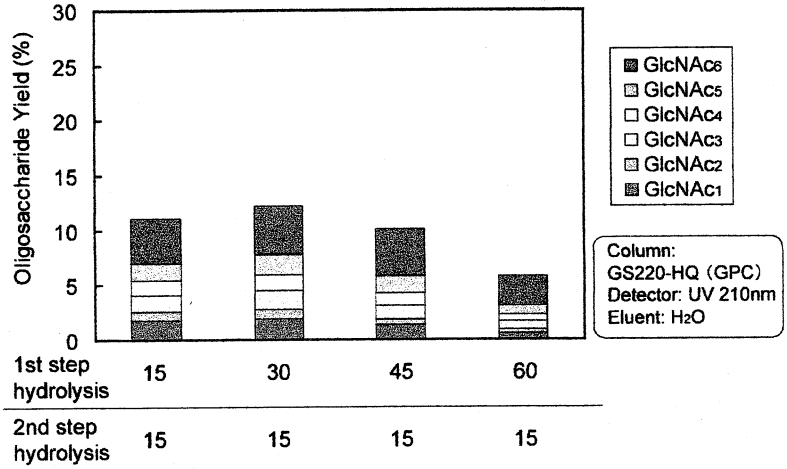

Fig.2　Oligosaccharides obtained in 2nd step hydrolysis.

分が比較的多く存在したためと考えられ、また、反応時間が 15 分と短かったことも原因と考えられる。水抽出量は第一段階での加水分解時間の短い試料ほど多くなった。

Fig.2 に第二段階加水分解のオリゴ糖分析結果について示した。第一段階加水分解を行った試料を再度、加水分解することで、オリゴ糖を抽出できた。第二加水分解ではオリゴ糖収量は少ないが、5、6 量体の収量が多く、2 段階加水分解で得られた糖の 50%以上を占めた。

3.2　分別溶解

3.2.1　アセトン濃度の影響

90%アセトン-H_2O 溶液 5ml を試料に加えて分別溶解を行った。以後、沈殿に H_2O の割合を 10%ずつ増やした溶液を加え、6 回繰り返し分別溶解を行った。

キチンオリゴ糖の溶解性はサイズごとに異なることが分かつた。1 回目の 90%アセトン抽出では(GlcNAc)1~3 のピークしか確認できず、4 量体以上のピークは確認されなかった。3 回目の 70%アセトン抽出から(GlcNAc)4 のピークが現れ、4 回目の 60%アセトンでの抽出から(GlcNAc)5 の大きなピークと、(GlcNAc)6 出始めピークが確認できた。最後の水(0%アセトン)での抽出では(GlcNAc)6 が現れた。

3.2.2　60%アセトンを用いた分別溶解

(GlcNAc)6 の分別溶解を目的に、抽出液量を 14mL に増やし、60%アセトンで 2 回抽出した後、水で抽出した(60%-60%-0%)。Fig.3 はその結果を示したものである。図から明らかなように、60%アセトンで 2 回抽出を行うことにより、(GlcNAc)1~5 のほとんどが分別できた。

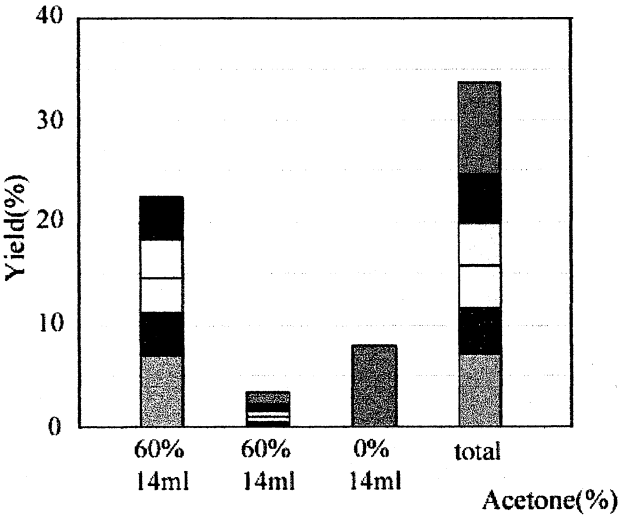

Fig.3 Effect of acetone conc. on yield of oligosaccharides.

次に、60%アセトンで 2 回分別溶解する操作を、1 回に省略できないか検討した。60%アセトン 30ml で分別溶解した後、水で残りのオリゴ糖の抽出を行ったところ、60%アセトン 1 回の分別溶解の操作でも(GlcNAc)1~5 を十分に抽出できている事が分った。しかし、1 回の分別溶解操作の場合では、収率は高くなるものの、2 回分別操作を行った場合のクロマトグラムと比較すると、やや他の成分が含まれているようである。分別溶解に用いる溶液量を増やすより、少量の溶液で抽出回数を増やしたほうが純度の高い(GlcNAc)6 が得られることが分かった。

3.3　キメラ酵素の特性解析

CGA、CGA の保存領域 1 を GDase の保存領域 1 へ変換したキメラ酵素（R1)、そして同様に保存領域 4 を変換したキメラ酵素(R4)の三糖基質であるマルトトリオースおよびパノースに対する比活性を Fig.4 および 5 に示した。 CGA は α-1,4 グルコシド結合を持つマルトトリオースに対する活性が高いが、GDase はほとんど活性がない。キメラ体は R1 そして R4 の順に活性が低くなった。一方、非還元末端側に α-1,6 グルコシド結合を持つパノースに対して R4 は GDase の約 10 倍の活性を示した。これらの結果は R4 が GDase に近い特性を持つこと、また、GDase が加水分解しにくい基質に対しても高めの活性を持つことを示している。これは、R4 が広い基質特異性を持

ったことを意味し、保存領域 4 は両酵素の基質特異性に関与するアミノ酸、もしくはアミノ酸群を含んでいることを示唆した。

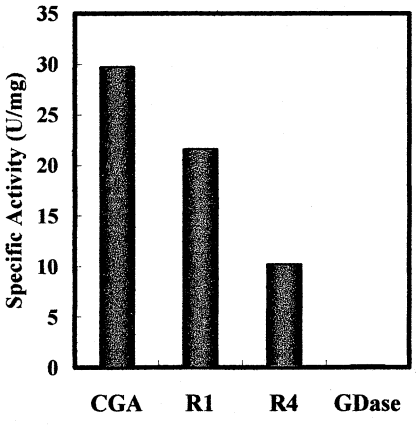

Fig.4 Specific activity of CGA, GDase, and chimera enzymes for maltotriose.

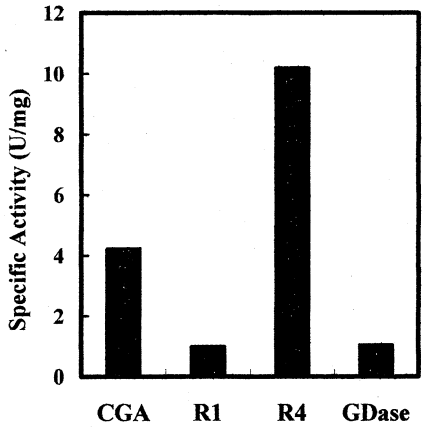

F Fig.5 Specific activity of CGA, GDase, and chimera enzymes for panose.

4 結論

抽出溶液(アセトン－水)の割合を変化させることにより、極性をコントロールし、キチンオリゴ糖をサイズごとに分別溶解を行うことができた。特に、(GlcNAc)6 は免疫増強作用や腫瘍成長抑制作用等の報告が一番多く、(GlcNAc)1~6 の中でも一番高価な物質である。一連の操作はアセトンと水しか用いないため安価であり、操作も単純である。また、セルロースオリゴ糖、デンプンオリゴ糖など、他のオリゴ糖混合物の分画にも有効な方法と考えられる。

糖質分解酵素 CGA の保存領域 4 には酵素の基質特異性に関与するアミノ酸、またはアミノ酸群が含まれており、この領域を解析すること、そしてこの領域と関連のあるアミノ酸を同定することで多機能の酵素を構築できる可能性を示唆している。

1) Ohnishi H, Kitamura H, Minowa T, Sakai H, Ohta T Molecular cloning of a glucoamylase gene from a thermophilic *Clostridium* and kinetics of the cloned enzyme. *Eur. J. Biochem.* **207**(2):413-418(1992)

2) Aleshin A.E, Feng P.H, Honzatko R.B, Reilly P.J. Crystal structure and evolution of a prokaryotic glucoamylase. *J. Mol. Biol.* **327**(1),61-73(2003)

3) Mizuno M, Tonozuka T, Suzuki S, Uotsu-Tomita R, Kamitori S, Nishikawa A, Sakano Y. Structural insights into substrate specificity and function of glucodextranase. *J. Biol. Chem.* **279**(11),10575-83(2004)

研究業績

1 Masayoshi Sakaguchi, Mika Matsuzaki, Keisuke Niimiya, Junichi Seino, Yasusato Sugahara and Masao Kawakita Role of proline residues in conferring thermostability on aqualysin I, *J.Biochem.***141**,213-220(2007)

2 Masayoshi Sakaguchi, Makoto Takezawa, Rie Nakazawa, Kazutaka Nozawa, Taro Kusakawa, Takeshi Nagasawa, Yasusato Sugahara, and Masao Kawakita, Role of disulphide bonds in a thermophilic serine protease aqualysin I from *Thermus aquaticus* YT-1., *J. Biochem.*, **143** (5) 625-632(2008)

3 Masayoshi Sakaguchi, Keisuke Niimiya, Makoto Takezawa, Tsutomu Toki, Yasusato Sugahara, and Masao Kawakita, Construction of an expression system for aqualysin I in *Escherichia coli* that gives a markedly improved yield of the enzyme Protein, *Biosci. Biotechnol. Biochem.*, **72**(8) 2012-2018(2008)

2. ナノ薄膜

2．1　超臨界流体を用いた有機薄膜作成技術の開発と発光素子への応用のための膜質制御と評価に関する研究

Organic Thin-Film Deposition Method using Supercritical Fluids and Its Application to Light Emitting Electronic Devices

工学院大学 工学部 電気システム工学科　坂本 哲夫

東京大学 環境安全研究センター、生産技術研究所　尾張 真則

Dept of Electrical Eng., Faculty of Eng., Kogakuin University　Tetsuo Sakamoto

Env. Sci. Center and Institute of Industrial Sci., the University of Tokyo Masanori Owari

Abstract

This study aims at the development of new methods for organic thin film deposition utilizing supercritical fluids. Supercritical fluids have unique properties such as high solvating power like a liquid and high diffusion coefficient like a gas. Two kinds of thin film deposition using supercritical fluid have been devised; supercritical fluid deposition (SFD) and rapid expansion of supercritical fluid solutions (RESS). Instruments for each technique have been made and fundamental properties of thin film deposition were investigated.

1．はじめに

有機薄膜は、発光素子・トランジスタ・太陽電池など今後著しい発展が期待される分野の基礎材料である。有機薄膜の作製は蒸着法と塗布法が利用されているが、それぞれ、適用できる有機材料に大幅な制限がある。また、塗布法の場合は異種材料の多層化が難しいという問題がある。パターニングや多層化を行うためにはウェットプロセスではなくドライプロセスが適当であるが、ドライプロセスは材料の加熱を伴うことが多く、材料の変性や分解の問題から、蒸発しやすい物質への適用に留まる。本研究ではこうした背景から、新しい有機薄膜作成技術を開発することを目的としている。超臨界流体は Fig.1 に示すように温度、圧力ともに臨界点を超えた流体のことで、物質の溶解力をもつ高密度の流体である。本研究では超臨界流体に一度材料を溶解したえうえで、流体条件を変化させることにより、材料を析出させ、流体(CO_2)そのものは瞬時に気化する性質を利用し、ドライプロセス化を実現するものである。

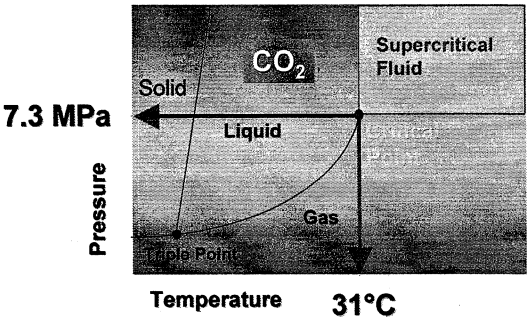

Fig.1: Schematic phase diagram of CO_2

2．急速膨張(RESS)法による有機材料の堆積

2-1 はじめに

前年度、超臨界溶媒中にて温度操作によって溶解度を低下させ、過飽和から材料を析出させる超臨界析出法(SFD)を検討した。その結果、微結晶が得られる傾向にあり、析出条件の制御が極めて難しいことがわかった。一方、もうひとつの方法として試行した超臨界急速膨張法(RESS)では装置がより簡便であり、また高分子系材料において平坦な膜が得られた。今年度は RESS 法を中心にさらに成膜条件を探索することとした。

2-2 ノズルの改良

これまでの実験ではキャピラリー先端から流体が噴出する際の冷却効果および流路内での圧力低下による溶質の析出によってキャピラリーが詰まることが多かった。ピンホールのようなもの

で超臨界部分と大気を隔てられればよいが、構造上難しい。これまで、内径 5 μm～30 μm のガラスキャピラリーを用いてきたが、析出を防ぐ方法として、Fig.2 に示すように、バーナーで先端を一度封じたあと、先端を研磨することで任意径の開口部を得る方法を試した。これにより、先端に近づくほど内径が狭くなる構造となり、流路での減圧と析出を抑えられるようになった。また、これまではノズル先端を積極的に温調することはなかったが、先端での圧力低下に伴う溶解度低下を補うべく、先端を材料セルよりも高温(～150℃ max)とすることで、詰まりを防止する工夫も凝らした。

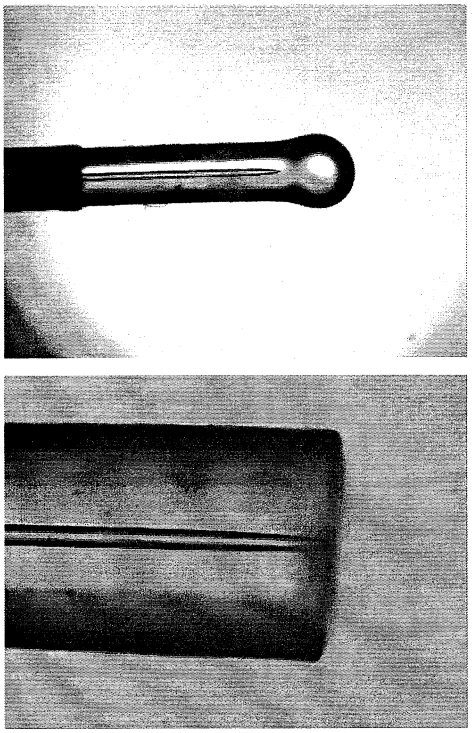

Fig.2: Micrographs of the melted tip of a capillary, and conical-shaped capillary

2-3 ノズル先端形状の効果

比較のため、従来どおり内径 5 μm のキャピラリーを用い、アントラセンを堆積させた。Fig.3 に示すように基板上の吹きつけ中心部ではミクロンオーダーの微粒子が積み重なるように堆積していた。その周囲には下に示すような棒状の析出物が散在していた。この棒の直径が約 5 μm であったため、恐らく、キャピラリー内で徐々に析出し、これが圧力で押し出されて形成されたものと思われた。これが続くとキャピラリーの詰まりにつながるものと考えられる。

次に、同様の条件において、ストレートキャピラリーノズルを使用した場合、今回新たに作成したコニカルノズルを使用した場合を比較した。Fig.4 に示すように、コニカルノズルを使用した場合は粒子が微細化しており、超臨界状態からの減圧がより高速に起こり、核の成長が抑えられていることがわかる。

2-4 ノズル・基板間の距離

RESS 法ではノズル先端で急激な溶解度の低下により核生成が起こるといわれている。2-3 での結果は溶解度の低下速度を変えた実験であったが、次にノズルから噴出した後の条件を変えてみた。ここでは、ノズルと基板間の距離を変化させた。Fig.5 に示すように距離が近い場合、堆積物の密度は高く、遠い場合は減少した。これは単にノズルからの噴出流がコーン状に広がるため、基板上への物質の堆積が距離に応じて減ることが理由である。一方、堆積物の粒子径に着目すると、距離が近い方が粒子径が大きくなっている。仮にノズルから噴出したあとの飛行中に粒子が成長するのであれば距離が遠い方が粒子径は大きいはずであるが、逆の傾向となった。これは、粒子の成長が気相ではなく、基板上で起こっていることを示唆するものである。また、超臨界圧力を 10 MPa としたところ、ノズル・基板間距離を 1 mm まで近づけた場合に比較的大きい結晶状の粒子が得られた(Fig.6)。大きいものでは 50 μm を超えており、ノズル内径よりも明らかに大きいため、基板上で成長したものと思われる。一方、基板までの距離を 8 mm とした場合、大きな結晶粒は見られなかった。

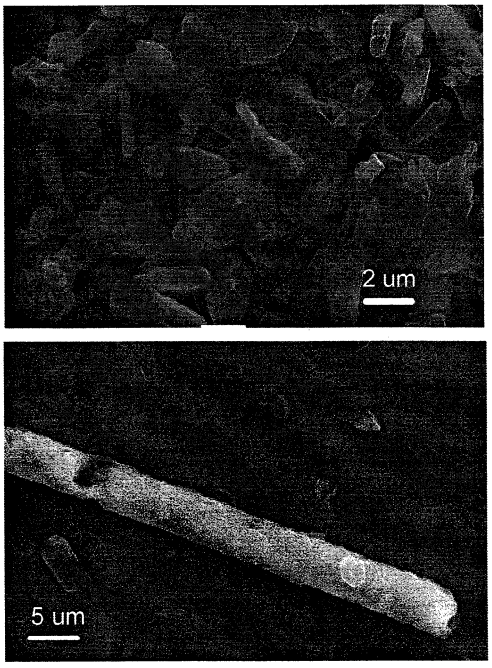

Fig.3: SEM images of anthracene deposited by RESS method at 25 MPa, 100℃. (upper: central part of deposition, lower: rod-type shape)

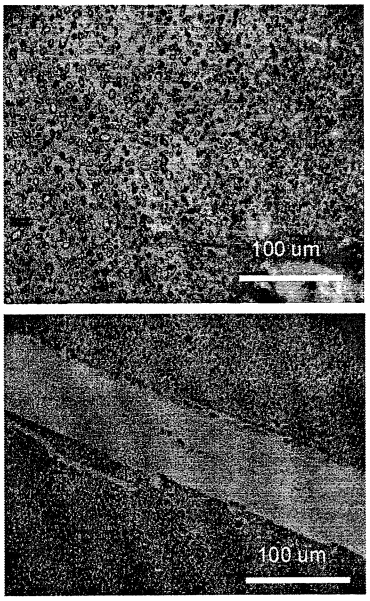

Fig.4: Micrographs of anthracene particles using a strait nozzle (5 μmid), and a conical nozzle (25 μmid)

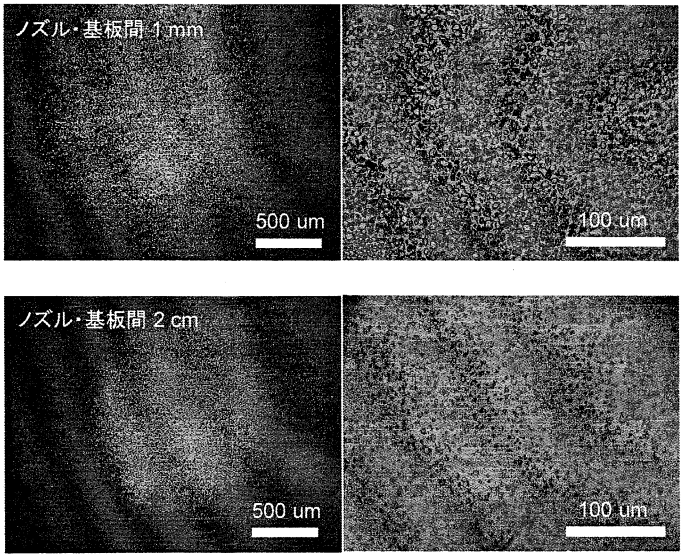

Fig.5: Micrographs of anthracene particles (upper: nozzle-substrate distance=1 mm, lower: 2 cm) at fluid condition 30 MPa, 120℃.

ここまでの結果を纏めると、ノズル・基板間の距離が近いと粒子径は大きくなる傾向があり、さらに超臨界圧力を低くするとその傾向が顕著となる。また、ノズルから噴出したあとに粒子の成長が起きていることが明らかとなった。この理由の解釈は難しいが、例えば、ノズルのすぐ近くに基板が位置する場合、過飽和の空間がノズル近辺に形成されやすくなり、結果として結晶の成長速度が上がるのではないかと考えられる。

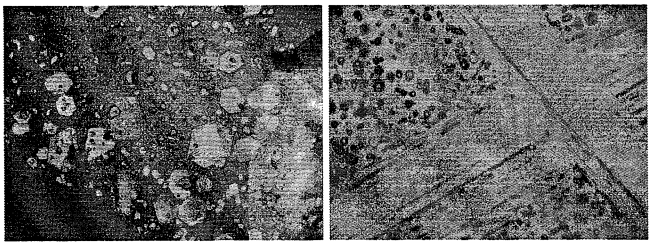

Fig.6: Anthracene particles fabricated at nozzle-substrate distance 1 mm (left), and 8 mm (right) with fluid condition 10 MPa, 100℃.

2-5 モディファイヤ添加の効果

これまでは超臨界 CO_2 単独での実験であったが、ここで微量の有機溶媒を添加する方法を検討した。一般にモディファイヤやエントレーナと呼ばれる微量溶媒は超臨界 CO_2 の溶解力を増大する効果があるといわれる[1]。Fig.7 にモディファイヤとしてアセトンを一定流量供給しながら RESS 堆積を行った結果を示す。これまでの結果とは様相が異なり、凹凸はあるものの、連続的な膜状の堆積物が得られた。蛍光像においても、連続膜であることが確認できた。モディファイヤは本来、溶解度を上げるために使われるものであるが、本実験では添加したアセトンがミストとなって基板上に供給されたことにより、僅かにアントラセンが溶解し、すぐにアセトンが揮発したのではないかと考えられる。ドライプロセスを目指す趣旨とは少し外れるが、連続膜を得る方法として今後検討の必要がある。

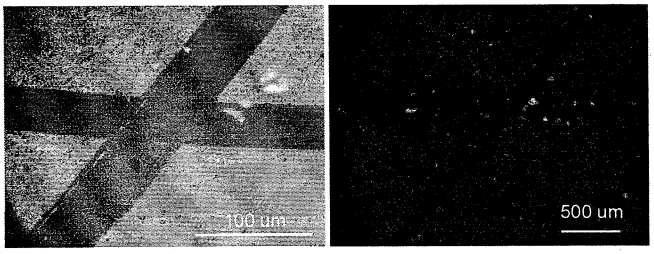

Fig.7: Anthracene film deposited with CO_2 fluid modified by acetone. (left: visible-light reflection image, right: UV-excited image)

3．エレクトロスプレー法による高分子有機薄膜の作成

3-1 概要

超臨界流体の場合、モディファイヤを加えても高分子系有機材料は溶解しにくい傾向となった。そこで、同様の目的でエレクトロスプレー法(ESD)を検討することとした。ESD はスピンコート法やインクジェット法と同様に材料を一度溶媒に溶かすことになるが、基板に噴霧する過程において溶媒が蒸発し、基板上ではドライプロセスになることが可能であると考えた。本年度はスプレー条件の検討を行った。

3-2 エレクトロスプレー堆積法

ESD では、有機材料を溶かした溶液を高電圧を印加した金属キャピラリーに送液する。キャピラリー先端では強電界により溶液がスプレー状に噴霧する。この方法は 2002 年の Fenn 博士のノーベル賞によりソフトイオン化法として一躍有名になった。スプレーの過程は以下のとおりである。キャピラリー先端に高電圧を印加し、強い電界を発生させると、溶液の表面張力と液滴表面の電荷のクーロン反発力が釣り合い、溶液が鋭く尖った円錐形の形状をとる。これが Taylor コーンである。電場強度がさらに大きくなると、Taylor コーンの先端から対極に向かって細かな液滴の噴霧が始まることになる[2,3]。

3-3 ESD による高分子系材料の成膜

典型的な高分子系有機 EL 材料として MEH-PPV を用いた。キャピラリーと基板の距離、溶媒の種類、溶質濃度など種々の検討を行った結果、Fig.8 に示すように若干の凹凸はあるものの、高分子系についても連続膜を得ることができた。これにアルミ電極を蒸着し、電圧を印加したところ、数秒間であるが発光が確認できた。

Fig.8: MEH-PPV film prepared with ESD (upper), and EL device (lower). (MEH-PPV solution at 0.04 wt%)

4．まとめと展望

低分子系有機材料については RESS 法により微粒子ならびにモディファイヤ使用時は連続膜が得られることが判った。今後は連続膜に焦点をあて、モディファイヤの最適化を図る。高分子系については ESD 法が有望であり、発光に至る手順の再現性を向上させることを目標とする。

【引用文献】

[1] J.J.Langenfeld et al, Analytical Chem. 66 (1994) 909.
[2] R.G.Forbes, Vacuum 48(1) (1997) 85.
[3] R.G.Forbes, J.Aerosol Sci. 31(1) (2000) 97.

【研究業績】

[1] 池田一洋、池田大成、宮田亘、坂本哲夫、超臨界流体組成のリアルタイム分析装置の開発、第 67 回応用物理学会学術講演会、31p-G-15、2006 年 8 月.
[2] 池田大成、池田一洋、宮田亘、坂本哲夫、超臨界流体を用いた有機微粒子・薄膜作製方法の開発、第 67 回応用物理学会学術講演会、29p-M-3、2006 年 8 月.
[3] 池田一洋、池田大成、宮田亘、坂本哲夫、超臨界流体組成のリアルタイム分析装置の開発、第 54 回応用物理学関係連合講演会、28p-SK-9、2007 年 3 月.
[4] 池田大成、池田一洋、宮田亘、坂本哲夫、超臨界流体を用いた微粒子・薄膜作製方法の開発(2)、第 54 回応用物理学関係連合講演会、30a-N-10、2007 年 3 月.
[5] Tetsuo SAKAMAOTO, Itaru YAMAGUCHI and Kenji OISHI, "Fabrication of Organic Thin Films and Particles using Supercritical Fluids", 4th Vacuum and Surface Sciences Conference of Asia and Australia (VASSCAA-4), p.418, 2008.10.
[6] Itaru YAMAGUCHI, Yuuki WATANABE and Tetsuo SAKAMOTO, "Organic Thin-Film Fabrication by means of Electrospray Deposition", 4th Vacuum and Surface Sciences Conference of Asia and Australia (VASSCAA-4), p.423, 2008.10.

２．２ イオンビームを用いたアモルファス炭素で構成される ナノ薄膜の付与による生分解性プラスチックスの多機能化

矢ケ崎隆義*、鷹野一朗**、佐藤年男***

Multi-Functionalization of Biodegradable Resin by Formation of Nano Thin Film Consisting of Amorphous Carbon with Ion Beam

by

Takayoshi Yagasaki*, Ichiro Takano** and Toshio Sato***

ABSTRACT: For a product made in environmental burden reduction material, authors tried to give amorphous carbon nano thin film to surfaces of various biodegradability plastic by film forming method used ion beam. In this study, we performed amorphous carbon nano film formation by film forming methods, the formation of the sedimentary film by the ion beam assist method. Through functional tests of the various biodegradability plastic plate which stuck in amorphous carbon nano film, it became clear thin film formation by the ion beam assist method was possible, and to have effective electric resistance value. Furthermore, it became clear that optimum conditions of amorphous carbon nano film formation were different by number of carbon of hydrocarbon gases.

1. 緒言

電気・電子用基板の廃棄物を終末処理するに際して、環境負荷軽減の立場から、基板材料に用いられている汎用プラスチックスの代替として二酸化炭素や水などの低分子化合物に完全分解される生分解性プラスチックス材料の適用が注目されている。しかしながら、汎用プラシチックスに比して生分解性プラスチックスの耐熱性は低く、また製造コストが高いという弱点があり、その適用分野が限定されているという現状にある。そこで報告者らは、生分解性プラスチック表面へのイオンビームを用いた各種金属薄膜の付与を試み、機能化を図ることによって適用範囲の拡大を目指してきた。その結果、水冷プロセスを組み込んだイオンビームミキシング法を用いることにより、生分解性プラスチックの表面に密着性の良い安定な金属薄膜を付与する技術を獲得するに至っている。

一方、薄膜を付与したプラスチックス製電気・電子用基板の更なる環境負荷軽減を求める場合、基板材料に生分解性プラスチックスを採用することに加え、薄膜材料の検討が必要不可欠と考えられる。そこで、環境に負荷をかけずに機能化の可能性を有する薄膜材料として、特定の結晶構造を持たないアモルファス構造を有するアモルファス炭素を選択することにした。アモルファス炭素薄膜の製膜法は多数あるが、主としてグラファイトなどの固体を薄膜の原料とする手法と、炭化水素気体を薄膜の原料とする手法とに大別される。前者の手法では炭素を主とするネットワーク構造中にほとんど水素を含まないアモルファス炭素薄膜が得られ、後者のそれによれば水素を含むアモルファス炭素薄膜が得られるとされている。因みに、薄膜中に含有される水素量は薄膜の物性（硬度、耐摩耗特性など）に大きな影響を及ぼし、さらに製膜時の印加電圧やガス流量などの製膜条件がアモルファス炭素の結合軌道に影響を与え構造を変化させ得ることが明らかとなっている。すなわち、アモルファス炭素薄膜の構造の制御が可能となれば、物性や機能性を選択的に発現し得る可能性を有していることになる。しかしながら、生分解性プラスチックスへのアモルファス薄膜の付与に関わる系統的な研究は未だほとんど為されてはいない現状にある。

これらの観点から、本研究は環境負荷低減型の電気・電子用基板の創製および生分解性プラスチック材料の適用範囲の拡大を図るために、各種炭化水素気体を薄膜原料としてイオンビームアシスト法により生分解性プラスチック表面にアモルファスナノ堆積薄膜の形成を試みることを通

*　工学院大学　工学部　マテリアル科学科、Dept. of Materials Sci. and Tec., Kogakuin University
**　工学院大学　工学部　電気工学科、Dept.of Elect.Eng., Kogakuin.University
***　共立工業株式会社　システム設計本部、Kyouritsu Industry Co.

し、堆積薄膜の形成条件の精査および得られたアモルファス炭素ナノ薄膜の構造と物性とを評価することを目的として遂行した。また、アモルファス炭素ナノ薄膜付与材料の加水分解挙動を精査した。本報では、これらの結果を報告する。

2．基板材料、薄膜材料および実験方法

2-1　基板材料および薄膜材料　薄膜付与する生分解性プラスチックの基板材料には、汎用プラスチック材料と同程度の物性を有する植物由来の生分解性プラスチックであるポリ乳酸 LACEA（H-100J：三井化学㈱）および比較材として石油由来の軟質系生分解性プラスチックであるポリブチレンサクシネート BIONOLLE（#1000：昭和高分子㈱）とを選定した。前者は、ガラス転移点が 50℃、融点が約 170℃であり透明性の優れた硬質の熱可塑性プラスチックスである。後者は、ガラス転移温度が - 32℃、融点が約 110℃の軟質の熱可塑性プラスチックである。図 1 にこれらの構造を示す。これらの供試材料を 10mm×10mm×3mm の形状寸法に機械加工した後、表面粗度が一定となるようにバフ研磨を施した上で基板として用いた。

(a)PLLA:Poly-L-lactic acid　　(b)PBS:Poly-butylene succinate

Fig. 1　Molecule chain of biodegradable resins.

薄膜材料とする炭化水素ガスにはトルエン、ナフタレン、ドデカンの 3 種類を用いた。トルエンガスについては金属基板上でのアモルファス炭素膜の形成が既に確認されており、一般的なメタンやエチレンガスより炭素数が大きいために短時間での製膜に適すると考えられる。ナフタレンは、アモルファス炭素薄膜の構造に影響を与えると考えられるπ電子をトルエンよりも多く含む構造であるために、ナフタレンガスより得られるアモルファス炭素薄膜の構造はトルエンガスより得られるそれより sp^2 の割合がリッチになると想定される。さらに、ドデカンは直鎖構造をしており炭素数が多くまた水素を多く含む構造であることから、短い製膜時間でトルエンと同程度以上の膜厚が得られ、且つ構造中に水素を多く含むためによりアモルファスな構造となるものと考えられることから選定した。薄膜原料ガスとして選択した炭化水素ガスの構造を図 2 に示す。

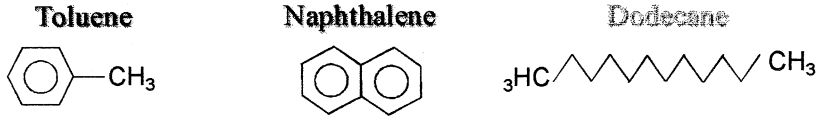

Fig.2　Structures of source gas.

2-2　製膜方法および製膜条件、解析・評価方法　薄膜の付与には大電流イオン注入装置（日立製作所：HIIB-200-B）を用い、イオンビームアシスト法により Table 1 に示す条件にて製膜を実施した。尚、その際、生分解性プラスチックス基板に与える熱影響を軽減するために、製膜時に基板ホルダーの水冷処理を施した。図 3 にイオンアシスト法による薄膜形成の概念を示す。基板上に形成したアモルファスナノ薄膜は、光学顕微鏡、レーザー顕微鏡および電子顕微鏡を用いて表

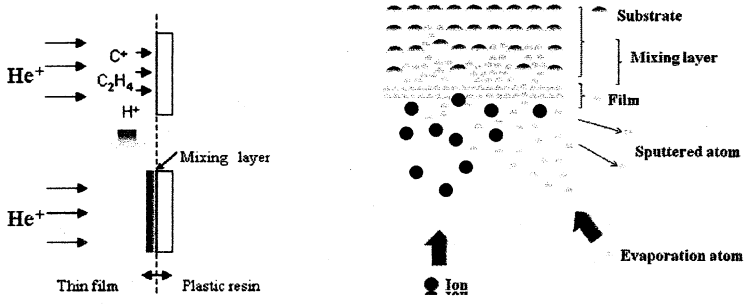

Fig.2　General idea of ion beam assist method.

Table 1　Formed conditions of amorphous carbon nano films.

Source gas	Toluene C_7H_8	Naphthalene $C_{10}H_8$	Dodecane $C_{12}H_{26}$
Ion species	He^+	He^+	He^+
Base pressure (Torr.)	6.0×10^{-5}	6.0×10^{-5}	6.0×10^{-5}
Gas pressure (Torr)	2.0×10^{-4}	2.0×10^{-4}	2.0×10^{-4}
Accelerative voltage (keV)	1	1	1
Current density ($\mu A/cm^2$)	40	40	40
Deposition time (s)	3600	3600	3600

面状態を観察した。また、膜厚はSTEMおよびFIB加工の後、断面を観察することにより求めた。薄膜の密着性は、連続加重式表面性測定機によるスクラッチ試験により評価した。薄膜の構造解析は、レーザラマン分光装置（日本分光社製：NRS-2100）により実施した。さらに、薄膜の表面抵抗率を極超絶縁計（東亜DKK社製：SM-8001、SM-8210）を用い二重リング電極法にて測定した。

3．実験結果および考察

3-1　成形薄膜の形態観察、膜厚の測定　異なる炭化水素ガスを原料としたイオンビームアシスト法による基板材料上への堆積薄膜の形成後、各薄膜の表面を光学顕微鏡および電子顕微鏡を用いて形状および形態等を観察した。いずれの薄膜も表面の色は褐色であり、特にナフタレンは濃い褐色であった。また、トルエンを原料とした薄膜が平滑で均質であるのに比して、ナフタレンのそれは厚く積層し表面粗さが目立っていた。また、ドデカンによる薄膜の表面にはマイクロオーダーの微粒子が付着しているのが観察され、基板表面にはイオンビームのスパッタリングやミキシングの影響によるものと考えられる形態変化が確認された。尚、これらの表面構造の変化は、BIONOLLE基板に比してLACEA基板で顕著であった。また、各堆積薄膜の膜厚を測定した結果、トルエンガスを原料とする堆積薄膜についてはおよそ200nm、ナフタレンのそれは500nmであった。また、ドデカンによる薄膜については、その存在が確認できなかった。

3-2　薄膜の構造解析　異なる製膜条件で形成したアモルファス炭素の堆積薄膜の構造を解析するために、薄膜に対してラマン分光分析測定を実施した。測定により得られたラマンスペクトルを図3に例示する。この結果より、トルエン、ナフタレンを用いた堆積製膜操作では、いずれの生分解性プラスチック基板であっても、アモルファス炭素の特徴であるGピーク（1590cm^{-1}付近のグラファイトのsp^2結晶構造成分）およびDピーク（1360cm^{-1}付近の歪んだsp^2結合由来）の存在が確認された。この事から、この製膜条件により生分解性プラスチック材料表面にアモルファス炭素薄膜の形成が可能となることが明らかとなった。また、トルエンとナフタレンのガスの種類による薄膜の顕著な構造の差異は認められなかった。

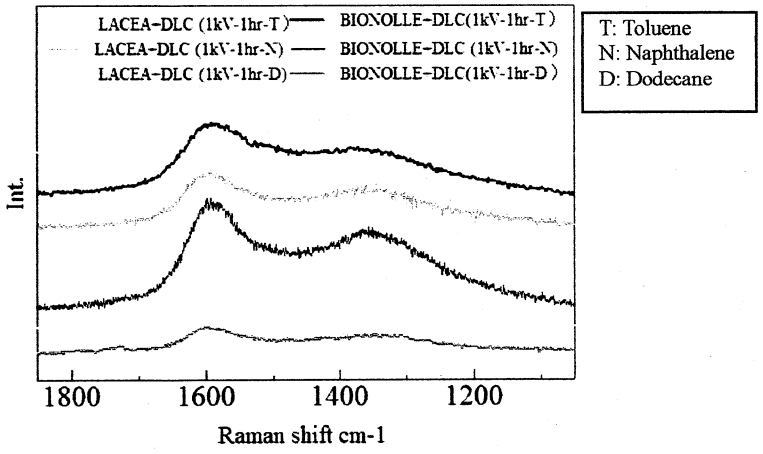

Fig.3 Raman spectrum of amorphous carbon thin film formed in different conditions.

他方、ドデカンガスを原料として製膜を実施したものについては、アモルファス炭素薄膜の存在を示す明確なピークは得られず、薄膜は形成されていなものと判断した。薄膜形成がなかった理由として、前者 2 種のガス種と比較した場合、ドデカンは直鎖の sp^3 結合成分を主とした安定な構造であることから立体的な障害が大きいため基板への吸着が起こりにくく、また分解されにくいためと考え得る。また、薄膜として成長する過程にて基板に吸着したドデカンがアモルファス炭素の構造に変化する前にイオンビームによるスパッタリングを受けてしまい、膜成長が律速されることも考えられる。ドデカンガスを用いた製膜条件については、更なる精査が必要である。

3-3　薄膜の密着性および薄膜の電気伝導性の測定　イオンビームアシスト法により種々の炭化水素ガスを原料として堆積成形したアモルファス炭素薄膜の表面抵抗率を測定した。その結果を図 4 に示す。表面観察と膜厚測定とによりアモルファス炭素薄膜の形成が確認されたトルエンおよびナフタレンガスによる薄膜の表面抵抗率は、いずれも形成されたアモルファス炭素薄膜が導電性に寄与し半導体域に相当する値を有することが確認された。また、トルエンよりナフタレンガスを用いて成形したアモルファス炭素薄膜の抵抗値が低くなる理由は、ラマン分光分析の結果より両者の構造が等しいと考えるのならば、膜厚の影響と考え得る。また、アモルファス炭素の明確な形成が認められなかったドデカンガスでの製膜結果についても、バージン材と比較すると表面抵抗値が若干低下していることがされた。これは、製膜の際に、イオンビーム照射により生分解性プラスチック基板の表面が部分的に改質され炭素化した結果であると考え得るが、今後の精査が必要である。

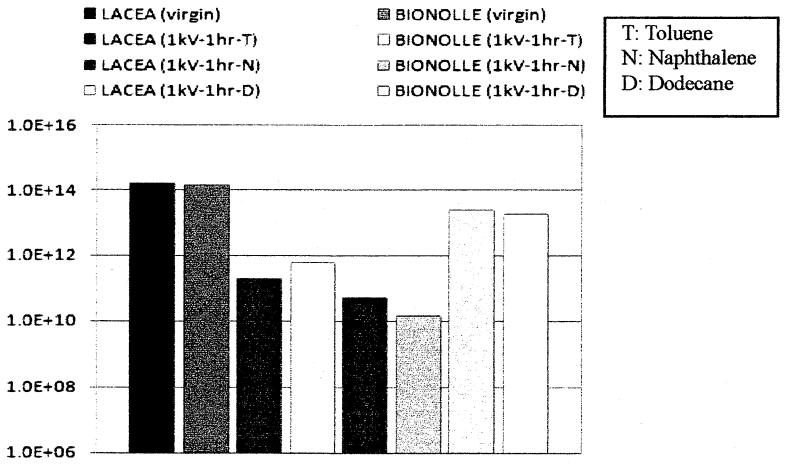

Fig. 4 Surface resistance value of amorphous carbon thin film formed in different conditions.

4．結言

環境負荷低減型の電気・電子用基板の創製および生分解性プラスチック材料の適用範囲の拡大を図るために、各種炭化水素ガスを薄膜原料としてイオンビームアシスト法により生分解性プラスチック表面にアモルファスナノ薄膜の堆積形成を試みることを通して、薄膜の形成条件の精査および得られたアモルファス炭素ナノ薄膜の構造と物性との関係を評価することを試みた。その結果、イオンビームアシスト法にて異なる炭化水素ガスを薄膜原料とするアモルファス炭素薄膜の創製が可能であり、有効な電気抵抗値を有する薄膜が得られること等が明らかとなった。他方、薄膜形成の最適条件が炭化水素ガスの種類により異なることが明らかとなった。さらに、原料とする炭化水素ガスの炭素数が大きい程、厚い薄膜が得られること等が明確となった。今後、更なる構造解析を試み構造と物性との関係を明確にしていくことにより、実用的なアモルファス炭素ナノ薄膜付与材料の創製が可能となるものと考えられる。

尚、アモルファス炭素ナノ薄膜の基板に対する密着性試験および薄膜付与材料の加水分解試験の結果については、研究成果報告会にて報告する。

引用文献

1）　矢ケ崎隆義、木村雄二、材料、47、84-89（1998）.
2）　山田香織、矢ケ崎隆義、木村雄二、鷹野一朗、54、79-84（2005）.
3）　金子睦、矢ケ崎隆義、鷹野一朗、木村雄二、下田高志、化学工学会第 73 回年会・研究発表講演集（2008）.

2．3　イオンビーム照射によるナノレベルでの表面モルフォロジー制御

Formation of Surface Nano-morphology Controlled by Ion Beam Irradiation

鷹野一朗（工学院大学 電気システム工学科）
Ichiro TAKANO (Department of Electrical Engineering, Kogakuin University)
佐々木道子（理化学研究所）
Michiko SASAKI (RIKEN)

Abstract

Recently the material control at nano-level leads to developments of new material or mechanism. The surface properties can be changed by controlling with nano-level even the surface on the material consisting of the same element. For example the leaves of some kinds have the roughness of nano-level. The roughness plays the role of repelling water. It's possible to produce the excellent properties such as the water repellant to the materials surface. In this study, the other PTFE (3M-PTFE) surface was irradiated by ion beams of He, N_2 or Ar gas. The morphology of PTFE was changed by the effects of sputtering and heating of ion beam. The surface morphology changed by the ion beams produced the high water repellency and the hydrophile property to the PTFE surface.

1. はじめに

PTFE（ポリテトラフルオロエチレン）の用途はあらゆる産業分野に広がっており，耐熱性，耐寒性，耐薬品性，耐候性，難燃性，電気特性，低摩擦特性など様々な特性を有する。その用途は，化学，電気・電子，機械，建設，食品などの各分野はもちろん，近年は環境・安全性，高機能性ニーズに応えて半導体，自動車，OA 機器，レジャー用品に至るまで拡大しており，今後ますますそれらの伸びが期待されている。このような素材の表面をさらに加工し，より高度な材料として使用することが，更なる高機能材料の開発へとつながる。

本来フッ素樹脂とは，フッ素原子を含むプラスチックの総称である。つまり，アクリル樹脂にフッ素原子が入れば含フッ素アクリル樹脂になり，ウレタン樹脂にフッ素原子が入れば含フッ素ウレタン樹脂となるためフッ素樹脂には非常に広い範囲が存在する。これらのフッ素樹脂を使った典型的なものとしては，フッ素樹脂コーティングされたフライパンが上げられる。フッ素樹脂コーティングされたフライパンの表面では，ハスの葉の上を水玉が転がるような非粘着性，油なしでも卵焼きが焦げ付かない離型性，さらに出来上がった調理物が滑る低摩擦性，直火で使用してもフッ素樹脂が炭化せず燃えにくい耐熱性と耐燃焼性を有する。人体に対しても，テフロンは他の物質と溶け合わず化学反応を起こさないので，胃や腸で吸収されることはなく，そのまま排出されてしまうため，全く無害である（日本弗素樹脂工業会及び FDA の研究による）。高い電気絶縁性・低誘電性の特長を生かし，かつ耐燃焼性が有ることより様々な情報通信のケーブルに使用され，無くてはならないものとなっている。このような特徴をフッ素樹脂は持っているが，そのなかで最も特徴の有るフッ素樹脂は PTFE である。これは，炭素原子に 2 個のフッ素原子が結合した形の繰り返しで，フッ素原子の代わりに水素原子が有ればポリエチレンとなる。PTFE の特徴は，このフッ素原子と炭素原子の組合せに由来している。PTFE の電気陰性度はあらゆる原子中で最も大きく炭素原子と結合する。炭素原子とフッ素原子が結合し，他の物質と結合しないため高い非粘着性を発揮しかつ低摩擦性を有する。一方，このような特徴を有するテフロンにも問題があり，例えば高い非粘着性と離型性を持っているため，強固に接着できる接着剤がない，高い耐熱性を持っているため熱処理による加工が難しい，耐薬品性が高いため化学的に除去することが難しいことが知られている。[1)]

前方では，窒素，アルゴン，ヘリウムの各イオンビームを PTFE（ポリテトラフルオロエチレン）に照射し，その特性の違いについて調査した。PTFE に対するイオン照射により，表面形態に大きな変化が得られたため，基板温度などを計算により求めたところ表面形態との関連性が良い一致を示しており，温度を実測して詳細なメカニズムを検討することができた。さらに，イオン種についても違いが現れた。

本研究の特徴は，イオンエネルギーにばらつきのあるプラズマを用いるのではなく，一様のエネルギーを持つイオンビームを利用することで，精密に表面形態変化を知ることができる。[2)]この変化が PTFE において

重要な特性とされている摩擦係数及び水の接触角にどのような影響を与えるかを調査した。PTFEを対象としたイオン照射の研究は井上ら[3]が報告しているように，様々なエネルギーや照射電流で Ar^+イオンを照射した場合，その表面形態は大きく変化し撥水性に強く影響するがそのメカニズムは明らかになっていない。しかし，これまでの筆者らの調査では，スパッタリング等の影響とともに熱的影響が大きく関与していることが予想されている。[4)5)]試料として用いた PTFE(ニチアス㈱)の物性は，溶解温度 357℃，密度 2.1g/cm^3，比熱 1.05kJ/(kg･K)，熱伝導率 25.1W/(m･K)であったが，同じ PTFE であっても各メーカにおいては微妙な違いが影響することが予想される。本報では，他社の PTFE(No.5490 住友スリーエム㈱)を用い同様の実験を行った。ここでは，PTFE を区別するため N-PTFE(ニチヤス(株))と 3M-PTFE(No.5490 住友スリーエム㈱)とした。

2. 実験装置

本研究では，直進型のマルチアパチャータイプの電極を持つ大電流イオン照射装置を用いる。イオン源のガス導入管から導入されたガスは，イオン源プラズマ室に入り，タングステンフィラメントを陰極，プラズマ室外壁を陽極として，低電圧で陰極より引き出された熱電子によって電離されプラズマ化される。生成されたプラズマは，プラズマ室内壁にあるサマリウムコバルト製の永久磁石によって発生された多極磁場により閉じ込められている。このプラズマから加速電極，接地電極間の強電界により，イオンビームを引き出している。この時，加速電極と接地電極は，イオンを引き出すと同時に，イオンを加速する働きを兼ねるため，両電極間には最大 40kV の電圧が印加される。電極は，多孔電極構造をしており，電極板には直径 5mm の丸い穴が 6mm 間隔で 192 個配置されている。これによって，直径 100mm のイオンビームが得られ，大きな面積の処理が可能になり，いわゆるイオンシャワーのような処理となる。試料処理チャンバーには，基板ホルダー，シャッター，電子ビーム蒸着装置 2 台，膜厚計 2 台，ファラデーカップが装備されている。イオン電流値は測定面積 1.0cm^2 のファラデーカップでモニタした。ファラデーカップは放出される二次電子をサプレッサ電極で受け止め電流値の補正を行うような構造となっている。チャンバーの排気系は油拡散ポンプ(DP)と油回転ポンプ(RP)によって排気される。

3. 実験方法

試料として用いる 3M-PTFE をサンプルホルダーに装着後，照射チャンバー内を 6×10^{-4}Pa まで排気し，He，N_2 または Ar ガスを導入して 1×10^{-2}Pa とした。イオンエネルギーは 10keV，照射量電流密度は 40μA/cm^2 とし，照射時間を変化した場合の硬さ，摩擦係数，水接触角測定と表面形態変化を観察した。硬さは超微小硬度計(SHIMADZU Co. Ltd.)を用い，ヌープ圧子によりテフロンのヌープ硬さを荷重 5mN の圧子押し込み試験により測定した。5 回測定しその値の最大最小の値を除いて平均したものをその試料の硬さとした。摩擦試験は表面性試験機(新東科学㈱)を用いて固定荷重 20gf とし，摺動幅 5mm の往復摩擦試験により相手材である SUJ2 球に対する摩擦係数を測定した。水接触角試験は接触角計(協和界面科学㈱)を用いて，蒸留水 1μℓを滴下して水滴の接触角を測定した。接触角は，液滴の左右端点と頂点を結ぶ直線の固体表面に対する角度から $\theta/2$ 法で求めた。

4. 実験結果

Fig.1 には各イオンを照射した 3M-PTFE のヌープ硬さを示す。表面形態が変化するため，ヌープ硬さの測定値は本質的な硬さではないが，ここでは比較評価として行った。いずれのイオン種においても照射時間

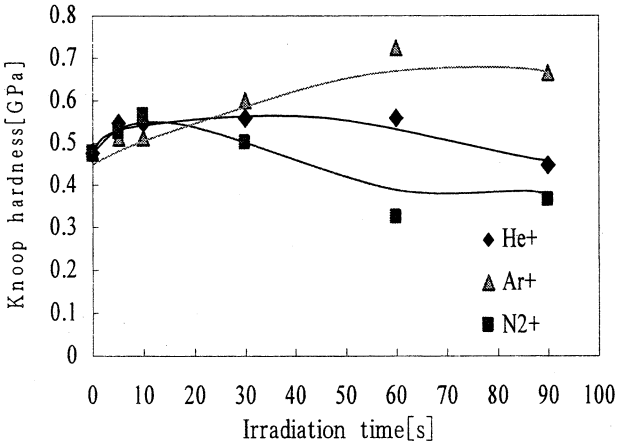

Fig.1 Knoop hardness of 3M-PTFE irradiated by He^+, N_2^+ or Ar^+ ion beam

20sまでは，大きな違いは現れなかったが，20s 以上ではイオン種ごとに差が確認された。最も高い硬さを示したのが Ar^+イオン照射した試料で，以下 He^+イオンと N_2^+イオンの順に硬さは低下した。未照射試料との関係をみると，硬さが上昇する Ar^+イオンに対して，N_2^+イオンは硬さが未照射より低下する傾向がある。硬さは表面形態の影響を大きく受けるため，表面での凹凸が増すと，実質的に密度低下となり硬さは低下することになる。

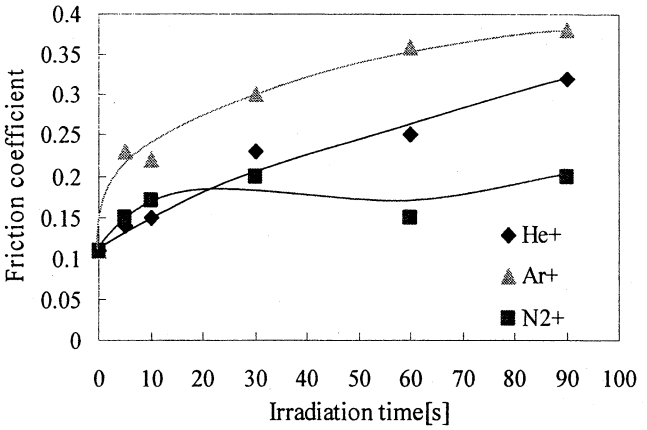

Fig.2 Friction coefficient of 3M-PTFE irradiated by He^+, N_2^+ or Ar^+ ion beam

Fig.2 には同様に各イオンにおける SUJ2 球に対する摩擦係数を示す。摩擦係数は，700s 間往復摺動測定を行いその平均値とした。各イオンにおいて，摩擦係数は未照射よりも上昇することが共通しており，PTFE の特徴である低摩擦性はイオン照射によって損なわれることが分かった。Ar^+イオン，He^+イオンともに照射時間が長くなると摩擦係数は上昇する傾向にある。一方，N_2^+イオン照射の場合は 20s 付近から飽和状態となり，0.15-0.2 の間で一定となった。摩擦係数の値も，表面の凹凸に大きく影響するため，摩擦係数が変化したものと言える。イオン種による違いは，硬さの場合と同順となり，硬さが大きい試料である Ar^+イオンは高い摩擦係数を示し，硬さが低い N_2^+イオンの試料は低い摩擦係数を示した。

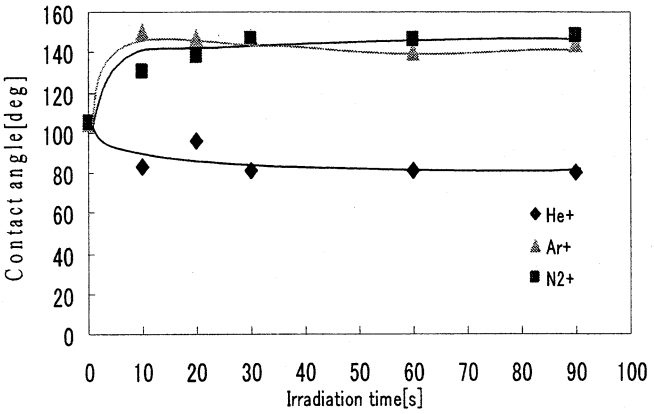

Fig.3 Contact angle of 3M-PTFE irradiated by He^+, N_2^+ or Ar^+ ion beam

Fig.3 には各照射試料に対する水の接触角の変化を示す。良く知られているようにPTFEは元々撥水性の高い材料である。一般に物体の表面では，物体の分子がもつ力によって近接する水の分子を引き寄せようとする性質があるが，その度合はその表面の物理的・化学的構造によって異なる。双方の関係は水の凝集力と基材表面引力との関係で決まるため，接触角 θ が 90° 以上の場合を撥水性，110° から 150° の場合が高撥水性，150° 以上の場合は超撥水性となる。ここでは，イオン照射した 3M-PTFE の撥水性がどのように変化するか測定した。Fig.3 の水接触角測定において，未照射 3M-PTFE の接触角初期値は 100° で，この値から出発して Ar^+及び N_2^+イオン照射とともに接触角は照射時間約 10s で急激に上昇し，その後飽和状態となり 150° 付近で一定値を示す。未照射と Ar^+イオン照射での水接触の写真は Fig.4 のようになる。一方，He^+イオンではまったく逆の変化が見られ，イオン照射時間とともに接触角 80° まで徐々に低下することがわかる。一般に，PTFE などのように表面に凹凸を形成した場合は，水と表面との接触面積が減少し接触角は高くなる傾向がある。ところが，He^+イオン照射の場合，Fig.4 の写真からもわかるように，接触角は低下する。このようなイオン種による明確な違いが表れたのは初めてであり注目に値する。

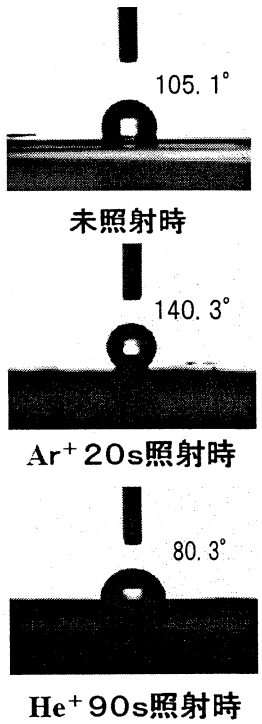

Fig.4 Photographs of contact angle measurement

以上のような硬さ，摩擦係数，水接触角の変化が，表面形態度とどの程

度かかわっているかを電子顕微鏡観察によって評価する。Fig.5 に示すように照射時間 60s における，各イオン照射後の表面写真を示す。未照射試料では写真のような突起物の個所は除き，ほぼ平面的な表面形態となっている。ところが Ar+イオン，N_2^+イオン，He^+イオン照射はどれも異なった表面形態に変化していることがわかる。従って，これまでの硬さや，摩擦係数，水接触角試験のイオン種ごとによる各値の違いは，表面形態の違いに起因することが予想される。Ar^+イオン照射では，細い針状のものが多数存在していることがわかる。N_2^+イオン照射では，Ar^+イオンに比べ凹凸が荒くなっており，凸部の塊は照射エネルギーにより溶融し結合した部分のようにも見える。このような形態は，前報での N-PTFE でも観察されており，イオンエネルギーによる熱的な影響によるものと判断している。また，He^+イオン照射では，凹部が徐々に形成される段階のように見え，他の 2 種類とは全く異なる様相を示しており，これにより親水性が生じていると考えられる。ただし，未照射に比べ凹凸は明らかに増えているため，合理的な説明をするためにはさらなる詳細な調査が必要である。各試料とも照射エネルギーは 24J/cm^2 が投入されている。一方，イオンが表面に及ぼす注入イオンの飛程は，He^+イオンが最も深く，次に N_2^+イオン，Ar^+イオンの順に浅くなる。言いかえると，単位体積当たりの付与エネルギーは Ar^+イオンが最も大きく，次に N_2^+イオン，そして He^+イオンの順となる。もし熱だけが変化の過程に関与するならば，He^+イオン，N_2^+イオンの表面形態のあとに Ar^+イオンの状態が来ることになる。しかし，He^+イオンのような水接触角が低下する状態は他のイオンでは確認されておらず，He^+イオン特有の表面形態と考える方が正しい。従って，今回の実験では熱的影響の他にイオン種の影響も関与していることは明らかとなり，イオン種やエネルギーによって詳細な表面形態のコントロールが可能であることが確認された。

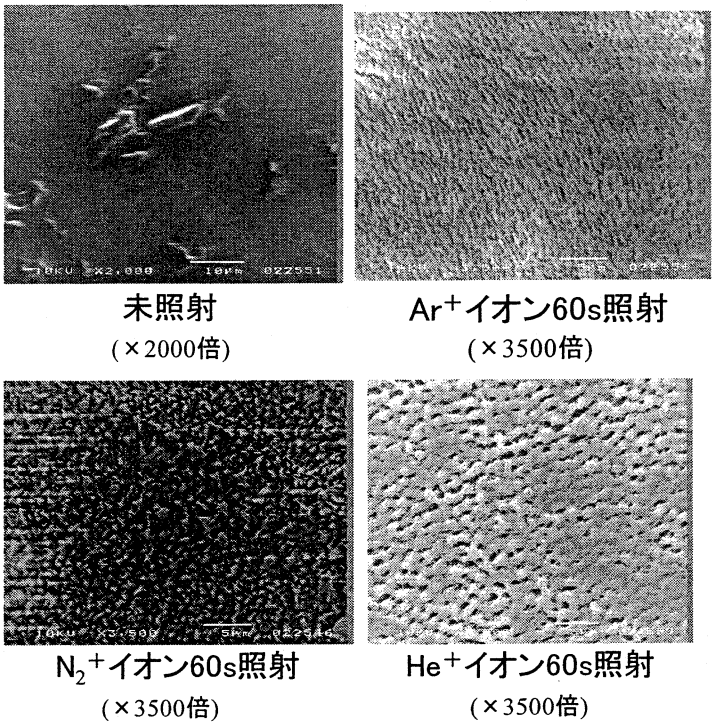

Fig.5 The surface morphology of PTFE irradiated by Ar^+ ,N_2^+ or He^+ ion beam

5. おわりに

今回 3M-PTFE に対するイオン照射を行い，表面形態に大きな変化が得られた。前報と同様にイオン照射による熱的な影響を考えると，表面形態との関連性は説明ができる。しかし，He^+イオンにより接触角が親水性側に移行するという新たな特性が得られたことで，イオン種自体の影響も十分に考慮する必要が生じた。また，N-PTFE と 3M-PTFE の特性の違いも確認されたため，PTFE 自体を詳細に検討することも必要である。

参考文献

1) 三井・デュポンフロロケミカル㈱，日本フッソ工業㈱,社報等

2)鷹野一朗，表面技術，**52**, 12 (2001) 9

3)井上陽一，吉村保廣，池田由紀子，河野顕臣，表面技術，**51** (2000) 512

4)鷹野一朗，他;“高分子材料へのイオンビーム照射による表面機能評価”日本真空協会・真空に関する連合講演会(2007.11)

5)佐々木道子，他;“低エネルギーAr^+イオン照射による PTFE の表面改質”表面技術協会・第 116 回講演大会(2007.9)

2．4 ポーラス構造を持つ薄膜材料を用いた新規ナノデバイスの開発
Fabrication of novel nano-devices based on thin solid films with porous structure

位置選択的な貴金属触媒の付与と湿式エッチングによる半導体表面のマイクロファブリケーション
Micro-fabrication of semiconductors by site-selective noble metal deposition and subsequent chemical etching

小野幸子*，阿相英孝*，安川雪子**
Sachiko ONO*, Hidetaka ASOH* and Yukiko YASUKAWA**

工学部応用化学科，,**総合研究所
*Faculty of Engineering, Dept. of App. Chem., *,**Res. Inst. Sci. Tchnol.

Abstract: Hole arrays of Si as well as the other semiconductors with ordered periodicities were fabricated by the site-selective chemical etching of a Si substrate using patterned noble metals as etching catalyst through self-assembled micro/nano-spheres as a mask. By using shape-controlled circular metal thin films, silicon micro holes containing metal thin films at bottom of each hole could be obtained easily. Micro pattering of GaAs in the same manner was also performed. The process presented is also suitable for the large-scale production of ordered metal honeycomb and isolated metal patterns on a Si substrate that are not achievable by conventional lithographic techniques.

1. 緒言

シリコン（Si）をフッ酸溶液中でアノード酸化することで得られる多孔度の高い微細構造を持ポーラスシリコンは，バルクシリコンにはない可視発光現象が発見されて以来，光学素子，センサー，生物分野など多方面への応用が期待されている。ポーラスシリコンの作製方法はフッ酸を含む電解液中でのアノード酸化が最も一般的であるが，近年，松村ら [1]により，貴金属の微粒子を付与したSi基板をフッ酸ー過酸化水素の混合液に浸漬することで，金属微粒子が基板内部に沈降しながら孔を形成する現象が報告された。貴金属微粒子の触媒作用によるポーラスシリコン層の形成は，太陽電池表面の反射率を低減する新たなテクスチャー技術として期待されるだけでなく，既存のマスク形成技術と組み合わせることにより，Si基板を位置選択的にエッチングすることが可能であり，発光デバイス，化学センサーなどの作製技術として応用が検討されている [2]。我々はNASICプロジェクト開始当初よりSi基板上に自己組織化的に形成した微粒子の規則配列構造（コロイド結晶）をマスクとして利用し，化学エッチングやアノード酸化によるSi基板の微細加工を検討してきた [3]。コロイド結晶などの自己組織化構造をマスクとして利用した構造転写技術は，既存のリソグラフィー技術に比べ，工程の簡易さ，低コスト，大面積加工などの特徴を持ち，トップダウン方式によらない微細加工技術として様々な分野での応用が期待される。本研究では，コロイド結晶を利用した構造転写法と金属触媒エッチングを組み合わせ，ナノメートルからマイクロメートルの周期を持つ各種半導体のホールアレイの作製を検討した。

2. 実験方法

図 1 に Si を代表例とした実験プロセスを模式図と共に示す。各処理後の表面形態は走査型電子顕微鏡（SEM），原子間力顕微鏡（AFM）で観察し，断面作製には収束イオンビーム加工装置（FIB）を用いた。

3. 結果および考察

3.1 ポリスチレンハニカムマスクを用いたエッチング

ハニカム状の PS 製マスクを作製し，イオンスパッタリングにより Pt/Pd または Au 薄膜を付与した。金属薄膜の厚さは，AFM 測定より Pt/Pd が 10 - 15 nm，Au は 8 - 25 nm で，厚さの均一性は前者がより高かった。金属薄膜付与後，フッ酸と過酸化水素の混合液中でエッチングすることで Si 基板にコロイド結晶のパターンを転写することを試みた。図 2 に Pt/Pd 薄膜を付与後，エッチングを 1 分間行った Si 基板表面の SEM 像を示す。Si 基板上にコロイド結晶の規則配列を転写したホールアレイが得られた。形成した孔の底部では円形状の Pt/Pd が薄膜の形状を維持したまま基板内部に沈降している様子が観察された。テンプレートとして用いたシリカ微粒子の直下に相当する位置に，選択的にイオンスパッタリングによる金属薄膜が付与されたと考えられる。エッチングの進行に伴い，六角形状のセル状構造が得られたが，孔壁の溶解が進行し，高アスペクト比を持つ孔を形成できなかった。同様に Pt/Pd を付与後，PS ハニカムマスクを除去してエッチングを行うことでエッチング時のマスクの有無に関する影響を検討した。図 3 にエッチングを行った後の Si 基板の表面及び破断面の SEM 像を示す。マスクを除去してエッチングした場合も触媒が連続した膜として基板内部に沈降している様子が観察されたが，この場合はサイドエッチングの影響が低減され，2 分間のエッチングで深さ 7μm の孔が得られた。しかし，エッチング時間の経過と共に，孔壁は溶解を受け，パターンの形状は徐々に崩れた。以上の結果から，孔壁の溶解メカニズムを次のように考察した。エッチング時に金属薄膜は触媒として作用し，Si の溶解を伴いながら基板内部に沈降する。この際に，金属薄膜の一部が微細な微粒子として孔壁に留まり，触媒作用を引き起こすことで孔壁の溶解が進行する。マスクを付けた状態でエッチングを行った際に高アスペクト比を持つ孔を形成できなかった原因は，マスクを除去した場合に比べ，孔壁に留まる金属触媒量が多いためと考えられる。

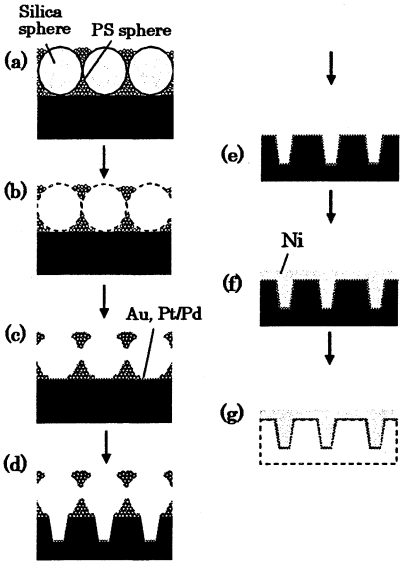

Fig. 1 Schematic model of fabrication of silicon macropore arrays: (a) formation of composite colloidal crystals on silicon substrate, (b) removal of silica sphere, (c) formation of metal catalyst layer, (d) chemical etching of silicon, (e) removal of PS honeycomb mask, (f) electrodeposition of nickel layer, and (g) removal of silicon by immersion of substrate in TMAH.

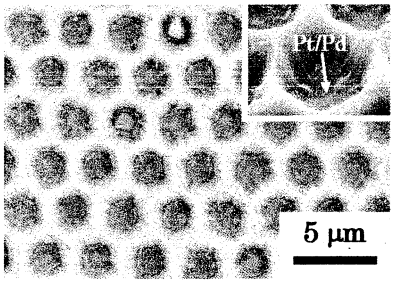

Fig. 2 SEM images of patterned Pt-Pd-coated silicon after chemical etching in 5 mol dm^{-3} HF / 1 mol dm^{-3} H_2O_2 for 1min.

次に，金属触媒種の影響を検討するため，イオンスパッタリングにより Au を付与した。図 4a に Au 薄膜を付与後，マスクを付けた状態で 1 分間エッチングを行った Si 基板表面の SEM 像を示す。直径 1μm 程度の細孔が 3μm の周期で観察され，Si 基板上にコロイド結晶の規則構造を転写したホールアレイを得ることができた。また，Pt/Pd の場合と同様に Au の薄膜が形状を維持したまま基板内部に沈降する様子が確認できた。図 4b,c にエッチングした Si 基板の FIB 断面の SIM 像を示す。エッチングの初期段階において孔底部の Au 薄膜の中央部は盛り上がったように観察された。以上の結果から，金属薄膜が Si 基板に沈降し，ホールを形成する過程を次のように考察

した。エッチング開始後は円形に付与した金属薄膜の周囲で優先的にエッチングが進行し，金属薄膜と Si の間に溝を形成する。その後，その溝から金属薄膜の中央部に向かってエッチング液が供給されることで金属薄膜と接している部分の Si の溶解が進行し，金属薄膜と Si の間に微少な間隙が形成される。この微小な間隙部にエッチング液が供給され続けることによって Si の溶解が進行し，孔を形成する。Pt/Pd 薄膜の場合でもエッチングの初期段階において同様の過程を経るものと推測される。また，エッチング時間を延長することで深さ約 5 μm のホールアレイの作製が可能であった。金属触媒に Au を用いることで，Pt/Pd の場合に比べサイドエッチングの影響が低減され，高アスペクト比を持つ孔の形成が可能であった。これは，Pt/Pd の場合，Au に比べ反応速度が速く，エッチング液中で活性が高いことに起因する。

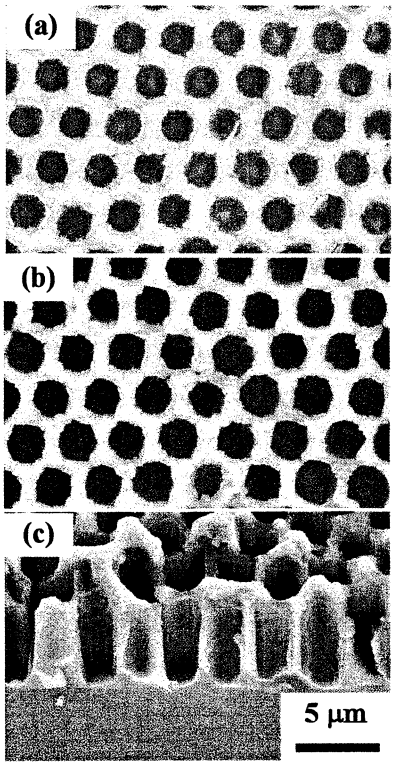

Fig. 3 SEM images of patterned Pt-Pd-coated silicon after chemical etching in 5 mol dm^{-3} HF / 1 mol dm^{-3} H_2O_2 for (a) 1 min, (b, c) 2 min. (a, b) Top view and (c) cross-sectional view.

3.2 Niレプリカによるホール形状の評価

次に，Siホールアレイの形状を評価するためにNiレプリカの作製を行った。図5aにPt/Pdを付与し，ハニカムマスクを除去後，エッチングして作製したSiホールアレイのNiレプリカのSEM像を示す。規則配列したロッド状の構造が得られ，ロッドの先端には円形状のPt/Pd薄膜が観察された。レプリカを観察した結果，孔壁は滑らかであり，孔の上部ほど孔壁の溶解が進行して広がっている様子がわかった。図5bにAu触媒により作製したホールアレイの形状を転写したNiレプリカのSEM像を示す。Au触媒の場合，孔壁はハニカムマスクを構成するPS微粒子の形状を反映した細い溝が観察された。このことからも，Pt/Pdに比べてサイドエッチングの影響が少ないと考えられる。また，孔の底部にある金の薄膜はPt/Pdの場合と異なり，エッチング時間の経過とともに徐々に構造が崩れた。これは，Au薄膜を構成するスパッタ粒子の大きさがPt/Pdに比べて大きく，金属薄膜の均一性において劣るため，膜の形状維持が困難であるためと推測される。

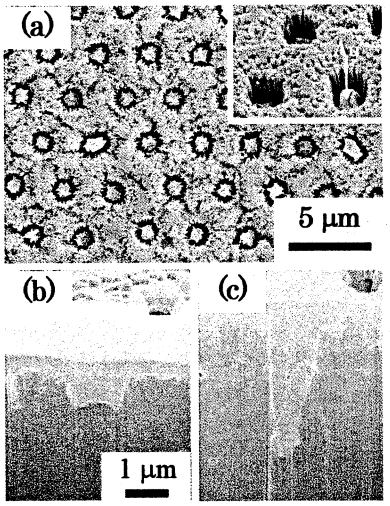

Fig. 4 SEM images of Au-coated silicon after chemical etching in HF/H_2O_2 for (a, b) 1 min and (c) 5 min. (a) Top view and (b, c) cross-sectional view of silicon prepared by FIB.

3.3 GaAsに形成されたホール構造

図6に基板としてGaAsを使用し，Siと同様にAu触媒を付与しエッチングを行った場合のホール構造を示す。エッチング速度は異なるが，Siと同様に六方配列したホールアレイを得ることが出来た。GaAsはエッチングに異方性を持つ特徴がある。

4. 結論

本年度までの結果をまとめると，コロイド結晶を出発マスクとし,貴金属触媒微粒子の析出位置を制御することで Si 凸型構造と Si ホールアレイの二種類の Si 微細構造を作製できた。Si ホールアレイはマスクとして用いる PS 微粒子の粒径を変化させることで，3 μm から 200 nm の周期まで微細化に成功した。ポリスチレンハニカムマスクを用いてスパッタリングにより Pt/Pd または Au 薄膜を付与し，エッチングを行った結果，両金属共にホールアレイを作製できた。Au を触媒とし

て用いることでサイドエッチングの影響を低減できることが分かり，高アスペクト比を持つホールアレイの作製が実現した。本手法は，コロイド結晶テンプレート法と金属触媒エッチングを融合した新規のリソグラフィー技術であり，Si 基板以外にも GaAs など化合物半導体などの固体基板の微細加工技術としての種々の応用が期待される。

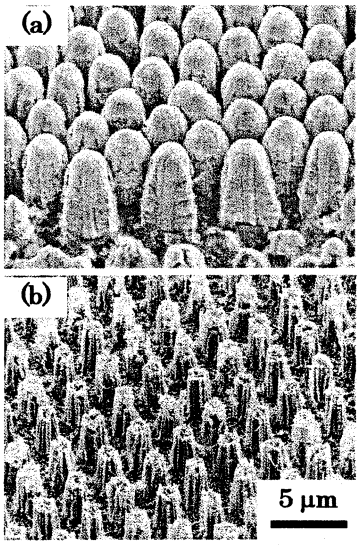

Fig. 5 SEM images of nickel replica of etched silicon. (a) Pt-Pd-coated silicon was etched for 2 min. (b) Au-coated silicon was etched for 3 min.

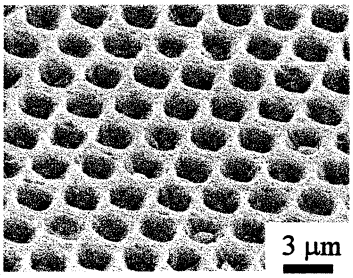

Fig. 6 GaAs hole arrays structured by Au-assisted chemical etching for 60 s.

文献

1) K. Tsujino and M. Matsumura, Adv. Mater., 17, 1045 (2005).

2) S. Chattopadhyay and P. W. Bohn, J. Appl. Phys., 96, 6888 (2004).

3) S. Ono, A. Oide and H. Asoh, Electrochim. Acta., 52, 2898 (2007).

4) 内堀航太，工学院大学修士論文，(2006).

【研究業績（2005 年 4 月－2009 年 3 月）】

査読つき論文 41 件（他：解説論文等 5 報，著書 4 報，
国際会議 50 件，国内会議 133 件，公開特許 7 件，出願中 1 件）

1. A. Kodama, S. Bauer, A. Komatsu, H. Asoh, S. Ono and P. Schmuki, Acta Biomaterialia (印刷中)
2. H. Asoh, F. Arai and S. Ono, Electrochimica Acta (印刷中)
3. S. Ono, K. Kuramochi and H. Asoh, Corrosion Science (印刷中)
4. H. Asoh, K. Uchibori and S. Ono, Corrosion Science (印刷中)
5. 小林勇太，阿相英孝，小野幸子，表面技術, **60** (3), 202-207 (2009.3)
6. 西村和子，板谷浩丘，長原和宏，高橋英明，阿相英孝，小野幸子，表面技術, **60** (3), 195-201 (2009.3)
7. 阿相英孝, 川目達也, 柴田稚子, 小野幸子，無機マテリアル学会会誌, **16** (338), 28-36 (2009.1)
8. 小野幸子，児玉アニタ，阿相英孝，軽金属, **58** (11), 593-598 (2008.11)
9. S. Ono, Y. Kobayashi, R. Kobayashi and H. Asoh, ECS Transactions, **16** (3), 353-358 (2008.10)
10. Y. Yasukawa, H. Asoh and S. Ono, ECS Transactions, **16** (3), 253-258 (2008.10)
11. S. Sakamoto, L. Philippe, M. Bechelany, J. Michler, H. Asoh and S. Ono, Nanotechnology, **19**, 405304/1-405304/6 (2008.10)
12. 朝比奈建史，石原秀憲，阿相英孝，小野幸子，軽金属, **58** (8), 375-380 (2008.8)
13. S. Ono, A. Kiyotake and H. Asoh, ECS Transactions, **11** (15), 1-8 (2008.6)
14. H. Asoh, F. Arai, K. Uchibori and S. Ono, Appl. Phys. Express, **1** (6), 067003/1-067003/3 (2008.5)
15. S. Ono, Y. Kobayashi and H. Asoh, ECS Transactions, **13** (3), 183-189 (2008.5)
16. Y. Yasukawa, H. Asoh and S. Ono, ECS Transactions, **13** (3), 83-92 (2008.5)
17. Y. Yasukawa, H. Asoh and S. Ono, Electrochemistry Communications, **10** (5), 757-760 (2008.5)
18. 新井房雄，阿相英孝，小野幸子, Electrochemistry, **76** (3), 187-190 (2008.3)
19. H. Asoh, S. Sakamoto and S. Ono, J. Colloid and Interface Science, **316** (2), 547-552 (2007)
20. 奥平浩平，阿相英孝，小野幸子, Electrochemistry, **75** (11), 873-878 (2007)
21. H. Asoh, K. Nakamura and S. Ono, Electrochimica Acta, **53** (1), 83-86 (2007)
22. H. Asoh, F. Arai and S. Ono, ECS Transactions, **6** (2), 431-437 (2007)
23. H. Asoh, F. Arai and S. Ono, Electrochemistry Communications, **9** (4), 535-539 (2007)
24. S. Ono, A. Oide and H. Asoh, Electrochimica Acta, **52** (8), 2898-2904 (2007)
25. H. Asoh, A. Oide and S. Ono, Electrochemistry Communications, **8** (12), 1817-1820 (2006)
26. S. Ono, K. Nakamura and H. Asoh, ATB Metallurgie, **45** (1-4), 480-483 (2006)
27. S. Ono, A. Oide and H. Asoh, ATB Metallurgie, **45** (1-4), 120-125 (2006)
28. 生出章彦，阿相英孝，小野幸子, Electrochemistry, **74** (5), 379-384 (2006
29. H. Asoh, A. Oide and S. Ono, Applied Surface Science, **252** (5), 1668-1673, (2005)
30. S. Ono, M. Saito and H. Asoh, Electrochimica Acta, **51** (5), 827-833, (2005)
31. H. Asoh and S. Ono, Applied Physics Letters, **87** (10), 103102/1-103102/3, (2005)
32. S. Ono, C. Wada and H. Asoh, Electrochimica Acta, **50** (25-26), 5103-5110, (2005)
33. H. Asoh, K. Sasaki and S. Ono, Electrochemistry Communications, **7** (9), 953-956, (2005)
34. A. Oide, H. Asoh and S. Ono, Electrochem. Solid-State Lett, **8** (7), G172-G175 (2005)　他

2．5 超音速フリージェットPVDによるナノ組織・ナノコンポジット膜の形成

工学院大学	機械システム工学科	丹羽 直毅，廣木 富士男，湯本 敦史
工学院大学	マテリアル科学科	塩田 一路，桑折 仁
工学院大学	機械工学科	藤江 裕道
東京大学大学院	新領域創成科学研究科	山本 剛久
NASIC客員研究員		鈴木 敏之
サレジオ高専		大杉 功，加藤 雅彦

Development of Nanostructure and Nanocomposite Coatings with Supersonic Free-Jet PVD

N. Niwa, F. Hiroki, A. Yumoto: Dept. of Mecanical Systems Eng., Kogakuin University
I. Shiota, H. Kohri: Dept. of Materials Science and technology, Kogakuin University
H. Fujie: Dept. of Mechanical Eng., Kogakuin University
T. Yamamoto: Dept. of Advanced Materials Science, University of Tokyo
T. Suzuki: NASIC
I. Ohsugi, M. Kato: Salesian Polytecnic

ABSTRACT: The aim of our present work is to produce Al films on a metal substrate with Supersonic Free-Jet PVD (SFJ-PVD) and to investigate the relationships between the microstructure and the tensile properties of it. With SFJ-PVD, We produce a film that has smooth, compact and defect-free microstructure both in the film and at the interface between the substrate and the film and excellent adhesive strength to the substrate.

1. 緒　言

アルミニウム（Al）は軽量かつ優れた機械的・化学的性質を有するため，古くから様々な基材に対する環境保護皮膜として活用されている．近年では，亜鉛資源の枯渇が危惧されていることから亜鉛めっき鋼板の代替としてAlめっき鋼板が検討されるなど，今後ますます工業製品に対するAl膜の重要性が高まってくることが予想されている．

当グループは，高い成膜速度で緻密な膜形成を可能とする新しいコーティング技術として超音速フリージェットPVD（以下SFJ-PVDと略記）を提案・開発している．SFJ-PVDは，不活性ガス雰囲気中で生成させたナノサイズの粒子（ナノ粒子）を，超音速ガス流により高速に加速させ基材に積層させることにより膜形成する技術である．

本研究は，Al膜形成技術として本法を確立させることを目指し，Al膜性状に影響を及ぼす諸因子を評価検討することを目的とする．本法による成膜因子としては主に，超音速ガス流を生み出す超音速ノズル，ガス流速に影響を及ぼすノズル温度，成膜速度を決定する蒸発加熱電力などがあるが，最も重要な因子はガス流を超音速に加速させるノズルの設計である．超音速ノズルは，圧縮性流体力学の理論に基づき，一次元等エントロピ流れの考えを基にした一次元ノズル，特性曲線法を用いた特性曲線ノズルなどいくつかの設計手法が提案されている[1,2]．本研究では，各種，一次元，特性曲線ノズルを設計製作し，各ノズル出口からの噴流を可視化することで超音速ガス

流の噴流形態を調査する．さらに，各ノズルを用いてAl膜を形成させることで噴流形態と膜性状の相関関係を調査し，超音速ノズルの設計の差異が及ぼすAl膜性状への影響を明らかにする．

2. 超音速フリージェットPVD（Supersonic Free-Jet PVD; SFJ-PVD）

SFJ-PVD装置の概略図を図1に示す．本装置はナノ粒子を生成するナノ粒子生成室，基材が設置してあり皮膜形成を行う膜形成室，および真空排気系で構成されている．ナノ粒子生成室と皮膜形成室は搬送管により連結されている．ガス中蒸発の原理を用いて，不活性ガス雰囲気としたナノ粒子生成室内において水冷銅るつぼ上に設置されたAl膜材料をアーク加熱により蒸発させナノ粒子を生成させる．真空排気されている膜形成室と，不活性ガス雰囲気のナノ粒子生成室の差圧によって生じるガスの流れにより，搬送管を通ってナノ粒子が膜形成室に搬送される．搬送管の先端には超音速ノズルが設置されており，ノズル内を通過するガスは超音速流となり，超音速ガス流によって高速に加速された粒子は，膜形成室X-Yステージ上に設置された基板へ吹き付けられる．

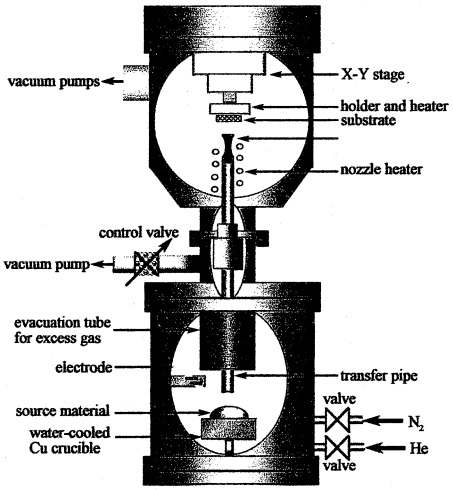

Fig. 1. Schematic diagram of SFJ-PVD apparatus.

3. 超音速ノズルの設計

3.1 超音速ノズル概要

通常，差圧により生まれるガス流は，音速（マッハ数　M=1）までが限界である．しかし，超音速ノズルはその特殊な内部構造によりガスの流れを超音速（マッハ数　M>1）に加速させることができる．超音速ノズルは，その形状から先細末広ノズル(convergent- divergent nozzle)，あるいは1884年に最初にこのノズルを提案したラバル(C.G.P. de Laval)の名からラバルノズル(Laval nozzle)とも呼ばれる[1]．

圧縮生流体力学の基礎理論において，超音速ガス流は上流側と下流側の圧力比により，所定のマッハ数が決定する．マッハ数の決定により，ノズル内の流れに様々な理論を適用することで種々の形状の超音速ノズルを設計することができる．

3.2 一次元ノズル

一次元ノズルは，スロートと呼ばれるノズル最小断面積部（スロート断面積(A*)）を設定することで式(1)によって表されるマッハ数(M)と断面積(A)の関係のみで形状が決まるノズルである．一次元ノズルの概念では，ノズル長さ（ガスの流れ方向）と断面形状は任意に決定することができる．このノズルは，摩擦やノズル内壁から流体への熱の授受の無い等エントロピ流れの概念を基本にしており，ノズル内の流れの圧力，速度や衝撃波の発生に関しては考慮に入れていない．

$$\frac{A}{A^*}=\frac{1}{M}\left[\frac{(\gamma-1)M^2+2}{\gamma+1}\right]^{\frac{\gamma+1}{2(\gamma-1)}} \qquad (1)$$

3.3 特性曲線ノズル

特性曲線ノズルは，流れ場を軸対称として設計するノズルである．設計方法はノズルスロート

からノズル出口までの流れの変化を特性曲線法により計算する[2]．この手法では，図 2 のようなガス流れを物理面と運動ベクトルであるホドグラフ面に分けて特性曲線網を構築していく．図 2 の要素 1-1～1-5 を既知とすると，式(2) から物理面の傾き dy/dx は，現在のガス流の傾き(θ)とマッハ角(α)の関係から各々の物理面における交点 2-1～2-4 が決定する．

$$\left(\frac{dy}{dx}\right)_{I,II} = \tan(\theta \mp \alpha) \qquad (2)$$

次に式(3) からホドグラフ面の dv/du の傾きが x 方向の速度ベクトル(u), x 方向の速度ベクトル(v),音速(a)によって決定することができる．

$$\left(\frac{dv}{du}\right)_{I,II} = \frac{uv \mp a\sqrt{u^2+v^2-a^2}}{a^2-v^2} - \frac{\sigma a^2 v}{a^2-v^2}\cdot\frac{1}{y}\left(\frac{dy}{du}\right)_{I,II} \qquad (3)$$

特性曲線ノズルは，特性曲線網を逐次構築することによって最終的に軸対称ノズルの出口において希望するマッハ数の一様な軸方向速度を持つ軸対称超音速ノズルを設計することができる．

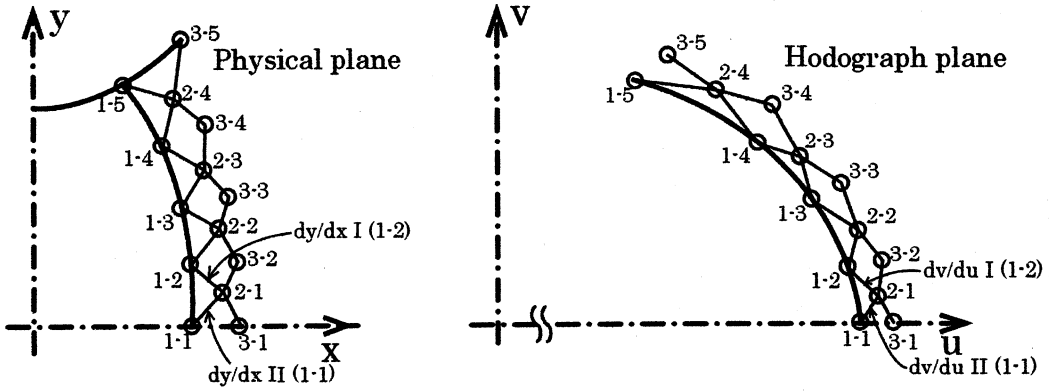

Fig. 2. Design of Characteristic-curve nozzle.

4. 実験方法・実験条件

4.1 噴流可視化実験方法・条件

可視化実験は，SFJ-PVD 装置内のノズル出口後の噴流を大気下で再現し，各ノズルからの噴流をシュリーレン法によって観察した．噴流可視化実験の条件を表 1 に示す．

実験には供給ガスを大気下に放出するため，大気との密度差の少ない窒素を用いた．一次元ノズルの長さは特性曲線ノズルと同じ長さとし，一次元ノズル，特性曲線ノズル共にノズル出口径に対するバレル長さ比が 0, 1.2, 6.9 の 3 種類のバレル長さのノズルを用いた．

Table 1. Visualization condition of free-jet flow.

使用気体	N_2					
マッハ数	3.6					
貯気槽部圧力	8.8(MPa)					
ノズル出口圧力	0.1(MPa)					
設計方法	一次元			特性曲線		
バレル長さ比	0	1.2	6.9	0	1.2	6.9

4.2 成膜実験条件

成膜実験のノズルは，マッハ数 4.2 の He 用ノズルで噴流可視化実験と同様にバレル長さの異なる 3 種類の一次元，特性曲線ノズルを用いた．皮膜は，成膜後断面を SEM 観察し評価した．

5. 実験結果

5.1　噴流可視化実験結果

噴流の可視化観察結果を図3に示す. 図3の結果からバレル無しの場合,一次元ノズルはノズル出口から噴流が広がるが,特性曲線ノズルはノズル出口から噴流が広がらず真っ直ぐ進むことが観察された.バレルを設けた場合,バレル無しに比べ一次元ノズルでは約5%噴流の最大幅が減少し，特性曲線ノズルでは約3%減少した.

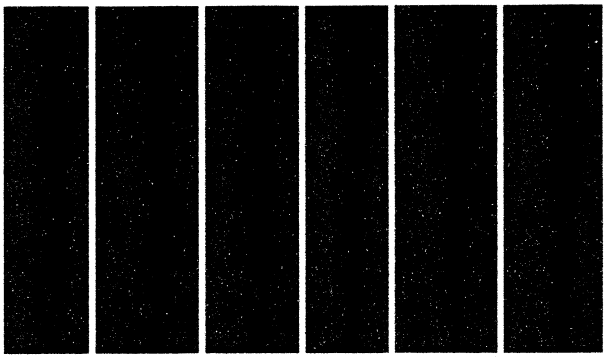

Fig. 3. Visualization of free-jet flow.

5.2　成膜実験結果

バレル長さの異なる一次元ノズル及び特性曲線ノズルにより成膜させた Al 膜の膜断面組織を観察した結果，ノズルタイプにより膜断面組織に差異があることが確認された.

6. 結　言

本研究では，一次元・特性曲線ノズルを設計製作し，各ノズル出口からの超音速ガス流の噴流形態を可視化観察した．さらに，各ノズルを用いてAl膜を形成させ，噴流形態と膜性状の相関関係を調査し，以下の結果を得た.

- 超音速ノズルの設計理論の差異によってノズル出口後の噴流形態が異なる.
- バレル部を設けると一次元ノズルは噴流形態が異なるが，特性曲線ノズルは噴流形態が変わらない.
- 一次元ノズルと特性曲線ノズルでAl膜性状に違いが見られた.

参考文献

(1)松尾，圧縮性流体力学　内部流れの理論と解析，(1994)，理工学社

(2)木村，ロケット工学，養賢堂，(1994)

研究業績

(1) 湯本, 丹羽, 廣木(出願タマティーエルオー株), 金属酸化膜の形成方法及び物理蒸着装置, 特願 2007-276907

(2) 湯本，丹羽，廣木（出願タマティーエルオー株)，繊維強化複合材料の製造方法，特願 2007-276906

(3) 湯本，丹羽，廣木，山本（出願タマティーエルオー株)，物理蒸着装置および物理蒸着方法，特許公開 2008-195996，公開日：平成 20 年 8 月 28 日，国際出願番号：PCT/JP2008/063525，2008 年 7 月 28 日

(4) 湯本，丹羽，廣木，塩田，山本，小宮山（出願タマティーエルオー株)，ハイドロキシアパタイト粒子分散金属膜及びその形成方法，特許公開 2008-194175，公開日：平成 20 年 8 月 28 日

(5) Takashi Hashimoto, Hitoshi Kohri, Atsushi Yumoto and Ichiro Shiota: Friction Coefficients and Wear Rates of MoS_2/Cu, BN/Cu Composites, Advances in Science and Technology Vol. 54 (2008) pp 174-179.

(6) Naotake Niwa, Atsushi Yumoto, Takahisa Yamamoto, Fujio Hiroki and Ichiro Shiota: Coating with Supersonic Free-Jet PVD, Materials Science Forum Vols. 561-565 (2007) pp. 981-984.

(7) 湯本敦史，廣木富士男，塩田一路，丹羽直毅：超音速フリージェット PVD による金属膜の形成と密着性評価，溶射技術第 26 巻 2 号（2007)，pp.44-50.

2．6 高い紫外光応答性をもつ可視光応答ルチル薄膜の分子プレカーサー法による形成

Visible-light-responsive rutile thin film with high UV-light sensitivity by molecular precursor method

佐藤光史[a*]・永井裕己[b]・望月千尋[a]・原広樹[a]・鷹野一郎[c]
Mitsunobu Sato[a*], Hiroki Nagai[b], Chihiro Mochizuki[a], Hiroki Hara[a], Ichiro Takano[c]
[a]共通課程, [b]化学応用学専攻, [c]電気工学科
[a] Department of General Education, Faculty of Engineering, Kogakuin University
[b] Department of Applied Chemistry, Graduate School, Kogakuin University
[c] Department of Electrical Engineering, Faculty of Engineering, Kogakuin University

Abstract

Rutile is the most stable crystal form of naturally abundant Titania. Rutile sensitive to visible light has not as yet found. Because the photoreactivity of anatase is always higher than that of rutile under UV irradiation, formation of the visible light responsive anatase has been much attention for the effective use of the wide range of solar light in the last decade. Here we report the fabrication of novel rutile thin film responsive to visible light and having high photoreactivity under UV light irradiation. This epoch-making rutile thin film was attained by forming the O-deficient Titania by molecular precursor method.

1. 序論

二酸化チタンの組成をもつアナターゼやルチルは，チタンの酸化物（チタニア）である。アナターゼは，紫外光照射によって励起するn型半導体である[1]。アナターゼは，この光励起によって表面に付着した有機物の分解が可能な優れた光反応材料として有用であり，湿式太陽電池の電極材料としても著名である[2, 3]。また，光誘起によるアナターゼ表面の超親水化が報告され，アナターゼの薄膜化も盛んに研究されている[4]。しかし，上述のとおりアナターゼの光励起には紫外光を要し，室内ではほとんど利用不可能で，屋外でも太陽光に含まれるわずか数%の紫外線のみが有効である。このため，光利用高効率化の観点から，アナターゼに遷移金属イオンや窒素イオンなどをドープして可視光励起を可能とする研究が活発に行われている[5-7]。これら従来の研究で得られた可視光応答型アナターゼは，不純物ドープによってバンド端を低エネルギー側にシフトさせ，応答波長限界を可視光域に移動させて実現された。しかし，いずれの可視光応答型アナターゼも，ドーパントによって不純物準位を形成するために，紫外光照射下での光反応活性が低下し，本来の目的であるアナターゼの光利用高効率化は達成されていない。

アナターゼよりも可視光域の光を吸収するルチルは，高い安全性と優れた遮蔽性をもつ白色顔料として知られており，ペイント，食品，化粧品や化学繊維などへの添加剤として広範な用途に使用されている。一方，アナターゼはルチルよりも紫外光照射下で高反応活性であることを西本らが報告して以来，ルチルの光反応活性はアナターゼより低いと長く信じられてきた[8]。ルチルの低い光反応活性の原因は，その結晶構造に起因するものと考えられている[9, 10]。

分子プレカーサー法は，欠陥のない金属酸化物透明薄膜を形成できる化学的湿式法である[11-15]。昨年度までの研究で，分子プレカーサー法を利用して不活性ガス気流中で熱処理して形成したアナターゼ薄膜は，薄膜内部に多量の酸素欠損を含むことがわかった。その薄膜内部に多量の酸素欠損を含む

アナターゼは，酸素欠損を含まないアナターゼに比べ，著しく光反応活性が高い[14]。したがって，内部に酸素欠損を含むルチル薄膜は，従来報告されてきた不純物をドープすることなしに，可視光で高い光反応活性をもつと考えられる。そこで我々は，分子プレカーサー法を用いて酸素欠損ルチル薄膜の直接形成を試みて，光反応活性の高い酸素異常欠損型ルチル薄膜を形成したので報告する[15]。

2. 実験

2.1 溶液合成と薄膜形成

EDTAを配位子とするTi^{4+}錯体濃度が0.4 mmol g^{-1}の分子プレカーサー溶液（S_{MP}）を合成し，部分的に加水分解されたチタノキサンポリマーを含むTi濃度が0.5 mmol g^{-1}のゾルーゲル溶液（S_{SG}）を調製した[12-15]。S_{MP}を利用して石英基板上にスピンコート法で塗布し，乾燥器中において70℃で10分間プレヒート後，石英管(40 mm φ)管状炉に0.1 L min^{-1}のArを通気しながら，室温から700℃まで昇温し，到達後30分間熱処理して透明薄膜**R**を得た。一方，S_{SG}を利用し，同条件で透明薄膜**A**を形成した。薄膜の膜厚は，いずれも100 nmであった。

2.2 測定

膜厚は，表面粗さ計で測定した。XRDによって結晶構造を，XPSにより膜の組成を調べた。表面形態をFE-SEMで観察し，密着性をスクラッチ試験(荷重0.50 kg，印加速度10.5 N m^{-1})で評価した。膜の吸収スペクトル測定結果から，Taucの式を用いて光学的バンド端エネルギーを求めた。

2.3 光応答性評価

これらの薄膜の光応答性を，光誘起によるチタニア表面の親水化試験で調べた。膜共存下でのメチレンブルー水溶液の退色反応速度も測定した。

3. 結果と考察

3.1 結晶構造と組成

得られた薄膜のXRDパターンをFig. 1に示す。分子プレカーサー法で形成した薄膜**R**は，典型的なルチルの回折パターンを示した。また，ゾルーゲル法で形成した薄膜**A**は，アナターゼであることが分かった。この結晶構造の選択的な形成は，2つのプレカーサー膜中のTiイオンの周りにある酸素量の違いが反映したと考えられる。すなわち，**R**膜中のTiに配位している酸素が不足しているために，当初生じたアナターゼ結晶が転移しやすくなり，より安定な結晶構造のルチルに低温で転移した結果と考えられる。

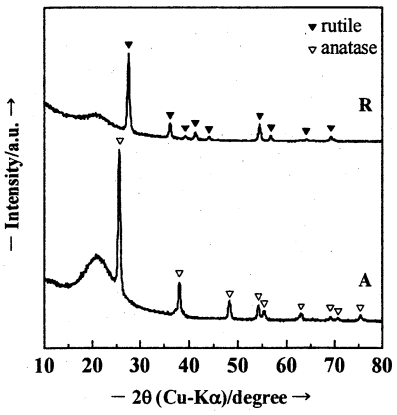

Fig. 1 XRD patterns of **R** and **A**

各膜のO 1sとTi $2p_{3/2}$に帰属できるXPSピークは，各々529.8 eVと458.8 eVに観測された。XPSのデプスプロファイルから求めたO/Tiピークの相対比は，**R**が1.78で，**A**が1.93であった。**A**の場合，チタノキサンポリマー中の酸素量は，化学量論的なTiO_2を形成するために若干不足するものの，十分と考えられる。一方，**R**は，熱処理によって配位子中のCやN，H成分が，酸素と化学結合しながら膜成分から除かれ，多量の酸素が欠損したと考えられる。

3.2 表面形態と密着性

FE-SEM で観察した薄膜の表面状態を Fig. 2 に示した。**R** の結晶粒はよく成長しており，**A** に比べて粒子サイズは明らかに大きかった。

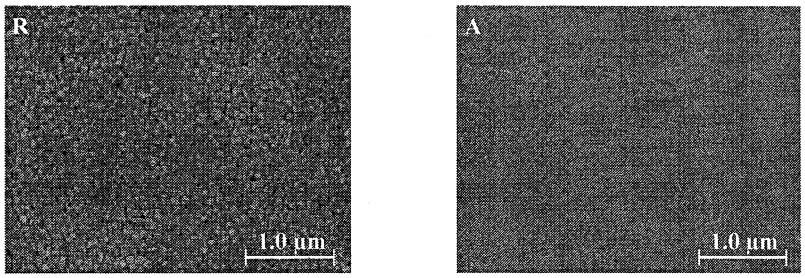

Fig. 2 Surface appearance of **R** and **A** observed by using a field emission scanning electron microscope.

スクラッチ試験による **R** と **A** の石英基板への密着性は，各々 1.75 GPa と 0.69 GPa であった。**R** の石英基板への密着性は，**A** の 2 倍以上である。**R** は，**A** に比べて酸素欠損が多いことから，基板との界面にある **R** 中の Ti イオンが，石英ガラス基板表面上にある多数の酸素原子と強く結合した結果と考えられる。

3.3 光学特性

薄膜の吸収スペクトルを Fig. 3 に示す。直接遷移型半導体とみなして求めた **R** と **A** の光学的バンド端エネルギーは，各々 3.10 eV と 3.63 eV であった。一般的に，薄膜の光学的バンド端は，基板と膜のひずみにより拡幅する。FE-SEM 像に観察されるように，**R** の結晶粒は **A** に比べて著しく大きい。したがって，結晶粒の成長過程において，膜と基板とのひずみが緩和され，**R** のバンド端エネルギーは，単結晶に近い値を示したと考えられる。この **R** は，410 nm 以下の可視光・紫外光に応答することが期待される。

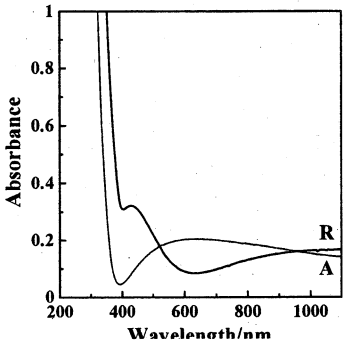

Fig. 3 Absorption spectra of **R** and **A**

3.4 光応答性

R と **A** の光応答性は，可視光および紫外光励起による薄膜表面の親水化試験で評価した[4]。これらの結果を Fig. 4 に示す。可視光への応答による親水化試験は，蛍光灯を光源として 400 nm 以下の波長を完全に除いて実施した（0.8 mW cm^{-2}, 0.0 mW cm^{-2} at 365 nm）。光照射前の **R** と **A** 表面に対する水の接触角度は，66°だった。しかし，可視光照射後 **R** 表面は高い親水性を示したが，**A** は全く親水性を示

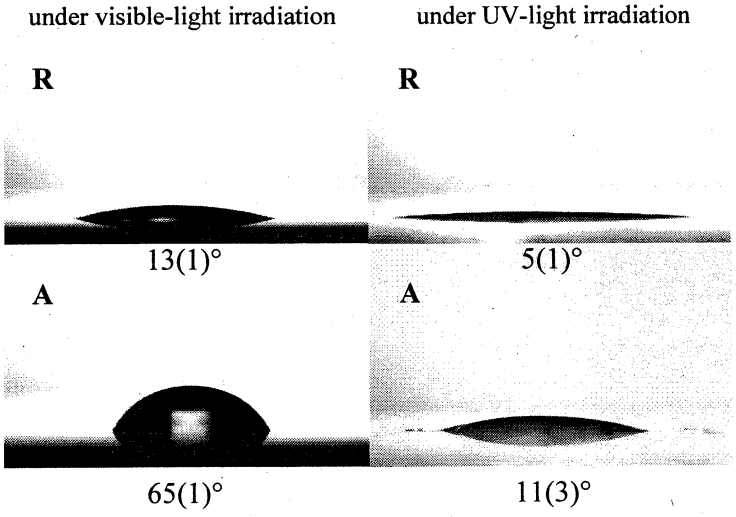

Fig. 4 Comparison of the contact angles of a 1.0-μL water droplet on **R** and **A**.

さなかった。また，弱い紫外光照射下（1.2 mW cm^{-2} at 365 nm）でも，**R** 表面は，超親水性を発現した。

メチレンブルー水溶液に膜形成ガラス板を浸漬し，親水化試験と同様な光源で退色試験を実施したところ，退色速度は親水化現象と一致する結果が得られた。

4. 結言

本研究で得られたルチル薄膜**R**は，膜内部に酸素欠損を多量に含んでいた。その結果，同条件下で形成したアナターゼを凌ぐ紫外光への応答性と，可視光照射下における高い光励起応答性を示した。したがって，従来可視光化に用いられてきた不純物をドープすることなく，すなわち不純物準位を形成することなく可視光応答チタニア薄膜の形成を達成した。ルチル内部に多量の酸素欠損を形成させて，バンド端エネルギーに対応する本質的で潜在的な可視光応答能力の顕在化を実現した。ここで，膜内部に酸素欠損を形成したルチルが光応答性を発現した要因を，Inner Part Electron Trap（IPET）効果とよぶことを提案する。分子プレカーサー法は，この効果を発現させることが可能な現在唯一の方法である。得られたルチル薄膜**R**は，従来アナターゼで実現できるとされた太陽電池材料や，太陽光や蛍光灯による汚染有機物質の除去，防曇材料などへの広い応用が期待される。

参考文献

[1] C. F. Doodeve, J. A. Kitchener, *Trans. Faraday Soc.*, **34**, 902-908 (1938). [2] A. Fujishima, X. Zhang, D. A. Tryk, *Surf. Sci. Rep.*, **63**, 515-582 (2008). [3] B. O'Regan, M. Grätzel, *Nature*, **353**, 737-739 (1991). [4] R. Wang, K. Hashimoto, A. Fujishima, M. Chikuni, E. Kojima, A. Kitamura, M. Shimohigoshi, T. Watanabe, *Nature,* **388**, 431-432 (1997). [5]M. Anpo, *Bull. Chem. Soc. Jpn.*, **77**, 1427-1442 (2004). [6] R. Asahi, T. MOrikawa, T. Ohwaki, K. Aoki, Y. Taga, *Science*, **293**, 269-271 (2001). [7] S. Sakthivel, H. Kisch, *Angew. Chem. Int. Ed.*, **42**, 4908-4911 (2003). [8] S. Nishimoto, B. Ohtani, H. Kajiwara, T. Kagiya, *J. Chem. Soc., Faraday Trans*, **81**, 61-68 (1985). [9]F. D. Ollis, E. Pelizzetti, N. Serpone, *Environ. Sci. Technol.*, **25**, 1523-1529 (1991). [10]M. A. Fox, M. T. Dulay, *Chem. Rev*, **93**, 341-357 (1993). [11]T. Nishide, M. Sato, H. Hara, *J. Mater. Sci.*, **35**, 465-469 (2000). [12]T. Nishide, M. Sato, H. Hara, Y. Sawada, *J. Mater. Chem.*, **6**, 1767-1770 (1996). [13]H. Nagai, C. Mochizuki, H. Hara, I. Takano, M. Sato, *Sol. Energy Mater. Sol. Cells,* **92**, 1136-1144 (2008). [14]H. Nagai, M. Hasegawa, H. Hara, C. Mochizuki, I. Takano, M. Sato, *J. Mater. Sci.*, **43**, 6902-6911 (2008). [15]H. Nagai, S. Aoyama, H. Hara, C. Mochizuki, I. Takano, N. Baba, M. Sato, *J. Mater. Sci.*, **44**, 861-868 (2009).

研究業績

【審査付き論文】

[1]H. Nagai, C. Mochizuki, H. Hara, I. Takano, M. Sato, *Sol. Energy Mater. Sol. Cells,* **92**, 1136-1144 (2008). [2]H. Nagai, M. Hasegawa, H. Hara, C. Mochizuki, I. Takano, M. Sato, *J. Mater. Sci.*, **43**, 6902-6911 (2008). [3]H. Nagai, S. Aoyama, H. Hara, C. Mochizuki, I. Takano, N. Baba, M. Sato, *J. Mater. Sci.*, **44**, 861-868 (2009).

【国際学会発表】

[1]H. Nagai, S. Aoyama, H. Hara, C. Mochizuki, I. Takano, N. Baba, M. Sato, 7th International Symposium on Advanced Technology, Beijing University of Chemical Technology, Oral, October 21, 2008. [2]H. Nagai, S. Aoyama, H. Hara, C. Mochizuki, Y. Mashiyama, T. Honda, I. Takano, N. Baba, M. Sato, 7th International Symposium on Advanced Technology, Beijing University of Chemical Technology, Poster, October 21, 2008. [3]H. Nagai, M. Hasegawa, C. Mochizuki, M. Sato, Sintering2008, Poster, San Diego, November 17, 2008. [4]S. Adachi, H. Nagai, C. Mochizuki, M. Sato, Sintering2008, Poster, San Diego, November 17, 2008. [5]H. Nagai, S. Aoyama, H. Hara, C. Mochizuki, M. Sato, 15th International SPACC-CSJ Symposium, Oral, Osaka, November 20, 2008. [6]S. Adachi, H. Nagai, C. Mochizuki, M. Sato, 15th The Society of Pure and Applied Coordination Chemistry-CSJ Symposium, Poster, Osaka, November 20, 2008.

3. ナノ界面・粒子

3. 1. 1. ナノ機能表面を有する生物規範型ロボットの開発研究
Development of Biomimetic Robots with Nano-Functional Surfaces

鈴木健司，髙信英明，三浦宏文
Kenji Suzuki, Hideaki Takanobu and Hirofumi Miura

工学院大学　工学部　機械システム工学科
Department of Mechanical Systems Engineering, Kogakuin University

This paper presents the insect-inspired robots with micro- and nano- functional surfaces. Two kinds of robots have been developed. One is the water strider robot that is able to stand and move on the surface of water using surface tension force. Various kinds of supporting legs with hydrophobic microstructures were developed utilizing MEMS techniques. The lift and pull-off forces of these legs were investigated experimentally. Then, a water strider robot with twelve microfabricated legs driven by a vibration motor was developed. The robot successfully moved on a water surface and also made left/right turns by utilizing differences in the resonant frequencies of the legs. The other robot is a wall-climbing robot based on adhesive mechanism of ants. Adhesive pads made of glass and PDMS were fabricated using MEMS processes and adhesive properties were measured. Then, a hexapod robot with glass and PDMS pads was developed. The robot successfully walked on vertical and inverted glass surfaces.

1．緒言

本研究は，生物の表面の構造と機能を規範として，表面の微細構造をナノ・マイクロ加工技術により再現することにより，生物と同様の機能を持つロボットの開発を目的とする．昆虫などの微小な生物では，スケールの効果により，重力などに比べて表面間の相互作用の影響が顕著に現れるため，表面の機能を積極的に利用して行動している．このような表面機能を工学的に解明し，小型ロボットに応用することによって，従来にはない新しいロボットの設計指針が得られると考えられる．本研究では，身近な昆虫であるアメンボの水面移動と，アリの壁面歩行に着目した．アメンボは，脚先の多数の毛と，撥水性の物質の分泌により表面張力を利用して水の上に立ち移動することができる [1]．また，アリは，脚の先端にある柔軟な付着パッドと，そこから分泌される液体を利用して垂直面や天井面に付着していると考えられている [2)3)]．これらは微小な昆虫に特有の能力であり，スケールの効果を生かした移動形態であると考えられる．これらの機能を小型ロボットに付与することにより，ロボットの活動領域が拡大され応用の可能性が広がるだけではなく，昆虫の運動機能のメカニズムの解明にもつながることが期待される．

2．表面張力を利用した水面移動ロボットの開発

2.1．表面に凹凸を持つ支持脚の製作

撥水性の物質は，表面に凹凸構造を設けることにより撥水性が強められることが知られている．アメンボの脚の表面も，多数の毛で覆われていることで撥水性が強化されている [1]．そこで，MEMS 技術を用いて，表面に凹凸構造を持つ 3 種類の撥水性の支持脚を開発した．

①櫛形構造の巻きつけによる細毛の加工 [Fig.1(a)]

シリコンウエハ上に厚膜フォトレジスト SU-8 で鋳型を作製し，PDMS(Polydimethylsiloxane) を流し込み櫛型の構造を製作する．これを φ0.5mm の黄銅線に巻き付け撥水剤 FS-1010 を塗布することで，アメンボの毛のような構造が得られる．

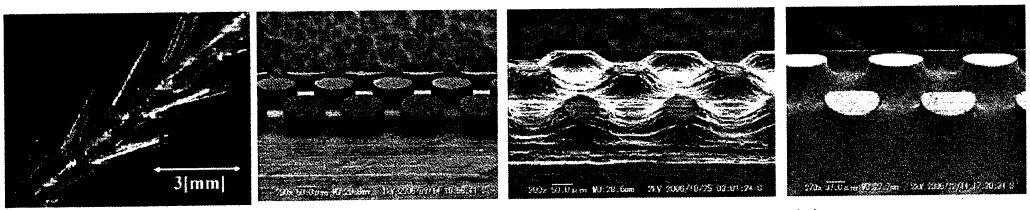

(a) PDMS　(b) SU-8　(c) Aluminum　(d) Brass

Fig.1 Supporting legs with microfabricated structures.

②SU-8 を使用した円筒面への凹凸加工 [Fig.1(b)]
SU-8 を浸漬により φ1.0mm の黄銅線に塗布し，円筒面を 5 回に分けて露光し，現像することで凹凸面を製作する．マスクパターンは直径 100 μm の円形で，間隔は 50 μm である．
③金属ワイヤのエッチングによる凹凸加工 [Fig.1(c) (d)]
紫外線フォトレジストの OFPR を浸漬により金属ワイヤに塗布し，円筒面を 5 回に分けてパターンを露光し，現像する．その後，金属ワイヤのウットエッチングにより凹凸面を製作する．金属材料は，アルミと真鍮を用いた．マスクパターンは直径 100 μm の円形で，間隔は 80 μm である．

2.2. 支持力の測定

前節で製作した支持脚を用いて，水面からの高さ（深さ）と支持力の関係を測定した．支持脚は長さ 30mm で，端部を上向き 60 度に折り曲げたものを用いた．支持脚を平行平板ばねの先端に水面と平行になるように固定し，Z 軸ステージで水面の高さを変化させる．水面と支持脚が接触する瞬間を高さのゼロ点として，支持脚が完全に水没するまで水面を上昇させ，水面と支持脚の相対高さと支持力を平行平板ばねとレーザー変位計を用いて測定した．また脚が水没した状態から水面を降下させた際に脚にかかる力（引き離し力）も測定した．各支持脚の直径，接触角を Table 1 に，支持力と水面からの高さの測定結果を Fig. 2 に示す．直径の大きい脚の方が大きな支持力が得られることが確認された．ただしこれは浮力の差によるものであり，脚の自重を差し引いた支持力はどの脚も同程度となる．一方，引き離し力は接触角が大きいほど小さくなる．

2.3. 共振を利用した水面移動ロボット

表面に凹凸加工を施した撥水性の支持脚を用いて，表面張力で水面に浮き，脚の共振を利用して移動するロボットを製作した．ロボットの外観と脚の配置を Fig.3 に示す．支持脚は，振動による表面構造の剥離を防ぐため，直径 0.5mm の真鍮線をエッチングしたものを用い，12 本の脚を放射状に配置した．アクチュエータには偏心質量を持つ振動モータを用い，PWM (Pulse Width Modulation) 制御により振動数を制御した．支持脚は 2 次モードの共振により円軌道を描いて振動し，水面を蹴ることによってロボットが推進する．また，Table 2 に示すように各脚の長さが異なっており，振動数によって共振する脚が変化し，109Hz で直進，115Hz で右旋回，132Hz で左旋回が可能である．リチウムポリマー電池とモータ，制御回路を搭載し，質量は 7.85g である．一方，脚の長さの合計は 1m であり，最大 16gf の支持力が得られるように設計されている．屋外で水面移動実験を行い，自立的に振動数を変化させ，水面上で直進，右旋回，左旋回を順次行わせることに成功した．風などの外乱があっても沈むことはなかった．移動速度は直進が 70mm/s，旋回が 50mm/s であり，旋回半径は右が 800mm，左が 700mm であった．これらの数値に差があるのは，共振する脚の長さと本数の違いによるものと考えられる．

Table 1 Supporting legs

Material	Diameter	Contact angle
PDMS	2.5mm	117°
SU8	1.1mm	128°
Aluminum	1.4mm	123°
Brass	1.0mm	123°

Table 2 Role and specifications of the legs

Leg No.	Role	Length	Resonant frequency	Duty factor
L-1,6, R-1,6	Support	85mm	—	—
L-3,4, R-3,4	Straight	90mm	109Hz	32%
L-2,5	Right turn	80mm	115Hz	34%
R-2,5	Left turn	70mm	132Hz	39%

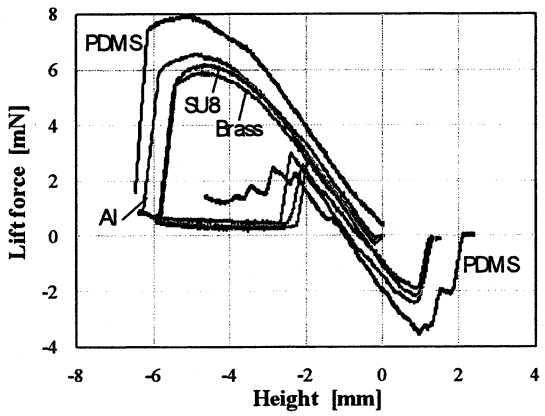

Fig.2 Lift and pull-off forces

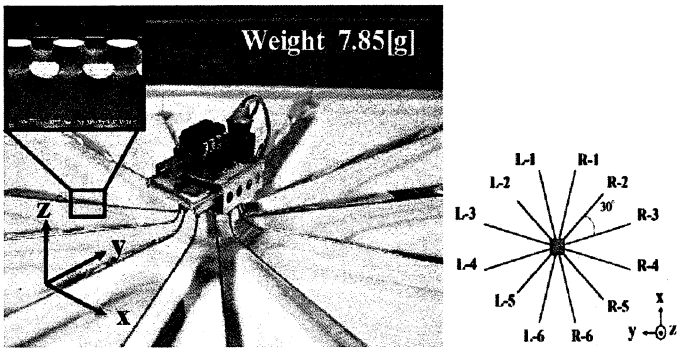

Fig.3 Water strider robot with microfabricated legs

3．液体を利用した壁面歩行ロボット

3.1　MEMS技術を利用した付着パッドの製作

アリの付着パッドを参考にして，ロボットの足底に装着する付着パッドを MEMS 技術を用いて製作した．付着面の材料としては，濡れ性が高くメニスカス力の利用が期待できるガラスと，柔軟で壁面との密着性が高く，大きな摩擦力が期待できる PDMS の２種類を製作した．パッドから液体を出せるように，パッド内部に流路を設け，付着面に直径 0.15mm の６個の穴を設けた．付着面の寸法は，ガラスパッドが 8×8mm, PDMS パッドが 8×7mm である．

3.2　付着力の測定

製作した２種類の付着パッドを用いて，ガラスウェーハ表面での垂直方向，接線方向の付着力を測定した．平行板ばねの先端にガラスウェーハを固定し，ウェーハ表面に付着パッドを垂直に押しつけて引き離すときの板ばねの変位をレーザー変位計で測定し，力を求めた．パッドがウェーハ表面から離れる瞬間の力を垂直方向の付着力とした．また，付着パッドをガラスウェーハに押し付け接線方向に引っ張るときの力を板ばねの変位より求め，パッドが滑りだした瞬間の力を接線方向の付着力とした．

PDMS パッドの付着力は，液体の有無でほとんど差が見られなかったため，液体を使わずにドライの状態で測定を行った．Fig.3 に垂直方向の押し付け力と付着力の関係を示す．押し付け力の増加とともに付着力の増加が見られた．これはパッドの変形により接触面積が増加したためと考えられる．また，接線方向には，押し付け力 20mN のとき 90mN の付着力が得られた．

ガラスパッドの付着力の測定では，液体として純水を用い，ピペットを用いて外部からウェーハ表面に供給して実験を行った．Fig. 4 は，ガラスパッドの垂直方向，接線方向の付着力と供給した水の量の関係を示したものである．垂直方向の付着力は，水が無いときにはほとんど働かず，水が 0.3μl のときに最大値 450mN の力が得られた．これは主にメニスカス力によるものと考えられる．一方，水平方向の付着力は 50mN 以下の小さい力しか得られなかった．

3.4. 壁面歩行ロボットの製作

前節の測定により得られた２種類の付着パッドの特性を生かして，壁面および天井面を歩行する６脚歩行ロボットを製作した．接線方向の付着のために各脚の先端に PDMS パッドを配置し，垂直方向の付着のために腹部にガラスパッドを１枚搭載した．ガラスパッドには 0.3μl の水を外部から供給し，接線力が小さいことを利用して歩行中は壁面上をすべらせるようにした．脚の機構には Fig.6 のようなリンク機構を用いて直角三角形に近い軌道を描くようにし，対角の３本の脚を同時に上げる交互三脚歩行を行わせるように設計した．脚を直角三角形の斜辺に沿って斜めに上げることにより，脚の引き離しに必要な力を小さくすることができる．ロボットの質量は，３本の PDMS パッドの接線方向の摩擦力で支持できるように，モータを含めて 9.5 g とした．垂直面では，重力により壁から離れようとする後脚まわりのモーメントを付着力で打ち消す必要があるため，ガラスパッドを前方に配置した．一方，天井面を歩行する際には，重力と付着力を釣り合わせるため，ガラスパッドの位置を後方の重心位置に変更した．

3.5. 歩行実験

ガラスパッドにあらかじめ純水を 0.3μl 付け，ロボットをガラス面に付着させた状態から垂直面，天井面での歩行実験を行った．その結果，どちらの面においても交互三脚による歩行に成功した．歩行の様子を Fig.7 に示す．

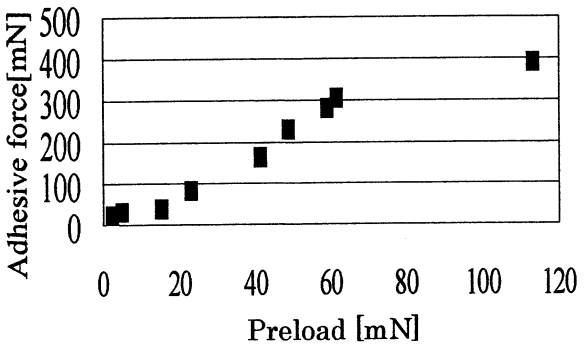

Fig.4　Normal adhesive force of PDMS pad

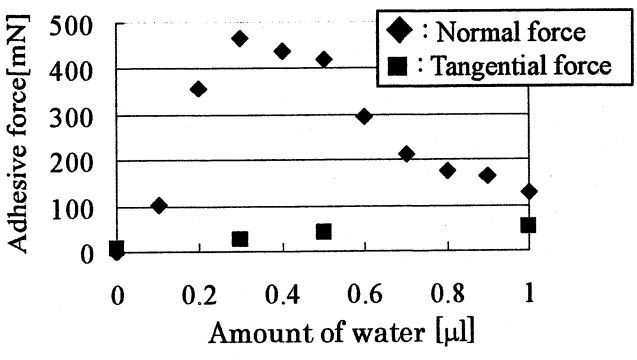

Fig.5　Adhesive force of glass pad

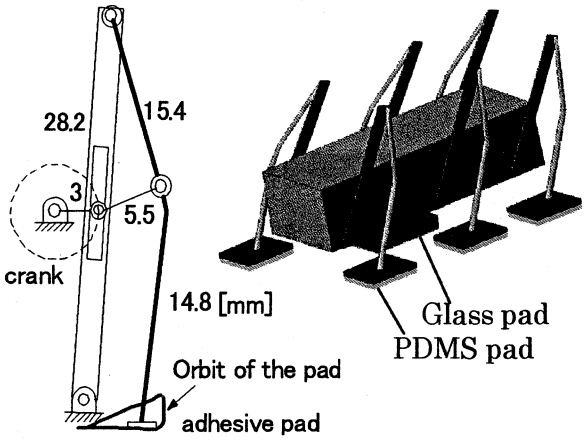

Fig. 6 Mechanism of leg and robot

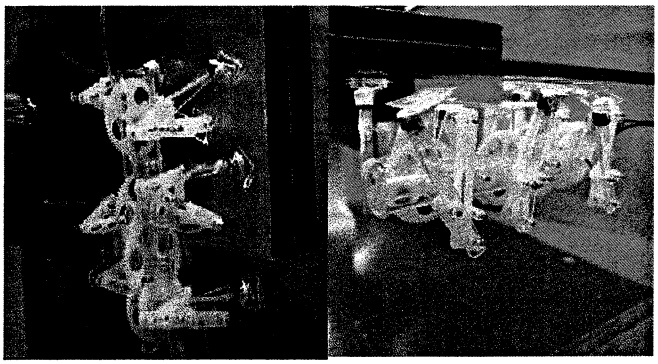

Fig.7 Photographs of hexapod robot walking on vertical and inverted glass surfaces

4．結言

本研究では，アメンボの水面移動，アリの壁面歩行と脚の表面構造の関係を調べ，MEMS 技術により昆虫と同様な機能を持つ表面構造を製作し、性能評価を行った，また，これらの機能性表面をロボットの脚に用いることにより，水面移動ロボット，壁面移動ロボットの開発を行った．水面移動ロボットに関して以下の成果が得られた．

1) MEMS 技術により真鍮線の表面に凹凸加工を施した 3 種類の撥水性支持脚を開発した．
2) 開発した脚の水面における支持力と引き離し力を測定し，支持力は脚の直径に依存し，引き離し力は接触角に依存することを確認した．
3) 開発した支持脚を用いた水面移動ロボットを製作し，脚の共振を利用して水面上での直進，旋回移動に成功した．

壁面歩行ロボットに関して以下の成果が得られた．

1) アリの付着パッドを規範として，ガラスと PDMS のパッドを MEMS 技術により製作した．
2) 付着パッドの付着力を測定し，ガラスパッドは垂直力が大きく，PDMS は接線力が大きいことを確認した．
3) 2 種類のパッドの特性を生かしたロボットを製作し，壁面，天井面での歩行に成功した．

参考文献

1) Davld L. Hu, et al., "The hydrodynamics Water Strider locomotion" Nature, Vol.424, 2003, pp. 663-666.
2) Kellar Autumn, et al.: Adhesive force of a single gecko foot-hair, NATURE, VOL 405, 2002, pp.681-685.
3) Walter Federle, et al.: Biomechanics of ant adhesive pads: frictional forces are rate- and temperature-dependent, Journal of Experimental Biology, 207, 2004, pp.67-74.

研究業績　（国内口頭発表は省略）

Ⅰ 審査付き論文

(1) 鈴木 健司，小池 裕之，髙信 英明，三浦 宏文，"表面張力を利用した水面移動ロボットの研究，機械学会論文集 C 編, Vol.75, No.3, 2009, (掲載決定).

Ⅱ 国際会議論文（審査付き）

(1) Kenji Suzuki, Hideaki Takanobu, Kota Noya, Hiroyuki Koike, and Hirofumi Miura, "Water Strider Robots with Microfabricated Hydrophobic Legs," Proceedings of the 2007 IEEE/RSJ International Conference on Intelligent Robots and Systems (IROS07), San Diego, CA, USA, Oct 29 - Nov 2, 2007, pp.590-595.

Ⅲ 解説記事

(1) 鈴木健司，"マイクロメカニズムにおける摩擦と潤滑，" 精密工学会誌, Vol. 74, No.9, 2008, pp.901-904.

Ⅳ 報道，インターネットでの公開

(1) 爆笑問題の日本の教養，FILE063「ロボットの虫」三浦宏文，NHK 総合，2009/2/24, 23:00-23:30. http://www.nhk.or.jp/bakumon/previous/20090224.html
(2) 未来をひらく昆虫テクノロジー (12)昆虫をまねて作るハイテクロボット，サイエンスチャンネル，2008/9/5 17:00-17:30. http://sc-smn.jst.go.jp/8/bangumi.asp?i_series_code=A070620&i_renban_code=012
(3) キャンパる：動物ロボ　自由自在 12 本足　アメンボ，毎日新聞　2007 年 10 月 26 日，夕刊, p.6, http://mainichi.jp/life/edu/news/20071026dde012070033000c.html.
(4) 工学院大がアメンボロボ 2 種開発，日刊工業新聞, 2007/5/21, p.19. http://robonable.typepad.jp/news/2007/05/20070521_7005.html

３．１．２ 作動温度低温化を目指した固体酸化物形燃料電池の電極・電解質材料開発と界面構造の制御

Development of SOFCs Working at Lower Temperatures by Controlling Interfacial Nano-Structures

長本英俊・大友順一郎*
工学院大学工学部環境化学工学科
*東京大学大学院新領域創成科学研究科環境システム学専攻

Nagamoto Hidetoshi and Junichiro Otomo*
Department of Environmental Chemical Engineering, Kogakuin University
*Department of Environment Systems, The University of Tokyo

The development of new electrolyte and electrode materials makes it possible to advance fuel cell systems that can satisfy the requirements of higher efficiency and reliability. Lowering operation temperature is an attractive solution for constructing reliable Solid Oxide Fuel Cell (SOFC) systems, whereas it increases overpotentials resulting from ohmic loss in electrolyte as well as charge transfer reactions on electrodes. Considering the above, the enhancements of ionic conductivity and electrode reactions are of significant importance. In this report, we investigate new approaches to enhancing ionic conductivity and electrode reactions in terms of controlling the interfacial microstructures of electrolyte and electrode materials.

1. 緒言　次世代の燃料電池として期待されている固体酸化物形燃料電池（SOFC）は、高温作動に起因する構成部材の劣化が問題になっており、その信頼性の向上は極めて重要な問題である。SOFC の作動温度を低温化は、その解決方法として有効であるが、低温作動の実現には従来材料よりも高いイオン伝導率を有する電解質材料や反応過電圧の低い電極材料の開発が必要である。本研究では、電解質および電極の微構造制御に着目し、特に界面の構造制御によるイオン伝導率の向上および電極の反応過電圧の低減を目的とした。昨年度まで（平成 19 年度以前）は、特に中温域(150–300 ℃)で作動する新規固体電解質形燃料電池の開発を目的とし、電解質の微構造制御およびプロトン伝導性酸素酸塩（リン酸二水素セシウム（CsH_2PO_4）等）の評価を行ってきた[1,2]。CsH_2PO_4/SiO_2 複合体の導電率と構造相転移挙動の観測を通じて、メソ細孔を有するシリカ粒子の添加により、降温過程において CsH_2PO_4 の高伝導相（立方晶）が臨界温度より低い温度まで保持されることが明らかとなった。また、観測された現象は、メソ多孔質シリカと CsH_2PO_4 の間における界面応力によって CsH_2PO_4 の構造相転移の過冷却現象が生じたためと結論づけた[3]。

本年度（平成 20 年度）は、SOFC の作動温度の低温化のための材料開発を行った。上述の酸素酸塩に限らず、ナノスケールの界面ではイオン輸送現象に関わる特異な現象が期待される。SOFC の電解質材料や電極材料においても、界面における結晶の不規則化や酸素空孔濃度の変化によるイオン導電率への影響が予想される。以上を考慮して、本検討では SOFC の中温作動用の電解質

材料候補である Y ドープ CeO_2(YDC)の薄膜化によるイオン導電率に対する影響について検討を行った。次に、空気極材料の微構造制御による空気極反応過電圧の低減に関する検討を行った。この系では、粒界（結晶/結晶界面）特性の利用による空気極性能の向上に着目し、緻密薄膜電極の微構造を制御することによって、空気極内部の粒界部分とバルク内部分が酸素還元反応の素過程に与える影響について検証した。すなわち、現在空気極材料として検討されている $La_{1-x}Sr_xCoO_{3-\delta}$ および $La_{1-x}Sr_xMnO_{3-\delta}$ の緻密薄膜の粒径制御を行う（粒界の体積分率を変化させる）ことで空気極の高効率化の検討を行い、SOFC の更なる低温化に向けた指針を得ることを目的とした。

2. 実験方法

2. 1. セリア（CeO_2）系薄膜電解質

単相膜作製に RF マグネトロンスパッタリング装置を使用した。ターゲット材料は YDC（10% Y ドープ CeO_2）粉末を用い、石英ガラスプレート上に各粉末をプレス成形した試料をターゲットとして用いた。成膜は Ar もしくは Ar:O_2= 9:1（モル比）の雰囲気で行った。RF 電力を 2.3～4.7 W/cm^2、基板とターゲットの距離を 50 mm、成膜時間を 0.25 h～5 h、Ar 圧力を 10～60 mTorr と変化させ、石英基板、シリコン基板、カーボン基板上に成膜を行った。定性分析は SEM、FE-SEM、XRD および TEM により行った。全導電率は交流インピーダンス法（2 端子法）により評価した。

2. 2. 緻密薄膜空気極（$La_{1-x}Sr_xCoO_{3-\delta}$, $La_{1-x}Sr_xMnO_{3-\delta}$）

電解質として錠剤成型器でプレスして作製した $Ce_{0.9}Gd_{0.1}O_{2-\delta}$ (GDC)基板 (相対密度 93～95 %、厚さ 1.0～1.2 mm、直径 9 mm)を用いた。空気極材料としては $La_{0.9}Sr_{0.1}CoO_{3-\delta}$(LSC)粉末と $La_{0.7}Sr_{0.3}MnO_{3-\delta}$ (LSM)粉末を用いた。試料を石英シャーレ上に設置し、RF マグネトロンスパッタ装置を用いて RF 出力 100 W、Ar 圧力 35 mTorr、基板温度 400 ℃でそれぞれ 3 h 成膜し、緻密薄膜を作製した。成膜後、空気中で 600 ℃もしくは 1000 ℃の熱処理による粒径制御を行うことで、粒界の体積分率を変化させた。FE-SEM を用いて薄膜の断面及び表面構造を観察し、XRD を用いて結晶組成の評価を行った。直流法及び交流インピーダンス法を用いて 400 ℃～600 ℃の領域で三端子法により電気化学測定を行った。作用極には空気極薄膜を成膜した試料を用いた。また対極には Pt ペーストを用いた。参照極には電解質に Pt 線を巻きつけて使用した。空気極薄膜の界面導電率 σ は式(1)より算出した。

$$\sigma = \frac{1}{SR} \quad \cdots(1)$$

（σ: 界面導電率 [S cm^{-2}]、 S: 空気極面積 [cm^2]、 R: 電極抵抗 [Ω]）

3. 実験結果および考察

3. 1. YDC 薄膜電解質の合成と導電率評価

3. 1. 1. YDC 単相膜の成膜

圧力（15～35 mTorr）、基板(シリカガラス, 結晶 Si)、基板温度の各パラメーターを変化させて成膜を試みた。XRD 測定の結果から、いずれの成膜条件においても目的物質である YDC の生成が確認された。Fig. 1 に Si 基板上に成膜した YDC 膜形態の SEM 断面写真を示す。Fig. 1(a) は基板無加熱で成膜した試料であり、Fig. 1(b) は基板加熱(600 ℃)で成膜した試料である。Fig. 1(a) の断面と比較して、Fig. 1(b) の断面はより均一で平滑な膜の形態を確認できた。また、熱処理を加えることで、(111)面方位に配向した結晶性

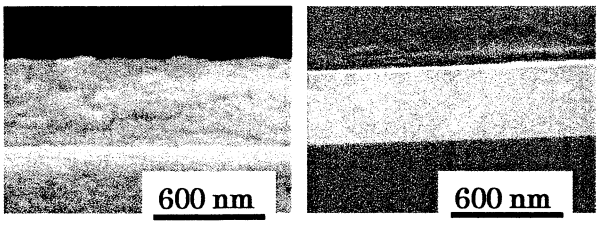

(a)基板無加熱　　(b)基板加熱(600℃)

Fig. 1 YDC 薄膜の SEM 断面写真
（Ar　35 mTorr, 出力 4.7 Wcm^{-2}）

の高い薄膜の生成を確認した。したがって、YDC 単相薄膜の作製は比較的低温の処理においても容易に作製可能であることがわかった。

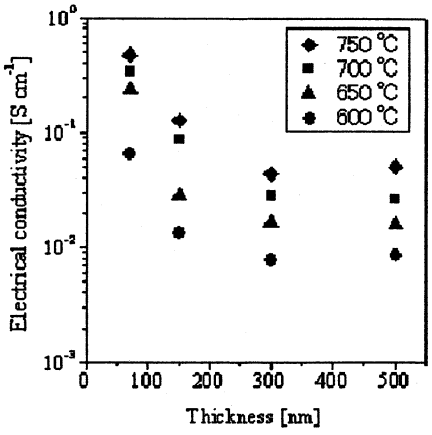

Fig. 2 YDC 薄膜における導電率の膜圧依存性

3. 1. 2. YDC のイオン導電率

基板温度 600 ℃、成膜時間 30 min、1 h、3 h で成膜した試料を用意した。膜厚はそれぞれ 70 nm、150 nm、300 nm、500 nm である。試料は 800 ℃で熱処理した後、導電率測定を行った。Fig. 2 に導電率の膜厚依存性を示す。この結果より、膜厚が薄くなるに従って導電率が上昇する現象が観測された。この傾向は 100 nm 以下の膜厚で顕著である。100 nm 以下の薄膜における導電率上昇の機構は明確ではないが、一つの可能性として、基板と YDC 薄膜の界面における YDC 結晶構造の不規則化によってもたらされた酸化物イオン伝導特性の向上による現象であることが推察される。微構造の制御によって導電率の上昇が生じることから、SOFC 低温作動の方策の一つとして有効な手段であると結果である。

3. 2. $La_{0.7}Sr_{0.3}MnO_{3-\delta}$(LSM)および $La_{0.9}Sr_{0.1}CoO_{3-\delta}$(LSC)緻密薄膜空気極の合成と導電率評価

3. 2. 1. LSM および LSC 緻密薄膜の成膜

XRD 測定結果より、GDC 基板上における LSM および LSC の合成が確認された。600℃および1000℃の熱処理を行うことにより XRD 回折パターンの半値幅が減少し、薄膜の結晶性が向上することが確認された。また、SEM 観察より、LSM および LSC の緻密薄膜が形成されていることを確認した。シェラーの式と SEM 画像から各試料の粒径を評価した結果、600℃および 1000℃の熱処理によって粒径の制御が可能であり（LSM、LSC 共に： 600℃：粒径 10 nm～20 nm の微粒子；1000℃：粒径約 500 nm)、これらの試料を用いて粒径（粒界）が空気極反応に及ぼす影響について検討した。

3. 2. 2. 電気化学測定

＜直流法＞ Fig. 3 に直流法を用いて測定した各試料の空気極分極曲線を示す。Fig. 3 より LSC 薄膜において微粒子化による界面導電率の顕著な上昇を確認し、粒界の寄与による効果である可能性が示唆された。一方、LSM 薄膜においては粒径が大きい場合に界面導電率が上昇する結果が得られた。従って、特に LSC 薄膜においては微構造の制御により粒界の特性が反応に顕著な影響を与えることが示唆された。

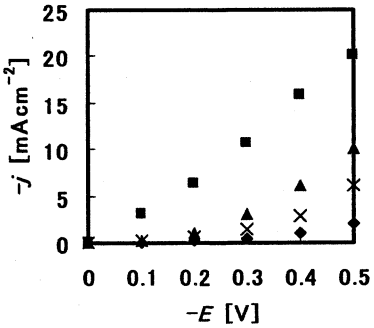

Fig. 3. 空気極分極曲線（測定温度：600℃）
■：LSC (600 ℃熱処理後)
▲：LSC (1000 ℃熱処理後)
◆：LSM (600 ℃熱処理後)
×：LSM (1000 ℃熱処理後)

＜交流インピーダンス法＞ Fig. 4 に交流インピーダンス測定から得られた Cole-Cole プロットの例を示す。Fig. 4 に示すように、3 つもしくは 2 つの半円が観測された。それぞれの半円の界面抵抗を R_H、R_M、R_L(または R_H、R_L)として、界面導電率 σ_H、σ_M、σ_L(または

σ_H、σ_L)を式(1)より算出した。時定数および電位依存性から、LSM と LSC 共に σ_L が電荷移動反応すなわち酸素還元反応に直接関与する界面導電率であると同定した。また、酸素分圧依存性の実験結果から、LSM 薄膜の場合、σ_L は酸素分圧の 0.26 次(≈1/4 次)に依存する結果が得られ、吸着酸素の電極表面拡散に由来すると考えた。一方、LSC 薄膜においての酸素分圧依存性を調べたところ、σ_L は負の依存性を示すことが確認された。Fig. 5 に粒径を変化させた場合の LSC と LSM の反応に関わる界面導電率(σ_L)の温度依存性を示す。Fig. 5 より、Fig. 3 と同様に LSC 薄膜における界面導電率の顕著な上昇が確認された。

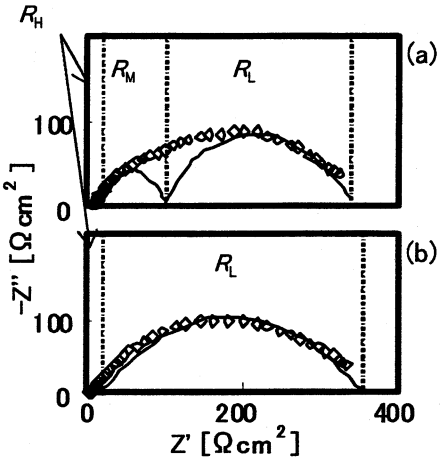

Fig. 4. Cole-Cole プロット
(a):LSM 1000 ℃熱処理後 600 ℃測定
(b):LSC 1000 ℃熱処理後 600 ℃測定

3. 2. 3. 粒界が酸素還元反応に及ぼす影響について

粒径制御が界面導電率に影響を及ぼした要因として、LSC と LSM の反応における律速過程の違いが考えられる。反応過程は、①：気相での酸素分子の拡散、②：電極表面での酸素原子の解離吸着、③：吸着酸素の電極表面拡散、もしくは③'：吸着酸素原子の電極バルク内への取り込みおよびバルク内拡散、④：空気極から電解質への酸化物イオンの移動、の４つの過程に分けられる。LSC 薄膜においては③'の過程の吸着酸素原子(O_{ad})が酸素空孔($V_O^{\cdot\cdot}$)に取り込まれる過程と後続のバルク内拡散が律速と考えられる。$V_O^{\cdot\cdot}$ は酸素濃度の減少に伴い増加することが予想され、$V_O^{\cdot\cdot}$ 濃度が吸着 O_{ad} の取り込み反応速度に影響を与えると考えられる。このことは、上述の LSC の σ_L が酸素分圧に対して負の依存性を示すことに矛盾しない。従って、粒界中の $V_O^{\cdot\cdot}$ 濃度がバルクのそれよりも高いことによって反応が促進されたと考えられる。一方、LSM 薄膜においては、酸素濃度依存性の結果から③の吸着酸素の表面拡散が律速であり、粒界の寄与が顕著でなかったと考えられる。

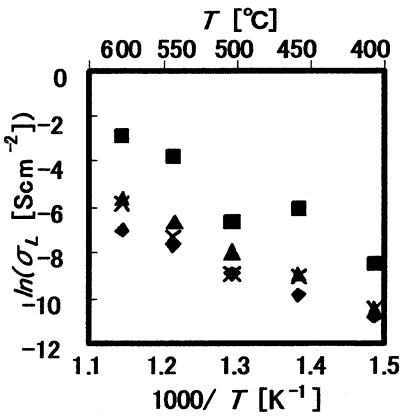

Fig. 5. 空気極分極曲線 測定温度 600℃
■：LSC (600 ℃熱処理後)
▲：LSC (1000 ℃熱処理後)
◆：LSM (600 ℃熱処理後)
×：LSM (1000 ℃熱処理後)

4. まとめ

SOFC の電解質および電極材料における微構造制御（界面構造制御）がイオン伝導および電極反応に及ぼす影響について検討し、微構造制御が SOFC の低温作動化に有効な手段であることを実験的に実証した。

引用文献

[1] J. Otomo, S. Wang, H.Takahashi and H. Nagamoto, *J. Membr Sci,* **279**(1-2), 256-265 (2006).

[2] J. Otomo, R. Kurokawa, H. Takahashi and H. Nagamoto, *Vacuum*, **81**(8), 1003-1011, (2007).

研究業績

[1] Junichiro Otomo, Takashi Ishigooka, Tomoyuki Kitano, Hiroshi Takahashi and Hidetoshi Nagamoto "Phase transition and proton transport characteristics in CsH_2PO_4/SiO_2 composites" *Electrochimica Acta* **53**(28), 8186–8195 (2008).

３．１．３ ナノコンポジットの結晶化挙動に及ぼす充填材の影響について

－カーボンナノファイバー充填ナノコンポジットの構造と物性－

Influence of Filler on Crystallization Behavior of Nanocomposites

－Structure and Physical Properties of Carbon Nano Fiber filled Nanocomposites－

西谷　要介，佐藤　貞雄

Yosuke Nishitani, Sadao Sato

工学院大学　工学部　機械工学科

Department of Mechanical Engineering, Faculty of Engineering, Kogakuin University

The internal structure and mechanical properties were investigated for two kind of carbon nanofiber (CNF) filled nanocomposites (VGCF/PBT, VGCF-S/PBT) and the ternary nanocomposites (VGCF/PBT/TPE), which are PBT filled with CNF and various functionalized TPE. Influence of fiber diameter of CNF and addition of TPE on internal structure, mechanical and tribological properties of these composites differed for each property. Izod impact properties and wear resistance were remarkably improved with the addition of various functionalized TPE It follows from results properties that the new tribomaterials with sufficient balances of mechanical and tribological properties for micro devices may be able to be developed.

１．緒言

近年，ナノサイズのフィラーを充填したナノコンポジットは，従来の高分子系複合材料とは異なり，ナノサイズによるユニークな性能や機能が発現されるので，盛んに研究開発が進んでいる[1]．一方，高分子材料および高分子系複合材料の性能は，材料の内部構造により左右されることも知られている[2]．特に結晶性高分子材料を用いた場合，結晶構造はマクロ物性に及ぼす影響が強く，結晶構造を制御する必要がある．しかしながら，結晶性高分子材料にナノフィラーを充填したポリマー系ナノコンポジットの結晶化挙動や結晶構造の制御を詳細に検討した研究はほとんどなく，データが不足しているのが現状である．そこで，筆者らはこれまでにナノコンポジットの結晶化挙動を把握するために，様々な検討を行ってきた．第一に，結晶化挙動を動的に観察するための手法として，従来のDSCを用いた手法とは異なり，CCDカメラを用いてリアルタイムに結晶化挙動を観察する手法を開発した[3]．第二に，その開発した結晶化挙動観察法を用いて，モンモリロナイトやマイカを充填したポリプロピレン（PP）系ナノコンポジット，さらにはポリ乳酸（PLA）やポリブチレンサクシネート（PBA）にナノフィラーを充填した生分解性樹脂系ナノコンポジットなどの結晶化挙動や，それらの機械的性質に及ぼす充填材の影響について検討してきた[4]．

今年度は，ナノコンポジットの結晶化挙動に及ぼす充填材の影響について，更に明らかにするため，エンプラなどの他の結晶性高分子やナノカーボン系充填材の適用，およびその応用例として機械摺動部材への展開を検討した．具体的には(1)カーボンナノファイバー（CNF）充填ナノコンポジット，(2)ポリアミド（PA）系ナノコンポジット，(3)生分解性樹脂系ナノコンポジットの３点である．本報告では，(1)CNF充填ナノコンポジットの代表例として，特にマイクロ機械向け摺動部材の候補であるCNF充填ポリブチレンテレフタレート（PBT）系ナノコンポジットについて，繊維径が異なる２種類のCNF充填やTPEの添加が，内部構造やそれらの諸物性に及ぼす影響を中心に検討した結果を報告する．

２．実験

２．１　材料

本研究に用いた材料は，２種類のCNF充填PBT複合材料（VGCF/PBTおよびVGCF-S/PBT）である．さらにCNFの分散状態および機械的性質の向上のため，VGCF/PBTにスチレン系熱可塑性エラストマー

(TPE)を添加した3成分系複合材料(VGCF/PBT/TPE)である. マトリックス樹脂は市販のPBT(PBT, 東レ(株)製, トレコン1100P), 充填材としては繊維径の異なる2種類のCNF(昭和電工(株)製, 気相成長炭素繊維, VGCFおよびVGCF-S)を用いた. Table1に2種類のCNFの物性を示す. VGCFおよびVGCF-Sの充填量は1,2,5,10vol.%である. また, TPEは全てスチレン系であり, エポフレンドAT501(SBS-EP, ダイセル化学工業(株)), セプトンHG252(SEEPS-OH, (株)クラレ), タフテックPシリーズMP10(SBBS-NH_2, 旭化成ケミカルズ(株))を用いた. また, SBS-EPはエポキシ基, SEEPS-OHは水酸基, SBBS-NH_2はアミン基を分子構造中に有するように変性処理を行ったグレードであり, 添加量は全て20wt.%に固定した. 3成分系複合材料(VGCF/PBT/TPE)の材料配合をTable 2に示す.

Table 1 Physical property of VGCF & VGCF-S

	Diameter	Length	Powder density	Aspect ratio
	nm	μm	g/cm^3	-
VGCF	150	10	0.04	67
VGCF-S	100	10	0.02	100

Table 2 Composition of ternary composites (vol.%)

Code	P	P1	P5	E	E1	E5	O	O1	O5	N	N1	N5
PBT	100	80	80	80	80	80	80	80	80	80	80	80
VGCF		1	5		1	5		1	5		1	5
SBS-EP				20	20	20						
SEEPS-OH							20	20	20			
SBBS-NH_2										20	20	20

2．2 成形

VGCF/PBTおよびVGCF/PBT/TPEの成形は, 予備乾燥(130℃×4h)させた各種材料をドライブレンドした後, 二軸押出機(東洋精機製作所(株), ラボプラストミルマイクロ2D15W)を用いて混練(250℃, 70rpm)した. その後, 再度予備乾燥を行い, 小型射出成形機(日精樹脂(株), NS20-2A)を用いて, 各種試験片を成形した. 成形機温度はノズル部, 前部, 中部および後部の順に, 250, 260, 250および240℃, 金型温度は80℃である. 射出成形により成形した各種形状の試験片を各種評価の試料とした.

2．3 実験

実験は, 結晶構造や内部構造などの観察, 溶融状態の動的粘弾性および各種機械的性質などを評価した. 結晶構造はDSC((株)島津製作所, DSC-50)を用い, 相対結晶化度を測定した. 各種複合材料中のVGCFの分散状態や添加材であるTPEの形態観察を行うため, 走査型電子顕微鏡(日本電子(株), JSM-6360LA, SEM)を用いた. SEM観察に用いた試料は, アイゾット衝撃試験後の試験片をトルエンに24時間浸し, 各種TPEを抽出させたものを, 金蒸着したものである. さらに複合材料中の構造を理解するために, SEMで撮影した画像を用いて, TPE分散相の粒径を定量的に評価した[5),6)]. 求めた値は, 個数平均径d_n, 面積平均径d_w, 体積平均径d_vおよび粒子間距離t_cである.

機械的性質としては, 引張り特性およびアイゾット衝撃特性を, さらに摩擦摩耗特性を評価した. 摩擦摩耗特性は, JIS K 7218A法に準拠し, 試験片および相手材(S45C)の表面を#800研磨紙で仕上げ, リングオンディスク型摩擦摩耗試験機(ORIENTEC(株)製, EFM-Ⅲ-E)を用いて測定した. 試験条件は, すべり速度を0.3m/s, 垂直荷重を50, 100および150N, 摩擦距離を1500mとした. なお, 試験開始から700m以降の摩擦係数から平均摩擦係数を算出した. なお, 流動成形時の基礎データ取得および, 材料の内部構造やその変化を把握するために, 平行円板型粘度計を用いた溶融状態の動的粘弾性も測定したが, 紙面の都合上, ここでは割愛する.

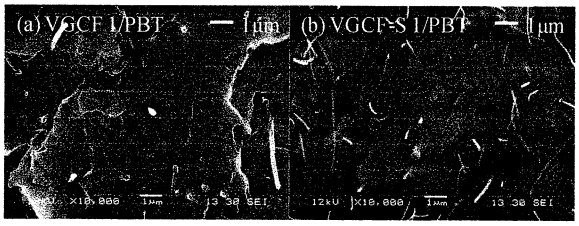

Fig. 1 SEM of VGCF/PBT and VGCF-S/PBT

3．実験結果と考察

3．1 CNF/PBTの物性に及ぼす繊維径の影響

Fig.1にVGCFとVGCF-Sをそれぞれ1vol.%充填した試験片のアイゾット衝撃試験後の破断面のSEM写真を示す. VGCFとVGCF-Sの充填系で比較すると, 両者の繊維径の違いだけでなく, 両者とも分散状態が良好であることがわかる. Fig.2に摩擦摩耗特性の代表的な結果としてVGCF/PBTおよびVGCF-S/PBTの比摩耗率V_sと繊維充填量の関係(150N)を示す. 比摩耗量V_sのV_f依存性は, 繊維径の違いに差はあるものの, 基本的にはV_fの増加に伴い, V_sは低下する. これはVGCFの充填により, 結晶構造が変化したこと

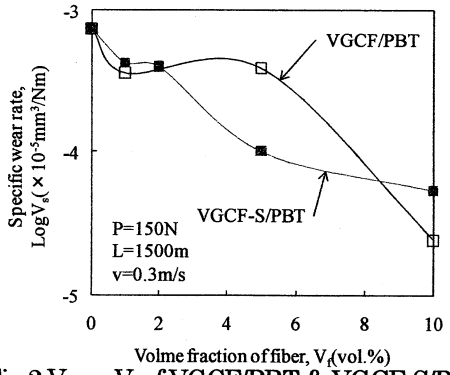

Fig.2 V_s vs. V_f of VGCF/PBT & VGCF-S/PBT

や弾性率等の機械的性質が変化したことによる影響が強く現れたためと考えられる．Fig.3 に VGCF/PBT および VGCF-S/PBT の相対結晶化度と V_fの関係を示す．V_f増加に伴い相対結晶化度が向上する．なお，スペースの都合上割愛するが引張り弾性率 E_t も V_fの増加に伴い上昇することを確認しており，CNF 充填により内部構造が変化し，それにより機械的性質や摩擦摩耗特性が改善されることを示している．

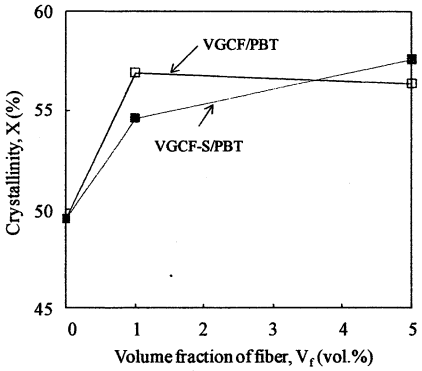

Fig. 3 Defgree of crystallinity vs. V_f of VGCF/PBT & VGCF-S/PBT

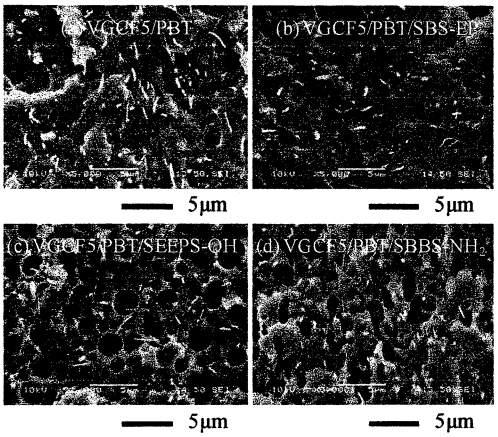

Fig. 4 SEM of the ternary nanocomposites

3．2　CNF/PBT に及ぼす TPE 添加の影響

3 成分系ナノコンポジット（VGCF/PBT/TPE）の内部構造を観察するために，アイゾット衝撃試験後の破断面をトルエンによりエッチング処理を施し，SEM 観察した結果の一例を Fig.4 に示す．VGCF が均一に分散しており，かつ TPE が独立した分散相を示している．また，SBS-EP 添加系で最も TPE 分散相の粒径が小さいことがわかる．この TPE 分散相の形状をより詳細に検討するために，SEM 画像から画像処理して求めた個数平均径 d_n，面積平均径 d_w，体積平均径 d_vおよび粒子間距離τ_cを Table3 に示す．TPE 分散相の粒径および粒子間距離は，エポキシ基（SBS-EP）＜水酸基（SEEPS-OH）＜アミン基（SBBS-NH_2）の順に大きくなり，エポキシ基を有する SBS-EP が最も PBT に対して微分散化するということがわかる．特に，τ_cを比較すると VGCF 無充填系では SBS-EP 添加系（No.E）に比べ SEEPS-OH 添加系（No.O）が 1.3 倍程度大きく，SBBS-NH_2添加系（No.N）が 3 倍程度大きい．これは SBS-EP 中に含まれるエポキシ基が他の官能基に比べ，PBT 中のエステル基との反応が強いためと考えられる．つまり，SBS-EP は PBT との相溶性が良好であるため，粒径および粒子間距離が小さくなることを示唆している．次に，Fig.5 にアイゾット衝撃値 a_{iN} と粒子間距離τ_cの関係を示す．a_{iN}は SBS-EP 添加系（No.E）に比べ SEEPS-OH 添加系（No.O）が 0.4 倍程度小さく，SBBS-NH_2添加系（No.N）も 0.2 倍程度小さい．つまり，前述したτ_cが小さくなるほど a_{iN} が高いことがわかる．この傾向は，Wu[6]による PA6/EPR の報告でも認められるものであり，官能基を付与した TPE 添加により TPE 分散相が微分散化するので，TPE とマトリックス樹脂間の界面領域が大幅に増加し，その結果としてせん断降伏変形による破壊エネルギーを吸収することが可能なるためと考えられる．最後に，摩擦摩耗特性として，比摩耗率 V_sと d_vの関係を Fig.6 に示す．d_vの減少に伴い比摩耗率 V_sは上昇し，耐摩耗性が低下することがわかる．これらの結果から，TPE 分散相を小さくすると衝撃特性は向上するが，分散相径が小さすぎると耐摩耗性は低下するので，使用される部位によりバランスを考えた材料配合設計が必要なことがわかる．

Table 3 Particle size of ternary nanocomposites

Code	d_n μm	d_w μm	d_v μm	d_w/d_n -	d_v/d_n -	τ μm
NH_2	1.13	1.77	3.13	1.56	2.76	0.47
NH_21	1.45	2.02	2.97	1.39	2.05	0.55
NH_25	0.95	1.09	1.41	1.15	1.49	0.32
OH	0.71	0.79	0.98	1.12	1.39	0.20
OH1	1.37	1.72	2.26	1.25	1.62	0.44
OH5	1.19	1.57	2.23	1.33	1.89	0.43
EP	0.51	0.57	0.71	1.11	1.39	0.16
EP1	0.45	0.50	0.58	1.11	1.31	0.14
EP5	0.49	0.54	0.64	1.08	1.29	0.16

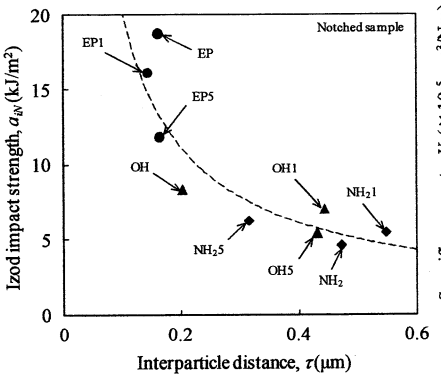

Fig.5 a_{iN} vs. τ_c of VGCF/PBT/TPE

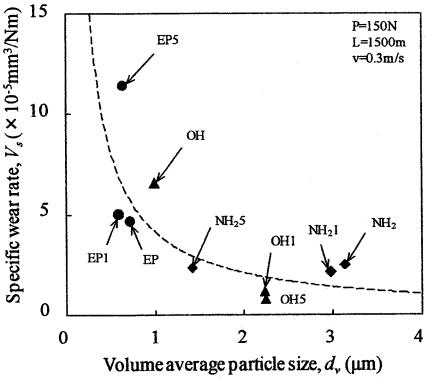

Fig.6 V_s vs. d_v of VGCF/PBT/TPE

4．結言

ナノコンポジットの結晶化挙動に及ぼす充填材の影響を検討するために，CNF 充填ポリブチレンテレフタレート（PBT）系ナノコンポジットについて，繊維径が異なる 2 種類の CNF 充填および TPE の添加が，内部構造やそれらの物性に及ぼす影響を中心に検討した結果，繊維径の異なる CNF の充填や TPE 添加により，内部構造が変化すること，およびそれらの物性が大きく影響を受けることを明らかにした．

謝辞

本研究で用いた VGCF および VGCF-S は昭和電工（株），またエポフレンドはダイセル化学工業（株），セプトンは（株）クラレ，タフテックは旭化成ケミカルズ（株）からそれぞれ提供を受けたものであり，各関係者のご支援に感謝致します．

引用文献

1) A. Schlarb, "Tribology of Polymeric Nanocomposites", Elsevier,(2008)
2) 小島盛男，"目で見る結晶性高分子入門" アグネ技術センター，(2006)
3) 佐藤貞雄，井上遼平，森下智史，高橋一矩，中島陽祐，高分子加工技術討論会講演要旨集，Vol.18th，No.12，(2006)
4) 満田諒，井上遼平，原良輔，佐藤貞雄，成形加工，19，730-735，(2007)
5) J.J. Huang, H. Keskkula, D.R. Paul, Polymer, 45, 4203, (2004)
6) S. Wu, Polymer, 26, 1855, (1985)

研究業績

Ⅰ審査付き論文

1) Yosuke Nishitani, Kohei Ohashi, Chiharu Ishii, Isamu Sekiguchi, Takeshi Kitano, "Influence of Addition of Styrene-ethylene/butylene-styrene Copolymer on Rheological, Mechanical and Tribological Properties of Polyamide Nanocomposites", Polymer Composites, in press, (DOI: 10.1002/pc.20767)
2) Yosuke Nishitani, Yoshinao Yamada, Chiharu Ishii, Isamu Sekiguchi, Takeshi Kitano, "Effects of Addition of Functionalized SEBS on Rheological, Mechanical and Tribological Properties of Polyamide 6 Nanocomposites", Polymer Engineering and Science, Submitted
3) 内藤貴仁，西谷要介，関口勇，石井千春，北野武，"気相成長炭素繊維充填 PBT 複合材料の機械的およびトライボロジー的性質に及ぼす熱可塑性エラストマー添加の影響"，成形加工，Submitted

Ⅱ研究報告

1) 満田諒，佐藤啓治，天野智啓，小野充智，佐藤貞雄，"PLA/PBS/天然繊維複合材の機械的物性に及ぼす充填材の影響"，工学院大学研究報告，Vol.105，11-16，2008 年 11 月
2) 満田諒，天野智啓，佐藤啓治，小野充智，佐藤貞雄，"ポリブチレンサクシネートアジペート(PBSA)複合材の機械的物性に及ぼす天然繊維(NF)の影響"，工学院大学研究報告，Vol.106　Submitted
3) R. INOUE, R.MITSUTA, Y. HARA, and S. SATO, "Influence of Fillers on Kinetic Crystallization Behavior and Mechanical Properties of Polypropylene Composites"，工学院大学研究報告，Vol.106　Submitted

Ⅲ研究発表（国際会議）

1) Yosuke Nishitani, Kohei Ohashi, Yoshinao Yamada, Sadao Sato, Isamu Sekiguchi, Takeshi Kitano, "Rheological, Mechanical and Tribological Properties of Nanocomposites Based on Polyamide with Functionalized SEBS Copolymers", Polymer Processing Society 24th Annual Meeting (PPS-24), Salerno, Italy, 17 June 2008, S11-455

Ⅳ研究発表（国内）

1) 満田諒，天野智啓，佐藤啓治，小野充智，佐藤貞雄，"PBS/天然繊維複合材の機械的物性"，成形加工'08，77-78，タワーホール船堀，東京，（口頭&ポスター発表）
2) 西谷要介，山田芳直，北野武，関口勇，"PA 系ナノコンポジットを 1 成分とするポリマーブレンドの溶融粘弾性"，成形加工'08，245-246，タワーホール船堀，東京，（口頭発表）
3) 内藤貴仁，西谷要介，北野武，佐藤貞雄，関口勇，"3 成分系ナノコンポジット（VGCF/PBT/TPE）を用いたトライボマテリアルの開発" 成形加工'08，247-248，タワーホール船堀，東京，（口頭&ポスター発表）
4) 西谷要介，内藤貴仁，関口勇，北野武，"VGCF/PBT の溶融粘弾性に及ぼす TPE 添加の影響"，成形加工シンポジア vol.2008，239-240，福井大学，福井，（口頭発表）
5) 満田諒，小野充智，佐藤貞雄，"PBS の結晶化挙動に及ぼす充填材の影響"，成形加工シンポジア'08，335-336，福井大学，福井，（ポスター発表）
6) 内藤貴仁，西谷要介，北野武，関口勇，"VGCF/PBT の機械的性質に及ぼす繊維径の影響"，成形加工シンポジア vol.2008，339-340，福井大学，福井，（ポスター発表）
7) 内藤貴仁，西谷要介，関口勇，北野武，"3 成分系（VGCF/PBT/TPE）複合材料における構造と物性の関係"，2008 年度材料技術研究協会研究討論会，P43（ポスター発表）（ゴールドポスター賞受賞）

３．１．４ コポリマーブラシを用いたナノ相分離構造薄膜の創製

Creation of thin films with nano-structure by intermolecular phase-separation of copolymer brush.

川井忠智、寺町信哉、伊藤雄三

Tadatomo KAWAI, Shinya TERAMACHI, Yuzo ITOH

マテリアル科学科

Department of Materials Science and Technology

Abstract: Hetero-arm cylindrical copolymer brushes were synthesized by free radical copolymerization of two kinds of macromonomers. Utilized macromonomers were polydimethylsiloxane, polystyrene, poly(methyl methacrylate) and poly(ethylene oxide) macromonomer. These macromonomers were copolymerized in the benzene solution. In the much combination system, there was the phase separation. The copolymer brushes were analyzed by dual detection size-exclusion chromatography, eluent gradient HPLC and FT-IR.

1. はじめに

ポリマクロモノマーは、末端に反応性基を持つ高分子(マクロモノマー)を重合することにより得られるブラシ状高分子で、側鎖間の排除体積効果により棒状分子としてふるまい液晶性を示すことが知られている。この棒の太さは、マクロモノマーの分子量により nm～数 10nm オーダーに調整できる。一方で、ブロックコポリマーやグラフトコポリマーは、それぞれの同じブロック鎖が集合し、ミクロ相分離構造を作ることがよく知られている。これらの性質を利用すれば、異種マクロモノマーの共重合により生成したブラシ状のコポリマクロモノマー、すなわちコポリマーブラシは、分子内相分離により自己組織化能を発揮し、配向したナノスケールの幅を調節できる縞状構造の表面を有する、ナノ相分離構造薄膜を創製することが期待できる。両ポリマクロモノマーの種類、主鎖および枝の分子量、などを調節することにより、こうした異種高分子によるナノスケールの縞状構造の実現は可能と考えられる。

本研究では、種々のマクロモノマーの組合せによる共重合を行いコポリマーブラシを合成し、その分子構造の解析を行う。それらのコポリマーブラシから薄膜を調製し、ナノ相分離構造薄膜の、分子構造と機能性の関係を明らかにすることを目的としている。

現在までに、ポリジメチルシロキサン(PDMS)、ポリスチレン(PS)、ポリメタクリル酸メチル(PMMA)、ポリエチレンオキシド(PEO)のマクロモノマー間の各組み合わせについて共重合を行い、共重合性について検討してきたが大部分の組み合わせは、異種ポリマー、共通溶媒系に特有の液-液相分離を示し、各々の相中で共重合が起こることが明らかとなった。本報告では、その主要な点を述べることとする。

2. 実験

2.1 試料

本研究では、ポリジメチルシロキサン-マクロモノマー(PDMS-m, MW 5,000, チッソ社提供)、ポリスチレン-マクロモノマー(PS-m, MW 6,000, 東亞合成社提供)、ポリメタクリル酸メチル-マクロモノマー(PMMA-m, MW 5,000, 東亞合成社提供)、ポリエチレンオキシド-マクロモノマー(PEO-m, MW 2,080 と MW 1,100, シグマアルドリッチ社製)を使用した。末端反応基は、いずれもメタクリル基である。なお示した分子量はカタ

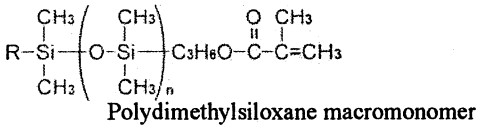

Polydimethylsiloxane macromonomer

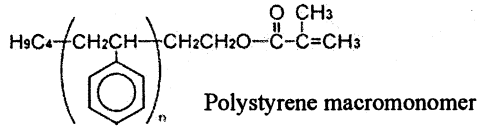

Polystyrene macromonomer

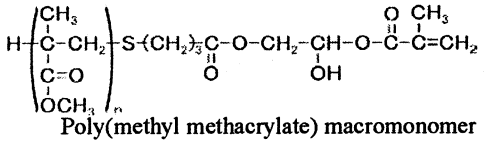

Poly(methyl methacrylate) macromonomer

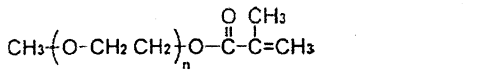

Poly(ethylene oxide) macromonomer

Fig.-1. Sample of macromonomers

ログ値である。

2.2 共重合系での相状態の確認

マクロモノマー(1)／マクロモノマー(2)／ベンゼン系の相状態を、反応温度と同じ60℃で確認した。

2.3 共重合

種々のマクロモノマーの仕込み組成において、溶媒にベンゼン、開始剤にAIBNを用い、60℃にてラジカル共重合を行った。共重合後、巨視的に2相分離状態が認められた系は、それぞれの相を分取しポリマー成分を回収した。

2.3 分子構造解析

コポリマーの生成確認には、SECを用いた。平均組成は、^{1}H NMRにより求めた。また、溶離液グラジエントHPLCにより組成分布の解析を、FT-IRにより高次構造の解析を、それぞれ試みた。

3. 結果と考察

3.1 Macromonomer 1／Macromonomer 2／Benzene系の相状態

相状態の確認は、Fig.-1 に示したマクロモノマーを組み合わせ行った。特徴的な組み合わせの擬三成分系相図をFig.-2に示す。

Fig.-2(a)には、PDMS-m／PS-m／Benzene系の相図を示した。溶媒約80%付近に相分離曲線が認められ、広い組成範囲で相分離することがわかった。さらに仕込み組成にかかわらず巨視的に相分離を起こし、相分離したそれぞれの相の組成が非常に偏り、上相は下相に比べ著しくスチレン含率が低かった。同様の結果は、PDMS-m／PMMA-m／Benzene系、PDMS-m／PEO-m／Benzene系、でも得られた。

Fig.-2(b)には、PS-m／PMMA-m／Benzene系の相図を示した。溶媒約50%付近に相分離曲線が認められ、若干曖昧さがあるものの巨視的に相分離を起こした。また、PS-m／PEO-m／Benzene系においても溶媒約50%付近に相分離曲線が認められたが、この系では、巨視的な相分離は起きず系全体が白濁した相分離状態であった。

Fig.-2(c) には、PEO-m／PMMA-m／Benzene 系の相図を示した。この系では、60℃において広い組成範囲で均一相となることが見出された。

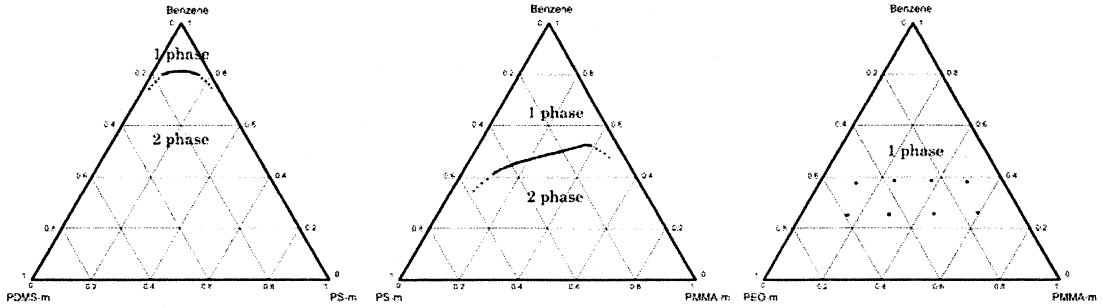

(a) PDMS-m／PS-m／Benzene (b) PS-m／PMMA-m／Benzene (c) PEO-m／PMMA-m／Benzene

Fig.-2 Cloud points curves of Macromonomer 1／Macromonomer 2／Benzene at 60℃

3.2 コポリマーブラシの合成と解析

コポリマーブラシの合成は、Fig.-1 に示したマクロモノマーの組み合わせで行った。そのうち PS-m／PMMA-m、PS-m／PEO-m について示す。

3.2.1 PS-m／PMMA-m／Benzene系

PS-m／PMMA-m／Benzene系では、均一系と相分離系で共重合を行った。

まず共重合に先立ち、溶媒50%での未反応の両相を分取しその組成を決定した。各相の組成は偏りが

Table 1. Preparation of Poly(PS-*co*-PMMA)by radical copolymerization in benzene at 60℃for 48h.

Sample Code	Feed (g)				Styrene Content (wt.%) [1]		
	PS-m	PMMA-m	Benzene	AIBN	phase	Composition in the respective phase	Fractionated Copolymer [2]
PSPMMA731	1.0507	0.4520	2.8198	0.0067			57.0
PSPMMA551	0.7750	0.7506	2.8100	0.0066			41.3
PSPMMA371	0.4497	1.0501	2.8306	0.0066			21.7
PSPMMA732	1.0575	0.4610	1.5252	0.0045	Upper	70.2	65.8
					Lower	44.9	44.0
PSPMMA552	0.7540	0.7590	1.5179	0.0045	Upper	55.6	45.9
					Lower	31.8	21.6
PSPMMA372	0.4532	1.0640	1.5096	0.0047	Upper	24.1	28.9
					Lower	23.7	21.6

1) Determined by ^{1}H NMR; JEOL ECX400, $CDCl_3$
2) Fractionated by SEC

あり、上相は下相に比べスチレン含率が高かった。

共重合は、種々のマクロモノマー仕込組成で、溶媒65%の均一系と溶媒50%の相分離系とで、開始剤にAIBNを用い60℃で48時間行った。均一系では重合終了まで均一1相で進行し、粗共重合体の回収率はほぼ100%であった。一方、相分離系では、重合の進行に伴い溶液の粘性が上昇した。重合後は、曖昧さはあるものの巨視的な2相分離状態であったため、それぞれの相を分取しポリマー成分を回収した。しかし粘性が高く回収に困難を伴ったため、回収率は85%から95%であった。回収した各試料の組成は、上相はスチレン含率が高く下相はスチレン含率が低く、概ね未反応系の各相の組成に対応していた。これは、重合過程において相分離した各々の相でマクロモノマーはその相の組成比で反応し、重合の進行に伴う各相の間での物質移動はあまり起こらないといえる。

SECにおいて、未反応マクロモノマーより高分子量側にコポリマーと考えられるピークが認められたため、SECによりコポリマーを分別しUV－RI二重検出SECにより見かけの分子量に対する組成を調べた。結果は、コポリマー部分のスチレン含率が未反応の各相に対応していた。相分離系では、それぞれの相で共重合が起こり、仕込み組成とは異なる組成のコポリマーが生成することが明らかとなった。

SEC分取したコポリマーを用い、HPLCによる組成分布の解析を試みた。しかし、いくつかの分離条件で検討したが、組成に応じた溶出位置とは異なる溶出のクロマトグラムが得られ、また、カラムへの試料残留が起こり、定量的な組成分布を明らかにすることはできなかった。コポリマーのカラムへの強い残留は、コポリマーブラシという特徴的な分子構造に由来することが示唆された。

これらコポリマーブラシについて高次構造の解析を、FT-IRにて試みた。粗共重合体の場合、仕込み組成に応じベンゼン環由来のシグナルのシフトと強度比変化がわずかに認められた。ただし、PMMA由来のシグナルには変化が認められなかった。一方、今年度SEC分取により得たコポリマーブラシは、粗共重合体の場合と異なり、変化は認められなかった。これらについて、ラマンによる解析を行い高次構造の詳細を検討する。

以上より、PS-m／PMMA-m／Benzene系では、未反応の組成と粗共重合体の組成および分別コポリマクロモノマーの組成があまり変化していないことから、相分離した各々の相での重合反応は、重合の進行に伴う各相の間での物質移動はあまり起こらないこと、さらに、両マクロモノマーの末端基が同じメタクリロイル基であることから、化学反応律速であれば予想されるように両者のモノマー反応性比は共に1に近い値であることが分かった。不均一系においても仕込み組成を検討することによりある程度任意の組成のコポリマーブラシを合成することは可能であると考えられる。

3.2.2 PS-m／PEO-m／Benzene系

PS-m／PEO-m／Benzene系では、PS-mとPEO-mの仕込組成は、3:7、5:5、7:3とし、溶媒65%の系と

溶媒55%で重合の進行に伴い相分離する可能性のある系とで、開始剤にAIBNを用い60℃で24時間行った。共重合開始直後は、均一相であったが重合の進行に伴い溶液の粘性が上昇し、すべての試料で白濁が認められたが、マクロな相分離は起こらなかった。また、溶媒 55%とした試料の多くにゲル成分を生じた。各試料は、凍結乾燥により回収した。

回収した粗共重合体の組成は、^{1}H NMR により求めたが、試料は、ゲル成分を含んだ状態で測定した。

この系では、未反応マクロモノマーとコポリマーは、SEC 的に分離が不可能であったため、透析により未反応PEO-m を溶媒抽出法により未反応PS-m の除去を試みた。未反応マクロモノマーの除去確認は、SECと、統計コポリマーの組成分別に有効であるHPLCを用い試みた。しかし、今回の試料は、ゲル成分の存在によりその解析ができなかった。なおPEO-m の単独重合も行い、ゲルの生成を確認したことから、PEO-m 中に二官能性モノマーが混在し架橋ゲルを生成した可能性があり、^{1}H NMR による組成解析からも可能性が示唆された。

Table 2. Preparation of Poly(PS-*co*-PEO)by radical copolymerization.[1)]

Sample Code	Feed (g)				Styrene Content (wt.%) [2)]
	PS-m	PEO-m	Benzene	AIBN	Composition in the respective phase
PSPEO(2)731	1.401	0.600	3.710	0.014	71.0
PSPEO(2)551	1.001	1.006	3.720	0.014	49.3
PSPEO(2)371	0.600	1.400	3.727	0.014	27.5
PSPEO(2)732	1.400	0.600	2.452	0.007	69.3
PSPEO(2)552	1.352	1.350	3.308	0.008	50.7
PSPEO(2)372	0.600	1.399	2.462	0.007	30.0

1) PEO macromonomer molecular weight: 2080, Solvent: benzene, Temp.: 60℃ Reaction Time; 24h.
2) Determined by ^{1}H NMR; JEOL ECX400, $CDCl_3$

Table 3. Preparation of Poly(PS-*co*-PEO)by radical copolymerization.[1)]

Sample Code	Feed (g)				Styrene Content (wt.%) [2)]
	PS-m	PEO-m	Benzene	AIBN	Composition in the respective phase
PSPEO(1)731	0.702	0.303	1.860	0.007	–
PSPEO(1)551	0.501	0.501	1.860	0.007	31.3
PSPEO(1)371	0.303	0.700	1.859	0.007	30.5
PSPEO(1)732	0.701	0.299	1.237	0.004	73.1
PSPEO(1)552	0.497	0.500	1.242	0.003	66.4
PSPEO(1)372	0.302	0.703	1.227	0.003	71.5

1) PEO macromonomer molecular weight: 1100, Solvent: benzene, Temp.: 60℃ Reaction Time; 24h.
2) Determined by ^{1}H NMR; JEOL ECX400, $CDCl_3$

これらコポリマーブラシについて高次構造の解析を、FT-IR にて試みた。粗共重合体と透析後のコポリマーブラシを比較すると、PEO 鎖-CH_2-由来のシグナルのシフトと強度比変化が認められた。主鎖構造となるPMMA 由来C=O シグナルには変化が認められないことから、未反応PEO-M が除去されることによりコポリマーブラシの側鎖構造が変化し、結果としてPEO鎖由来のシグナル変化が認められたと思われる。これらの変化が、どのような高次構造を示しているのかは、今後さらなる解析が必要である。

3.2.4 その他の系

PS-m／PDMS-m／Benzene 系、PDMS-m／PEO-m／Benzene 系とPDMS-m／PMMA-m／Benzene 系は、均一系ではマクロモノマー濃度が低いため、相分離系でラジカル共重合を行った。これらの系は均一相がきわめて狭く、このため極端に偏ったコポリマーブラシが合成された。PMMA-m／PEO-m／Benzene 系は、広い組成範囲で均一相となったため、種々のマクロモノマー濃度における共重合を検討した。結果、高PEO-m 組成においてゲル化が起こり多官能性PEO-m の混在も疑われた。この系でも、FT-IR による高次構造解析を試みた。現在その構造を解析中である。

4. まとめ

以上より、低マクロモノマー濃度領域では、反応性末端濃度が極端に低いため共重合が起こりにくい。重合が起こるためには、末端基濃度を上げる、すなわちマクロモノマー濃度を上げる必要がある。このため、マクロモノマーの組み合わせによって相分離した系となるが、均一相がきわめて狭い相分離系でなければ、ある程度はコポリマーブラシの組成を任意に調節することが可能であることが、PS-m／PMMA-m／Benzene 系により明らかとなった。

３．２．１　溶液からの核発生および結晶粒径分布の制御
Control of Nucleation and Size Distribution of Crystals from Solution

環境化学工学科　加藤　尚武
環境化学工学科　仲田　努
早稲田大学　平沢　泉
Department of Environmental Chemical Engineering　Naotake Katoh
Department of Environmental Chemical Engineering　Tsutomu Nakata
Waseda University Izumi Hirasawa

(Abstract) In order to generate nano-size crystals, we attempted to irradiate ultrasonic wave into a batch cooling crystallizer. In case of usual batch cooling operation, nucleation did not occurred at saturation concentration and occurred at supersaturation condition. Conversely, in case of batch cooling operation with ultrasonic wave, nucleation occurred at undersaturation concentration. Experimental results showed that KNO_3 crystal size of order 1 micrometer was obtained at undersaturation concentration by use of ultrasonic wave. Furthermore, we attempted to irradiate ultrasonic wave into a batch reactive crystallizer. Experimental results showed that by use of ultrasonic wave reaction and nucleation process were strongly influenced whereas crystal growth process was not influenced and $CaCO_3$ crystal size of order of 3 micrometer was obtained.

1.緒言

最近注目されている技術にナノレベルでの超微粒子の製造がある。超微粒子は通常の結晶では見られない、量子サイズ効果、面積効果、化学結合効果、体積効果などの多くの性質を有しており、その用途は医薬品や機能化学品、食品や触媒など多岐にわたって期待されている。

本研究では、まず、晶析操作の中で最も基本的な冷却回分晶析をとり上げ、これまでの種晶添加操作に加え超音波照射という新たな操作、さらにそれらをオンライン粒度分布測定装置(FBRM)によって観察した。そこから超音波照射を伴う晶析現象の理解、さらに操作条件の影響を把握し、最終的に超微粒子結晶の生成を目指すことを目的とした。

実験は硝酸カリウム（KNO_3）の冷却回分晶析を用いた。

次に、反応晶析に対して、超音波放射がどのような影響を与えるか、とくに反応物と生成物への超音波の影響そして核発生や結晶粒径およびその分布への影響を検討した。

実験は、塩化カルシウム($CaCl_2$)と炭酸ナトリウム(Na_2CO_3)から炭酸カルシウム($CaCO_3$)の結晶を生成する反応晶析を用いた。

2.理論

結晶成長が起こるためには溶液中に存在する溶質分子が脱水和を起こし、結晶の界面に拡散・吸着する必要がある[1)]。すなわち、界面に存在する溶媒分子を押しのけて、溶質分子が吸着しなければならない。一方、平沢らは、超音波照射により生成する気泡が壊れるときに周辺が非常に高圧になり、この圧力差を推進力として一次核化が起こり、そして結晶が生成するとしている[2)]。

このように、核発生、結晶成長への超音波の影響について諸説があるが、実験的に十分検討されているわけではない。

3.実験装置および方法

3.1 実験装置

実験装置の概略を Fig.1 に示す。

本実験の特長は、①のオンライン粒度分布測定装置（米国レーゼンテック社製）を用いて晶析槽内の結晶生成の刻々の変化を観察できることである。この装置の原理は、レーザービームが粒子を横切る時間と粒子径とが比例するということにもとづく。

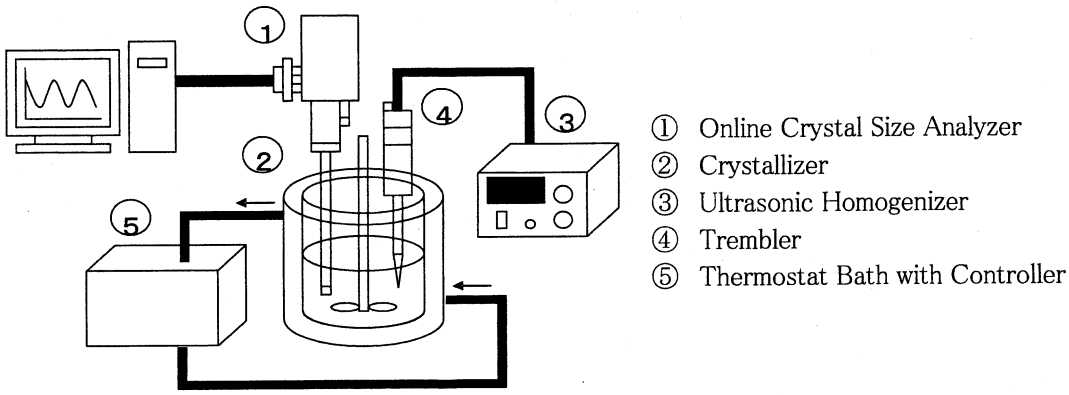

Fig.1 Schematic diagram of experimental apparatus

3.2 実験方法

3.2.1 冷却晶析

実験手順の概略を Fig.2 に示す。純水 200 [mL]を容量 500 [mL]のジャケット付晶析槽②に入れ、冷却水をジャケットに流し、純水を 35 [℃]程度にする。次に硝酸カリウム(KNO_3)を 75.68[g]純水に投入し、完全に溶かす。この 75.68 [g]は、純水 25 [℃]、200 [mL]での硝酸カリウムの溶解度に対応する。温度を測定開始温度 28 [℃]まで下げ、FBRM①による核発生および結晶成長の測定を開始し、プログラムバス⑤(東京理科器械社PCC-7000)によって 40 [min]かけて 20[℃]まで冷却した。超音波発生装置③(エスエムテー UH-50)は周波数 20 [kHz]、出力 50 [W]で測定開始とともに照射し、測定終了まで照射し続けた。前述したように本実験の特長は、回分冷却晶析における結晶成長の様子が FBRM①により、オンラインで測定できること、したがって、超音波の核発生、結晶成長への影響を刻々知ることができることである。また、FBRM は 0.5 μmから 1000μmまでの粒径を測定することができる。

超音波により晶析槽内に気泡が発生することは十分考えられる。そこで、結晶の有無、粒径は光学顕微鏡（オリンパス製、BX51）によっても測定した。このとき、サンプルの温度と室温がほぼ同じになるようにしてサンプル中の結晶の生成や溶解を防ぐために、温度範囲を 20℃から 28℃とした。

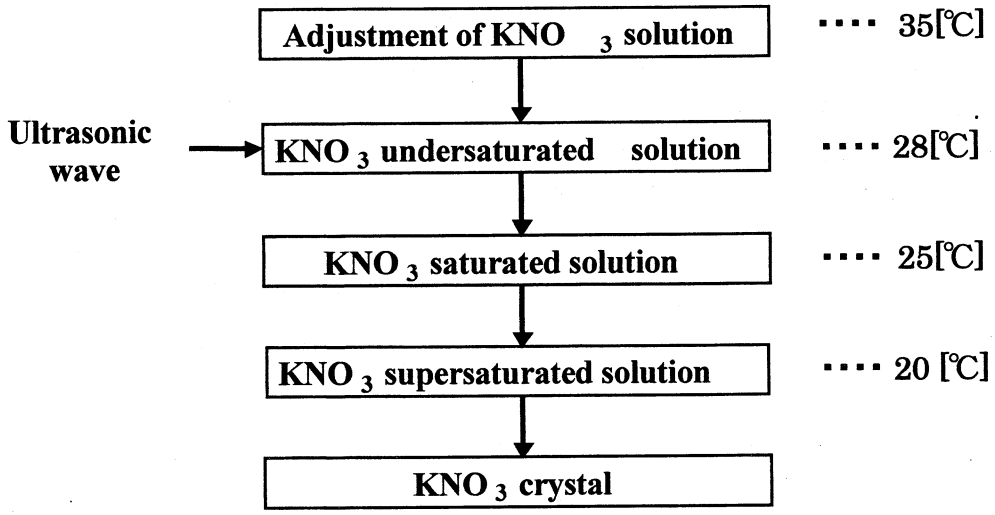

Fig.2 Experimental scheme

3.2.2 反応晶析

実験装置はほぼ Fig.1 と同様である。300mL の晶析槽に塩化カルシウム水溶液 100mL を投入、次に炭

酸ナトリウム水溶液を一気に供給すると同時に FBRM による核発生および結晶成長の観察、イオンメーターによる Ca^{2+}イオン濃度の測定を行なった。

4.結果及び考察

4.1 冷却晶析

超音波照射の核化、結晶成長および晶析槽内温度への影響を検討した。

超音波無照射の場合の実験結果を Fig.3 に示す。縦軸のカウント数はレーザー光線が粒子に当たり、その反射光を計数したもので、結晶個数に対応する。Fig.3 の通常の回分冷却晶析では、槽内温度が飽和温度 25℃に下がっても、結晶は観測されず、10 分ほど遅れて、約 23.3℃で結晶の生成が認められる。そして晶析熱により 2 分ほど温度が低下せず一定になっていることが認められる。実験開始から約 27 分までは FBRM のカウント数はゼロであり、光学顕微鏡による観察でも結晶は認められなかった。実験終了時,t=40 分における結晶粒径分布（CSD）を光学顕微鏡で観察した結果も Fig.3 に示す。このと FBRM によるカウント数の結果を比較すると両者の測定結果は大体一致している。

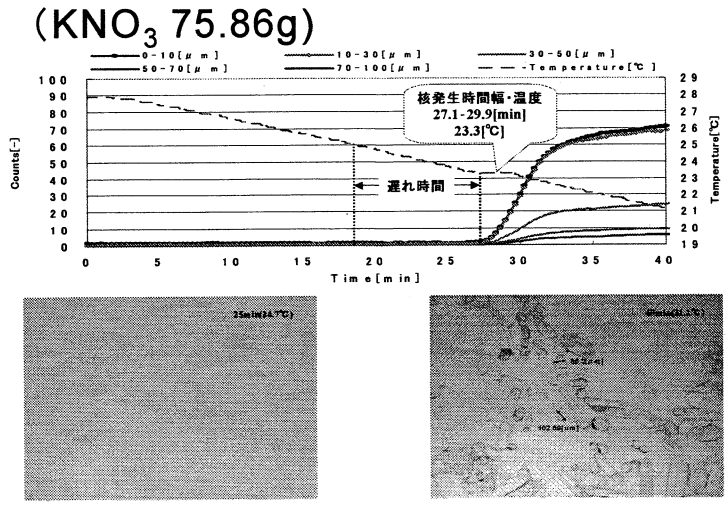

Fig.3 CSD and Temperature transients(without irradiation)

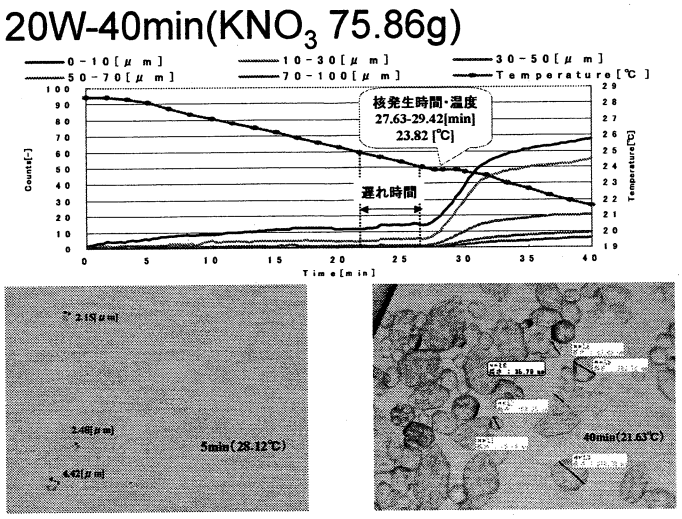

Fig.4 CSD and temperature transients(with irradiation)

Fig.4 は、槽内温度が 28℃になったときに超音波を照射したときの結果である。超音波のないときに比べて冷却による核発生の温度が 23.8℃と,Fig.3 の場合よりやや高い温度になっているがそれほどの差はない。興味深いのは、実験開始から冷却による急激な核発生にいたるまで、粒径 0～10μm および 10～30μm の微細結晶のカウント数がすこしずつ増加していることである。このカウント数は超音波による気泡の発生の影響を受けている可能性もあるので、晶析槽内の溶液を約 0.1mL サンプリングし、すばやく光学顕微鏡で観察した。その結果も Fig.4 に示す。 t =5min の場合は飽和温度 25℃以上の未飽和領域であり、それでも 1～5μm の範囲の結晶が生成している点が注目される。　超音波により、局所的に過飽和領域が実現された

ものと推測される。

4.2 反応晶析

超音波を照射しない場合の結果を Fig.5 に、照射した場合の結果を Fig.6 に示す。

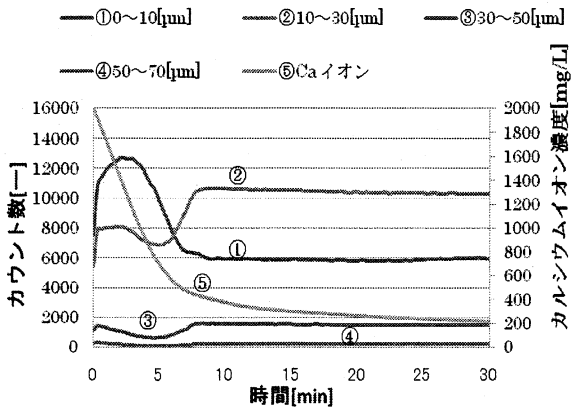

Fig.5 Experimental results(without irradiation)

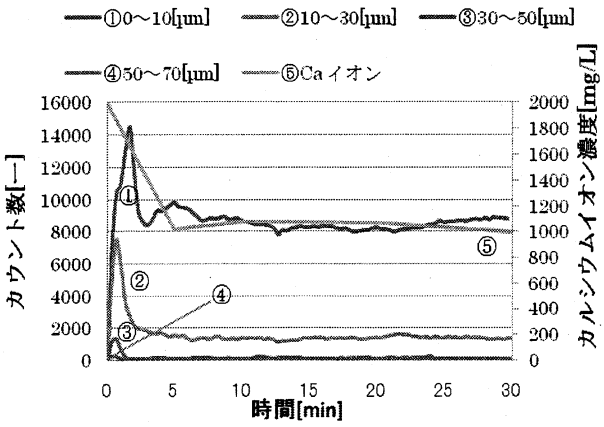

Fig.6 Experimental results(with irradiation)

Fig.5 では実験開始後約 7 分で①の微粒子結晶個数（カウント数）が減少し、②の 10～30 μm の大きな結晶個数が上まわっている。Ca^{2+}イオン濃度は 30 分後にはほぼ 90%が消費されている。典型的な逐次反応の形を示している。Fig.6 では、①と②の個数の逆転現象は起こらず、Ca^{2+}イオン濃度は 30 分後でも 50%しか消費されていない。これは超音波照射によって、①の微細結晶が再溶解する現象が起きていると考えることにより説明できる。

Fig.5,Fig.6 に対応して生成した結晶の顕微鏡写真をそれぞれ Fig.7,Fig.8 に示す。超音波を照射しない Fig.7 では、$CaCO_3$結晶の平均粒径は約 15 μm、また結晶の形状は丸い形であることがわかる。超音波を照射した Fig.8 では、結晶の平均粒径は約 3 μm となっており、超音波効果により生成結晶が微細化していることがわかる。結晶形状は歪になっておりこれも超音波効果によるものと考えられる。すなわち、超音波効果により、反応・核発生過程の促進、結晶成長過程の抑制が起きていることがわかる。

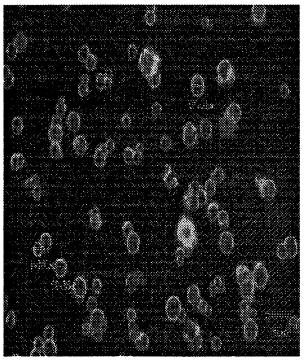

Fig.7 Crystal picture(t=30min) (without irradiation)

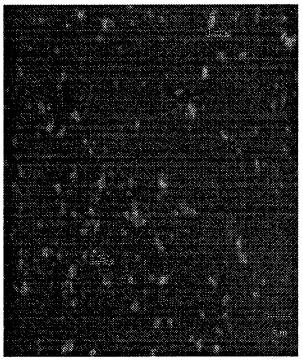

Fig.8 Crystal picture(t=30min) (with irradiation)

5. 結言

KNO_3 を用いた回分冷却晶析操作に超音波を照射する実験を行い次の知見を得た。

（1） 未飽和領域で 1～4 μm の微細結晶が生成していることを FBRM,光学顕微鏡で確認した。

（2） 超音波は冷却による結晶成長にはほとんど影響しないことがわかった。

$CaCl_2$ と $NaCO_3$ から $CaCO_3$ を生成する反応晶析操作に超音波を照射する実験を行い次の知見を得た。

（3） 反応・核発生過程では核発生を促進するが、再溶解により反応を抑制する効果を示した。

（4） 結晶成長過程では超音波効果は認められなかった。

引用文献 1）佐藤 清隆他：溶液からの結晶成長,p95、共立出版（2002） 2）小寺、黒谷、平沢：化学工学会第 39 回秋季大会（2007）

研究業績 1．長谷部 拓、加藤 尚武、平沢 泉：化学工学会第 72 回年会、福岡（2007） 2．後藤 雄一、加藤 尚武、平沢 泉：化学工学会第 40 回秋季大会(2007) 3．長谷部 拓：工学院大学修士論文（2007） 4．後藤 雄一：工学院大学修士論文（2008） 5．仲田 努：工学院大学修士論文(2009)

３．２．２　ナノ表面制御による白金族触媒の白金族使用量の低減または代替

Reduction in platinum use or substitution of platinum by nano surface control for platinum-based catalyst

五十嵐 哲、飯田 肇
Akira IGARASHI, Hajime IIDA
工学院大学工学部 環境化学工学科
Department of Environmental Chemical Engineering,
Faculty of Engineering, Kogakuin University

Abstract

In order to reduce in the Pt use for the Pt-Re/TiO_2(R: Rutile) catalyst for water gas shift reaction at low-temperature, the effect of the drying conditions in the catalyst preparation on the catalytic properties and activities of Pt-Re/TiO_2(R) catalysts was examined. As the results, the SubCD (Sub-Critical Drying) was an effective preparation method for the enhancement in the Pt dispersion. The SubCD catalyst prepared with $Pt(C_5H_7O_2)_2$ exhibited superior catalytic activity for LT-WGS at 250 °C compared with a commercial Cu/Zn catalyst.

1.　緒言

白金族触媒は、石油化学工業における重質ナフサの改質やオレフィンの水素化を始めとして、自動車の排ガス浄化や揮発性有機化合物(VOC)の分解など、さまざまな触媒反応に使用されている。通常、白金族触媒は、担体とよばれる高比表面積をもつ活性炭および無機酸化物などの表面上に金属を分散させた担持金属触媒として使用される。白金族は、資源量の制約があり高価であるにもかかわらず、最近では環境保全触媒としての利用が急増しており、これらの触媒の白金族使用量の低減あるいは白金族代替触媒の開発が切望されている。

さて、固体高分子形燃料電池(PEFC)のための炭化水素の水蒸気改質による水素製造プロセスでは、PEFC の燃料極を被毒する CO の低減のために、改質工程に続いて低温水性ガスシフト(LT-WGS)反応が行なわれる。通常、LT-WGS 反応に用いられる Cu-Zn 系触媒は低温ですぐれた活性を示すものの、酸化雰囲気下での耐久性に問題があることから、白金族触媒を適用する試みがある。しかし、白金族触媒は Cu-Zn 系触媒と比べて低温活性が低いことから、触媒反応器の小型化および白金族使用量の低減のために、すぐれた触媒活性を示す担持白金族触媒の開発が必要とされている。

そこで本研究においては、白金族のなかでも LT-WGS 反応にすぐれた触媒活性を示す担持 Pt 触媒の活性向上および Pt 使用量の低減のために、担体の種類、Re 添加、および Pt 出発原料が Pt 分散度や触媒活性に与える影響について検討を加えたところ、前年度までにビスアセチルアセトナト白金を用いて調製した Pt-Re/TiO_2(R)がすぐれた触媒活性を示すことを見いだした。本年度は、担体上への Pt の高分散担持のために、触媒調製法について検討を加え、Pt-Re/TiO_2(R)の一層の高機能化を図った。

2.　前年度までの研究成果

触媒の調製方法、触媒の性能試験や物性測定は、既報 [1), 2)]に示した通りである。まず、担体の種類が触媒活性や Pt 分散度に与える影響について検討を加えた。Table 1 に担持 Pt 触媒の触媒活性と物性を

Table 1 Effect of support on the catalytic activity and properties

Catalyst[1]	BET surface area (m^2/g)	Pt particle size[2] (nm)	Pt dispersion[2] (%)	CO conversion[3]	Catalytic activity per unit mass of Pt (mol-CO/(h g-Pt))
Pt/Al_2O_3	180	2.24	50.5	1.7	0.30
Pt/ZrO_2	75	2.38	47.6	16.9	1.76
Pt/TiO_2(R)	44	2.94	38.6	52.3	6.05

1) Pt 3wt%, Pt precursor: H_2PtCl_6 $6H_2O$

2) After LT-WGS

3) Feed gas: CO(99.95%), Reaction temperature: 250°C, H_2O/CO = 1.5, S.V. (on the basis of CO) = 9,500 h^{-1}

示したが、Pt/TiO_2(R:Rutile)は Pt/Al_2O_3 や Pt/ZrO_2 と比べてBET表面積とPt分散度が低いにもかかわらず、CO転化率が高いことがわかる。このことは、Ptの分散状態よりもPtと担体の相互作用による活性点の質的な変化が触媒活性に大きな影響を与えていることを示唆している。Pt 1g当たりの触媒活性を比較すると、Pt/TiO_2(R)のそれは Pt/Al_2O_3 の約20倍であり、TiO_2(R)の使用が大幅な触媒活性の向上とPt使用量の低減に効果があることが示された。

つぎに、Reの添加について検討を加えた。Table 2に Pt/TiO_2 (R)と $Pt\text{-}Re/TiO_2$ (R)のTEM像から得ら

Table 2 Catalytic activities and properties of Pt(3wt%) and Pt-Re(3wt%-2wt%) catalysts (Pt precursor: H_2PtCl_6 $6H_2O$)

Catalyst	Pt particle size[1] (nm)	CO conversion[2] (%)	TOF[2),3)] $\times 10^2$ (s^{-1})	Catalytic activity per unit mass of Pt (mol-CO/(h g-Pt))
Pt/TiO_2 (R)	3.2	33.0	16.9	1.11
$Pt\text{-}Re/TiO_2$ (R)	2.1	65.0	21.6	2.18

1) Pt particle size was estimated from TEM images.

2) Feed gas: Mixed gas (CO(10%)-CO_2(15%)-H_2(75%)), Reaction temperature: 225 °C, H_2O/CO = 5.0, S.V.(Total) = 40,000 h^{-1}.

3) TOF was calculated from the Pt particle size on TEM micrograph.

れたPt粒子の平均径(メジアン径)とCO転化率、それらから算出したTOF、Pt 1gあたりの触媒活性を示した。表から、Pt/TiO_2 (R)へのRe添加がPt粒子の微細化をもたらし、それが触媒活性の向上に寄与していることがわかる。また、Pt 1g当たりの触媒活性は、Reの添加によって約2倍に増加し、Reの添加がPt使用量の低減をもたらすことが示唆された。

さらに、種々のPt出発原料を用いて $Pt\text{-}Re/TiO_2$ (R)触媒を調製し、触媒活性に与える影響について検討を加えた。Table 3に種々のPt出発原料から調製した $Pt\text{-}Re/TiO_2$ (R)触媒の触媒活性と物性をまとめ

Table 3 Catalytic activities and properties of Pt-Re (1.0wt%-0.67wt%)/TiO_2 (R) catalysts prepared from various Pt precursors

Precursor	CO conversion[1] (%)	Pt dispersion[2] (%)	Catalytic activity per unit mass of Pt (mol-CO/(h g-Pt))	Pt dispersion[2] (%)
$Pt(C_5H_7O_2)_2$	80.5	52.5	28.9	52.5
$H_2PtCl_6 \cdot 6H_2O$	69.6	38.5	23.8	38.5
$[Pt(NH_3)_4]Cl_2$	65.5	27.6	23.1	27.6
$[Pt(NH_3)_4](NO_3)_2$	52.3	24.5	18.4	24.5
cis-$[Pt(NO_2)_2(NH_3)_2]$	38.1	11.0	13.7	11.0
Commercial Cu/ZnO	71.6	-	-	-

1) Feed gas: CO(99.95%), Reaction temperature: 250 °C, H_2O/CO = 1.5, S.V.(on the basis of CO) = 9,500 h^{-1}.

2) Pt dispersion was calculated from the amount of CO chemisorbed on the catalyst after reaction (CO/Pt = 1).

た。表から、ビスアセチルアセトナト白金($Pt(C_5H_7O_2)_2$)から調製した触媒はPt分散度とCO転化率がもっとも高いことがわかる。Pt 1g当たりの触媒活性は、従来の塩化白金酸六水和物から調製した触媒のそれの約1.2倍である。さらに、同触媒の触媒活性は、反応温度250 °Cで市販のCu-ZnO触媒を超えていることから、ビスアセチルアセトナト白金の使用によってPt使用量を1.0 wt%以下に低減できることが示唆された。

3. 本年度の研究成果

3.1 はじめに

当研究室では、高温超臨界乾燥法(HTSCD)が活性金属の高分散化による担持金属触媒の高機能化に有効であることを見いだしている[3]ことから、HTSCDあるいは乾燥溶媒の臨界温度以下の条件で乾燥させる亜臨界乾燥法(SubCD)により触媒を調製し、調製条件がPt分散度や触媒活性に与える影響について検討を加えた。

3.2 実験

触媒は以下の手順で調製した。まず、焼成(500 ℃, 1 h 昇温, 1 h保持, 空気気流中)したTiO_2担体(触媒学会参照触媒JRC-TIO-6, 細孔容積 0.5 ml/g)に、過レニウム酸アンモニウムエタノール溶液をRe仕込み量0.67 wt%となるように含浸し、同条件で焼成してRe/TiO_2(R)を得た。つぎに、ビスアセチルアセトナト白金トルエン溶液をPt仕込み量1 wt%となるように含浸(溶媒/細孔容積比 = 2.3, 室温 24 h 放置)した後、n-ペンタン (臨界温度: 196.8 ℃, 臨界圧力: 3.32 MPa)を乾燥溶媒としてSubCD(150 ℃, 3.0, 15.0, 20.0 MPa, 0.5h)、またはHTSCD(300 ℃, 20.0 MPa, 0.5h)を行ない、同条件で焼成してSubCD触媒とHTSCD触媒を得た。また、熱乾燥(TD)触媒は、TD(100 ℃, 0.1 MPa, 12h)を施して調製した。触媒性能試験、触媒物性測定は既報[1), 2)]と同様である。

3.3 結果と考察

Table 4に乾燥方法がPt担持量とPt分散度に与える影響を示した。まず、ビスアセチルアセトナト白金

Table 4 Effect of drying method on catalytic properties

Drying method	Pt precursor	Drying temperature (℃)	Pt content (%)	Amount of CO chemisorbed[2] (cm^3-STP/g-cat.)	Pt dispersion[2] (%)
TD	$Pt(C_5H_7O_2)_2$	100	1.0	0.51	46.8
	$H_2PtCl_6\ 6H_2O$	100	1.0	0.46	38.1
HT-SCD[1]	$Pt(C_5H_7O_2)_2$	350	0.8	0.37	42.5
		300	0.8	0.43	46.3
	$H_2PtCl_6\ 6H_2O$		0.8	0.07	7.8
SubCD[1]	$Pt(C_5H_7O_2)_2$	200	1.0	0.48	40.6
		150	1.0	0.56	49.1
	$H_2PtCl_6\ 6H_2O$		0.7	0/09	10.9

1) 20 MPa, S/P ratio = 2.3
2) After reduction at 500 ℃

から調製した触媒については、HTSCD触媒のPt担持量は0.8wt%であるのに対して、SubCD触媒とTD触媒のそれは、仕込み量である1wt%であることがわかる。このことから、HTSCDでは乾燥過程におけるPtの流失が問題となることが明らかとなった。また、SubCD触媒のPt分散度は、TD触媒やHTSCD触媒のそれよりも高い。一方、塩化白金酸六水和物($H_2PtCl_6\ 6H_2O$)から調製した触媒については、SubCD触

媒は TD 触媒よりも Pt 担持量、Pt 分散度ともに低いことがわかる。このことから、ビスアセチルアセトナト白金を用いた SubCD が Pt を損なうことなく、触媒上に高分散担持させる方法として有効であることが明らかとなった。つぎに、Fig. 1 は、ビスアセチルアセトナト白金を用いて種々の乾燥法により調製した触媒の Pt 分散度と触媒活性の関係を示した。乾燥過程での Pt の流失が認められた HTSCD 触媒を除いて、Pt 分散度と CO 転化率の間には直線の相関が認められた。これは、乾燥法によらず比活性（活性サイトである Pt の露出表面積あたりの活性）が一定であり、触媒活性が Pt 分散度に依存していることを示している。調製した触媒のなかで、高い Pt 分散度をもつ SubCD 触媒は、TD 触媒や HTSCD 触媒よりもすぐれた触媒活性を示している。以上のことから、ビスアセチルアセトナト白金を用いた SubCD が Pt-Re/TiO_2(R)の活性向上および Pt 使用量の低減に有効であることが示された。

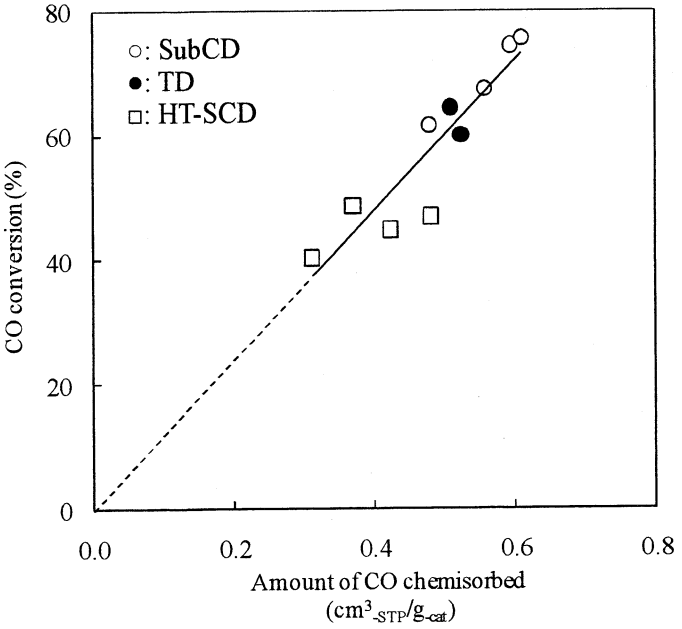

Feed gas: Mixed gas (CO(10%)-CO_2(15%)-H_2(75%)),
Reaction temperature: 250 °C H_2O/CO = 5.0,
S.V.(Total) =40,000h^{-1}

Fig. 1 Relation between the amount of CO chemisorbed and the CO conversion

4. 総括

LT-WGS 反応にすぐれた触媒活性を示す担持 Pt 触媒の活性向上および Pt 使用量の低減のために、担体の種類、Re 添加、および Pt 出発原料の種類や触媒調製法について検討を加えたところ、ビスアセチルアセトナト白金を用いて SubCD により調製した Pt-Re/TiO_2(R)触媒が Pt 担持量 1wt%で市販の Cu/Zn 触媒を超える触媒活性を示すことを見いだした。

引用文献

1) H. Iida and A. Igarashi, Appl. Catal. A: Gen., 298, 152 (2006).
2) H. Iida and A. Igarashi, Appl. Catal. A: Gen., 303, 192 (2006).
3) S. Sugita, M. Ohta, and A. Igarashi, 2000 International Chemical Congress of Pacific Basin Societies (PACIFICHEM 2000), INOR 540 (2000).

研究業績《審査付論文》

1) "Characterization of a Pt/TiO_2 (rutile) catalyst for water gas shift reaction at low-temperature", H. Iida and A. Igarashi, *Appl. Catal. A: Gen.*, **298**, 152 (2006).
2) "Structure Characterization of Pt-Re/TiO_2 (Rutile) and Pt-Re/ZrO_2 catalysts for Water Gas Shift Reaction at Low-temperature", H. Iida and A. Igarashi, *Appl. Catal. A: Gen.*, **303**, 192 (2006).
3) "Difference in the Reaction Behavior between Pt-Re/TiO_2 (Rutile) and Pt-Re/ZrO_2 Catalysts for Low-temperature Water Gas Shift Reactions", H. Iida and A. Igarashi, *Appl. Catal. A: Gen.*, **303**,48 (2006).
4) "Effect of Pt Precursors on Catalytic Activity of Pt/TiO_2 (Rutile) for Water Gas Shift Reaction at Low-temperature", H. Iida, K. Kondo, and A. Igarashi, *Catal. Commun.*, **7**, 240 (2006).
5) "Catalytic Activities and Properties of Pt-Re/TiO_2 Catalysts Prepared from Various Pt precursors for Low-temperature Water Gas Shift Reaction", H. Iida, M. Someya, K. Kondo, and A. Igarashi, *Stud. Surf. Sci. Catal.*, **172**, 265 (2007).
6) "Low-temperature Water Gas Shift Reaction over Pt-Re/TiO_2 Catalysts Prepared by a Sub-Critical Drying Method", H. Iida, K. Yonezawa, M. Kosaka, and A. Igarashi, *Catal. Commun.*, **10**, 627 (2009).

３．２．３　触媒活性を有する遷移金属ナノクラスターの合成と応用

Synthesis of Novel Transition-Metal Nano-Clusters and Their Application to Organic Synthesis

河野博之[†]，南雲紳史[‡]

Hiroyuki KAWANO[†] and Shinji NAGUMO[‡]

[†]工学院大学　工学部　共通課程，[‡]工学院大学　工学部　応用化学科

[†]General Education, Faculty of Engineering, Kogakuin University
[‡]Department of Applied Chemistry, Faculty of Engineering, Kogakuin University

Abstract: A dihydridoruthenium complex $RuH_2(CO)(PPh_3)_3$ is a good starting compound for generating a zerovalent ruthenium atom. The zerovalent ruthenium atom combines with each other to form a novel ruthenium-metal particle with diameters less than 1000 nm. On the other hand, the active zerovalent ruthenium atom reacts with another metal complex to form Ru/Rh-, Ru/Pt-, Ru/Pd-mixed metal nano-sized particles. The Ru/Rh-mixed metal nano-sized particle shows a moderate activity in catalytic hydrogenation and oxidation depending on the particle size.

Index Terms: Inorganic and Organometallic Chemistry, Ruthenium Complexes, Nano-Sized Metal-Containing Particles, Chemical Process for Nano-Particles.

緒言

1．金属ナノ粒子の化学的合成法

金属ナノ粒子とは、その直径がナノメートル(nm, 10^{-6}-10^{-9} m)サイズの金属微粒子であり、数十から千個程度の金属原子から構成されている。この大きさの金属微粒子には高い比表面積効果や量子サイズ効果が期待されること、生体細胞の細胞膜を傷つけずに通過できることなどから、金属ナノ粒子は、近年ナノサイエンスあるいはナノテクノロジーの分野における重要な素材として注目されている。

これまで、金属ナノ粒子はバルク金属を粉砕する「物理的」な方法で調製されてきた(Scheme 1)。しかし、最近、金属イオンを「化学的」に還元して電荷をもたない単独の金属原子を発生させる金属ナノ粒子合成法が精力的に研究されている。化学的金属ナノ粒子合成法では、制御された条件下で凝集をコントロールすることでき、ナノメートルサイズの金属微粒子を大量に得ることができる。

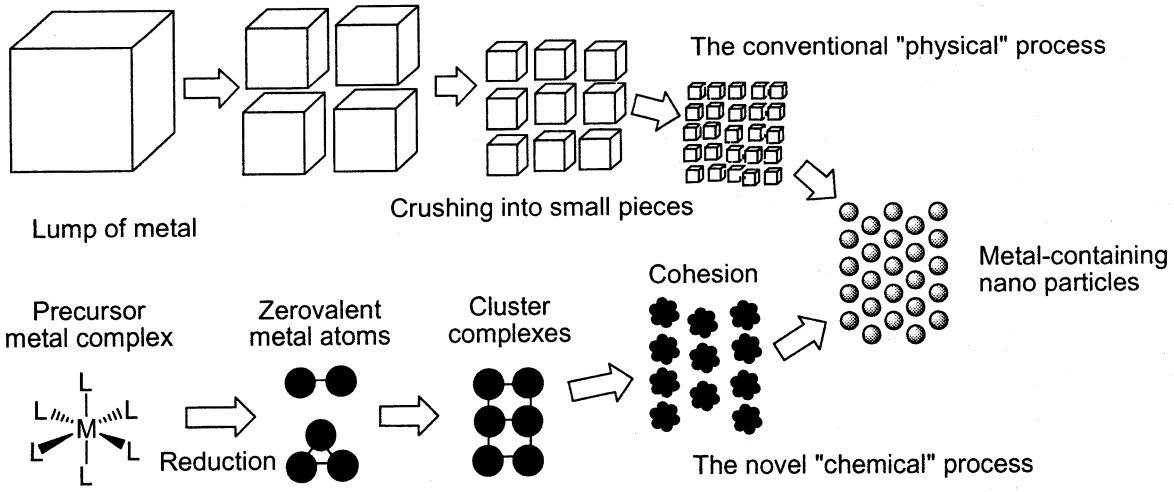

Scheme 1. The "physical" process vs. the "chemical" process for the metal-containing nano particles.

化学的金属ナノ粒子合成法の出発物質としては金属錯体がよく利用される。一般に裸の金属原子や金属イオンは不安定で、多くの場合はただちに酸化されたり凝集したりして単独では存在できないが、配位子と錯形成させることで安定化され、一個の金属中心を持つ錯体分子となる。一方、金属ナノ粒子も、通常は保護剤とよばれる分子でナノ粒子の周囲を囲むことで凝集を防ぎ、安定化されている。したがって、金属錯体分子にとっての配位子と金属ナノ粒子にとっての保護剤の作用は共通であり、このことから金属錯体の配位子を一部取り除き、制御した条件下で凝集させれば金属ナノ粒子が生成すると予想できる。この考えが本研究課題の動機である。

2. 遷移金属錯体とナノマテリアルの関係

遷移元素を中心金属とする遷移金属錯体の特徴は、複数の配位子が、遷移金属原子の周囲に多面体型の構造をかたちづくるように結合していることと、それら配位子の種類と配列が制御されることで中心金属の反応性が多様に変化することである。遷移金属錯体が有するこれらの特徴は、金属錯体を利用するナノマテリアルへの応用と密接に関連している。

本研究課題の対象の中心となるルテニウム錯体の場合、ルテニウムの酸化状態は-2 から+8 までのあらゆる状態を取ることができ、それに結合している配位子数も 4 から 7 までとバラエティに富んでいるので、様々な構造のルテニウム錯体が形成される。また、ルテニウム原子間で結合し、ルテニウム中心を複数有する多核錯体をしばしば形成することも特徴の一つであり、このことはルテニウム原子が凝集したルテニウム含有ナノ粒子が容易に生成する可能性を示している。

また、化学的金属ナノ粒子合成法では、異種金属を一つのナノ粒子中に含む混合金属ナノ粒子を合成できることが利点である。ナノ粒子合成の際に異種の金属錯体を共存させることで、混合金属ナノ粒子を比較的簡単に得ることができる。ここでは金属錯体間の自己組織化を利用しているので、組成や構造が良く揃った混合金属ナノ粒子が生成する。触媒反応への展開を考える場合、このような混合金属ナノ粒子は、異種金属それぞれが異なった機能を分担することで、より効率的な触媒となる可能性がある。例えば、一方の金属は主として基質分子の捕捉に関与し、もう一方の金属が基質の変換を担当するといったことが考えられる。したがって、混合金属ナノ粒子のもつ触媒反応活性の研究は、既に工業的に利用されている多元系不均一系触媒の研究モデルとして重要であると同時に、異種金属を含む特徴を利用した新反応の開発につながるものである。

研究成果

1. ルテニウム錯体触媒からルテニウム金属ナノ粒子への展開

ルテニウム(0)錯体触媒を用いる芳香環 C-H 結合のオレフィンへの付加反応[1, 2]は、通常活性化されにくい有機化合物の C-H 結合や C-C 結合をルテニウム(0)錯体で直接活性化・切断することを鍵反

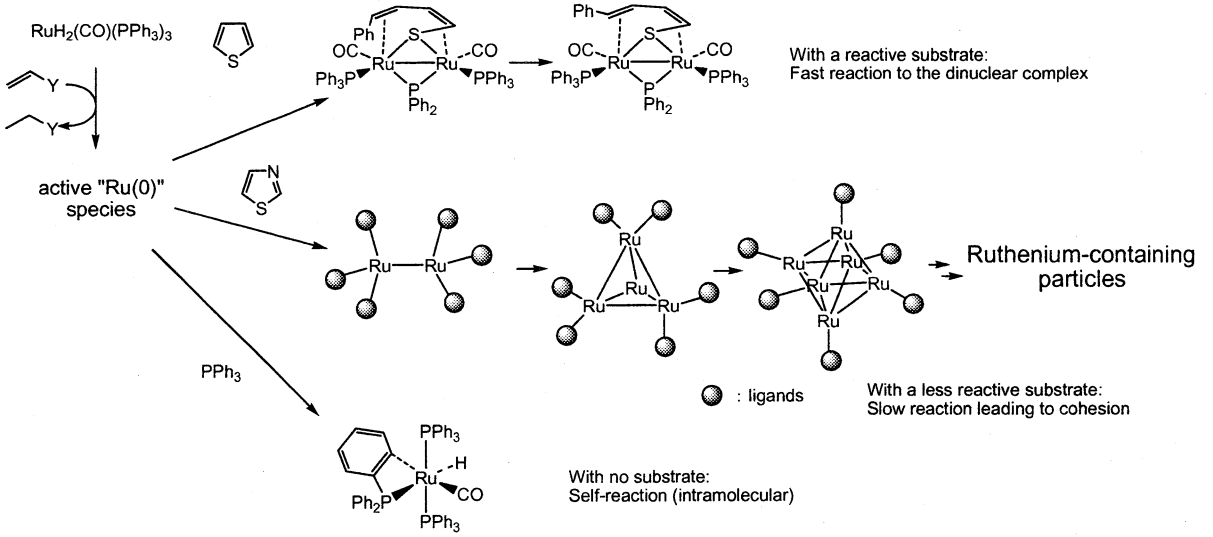

Scheme 2. A possible route to the nano-sized ruthenium-containing particles.

応としており、低原子価ルテニウム錯体が不活性な結合を効果的に活性化できることを証明した。

この分野において、我々はジヒドリドルテニウム(II)錯体、$[RuH_2(CO)(PPh_3)_3]$とオレフィンとの反応で反応溶液中に発生する活性ルテニウム(0)錯体種(現時点で組成は$[Ru(CO)(PPh_3)_n]$ (n = 2 or 3)と推定されている)が、芳香環上のC-H結合やメチル基のC-H結合を活性化できることを明らかにしてきた。また、ルテニウム(0)錯体種が生成した後、直ちに反応する有機化合物が周囲に存在しない場合には、自分自身に結合したPPh_3配位子のC-H結合まで切断してしまうことが明らかとなった[3]。

このことは、芳香環C-H結合を有する化合物よりも活性ルテニウム(0)錯体との反応が遅い化合物を利用すれば、分子内でのPPh_3配位子C-H結合切断を抑えつつ、ルテニウム錯体分子間の凝集を制御できる可能性を示している(Scheme 2)。本研究課題以前の取り組みでは、チオフェンを活性ルテニウム(0)錯体と反応させた場合に、チオフェン1分子に対しルテニウム錯体が2分子反応した二核錯体が得られた[4]。

そこで、活性ルテニウム(0)錯体に、より反応しにくいチアゾールを接触させたところ、予想通り単核あるいは二核のルテニウム錯体種の生成は確認できず、ルテニウム(0)錯体、すなわち配位子をまとったルテニウム原子の凝集が進み、多核クラスターを経て1000ナノメートル未満の粒径のものを含むルテニウム金属微粒子が生成した。同様の微粒子は、ルテニウム(0)錯体とベンゾフランとの反応でも生成した。これらの微粒子の粒径はさらなる配位子PPh_3の添加で制御可能であり、配位子PPh_3が微粒子表面のルテニウム原子に配位して凝集による粒径の増大を抑えていることがわかった。

2. ルテニウム含有混合金属微粒子の合成

ルテニウム(0)錯体の凝集を制御することでルテニウム金属微粒子を合成できることが明らかになったので、さらに混合金属微粒子の合成にこの手法を応用した。主として、ルテニウム(0)錯体とロジウム(I)錯体との組み合わせを検討したが、ルテニウム(0)錯体と酸化状態の異なるルテニウム(II)錯体およびパラジウム(II)錯体あるいは白金(II)錯体などを共存させての混合金属微粒子合成も試みた。

ルテニウム(0)錯体に等しい物質量のロジウム(I)錯体$[RhCl(PPh_3)_3]$、二種のルテニウム(II)錯体、$[RuCl_2(1,5\text{-cyclooctadiene})]_n$、$[RuCl_2(PPh_3)_3]$、パラジウム(II)錯体$[PdCl_2(PPh_3)_2]$、および白金(II)錯体$[PtCl_2(PPh_3)_2]$を反応させたところ、いずれの場合にもルテニウム(0)原子と異種金属イオンが1:1で反応した組成の生成物が再現性良く得られた。生成物を溶媒に再分散させて粒径を測定したところ、数10ないし数100ナノメートルの粒径をもつ混合金属微粒子であることが判った。ここでルテニウム(0)錯体との反応用いた金属錯体には、いずれにも塩化物イオン(Cl^-)が配位子として含まれている。生成した微粒子には、すべて塩化物イオンが含まれていた。すなわち、これらの微粒子は単純な金属微粒子ではなく金属塩化物からなる化合物微粒子であることが明らかになった。再分散させたこれらの微粒子の凝集挙動は出発物質に用いた遷移金属錯体の種類により異なっていたが、一般に凝集しやすく配位子PPh_3を添加しても微粒子の凝集を完全に制御することはできなかった。

ルテニウム(0)錯体とロジウム(I)錯体の混合比を変え、ロジウムが過剰の条件で反応を試みると、過剰分に相当する量のロジウム二核錯体$[Rh_2Cl_2(PPh_3)_4]$が、オレンジ色の沈殿として反応溶液中に生成した。反応溶液から得られたRu/Rh混合金属微粒子の組成は、ルテニウムとロジウムの混合比率にかかわらず、ほぼ$RhRuCl(PPh_3)_{1.5}$であった。このことから、ルテニウムとロジウムが混合金属微粒子を生成する際には、まず、ルテニウム(0)錯体とロジウム(I)錯体との間で、Ru/Rh二核錯体が生成し、この錯体が自己組織化することでRu/Rh混合金属微粒子が生成していると考えられる(Scheme 3)。

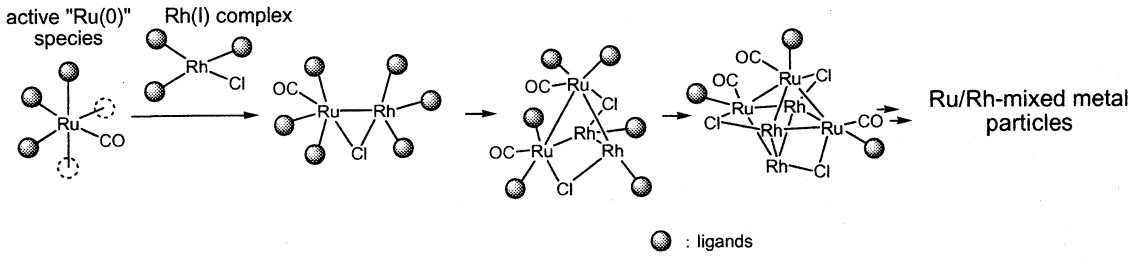

Scheme 3. Formation of the Ru/Rh(1:1)-mixed metal particles.

3. Ru/Rh 混合金属微粒子の触媒作用の検討

ここで得られた Ru/Rh 混合金属微粒子は、粒径測定からそのサイズが 100 ナノメートル程度以下であった。微粒子の詳細な構造は未だ不明であるが、この大きさの金属粒子には高い比表面積の効果や量子サイズ効果が期待されるので、Ru/Rh 混合金属ナノ粒子の有機化合物に対する反応性には興味がもたれる。そこで、ロジウム(I)錯体を触媒とする、化合物 **1** の分子内付加環化反応[5, 6]をモデルに、触媒活性の検討を行った(Table 1)。

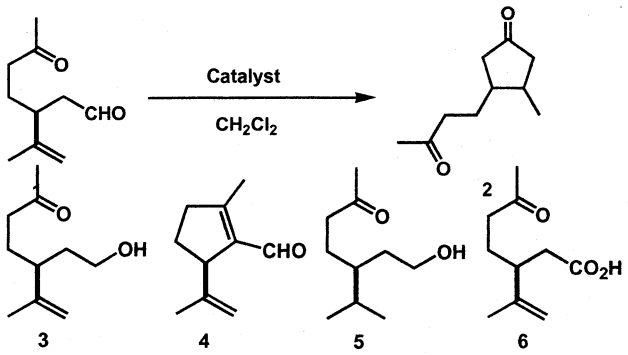

Ru/Rh 混合金属ナノ粒子を触媒に用いたところ、当初想定した分子内環化生成物 **2** は生成せず、官能基の酸化還元反応が進行することが明らかになった。まず、Ru/Rh 混合金属ナノ粒子単独の場合には、アルデヒドの還元体 **3** と、アルドール反応生成物 **4** が生成した。そこで反応を促進させるため、水素気流下で行ったところ、二重結合も還元され **5** が生成することが確認された。また配位子の PPh_3 を添加したところアルデヒドの酸化が起こり、酸素の有無にかかわらずカルボン酸 **6** が生成した。PPh_3 の添加は、ナノ粒子のサイズないし凝集状態を制御すると考えられるので、Ru/Rh 混合金属ナノ粒子は、粒子サイズによって異なる反応を触媒する、非常に特異な作用を示すことが明らかになった。

Table 1. Catalytic activity of the Ru/Rh-mixed metal nano particle.

Entry	Catalyst	Solvent	Additive	Gas	Time	Product
1	$RhCl(PPh_3)_3$	CH_2Cl_2	-	Ar	20 h	2 (quant.)
2	$RuH_2(CO)(PPh_3)_3$	CH_2Cl_2	-	Ar	6 days	3 (22%)
3	$RuH_2(CO)(PPh_3)_3$	CH_2Cl_2	-	H_2	10 days	3 (47%)
4	Ru/Rh ナノ粒子	CH_2Cl_2	-	Ar	38 days	3 (3%), 4 (6%)
5	Ru/Rh ナノ粒子	CH_2Cl_2	-	H_2	8 days	5 (39%)
6	Ru/Rh ナノ粒子	CH_2Cl_2	PPh_3	Ar	5 days	6 (26%)
7	Ru/Rh ナノ粒子	CH_2Cl_2	PPh_3	O_2	11 days	6 (29%)

結論

以上に述べたように、ルテニウム(0)錯体種をルテニウム原子の供給源とする化学的金属ナノ粒子合成法で、ルテニウム金属ナノ粒子および混合金属化合物微粒子を合成できることと、混合金属微粒子が生成する機構が明らかとなった。また、混合金属微粒子は、それらの成分金属が持たない特異な触媒作用を示すことも明らかになった。この成果は、精密触媒機能など高付加価値を有するナノ粒子の設計と合成を可能にするものであるといえる。

引用文献

[1] The first report on the synthetic use of the active ruthenium species: S. Murai, F. Kakiuchi, S. Sekine, Y. Tanaka, A. Kamatani, M. Sonoda, N. Chatani, *Nature*, **366**, 529 (1993).

[2] F. Kakiuchi, S. Sekine, Y. Tanaka, A. Kamatani, M. Sonoda, N. Chatani, S. Murai, *Bull. Chem. Soc. Jpn.*, **68**, 62 (1995).

[3] K. Hiraki, S. Kira, H. Kawano, *Bull. Chem. Soc. Jpn.*, **70**, 1583 (1997).

[4] H. Kawano, H. Narimatsu, D. Yamamoto, K. Tanaka, K. Hiraki, M. Onishi, *Organometallics*, **21**, 5526 (2002),

[5] Y. Taura, M. Tanaka, K. Funakoshi, K. Sakai, *Tetrahedron Lett.*, **30**, 6349 (1989).

[6] Y. Taura, M. Tanaka, X.-M. Wu, K. Funakoshi, K. Sakai, *Tetrahedron*, **47**, 4879 (1991).

関連する研究業績

[1] 年会特別企画「化学的金属ナノ粒子合成法の進歩」, 日本化学会第 87 春季年会（関西大学）2007 年 3 月；上記シンポジウムの企画・開催・趣旨説明.

[2] S. Nagumo, Y. Ishii, G. Sato, M. Mizukami, M. Imai, N. Kawahara, H. Akita, *Tetrahedron Lett.*, **50**, 26 (2009).

３．２．４ 高分散性セラミックナノ粒子・ナノポア構造体の創製とキャラクタリゼーション

Development and Characterization of Nano-porous Ceramics and High-dispersive Ceramic Nano-particles

大倉 利典、門間 英毅（工学院大学工学部マテリアル科学科）

Toshinori Okura and Hideki Monma (Faculty of Engineering, Kogakuin University)

川副 博司（川副フロンティアテクノロジー株式会社）

Hiroshi Kawazoe (Kawazoe Frontier Technology Co. Ltd.)

Firstly, a low crystalline silicoaluminophosphate with the chabazite-type nano-pore-containing structure was clarified to be easily subject to change from crystalline into amorphous by evacuation at 200°C. Such a structural change seemed to correspond to the loss of structural OH and H_2O. A similar change was observed around 1055°C on furnace heating, and also by mechanical grinding. Secondly, magnesium phosphate (MP) glasses with a nano-order network structure were demonstrated to be superior for the immobilization of Simulated High Level Nuclear Wastes (SHLW), compared to currently used borosilicate (BS) glasses. The introducible amount of SHLW was much more in MP glasses than in BS glasses. The water-leaching rate of a MP glass with 50 mass% SHLW was in the order of 10^{-6} g/cm^2·day at 90°C, which is lower than that of BS glasses. These properties could be discussed from the standpoint of isolated ions such as dimeric $(P_2O_7)^{4-}$ and monomeric $(PO_4)^{3-}$. Thirdly, $Na_5YSi_4O_{12}$-type glass-ceramic Na^+-superionic conductors (Na_5YXSi) were prepared by crystallization of glasses. Polycrystalline Na_5YXSi glass-ceramics have been obtained with X = B, Al, Ti, Te, Ge, P, V and Mo. The effects of X elements on the crystallization of the phase and the microstructural effects on the conduction properties of the glass-ceramics were discussed, and the crystallization kinetics of the glasses was examined by DTA analysis. The conductivity of the glass-ceramic Na_5YBSi with the $Na_{3.7}Y_{0.8}B_{0.1}Si_{2.9}O_9$ composition was 4.31×10^{-2} S/cm at 300°C, and the activation energy of the specimen was 17.0 kJ/mol.

1. はじめに

環境保全およびバイオ系新素材としての非晶質リン酸カルシウム（ACP）コロイド粒子、および環境・エネルギー関連の基礎素材としてのアルミナ系ナノポアセラミックス（NPC）構造体、それぞれの創製と組成・構造・モルフォロジー制御を追究する。約 6 nm の一次粒子径をもつ ACP に関しては沈殿合成では凝集粒子として沈殿してしまい、高分散安定化技術はまだ達成できていない。アルミナ系 NPC 構造体については、ケイ酸、リン酸、各種希土類元素の組成系で構造設計の指針を考え、ガラス化法およびガラス結晶化法を採用して、超イオン伝導性のナノポア分散構造体の合成条件を明らかにした。現在、ナノポアをイオン伝導パスとした固体電解質、ナノオーダーネットワーク構造を利用した高レベル放射線廃棄物固定化ガラスといった機能材料への展開を図っている。これらの研究成果は材料化学技術，資源・環境・エネルギー関連分野の発展に大きく寄与するものである。以下、これら成果の概要を報告する。

2. Chabazite 型ナノポーラス SAPO の合成とアモルファス化現象

(Synthesis of Chabazite-type Nano-porous SAPO and its Change from Crystalline into Amorphous)

SAPO（Silicoaluminophosphate）は、Si、Al および P の混合酸化物ネットワーク構造を持ち、これらの組成比によりナノオーダーの細孔径と骨格上に局在する過剰電荷を制御できる。Chabazite 型 SAPO（SAPO-CHA）は、骨格上の過剰電荷を補償するために細孔内に対イオンが包摂され、中温度域作動固体電解質としての応用が期待される。本研究では、SAPO-CHA の吸脱着等温線測定時に見いだした新現象、すなわち、同一 N_2 平衡圧での N_2 吸着量が「吸着過程＞脱着過程」となる一般的な関

係と逆転する現象に関して、その原因を追究した。

SAPO-CHA の合成は以下のように行った。モル比で、0.60 (SiO_2) : 1.0 (Al_2O_3) : 0.80 (P_2O_5) : 1.70 ($C_6H_{11}NH_2$) : 1.0 (HF) : 80 (H_2O)、のように配合した分散液を撹拌・混合し、オートクレーブ中 180℃で 192 時間静置して生成物をろ過・乾燥後、560℃で 24 時間仮焼し、SAPO-CHA を得た。この生成物について、脱ガス処理、熱処理および摩砕処理による構造変化（アモルファス化）を検討した。

SAPO-CHA の窒素吸着測定において、前処理である脱ガスの時間を長くするとともに XRD パターンはブロードになり、アモルファス化が進行した。すなわち、この脱ガス処理の時点で構造変化していることがわかった。吸脱着等温線の逆転は脱ガス処理の構造変化による比表面積の減少を反映したものと結論した。脱ガス時間の増加により 3400 cm^{-1} 付近の O-H 伸縮振動と 1650 cm^{-1} 付近の H_2O の変角振動の減少が観察され、アモルファス化は SAPO-CHA 構造内の H_2O 分の減少を伴っていた。乾式加熱では、900℃付近からアモルファス特有の XRD ハローが現れ、1055℃付近でアモルファスになり、1070℃付近から再び結晶化し、SAPO-CHA とは異なる結晶となった。H_2O 分に関しては、加熱 1055℃付近から O-H 伸縮振動が減少したことから、SAPO-CHA は 1000℃においても構造内に H_2O 分を保持できる極めて安定なサイトをもつことがわかった。このようなアモルファス化は摩砕処理によっても同様に生じることもわかった。

3. リン酸塩ガラスによる模擬高レベル放射性廃棄物（SHLW）の固定化
（Immobilization of Simulated High Level Nuclear Wastes with Phosphate Glasses）

原子力発電所から発生する使用済核燃料の再処理工程で高レベル放射性廃液（HLW）が分離される。この高レベル放射性廃液は、ガラスと混ぜて溶かし、「キャニスター」と呼ばれるステンレス製の容器に注入したあと、冷やして固める（ガラス固化体）。現在、固化ガラスにはホウケイ酸塩ガラスが使用されており、HLW 含有量は最大で 25mass%となっている。しかし、このガラスは P_2O_5 の濃度が増加すると分相してしまうことが報告されている。HLW 成分の中には分相傾向を一層増大するようなモリブデンなどの元素も存在する。本研究では、HLW 固化ガラスのベースガラスとして、融点が低く、より多く様々な種類の元素を取り込める特性を持つリン酸塩ガラスに着目した。多くのリン酸塩ガラスは鎖状構造を有することが知られているが、とくにリン酸マグネシウムガラスは組成により二つのタイプの構造を含むと考えられ、一つは $MgO/P_2O_5<1$ のときでテトラメタリン酸構造を含むもの、もう一つは $MgO/P_2O_5>1$ のときでピロリン酸構造を含むものである。本研究では、リン酸マグネシウムガラスを用いて、SHLW 元素（Na, Sr, La, Mo, Mn, Fe, Te）を固化させたガラス固化体について、熱的安定性や耐水性の評価、振動スペクトルを用いた構造変化の検討を行い、さらにγ線を照射させたときの影響についても検討した。

母体ガラスとした $MgO-P_2O_5$ 系ガラス（M-P ガラス）および $CaO-P_2O_5$ 系ガラス（C-P ガラス）は $MgO:P_2O_5$=40:60, 47:53, 50:50, 55:45 および $CaO:P_2O_5$=40:60, 50:50, 55:45 混合物（モル比）を 600℃で 3 時間加熱後、さらに 1250℃で 1 時間加熱溶融し、急冷して得た。SHLW 固化ガラスは、M-P ガラスあるいは C-P ガラスを粉砕し、それに SHLW 含有率が 25 および 45 mass%になるようにそれぞれ混合し、1250℃で 2 時間溶融後、急冷して得た。得られたガラスについて、密度測定、DTA による「ガラス転移点（*Tg*）－結晶化開始温度（*Tc*）」を指標としたガラス安定性、500℃で 2 時間加熱した試料の結晶化の有無、SHLW 含有量の増加によるガラスの FT-IR および Laser-Raman からみた構造変化、粉砕試料の水中 90℃での 20 日間保持後の質量減少率からみた水中浸出性（MCC 法）、を評価した。加えて、ガラス固化体が放射線を常に照射される状態を考え、γ線（Co-60、全線量 10 μR）を照射したガラス固化体についての構造・物性も検討した。

M-P ガラスは SHLW 含有量を増加しても均一なガラス試料を作製できた。C-P ガラスでは SHLW を含有させるとすべての組成において結晶化した。ガラスの安定性は SHLW 含有量が増加すると低下したが、$MgO:P_2O_5$=40:60 以外の M-P ガラスと $CaO:P_2O_5$=50:50 の C-P ガラスは、SHLW 含有量にあまり影響を受けないことがわかった。M-P ガラスにおいては、ピロリン酸構造を多く含む組成の方が安定性は高くなるのではないかと考えられる。耐水性は M-P および C-P ガラスのどちらもそれら自体は悪いが、SHLW 含有量が増加するにつれて高くなる特徴が判明した。M-P ガラスにおいては、$MgO:P_2O_5$=47:53 で SHLW 含有量 45mass%の固化ガラスの水浸出率は $10^{-6}g/cm^2$・day オーダーとなり、現在使用

されているホウケイ酸塩ガラス固化体（HLW 含有量 25 mass%）の浸出率 2.5×10^{-5}g/cm^2・day と比べてかなり低い値となり、この組成が固化ガラスとして適していると考えられる。C-P ガラスにおいては $CaO:P_2O_5=50:50$ で SHLW 含有量 45mass%の固化ガラスの浸出率が比較的低い値 6.85×10^{-5}g/cm^2・day を示したが、ホウケイ酸塩ガラス固化体よりは高い値となった。FT-IR および Laser Raman スペクトルから、M-P および C-P ガラスのどちらにおいても、環状や鎖状の構造が SHLW 元素によって切断されるために、$P_2O_7^{4-}$やPO_4^{3-}などは増加せず、このような構造が増加するとガラスネットワーク中のクロス・リンケージの密度が増加し、耐水性を向上させたものと考えられる。γ 線を照射することによって、浸出率は 1 桁近く悪くなったが、FT-IR、Laser Raman どちらのスペクトルにも照射前後に変化が見られず、大きな構造的変化は起きないことが分かった。

4. $Na_5YSi_4O_{12}$ 型 Na^+導電性結晶化ガラスの作製と Si 置換効果

（Synthesis and Effects of Si Substitution on Various Properties of $Na_5YSi_4O_{12}$-type Glass-ceramic Na^+-Superionic Conductors）

＜研究の背景と目的＞

Na_2O-R_2O_3-SiO_2（R＝希土類元素）系化合物は、組成や結晶化熱処理温度によって、$Na_3RSi_3O_9$（N3 型）、$Na_5RSi_4O_{12}$（N5 型）、$Na_9RSi_6O_{18}$（N9 型）の三つの結晶相を持つ。なかでも N5 型は SiO_4 四面体の 12 員環構造を R で結合した 3 次元のトンネル構造を持ち、Na^+をキャリアーとした安定で高いイオン導電性をもつ。これまで R を Y とし、Si の一部をイオン半径および価数の異なる元素で置換した結晶化ガラスを作製し、電気的評価を行ってきた。これらの化合物は 300℃で 10^{-2} S/cm 程度の高い電導度を示した。本研究では R を Y とし、Si の一部を B、P、V、Mo、Ti、Te で一部置換した一般組成式 $Na_{3+3x+y}Y_{1-x}B_ySi_{3-y}O_9$（NaYBSi）、$Na_{3+3x}Y_{1-x}$（Ti, Te）$_ySi_{3-y}O_9$（NaYTiSi, NaYTeSi）、$Na_{3+3x-y}Y_{1-x}$（P, V）$_ySi_{3-y}O_9$（NaYPSi, NaYVSi）、$Na_{3+3x-2y}Y_{1-x}Mo_ySi_{3-y}O_9$（NaYMoSi）からなる N5 型単一相の結晶化ガラスを作製し、Si を置換する元素の違いによる結晶化の活性化エネルギーの変化、格子定数の変化、電導度および電導の活性化エネルギーの変化、SEM による観察から微構造の違いを調べた。

＜実験＞

ガラスの作製には溶融急冷法を用いた。出発原料として Na_2CO_3、Y_2O_3、SiO_2 および Si を置換する元素として H_3BO_3、$NH_4H_2PO_4$、V_2O_5、MoO_3、TiO_2、TeO_2 を一般組成式に基づいてそれぞれの配合比で秤り取り、粉砕・混合し、1350℃で 1 時間溶融した。融液を円筒状のグラファイト型に流し込み、急冷、アニーリング後、ガラス試料を得た。これらのガラスの結晶化挙動を調べるために、昇温速度 α を変えて DTA 測定を行い、ガラス転移温度 T_g、結晶化開始温度 T_c、結晶化の発熱ピーク温度 T_0 を求めた。DTA のデータをもとに修正 Kissinger の式（1）を用いて結晶化（結晶成長）の活性化エネルギー（E）を算出した。

$$\ln\left(\frac{\alpha^n}{T_0^2}\right) = -\frac{mE}{RT_0} + \text{const.} \qquad (1)$$

得られた結晶化ガラスに対し、XRD によって結晶相を同定し、格子定数を算出した。SEM を用いて微構造の観察を行った。また交流二端子法による複素アドミッタンス測定から電導度を求め、アレニウスプロットの傾きから電導の活性化エネルギーを算出した。

＜結果および考察＞

Si の一部を他の元素で置換した場合でも目的とした N5 型単一相が得られた。a 軸と単位格子体積において Si の一部を置換する元素のイオン半径が大きくなるにつれ、格子定数 a と単位格子体積は大きくなった。c 軸では Si を一部置換する元素のイオン半径に依らず、傾向を示さなかった。

本試料は 3 次元体積核生成とし、(1) 式において m=3、n=4 を用いて計算を行った。Si の一部を置換する元素のイオン半径が大きくなるにつれ、結晶化の活性化エネルギーが増大した。しかし、P で一部置換した場合はこれに当てはまらず、結晶化の活性化エネルギーはイオン半径が最も小さい B よりも小さな値を示した。これはケイ酸塩ガラスに P を添加することで結晶化温度が低下するという報告があり、本試料においても P を添加したことで結晶化温度が低下し、その影響で結晶化の活性化エネルギーも小さくなったものと考えられる。

$Na_{3.7}Y_{0.8}B_{0.1}Si_{2.9}O_9$ 組成の結晶化ガラスの複素アドミッタンス軌跡を Fig. 1 に、アレニウスプロットを Fig. 2 に示した。150℃で二つの円弧を描き、200℃以上では一つの円弧を描く複素アドミッタンス軌跡が観察された。測定温度が上昇するにつれ、粒界の電導度が大幅に上昇したために、粒内の円弧が粒界の円弧に飲み込まれ、見かけ上一つの円弧になったと考えられる。$Na_{3.7}Y_{0.8}B_{0.1}Si_{2.9}O_9$ 組成の結晶化ガラスの 300℃での電導度は 4.31×10^{-2} S/cm、活性化エネルギーは 17.0 kJ/mol の値を得た。

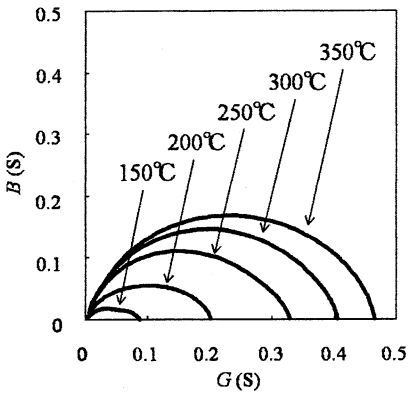

Fig. 1 Complex admittance diagrams of $Na_{3.7}Y_{0.8}B_{0.1}Si_{2.9}O_9$ glass-ceramics.

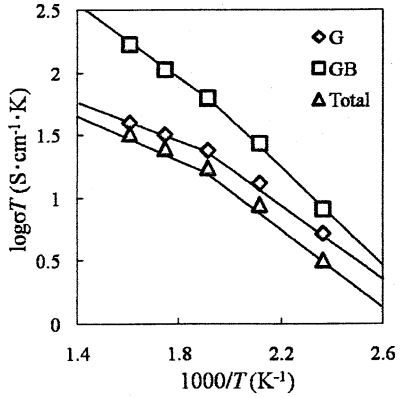

Fig. 2 Arrhenius plots of conductivities of $Na_{3.7}Y_{0.8}B_{0.1}Si_{2.9}O_9$ glass-ceramics.

研究業績（2005 年 4 月～2009 年 3 月）

審査付論文

1. 門間,西村,大倉, Characterization of Layer-Structured Octacalcium Phosphate/Dicarboxylate Composite, Phosphorus Research Bulletin, Vol. 18 127-134 (2005)
2. 門間,守吉,浦野,大倉, Preparation of Hydroxyapatite Porous Body and Tubular Particles from Gypsum, Phosphorus Research Bulletin, Vol. 19 166-171 (2005)
3. 古高,門間,大倉, Characteristic Reaction Processes in the System Brushite-NaOH solution, J. Eur. Ceram. Soc., 26, [4-5] 543-547 (2006)
4. 大倉,宮地,門間, Properties and Vibrational Spectra of Magnesium Phosphate Glasses for Nuclear Waste Immobilization, J. Eur. Ceram. Soc., 26, [4-5] 831-836 (2006)
5. 大倉,門間,山下, Superionic Conducting $Na_5SmSi_4O_{12}$- Type Glass-Ceramics: Crystallization Condition and Ionic Conductivity, J. Eur. Ceram. Soc., 26, [4-5] 619-622 (2006)
6. 大倉, ガラスによる高レベル放射性廃棄物の固化処理, J. Soc. Inorg. Mater. Japan, 13, 448-455 (2006)
7. 吉田,竹内,大倉,門間,若村,大崎,渡部, Super-Hydrophobic Photocatalytic Coatings Utilizing Apatite-Based Photocatalyst, Thin Solid Films, 502, 108-111 (2006)
8. 大倉,門間,山下, Na^+ Superionic Conducting Glass-Ceramics of Silicophosphates: Crystallization, Microstructure and Conduction Properties, Phosphorus Research Bulletin (Review), Vol. 20 111-118 (2006)
9. 根岸,大倉,関谷, $CaSO_4$-H_3PO_4-H_2O 系における二水セッコウの準安定性, J. Soc. Inorg. Mater. Japan, 14, 294-299 (2007)
10. 大倉,門間, ゾル - ゲル法による SiO_2-P_2O_5-GeO_2 系非晶質バルク体の合成, J. Soc. Inorg. Mater. Japan, 14, 363-368 (2007)
11. 門間,大倉,石田,守吉, Dry-Mechanochemical Conversion of Gypsum to Apatite, J. Soc. Inorg. Mater. Japan, 15, 37-41 (2008)
12. 大倉,門間, Ionic Conductivity of Na^+-Ion Implanted Na_2O-P_2O_5-SiO_2 Glass, J. Soc. Inorg. Mater. Japan, 15, 171-173 (2008)
13. 大倉,高橋,門間,山下, Effect of Substitution of Si with V and Mo on Ionic Conductivity of $Na_5YSi_4O_{12}$-Type Glass-Ceramics, Solid State Ionics, 179, 1291-1295 (2008)
14. 大倉,門間,山下, Na^+-Fast Ionic Conducting Glass-Ceramics of Silicophosphates, J. Electroceram. (Review), in press
15. 大倉,才丸,門間,山下, Ionic Conductivities of Nasicon-Type Glass-Ceramic Superionic Conductors in the System Na_2O-Y_2O_3-XO_2-SiO_2 (X=Ti, Ge, Te), Solid State Ionics, in press
16. 門間,大倉,原,守吉, Mechanochemical Properties of Octacalcium Phosphate and Brushite, Phosphorus Research Bulletin, in press

その他

著書　6
学術雑誌、研究機関への研究報告、展望、解説、論説など　11
国際学会の口頭発表　8
国内学会の口頭発表　51
特許　1

4. デバイスへの応用

4．1　電子デバイス微細接合部の熱サイクル信頼性評価

—Al ボンディングワイヤーの疲労特性—

後藤芳樹，立野昌義，小久保邦雄（機械工学科）

Fatigue Properties of Aluminum Bonding Wire

Yoshiki GOTOH, Masayoshi TATENO, Kunio KOKUBO

Abstract: The evaluation of mechanical properties including static and fatigue behavior is essential issue for developing a reliable micro-sized machine in service operation. But there has been an absence of the standard test procedure for micro-sized materials. Therefore, the evaluation of mechanical properties including reliability and durability has not been performed.

In the present study, fatigue tests have been performed for Aluminum bonding wire specimen with 25μm diameter, and the S-N curves have been obtained. It was investigated that the fatigue limit of specimen using PI tab increased rather than PP tab, and the ratio of fatigue limit to tensile strength was 0.88 and necking was observed at the final stage of fatigue life.

Key words: Aluminum bonding wire, Fatigue Properties, S-N curves, Polyimide tub

1. はじめに

従来から IC チップとパッケージの接続にはボンディングワイヤーが使用されているが，電子デバイスの信頼性の向上のためには，このような極細線の機械的性質を評価する必要がある。しかし，現状では，このような微小寸法材料を評価するための標準的な試験方法は確立されておらず，信頼性の高いデータを得るためには試験方法の標準化は不可欠である。細線をプラスチックタブに接着し，タブを保持して繰返し荷重を加えて疲労試験を行なう方法は，直接チャッキングした場合にチャッキングにより破断する可能性のある細線の試験において，一つの有望な試験方法である。

我々は，これまでに，プラスチックタブを用いることにより，細線の引張試験[1)]や疲労試験[2)]が可能であることを報告してきた。しかし，プラスチックタブを用いる疲労試験については，光ファイバー[3)]，アラミド繊維[4)]および Cu 細線[5)]についての報告があるが，まだまだデータの少ないのが現状である。

本研究は，一定繰返し変位を負荷できる自作の疲労試験機を用い，タブや疲労試験機の改良を行い，プラスチックタブを用いた疲労試験の信頼性の向上を目的として，アルミニウムボンディングワイヤーの疲労試験を行ったので，その結果について報告する。

2. 試験方法

2.1 疲労試験機

Fig.1 に示すような自作の小型疲労試験機を用いた。アクチュエータは容量 9.8N の電磁式加振機(周波数 1.0～2000Hz)，繰返し変位はレーザー変位センサーで計測し，荷重の測定は容量500mNのロードセルを用いている。

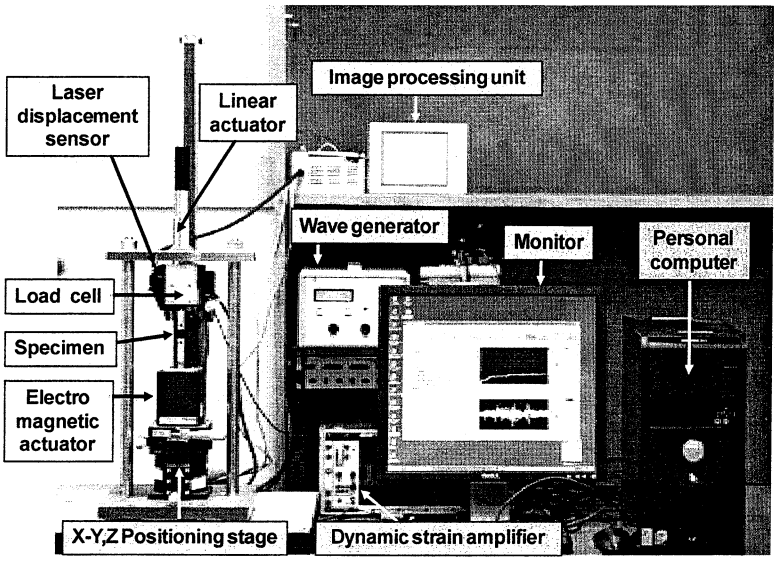

Fig.1 Fatigue tester

疲労試験システムを Fig.2 に示す。この試験機は，最大荷重の制御を行っている。最大荷重が設定荷重値を下回って 10sec 経過したとき，ロードセルの上部に設置されたリニアアクチュエータが，1回の作動で試験片を引張速度 1.0 μ /s で 1.0 μ m の変位を与え，試験片に引張りの変位を加えることにより，最大荷重を一定に保つように制御している。

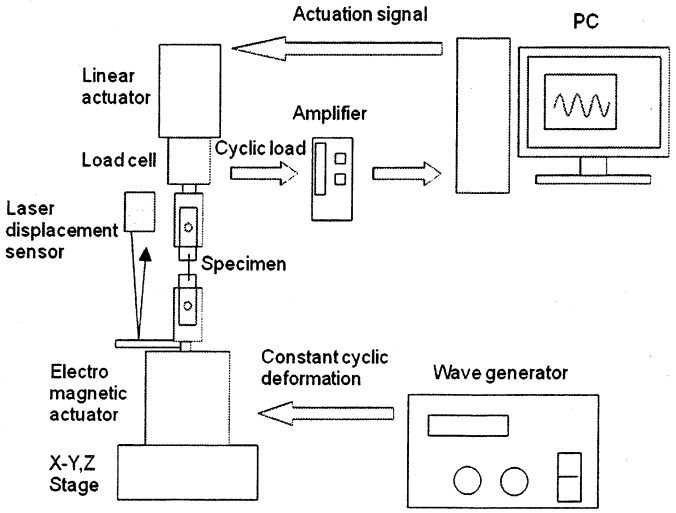

Fig.2 Schematic diagram of fatigue test system

2.2 供試材料および試験片

試験片には、Kulicke&Soffa，Ltd. 製および田中貴金属工業（株）製の直径 25 μ m のアルミニウムボンディングワイヤーを用いた. この Al 線を所定の長さに切断して試験片とした。試験片を Fig.3 に示すプラスチックタブに接着し，タブを試験機に取り付けた後，Fig.3 に示すタブの斜線部を切り離した後，試験片にのみ荷重が加わる状態で試験に供した。タブの材料は，熱可塑性プラスチックのポリプロピレン（PP）および熱硬化性プラスチックのポリイミド（PI）を使用した。タブの作製はレーザーマーカーを用い，レーザー加工でシートから切り出すことにより，加工精度の均一なタブを製作し，タブの寸法のばらつきを少なくしている。試験片のタブへの接着にはシア

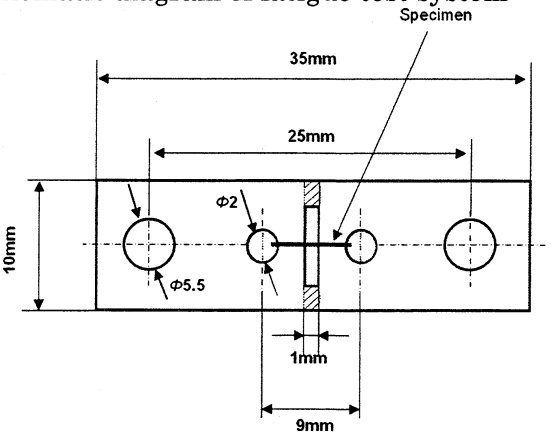

Fig.3 Tub and specimen for fatigue test

ノアクリレート系瞬間接着剤と，接着強度の向上を図る為に表面改質剤を用いた。また試験片のねじれを除くために，試験片を Fig.3 に示すタブの補助穴に通し，その後 0.1g の重りを試験片の両端部に取り付けた後，接着した。

2.3 疲労試験方法

疲労試験は加振機で一定変位の正弦波を加え，片振引張りの繰返し荷重を加えた。繰り返し速度 25Hz とし，繰返し数が 10^7cycle に達しても破断しなかった場合はその時点で試験を終了した。なお，試験機は恒温層の中に設置され，試験温度一定（２３±１° C）で行った。温度疲労試験終了後，走査型電子顕微鏡（KEYENCE 製 VE-8800S）を用いて破断面の観察を行った.

3. 実験結果および考察

Fig.4 に S-N 曲線を示す。PP タブを用いたものの疲労限度は 230MPa，熱硬化性樹脂の PI タブを用いたものは 290MPa 付近にあり，PP タブに比べて PI タブを用いたものは疲労強度が増加する結果となった。この理由としては，温度によりプラスチックタブが硬化あるいは軟化することによる繰返し荷重の変動が考えられる。熱可塑性樹脂のポリプロピレンタブのみで疲労試験を行ったところ，試験温度１℃当たり試験荷重が７MPa 程度変化をすることが明らかとなり，温度の影響を受けにくい熱硬化性のポリイミドのタブを用いた方が疲労強度は増加したものと考えられる。

また，供試 Al ボンディングワイヤーの引張り強さは 330MPa であることから，10^7cycle の疲労限度は引張り強さの約 88%となり，Al バルク材に比べて疲労限度の割合が高いことが分かった。

繰返し最大応力 321MPa の試験片の破断面を Fig.5 に示す。この破断面から，Al ボンディングワイヤーは，破断部にくびれを生じ，ネッキングを起こして破断しており，き裂進展がほとんどないまま，不安定破断に到ったと推定される。また，この破断面の形状は，引張りによる破断面の形状と非常によく似ていることが分かる。次に，繰り返し最大応力 301MPa の試験片の破断面を Fig.6 に示す。これもネッキングを起こして破断しているが，繰返し応力が低くなったためか，最終破断部にせん断変形の部分が観察される。微小寸法材料においては，これらのようなネッキングによる破断が生じる[6) 7)]ことが知られている。

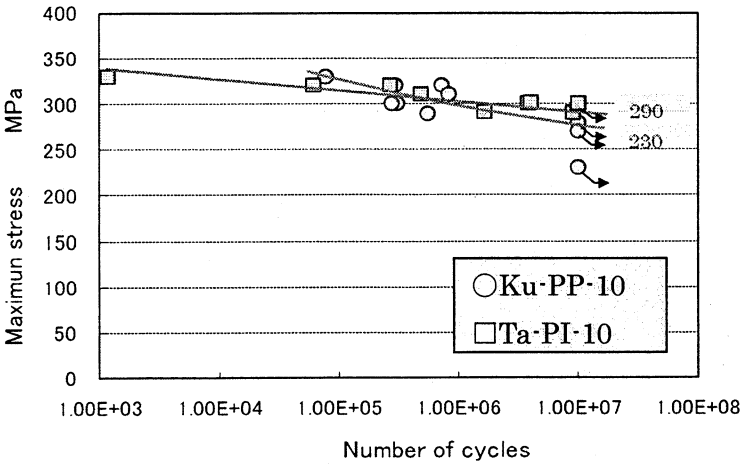

Fig.4 S-N diagram of Al bonding wire

Fig.5 Fracture surface of Al bonding wire (σ max=321MPa,N=6.14×10^4, El=21μm)

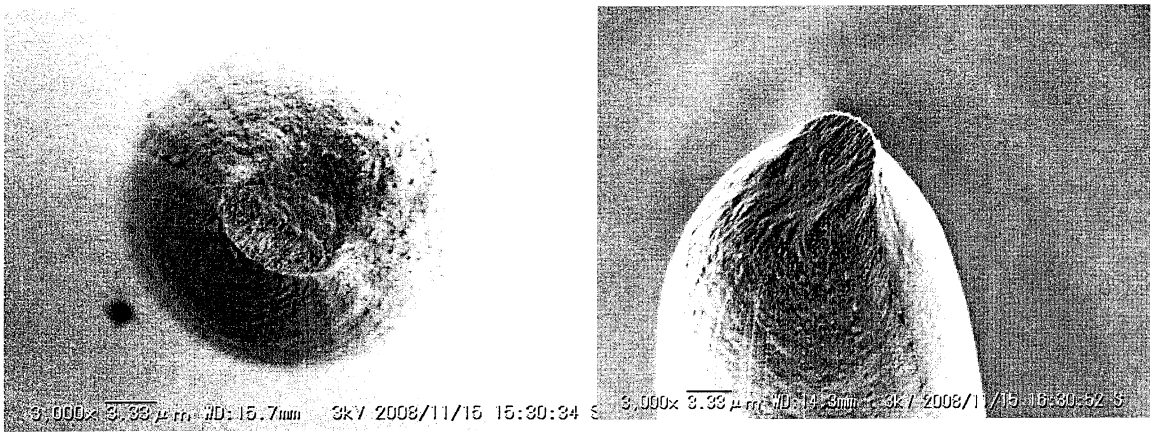

Fig.6 Fracture surface of Al bonding wire (σ max=301MPa, N=3.84×10^6, El=30μm)

4. 結 論

1）PI タブを用いることにより，直径 25μm の Al ボンディングワイヤーの信頼性の高い疲労試験を行うことが可能である。

2）リニアアクチュエータを用いて疲労試験中の試験片の伸びを補正することにより，最大荷重一定の荷重制御試験を行うことができた。

参考文献: 1）後藤 他5名：材料試験技術，Vol.53，No.1，pp.38-42（2008） 2）井口 他5名：材料試験技術，Vol.54，No.1，pp.47-49（2009） 3）箕島 他2名：日本材料学会 第269回疲労部門委員会 第27回マイクロマテリアル部門委員会研究討論資料，p.44-45（2004-5） 4）箕島 他2名：日本材料学会 第269回疲労部門委員会 第27回マイクロマテリアル部門委員会研究討論資料，p.35-43（2004-5） 5）原 他3名：第4回マイクロマテリアルシンポジュウム講演論文集, pp.18-23(2008) 6）中井 他2名:材料, Vol.54,No.3, pp.284-289(2005) 7）中村 他3名:第4回マイクロマテリアルシンポジュウム講演論文集，pp.12-17(2008)

研究業績: 1）後藤，新井，宮坂，立野，小林，小久保：材料試験技術，Vol.53，No.1，pp.38-42（2008） 2）井口，上杉，後藤，立野，小林，小久保：材料試験技術，Vol.54，No.1，pp.47-49（2009）

4．2　原子レベルで界面を制御したヘテロエピタキシャル半導体による新機能発光・電子デバイスの開発研究

川西英雄、本田　徹

工学院大学　工学研究科　電気・電子工学専攻

Abstract

Importance of crystal quality control of the AlN and AlGaN epitaxial layers has been acknowledged for deep-UV LEDs and LDs device applications. We have demonstrated epitaxial growth of high quality AlGaN layer and AlN template on the SiC or Al2O3 substrate by both using (AlN/GaN) multi-buffer layer structure (MBLS for short) and Alternate Source-Feeding Low Pressure MO-VPE (ASF LP-MO-VPE for short) technique. However, the FWHM of (1-102) ϕ-scan was as wide as 900-1400 [arcsec] for the AlN template grown on the SiC. This means that high dense edge-type dislocation was included in the epitaxial layer with residual tensile strain along a-axis.

The purpose of this paper is to report our recent drastic improvement on FWHM of (10-12) ϕ-scan for the AlGaN and AlN template grown on SiC and Al2O3 substrate down to 35-50 [arcsec]. This means that the edge-type dislocation density can be decreased drastically in the AlN and AlGaN template grown on the substrates by our newly improved ASF LP-MO-VPE growth technique.

1．はじめに

AlN や AlGaN は紫外から深紫外域に対応した広いバンドギャップを有していることから、この波長域の発光ダイオード（LED）や半導体レーザ（LD）などの半導体発光デバイスを実現が可能な半導体材料である。一方、これらの半導体を SiC、サファイア、さらに近年可能となった GaN などの基板にエピタキシャル成長するとき、格子整合が不可能なことから、ヘテロ界面に起源を発するミスフィット転位を発生、多くのらせん転位、刃状転位、混合転位などの転位とエピタキシャル結晶内に高密度の欠陥が含まれることとなり、発光デバイスの実現を阻んできた。

これらを克服する方法として、この分野の研究機関では、先ず、バッファ層構造によりこれを解決してきた。それらには、「(AlN/GaN)ヘテロ結晶界面における転位の制御」及び「その上に成長した AlN への歪みの導入による転位の曲げ」の二つの効果を含んだ（AlN/GaN）多重バッファ層構造、後者の効果のみを利用した(AlGaN/AlN)超格子構造などがある。　他方、結晶成長法による解決法も試みられてきた。それまでの同時供給法に対し、種々の「交互供給法」が提案、導入されてきた。この方法の導入により、AlGaN や有するバンドギャップとしての財産を総て利用した紫外から深紫外域に対応した LED や光励起によるレーザ発振や誘導放出がすでに達成され、AlGaN 半導体が、結晶品質を向上することで、レーザ発振に十分な光学利得を得ることが可能である事が証明された。

その結果として、先ず、高品質な AlN テンプレートを下地として準備、その上に、デバイス構造を製作する手法・構造を採用した。「テンプレート」と呼ぶこの下地の結晶品質が、その上に成長する AlGaN の結晶品質に大きく影響を与えるからである。

この結果、AlN テンプレートの結晶品質は、らせん転位密度に関係する(0002)面 ω-スキャン半値幅で、約 50-70　[arcsec]まで狭窄化した。一方、刃状転位密に関係する（1-102）面）ϕ-スキャン半値幅は SiC 基板の場合は 900ー1400[arcsec]が最も良く、下限値であった。刃状転位密度がエピタキシャル成長層内に多く含まれていた。

一方、半導体としての特長を生かした、紫外から深紫外域に対応した電流注入型半導体レーザ（LD）の実現が望まれる。現在は、その最短波長は、おおよそ 342nm であり、しかもパルス動作に止まっている。AlGaN 層の電気抵抗値が大きく、駆動電圧はおおよそ 50V 前後と極端に高くなってしまっている。これを解決するための課題は、高 Al 組成の AlGaN の電気伝導制御にその課題が集約されて来ているように思える。

現時点では、この課題を、結晶品質を向上することで解決しようとしている。

本稿は、これまで課題であった刃状転位密度を減少させるために、「交互供給法」を周期的に導入した。その結果、（1-102）面）ϕ-スキャン半値幅が、それまで 900ー1400[arcsec]であったものを、35ー60[arcsec]と大幅に減少、刃状転位密度が大きく低減した。更に、この結果は、TEM 断面観測からも確認出来、交互供給法による成長法では「どんなことが起きているのか」を議論し、明らかにしたい。

2．実験

AlN、AlGaN テンプレートは SiC 基板上に、減圧 MO-VPE 法によって成長した。　通常の「同時供給法」の成長法が主体であるが、今回は、新しく「交互供給法」を、同時供給法の合間に、周期的に加える工夫をした。この時の交互供給法の繰り返し数（周期と以下呼ぶ）は、暫定的に 5 回とした。尚、それに先立ち、基板とテンプレート層の間には、これまでと同様に（AlN/GaN）多重バッファ層構造を導入している。　この時の結晶断面構造を模式的及び高解像度 SEM 断面写真を示したのが、それぞれ、　図. 1-(a)及び図. 1-(b)であ

る。テンプレート層の層厚は 1ー2 [μm]であった。　更に、交互供給法で成長した試料の断面では、それに対応した薄い層が僅かに観測され、その存在が認識できるとともに、同時供給法で成長した結晶と、交互供給法で成長した結晶の品質が異なる事が,SEM によってもあることが予見される。

成長層の結晶品質はX線解析装置により評価した。特に、ω-スキャン及びφ-スキャン半値幅と、らせん転位密度や刃状転位密度と関係は、本研究室で、TEM 断面観測と比較しほぼ校正したものである。

尚、ω-スキャンには、(0002)面を、φ-スキャンには、(10-12)面の非対称散乱面など良く用いられている面を用いた。

3. 実験結果と考察

3-1.　XRC による転位の間接観測

本稿での XRC 解析では、らせん転位に関するω-スキャン、及び、刃状転位に関するφ-スキャンは、それぞれ　(0002)面、及び、(10-12)面 (非対称散乱を利用) とし議論をする。尚、これに関する理論曲線も報告されているが、本研究でも、TEM 断面観測による転位密度と各スキャンの半値幅との関係を実験的に確認し、XRC の各半値幅測定により、転位密度が見積もられる事を確認している。以下はその結果を基礎に述べることとする。

(0001)面 SiC 基板に同時供給法のみ、及び、5 周期の交互供給法を加え成長した AlN テンプレート (エピタキシャル層厚は 1.5μm) のそれぞれのXRD及びXRCの測定結果の一例を、図.2-(a), 2-(b), 2-(c)にまとめた。

AlN テンプレートを同時供給法のみで成長した試料のω-スキャン、及びφ-スキャンの半値幅はそれぞれ、150[arcsec]、及び、1070[arcsec]となった。この結果から見積もったらせん転位密度、及び、刃状転位密度は、それぞれ、$1x10^{8}$ [cm^{-2}] 及び、$9 x 10^{9}$ [cm^{-2}] となる。

一方、同時供給法の間に、交互供給法を 5 周期挿入した試料のω-スキャン、及びφ-スキャン半値幅はそれぞれ、154[arcsec]、及び、50ー60 [arcsec], 最も狭いもので図.2-(c)に示すように、36[arcsec]のものも得られた。この結果から見積もったらせん転位密度は、同時供給法と同じ密度であるのに対し、刃状転位密度は、$5x10^{7}$ [cm^{-2}] と約 180 分の 1 程度まで減少した。

1ー2μm の層厚の AlN テンプレートの試料に対するω-スキャンの半値幅は、狭いもので約 50ー70[arcsec]を得たが、交互供給法を挿入した場合でもこの値には大きな変化は認められなかった。この実験結果は、各転位の中で、らせん転位成分は、交互供給法によって制御は出来ない可能性を示している。(ただし、この成分は多重バッファ層構造や、超格子構造によって制御できることは、以前にすでに報告しているので参照願いたい。)

一方、刃状転位成分は、交互供給法によって制御可能であることを強く示唆している。

この様に、XRC 解析の結果から、これら二つの試料の間で、結果の違いが認められ、刃状転位の制御の可能性を示唆しているが、これを確かめるのは、次に述べる、断面 TEM 観測の結果を見なければならない。

3-2.　刃状転位の直接観測 (TEM 断面観測)

交互供給法により成長する事により転位がどの様に振る舞うかを、直接観測するために、断面 TEM 観測を行った。　(刃状転位+混合転位) のみを観測するために、(-1-120) スポットを用いた暗視野像である。従って、(刃状転位+混合転位) は「白く」現れている。また、この TEM 断面観測に含まれる混合転位成分は、別途行った(0000)明視野像、及び、(0002)暗視野像の観測結果との比較から、分類、判別し、刃状転位成分のみを抽出することが出来る。

図.3 は、交互供給法を挿入していない試料の (-1-120) スポットを用いた暗視野像の一例である。この試料のφ-スキャン半値幅は、835[arcsec]であった。　SiC 基板と AlN テンプレートの間に 5 周期の(AlN/GaN)多重バッファ層構造を挿入しているが、界面に発生した多くの (刃状転位+混合転位) が、激しく、先ず、減少している。明視野像、及び (0002) スポット暗視野像によっても同様な様子が観測されており、らせん転位成分も、このバッファ層により減少していることが分かった。この時の様子は、転位が各ヘテロ界面で「終端している様子」とともに、「曲線を描いている様子」とが、併せて観測された。このバッファ層構造により、基板と窒化物半導体界面で発生した多くの転位の内、らせん転位を主体に、刃状転位も断面図の示すように、減少する傾向が観測された。同様な現象は、AlN テンプレートとその上に成長した、AlGaN とのヘテロ界面においても観測されている。

同様な観測を、交互供給法を挿入した AlN テンプレート層についても観測した。

図.4 は、図.1-(b)の SEM 写真に対応した交互供給法を挿入した試料の(-1-120)スポットによる暗視野像である。この試料にも、SiC 基板と AlN テンプレートの間に 5 周期の(AlN/GaN)多重バッファ層構造を挿入しており、らせん転位を主体に、図.3 と同様、各種の転位が減少している。

更に詳しく議論するために、高解像度 SEM 断面写真と対にして整理した。

これらの結果から、以下のことが判明する。すなわち、(AlN/GaN)多重バッファ層構造によって導入した「a 軸方向の引っ張り歪み」の導入により、刃状転位が、同時供給法で成長した AlN テンプレート層の「途中で僅かに停止するもの」様子が観測されるとともに、「5 周期の交互供給法で成長した層の付近」で、刃状転位が停止している様子がはっきりと確認出来る。この結果から、交互供給法の挿入によって、刃状転位を制御できる可能性が強く示唆される。

今回の検討から、次のようなことが結論される。この様な転位の振る舞いが、XRC 解析結果にも反映され、らせん転位を反映するω-スキャン半値幅、及び、刃状転位を反映する

φ-スキャン半値幅の双方に効果を現し、それぞれの半値幅の急激な減少が実現できた。特に、刃状転位は、(AlN/GaN)多重バッファ層構造により導入された歪み制御よっても減少できるが、その効果は限定的であった。むしろ、らせん転位の減少に、この構造は優位である。一方、交互供給法は、刃状転位の減少にむしろ効果的である事が、X線解析及び、断面TEM解析によって、間接的及び直接的に確認する事が出来た。

4. まとめ

本稿では、AlN テンプレートの結晶品質、特に、これまで未解決であった刃状転位の減少に対して、「交互供給法による減圧MO-VPE」を通常の同時供給法の間に周期的に導入することが極めて有効であることを、実験的に明らかにした。また、刃状転位の挙動を断面TEMにより観測することで、直接観測することが出来た。その結果、AlN テンプレート層内に含まれる刃状転位密度は 5×10^7 [cm^{-2}] 程度まで、減少することが出来、いっそうの高品質AlN結晶が実現できる様になった。

謝辞

本研究は、大学院生、武田(修士1年在学)、学部生、安斉君 (H20年度卒論研究)、中館君 (H20年度卒論研究)、及び、TEM解析は、村川君(現NECエレクトロニクス)、X線解析は、新倉君 (現ローム) によってなされたものである。彼等の協力に心より感謝する。尚、筑波大名誉教授　長谷川文夫先生には、日頃より有意義な議論を頂き、ここに深く感謝する。

(本研究に関する発表：H)

1. Hideo Kawanishi, "Structure and Properties of Deep-UV AlGaN MQW Laser", Proceedings of iNow2008 (印刷中).
2. Ken-ichi Isono, Eiichiro Niikura, Koichi Murakawa, Fumio Hasegawa, and Hideo Kawanishi, "Improvement of Crystal Quality of n-AlGaN by Alternate-Source-Feeding Metal Organic Vapor Phase Epitaxy", Japan J. Appl. Phys., Vol.46, No.9A, 5711-5714 (2007.09)
3. Kouichi Murakawa, Eiichiro Niikura, Fumio Hasegawa, and Hideo Kawanishi, "Reduction of Threading Dislocations in AlGaN/AlN/SiC Epitaxial Layers by Controlled Strain with (AlN/GaN) Multibuffer-layer Structure", Japan. J. Appl. Phys., Vol.46, No.6A, 3301-3304 (2007.06)
4. Hideo Kawanishi, Masanori Senuma, and Takeaki Nukui, "Tm-mode lasing and anisotropic polarization properties of AlGaN multiple quantum well lasers in deep-ultraviolet spectral region", Proceeding of SPIE Photonics West 2007, Vol.6473, 64731D (2007.2)
5. Eiichiro Niikura, Kouichi Murakawa, Fumio Hasegawa, and Hideo Kawanishi, "Improvement of crystal quality of AlN and AlGaN epitaxial layers by controlling the strain with the (AlN/GaN) multi-buffer layer", Journal of Crystal Growth, Vol.298, 345-348. (2007.01)
6. Hideo Kawanishi, Eiichiro Niikura, Mao Yamamoto, and Shoichiro Takeda, "Experimental energy difference between heavy- or light-hole valence band and crystal-field split-off-hole valence band in $Al_xGaN_{1-x}N$", Appl. Phys. Lett., Vol.89, No.25, 251107-1 - 251107-3 (2006.12)
7. Hideo Kawanishi, Masanori Senuma, Mao Yamamoto, Eiichiro Niikura, and Takeaki Nukui, "Extremely weak surface emission from (0001) c-plane AlGaN multiple quantum well structure in deep-ultraviolet spectral region", Appl. Phys. Lett, Vol.89, No.8, 081121-1 - 081121-3 (2006.08)
8. Hideo Kawanishi, Masanori Senuma, and Takeaki Nukui, "Anisotropic polarization characteristics of lasing and spontaneous surface and edge emissions from deep-ultraviolet ($\lambda \approx 240$ nm) AlGaN multiple-quantum-well lasers", Appl. Phys. Lett., Vol.89, No.4, 041126-1 - 041126-3 (2006.7)
9. 川西英雄、瀬沼正憲、貫井猛晶、「深紫外AlGaN多重量子井戸半導体レーザー光の光学的異方特性」、日本光学会 (応用物理学会) 光学、35巻、5号、265-267 (2006. 05)
10. Naoyuki Obinata, Koichi Sugimoto, Kazuyuki Ijima, Masaya Ishibiki, Shinichi Egawa, Tohru Honda, and Hideo Kawanishi, "Relationship between Excess Ga and Residual Oxides in Amorphous GaN Films Deposited by Compound Source Molecular Beam Epitaxy", Japan. J. Appl. Phys. Vol.44, No.12, 8432-8434 (2005.12)
11. 川西英雄、高野隆好、瀬沼正憲、貫井猛晶、「光励起によるAlGaN多重量子井戸型深紫外レーザーの発振特性-発振波長域240ー360nm」応用物理、第74巻、第11号、1458-1462 (2005.11)
12. Tohru Honda, Yohta Aoki, Miwako Akiyama, Naoyuki Obinata, Shinichi Egawa, and Hideo Kawanishi, "GaN films deposited at low temperature on (111) Si by compound-source molecular beam epitaxy technique", J. Vac. Sci. Technol, B23(4) (2005.07)

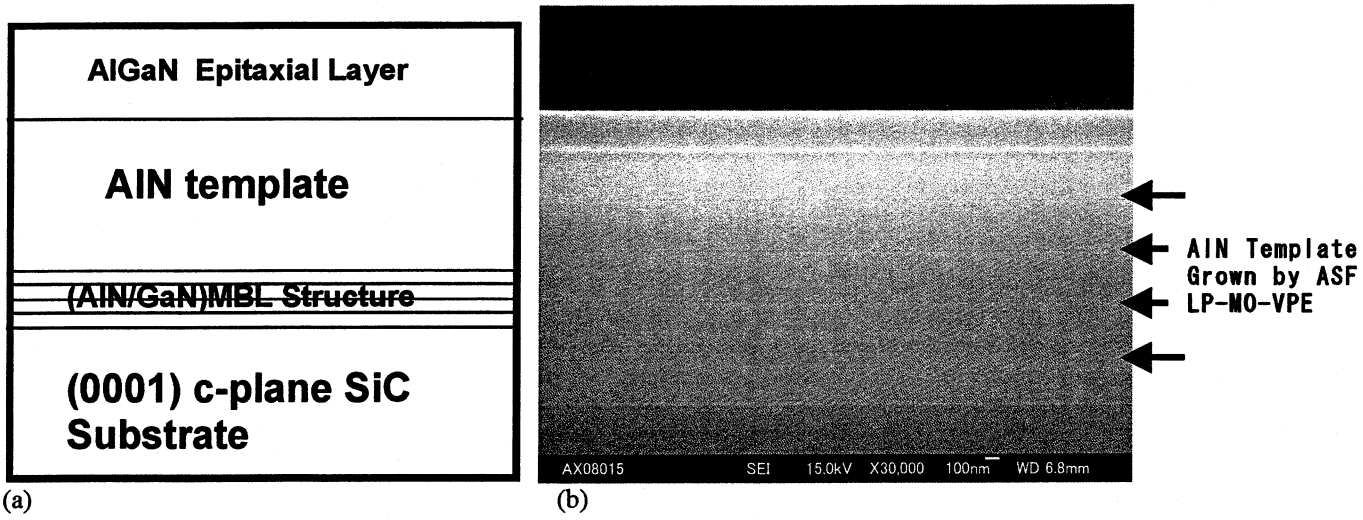

Fig. 1 (a) and (b): Layer structure and cross sectional SEM image of quality controlled AlN template grown on SiC substrate by ASF LP-MO-VPE with (AlN/GaN) MBL Structure. Residual strain in the AlN template can control by changing layer thicknesses of AlN and GaN of the (AlN/GaN) MBL structure in atomic scale.

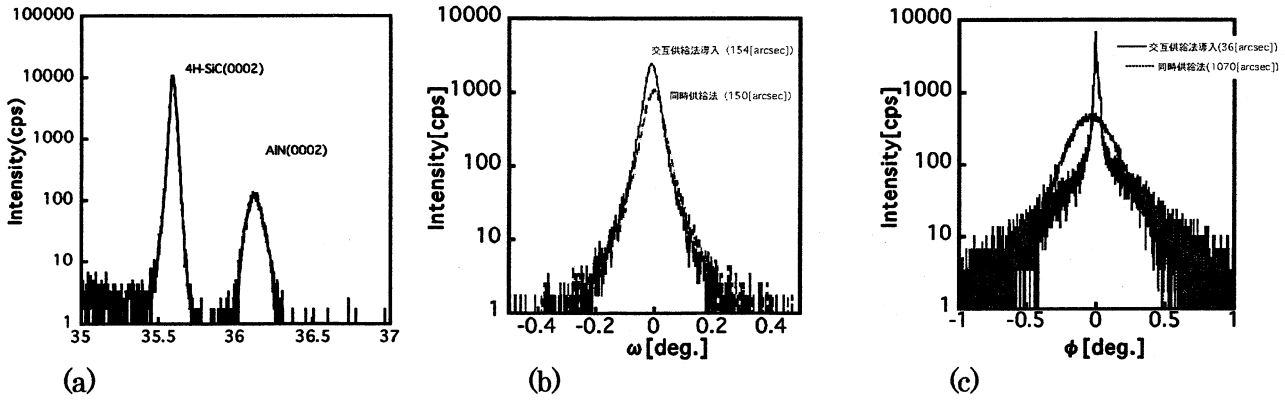

Fig.2: X-ray analysis of AlN template grown on SiC substrate.
(a) (2 θ - ω) scan of AlN template (1.5μm thick) grown on (0001) plane SiC substrate.
(b) (0002) ω–scan of AlN template grown by conventional and ASF LP-MO-VPE.
(c) (10-12) ϕ–scan of AlN template grown by conventional and ASF LP-MO-VPE. The narrowest FWHM was 36 [arcsec] as shown in this figure (c).

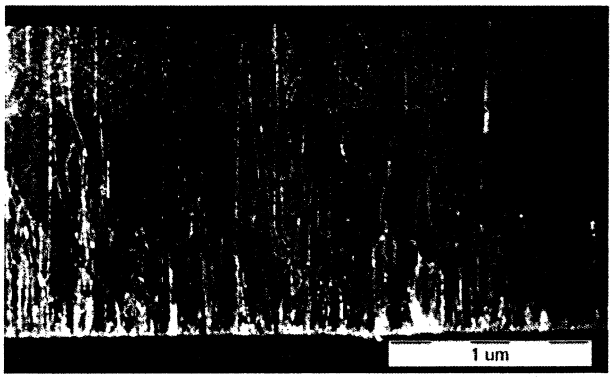

Fig. 3: Cross sectional TEM image of AlN template grown by conventional simultaneous LP-MO-VPE (for (-1-120) Spot). FWHM for (10-12) plane ϕ -scan was around 845 [arcsec].

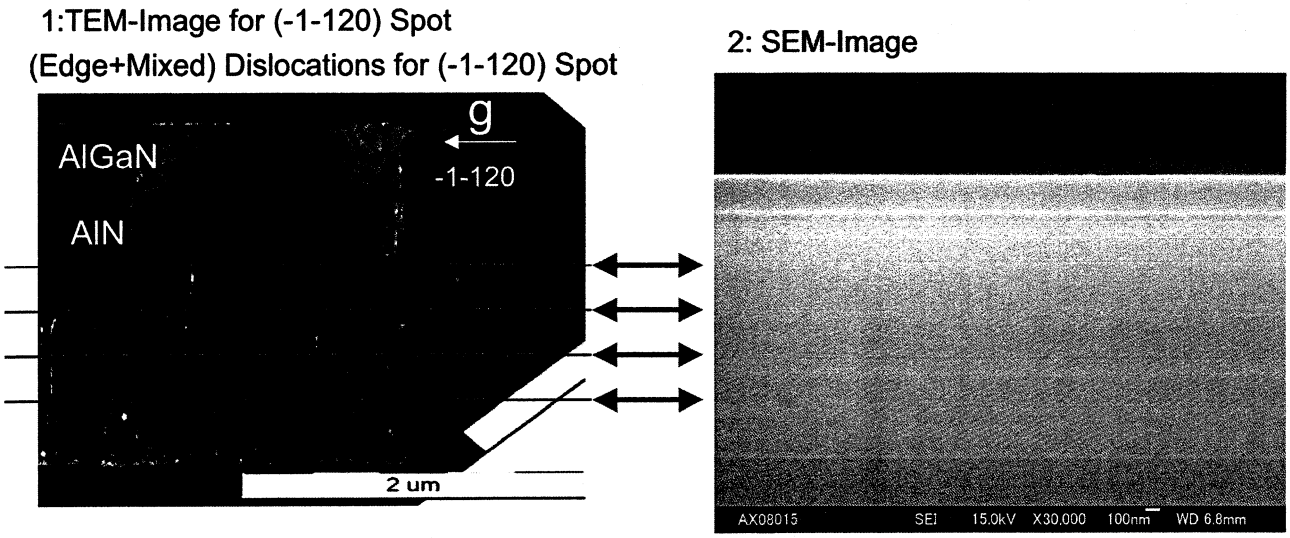

Fig. 4: Cross sectional TEM and high-resolution SEM images of AlN template grown by ASF LP-MO-VPE (for (-1-120) Spot). FWHM for (10-12) plane ϕ -scan was around 50 [arcsec].

4.3 液晶分子に対して双安定配向特性をもつ基板表面の形成とそのＬＣＤへの応用

-----紫外線硬化樹脂を用いて基板上に形成した回折格子状溝構造表面を溝と垂直方向にラビングすることによる双安定配向-----

齊藤　　進　工学部情報通信工学科
高橋　泰樹　工学部情報通信工学科

Formation of Bistable Alignment Layer on Substrate Surface for LC Molecules and Its Applicalion to LCDs

-----Bistable Alignment Resulted from Rubbed Groove Structure Formed on Substrate Surface Using UV Curable Resin----

Susumu SAITO and Taiju TAKAHASHI
Department of Information and Communications Engineering, Faculty of Engineering, Kogakuin Univ.

Periodical groove structure was formed on the substrate surface by copying the structure on the grating film on the market to the photo curable resin coated on the substrate surface. And then, the substrate surface with groove structure was rubbed along the direction perpendicular to the groove. Alignment of LC on such substrate surface was experimentally investigated. In a cell constructed using such substrate and the substrate treated by a vertical alignment material, distinctive domains with different orientation direction were observed. This suggests us that the bistable alignment property can be adapted on the substrate surfaces by this method.

1. 研究背景

近年、紙媒体とデジタル媒体の長所を兼ね備えたディスプレイである電子ペーパーが注目を集めている。現在様々な種類のディスプレイモードが提案され実用化されているが、液晶ディスプレイはその薄型・軽量・低消費電力・安価といった特徴から電子ペーパーへの応用に適している表示モードの一つである。

しかし、電子ペーパーのような携帯端末への応用を考えた場合、更なる低消費電力化と低コスト化が望まれている。液晶ディスプレイの更なる低消費電力化と低コスト化を図るための方法として、バックライトを用いず、TFT 等のアクティブ素子の形成を必要としない反射型のパッシブ・マトリック型 LCD が見直されている。パッシブ・マトリックス型 LCD でアクティブ・マトリックス型 LCD 並みの高密度表示を実現するためには、配向のメモリ性を有する双安定型 LCD が注目され、これまでに様々なモードが提案されてきた。

それらの双安定型 LCD は、配向層に単安定な配向特性をもつものを用いるか、双安定な配向特性を持つものを用いるかによって二つに分類される。前者の例としては、液晶の双安定なテクスチャー変化を利用する双安定コレステリック LCD[1]や液晶のツイスト角を変化させる双安定ツイストネマティック LCD[2][3]等があり、後者の配向層に双安定配向性を付与する方法として、特定の条件で形成した SiO の斜方蒸着膜を用いる方法[4]、基板表面にグレーティング状の溝を形成し、その表面に垂直配向処理を施す方法[5]、互いに隣接する微少領域のラビング方向が直交するようにＡＦＭの探針でラビングするナノラビング法[6]等が提案されている。しかし、これらの配向層に双安定な配向性を付与するための方法は、大面積化が困難な点で実用上問題視されており、実用化に至っていない。

基板間で液晶分子を均一に配向させることは、液晶ディスプレイを実現する上で極めて重要な技術であるだけでなく、液晶の基礎的な物性を研究する上でも重要な技術である。本研究では、

液晶と固体基板の界面を出来るだけミクロな視点から捉え、液晶の配向のメカニズムを考究し、特に基板表面に大面積にわたって均一に双安定な配向性を付与する技術を開発し、それを超低消費電力の双安定型液晶ディスプレイに応用するための基礎技術を確立することを目標としている。

2. 研究経過

大面積に亘って、均一に双安定な配向特性を持つ配向層を得るための方法として、これまでに以下の五つの方法を検討してきた。

① 未架橋時にラビング方向と直交する方向に液晶分子を配向させるポリビニルシンナメート（ＰＶＣi）とラビング方向に平行な方向に配向させるポリイミド（ＰＩ）系配向材の混合溶液をスピンコートし、熱処理後、一方向にラビングする方法[7][8][9]

② 偏光ＵＶ光照射によって偏光方向と平行な方向に配向規制力を生じる光配向材と偏光方向と直交する方向に配向規制力を生じる光配向材の混合溶液を配向材としてスピンコートし、全体への偏光ＵＶ光照射とストライプ状光学マスクを通して偏光ＵＶ光照射を行う方法

③ 垂直配向規制力の弱いポリイミド系配向材（日産化学工業製　ＲＮ1338）をスピンコートし、熱処理後、ｐ偏光ＵＶ光を斜め照射することによって特定の方向の主鎖を選択的に分解することによって配向規制力に非対称性を誘起する方法

④ 市販の回折格子フィルムの溝構造を基板に塗布した紫外線硬化樹脂に転写することによって形成した溝構造表面を溝と直交する方向にラビングする方法[10]

⑤ ＩＴＯ基板上に真空蒸着したアルミニウム薄膜をフォトリソグラフィー技術によって幅0.5 ミクロン間隔のストライプ状パターンにエッチング後、Al を陽極酸化することによって、Al の酸化膜上で得られる垂直配向規制力と Al がエッチング除去されたことによって生じた溝による平行配向規制力を用いる方法[11]

前回の研究成果報告会では①の方法でえられる双安定配向特性について報告した。今回は③の方法についてその詳細を報告する。

3. 紫外線硬化樹脂を用いて基板上に形成した回折格子状溝構造表面を溝と垂直方向にラビングすることによる双安定配向[9]

本研究では、市販のフィルムグレーティングの溝構造を基板に塗布した紫外線硬化樹脂に転写することによって形成した溝構造表面を溝と直交する方向にラビングした基板を用いることによって双安定配向が得られることを確認し、インプレーン電界の印加による二状態間のスイッチングについて検討する。

3-1 供試セルの作製

Fig.1 に示すような櫛歯電極付きガラス基板（電極幅 53μm、電極間距離 120μm）に感光性樹脂(テクノビット 2000LC)（Heraeus Kulzer GmbH&Co.KG 社製）を塗布した後、回折格子フィルムの溝構造を転写した。

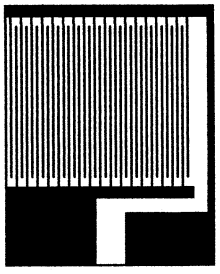

Electrode width　:53 μm

Interelectrode distance　:120 μm

Fig. 1 Electrode pattern

紫外線照射エネルギーは 7 J/cm^2、回折格子フィルムには、ピッチが 1μm のものを使用した。その後、溝構造の溝に直交する方向にラビング処理を 3 回施した。Fig.2(a)は回折格子フィルムのレー

ザ顕微鏡写真であり、Fig.2(b)は櫛歯電極付きガラス基板上に転写された溝構造のレーザ顕微鏡写真である。Fi.2(c)は転写された溝構造表面を溝と直交する方向ラビングしたもののレーザ顕微鏡写真である、ラビングしたことによって溝の山が削られていることが分かる。垂直配向処理を施した基板と貼り合せ試料セルを作製した。垂直配向材はSE-1211(日産化学工業社製)、液晶材料はネマティック液晶5CB(メルク社製)（$\Delta\varepsilon > 0$)、セル厚を約6μmとした。

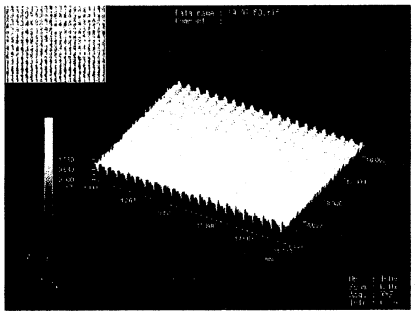

Fig. 2(a) Diffraction grating film original

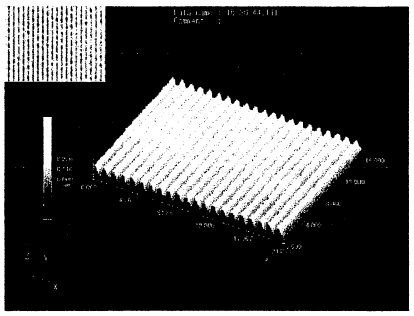

Fig. 2(b) Copy-printing groove structure on the glass substrate

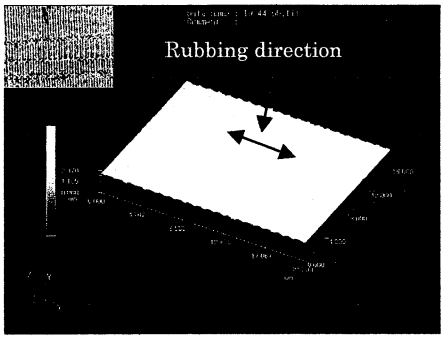

Fig. 2(c) After processing rubbing treatment

3-2　実験結果および考察

試料セルの配向容易軸間の切り換えを面内電界を印加することによって試みた。電圧印加前、および周波数1Hz、±20Vの方形波を印加後の偏光顕微鏡写真をそれぞれFig.3(a)、Fig.3(b)に示す。それぞれのドメイン内の液晶分子の配向方向は、偏光顕微鏡と光学補償フィルムを用いて確認したところ、図中に示したn_1、n_2の二方向であった。Fig.3(a)をFig.3(b)と比較することによって、電圧を印加することによって、部分的ではあるが、n_1の領域がn_2に、n_2の領域がn_1に遷移したことが分かる。しかし、電極パターンの都合上、逆方向の切り替えをすることは出来なかった。

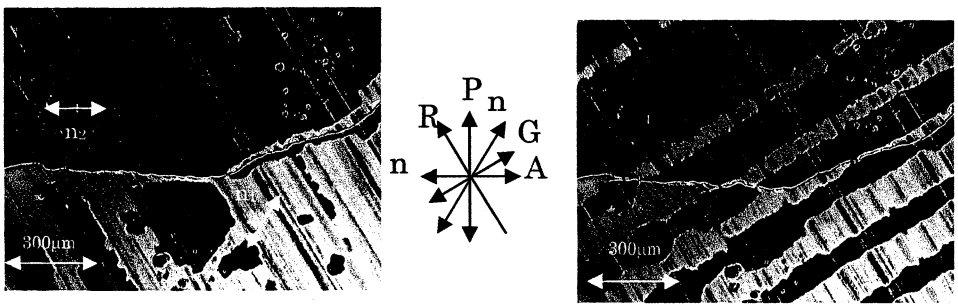

Fig 3(a) Before voltage Application

Fig.3(b) Just after removing the voltage application(5min)

A : Analyzer　　G : Groove structure

P : Polarizer　　n_1, n_2 : Directers

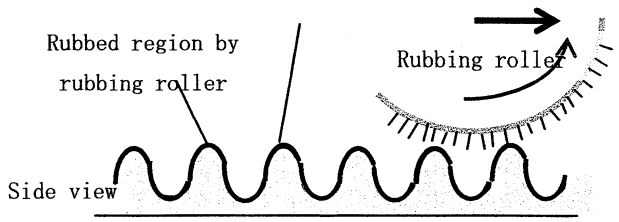

Fig. 4 Substrate with periodical groove structure

今回行った配向処理によって二つの配向容易軸が生じたのは、Fig.4 のようにラビングされなかった谷部分では溝構造による溝に平行な方向への配向する傾向が強く、ラビングされた山の上の部分ではラビング処理により細かい溝が形成され、溝と直交するラビング方向に配向する傾向が強くなると考えられる。これらが周期的に存在することが原因ではないかと考えられる。

また、今回用いた樹脂を平坦に塗布した後に硬化させた基板表面をラビングして作製したセルでは、プレチルト角の発生は見られなかった。しかし、今回の溝構造をラビング処理したセルではプレチルト角の発生が確認されている。このプレティルト角は、山の頂上前後でラビングの度合いが異なることによって生じたと考えられる。

3-3.結論

市販のフィルムグレーティングの溝構造を基板に塗布した紫外線硬化樹脂に転写することによって形成した溝構造表面を溝と直交する方向にラビングした基板を用いることによって双安定配向が得られることを確認した。さらに、インプレーン電界の印加により二つ配向容易軸間で一方向の切り替えに成功した。しかし、双向のスイッチングを実現するためには、電極構造と電圧印加法の更なる検討が必要である。

4. 謝辞

本研究を遂行するに当たって、実験に協力してくれた大学院生の椎名哲也君に感謝します。また、本プロジェクトに関わるこれまでの研究に協力してくれた大学院生の下山和則君（平成 19 年度修了生)、塚田和成君、久保田直樹君、今井恵司君に感謝します。

参考文献

[1] M. Okada, T. Hatano and K. Hashimoto: SID Dig., 1997, p.101

[2]D. W. Berreman:Phys. Lett., 28, 1683(1972)

[3] I. Dozov, M. Nobili and G. Durand: Lett., 70, (1997)1179

[4] R. Barberi and G. Durand : Appl. Phys. Lett. 58, p2907 (1991)

[5] G. P. Bryan, C. V. Brown, J. C. Jones, E. L. Wood, I. C. Sage, P. Brett and J. Rudin:SID'97 Digest, 37 (1997)

[6] J. H. Kim, M. Yoneya, J. Yamamoto, and H. Yokoyama: Appl. Phy. Lett., 78, p.3055(2001)

本研究に関する発表論文

[7] K. Shimoyama, T. Takahishi, and S. Saito; IDW '07,(Sapporo),(2007)

[8] K. Shimoyama, T. Takahashi and S. Saito; Euro Display '07. (Moscow), (2007)

[9] **塚田和成、高橋泰樹、齊藤進**; 日本液晶学会討論会予稿集、ＰＡ32 (2008)

[10] T. Shiina, S. Saito, and T. Takahashi; The 22nd International Liquid Crystal Conference, Korea, Poster 1-APP30, (2008), Mol. Cryst. And Liq. Cryst. (Accepted)

[11] K. Imai, A. Yokoyama, S. Saito, and T. Takahashi; The 22nd International Liquid Crystal Conference, Korea, Poster 1-APP29, (2008)

研究業績

1. 生体分子のナノ表面

Available online at www.sciencedirect.com
SCIENCE DIRECT®
Digestive and Liver Disease
Digestive and Liver Disease 37 (2005) 190–194
www.elsevier.com/locate/dld

Liver, Pancreas and Biliary Tract

Urine diacetylspermine as a novel tumour maker for pancreatobiliary carcinomas

K. Yamaguchi[a,*], M. Nakamura[a], K. Shirahane[a], H. Konomi[a], N. Torata[a], N. Hamasaki[b], M. Kawakita[c], M. Tanaka[a]

[a] *Department of Surgery and Oncology, Graduate School of Medical Sciences, Kyushu University, Fukuoka 812-8582, Japan*
[b] *Department of Clinical Chemistry and Laboratory Medicine, Graduate School of Medical Sciences, Kyushu University, Fukuoka, Japan*
[c] *Department of Applied Chemistry, Faculty of Engineering, Kogakuin University, Tokyo, Japan*

Received 17 May 2004; accepted 11 October 2004
Available online 15 December 2004

Abstract

Background. Serum carcinoembryonic antigen (highly specific) and carbohydrate antigen 19-9 (highly sensitive) have been used as tumour markers for pancreatobiliary caners. A novel urine tumour marker, diacetylspermine, was compared with the two conventional serum tumour markers in 125 patients with pancreatobiliary diseases.

Results. When the diagnosis of benign or malignant condition was examined, the sensitivity of urine diacetylspermine (75%) was higher than that of serum carcinoembryonic antigen (44%; $P = 0.048$) and the same as that of serum carbohydrate antigen 19-9 (75%). The specificity of urine diacetylspermine (81%) was lower than that of serum CEA (92%) and as high as that of serum carbohydrate antigen 19-9 (80%). The efficiency of urine diacetylspermine (79%) was higher than that of serum carcinoembryonic antigen (74%) and the same as that of serum carbohydrate antigen 19-9 (79%).

Conclusion. These results suggest that urine diacetylspermine is a marker for pancreatobiliary carcinoma, which is as highly sensitive and specific as serum carbohydrate antigen 19-9.

Keywords: Carbohydrate antigen 19-9; Carcinoembryonic antigen; Diacetylspermine

1. Introduction

Polyamines are ubiquitous organic polycations that are synthesised in substantial amounts by rapidly growing and dividing cells, including cancer cells [1]. Polyamines excreted in the urine are mainly in the monoacetylated form. Among them, acetylputrescine is most abundant followed by acetylcadaverine, N^1-acetylspemidine and N^8-acetylspermine. Diacetylated forms are minor components and the average amounts of diacetylspermidine and diacetylspermine are only 1.4 and 0.46%, respectively [2]. These diacetylated polyamine species have not been identified because they are of limited quantity in the urine and are undetectable by conventional methods due to a lack of the primary amino groups.

Russell [3] first reported increased excretion of polyamines in the urine in cancer patients, which evoked a surge of studies on polyamine analysis in the urine in 1970s [1]. However, the following results were disappointing because there were too many false negative and false positive results as far as total polyamine levels and its monoacetyl compounds were examined [4], although their average urinary levels were certainly higher in patients with cancer than in healthy persons [4,5]. Therefore, diagnostic utility of urine polyamines has been abandoned for a long time.

Recently, Hiramatsu et al. [2,6,7] reported that diacetylspermine, one of spermine derivatives, is more frequently expressed in the urine of patients with malignant conditions compared to benign diseases using high-performance liquid

* Corresponding author. Tel.: +81 92 642 5441; fax: +81 92 642 5458.
E-mail address: yamaguchi@surg1.med.kyushu-u.ac.jp (K. Yamaguchi).

1590-8658/$30 © 2004 Published by Elsevier Ltd on behalf of Editrice Gastroenterologica Italiana S.r.l.
doi:10.1016/j.dld.2004.10.006

chromatography (HPLC) procedure. However, HPLC is difficult, not so popular and cannot be used as a clinical laboratory test. Thereafter, Hiramatsu et al. [8] developed a sensitive and accurate enzyme-linked immunosorbent assay (ELISA) system with the use of an affinity-purified polyclonal antibody against diacetylspermine. ELISA is easy to use, and therefore, appropriate to be used in the clinical laboratory.

Serum carcinoembryonic antigen (CEA) [9,10] and carbohydrate antigen (CA) 19-9 [11] have been used as tumour markers for pancreatobiliary caners. Serum CEA is highly specific for pancreatobiliary cancers and serum CA19-9 is highly sensitive. Their positivity increases with the progression of the diseases. They are not useful in detecting early cancers but are used as a marker of the recurrence of the tumour after surgical resection.

There are few reports of urine diacetylspermine levels in patients with pancreatobiliary diseases. In this series, clinical implications of this novel urine tumour marker, diacetylspermine, were examined by comparing with two conventional tumour markers, serum CEA and CA19-9, in 125 patients with pancreatobiliary diseases.

2. Materials and methods

This series consisted of 125 patients with pancreatobiliary diseases who were treated in the Department of Surgery I, Kyushu University Hospital, Fukuoka, Japan from November 2002 to January 2003. The 125 patients were 70 men and 55 women and their age ranged from 28 to 86 years with a mean of 63.5 ± 12.2 years. The 125 patients included 52 patients in the preoperative or postoperative state of benign diseases (control group), 22 patients in the preoperative state of malignant diseases, and the other 51 patients in the postoperative state (more than 3 months) of malignant conditions. Of the 51 postoperative patients, 10 had unequivocal signs of recurrence as judged by the clinical findings including imaging and the others had no definite evidence of recurrence as proven by subsequent clinical follow-up as well. Therefore, a total of 32 patients were considered to have malignant pancreatobiliary tumours. The 52 patients in the control group consisted of 28 with benign inflammatory diseases [15 in the preoperative state (9 chronic pancreatitis, 3 hepatolithiasis, 1 cholecystolithiasis, 2 adenomyomatosis of the gallbladder) and 13 in the postoperative state (10 chronic pancreatitis, 1 cholecystolithiasis, 1 choledocholithiasis and 1 choledochal cyst)] and 24 with adenoma (8 in the preoperative state of intraductal papillary-mucinous adenoma of the pancreas, 15 in the postoperative state of the same disease, 1 in the postoperative state of adenoma of the papilla of Vater). Urine diacetylspermine is known to be elevated in acute inflammatory conditions including acute pancreatitis, acute cholecystitis and the early postoperative state due to the rapid turnover of cells (personal communication with Dr. M. Kawakita). All patients who suffered from acute inflammatory diseases and were within 3 months after the operation were excluded from the present series. The patients with pancreatic endocrine tumours and hepatocellular carcinomas were also excluded because we intended to compare urine diacetylspermine and serum CEA and CA19-9. Urine diacetylspermine and serum CEA and CA19-9 were examined in all these 125 patients.

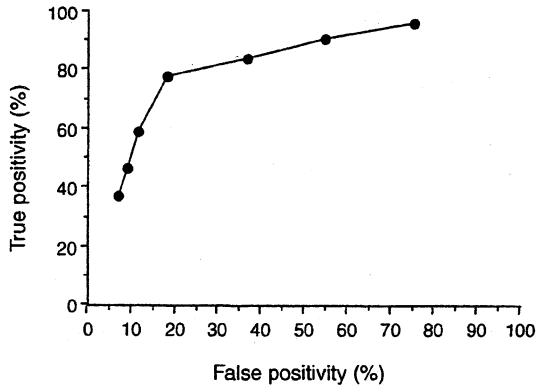

Fig. 1. Receiver operating characteristic curve indicating test performance for pancreatobiliary carcinoma for the following threshold values: 175, 225, 275, 325, 375, 425 and 475 nmol/g Creatinine. (●–●) Performance in distinguishing malignant from benign pancreatobiliary diseases.

Urine and peripheral blood were obtained in the morning. Diacetylspermine was measured by using ELISA system, which was created by Transgenic Co. Ltd, Kumamoto, Japan according to the Hiramatsu's method [8] in CRC Co. Ltd., Fukuoka, Japan. The cut-off level was set at 325 nmol/g Creatinine by constructing a receiver operating characteristics curve (Fig. 1). The serum levels of CEA and CA19-9 were measured in the Clinical Laboratory of Kyushu University Hospital. Their cut-off levels were 2.5 ng/ml and 37.4 IU/ml, respectively.

The clinical stage of malignant pancreatobiliary diseases was determined according to TNM Classification of Malignant Tumours issued by the UICC [12]. The 32 patients with primary or metastatic pancreatobiliary adenocarcinoma consisted of six in Stage IIb, two in Stage III and 24 in Stage IV.

Informed consent was obtained from each patient. The protocol was submitted to and preapproved by the Senior Staff Committee of the Department.

Values were expressed as mean ± standard deviation. Mean values were compared by Student's t test and the distribution of patients was measured by the chi-square test. The sensitivity, specificity, positive predictive value, negative predictive value and efficiency were measured. $P < 0.05$ was considered as statistically significant.

3. Results

3.1. Measurements of urine diacetylspermine

Urine diacetylspermine levels of the 52 patients in the control group and 32 with pancreatobiliary adenocarcinoma were 267.2 ± 143.0 and 621.5 ± 584.0 nmol/g Creatinine,

Table 1
Malignant and benign diagnosis by urinary diacetylspermine, serum CEA and CA19-9

	Diacetylspermine		CEA		CA19-9	
	Positive	Negative	Positive	Negative	Positive	Negative
Malignant	22	10	14	18	21	11
Benign	8	44	4	48	7	45
Sensitivity (%)	75[a]		44[a]		75	
Specificity (%)	81		92		80	
Positive predictive value (%)	71		78		86	
Negative predictive value (%)	84		73		87	
Efficiency (%)	79		74		79	

[a] $P = 0.044$.

respectively ($P < 0.001$). The serum CEA and CA19-9 values of the two groups were 1.2 ± 0.8 and 39.2 ± 158.5 ng/ml in the controls and 16.8 ± 21.3 and $7{,}825.2 \pm 23{,}996.8$ U/ml in the malignant group ($P = 0.0209$), respectively. The values of eight patients with intraductal papillary-mucinous adenoma were 243.2 ± 96.1 nmol/g Creatinine, 1.4 ± 1.2 ng/ml and 9.0 ± 5.0 U/ml, which were similar to those of the control group and were lower than those in patients with adenocarcinoma, but the differences were not statistically significant.

3.2. Diagnosis of benign and malignant conditions

Data concerning benign and malignant conditions are shown in Table 1. The sensitivity of urine diacetylspermine for malignant conditions was 75%, which was higher than 44% ($P = 0.044$) of serum CEA and as high as 75% of serum CA19-9. The specificity of urine diacetylspermine was 81%, which was lower than 92% of serum CEA and as high as 82% of serum CA19-9. Efficiency of urine diacetylspermine was 79%, which was similar to 74% of serum CEA and 79% of serum CA19-9.

3.3. Detection of recurrence of pancreatobiliary carcinoma

Data are present in Table 2. The sensitivity of urine diacetylspermine for the presence of recurrence of malignant pancreatobiliary diseases was 80%, which was higher than 70% of serum CEA and 70% of serum CA19-9. The specificity of urine diacetylspermine was 66%, which was lower than 78% of CEA and 83% of CA19-9.

Table 3
Tumour stage and urine diacetylspermine, serum CEA and CA19-9

Stage	Diacetylspermine		CEA		CA19-9	
	Positive	Negative	Positive	Negative	Positive	Negative
IIb	3	3	0	6	4	2
III	2	0	1	1	1	1
IV	19	5	11	13	16	8

3.4. Tumour stage and three markers

The mean values of urine diacetylspermine of patients with Stages IIb, III and IV carcinoma were 347.8 ± 139.7, 605.1 ± 375.9, 691.3 ± 651.7 nmol/g Creatinine, serum CEA 0.9 ± 0.1, 15.6 ± 20.9 and 50.8 ± 182.4 ng/ml and serum CA19-9 134.2 ± 154.6, 1726.1 ± 2438.2 and $10{,}256.3 \pm 27{,}405.1$ U/ml, respectively. The positivity of the three markers increased with the progression of tumours (Table 3). Three of the six patients with Stage IIb carcinoma showed a positive urine diacetylspermine result. None of them showed elevation of serum CEA, but four of them did show elevation of serum CA19-9.

3.5. Predictivity for unresectability of carcinoma by three markers

The sensitivity for prediction of unresectability of urine diacetylspermine (81%) was higher than that of serum CEA

Table 2
Recurrence and urinary diacetylspermine, serum CEA and CA19-9

	Diacetylspermine		CEA		CA19-9	
	Positive	Negative	Positive	Negative	Positive	Negative
Recurrence						
Yes	8	2	7	3	7	3
No	14	27	9	32	7	34
Sensitivity (%)	80		70		70	
Specificity (%)	66		78		83	
Positive predictive value (%)	36		44		50	
Negative predictive value (%)	93		91		92	
Efficiency (%)	69		76		80	

Table 4
Unresectability and three markers

	Diacetylspermine		CEA		CA19-9	
	Positive	Negative	Positive	Negative	Positive	Negative
Unresectability						
Yes	21	5	14	12	17	9
No	3	3	0	6	4	2
Sensitivity (%)	81[a]		54[a]		65	
Specificity (%)	50		100		33	
Positive predictive value (%)	88		100		81	
Negative predictive value (%)	38		33		18	
Efficiency (%)	75		63		59	

[a] $P=0.039$.

(54%, $P=0.039$) and serum CA19-9 (65%) (Table 4). The specificity of serum CEA was highest of the three markers. The efficiency of urine diacetylspermine (75%) was higher than that of serum CEA (63%) and serum CA19-9 (59%), but the differences were not significant.

4. Discussion

Serum levels of CA19-9 (highly sensitive) and CEA (highly specific) have been used as tumour markers for pancreatobiliary diseases. Usefulness of urine diacetylspermine as a tumour marker was studied in 125 patients with pancreatobiliary diseases. The sensitivity of urine diacetylspermine was higher than that of serum CEA and as high as that of CA19-9 and the specificity of urine diacetylspermine was also as high as those of serum CEA and CA19-9. A half of the patients with Stage IIb pancreatobiliary carcinoma gave a positive result for urine diacetylspermine. Urine diacetylspermine is a novel tumour marker for pancreatobiliary carcinoma, being as highly sensitive and specific as serum CA19-9.

It is true that ideal tumour markers should have high specificity and sensitivity for target malignant conditions. This urine diacetylspermine showed sensitivity and specificity similar to serum CA19-9 and CEA, respectively. Because the urine sample is easy to obtain and the measurement could be done by the ELISA kit, urine diacetylspermine is a novel convenient tumour marker for pancreatobiliary carcinomas.

The clinical outcome of patients with pancreatobiliary carcinoma remains dismal despite the recent progress of diagnostic and therapeutic modalities. Therefore, early diagnosis of pancreatobiliary carcinoma is mandatory. Conventional tumour markers such as serum CA19-9 and CEA have been reported to be not useful in detecting early pancreatic carcinoma. Urine diacetylspermine was positive in a half of patients with Stage IIb pancreatobiliary carcinoma, although the total number of patients examined was small. Therefore, this marker may be of value to detect early pancreatobiliary cancer.

Clinical differentiation between benign inflammatory diseases and malignant diseases is important as well as that of benign and malignant neoplasms. The urine diacetylspermine level is increased in the conditions where cell turnover is accelerated. Thus, patients in the phase of acute inflammation and in the early postoperative state were excluded from the present series. Urine diacetylspermine in patients with benign pancreatobiliary neoplasms were as low as that in those with chronic inflammatory pancreatobiliary diseases, and both the levels were lower than that of pancreatobiliary carcinoma. Therefore, urine diacetylspermine seems to be useful to distinguish malignant pancreatobiliary diseases from benign ones.

It is true that the surgical decision is made by imaging and/or macroscopic findings, but the prediction of resectability by serum tumour markers, if possible, is of great value for surgeons. The positivity and values of urine diacetylspermine increased with the progression of the malignant diseases. Therefore, the urine diacetylspermine level may be of some value to predict the choice of the treatment.

One of the other purposes of tumour marker determination is to predict the clinical outcome of patients with pancreatobiliary carcinoma. This series is a preliminary report on urine diacetylspermine in patients with pancreatobiliary diseases and there is no long-term information. Therefore, further examination is mandatory to identify the usefulness of this novel maker as a prognostic indicator.

Theoretically, urine diacetylspermine is considered to be not specific for a special type of malignancy but for all malignant conditions of any organs. Sugimoto et al. [6] reported that urine diacetylpolyamine was markedly increased in patients with urogenital malignancies and van den Berg et al. [13] reported a high concentration of diacetylspermine in the urine of patients with non-Hodgkin's lymphoma by capillary gas chromatography. In this series, a high concentration of urine diacetylspermine was proved in patients with pancreatobiliary carcinoma. Concerning pancreatic cancer, we previously reported a high incidence of pancreatic cancer in selected patients with diabetes mellitus [14] and intraductal papillary-mucinous neoplasm of the pancreas [15]. This novel marker may be of great value in mass screening and follow-up of patients at high risks of the development of malignancy such as familial adenomatosis coli, ulcerative coli-

tis, pancreatobiliary malunion, congenital choledochal cyst, diabetes mellitus, intraductal papillary-mucinous tumour of the pancreas [16], Barret's oesophagus and so on.

Although this is a preliminary report on urine diacetylspermine in patients with pancreatobiliary diseases, this novel urinary marker is as sensitive and specific for pancreatobiliary carcinomas as serum CA19-9. Urine diacetylspermine may be a universal tumour marker for malignant conditions and useful in mass screening and follow-up of high-risk groups.

Conflict of interest statement

None declared.

Acknowledgement

This study is partially supported by grant from Fukuoka Industry, Science and Technology Foundation, Fukuoka, Japan, 2002 and 2003.

References

[1] Tabor C, Tabor H. 1-4-Diaminobutane (putrescine), spermidine and spermine. Annu Rev Biochem 1976;45:285–306.
[2] Hiramatsu K, Sugimoto M, Kamei S, Hoshino M, Kinoshita K, Iwasaki K, et al. Determination of amounts of polyamines excreted in urine: demonstration of *N*1,*N*8-diacetylspermidine and *N*1,*N*12-diacetylspermine as components commonly occurring in normal human urine. J Biochem 1995;117:107–12.
[3] Russell D. Increased polyamine concentrations in the urine of human cancer patients. Nat New Biol 1971;233:144–5.
[4] Scalabrino G, Ferioli E. Polyamines in mammalian tumors. Part II. Adv Cancer Res 1982;36:1–102.
[5] Bachrach U. Polyamines as markers of malignancy. Prog Drug Res 1992;39:9–33.
[6] Sugimoto M, Hiramatsu K, Kamei S, Kinoshita K, Hoshino M, Iwasaki K, et al. Significance of urinary *N*1,*N*8-diacetylspermidine and *N*1,*N*12-diacetylspermine as indicators of neoplastic diseases. J Cancer Res Clin Oncol 1995;121:317–9.
[7] Hiramatsu K, Sugimoto M, Kamei S, Hoshino M, Kinoshita K, Iwasaki K, et al. Diagnostic and prognostic usefulness of *N*1,*N*8-diacetylspermidine and *N*1,*N*12-diacetylspermine in urine as novel markers of malignancy. J Cancer Res Clin Oncol 1997;123:539–45.
[8] Hiramatsu K, Miura H, Kamei S, Iwasaki K, Kawakita M. Development of a sensitive and accurate enzyme-linked immunosorbent assay (ELISA) system that can replace HPLC analysis for the determination of *N*1,*N*12-diacetylspermine in human urine. J Biochem 1998;124:231–6.
[9] Gold P, Freedman S. Demonstration of tumor-specific antigens in human colonic carcinomata by immunological tolerance and absorption techniques. J Exp Med 1965;121:439–62.
[10] Gold P, Freedman S. Specific carcinoembryonic antigens of the human digestive system. J Exp Med 1965;121:467–81.
[11] Koprwoski H, Steplewski Z, Mitchell K, Herlyn M, Herlyn D, Fuhrer P. Colorectal carcinoma antigens detected by hybridoma antibodies. Somatic Cell Genet 1979;5:957–72.
[12] International Union Against Cancer: TNM classification of malignant tumours. 6th ed. International Union Against Cancer. New York: John Willey & Sons, Inc., Publication; 2002.
[13] van den Berg GA, Muskiet FA, Kingma AW, van der Slik W, Halie MR. Simultaneous gas-chromatographic determination of free and acetyl-conjugated polyamines in urine. Clin Chem 1986;32:1930–7.
[14] Ogawa Y, Tanaka M, Inoue K, Yamaguchi K, Chijiiwa K, Mizumoto K, et al. A prospective pancreatographic study on prevalence of pancreatic cancer in diabetic patients. Cancer 2002;94:2344–9.
[15] Yamaguchi K, Ohuchida J, Ohtsuka T, Nakano K, Tanaka M. Intraductal papillary-mucinous tumor of the pancreas concomitant with ductal carcinoma of the pancreas. Pancreatology 2002;2:484–90.
[16] Yamaguchi K, Yokohata K, Noshiro H, Chijiiwa K, Tanaka M. Mucinous cystic neoplasm of the pancreas or intraductal papillary-mucinous tumor of the pancreas. Eur J Surg 2000;166:141–8.

Journal of Carbohydrate Chemistry, 24:705–715, 2005

ISSN: 0732-8303 print 1532-2327 online
DOI: 10.1080/07328300500208107

Taylor & Francis
Taylor & Francis Group

Effect of Anomeric Linkage on the Sialylation of Glycosides by Cells

Maria Carmelita Z. Kasuya

Institute of Industrial Science, University of Tokyo, Tokyo, Japan

Maki Ikeda

Institute of Industrial Science, University of Tokyo, Tokyo, Japan and Faculty of Engineering, Kougakuin University, Tokyo, Japan

Kazuhiko Hashimoto

Faculty of Engineering, Kougakuin University, Tokyo, Japan

Toshinori Sato

Graduate School of Science and Engineering, Keio University, Yokohama, Japan

Kenichi Hatanaka

Institute of Industrial Science, University of Tokyo, Tokyo, Japan

The synthesis of sialylated glycosides using saccharide primers and cells was investigated. α- and β-Saccharide primers were chemically synthesized and introduced into B16 melanoma cells to prime oligosaccharide synthesis. Incorporation of α- and β-dodecyl lactosides into B16 cells resulted in the sialylation of the galactose residue to give GM3-type oligosaccharides. The β-dodecyl galactoside primer was sialylated but the α-dodecyl galactoside primer was not. Both the α- and β-dodecyl glucoside primers were not elongated. In the glycosylation of primers by cells, this research confirmed that sialyl transferases tolerate acceptor modifications and are permissive to primer elongation regardless of the α- or β-linkage to the aglycon unit. However, the

Received June 21, 2004; accepted April 30, 2005.
Address correspondence to Kenichi Hatanaka, Institute of Industrial Science, University of Tokyo, 4-6-1 Komaba, Meguro-ku, Tokyo 153-8505, Japan. E-mail: hatanaka@iis.u-tokyo.ac.jp

presence of the terminal galactose residue that is β-linked to the adjacent saccharide or aglycon unit is essential for sialylation by cellular enzymes to occur.

Keywords Sialylation, Glycoside primer, Oligosaccharide, Ganglioside, α,β Anomer

INTRODUCTION

Sialic acid, located at the nonreducing end of carbohydrate chains of glycoconjugates, plays an important role in a number of biochemical and immunochemical events.[1–3] Sialylated oligosaccharides have useful applications to study protein and carbohydrate interactions, for drug delivery, and as potential inhibitors.[4,5] Sialic acid-containing gangliosides are located at the outer cell surface of plasma membranes and serve as binding sites for enzymes, hormones, toxins, lectins, and viruses.[6]

Considering the roles played by sialic acid-containing glycoconjugates in biochemical and cellular processes, development of methods for the rapid and efficient synthesis of sialylated oligosaccharides is necessary to clarify their vital functions.[7] Several strategies involve a chemical or an enzymatic synthetic approach.[8] However, the stereoselective glycosylation of sialic acid by the creation of α-glycosidic linkage is a daunting task.[9,10] Aside from poor stereoselectivity, low yield is also one among the many shortcomings.[11] The carboxyl group attached to the anomeric position reduces reactivity in glycosylation. Although organic synthesis yields a reasonable amount of sialylated oligosaccharide with high purity, the approach requires a multistep operation involving tedious protection and deprotection schemes.

New methods of glycosylation are undertaken to afford sialylated oligosaccharides with high stereoselectivity and yield.[12] Recently, a biocombinatorial method of preparing GM3-type oligosaccharides (sialylated lactosides) has been reported.[13,14] This approach involves the use of saccharide primers (simple amphiphilic building blocks) and cells. Elongation of the saccharide primers is cellular enzyme-mediated. Depending on the type of cell used, a single building block could yield a number of oligosaccharides that are released to the culture medium.[15] As part of our continued interest in the synthesis of oligosaccharides using this strategy, we embarked on the fast and easy preparation of sialylated oligosaccharides by introducing chemically synthesized lactoside, galactoside, and glucoside primers into B16 melanoma cells. To establish the significance of the glycosidic linkage in priming oligosaccharide synthesis, primers with α- and β-linked aglycon units were used. The efficiency of glycosylation is dependent not only on the saccharide unit but also on the aglycon structure. The alkyl chain length of the aglycon plays an important role to allow the incorporation of primers into the cell and the subsequent release of the elongated products to the culture medium. The alkyl chain length

of dodecyl has been reported to be the most appropriate and thus, dodecyl was used as aglycon for all the primers in this research. [15]

RESULTS AND DISCUSSION

Chemical Synthesis of Saccharide Primers

The preparation of the saccharide primers is shown in Scheme 1. Generally, the saccharide primers were prepared in two steps: glycosylation followed by deacylation. Glycosylation of lactose peracetate (**1**) with dodecanol in the presence of a Lewis acid afforded α,β mixture of the dodecyl lactoside derivatives that was separated by column chromatography. Usual *O*-deacylation with NaOMe-MeOH gave the α- and β-linked dodecyl D-lactoside primers. The structures of the desired compounds were confirmed by both ^{1}H NMR and ^{13}C NMR results. The anomeric configuration of the α- and β-lactoside was confirmed by the chemical shift for H-1 and the $J_{1,2}$ coupling constant. Resonances at 4.60 ($J = 3.84$ Hz) and at 4.15 ($J = 7.68$ Hz) in the ^{1}H NMR spectra confirmed the formed α- and β-anomeric linkage, respectively.

The reaction of 2,3,4,6-tetra-*O*-benzylgalactosyl chloride (**3**) with dodecanol in the presence of AgOTf gave a mixture of α- and β-glycosylation products that were separated by column chromatography. Subsequent deprotection with Pd/C afforded n-dodecyl α-D-galactopyranoside and n-dodecyl β-D-galactopyranoside. Resonances at 4.58 ($J = 3.84$ Hz) and 4.22 ($J = 7.83$ Hz) in the ^{1}H NMR spectra confirmed the α- and β-anomeric linkage, respectively.

Reaction of 2,3,4,6-tetra-*O*-benzylglucosyl imidate (**5**) with dodecanol in the presence of TBDMSOTf gave a mixture of α- and β-glycosylation products. Separation of glycosylation products by column chromatography followed by deprotection with Pd/C afforded n-dodecyl α-D-glucopyranoside and n-dodecyl β-D-glucopyranoside. Resonances at 4.59 ($J = 3.84$ Hz) and at 4.08 ($J = 7.74$ Hz) in the ^{1}H NMR spectra confirmed the α- and β-anomeric linkage, respectively.

Effect of Saccharide Primer on Cell Growth and Cellular Glycosylation of the Saccharide Primers

Fifty μM of each of the saccharide primers were administered to mouse B16 melanoma cells for their feasibility as substrate for GM3 oligosaccharide biosynthesis. β-glucoside primer exhibited cytotoxicity. The α-glucoside primer and α-galactoside primer significantly reduced the number of cells by 50% and 70%, respectively, relative to control. The rest of the primers did not exhibit adverse effects to cell morphology and viability as shown in Table 1.

After incubation for 48 hr, lipids from the culture media were collected by using SepPak C18 column, while lipids from the cell homogenates were

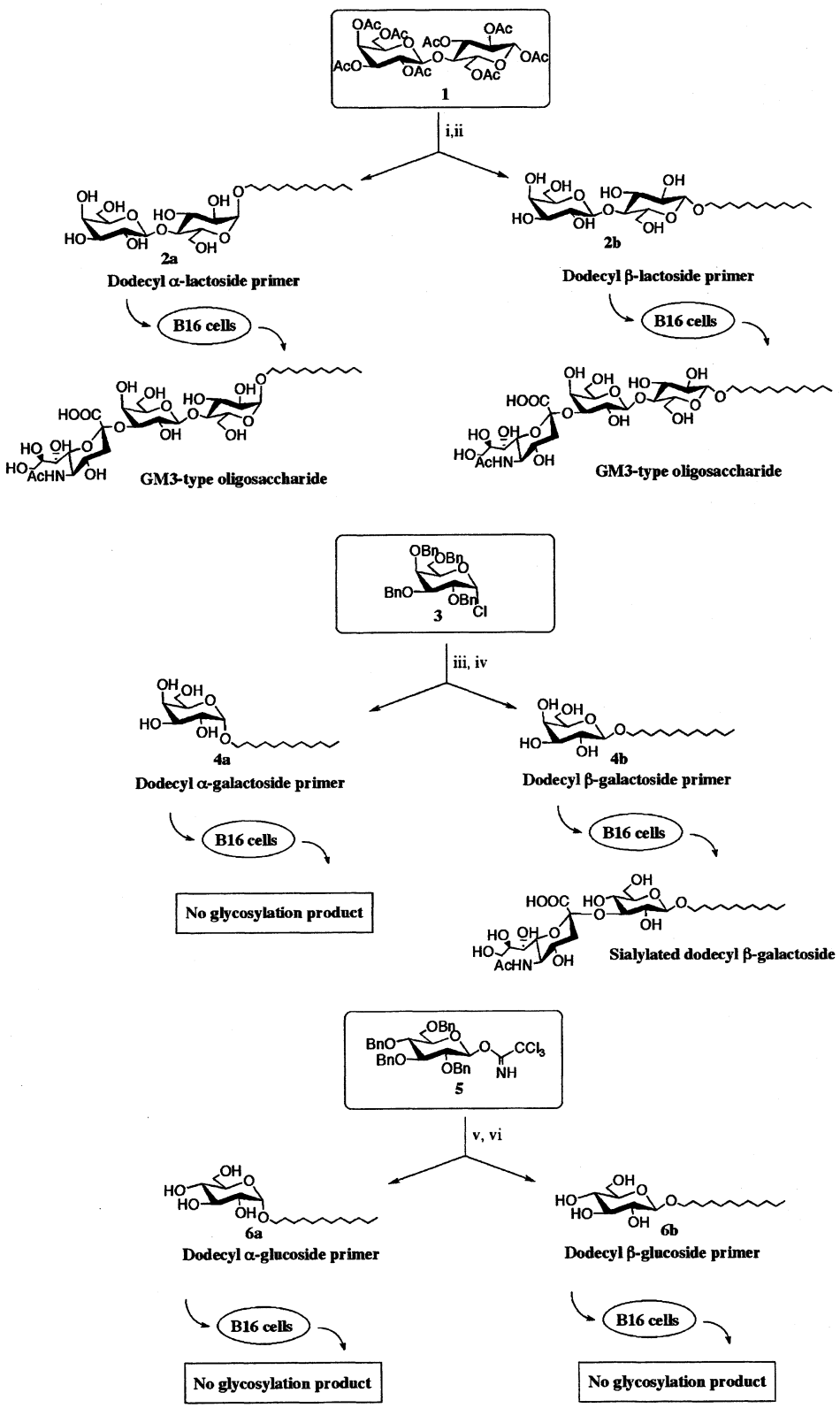

Scheme 1: Chemical synthesis of glycoside primers and subsequent uptake by B16 cells to prime oligosaccharide synthesis. Reagents and conditions: i. $CH_3(CH_2)_{11}OH$, $BF_3 \cdot OEt_2$, $ClCH_2$, CH_2Cl, 20 hr, 50°C; ii. NaOMe, MeOH, 12 hr, rt iii. $CH_3(CH_2)_{11}OH$, AgOTf, toluene, 12 hr–15°C; iv. 5% Pd/C, EtOH, 3 days, rt; v. $CH_3(CH_2)_{11}OH$, diethyl ether, TBDMSOTf, 6 hr, rt; vi. 5% Pd/C, EtOH, 6 days, rt.

Table 1: Cell number after 48-hr incubation of cells with the saccharide primer.

Saccharide Primer	Cell Number[a]
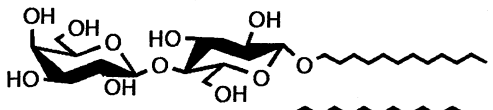	9.1×10^6
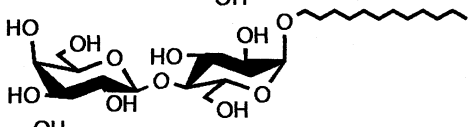	7.6×10^6
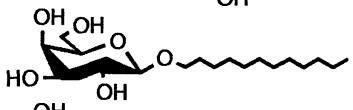	6.4×10^6
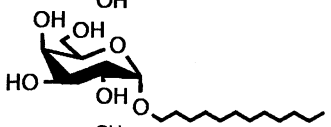	3.5×10^6
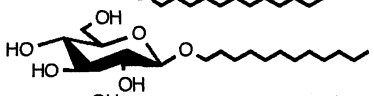	Cells died
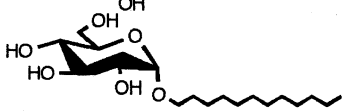	5.1×10^6

[a]Control: 10.8×10^6.

collected by extraction with chloroform:methanol and then with chloroform:2-propanol:water. HPTLC results of the lipid extracts from the culture media showed new bands corresponding to glycosylated products from the α-lactoside primer, the β-lactoside primer, and the β-galactoside primer. The HPTLC results of the lipid extracts from the cell fraction show the presence of the band corresponding to the α-galactoside primer and the α-glucoside primer, indicating that both primers were taken up by cells. However, neither the α-galactoside primer nor the α-glucoside primer gave any glycosylation product.

Identification of the Glycosylated Lactoside

To elucidate the glycan structure modified in the cells, the glycosylated products were scraped from the HPTLC plate, extracted with methanol, and dried. Since the glycosylated products were obtained in minute amounts, analysis by NMR was not possible and thus, identification was carried out by mass spectral analysis and the use of appropriate enzymes to confirm the structure. MALDI TOF mass spectral results obtained for each of the glycosylated primers revealed peaks at m/z 823.84, at m/z 823.62, and at m/z 662.22 that correspond to a monosialylated α-lactoside, a monosialylated β-lactoside, and a monosialylated β-galactoside, respectively. Treatment of glycosylated

products with α-2,3-sialidase confirmed that the glycosylation products are GM3-type oligosaccharides (sialylated dodecyl α-lactoside and sialylated dodecyl β-lactoside) and sialylated dodecyl β-galactoside. Thus, uptake of either the α- or the β-lactoside primers by B16 cells resulted in the sialylation of the galactose residue to give a glycosylated product having the same glycan structure as ganglioside GM3. Similarly, uptake of the β-galactoside primer resulted in sialylation of the galactose residue.

Sialyltransferases reside in the Golgi compartment and transfer a sialic acid residue from CMP-sialic acid to the C-6 or C-3 hydroxyl groups at the nonreducing Gal-, Gal NAc-, or GlcNAc residue. For glycosylation by cells to occur, the primers must diffuse through the plasma membrane and enter the Golgi. Results revealed that cells are not selective to the type of anomeric linkage of the primers they take in. Both the α- and β-lactoside primers could pass through the plasma membrane and function as acceptors for GM3 synthase, α2-3 sialyl transferase. It is noteworthy that sialyltranferases used the α-lactoside primer as substrate even if the anomeric linkage to the aglycon is different from lactosyl ceramide, the common natural intermediate in glycosphingolipid biosynthesis. Although the α-galactoside and the α-glucoside primers were not glycosylated, HPTLC results showing the presence of these primers in the cell fraction confirmed that these primers have been taken up by the cell. Thus, the anomeric linkage of the aglycon unit seems irrelevant for primer incorporation into cells and elongation. However, the anomeric linkage of the terminal galactoside residue that is the site for sialylation of the primers plays a significant role.

Cells take up saccharide primers that act as substrates to give sialylated oligosaccharides. In the biosynthetic pathway, cellular enzymes recognize and sialylate the terminal galactose residue of lactosyl ceramide. Results showed that sialylation occurred only with the α- and β-lactoside primers and with the β-galactoside primer. These primers have a terminal galactose residue that is β-linked. On the other hand, the α-galactoside primer and the α- and β-glucoside primers that do not have a terminal β-linked galactose moiety were not recognized as acceptors by α-(2 → 3)-sialyl transferase and were not sialylated. Thus, a terminal galactose moiety that is β-linked to the adjacent saccharide or aglycon unit is essential for the efficient saccharide sialylation by cellular enzymes.

EXPERIMENTAL

General Methods

Specific rotations were determined with a JASCO DIP 1000N digital polarimeter at 28.5°C, and ^{1}H NMR spectra were recorded at a 600 MHz

JEOL spectrometer in Me_2SO-d_6, MeOH-d_3, or $CDCl_3$ using Me_4Si as internal reference. All reactions were monitored by thin layer chromatography (TLC) on Silica Gel 60 F-254 (E. Merck), with detection by UV light or by visualizing by spraying with anisaldehyde-H_2SO_4 and heating. Column chromatography was performed on Silica Gel 60 (70–230 mesh, E. Merck, Darmstadt). The MALDI TOF mass spectrum was recorded on a Bruker MALDI TOF mass spectrometer with a 2,5-dihydrobenzoic acid (DHB) matrix.

Chemical Synthesis of Glycoside Primers

*n-Dodecyl α-D-lactoside and n-dodecyl β-D-lactoside (**2a** and **2b**).* To a suspension of molecular sieves in 100 mL 1,2-dichloroethane was added 20.0 g (29.5 mmol) of peracetyllactose (**1**) and dodecanol (27.5 g, 147 mmol) and stirred at 50°C for 2 hr under a stream of nitrogen. $BF_3 \cdot Et_2O$ (18.5 ml, 147 mmol) was added and the mixture was stirred at 50°C for 20 hr. The reaction was stopped by the addition of saturated sodium bicarbonate and filtered through a bed of celite. Chloroform was added and the organic layer was washed successively with water and with satd. sodium chloride. The organic layer was dried over anhydrous sodium sulfate, filtered, and evaporated to dryness to afford the $\alpha:\beta$ mixture of glycosylation product (7.48 g, 31.4%), which was separated by silica gel column chromatography (ethyl acetate:hexane, 1:2). When a sufficient amount of products necessary for cellular experiments was obtained in pure form (i.e., α-glycosylation product and β-glycosylation product), separation of the rest of the glycosylation product was stopped and thus, the rest of the glycosylation product remained as mixture. Deacylation was carried out by dissolving the α-glycosylation product (1.94 g, 2.41 mmol) in methanol (24.5 mL) and to the solution was added a catalytic amount of sodium methoxide. The mixture was stirred for 12 hr at rt. Deacylation of the β-glycosylation product (330 mg, 0.410 mmol) in methanol (4 mL) was likewise carried out. After completion of the reaction, the respective mixture was neutralized with cation-exchange resin (DIAION SK1B H^+ form), filtered, and evaporated to afford n-dodecyl α-D-lactoside **(2a)** and n-dodecyl β-D-lactoside **(2b)**, both as an amorphous mass in 86% and 49% yield, respectively.

n-Dodecyl 4-*O*-(2′,3′,4,′6′-tetra-*O*-acetyl-β-D-galactopyranosyl)-(1 → 4)-2,3,6-tri-*O*-acetyl-α-D-glucopyranoside: $[\alpha]_D$ +2.2° (*c* 1.0, MeOH); ^1H NMR ($CDCl_3$): δ 5.47 (t, 1H, $J = 9.36$ Hz, H-3), 5.35 (s, 1H, H-4′), 5.12 (t, 1H, H-2′), 4.97 (s, 1H, H-1), 4.96 (s, 1H, H-3′), 4.77 (dd, 1H, H-2), 4.50 (d, 1H, $J = 8.22$ Hz, H-1′), 4.43 (d, 1H, H-6), 4.15–4.09 (m, 3H, H-6′a,b, H-6), 3.73 (t, 1H, $J = 9.90$ Hz, H-4), 3.66, 3.38 (q, 2H, OCH_2), 2.150–1.96 (s, 21H, OAc), 1.58 (m, 2H, OCH_2CH_2), 1.36–1.26 (m, 18H, CH_2) 0.88 (t, 3H, CH_3). Anal. calcd for $C_{38}H_{60}O_{18}$ (804.9): C, 56.71%; H, 7.51%; found: C, 56.58%; H, 7.85%. n-dodecyl α-D-lactoside **(2a)**: ^1H NMR (Me_2SO-d_6): δ 4.16 (d, 1H, $J = 7.2$ Hz,

H-1′), 4.60 (d, 1H, $J = 3.84$ Hz, H-1), 1.51 (m, 2H, $OCH_2C\underline{H}_2$), 1.23 (m, 18H, $C\underline{H}_2$), 0.85 (t, 3H, CH_3). MALDI TOF MS: calcd for $C_{24}H_{46}O_{11}$ $(M + Na)^+$, 533.3; found: $(M + Na)^+$, 532.98.

n-dodecyl 4-*O*-(2′,3′,4,′6′-tetra-*O*-acetyl-β-D-galactopyranosyl)-(1 → 4)-2,3,6-tri-*O*-acetyl-β-D-glucopyranoside: $[\alpha]_D$ −0.93° (*c* 1.0, MeOH); ^1H NMR ($CDCl_3$): δ 5.26 (s, 1H, H-4′), 5.11 (t, 1H, $J = 9.36$ Hz H-3), 5.02 (t, 1H, $J = 8.22$ Hz, H-2′), 4.87 (dd, 1H, $J = 10.44$ Hz, H-3′), 4.79 (t, 1H, $J = 8.22$ Hz, H-2), 4.44 (d, 1H, $J = 8.28$ Hz, H-1′), 4.37 (d, 1H, $J = 8.28$ Hz, H-1), 4.05–4.01 (m, 3H, H-6, 6′a,b), 3.80 (t, 1H, $J = 7.14$ Hz, H-5′), 3.57–3.69 (m, 2H, H-4, OCH_2), 3.52 (m, 1H, H-5), 3.36 (q, 1H, OCH_2), 2.04–1.94 (s, 21H, O$\underline{Ac}$), 1.45 (m, 2H, $OCH_2C\underline{H}_2$), 1.71–1.64 (m, 18H, $C\underline{H}_2$), 0.79 (t, 3 H, CH_3). Anal. calcd for $C_{38}H_{60}0_{18}$ (804.9): C, 56.71%; H, 7.51%; found: C, 56.45%; H, 7.43%. n-dodecyl β-D-lactoside **(2b)**: ^1H NMR (Me_2SO-d_6): δ 4.18 (d, 1H, $J = 6.6$ Hz, H-1′), 4.15 (d, 1H, $J = 7.68$ Hz, H-1), 2.98 (t, 2H, $OC\underline{H}_2CH_2$), 1.50 (m, 2H, $OCH_2C\underline{H}_2$), 1.23 (m, 18H, $C\underline{H}_2$), 0.85 (t, 3H, CH_3). MALDI TOF MS: calcd for $C_{24}H_{46}O_{11}$ $(M + Na)^+$, 533.3; found: $(M + Na)^+$, 532.98.

*n-Dodecyl α-D-galactopyranoside and n-dodecyl β-D-galactopyranoside **4a** and **4b**).* 2,3,4,6-Tetra-*O*-benzylgalactosyl chloride (0.80 g, 1.43 mmol) **(3)** and dodecanol (1.33 g, 7.15 mmol) were added to a suspension of molecular sieves and 15.0 mL toluene, and the resulting mixture was stirred at −15°C under a stream of nitrogen. Silver triflate (1.10 g, 4.29 mmol) was added and the mixture was stirred for 12 hr. The reaction was stopped by the addition of saturated sodium bicarbonate and filtered. Chloroform was added to the filtrate and washed with sodium bicarbonate, water, and saturated sodium chloride, dried with anhydrous sodium sulfate, filtered, and evaporated to dryness. The α:β mixture of the glycosylation product was separated by silica gel column chromatography (ethyl acetate:hexane, 1:4) to afford 217 mg (21.4%) of dodecyl 2,3,4,6-tetra-*O*-benzyl-α-D-galactopyranoside the α-glycosylation product and 290 mg (29%) of the β-glycosylation product. The α-glycosylation product (200 mg, 0.282 mmol) in ethanol (30 mL) and the β-glycosylation product (250 mg, 0.353 mmol) in ethanol (30 mL) were hydrogenolyzed respectively over 5% Pd/C for 3 days at rt. After completion of the reaction, the mixture was filtered through a bed of celite and concentrated to afford the syrupy n-dodecyl α-D-galactopyranoside **(4a)** and n-dodecyl β-D-galactopyranoside **(4b)** primers in 78% and 70% yield, respectively.

n-dodecyl 2,3,4,6-tetra-*O*-benzyl-α-D-galactopyranoside: ^1H NMR ($CDCl_3$):δ 7.28–7.24 (m, 20H, 4Bn), 4.82 (s, 1H, H-1), 3.59 (q, 1H, OCH_2), 3.40 (q, 1H, OCH_2), 1.59 (m, 2H, $OCH_2C\underline{H}_2$), 1.35–1.20 (m, 18H, $C\underline{H}_2$), 0.85 (t, 3H, CH_3). Anal. calcd for $C_{46}H_{60}0_6$ (708.97): C, 77.93%; H, 8.53%; found: C, 77.98%; H, 8.32%. n-dodecyl α-D-galactopyranoside **(4a)**: ^1H NMR (Me_2SO-d_6) δ 4.58 (d, 1H, $J = 3.84$ Hz, H-1), 1.45 (m, 2H, $OCH_2C\underline{H}_2$), 1.30–1.10 (m, 18H, $C\underline{H}_2$), 0.80 (t, 3H, $CH_2C\underline{H}_3$). MALDI TOF MS: calcd for $C_{18}H_{36}O_6$ $(M + Na)^+$, 371.25; found: $(M + Na)^+$, 371.19.

n-dodecyl 2,3,4,6-tetra-*O*-benzyl-β-D-galactopyranoside: ^{1}H NMR ($CDCl_3$): δ7.32–7.26 (m, 20H, 4Bn), 4.33 (d, 1H, $J = 7.74$ Hz, H-1), 3.92 (q, 1H, Hz, OCH_2), 3.88 (s, 1H, H-2), 3.808 (t, 1H, $J = 8.76$ Hz, H-6), 3.5 (d, 1H, $J = 6.0$ Hz, H-3), 1.62–1.58 (m, 2H, $OCH_2C\underline{H}_2$), 1.26–1.24 (m, 18H, $C\underline{H}_2$), 0.88 (t, 3H, CH_3). Anal. calcd for $C_{46}H_{60}0_6$ (708.97): C, 77.93%; H, 8.53%; found: C, 77.88%; H, 8.62%. n-dodecyl β-D-galactopyranoside **(4b)**: ^{1}H NMR (Me_2SO-d_6) δ 4.22 (d, 1H, $J = 7.83$ Hz, H-1), 1.59 (m, 2H, $OCH_2C\underline{H}_2$), 1.21–1.28 (m, 18H, $C\underline{H}_2$), 0.80 (t, 3H, $CH_2C\underline{H}_3$). MALDI TOF MS: calcd for $C_{18}H_{36}O_6$ $(M + Na)^+$, 371.25; found: $(M + Na)^+$, 371.11.

*n-Dodecyl α-D-glucopyranoside and n-dodecyl β-D-glucopyranoside (**6a** and **6b**).* 2,3,4,6-Tetra-*O*-benzylglucosyl imidate (1.50 g, 2.19 mmol) (**5**) and dodecanol (1.63 mL, 8.75 mmol) were added to a suspension of molecular sieves and 40.0 mL diethyl ether and stirred under a stream of nitrogen. TBDMSOTf (0.80 mL, 1.00 mmol) was added and the mixture was stirred at rt for 5 hr. The reaction was stopped by the addition of sodium bicarbonate and ether was added. The organic layer was washed successively with saturated sodium bicarbonate, water, and saturated sodium chloride, dried with anhydrous sodium sulfate, filtered, and evaporated to dryness. The α:β mixture of glycosylation product was separated by silica gel column chromatography (ethyl acetate:hexane, 1:9) to afford 420 mg (27%) of the α-glycosylation product and 450 mg (29%) of the β-glycosylation product. The α-glycosylation product (302 mg, 0.427 mmol) in ethanol (50 mL) and the β-glycosylation product (226 mg, 0.319 mmol) in ethanol (30 mL) were hydrogenolyzed respectively over 5% Pd/C for 6 days at rt. After completion of the reaction, the mixtures were filtered through a bed of celite and concentrated to afford the syrupy n-dodecyl α-D-glucopyranoside **(6a)** and n-dodecyl β-D-glucopyranoside primers **(6b)** in 77% and 68% yield, respectively.

n-dodecyl 2,3,4,6-tetra-*O*-benzyl-α-D-glucopyranoside: $[\alpha]_D$ +0.94° (*c* 1.0, MeOH); ^{1}H NMR ($CDCl_3$): δ 7.35–7.26 (m, 20H, 4Bn), 4.78 (s, 1H, H-1), 3.77 (d, 1H, $J = 9.9$ Hz, H-6), 3.56 (d, 1H, $J = 9.9$ Hz, H-6), 3.41 (q, 1H, OCH_2), 1.62 (m, 2H, $OCH_2C\underline{H}_2$), 1.35–1.25 (m, 18H, $C\underline{H}_2$), 0.88 (t, 3 H, CH_3). Anal. calcd for $C_{46}H_{60}0_6$ (708.97): C, 77.93%; H, 8.53%; found: C, 77.83%; H, 8.52%. n-Dodecyl α-D-glucopyranoside primers **(6a)**: ^{1}H NMR (MeOH-d_3) δ 4.59 (d, 1H, $J = 3.84$ Hz, H-1), 3.57 (m, 2H, OCH_2, H-5), 3.48–3.38 (m, 2H, H-2, H-4), 3.34–3.26 (m, 2H, H-3, OCH_2), 3.16 (dd, 1H, $J = 9.36$ Hz, H-6), 3.04 (t, 1H, $J = 9.36$ Hz, H-6), 1.501 (m, 2H, $OCH_2C\underline{H}_2$), 1.30–1.23 (m, 18H, $C\underline{H}_2$), 0.85 (t, 3H, $CH_2C\underline{H}_3$). MALDI TOF MS: calcd for $C_{18}H_{36}O_6$ $(M + Na)^+$, 371.25; found: $(M + Na)^+$, 371.31.

n-Dodecyl 2,3,4,6-tetra-*O*-benzyl-β-D-glucopyranoside: $[\alpha]_D$ − 0.32° (*c* 1.0, MeOH); ^{1}H NMR ($CDCl_3$): δ 7.34–7.26 (m, 20H, 4Bn), 4.39 (d, 1H, $J = 7.68$ Hz, H-1), 3.97 (q, 1H, OCH_2), 3.65 (t, 1H, $J = 9.36$ Hz, H-6), 3.58 (t, 1H, $J = 9.36$ Hz, H-6), 3.52 (q, 1H, OCH_2), 1.66 (m, 2H, $OCH_2C\underline{H}_2$), 1.41–1.25 (m, 18H, $C\underline{H}_2$), 0.89 (t, 3 H, CH_3). Anal. calcd for $C_{46}H_{60}0_6$ (708.97): C,

77.93%; H, 8.53%; found: C, 77.91%; H, 8.64%. n-Dodecyl β-D-glucopyranoside primers **(6b)**: ^{1}H NMR (MeOH-d_3) δ 4.08 (d, 1H, J = 7.74 Hz, H-1), 3.73 (q, 1H, OCH_2), 3.63 (d, 1H, J = 10.98 Hz H-5), 3.44–3.41 (m, 2H, H-4, OCH_2), 3.12 (t, 1H, J = 8.28 Hz, H-6), 3.03 (s, 2H, H-2, H-3), 2.91 (t, 1H, J = 8.22 Hz, H-6), 1.49 (m, 2H, $OCH_2C\underline{H}_2$), 1.32–1.18 (m, 18H, $C\underline{H}_2$), 0.84 (t, 3H, $CH_2C\underline{H}_3$). MALDI TOF MS: calcd for $C_{18}H_{36}O_6$ $(M+Na)^+$, 371.25; found: $(M+Na)^+$, 371.40.

Cellular Uptake of Glycoside Primers

Cell culture and incubation of cells with lactoside primer were carried out according to the literature.[13]

Identification of Glycosylated Product

The glycosylated products were extracted according to the literature and the MALDI TOF mass spectra were taken. Treatment of the glycosylated products with α2,3-sialidase (cloned from *Salmonella typhimurium* LT2 and expressed in *Escherichia coli*) was carried out to confirm their structure.[16]

REFERENCES

[1] Varki, A.; Cummings, R.; Esko, J.D.; Freeze, H.H.; Hart, G.; Marth, J. *Essentials of Glycobiology*; Cold Spring Harbor Laboratory Press: New York, 1999; 195–207.

[2] Lemieux, T.; Bertozzi, C. Modulating cell surface immunoreactivity by metabolic induction of unnatural carbohydrate antigens. Chemistry and Biology **2001**, *8*, 265–275.

[3] Roy, R.; Laferriere, C.; Gamian, A.; Jennings, H. N-Acetylneuraminic acid: neoglycoproteins and pseudopolysaccharides. J. Carbohydrate Chemistry **1987**, *6* (1), 161–165.

[4] Pritchett, T.; Paulson, J. Basis for the potent inhibition of influenza virus infection by equine and guinea pig α2-macroglobulin. J. Biol. Chem. **1989**, *264* (17), 9850–9858.

[5] Sun, X.-L.; Kanie, Y.; Guo, C.-H.; Kanie, O.; Suzuki, Y.; Wong, C.-H. Synthesis of C-3 modified sialylglycosides as selective inhibitors of influenza hemagglutinin and neuraminidase. Eur. J. Org. Chem. **2000**, 2643–2653.

[6] Hakomori, S. Glycosphingolipids in cellular interaction, differentiation, and oncogenesis. Ann. Rev. Biochem. **1981**, 733–764.

[7] Gan, Z.; Roy, R. Sialoside clusters as potential ligands for siglecs (sialoadhesins). Can. J. Chem. **2002**, *80*, 908–916.

[8] Okamoto, K.; Goto, T. Glycosidation of sialic acid. Tetrahedron **1990**, *46* (17), 5835–5857.

[9] Martichonok, V.; Whitesides, G. Studies on α-sialylation using sialyl donors with an auxiliary 3-thiophenyl group. Carbohydr. Res. **1997**, *302*, 123–129.

[10] Castro-Palomino, J.; Tsvetkov, Y.; Schmidt, R. 8-*O*-Sialylation of neuraminic acid. J. Am. Chem. Soc. **1989**, *111*, 8505–8510.

[11] Ito, Y.; Numata, M.; Sugimoto, M.; Ogawa, T. Highly stereoselective synthesis of ganglioside GD3. J. Am. Chem. Soc. **1998**, *120*, 5435–5440.

[12] Kiefel, M.; von Itzstein, M. Recent advances in the synthesis of sialic acid derivatives and sialylmimetics as biological probes. Chem. Rev. **2002**, *102*, 471–490.

[13] Kasuya, M.C.; Wang, L.; Lee, Y.C.; Mitsuki, M.; Nakajima, N.; Sato, T.; Hatanaka, K.; Yamagata, S.; Yamagata, T. Azido glycoside primer: a versatile building block for the biocombinatorial synthesis of glycosphingolipid analogues. Carbohydr. Res. **2000**, *329*, 755–763.

[14] Miura, Y.; Yamagata, T. Glycosylation of lactosylceramide analogs in animal cells: amphiphatic disaccharide primers for glycosphingolipid synthesis. Biochem. Biophys. Res. Comm. **1997**, *241*, 698–703.

[15] Nakajima, H.; Miura, Y.; Yamagata, T. Glycosylation of amphiphatic lactoside primers with consequent inhibition of endogenous glycosphingolipid synthesis. J. Biochem. **1998**, *124*, 148–156.

[16] Kasuya, M.C.; Cusi, R.; Ishihara, O.; Miyagawa, A.; Hashimoto, K.; Sato, T.; Hatanaka, K. Fluorous-tagged compound: a viable scaffold to prime oligosaccharide synthesis by cellular enzymes. Biochem. Biophys. Res. Commun. **2004**, *316* (3), 599–604.

REGULAR ARTICLE

Polymer Journal

The Synthesis of the Glycopolymers Containing Pendant D,L-Xylaric and L-Tartaric Moieties and Their Inhibition Behavior on the β-Glucuronidase Activity

*By Asei William KAWAGUCHI, Takafumi KAIDA, Haruki OKAWA, and Kazuhiko HASHIMOTO**

New styrene derivatives having D,L-xylaric and L-tartaric moieties, *N*-*p*-vinylbenzyl-D,L-xylaramic and *N*-*p*-vinylbenzyl-L-tartaramic acids (VB-D,L-XylarH **10** and VB-L-TartaH **11**), were synthesized by the ring-opening reaction of 2,3,4-tri-*O*-acetyl-meso-xylaric anhydride and 2,3-di-*O*-acetyl-L-tartaric anhydride with *p*-vinylbenzylamine, respectively, and their subsequent hydrolysis under basic condition. The glycomonomers were copolymerized with acrylamide (AAm) to give novel polymers having xylaric and tartaric moieties in the pendants (P(VB-D,L-XylarH-*co*-AAm) **12** and P(VB-L-TartaH-*co*-AAm) **13**) respectively. The inhibition abilities of the resulting glycopolymers on the β-glucuronidase activity were found to be much higher than not only that of the corresponding saccharic acids but also that of the glycomonomers, especially at the lower concentration of saccharic unit by the spectrophotometry. However, the inhibition values were lower than those of the glycopolymers bearing D-glucaric pendant, P(VB-6-D-GlucaH-*co*-AAm) (**5**) and P(VB-1-D-GlucaH-*co*-AAm) (**6**), reported in our previous work. The Lineweaver-Burk plot suggested that the glycopolymer **13** and the corresponding monomer **11** inhibit the β-glucuronidase activity noncompetitively, whereas the inhibition behavior of glycopolymer **12** and monomer **10** is more complicated, probably a mix-type of uncompetitive and noncompetitive ones. These are in contrast to the competitive inhibition in the presence of the glycopolymer **5** and its monomer **1**.

KEY WORDS: Glycopolymer / Xylaric Acid / Tartaric Acid / β-Glucuronidase / Inhibitor / Xenobiotics /

When xenobiotics such as toxic and medical substances are absorbed into the human body, they are sent to the liver and oxidized to β-glucuronide conjugates.[1] This reaction is a kind of detoxication metabolism. If the molecular weight of the conjugates is more than 400, they should be exhausted *via* the small intestines. However, most of them are hydrolyzed by the β-glucuronidase in the small intestine. The free xenobiotics are absorbed and returned to the liver to be metabolized again.[1] If the xenobiotics are toxic, this cycle may be serious for health. Therefore the inhibition of the β-glucuronidase activity would be effective for exhausting of the xenobiotics from the body.[2–7]

D-Glucaric acid and their lactone derivatives are known to be efficient inhibitors for β-glucuronidase.[8–16] However, even if these saccharic derivatives were administered orally, they would be absorbed before reaching the small intestine.

In our previous work,[5–7] four styryl-type monomers having D-glucaric, L-gulonic, and D-gluconic moieties, *N*-*p*-vinylbenzyl-6-D-glucaramic acid (VB-6-D-GlucaH, **1**), *N*-*p*-vinylbenzyl-1-D-glucaramic acid (VB-1-D-GlucaH, **2**), *N*-*p*-vinylbenzyl-6-L-gulonamide (VB-6-D-Glco, **3**), and *N*-*p*-vinylbenzyl-6-D-gluconamide (VB-6-D-Glco, **4**), were synthesized through the ring-opening reaction of D-glucaro-6,3-lactone, D-glucaro-1,4-lactone, L-gulono-1,4-lactone and D-glucono-1,5-lactone, respectively, with *p*-vinylbenzylamine. Although these lactones are commercially available, D-glucarolactones are relatively expensive and prepared from D-glucose.

The water soluble random copolymers of **1** and **2** with acrylamide, poly(*N*-*p*-vinylbenzyl-6-D-glucaramic acid-*co*-acrylamide) (P(VB-6-D-GlucaH-*co*-AAm), **5**), poly(*N*-*p*-vinylbenzyl-1-D-glucaramic acid-*co*-acrylamide) (P(VB-1-D-GlucaH-*co*-AAm), **6**), respectively, were found to suppress

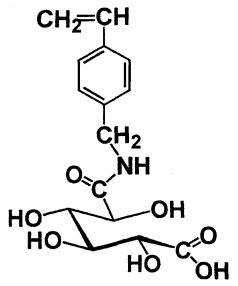

VB-6-D-GlucaH, 1

Scheme 1.

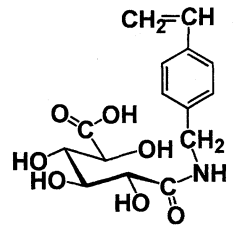

VB-1-D-GlucaH, 2

Scheme 2.

Department of Materials Science and Technology, Faculty of Engineering, Kogakuin University, Nakano-Cho, Hachioji 192-0015, Japan
*To whom correspondence should be addressed (Tel: +81-42-628-4616, E-mail: hashimot@cc.kogakuin.ac.jp).

 doi:10.1295/polymj.PJ2008105

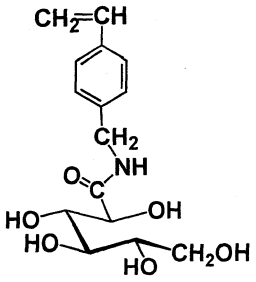

VB-6-D-Glco, 3

Scheme 3.

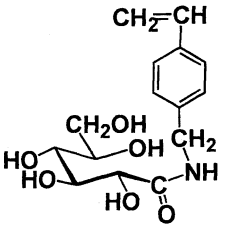

VB-1-D-Glco, 4

Scheme 4.

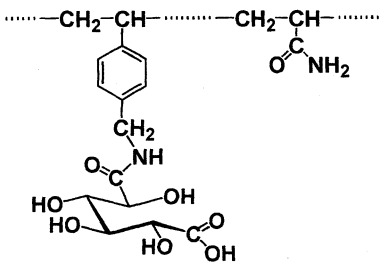

P(VB-6-D-GlucaH-*co*-AAm), 5

Scheme 5.

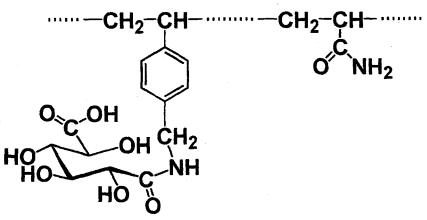

P(VB-1-D-GlucaH-*co*-AAm), 6

Scheme 6.

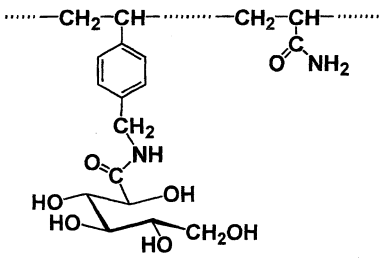

P(VB-6-D-Glco-*co*-AAm), 7

Scheme 7.

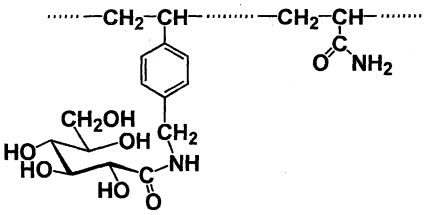

P(VB-1-D-Glco-*co*-AAm), 8

Scheme 8.

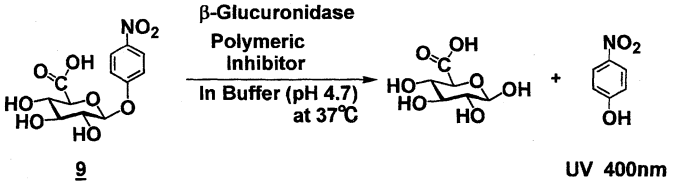

9

Scheme 9.

the hydrolysis of a model compound for the xenobiotics-β-D-glucuronide conjugates, *p*-nitrophenyl β-D-glucuronide (**9**). However, the copolymers, poly(*N*-*p*-vinylbenzyl-6-L-gulonamide-*co*-acrylamide) (P(VB-6-D-Glco-*co*-AAm), **7**), and poly(*N*-*p*-vinylbenzyl-1-D-gluconamide-*co*-acrylamide) (P(VB-1-D-Glco-*co*-AAm), **8**), respectively, scarcely inhibited the hydrolysis (Scheme 9).[5–7] Therefore the absence of the carboxy group in the glycopolymers **7** and **8** should be a main reason for their poor inhibition ability. Moreover, the kinetic analysis of the hydrolysis using Lineweaver-Burk plot[17,18] suggested that glycopolymer **5** inhibits the enzyme competitively but the glycopolymer **6** does uncompetitively.[5,7]

The inhibition behavior is roughly classified into three kinds that are competitive, noncompetitive and uncompetitive. Competitive inhibition is that the inhibitor binds to the active site of the enzyme to form the enzyme-inhibitor complex (EI) and prevent the substrate binding the same site of the enzyme. Noncompetitive inhibition takes place when the inhibitor binds to both the enzyme and the enzyme-substrate complex (ES) and becoming EI and the enzyme-substrate-inhibitor complex (ESI). Uncompetitive inhibition occurs when the inhibitor binds to only the enzyme-substrate complex (ES) to form ESI. EI and ESI are inactive, respectively.

In order to examine the inhibition of the glycopolymers containing five- and four-carbon saccharic pendants, two new glycomonomers, *N*-*p*-vinylbenzyl-D,L-xylaramic acid (VB-D,L-XylarH, **10**) and *N*-*p*-vinylbenzyl-L-tartaramic acid (VB-L-TartaH, **11**), respectively, were synthesized in this article. The

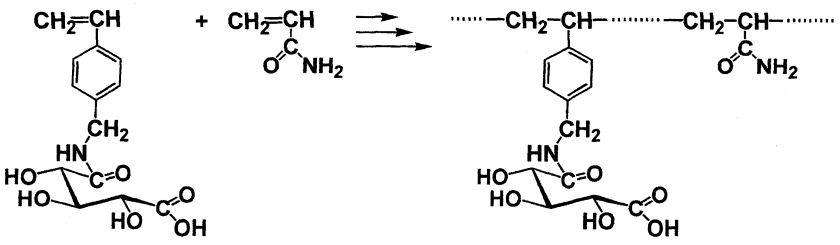

VB-D,L-XylarH, 10 P(VB-D,L-XylarH-*co*-AAm), 12

Scheme 10.

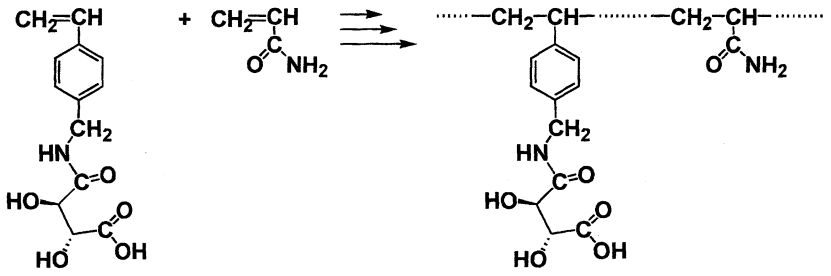

VB-L-TartaH, 11 P(VB-L-TartaH-*co*-AAm), 13

Scheme 11.

inhibition behavior of their random copolymers with acrylamide, Poly(*N*-*p*-vinylbenzyl-D,L-xylaramic acid-co-acrylamide) and Poly(*N*-*p*-vinylbenzyl-L-tartaramic acid-co-acrylamide) (P(VB-D,L-XylarH-*co*-AAm), **12** and P(VB-L-TartaH-*co*-AAm), **13**), was also investigated kinetically and compared with that of the corresponding glycomonomers and saccharic acids.

EXPERIMENTAL

Materials

2,3,4-Tri-*O*-acetyl-meso-xylaric anhydride was synthesized from acetic anhydride and xylaric acid which was previously prepared through the oxidation of D-xylose with nitric acid.[19] *p*-Vinylbenzylamine was obtained through the azidation of *p*-vinylbenzyl chloride and the following reduction with lithium aluminum hydride.[20] *p*-Vinylbenzyl chloride was kindly supplied by Seimi Chemical Co. Ltd. (Chigasaki, Kanagawa, Japan). meso-Xylose and 2,3-diacetyl-L-tartaric anhydride were purchased from Tokyo Kasei Co. Ltd. 28%-Ammonia aqueous solution was obtained from Taisei Kagaku Co. Ltd. β-Glucuronidase (bovine liver) and *p*-nitrophenyl β-glucuronide were purchased from Sigma and used as received. DMSO was dried over calcium hydride and distilled under reduced pressure.

Instruments

^{1}H NMR spectra were taken with a JEOL JNM-EX-270 Fourier transform high-resolution spectrometer. Size-exclusion liquid chromatography was measured with a TOSOH model HLC-8120 high-performance liquid chromatogram apparatus using TOSOH TSK-gel α-M, φ7.8 × 600 mm in acetic buffer solution (0.8 mL/min.). Molecular devise SPECTRSA$_{MAX}$™ 250 microplate spectrophotometer was used for determination of *p*-nitrophenol generating during the hydrolysis test. Optical rotation was determined with a P1010 (JASCO) polarimeter.

Monomer Synthesis

VB-D,L-XylarH (**10**) was prepared as follows: 4.8 g (17 mmol) of 2,3,4-*tri*-*O*-acetylxylaric anhydride and 4.5 g (3.4 mmol) of *p*-vinylbenzylamine were stirred in 53 mL of ethyl acetate at 40 °C for 1 d, and the solvent was distilled out under reduced pressure. Then, 50 mL of chloroform and 5 mL of acetic anhydride were added to the residue, and the mixture was stirred for 2 h and concentrated under reduced pressure. In order to remove the acetyl group in the glycomonomer, the mixture was stirred with 100 mL of ammonia-methanol solution (1:1) at room temperature for 2 d. After the removal of excess ammonia-methanol solution under reduced pressure, the co-products such as *N*-*p*-vinylbenzyl acetamide were extracted with chloroform from the residue, and then the ethanol soluble part was collected and concentrated again. The residual, the xylaric type monomer (**10**), was collected on the glassfilter and purified by the reprecipitation from ethanol-*n*-hexane system; Yield, 2.8 g (56%), m.p., 141–142 °C. ^{1}H NMR (7.5%, DMSO-d_6, 25 °C) δ, ppm; 8.2 (t, 1H, amide N*H*), 7.4 (d, 2H, 2,6-position of phenyl C*H*), 7.3 (d, 2H, 3,5-position of phenyl C*H*), 6.7 (dd, 1H, C*H*=CH$_2$), 5.8 (d, 1H, CH=C*H*$_2$(cis)), 5.2 (d, 1H, CH=C*H*$_2$(trans)), 4.3 (d, 2H, benzyl C*H*$_2$), 4.1 (d, 1H, $^{2\text{ or }4}$C*H*-CONH), 4.0 (t, 1H, $^{4\text{ or }2}$C*H*-COOH), 3.9 (d, 1H, ^{3}C*H*), 3.0–4.2 (bs, 4H, O*H*), ^{13}C NMR (7.5%, DMSO-d_6, 25 °C) δ, ppm; 175.6 (NH-*C* O), 173.1 (*C* OOH), 139.4 (NH-CH$_2$-*C* (phenyl)),

Polymer Journal

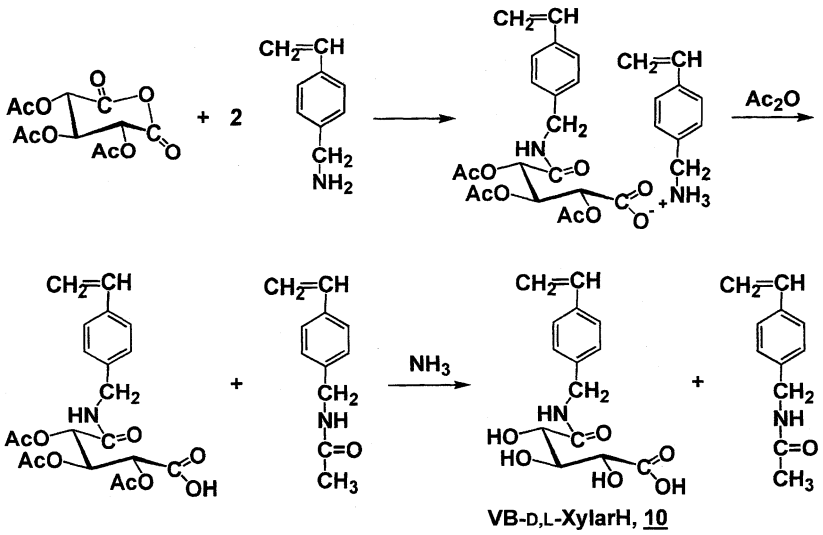

Scheme 12.

136.2 (CH_2=$\underline{C}$ H), 135.3 (CH_2=CH-$\underline{C}$ (phenyl)), 127.2 (3,5-position of phenyl $\underline{C}$), 125.8 (2,6-position of phenyl $\underline{C}$), 113.4 ($\underline{C}$ H_2=CH), 72.7 ($^{2\text{ or }4}\underline{C}$), 72.0 ($^{3}\underline{C}$), 70.7 ($^{2\text{ or }4}\underline{C}$), and 41.4 (benzyl $\underline{C}$ H_2). IR (KBr disk): 3486, 3436, 3390, 3324, 3253 cm^{-1} ($\nu_{O\text{-}H}$ and $\nu_{N\text{-}H}$), 1724 cm^{-1} ($\nu_{C=O}$, carboxyl), 1610 cm^{-1} ($\nu_{C=O}$, amide), 1537 cm^{-1} ($\nu_{N\text{-}H}$). $[\alpha]^{25}_{D} = +0,3°$ (DMSO, C 1.0).

Tartaric type monomer (**11**) was also prepared in a similar method to that for **10**; Yield, 56%. m.p., 186–187 °C. ^{1}H NMR: (7.5%, DMSO-d_6, 25 °C) δ, ppm; 8.1 (t, 1H, amide N*H*), 7.4 (d, 2H, 2,6-position of phenyl C*H*), 7.3 (d, 2H, 3,5-position of phenyl C*H*), 6.7 (dd, 1H, C*H*=CH_2), 5.8 (d, 1H, CH=C*H*$_2$(cis)), 5.2 (d, 1H, CH=C*H*$_2$(trans)), 4.3 (d, 1H, ^{2}C*H*), 4.2 (d, 2H, benzyl C*H*$_2$), 4.0 (d, 1H, ^{3}C*H*), 5.5–6.8 (bs, 2H, O*H*), ^{13}C NMR (7.5%, DMSO-d_6, 25 °C) δ, ppm; 173.9 (NH-$\underline{C}$ O), 171.6 ($\underline{C}$ OOH), 139.3 (NH-CH-$\underline{C}$ (phenyl)), 136.5 (CH_2=$\underline{C}$ H), 135.6 (CH_2=CH-$\underline{C}$ (phenyl)), 127.4 (3,5-position of phenyl $\underline{C}$), 126.0 (2,6-position of phenyl $\underline{C}$), 113.8 ($\underline{C}$ H_2=CH), 73.2 (NH-CO-$\underline{C}$), 71.8 ($\underline{C}$ -COOH), and 40.8 (benzyl $\underline{C}$ H_2). IR (KBr disk): 3507, 3382, 3282 cm^{-1} ($\nu_{O\text{-}H}$ and $\nu_{N\text{-}H}$), 1733 cm^{-1} ($\nu_{C=O}$, carboxyl), 1633 cm^{-1} ($\nu_{C=O}$, amide), 1537 cm^{-1} ($\nu_{N\text{-}H}$). $[\alpha]^{25}_{D} = +57,7°$ (DMSO, C 1.0).

Copolymerization of Glycomonomers with Acrylamide (AAm)

VB-D,L-XylarH (**10**) or VB-L-TartaH (**11**), acrylamide (AAm) and azobisisobutyronitrile were dissolved in dimethyl sulfoxide in testing tubes. After degassing three times in a cooling bath, the tubes were sealed and heated in a bath controlled at 60 °C for 24 h. Then, the tubes were cooled down at −20 °C for quenching. After the seal was broken, the solution was poured to a large amount of chloroform and the resulting polymers were collected on a glassfilter. The polymers were purified by dialysis (cut off 3500) with water and the lyophilization. The copolymer composition was estimated from the intensity ratio of the signals in the ^{1}H NMR.

Estimation of Inhibition Value of Different Glycopolymers and Monomers for β-Glucuronidase Activity

A model compound, for the β-D-glucuronide conjugates *p*-nitrophenyl β-D-glucuronide (**9**) (7 mmol/L), was hydrolyzed with 14 IU/L of β-glucuronidase in an acetic buffer solution (pH = 4.7) at 37 °C in presence or absence of 0.002–6.67 mmol/L of the glyco unit in the glycopolymers or glycomonomers. The same lot No. of the β-glucuronidase was used for the hydrolytic test in the absence and presence of each inhibitor. The hydrolytic rate was estimated from the time dependence of the absorbance of the freed *p*-nitrophenol at 400 nm. The inhibition value of the glycopolymers (%) was calculated from the hydrolytic rate in the presence or absence of 0.002–6.67 mmol/L of the glyco unit in the glycopolymers.

The Lineweaver-Burk plot was attempted by using the data determined in 0.4–1.4 mM of *p*-nitrophenyl β-D-glucuronide in the presence of different amounts of the glycomonomers and glycopolymers.

RESULTS AND DISCUSSION

Monomer Synthesis

A styrene monomer, *N*-*p*-vinylbenzyl-D,L-xylaramic acid (VB-D,L-XylarH, **10**), was newly synthesized as shown in Scheme 12. Two equivalents of *p*-vinylbenzylamine were added to 2,3,4-tri-*O*-acetyl-meso-xylaric anhydride in ethyl acetate and the mixture was stirred at 40 °C for 1 d. The resulting crude salt (**14**) was acetylated with acetic anhydride in chloroform for 2 h. Then acetyl groups in the glycomonomer were selectively hydrolyzed in ammonia-methanol solution at room temperature for 2 d. The co-products such as *N*-*p*-vinylbenzyl acetamide were removed as a chloroform soluble part from the residue and subsequently the glycomonomer (**10**) was obtained as an ethanol soluble part at 40 °C. Total yield was about 56%; m.p. 141–142 °C.

Another monomer, *N*-*p*-vinylbenzyl-L-tartaramic acid (VB-L-TartaH, **11**), was also prepared using L-tartaric anhydride as a

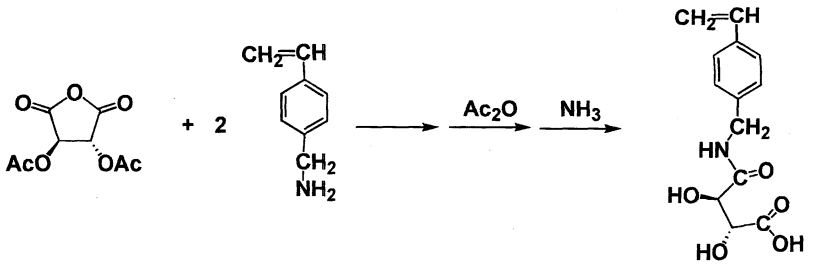

VB-L-TartaH, 11

Scheme 13.

Table I. The radical copolymerization of the glycomonomers (10 and 11) with acrylamide[a]

Run No.	Glycomonomer M_1	Glycomonomer mg (mmol)	AAm mmol	Mole fraction of M_1 in feed	$[M]_0$ mol/L	AIBN mol%	Time h	Polymer: Resulting polymer	Polymer: Yield mg	Polymer: Mole fraction of 10 or 11[b]	M_n[c] $\times 10^{-4}$	M_w/M_n[c]
1	10	177(0.6)	2.4	0.20	3.0	1.00	24	12	217	0.25	1.56	1.90
2	10	177(0.6)	2.4	0.20	3.0	0.25	24	12	177	0.35	2.96	1.72
3	10	177(0.6)	2.4	0.20	3.0	0.05	36	12	124	0.42	4.14	1.98
4	10	170(0.6)	2.4	0.20	1.5	1.00	24	12	210	0.22	0.84	1.53
5	10	295(1.0)	4.0	0.20	1.0	0.30	24	12	336	0.41	1.32	1.57
6	11	316(1.2)	4.8	0.20	6.0	0.13	12	13	318	0.30	8.80	2.62
7	11	158(0.6)	2.4	0.20	1.5	1.00	12	13	110	0.23	0.88	2.95
8	11	474(1.8)	4.2	0.30	6.0	0.13	12	13	408	0.41	11.3	2.70
9	11	239(0.9)	2.1	0.30	3.0	0.25	12	13	72	0.50	4.7	1.91

[a]Solvent, DMSO; temp., 60 °C. [b]By ^{1}H NMR in D_2O. [c]By SEC in acetic buffer (standard, PEG).

starting material in a similar method (Scheme 13); yield, 68%; m.p. 186–187 °C.

Both two new monomers 10 and 11 are soluble in water, DMF, and DMSO at room temperature and in ethanol and methanol at 60 °C, but insoluble in chloroform, diethyl ether, benzene and acetone.

Copolymerization of the Glycomonomers (10 and 11) with Acrylamide (AAm)

The radical copolymerization of the glycomonomers containing D,L-xylaric and L-tartaric pendants (10 and 11) with acrylamide (AAm), on which the mole fraction of the glycomonomers in feed was 0.2 or 0.3, proceeded in DMSO in a homogeneous phase at 60 °C. The resulting copolymers were precipitated in chloroform, purified by dialysis (cut off 3500) in water and isolated by the subsequent lyophilization (Table I).

The resulting copolymers, P(VB-D,L-XylarH-*co*-AAm) (12) and P(VB-L-TartaH-*co*-AAm) (13), were dissolved in water, methanol and DMSO, at room temperature, but were insoluble in chloroform, benzene, diethyl ether and ethyl acetate. The number average molecular weight estimated by size-exclusion chromatography in acetic buffer (pH = 4.7) was found to be controlled by the initial monomer concentration and the initiator concentration in the range from 8.8×10^3 to 11×10^4. The copolymer composition was determined from the signal intensity in their ^{1}H NMR spectrum as shown in Table I. The copolymers obtained in the present work are speculated to be the random copolymers, because the copolymer composition of a similar glycopolymer, P(VB-6-D-GlucaH-*co*-AAm) 5, depended upon the mole fraction of glycomonomer in feed on the radical copolymerization as reported in our previous article.[6]

Inhibition of β-Glucuronidase Activity by Different Glycopolymers and Glycomonomers

A model compound for the β-D-glucuronide conjugates of xenobiotics, *p*-nitrophenyl β-D-glucuronide (9), was hydrolyzed with β-glucuronidase in the absence or presence of the resulting glycopolymers (12 and 13), the corresponding monomers (10 and 11) or saccharic acids. The inhibition value (%) was calculated from the hydrolytic rates of the substrate in the absence and presence of the copolymers, monomers or saccharic acids (v_0 and v, respectively) as shown in eq 1.

$$\text{Inhibition value (\%)} = \{(v_0 - v)/v_0\} \times 100 \quad (1)$$

As shown in Figure 1, inhibition value of the glycopolymer bearing D,L-xylaric moiety, P(VB-D,L-XylarH-co-AAm) (12), was found to be 50% even at the lower range of the concentration of the saccharic unit such as 0.05 mmol/L, and increased with the concentration of up to 70% at 6.67 mmol/L. On the other hand, the corresponding glycomonomer, VB-D,L-XylarH (10), and meso-xylaric acid inhibited insignificantly at a lower concentration (<0.1 mmol/L), although their inhibition values rose at higher concentration, except L-tartaric acid.

As summarized in Figure 2, the glycopolymer bearing L-tartaric moiety, P(VB-L-TartaH-*co*-AAm) (13), inhibited the enzyme effectively at the lower concentration range of the saccharic unit, and the inhibition value deteriorated similarly in the order of the copolymer (13), monomer (11), and L-tartaric acid.

Polymer Journal

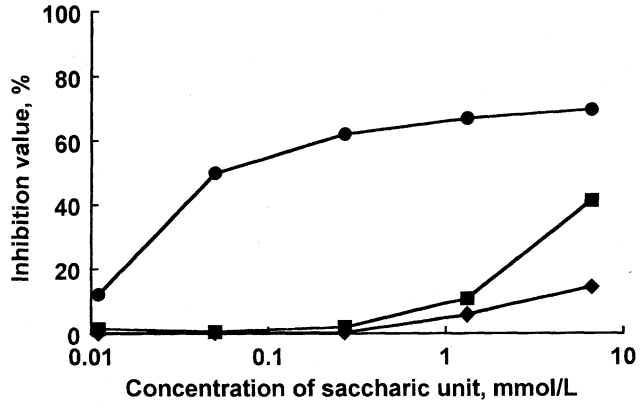

Figure 1. Inhibition of the β-glucuronidase activity by the xylaric series inhibitors at 37 °C (*p*-nitrophenyl β-D-glucuronide (**9**), 7 mmol/L; β-glucuronidase, 14 IU/L). ●; P(VB-D,L-XylarH-*co*-AAm) (**12**), glycomonomer unit, 22%, $M_n = 0.84 \times 10^4$: ■; VB-*meso*-XylarH (**10**): ◆; D-Xylaric acid.

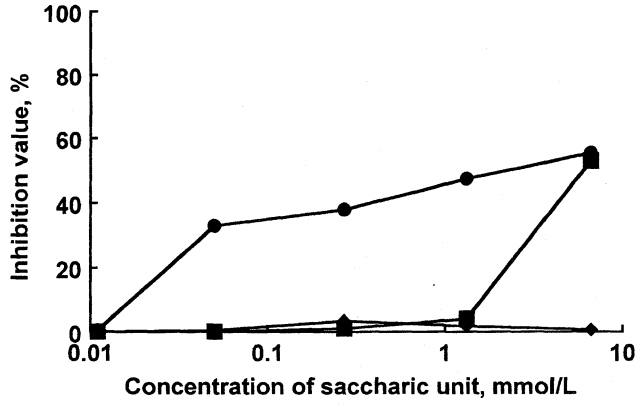

Figure 2. Inhibition of the β-glucuronidase activity by the tartaric series inhibitors at 37 °C (*p*-nitrophenyl β-D-glucuronide (**9**), 7 mmol/L; β-glucuronidase, 14 IU/L). ●; P(VB-L-TartaH-*co*-AAm) (**13**), glycomonomer unit, 23%, $M_n = 0.88 \times 10^4$: ■; VB-L-TartaH (**11**): ◆; L-Tartaric acid.

Another noteworthy point is in the fact that glycomonomers **10** and **11** having *p*-vinylbenzyl group inhibited more strongly than the corresponding saccharic acids at a higher concentration. The hydrophobicity of *p*-vinylbenzyl group may also participate in the inhibition behavior. The effect of the hydrophobic group is now being investigated from the view point of the interaction with a hydrophobic part in the enzyme, and will be reported in the near future.

These effective inhibitions of the glycopolymers (**12** and **13**) should be caused by the linkage of the glycomonomer unit along the polymer chain. Therefore the glycomonomer units are inferred to exist as a cluster even in the lower concentration and the glycopolymers show a positive cluster effect on the inhibition.

Figure 3 shows that the inhibition values of copolymer **12** (P(VB-D,L-XylarH-*co*-AAm)) and copolymer **13** (P(VB-L-TartaH-*co*-AAm)) were lower than that in the case of glycopolymer **5** (P(VB-6-D-GlucaH-*co*-AAm)) reported in our previous work.[6,7] The glucaric moiety in copolymer **5** has potentially similar conformation to the glucuronic moiety in

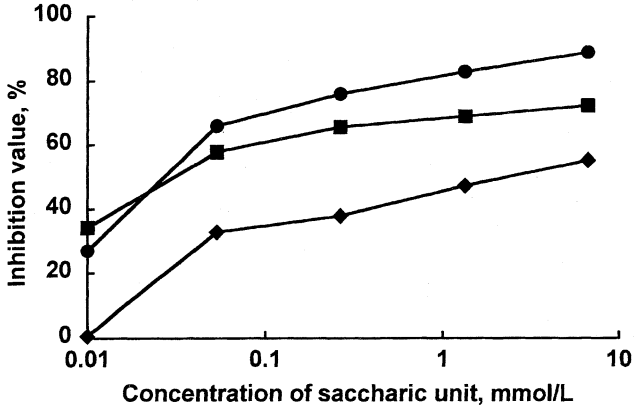

Figure 3. Inhibition of the β-glucuronidase activity by the different glycopolymers at 37 °C (*p*-nitrophenyl β-D-glucuronide (**9**), 7 mmol/L; β-glucuronidase, 14 IU/L). ●; P(VB-6-D-GlucaH-*co*-AAm) (**5**), glycomonomer unit, 27%, $M_n = 0.73 \times 10^4$: ■; P(VB-D,L-XylarH-*co*-AAm) (**12**), glycomonomer unit, 22%, $M_n = 0.84 \times 10^4$: ◆; P(VB-L-TartaH-*co*-AAm) (**13**), glycomonomer unit, 23%, $M_n = 0.88 \times 10^4$.

the β-D-glucuronide conjugates. In contrast, the chain length of xylaric and tartaric moieties in glycopolymer **12** and **13** are shorter than that of D-glucaric acid. Therefore, the similarity of the molecular structure, especially, the chain length may also be one important factor for the inhibition.

Although the tartaric-type inhibitor (**13**) was less effective to the β-glucuronidase activity than the glucaric- and xylaric-type inhibitors (**5** and **12**), it is still useful, because L-tartaric anhydride, which is a key starting material for the corresponding glycopolymer (**13**), is commercially available and less expensive. On the other hand, D-glucaro-6,3-lactone and xylaric anhydride for the synthesis of the glycomonomers (**1** and **10**), respectively, are expensive and/or necessary to be prepared in the laboratory before use.

Lineweaver-Burk Plot

The inhibition behavior can be distinguished by judging from the each extrapolating line on Lineweaver-Burk plot[17,18] and typical examples of Lineweaver-Burk plot were shown in Figure 4.

In the case of competitive inhibition, each line crosses on the vertical axis (Figure 4A), whereas in the case of noncompetitive inhibition, each line crosses on the horizontal axis (Figure 4B). In the case of uncompetitive inhibition, each line becomes parallel (Figure 4C). On the other hand, each line intersects in the second quadrant in the case of the mix-type of competitive and noncompetitive inhibition (Figure 4D) and cross in third quadrant in the case of the mix-type of noncompetitive and uncompetitive inhibition (Figure 4E), respectively.

The hydrolytic rate (v) in different concentration of β-glucuronide **9** with β-glucuronidase was determined in the presence of the glycopolymers having tartaric and xylaric pendants (**13** and **12**) (Figures 5 and 6). V_{max}, K_m and (K_m/V_{max}) for the line in the absence of the inhibitor and the apparent values of $V_{max}{}^I$, $K_m{}^I$ and $(K_m/V_{max})^I$ for the line in

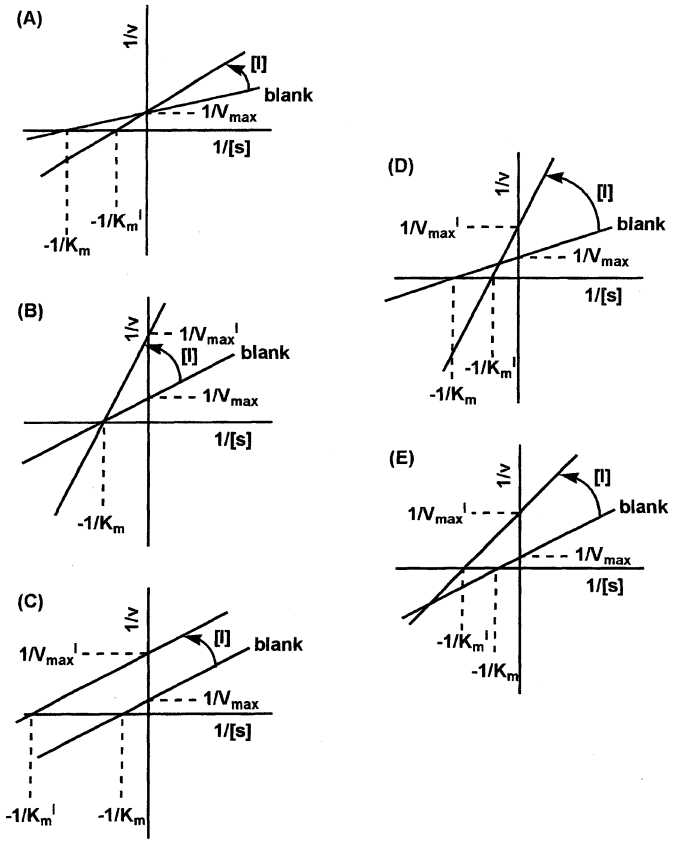

Figure 4. The typical examples of Lineweaver-Burk plot. (A) competitive inhibition, (B) noncompetitive inhibition, (C) uncompetitive inhibition, (D) mix-type of competitive and noncompetitive inhibition and (E) mix-type of noncompetitive and uncompetitive inhibition.

the presence of the inhibitors were estimated from the slope and intercepts of each line and summarized in Table II.

In the case of hydrolytic test using glycopolymer **13** as a macromolecular inhibitor (Figure 5), the intercept of the horizontal axis was found to be constant and not to depend on the concentration of the macromolecular inhibitor (**13**), but the intercept of the vertical axis to be dependent upon the concentration. In other words, K_m and $K_m{}^I$ were constant and independent upon the concentration of the inhibitor, and V_{max} and $V_{max}{}^I$ were dependent upon the concentration of the inhibitor as shown in Table II. Thus, the tartaric-type glycopolymer is presumed to inhibit the enzyme noncompetitively. The tartaric-type glycopolymer binds probably not only the enzyme (E) but also the enzyme-substrate complex (ES). This fact is remarkably different from the competitive inhibition by glucaric-type copolymer **5** reported in our previous article.[6] In the Lineweaver-Burk plot for the copolymer **5**, the intercept of the vertical axis, that corresponds to $1/V_{max}$ and $1/V_{max}{}^I$, was constant and independent on the concentration of the copolymer **5**, but that of the horizontal axis, that corresponds to $-1/K_m$ and $-1/K_m{}^I$, depend upon the concentration. The glucaric-type glycopolymer should bind to the active site of the enzyme and prevent the binding of the substrate.

The Lineweaver-Burk plot for the xylaric-type glycopolymer **12** was more complicated (Figure 6). Both intercepts of horizontal and vertical axes were dependent upon the concen-

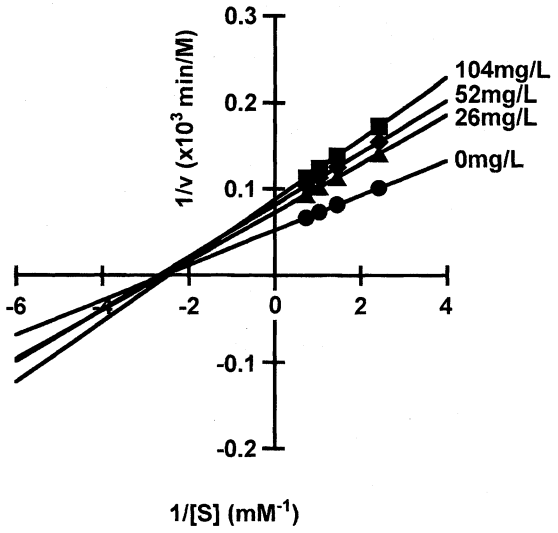

Figure 5. Lineweaver-Burk plot for the kinetic data on the hydrolysis of *p*-nitrophenyl β-D-glucuronide (**9**) by β-glucuronidase in the presence of P(VB-L-TartaH-*co*-AAm) (**13**). glycomonomer unit, 23%, $M_n = 0.80 \times 10^4$.

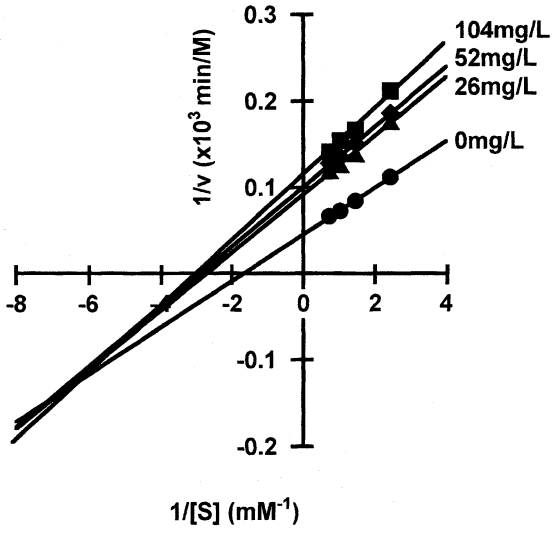

Figure 6. Lineweaver-Burk plot for the kinetic data on the hydrolysis of *p*-nitrophenyl β-D-glucuronide (**9**) by β-glucuronidase in the presence of P(VB-D,L-XylarH-*co*-AAm) (**12**). glycomonomer unit, 41%, $M_n = 1.32 \times 10^4$.

Table II. The kinetic data on the hydrolysis of *p*-Nitrophenyl β-glucuronide with β-glucuronidase in the presence of macromolecular inhibitors at 37 °C

Macromolecular Inhibitor (mg/L)	V_{max} or $V_{max}{}^I$ ×10^{-3} (M/min)	K_m or $K_m{}^I$ (mM)	(K_m/V_{max}) or $(K_m/V_{max})^I$ ×10^{-1} (min)
13			
0	19.1	0.4	0.2
26	13.7	0.4	0.3
52	12.2	0.4	0.3
104	11.4	0.4	0.4
12			
0	22.1	0.6	0.3
26	10.9	0.4	0.3
52	9.9	0.3	0.3
104	8.7	0.3	0.4

Polymer Journal

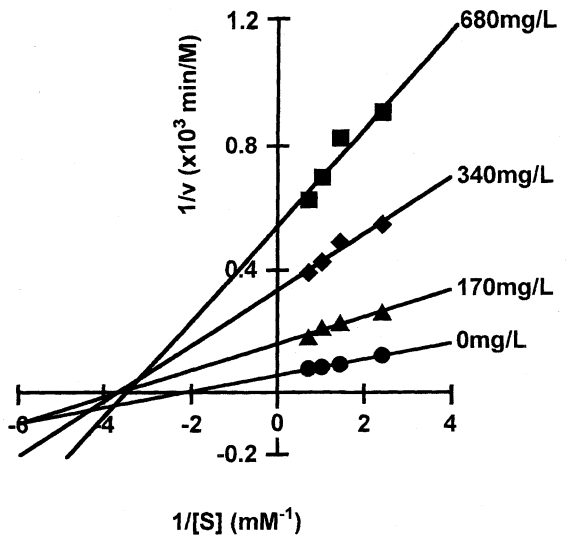

Figure 7. Lineweaver-Burk plot for the kinetic data on the hydrolysis of *p*-nitrophenyl β-D-glucuronide (**9**) by β-glucuronidase in the presence of VB-L-TartaH (**11**).

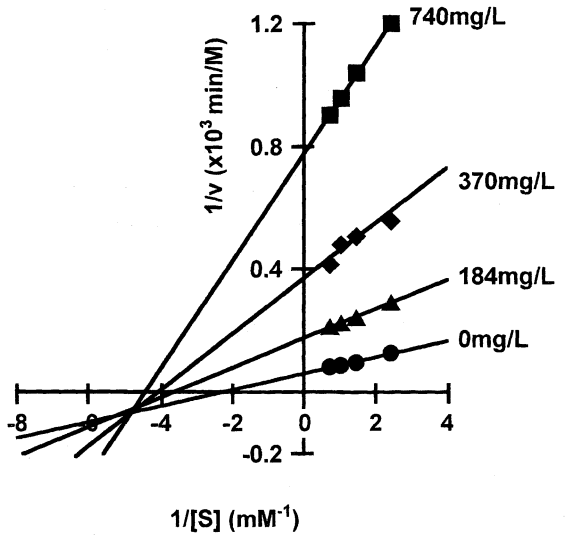

Figure 8. Lineweaver-Burk plot for the kinetic data on the hydrolysis of *p*-nitrophenyl β-D-glucuronide (**9**) by β-glucuronidase in the presence of VB-D,L-XylarH (**10**).

tration. In addition, the extrapolating lines on the all glycopolymer concentration and the line in the absence of the glycopolymer were found to cross over in the third quadrant. Judging from the intersection position the behavior of glycopolymer **12** is supposed to be a mix-type of noncompetitive and uncompetitive inhibition. Such a inhibition behavior may reflect the fact that the glycopolymer **12** contains both D- and L-xylaric moieties.

Lineweaver-Burk plot was also applied to the kinetic data on the hydrolysis in the presence of the corresponding glycomonomers (**11** and **10**) (Figures 7 and 8) and V_{max}, K_m and K_m/V_{max} in the absence of the inhibitor and the apparent values of $V_{max}{}^I$, $K_m{}^I$ and $(K_m/V_{max})^I$ in the presence of glycomonomers were shown in Table III.

As shown in Figures 7 and 8, both Lineweaver-Burk plots of the glycomonomers were quite similar to those of the

Table III. The kinetic data on the hydrolysis of *p*-Nitrophenyl β-glucuronide with β-glucuronidase in the presence of monomeric inhibitors at 37 °C

Macromolecular Inhibitor (mg/L)	V_{max} or $V_{max}{}^I$ ×10⁻³ (M/min)	K_m or $K_m{}^I$ (mM)	(K_m/V_{max}) or $(K_m/V_{max})^I$ ×10⁻¹ (min)
11			
0	18.1	0.5	0.3
170	6.2	0.3	0.4
340	3.0	0.3	0.9
680	1.8	0.3	1.5
10			
0	16.8	0.4	0.3
184	15.8	0.3	0.5
370	2.7	0.2	0.9
740	1.3	0.2	1.8

corresponding glycopolymers, respectively. Taking into consideration of the low inhibition ability of polyacrylamide as reported previously,[6] the mechanism of the glycopolymer can be mainly caused by their corresponding glycomonomer. Thus, the inhibition with glycomonomer **11** should be noncompetitive, whereas that with the glycomonomer **10** may be a mix-type of noncompetitive and uncompetitive inhibition.

Although the figure is not presented here, the inhibition with glycomonomer **1** is competitive, and similar to that of glycopolymer **5**, which will be reported in a separated paper in the near future.

As above-mentioned, the competitive inhibition by the glucaric-type copolymer, **5**, may reflect the similarity of its molecular structure to that of the β-glucuronide unit in the substrate (**9**). In other words, the noncompetitive inhibition by the tartaric-type copolymer **13** and a mixed-type inhibition by the xylaric copolymer **12** might reflect the unsimilarity of their molecular structure to that of the β-glucuronide unit. The length of the carbon chains and the configuration of the saccharic units in the glycopolymers **12** and **13** are significantly different from those of the β-glucuronide unit in the substrate **9** as shown in Figure 9. Nevertheless, the glycopolymers **12** and **13** should be useful because of their inhibition ability.

In summary xylaric and tartaric copolymers **12** and **13** synthesized in the present work were found to inhibit the activity of β-glucuronidase and to show "cluster effect" as well as the glucaric copolymer **5** reported in our previous work. The inhibition tendency became lower with the shortening of the

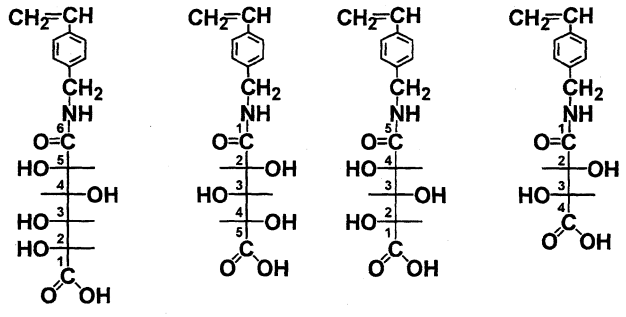

Figure 9. Fisher projections of VB-6-GlucaH (**1**), VB-D,L-XylarH (**10**), and VB-L-TartaH (**11**).

carbon chain in the saccharic moieties. However, the inhibition behavior of the copolymers **12** and **13** is different from that of glucaric-type copolymer **5**, which inhibits the enzyme competitively.

Acknowledgment. The authors thank Professors Masao Kawakita and Yasutada Imamura of Kogakuin University for their experimental guidance and helpful discussion on the present results. This work was partly supported by Grant-in-Aid for High Technology Research Center in Private Universities from the Japanese Ministry of Education, Culture, Sports, Science and Technology.

Received: April 26, 2008
Accepted: June 19, 2008
Published: August 6, 2008

REFERENCES

1. A. J. Glazko, W. A. Dill, and L. M. Wolf, *J. Pharmacol. Exp. Ther.*, **104**, 452 (1952).
2. C. Sacco and J. E. J. Calabrese, *J. Environ. Sci. Health Toxical.*, **A27**, 1249 (1992).
3. C. Sacco, W. E. McEwen, and E. Calabrese, *J. Hum. Exp. Toxical.*, **12**, 181 (1993).
4. C. Sacco and E. J. Calabrese, *J. Hum. Exp. Toxical.*, **13**, 759 (1994).
5. K. Hashimoto, R. Ohsawa, N. Imai, and M. Okada, *J. Polym. Sci., Part A: Polym. Chem.*, **37**, 303 (1999).
6. K. Hashimoto, R. Ohsawa, and H. Saito, *J. Polym. Sci., Part A: Polym. Chem.*, **37**, 2773 (1999).
7. K. Hashimoto, H. Saito, and R. Ohsawa, *J. Polym. Sci., Part A: Polym. Chem.*, **44**, 4895 (2006).
8. M. C. Karunairatnam and G. A. Levvy, *Biochem. J.*, **44**, 599 (1949).
9. G. A. Levvy, *Biochem J.*, **52**, 464 (1952).
10. T. Delahunty and D. Hollander, *Comp. Biochem. Physiol.*, **86**, 565 (1987).
11. C. A. March, *Biochem. J.*, **99**, 22 (1966).
12. A. Kiyomoto, S. Harigaya, S. Ohshima, and T. Morita, *Biochem. Pharmacal.*, **12**, 105 (1963).
13. M. Marselos, G. Dutton, and O. Hanninen, *Biochem. Pharmacol.*, **24**, 1855 (1975).
14. A. Macfadyen and K. Ho, *J. Hepatology*, **9**, 552 (1989).
15. C. Dwivedi, W. I. Heck, A. A. Donie, S. Larroya, and T. E. Webb, *Biochem. Med. Metab. Biol.*, **43**, 83 (1990).
16. Z. Walaszek, M. Hanausek-Qalaszek, and T. Webb, *Carcinogenesis*, **5**, 767 (1984).
17. L. Stryer, in "Biochemistry," 3rd ed., Freeman, New York, 1993, p. 189.
18. H. Lineweaver and D. Burk, *J. Am. Chem. Soc.*, **56**, 658 (1934).
19. C. E. Cantrell, D. E. Kiely, G. J. Abruscato, and J. M. Riordan, *J. Org. Chem.*, **42**, 3562 (1977).
20. W. Zhou, M. J. Kurth, Y. Hsieh, and J. M. Krochta, *Macromolecules*, **32**, 5507 (1999).

Synthesis of Glycopolymers Bearing Mannaric Pendants as Inhibitors on the β-Glucuronidase Activity: The Inhibition Mechanisms of Mannaric- and Glucaric-Compounds

ASEI WILLIAM KAWAGUCHI, HARUKI OKAWA, KAZUHIKO HASHIMOTO

Department of Materials Science and Technology, Faculty of Engineering, Kogakuin University, Nakano-Cho, Hachioji, Tokyo 192-0015, Japan

Received 25 September 2008; accepted 18 January 2009
DOI: 10.1002/pola.23308
Published online 00 Month 2009 in Wiley InterScience (www.interscience.wiley.com).

ABSTRACT: A new styrene derivative having D-mannaric moiety, *N*-*p*-vinylbenzyl-D-mannaramic acid (VB-D-ManaH, **8**) was synthesized though the ring-opening reaction of D-mannaro-1,4:6,3-dilactone (D-MDL) with *p*-vinylbenzylamine. VB-D-ManaH was copolymerized with acrylamide (AAm) to give novel polymers having D-mannaric moiety in the pendants, P(VB-D-ManaH-*co*-AAm), **10**. The resulting glycomonomer and polymer (**8** and **10**) bearing D-mannaric pendants were found to inhibit the β-glucuronidase activity, although the inhibition ability of the corresponding saccharodilactone (D-MDL) was known to be low. Additionally, the inhibition ability of P(VB-D-ManaH-*co*-AAm), **10**, was almost the same as that of the glycopolymer having D-glucaric pendants, P(VB-6-D-GlcaH-*co*-AAm), **1**, which was one of the most effective inhibitors for β-glucuronidase, reported in our previous work. Thus, **10** and **8** may be the first D-mannaric strong inhibitors to the β-glucuronidase activity. The Lineweaver–Burk plot suggested that the inhibition mechanisms of **10** and **8** were more complicated than in the case of the competitive and uncompetitive inhibition of *N*-*p*-(vinylbenzyl)-6-D-glucaramic (**11**) and *N*-*p*-(vinylbenzyl)-1-D-glucaramic acids (**12**), respectively. ©2009 Wiley Periodicals, Inc. J Polym Sci Part A: Polym Chem 47: 2032–2042, 2009

Keywords: glycopolymer; inhibitor; molecular recognition; polystyrene; proteins

INTRODUCTION

Recently, many kinds of glycopolymers have been studied vigorously since they can be used for the many potential applications. For examples, they were used as a mimic for the glycosaminoglycan heparin by Ayres et al.[1] and as a macroinitiator by Haider and Williams.[2] This article is concerned with a new potential application of the glycopolymer to an inhibitor for β-glucuronidase activity.

β-Glucuronidase exists in almost all parts of mammalian, especially in liver, spleen, kidney, and intestine.[3] This enzyme of humans consists of four same subunits containing 651 amino acid units.[4] The catalytic residues are known to be Glu-451 and Glu-540,[5] and to hydrolyze glucuronide conjugates to the free xenobiotics such as drugs and medical substances and D-glucuronic acid in the intestine.[6] The free xenobiotics are absorbed through the intestinal mucosa and returned to the liver. Consequently, the

Correspondence to: A. W. Kawaguchi (E-mail: bd06001@ns.kogakuin.ac.jp) or K. Hashimoto (E-mail: hashimot@cc.kogakuin.ac.jp)

Journal of Polymer Science: Part A: Polymer Chemistry, Vol. 47, 2032–2042 (2009)

J_ID: Z8G Customer A_ID: 23308 Cadmus Art: POLA 23308 Ed. Ref.: 08-1001.R1 Date: 27-February-09 Stage: Page: 2033

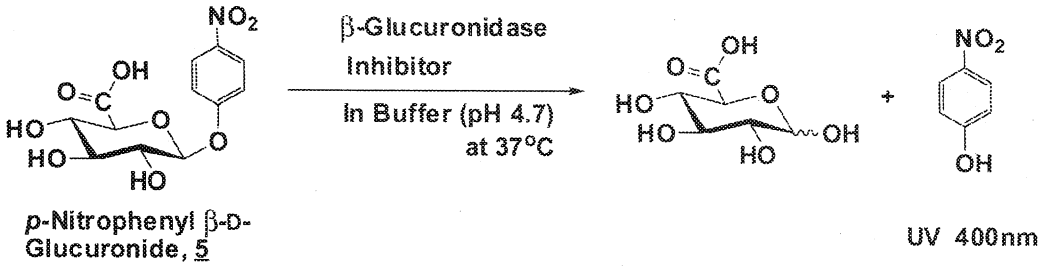

p-Nitrophenyl β-D-Glucuronide, 5

Scheme 1. Method of inhibition test for β-glucuronidase activity by synthetic glycopolymer.

xenobiotics are hardly excreted. If the xenobiotics are toxic, such an enterohepatic circulation may be serious for the human body. Therefore, the inhibition of the β-glucuronidase activity would be an effective way to excrete the xenobiotics from the body.

Several types of inhibitors such as amino acids,[7] metal ions,[8] and saccharic acids[9,10] have been investigated for β-glucuronidase. Among them, D-glucaric derivatives are the most effective inhibitor for β-glucuronidase.[7,9,10] However, even if the saccharic derivatives were administered orally, most of them would not be carried to the intestine because of their low-molecular weight. Therefore, the exclusive transport of the inhibitors into the intestine is important for clinical research on their activity in the human body.[10–16]

In our previous work,[14–16] novel water-soluble glycopolymers containing aldaric [P(VB-6-D-GlcaH-*co*-AAm), **1**, and P(VB-1-D-GlcaH-*co*-AAm), **2**] and aldonic [P(VB-6-D-Glco-*co*-AAm), **3**, and P(VB-1-D-Glco-*co*-AAm), **4**] moieties were synthesized by the radical copolymerization of the corresponding glycomonomers with acrylamide (AAm), respectively. Among them, **1** and **2** inhibited the hydrolysis of a model compound for xenobiotics-β-D-glucuronide conjugates, *p*-nitrophenyl β-D-glucuronide (**5**) (Scheme 1).

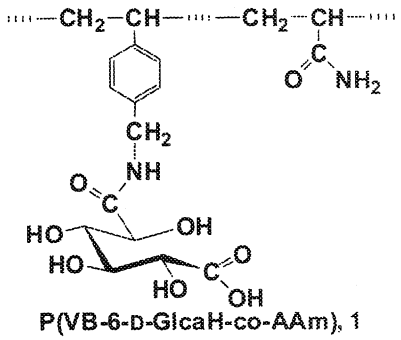

P(VB-6-D-GlcaH-co-AAm), 1

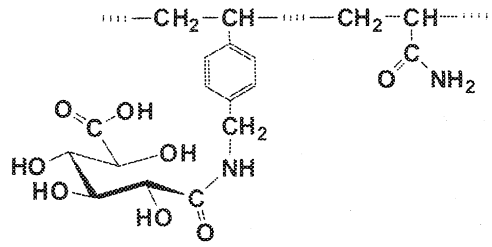

P(VB-1-D-GlcaH-co-AAm), 2

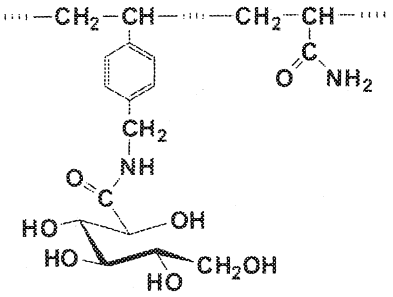

P(VB-6-D-Glco-co-AAm), 3

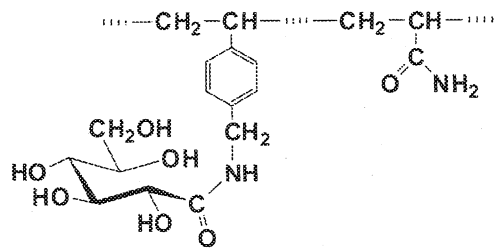

P(VB-1-D-Glco-co-AAm), 4

However, **3** and **4** hardly suppressed the hydrolysis. Therefore, the absence of the carboxy group in P(VB-6-D-Glco-*co*-AAm) (**3**) and P(VB-1-D-Glco-*co*-AAm) (**4**) should be a major occasion for their

ID: kumarpr | Black Lining [ON] | Time: 12:05 | Path: //xinchnasjn/01Journals/Wiley/3b2/POLA/Vol04708/090052/APPFile/C2POLA090052

J_ID: Z8G Customer A_ID: 23308 Cadmus Art: POLA 23308 Ed. Ref.: 08-1001.R1 Date: 27-February-09 Stage: Page: 2034

low inhibition ability. Moreover, in our another previous work,[10] the inhibition ability of the glycopolymers was found to be lower in the order of **1**, P(VB-D,L-XylaH-*co*-AAm) (**6**), and P(VB-L-TartH-*co*-AAm) (**7**).

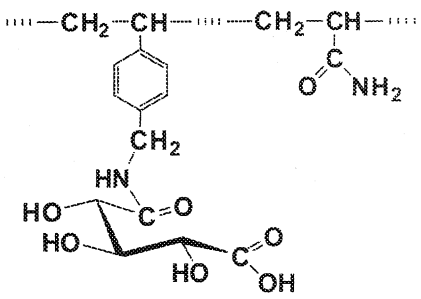

P(VB-D,L-XylaH-co-AAm), 6

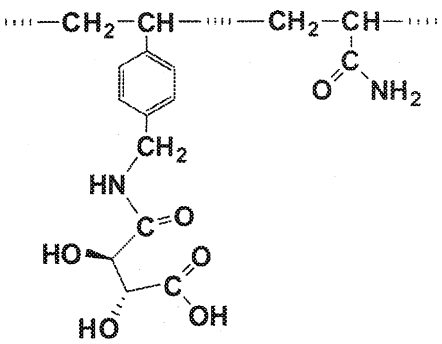

P(VB-L-TartH-co-AAm), 7

In the present work, the new glycomonomer and glycopolymer having D-mannaric pendants, of which the configuration was different from those of D-glucaric pendants, were synthesized and their inhibition mechanism was investigated, although Levvy had reported that among the 6-carbon saccharic acids, D-mannaric dilactone was not effective for the inhibition of β-glucuronidase activity, which was different from D-glucaric and D-galactaric compounds.[17] Thus, *N*-*p*-vinylbenzyl-D-mannaramic acid (VB-D-ManaH, **8**), was synthesized from D-mannaro-1,4:6,3-dilactone (D-MDL, **9**) and *p*-vinylbenzylamine and copolymerized with AAm to give a new water soluble glycopolymer, P(VB-D-ManaH-*co*-AAm), **10**, (Schemes 2 and 3).

S2, S3

The inhibition abilities of **10**, **8**, and **9** for β-glucuronidase activity were compared with those of **1**, **2** and the corresponding glucaric-type monomers, *N*-(*p*-vinylbenzyl)-6-D-glucaramic and *N*-(*p*-vinylbenzyl)-1-D-glucaramic acids (VB-6-D-GlcaH, **11**, and VB-1-D-GlcaH, **12**, respectively), from the view of their configuration.

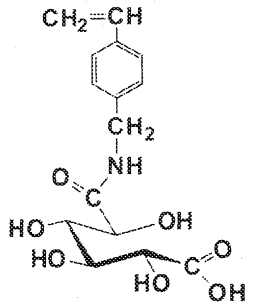

VB-6-D-GlcaH, 11

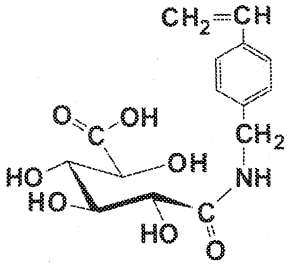

VB-1-D-GlcaH, 12

EXPERIMENTAL

Materials

p-Vinylbenzylamine was prepared as reported in the literature.[18] *p*-Vinylbenzyl chloride was kindly supplied by Seimi Chemical Co. Ltd. (Chigasaki, Kanagawa, Japan). β-Glucuronidase (bovine liver) and *p*-nitrophenyl β-D-glucuronide were purchased from Sigma and used as-received. DMSO was dried over calcium hydride and distilled under reduced pressure. Azobisisobutyronitrile (AIBN) was purchased from Tokyo Chemical Industry Co. Ltd. (Tokyo, Japan) and recrystallized with methanol before use. D-MDL was synthesized by the oxidation of D-mannitol and subsequent dehydration.[19] D-MDL hydrolysate was prepared as its acetic buffer solution (pH 4.7) by the hydrolysis of D-MDL with ~~potassium~~ hydroxide aqueous solution and subsequent pH control with acetic acid. D-Mannitol was purchased from Kanto

ID: kumarpr | Black Lining: [ON] | Time: 12:05 | Path: //xinchnasjn/01Journals/Wiley/3b2/POLA/Vol04708/090052/APPFile/C2POLA090052

J_ID: Z8G Customer A_ID: 23308 Cadmus Art: POLA 23308 Ed. Ref.: 08-1001.R1 Date: 27-February-09 Stage: Page: 2035

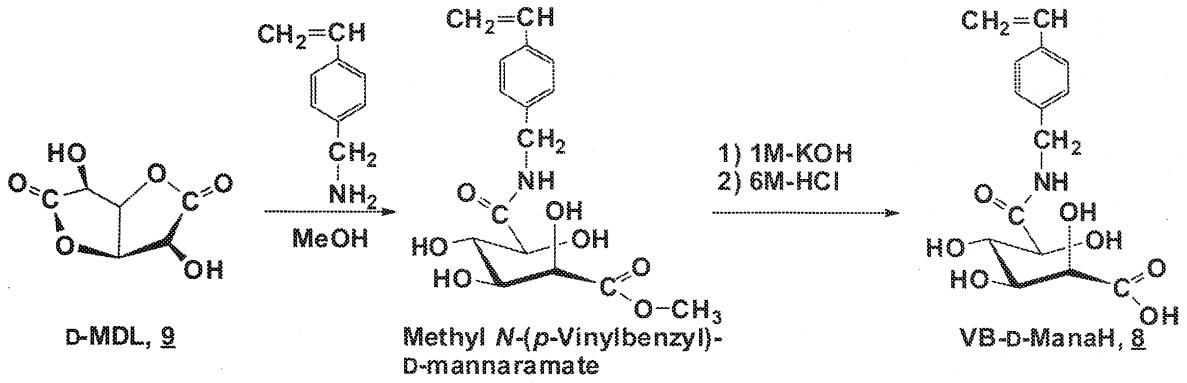

Scheme 2. Synthesis of VB-D-ManaH (8).

Kagaku Co. VB-6-D-GlcaH (**11**) and VB-1-D-GlcaH (**12**) were synthesized as reported in the previous literature.[14,16]

Instruments

^{1}H NMR and ^{13}C NMR spectra were taken with a JEOL JNM-ECX-400 Fourier transform high-resolution spectrometer. FTIR spectra were recorded on a JEOL JIR-WINSPEC50 FTIR spectrophotometer. Size-exclusion liquid chromatography was carried out with a TOSOH model HLC-8120 high-performance liquid chromatogram apparatus using TOSOH TSK-gel α-M, ϕ 7.8 × 600 mm in acetic buffer solution (0.6 mL/min.). Molecular devices SPECTRA$^{TM}_{MAX}$ 190 microplate spectrophotometer was used for the determination of *p*-nitrophenol generating during the hydrolysis test. Optical rotation was determined with a JASCO P1010 polarimeter. Elemental analysis was carried out with CHN/O Analyzer 2400II (Perkin-Elmer). The amino acid sequence of β-glucuronidase was obtained from Protein Data Base, Japan.

Synthesis of VB-D-ManaH (8)

D-MDL (**9**) (0.87 g, 5.0 mmol) was dissolved in methanol (50 mL) and *p*-vinylbenzylamine (0.73 g, 5.5 mmol) was slowly dropped to the solution, which was stirred at 35 °C for 3 days. The white powdered by-product, *N,N'*-bis(*p*-vinylbenzyl)-D-mannarodiamide, was filtered off and the filtrate was concentrated under reduced pressure. Then chloroform (150 mL) was added to the filtrate to enhance the crystallization of the product, methyl *N*-(*p*-vinylbenzyl)-D-mannaramate. Yield: 30% (0.54 g).

^{1}H NMR(400 MHz, DMSO-d_6, 25 °C) δ, ppm; 8.4 (t, 1H, amide N*H*), 7.4 (d, 2H, 3,5-position of phenyl C*H*), 7.3 (d, 2H, 2,6-position of phenyl C*H*), 6.7 (dd, 1H, C*H*=CH$_2$), 5.8 [d, 1H, CH=C*H*$_2$(cis)], 5.6 (d, 1H, O*H*), 5.4 (d, 1H, O*H*), 5.2 [d, 1H, CH=C*H*$_2$(trans)], 4.7 (d, 1H, O*H*), 4.5 (d, 1H, O*H*), 4.3 (d, 2H, benzyl C*H*$_2$), 3.9 (dd, 2H, ^{3}C*H*, and ^{4}C*H*), 3.7 (t, 2H, ^{2}C*H*, and ^{5}C*H*), and 3.6, (s, 3H, —OCO—C*H*$_3$). ^{13}C NMR (100 MHz, DMSO-d_6, 25 °C) δ, ppm; 175.6 and 173.1 (NH—CO and *C*OOCH$_3$), 139.4 [NH—CH$_2$—*C* (phenyl)], 136.2

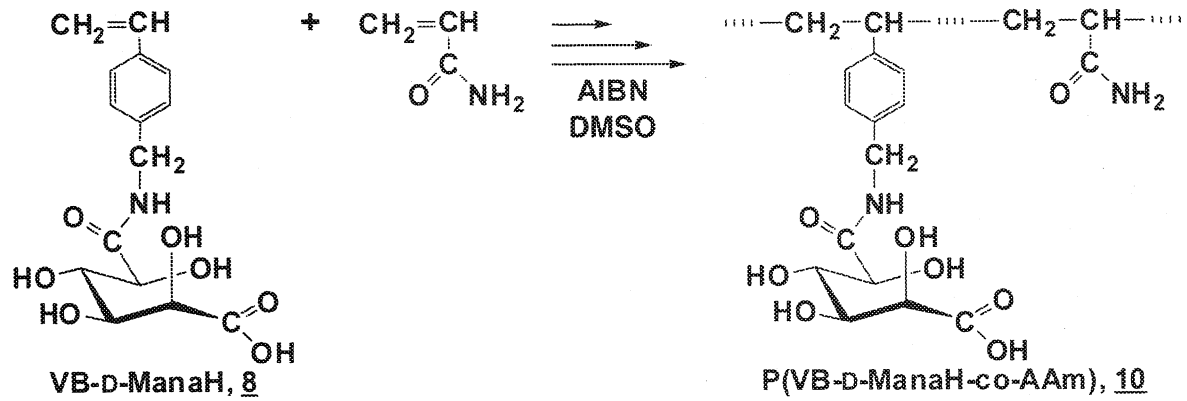

Scheme 3. Copolymerization of VB-D-ManaH (8) with acrylamide.

ID: kumarpr | Black Lining [ON] | Time: 12:05 | Path: //xinchnasjn/01Journals/Wiley/3b2/POLA/Vol04708/090052/APPFile/C2POLA090052

J_ID: Z8G Customer A_ID: 23308 Cadmus Art: POLA 23308 Ed. Ref.: 08-1001.R1 Date: 27-February-09 Stage: Page: 2036

(CH_2=CH), 135.3 [CH_2=CH—C (phenyl)], 127.2 (3,5-position of phenyl C), 125.8 (2,6-position of phenyl C), 113.4 (CH_2=CH), 71.3 and 71.0 (^2C and ^5C), 70.7 and 70.2 (^3C and ^4C), 50.6 (—OCO—CH_3) and 41.4 (benzyl CH_2).

The precursor (0.54 g, 1.6 mmol) was hydrolyzed with 1 M ~~potassium~~ hydroxide aqueous solution, and subsequently neutralized with 6 M hydrochloric acid to obtain VB-D-ManaH, immediately. The crystal was collected on a glass-filter and further washed with a small amount of water. Yield of **8**: 57% (0.30 g).

M.p.: 167–168 °C. ^{1}H NMR(400 MHz, DMSO-d_6, 25 °C) δ, ppm; 12.2 (bs, COOH), 8.4 (t, 1H, amide NH), 7.4 (d, 2H, 3,5-position of phenyl CH), 7.3 (d, 2H, 2,6-position of phenyl CH), 6.7 (dd, 1H, CH=CH_2), 5.8 [d, 1H, CH=CH_2(cis)], 5.6 (d, 1H, OH), 5.4 (d, 1H, OH), 5.2 [d, 1H, CH=CH_2(trans)], 4.7 (d, 1H, OH), 4.5 (d, 1H, OH), 4.2 (d, 2H, benzyl CH_2), 4.1 (dd, 2H, ^{3}CH and ^{4}CH), 4.0 (t, 2H, ^{2}CH and ^{5}CH). ^{13}C NMR (100 MHz, DMSO-d_6, 25 °C) δ, ppm; 175.3 and 174.2 (NH—CO and COOH), 139.7 [NH—CH_2—C (phenyl)], 136.9 (CH_2=CH), 136.1 [CH_2=CH—C (phenyl)], 127.9 (3,5-position of phenyl C), 126.5 (2,6-position of phenyl C), 114.3 (CH_2=CH), 72.0 and 71.7 (^2C and ^5C), 71.3 and 71.0 (^3C and ^4C), and 41.4 (benzyl CH_2). IR (KBr disk, cm^{-1}): 3486, 3436, 3390, 3324, 3253 (ν_{O-H} and ν_{N-H}), 1720 ($\nu_{C=O}$, carboxyl), 1610 ($\nu_{C=O}$, amide), 1537 (ν_{N-H}). $[\alpha]_D^{25}$: −25.6 (c = 1.00, DMSO). Anal. calcd. for $C_{15}H_{19}NO_7$: C, 55.38; H, 5.89; N, 4.31. Found: C, 55.53; H, 5.96; N, 4.43.

Copolymerization of VB-D-ManaH (8) with AAm

VB-D-ManaH, AAm and AIBN were put in a test tube and dissolved in dimethyl sulfoxide. After degassing three times in a cooling bath, the tube was sealed and heated in a bath controlled at 60 °C for 24 h. Then, the tube was cooled down at −20 °C for quenching. After the seal was broken, the solution was poured to a large amount of chloroform and the resulting polymer was collected on a glassfilter. The polymer was purified by the dialysis (cut off 3500) in water and isolated by the subsequent lyophilization. The copolymer composition was estimated from intensity ratio of the signals in the ^{1}H NMR.

Inhibition Test of the Glycopolymer for β-Glucuronidase Activity

A model compound for the β-D-glucuronide conjugates of xenobiotics, *p*-nitrophenyl β-D-glucuronide, was hydrolyzed with β-glucuronidase in the absence or presence of the resulting glycopolymer. The amount of *p*-nitrophenol liberated from the glucuronide was determined by spectroscopy. The inhibition value (%) was calculated from the hydrolytic rates of the substrate in the absence and presence of the copolymer. The inhibition values of VB-ManaH or D-MDL were also determined in a similar method. The Lineweaver–Burk plot was tried by using the data determined in 0.4–1.4 mM of *p*-nitrophenyl β-glucuronide in the presence of different amount of the glycomonomers and glycopolymers.

RESULTS AND DISCUSSION

Monomer Synthesis

To synthesize the new glycomonomer having D-mannaric moiety, *N*-(*p*-vinylbenzyl)-D-mannaramic acid (VB-D-ManaH) (**8**), methyl *N*-(*p*-vinylbenzyl)-D-mannaramate was firstly synthesized by the ring-opening addition reaction of D-MDL with *p*-vinylbenzylamine in methanol. Although *N*,*N*′-bis(*p*-vinylbenzyl)-D-mannarodiamide was obtained as the by-product, that was one reason for low yield of methyl *N*-(*p*-vinylbenzyl)-D-mannaramate, we used the excess amine to convert all D-MDL to mono- and diamide and to simplify the isolation of the precursor monomer. The long reaction time for producing the precursor was for the ring-opening esterification of the remaining lactone after the amidation reaction. The hydrolysis of the precursor monomer and subsequent neutralization with hydrochloric acid precipitated VB-D-ManaH (**8**), immediately. The resulting monomer was very pure and therefore its subsequent purification was not necessary. VB-D-ManaH (**8**) was dissolved in water and DMSO at room temperature, but insoluble in chloroform, benzene, diethyl ether, and ethyl acetate.

Copolymerization of VB-D-ManaH (8) with AAm

The radical copolymerization of **8** with AAm, on which the mole fraction of the glycomonomer in feed was 0.15 or 0.2, proceeded in DMSO in a homogeneous phase at 60 °C. The resulting copolymers were precipitated in chloroform, purified by dialysis (cut off 3500) in water and isolated by the subsequent lyophilization (Table 1). T1

The obtained copolymer, P(VB-D-ManaH-*co*-AAm) **10**, was dissolved in water, methanol and DMSO at room temperature, but insoluble in

ID: kumarpr | Black Lining [ON] | Time: 12:05 | Path: //xinchnasjn/01Journals/Wiley/3b2/POLA/Vol04708/090052/APPFile/C2POLA090052

J_ID: Z8G Customer A_ID: 23308 Cadmus Art: POLA 23308 Ed. Ref.: 08-1001.R1 Date: 27-February-09 Stage: Page: 2037

Table 1. The Radical Copolymerization of VB-D-ManaH (**8**) with Acrylamide (AAm)[a]

Run No.	**8** (mg) (mmol)	AAm (mg) (mmol)	Mole Fraction of **8** in Feed	$[M]_0$ (mol/L)	AIBN (mol %)	Time (h)	Resulting Polymer Yield (mg)	Resulting Polymer Mole Fraction of **8**[b]	$M_n \times 10^{-4}$ [c]	M_w/M_n[c]
1	195 (0.6)	170 (2.4)	0.20	1.50	1.00	24	184	0.34	1.4	1.9
2	195 (0.6)	170 (2.4)	0.20	3.00	0.25	24	168	0.34	3.1	3.5
3	292 (0.9)	362 (3.1)	0.15	3.00	0.05	36	208	0.30	6.4	2.0

[a] Solvent, DMSO; temp., 60 °C.
[b] By ^{1}H NMR in D_2O.
[c] By SEC in acetic buffer (standard, PEG).

chloroform, benzene, diethyl ether and ethyl acetate. The number average molecular weight estimated by size-exclusion chromatography in acetic buffer (pH 4.7) was found to be controlled by the initial monomer concentration and the initiator concentration in the range from 1.4×10^4 to 6.4×10^4. The copolymer composition was determined from the signal intensity in their ^{1}H NMR spectrum as shown in Table 1.

Inhibition of β-Glucuronidase Activity by Mannaric-Type Glycopolymer and Glycomonomer

A model compound for the β-D-glucuronide conjugates of xenobiotics, *p*-nitrophenyl β-D-glucuronide, was hydrolyzed with β-glucuronidase in the absence or presence of P(VB-D-ManaH-*co*-AAm) (**10**), VB-D-ManaH (**8**), D-MDL (**9**), or D-MDL hydrolysate, that was kinetically traced by spectroscopy. The inhibition value (%) was calculated from the hydrolytic rates of the substrate in the absence and presence of the copolymers, monomers or saccharic acids (v_0 and v, respectively), as shown in eq 1.

$$\text{Inhibition value } (\%) = \{(v_0 - v)/v_0\} \times 100 \quad (1)$$

F1 As shown in Figure 1, P(VB-D-ManaH-*co*-AAm) (**10**) inhibited the β-glucuronidase activity more efficiently than VB-D-ManaH (**8**) and D-MDL (**9**), especially at the range from 0.05 to 1.33 mM.

This fact may be due to show the broadly-defined cluster effect,[20,21] which is similar to those in the cases of other polymeric inhibitors reported in our previous articles.[8,12–14] Since saccharic units are linked to the amino groups along the polymer chain, the saccharic concentration may become higher locally, even at the lower concentration. Consequently, polymeric inhibitor could inhibit the enzyme effectively.

Another noteworthy point is in the fact that VB-D-ManaH (**8**) inhibited the β-glucuronidase activity much more efficient than D-MDL at 6.67 mM of saccharic concentration. A main structural difference of VB-D-ManaH (**8**) from D-MDL (**9**) is the existence of the hydrophobic part due to a *p*-vinylbenzyl group. Hence, this part should participate in the inhibition, which will be reported in the near future.

As mentioned earlier, Levvy reported that D-MDL did not inhibit the β-glucuronidase activity;[15] that was confirmed also in our present work as shown in Figure 1. This fact should be noted because of the high inhibition abilities of D-glucaric analogues, D-glucaro-1,4-lactone, D-glucaro-6,3-lactone, and D-glucaro-1,4:6,3-dilactone. Since D-glucaro-1,4:6,3-dilactone is known to be hydrolyzed easily in the aqueous solution, all of them have free carboxy group in the aqueous solution.[22] Therefore, D-MDL hydrolysate was also investigated, but the inhibition ability of the hydrolysate

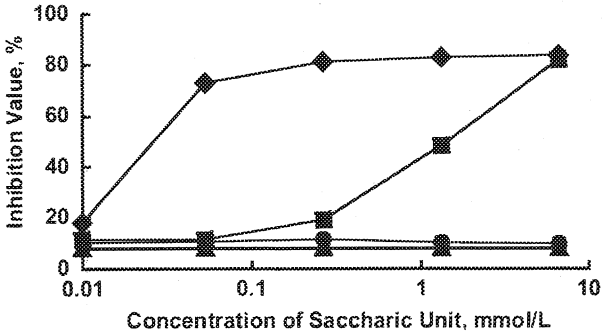

Figure 1. Inhibition of the β-glucuronidase activity by the mannaric series inhibitors at 37°C (*p*-nitrophenyl β-D-glucuronide (**5**), 6.67 mM; β-glucuronidase, 14IU/L). ◆ P(VB-D-ManaH-*co*-AAm) **10**, glycomonomer unit, 34%, $M_n = 1.4 \times 10^4$; ■ VB-D-ManaH (**8**); ● D-MDL (**9**); ▲ the hydrolysate of D-MDL.

ID: kumarpr | Black Lining [ON] | Time: 12:05 | Path: //xinchnasjn/01Journals/Wiley/3b2/POLA/Vol04708/090052/APPFile/C2POLA090052

J_ID: Z8G Customer A_ID: 23308 Cadmus Art: POLA 23308 Ed. Ref.: 08-1001.R1 Date: 27-February-09 Stage: Page: 2038

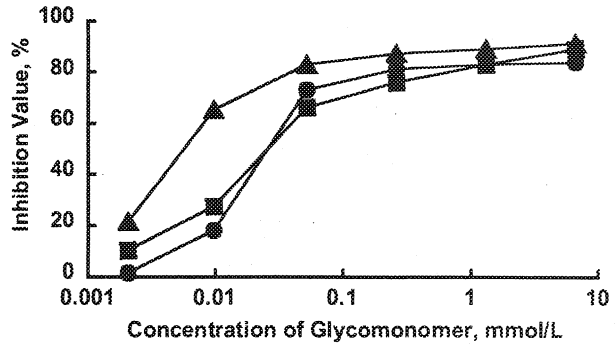

Figure 2. Inhibition of the β-glucuronidase activity by the different glycopolymers at 37°C (*p*-nitrophenyl β-D-glucuronide (**5**), 6.67 mM; β-glucuronidase, 14 IU/L) ● P(VB-D-ManaH-*co*-AAm) (**10**), glycomonomer unit, 34%, $M_n = 1.4 \times 10^4$; ■ P(VB-6-D-GlcaH-*co*-AAm) (**1**), glycomonomer unit, 27%, $M_n = 0.73 \times 10^4$; ▲ P(VB-1-D-GlcaH-*co*-AAm) (**2**), glycomonomer unit, 22%, $M_n = 0.65 \times 10^4$.

was still low (Fig. 1). Thus, mannaric acid itself may not have the ability for the inhibition of the β-glucuronidase activity.

F2 In Figure 2, the inhibition ability of P(VB-D-ManaH-*co*-AAm) (**10**) was comparable with those of P(VB-1-D-GlcaH-*co*-AAm) (**2**) and P(VB-6-D-GlcaH-*co*-AAm) (**1**), which were reported to be effective inhibitors.[14–16]

At a lower saccharic concentration, however, the inhibition ability of the mannaric-type polymeric inhibitor, P(VB-D-ManaH-*co*-AAm) (**10**), was lower than that of P(VB-1-D-GlcaH-*co*-AAm) (**2**). On the other hand, it was almost the same as that of P(VB-6-D-GlcaH-*co*-AAm) (**1**) at any range of the concentration. Thus P(VB-D-ManaH-*co*-AAm) (**10**) may be one of the efficient inhibitors for β-glucuronidase.

Inhibition Mechanism

There are three-type inhibition mechanisms, which are competitive, uncompetitive and noncompetitive inhibition. In the case of competitive inhibition, the inhibitor combines with the enzyme active site to form the enzyme-inhibitor (EI) complex and prevent the binding of the substrate at the same site of the enzyme. The uncompetitive inhibition takes place through the binding of the inhibitor to only the enzyme-substrate (ES) complex to form the corresponding enzyme-substrate-inhibitor (ESI) complex. In the case of noncompetitive inhibition, the inhibitor binds to both the enzyme and the ES complex to form EI and ESI complexes at the same rate. These inhibition mechanisms can be distinguished from the each extrapolating line on the Lineweaver–Burk plot (eq 2).[23,24]

$$1/v = (1 + [\mathrm{I}]/K_\mathrm{i})\{K_\mathrm{m}/V_\mathrm{max}\}(1/[\mathrm{S}]) + (1 + [\mathrm{I}]/K'_\mathrm{i})/V_\mathrm{max} \quad (2)$$

where S, I, K_m, K_i, K'_i, and V_{max} are the substrate, inhibitor, equilibrium coefficient for the enzyme-substrate complex, coefficient for the enzyme-inhibitor complex (inactive), coefficient for the enzyme-substrate-inhibitor complex (inactive) and maximum value of v, respectively. Additionally, V_{max}, K_m, and (K_m/V_{max}) can be estimated from the plot easily as the reciprocal of the vertical intercept, the reciprocal of the horizontal intercept multiplied by −1 and the slope of the line, respectively (Fig. 3).[23,24] F3

The hydrolytic rate (v) in different concentration of *p*-nitrophenyl β-D-glucuronide with β-Glucuronidase was determined in the presence of P(VB-D-ManaH-*co*-AAm) (**10**) and VB-D-ManaH (**8**) as shown in Figures 4 and 5, respectively. The F4, F5 results of V_{max}, K_m and (K_m/V_{max}) for the line in the absence of the inhibitors and the apparent values of V^I_{max}, K^I_m and $(K_m/V_{max})^I$ for the lines in the presence of the inhibitors were estimated from the slopes and intercepts of each line and summarized in Table 2. T2

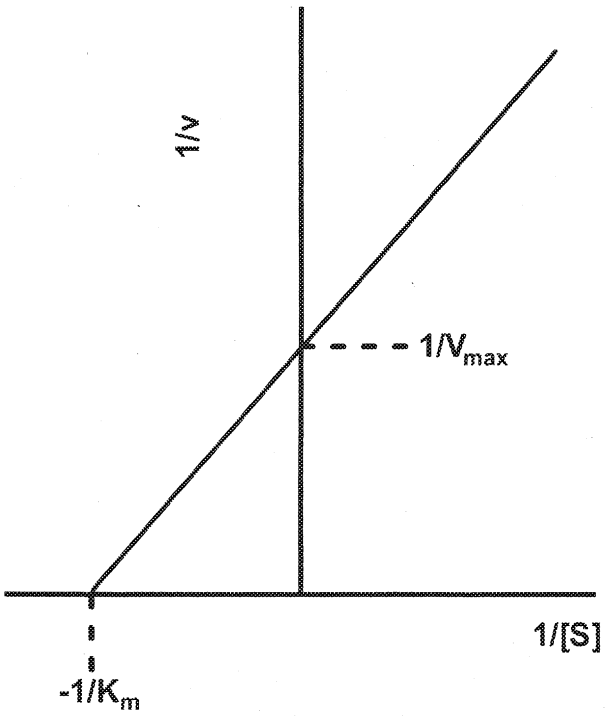

Figure 3. The typical Lineweaver–Burk plot.

ID: kumarpr | Black Lining: [ON] | Time: 12:05 | Path: //xinchnasjn/01Journals/Wiley/3b2/POLA/Vol04708/090052/APPFile/C2POLA090052

J_ID: Z8G Customer A_ID: 23308 Cadmus Art: POLA 23308 Ed. Ref.: 08-1001.R1 Date: 27-February-09 Stage: Page: 2039

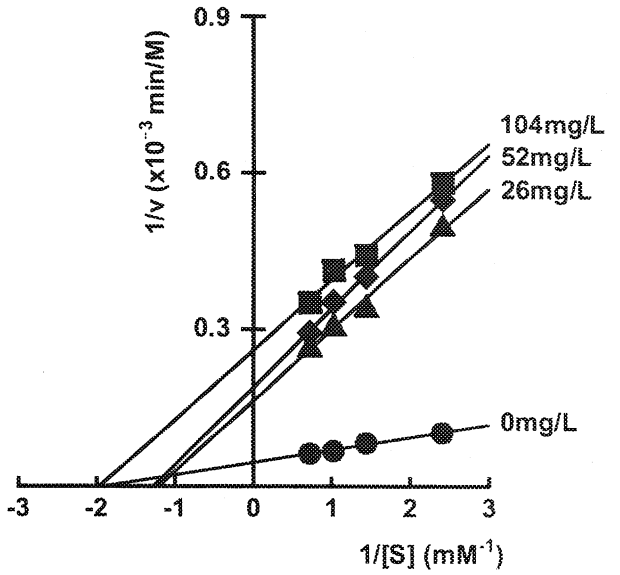

Figure 4. Lineweaver–Burk plot for the kinetic data on the hydrolysis of *p*-nitrophenyl *β*-D-glucuronide (**5**) by *β*-glucuronidase in the presence of P(VB-D-ManaH-*co*-AAm) (**10**). Glycomonomer unit, 34%, $M_n = 1.4 \times 10^4$.

In the case of the hydrolytic test with P(VB-D-ManaH-*co*-AAm) (**10**), the vertical intercepts were found to depend on the concentration of the inhibitor (Fig. 4). Additionally, the extrapolating lines in the presence of the polymeric inhibitor of 26, 52, and 104 mg/L became parallel. Thus, at a glance, the inhibition mechanism of P(VB-D-ManaH-*co*-AAm) (**10**) seemed to be uncompetitive. However, in the case of the typical uncompetitive inhibition, not only each line becomes parallel but also the horizontal intercept becomes smaller than that of line in the absence of the inhibitor 0 mg/L. In other words, the apparent affinity between the enzyme and the substrate becomes lower when the inhibitors are added. In contrast, in the case of the typical competitive inhibition, the intercepts of the lines become bigger than that of the blank line. In this case, the intercepts of the line of 26 and 52 mg/L were bigger than that of 0 mg/L. Hence the inhibition mechanism of P(VB-D-ManaH-*co*-AAm) (**10**) was not just competitive and uncompetitive.

In the case of VB-D-ManaH (**8**), the horizontal intercepts became bigger until the line of 52 mg/L, as the inhibitor concentration was increased and then it became smaller at the line of 104 mg/L (Fig. 5). The vertical intercepts of the line of 0, 26, and 52 mg/L were close to each other but the intercept of the line of 104 mg/L was far from them. Thus, the inhibition mechanism of VB-D-ManaH (**8**) seemed to be mainly the competitive inhibition at 26 and 52 mg/L. Then, the element of the uncompetitive inhibition might appear at the line of 104 mg/L. Hence, the inhibition mechanism of VB-D-ManaH (**8**) was not so simple and depended on the inhibitor concentration (although the actual inhibition mechanism might be noncompetitive instead of uncompetitive, the word "uncompetitive" was used since the definition of noncompetitive inhibition contained both competitive and uncompetitive inhibition).

To consider the inhibition mechanism of VB-D-ManaH (**8**) in detail, inhibition mechanisms of VB-6-D-GlcaH (**11**), and VB-1-D-GlcaH (**12**), of which configurations differed from that of VB-D-ManaH (**8**), were also determined (Figs. 6 and 7, respectively) because their glycopolymers, P(VB-6-D-GlcaH-*co*-AAm) (**1**) and P(VB-1-D-GlcaH-*co*-AAm) (**2**), were reported to inhibit the enzyme competitively and uncompetitively, respectively, in our previous articles.[15,16] Table 3 shows the values of V_{max}, K_m, and (K_m/V_{max}) for the line in the absence of the inhibitors and the apparent values of V^I_{max}, K^I_m, and $(K_m/V_{max})^I$ for the line in the presence of the inhibitors were estimated from the slope and intercepts of each line.

F6, F7

T3

In the case of VB-6-D-GlcaH (**11**) shown in Figure 6, the horizontal intercepts were found to depend on the inhibitor concentration, but the vertical intercepts were independent of the

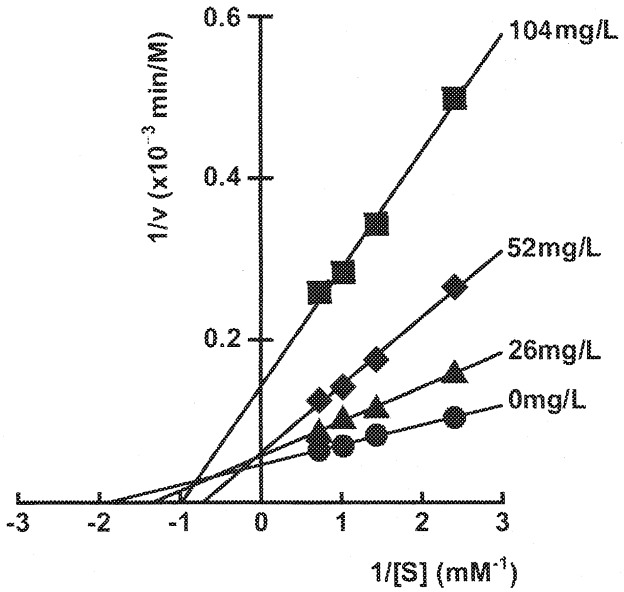

Figure 5. Lineweaver–Burk plot for the kinetic data on the hydrolysis of *p*-nitrophenyl *β*-D-glucuronide (**5**) by *β*-glucuronidase in the presence of VB-D-ManaH (**8**).

ID: kumarpr | Black Lining [ON] | Time: 12:05 | Path: //xinchnasjn/01Journals/Wiley/3b2/POLA/Vol04708/090052/APPFile/C2POLA090052

J_ID: Z8G Customer A_ID: 23308 Cadmus Art: POLA 23308 Ed. Ref.: 08-1001.R1 Date: 27-February-09 Stage: Page: 2040

Table 2. The Kinetic Data on the Hydrolysis of *p*-Nitrophenyl β-Glucuronide with β-Glucuronidase in the Presence of P(VB-D-ManaH-*co*-AAm) (**10**) and VB-D-ManaH (**8**) at 37°C

Mannaric Inhibitor	(mg/L)	V_{max} or V^I_{max} × 10^{-3} (M/min)		K_m or K^I_m (mM)		(K_m/V_{max}) or $(K_m/V_{max})^I$ × 10^{-1} (min)	
10	0	22.3		0.5		0.2	
	26		6.1		0.8		1.3
	52		5.3		0.8		1.5
	104		3.9		0.5		1.3
8	0	23.0		0.6		0.2	
	26		17.8		0.8		0.4
	52		17.0		1.4		0.8
	104		7.1		1.0		1.5

concentration. In other words, K_m increased with the inhibitor concentration, but V_{max} was constant. These results suggest that VB-6-D-GlcaH (**11**) inhibited the enzyme competitively, as well as P(VB-6-D-GlcaH-*co*-AAm) (**1**) in our previous article.[15] In the case of VB-6-D-GlcaH type inhibitor, a point of difference was the value of $1/V_{max}$; $1/V_{max}$ of P(VB-6-D-GlcaH-*co*-AAm) (**1**) was much higher than that of VB-6-D-GlcaH (**11**) on the same saccharic concentration, which meant that glycopolymer inhibited the enzyme more effectively than its monomer did, that caused by the polymeric cluster effect. Since the glycopolymer should move dynamically in the solution, its average concentration can be used to estimate the inhibition mechanism with Lineweaver–Burk plot, even though the concentration of the saccharic units fluctuated.

In contrast, both horizontal and vertical intercepts in Figure 7 were found to depend on the inhibitor concentration in the case of VB-1-D-GlcaH (**12**). Additionally, all the lines became almost parallel. These results are consistent with the typical uncompetitive inhibition mechanism. Therefore, the inhibition mechanisms of VB-6-D-GlcaH (**11**) and VB-1-D-GlcaH (**12**) seem to be reflected on those of the corresponding glycopolymer. The

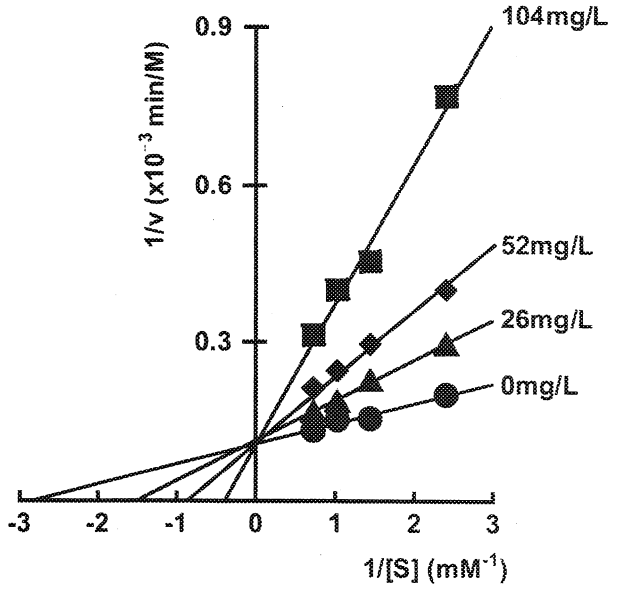

Figure 6. Lineweaver–Burk plot for the kinetic data on the hydrolysis of *p*-nitrophenyl β-D-glucuronide (**5**) by β-glucuronidase in the presence of VB-6-D-GlcaH (**11**).

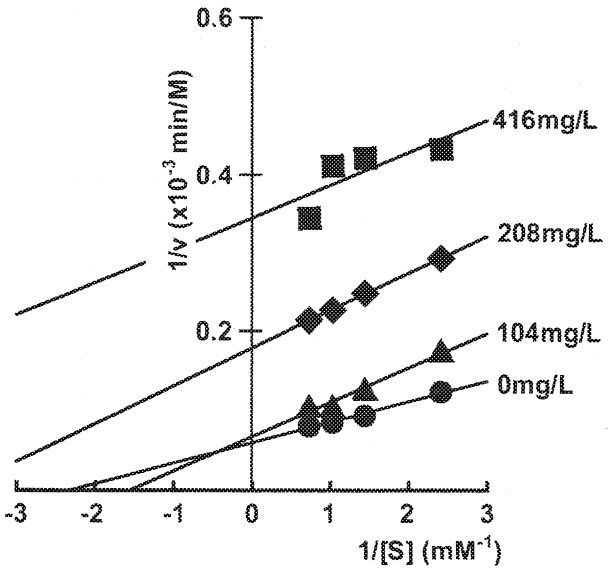

Figure 7. Lineweaver–Burk plot for the kinetic data on the hydrolysis of *p*-nitrophenyl β-D-glucuronide (**5**) by β-glucuronidase in the presence of VB-1-D-GlcaH (**12**).

ID: kumarpr | Black Lining [ON] | Time: 12:05 | Path: //xinchnasjn/01Journals/Wiley/3b2/POLA/Vol04708/090052/APPFile/C2POLA090052

Technology Research Center in Private Universities from the Japanese Ministry of Education, Culture, Sports, Science and Technology.

REFERENCES AND NOTES

1. Ayres, N.; Holt, D. J.; Jones, C. F.; Corum, L. E.; Grainger, D. W. J Polym Sci Part A: Polym Chem 2008, 46, 7713–7724.
2. Haider, A. F.; Williams, C. K. J Polym Sci Part A: Polym Chem 2008, 46, 2891–2896.
3. Fishman, W. H. Adv Enzymol Relat Areas Mol Biol 1955, 16, 361–409.
4. Oshima, A.; Kyle, J. W.; Miller, R. D.; Hoffmann, J. W.; Powell, P. P.; Grubb, J. H.; Sly, W. S.; Tropak, M.; Guise, K. S.; Gravel, R. A. Proc Natl Acad Sci USA 1987, 84, 685–689.
5. Islam, M. R.; Tomatsu, S.; Shah, G. N.; Grubb, J. H.; Jain, S.; Sly, W. S. J Biol Chem 1999, 274, 23451–23455.
6. Paigen, K. Prog Nucleic Acid Res Mol Biol 1989, 37, 155–205.
7. Kreamer, B. L.; Siegel, F. L.; Gourley, G. R. Pediatr Res 2001, 50, 460–466.
8. Gupta, G. S.; Singh, G. P. Biochim Biophys Acta 1983, 748, 398–404.
9. Karunairatnam, M. C.; Levvy, G. A. Biochem J 1949, 44, 599–604.
10. Kawaguchi, A. W.; Kaida, T.; Okawa, H.; Hashimoto, K. Polym J 2008, 40, 1–9.
11. Sacco, C.; Calabrese, E. J. J Environ Sci Health 1992, A27, 1249–1272.
12. Sacco, C.; McEwen, W. E.; Calabrese, E. J. Hum Exp Toxicol 1993, 12, 181–184.
13. Sacco, C.; Calabrese, E. J. Hum Exp Toxicol 1994, 13, 759–763.
14. Hashimoto, K.; Osawa, R.; Imai, M.; Okada, M. J Polym Sci Part A: Polym Chem 1999, 37, 303–312.
15. Hashimoto, K.; Osawa, R.; Saito, H. J Polym Sci Part A: Polym Chem 1999, 37, 2773–2779.
16. Hashimoto, K.; Saito, H.; Osawa, R. J Polym Sci Part A: Polym Chem 2006, 44, 4895–4903.
17. Levvy, G. A. Biochem J 1952, 52, 464–472.
18. Zhou, W. J.; Kurth, M. J. Macromolecules 1999, 32, 5507–5513.
19. Linstead, R. P.; Owen, L. N.; Webb, R. F. J Chem Soc 1953, 1225–1231.
20. Lee, Y. C.; Lee, R. T. In Neoglycoconjugates; Lee, R. T.; Lee, Y. C., Eds.; Academic Press: London, 1994; Chapter 2, pp 23–38.
21. Lee, Y. C.; Lee, R. T. In Neoglycoconjugates Part A Synthesis; Lee, Y. C.; Lee, R. T., Eds.; Academic Press: London, 1994; Section III, Synthetic Polymers, pp 294–304.
22. Hirasaka, Y.; Umemoto, K. Chem Pharm Bull (Tokyo) 1965, 13, 325–329.
23. Stryer, L. Biochemistry, 3rd ed.; W. H. Freeman and Co.: New York, 1988; p 189.
24. Lineweaver, H.; Burk, D. J Am Chem Soc 1934, 56, 658–666.

J_ID: Z8G Customer A_ID: 23308 Cadmus Art: POLA 23308 Ed. Ref.: 08-1001.R1 Date: 27-February-09 Stage: Page: 2041

Table 3. The Kinetic Data on the Hydrolysis of *p*-Nitrophenyl β-Glucuronide with β-Glucuronidase in the Presence of VB-6-D-GlcaH (**11**) and VB-1-D-GlcaH (**12**) at 37 °C

Glucaric Type Inhibitor	(mg/L)	V_{max} or V^I_{max} × 10^{-3} (M/min)		K_m or K^I_m (mM)		(K_m/V_{max}) or $(K_m/V_{max})^I$ × 10^{-1} (min)	
11	0	9.4		0.4		0.4	
	26		8.9		0.7		0.8
	52		9.5		1.2		1.3
	104		9.3		2.5		2.7
12	0	16.9		0.4		0.3	
	104		15.0		0.7		0.4
	208		5.6		0.3		0.5
	416		2.9		0.1		0.4

similar cluster effect was observed between P(VB-1-D-GlcaH-*co*-AAm) (**2**) and VB-1-D-GlcaH (**12**). Thus, these results suggested that the inhibition mechanisms of one glycomonomer and its glycopolymer should be considered not separately, but continuously. They also suggested that the inhibition mechanisms of the glycopolymer and its glycomonomer indicate the mechanism at the higher and lower inhibitor concentration parts, respectively. Taking these results into consideration, the inhibition mechanism of the mannaric type inhibitors may be competitive inhibition at the lower inhibitor concentration and the element of the uncompetitive inhibition might appear with increasing the inhibitor concentration.

Figure 8 shows that the configurations enclosed with a continuous line and a dash line of VB-ManaH (**8**) are similar to those of VB-6-D-GlcaH (**11**) and VB-1-D-GlcaH (**12**), respectively. Thus, the elements of the competitive and uncompetitive inhibition for VB-D-ManaH (**8**) might be caused by the configurations enclosed with a continuous and a dash line, respectively. F8

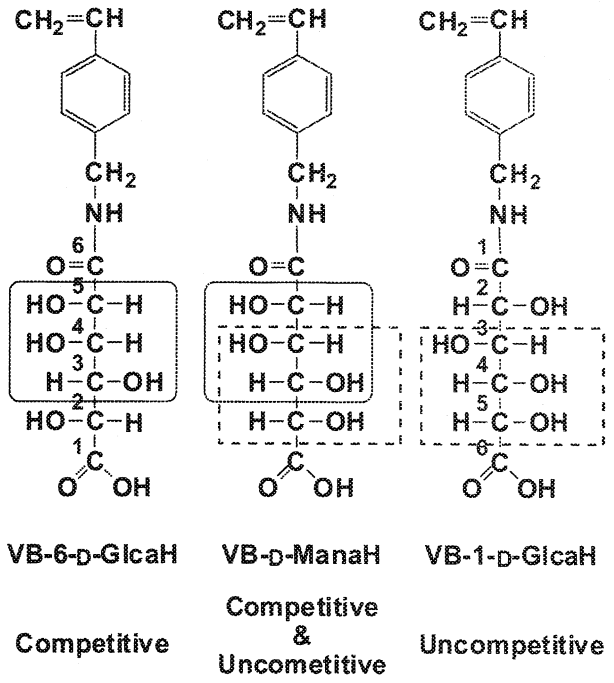

Figure 8. Fischer projections of VB-D-ManaH (**8**), VB-6-D-GlcaH (**11**), and VB-1-D-GlcaH (**12**).

CONCLUSIONS

The glycopolymer, P(VB-D-ManaH-*co*-AAm) (**10**), was synthesized from VB-D-ManaH (**8**) and AAm was found to inhibit the β-glucuronidase activity more efficiently then the corresponding monomer, **8**, and D-MDL (**9**), especially at the lower saccharic unit concentration. This result is caused by the cluster effect which is the same as those in the cases of other glycopolymers shown in our previous articles.[10,14–16] Additionally, the inhibition ability of P(VB-D-ManaH-*co*-AAm) (**10**) was almost as same as that of P(VB-6-D-GlcaH-*co*-AAm) (**1**) that was one of effective inhibitors.

Lineweaver–Burk plot suggested that the inhibition mechanism of mannaric-type inhibitor was a mix-type of competitive and uncompetitive (noncompetitive) inhibition that was probably caused by the configuration of the VB-D-ManaH (**8**) which was partly similar to both VB-6-D-GlcaH (**11**) and VB-1-D-GlcaH (**12**).

The authors thank Professor Yasutada Imamura of Kogakuin University for their experimental guidance and helpful discussion on the present results. This work was supported, in part, by Grant-in-Aid for High

ID: kumarpr | Black Lining [ON] | Time: 12:05 | Path: //xinchnasjn/01Journals/Wiley/3b2/POLA/Vol04708/090052/APPFile/C2POLA090052

A novel glycopolymer, P(VB-D-ManaH-*co*-AAm), was prepared by the copolymerization of a new glycomonomer having D-mannaric moieties, VB-D-ManaH, with acrylamide. The resulting glycopolymer and VB-D-ManaH were found to inhibit the β-glucuronidase activity, although D-mannaro-1,4:6,3-dilactone (D-MDL) was known not to do. Additionally, the inhibition ability of P(VB-D-ManaH-*co*-AAm) was much higher than that of VB-D-ManaH, which was caused by the polymeric cluster effect. Thus, P(VB-D-ManaH-*co*-AAm) and VB-D-ManaH may be the first D-mannaric strong inhibitors to the β-glucuronidase activity. Lineweaver–Burk plot suggests that the inhibition mechanism of P(VB-D-ManaH-*co*-AAm) and VB-D-ManaH were not so simple.

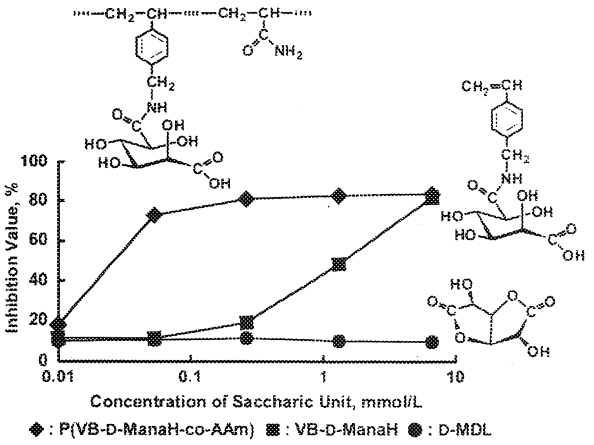

J Appl Phycol (2008) 20:283–288
DOI 10.1007/s10811-007-9245-9

Development of laboratory-scale photobioreactor for water purification by use of a biofilter composed of the aerial microalga *Trentepohlia aurea* (Chlorophyta)

Katsuya Abe · Emi Takahashi · Morio Hirano

Received: 20 January 2007 / Revised and Accepted: 22 June 2007 / Published online: 19 September 2007

Abstract Biofilms formed by the green alga *Trentepohlia aurea* could be a useful tool in the removal of nitrate and phosphate from water. When a prepared biofilter was dampened with medium and incubated under low light intensity (10 μmol photons m^{-2} s^{-1}) between 5 and 50 μmol photons m^{-2} s^{-1}, the efficiency of removal of inorganic compounds from water was higher without the decomposition of chlorophylls in the cells. Algal cells immobilized on a glass fiber filter could be kept for 12 weeks under dark conditions at 4°C in the refrigerator. We tried to construct a laboratory-scale photobioreactor for the removal of inorganic nitrogen and phosphate from water by the biofilm. In this study, the synthetic wastewater was prepared by diluting 18-fold Bold's basal medium with deionized water. The photobioreactor could efficiently remove nitrate and phosphate from the synthetic wastewater under continuous illumination. The removal ability of nitrate and phosphate per sheet of the biofilter in the photobioreactor exhibited about an 8- and 16-fold increase, respectively, in 3 days, compared with the bath experimental results. This study showed that the cycling of wastewater in the reactor by the pump led to a significant improvement in the efficiency of the inorganic ion uptake from water.

Keywords *Trentepohlia aurea* · Aerial microalga · Biofilter · Bioreactor · Eutrophication · Water treatment

K. Abe (✉) · E. Takahashi · M. Hirano
Faculty of Engineering, Department of Applied Chemistry,
Kogakuin University,
2665-1, Nakano-machi, Hachioji,
Tokyo 192-0015, Japan
e-mail: bt10335@ns.kogakuin.ac.jp

Introduction

The great potential of algae in wastewater treatment has frequently been noted and utilized in the form of using suspended algae to remove inorganic nutrients and organic matter (Grossi et al. 2001; Lee and Lee 2001; Mallick 2002; Todd et al. 2002; Lima et al. 2003; da Costa and França 2003; Lebeau and Robert 2006). Hammouda et al. (1995) reported on the performance of an algal aquaculture wastewater treatment system using the green algae *Scenedesmus* spp. and *Chlorella vulgaris*. The cyanobacterium *Spirulina platensis* has also been used to evaluate the possibility of employing microalgal biomass to remove nitrate and phosphate from wastewater (Lodi et al. 2003). When some microalgae are used as biological agents for wastewater treatment, they produce fine chemicals such as pigments, polysaccharides, polyunsaturated fatty acids and so on. Microalgae, immobilized in alginate beads, chitosan, synthetic polymer, porous glass, etc., have also been used because of the high physiological stability of the cells and ease of separating treated water and organisms (e.g., de la Noüe and Proulx 1988; McLean et al. 2000; Schumacher and Sekoulov 2002; Delahaye et al. 2005; Hernandez et al. 2006). Immobilization improves the ability to handle microorganisms and to control the process. For example, Gaffney et al. (2001) constructed a laboratory-scale photobioreactor for the removal of inorganic phosphate from water by the cyanobacterium *Anabaena variabilis* where the cyanobacteria were immobilized by adsorption onto polyurethane foam. The efficiency of phosphorus uptake by the immobilized cells was higher than that by free-living cells and an uptake efficiency of about 90% could be achieved with this photobioreactor. In addition, when the performance of "microalgal biofilms" systems (which are different from the process using immobilized cells) was

compared with suspended algae systems (Lin et al. 2003), the use of microalgal biofilm systems (in flat plate photobioreactors) was shown to be especially suitable for nutrient removal. In one study, an algal biofilm was formed by different species of algae, mainly by the green algae *Ulothrix*, *Stigeoclonium* and *Chlamydomonas* and the blue-green alga *Oscillatoria* (Schumacher and Sekoulov 2002). In another study, it was shown that small wastewater treatment plants for nutrient removal and bacteria reduction could be developed with the aid of microalgal biofilms. The authors have also examined the capability of the aerial microalga *Trentepohlia aurea*, grown on the surface of a substrate such as cellulose filter paper, in removing inorganic nitrogen from water (Abe et al. 2003). It was reported that growth inhibition of the cyanobacterium *Spirulina platensis* was noticeable in SOT medium treated with the algal biofilm. In general, because aerial microalgae can also grow on surfaces of rocks, concrete and tree bark exposed to full sunlight, they are believed to have a high level of tolerance and adaptability to severe conditions such as desiccation. In another study, the aerial microalga *Coelastrella striolata* var. *multistriata* was shown to have a unique ability to exhibit a reddish-orange (indicative of carotenoid formation) to green color (chlorophyll formation) depending on the nitrogen source concentration in the medium. By analyzing the rate of chlorophyll formation, it was possible to estimate spectrophotometrically the total nitrogen content in water collected from aquatic systems (Abe et al. 2004). Additionally, even if the culture was kept in the dark at 4°C, the alga was physiologically stable for at least 90 days.

The aim of this work is to characterize the removal of inorganic nitrogen and phosphorus compounds from nutrient-rich water by a biofilter using the aerial microalga *T. aurea* under various conditions of light intensity, pH and other conditions, and to develop a photobioreactor with the biofilter for water purificaion.

Materials and methods

The aerial microalga *Trentepohlia aurea* was collected in Shizuoka, Japan (Abe et al. 1998). The algal cells were cultured and maintained in modified Bold's basal medium (using NH_4Cl instead of $NaNO_3$ as N source) as reported previously (Abe et al. 1999). Cultures were bubbled with air in 500 mL Erlenmeyer flasks. The modified BB medium contained 1,000 mg NH_4Cl, 175 mg KH_2PO_4, 75 mg K_2HPO_4, 25 mg $MgSO_4 \cdot 7H_2O$, 25 mg NaCl, 50 mg EDTA, 30 mg KOH, 5 mg $FeSO_4 \cdot 7H_2O$ and 11 mg H_3BO_3 in 1 l of deionized water. The pH was adjusted to 8.0 with NaOH prior to autoclaving.

Preparation of algal biofilms

Under sterile conditions, algal cells suspension were applied dropwise onto a glass fiber filter (ADVANTEC, Filter paper GA-55, size: 20×100 mm) by Pasteur pipette. The algal cells on the filter were about 4 mg dry weight. Chlorophyll concentration was 20 mg g^{-1} dry wt. The filter papers were placed in a flat-bottomed test tube (25Φ× 125 mm) with 10 mL of BB medium (containing 250 mg $NaNO_3$ L^{-1} as N source). After covering the test tube mouth with a plastic cup, the biofilm was dampened with medium and incubated under continuous illumination with cool-white fluorescent lamps (10 μmol photons m^{-2} s^{-1}) at 25°C. Such a system is called "bath system" in this study.

Observation of biofilms

Algal biofilms of *T. aurea* were observed using a digital camera (Sony, DSK-F505K) and light microscopy (Nikon, E-800).

Algal growth was measured by carefully washing the immobilized cells on the glass fiber filters with a filter funnel and distilled water, and then drying under reduced pressure before weighing. Growth was estimated by measuring the quantity of biomass expressed as dry weight.

Photobioreactor Design

A laboratory-scale photobioreactor was constructed for the removal of inorganic nitrogen and phosphorus from water by *T. aurea* cells. As shown in Fig. 1, the photobioreactor glass column (50 cm in length×4.5 cm diameter) was filled with funnels with algal biofilter attached. The column was maintained at 25°C and illuminated with a cool-white fluorescent lamp (10 μmol photons m^{-2} s^{-1}) and a light reflector (e.g., aluminum foil). The flow rate was 12 mL min^{-1}.

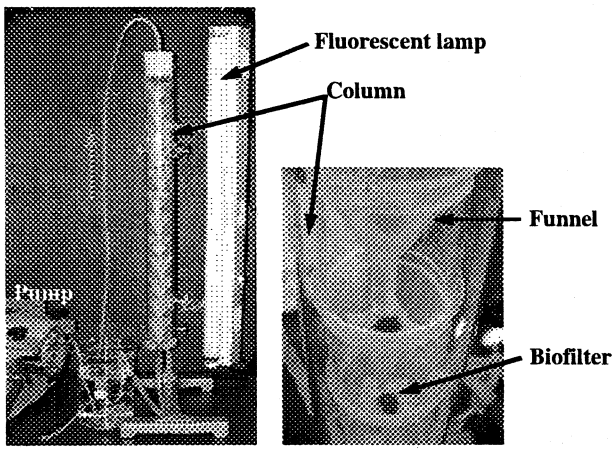

Fig. 1 The laboratory-scale photobioreactor filled with the biofilters using *T. aurea* for removal of nitrate and phosphate from water

Analyses

Total chlorophyll was estimated according to Mackinney (1941). Nitrate and phosphate were measured by non-suppressed ion chromatography (TOA DKK, IA-200) using an anion-exchange column (TOA DKK, PCI-211) at 1.1 mL min^{-1} and 40°C and equipped with a three-electrode detector. The mobile phase consisted of phthalic acid (2.3 mM), 6-aminohezanoic acid (2.8 mM), and boric acid (200 mM).

Removal ratios (R) of nitrate and phosphate were defined as: R=[(I-F)/I] × 100%, in which I and F are the initial and final concentrations of the inorganic ions, respectively. For example, a removal ratio of 100% was obtained when no nitrate was detected in the water (i.e., F=0).

Results and discussion

In this study, cells suspensions of *Trentepohlia aurea* were applied dropwise onto a glass fiber filter. The prepared biofilm was incubated in damp medium under continuous illumination. Observation by light microscopy showed that the filaments of *T. aurea* twined around the glass fibers in the filter, in a manner similar to the immobilized cells on the cellulose paper in the previous study (Abe et al. 2003). We selected the glass fiber filter for cell immobilization because this study found that glass fiber filter had more durability in water (for example, it did not become soggy for an extended period of time) than cellulose paper.

Effect of light intensity and pH on removal of nitrate and phosphate

The cells dropped on the glass fiber filter were about 4 mg (initial biomass) dry weight and the culture medium was adjusted to pH 8.0 (initial value). Fig. 2 shows the effect of light intensity on biomass and removal of nitrate and phosphate. As a result, the removal ratios (and specific nitrate removal: removal NO_3 mg dry weight mg^{-1} L^{-1} day^{-1}) of nitrate by the algal biofilter attained were 12 (0.94), 15 (1.10), 13 (1.02), and 11% (0.80) when treated with 5, 10, 20, and 50 μmol photons m^{-2} s^{-1} for 4 days, respectively. On the other hand, the removal ratios (and specific phosphate removal: removal PO_4 mg dry weight mg^{-1} L^{-1} day^{-1}) of phosphate by the biofilter were, respectively, 0.6 (0.04), 3 (0.20), 5 (0.35), and 6% (0.40) under these light conditions at 4 days. In the past, inorganic ions removal from water by *Dunaliella salina* immobilized in alginate beads was investigated (Thakur and Kumar 1999). The removal ratio of nitrogen and phosphate by the immobilized cells in beads attained 14 and 64% after 1.5 days. The alga

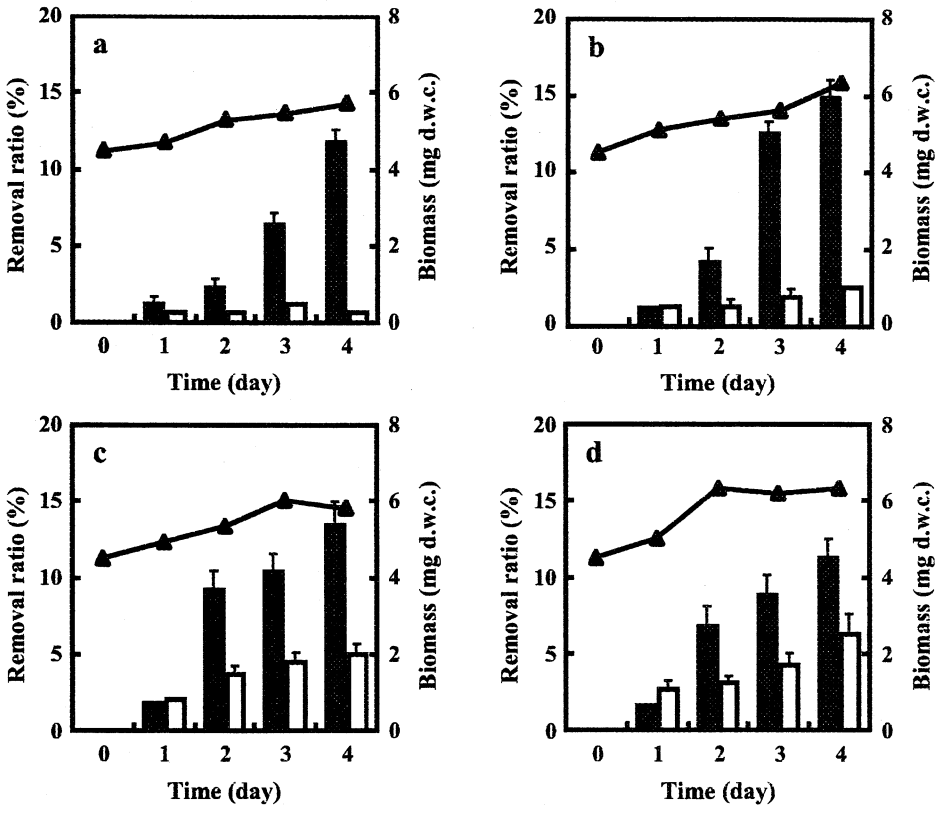

Fig. 2 Time course of the removal ratio of nitrate (*black bars*) and phosphate (*white bars*) by the algal biofilm and biomass (▲) of *T. aurea* on glass fiber filter under 5 (**a**), 10 (**b**), 20 (**c**), and 50 μmol photons m^{-2} s^{-1} (**d**). The culture medium was adjusted to pH 8.0 (initial value) at 25°C. The initial concentrations of nitrate and phosphate were 182 mg L^{-1} and 163 mg L^{-1} in the BB medium, respectively. Data are represented as mean ± SD obtained from three independent experiments

cells contained chlorophylls between 15 and 22 mg g^{-1} dry weight during the 4 days, although there was a tendency for the chlorophyll content of *T. aurea* on glass fiber filter to decrease with increasing light intensities (Fig. 3). In particular, the decomposition of the chlorophylls was observed in the alga cells cultured for over 1 week with a light intensity above 20 μmol photons m^{-2} s^{-1}. *Trentepohlia aurea* could grow to a small degree on the surface of a glass fiber filter moistened with the medium for 4 days with the indicated light intensities. It was found that the biofilter with the alga was affected by the light intensity in the removal of nitrate and phosphate from water, as well as the biomass on the glass fiber filter. Consequently, when the prepared biofilter was dampened with medium and incubated under a lower light intensity (10 μmol photons m^{-2} s^{-1}), the efficiency of removal of the inorganic compounds from water is higher without the problem of decomposition of chlorophylls in the cells. The ability of the biofilter to remove inorganic compounds remained constant throughout the experimental period even after the biofilter was re-used more than 5 times.

We tried to examine the effect of medium pH on the removal of nitrate and phosphate by the algal biofilter, when the illumination was held constant at 10 μmol photons m^{-2} s^{-1}. It was found that the values of the initial medium pH changed from pH 4.0, 5.0 6.0, 7.0, and 8.0 to pH 6.0, 6.1, 6.7, 7.4, and 8.2, respectively, in the bath system for 4 days. As shown in Fig. 4, the removal ratios of nitrate by the algal biofilter reached around 14% at pH 6 to 8 (initial medium pH) in 4 days. There would be

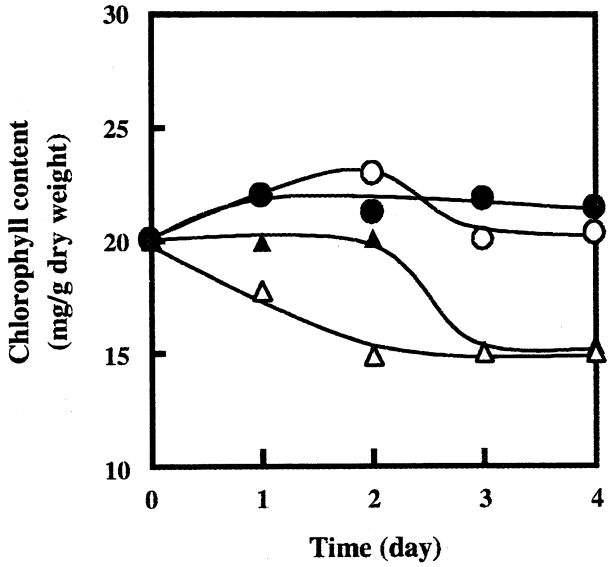

Fig. 3 Time course of the chlorophyll content of *T. aurea* on glass fiber filter under 5 (•), 10 (○), 20 (▲), and 50 μmol photons m^{-2} s^{-1} (Δ). The culture medium was adjusted to pH 8.0 (initial value) at 25°C. Values are means (n=3)

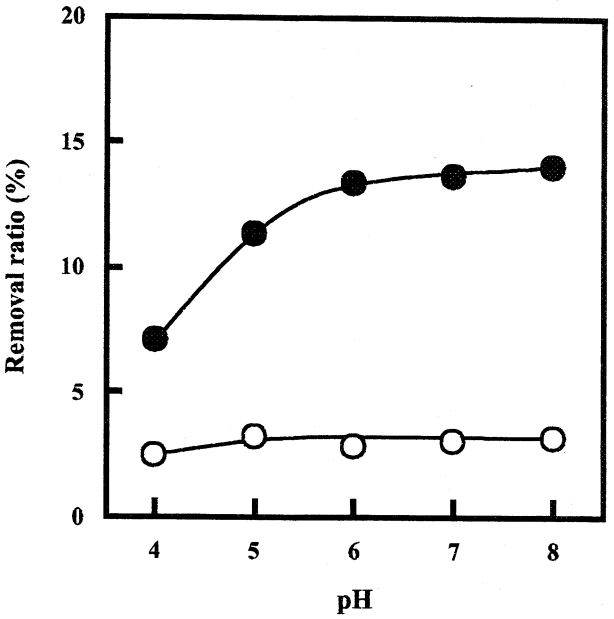

Fig. 4 Effect of medium pH on removal ratio of nitrate (•) and phosphate (○) of the algal biofilm. The algal biofilter was incubated damping with medium for 4 days at 10 μmol photons m^{-2} s^{-1} and 25°C. Values are average values (n=3)

physiological or metabolic damage to the algal cells of *T. aurea* under the condition of the lower initial medium pH. The removal ability of inorganic phosphorus compounds (containing HPO_4^{2-} and $H_2PO_4^-$) from water was unchanged between pH 4 to 8. It was observed that the chlorophyll content of the alga decreased by 16 mg g^{-1} dry weight when cultured for 4 days at pH 4.0. The decrease of the removal ratio of inorganic nitrogen compounds from water under pH would result in decrease in the chlorophyll content of the alga (e.g., removal ratio and specific nitrate removal at pH 3: 3% and 0.23 mg dry weight mg^{-1} day^{-1}).

It was found that the biofilter using *T. aurea* was physiologically stable and could ingest nitrogen and phosphate sources when the algal filter was kept for 12 weeks under dark conditions at 4°C. After 12 weeks under these conditions, the removal ratios of nitrate and phosphate by the biofilter were 9% and 2% when placed in the BB medium at pH 8, 10 μmol photons m^{-2} s^{-1} and 25°C for 4 days, respectively. Since the alga could continue to survive on the glass fiber filter in the refrigerator for a long time, a large quantity of the biofilter could be prepared in advance.

Effect of biomass on removal of nitrate and phosphate

This study examined the removal of nitrate and phosphate by means of different kinds of algal biofilters, namely, two sheets of the glass fiber filters partially placed dropping algal cells suspension of ca. 4 mg by dry weight (called 2 sheets-biofilter), one sheet of the filter using algal cells suspension

of ca. 8 mg as dry weight of cells (2 times-biomass), and one sheet of filter using algal cells suspension of ca. 4 mg as dry weight of cells (control). These biofilms in the bath culture were dampened with medium and incubated for 4 days at 10 μmol photons m^{-2} s^{-1}, pH 8.0, and 25°C. As shown in Fig. 5, the removal ratios of nitrate and phosphate from water by the 2 sheets-biofilter and 2 times-biomass algal biofilters were about twice that of control in the bath system.

Removal of nitrate and phosphate by photobioreactor

We tried to construct a laboratory-scale photobioreactor for the removal of nitrate and phosphate from water. Twelve sheets of the biofilm composed of *T. aurea* cells (chlorophyll concentration: 20 mg g^{-1} dry weight cells) were used, as shown Fig. 1. In this study, the synthetic wastewater was prepared by diluting 18-fold the BB medium with deionized water. The initial concentrations of nitrate and phosphate in the prepared wastewater were 10 and 9 mg L^{-1}, respectively. These concentrations in the synthetic wastewater made reference to water of a lake in Japan. Experiments showed that the photobioreactor filled with the *T. aurea* biofilters removed nitrate and phosphate from the water when light was illuminated at 10 μmol photons m^{-2} s^{-1} (Fig. 6). In particular, complete removal of nitrate was achieved within 72 h by the bioreactor under continuous illumination. The photobioreactor could ingest 40% of the phosphate in the wastewater in 3 days. The past study showed a possibility of polishing secondary effluent by a small

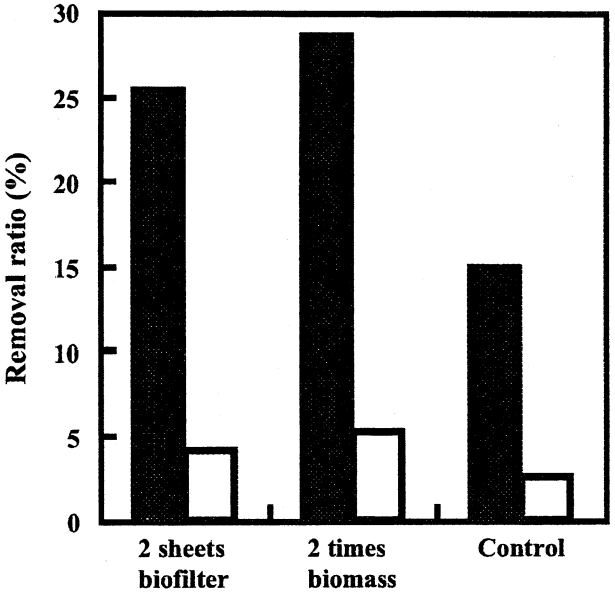

Fig. 5 Effect of biomass on removal ratio of nitrate and phosphate of the algal biofilm. The algal biofilter was incubated damping with medium for 4 days at 10 μmol photons m^{-2} s^{-1} and 25°C. Values are means (n=3)

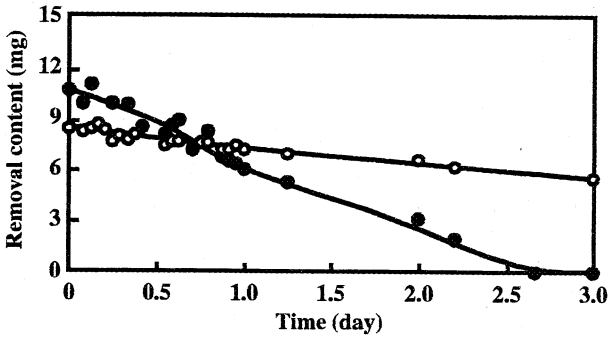

Fig. 6 Time course of removal of nitrate (•) and phosphate (○) by the photobioreactor filled with the biofilters using *T. aurea* at 10 μmol photons m^{-2} s^{-1} at 25°C

wastewater treatment plant (the surface size of a plant: 1.65 m width and 2 m length) using an algal biofilm composed of different green and bluegreen algae (Schumacher and Sekoulov 2002). In this case, the plant using algal biofilm could ingest about 90% of total phosphorus and total inorganic nitrogen for 6 h. A laboratory-scale photobioreactor was previously constructed for removal of inorganic phosphorus from water by polyurethane foam-immobilized *Anabaena variabilis* cells (Gaffney et al. 2001). It was reported that the photobioreactor could remove almost all orthophosphate from water in the period of 26 days. In this study, the synthetic wastewater was continuously returned to a water reservoir in a closed system. This system was possible to measure the uptake of the inorganic ions in the water. The removal efficiency of nitrate and phosphate per sheet of the biofilter composed of *T. aurea* cells in the photobioreactor (cycling system) exhibited about an 8- and 16-fold increase, respectively, in 3 days, compared with the bath system using a sheet of the biofilm in the wastewater under the same conditions. The study showed that the cycling of wastewater in the reactor by the pump (flow rate: 12 mL min^{-1}) provided significant improvement in the efficiency of the inorganic ion uptake from water.

Conclusions

In this study, the biofilms of *T. aurea* could represent a useful tool for removing nitrate and phosphate from water. Observation by light microscopy showed that the filaments of *T. aurea* twined around the glass fiber in the filter. *T. aurea* could grow to a small degree on the surface of a glass fiber filter moistened with the medium. It was found that the algal filter could be kept for 12 weeks under dark conditions at 4°C in the refrigerator. We made a laboratory-scale photobioreactor for the removal of nitrate and phosphate from water by the biofilm. The photobioreactor could efficiently remove nitrate and phosphate from the

synthetic wastewater under continuous illumination. This study showed that the cycling of wastewater in the reactor by the pump led to a significant improvement in the efficiency of the inorganic ion uptake from water. The logical next step would be to optimize the removal of nitrogen and phosphorus source uptake from water by the photobioreactor.

Acknowledgement This work was partly supported by a grant from MEXT Kakenhi (Houga: 16658135).

References

Abe K, Mihara H, Hirano M (1998) Characteristics of growth and carotenoids accumulation of the aerial microalga *Trentepohlia aurea*. J Mar Biotechnol 6:53–58

Abe K, Nishimura N, Hirano M (1999) Simultaneous production of β-carotene, vitamin E, and vitamin C by the aerial microalga *Trentepohlia aurea*. J Appl Phycol 11:331–336

Abe K, Matsumura I, Imamaki A, Hirano M (2003) Removal of inorganic sources from water by the algal biofilm of the aerial microalga *Trentepohlia aurea*. World J Microbiol Biotechnol 19:325–328

Abe K, Takizawa H, Kimura S, Hirano M (2004) Characteristics of chlorophyll formation of the aerial microalga *Coelastrella striolata* var. *multistriata* and its application for environmental biomonitoring. J Biosci Bioeng 98:34–39

da Costa AC, de França FP (2003) Cadmium interaction with microalgal cells, cyanobacterial cells, and seaweeds; toxicology and biotechnological potential for wastewater treatment. Mar Biotechnol 5:149–156

Delahaye E, Boussahel R, Petitgand T, Duguet JP, Montiel A (2005) Use of fixed micro-algae as a direct, simple and quickly measurable indicator of biofilm density in biofilters in order to improve washing operations. Desalination 177:273–279

de la Noüe, J Proulx, D (1988) Biological tertiary treatment of urban wastewaters with chitosan-immobilized *Phormidium*. Appl Microbiol Biotechnol 29:292–297

Gaffney AM, Markov SA, Gunasekaran M (2001) Utilization of cyanobacteria in photobioreactors for orthophosphate removal from water. Appl Biochem Biotechnol 91–93:185–193

Grossi V, Blokker P, Sinninghe Damsté JS (2001) Anaerobic biodegradation of lipids of the marine microalga *Nannochloropsis salina*. Org Geochem 32:795–808

Hammouda O, Gaber A, Abdel-Raouf N (1995) Microalgae and wastewater treatment. Ecotoxicol Environ Safety 31:205–210

Hernandez JP, de-Bashan LE, Bashan Y (2006) Starvation enhances phosphorus removal from wastewater by the microalga *Chlorella* spp. co-immobilized with *Azospirillum brasilense*. Enzyme Microbial Technol 38:190–198

Lebeau T, Robert JM (2006) Biotechnology of Immobilized Micro Algae: A Culture Technique for the Future? In: Subba Rao DV (ed) Algal Culture, Analogues of Blooms and Applications. Science Publishers, New Hampshire, USA, pp 801–837

Lee K, Lee CG (2001) Effect of light/dark cycles on wastewater treatments by microalgae. Biotechnol Bioproc Eng 6:194–199

Lima SAC, Castro PML, Morais R (2003) Biodegradation of p-nitrophenol by microalgae. J Appl Phycol 15:137–142

Lin YH, Leu JY, Lan CR, Lin PHP, Chang FL (2003) Kinetics of inorganic carbon utilization by microalgal biofilm in a flat plate photo reactor. Chemosphere 53:779–787

Lodi A, Binaghi L, Solisio C, Converti A, Del Borghi, M (2003) Nitrate and phosphate removal by *Spirulina platensis*. J Ind Microbiol Biotechnol 30:656–660

Mackinney J (1941) Adsorption of light by chlorophyll solution. J Biol Chem 140:315–322

Mallick N (2002) Biotechnological potential of immobilized algae for wastewater N, P, and metal removal: A review. Biometals 15:377–390

McLean BM, Baskaran K, Connor MA (2000) The use of algal-bacterial biofilms to enhance nitrification rates in lagoons: experience under laboratory and pilot-scale conditions. Water Sci Technol 42:187–194

Schumacher G., Sekoulov I (2002) Polishing of secondary effluent by an algal biofilm process. Water Sci Technol 46:83–90

Thakur A, Kumar HD (1999) Nitrate, ammonium, and phosphate uptake by the immobilized cells of *Dunaliella salina*. Bull Environ Contam Toxicol 62:70–78

Todd SJ, Cain RB, Schmidt S (2002) Biotransformation of naphthalene and diaryl ethers by green microalgae. Biodegradation 13:229–238

Available online at www.sciencedirect.com
SCIENCE DIRECT
Food Chemistry 100 (2007) 656–661
Food Chemistry
www.elsevier.com/locate/foodchem

Accumulation and antioxidant activity of secondary carotenoids in the aerial microalga *Coelastrella striolata* var. *multistriata*

Katsuya Abe, Hiroaki Hattori, Morio Hirano *

Department of Applied Chemistry, Faculty of Engineering, Kogakuin University, 1-24-2 Nishi-Shinjuku, Shinjuku-ku, Tokyo 163-8677, Japan

Received 20 June 2005; accepted 11 October 2005

Abstract

The growth and nitrate uptake of the aerial microalga *Coelastrella striolata* var. *multistriata*, which was isolated from the surface of rocks, were characterized under a variety of conditions in this study. The maximum specific growth rate of the alga, having prominent inorganic nitrogen uptake in the fresh medium, was 0.30 d^{-1}, as calculated in the growth logarithmic phase. It was also shown that the alga had abilities to be reddish orange to green colour (depending on the nitrogen source concentration in the medium) and to synthesize very high amounts of a complex mixture of carotenoids, such as canthaxanthin, astaxanthin and β-carotene. The reddish orange cells of the alga could accumulate 56.0 mg of major secondary carotenoids per g biomass. In the content of carotenoids, canthaxanthin, astaxanthin and β-carotene in the cells were 47.5, 1.5, and 7.0 mg/g dwc, respectively. Additionally, it was shown that the algal extract containing those carotenoids had an antioxidant potential in lipid foods. In the near future, the aerial microalga *C. striolata* var. *multistriata* will be used as a functional material in a variety of commercial applications, such as feed supplements, natural antioxidants and food dyes.

Keywords: Aerial microalga; *Coelastrella striolata* var. *multistriata*; Canthaxanthin; Antioxidant

1. Introduction

Reactive oxygen species (single oxygen and peroxyl radicals) may react with biologically important components, such as DNA, proteins, or lipids, impairing their physiological functions (Halliwell, 1996; Sies, 1985). Such processes are considered as initial events in the pathogenesis of several diseases, including cancer, cardiovascular diseases, or age-related macular degeneration. Several classes of biological molecules are susceptible to attack by these free radicals, including certain amino acids, which react with radicals at quite rapid rates. In the lipids, polyunsaturated fatty acids also react at much slower rates, increasing with the number of double bonds in the molecule, to form lipid hydroperoxides (Kiritsakis & Dugan, 1985; Terao, Hirota, Kawakatsu, & Matsushita, 1981; Terao & Matsushita, 1977). Such lipid oxidation, not only results in an undesirable off-flavour, but also decreases the nutritional quality of lipid foods due to the loss of essential fatty acids. It was reported, 35 years ago, that singlet oxygen participates in the initiation step of oil oxidation, and the reaction rate of singlet oxygen with linoleic acid is about 1450 times greater than that of triplet oxygen (Rawls & Van Santen, 1970).

Carotenoids play major roles in oxygenic photosynthesis, where they function in light harvesting and protect the photosynthetic apparatus from excess light by energy dissipation. Most carotenoids are efficient antioxidants, quenching singlet oxygen, and trapping peroxyl radicals (Jyonouchi, Sun, & Gross, 1995; Krinsky, 1992, 1993; Miki, 1991; Surai et al., 2003). The effects of naturally occurring and food-approved carotenoids (for example, β-carotene and canthaxanthin) on the singlet oxygen oxidation of vegetables oils have previously been examined (Goulson & Warthesen, 1999; Jung & Min, 1991; Pánek,

* Corresponding author. Fax: +81 3340 0147.
E-mail address: bt10807@ns.kogakuin.ac.jp (M. Hirano).

0308-8146/$ - see front matter © 2005 Elsevier Ltd. All rights reserved.
doi:10.1016/j.foodchem.2005.10.026

Fantová, Trojáková, Réblová, & Pokorný, 2001; Psomiadou & Tsimidou, 2002; Rahmani & Csallany, 1998). The singlet-oxygen quenching rates of the food-approved carotenoids increased as the number of conjugated double bonds of the carotenoids increased (Jung & Min, 1991). It has been shown in vitro that canthaxanthin also has antioxidant capabilities. The antioxidant activity of canthaxanthin has been recorded in membrane model systems, liposomes, and cell models (Clark, Faustman, Chan, Furr, & Riesen, 1999; Palozza et al., 1996; Rengel et al., 2000).

Among the ketocarotenoids found in higher plants, algae, fungi, or bacteria, astaxanthin (3,3′-dihydroxy-β,β-carotene-4,4′-dione) and canthaxanthin (β,β-carotene-4,4′-dione) are the most important from the biotechnological viewpoint. Thus, there is growing commercial interest in the biotechnological production of such secondary carotenoids (Baker, 2002). The secondary carotenoids are functionally defined as carotenoids that are not essential for photosynthesis and are not localized in the thylakoid membranes of the chloroplast. The ketocarotenoid astaxanthin is commonly used as a feed supplement in aquaculture for the production of salmon, trout and shrimp (Lorenz & Cysewski, 2000), while canthaxanthin is mainly used as a food dye for colouring egg yolks and chicken skin (Surai et al., 2003). In the past, astaxanthin has been found and identified in many species of algae, such as *Haematococcus pluvialis* (Grünewald, Hirschberg, & Hagen, 2001), *Chlorococcum* sp. (Zhang & Lee, 2001), *Chlorella zofingiensis*, *Neochloris wimmeri*, *Scenedesmus vacuolatus*, *Scotiellopsis oocystiformis* and *Protosiphon botryoides* (Orosa, Torres, Fidalgo, & Abalde, 2000). On the other hand, canthaxanthin production has been reported only in a few algal species {*C. zofingiensis* (Pelah, Sintov, & Cohen, 2004), *Chlorococcum* sp., and *Tetracystis intermedium* (Campo et al., 2000)}. The fresh water microalga *C. zofingiensis* could accumulate 8.79 mg/g biomass of total secondary carotenoids (containing about 97% canthaxanthin), when the alga was grown for 9 days under conditions of salt stress and low light.

We previously reported the growth and ammonium uptake of the aerial microalga, *C. striolata* var. *multistriata*, which was isolated from the surface of rocks at Shizuoka (Japan) (Abe, Takizawa, Kimura, & Hirano, 2004). It was shown that the alga had a unique ability to be a reddish-orange to green colour depending on the nitrogen source concentration in the medium. Using the chlorophyll formation of the alga, it was possible to estimate, spectrophotometrically, the total nitrogen content in water collected from the aquatic system. In addition, the reddish-orange cells of the alga were able to accumulate significant quantities of carotenoids (mainly as canthaxanthin, astaxanthin, and β-carotene). The aim of the present work is to study secondary carotenoid accumulation during culture of the aerial microalga, *C. striolata* var. *multistriata* under the stress condition of nitrogen deficiency and to examine activities of natural antioxidants in oil.

2. Materials and methods

2.1. Regents

All solvents and reagents were of analytical or laboratory grade. Deionized water was used throughout.

2.2. Algal material and culture conditions

Colonies of the microalga, *C. striolata* var. *multistriata*, were isolated from the surface of rocks at Shizuoka, Japan. The microalga was cultured and maintained in Bold's basal (BB) medium at 25 °C under continuous illumination by cool-white fluorescent lamps (40 μmol photons/m^2/s). Batch cultures were bubbled with air in flat glass bottles. The BB medium contained 250 mg of $NaNO_3$, 175 mg of KH_2PO_4, 75 mg of K_2HPO_4, 25 mg of $MgSO_4 \cdot 7H_2O$, 25 mg of NaCl, 50 mg of EDTA, 30 mg of KOH, 5 mg of $FeSO_4 \cdot 7H_2O$ and 11 mg of H_3BO_3 in 1 l of deionized water. The pH was adjusted to 8.0 with NaOH prior to autoclaving.

2.3. Measurement of algal growth

The growth of algal cells was determined by turbidity at 750 nm. For the dry weight measurement, cells were collected using a 10 μm membrane filter (Nihon Millipore, Tokyo), washed with distilled water, and then dried under reduced pressure before weighing.

2.4. Pigment analysis

Chlorophylls were extracted using methanol. Total amounts of chlorophyll were estimated using a spectrometer (UV-2450; Shimadzu, Kyoto) according to the method of Mackinney (1941). Monitoring of the free carotenoids and carotenoid esters in the pigment extract was carried out according to an HPLC method, as described previously (Abe et al., 2004). The HPLC analysis was performed with a reversed phase column (250 × 4.6 mm i.d., ODS-P Inertsil; GL Sciences, Tokyo), and a pump (PU-980; Jasco, Tokyo) equipped with a UV/Vis detector (UV-970; Jasco). Aliquots of 10 μl were used for HPLC analysis. The mobile phase consisted of eluents A (dichloromethane:methanol:acetonitrile:water, 5.0:85.0:5.5:4.5 v/v) and B (dichloromethane:methanol:acetonitrile:water, 25.0:28.0:42.5:4.5 v/v). For separation of carotenoids, the following gradient procedure was used (0% of B for 8 min; a linear gradient from 0% to 100% of B for 6 min; 100% of B for 40 min, at a flow rate of 1.0 ml/min and 25 °C). The absorbance detector was set at 480 nm. Pigments were extracted with 1 ml of dichloromethane and methanol (25:75, v/v). Saponification of carotenoid esters was performed as follows: NaOH (0.016 M) dissolved in methanol (0.25 ml), which was freshly prepared, was added to the pigment extract solution under a nitrogen atmosphere. The mixture was kept at 5 °C in darkness under nitrogen for 24 h for complete hydrolysis

of carotenoid esters. The saponified pigment extract solution was directly analyzed by HPLC. Pure standards of astaxanthin, lutein, and β-carotene were purchased from Sigma Chemical (St. Louis, MO, USA), and canthaxanthin and neoxanthine were from Wako.

2.5. Fatty acid analysis

After 1 ml of 5%HCl–methanol (Kokusan Chemical, Tokyo) was added to 10 mg of freezed-dried cells, the mixture was refluxed by heating at 100 °C for 3 h. After cooling to room temperature, fatty acid methyl esters were extracted into 1 ml of hexane. The obtained hexane layer was dehydrated, and then 1.5 μl of the hexane layer was withdrawn with a microsyringe and its fatty acid methyl ester content was determined by a gas chromatography system (GC-14B; Shimadzu, Kyoto) equipped with a capillary column (30 m × 0.25 mm internal diameter; J&W Scientific, CA, USA) and a hydrogen flame ionization detector. In this case, heptadecanoic acid was used as the internal standard for quantitative analysis.

2.6. Nitrate analysis

Ammonium was analyzed using an ammonium electrode (5002A-10C; Horiba, Kyoto). Nitrate ion was measured spectrophotometrically using the methods of the Japanese industrial standard for industrial wastewater (Japanese Industrial Standard, 1998). Nitrate was determined at 410 nm with 4-aminobenzenesulfonamide (Wako) and brucine (Tokyo Kasei Kogyo, Tokyo).

2.7. Photooxidation of methyl linoleate

Methyl linoleate (600 mg, Wako), containing oily pigment extract, was placed in test tube and subjected to oxidation under a fluorescent lamp for 4 h. The light intensity and temperature were 65 μE/m^2/s and 20 °C. The oxidation of methyl linoleate was determined by measuring peroxide values according to the JOCS method (Endo, Usuki, & Kaneda, 1984).

3. Results and discussion

3.1. Effects of nitrogen, light, and vessel on algal growth

In order to examine the effect of nitrogen concentration on growth, cells of the aerial microalga *C. striolata* var. *multistriata* were cultured using a flat glass bottle (700 ml) for 30 days in BB medium under various concentrations of nitrate (0, 250, 500 and 1000 mg/l $NaNO_3$ as the nitrogen source) at 40 μmol photons/m^2/s and 25 °C. The batch cultures were bubbled with air in flat glass bottles. Although the culture in the nitrogen-free medium inhibited cell division, higher biomass was obtained when the alga was cultured in BB medium containing more than 500 mg/l $NaNO_3$, as shown in Fig. 1(a). The alga entered the stationary phase of growth after 20 days with the higher rate of nitrate depletion. It was found that the maximum uptake rates of nitrate of the alga were almost the same under various concentrations of the nitrate-N (Fig. 1(b)). Because nitrogen deficiency will be a potential inducer, of secondary carotenoid formation in the microalga, the algal cells were grown in the medium containing 500 mg/l $NaNO_3$ (initial concentration), to promote production and accumulation of large amounts of secondary carotenoids in this study. To examine the effect of light intensity on growth, the algal cells were cultured for 30 days in BB medium containing 500 mg/l $NaNO_3$ at various light intensities (0, 7, 40, 65, 105, and 130 μmol photons/m^2/s) and 25 °C. As a result, the higher specific growth rate of 0.22 d^{-1} attained when the alga was cultured over 65 μmol photons/m^2/s (Fig. 2). Moreover, we tried to develop a culture method for the growth of *C. striolata* var. *multistriata* using two kinds of vessel. The alga was grown using a flat glass bottle (700 ml) and/or a slender test tube (400 mm × ∅ 30 mm) for 30 days in BB medium containing 500 mg/l $NaNO_3$ at 65 μmol photons/m^2/s and 25 °C. The maximum specific growth rate of 0.30 d^{-1} was obtained if the algal cells were cultured in the test tube. The alga entered the stationary phase of growth after 20 days with the highest rate of nitrate depletion in Fig. 3. The nitrate uptake rate reached 0.4 mg/

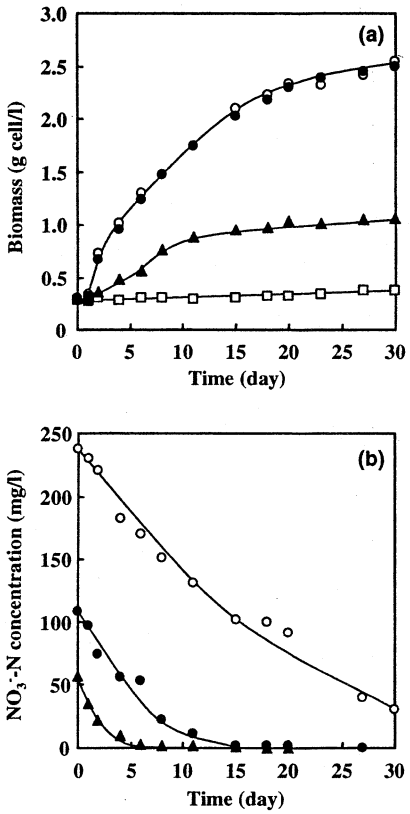

Fig. 1. Time course of the growth (a) and nitrate-N concentration of the medium (b) in a culture of *C. striolata* var. *multistriata*. The alga was cultured using a flat glass bottle for 30 days in BB medium under various concentrations of 0 (□), 250 (▲), 500 (●), and 1000 (○) mg/l $NaNO_3$ as the nitrogen source at 40 μmol photons/m^2/s and 25 °C.

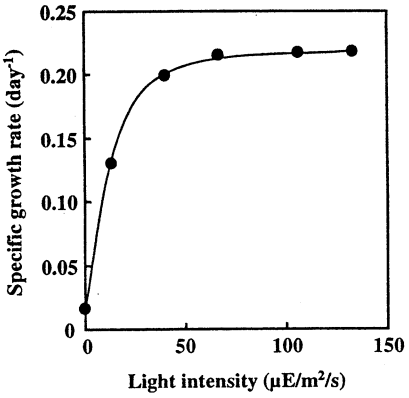

Fig. 2. Effect of light intensity on the specific growth rate in a culture of *C. striolata* var. *multistriata*. The alga was cultured using a flat glass bottle for 30 days in BB medium with 500 mg/l $NaNO_3$ added as the nitrogen source at 25 °C.

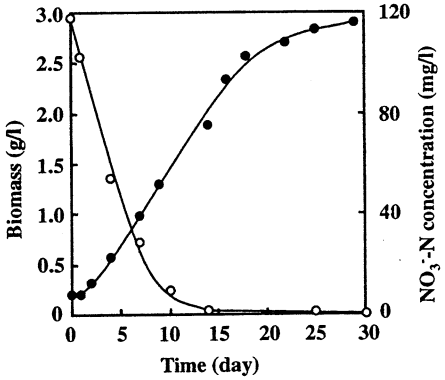

Fig. 3. Time course of growth (●) and nitrate-N concentration (○) of the medium in a culture of *C. striolata* var. *multistriata*. The alga was cultured using a slender test tube for 30 days in BB medium under various concentrations of 500 mg/l $NaNO_3$ as the nitrogen source at 65 μmol photons/m^2/s and 25 °C.

l/h, which was the same as that by *C. striolata* var. *multistriata* cultured in the medium with added NH_4Cl instead of $NaNO_3$ as the nitrogen source. This uptake rate was twice that obtained by other microalgae, such as *C. pyrenoidosa* and *Scenedesmus* sp. (Tam & Wong, 1989). The aerial microalga, *C. striolata* var. *multistriata* shows prominent ammonium and nitrate-N uptake in the fresh medium. When the alga was cultured in nitrogen-deficient medium under the same conditions, the cells were observed, in the slender test tube, to change from green to reddish-orange more rapidly than in the flat glass bottle (Fig. 4). Accordingly, the optimal growth of *C. striolata* var. *multistriata* was obtained at a combination of 500 mg/l $NaNO_3$ and a light irradiance of 65 μmol photons/m^2/s in the slender test tube to induce carotenoid synthesis.

3.2. Analyses of pigments and fatty acids of algal cells

The contents of carotenoids and chlorophylls in the extract solutions from the aerial microalga *C. striolata* var. *multistriata* cells were analyzed by HPLC and GC.

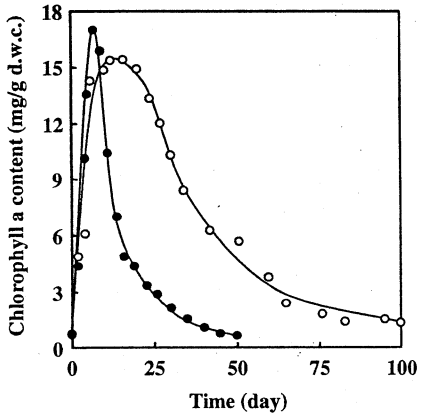

Fig. 4. Effect of culture vessel on chlorophyll content in a culture of *C. striolata* var. *multistriata*. The alga was cultured using a flat glass bottle (○) and a slender test tube (●) for 30 days in BB medium under various concentrations of 500 mg/l $NaNO_3$ as the nitrogen source at 65 μmol photons/m^2/s and 25 °C.

Analytical data of the pigment extracts from the green and reddish-orange cells of the alga are shown in Table 1. As a result, the reddish orange cells of the alga grown for 50 days under above-mentioned conditions could accumulate 56.0 mg of major secondary carotenoids per g dry weight cells (dwc) after the saponification treatment. This result is particularly surprising in view of the fact that the content of canthaxanthin in the cells was 47.5 mg/g dwc. While astaxanthin is a high-value carotenoid and identified in many kinds of microorganisms, canthaxanthin has also been characterized by comparatively high antioxidant activities in some in vitro systems. Natural canthaxanthin production has been investigated only in a few algal species. It was previously reported that the fresh water green microalga, *C. zofingiensis*, growing under conditions of salt stress and low light, accumulated high amounts of canthaxanthin (8.5 mg/g dwc) (Pelah et al., 2004). This study shows that the aerial microalga, *C. striolata* var. *multistriata*, has the ability to synthesize very high amounts of a complex mixture of carotenoids, such as canthaxanthin, astaxanthin, and β-carotene. These ketocarotenoids are commonly used as a feed supplement in aquaculture for the production of salmon, trout and shrimp. The biosynthesis of the ketocarotenoids in the algal cells will be

Table 1
Carotenoid content (mg/g dry weight cells) in the pigment extracts from the green and reddish orange cells of the aerial microalga, *C. striolata* var. *multistriata*, growing using a slender test tube in BB medium containing 500 mg/l $NaNO_3$ at 65 μmol photons/m^2/s and 25 °C

Pigment	Green cells	Reddish-orange cells[a]
Chlorophyll *a*	18.3	0.3
Chlorophyll *b*	6.0	0.3
β-Carotene	5.2	7.0
Canthaxanthin	3.2	47.5
Astaxanthin	n.d[b]	1.5

[a] After saponification treatment.
[b] n.d., not detected.

up-regulated under stress conditions, such as high light irradiance, salt addition and desiccative treatment.

In the fatty acid analysis, it is apparent that the alga contained fatty acids having 16 and 18 carbon atoms. Both saturated and unsaturated acids were present in the green and reddish orange cells of the alga (Table 2). The predominant saturated was palmitic acid (16:0) in both green and reddish-orange cells. On the other hand, it was found that the predominant unsaturated fatty acids in the green and reddish-orange cells were linoleic acid (18:2) and oleic acid (18:1), respectively. The reddish-orange cells of the alga could produce large amounts of fatty acids (total fatty acid content: 319 mg/g dwc), especially, 113.4 mg of oleic acid per g dwc.

3.3. Effect of algal extracts on photooxidation of oil

Effect of the algal extract (from *C. striolata* var. *multistriata* cells) on the peroxide value of methyl linoleate (ML) at 65 μmol photons/m^2/s and 20 °C is shown in Fig. 5. Using 20 mg of dried samples of the green and reddish-orange cells, the algal extract was prepared with dichloromethane and methanol, followed by saponification of carotenoid esters and fatty acids. As a result, the peroxide values of ML containing the algal extract from the orange cells were lower than that of the oil containing authentic carotenoid mixture, which was the same composition as carotenoids contained in the algal extract (0.95 mg canthaxanthin, 0.14 mg β-carotene and 0.03 mg astaxanthin). It was found that the algal extract sufficiently acted as antioxidants in ML, because it contained other natural antioxidants, such as tocopherols. On the other hand, the peroxide values of ML mixed with the algal extract from the green cells were higher, than that of the oil without the extract. This result was due to the chlorophyll-photosensitized singlet-oxygen oxidation of the oil. Consequently, the peroxide result suggests that canthaxanthin, with long-conjugated double bonds, has considerably greater antioxidant activity (same as astaxanthin). The algal extract from the cells of the aerial microalga *C. striolata* var. *multistriata* was demonstrated to have an antioxidant potential in lipid foods in this study. We will try to determine oxidation of oils by measuring peroxide formation and studying quenching mechanisms and quenching rate constants of the algal extract by using steady-state kinetic equations.

Table 2
Fatty acid content (mg/g dry weight cells) of the aerial microalga, *C. striolata* var. *multistriata*, growing using a slender test tube in BB medium containing 500 mg/l $NaNO_3$ at 65 μmol photons/m^2/s and 25 °C

Fatty acid	Green cells	Reddish-orange cells
C16:0	17.9	60.3
C16:1*cis*	1.0	19.9
C16:1*trans*	4.3	7.6
C18:	1.3	11.9
C18:1*cis*	13.1	113
C18:1*trans*	2.2	3.8
C18:2	22.7	54.1
C18:3α	28.3	48.3
Total fatty acid	90.8	319

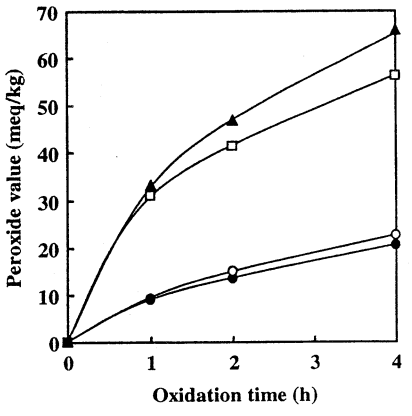

Fig. 5. Effect of the algal extracts of *C. striolata* var. *multistriata* on photooxidation of methyl linoleate. The photooxidation of methyl linoleate was carried out at 65 μmol photons/m^2/s and 20 °C. Symbols: □, control; ▲, the algal extract from the green cells; ○, authentic carotenoids mixture (containing 0.95 mg canthaxanthin, 0.14 mg β-carotene, and 0.03 mg astaxanthin); ●, the algal extract from the reddish orange cells (after the saponification).

In summary, the growth and nitrate uptake of the aerial microalga *C. striolata* var. *multistriata*, which was isolated from the surface of rocks, were characterized in the present study. The maximum specific growth rate of the alga, showing prominent inorganic nitrogen uptake in the fresh medium, was 0.30 d^{-1}, as calculated in the growth logarithmic phase. It was also shown that the alga had the ability to synthesize very high amounts of a complex mixture of carotenoids, such as canthaxanthin, astaxanthin and β-carotene. The algal extract containing these carotenoids had an antioxidant potential in lipid foods. In the near future, the aerial microalga, *C. striolata* var. *multistriata*, will be used as a functional material in a variety of commercial applications, such as feed supplements, natural antioxidants and food dyes.

References

Abe, K., Takizawa, H., Kimura, S., & Hirano, M. (2004). Characteristics of chlorophyll formation of the aerial microalga *Coelastrella striolata* var. *multistriata* and its application for environmental biomonitoring. *Journal of Bioscience and Bioengineering, 98*, 34–39.

Baker, R. T. M. (2002). Canthaxanthin in aquafeed applications: is there any risk? *Trends in Food Science and Technology, 12*, 240–243.

Campo, J. A. D., Moreno, J., Rodríguez, H., Vergas, A., Rivas, J., & Guerrero, M. G. (2000). Carotenoid content of chlorophycean microalgae: factors determining lutein accumulation in *Muriellopsis* sp.. *Journal of Biotechnology, 76*, 51–59.

Clark, T. H., Faustman, C., Chan, W. K. M., Furr, H. C., & Riesen, J. W. (1999). Canthaxanthin as an antioxidant in a liposome model system and in minced patties from rainbow trout. *Journal of Food Science, 64*, 982–986.

Endo, Y., Usuki, R., & Kaneda, T. (1984). Prooxidant activities of chlorophylls and their decomposition products on the photooxidation

of methyl linoleate. *Journal of the American Oil Chemists Society, 68*, 653–658.

Goulson, M. J., & Warthesen, J. J. (1999). Stability and antioxidant activity of beta carotene in conventional and high oleic canola oil. *Journal of food science, 64*, 996–999.

Grünewald, K., Hirschberg, J., & Hagen, C. (2001). Ketocarotenoid biosynthesis outside of plastids in the unicellular green alga *Haematococcus pluvialis*. *Journal of Biological Chemistry, 276*, 6023–6029.

Halliwell, B. (1996). Cellular stress and protection mechanisms. *Biochemistry Society Transactions, 24*, 1023–1027.

Japanese Industrial Standard. (1998). *Testing methods for industrial wastewater JIS K 0102: 1998(J)* (pp. 160, 167). Tokyo: Japanese Standards Association (in Japanese).

Jung, M. Y., & Min, D. B. (1991). Effect of quenching mechanisms of carotenoids on the photosensitized oxidation of soybean oil. *Journal of the American Oil Chemists Society, 68*, 653–658.

Jyonouchi, H., Sun, S., & Gross, M. (1995). Effect of carotenoids on in vitro immunoglobulin production by human peripheral blood mononuclear cells: astaxanthin, a carotenoid without vitamin A activity, enhances in vitro immunoglobulin production in response to a T-dependent stimulant and antigen. *Nutrition and Cancer, 23*, 171–183.

Kiritsakis, A. K., & Dugan, L. R. (1985). Studies in photooxidation of olive oil. *Journal of the American Oil Chemists Society, 62*, 892–896.

Krinsky, N. I. (1992). Mechanism of action of biological systems. *Proceedings of the Society for Experimental Biology and Medicine, 200*, 248–254.

Krinsky, N. I. (1993). Actions of carotenoids in biological systems. *Annual Review of Nutrition, 13*, 561–587.

Lorenz, R. T., & Cysewski, G. R. (2000). Commercial potential for Haematococcus microalgae as a natural source of astaxanthin. *Trends in Biotechnology, 18*, 160–167.

Mackinney, G. (1941). Absorption of light by chlorophyll solution. *Journal of Biological Chemistry, 140*, 315–322.

Miki, W. (1991). Biological functions and activities of animal carotenoids. *Pure and Applied Chemistry, 63*, 141–1465.

Orosa, M., Torres, E., Fidalgo, P., & Abalde, J. (2000). Production and analysis of secondary carotenoids in green algae. *Journal of Applied Phycology, 12*, 553–556.

Palozza, P., Luberto, C., Ricci, P., Sgarlata, E., Calviello, G., & Bartoli, G. M. (1996). Effect of β-carotene and canthaxanthin on *tert*-butyl hydroperoxide-induced lipid peroxidation in murine normal and tumor thymocytes. *Archives of Biochemistry and Biophysics, 325*, 145–151.

Pánek, J., Fantová, L., Trojáková, L., Réblová, Z., & Pokorný, J. (2001). Effectiveness of natural antioxidants in sunflower oil. *Special Publication – Royal Society of Chemistry, 269*, 371–374.

Pelah, D., Sintov, A., & Cohen, E. (2004). The effect of salt tress on the production of canthaxanthin and astaxanthin by *Chlorella zofingiensis* grown under limited light intensity. *World Journal of Microbiology & Biotechnology, 20*, 483–486.

Psomiadou, E., & Tsimidou, M. (2002). Stability of virgin olive oil. 2. Photo-oxidation studies. *Journal of Agricultural and Food Chemistry, 50*, 722–727.

Rahmani, M., & Csallany, A. S. (1998). Role of minor constituents in the photooxidation of virgin olive oil. *Journal of the American Oil Chemists Society, 75*, 837–843.

Rawls, H. R., & Van Santen, P. J. (1970). Possible role for singlet oxygen in the initiation of fatty acid autoxidation. *Journal of the American Oil Chemists Society, 47*, 121–125.

Rengel, D., Díez-Navajas, A., Serna-Rico, A., Veiga, P., Muga, A., & Milicua, J. C. G. (2000). Exogenously incorporated ketocarotenoids in large unilamella vesicles. Protective activity against peroxidation. *Biochimica et Biophysica Acta, 1463*, 179–187.

Sies, H. (1985). Oxidative stress: Introductory remarks. In H. Sies (Ed.), *Oxidative stress* (pp. 1–8). London, UK: Academic Press.

Surai, A. P., Surai, P. F., Steinberg, W., Wakeman, W. G., Speake, B. K., & Sparks, N. H. C. (2003). Effect of canthaxanthin content of the maternal diet on the antioxidant system of the developing chick. *British Poultry Science, 44*, 612–619.

Tam, N. F., & Wong, Y. S. (1989). Wastewater nutrient removal by *Chlorella pyrenoidosa* and *Scenedesmus* sp. *Environmental Pollution, 58*, 19–34.

Terao, J., Hirota, Y., Kawakatsu, M., & Matsushita, S. (1981). Structural analysis of hydroperoxides formed by oxidation of phosphatidylcholine with singlet oxygen. *Lipids, 16*, 427–432.

Terao, J., & Matsushita, S. (1977). Productions formed by photosensitized oxidation of unsaturated fatty acid esters. *Journal of the American Oil Chemists Society, 54*, 234–238.

Zhang, D.-H., & Lee, Y.-K. (2001). Two-step process for ketocarotenoid production by a green alga, *Chlorococcum* sp. Strain MA-1. *Applied Microbiology and Biotechnology, 55*, 537–540.

2. ナノ薄膜

29P 048

Fabrication of Organic Thin Films and Particles using Supercritical Fluids

Graduate School of Electrical and Electronic Engineering, Kogakuin University

°Tetsuo SAKAMAOTO, Itaru YAMAGUCHI and Kenji OISHI

ct13087@ns.kogakuin.ac.jp

1. Introduction

A novel process to make organic thin films was developed. Supercritical fluid, which is a state above critical point defined with pressure and temperature, was used as a solvent to deliver materials to substrate surfaces. In this paper, instrumentation and initial results of thin film fabrication will be reported.

2. Apparatus

An instrument for the purpose was constructed in laboratory. Figure1 shows a schematic illustration of the apparatus. It consists of a pump for pressurize liquefied CO_2, a heater and a backpressure regulator. Supercritical CO_2 was obtained by adjusting its pressure and temperature above the critical point.

Organic material is located in the first cell-1. Dissolved material is transferred through the stainless tubing into cell-2, where the organic material is deposited onto a substrate.

3. Experimental

Typical organic materials (anthracene and Alq_3) were used to examine the deposition. Each of the materials was fed into cell-1, then supercritical CO_2 was supplied. An ITO glass substrate was located in cell-2. Deposited materials were observed with an optical microscope.

4. Results and Discussion

Figure2 shows optical microscope images of deposited anthracene. The morphology depends on both supercritical pressure and temperature. When the cell-1 temperature was gradually decreased, microcrystallines of anthracene were obtained as shown in Fig.2a. The other side, the temperature was kept constant, thin film deposition was observed.

The other material, Alq_3 exhibits different behavior. It preferred rather high temperature (100°C) and pressure (20 MPa) for thin film deposition.

5. Conclusion

It was found that both anthracene and Alq_3 can be dissolved in supercritical CO_2, and they are deposited onto substrates in supercritical CO_2 with different temperature.

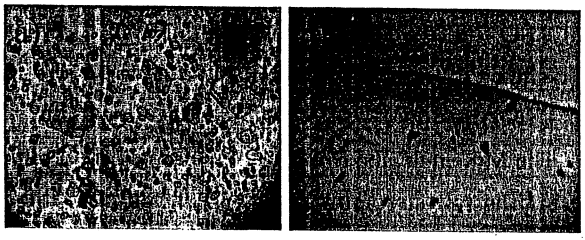

Fig.2 Optical microscope images of a) anthracene crystals at 12.5 MPa, 70°C, and b) thin films deposited on ITO glass plate in supercritical CO_2 at 12.5 MPa, 30°C.

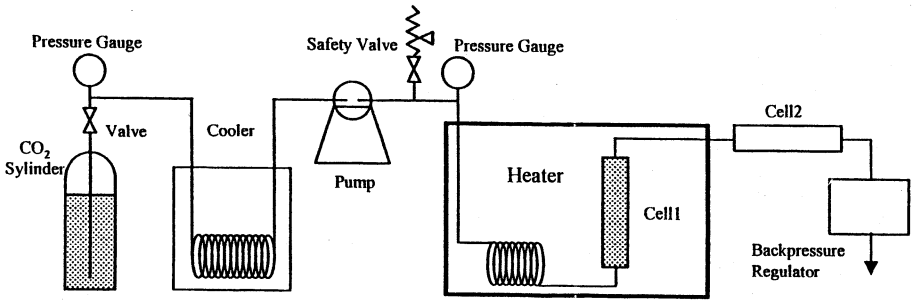

Fig.1 Supercritical fluid deposition apparatus.

29P 053

Organic Thin-Film Fabrication by means of Electrospray Deposition

○Itaru YAMAGUCHI, Yuuki WATANABE and Tetsuo SAKAMOTO
Graduate School of Electrical and Electronic Engineering, Kogakuin University
cm08035@ns.kogakuin.ac.jp

Organic electroluminescence device have been developed by many researchers because of its features compared with conventional inorganic devices. There are two kinds of organic materials used for organic EL: low molecular weight and polymer materials. In the latter cases, wet -process such as spin-coating or printing methods is employed. However, it is very difficult to make multilayer films consisting of different materials.

In the present study, electro-spray method is applied to thin film fabrication from organic solutions. This method is aiming at a dry-process while it uses a solution as a material.

The advantages of the electro-spray method are the following three points: i) since it is a dry-process, multilayer thin films can be obtained, ii) there is less thermal damage polymer material in fabrication, iii) patterning can be performed with a shadow-mask like vacuum deposition.

Figure 1 shows a schematic diagram of the apparatus. It consists of a stainless-steel tube with a sharpened tip, a counter electrode where a substrate is fixed. Distance between the tip and the counter electrode can be changed using a rail. The spray current can be monitored with an digital electrometer connected to the counter electrode. A high-voltage (5 kVmax) is applied to the stainless-steel. Solution containing materials is fed through a PTFE tube from a syringe pump. The flow rate of the syringe pump is adjusted around 0.1mL/h steps.

Figure 2 shows an optical micrograph of the deposit with this method. In this experiment Alq_3 was used as a material. It was dissolved in acetone at 0.40 wt.%. The distance between the tip and the counter electrode was 30 mm, while the tip voltage was 4.00 kV. It was seen that organic EL material can be sprayed and deposit by the electro-spray method.

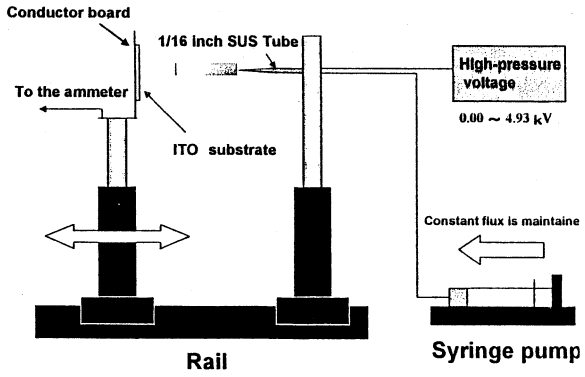

Fig.1 schematic diagram of the experiment

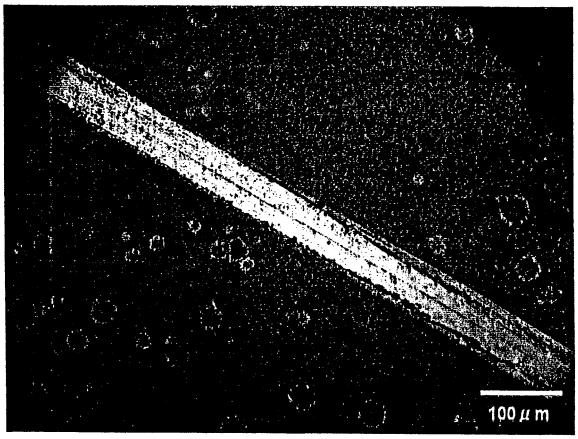

Fig.2 deposited for Alq_3 by the ESD method

G Model
EA143201-7

Electrochimica Acta xxx (2009) xxx–xxx

Contents lists available at ScienceDirect

Electrochimica Acta

journal homepage: www.elsevier.com/locate/electacta

Effect of noble metal catalyst species on the morphology of macroporous silicon formed by metal-assisted chemical etching

Hidetaka Asoh, Fusao Arai, Sachiko Ono*,[1]

Department of Applied Chemistry, Kogakuin University, 2665-1 Nakano, Hachioji, Tokyo 192-0015, Japan

ARTICLE INFO

Article history:
Received 1 December 2008
Accepted 16 January 2009
Available online xxx

Keywords:
Silicon
Metal-assisted chemical etching
Noble metal
Colloidal crystal templating

ABSTRACT

Macroporous silicon with ordered pore intervals was fabricated by the site-selective chemical etching of a Si substrate using patterned noble-metal thin films as a catalyst. The morphology of the etched silicon surface and the etching rate was affected by the shape of deposits and metal catalyst species such as Pt–Pd, Au, and Pt. The etching rate increased in the following order: Au < Pt ≤ Pt–Pd. The pores of macroporous silicon prepared by using Pt–Pd catalyst were conical in shape because of the chemical dissolution of the surface of the macropores. On the other hand, by using Au catalyst, relatively straight pores with uniform diameter were formed in the direction of pore depth. The morphology of macroporous silicon was assumed to be affected by the difference in the shape of metal catalysts and the diffusion behaviour of injected positive holes at the silicon/metal interface.

1. Introduction

Three-dimensional silicon microstructures such as pillars, tubes, and macropores are fabricated by electrochemical etching in hydrofluoric acid (HF). This is a promising technique for the micromachining of silicon [1–3]. Among three-dimensional silicon microstructures, silicon with a regular porous structure of the order of submicrons to nanometres, which is normally fabricated by electrochemical etching, has been studied intensively from the viewpoint of both basic research and commercial applications over the past few decades [4]. A novel technique for fabricating porous silicon without applying an external bias, so-called metal-assisted chemical etching, was proposed by Li and Bohn in 2000 [5]. According to their report, a porous silicon layer can be formed easily and efficiently by immersing silicon wafers coated with a noble metal (i.e. Au, Pt, or Au–Pd) in HF mixed with hydrogen peroxide (H_2O_2) solution. A mechanism involving a localized electrochemical process has been proposed to explain the mechanism of metal-assisted chemical etching as follows [5]:

Cathode reaction (at noble metal surface as a local cathode):

$$H_2O_2 + 2H^+ \rightarrow 2H_2O + 2h^+,$$

$$2H^+ \rightarrow H_2\uparrow + 2h^+.$$

Anode reaction (at silicon surface):

$$Si + 4h^+ + 4HF \rightarrow SiF_4 + 4H^+,$$

$$SiF_4 + 2HF \rightarrow H_2SiF_6.$$

Overall reaction:

$$Si + H_2O_2 + 6HF \rightarrow 2H_2O + H_2SiF_6 + H_2\uparrow.$$

In other words, when oxidants (H_2O_2) are reduced on the surfaces of noble metal catalysts, positive holes (h^+) are generated. After the removal of electrons from metal particles, the potential of the metal shifts towards a positive value to a level enabling the injection of h^+ into the silicon substrate. Finally, anodic oxidation and the dissolution of silicon take place in the chemical etchant containing HF.

Various types of silicon microstructures such as deep straight nanopores and helical silicon nanopores have been prepared by metal-assisted chemical etching [6–9]. These microstructures are expected to be used for improving the light-emitting properties and conversion efficiency of solar cells. The formation of porous silicon by metal-assisted chemical etching can be proceed in the presence of not only Au, Pt, and Au–Pd particles but also other noble metals such as Ag and Pd.

Recently, we have reported the fabrication of ordered silicon microstructures such as silicon convex arrays and silicon nanopore patterns with regular periodicity of the order of micrometres by combining colloidal crystal templating and site-selective chemical etching using patterned noble-metal thin films as catalysts [10–12]. In addition, by using a shape-controlled Pt–Pd thin film as a cata-

* Corresponding author. Tel.: +81 3 3340 2732; fax: +81 3 3340 2732.
E-mail address: sachiono@cc.kogakuin.ac.jp (S. Ono).
[1] ISE member.

0013-4686/$ – see front matter © 2009 Published by Elsevier Ltd.
doi:10.1016/j.electacta.2009.01.050

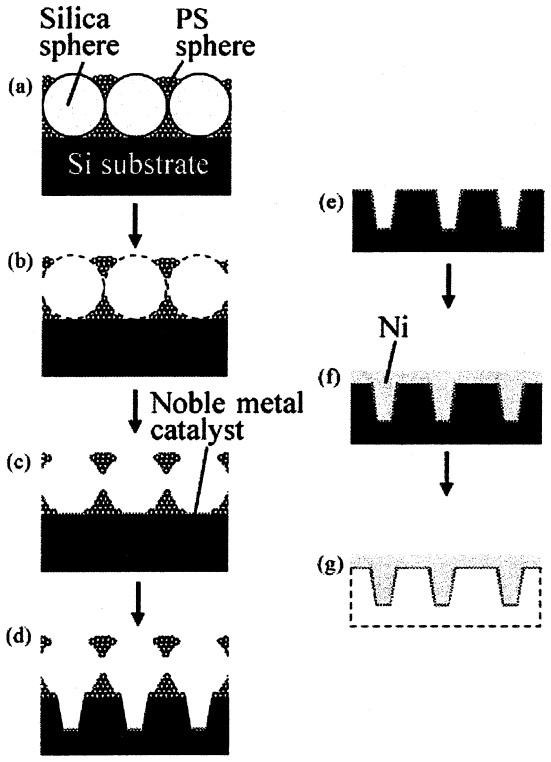

Fig. 1. Schematic model of fabrication of silicon macropore arrays: (a) formation of composite colloidal crystals on silicon substrate, (b) removal of silica sphere, (c) formation of metal catalyst layer, (d) chemical etching of silicon, (e) removal of PS honeycomb mask, (f) electrodeposition of nickel layer, and (g) removal of silicon by immersion of substrate in TMAH.

lyst, we have fabricated silicon microwells containing Pt–Pd thin films [13]. We carry out a preliminary study to examine the effect of noble metal catalyst species on the morphology of macroporous silicon prepared by metal-assisted chemical etching. We mainly focus on the correlation between the morphology of etched silicon microstructures, etching rate, and catalyst species.

2. Experimental

The principle of pattern transfer, which is similar to that described in our previous study [13], is schematically shown in Fig. 1. Silicon substrates were precleaned in 1 wt% HF to remove organic contaminants and native oxides. A mixed suspension consisting of equal volumes of a 0.2-wt% suspension of polystyrene (PS) nanospheres with a diameter of 200 nm (Polysciences, Inc.) and a 0.5-wt% suspension of silica microspheres with diameter of 3 μm (Bangs Laboratories, Inc.) was dropped on the substrates. The suspension on the substrates was dried in air for more than one day, during which the mixture containing spheres of two different diameters self-assembled into a close-packed structure due to the capillary forces. After the complete evaporation of the solvent, the silicon substrates with binary colloidal crystals formed from the spheres were heated at 100 °C for 1 h to combine the adjacent PS nanospheres [Fig. 1(a)]. After heating, the silica spheres, which were used as a template, were selectively removed by immersing the specimens in 10 wt% HF for 10 min [Fig. 1(b)].

Metal thin films were deposited on the silicon substrates by ion sputtering (Hitachi E-1010) using a PS honeycomb mask composed of densely packed PS nanospheres. The sputtering was carried out at a discharge current of 15 mA in a vacuum with the pressure below 10 Pa [Fig. 1(c)]. Pt–Pd (80% Pt and 20% Pd), Au, and Pt targets were used as sputtering targets. The deposition rates of Pt–Pd, Au, and Pt were 6, 10, and 6 nm min^{-1}, respectively. The morphology and thickness of the deposited metal layers were examined by atomic force microscopy (AFM, Digital Instrument NanoScope IIIa). After

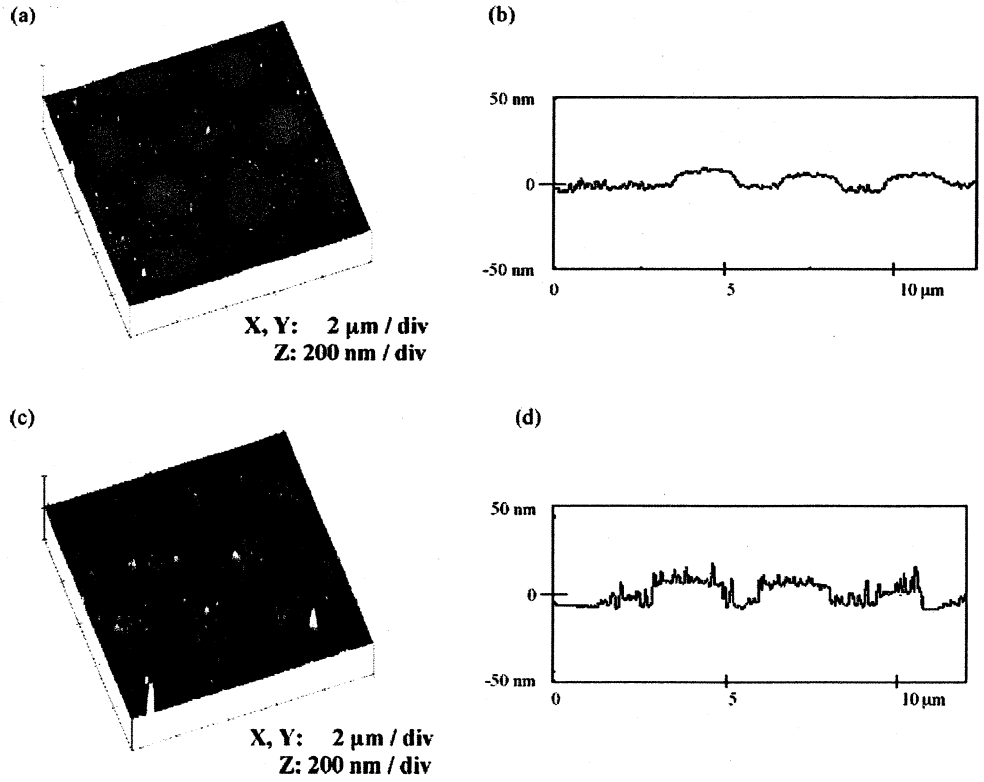

Fig. 2. AFM tapping-mode images of silicon surface after ion sputtering for (a, b) 5 min using Pt–Pd and (c, d) 3 min using Au. (b, d) Typical line scan images of cross-section of each specimen.

Please cite this article in press as: H. Asoh, et al., Effect of noble metal catalyst species on the morphology of macroporous silicon formed by metal-assisted chemical etching, Electrochim. Acta (2009), doi:10.1016/j.electacta.2009.01.050

sputtering, the specimens with locally deposited metal films were etched in a mixed solution of 5 mol dm^{-3} HF and 1 mol dm^{-3} H_2O_2 at room temperature [Fig. 1(d)]. Finally, the PS honeycomb mask was removed by immersing the specimens in 97% toluene [Fig. 1(e)].

To examine the morphology of the silicon macropores in the direction of pore depth, a metal replica was prepared by metal plating. After coating the surface of silicon microstructures with metal catalyst layers by ion sputtering, nickel layers were electrodeposited using conventional nickel plating solution [Fig. 1(f)]. Finally, the silicon substrates were selectively removed by immersing the specimens in tetramethylammonium hydroxide (TMAH) [Fig. 1(g)]. The ordered geometric pattern formed on the silicon substrates was evaluated by scanning electron microscopy (SEM, Hitachi S-4200) and focused ion beam microscopy (FIB, Hitachi FB-2100).

3. Results and discussion

When ion sputtering was carried out using the PS honeycomb mask, isolated circular metal thin films with a diameter of approximately 1.6 μm were deposited in the interspaces of the PS mask [13]. Fig. 2(a) shows a typical AFM image of the Pt–Pd thin film arrays deposited on a silicon substrate. From the cross-section analysis of the AFM image, the maximum thickness of the Pt–Pd layer deposited by using the PS honeycomb mask after a sputtering time of 5 min was estimated to be 10–15 nm. The thickness of the deposited layer was less than half the thickness estimated from the sputtering rate of Pt–Pd. The decrease in the deposition thickness is assumed to be caused by the use of the PS honeycomb with a thickness of approximately 2 μm during sputtering.

In addition, from a high-magnification AFM image of the same specimen, it was confirmed that the isolated circular Pt–Pd thin films were composed of clusters of Pt–Pd nanoparticles with a size range of 5–15 nm, as shown in Fig. 3(a). Ion sputtering, which is generally used for coating nonconducting materials with a metal layer for SEM observations, was used for depositing Pt–Pd in order to form a smoothly shaped metal thin film and to prevent the formation of a granular coating.

On the other hand, from the cross-section analysis of the AFM image of the deposited Au layer, the layer thickness was estimated to be 10–25 nm for a sputtering time of 3 min, as shown in Fig. 2(d). The isolated Au circular thin films were also composed of clusters of Au nanoparticles with a size range of 10–30 nm, as shown in Fig. 3(b). As compared to the isolated circular Pt–Pd thin films, the Au nanoparticles in the isolated circular Au thin films varied considerably in size, and the surface of the deposit was markedly uneven with granular particles.

After the sputtering of each metal catalyst, the specimens were immersed in a mixed solution of 5 mol dm^{-3} HF and 1 mol dm^{-3} H_2O_2 at room temperature. Fig. 4(a) shows an SEM image of the silicon surface after chemical etching for 1 min using Pt–Pd catalyst. Metal-assisted chemical etching was carried out without removing the PS honeycomb mask. The central part of the silicon substrate surrounded by the wall of the PS honeycomb mask sagged during chemical etching, yielding an ordered array of macropores with uniform diameter. The periodicity of the pores, which was basically determined by the diameter of the silica spheres, was approximately 3 μm. These results indicate that chemical etching proceeded only in the Pt–Pd-coated area on the silicon surface.

From the tilted view of the specimen shown in Fig. 4(b), it was confirmed that the shape of the pores was conical, and the pore depth was approximately 2 μm. The diameter of the silicon macropores was approximately 3 μm due to the chemical dissolution of the horizontal plane at the outermost surface. When the contact of two adjacent pores was accomplished, the expansion of pore diameter was stopped. Finally, pores with ideal hexagonal openings were obtained. It should be noted that the Pt–Pd catalyst remained in the

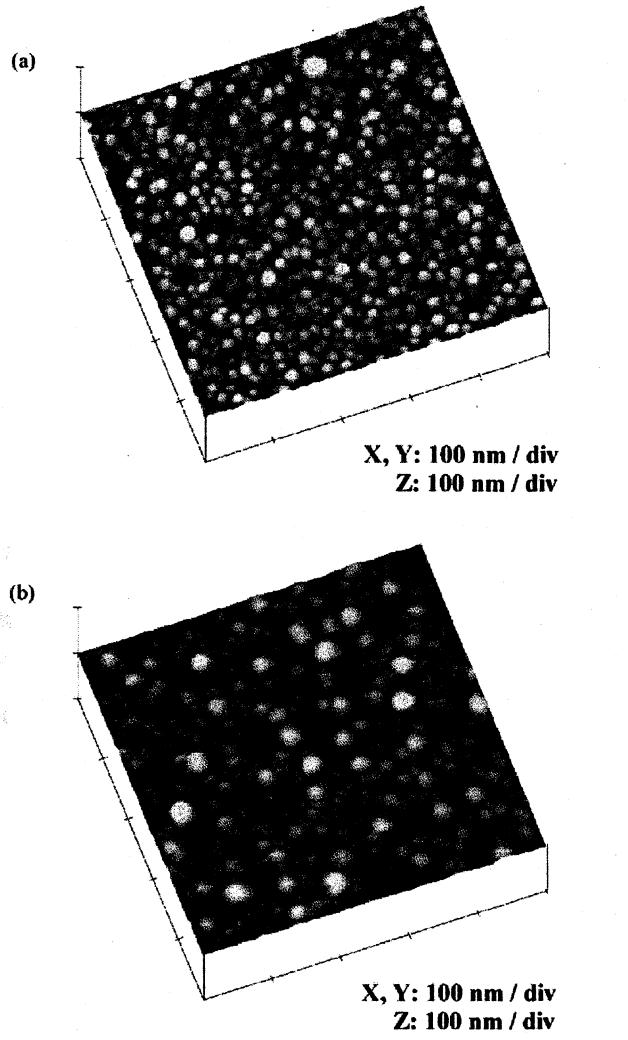

Fig. 3. High-magnification AFM images of (a) Pt–Pd and (b) Au films sputtered on Si substrate. Scan area was 500 nm^2.

form of circular thin continuous films at the bottom of each pore after the etching process was stopped.

To investigate the effect of etching time on the resultant patterns, the etching time was increased from 1 to 2 min. Although the diameter of each silicon macropore remained unchanged with the increase in the etching time, as shown in Fig. 4(c), the depth of the pores increased clearly with the increasing etching time, as shown in Fig. 4(d). However, it was difficult to obtain macropores with a high aspect ratio because the pore walls crumbled gradually due to chemical dissolution. In this case, injected positive h^+ were assumed to have diffused into silicon bulk, resulting in the oxidization of silicon at locations away from the metal-coated silicon surface and the excessive widening of pores at the outermost silicon surface. A similar phenomenon observed during metal-assisted chemical etching using Ag catalyst was reported by Chartier et al. in 2008 [14].

To examine the effect of the catalyst species on the morphology of the etched silicon structure, chemical etching was also carried out using patterned Au thin films. Fig. 5 shows the surfaces and cross-sectional images of silicon after chemical etching using the patterned Au thin films. Before carrying out FIB processing to observe the cross-section of the pores, tungsten was deposited on surface of the specimens to prevent damage to the etched silicon surface by gallium ion beam. Although metal-assisted chemical etching was carried out using Au catalyst under the same etch-

Please cite this article in press as: H. Asoh, et al., Effect of noble metal catalyst species on the morphology of macroporous silicon formed by metal-assisted chemical etching, Electrochim. Acta (2009), doi:10.1016/j.electacta.2009.01.050

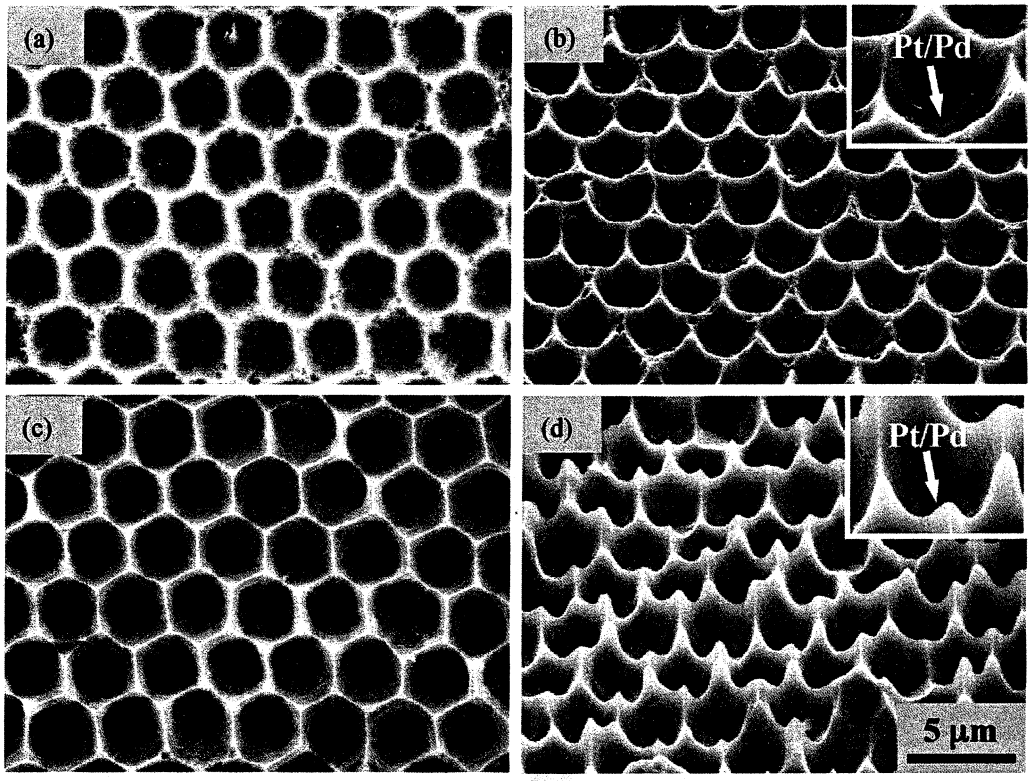

Fig. 4. SEM images of Pt–Pd-coated silicon after chemical etching in HF/H_2O_2 for (a, b) 1 min and (c, d) 2 min. In the case of (b, d), the specimen was observed at an angle of 45° from the surface. The periodicity of the PS honeycomb mask was 3 μm.

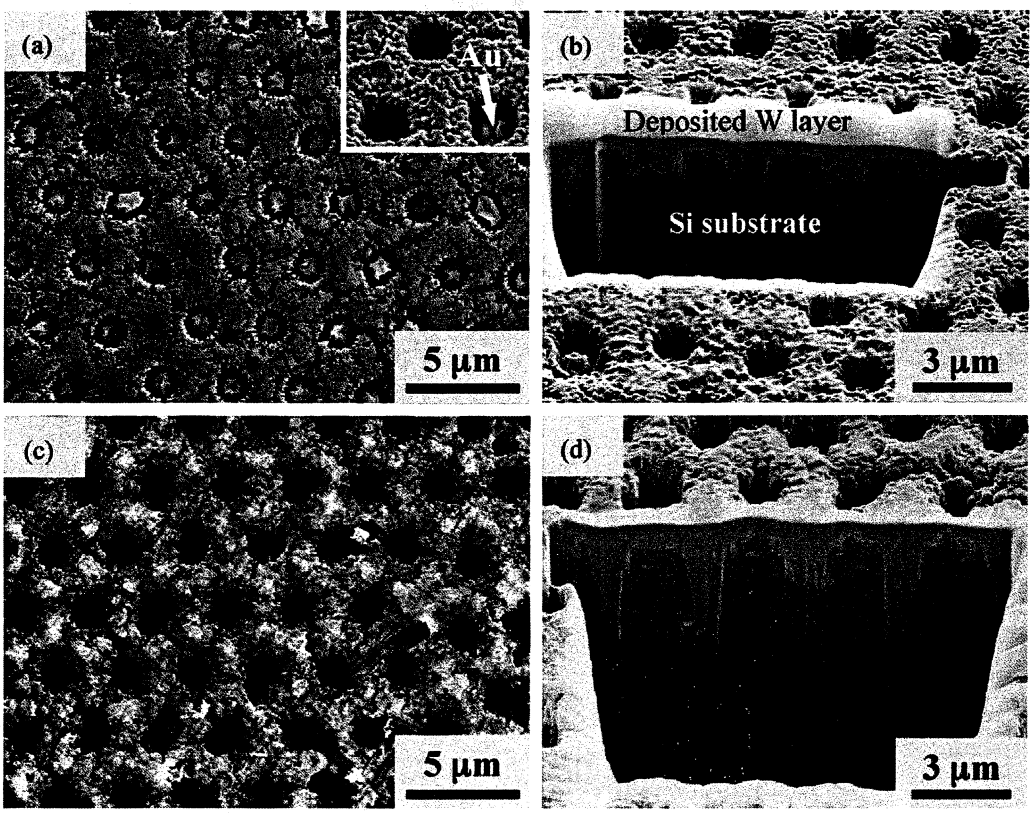

Fig. 5. SEM images of Au-coated silicon after chemical etching in HF/H_2O_2 for (a, b) 1 min and (c, d) 5 min. (a, c) Top view and (b, d) cross-sectional view of silicon prepared by FIB. The periodicity of the PS honeycomb mask was 3 μm.

Please cite this article in press as: H. Asoh, et al., Effect of noble metal catalyst species on the morphology of macroporous silicon formed by metal-assisted chemical etching, Electrochim. Acta (2009), doi:10.1016/j.electacta.2009.01.050

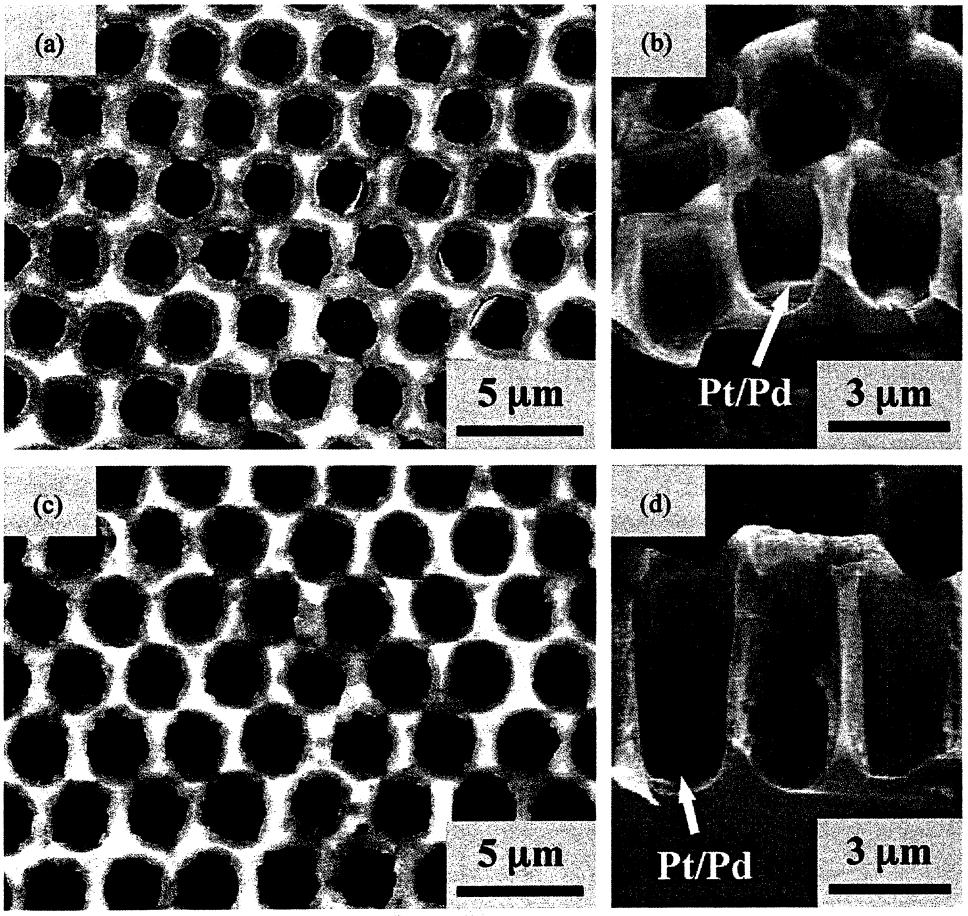

Fig. 6. SEM images of Pt–Pd-coated silicon after chemical etching in HF/H_2O_2 for (a, b) 1 min and (c, d) 2 min. (a, c) Top view and (b, d) cross-sectional view of Pt–Pd-coated silicon. Chemical etching was carried out after removing the PS honeycomb mask.

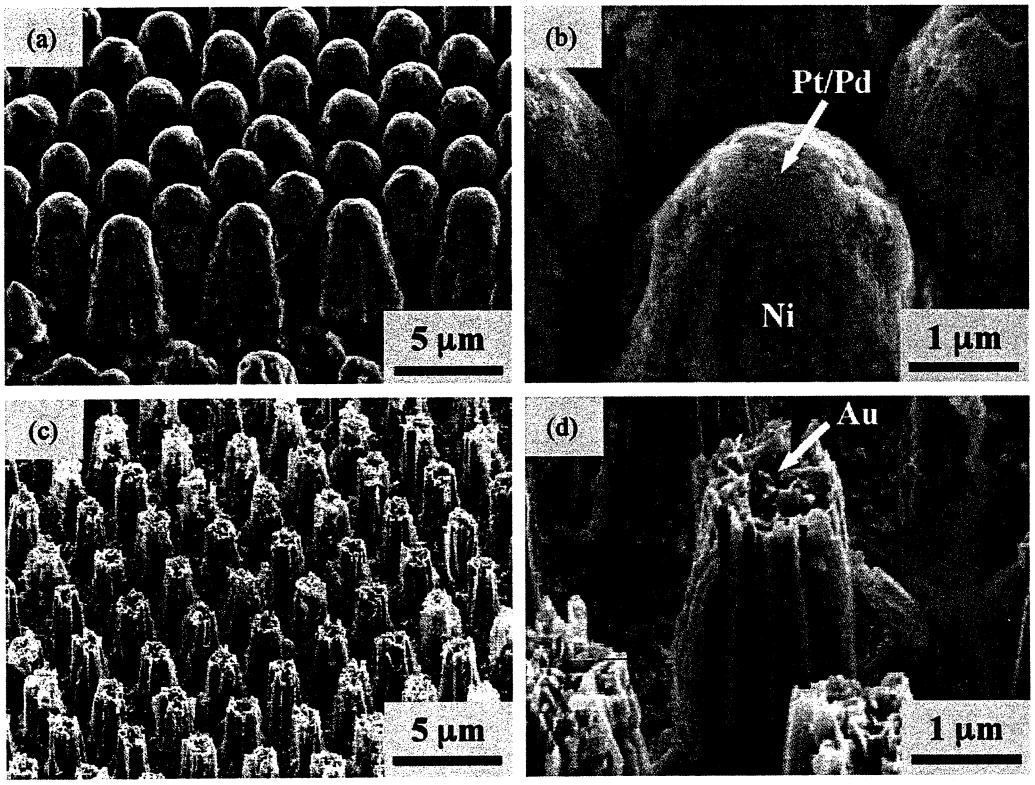

Fig. 7. SEM images of nickel replica of etched silicon: (a, b) Pt–Pd-coated silicon etched for 2 min and (c, d) Au-coated silicon etched for 3 min. (b, d) High-magnification images of each specimen. SEM observation was carried out at an angle of 45° from the surface.

Please cite this article in press as: H. Asoh, et al., Effect of noble metal catalyst species on the morphology of macroporous silicon formed by metal-assisted chemical etching, Electrochim. Acta (2009), doi:10.1016/j.electacta.2009.01.050

ing conditions indicated in Fig. 4, the morphology of the resultant porous structure was significantly different from that of the silicon macropores formed using Pt–Pd catalyst.

When the etching time was equal to 1 min, the localized dissolution of silicon was observed only on the silicon surface covered with Au thin films [Figs. 5(a) and (b)]. After carrying out metal-assisted chemical etching for 5 min, the pore depth increased up to 5 μm. The etching rate was estimated to be approximately 1 μm min^{-1}. One of the notable features of metal-assisted chemical etching using Au catalyst is the suppression of pore widening at the outermost surface of silicon. The diameter of the pores hardly increased during chemical etching. The dissolution of silicon was accelerated locally at the silicon/metal interface in the direction of the pore depth, resulting in the formation of macropores with a relatively high aspect ratio.

The following factors are considered as the reasons behind the suppression of pore widening. (I) As discussed previously, the isolated Au circular thin films are composed of clusters of Au nanoparticles with a relatively large size. Thus, the configuration of metal catalysts affects the morphology of pores due to the catalytic action of the catalysts. (II) The diffusion area of h^+ during pore formation in the presence of Au catalyst is narrower than that of Pt–Pd catalyst. The injection/diffusion behaviour of h^+ is assumed to be affected by a Schottky barrier formed at the silicon/metal interface and the work function of each noble metal.

Fig. 6 shows the SEM images of Pt–Pd-coated silicon after chemical etching in HF/H_2O_2. In this case, chemical etching was carried out after removing the PS honeycomb mask. A comparison with Fig. 4 showed that despite employing the same etching conditions, the preferential dissolution of silicon in this case remarkably proceeded in the direction of pore depth. It was also apparent that pore widening at the silicon surface was effectively suppressed. After metal-assisted chemical etching for 2 min, the pore depth increased up to 7 μm. The etching rate, which was estimated to be approximately 3.5 μm min^{-1}, was ~2 times faster than that of etching carried out using the PS mask and Pt–Pd catalyst, as shown in Fig. 4, and ~3.5 times faster than that of Au catalyst, as shown in Fig. 5. When metal catalysts were located for isolation on the silicon substrate and the PS honeycomb mask was not used, the diffusion of hydrogen produced by the reduction of protons and the dissolution of silicon probably proceeded effectively. As a result, straight macropores were formed within a relatively short etching time, and excessive pore widening at the outermost surface of macroporous silicon was prevented.

To evaluate the morphology of the porous structure in the direction of pore depth, a nickel replica was prepared by metal plating using obtained macroporous silicon as a template. From the SEM image of the obtained nickel replica shown in Fig. 7, it was confirmed that the height of nickel rods, that is, the depth of the pores was almost uniform in both specimens. These images of the nickel replica were basically compatible with the SEM images of macroporous silicon. However, the shape of the side surface of the nickel rods was found to differ in the case of each specimen. In the case of Pt–Pd catalyst, the side surface of nickel rods, that is, the side walls of the silicon macropores were relatively smooth. It should be noted that the obtained nickel rods had Pt–Pd thin films at their tips. This result also revealed that metal-assisted chemical etching proceeded only in the Pt–Pd-coated area on the silicon surface. On the other hand, in the case of Au catalyst, a number of channels were observed on the side surface of the nickel rods. Such structure is thought to be reflected in the traces of Au nanoparticles divided from circular thin film. In other words, the outer surface of silicon macropores was composed of the cluster of nanopores with sizes in the range of 50–100 nm. Suppression of pore widening during metal-assisted chemical etching using Au catalyst may be caused by the specific catalytic action of Au nanoparticles.

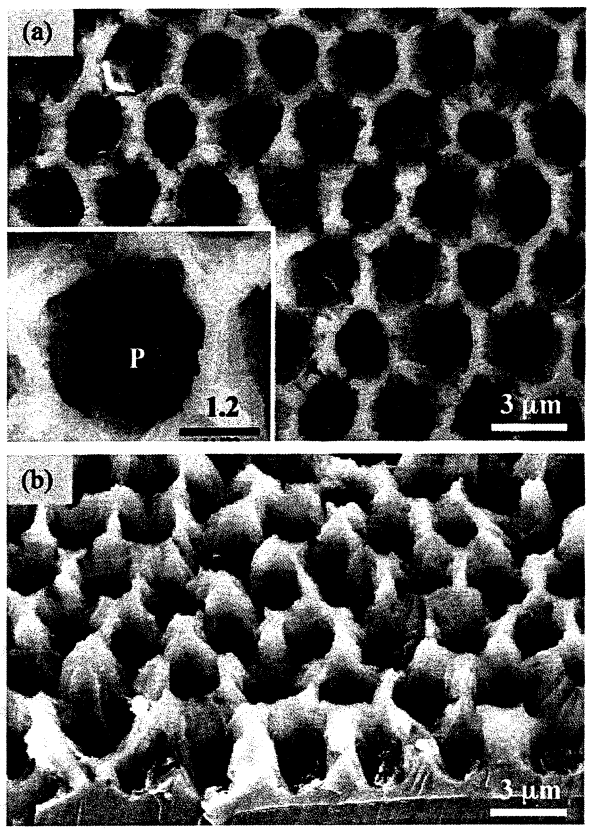

Fig. 8. SEM images of Pt-coated silicon after chemical etching in HF/H_2O_2 for 1 min: (a) top view and (b) cross-sectional view. Chemical etching was carried out after removing the PS honeycomb mask. Inset shows a high-magnification top view of the same specimen.

On the basis of the present method, ordered macropore arrays could be formed independent of noble metal catalyst species. Fig. 8 shows the silicon macropore arrays formed by metal-assisted chemical etching using Pt single catalyst. Metal-assisted chemical etching was carried out after removing the PS honeycomb mask. The etching behaviour when Pt catalyst was used was basically similar to that in the case of Pt–Pd catalyst. From the tilted view of the

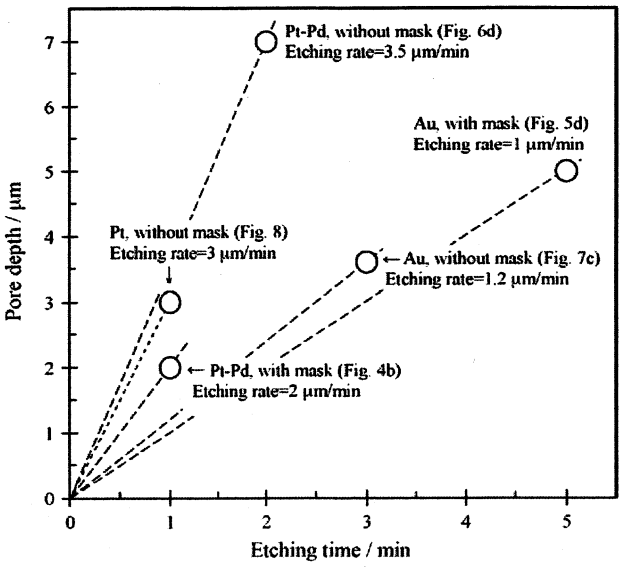

Fig. 9. Relationship between depth of pores formed by metal-assisted chemical etching and corresponding etching time.

Please cite this article in press as: H. Asoh, et al., Effect of noble metal catalyst species on the morphology of macroporous silicon formed by metal-assisted chemical etching, Electrochim. Acta (2009), doi:10.1016/j.electacta.2009.01.050

specimen shown in Fig. 8(b), the pore depth after metal-assisted chemical etching for 1 min was estimated to be approximately 3 μm. A detailed study is under way for the clarification of the effect of Pd single catalyst.

The relationship between the pore depth and the etching time is summarized in Fig. 9. In addition to the results for the metal-assisted chemical etching carried out using the PS mask, the results obtained without using the PS mask are also plotted for each metal species. In the present study, etching rate increases in the following order: Au < Pt ≤ Pt–Pd. If the metal catalyst species are the same, the etching rate without using the mask is faster than that obtained using the mask. Further research on metal-assisted chemical etching using metal thin films as a catalyst would clarify the relationship between the mechanism for controlling the morphology of the resultant pattern and the etching conditions, such as the composition and concentration of an etchant, substrate parameters, resistivity, and doping density.

4. Conclusion

We described the differences in the catalytic action of Pt–Pd (or Pt) and Au catalysts on the morphology of etched silicon microstructures. In the case of Pt–Pd, although etching rate was faster than that of Au, there was excessive pore widening at the outermost surface due to the chemical dissolution of the horizontal plane. On the other hand, straight pores with relatively small diameter were obtained by using Au catalyst under the same etching conditions. Thus, the dissolution of silicon by using Au thin films as a catalyst was locally accelerated at the silicon/metal interface in the direction of the pore depth. The morphology of the resultant porous structure was assumed to be affected by the difference in the shape of metal catalyst and the diffusion behaviour of injected positive holes at the silicon/metal interface.

The process presented in this paper is suitable for the large-scale production of ordered silicon macropores containing noble metal thin films, which cannot be fabricated by conventional lithographic techniques, because this patterning process involves colloidal crystal templating based on a relatively easy chemical treatment. On the basis of the present process, different types of noble metal films can also be embedded within a silicon substrate. Further research on the preparation of three-dimensional silicon microstructures by metal-assisted chemical etching would help us to determine their potential applications in optical devices, chemical sensors, and silicon-based biofunctional devices.

Acknowledgements

Part of this work was financially supported by a Grant-in-Aid for Scientific Research from the Japan Society for the Promotion of Science and the Light Metal Education Foundation of Japan. Thanks are also due to the "High-Tech Research Center" Project for Private Universities: matching fund subsidy from the Ministry of Education, Culture, Sports, Science and Technology.

References

[1] V. Lehmann, H. Föll, J. Electrochem. Soc. 137 (1990) 653.
[2] P. Kleimann, J. Linnros, R. Juhasz, Appl. Phys. Lett. 79 (2001) 1727.
[3] S. Matthias, F. Müller, C. Jamois, R.B. Wehrspohn, U. Gösele, Adv. Mater. 16 (2004) 2166.
[4] V. Lehmann, Electrochemistry of Silicon, Wiley–VCH, Weinheim, 2002.
[5] X. Li, P.W. Bohn, Appl. Phys. Lett. 77 (2000) 2572.
[6] S. Yae, Y. Kawamoto, H. Tanaka, N. Fukumuro, H. Matsuda, Electrochem. Commun. 5 (2003) 632.
[7] K. Tsujino, M. Matsumura, Adv. Mater. 17 (2005) 1045.
[8] K. Tsujino, M. Matsumura, Electrochem. Solid-State Lett. 8 (2005) C193.
[9] S. Yae, M. Abe, N. Fukumuro, H. Matsuda, Electrochemistry 76 (2008) 144.
[10] H. Asoh, F. Arai, S. Ono, Electrochem. Commun. 9 (2007) 535.
[11] H. Asoh, F. Arai, S. Ono, ECS Trans. 9 (2007) 535.
[12] F. Arai, H. Asoh, S. Ono, Electrochemistry 76 (2008) 187.
[13] H. Asoh, F. Arai, K. Uchibori, S. Ono, Appl. Phys. Express 1 (2008) 067003.
[14] C. Chartier, S. Bastide, C. Lévy-Clément, Electrochim. Acta 53 (2008) 5509.

Please cite this article in press as: H. Asoh, et al., Effect of noble metal catalyst species on the morphology of macroporous silicon formed by metal-assisted chemical etching, Electrochim. Acta (2009), doi:10.1016/j.electacta.2009.01.050

Corrosion Science xxx (2008) xxx–xxx

Contents lists available at ScienceDirect

Corrosion Science

journal homepage: www.elsevier.com/locate/corsci

Effects of electrolyte pH and temperature on dielectric properties of anodic oxide films formed on niobium

Sachiko Ono *, Ken Kuramochi [1], Hidetaka Asoh

Department of Applied Chemistry, Faculty of Engineering, Kogakuin University, 2665-1 Nakano, Hachioji, Tokyo 192-0015, Japan

ARTICLE INFO

Article history:
Received 5 September 2008
Accepted 24 November 2008
Available online xxxx

Keywords:
Niobium
Dielectric property
Anodic oxide film
High capacitance
Anion incorporation

ABSTRACT

The effects of electrolyte pH and temperature on the structure and properties of anodic oxide films formed on niobium in phosphoric acid solution with the addition of NH_4OH for pH adjustment have been investigated. The film thickness formed at the same voltage slightly increased with increasing pH and significantly increased with increasing electrolyte temperature. The capacitance of the film was independent of electrolyte pH in an acid region, while it notably increased with increasing pH in an alkaline region. The relative permittivity of the film changed 43.7–80.5 when the electrolyte pH was increased from 1.6 to 10. The incorporation depth and content of phosphorus in the film were markedly suppressed at pH 10, and nitrogen was found to penetrate into a depth of 70%. Furthermore, the apparent transport number of Nb^{5+} ion decreased from 0.26 to 0.02 by a pH increase from 1.6 to 10. The notable changes in structure and dielectric properties of the anodic niobia film formed in the alkaline region would primarily be caused by the different incorporation behavior of electrolyte species such as phosphorous and nitrogen.

1. Introduction

Anodic oxide film formed on niobium has generated considerable attention because of its use as an alternative to tantalum oxide in the capacitor industry. Niobium has similar physical and chemical properties to tantalum as both elements belong to the same group in the periodic table and is more abundant as producing reserves. Furthermore, the permittivity of niobium oxide is almost twice that of tantalum oxide. Other than the importance for a practical application in industry, clarification of the factors controlling the dielectric properties of anodic oxide film has essential importance for an understanding of the fundamental anodization mechanism. A number of studies concerning the structure and dielectric property of anodic barrier films on valve metals including niobium have been reported in relation to the incorporated electrolyte anions [1–6], as well as defect formation by the rapid oxide crystallization under an electric field [7–10]. The growth of anodic oxide films proceeds at both film/electrolyte interface by the migration of metal ions and film/substrate interface by the migration of oxygen ions giving a duplex structure [1,2,7,11,12]. The oxide layer formed at the former interface includes electrolyte anions, while a pure oxide layer is formed at the latter interface. The thickness ratios of each layer, respectively, represent transport numbers of metal ion and oxygen ion if the incorporated anions are immobile in the film. Phosphorus incorporation proceeds by inward migration into the films to approximately 50% depth under the electric field, which reduces the permittivity but increases the electric field strength, i.e., the sustainability of the electric field of the oxide layer [1,5]. The authors [5] reported the fundamental aspects of anodic oxide films formed on niobium with emphasis on the effects of anodizing conditions including current density, concentration, temperature and type of electrolyte on the anion incorporation that influenced to the dielectric properties.

For the further control of dielectric properties, the addition of nitrogen or silicon into the niobium substrate as alloying elements was reported [13,14] by inducing the elemental doping into the anodic niobia film, which results in low leakage current and high thermal stability, leading to enhanced reliability as a capacitor. However, in general, only limited acidic electrolytes such as phosphoric acid and sulfuric acid solutions are used; nevertheless, contaminating species into the anodic films could be a possible factor controlling the oxide properties.

In this study, the effects of electrolyte pH and temperature on the dielectric properties of anodic niobia films were investigated with focus on the oxide film structure and incorporated species by oxide characterization using electrochemical analysis, SEM and TEM observations, and determination of the depth profiles of constituent elements by glow discharge optical emission spectroscopy (GDOES).

* Corresponding author. Tel./fax: +81 42 628 4843.
E-mail address: sachiono@cc.kogakuin.ac.jp (S. Ono).
[1] Present address: Hitachi AIC Inc., 1065, Oaza-Kugeta, Ninomiyamachi, Haga-gun, Tochigi 321-4521, Japan.

0010-938X/$ - see front matter © 2008 Published by Elsevier Ltd.
doi:10.1016/j.corsci.2008.11.027

2. Experimental

Pure (99.93%) niobium foil was chemically etched in a 1:4 mixture of HF and HNO_3 solutions and anodized in 0.1 mol dm^{-3} phosphoric acid solution (pH 1.6) with and without the addition of NH_4OH for pH adjustment at a constant current density of 1 mA cm^{-2} until the voltage increased to 60 V. Subsequent voltage holding was carried out for 30 min. Adjustment of pH was performed at room temperature. The effect of electrolyte temperature was evaluated by changing the temperature in the range from 20 to 80 °C. For the estimation of relative film thickness, a voltage–time curve was measured during reanodization at 0.1 mA cm^{-2} of each anodized specimen in 100 g dm^{-3} diammonium adipate at 50 °C. The withstand voltage of the film was evaluated by measuring the initial voltage jump (V_j) at the reanodization from the extrapolation of the voltage–time curve to 0 min, where V_j is suggested to be proportional to the film thickness if the oxide property is the same. Details were described in the previous paper [4]. The leakage current was measured by applying 45 V, i.e., 75% of the formation voltage in 0.1 mol dm^{-3} phosphoric acid at 20 °C. The dielectric property was evaluated by measuring the capacitance of the anodic film in the series equivalent circuit with a signal level of 1 V at 120 Hz in 150 g dm^{-3} diammonium adipate using an LCR meter (LCR Hi-TESTER, HIOKI 3511-50). To elucidate the depth property of the anodic oxide, a stepwise chemical dissolution by dipping in 1 mol dm^{-3} sodium hydroxide solution at 50 °C for different durations was carried out. The change in the chemical dissolution rate of the film was evaluated by measuring the voltage jump V_j at reanodization in 100 g dm^{-3} diammonium adipate at 50 °C. The morphology of the anodic film was observed using a field-emission scanning electron microscope (SEM, Hitachi S-4200) after preparing fracture sections. For the direct evaluation of the film thickness, cross-sectional investigation was carried out using a transmission electron microscope (TEM, JEOL JEM-2100F) coupled with focused ion beam micro processing (FIB, Hitachi FB-2100). GDOES (Jobin-Yvon JY5000RF) was used to measure the depth profiles of constituent elements in the films accompanied by argon ion sputtering at 40 W.

3. Results and discussion

3.1. Change in anodizing behavior with pH and temperature

Voltage–time curves during anodization of niobium at 1 mA cm^{-2} until the voltage increased to 60 V in 0.1 mol dm^{-3} phosphoric acid at 20 °C are shown in Fig. 1 at the various electrolyte pHs adjusted with NH_4OH. The slope of the V–t curve decreased with increasing pH. In the case of pH 10, the slope was about 20% lower than that in the case of pH 1.6. The slope, dV/dt, is summarized in Fig. 2 with the effect of electrolyte pH and temperature. If the film property is the same and if the oxide dissolution during film growth is negligible, the thickness of the film increases with increasing pH and temperature because of increasing electricity consumption until the voltage reaches to 60 V. When the temperature was increased to 80 °C from 20 °C, the electricity consumption increased approximately 20% for the film formed in the electrolyte at pH 1.6.

Current density–time curves during anodization up to 60 V and subsequent voltage holding at 60 V are shown in Fig. 3 with the effect of electrolyte pH at 20 °C. In the case of pH higher than 8, the residual current density increased. A similar phenomenon is ascertained at all the other temperatures. The total electricity including both "constant current" and "constant voltage" regions for the film formed in the electrolyte at pH 10 was 127% to that of pH 1.6.

3.2. Evaluation of dielectric properties

Fig. 4 shows the V–t curves at reanodization of the anodized specimens for the evaluation of withstand voltage expressed as voltage jump V_j, for the various electrolyte pH at 20 °C. As shown in this figure, the withstand voltages were almost the same regardless of electrolyte pH even though the consumed electricity was different. This result indicates that the film thickness evaluated electrochemically was independent of electrolyte pH. However, as revealed in Fig. 5, the withstand voltage was dependent on temperature and increased almost linearly, as we reported previously [4,5]. As shown in Figs. 6 and 7, the leakage current measured by applying 45 V on the anodized specimens increased appreciably with increasing pH, and decreased with increasing temperature. This temperature dependence of the leakage current could be explained on the basis of the increased film thickness with the increase in temperature. On the other hand, the reason for the noticeable increase in leakage current with the increase in pH is not clear at this stage. This can be explained by the change in the oxide property with the change in the electrolyte pH as discussed later.

Changes in the capacitance of the films with electrolyte pH and temperature are shown in Fig. 8. The capacitances of the oxide films formed in the acid to neutral region were almost the same while those formed in the alkaline region increased to a large degree with increasing pH. The capacitance of 2.6 mF m^{-2} at pH 1.6 increased to 4.6 mF m^{-2} at pH 10, i.e., approximately 1.8 times.

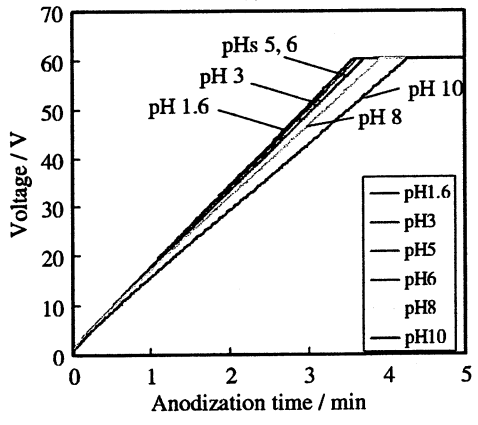

Fig. 1. Voltage–time curves during anodization of niobium at 1 mA cm^{-2} until the voltage increased to 60 V in 0.1 mol dm^{-3} phosphoric acid at 20 °C for various electrolyte pHs adjusted with NH_4OH.

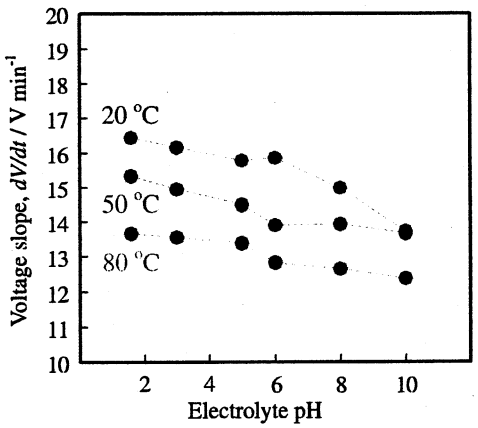

Fig. 2. Slope of voltage–time curves during anodization up to 60 V in phosphoric acid for various electrolyte pHs and temperatures.

Please cite this article in press as: S. Ono et al., Effects of electrolyte pH and temperature on dielectric properties of anodic ..., Corros. Sci. (2008), doi:10.1016/j.corsci.2008.11.027

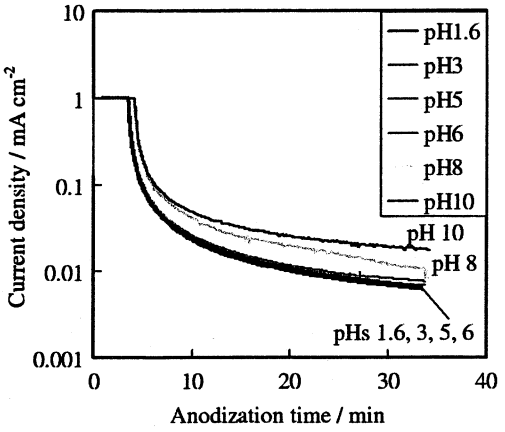

Fig. 3. Current density–time curves during anodization up to 60 V in phosphoric acid and subsequent voltage holding for 30 min at 60 V for various electrolyte pHs at 20 °C.

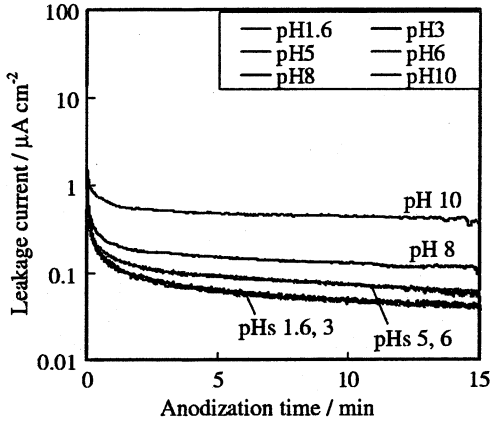

Fig. 6. Leakage current measured by applying anodization voltage of 45 V on anodized specimens. Anodic films were formed at 60 V for 30 min in phosphoric acid for various electrolyte pHs at 20 °C.

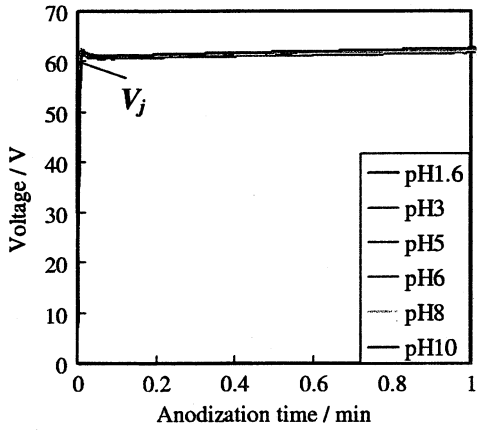

Fig. 4. Voltage–time curves at reanodization of anodized specimens at 0.1 mA cm^{-2} in 100 g dm^{-3} ammonium adipate for the evaluation of withstand voltage measured as voltage jump V_j. Anodic films were formed at 60 V for 30 min in various electrolyte pHs at 20 °C.

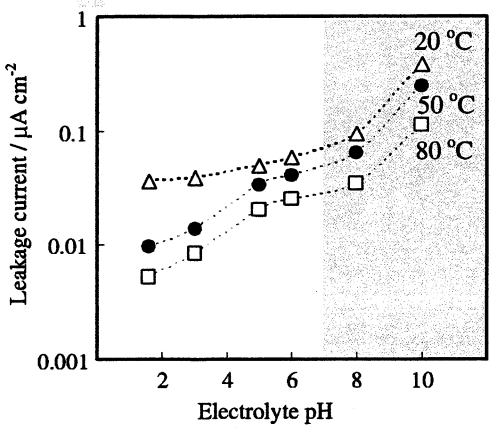

Fig. 7. Leakage current determined 15 min after applying 45 V on anodized specimens. Anodic films were formed at 60 V for 30 min in phosphoric acid for various electrolyte pHs and temperatures.

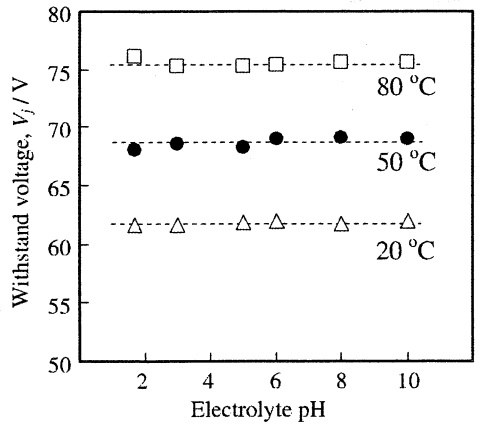

Fig. 5. Withstand voltages of the anodic films formed at 60 V for 30 min in phosphoric acid for various electrolyte pHs and temperatures. All *V–t* curves are coincident.

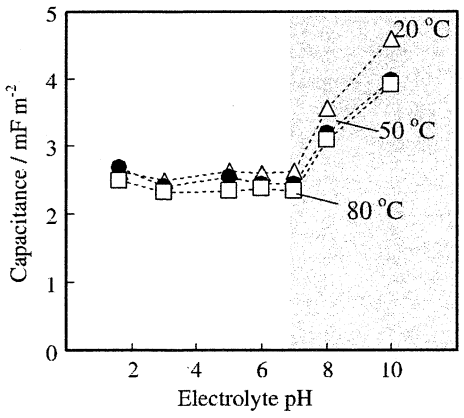

Fig. 8. Capacitance of the anodic films formed at 60 V for 30 min in phosphoric acid for various electrolyte pHs and temperatures.

Such pH dependence of capacitance is found regardless of electrolyte temperature. The capacitance of the film is slightly lower when the temperature is higher because of the increase in the film thickness. To evaluate the charging ability of the dielectric oxide film, the *CV* value, i.e., capacitance *C* multiplied by withstand voltage *V*, was calculated in relation to pH as shown in Fig. 9. The *CV* value, which is proportional to permittivity as shown later using an equation, appears to be higher when the electrolyte temperature is higher.

Please cite this article in press as: S. Ono et al., Effects of electrolyte pH and temperature on dielectric properties of anodic ..., Corros. Sci. (2008), doi:10.1016/j.corsci.2008.11.027

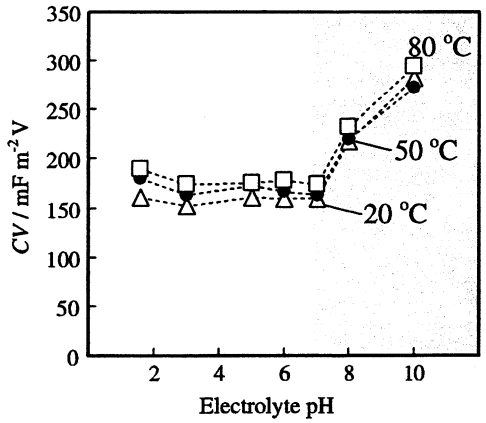

Fig. 9. *CV* value (product of capacitance and withstand voltage) of the anodic films formed at 60 V for 30 min in phosphoric acid for various electrolyte pHs and temperatures.

3.3. Analysis of film structure

For the evaluation of oxide film thickness, the individual interference color was observed as shown in Fig. 10. Despite the same withstand voltage of the films, the interference color changed with the change in electrolyte pH at all temperature ranges. Thus, it became clear that the film thickness increased with both increasing pH and temperature, suggesting the simultaneous decrease in voltage sustainability per unit thickness of the anodic oxide.

The structure of the anodic oxide films formed in phosphoric acid with different electrolyte pHs of 1.6 and 10 at 20 °C was evaluated using SEM and TEM as shown in Fig. 11. SEM images of the fracture sections indicated a flat and homogeneous structure, suggesting a dense and barrier-type amorphous oxide without forming pores or cracks. As revealed in the insets of Fig. 11, the TEM images of the anodic films formed in phosphoric acid with different electrolyte pHs showed that the films were composed of two layers: the outer layer having light contrast and the inner layer having dark contrast as indicated in the interface by dotted lines. Pt was deposited on the specimens for the sample preparation. In addition, the film formed at pH 10 was slightly thicker than the film formed at pH 1.6, i.e., 155 and 147 nm, respectively. From the film thickness, the relative permittivity ε_r of the oxide could be estimated using the following equation.

$$C = \varepsilon_r \varepsilon_0 S/d, \quad \text{namely, } \varepsilon_r = Cd/\varepsilon_0 S$$

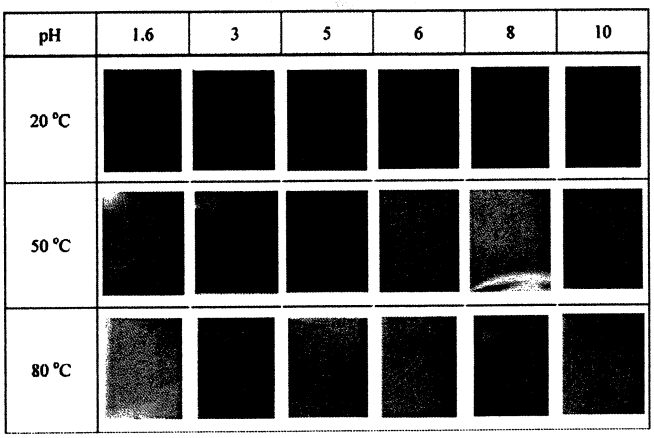

Fig. 10. Interference colors of anodic films formed at 60 V for 30 min in phosphoric acid for various electrolyte pHs and temperatures.

Here, C is the capacitance, ε_0 is the permittivity of vacuum, S is the surface area of the dielectric film, and d is the film thickness. As a result, the relative permittivity of each film was determined as 43.7 for pH 1.6 and 80.5 for pH 10, respectively. Thus, the capacitance of the film formed at pH 10 was markedly higher than that of the film formed at pH 1.6. In addition, it is revealed that the *CV* value is proportional to the permittivity because the withstand voltage is proportional to the film thickness.

3.4. Transport number of Nb^{5+} and depth profiles of constituent elements

The film composition has a connection with the transport numbers of Nb^{5+} and O^{2-} and anion incorporation behavior. To elucidate the oxide film composition in relation to the peculiar high permittivity of the anodic film formed in alkaline electrolyte, the depth profiles of the constituent elements were measured by GDOES as shown in Fig. 12. To evaluate the transport number of Nb^{5+} ions, Si was used as an immobile marker. Namely, a niobium substrate was preanodized in 20% sodium silicate at 0.1 mA cm^{-2} until the voltage reached 2 V before anodization in a phosphoric acid solution. The reason of high intensity of Si in substrate would be Si impurity included in Nb substrate in ppm level, since the wavelength of 220 nm for Si detection is not fitted for the other elements. The transport number of Nb^{5+} ions of the film formed in the electrolyte of pH 1.6 is 0.27, while that of the film formed at pH 10 is as low as 0.02, as indicated by the peak position of the Si marker. This implies that the anodic film growth proceeds mostly at the film/substrate interface when the electrolyte pH is high. This phenomenon is somewhat similar to that observed in the anodic films formed on niobium [5] and aluminum [4] at high temperature, where the apparent transport number is lowered (TNb^{5+} is 0.16 at 80 °C), and the film thickness considerably increases, suggesting the lower electric field strength across the oxide layer [5]. In fact, the anion incorporation depth and the content decrease with increasing electrolyte temperature in both cases. The ratio of the incorporation depth of phosphorous of the present niobium anodic film was approximately 0.5 in the case of pH 1.6 but it decreased to 0.1 in the case of pH 10, in accordance with the lighter contrast regions of the films observed in the TEM images. Thus, the outer layer having a lighter contrast is a phosphorous-containing layer, while the inner layer consists of pure niobium oxide. Furthermore, the spectrum intensity, i.e., the phosphorous content, was markedly suppressed when the film was formed in the electrolyte of pH 10, as shown in Fig. 12b. The anion penetration progresses as a result of inward migration under the electric field; therefore, the notable suppression of phosphorous incorporation in the alkaline region could be, even partly, caused by the decrease in the electric field strength induced by the film thickening. This is also applicable for the case of higher temperature as we reported previously [5]; however, the suppression rate of anion incorporation in the film formed at pH 10 is much higher. Moreover, the capacitance of the film formed at 80 °C in the acid region is low. Although the permittivity of the anion-free pure oxide layer is higher than that of the anion-contaminated layer [4], the reason for high suppression rate of anion penetration other than the peculiar high capacitance of the film formed in alkaline region has not been fully clarified.

Since the total electricity of the film formed at pH 10 was 127% compared to that of the film formed at pH 1.6, the film thickness should be 186 nm (147 nm × 1.27) if the film density is the same and oxide dissolution is not occurred. Therefore, the difference in thickness between hypothetical and actual alkaline films is 31 nm (186 − 155 nm), corresponding to 0.17 (31 nm/186 nm) of the thickness ratio. This ratio also represents the hypothetical transport number of Nb^{5+} of the alkaline film if all the migrated

Please cite this article in press as: S. Ono et al., Effects of electrolyte pH and temperature on dielectric properties of anodic ..., Corros. Sci. (2008), doi:10.1016/j.corsci.2008.11.027

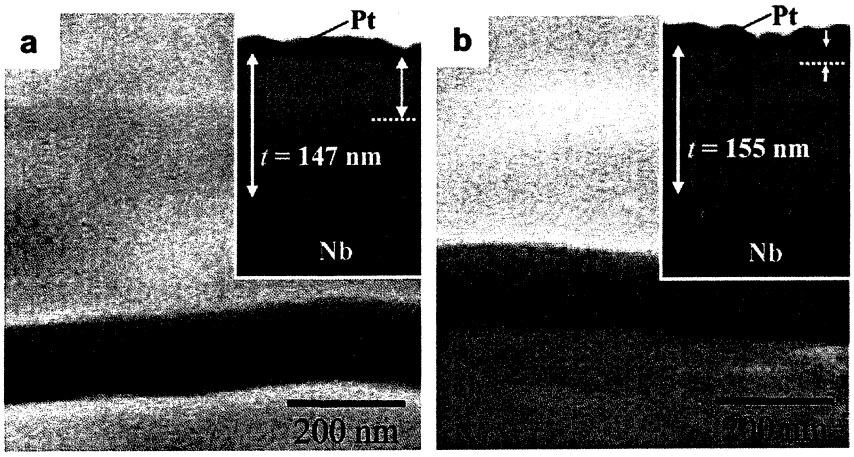

Fig. 11. SEM and TEM (insets) images of cross-section of anodic films formed at 60 V for 30 min in phosphoric acid at (a) pH 1.6 and (b) pH 10 at 20 °C.

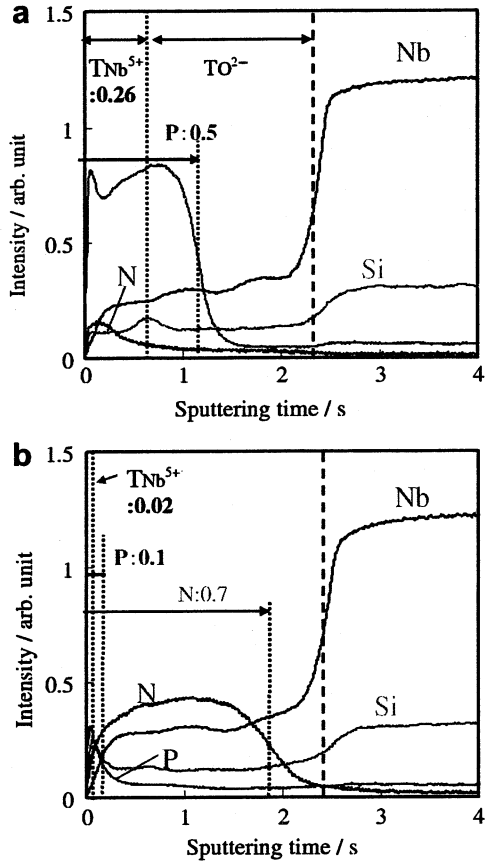

Fig. 12. Depth profiles of constituent elements measured by GDOES of anodic films formed at 60 V for 30 min in phosphoric acid at (a) pH 1.6 and (b) pH 10 at 20 °C.

niobium ions reached to the film/electrolyte interface are directly ejected to the electrolyte. Thus, it is clear that the ion transport number of Nb^{5+} of the film formed in alkaline electrolyte is, at any rate, lower than that of the film formed in acid electrolyte. Even if this hypothesis is appropriate, the lower ratio of phosphorus containing layer of 0.1 is inexplicable since phosphorus could migrate under the electric field across the film.

In contrast to the low phosphorus incorporation, nitrogen penetration into the film of 70% thickness ratio was detected in the case of pH 10. The origin of nitrogen doping should be ammonium ions although they are cations. A certain mechanism for nitrogen penetration into anodic films must exist, since nitrogen doping is always found when ammonium salt is used as an electrolyte species for various valve metals including aluminum.

Although the electricity consumed for the formation of anodic niobia film up to 60 V in the electrolyte of pH 10 was 20% larger than that associated with pH 1.6, the actual film was merely 5% thicker. Because the oxide density seems to have no big difference, the oxide would be dissolved, or more likely, niobium ions corresponding to the remaining 15% would directly migrate into the electrolyte. At any rate, the actual transport number of Nb^{5+} ion of the film formed in the alkaline region would be smaller than that associated with the acid region.

3.5. Dissolution behavior of anodic films formed in electrolytes with different pHs

To elucidate the in-depth property of the anodic niobium oxide films, a stepwise chemical dissolution by dipping in a 1 mol dm^{-3} sodium hydroxide solution at 50 °C and subsequent reanodization at 0.1 mA cm^{-2} in diammonium adipate solution, to estimate the changes in the film thickness by measuring the jumping voltage V_j, were carried out. Fig. 13 shows the variation of the V_j of the films formed at different electrolyte pHs with dissolution time. As reported previously [5], the anodic film formed in phosphoric acid was composed of three different layers with different solubilities. The outer layer, which consists of 10% of the film thickness,

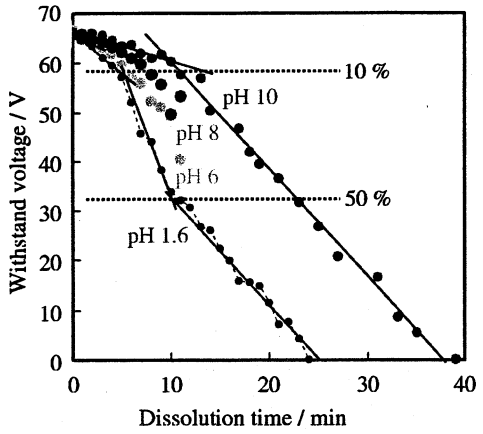

Fig. 13. Change in the withstand voltage with dissolution time in 1 mol dm^{-3} sodium hydroxide at 50 °C of the films formed at 60 V for 30 min in phosphoric acid at different electrolyte pHs.

Please cite this article in press as: S. Ono et al., Effects of electrolyte pH and temperature on dielectric properties of anodic ..., Corros. Sci. (2008), doi:10.1016/j.corsci.2008.11.027

shows relatively low solubility, and the intermediate layer with a thickness of 10–50% was most soluble. Because the depth of intermediate layer coincides with the phosphorous-containing depth of 50%, the high solubility is caused by anion incorporation, although the low solubility of the outer layer requires further explanation. In the case of the films formed in alkaline electrolytes, the film was composed of two layers. The dissolution rate of the outer layer decreased with increasing electrolyte pH, whereas that of the inner layer of a pure oxide remained unchanged. This can be explained by the suppressed phosphorous content with increasing pH in the outer layer and no phosphorus inclusion in the inner layer of all the films. Although the cause of the solubility of the outer layer being lower than that of the intermediate layer of the acid film despite the same phosphorous content is yet unknown, it is deduced that the chemical property in the depth of anodic films is strongly affected by the anion distribution, which is also dependent on the electrolyte pH.

4. Conclusions

The effects of electrolyte pH and temperature on the structure and properties of anodic films formed on niobium were investigated. The film thickness electrochemically evaluated on the basis of withstand voltage increased linearly with increasing electrolyte temperature, whereas it was independent of pH. However, the direct TEM observation of the cross-sections and the interference color of the films suggested that the thickness slightly increased with increasing pH. The leakage current of the film increased with increasing pH and decreased with increasing temperature. The capacitance of the film was independent of the electrolyte pH in an acid region but notably increased with increasing pH in an alkaline region. The capacitance was lower at the higher temperature owing to the increase in the film thickness. The relative permittivity estimated from the capacitance and film thickness increased from 43.7 to 80.5 when the electrolyte pH was increased from 1.6 to 10. The depth profiles of the constituent elements of the film suggested that the incorporation depth and phosphorus content markedly decreased with increasing pH, and nitrogen was found to penetrate into the depth of 70% at pH 10. Furthermore, the apparent transport number of Nb^{5+} ion decreased from 0.26 to 0.02 with the pH increase from 1.6 to 10, which implied direct migration of Nb^{5+} ion into the electrolyte without forming oxide at the alkaline region.

From these results, it is concluded that the changes in the structure and dielectric properties of the niobium anodic films with the changes in electrolyte temperature and pH are primarily caused by the different incorporation behavior of electrolyte species such as phosphorous and nitrogen. However, the notable increase in capacitance with pH is controlled by additional unknown factors besides the change in electric field strength across the anodic niobia films.

5. Uncited reference

[15]. Q1

Acknowledgements

Part of this work was financially supported by a Grant-in-Aid for Scientific Research from the Japan Society for the Promotion of Science and the Light Metal Education Foundation of Japan. Thanks are also due to the "High-Tech Research Center" Project for Private Universities: matching fund subsidy from the Ministry of Education, Culture, Sports, Science and Technology.

References

[1] J.J. Randall Jr., W.J. Bernard, R.R. Wilkinson, Electrochim. Acta 10 (1965) 183.
[2] C.J. Dell'Oca, L. Young, J. Electrochem. Soc. 117 (1970) 1548.
[3] Y.M. Li, L. Young, J. Electrochem. Soc. 147 (2000) 1344.
[4] S. Ono, F. Mizutani, M. Ue, N. Masuko, in: Corrosion and Corrosion Protection/2001, PV 2001-22, The Electrochemical Society Proceedings Series, Pennington, NJ, 2001, p. 1129.
[5] S Ono, M Baba, M Shimoyama, H Asoh, in Surface Oxide Films/2003, PV 2003-25, The Electrochemical Society Proceedings Series, Pennington, NJ, 2004, p. 133.
[6] K. Nagahara, M. Sakairi, H. Takahashi, K. Matsumoto, K. Takayama, Y. Oda, Electrochemistry 72 (2004) 624.
[7] N.F. Jackson, J. Appl. Electrochem. 3 (1973) 91.
[8] N.F. Jackson, J.C. Hendy, Electrocomponent Sci. Technol. 1 (1974) 27.
[9] D.M. Lakhiani, L.L. Shreir, Nature 188 (1960) 49.
[10] H. Asoh, H. Odate, S. Ono, J. Surf. Finish. Soc. Jpn. 55 (2004) 952.
[11] J.A. Davies, B. Domeij, J.P. Pringle, F. Brown, J. Electrochem. Soc. 112 (1965) 675.
[12] J.W. Diggle, T.C. Downie, C.W. Goulding, Chem. Rev. 69 (1969) 365.
[13] G.E. Thompson, Y. Xu, P. Skeldon, K. Shimizu, S.H. Han, G.C. Wood, Phil. Mag. B 55 (1987) 651.
[14] H. Habazaki, T. Matsuo, H. Konno, K. Shimizu, S. Nagata, K. Takayama, Y. Oda, P. Skeldon, G.E. Thompson, Thin Solid Films 429 (2002) 159.
[15] H. Habazaki, T. Matsuo, H. Konno, K. Shimizu, S. Nagata, K. Matsumoto, K. Takayama, Y. Oda, P. Skeldon, G.E. Thompson, Electrochim. Acta 48 (2003) 3519.

Corrosion Science xxx (2008) xxx–xxx

Contents lists available at ScienceDirect

Corrosion Science

journal homepage: www.elsevier.com/locate/corsci

Structural features of anodic oxide films formed on aluminum substrate coated with self-assembled microspheres

Hidetaka Asoh *, Kota Uchibori, Sachiko Ono

Department of Applied Chemistry, Faculty of Engineering, Kogakuin University, 2665-1 Nakano, Hachioji, Tokyo 192-0015, Japan

ARTICLE INFO

Article history:
Received 26 August 2008
Accepted 14 November 2008
Available online xxxx

Keywords:
Aluminum
Anodic films
Anodizing ratio
Self-assembled microspheres
Microporous alumina

ABSTRACT

The structural features of anodic oxide films formed on an aluminum substrate coated with self-assembled microspheres were investigated by scanning electron microscopy and atomic force microscopy. In the first anodization in neutral solution, the growth of a barrier-type film was partially suppressed in the contact area between the spheres and the underlying aluminum substrate, resulting in the formation of ordered dimple arrays in an anodic oxide film. After the subsequent second anodization in acid solution at a voltage lower than that of the first anodization, nanopores were generated only within each dimple. The nanoporous region could be removed selectively by post-chemical etching using the difference in structural dimensions between the porous region and the surrounding barrier region. The mechanism of anodic oxide growth on the aluminum substrate coated with microspheres through multistep anodization is discussed.

1. Introduction

From many morphological studies, it has been known that an anodic oxide film formed on an aluminum substrate in an appropriate acidic solution consists of two regions: a thick outer region of porous-type oxide and a thin inner region of barrier-type oxide lying adjacent to the aluminum substrate [1–3]. Over the past several decades, although studies to protect or design aluminum surfaces for commercial application have been carried out, little attention has been given to the regularity of self-organized cell structures in porous anodic oxide films. In 1995, Masuda and Fukuda reported for the first time that pore configurations with long-range ordering are formed in porous anodic oxide films under optimized anodization conditions [4]. Since then, there has been renewed interest in porous anodic oxide films, so-called nanoporous alumina films, as a template for nanodevice preparation, particularly in terms of the controllability and regularity of porous oxide films. We have also studied the self-ordering conditions of pore configurations in porous anodic oxide films grown in solutions of various organic acids such as citric acid [5], malonic acid [6] and tartaric acid [6], and confirmed new self-ordering conditions in such organic acid electrolytes using the previously suggested mechanism of anodization at a high electric field in a barrier layer [7–9].

In conventional anodization, however, the formation of microporous alumina with large pore intervals (>1 μm) is difficult owing to "burning" under high formation voltages of more than 400 V. Against this background, the proposal of a new fabrication process for porous anodic oxide films with large pore intervals on the micrometer scale has been thought to be necessary to achieve various functional applications. In this paper, we describe the morphology and growth mechanism of anodic oxide films on an aluminum substrate coated with self-assembled microspheres and their application to the fabrication of microporous anodic oxide films with large pore intervals of more than 1 μm.

2. Experimental

Fig. 1 shows the schematic of the fabrication of the microporous alumina structure on an aluminum substrate. The process used to fabricate the microporous structure was based on a combination of the templating of self-assembled microspheres and the subsequent multistep anodization. A monodisperse suspension of 3-μm-diameter polystyrene (PS) spheres (Polysciences, Inc.) was dropped onto the aluminum substrate. The suspension drop was dried in air, and the microspheres were allowed to self-assemble into a closely packed structure via attractive capillary forces (Fig. 1a). After the complete evaporation of the solvent, the aluminum substrate coated with the PS spheres was anodized in a mixture of 0.5 mol dm^{-3} boric acid and 0.05 mol dm^{-3} sodium tetraborate solution at a constant current density of 1 Am^{-2} up to a predefined voltage at 20 °C (Fig. 1b). After the first anodization, the sample was immersed in 97% toluene to dissolve the PS spheres used as a mask (Fig. 1c). Then, to form the nanoporous alumina, a second anodization was conducted in oxalic acid solution at a voltage low-

* Corresponding author. Tel.: +81 42 628 4537; fax: +81 42 628 4537.
E-mail address: asoh@cc.kogakuin.ac.jp (H. Asoh).

0010-938X/$ - see front matter © 2008 Published by Elsevier Ltd.
doi:10.1016/j.corsci.2008.11.018

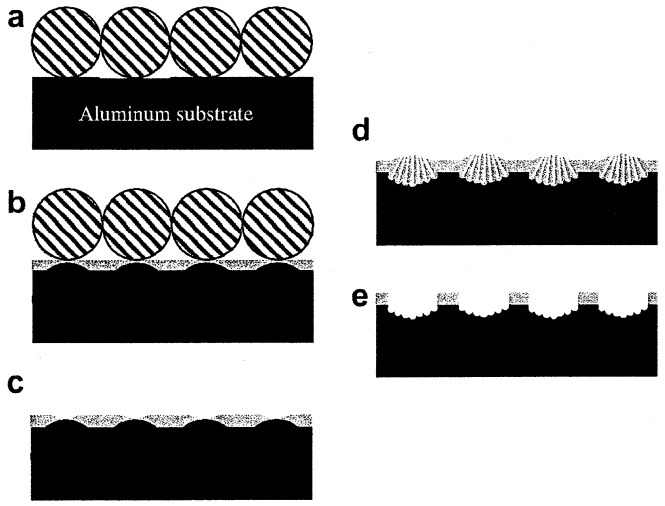

Fig. 1. Scheme for fabricating microporous alumina by templating and multistep anodization: (a) self-assembly of PS spheres, (b) first anodization in neutral solution, (c) removal of spheres, (d) second anodization in acid solution, and (e) removal of nanoporous layer.

er than that of the first anodization (Fig. 1d). After the second anodization, the sample was immersed in 5 wt.% phosphoric acid solution at 30 °C to dissolve the nanoporous alumina region (Fig. 1e). The resultant anodic oxide films formed on the aluminum substrate were evaluated by field-emission scanning electron microscopy (SEM, Hitachi S-4200) and atomic force microscopy (AFM, Digital Instrument Nano Scope IIIa).

3. Results and discussion

Fig. 2a shows a SEM image of ordered dimple arrays in the anodic oxide film formed by first anodization up to 100 V in a neutral solution. After the removal of microspheres used as a mask, SEM observation was conducted to evaluate the surface morphology of the anodic oxide film. The voltage–time curve at a constant current density for the anodization of the aluminum substrate coated with the PS spheres was almost the same as that for a conventional electropolished aluminum substrate. That is, the formation voltage increased linearly with increasing anodization time following barrier-type oxide film growth. From the cross-sectional SEM image in Fig. 2b, it was confirmed that the thickness of the barrier-type film, indicated by arrow A, was approximately 140 nm, in almost agreement with the expected value calculated by (anodizing ratio: nm V^{-1}) × (formation voltage: V). Namely, if the selected formation voltage is 100 V, the film thickness is assumed to be 140–150 nm while taking into account the anodizing ratio (1.4–1.5 nm V^{-1} [10,11]).

On the other hand, it must be noted that the thickness of the barrier-type film of the contact area between the spheres and the underlying aluminum substrate, indicated by arrow B, was smaller than that of the surrounding film. The thickness of the central part of the dimple was smallest at approximately 95 nm, i.e., 2/3 of that of the surrounding film, corresponding to a formation voltage of 68 V while taking into account the anodizing ratio (1.4 nm V^{-1}). In addition, one of the notable features of the obtained anodic oxide film is that the film thickness increased gradually from the center outward owing to the curvature of the microspheres used as a mask. These results indicate that each microsphere can act as a mask for anodizing by suppressing ionic current flow. That is, the exposed aluminum surface of the interspaces among spheres was anodized preferentially.

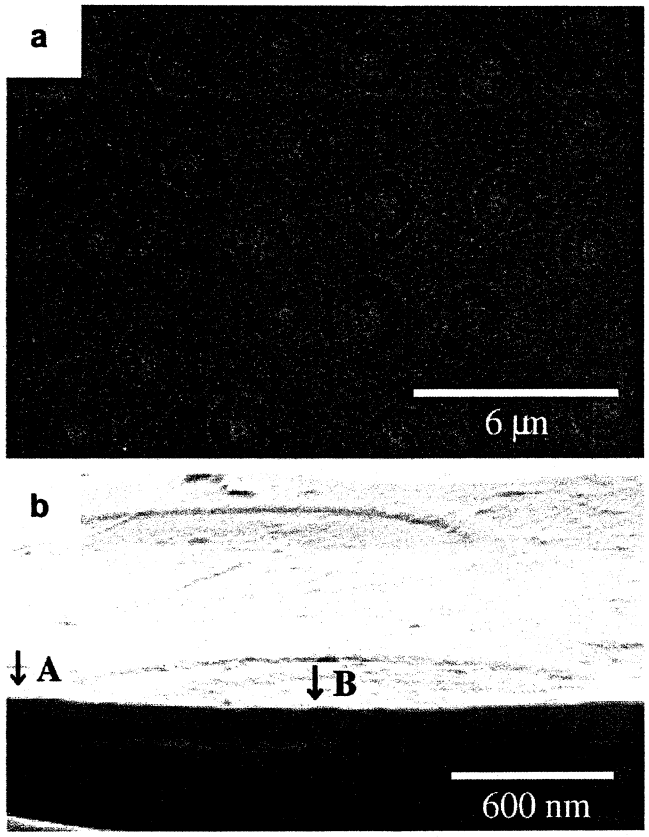

Fig. 2. SEM images of anodized Al after removal of microspheres: (a) surface view and (b) cross-sectional views. The first anodization was conducted in a mixture of 0.5 mol dm^{-3} boric acid and 0.05 mol dm^{-3} sodium tetraborate solution at a constant current density of 1 Am^{-2} up to 100 V at 20 °C.

Intrinsic defects (vacancies and dislocations) are often observed at the present stage as shown in Fig. 2a. These disordered patterns are thought to be the cause of inappropriate conditions for the evaporation of solvent during the formation of two-dimensional arrays of PS spheres. For the general background of the mechanism of self-assembly of colloidal spheres, see Refs. [12,13]. In our previous work using silicon wafers as an underlying substrate, however, the PS spheres could be self-assembled into ordered two-dimensional arrays with a relatively large domain exceeding several ten micrometers in area [14,15]. Therefore, the intrinsic defects might be caused by the detachment of the PS spheres from the substrate during anodization. A detailed study on the effect of heat treatment conditions such as the temperature and treatment time is also now in progress to fix perfectly each sphere to the aluminum substrate.

Fig. 3 shows a cross-sectional SEM image of the anodic oxide film after the second anodization at a constant voltage of 80 V in oxalic acid solution. To form a nanoporous film only in the central part of the dimple, the formation voltage of second anodization needs to be higher than the voltage calculated from the thickness of the central part of the dimple shown in Fig. 2b and the anodizing ratio, that is, 68 V. In addition, to restrict the pore initiation of the anodic film within each dimple, it needs to be lower than that of the first anodization, that is, 100 V. Therefore, the second formation voltage was set to 80 V, in which the thickness of the barrier layer of porous film was about 1 nm V^{-1}. In this case, pore initiation could start at the barrier film within a thickness of approximately 100 nm. From the SEM image shown in Fig. 3, it was confirmed that nanopores were generated only in the thinner part of the barrier film of the dimple in the initial stage of porous film

Please cite this article in press as: H. Asoh et al., Structural features of anodic oxide films formed on aluminum substrate coated ..., Corros. Sci. (2008), doi:10.1016/j.corsci.2008.11.018

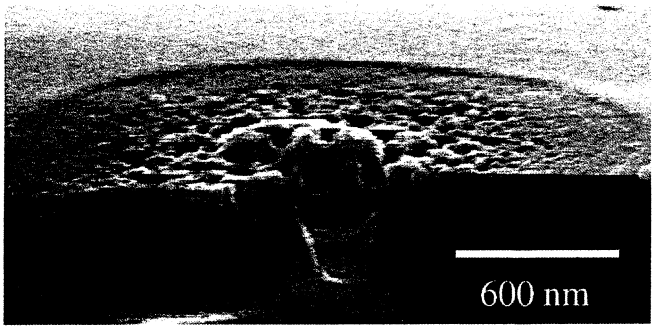

Fig. 3. Cross-sectional SEM image of anodized Al after second anodization in 0.05 mol dm^{-3} oxalic acid solution at 80 V for 5 min at 20 °C. The first anodization conditions were the same as those in Fig. 2.

growth. Further anodization resulted in the spread of the nanoporous region within each dimple. Namely, the surrounding dense barrier layer, which was formed on the bulk aluminum substrate by the first anodization at a relatively high voltage of 100 V in neutral solution, could act as an effective anodization mask during the second anodization at a low formation voltage of 80 V.

Subsequently, a similar multistep anodization was conducted under different anodization conditions. Fig. 4 shows typical surface images of the anodic oxide films after the second anodization. The formation voltages of the first and second anodizations decreased by half, as described in Fig. 4, that is, to 50 and 40 V, respectively.

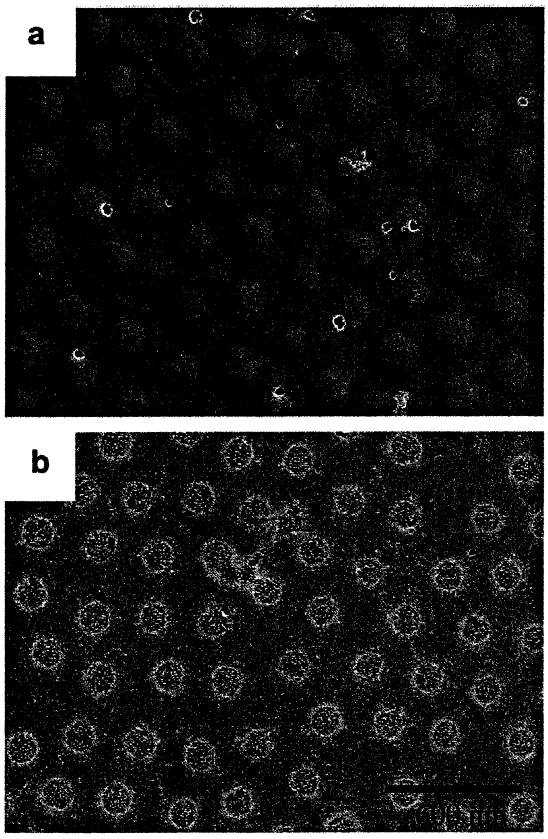

Fig. 4. SEM image of surface of anodized Al after second anodization: (a) as-anodized film and (b) after post-chemical etching in 5 wt.% phosphoric acid solution at 30 °C for 40 min. The first anodization was conducted in a mixture of 0.5 mol dm^{-3} boric acid and 0.05 mol dm^{-3} sodium tetraborate solution at a constant current density of 1 Am^{-2} up to 50 V at 20 °C. After the removal of PS spheres, the second anodization was performed in 0.3 mol dm^{-3} oxalic acid solution at 40 V for 5 min at 30 °C.

The detachment of the PS spheres from the aluminum substrate during the first anodization was effectively inhibited by changing the formation voltage from 100 to 50 V.

The periodicity of the circular nanoporous region was approximately 3 μm, as shown in Fig. 4a. After post-chemical etching, the border between the dense barrier region and the nanoporous region can be clearly distinguished, as shown in Fig. 4b. As in Fig. 3, these results indicate that the formation of porous films was restricted within each dimple because the formation of porous films at 40 V could not be achieved in the surrounding barrier region, which was formed on an exposed aluminum substrate by the first anodization at a relatively high voltage of 50 V in neutral solution.

Afterward, post-chemical etching was conducted to fabricate a microporous alumina film with large pore intervals by removing the porous region selectively. To investigate the removal of the

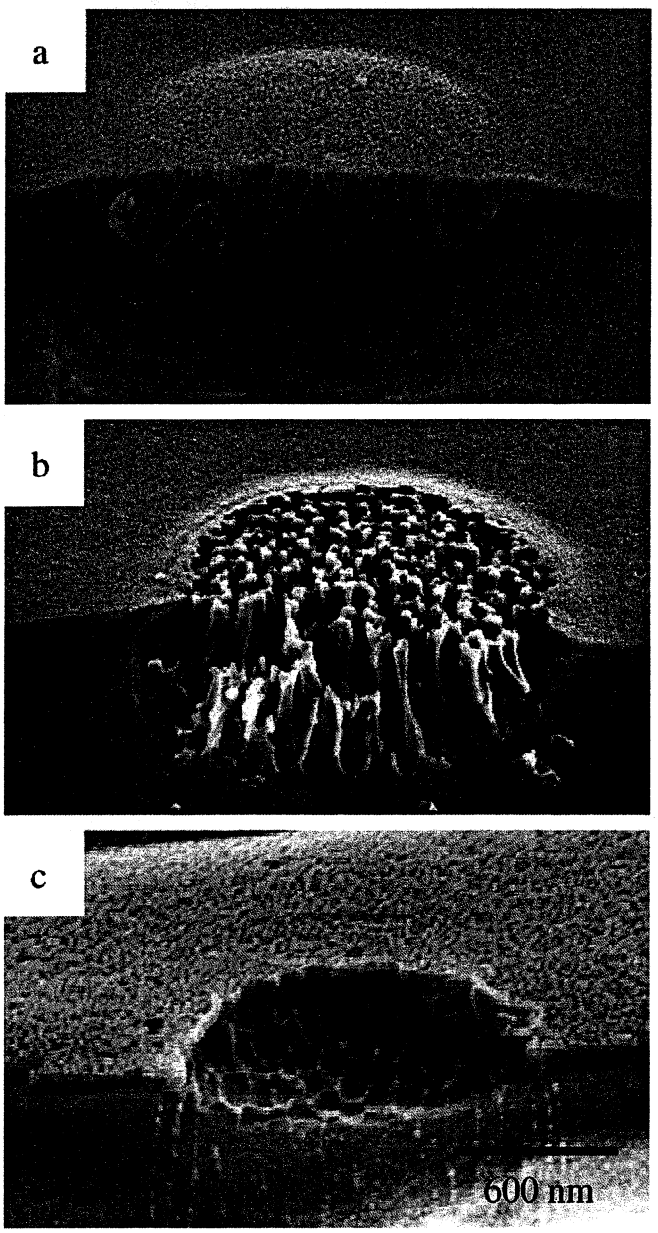

Fig. 5. Cross-sectional SEM images of anodized Al after immersing in phosphoric acid solution for different times. (a) without treatment, (b) 40 min, and (c) 80 min. The anodization conditions were the same as those in Fig. 4.

Please cite this article in press as: H. Asoh et al., Structural features of anodic oxide films formed on aluminum substrate coated ..., Corros. Sci. (2008), doi:10.1016/j.corsci.2008.11.018

nanoporous region in detail, the transformation of the microstructure of the anodic oxide film formed by multistep anodization was observed by SEM at different stages. Concerning the as-anodized film before chemical etching, it was confirmed from the cross-sectional view shown in Fig. 5a that the nanoporous region clearly became dome-shaped in comparison with the surrounding barrier region owing to the volumetric expansion of aluminum to alumina and the preferential growth of porous-type anodic oxide films perpendicular to the aluminum substrate. In addition, the bottom part of the nanoporous region with semispherical faces protruded into the underlying aluminum substrate locally because the porous film was grown and radiated outward.

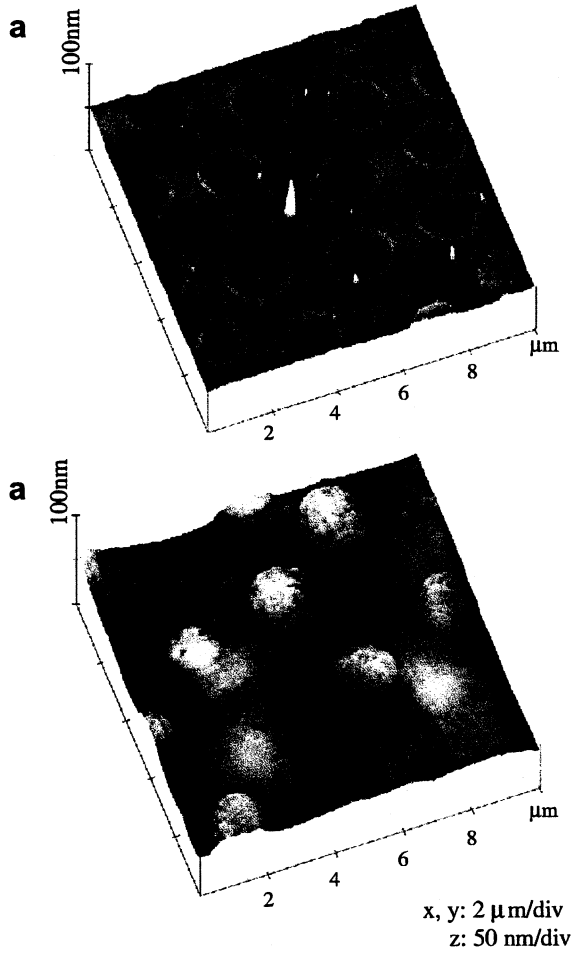

Fig. 6. AFM tapping-mode images of (a) surface of anodized aluminum after first anodization and (b) surface of aluminum after removal of oxide film in mixture of phosphoric acid and chromic acid. (c) Schematic model of interface between barrier film and aluminum substrate. The anodization conditions were the same as those in Fig. 4.

Fig. 5b and c show cross-sectional SEM images of the anodized specimens after post-chemical etching. When each specimen was immersed in phosphoric acid solution for 40 min, the cell wall of alumina almost disappeared with lateral etching. Further chemical etching results in a through-hole in the barrier layer of each cell, indicating the complete removal of the nanoporous region, as shown in Fig. 5c. The diameter of the circular opening was approximately 1.3 μm, which could not be obtained by conventional anodization.

Although the thickness of the surrounding barrier region also decreased during chemical etching, and fine pores were generated on the surface of the surrounding barrier region, no paths reached the surface of the aluminum substrate were observed. As mentioned previously, the anodizing ratio of the cell wall and the barrier layer for the porous films formed in acid solution is approximately 1.0 nm V^{-1} and less than that of the barrier-type film formed in neutral solution (1.4–1.5 nm V^{-1}) [10,11]. Therefore, the nanoporous region could be removed preferentially because the thicknesses of the cell wall and barrier layer formed at 40 V in oxalic acid solution were considerably smaller than that of surrounding dense barrier layer formed at a higher voltage of 50 V. As a result, the microporous alumina film with a 3 μm pore interval could be obtained.

To clarify the oxide growth in the contact area between the spheres and the underlying aluminum substrate during the first anodization in neutral solution, the distribution of film thickness was investigated using AFM. Fig. 6a shows an AFM image of the surface of the anodized aluminum substrate. Cross-sectional analysis revealed that the depth of the dimple was approximately 5 nm. This result was the average of seven measurements in different scan areas. After removing the oxide film in a boiling solution of 6 wt.% phosphoric acid and 2 wt.% chromic acid for 10 min, the topography of the aluminum surface was analyzed by AFM, as shown in Fig. 6b. The height of the protrusion of the aluminum substrate was approximately 14 nm on average. Considering these measurements at a formation voltage of 50 V, the morphology of the barrier-type film grown on the aluminum substrate in the presence of spheres as an anodizing mask is summarized as a schematic model in Fig. 6c. When patterned anodic barrier films having different thicknesses are subjected to a second anodization at a constant voltage in oxalic acid solution, the electric field strength is highest in the central part of the dimple because the thickness of oxide film is smallest in the central part. Therefore, the formation of a nanoporous film in the second anodization in acid solution can proceed even at a voltage lower than that of first anodization in neutral solution and the film will grow from the center outward.

4. Conclusions

We described the morphology and growth mechanism of anodic oxide films under PS microspheres used as an initial mask. In the first anodization in neutral solution, the growth of a barrier-type film was partially suppressed in the contact area between the spheres and the underlying aluminum substrate. Namely, each microsphere can act as a mask for anodization by suppressing ionic current flow. As a result, ordered dimple arrays were formed in the anodic oxide film. Using such patterned anodic barrier films having different thicknesses, the distribution of pore generation was restricted within each dimple in the second anodization in acid solution. The nanoporous region could be removed selectively during post-chemical etching because the thicknesses of the cell wall and barrier layer of the porous film were smaller than that of the surrounding dense barrier layer formed by the first anodization at a relatively high voltage in neutral solution. Eventually, a com-

Please cite this article in press as: H. Asoh et al., Structural features of anodic oxide films formed on aluminum substrate coated ...., Corros. Sci. (2008), doi:10.1016/j.corsci.2008.11.018

bination of multistep anodization and post-chemical etching produced a microporous anodic oxide film with a large pore interval of more than 1 μm, which cannot be obtained by conventional anodization. The obtained new-model microporous alumina with a large pore interval of more than 1 μm has potential technological and scientific applications as catalytic supports and separation media other than as an etching mask.

Acknowledgements

Part of this work was financially supported by a Grant-in-Aid for Scientific Research from the Japan Society for the Promotion of Science and the Light Metal Education Foundation of Japan. Thanks are also due to the "High-Tech Research Center" Project for Private Universities: matching fund subsidy from the Ministry of Education, Culture, Sports, Science and Technology.

References

[1] F. Keller, M.S. Hunter, D.L. Robinson, J. Electrochem. Soc. 100 (1953) 411.
[2] J.W. Diggle, T.C. Downie, C.W. Goulding, Chem. Rev. 69 (1969) 365.
[3] J.P. O'Sullivan, G.C. Wood, Proc. R. Soc. Lond. A 317 (1970) 511.
[4] H. Masuda, K. Fukuda, Science 268 (1995) 1466.
[5] S. Ono, M. Saito, M. Ishiguro, H. Asoh, J. Electrochem. Soc. 151 (2004) B473.
[6] S. Ono, M. Saito, H. Asoh, Electrochim. Acta 51 (2005) 827.
[7] S. Ono, K. Takeda, N. Masuko, in: Proceedings of the Second International Symposium on Aluminum Surface Science Technology (2000) 398.
[8] S. Ono, N. Masuko, Surf. Coat. Technol. 169–170 (2003) 139.
[9] S. Ono, M. Saito, H. Asoh, Electrochem. Solid State Lett. 7 (2004) B21.
[10] S. Ono, F. Mizutani, M. Ue, N. Masuko, in: Corrosion and Corrosion Protection, J. D. Sinclair, R. P. Frankenthal, E. Kálmán, (Eds.), PV 2001-22, The Electrochemical Society Proceedings Series, Pennington, NJ (2001) 1129.
[11] S. Ono, C. Wada, H. Asoh, Electrochim. Acta 50 (2005) 5103.
[12] N.D. Denkov, O.D. Velev, P.A. Kralchevsky, I.B. Ivanov, H. Yoshimura, K. Nagayama, Langmuir 8 (1992) 3183.
[13] Y. Xia, B. Gates, Y. Yin, Y. Lu, Adv. Mater. 12 (2000) 693.
[14] H. Asoh, A. Oide, S. Ono, Electrochem. Commun. 8 (2006) 1817.
[15] H. Asoh, S. Sakamoto, S. Ono, J. Colloid Interface Sci. 316 (2007) 547.

Q2

Paper

Journal of the Society of Inorganic Materials, Japan **16**, 28–36 (2009)

アルカリ処理を施したチタン基板への水酸アパタイトの電解析出

阿相　英孝・川目　達也・柴田　稚子・小野　幸子
（工学院大学工学部応用化学科）

Electrodeposition of Hydroxyapatite on Alkali Treated Titanium

Hidetaka ASOH, Tatsuya KAWAME, Wakako SHIBATA and Sachiko ONO
(Department of Applied Chemistry, Faculty of Engineering, Kogakuin University
2665-1 Nakano, Hachioji-shi, Tokyo 192-0015, Japan)

Electrodeposition behavior of hydroxyapatite on titanium substrates with morphologically controlled surface induced by alkali treatment in sodium hydroxide was investigated. From the results obtained by electron microscopic analysis, it was found that the microstructure of porous network layer formed by the alkali treatment, which was mainly composed of noncrystalline and microcrystalline titanium oxide, was influenced by sodium hydroxide concentration and immersing time. The pore size and thickness of porous titanium dioxide layer formed by alkali treatment in 5 $mol \cdot dm^{-3}$ sodium hydroxide solution for 2.5 h were several hundreds nanometers and approximately 1 μm as a maximum, respectively. Alkali-treated titanium was used as a substrate for electrodeposition of hydroxyapatite, and acid-treated titanium with relatively flat surface was also examined as a reference. Although inhomogeneous deposition of hydroxyapatite proceeded on acid-treated titanium, hydroxyapatite layer was uniformly deposited on alkali-treated titanium over a wide range even at the initial stage of electrodeposition. The nucleation of hydroxyapatite occurred in the porous titanium dioxide layer, resulting in the growth of plate-like crystalline hydroxyapatite in a direction perpendicular to the titanium substrate. Improved distribution of hydroxyapatite deposits is attributable to uniform hydrogen gas evolution through the porous network structure formed by alkali treatment. In addition, the quantity of deposits on alkali-treated titanium was much larger than those of the acid-treated titanium under the same quantity of electricity. The adhesion between the deposited hydroxyapatite layer and the underlying titanium substrate was also effectively improved by the anchor effect of microstructural roughness induced by alkali treatment.

(Received Aug. 18, 2008)
(Accepted Sep. 19, 2008)

Key words : Hydroxyapatite, Electrodeposition, Titanium, Alkali treatment

1 緒　　言

水酸アパタイト[$Ca_{10}(PO_4)_6(OH)_2$，以下 HAp]の優れた生体親和性が注目され，医・歯学の分野で種々の機能・特性をもつ基板材料との複合化が検討されている．中でもチタンおよびチタン合金は軽量，高比強度で耐食性に優れることから，その表面に HAp をコーティングし，歯科用インプラントや人工関節などの硬組織代替器具として実用化する様々な研究が進んでいる[1)~4)]．筆者らはこれまでに交互浸漬法あるいはカソード電着法を用いた HAp のコーティングに関して，種々の導電性基板を用いた場合，基板表面の微細構造と材質が HAp の生成に強く影響を及ぼすことを報告してきた[5),6)]．また，下地基板としてチタンを用いカソード電着法で HAp を析出させた際には，平滑なチタン表面に比べアルカリ処理等で凹凸を付与したチタン基板において HAp の析出が促進されることを報告した[7)~9)]．

チタンを水酸化ナトリウム水溶液などのアルカリ溶液に浸漬するアルカリ処理に関しては，処理後のチタン表面に多孔質酸化チタン層が形成されること[10)]に加え，アルカリ処理後のチタンの生体適合性が著しく改善されることが報告されている[11)~15)]．このアルカリ処理は HAp 層とチタン基板を強固に結合させる効

果的な前処理と位置づけられ，擬似体液中においてチタン表面にHAp層を形成する際の前処理として広く用いられている．しかしながら，アルカリ処理後のチタン表面に対してカソード電着を行った際のHApの析出過程に関して詳細に研究を行った報告例はない．

本報告では，アルカリ処理を施したチタン基板の表面形態とカソード電着によるHApの析出挙動の関係について検討した．特に，電解初期のHApの成長過程に着目し，硝フッ酸処理を施したチタン基板上での電着挙動との比較に加え，電子顕微鏡による微細構造の観察を通じてHApの析出形態に及ぼすアルカリ処理の効果を明らかにすることを目的とした．

2 実験方法

純度99.5％のチタン板（厚さ0.5 mm）を10×20 mmの短冊状に切断し試料とした．アルカリ処理は，濃度1～8 mol·dm^{-3}の水酸化ナトリウム（NaOH）水溶液（60°C）中に1～24時間浸漬して行った．

HApの電着は既報[16]を参照し，0.03 mol·dm^{-3}硝酸カルシウム四水和物–0.03 mol·dm^{-3}リン酸水素二アンモニウム混合溶液（Ca/P＝1.67, 80°C, pH 4付近）を電解液とし，対極にステンレス（316L）板を用い，電流密度10 A·m^{-2}の定電流カソード電解で行った．

アルカリ処理後のチタン表面の微細構造は走査型電子顕微鏡（SEM, Hitachi S-2600, S-4200）および原子間力顕微鏡（AFM, Digital Instruments Nano Scope Ⅲa）で観察し，深さ方向の元素分布はグロー放電発光分光法（GD-OES, Jobin-Yvon JY7500RF）で測定した．電着後のHApの析出状態はSEMを用い析出分布および析出形態を評価し，結晶構造はX線回折法（XRD, Rigaku製MiniFlex）ならびに薄膜X線回折法（TF-XRD，マックサイエンス社製MXP-18AHF22）で同定した．

また，HAp/チタン基板界面の微細構造を観察するために断面観察用試料を収束イオンビーム加工装置（FIB, SSI SMI2050MS）で作製後，透過型電子顕微鏡（TEM, JEOL JEM-2100F）を用いた構造解析に加え，エネルギー分散X線分析（EDS, JEOL JEM-2300T）を用いた組成解析を行った．

3 結果および考察

3・1 硝フッ酸処理したチタン表面におけるHApのカソード電着

チタンの表面処理技術として一般に硝フッ酸を用いた酸洗いやバフ研磨などが知られており[17]，HApをカソード電着によりチタン上にコーティングする際にもその表面の微細構造がHApの析出形態および析出

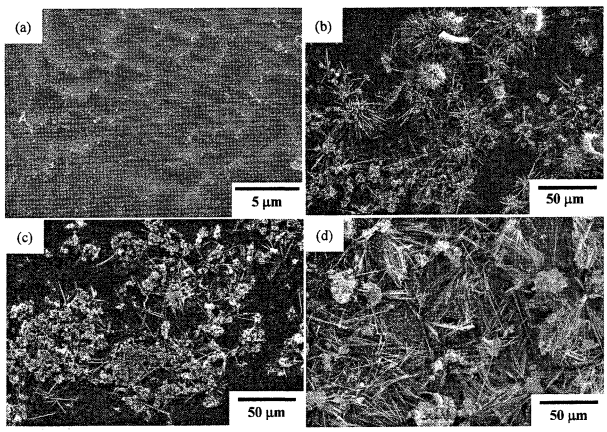

Fig. 1 (a) SEM image of titanium surface after acid treatment in 4 mol·dm^{-3} HNO_3–0.5 mol·dm^{-3} HF solution for 2 min. (b–d) SEM images of acid-treated titanium substrates after electrodeposition for (b) 10 min, (c) 20 min and (d) 60 min.

分布に影響を与えると考えられる．

図1に硝フッ酸処理後のチタン表面および硝フッ酸処理後カソード電着を行った試料の表面SEM像を示す．ここでの前処理は，チタン表面の不純物を除去し平滑性を付与する目的で4 mol·dm^{-3}硝酸－0.5 mol·dm^{-3}フッ酸の混合溶液中にチタン板を2分間浸漬して行った．

硝フッ酸処理後のチタン表面にはエッチングにより生じた2, 3 μm径の凹凸が存在した（図1a）．図1aのSEM像のみ図1b, c, dに比べ高倍率で表示しているが，他の像と同じ倍率で比較すれば巨視的にはほぼ平坦な表面とみなすことができる．

硝フッ酸処理を施したチタン板に対し10分間カソード電着した試料においては，図1bに示したようにチタン表面の一点を中心として放射状に板状の析出物が成長し，同時に板状の析出物の上部に綿毛状の析出物が成長している様子が観察された．カソード電解によるHApの析出は，水素ガス発生による局所的なpH上昇に起因する[18]ことから，図1aに示したチタン表面の微細な凹凸が影響し，チタン基板上の電流の優先的な通過点が核となり電着が開始し，その核を中心として放射状にHApが析出したと考えられる．下地基板が既報[15]のステンレス（SUS304）板とは異なるものの，電解液中のCa/Pモル比をHApにおける化学量論値1.67と一致させた場合においては，基板垂直方向に成長した板状の析出物が観察され，基本的なHApの析出挙動は既報[15]と一致した．しかしながら，硝フッ酸処理を施したチタン板上においては図1c, dに示すように電解時間の経過にともない板状，綿毛状の析出物はともに増加するが，チタン全面をち

密なHAp層で覆うような均一な析出分布ではなかった．

図2に硝フッ酸を用いた化学エッチング後，60分間カソード電着を行った試料のXRDの結果を示す．$2\theta=26°$, 53°付近にHApの(002), (004)面に帰属される相対強度の大きなピークが認められることから，電着で生成したHApはc軸配向性が強いことがわかる．その他にも，$2\theta=30°$～35°付近に検出された(211), (112), (300), (202)面に帰属されるピークに加え，45°～50°付近にもHAp固有の回折ピーク(JCPDS　No. 09-0432)が検出された．

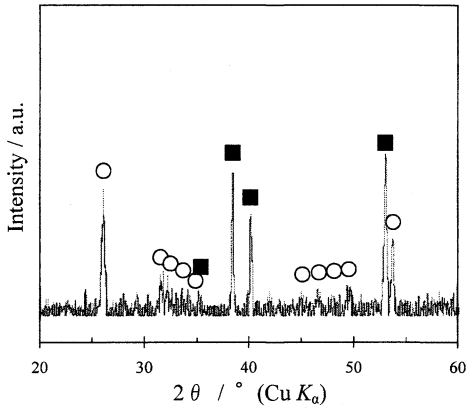

Fig. 2　XRD pattern of HAp deposit after electrodeposition for 60 min on acid-treated titanium.
■: Ti, ○: HAp

図3に硝フッ酸を用いた化学エッチング後，60分間カソード電着を行った試料のFIB断面のTEM観察結果を示す．板状の析出物がチタン基板垂直方向に成長し，板状物質の間げきと上部に細長い繊維状の物質が析出している様子がわかった．図3において板状の析出物Aの部分における電子回折パターンは(002)面の回折スポットを示したことから，板状の析出物は析出直後の状態で結晶性をもつことがわかる．また，同箇所におけるEDSの結果より，Ca/P比は1.11～1.35で1 mol%未満の微量のチタンを含むことがわかった．一方，Bの部分における電子回折パターンはリング状で(211)面および(112)面に帰属され，Aの板状結晶とは析出形態が異なる繊維状の微結晶の集合体であることが確認された．同箇所におけるEDSの結果より，Ca/P比は1.12～1.39であった．図2に示したXRDの結果では析出物はHApと同定されたが，EDSの結果とHApの化学量論値(1.67)を考慮するとA, Bいずれの領域においても，Ca/P比が小さいことから結晶性のHAp以外にCa欠損型HApあるいはCa/P比の小さなリン酸カルシウム(ブラッシャイト：$CaHPO_4 \cdot 2H_2O$，モネタイト：$CaHPO_4$など)の共存の可能性が示唆された．

3・2　チタン表面の微細構造に及ぼすアルカリ処理条件の影響

図4に異なる濃度の水酸化ナトリウム水溶液を用い

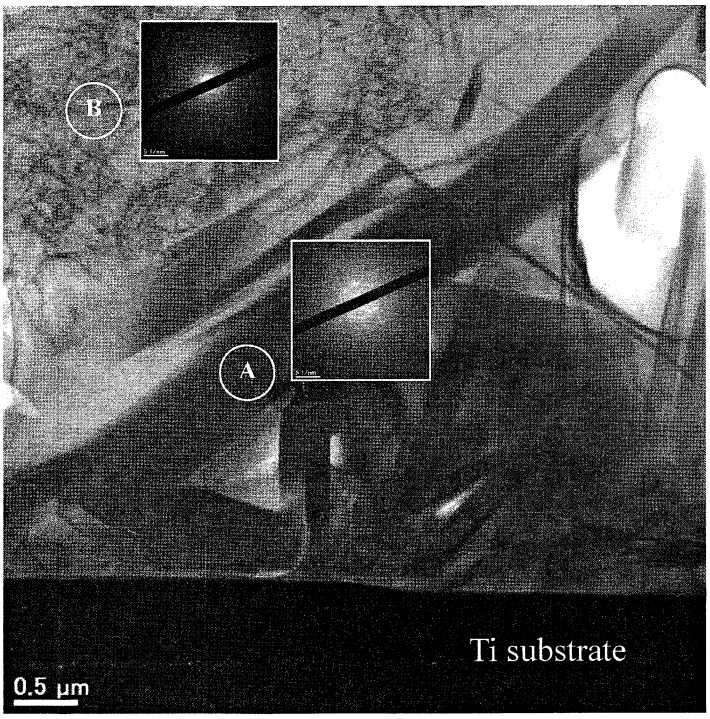

Fig. 3　TEM image and electron diffraction patterns (inset) of HAp deposits after electrodeposition for 60 min on acid-treated titanium.

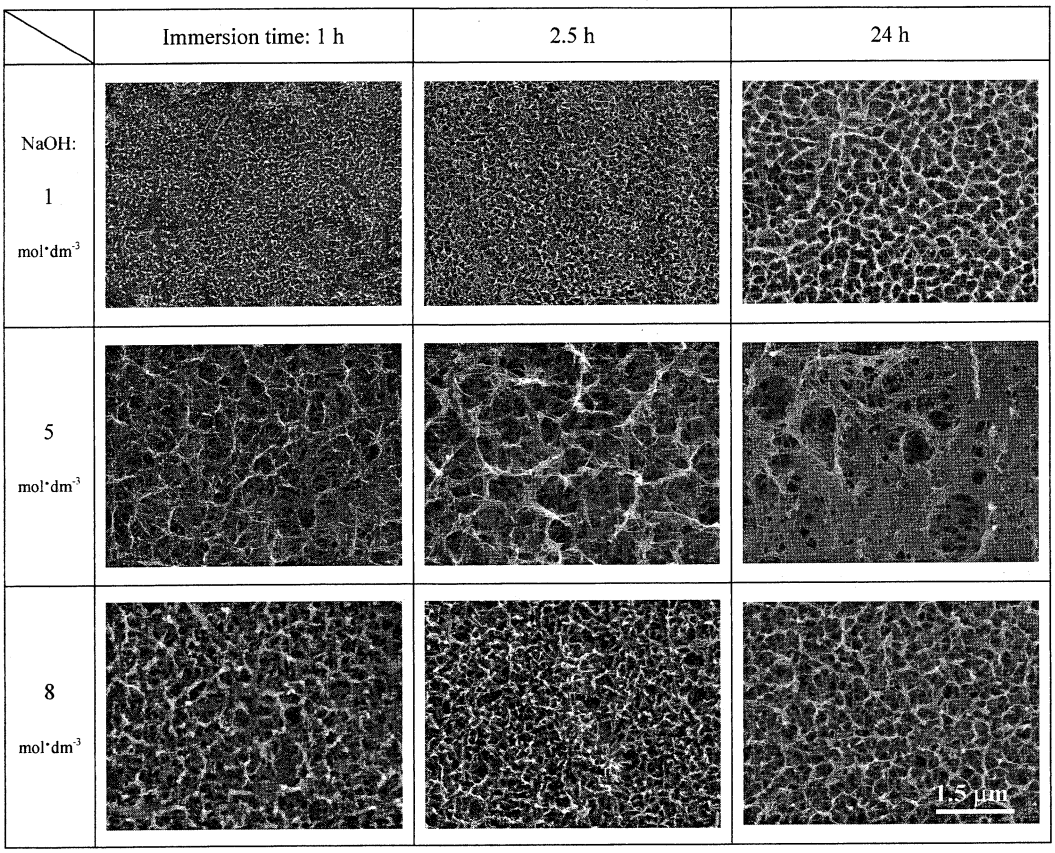

Fig. 4　SEM images of the surfaces of alkali-treated titanium in various conditions.

てアルカリ処理を施したチタン表面の SEM 像を示す．いずれの条件においても数 10 nm から数 100 nm の孔径をもつ網目状の構造がチタン基板上に生成した．5 mol·dm^{-3} NaOH で処理したチタン表面は 1 mol·dm^{-3} NaOH で処理したチタン表面に比べ粗い網目構造であり，処理時間が長くなるにつれチタンの溶解が進み，さらに大きな孔径をもつ粗い網目構造となった．一方，8 mol·dm^{-3} NaOH で処理したチタン表面は 1 mol·dm^{-3} NaOH で処理したチタンの表面形態と似ており，必ずしも高濃度ほど粗い網目構造を形成するわけではなかった．

図 5 に 1 mol·dm^{-3} および 5 mol·dm^{-3} NaOH で 2.5 時間処理したチタン表面の AFM 像を示す．各試料の二乗平均粗さ（*RMS*）と最大谷深さ（R_{max}）は，1 mol·dm^{-3} NaOH での処理で，*RMS*＝43 nm，R_{max}＝530 nm（図 5a），5 mol·dm^{-3} NaOH で処理した場合，*RMS*＝90 nm，R_{max}＝980 nm であり，チタン表面には最大で深さ約 1 μm の網目構造が観察された（図 5b）．

大石ら[10]は，アルカリ処理によってチタン表面に生成した網目構造は，非晶質あるいは結晶性の低い二酸化チタンであり，チタン酸塩や水酸化物としての存在が予想されるナトリウムは検出されないと報告して

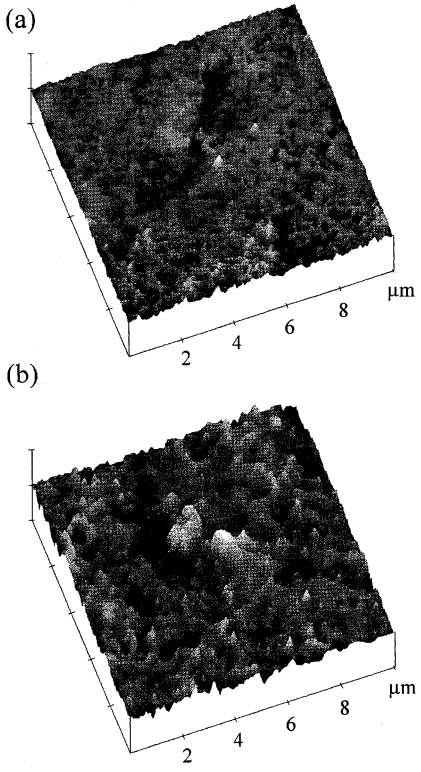

Fig. 5　AFM images of titanium surfaces after alkali treatment for 2.5 h in (a) 1 mol·dm^{-3} NaOH and (b) 5 mol·dm^{-3} NaOH. Scan area was 10 μm square (x, y : 2 μm/div and z : 1 μm/div).

いる．一方，金ら[12]は，5 mol·dm^{-3} NaOH で 24 時間処理したチタン表面の TF-XRD から，チタン表面に非晶質のチタン酸ナトリウム水和ゲル層が生成し，600℃ の熱処理を経てルチル(TiO_2)およびチタン酸ナトリウム($Na_2Ti_5O_{11}$)が生成すると報告している．

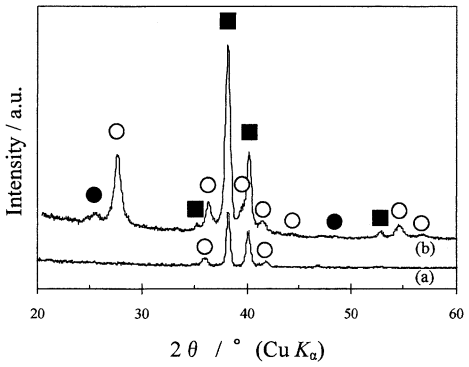

Fig. 6　TF-XRD patterns of alkali-treated titanium (a) before and (b) after heat treatment at 600℃ for 1 h. Alkali treatment was conducted in 5 mol·dm^{-3} NaOH for 2.5 h.
■ : Ti, ○ : TiO_2(rutile), ● : TiO_2(anatase)

図 6 に 5 mol·dm^{-3} NaOH で 2.5 時間処理したチタン基板の TF-XRD による回折スペクトルを示す．筆者らの TF-XRD 結果では，アルカリ処理後の試料ではチタン酸ナトリム由来のピークは検出されず，600℃, 1 時間の熱処理後においてもルチルに加えアナターゼの結晶性ピークがわずかに検出されるのみであった．よって，アルカリ処理後に生成する網目状の構造は，主に非晶質あるいは結晶性の低い二酸化チタンで構成されていると考えられる．一般にアルカリ処理後，熱処理を経て生成するといわれているチタン酸ナトリウムのピークが検出されなかった理由として，本系の場合アルカリ処理時間が 2.5 時間と短く，チタン酸ナトリウム水和ゲル層の生成が少なかったことが考えられる．

図 7 に GD-OES により測定したアルカリ処理後のチタン表面における元素の深さ方向分布を示す．ここでは，NaOH の濃度を 1 と 5 mol·dm^{-3}，処理時間を 1 と 2.5 時間に設定し，4 条件での処理結果を比較した．いずれの条件においても，チタン表面に形成された網目状のチタン酸化物内に XRD では検出できなかったナトリウムの混入が確認された．今回の GD-

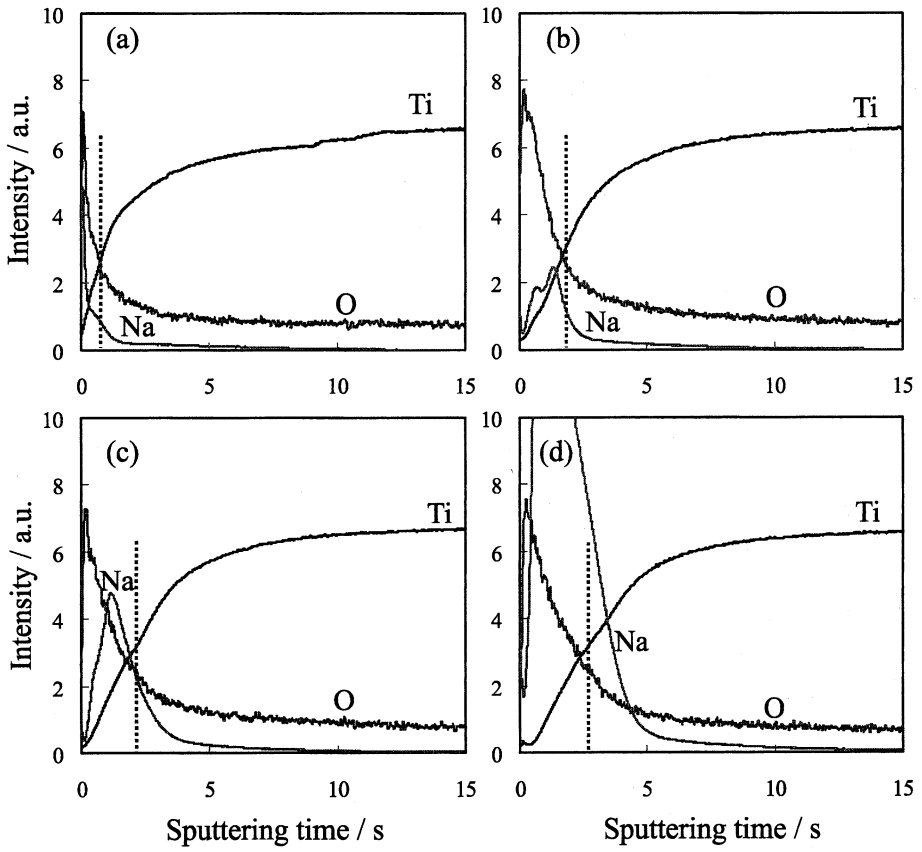

Fig. 7　GD-OES depth profiles of the surfaces of alkali-treated titanium in (a) 1 mol·dm^{-3} NaOH for 1 h, (b) 1 mol·dm^{-3} NaOH for 2.5 h, (c) 5 mol·dm^{-3} NaOH for 1 h, and (d) 5 mol·dm^{-3} NaOH for 2.5 h. Dashed lines indicate the position of interface between porous titanium dioxide layer and titanium substrate.

OES 測定結果では，ナトリウム量を定量的に評価することはできないが，その混入量を相対的に比較すると処理液の濃度が濃いほど，また処理時間が長いほどナトリウムの混入量は増加傾向にあった．図 6 に示した TF-XRD の結果では，チタン酸ナトリウムの存在を確認できなかったが，GD-OES による結果を考慮すると，本系においても非晶質のチタン酸ナトリウム水和ゲル層がチタン酸化物の表面に形成されていると推察される．

また，チタンのプロファイルに着目し，その発光強度が素地に対して 50％まで増加する地点をチタン酸化物層/チタン素地の界面とすれば，チタン酸化物層の厚さを相対的に評価することができる．界面まで到達するに要するスパッタリング時間を相対的な皮膜厚さと考えれば，4 試料の中では 5 mol·dm^{-3} NaOH で 2.5 時間処理した試料(図 7d)が最もチタンの溶解が進行し，厚い網目状のチタン酸化物層を形成したといえる．この結果は前述した図 5 の AFM 観察結果とも一致した．

3・3　アルカリ処理を施したチタン表面における HAp のカソード電着

図 8 に 5 mol·dm^{-3} NaOH で 2.5 時間処理したチタン上に HAp をカソード電着した試料の表面 SEM 像を示す．アルカリ処理は，同電着条件下における予備実験において HAp の析出分布を評価し，最も均一に HAp を析出させることができた 5 mol·dm^{-3} NaOH 中 2.5 時間の浸漬処理を適用した．

図 9 に同試料を 30°傾斜させ斜め観察を行った SEM 像を示す．電解 1 分間の試料では，基板表面を長さの比較的短い特徴的な薄片状の物質が覆っており，電解 10 分間の試料では板状の析出物の上部に綿毛状結晶が析出している様子がわかる．図 9c は析出した HAp 層の割れ目部分を観察した結果であるが，電解 30 分間において基板との界面に厚さ 10～20 μm ほどの比較的ち密な析出層，その上部に板状結晶が垂直方向に成長している様子がわかる．

図 10 にアルカリ処理後，60 分間カソード電着を行

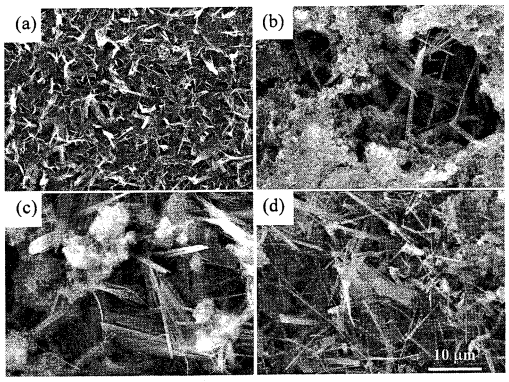

Fig. 8　SEM images of alkali-treated titanium after electrodeposition for (a) 1 min, (b) 10 min, (c) 30 min and (d) 60 min. Alkali treatment was conducted in 5 mol·dm^{-3} NaOH for 2.5 h.

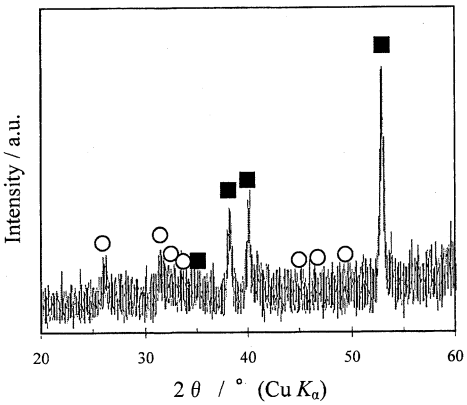

Fig. 10　XRD pattern of HAp deposit after electrodeposition for 60 min on alkali-treated titanium.
■ : Ti, ○ : HAp

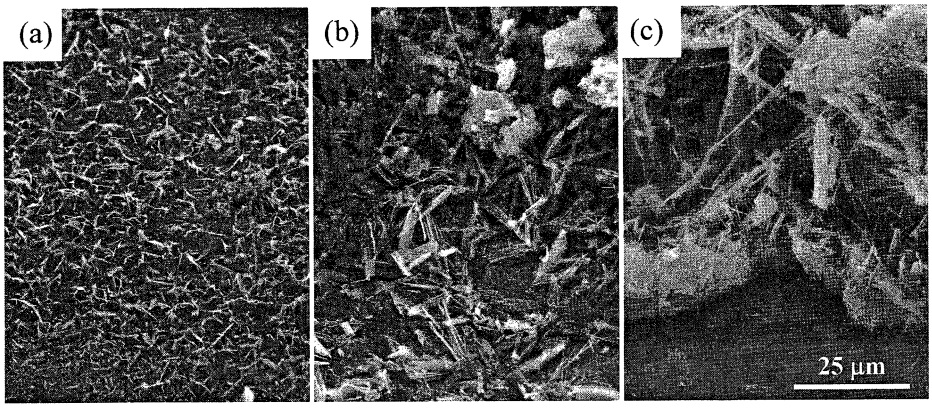

Fig. 9　Tilted (30°) view of the same specimens as those in Fig. 8a–c. Figure 9c was observed at a cleavage in HAp deposit layer.

った試料のXRDの結果を示すが，図2同様，電着によって生成した析出物はHApであった．

アルカリ処理を施したチタン基板は硝フッ酸を用いた化学エッチング後の基板より同一電気量における電解後のHApの析出量が多く，ミクロスパチュラによる簡易的な引っかき試験の結果，アルカリ処理基板上に析出したHAp層は容易にはく離せず，基板との接着性は硝フッ酸処理基板よりも良好であった．また，硝フッ酸を用いた化学エッチング後の基板上では電解初期(電解時間10分間)に放射状の析出物の分散(図1b)が観察されるのに対し，アルカリ処理後の基板上では電解1分間の時点においても密にHApが析出していることがわかる(図8a)．カソード電着によるHAp層の生成は，基板上での水素ガス発生とHApの析出が同時に起こるため，電解の途中でHApのはく離が生じるなど不均一になりやすいといわれている．しかしながら，アルカリ処理により生成した微細でかつ最大1 μmに達する深い網目状チタン酸化物層が予めチタン基板上に存在することで，カソード電着時の水素ガス発生が広範囲に均一分散し，局所的なpHの偏りが抑制された結果，均一なHAp層の形成が実現したと考えられる．

3・4　HAp/チタン基板界面の微細構造

アルカリ処理後のチタン基板とHAp析出層の界面の構造を詳細に観察するため，FIBでTEM断面観察用試料を作製した．**図11**にアルカリ処理後のチタン上に10分間電着した試料をFIBで加工した際の断面走査イオン顕微鏡(SIM)像を示す．チタン基板表面に厚さ500 nm程の網目状チタン酸化物層が存在し，その上部に厚さ5 μmほどの板状結晶が成長している層が観察された．さらにその最表層には白色のコントラストを呈する綿毛状結晶が析出し，チタン上に生成したHAp層の全膜厚は10～15 μmであった．図8に示した表面SEM像からは，深さ方向のHApの析出形態を確認することは困難であったが，FIBによる断面加工を用いることによって，HAp析出層と基板界面の微細構造を詳細に観察することが可能になった．

図12に同試料の断面TEM像を示す．基板表面にアルカリ処理時に形成されたチタン酸化物からなる網目構造が観察され，その網目構造を起点として板状のHApが成長していることがわかった．また電子回折およびEDS分析から以下のことが明らかとなった．

1)　下地チタン基板の網目状層に近い図中Aの部分におけるHApは結晶性を示し，主成分はCa, P, Oで微量のTiを含む．周辺の板状析出物はいずれも結晶性を示し多結晶である．

2)　図中Bの表層側においても図中Aの部分同様に結晶性を示す．Ca, P, Oを主成分とするが基板由来のTiは含まない．

3)　アルカリ処理によって生成した網目構造の図中C点は非晶質でTi, Oを主成分としCa, Pを微量含む．なお，C点のEDSスペクトル中における，Ga, Moのピークはそれぞれ，加工に用いたイオン源ならびに試料ホルダーに起因しており，析出物の組成とは無関係である．

図13に5 mol·dm^{-3} NaOHで2.5時間処理したチタン上にHApを60分間電着した試料の断面SEM像を示す．基板との界面に厚さ10 μmほどの比較的ち密な析出層，その上部に長さ20 μmほどの板状結晶が垂直方向に生成し，最表面には綿毛状結晶が析出している様子が観察された．硝フッ酸で処理したチタン基板を用いた60分間の電着結果(図3)と比較し，アルカリ処理を施したチタン基板ではHApの析出分布が均一化し，基板上にち密な析出層が形成されるのが特徴である．

また，同一電気量の電解において硝フッ酸で処理し

Fig. 11　SIM image of cross section of HAp deposit layer prepared by FIB. Electrodeposition was conducted for 10 min after alkali treatment in 5 mol·dm^{-3} NaOH for 2.5 h.

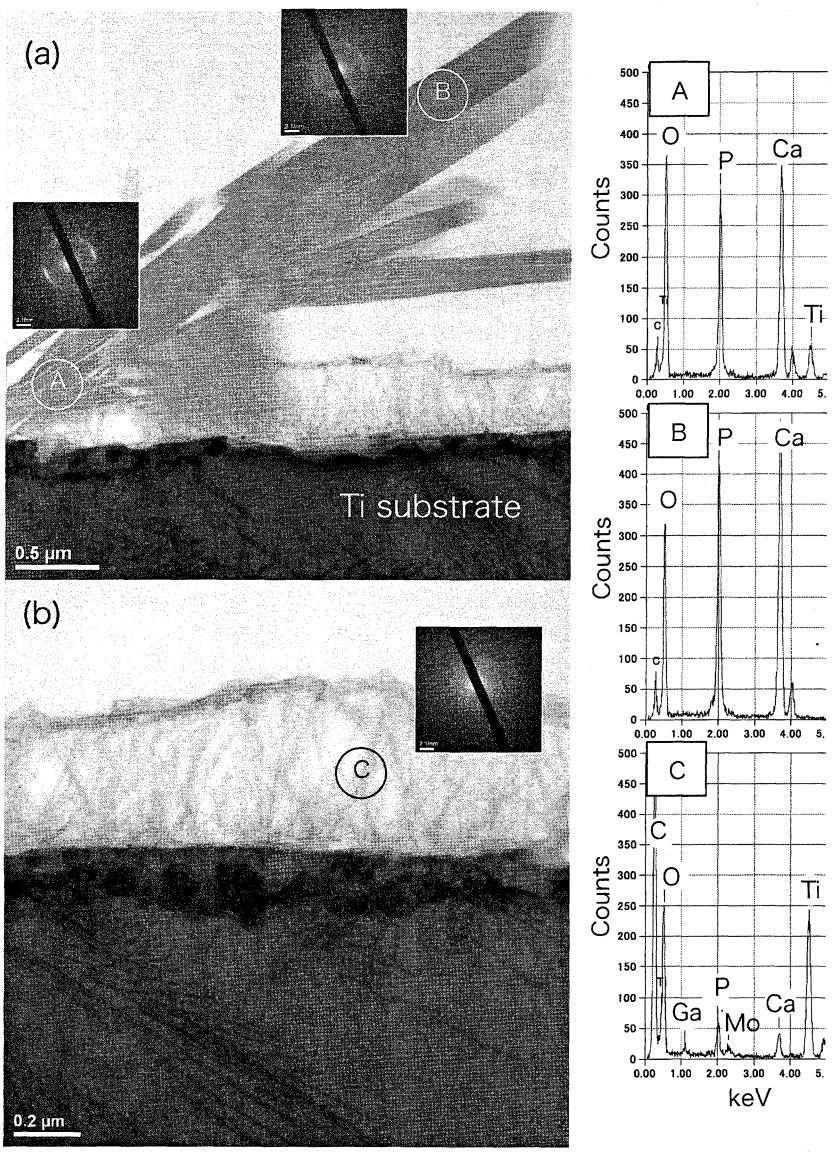

Fig. 12　TEM images, electron diffraction patterns (inset), and typical EDS spectra of HAp deposits after electrodeposition for 10 min on alkali-treated titanium. (a) low-magnification view of cross section of HAp deposit on titanium and (b) high-magnification view of porous network structure. EDS spectra were taken at labeled points in TEM images.

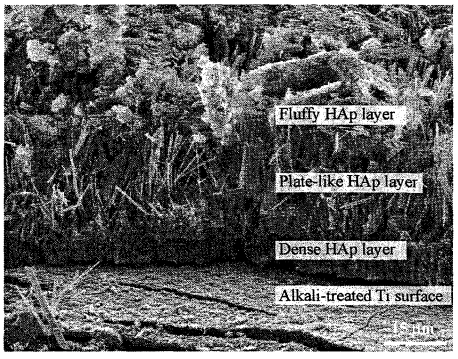

Fig. 13　Fracture section of alkali-treated titanium after electrodeposition for 60 min.

たチタン上に析出したHAp層は，荷重100 gの鉛筆引っかき試験(付着強度測定：JIS K5400)において鉛筆硬度6Bにおいて容易にはく離するのに対し，アルカリ処理を施した試料では，鉛筆硬度6Hでも HAp層のはく離が観察されず，下地基板との接着性が著しく向上した．下地基板に対してHAp層の接着強度が向上した大きな要因として，チタン基板上に生成したチタン酸化物の微細な多孔質構造が挙げられる．本系の場合，網目状酸化物のインターロック構造が，HApの核生成を広範囲に均一分散させ，析出したHApはアンカー効果により網目状酸化物内に強固に固定されたと考えられる．

4 結　　論

アルカリ処理を施したチタン基板の表面形態とカソード電着によるHApの析出挙動の関係について，硝フッ酸処理を施したチタン基板上での電着挙動との比較を通じて以下の結論を得た．

1) 硝フッ酸で処理した比較的平坦な表面を持つチタン上でのカソード電着では，局所的な水素ガス発生に起因し放射状に板状結晶が成長し，その析出分布は不均一である．また，析出したHAp層とチタン基板との密着性は低く引っかき試験において容易にはく離する．

2) アルカリ処理によって生成する微細な網目構造の孔径や深さは，処理液の濃度，浸漬時間に依存し，5 mol·dm^{-3} NaOHで2.5時間処理したチタン表面には最大で深さ約1 μmの網目構造が生成する．網目構造は主に非晶質あるいは結晶性の低い二酸化チタンで構成され，表層付近には非晶質のチタン酸ナトリウム水和ゲル層の存在が示唆される．

3) アルカリ処理を施したチタン基板に対してカソード電着を行うことで，ち密なHAp析出層がチタン表面に均一に形成される．HApの析出は網目状チタン酸化物層内部を起点とし，板状のHApが基板垂直方向に成長する．析出分布の改善に加え析出量が増加した要因としては，アルカリ処理によって生成した網目状チタン酸化物層を介してカソード電着を行うことで水素ガス発生が広範囲に均一化し局所的なpHの偏りが抑制されたことが挙げられる．

4) HAp析出層と基板との密着性は，網目状チタン酸化物層の微細な多孔質構造に起因して発現するアンカー効果によって著しく向上する．

謝　辞

本研究の一部は，軽金属奨学会教育研究資金，科学研究費補助金(基盤B)，文部科学省私立大学学術研究高度化推進事業の助成を受けて行われた．

文　　献

1) 新家光雄，金属，**73**, 448–453 (2003).
2) 塙　隆夫，軽金属，**55**, 553–556 (2005).
3) 成島尚之，軽金属，**55**, 561–565 (2005).
4) 興戸正純，まてりあ，**44**, 808–811 (2005).
5) 清武篤嗣，阿相英孝，小野幸子，古高　圭，門間英毅，“無機マテリアル学会第109回学術講演会講演要旨集”，(2004) p. 4.
6) 小野幸子，柴田稚子，阿相英孝，“無機マテリアル学会第112回学術講演会講演要旨集”，(2006) p. 76.
7) 小野幸子，阿相英孝，“無機マテリアル学会第113回学術講演会講演要旨集”，(2006) p. 48.
8) 阿相英孝，小野幸子，“無機マテリアル学会第114回学術講演会講演要旨集”，(2007) p. 6.
9) 小野幸子，児玉アニタ，阿相英孝，軽金属(印刷中)．
10) 大石哲雄，松原孝治，片桐　晃，*Electrochem.*, **68**, 106–111 (2000).
11) H. M. Kim, F. Miyaji, T. Kokubo, T. Nakamura, *J. Mater. Sci.: Mater. Med.*, **8**, 341–347 (1997).
12) 金　鉉敏，宮路史明，小久保　正，日本金属学会誌，**62**, 1102–1107 (1998).
13) S. Nishiguchi, T. Nakamura, M. Kobayashi, H. M. Kim, F. Miyaji, T. Kokubo, *Biomater.*, **20**, 491–500 (1999).
14) 李　敏鎬，朴　炯鎬，金　炳日，日本金属学会誌，**64**, 578–583(2000).
15) 久森紀之，丸山裕治，高井健一，材料，**53**, 101–107 (2004).
16) M. Murayama, T. Ogata, N. Katoh, K. Kuwabara, *J. Soc. Inorg. Mater. Japan*, **11**, 119–124 (2004).
17) 屋敷貴司，上窪文生，軽金属，**50**, 577–583 (2000).
18) H. Monma, *J. Soc. Inorg. Mater. Japan*, **8**, 491–497 (2001).

特集号：研究論文

軽金属　第58巻 第11号（2008），593–598

球状チタン焼結体で構成された多孔体電極への水酸アパタイトの電着挙動

小野　幸子*・児玉　アニタ*・阿相　英孝*

Journal of Japan Institute of Light Metals, Vol. 58, No. 11 (2008), pp. 593–598

Electrodeposition behavior of hydroxyapatite on porous electrode composed of sintered titanium spheres

Sachiko ONO*, Anita KODAMA* and Hidetaka ASOH*

Electrodeposition of HAp on a porous electrode of sintered titanium spheres has been studied. It took place only at the outer surfaces, but not at the inside of the porous electrode if the maximum size of spheres was 150 μm or lower. It is caused by the intricate fine structure of the electrodes composed of micro-sized titanium particles, which prevents the uniform current flow at the entire titanium surface. However, by applying pretreatments on titanium spheres electrode, deposition of HAp was remarkably improved in the following order; anodic film formation at 10 V<anodic breakdown film at 110 V<alkali treatment in NaOH. This is explicable by the addition of uniform resistance to titanium sphere surfaces at both outside and inside of the electrode, which originates from roughly structured oxide layers. As a result, uniform current flow followed by uniform hydrogen gas evolution at the entire titanium surface was induced. Furthermore, when electrolysis was performed under ultrasonic wave in addition to the oxide layer formation, electrodeposition of HAp at the inside of the electrode was dramatically improved to fulfill the space among titanium spheres. The vibration of ultrasonic wave acted an important roll to activate the evolved hydrogen gas to enhance ion migration and convection of the electrolyte. Thus, high controllability of HAp deposition on porous titanium could be attained.

(Received May 7, 2008　Accepted July 30, 2008)

Keywords: *electrodeposition, hydroxyapatite, sintered titanium spheres, porous titanium, titanium oxide layer*

1. 緒　　言

医・歯学の医療分野で水酸アパタイト $Ca_{10}(PO_4)_6(OH)_2$（HAp）の優れた生体親和性が注目され，種々の機能・特性を持つ材料との複合化が検討されている。中でもチタン系合金は耐食性に優れ高比強度であることから，人工骨や人工関節などの医用材料として用いられ，HAp コーティングに関する研究例は近年著しく増加している[1)~6)]。医用金属材料が生体内で長期間安定に存在し，生体骨との結合を強固に維持するためには，金属表面に生体活性化を促す処理が必要である。チタン系合金の場合には前処理としてアルカリ浸漬とその後の加熱処理を施すことで表面に活性層を付与し，擬似体液中でのアパタイト形成能が改善できることが知られている[7)]。著者らはこれまでに比較的簡便な手法でアパタイト付与が可能なカソード電解による電解析出（電着法）を用い，チタン基板上への HAp の電着に対する電解条件と素地表面形態の影響を検討してきた[8),9)]。その結果，平滑なチタン表面に比べアルカリ処理等で凹凸構造を持つ酸化物層を付与したチタン基板において HAp の電解析出が顕著に促進され，析出分布・接着強度が改善されることを析出形態と構造解析結果により明らかにした[9),10)]。

最近，チタン板より比表面積が大きく人体骨と同程度の低ヤング率・高強度を持つ真球状チタン粉末の焼結体を生体内で使用することが注目されている[11),12)]。また，インプラント材としてのポーラスチタンに対する擬似体液中での骨伝導性や機械強度の検討が行われ，多孔体中においてはより効果的な HAp 成長が進行すると報告されている[13),14)]。しかし，多孔体としての複雑な構造を持つチタン焼結体に対しては，高度な骨親和性を付与するための HAp コーティング条件を詳細に探索する必要がある。ポーラスチタンに対する電着法によるアパタイト付与に関する報告は少なく[15),16)]，またチタン多孔体の外部と微細な孔内部での析出形態や析出量の違いも十分検討されていない。多孔体電極において，電着法を用いることで HAp 成長を複雑な形態内で均一に制御して付与できれば，その後の生体内での骨伝導性を改善するとともに，骨との密着性をより強固にすることが可能であろう。本研究では，電着法を用いたチタン多孔体中への HAp の析出挙動を基礎的に明らかにし，析出分布の向上と析出量の制御を可能にすることを目的とした。

2. 実 験 方 法

基板として用いた真球状チタン焼結体である多孔体電極は，

* 工学院大学工学部応用化学科（〒192–0015　東京都八王子市中野町2665–1）。Department of Applied Chemistry, Faculty of Engineering, Kogakuin University (2665–1 Nakano-cho, Hachioji, Tokyo 192–0015).

㈱大阪チタニウムテクノロジーズ製の商品名タイポラス-45, -150, および -250（T-45, T-150, T-250 とそれぞれ表記するが数字部分は最大粒径の μm 表示で，電極厚さは 0.5 mm）を用いた。空孔率はそれぞれ，37±5%, 45±5%, 50±5%，表面積は 0.07 $m^2 g^{-1}$, 0.025 $m^2 g^{-1}$, 0.01 $m^2 g^{-1}$ である。

チタン多孔体電極の前処理として，①アルカリ処理あるいは②アノード酸化皮膜の付与を行った。①では 5 mol dm^{-3} 水酸化ナトリウム水溶液（60°C）中に 60 分浸漬した。②では 0.1 mol dm^{-3} りん酸電解液（20°C）中，電流密度 50 A m^{-2} で定電流電解した。アノード酸化では，電圧が 10 V あるいは絶縁破壊電圧である 100 V にそれぞれ達した後，定電圧で 10 分間アノード酸化を行った。HAp の電着は既報を参照し[17),18)]，0.03 mol dm^{-3} 硝酸カルシウム四水和物 −0.03 mol dm^{-3} りん酸水素二アンモニウム混合溶液（Ca/P=1.67, 80°C, pH4 付近）を電解液とし，ステンレス対極を用いて電流密度 10 Am^{-2} の定電流カソード電解を 1 時間行った。電流密度はチタン球状粒子の実表面積を考慮して決定した。また，HAp の析出分布の改善を目的とし，超音波（40 kHz）下での電着を試みた。電着前後のチタン（Ti）多孔体電極試料は，表面および破断面の SEM 観察および薄膜 X 線回折（XRD）による析出物の同定を行った。

3. 結果および考察

3. 1 粒径の異なるチタン焼結体における HAp 電着挙動

初めに，電解処理前の粒径の異なる 3 種のチタン多孔体電極表面の SEM 像を **Fig. 1** に示す。真球に近いチタンが焼結により相互に連結しており，最大球径が大きいほどチタン球の間隙サイズも大きくなる。真球状粉末の焼結体であるため間隙部はほぼ均一に分散し，空隙間の平均孔径は T-150 の場合で約 25 μm である。3 種のチタン多孔体電極に対し，HAp 電着のためにカソード電解を行った後の電極試料の破断面 SEM 像を **Fig. 2** に示す。粒径が大きく間隙部も大きな T-250 では，矢印で示す上下両表面側（Fig. 2a）に加え電極内部（Fig. 2b）にもチタン球を包み込むように HAp が析出した。なお，Fig. 2b と 2d 中に矢印 A で示した部分は焼結粒子の連結部が破断した面であり，図中の点線は多孔体内部の観察部位を示す。

一方，T-150 の場合（Fig. 2c），電極内部への HAp の析出は見られず，電極の両表面付近にのみ析出した。この原因は粒子間隙部の空間が T-250 に比べ微細なためであり，電極構造に起因した電流分布の偏りやイオン拡散の不均一性に依存すると考えられる。Fig. 2c 中の挿入図は電極表面における HAp 電着層の SEM 像であるが，HAp の析出形態はチタン平板基板上において同条件下で電解析出した HAp の形態と同様に

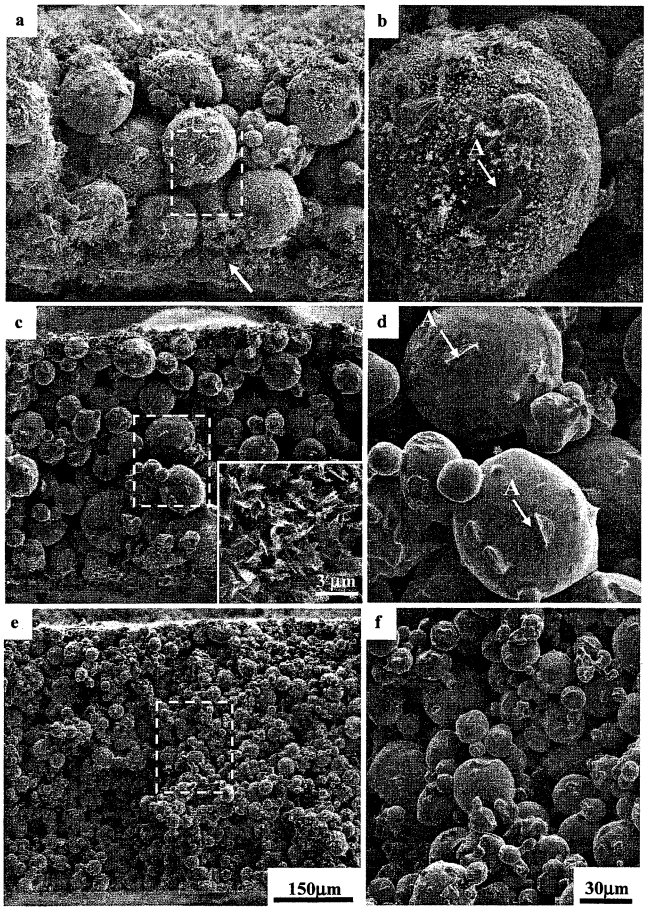

Fig. 2 SEM images of fracture section of titanium porous electrodes after electrodeposition at 10 Am^{-2} for 60 min at 80°C. (a) T-250, (c) T-150 with inset of top view, (e) T-45, (b, d, f) Magnified views of the center of each specimens marked by square dots line. Arrows in (a) indicate electrode surfaces. Arrows A indicate fractured connecting points of Ti spheres.

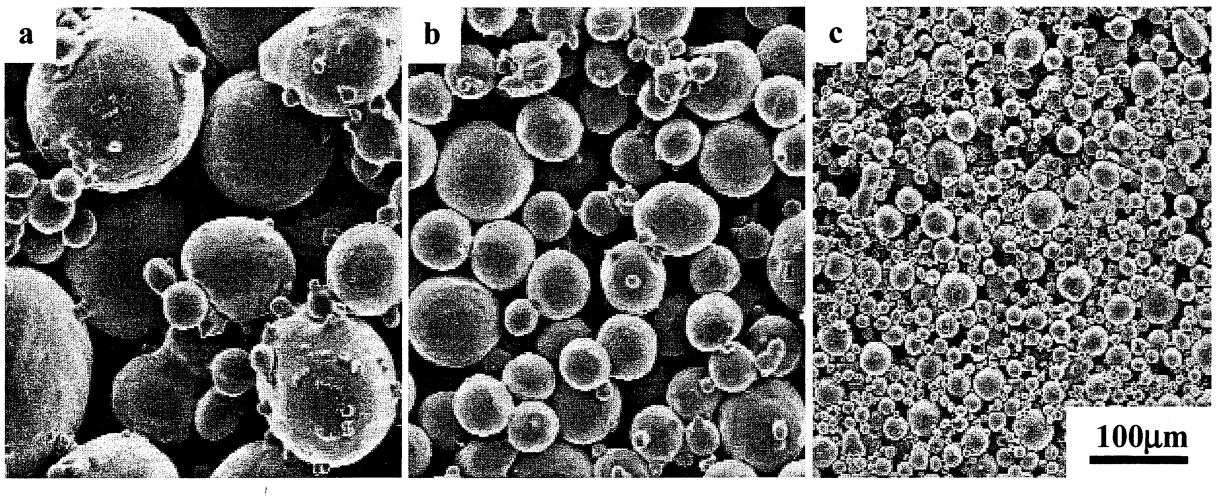

Fig. 1 SEM images of sintered spherical titanium specimens. (a) T-250, (b) T-150, (c) T-45.

板状であった。また，Fig. 2 (e, f) に示されるように，T-45 もT-150と同様な結果で，析出は両表面のみに限定され内部への析出は観察されなかった。

HApのカソード電着メカニズムは門間ら[17]の考察を参照し，以下の式で説明される。

$$H_2O+e^- \rightarrow 1/2H_2\uparrow+OH^-$$

$$H_2PO_4^-+OH^- \rightarrow HPO_4^{2-}+H_2O$$

$$10Ca^{2+}+6HPO_4^{2-}+2OH^- \rightarrow [HAp]\downarrow+6H^+$$

$$6H^++6e^- \rightarrow 3H_2\uparrow$$

カソード電極上で起こる水素発生に伴い，電極近傍は OH^- イオンの増加によってアルカリ性に傾き，HApの析出に至る。したがって，水素ガス発生が素地全表面で均一に進行することが均一な電着を導くために重要である。

3.2 チタン焼結体に施す前処理がHAp析出に与える効果

電極内部へのHAp析出の改善を目的とし，アノード酸化皮膜を① 10 V あるいは② 110 V まで付与するか，③アルカリ処理を行った。これらの処理後にT-150の表面形態を観察した結果を **Fig. 3** に示す。10 V でのアノード酸化後のチタン球表面 (Fig. 3a) はほぼ平滑であったが，110 V では絶縁破壊のため，顕著な凹凸構造がチタン球表面に生成した (Fig. 3b)。これはアナターゼ型 TiO_2 結晶とボイドを含む厚さ 150 nm 程度のアノード酸化皮膜層である。アルカリ処理の場合はチタン球表面に網目構造が観察される (Fig. 3c)。既報[9),10)]に述べたように，XRD解析の結果よりこの厚さ 500 nm 程度の粗い網状の層からは結晶性の低いルチル型 TiO_2 が検出され，600°C での加熱後はアナターゼ型も検出された。しかしKim[7)]らの報告にあるようなチタン酸ナトリウムなどに相当するピークは検出されなかった。

これらの前処理を施したチタン多孔体電極にHAp電着を行った結果を **Fig. 4** に示す。あらかじめ 10 V のアノード酸

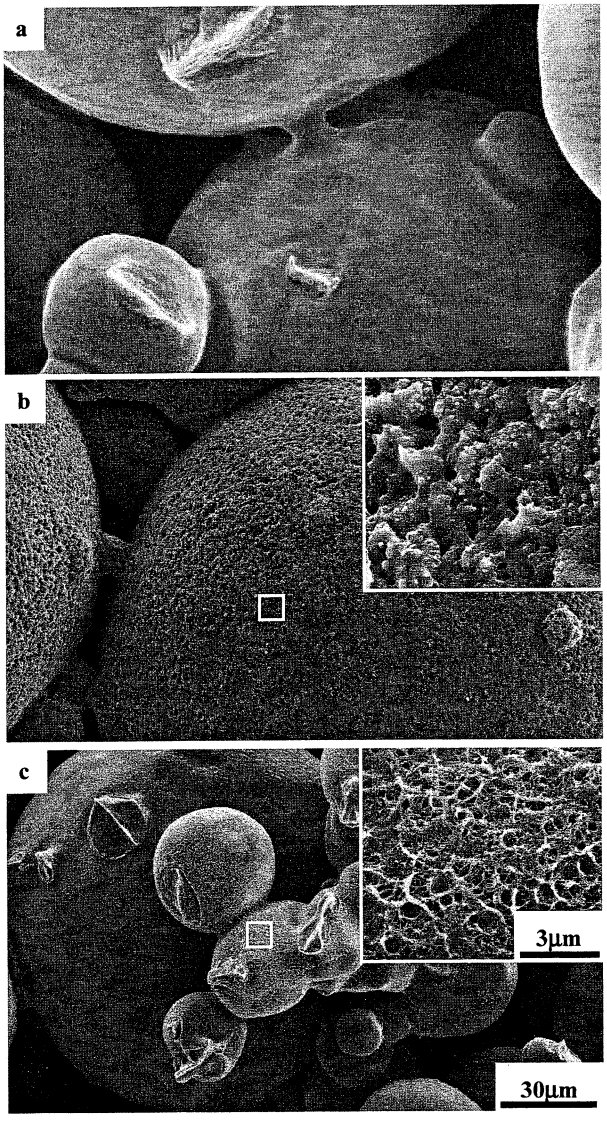

Fig. 3 SEM images of Ti sphere surfaces of T-150 after different pretreatments. (a) Anodizing in phosphoric acid at 10 V, (b) anodizing in phosphoric acid at breakdown voltage of 110 V and (c) alkali treatment in 5 mol dm^{-3} NaOH for 60 min at 60°C. Insets show magnified images of Ti surfaces marked by square lines.

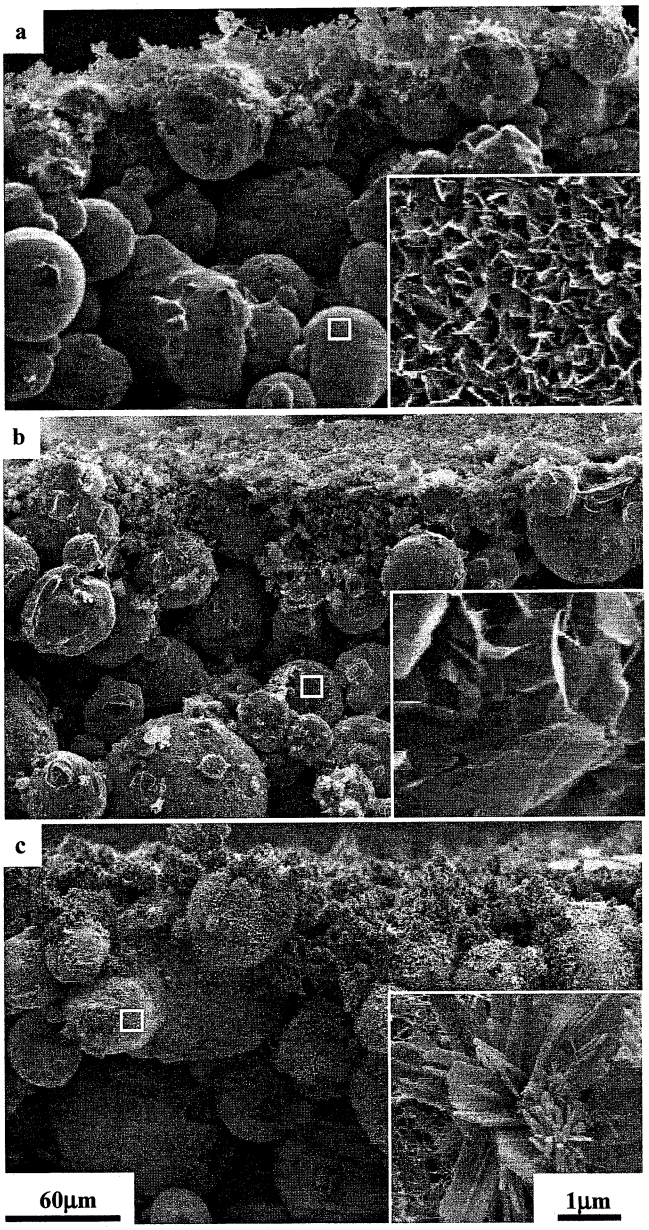

Fig. 4 Fracture sections of differently pretreated T-150 after electrodeposition of HAp. (a) Anodizing in phosphoric acid at 10 V, (b) at breakdown voltage of 110 V and (c) alkali treatment. Insets show magnified views indicated by square lines.

化皮膜を付与した場合，チタン球表面に薄片状のアパタイト析出が観察された（Fig. 4a)。この薄片状HApのひらひらした形態は，チタン平板での電着の初期に，板状HApの析出に先立って観察される構造と類似していた[10]。一方，110Vで絶縁破壊皮膜を付与した試料に電着を行った場合は，Fig. 4bに示すようにチタン球表面への薄片状アパタイト析出と同時に，電極内部のチタン球表面を包むような析出も観察された。Fig. 4cに示すアルカリ処理を施した電極への電着の場合は，内部チタン球表面に板状のHApが析出し，電極内部の空隙部への析出もさらに進行した。このように，多孔体内部への析出の促進効果は，チタン酸化物が粗なポーラス構造を持つほど高かった。

HApの析出はチタン平板であっても下地基板表面の微細構造に強く影響され，アノード酸化皮膜の付与やアルカリ処理によって顕著に促進される効果を持つ[8)~10)]。多孔体電極においてはさらに，球状チタンの全表面に付与した上記の酸化皮膜の均一で適度な抵抗の効果によって，電極表面側のみへの電流の集中が抑制されたと考えられる。しかし，アルカリ処理を施し電着を行った結果においても，チタン焼結体内部空間へのHApの析出は十分とは言えなかった。

3.3 超音波処理がチタン多孔体電極内部への析出に与える効果

電極構造に起因する電着時の表面側への電流の偏りを，チタン球表面にチタン酸化物を生成させることで抑制できたが，多孔体内部の空隙部を埋めチタン球を完全に覆うほどHApは成長しなかった。これは電着時の多孔体表面と内部での水素発生の均一化が不十分なためと考えられる。この点の改善を目的とし，超音波発生装置内での電着を試みた。

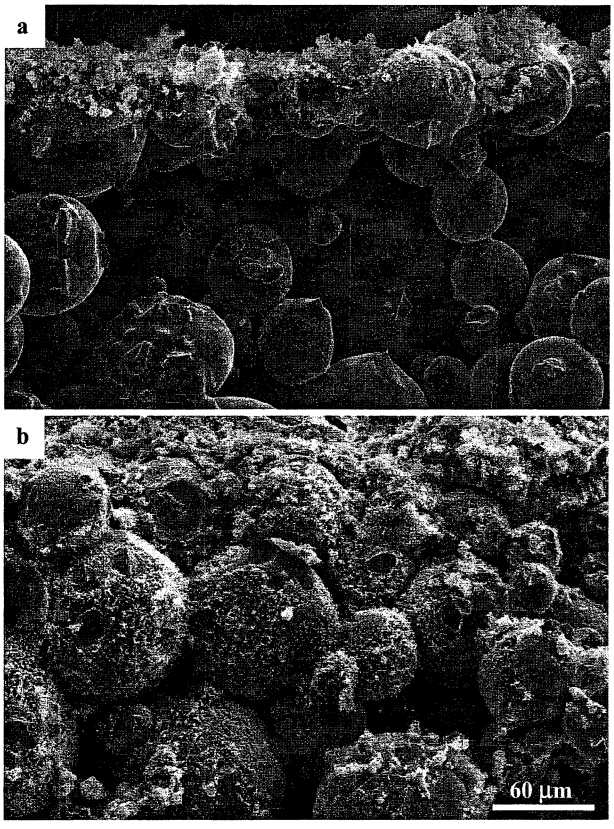

Fig. 5 Fracture sections of T-150 after electrodeposition. (a) Without and (b) with ultrasonic wave at 40 kHz.

まず初めに，前処理を施していないチタン焼結体電極へのカソード電解を超音波装置内で行った。超音波処理を施さない場合は，**Fig. 5a**に示すようにHAp電着は電極の外表面のみで進行し，内部への析出はまったく見られなかった。一方，超音波処理を施した場合，Fig. 5bに示すように，電極外部ばかりでなく内部の空隙にもチタン球を包むようにかなりのHAp電着が観察された。超音波がチタン球表面での水素ガス発生の効率化と均一化を促進すると同時に，電解液すなわちイオンの拡散を高める結果となり，前処理なしでもHAp電着を多孔体内部で十分進行させることが可能になったと考えられる。

次に，前処理を施したチタン焼結体電極に対して超音波装置内でカソード電解を行った。アノード酸化で10Vの皮膜を付与した場合と，110Vで絶縁破壊皮膜を付与した場合の結果を**Fig. 6a**およびFig. 6bに示す。アノード酸化皮膜を付与することで，チタン多孔体電極内部に相当量のHAp析出が進行し，Fig. 5bに示した前処理なしの試料への超音波併用の結果と比較すると，電着の均一化が顕著に改善されたことがわかる。特に絶縁破壊皮膜を付与した場合は，多孔体内部空間でのHAp電着量が増加し，チタン球の間隙を埋めるように析出した。

前処理としてアルカリ処理を施した場合の超音波装置内での電着後の破断面SEM像を**Fig. 7**に示す。HAp電着量はさらに増加し，チタン多孔体電極の空隙はほとんど隙間なく埋められた。チタン球上の電着層を高倍率でSEM観察した結果をFig. 7b,cに示すが，析出物はチタン球面に垂直に成長し

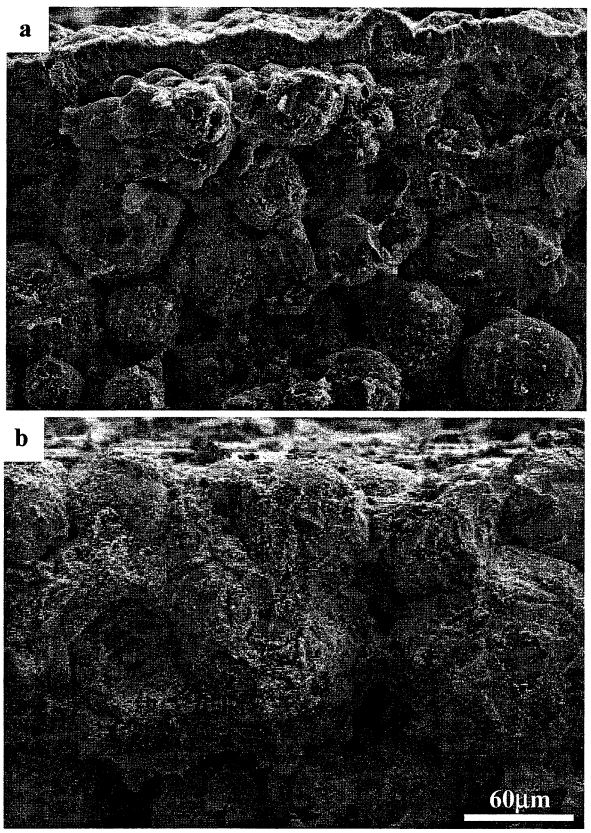

Fig. 6 Fracture sections of pretreated T-150 after electrodeposition of HAp under ultrasonic wave at 40 kHz. (a) Anodizing in phosphoric acid at 10 V and (b) at breakdown voltage of 110 V.

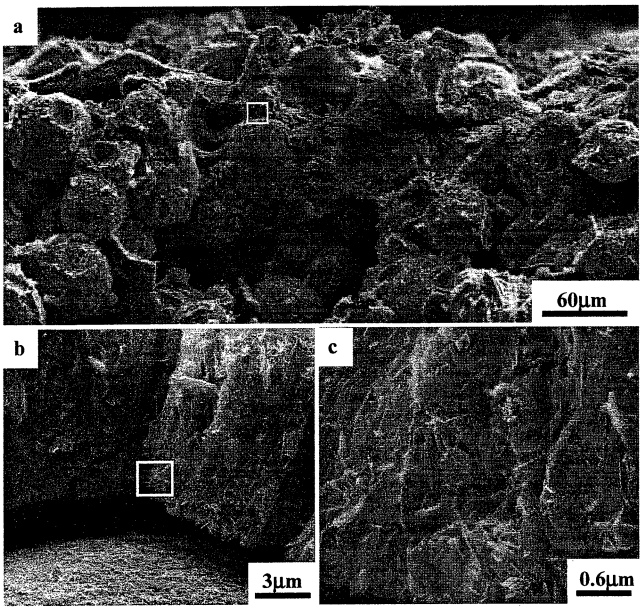

Fig. 7 SEM images of alkali-treated T-150 after electrodeposition under ultrasonic wave at 40 kHz. (a) Fracture section and (b, c) magnified images of HAp deposits indicated by square lines.

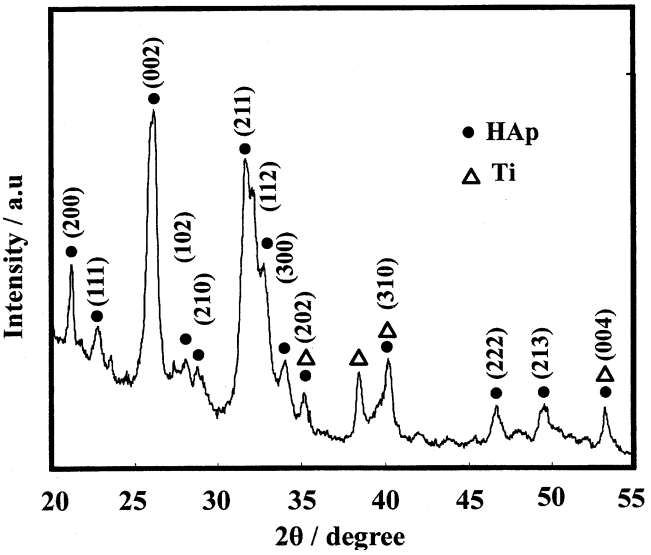

Fig. 8 TF-XRD pattern and identification of alkali-treated T-150 after electrodeposition under ultrasonic wave.

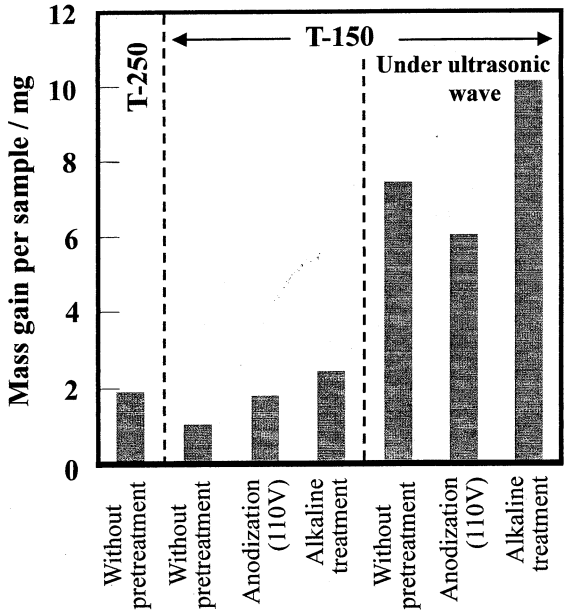

Fig. 9 Average mass gain of differently pretreated T-150 and T-250 after electrodeposition with and without ultrasonic wave.

た板状 HAp が極めて緻密に重なって形成されていることが明らかになった。なお，T-45 においても，アルカリ処理と超音波処理を施した場合はチタン粒子の間隙をほぼ完全に埋めて HAp が析出した。

アルカリ処理と超音波を併用して電着を行って得られた試料の薄膜 XRD による回折スペクトルと解析結果を **Fig. 8** に示す。電着物の回折スペクトルは JCPDS (09-0432) とよく一致し，水酸アパタイト $Ca_{10}(PO_4)_6(OH)_2$ と同定された。各面のピーク強度の比較から，(002) 面の回折強度が高く，c 軸配向性が強いことがわかる。

電着後の電極試料 1 個あたりの平均質量増加を測定した結果を **Fig. 9** に示す。この質量増加は電極表面と内部を合せた全 HAp 電着量に相当する。チタン球のサイズが 250 μm と大きい方が 150 μm より電着量が多いのは，間隙部の空間が大きく内部にも析出するためである。また前処理なしに比較し，絶縁破壊アノード酸化 (110 V)，アルカリ処理の順に電着量が増加した。さらに，超音波照射下で電解を行うと顕著に電着が促進された。超音波処理下でのチタン前処理なしの場合が絶縁破壊処理の場合より電着量が多くなった理由は明らかでないが，これらの測定結果は破断面の SEM 観察からの推測とおおよそ一致している。

3.4 チタン多孔体電極内部におけるアパタイト電着の促進メカニズム

本研究で用いた球状焼結体粉末のような複雑な電極構造を持つ場合，電極構造に依存した溶液抵抗の増加や電解液の対流の妨害，イオン拡散の抑制が生じることが予測される。その結果，電流は電極外表面に優先的に流れ，カソード反応としての水素ガス発生が均一に生起せず，多孔体外表面のみで電着が進行するであろう。T-250 においての結果は，そのチタン粒子の間隙が上記のような阻害を起こさないために十分な大きさであったことを示している。T-150 以下のチタン球のサイズにおいては，いずれもチタン球の全表面にアノード酸化，あるいはアルカリ処理で多孔質構造を持つチタン酸化物皮膜を付与することで，多孔体内部にも電着が可能になった。この原因は，上記の酸化皮膜の均一で適度な抵抗の効果によって，電極表面への電流の過度な集中が抑制されたためと考えられる。付与された酸化皮膜は，電極外表面において内部より成長が促進されるため，酸化物としての抵抗はより高くなると考えられ，結果として多孔体電極内部への電流通過が促されるであろう。その効果は，アルカリ処理で生成した網目状のチタン酸化物皮膜においてより高いが，微細でかつ 500 nm に達する深い網目状構造[10] が，水素ガスがより分散して発生するために大きな役割を果たすのであろう。

電着中に超音波振動を併用することで電極内部への電着が著しく改善されるメカニズムは，超音波が発生する水素ガス

をより微細化・活性化し，それに伴って電解液中のイオンの拡散が促進され，電解液の対流と濃度の均一化が生起し，結果として電流分布の均一化につながると説明できる。同時に，HAp析出の微細化と緻密化にも寄与しているだろう。したがって，超音波を素地表面構造の改善と併用することで，複雑な多孔体構造を持つチタン焼結体電極内部へのHApの析出分布の大幅な改善を実現できたと考えられる。

実際に生体内部において骨伝導を効果的に進行させるためには，チタン多孔体内部を完全に電着HApで埋める必要はなく，より短時間の電着で十分である。しかし，多孔体内部表面への骨成長への前駆体としての均一で緻密な電着HAp付与は極めて重要な課題であり，本報告で明らかになったチタンの前処理と超音波照射の効果は今後有効な手段として活用されるであろう。

4. 結　　言

微細で複雑な形状を持つ球状チタン焼結体内部への均一なHAp付与を目的とし，カソード電解による電着法でのコーティングを検討した結果，以下の結論を得た。

(1) チタン粒径が250 μmであるT-250では多孔体内部にもHAp電着が可能であったが，T-150およびT-45では微細な電極構造に起因して内部へのHAp析出が阻害され，電極表面のみに電着された。

(2) 電着時の電極表面への電流の偏りは，チタン球の素地表面にアノード酸化皮膜やアルカリ処理によるチタン酸化物を付与することで抑制され，電極内部にHAp電着が進行した。これはチタン表面に適度な酸化物の抵抗を付与し，電流分布（水素ガス発生）を均一化できたためである。その効果は，チタン酸化物がより微細なポーラス構造を持つほど高かった。

(3) 超音波装置内で電着を行うと，多孔体内部への電着が顕著に促進された。超音波が発生する水素ガスをより微細化，活性化し，イオンの拡散や電解液の対流を促進した結果である。

(4) 超音波振動とチタン素地への絶縁破壊アノード酸化皮膜付与やアルカリ処理を併用することで，チタン焼結体内部の間隙を完全に埋める程のHApを付与することが可能になった。

謝　辞

本研究の一部は，財団法人軽金属奨学会教育研究資金，科学研究費補助金（基盤B），文部科学省私立大学学術研究高度化推進事業の助成を受けて行われた。また，ポーラスチタン試料をご提供頂いた㈱大阪チタニウムテクノロジーズの小笠原忠司氏および大西　隆氏に謝意を表する。

参 考 文 献

1) 新家光雄：金属，**73** (2003)，448–453.
2) 塙　隆夫：軽金属，**55** (2005)，553–556.
3) 成島尚之：軽金属，**55** (2005)，561–565.
4) 興戸正純：まてりあ，**44** (2005)，808–811.
5) 青木秀希，矢島龍彦，小山利幸：表面技術，**58** (2007)，744–750.
6) 塙　隆夫，米山隆之：金属バイオマテリアル，コロナ社，(2007).
7) H. M. Kim, F. Miyaji, T. Kokubo and T. Nakamura: J. Mater. Sci., Mater. Med., **8** (1997), 341–347.
8) 小野幸子，阿相英孝：2006年電気化学会秋季大会講演要旨集，(2006)，270.
9) 阿相英孝，川目達也，小野幸子：2007年電気化学会春季大会講演要旨集，(2007)，374.
10) 阿相英孝，小野幸子：無機マテリアル学会第114回学術講演会講演要旨集，(2007)，6–7.
11) 花田修治：粉砕，**49** (2005)，12–21.
12) M. Nakai, M. Niinomi, T. Akahori, H. Yamanoi, S. Ituno, N. Haraguchi, Y. Itoh, T. Ogasawara and T. Onishi: Funtai oyobi Funmatsu Yakin, **55** (2008), 312–317.
13) M. Takemoto, S. Fujibayashi, M. Neo, J. Suzuki, T. Kokubo and T. Nakamura: Biomaterials, **26** (2005), 6014–6023.
14) B. Otsuki, M. Takemoto, S. Fujibayashi, M. Neo, T. Kokubo and T. Nakamura: Biomaterials, **27** (2006), 5892–5900.
15) D. J. Blackwood, Y. K. Chay, B. R. Chew, H. B. Tan and K. H. W. Seah: Inter. Corros. Cong., Frontiers in Corros. Sci. and Tech., 15th, Granada, Spain, (2002), 384/1–384/8.
16) M. G. Kutty, W. A. Prisbery, S. Bhaduri, J. R. Jokisaari and S. B. Bhaduri: Ceram. Eng. and Sci. Proc., **23** (2002), 745–752.
17) 門間英毅：J. Soc. Inorg. Mater. Jpn., **8** (2001)，491–497.
18) 村山美和，尾形剛志，加藤中英，桑原勝美：J. Soc. Inorg. Mater. Japan, **11** (2004)，119–124.

Abstract

Volume 16, Issue 3
214th ECS Meeting, October 12 - October 17, 2008, Honolulu, HI
Porous Semiconductors: A Symposium Held in Memory of Vitali Parhutik and Volker Lehmann
Editor(s): P. Schmuki, H. Foell, U. Goesele, J. Kelly, D. Lockwood, Y. Ogata

Fabrication of Self-Organized Nanoporous Oxide Semiconductors by Anodization

Sachiko Ono, Yuta Kobayashi, Ryohei Kobayashi, and Hidetaka Asoh
Kogakuin Univeristy

Self-organized nanoporous semiconductors such as ZnO and SnO2 having high aspect ratio was prepared by a simple, high throughput and non-costly wet electrochemical process without use of catalyst. By using anodization of metal plate of zinc in sodium hydroxide solution, tubular oxide with a pore interval of 10-20 nm and the thickness up to several ten microns was obtained. Photocatalytic activity of anodic film on zinc was improved by increasing annealing temperature up to 400 oC associated with increasing crystallinity, although the specific surface area of the oxide film decreased as a result of decreasing grain size caused by sintering. Anodic film formed on tin in sodium hydroxide solution showed cellular structure with the size of 50 nm consisted of microcrystal and the thickness up to 60 μm in only 1 h. Photo catalytic activity of the anodic SnO2 was ascertained by a methylene blue degradation test under UV irradiation. If sulfuric acid was used as an anodizing electrolyte for tin, a peculiar tubular film composed of mixture of crystalline SnO, SnO2 and Sn3O(OH)2SO4 was found.

doi:10.1149/1.2982575

Abstract

Volume 16, Issue 3
214th ECS Meeting, October 12 - October 17, 2008, Honolulu, HI
Porous Semiconductors: A Symposium Held in Memory of Vitali Parhutik and Volker Lehmann
Editor(s): P. Schmuki, H. Foell, U. Goesele, J. Kelly, D. Lockwood, Y. Ogata

GaAs Microarrays by Noble-Metal Assisted Chemical Etching

Yukiko Yasukawa, Hidetaka Asoh, and Sachiko Ono
Kogakuin Univeristy

Microarrays of n-GaAs were fabricated for both (100) and (111) by colloidal crystal templating, ion sputtering and chemical etching using nanosized Au particles as the etching catalyst. Since self-organized polystyrene spheres were used as a mask, Au particles were selectively deposited at sites resulting in the formation of Au honeycomb pattern on GaAs. Microsized GaAs column arrays were achieved by chemical etching of GaAs, where the honeycomb-patterned Au metals were deposited. Although ordered column structures were obtained for both planes, different anisotropic etching patterns were observed by Au-assisted chemical etching between n-GaAs (100) and (111). The crystal-face orientation strongly affects the etching morphology and the rate of metal-assisted chemical etching.

doi:10.1149/1.2982563

Article Options Go ? View Cart
Full Text: PDF Order

See Also

- GaAs Microarrays by Noble-Metal Assisted Chemical Etching
  Yukiko Yasukawa *et al.*
  Meet. Abstr. - Electrochem. Soc. **802**, 1811 (2008)

Back To Hit List | Previous / Next Document | Issue Table of Contents

IOP PUBLISHING NANOTECHNOLOGY

Nanotechnology **19** (2008) 405304 (6pp) doi:10.1088/0957-4484/19/40/405304

Ordered hexagonal array of Au nanodots on Si substrate based on colloidal crystal templating

S Sakamoto[1], L Philippe[2], M Bechelany[2], J Michler[2], H Asoh[1] and S Ono[1]

[1] Department of Applied Chemistry, Faculty of Engineering, Kogakuin University, 2665-1 Nakano, Hachioji, Tokyo 192-0015, Japan

[2] Swiss Federal Laboratories for Materials Testing and Research (EMPA), Laboratory of Nanostructures and Mechanics, Feuerwerkerstrasse 39, CH-3602 Thun, Switzerland

E-mail: laetitia.philippe@empa.ch

Received 5 May 2008, in final form 11 July 2008
Published 20 August 2008
Online at stacks.iop.org/Nano/19/405304

Abstract

We report two types of site-selective metal deposition methods based on colloidal crystal templating. We discuss in particular the controllability of the morphology and crystallinity of Au nanodots depending of the choice of method.

(Some figures in this article are in colour only in the electronic version)

1. Introduction

Metal nanoparticles and nanodots have been a focus of intense research due to their novel physical properties in reference to their bulk counterparts [1]. In addition, collective properties can arise due to the interactions of the individual nanoparticles in ordered arrays [2, 3]. This is why the control of individual dot properties (with controllable size and shape) and their relative arrangements (density, pattern shape) are crucial [4]. Nanodots patterned in ordered arrays, especially gold nanodots, have been proposed for a wide range of applications, such as magnetic data storage [5–8], optoelectronic devices [9], biosensors [10, 11] and catalysts for the growth of aligned one-dimensional nanostructures [12, 13].

In the past few years many methods have been developed for nanodot array patterning, such as focused ion beam or e-beam lithography [14, 15], molecular beam epitaxy (MBE) [16], chemical vapor deposition (CVD) [17], self-assembly [18, 19] and template-based methods by using porous anodic alumina (PAA) membranes as evaporation masks [20, 21]. However, most fabrication processes mentioned above are not satisfactory due to some drawbacks, such as low throughput, high cost of equipment and low uniformity of the shapes and sizes of dots. Besides these methods, the application using two-dimensional (2D) colloidal crystals, 'natural lithography', which has been proposed by Deckman and Dunsmuir, has attracted attention due to it being a relatively easy process in comparison with conventional lithography [22]. Based on such a process, uniformly sized microstructures could be produced on a substrate using a monolayer coating of colloidal spheres instead of a conventional resist. In recent years, various techniques, which are often called 'colloidal lithography' or 'nanosphere lithography', have been reported on the nano/microfabrication or nano/micropatterning of a wide variety of solid substrates including semiconductors [23], metals [24, 25] and ceramics. In the case of the use of 2D colloidal crystals as a physical mask, however, the target position for lithography is restricted to only interspaces among spheres. For more details on the different strategies for the self-assembly into ordered 2D crystalline arrays and their applications, see the review papers [26, 27].

We reported previously that metal patterns of two different types, that is, network-like honeycomb and isolated-island patterns with ordered periodicities (200 nm–3 μm), were formed on an Si(100) substrate by a combination of colloidal crystal templating, hydrophobic treatment and subsequent site-selective electrodeless deposition [24, 25]. Based on this strategy, it is possible to control the configuration of metal dot arrays by changing the mask structure for metal deposition.

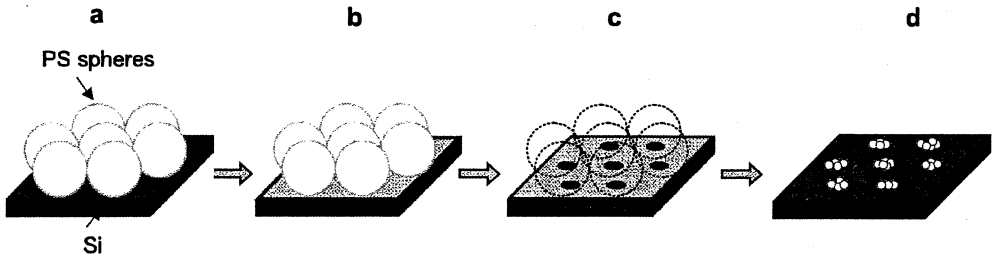

Figure 1. Schematic model of patterning of Au nanodot arrays using hydrophobic treatment for electrodeless deposition: (a) colloidal crystals on Si substrate, (b) colloidal crystals on HMDS-coated Si substrate, (c) HMDS honeycomb mask formed by removal of PS spheres, (d) electrodeless plating through an HMDS mask.

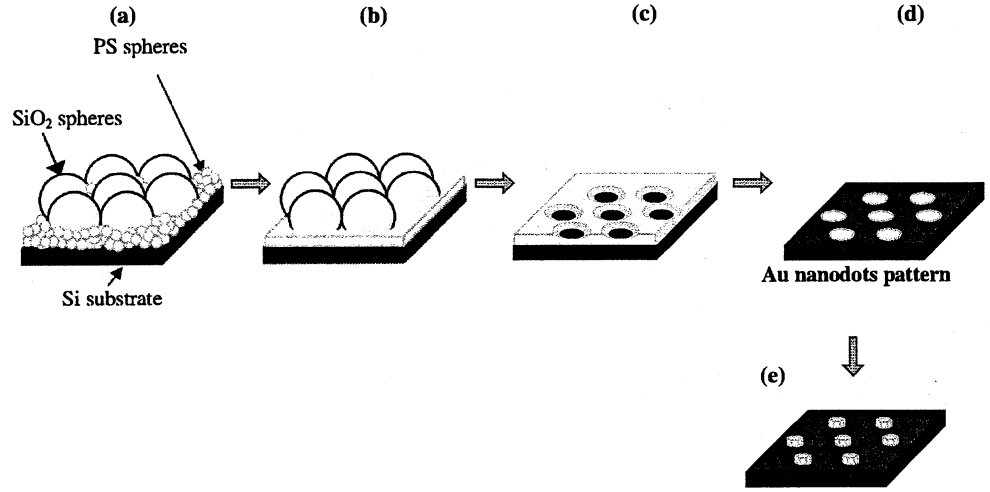

Figure 2. Schematic model of patterning of Au nanodot arrays using PS honeycomb mask for sputtering (a) binary colloidal crystals composed of silica and PS spheres on Si substrate, (b) binary colloidal crystals composed of silica and PS spheres on Si substrate after heat treatment at 100 °C, (c) PS honeycomb mask formed by removal of silica spheres, (d) Au sputter coating and removal of PS honeycomb mask and (e) crystallized Au nanodot arrays formed by annealing under an Ar atmosphere.

In this paper we describe the fabrication of an ordered hexagonally shaped Au nanodot array on an Si(111) surface. It is known that the intrinsic properties of noble metal nanoparticles are mainly determined by their size, shape, density, composition and crystallinity [28–30]. For that purpose two types of site-selective metal deposition methods based on colloidal crystal templating will be described for the synthesis of different sizes and densities of Au nanodots. We will focus in particular on the controllability of the morphology and crystallinity of Au nanodots and try to control the heteroepitaxial growth of Au dots on Si surfaces by high-temperature annealing above the eutectic temperature in an Au–Si system.

2. Experimental procedure

2.1. Metal patterning using hydrophobic treatment for electrodeless deposition

The principle of the patterning processes, described already elsewhere [25, 31, 32], is schematically shown in figures 1 and 2. In this study, subsequent to the patterning, two methods of deposition were used, which are, respectively, electrodeless deposition and physical vapor deposition methods. p-type Si wafers (5–10 Ω cm, (111) crystal orientation) of dimensions 1.5 cm^2 were used as substrates. Prior to patterning the Si specimens were precleaned in acetone for 5 min and 1 wt% HF for 5 min to remove organic contaminants and native oxide. Additionally, the specimens were immersed in 95–97% H_2SO_4 overnight to achieve a hydrophilic surface. Hydrophilic surfaces were formed by the terminal silanol (SiOH) groups [33].

After this pretreatment, a monodisperse suspension of polystyrene (PS) microspheres (Polysciences, Inc.) was dropped onto a delimited region by a 12 mm diameter silicon rubber O-ring onto the substrate. The suspension on the substrate was dried in air at ambient temperature overnight, and spheres self-assembled into a close-packed structure with three-dimensional ordered lattices via attractive capillary forces were observed.

In order to modify the exposed Si surfaces, specimens were placed in hexamethyldisilazane (HMDS) vapor at room temperature for more than one day. HMDS is a popular reagent for forming hydrophobic surfaces based on the immobilization of trimethylsilyl ($(CH_3)_3Si$–) groups on a silanol surface, namely HMDS-coated Si parts show localized hydrophobicity

and are expected to inhibit Au deposition [34]. After removal of the colloidal crystals used as a mask in 97% toluene, the Si substrate was immersed in an electrodeless gold plating solution containing 10^{-3} mol dm^{-3} $NaAuCl_4$ and 0.15 mol dm^{-3} HF for 30 s to fabricate an Au nanodot array.

2.2. Metal patterning using PS honeycomb mask for sputtering

Firstly, the Si substrate is cleaned in dilute HF as described above. Then, a mixed suspension consisting of equal volumes of a 0.2 wt% suspension of PS nanospheres of 200 nm diameter (Polysciences, Inc.) and a 0.5 wt% suspension of silica microspheres of 3 μm diameter (Bangs Laboratories, Inc.) was dropped onto the substrate. The suspension on the substrate was dried in free air for more than one day at room temperature, during which the mixture of spheres of two sizes was self-assembled into a close-packed structure by capillary forces. After the complete evaporation of the solvent, the Si substrate with the binary colloidal crystals formed by the spheres was heated at 100 °C for 1 h, which is higher than the glass transition point ($T_g \sim 93$ °C) of polystyrene, to combine the adjacent PS nanospheres. After heating, the silica spheres, which were used as a template, were selectively removed by immersing the specimens in 10 wt% HF for 10 min.

To fabricate an Au thin film pattern using a dry process, the honeycomb structure composed of the densely packed PS nanospheres was used as a deposition mask. Au thin films were deposited onto the Si substrate through the PS honeycomb mask by a Balzers SCD 040 sputter coater at a discharge current of 25 mA in a vacuum with pressure below 1 Pa for 10 min.

After sputtering, the PS honeycomb mask was removed by immersing the specimens in 97% toluene. Finally, the specimens were annealed at 600 °C for 1 h (heating rate 10 °C min^{-1}) under an argon atmosphere then cooled down at room temperature. Ordered geometric patterns formed on the Si substrate were always observed by scanning electron microscopy (SEM, Hitachi S-4200, S-4800) and electron backscatter diffraction analysis (EBSD, Genesis 4000 EDAX/TS) was performed in the case of patterns produced by sputtering.

3. Results and discussion

Figures 3(a) and (b) show the isolated pattern of the Au particles deposited by selective electrodeless plating using HMDS-coated Si. The isolated Au dot patterns with long range ordering were composed of clusters of Au nanoparticles with a size range of 10–50 nm and a density of $\sim 2.5 \times 10^8$ cm^{-2}, which is similar to the deposited Cu particles previously reported on Si(100) [25]. This result indicates that the HMDS-coated parts, which are located in the interspaces among the spheres on the Si substrate, possess effective hydrophobicity and can act as a mask for localized electrodeless plating, regardless of the different crystal orientations of Si.

In this case, the diameter of the spheres used as a mask for hydrophobic treatment was 1 μm. The contact area between the PS spheres and the underlying Si substrate was expected to serve as a point contact. From the distribution of Au nanoparticles shown in figure 3(b), the diameter of the circular contact area was estimated to be 0.3–0.4 μm, which was nearly equivalent to a third of the diameter of the PS spheres used as a mask. After annealing for 1 h at 600 °C above the eutectic temperature (363 °C) in an Au–Si system, dispersed Au nanoparticles were self-assembled into spherical

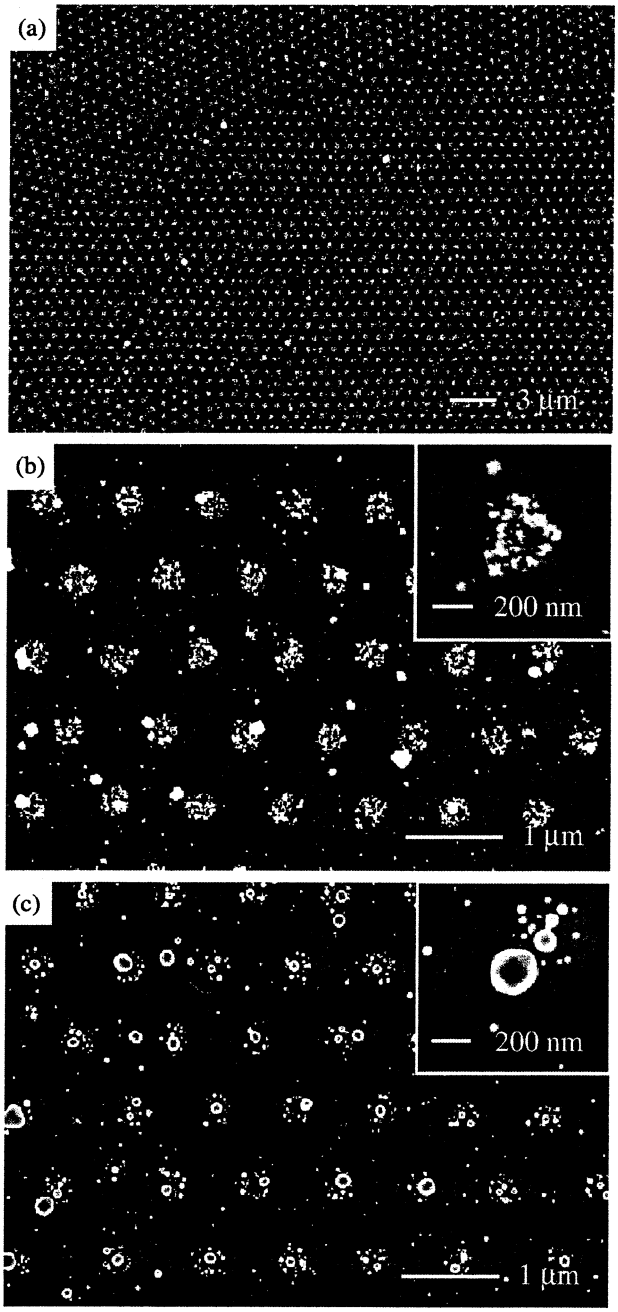

Figure 3. (a) Low-magnification SEM image of an isolated pattern of Au particles with 1 μm periodicity formed on Si. (b) High-magnification image of (a). Electrodeless plating was conducted in 10^{-3} mol dm^{-3} $NaAuCl_4$/0.15 mol dm^{-3} HF for 30 s through an HMDS honeycomb mask. (c) Au nanodot arrays after annealing at 600 °C for 1 h under an Ar atmosphere.

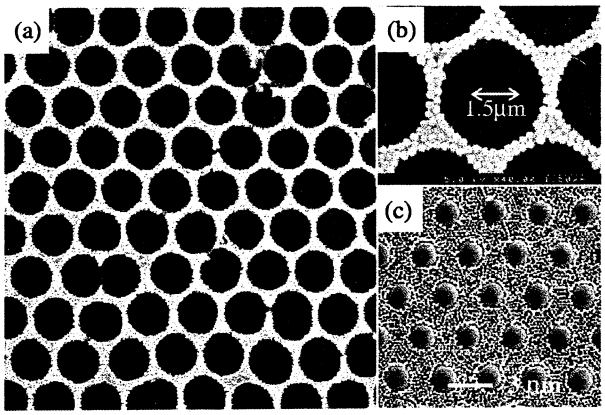

Figure 4. PS honeycomb mask with 3 μm in periodicity formed by the removal of silica spheres (a). Insets show an enlarged image of honeycomb mask (b) and binary colloidal crystals composed of 3 μm diameter silica and 200 nm diameter PS spheres on an Si substrate before removal of silica (c).

Au nanoislands by thermomigration. The central Au island had a diameter of 100–140 nm. Some fine Au particles, which were detected as small bright spots, remained around the central Au nanoisland. If we consider only the central Au island, the heat treatment under argon does not modify the density of Au nanodots.

To fabricate an Au thin film pattern using sputtering, a deposition mask was formed by a replication process based on crystal templating [32]. Figure 4 shows an SEM image of the inverse opal structure derived from using large silica spheres as a template with small PS spheres. The holes of the honeycomb-like inverse opal structure were arranged hexagonally over the entire area of the specimen. It can be clearly seen that the walls of the inverse opal structure were composed of an aggregation of small PS spheres. The inset shows an SEM image of the arrangement of the mixture of spheres with two different sizes before removal of the silica spheres. The large silica spheres formed an ordered hexagonal array and the small PS spheres filled the interspaces. This result indicates that the center-to-center distance between the holes of the PS honeycomb mask could be basically determined by the diameter of the large silica spheres.

In the present study, the obtained PS honeycomb structure was applied as a mask for metal deposition. When sputtering was conducted through the PS honeycomb mask, isolated circular Au thin films with approximately 1.5 μm diameter and a density of $\sim 1 \times 10^7$ cm^{-2} were deposited in the interspaces of the PS mask as shown in figure 5(a). Each thin film consisted of polycrystalline granular Au particles with 20–40 nm grains. After the deposition of the Au thin films on the Si(111) substrate, the specimens were annealed under an argon atmosphere to control the morphology and the crystallinity of the deposited Au. Figure 5(b) shows an SEM image of the Au nanodot arrays after heat treatment. The Au dots were arranged hexagonally over the entire area of the specimen. The diameter of each Au dot was approximately 650 nm (inset). Chemical analyses by EDX show that the heat treatment under argon does not change the chemical

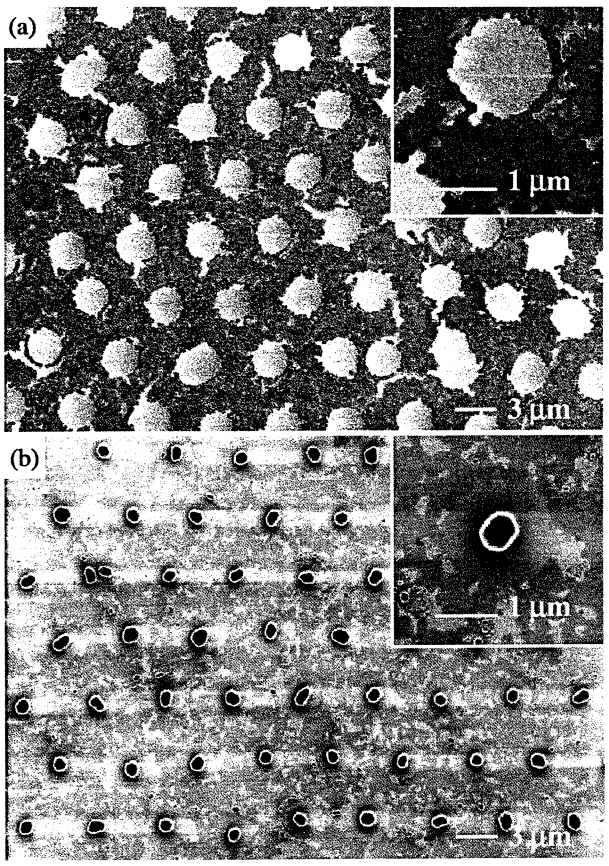

Figure 5. (a) Au thin film pattern formed by sputter coating through PS honeycomb mask and the removal of PS honeycomb mask. (b) Hexagonally arranged Au nanodot arrays formed by annealing under an Ar atmosphere.

composition of the nanodots. The density of the nanodots is also still unchanged. From the tilted view, it was confirmed that the shape of the Au nanodots was a truncated hexagonal dipyramid with defined facets (figure 6(a)). The height of the thermally crystallized Au dot was approximately 260 nm. To identify the crystal structure of the Au dot, EBSD analysis was performed. In fact, electron backscatter diffraction (EBSD) is a technique which allows crystallographic information to be obtained from samples in the scanning electron microscope (SEM). In EBSD a stationary electron beam strikes a tilted crystalline sample and the diffracted electrons form a pattern on a fluorescent screen. This pattern is characteristic of the crystal structure and orientation of the sample region from which it was generated. The diffraction pattern can be used to measure the crystal orientation, measure grain boundary misorientations, discriminate between different materials and provide information about local crystalline perfection. When the beam is scanned in a grid across a polycrystalline sample and the crystal orientation measured at each point, the resulting map will reveal the constituent grain morphology, orientations and boundaries. This data can also be used to show the preferred crystal orientations present in the material. Figure 6(b) shows EBSD mapping images of a side view of one dot. From EBSD analysis, it was ascertained that

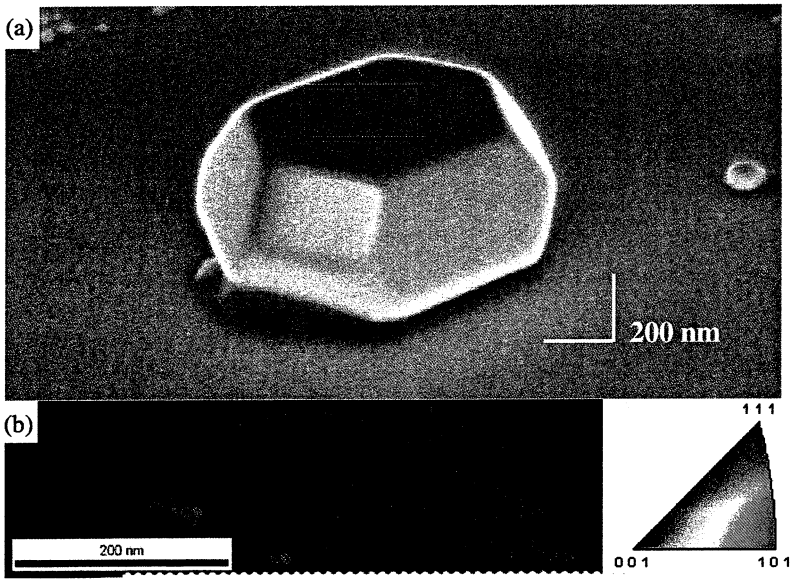

Figure 6. (a) Tilted (60°) SEM image of Au nanodots. (b) Color mapping (colour online) of crystal orientation of Au nanodots by EBSD analysis (the area analyzed by EBSD is marked by the rectangle in (a)). A pattern quality map is plotted in the background and data is cleaned. (The OIM software provides an algorithm to clean erroneous data by replacing it by the most common neighboring orientation.)

Au nanodots formed on Si(111) were almost single crystals with a (111) crystal face. We do not observe another crystal orientation. The shape difference observed in figure 5(b) can be related to the fact that all the nanodots under this heat treatment condition do not possess the perfect equilibrium structure (truncated hexagonal dipyramid with defined facets), see [35]. More experiments are in progress to better understand and control this shape difference. This specific growth of Au dots was assumed to be caused by the crystal orientation of the underlying Au/Si intermixed layer, that is, the Au silicide interfacial layer. Several studies have been carried out on interfacial phenomena between metals (Au) and semiconductors (Si) due to its importance in electronic devices and interconnects, and it is well known that Au silicide is formed due to diffusion of Si through the Au film during the annealing process [36–38]. In addition, epitaxial growth of truncated hexagonal dipyramidal Au nanodots on the Au silicide phase of Au_7Si has been reported by Wu *et al* [39]. According to their report, metallic Au was grown epitaxially on the $Au_7Si(111)$ because the lattice spacing matches well, that is, the lattice mismatch is 3.4% with two unit cells of Au matching a single unit cell of Au_7Si in the ⟨111⟩ orientation. In the present study, it is inferred from the specific morphology of the Au nanodot that the epitaxial growth of Au nanodots could be controlled by the crystal orientation of the underlying Au silicide as well as Si(111). We assume that the difference between the shape of Au nanodots after the heat treatment under argon (circular in the case of electrodeless deposition and truncated hexagonal in the case of sputtering) is more related to a size effect than to the metal deposition method. Experiments are in progress in order to understand the influence of this size effect on the morphology and crystallinity of Au nanodots.

4. Conclusion

We have described the epitaxial growth of truncated hexagonal dipyramidal and spherical Au dot arrays on an Si(111) surface by a combination of colloidal crystal templating, metal deposition and subsequent annealing processes. These methods allow the fabrication of Au nanodots with controllable size and density. The heat treatment allows the modification of the shape and the crystallinity. The obtained Au dot arrays have potential applications in optical devices, chemical sensors and Si-based biofunctional devices, and can also be expected to act as a catalyst for epitaxial growth of 1D nanostructures for vapor–liquid–solid process (the synthesis of ordered arrays of Si nanowires with different sizes by chemical vapor deposition is under investigation in our group). More experiments are in progress in order to study the physical properties of these nanodots (surface-enhancement Raman spectroscopy and mechanical properties by *in situ* compression) and to understand the effect of the crystal orientation of the Si substrate and the size of Au nanodots on the morphology and crystallinity after the heat treatment under argon.

Acknowledgment

Financial support by the European Commission in the framework of project HYDROMEL is gratefully acknowledged.

References

[1] Daniel M C and Astruc D 2004 *Chem. Rev.* **104** 293
[2] Motte L, Billoudet F, Lacaze E, Douin J and Pileni M P 1997 *J. Phys. Chem.* B **101** 138
[3] Wang S, Yu G J, Gong J L, Zhu D Z and Xia H H 2007 *Nanotechnology* **18** 015303

[4] Weitz I S, Sample J L, Ries R, Spain E M and Heath J R 2000 *J. Phys. Chem.* B **104** 4288
[5] Gai Z, Howe J Y, Guo J D, Blom D A, Plummer E W and Shen J 2005 *Appl. Phys. Lett.* **86** 023107
[6] Chio J H, Kim T H, Seo J, Kuk Y and Suh M S 2004 *Appl. Phys. Lett.* **85** 3235
[7] Terris B D and Thomson T 2005 *J. Phys. D: Appl. Phys.* **38** R199–222
[8] Albrecht M, Hu G, Guhr I L, Ulbrich T C, Boneberg J, Leiderer P and Schatz G 2005 *Nat. Mater.* **4** 203
[9] Xu W L, Zheng M J, Ding G Q and Shen W Z 2005 *Chem. Phys. Lett.* **411** 37
[10] Sato K, Hosokawa K and Maeda M 2005 *J. Am. Chem. Soc.* **125** 8102
[11] Maxwell D J, Taylor J R and Nie S 2002 *J. Am. Chem. Soc.* **124** 9606
[12] Ross F M, Tersoff J and Reuter M C 2005 *Phys. Rev. Lett.* **95** 146104
[13] Dailey J W, Taraci J, Clement T, Smith D J, Drucker J and Picraux S T 2004 *J. Appl. Phys.* **96** 7556
[14] Buckmaster R, Hanada T, Kawazoe Y, Cho M W, Yao T, Urushihara N and Yamamoto A 2005 *Nano Lett.* **5** 771
[15] Stodolka J, Nau D, Frommberger M, Zanke C, Giessen H and Quandt E 2005 *Microelectron. Eng.* **78** 442
[16] Chun Y J, Nakajima S and Kawabe M 1996 *Japan. J. Appl. Phys.* **35** L1075
[17] Donbaars S P, Reaves C M, Bressler-Hill V, Varma S and Weinberg H 1994 *J. Cryst. Growth* **145** 712
[18] Gai Z, Howe J Y, Guo J D, Blom D A, Plummer E W and Shen J 2005 *Appl. Phys. Lett.* **86** 023107
[19] Santhanam V, Liu J, Agarwal R and Andres R P 2003 *Langmuir* **19** 7881
[20] Masuda H, Yasui K and Nishio K 2000 *Adv. Mater.* **12** 1031
[21] Gong J L, Zhu D Z and Xia H H 2007 *Nanotechnology* **18** 015303
[22] Deckman H W and Dunsmuir J H 1982 *Appl. Phys. Lett.* **41** 377
[23] Huang Z, Fang H and Zhu J 2007 *Adv. Mater.* **19** 744
[24] Asoh H, Arai F and Ono S 2007 *Electrochem. Commun.* **9** 535
[25] Asoh H, Sakamoto S and Ono S 2007 *J. Colloid Interface Sci.* **316** 547
[26] Velev O D and Kaler E W 2000 *Adv. Mater.* **12** 531
[27] Xia Y, Gates B, Yin Y and Lu Y 2000 *Adv. Mater.* **12** 693
[28] Sun Y and Xia Y 2002 *Science* **298** 2176
[29] Sun Y, Mayers B and Xia Y 2003 *Nano Lett.* **3** 675
[30] Xue C, Li Z and Mirkin C A 2005 *Small* **1** 513
[31] Sivakov V, Heyroth F, Falk F, Andrä G and Christiansen S 2007 *J. Cryst. Growth* **300** 288
[32] Asoh H, Arai F, Uchibori K and Ono S 2008 *Appl. Phys. Express* **1** 067003
[33] Schyberg C, Plossu C, Barbier D, Jaffrezic-Renault N, Martelet C, Maupas H, Souteyrand E, Charles M H, Delair T and Mandrand B 1995 *Sensors Actuators* B **27** 457
[34] Jonas U and Krüger C 2002 *J. Supramol. Chem.* **2** 255
[35] Shi H and Stampfl C 2008 *Phys. Rev.* B **77** 094127
[36] Ressel B, Prince K C, Heun S and Homma Y 2003 *J. Appl. Phys.* **93** 3886
[37] Flammini R, Wiame F, Belkhou R, Taleb-Ibrahimi A, Gregoratti L, Barinov A, Marsi M and Kiskinova M 2004 *Surf. Sci.* **564** 121
[38] Negishi R, Mochizuki I and Shigeta Y 2006 *Surf. Sci.* **600** 1125
[39] Wu J S, Chen Y F, Dhara S, Wu C T, Chen K H and Chen L C 2003 *Appl. Phys. Lett.* **82** 4468

研究論文

軽金属　第58巻 第8号（2008），375–380

アルミニウムアノード酸化ポーラス皮膜の孔発生過程に及ぼす素地結晶方位および表面トポグラフィの影響

朝比奈　建史*・石原　秀憲**
阿相　英孝***・小野　幸子***

Journal of Japan Institute of Light Metals, Vol. 58, No. 8 (2008), pp. 375–380

Influence of crystal orientation and surface topography of aluminum substrate on pore nucleation of anodic porous alumina

Tatsushi ASAHINA*, Hidenori ISHIHARA**
Hidetaka ASOH*** and Sachiko ONO***

Pore nucleation and growth processes of anodic oxide films formed on aluminum substrate were investigated by atomic force microscopy with focusing on the crystal orientation and surface topography of aluminum substrate. Nanotopographies of electropolished aluminum were extremely affected by the crystal orientation of aluminum substrate. For as-received aluminum, regularly aligned striped structure appeared after electropolishing. On the other hand, aluminum substrate annealed at 300°C exhibited isotropic hexagonal cell structure. From X-ray diffraction patterns, it was confirmed that the preferential crystal orientation of aluminum was changed from (110) to (100) when annealing temperature was higher than 300°C. In the initial stage of anodization, specific nanotopography of electropolished aluminum surface was served as the initiation sites for pore generation, and accordingly it influenced cell arrangement. Using planarized aluminum with less than 0.3 nm asperities, however, a large number of fine pores initiated on the oxide film surface. Thus, the growth of anodic oxide films was seriously influenced by the surface topography of aluminum substrate.

(Received February 20, 2008　Accepted May 2, 2008)

Keywords: *anodic porous alumina, anodization, pore initiation, crystal orientation, atomic force microscopy*

1. 緒　　言

アルミニウム（Al）をアノード酸化することで表面にポーラス酸化皮膜を形成し，高い耐食性や装飾性を付与するアノード酸化処理は，一般にアルマイト処理と呼ばれ，建材や器物を始めとして広く工業的に利用されてきた。近年は，その特異的なポーラス構造の規則性や制御性が注目されナノ材料としての応用研究が注目を集めている[1)~5)]。アノード酸化処理はめっきや化成処理などの表面被覆処理とは異なり，電解初期に生成した皮膜が電解終了時の最表面に存在することから，電解初期に形成される皮膜構造の制御は重要な課題であり，皮膜表面の微細構造は他物質との接着性，摩擦，潤滑性，吸着特性に加え視感，触感に対しても大きな影響を及ぼすと考えられる。しかし，アノード酸化技術は幅広く普及し工業利用されているにもかかわらず，皮膜表面の形態制御に関しては不明点が多く，特にアノード酸化初期における孔の発生過程および皮膜の生成過程については十分明らかにされているとは言えない。

これまでにも走査型電子顕微鏡（SEM）や透過型電子顕微鏡（TEM）[6)~11)] あるいは原子間力顕微鏡（AFM）[12)] を用いて，アノード酸化初期における皮膜の成長過程を研究した例がいくつか報告されているが，観察技術や試料調整上の問題のため，孔発生過程に対する考察は十分とは言えず不明確な部分が残されている。過去の研究では，アノード酸化に先立ちAl表面を平滑にするための前処理として電解研磨が用いられてきた。しかし電解研磨後のAl素地表面には微視的に見ると電解研磨条件に依存した微細な凹凸構造が存在するため，アノード酸化初期に生成した皮膜の微細孔と電解研磨の際に生じた凹凸構造を区別することは難しいと考えられる。したがって，孔発生過程の本質を見極めるには，まず初めに皮膜の成長過程に及ぼす素地表面形態の影響を明確にする必要がある。そこで本研究では，アノード酸化ポーラスアルミナの孔発生過程に及ぼすAl素地表面の凹凸構造の影響を，素地の前処理の効果を含めてAFMを用いて検討した。

2. 実験方法

2.1　Al素地の熱処理および前処理

試料は純度99.99%のAl圧延板（東洋アルミニウム株式会

* 工学院大学大学院生〔現在：新日軽㈱〕Graduate student, Kogakuin University〔Present: Shin Nikkei Company, Ltd.〕
** 工学院大学学部学生〔現在：ダイセン・メンブレン・システムズ㈱〕Student, Kogakuin University〔Present: Daicen Membrane-Systems, Ltd.〕
*** 工学院大学工学部応用化学科（〒192–0015　東京都八王子市中野町2665–1）。Department of Applied Chemistry, Faculty of Engineering, Kogakuin University (2665–1 Nakano, Hachioji, Tokyo 192–0015).

社製，Cu; 40 ppm, Fe; 15 ppm, Si; 20 ppm，厚さ 0.5 mm）を用い，試料面積 25 mm×20 mm の旗型に切断後，アセトン中で 3 分間超音波脱脂を行った。その後，Al 素地の結晶配向性の制御を目的として，大気中 100～500°C で 1 時間あるいは 2 時間熱処理を行った。熱処理前後の結晶配向性は X 線回折装置（XRD; Rigaku 製 MiniFlex）を用いて評価した。

Al 素地表面の凹凸を除去する目的で，熱処理後の試料をエタノール（99.5%）－過塩素酸（60%）（体積比 4:1, 10°C 以下）混合溶液を用いて 25 V 定電圧で 3 分電解研磨を行った。さらに，電解研磨に伴って生成する微細なセル構造を除去するために平滑化処理に関して検討した。平滑化処理は，電解研磨後の試料を，0.5 mol dm^{-3} ほう酸－0.05 mol dm^{-3} 四ほう酸ナトリウム（20°C）混合水溶液を用いて電流密度 5 A m^{-2} で定電流アノード酸化（設定電圧 80 V に到達後 20 分電圧保持）しバリヤ型皮膜を生成させた後，0.2 mol dm^{-3} りん酸－0.52 mol dm^{-3} クロム酸混合水溶液で 2 分煮沸して酸化皮膜のみを溶解除去することで行った。

2.2 アノード酸化ポーラス皮膜初期成長過程の AFM 観察

前処理後の試料を 0.3 mol dm^{-3} しゅう酸水溶液（30°C）中，電流密度 100 A m^{-2} で定電流アノード酸化し，その際の電圧の経時変化を測定した。生成した皮膜表面および皮膜を選択的に溶解除去した素地表面を AFM（Digital Instruments 製 Nano Scope IIIa）を用いて大気中タッピングモードで観察し，アノード酸化時の経時変化に伴うポーラス皮膜の成長過程を観察した。

3. 結果と考察

3.1 電解研磨後の Al 素地表面形態

Fig. 1(a) に電解研磨後の Al 素地表面の AFM 像を示す。試料表面には縞状の凹凸構造（以降，縞状構造）が観察された。Fig. 1(b) の断面プロファイルより，縞の間隔は約 50 nm，深さは約 3 nm の規則的なパターンであることがわかった。同試料を 0.3 mol dm^{-3} しゅう酸水溶液（30°C）中，電流密度 100 A m^{-2} で 10 分定電流アノード酸化した試料表面の SEM 像を Fig. 1(c) に示す。結晶粒ごとに縞の配列する向きは異なるものの結晶粒内では規則的な縞状構造を形成していた。電解研磨後の素地表面形態と孔発生過程の詳細については 3.5 項で後述する。次に，Al 素地を 300°C で 1 時間熱処理した後，電解研磨した Al 素地表面の AFM 像を **Fig. 2**(a) に示す。試料表面には縞状構造はほとんど存在せず，最密充填したセル状の凹凸構造（以降，セル状構造）が観察された。Fig. 2(b) の断面プロファイルより，セル径は約 50 nm，深さは約 3 nm であった。熱処理を施した Al 試料において，電解研磨後の素地表面形態が等方的に変化したのは，Al 素地の結晶方位の変化による影響と考えられる。また，熱処理の有無によらず電解研磨後の凹凸構造の周期はどちらも約 50 nm，深さは約 3 nm であることから，凹凸構造の周期および深さは，電解研磨時の電圧に依存すると推定された。Fig. 2(c) に異なる電圧で 3 分電解研磨した Al 素地表面の AFM 像を示す。電解研磨時の生成電圧が高い場合には凹凸構造の周期は長くなり，縞状構造およびセル状構造の凹凸周期には共に電圧依存性が見られた。この結果は，電解研磨による素地のアノード溶解も，印加した電圧に依存したセル構造を形成して進行することを意味している。

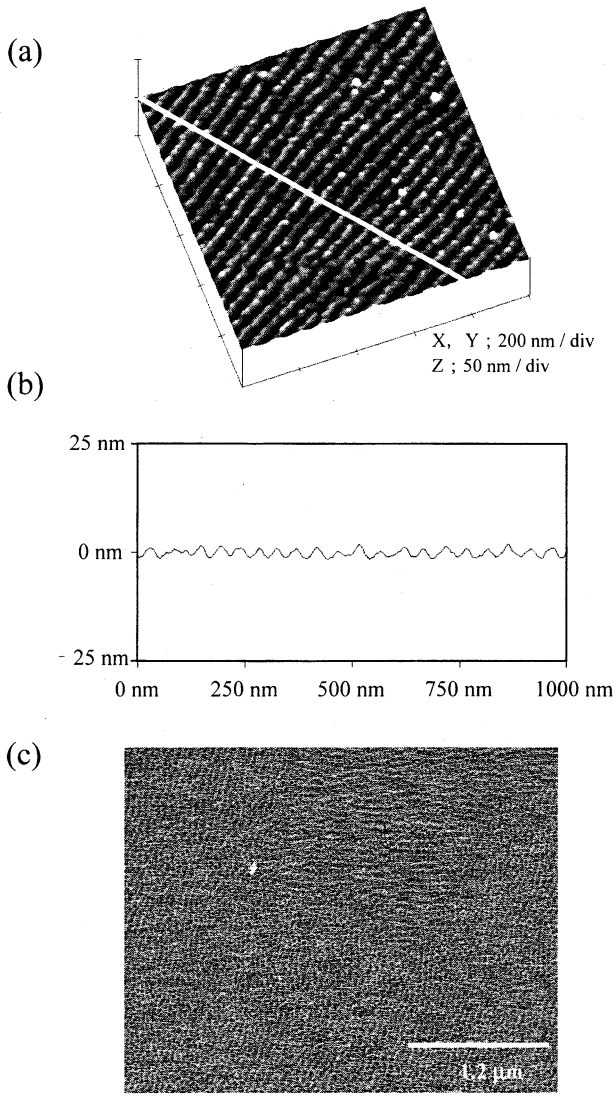

Fig. 1 (a) AFM top view image of electropolished as-received Al and (b) section profile along the line marked in Fig. 1(a). (c) SEM image of surface of anodic film formed on electropolished Al.

3.2 熱処理温度による Al 素地の結晶配向性の変化

熱処理に伴う Al 素地の結晶配向の変化を確認するために，100～500°C の範囲において 50°C ずつ処理温度を変え，1 時間熱処理を行った。**Fig. 3** に加熱後の Al 試料の X 線回折結果を示す。加熱前の試料（a）に加え，比較的低い熱処理温度領域（b: 100°C から e: 250°C）においては，2θ=65° に（220）面に帰属される強いピークと，2θ=78° に（311）面に帰属されるピークが確認された。そのほかにも，（111），（200），（420），（422）に由来するピークが検出されたが，ピーク強度を考慮すれば，Fig. 1(a) に示した縞状構造は（220）面の影響を強く受けたと考えられる。つまり加熱前の試料に代表される Al 試料は（220）面，つまり（110）配向の占有率が高いと考えられた。

一方，比較的高い熱処理温度領域（f: 300°C から i: 500°C）においては 2θ=65° の（220）面のピーク強度は減少し，2θ=45° に（200）面，2θ=100° に（400）面の存在を示す強いピークがそれぞれ確認された。このことから 300°C 以上の

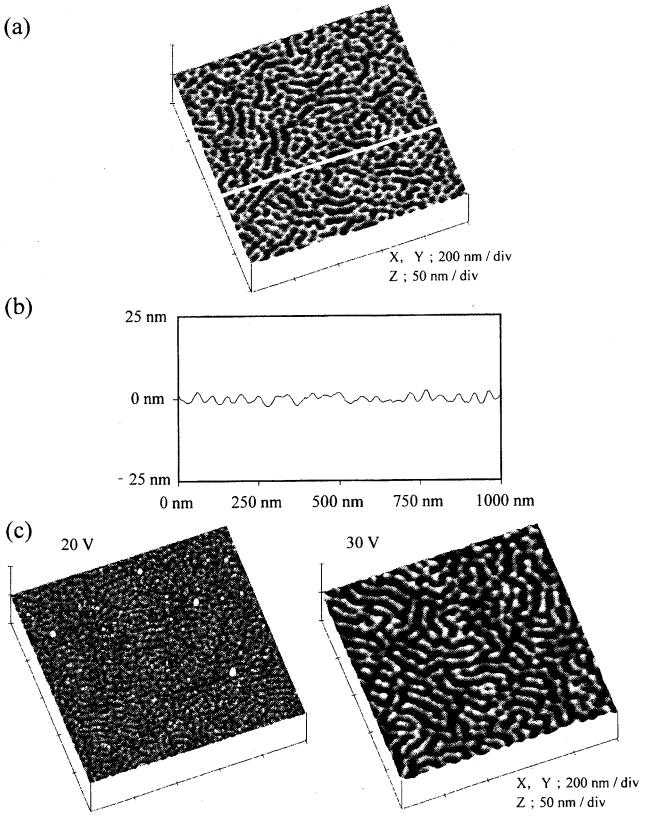

Fig. 2 (a) AFM top view image of electropolished heat-treated Al at 25 V and (b) section profile along the line marked in Fig. 2(a). Heat treatment was conducted at 300°C for 1 h. (c) AFM images of electropolished Al at different voltage; (left) 20 V and (right) 30 V.

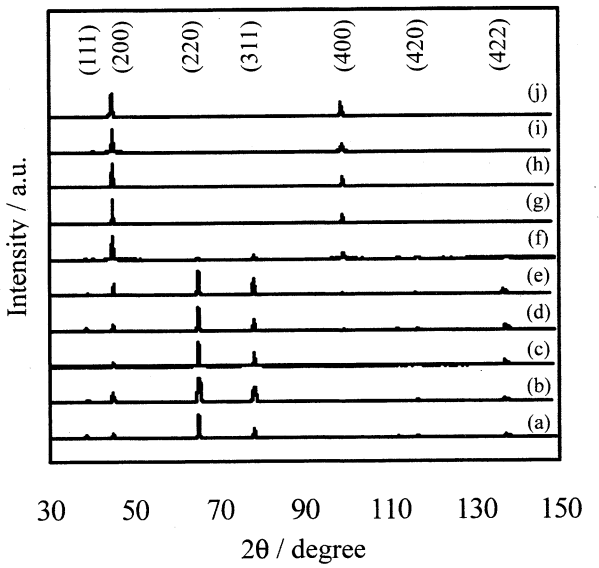

Fig. 3 X-ray diffraction patterns of Al substrate after heat treatment for 1 h. (a) As-received, (b) 100°C, (c) 150°C, (d) 200°C, (e) 250°C, (f) 300°C, (g) 350°C, (h) 400°C, (i) 450°C, (j) 500°C.

温度で熱処理を行ったAl試料は（100）面の占有率が高く，Fig. 2(a) に示したセル状構造は（100）面の影響を強く受けたと考えられる。電解研磨後にAl素地表面に現れる特異的なパターン（縞状構造，セル状構造）の結晶面依存性は既報の結果とも一致した[13]。なお，熱処理時間を2時間にした試

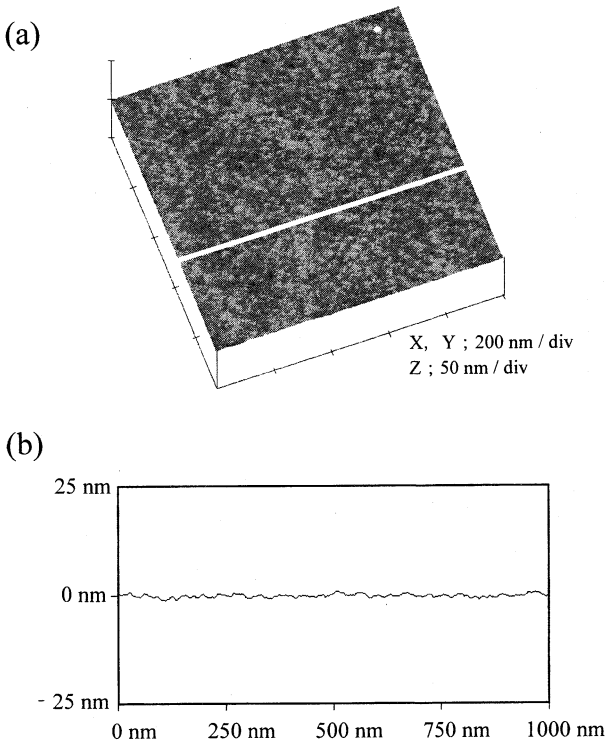

Fig. 4 (a) AFM top view image of flattened Al surface and (b) section profile along the line marked in Fig. 4(a).

料のX線回折パターンは，Fig. 3の結果とほぼ同様であり，結晶配向の変化に及ぼす熱処理条件の影響は，処理時間よりも処理温度の影響が大きいことがわかった。すなわち，300°C以上で1時間熱処理を施すことで結晶の優先配向性は（110）から（100）面に変化すると考えられた。

3.3 Al素地表面の平滑化

アノード酸化ポーラスアルミナの孔発生は，素地表面に存在する微細な凹凸構造に強く影響を受けるため，Fig. 1(a)，Fig. 2(a) に示す電解研磨面では凹凸構造に沿って皮膜の成長が進行すると予測される。そこで，アノード酸化に先立ち平滑化処理を行うことで電解研磨時に生成した凹凸構造の影響を軽減することを検討した。**Fig. 4**(a) にAl素地を300°Cで1時間熱処理後，平滑化処理を行ったAl試料の表面AFM像を示す。またFig. 4(b) に同試料の断面プロファイルを示す。素地表面には幅約20 nm，深さ約0.5 nmの分子レベルの凹凸が観察されるのみで，平滑化処理を施すことで，セル径約50 nm，深さ約3 nmの凹凸を持つFig. 2(a)の電解研磨面に比べて極めて平滑な表面が得られることがわかった。これは，80 Vまでの厚さのバリヤ型酸化皮膜を成長させることで，素地のレベリングが行われる現象を利用している。この平滑化処理を施したAl表面には連続したくぼみ構造が存在しないため，アノード酸化初期に発生する孔はくぼみ構造に誘導されず，孔発生過程の本質を観察することができると推測される。また，熱処理を施していないAl板で平滑化処理を行った場合，平滑化処理後にも電解研磨面の縞状構造が残存したため，平滑な素地表面を得るための前処理としては300°Cで1時間熱処理を行った上で平滑化処理を施した。

3.4 定電流アノード酸化時の電圧－時間曲線に及ぼす素地表面形態の影響

3種類の異なった素地表面形態（縞状構造，セル状構造，

平滑化処理面）を持つAl試料を0.3 mol dm^{-3}しゅう酸水溶液（30°C）中で定電流アノード酸化した際の電圧－時間曲線を**Fig. 5**に示す。3種類とも電解開始とともに直線的に電圧が上昇し，極大値を取った後に定常状態に至る典型的なポーラス型皮膜生成時の電圧－時間曲線を示した。しかし用いたAl素地の表面形態により極大電圧に差が見られた。すなわち，(100) 配向の電解研磨面（セル状構造）においては最も極大電圧が低く，次に（110）配向の電解研磨面（縞状構造）で，平滑化処理面においては最も高い極大電圧を示した。電解研磨後（100）面に形成されたセル状構造はアノード酸化ポーラスアルミナのセル配列に類似した構造であり，あらかじめ素地表面に存在するセル状のくぼみの中心に新規な孔が発生し酸化皮膜の成長が進行するため，電流の通過に対する皮膜生成時の電気抵抗が小さい，あるいはセル状構造を持つAl素地表面は平滑な試料に比べ表面積が大きいことから，実効電流値が設定値よりも低くなったために皮膜生成時の電圧が他の条件に比べ抑制されたと考えられる。一方，Al素地表面が平滑な試料は孔の発生位置が限定されていないため，定電流電解における皮膜生成時の電気抵抗は最も高く，電圧の極大値が高くなったと推定される。いずれの試料も2分後の定常電圧は約40 VでAl素地表面形態の違いは見られない。これは初期の素地形態によらず，電解2分の時点ではすでにポーラスアルミナのセル構造が確立していることによると考えられる。

3.5 アノード酸化ポーラスアルミナの孔発生過程に及ぼす素地表面形態の影響

Fig. 5に示した電圧－時間曲線中の5つの地点（I；電圧上昇前期，II；電圧上昇後期，III；電圧極大地点，IV；電圧下降期，V；電圧定常期）におけるアノード酸化皮膜表面の形態および皮膜を溶解除去したAl素地表面の形態をAFMで観察し，各地点におけるセル径およびAl素地上に形成されたくぼみの深さの変化を測定した。酸化皮膜表面における観察では発生初期の孔径およびその後の溶解による孔形状の変化しか評価できず，皮膜厚さ，セル形状自体の変化を評価することはできない。そこで本研究においては，生成した皮膜を選択的に溶解除去し，Al素地表面の形態を観察することで間接的にセル形状の経時変化を評価した。**Fig. 6**に（110）優先配向のAl試料を電解研磨後，定電流アノード酸化した際の皮膜表面のAFM像を示す。縞状構造の溝部分に孔が発生し，溝に沿って孔が配列している様子がわかる。アノード酸化では電解初期に形成された皮膜が最表面に残るため，挿入図として示した皮膜表面の拡大像からも，2分後の定常状態において皮膜表面の形態は縞状のままであり，電解初期の皮膜表面構造とほぼ同一であることが観察された。一方，皮膜を除去した素地表面の観察結果から，地点Iにおいては電解研磨面の縞状構造に対応した凹凸構造が確認されたが，地点II以降になると縞状のパターンは消失し，セルの最密充填配置が観察された。

Fig. 7に（100）優先配向のAl試料を電解研磨後，定電流アノード酸化した際の皮膜表面のAFM像を示す。（110）配向の場合と同様に，皮膜表面の形態は電解初期と定常状態で大きな変化はなく，孔間距離（セル径）はいずれも約50 nmであった。地点Iに比べ地点Vにおける孔径が若干大きいのは電解液による皮膜の化学溶解に起因すると推定される。一方，皮膜を除去した素地表面のAFM像から，地点Iにおいては電解研磨面に存在したセル状構造のくぼみ部分に孔が誘導され直径約50 nmのセルを形成していることが観察された。その後，微細孔が定常孔へ成長する過程でセル数は減少し，セル径が増大する様子が観察された。

Fig. 8に平滑化処理を施したAl試料を定電流アノード酸化した際の皮膜表面のAFM像を示す。皮膜表面の観察結果から，前述のFig. 6, Fig. 7では見られなかった無数の微細な凹凸が電解開始直後の地点Iにおいて確認された。その微細な凹凸のくぼみ間距離は約30 nm，各くぼみの深さは約4 nmであり，定常状態においては孔間距離約35 nmの定常孔に成長した。一方，皮膜を除去した素地表面の観察結果から，地点Iにおいて素地表面には直径約30 nm，深さ約1 nmのセル

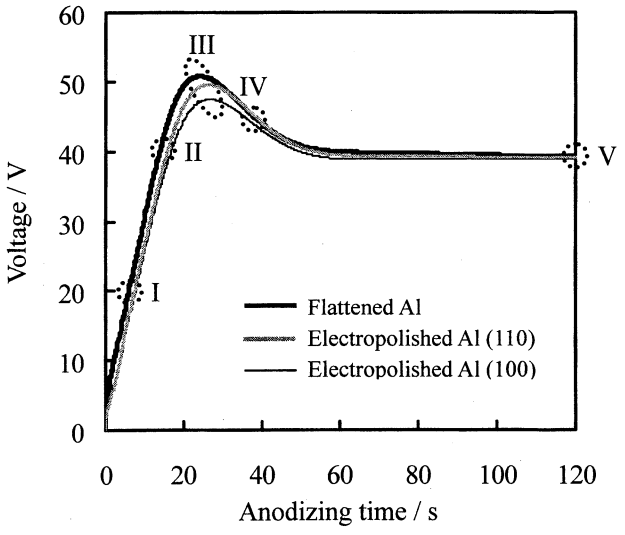

Fig. 5 Voltage-time curves measured during anodization of Al. Anodization was conducted at constant current in oxalic acid. Roman numbers mark the average times during the capture of images I, II, and V in Figs. 6–8.

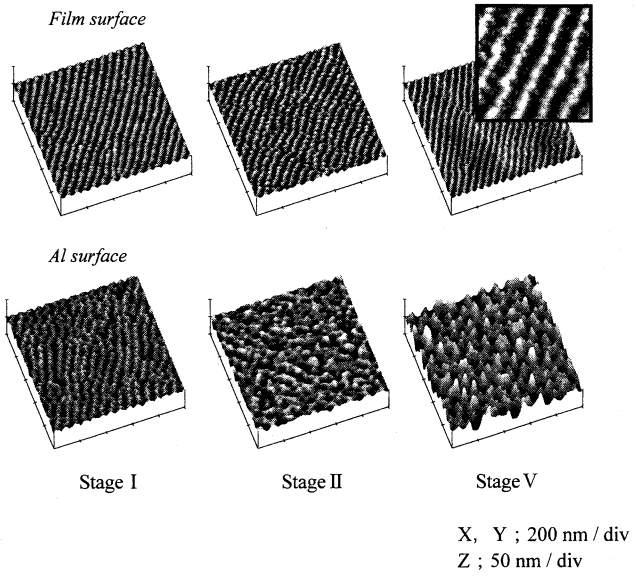

Fig. 6 AFM images of surface morphologies of oxide film and Al substrate: for electropolished (110) Al. Inset shows top view image of oxide film formed on Al at stage V. Scan area was 200 nm square.

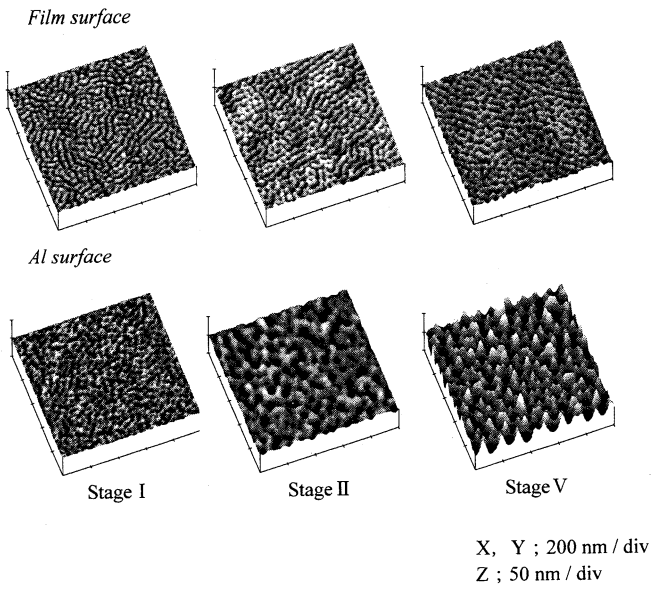

Fig. 7 AFM images of surface morphologies of oxide film and Al substrate: for electropolished (100) Al.

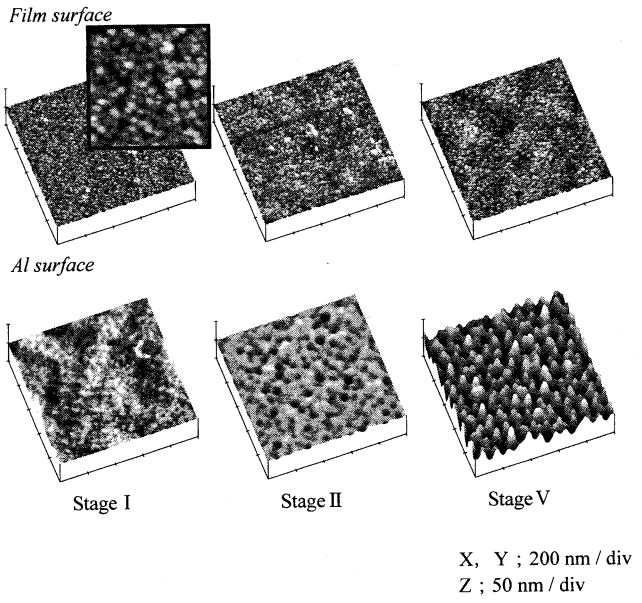

Fig. 8 AFM images of surface morphologies of oxide film and Al substrate: for flattened Al. Inset shows top view image of oxide film formed on Al at stage I. Scan area was 200 nm square.

構造が観察され，このセルサイズは電解前の素地表面に存在するくぼみ直径 20 nm よりも大きいことがわかった。また，その数も時間経過により増加していることから，電解直後の電圧上昇地点で孔発生に伴うセル形成が進行していると言える。地点 II においてはセル径がさらに増大しくぼみも深くなり，地点 V においては他の前処理条件と同様にセル構造の確立が観察された。

定電流アノード酸化した際の素地表面の形態変化を異なる前処理ごとに AFM で観察し，測定したセル径およびくぼみ深さの時間変化を **Fig. 9** にまとめて示す。まず始めに素地上に残存したくぼみ間の周期，つまりセル径の経時変化を異なる前処理ごとに比較すると，いずれの試料も時間経過に伴いセル径の増大が観察された（Fig. 9(a)）。言い換えれば，電解

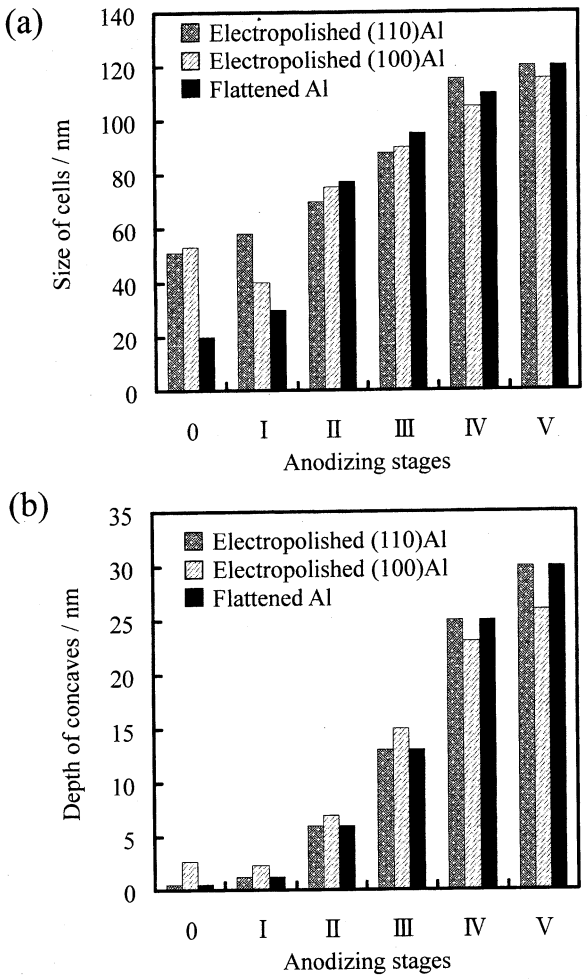

Fig. 9 Transition of (a) size of cells and (b) depth of concaves during anodization of each sample.

初期に微細な孔が多数発生するが，皮膜成長に伴い多くの微細孔は成長を停止し，残りの微細孔が定常孔へと成長することで，セル数が減少したことを示している。Fig. 1(a) に示した縞状構造あるいは Fig. 2(a) に示したセル状構造を持つ Al 素地は，電解前の時点で共に約 50 nm のくぼみ径を持つことから，電解初期の地点 I においては初期のくぼみに孔発生が誘導されたと考えられる。Fig. 2(a) に示したセル状構造を持つ Al 素地の場合，素地上に観察されるセル径が約 40 nm と電解前のくぼみ径に比べて小さいが，これはあらかじめ表面に存在するセル状のくぼみの中心に新規な孔が発生したことに起因すると推定される。したがって地点 I においては，孔の発生によりもたらされた素地上のくぼみ自体が電解前にすでに存在していたくぼみ構造を反映すると考えられる。その後，地点 II から地点 V に至る過程では，前処理条件によらず観察されたセル径の経時変化はほぼ同じ挙動であるため，地点 II 以降は電解前の素地表面形態の影響を受けていない深さ方向への皮膜成長を反映した結果と言える。

一方，平滑化処理を施した試料に着目すると，電解前は直径約 20 nm の浅いくぼみが点在するのみで極めて平滑な素地表面であるが，電解初期の地点 I において素地上に形成されたセルの直径は約 30 nm であることが観察された。皮膜の成長過程を観察した過去の多くの報告では，電解研磨時に生成したくぼみ構造の影響で，アノード酸化初期におけるセル径

を正確に観察することが困難であったと考えられるが，今回平滑化処理を施したAl試料を用いたことで，電圧上昇前期ですでに孔発生が起こり直径約30nmのセルを形成していることが明らかになった。Fig. 9(b) より，電解初期（地点I, II）に生成したセルの素地側への突出は極めて浅くセル径の10%未満であったが，セル径に対するセル底のくぼみ深さの割合は，皮膜成長に伴い増加し，地点IVと定常状態のVにおいては約25%であった。また，セル径の生成電圧に対する比率は地点IIの約1.8nm/Vから定常状態の地点Vでは約3nm/Vと増加した。

3.6 孔発生過程のモデル図

アノード酸化皮膜表面およびAl素地の形態変化をAFMで直接観察した結果より得られた，アノード酸化初期における孔の発生過程，皮膜の成長過程を**Fig. 10**に模式的に示す。電解研磨処理のみではAl素地表面に孔発生を誘導するくぼみ構造が残るため，ここでは平滑化処理を施したAl上における皮膜成長を考察する。

電解前のAl素地表面は極めて平滑であり，厚さ数nmの自然酸化皮膜に覆われていると考えられる（Fig. 10(a)）。アノード酸化の初期段階である電圧上昇前期（Fig. 5の地点I）では電圧の立ち上がりと同時にバリヤ層厚さが増加し，その表面には約30nm周期で深さ4nm程度の微細な孔が無数に発生する（Fig. 10(b)）。バリヤ層の厚さ（nm）を生成電圧（V）の約1（nm/V）倍[8]と仮定すれば，生成電圧が20Vの地点で，バリヤ層の厚さは20nm程度と推測される。電圧上昇後期（Fig. 5の地点II）ではバリヤ層の厚さは40nmに増加し，微細孔が成長し，電圧に応じた直径80nm，深さ5nm程度のセルが素地表面に観察される（Fig. 10(c)）。電圧極大地点（Fig. 5の地点III）ではバリヤ層の厚さは最大50nm程度になり，電圧下降期（Fig. 5の地点IV）では直径110nm，深さ25nm程度のセル構造を形成する（Fig. 10(d)）。以降定常電圧を示す領域においては，セル径はほぼ変わらず，素地上へのバリヤ層の突出が約30nmとなり，ポーラス層の厚さが時間とともに増加する。極大値以降に観察される皮膜の成長挙動は，これまでにTEM観察やAFM観察を通じて議論されてきた結果と基本的には一致するが，セル形態の変化を素地の表面トポグラフィとの関係から初めて説明することができた。さらに，Al素地の熱処理と平滑化処理を用いた本研究を通じて，アノード酸化の初期段階（電圧上昇前期）においてすでにバリヤ型皮膜の表面に微細な孔が発生していることを明確にできた。またアノード酸化時のセル形態の変化に関して，皮膜除去後のAl素地表面をAFMで直接観察することで，電解初期に電解研磨時に生成するくぼみ構造よりも小さなセルが多数発生することを初めて明らかにできた。

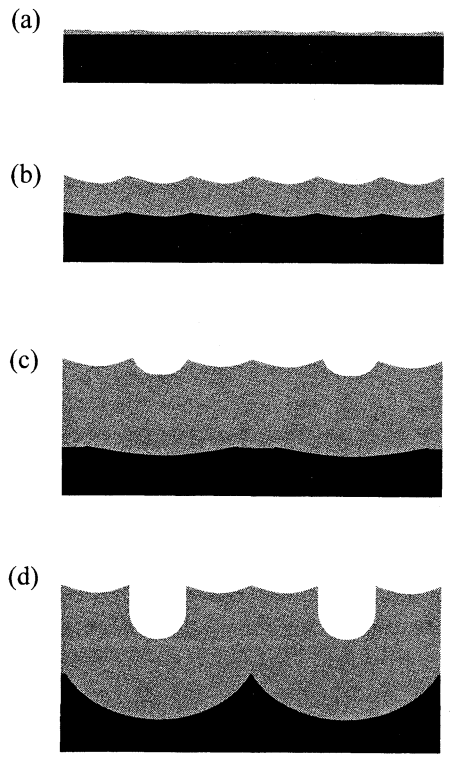

Fig. 10 Schematic diagram of cross section of anodic oxide films formed on flattened Al surface.

4. 結　　言

AFMを用いてアノード酸化ポーラスアルミナの孔発生過程に及ぼすAl素地表面の凹凸構造の影響を定量的に検討した結果，以下の事実が明らかになった。熱処理を施していないAl素地を電解研磨すると異方性を持つ縞状構造が現れるが，300°Cで1時間熱処理を施したAl素地を電解研磨すると等方性のセル状構造が観察される。熱処理を行っていない試料に加え，250°Cまでの比較的低い温度範囲で熱処理を行ったAl素地は（110）面が優先配向していた。一方，300~500°Cまでの比較的高い温度範囲で熱処理を行ったAl素地は（100）面優先配向に変化することから，縞状構造は（110）配向に由来することが確認された。電解研磨後のAl表面に，縞状構造あるいはセル状構造を持つ試料および平滑化処理した試料をそれぞれ定電流アノード酸化したときの孔発生過程の検討から，酸化皮膜の表面形態は電解前の素地表面のトポグラフィに強く依存することが示された。しかし平滑化処理を施したAl試料においては，孔発生を誘導する素地表面の凹凸構造を持たないことから，他の条件では観察されない微細な孔が電解初期に多数発生した。本研究の結果は同時に，皮膜の機械的特性や塗膜との密着性にも関連するアノード酸化皮膜の表面形態が，用いるAl素地の表面形態に強く依存することを明確に示した。

参 考 文 献

1) H. Masuda and K. Fukuda: Science, **268** (1995), 1466–1468.
2) H. Asoh, M. Matsuo, M. Yoshihama and S. Ono: Appl. Phys. Lett., **83** (2003), 4408–4410.
3) S. Ono, M. Saito, M. Ishiguro and H. Asoh: J. Electrochem. Soc., **151** (2004), B473–B478.
4) A. Oide, H. Asoh and S. Ono: Electrochem. Solid-State Lett., **8** (2005), G172–G175.
5) S. Ono, M. Saito and H. Asoh: Electrochimica Acta, **51** (2005), 827–833.
6) T. P. Hoar and J. Yahalom: J. Electrochem. Soc., **110** (1963), 614–621.
7) J. P. O'Sullivan and G. C. Wood: Proc. R. Soc. London, **A317** (1970), 511–543.
8) 永山政一，高橋英明：日本化学会誌，(1972)，850–855.
9) 福田芳雄：日本化学会誌，(1974)，1868–1875.
10) G. E. Thompson, R. C. Furneaux, G. C. Wood, J. A. Richardson and J. S. Goode: Nature, **272** (1978), 433–435.
11) K. Shimizu, K. Kobayashi, G. E. Thompson and G. C. Wood: Philosophocal Magazine A, **66** (1992), 643–652.
12) H. Wu, X. Zhang and K. R. Hebert: J. Electrochem. Soc., **147** (2000), 2126–2132.
13) V. V. Konovalov, G. Zangari and R. M. Metzger: Chem. Mater., **11** (1999), 1949–1951.

Pt–Pd-Embedded Silicon Microwell Arrays

Hidetaka Asoh*, Fusao Arai, Kota Uchibori, and Sachiko Ono

Department of Applied Chemistry, Kogakuin University, 2665-1 Nakano, Hachioji, Tokyo 192-0015, Japan

Received March 3, 2008; accepted April 25, 2008; published online May 23, 2008

Si microwell arrays containing Pt–Pd thin film were fabricated by the chemical etching of a Si substrate through a polystyrene honeycomb mask using a patterned metal catalyst. The honeycomb mask, which was formed by the utilization of binary colloidal crystals composed of large silica spheres and small polystyrene spheres, acted as a mask for metal deposition. After immersing a locally Pt–Pd-coated Si substrate into a solution containing hydrofluoric acid and hydrogen peroxide, an ordered Si microwell array with a hexagonal arrangement could be obtained by site-selective metal-assisted chemical etching. Moreover, the notable feature of this process is that an isolated circular Pt–Pd film used as a catalyst remained at the bottom of each well after chemical etching.

DOI: 10.1143/APEX.1.067003

Porous silicon with a regular porous structure on the submicron to nanometer order has received much attention over several decades due to its applications in various fields such as optical devices, chemical sensors, and biosensors. Although porous silicon is normally produced by the anodization of Si in an electrolyte containing hydrofluoric acid (HF),[1] a novel technique of fabricating porous silicon without applying an external bias was proposed by Li and Bohn in 2000.[2] According to their report, a porous silicon layer could be formed simply and efficiently by immersing Si wafers coated with a noble metal (i.e., Au, Pt, or Au–Pd) into HF mixed with hydrogen peroxide (H_2O_2) solution. Since then, on the basis of this metal-assisted chemical etching technique, the formation of deep straight nanoholes with a depth greater than 500 μm in Si using Ag nanoparticles[3] and helical Si nanoholes using Pt nanoparticles as a catalyst[4] have been reported by Tsujino and Matsumura. Yae *et al.* have reported the fabrication of Si square holes with approximately 30 μm diameter using patterned Pd catalyst deposited through a stainless mesh screen.[5]

Recently, we have reported the fabrication of Si convex arrays and Si hole arrays with regular periodicity on the micrometer order by a combination of colloidal crystal templating and subsequent site-selective chemical etching using patterned Ag nanoparticles as a catalyst.[6] The fabrication of Si nanowire arrays has also been achieved by a similar approach using a colloidal crystal mask.[7] Here, we report the fabrication of Si microwell arrays using a shape-controlled metal thin film as a catalyst for metal-assisted chemical etching. Moreover, the formation of a polystyrene (PS) honeycomb mask using an ordered arrangement of two types of spheres with a large diameter ratio is also investigated from the viewpoint of applying a two-dimensional (2D) crystalline array of colloidal spheres as a physical mask for "natural lithography". To our knowledge, there have been no studies in which the fabrication of Si microhole arrays has been attempted without using conventional lithography and/or anodic etching.

The principle of the fabrication process is schematically shown in Fig. 1. A *p*-type Si wafer [10 Ωcm, (100) crystal orientation] was cut into 1 × 1 cm^2 pieces, which were used as substrates. The Si specimens were precleaned in 1 wt % HF to remove organic contaminants and native oxide. A

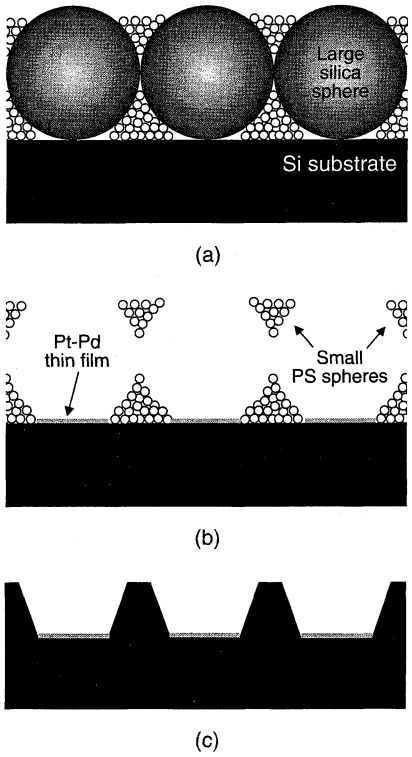

Fig. 1. Schematic model of fabrication of Si microwell arrays. (a) Binary colloidal crystals on Si substrate, (b) removal of silica spheres and deposition of metal layer, and (c) chemical etching and removal of PS honeycomb mask.

mixed suspension (~0.15 ml) consisting of equal volumes of a 0.2 wt % suspension of PS nanospheres of 200 nm diameter (Polysciences, Inc.) and a 0.5 wt % suspension of silica microspheres of 3 μm diameter (Bangs Laboratories) was dropped into the region surrounded by the silicon rubber O-ring of 5.5 mm inner diameter on the substrate. The suspension on the substrate was dried in air for more than one day, during which the mixture of spheres of two sizes was self-assembled into a close-packed structure by capillary forces. After the complete evaporation of the solvent, the Si substrate with the binary colloidal crystals formed by the spheres was heated at 100 °C for 1 h, which is higher than the glass transition point (T_g ~ 93 °C) of PS,[8] to combine the adjacent PS nanospheres [Fig. 1(a)]. After heating, the silica spheres, which were used as a template, were selectively removed by immersing the specimens in 10 wt % HF for 10 min.

*E-mail address: asoh@cc.kogakuin.ac.jp

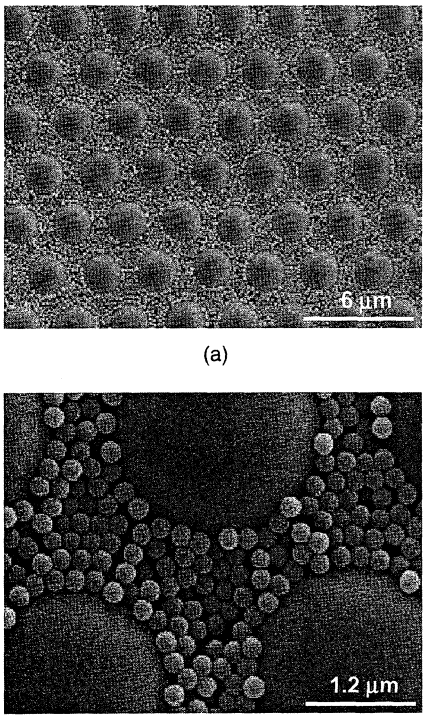

Fig. 2. SEM images of binary colloidal crystals. The diameters of the large silica and small PS spheres were 3 μm and 200 nm, respectively. (a) Low- and (b) high-magnification view.

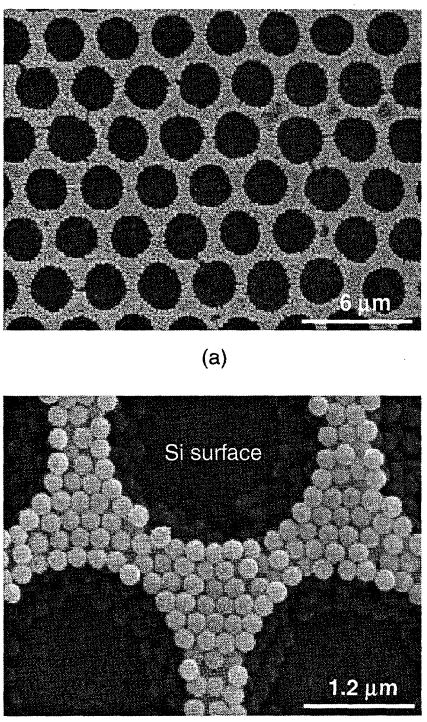

Fig. 3. SEM images of PS honeycomb mask after removing silica spheres by immersion in 10 wt % HF for 10 min. (a) Low- and (b) high-magnification view.

To fabricate a metallic catalyst pattern using a dry process, the honeycomb structure composed of the densely packed PS nanospheres was used as a deposition mask. Metal thin films were deposited onto the Si substrate through the PS honeycomb mask by ion sputtering (Hitachi E-1010) at a discharge current of 15 mA in a vacuum with pressure below 10 Pa [Fig. 1(b)]. Pt–Pd target (80% Pt and 20% Pd) was used as a sputtering target. The deposition rate of Pt–Pd was 6 nm/min. Here, the ion sputtering of Pt–Pd, which is generally used as a method of coating nonconducting materials with a metal for scanning electron microscopy (SEM) observation, was chosen for the purpose of forming a smoothly shaped metal thin film and to avoid a granular coating, such as for the case of Au deposition.

After sputtering, the specimens with locally deposited metal films were etched in a mixed solution of 5 mol dm^{-3} HF and 1 mol dm^{-3} H_2O_2 at room temperature. Finally, the PS honeycomb mask was removed by immersing the specimens in 97% toluene [Fig. 1(c)]. The ordered geometric pattern formed on the Si substrate was evaluated by SEM (Hitachi S-4200) and atomic force microscopy (AFM; Digital Instrument Nano Scope IIIa).

The 2D self-assembly of spheres (e.g., PS and silica) forms a close-packed structure with triangular interspaces among three neighboring spheres. In the case of 2D colloidal crystal templating, which is often called "colloidal lithography" or "nanosphere lithography", the ordered triangular interspaces can act as etching sites or deposition sites for conventional lithography.[9,10] Therefore, it is well-known that the resultant pattern is restricted to only the gaps between the 2D array of spheres. To expand the range of applications of colloidal crystal templating, the use of a multistep replication process, which allows variable patterns including an inverse opal structure, is a promising strategy. In this work, two-step replication using spheres of two different sizes was applied for the fabrication of the deposition mask, as shown in Fig. 1. Although several previous studies have reported on the ordered arrangement of spheres with two different sizes in a 2D plane,[11–13] little attention has been focused on the applications of the resultant pattern.

Figure 2(a) shows an SEM image of the arrangement of the mixture of spheres with two different sizes. The large silica spheres were ordered in domains with hexagonal packing and covered the silicon surface in a 2D array, that is, a monolayer was formed. When the suspension concentration was higher, thick multilayers were often observed. From the high-magnification SEM image shown in Fig. 2(b), it was confirmed that binary colloidal crystals were formed by the two types of spheres with a large diameter ratio. The large silica spheres formed an ordered hexagonal array and the small PS spheres filled the interspaces. To form ordered binary colloidal crystals, it was essential to adjust the diameter ratio of the two different spheres. If the large and small spheres are designated A and B respectively, the diameter ratio D_B/D_A was approximately 0.067 in the present case. When D_B/D_A was larger than 0.2, the large silica spheres had a disordered arrangement and stacking defects were observed over the entire substrate surface.

The binary colloidal crystals shown in Fig. 2(a) were immersed in dilute HF to dissolve the silica spheres used as the template. Figure 3(a) shows an SEM image of the inverse opal structure derived from using large silica spheres as a template with small PS spheres. The holes of the

honeycomb-like inverse opal structure were arranged hexagonally over the entire area of the specimen. It can be clearly seen in Fig. 3(b) that the walls of the inverse opal structure were composed of an aggregation of small PS spheres. In this case, the connections among neighboring spheres are thought to be produced by the heat treatment at 100 °C. This crosslinking yields a mechanically stable and continuous mask structure. The center-to-center distance between the holes of the PS honeycomb mask, which was basically determined by the diameter of the large silica spheres, was approximately 3 μm. The shrinkage of holes was negligible due to the stability of silica to heat.

In the present study, the obtained PS honeycomb structure was applied as a mask for metal deposition and subsequent metal-assisted chemical etching. When ion sputtering was conducted through the PS honeycomb mask, isolated circular Pt–Pd thin films with approximately 1.6 μm diameter were deposited in the interspaces of the PS mask, as shown in Fig. 1(b). This area of a circle almost corresponded with the value estimated from the curvature of the two types of spheres. The maximum thickness of the Pt–Pd layer was estimated to be 10 nm after a sputtering time of 100 s.

After the deposition of the Pt–Pd thin films on the Si substrate, the specimens were immersed in a mixed solution of HF and H_2O_2 to etch the Si substrate by metal-assisted chemical etching. During chemical etching, the central part of Si substrate surrounded by the wall of the PS honeycomb mask gradually sagged downward. Figures 4(a)–4(c) show plane-view and tilted-view SEM images of the Si surface etched using the patterned Pt–Pd catalyst. The chemical etching proceeded only in the Pt–Pd-coated area on the Si surface, in agreement with the proposed mechanism.[2)]

From the tilted view shown in Fig. 4(c), it was conformed that the pores were conical. The diameter of the opening of each Si microwell was approximately 3 μm due to the chemical dissolution of the horizontal plane. The depth of each Si microwell was estimated to be approximately 2 μm. The crest and side walls of the Si microwells were extremely smooth. In addition, the most noteworthy point is that the circular Pt–Pd thin films used as the catalyst remained at the bottom of each well. The SEM images shown in Figs. 4(b) and 4(c) revealed that the residual detected as bright contrast was the Pt–Pd catalyst. In previous studies, the diameter of the holes formed by metal-assisted chemical etching had a range of 50–100 nm, corresponding to the diameter of the nanoparticles deposited by electroless plating, and the metal particles were observed at the bottom of the holes, similar to the present case.[3,4,6)] By using circular metal thin films as a catalyst, however, the formation of Si microwells with micrometer-scale openings was achieved. The present process can thus be defined as "natural lithography", since it does not require the use of specific lithography techniques.

We have described the fabrication of Si microwell arrays by a combination of colloidal crystal templating and subsequent site-selective metal-assisted chemical etching. The formation of ordered Si microstructures having a short periodicity can also be achieved easily by downsizing the diameter of the silica spheres used in the initial template. The obtained Si microwells containing Pt–Pd thin film have potential applications in optical devices, chemical sensors, and Si-based biofunctional devices. On the basis of the present process, different types of noble metal films can also be embedded within a Si substrate.

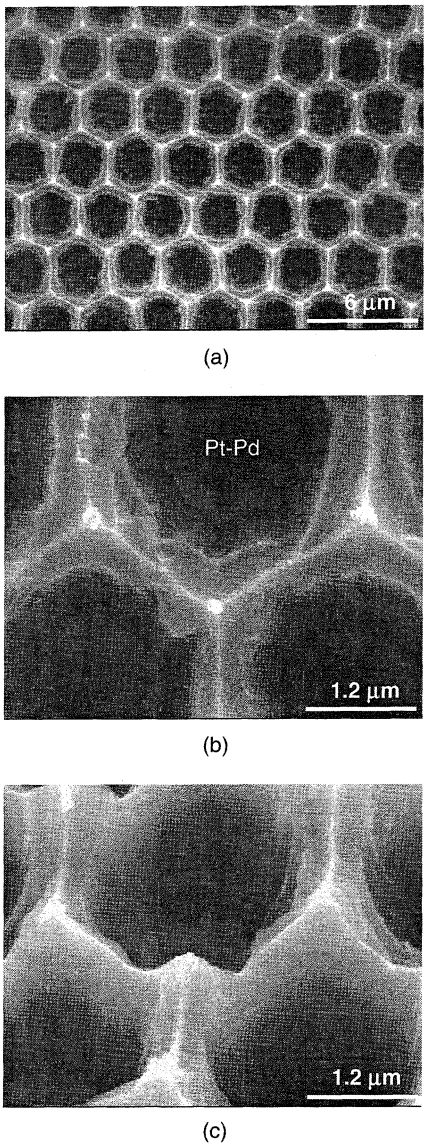

Fig. 4. (a) SEM images of Si microwell array containing Pt–Pd film with 3 μm periodicity, (b) high-magnification view, and (c) tilted (45°) view. Chemical etching was conducted in HF/H_2O_2 for 3 min.

1) V. Lehmann and H. Föll: J. Electrochem. Soc. **137** (1990) 653.
2) X. Li and P. W. Bohn: Appl. Phys. Lett. **77** (2000) 2572.
3) K. Tsujino and M. Matsumura: Adv. Mater. **17** (2005) 1045.
4) K. Tsujino and M. Matsumura: Electrochem. Solid-State Lett. **8** (2005) C193.
5) S. Yae, M. Abe, N. Fukumuro, and H. Matsuda: Electrochemistry **76** (2008) 144.
6) H. Asoh, F. Arai, and S. Ono: Electrochem. Commun. **9** (2007) 535.
7) Z. Huang, H. Fang, and J. Zhu: Adv. Mater. **19** (2007) 744.
8) B. Gates, S. H. Park, and Y. Xia: Adv. Mater. **12** (2000) 653.
9) H. W. Deckman and J. H. Dunsmuir: Appl. Phys. Lett. **41** (1982) 377.
10) Y. Xia, B. Gates, Y. Yin, and Y. Lu: Adv. Mater. **12** (2000) 693.
11) J. V. Sanders and M. J. Murray: Nature **275** (1978) 201.
12) C. J. Kiely, J. Fink, M. Brust, D. Bethell, and D. J. Schiffrin: Nature **396** (1998) 444.
13) K. P. Velikov, C. G. Christova, R. P. A. Dullens, and A. van Blaaderen: Science **296** (2002) 106.

Abstract

Volume 13, Issue 3
213th ECS Meeting, May 18 - May 23, 2008, Phoenix, AZ
State-of-the-Art Program on Compound Semiconductors 48 (SOTAPOCS 48) -and- ZnO, InZnO, and InGaO Related Materials and Devices for Electronic and Photonic Applications
Editor(s): M. Overberg, F. Ren, B. Gila, H. Ouyang, P. Nam, L. Chen, J. Kim, J. LaRoche

Self-Organized and High Aspect Ratio Nanoporous Zinc Oxide Prepared by Anodization

Sachiko Ono, Yuta Kobayashi, and Hidetaka Asoh
Kogakuin University

We have fabricated self-organized nanoporous zinc oxide having an extremely high aspect ratio by a simple, high throughput and non-costly wet electrochemical process without use of catalyst: anodization of zinc plate in aqueous solutions. By optimizing the anodizing condition, we could obtain a film with the thickness more than 90 mm. BET specific surface area of the anodic porous ZnO was approximately 28.5 m2/g. XRD measurement of the anodic ZnO reveals diffraction spectra of polycrystalline ZnO. From UV and visible light optical absorption spectra of thick anodic ZnO films, the absorption edge and the estimated band gap were 370 nm and 3.35 eV respectively. Photo catalytic activity of the anodic ZnO was ascertained by a methylene blue degradation test under UV irradiation at the wavelength of 365 nm. The proposed process with use of anodization of zinc could be expanded to other metals to obtain various oxides semiconductors, and has potential technological applications in the fields of catalysis, supports, and sensors.

doi:10.1149/1.2913094

See Also

- Self-Organized and High Aspect Ratio Nanoporous ZnO prepared by Anodization
  Sachiko Ono *et al.*
  Meet. Abstr. - Electrochem. Soc. **801**, 800 (2008)

Abstract

Volume 13, Issue 3
213th ECS Meeting, May 18 - May 23, 2008, Phoenix, AZ
State-of-the-Art Program on Compound Semiconductors 48 (SOTAPOCS 48) -and- ZnO, InZnO, and InGaO Related Materials and Devices for Electronic and Photonic Applications
Editor(s): M. Overberg, F. Ren, B. Gila, H. Ouyang, P. Nam, L. Chen, J. Kim, J. LaRoche

Site-Selective Metal Patterning/Metal-Assisted Chemical Etching on GaAs Substrate through Colloidal Crystal Templating

Yukiko Yasukawa, Hidetaka Asoh, and Sachiko Ono
Kogakuin University

Systematic research on an n-GaAs substrate through a combination of colloidal crystal templating, electroless plating/two-step catalyzation and subsequent metal-assisted chemical etching was carried out. Using self-organized polystyrene spheres as a mask, metal particles, i.e., Cu, Ag and Pd, were selectively deposited at sites resulting in the formation of metal honeycomb patterns on GaAs. Ordered GaAs convex arrays were fabricated by the chemical etching of GaAs originating from the honeycomb-patterned Ag and Pd metals, which acted as etching catalysts, whereas the effectiveness of Cu as a catalyst in metal-assisted etching was not confirmed. Each metal catalyst resulted in the formation of a characteristic etched structure and etching depth, and thus, etching rate. In addition, different anisotropic etching structures were obtained by Ag-assisted etching for (100)- and (111)-oriented substrates. The crystal-face orientation as well as the metal used affects the rate of metal-assisted chemical etching and the morphology obtained.

doi:10.1149/1.2913083

Abstract

Volume 11, Issue 15
212th ECS Meeting, October 7 - October 12, 2007, Washington, DC
Light Alloys 3
Editor(s): A. Davenport, S. Virtanen, B. Shaw, R. Buchheit, N. Missert

Effect of Nanostructured Surface of Light Metals on Hydroxyapatite Coating

Sachiko Ono, Atsushi Kiyotake, and Hidetaka Asoh

Kogakuin University

Hydroxyapatite coating by alternative dipping method on light metals such as Al, Mg and Ti having porous surface was studied with focusing on the morphology and composition of the surface layer. HAp coating is significantly enhanced by porous substrates having a pore size of 10 nm ~ 30 nm, i.e., mesoporous range. Incorporated electrolyte species into the substrates assist the precipitation of HAp in the following order: Sulfuric acid ≧ NaOH > Oxalic acid > Phosphoric acid. Plate-like deposit was formed on Mg substrate having thin natural oxide or defective anodic films. However, no deposit was found on chemically etched surface. Thus, it was clarified that the meso-porous size as well as incorporated anions of porous substrate strongly affected to the HAp coating.

doi:10.1149/1.2899042

Article Options | Go | ? | View Cart

Full Text: PDF Order

See Also

- Effect of Nanostructured Surface of Light Metals on Hydroxyapatite Coating
  Sachiko Ono *et al.*
  Meet. Abstr. - Electrochem. Soc. **702**, 902 (2007)

Back To Hit List | Previous Document | Issue Table of Contents

Available online at www.sciencedirect.com
ScienceDirect
Electrochemistry Communications 10 (2008) 757–760
electrochemistry communications
www.elsevier.com/locate/elecom

Site-selective chemical etching of GaAs through a combination of self-organized spheres and silver particles as etching catalyst

Yukiko Yasukawa [a], Hidetaka Asoh [a,b], Sachiko Ono [a,b,*]

[a] *Research Institute for Science and Technology, Kogakuin University, Japan*
[b] *Department of Applied Chemistry, Kogakuin University, 2665-1 Nakano-cho, Hachiouji, Tokyo 192-0015, Japan*

Received 30 January 2008; received in revised form 14 February 2008; accepted 15 February 2008
Available online 21 February 2008

Abstract

Microfabrication of the *n*-GaAs substrate surface was investigated by a combination of colloidal crystal templating, electroless plating and subsequent metal-assisted etching using noble metals as a catalyst. Ag and Cu nanosized particles were deposited site selectively to form metal-honeycomb patterns on GaAs using self-organized polystyrene spheres as a mask. By Ag-assisted etching, GaAs was effectively etched into a convex-array structure. Different anisotropic etching patterns were observed throughout the substrate after Ag-assisted etching, by changing the crystal-face orientation of *n*-GaAs from (100) to (111).

Keywords: Compound semiconductor; Metal-assisted chemical etching; Self-organized structure; Electroless plating; Colloidal crystals

1. Introduction

To fabricate multifunctional porous Si, "metal-assisted chemical etching" was proposed as a useful technique [1]. The method utilizes the catalytic ability of noble-metal thin films/particles in an etchant composed of a mixture of HF and H_2O_2 solutions without the use of any electrical connections or strong oxidizing agents [2]. Thus, the effects of metal-assisted etching with Au, Pt, Ag and Pd were systematically investigated for Si (100) [2,3]. However, the investigation of this etching method in group III–V compound semiconductors is rare in contrast to the case of Si, so it is less understood. Therefore, we describe here the effectiveness of metal-assisted etching for the most widely utilized group III–V compound semiconductor, GaAs, as a function of crystal-face orientations, i.e., (100) and (111) possessing a resistivity level of 10^{-3} Ω cm order. The morphological control of the GaAs surface is of interest from the standpoint of fundamental science, and further, the application to devices in the future.

A templating technique based on self-organized polystyrene (PS) spheres has been reported for the fabrication of Si hole arrays [4], dot arrays [4], disk arrays [5], pillar arrays [5] and porous alumina possessing 2D/3D composite structures [6] by means of anodization as well as the control of pit initiation sites on aluminum [7]. Here, PS spheres can be dissolved easily by ultrasonic cleaning in toluene after the experimental processes. Therefore, PS spheres forming the self-organized structure were selected as a mask, aiming for the "site-selective" etching of GaAs. As a result of previous studies [8,9], electroless Cu plating on Si has been clarified and the technique was well established. Also, deep cylindrical nanoholes have been generated by etching the *p*-Si substrate by depositing Ag particles [10], however, there is no report on successful electroless Cu and Ag plating of GaAs. Thus, Cu and Ag were chosen as metal sources for the metal-assisted etching in the present study.

* Corresponding author. Address: Department of Applied Chemistry, Kogakuin University, 2665-1 Nakano-cho, Hachiouji, Tokyo 192-0015, Japan. Tel./fax: +81 426 28 4843.
E-mail address: sachiono@cc.kogakuin.ac.jp (S. Ono).

1388-2481/$ - see front matter © 2008 Elsevier B.V. All rights reserved.
doi:10.1016/j.elecom.2008.02.024

2. Experimental

A GaAs wafer was cleaved to 1 cm × 1 cm in size and used as a substrate. Before forming a mask on the substrate, the native-oxide film was removed by immersing the substrate in 46 wt% HF solution for 15 min. Schematic explanation of the present experimental procedure and site-selective chemical etching of GaAs is shown in Fig. 1. A solution with PS spheres of 1 μm diameter was adjusted to the suspension concentration of 0.25%, supplied dropwise onto the substrate, and then dried in air. After the complete evaporation of the solvent, PS spheres forming a close-packed structure were obtained as a mask. To fix the mask on the substrate, a heat treatment was carried out at 100 °C for 1–2 h (Fig. 1a). Subsequently, electroless Cu plating was proceeded in a solution consisting of 0.01 wt% $CuSO_4 \cdot 5H_2O$ and 46 wt% HF without any reductants [8,9], with the bath temperature maintained at 25 °C for 12 ~ 20 min. Immersion plating in an aqueous solution containing 10^{-4} mol dm^{-3} $AgClO_4$ and 10^{-3} mol dm^{-3} NaOH at room temperature was conducted for 20 min [10] for Ag deposition (Fig. 1b). It was immediately followed by chemical etching in a mixture of 5 mol dm^{-3} HF and 1 mol dm^{-3} H_2O_2 solutions at room temperature (Fig. 1c–e). Finally, ultrasonic cleaning in toluene was carried out to remove the mask. The obtained surface morphologies of GaAs were observed by scanning electron microscopy (SEM, Hitachi S-4200) and atomic force microscopy (AFM, Digital Instrument Nano Scope IIIa).

3. Results and discussion

Fig. 2 represents a SEM image of a Cu-honeycomb pattern formed on the *n*-GaAs (100) substrate by electroless plating for 16 min. Cu particles were deposited site selectively only on the exposed areas of the substrate, i.e., the apertures between PS spheres, whereas essentially no Cu particles were deposited at the contact areas of the PS sphere and the underlying GaAs substrate. It was found that the Cu-honeycomb pattern consists of an aggregation of Cu particles of ~75 nm on average, though the size of particles is somewhat scattered. The present study could be the first report on Cu plating of GaAs without bias because the surface processing technique of GaAs has not

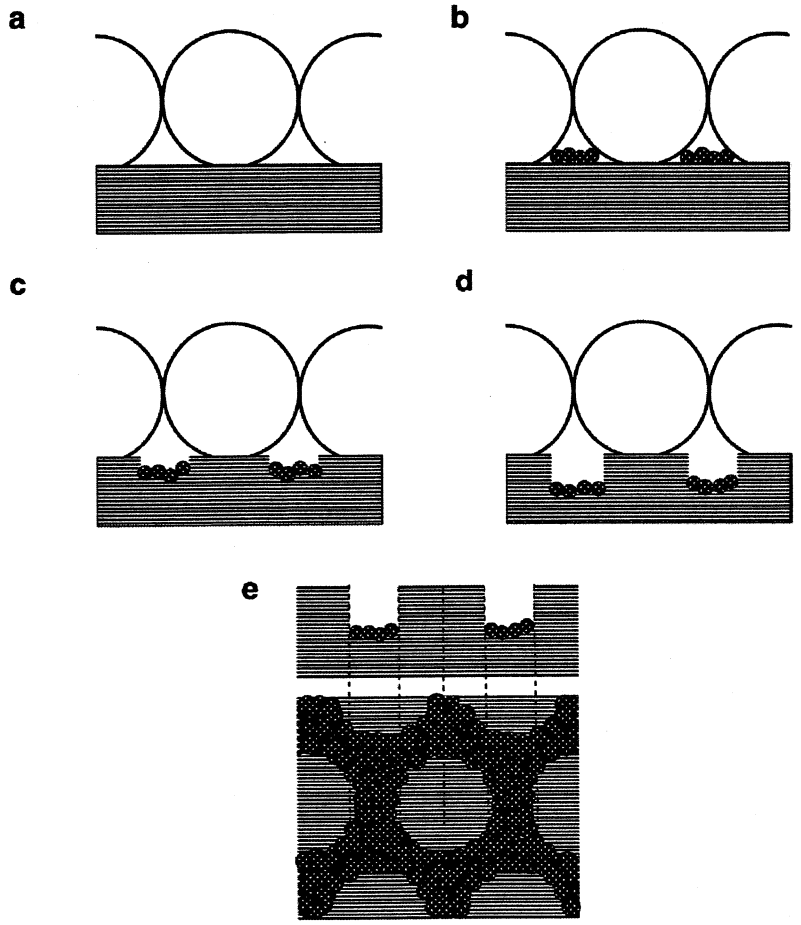

Fig. 1. Schematic explanation of site-selective chemical etching of GaAs. (a) Colloidal crystals formed on substrate as a mask, (b) deposition of noble-metal particles, (c) the initial stage of chemical etching of GaAs using a metal catalyst, (d) after completion of chemical etching, and (e) obtained cross section and corresponding top view after removal of the mask.

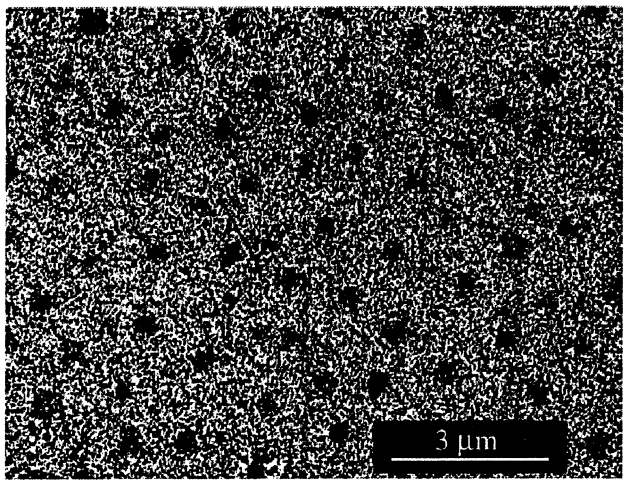

Fig. 2. SEM micrograph of Cu-honeycomb pattern formed on present *n*-GaAs (100) substrate. PS spheres of 1 μm diameter were utilized as a direct mask.

been sufficiently established and the removal of the native-oxide film from the surface is difficult [11]. A similar honeycomb pattern and particle size of Ag were obtained by Ag immersion plating. Afterward, the Cu- and Ag-plated substrates were exposed to an etching solution for 60 s. Fig. 3a shows a GaAs substrate after Ag plating and subsequent etching. Upon etching, the anisotropic GaAs convex arrays were formed. In the preliminary set of experiments, the etching behavior of the GaAs (100) substrate possessing colloidal crystals as the mask but without any metal catalysts, i.e., the conventional "chemical etching", was first investigated. As a result, GaAs was etched by the present HF-based etching solution itself. By comparing the chemically etched specimen described above with the specimen etched with Ag assistance represented in Fig. 3a, the difference in etching structures between the two specimens is clearly revealed. Therefore, it was confirmed that the obtained GaAs convex structure shown in Fig. 3a is due not to chemical etching but is originated from "metal-assisted" chemical etching with Ag. Essentially, the structure shown in Fig. 3a has an inverse relation to the Ag-honeycomb pattern exhibiting a pattern similar to that in Fig. 2. Note that the etching structure originated from the use of PS "spheres" with 1 μm diameter, though the achieved pattern showed an anisotropic shape. On the other hand, effective metal-assisted etching was not achieved for the Cu-plated specimen because Cu is less noble compared with Ag. An AFM image of the corresponding GaAs convex structure is shown in Fig. 3b. The average etching depth of 35 nm is much shallower than that of *p*-Si (100) [*ca.* 100 nm] etched with Ag assistance [12] under identical experimental conditions. *p*-Si (100) exhibited an isotropic etching structure with an etching rate of ~1.7 nm/s by Ag-assisted etching [12], while the present *n*-GaAs (100) shows an anisotropic configuration, and the average etching velocity was estimated to be ~0.6 nm/s on the bases of a line analysis of the AFM image

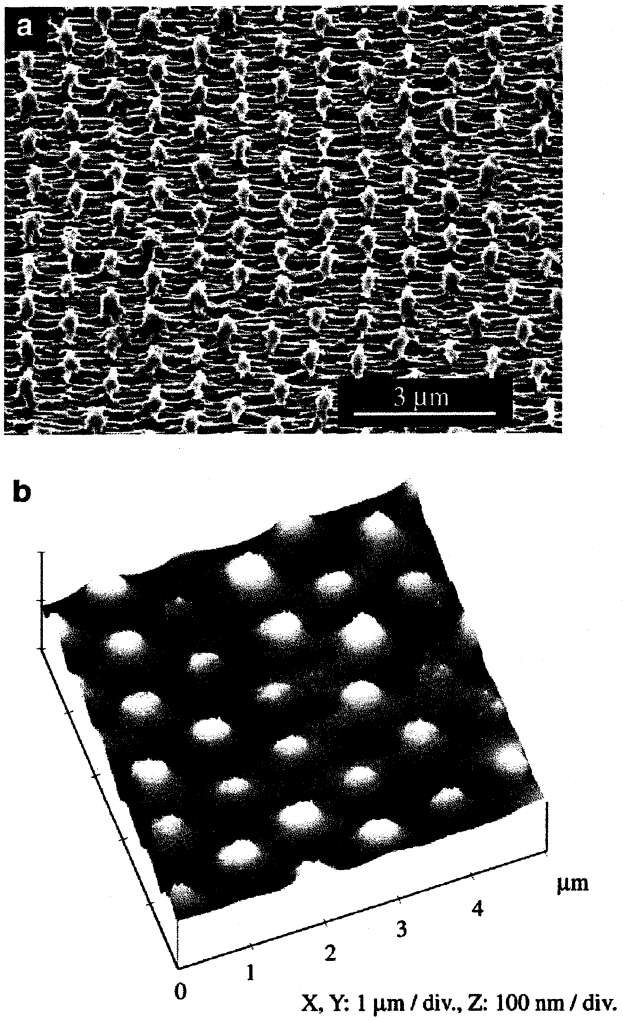

Fig. 3. Surface structures of *n*-GaAs (100) substrate obtained by a combination of self-organized structural mask consisting of PS spheres (∅1 μm), electroless plating and metal-assisted etching. Typical patterns obtained from (a) SEM micrograph observed from 45° to the surface, and (b) AFM image.

shown in Fig. 3b. Concerning the mechanism for the Ag-assisted chemical etching of Si, Li and Bohn reported as follows [2]: (I) When the oxidants (H_2O_2) are reduced on the surfaces of Ag particles, positive holes (h^+) are generated as cathode reaction. (II) The oxidative dissolution of Si occurs in HF-containing etchant as anode reaction. (III) Finally, porous silicon can be generated as a localized electrochemical process. The fundamental mechanism of metal-assisted etching of GaAs might be somewhat analogous to that of Si, but underlying mechanisms must be more complicated for GaAs since GaAs is composed of two different constituents. Also, chemical reactivities [11] and valences of Ga and As are different so that the contributions of Ga and As elements to metal-assisted etching might not be identical at the atomic level. Thus, Si and GaAs exhibit dissimilar etching configurations and etching rates even when the same experimental conditions and the same catalytic metal are utilized.

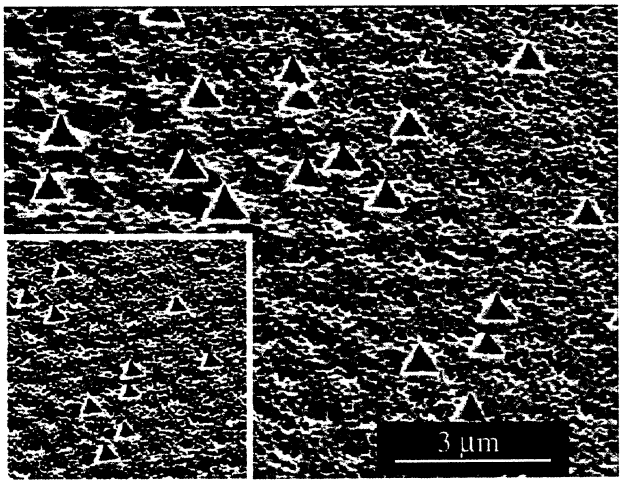

Fig. 4. SEM micrograph of Ag-assisted etching for *n*-GaAs (1 1 1) substrate observed from 45° to the surface. All the experimental conditions were the same as in the case of Fig. 3 Inset shows low-magnification view of obtained specimen.

Ag-assisted etching was also studied on the *n*-GaAs (1 1 1) substrate under the same experimental conditions. Although it is not confirmed, the obtained structure seems to be etched with Ag assistance and form convex configurations. On the other hand, the contact areas between the PS sphere and the substrate were etched owing to the removal of the mask during etching, i.e., traces of chemical etching at the convex portion are seen in Fig. 4. Therefore, the SEM image shows two different types of etching effects simultaneously. In contrast to the (1 0 0) substrate, the observed convex arrays imply that Ag-assisted etching proceeds relatively isotropically and at a shallow depth on the (1 1 1) substrate. According to a previous report [10], no marked difference between *p*-Si (1 0 0) and *p*-Si (1 1 1) substrates was seen in the electroless-deposited Ag particles. However, subsequent Ag-assisted etching generated different patterns on the two planes, i.e., etched holes tended to be generated on the surface of Si (1 1 1), but much deeper holes in the direction perpendicular to the substrate surface were formed on Si (1 0 0). Thus, the present result is consistent with that for Si. In addition, the shape of Ag particles is one of the dominant factors in the control of the orientation and the depth of etched holes in Ag-assisted Si etching [3]; the deeper cylindrical holes in the direction perpendicular to the surface originated as a consequence of the more spherical shape of Ag particles and the subsequent etching. Therefore, the shallower etching structure seen in GaAs (1 1 1) implies that the (1 1 1) substrate is chemically inactive compared with the (1 0 0) substrate in terms of Ag-assisted etching, or deformed Ag particles [3] were generated on (1 1 1). Although a reason for the generation of triangular pits seen in Fig. 4 is not yet confirmed, they could be composed of {1 1 2} pit walls because {1 1 2} is the most stable plane enveloping directions of <1 1 1> [13].

4. Conclusion

In conclusion, we demonstrated that electroless Cu and Ag plating yielded patterned structures reflecting the self-organized structural mask, and consequently, Ag-assisted etching was accomplished on the *n*-GaAs substrate. In the present etching method, the crystal-face orientation, i.e., *n*-GaAs (1 0 0) and (1 1 1), considerably affect the resultant etching structure and the etching rate. As a suggestion of future work, we will try to fabricate novel surface structures by using the difference in etching patterns between the crystal-face orientations of *n*-GaAs.

References

[1] S. Yae, Y. Kawamoto, H. Tanaka, N. Fukumuro, H. Matsuda, Electrochem. Commun. 5 (2003) 632.
[2] X. Li, P.W. Bohn, Appl. Phys. Lett. 77 (2000) 2572.
[3] K. Tsujino, M. Matsumura, Electrochim. Acta 53 (2007) 28.
[4] H. Asoh, A. Uehara, S. Ono, Jpn. J. Appl. Phys. 43 (2004) 5667.
[5] H. Asoh, A. Oide, S. Ono, Electrochem. Commun. 8 (2006) 1817.
[6] H. Asoh, S. Ono, Appl. Phys. Lett. 87 (2005) 103102.
[7] H. Asoh, K. Nakamura, S. Ono, Electrochim. Acta 53 (2007) 83.
[8] H. Asoh, S. Sakamoto, S. Ono, J. Colloid Interface Sci. 316 (2007) 547.
[9] S. Ono, A. Oide, H. Asoh, Electrochim. Acta 52 (2007) 2898.
[10] K. Tsujino, M. Matsumura, Adv. Mater. 17 (2005) 1045.
[11] I. Shiota, K. Motoya, T. Ohimi, N. Miyamoto, J. Nishizawa, J. Electrochem. Soc. 124 (1977) 155.
[12] H. Asoh, F. Arai, S. Ono, Electrochem. Commun. 9 (2007) 535.
[13] S. Langa, J. Carstensen, M. Christophersen, H. Föll, I. Tiginyanu, Appl. Phys. Lett. 78 (2004) 1074.

— Communication —

無電解めっきによる貴金属微粒子触媒層の付与と湿式エッチングによるシリコンのマイクロパターニング

新井　房雄，阿相　英孝，小野　幸子

工学院大学工学部応用化学科（〒192-0015　八王子市中野町2665-1）

Electroless Deposition of Noble Metal Nano Particles as Catalyst and Subsequent Micropatterning of Silicon Substrate by Wet Chemical Etching

Fusao ARAI, Hidetaka ASOH, and Sachiko ONO

Department of Applied Chemistry, Faculty of Engineering, Kogakuin University (2665-1 Nakano, Hachiouji, Tokyo 192-0015, Japan)

Received November 28, 2007 ; Accepted December 27, 2007

Noble metal particles such as Ag and Pd were deposited site-selectively on Si substrate using colloidal crystal composed of polystyrene spheres as a mask for electroless plating to obtain metallic honeycomb pattern. After metal-assisted chemical etching of Si in HF/H_2O_2, ordered Si convex arrays were formed. On the other hand, isolated-island metal pattern was obtained on Si substrate by hydrophobic treatment with colloidal crystal templating, which acted as a mask for subsequent electroless plating. Si hole arrays formed after chemical etching corresponded to inverse structure of above-mentioned Si convex arrays. The dimensions of the resultant pattern could be adjusted with feature sizes ranging from 3 μm to 200 nm by changing the diameter of the polystyrene spheres used as an initial mask.

Key Words : Silicon, Metal-assisted Chemical Etching, Colloidal Crystal Templating

1　緒　言

シリコンをフッ酸溶液中でアノード酸化することで形成されるポーラスシリコンは，基板の比抵抗や電解条件に応じてミクロ孔からマクロ孔まで孔径の制御が可能であり，その高い多孔度を利用して電気化学センサーや光電気化学セルなどへの応用が検討されると共に，バルクシリコンにはない可視発光特性を制御した発光素子としての応用研究も盛んに行われている[1,2]．ポーラスシリコンの作製方法はフッ酸を含む電解液中でのアノード酸化が最も一般的であるが，Bohnら[3]はイオンスパッタリングを用いて金や白金，パラジウムなどの貴金属薄膜を付与したシリコン基板をフッ酸－過酸化水素の混合液中に浸漬させることで電気化学的手法を用いること無くポーラスシリコン層の形成が可能であることを報告した．一方，八重ら[4]は無電解めっきにより白金やパラジウムなどの貴金属の微粒子を析出させたシリコン基板をフッ酸に浸漬するだけでもエッチングが進行し，過酸化水素などの酸化剤がなくてもポーラスシリコンを形成できることを報告した．また，松村ら[5]の報告によれば，銀微粒子を析出させたシリコン基板をフッ酸－過酸化水素の混合液に浸漬することで銀微粒子がエッチングの触媒として作用し，直径100 nm程度の銀微粒子が基板内部に沈降しながら深さ500 μmの孔を形成することも可能である．貴金属微粒子の触媒作用によるポーラスシリコン層の形成は，太陽電池表面の反射率を低減する新たなテクスチャー技術として期待されるだけでなく，既存のマスク形成技術と組み合わせることによりシリコン基板を位置選択的にエッチングすることが可能であり，拡散膜，発光デバイス，化学センサーなどの作製技術として応用が検討されている[6]．

我々はこれまでにシリコン基板上に形成したポーラスアルミナやコロイド結晶の自己組織化構造をマスクとして利用し，化学エッチングやアノード酸化によるシリコン基板の微細加工を検討してきた[7-9]．また，自己組織化的に形成されるコロイド結晶の規則構造に着目し，前述した金属触媒エッチングを組み合わせることで，コロイド結晶の規則配列を転写したマイクロメートル周期のシリコン凸型及び凹型構造を作製できることを報告した[10]．自己組織化構造をマスクとして利用した構造転写技術は，既存のリソグラフィー技術に比べ，パターンの多様性や加工精度には欠けるものの，工程の簡易さ，低コスト，大面積加工などの特徴を持ち，トップダウン方式によらない微細加工技術として様々な分野での応用が期待される．

本研究では，粒径3 μmから200 nmの範囲のポリスチレン微粒子をマスクとして用い，シリコン凹凸構造の周期をナノメートルオーダーまで微細化させることを検討した．また，二液法活性化前処理を用いてパラジウム微粒子触媒の位置選択的付与を検討し，無電解めっきで析出させた銀微粒子を比較対照に，シリコンのエッチング挙動に及ぼす触媒付与形態の影響を検討した．

2 実験方法

2．1 エッチングマスクの作製

Fig. 1に実験プロセスの模式図を示す．p型（100）配向単結晶シリコン基板（抵抗値10-20 Ωcm）を1 cm角に切り出し，アセトン中で超音波脱脂後，1 wt%フッ酸に1分間浸漬して自然酸化皮膜を除去した．前処理済みのシリコン基板上に内径5.5 mmのOリングを設置し，0.2%ポリスチレン（PS）微粒子分散懸濁液（Polysciences, Inc.製）を滴下，乾燥させることでエッチングマスクとなるコロイド結晶を形成した（Fig. 1 (a)）．その後，100℃，1時間の加熱処理を行い，PS微粒子を基板上へ固定した．一方，コロイド結晶を形成したシリコン基板をヘキサメチルジシラザン（HMDS）雰囲気下で密閉容器内に一晩静置し，シリコン露出面を疎水化処理した（Fig. 1 (e)）．HMDS処理後，シリコン基板上のコロイド結晶はトルエン中で溶解除去した（Fig. 1 (f)）．

2．2 貴金属触媒を用いた湿式エッチング

コロイド結晶を形成したシリコン基板を過塩素酸銀（10^{-3} mol dm^{-3}）－水酸化ナトリウム（10^{-3} mol dm^{-3}または10^{-2} mol dm^{-3}）の混合水溶液に20 min浸漬し，シリコン表面に銀微粒子を付与した（Fig. 1 (b)）．その後，5 mol dm^{-3}フッ酸－1 mol dm^{-3}過酸化水素の混合水溶液にシリコン基板を浸漬しエッチングを行った（Fig. 1 (c)）．コロイド結晶を直接マスクとした場合には，エッチング後の試料をトルエンに浸漬しコロイド結晶を除去した（Fig. 1 (d)）．一方，HMDS処理を施したシリコン基板に対しても同様に，位置選択的に銀微粒子を付与後（Fig. 1 (g,)），エッチングを行った（Fig. 1 (h)）．各処理後のシリコン表面形態は電界放射型走査電子顕微鏡（FESEM, HITACHI S-4200）で観察した．

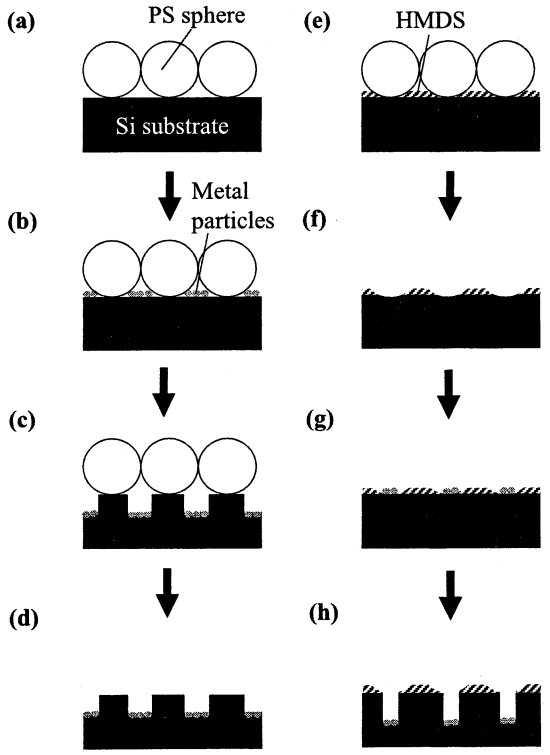

Fig. 1 Schematic model of site-selective chemical etching of Si: (a) Colloidal crystals on Si substrate, (b,g) electroless plating, (c,h) chemical etching of Si using metal particles as catalyst, (d,f) After removal of colloidal crystals, and (e) HMDS coating.

次に，シリコンのエッチング挙動に及ぼす触媒付与形態の影響を銀と比較するため，二液法活性化前処理を用い，パラジウム微粒子の位置選択的付与を検討した．はじめにシリコン基板を0.46 mol dm^{-3}塩酸－0.05 mol dm^{-3}塩化スズ（Ⅱ）の混合水溶液に5 min浸漬し，その後同基板を0.03 mol dm^{-3}塩酸－1.4×10^{-3} mol dm^{-3}塩化パラジウム（Ⅱ）の混合水溶液に5 min浸漬した．それぞれの処理後には純水洗浄を行った．二液法活性化前処理は一般に次の化学反応式（1）で表され，還元剤としてSn^{2+}を予め基板に吸着させる感受性化工程とパラジウムを還元析出させる活性化工程から成り立つ．

$$Pd^{2+} + Sn^{2+} \rightarrow Pd + Sn^{4+} \qquad (1)$$

二液法活性化前処理によりパラジウムを付与したシリコン基板は，銀を付与したシリコン基板同様にフッ酸－過酸化水素混合水溶液中でエッチングを行った．

3 結果および考察

3．1 コロイド結晶を直接マスクとした銀触媒エッチングによるシリコン凸型構造の作製

均一な粒子径を持つPS微粒子の懸濁液を固体基板上に滴下し，自然乾燥させると溶媒蒸発時の移流集積によって微粒子は最密充填構造を自発的に形成する[11]．コロイド結晶をマ

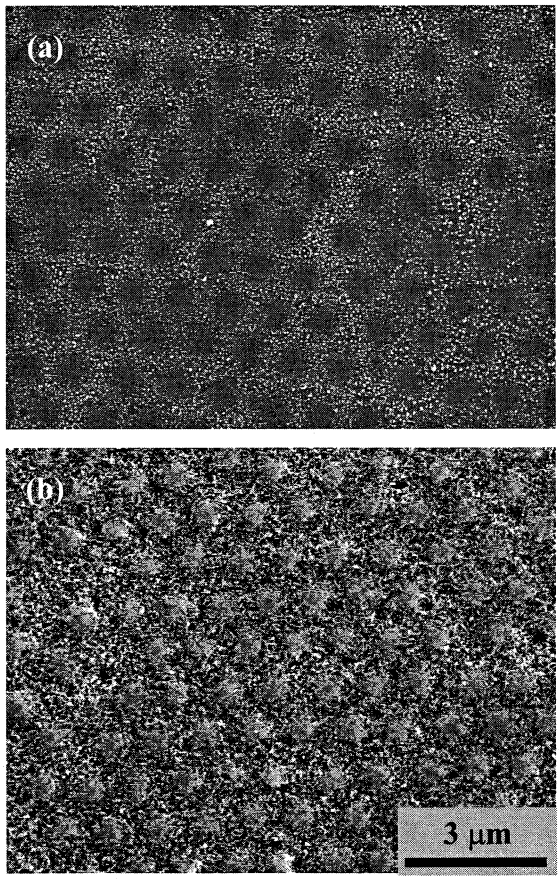

Fig. 2 (a) SEM image of Ag particles deposited on Si with colloidal crystal mask. Electroless plating was conducted in 10^{-3} mol dm^{-3} $AgClO_4$ and 10^{-2} mol dm^{-3} NaOH for 20 min. (b) SEM image of surface of etched Si in HF / H_2O_2 for 1 min. The polystyrene sphere used as a mask was 1 μm in diameter.

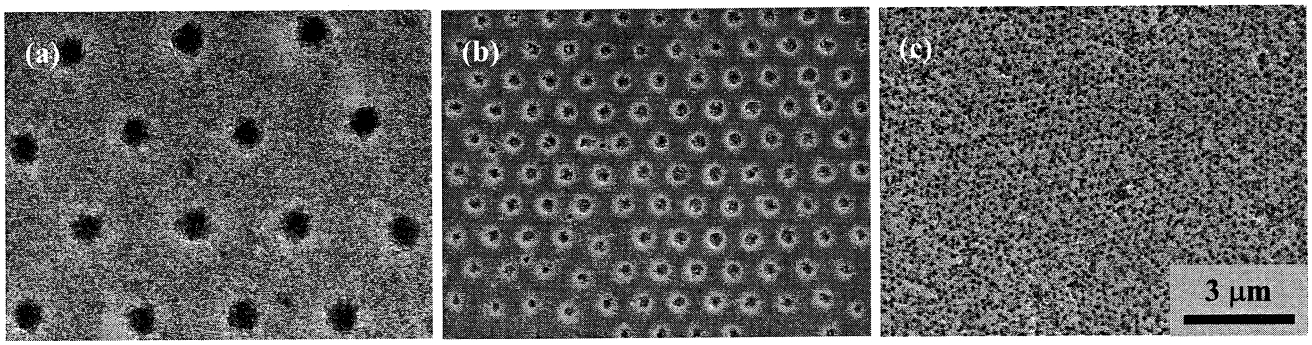

Fig. 3 SEM images of Si hole arrays with different periodicity: (a) 3 μm (b) 1 μm and (c) 200 nm. Electroless plating was conducted in 10^{-3} mol dm^{-3} $AgClO_4$ and 10^{-3} mol dm^{-3} NaOH for 20 min. Chemical etching was carried out in HF/H_2O_2 for (a) 5 min and (b, c) 30 s.

スクとして無電解銀めっきを施したシリコン基板上には粒径30-100 nmの銀微粒子が析出し，その銀微粒子の集合体がハニカム状パターンを形成した（Fig. 2 (a)）．Fig. 2 (a) においてコントラストの暗い部分はPS微粒子とシリコン基板の接触面に相当し，周囲の白色の点が析出した銀微粒子である．このパターンの周期がPS微粒子の直径に一致することは，PS微粒子が無電解めっき時のマスクとして作用し，PS微粒子とシリコン基板が接触していた面には銀微粒子は析出せず，その周囲の露出したシリコン基板表面のみに銀微粒子が析出したことを意味する．エッチング後，シリコン表面に六方配列した周期1 μmの凸型構造が得られた（Fig. 2 (b)）．Fig. 2 (b) において周囲より高いシリコンの凸部は明るいコントラストを呈し，周囲のポーラスシリコン層においては孔の部分が暗く，孔壁はエッジ効果で白く観察される．銀微粒子が析出したシリコン表面でのみ選択的にエッチングが基板垂直方向に進行し，ハニカム状にポーラスシリコン層を形成したと考えられる．その結果，PS微粒子とシリコン基板の接触面はエッチングを受けずに円盤状に残存し，その直径は400-500 nmであった．本手法で得られるパターンの周期は，基本的にマスクとして用いるPS微粒子径に依存することから，今回粒径1 μmのPS微粒子を用いることで，既報[10]の3 μm周期のパターンに対し，周期を1/3に微細化できた．しかしながら，エッチング部位が連続したハニカム構造であるため，1 min以上エッチングを継続した場合，シリコン基板表面に対して水平方向へのエッチングも著しく進行すると共にステイン層[3,5]が形成され，表面の規則配列を維持したままアスペクト比の高い突起構造を形成することはできなかった．

3．2　HMDS疎水性パターンをマスクとした銀触媒エッチングによるシリコン凹型構造の作製

上述したコロイド結晶をマスクとした構造転写法を応用し，2段階の転写プロセスによりシリコン凸型構造の反転構造に相当する凹型構造の作製について検討した．コロイド結晶を第一マスクとし，シリコン基板との接触面以外をHMDS処理することで，微粒子間隙部に相当する露出したシリコン基板表面は最表面がメチル基で覆われた疎水性表面となる[12]．その疎水性表面部と微粒子直下の位置に相当するシリコン露出面との濡れ性の違いを利用し，無電解銀めっきを行った．HMDS処理後，無電解銀めっきを行ったシリコン基板にはPS微粒子の配列に対応した銀微粒子の集合体からなる島状パターンが形成された．これは，PS微粒子の間隙部に相当するHMDS修飾面には銀微粒子は析出せず，親水性を持つ面のみに選択的に銀が析出したことを意味する．このようにHMDSによる疎水性パターンを無電解めっき時の第二マスクとして利用することで銀微粒子の集合体を規則的に配列させることが可能であった．

次にHMDS疎水性パターンをマスクとして銀微粒子を島状に析出させたシリコン基板をフッ酸－過酸化水素混合液中でエッチングし，シリコン凹型構造の作製を検討した．Fig. 3 (a) は第一マスクとして粒径3 μmのPS微粒子を用い，疎水化処理後の無電解めっきに続き，エッチングを5 min行ったシリコン基板表面のSEM像である．Fig. 3 (b), (c) はそれぞれ第一マスクとして粒径1 μm，200 nmのPS微粒子を用い，島状に銀触媒を付与後，エッチングを30 s行ったシリコン基板表面のSEM像である．エッチング後のシリコン基板にはいずれも六方配列したホールアレイが観察された．このホールアレイの周期はエッチング前の銀微粒子の島状パターン周期に一致し，コロイド結晶を構成するPS微粒子の粒径を変化させることにより制御が可能であった．上述のシリコン凸型構造の場合は銀微粒子が連続した網目構造を形成するため，サイドエッチングの影響で1 μm以下の周期に微細化することが困難であったが，反転構造の場合，銀微粒子の析出形態は孤立した島状構造であるため，サイドエッチングの影響が低減され，3 μmの周期から200 nmの周期までパターンの微細化が実現した．

3．3　パラジウムを触媒としたシリコンのエッチング

コロイド結晶を直接マスクとして二液法活性化前処理を行い，パラジウム微粒子触媒の位置選択的付与を行った．PS微粒子の間隙部に相当するシリコン面には直径50 nm以下の微粒子が隙間無く密に析出し，100-200 nmの比較的大きなパラジウム微粒子も不均一に析出した．

Fig. 4にパラジウム触媒付与後，エッチングを1 min行ったシリコン基板表面のSEM像を示す．Fig. 2 (b) に示した銀微粒子触媒の結果と同様にハニカム状に触媒を付与した周辺部で選択的にエッチングが進行した．六方配列したシリコン凸型構造の先端は平坦であり，その直径は約600 nmであった．シリコン突起部の直径はエッチング前のパラジウムが析出していない面の直径と一致し，1 minのエッチングではサイドエッチングの影響は顕著に表れなかった．粒径1 μmのPS微粒子をマスクとした場合は接着面の大きさが粒径の40-50％であったのに対し，3 μmのPS微粒子をマスクとした場合は接着面の大きさが粒径の約20％であった．加熱固

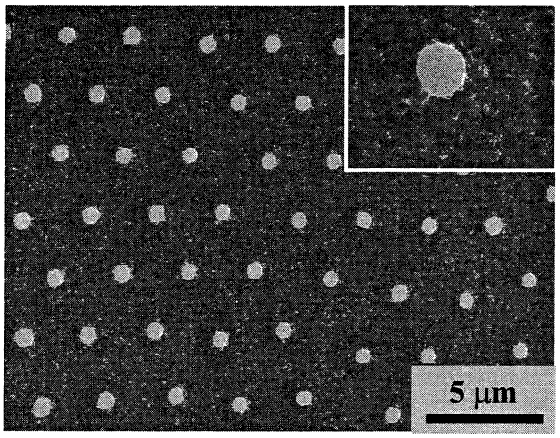

Fig. 4 SEM image of Pd-coated Si after etching in HF/H_2O_2 for 1 min. The polystyrene sphere used as a mask was 3 μm in diameter. Inset shows a high-magnification view of the silicon tip.

定の条件が同じでもPS微粒子の大きさによって熱変形の度合いが異なるため，PS微粒子の粒径に対する接着面の割合が異なったと考えられる．パラジウム微粒子触媒を利用したエッチングでは，銀微粒子触媒を利用した系に比べ，触媒を付与した領域においてシリコンの溶解が均一に進行し，Fig. 2 (b) に比べ，得られたシリコン凸型構造の輪郭は明瞭であった．触媒層を形成する平均的なパラジウム微粒子は，Fig. 2 (a) に示した銀微粒子と比べて粒径が小さく，緻密に析出したため，シリコンの溶解反応が均一に進行したと考えられる．しかし，Fig. 2 (b) に示した銀の場合と同様，エッチングを継続した場合にはサイドエッチングが進行し，表面の規則構造を維持することはできなかった．パラジウムの触媒作用に関しては，銀と同様にパラジウムの微粒子が沈降しながら孔形成するが，銀に比べて細孔の直線性が劣ると報告されている[5]．本研究で，パラジウム触媒の場合に残存したシリコン突起の凸型構造の輪郭が明瞭であった原因として，エッチング進行方向の不均一性も考慮する必要があるだろう．触媒付与形態や，金属種によるエッチングの違いについては，今後さらに詳細に検討すべき課題である．

4 結 言

3 μmから200 nmまで広範囲なサイズのコロイド結晶をマスクとして用いてSi基板上に湿式法による位置選択的な銀微粒子及びパラジウム微粒子触媒を付与することが可能であった．また金属微粒子を付与したシリコン基板をフッ酸－過酸化水素混合液中に浸漬すると，両金属共に触媒として作用し，触媒を付与した領域においてシリコン基板上に規則的な凹凸パターンを形成することができた．触媒種によりエッチング形態が異なることから，今後触媒粒子の形状，粒径，析出分布，密度などの触媒層の形態がその後のエッチングに及ぼす影響に関してより詳細に検討する必要がある．しかし，本手法は，コロイド結晶テンプレート法と金属触媒エッチングを融合した新規のリソグラフィー技術であり，シリコン基板以外にも化合物半導体などの固体基板の微細加工技術としての種々の応用が期待される．

文 献

1) V. Lehmann and H. Foll, *J. Electrochem. Soc.*, **137**, 653 (1990).
2) Y. H. Ogata, *Kino Zairyo* (*Function & materials*), **23**, 27 (2003) [in Japanese].
3) X. Li and P. W. Bohn, *Appl. Phys. Lett.*, **77**, 2572 (2000).
4) S. Yae, Y. Kawamoto, H. Tanaka, N. Fukumuro, and H. Matsuda, *Electrochem. Commun.*, **5**, 632 (2003).
5) K. Tsujino and M. Matsumura, *Adv. Mater.*, **17**, 1045 (2005).
6) S. Chattopadhyay and P. W. Bohn, *J. Appl. Phys.*, **96**, 6888 (2004).
7) A. Oide, H. Asoh, and S. Ono, *Electrochem. Solid-State Lett.*, **8**, G172 (2005).
8) H. Asoh, A. Oide, and S. Ono, *Electrochem. Commun.*, **8**, 1817 (2006).
9) S. Ono, A. Oide, and H. Asoh, *Electrochim. Acta*, **52**, 2898 (2007).
10) H. Asoh, F. Arai, and S. Ono, *Electrochem. Commun.*, **9**, 535 (2007).
11) N. D. Denkov, O. D. Velev, P. A. Kraichevsky, I. B. Ivanov, H. Yoshimura, and K. Nagayama, *Langmuir*, **8**, 3183 (1992).
12) H. Asoh, S. Sakmoto, and S. Ono, *J. Collid. Interface. Sci.*, **316**, 547 (2007).

J Mater Sci (2009) 44:861–868
DOI 10.1007/s10853-008-3185-x

Rutile thin film responsive to visible light and with high UV light sensitivity

Hiroki Nagai · Sohei Aoyama · Hiroki Hara · Chihiro Mochizuki · Ichiro Takano · Norio Baba · Mitsunobu Sato

Received: 22 September 2008 / Accepted: 11 December 2008 / Published online: 31 December 2008

Abstract A transparent rutile thin film 100 nm thick was fabricated on a quartz glass substrate; it was responsive to visible light and had a higher sensitivity to UV light than an anatase thin film formed by sol–gel method under identical conditions. The crystal structure was determined by observations using X-ray diffraction, Raman spectra, and a transmission electron microscope. The oxygen/titanium ratio of the rutile thin films was 1.78 according to the XPS peaks. The photoreactivity and photoinduced hydrophilicity of the rutile thin films was examined by measuring the pseudo first-order rate for the decoloration of methylene blue in an aqueous solution and the water contact angle, respectively. The high photoreactivity and photosensitivity of the O-deficient rutile thin film, whose optical band edge and refractive index were 3.10 eV and 2.2, respectively, were due to electron traps and assisted by O-defects within the rutile particles.

H. Nagai · S. Aoyama · H. Hara · C. Mochizuki · M. Sato (✉)
Coordination Engineering Laboratory, Faculty of Engineering, Kogakuin University, 2665-1 Nakano, Hachioji City, Tokyo 192-0015, Japan
e-mail: lccsato@cc.kogakuin.ac.jp; ft10302@ns.kogakuin.ac.jp

H. Nagai
e-mail: bd06002@ns.kogakuin.ac.jp

I. Takano
Department of Electrical Engineering, Faculty of Engineering, Kogakuin University, 2665-1 Nakano, Hachioji City, Tokyo 192-0015, Japan

N. Baba
Department of Information Science, Faculty of Informatics, Kogakuin University, 2665-1 Nakano, Hachioji City, Tokyo 192-0015, Japan

Introduction

Titania (TiO_2) has received considerable attention as a naturally abundant photosensitive material; rutile and anatase, both titania polymorphs, are industrially available. Rutile is the most stable crystal form of titania [1–4]. So far, anatase has been found to be more photosensitive than rutile. Since Nishimoto et al. showed that anatase is more sensitive to UV light than rutile in a photoreaction, rutile was believed to be inferior to anatase in terms of photoreactivity [5, 6]. Anatase is important for photocatalysis in pollutant degradation and in the development of photofunctional materials, such as films with hydrophilic surfaces, under UV light irradiation. The poor photoreactivity and photosensitivity of rutile are generally believed to be due to its crystal structure [6, 7], so rutile is primarily known as a useful pigment for white paint due to its chemical stability. Rutile more photosensitive than anatase has not yet been discovered; however, in 1972 Fujishima and Honda observed that water molecules photodecomposed on rutile being irradiated by UV light when a certain electric potential was applied to a Pt counter electrode [8].

Anatase, which responds only to UV light, has recently become the focus of research studies attempting to get it to respond to visible light in order to utilize solar and interior light efficiently. Layer-structured anatase thin films, when fabricated by heat treating molecular precursor films under an argon gas flow, were found to respond to visible light with enhanced UV sensitivity by the authors of this study in a previous article [9]. Recently, further details were provided revealing that the uniquely enhanced UV sensitivity of these anatase thin films was caused by oxygen deficiencies embedded within the anatase [10].

Because the band edge of a rutile single crystal is 3.0 eV, rutile has the potential to respond to visible light

[11]. Based upon this knowledge and building upon the results from the previous experiments on anatase responsiveness to visible light, this article details an attempt toward the direct fabrication of O-deficient rutile thin films with high photoreactivity by using a molecular precursor method. The first visible light-responsive thin film created from O-deficient rutile is discussed here; it works without applying any electric potential because of its unprecedented high photosensitivity under UV light irradiation. The findings of this study should facilitate widespread practical use of rutile in light-related applications.

Experimental

Materials

Ethylenediamine-*N,N,N′,N′*-tetraacetic acid (EDTA), methylene blue (MB), and titanium tetraisopropoxide ($Ti(O^iPr)_4$) were purchased from Kanto Chemical Co., Inc. Dibutylamine and 30% H_2O_2 were purchased from Wako Pure Chemical Industries, Ltd., and from Santoku Chemical Industries Co. Ltd., respectively. Methanol and 60% HNO_3 were purchased from Taisei Chemical Co. Ltd. Ethanol was purchased from Ueno Chemical Industries, Ltd. These solvents were dried in 4A molecular sieves before use. Other materials were used without further purification. Quartz glass was purchased from Akishima Glass. The glass substrates with dimensions of $20 \times 20 \times 1.1$ mm^3 were washed in 2-propanol for 15 min with sonicated stirring and then dried in a drying oven at 70 °C.

Preparation of the precursor solution S_{MP} involving the Ti^{4+} complex of EDTA

The precursor solution containing Ti^{4+} complex of EDTA was obtained by a method modified from the one previously reported by the authors [9, 10, 12]. Dibutylamine, 3.58 g (27.7 mmol) and EDTA, 3.56 g (12.2 mmol) were added to a mixture of 10 g each of ethanol and methanol, respectively. The solution was refluxed for 2 h with stirring and then cooled to room temperature. After adding 3.47 g (12.2 mmol) of $Ti(O^iPr)_4$, the solution was refluxed for 4.5 h. After cooling the reacted solution to room temperature, 1.56 g (13.8 mmol) of 30% H_2O_2 was carefully added. The solution was then refluxed for 0.5 h. The concentration of titanium was 0.4 mmol g^{-1}.

Preparation of the sol–gel solution S_{SG}

A conventional sol–gel solution was prepared by reacting 4.31 g (15.2 mmol) of $Ti(O^iPr)_4$ with 1.10 g (10.5 mmol) of 60% nitric acid and 0.84 g (46.7 mmol) of water in 25 g of ethanol [13, 14]. The concentration of titanium was 0.5 mmol g^{-1}.

Coating, heat-treating procedures, and film thickness

The thin films were formed by heat-treating the precursor films (15×15 mm^2) spin-coated onto a quartz glass substrate; the solutions S_{MP} and S_{SG} were applied with an argon gas flow. A spin-coating method to form the titania precursor films were formed with a spin-coating method employed with a double step each time: first at 500 rpm for 5 s, then at 2,000 rpm for 30 s. Transparent precursor films formed by spin-coating the solutions and pre-heating in a drying oven at 70 °C for 10 min were heat-treated at 700 °C for 30 min in a furnace made from a quartz tube (φ 40 mm) with an argon gas flow rate of 0.1 L min^{-1}. When S_{MP} was used, a transparent rutile thin film **R** formed; when S_{SG} was used, a transparent anatase thin film **A** formed. The film thickness, measured using the stylus profilometer DEKTAK3, was 100 nm in both cases.

In order to prepare the samples for transmission electron microscope observation, ultra-thin films with film thicknesses of 10 nm were prepared using 1/10-diluted solutions of S_{MP} and S_{SG} and under the same conditions except for the solution concentration and the substrate. NaCl single crystals were employed for the substrate instead. The ultra-thin films were fabricated and then recovered by dissolving the NaCl substrate with water.

Structure and chemical identity of thin films

The X-ray diffraction (XRD) pattern of each film was measured with an X-ray diffractometer (MXP-18 AHF22, Bruker AXS), with Cu–$K\alpha$ rays generated at 45 kV and 300 mA. Parallel beam optics with an incident angle of 3.0° was employed. Cell parameters were refined by the least square method.

The structure and lattice image of each film were observed with a transmission electron microscope (TEM H8100, Hitachi) at an accelerating voltage of 200 kV and the ultra-thin films applied on a Cu grid.

A Phi Quantum 2000 Scanning ESCA Microprobe (Shimadzu) with a focused monochromatic Al–$K\alpha$ X-ray (1486.6 eV) source was employed in order to evaluate the element states and quantities—Ti, O, N, and C—in the films. Chemical shift data were charge-referenced to the center of the C–C/C–H peak at 284.6 eV. The resolution was 0.2 eV for each measurement. The depth profile was obtained with the same instrument. The stepwise etching was performed by bombarding the Ar^+ ion with 2 kV and 18 μA cm^{-2} for 3 min before measuring each layer. The XPS peaks for all the 15 layers were measured in order to obtain the depth profile.

Surface morphology and mechanical strength

The surface appearance of the thin films coated with gold was observed with a field-emission scanning electron microscope (FE-SEM S-4200, Hitachi) at an accelerating voltage of 5 kV.

The adhering strength of the films to the quartz substrate was examined with a scratch tester (HEIDON-22, Shinto Scientific) using a load of 0.50 kg and a scanning rate of 10.5 N min^{-1}.

Optical properties of thin films

The transmittance and absorption spectra of the thin films were measured in the 200–800 nm range with a double-beam mode; the quartz glass substrate was used as the reference for each measurement. The measurements were performed with a U-2800 spectrophotometer (Hitachi). The optical band edge E_g of the thin films was determined by using the following Tauc expression:

$$\alpha = \frac{A(E - E_g)^{1/2}}{E} \quad (1)$$

where E is the photon energy ($\equiv h\nu$); A is the constant; and α is the absorption coefficient at the wavelength [15].

A MARY-102 (Five Lab) scanning ellipsometer was employed to measure the refractive index of the thin films with a He–Ne laser beam of 632.8 nm and an incidence angle of 70.8°. The refractive index was measured three times at eight different points on the thin films and averaged to determine the value.

Photoreactivity measurements

The photoreactivity of each film was examined using the decoloration rate of methylene blue (MB) in 10 mL of aqueous solution (0.01 mmol L^{-1}). A black light (FL10BL-B, National), was used for UV light irradiation. The distance of the black light source from the sample surfaces was adjusted in order to maintain a UV light intensity of 1.2 mW cm^{-2} at 365 nm; the intensity was measured with an ultraviolet meter (UVR-400, Iuchi). The visible light intensity on the samples was 0.8 mW cm^{-2} with the fluorescent light (True light, Duro Test) after removing wavelengths shorter than 400 nm by using a cut-off filter; the intensity was measured with an illuminometer (LX-105, Custom). The removal of UV light was confirmed by checking the UV light intensity for a value of 0.0 mW cm^{-2} at 365 nm with the UV meter.

The MB concentration was determined by measuring the absorption spectra of the aqueous solution with the U-2800 spectrophotometer. For the decoloration test, 3 mL of the solution was transferred into a quartz cell of dimensions $1 \times 1 \times 4.5$ cm^3 at 20-min intervals. After spectral measurement, the solution was immediately returned to the vessel and mixed with the aliquot. The mixed solution continued to be used until the test for each film was completed. The temperature of the test solution was maintained at 20 ± 1 °C throughout the measurement.

The pseudo first-order rate for the decoloration reaction of the MB aqueous solutions was obtained three times for each film; the averaged value was assigned to the rate v. In order to examine the effects of both the adsorption and the self-decoloration for MB, the same measurement was performed on the same samples without irradiation as a reference. The v value for each film was calculated as follows. The MB concentration C(t) after irradiation for t min was determined as

$$C(t) = 10 \times \frac{Abs(t)}{Abs(0)} [\mu\text{mol L}^{-1}] \quad (2)$$

where $Abs(0)$ and $Abs(t)$ represent the absorption value at 664 nm for the solution immediately before irradiation and after irradiation for t min, respectively. An approximate line for the function of C(t) versus t was obtained in the range $0 \leq t \leq 80$ min by the least square method. The rate v for each film was estimated as the averaged gradient of the lines:

$$v = \frac{|\sum v_n|}{3} \times 10^3 \quad [\text{nmol L}^{-1}\,\text{min}^{-1}], \quad (3)$$

where v_n indicates each of the individual gradients (n = 1, 2, 3) obtained independently.

Photo-induced hydrophilicity measurements

The contact angle for a 1.0-μL water droplet on the thin films was measured with a contact angle meter (FACE, Kyowa Kaimenkagaku). The measurement was performed after irradiation of the samples with visible or UV light in atmospheric air at 26 °C and 40% humidity. The same light sources employed in the decoloration test for the MB solution mentioned above were used. In this experiment, the position of the black light source was adjusted in order to maintain a UV intensity of 4.5 mW cm^{-2} at 365 nm on the samples. The contact angle for the water droplet before the light irradiation on **R** (68°) was almost the same as for **A** (70°) under the same atmospheric conditions.

Results

Crystal structure and chemical identity of the thin films

Figure 1 shows the XRD patterns for **R** and **A**. In **R**, the peaks were found at 2θ = 27.5, 36.2, 39.3, 41.4, 44.3, 54.5,

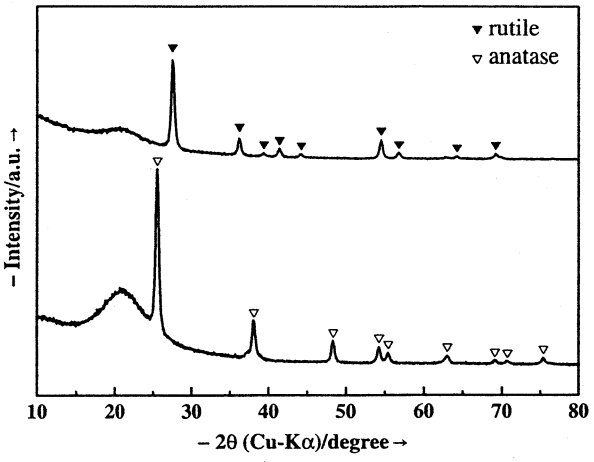

Fig. 1 XRD patterns for **R** (rutile) and **A** (anatase) fabricated by heat treating the corresponding precursor film at 700 °C in an Ar gas flow

56.7, 64.2, and 69.2°, corresponding to the (110), (101), (200), (111), (210), (211), (220), (310), and (301) phases of rutile [16]. In **A**, the peaks were observed at $2\theta = 25.6$, 38.1, 48.4, 54.2, 55.5, 62.9, 69.1, 70.7, and 75.3°, corresponding to the (101), (004), (200), (105), (211), (204), (116), (220), and (215) phases of anatase [17]. The precise cell parameters for the tetragonal lattices were $a = 0.459(1)$ nm and $c = 0.296(1)$ nm for **R**, and $a = 0.377(1)$ nm and $I = 0.953(4)$ nm for **A**. These values correlated well with the corresponding lattices for the rutile and anatase crystals. Thus, the crystal structures of **R** and **A** were demonstrated to be the single phases of rutile and anatase, respectively.

The Raman spectra of **R** and **A** thin films are shown in Fig. 2. The absorption bands at 139, 441, and 609 cm^{-1} correspond to rutile in the spectrum for **R**. The absorption bands at 146, 400, 521, and 641 cm^{-1} correspond to anatase in the spectrum for **A** [18].

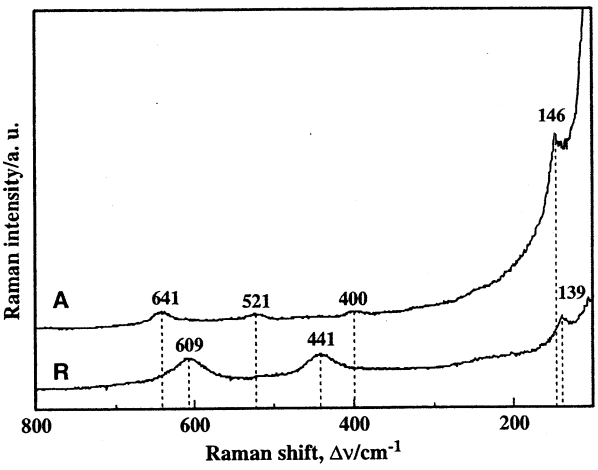

Fig. 2 Raman spectra for **R** and **A** thin films fabricated by heat treating the corresponding precursor film at 700 °C in an Ar gas flow

The transmission electron microscope (TEM) images and electron diffraction patterns for the ultra-thin films corresponding to **R** and **A** are presented in Fig. 3, along with the phase assignment and dimension. The diffraction patterns indicated a typical tetragonal structure for rutile and anatase with the corresponding cell parameters. These results were consistent with those determined by the XRD patterns for **R** and **A**.

The XPS peaks corresponding to O 1s and Ti $2p_{3/2}$ were found at 529.8 eV and 458.8 eV, respectively, for each film; these values are typical for titania [19]. The averaged O/Ti peak area ratio was 1.78 for **R** and 1.93 for **A**. The homogeneity in the vertical direction of the thin films was confirmed by the depth profiles of the XPS peaks, which were measured with an Ar^+ ion etching mode.

Surface morphology and mechanical strength of the thin films

The surface appearance of the thin films is shown in Fig. 4.

The adhering strength of **R** and **A** to the quartz substrate was 1.75 and 0.69 GPa, respectively.

Optical properties of the thin films

The transmittance spectra of the thin films are presented in Fig. 5. The optical band edge for **R**, determined from the corresponding absorption spectrum by assuming a direct-transition semiconductor, was 3.10 eV; it was considerably smaller than for **A** (3.63 eV).

The refractive indices of **R** and **A** were 2.2 and 2.5, respectively.

Photoreactivity of thin films

The photoreactivity of the thin films was evaluated by the decoloration rate of the MB solution, which served as a model for organic pollutants in water [20, 21]. The results measured under visible and UV light irradiation are summarized in Table 1 along with those measured under dark conditions (reference values); they indicate the effects of adsorption on the samples and vessels and self-decoloration of MB under each condition [9, 10]. The v values, where v is the pseudo first-order rate, were found to be larger than when under dark conditions, indicating the degree of photoreaction induced by the light irradiation on the films. Rapid decoloration of the MB solution due to the redox reaction caused by **R** was clearly observed when irradiating the films with only visible light. Moreover, the photoreactivity of **R** was also extremely high under UV light

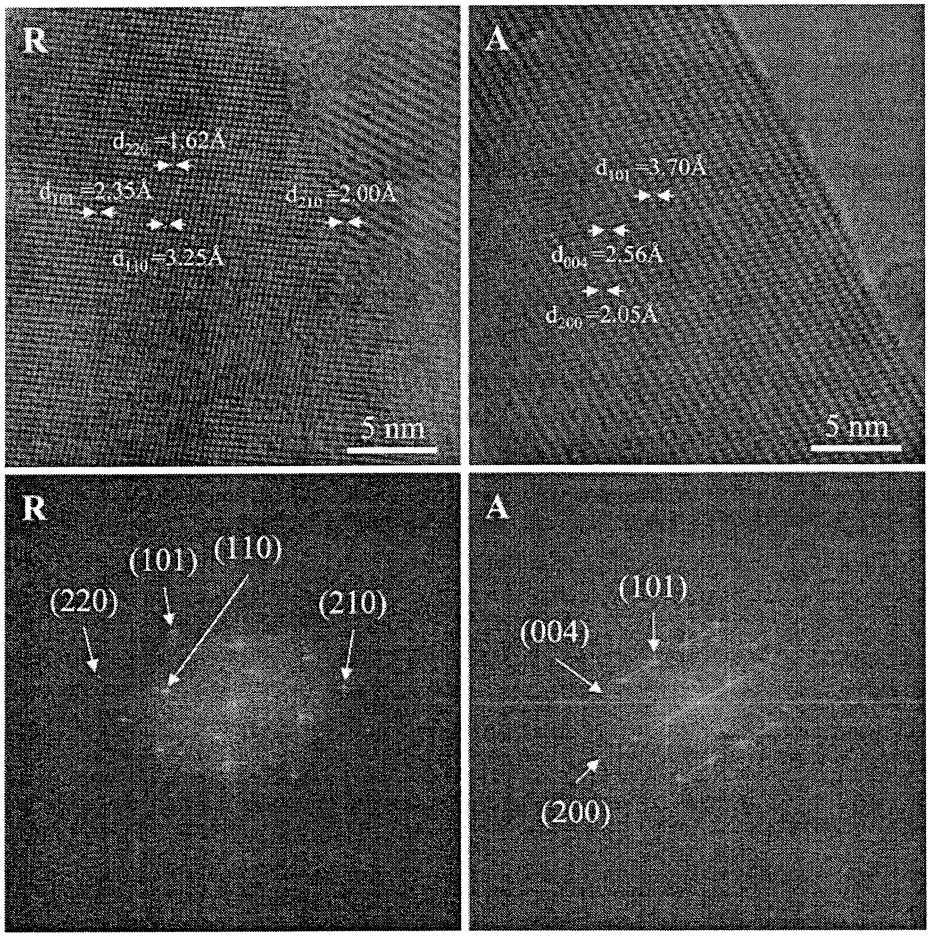

Fig. 3 Structure and lattice image of the ultra-thin films corresponding to **R** and **A**, observed with a transmission electron microscope. The TEM images (above) and the corresponding diffraction patterns (below) of the films are described, respectively. The crystal structure was analyzed using Fourier-transformed patterns

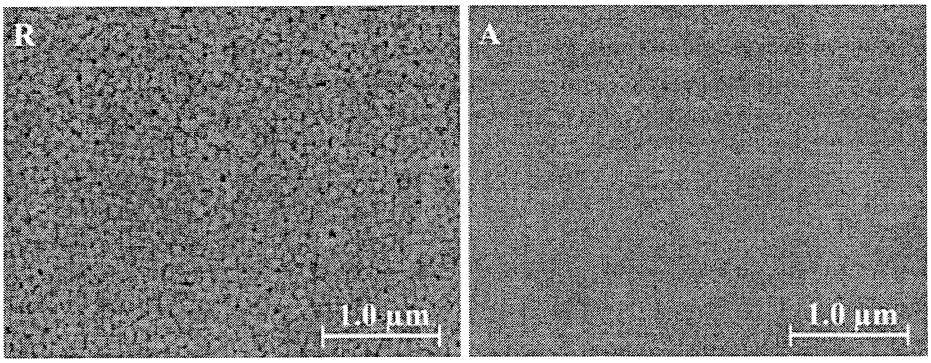

Fig. 4 Surface appearance of **R** and **A** observed by using a field emission scanning electron microscope

irradiation and higher than the photoreactivity of **A**, which is without precedent.

Photoinduced hydrophilicity of thin films

The photosensitivity of **R** and **A** was also examined by measuring the effects of visible and UV light irradiation on the water contact angle for the surfaces of the thin films [22–24]. The results are shown in Fig. 6. The rutile thin-film **R** exhibited visible light-induced hydrophilicity with a fluorescent light even though high-energy light with wavelengths shorter than 400 nm was eliminated. In contrast, visible light alone did not effectively reduce the contact angle on **A** under the same conditions. Furthermore, a rapid decrease in the water contact angle for **R** was observed with weak UV light irradiation. The superhydrophilic property of **R** appeared after only 1 h. When fluorescent light with a UV component was employed, the

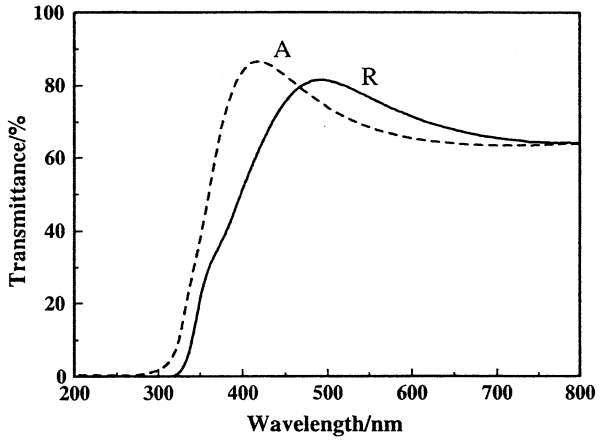

Fig. 5 Transmittance spectra of **R** and **A** for the 100-nm-thick film on a quartz substrate. The solid and broken lines indicate the **R** and **A** thin films, respectively

Table 1 The pseudo first-order kinetic rate v for the decoloration reaction in an aqueous solution containing 0.01 mol L^{-1} of methylene blue under both visible and UV light irradiation and under dark conditions

Notation	v [nmol L^{-1} min^{-1}][a]		
	Under visible light	Under UV light	Under dark conditions
R	13.3 (2)	26.7 (2)	4.2 (1)
A	3.8 (1)	19.3 (1)	3.8 (1)

[a] Estimated standard deviations are presented in parentheses

contact angle on **R** reduced more rapidly and the values reached 38° and 10° after irradiation for 1 and 24 h, respectively.

Discussion

Selective formation of rutile and anatase

Both the rutile and anatase thin films were easily formed selectively at 700 °C despite employing the different coating solutions. Each structure was characterized using XRD, Raman spectra, and TEM observations. The selectivity was due to the fact that the O-vacant sites in the oxide thin films formed at different levels due to the difference in the amount of oxygen between the two precursors; in this study, the oxygen source required to structure titania was available only in the precursor films when these thin films were fabricated. Therefore, crystallization into rutile, which has many O-vacant sites, and the accompanying rapid elimination of organic residues from the **R** precursor film occurred because of the heat treatment.

In contrast, the amount of oxygen available to the Ti^{4+} ions in the titanoxane polymers, though significant, was insufficient to develop stoichiometric TiO_2 from **A**. The oxygen defects in an anatase lattice generally lower the temperature of the phase transformation from anatase to rutile [25]. Thus, selective formation occurred according to differing levels in O-deficiency.

Optical property, surface morphology, and mechanical strength of the thin films

The band edge of **R** was comparable to that for a single crystal of rutile (3.0 eV) [1]. On the other hand, the band edge of **A** was higher than that for a single crystal of anatase, but comparable to anatase thin films with internal stresses caused by a lattice mismatch with the substrate [26]. The well-developed grain boundary in **R** was observed using the FE-SEM and is shown in Fig. 4. When compared to the size of the anatase grains in **A**, the grain sizes of the rutile crystals in **R** were undoubtedly larger. The internal stresses in **R** were relaxed by grain growth, thus reducing the band edge differences between a thin film and a single crystal.

In addition, the refractive index of **R** was lower than for **A**, although in general the index for rutile is higher than anatase [26, 27]. Permittivity is described by the following equation

$$\nabla \cdot \mathbf{E} = \frac{\rho}{\varepsilon_0}, \tag{4}$$

where **E** is the electric field intensity, ρ the charge density, and ε_0 the vacuum permittivity. The fact that the refractive index of **R** was smaller than for **A** suggested that the permittivity of **R** showed an extraordinary decrease due to the low charge density from a high O-deficiency compared to **A**. Therefore, the optical properties of **R** were found to be strongly related to its large O-deficiency.

Furthermore, the adhering strength of **R** to the quartz substrate was more than twice the strength of **A**. The titanium ions of **R** linked covalently to the O atoms belonging to the quartz molecules to form a robust interface between the quartz glass substrate and **R**. The strong adherence to the substrate was assumed to occur because of the many O-defects of **R** compared to **A**.

Inner part electron trap (IPET) effect

From the abovementioned results, the rutile thin film **R** with many O-defects was shown to have high photoreactivity and photoinduced hydrophilicity under both visible and UV light irradiation. Linsebigler et al. proposed that O-vacancies on a titania surface suppress the recombination of photoinduced electron–hole pairs with electron traps and

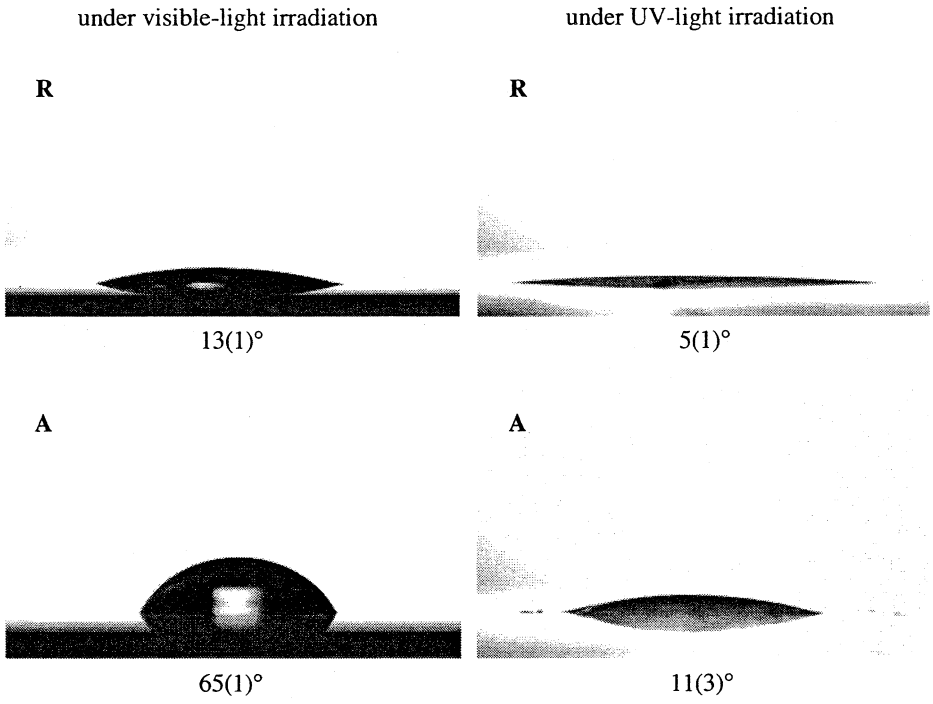

Fig. 6 Comparison of the contact angles for a 1.0-μL water droplet on **R** and **A**. Before measurement, the thin films were exposed either to only visible light (samples on the left), obtained by removing the UV component from the light emitted by a fluorescent lamp, or to UV irradiation (samples on the right), obtained with a black light

thus extend their lifetime [28]. This might lead to the high photoreactivity of O-vacant titania. Previously, several researchers examined the formation of O-vacant sites on a rutile thin-film surface by physical injection of or chemical reduction with hydrogen [29, 30]. However, photoinduced properties for rutile with an O-vacant surface were not observed in those studies, though the modification of its electric properties was shown. This suggests that the photoinduced properties of titania are not effectively assisted by the O-vacant sites on its surface alone. As shown by the XPS examination, many O-defects for **R** were spread throughout much of the rutile thin films formed in this study. Thus, the electron traps caused by O-deficiencies embedded deeply in **R** can be concluded to provide an essential contribution to its effective photoreactivity and photoinduced hydrophilicity under both visible and UV light.

Conclusion

This study presents an alternative method for enabling titania to respond to visible light without using the doping impurities usually employed for visualizing anatase, where the original photoreactivity under UV light irradiation is suppressed by generated impurity levels. This article showed that a certain level of O-deficiency embedded deeply within rutile crystals in the thin film can actualize the intrinsic and potential properties of rutile to respond to visible light. This article proposed an inner part electron trap (IPET) effect by using an O-deficient rutile thin film. In addition, the results led to the recommendation to differentiate rutile and anatase, which are frequently expressed simply as titania, in future study to avoid any confusion while discussing on their respective photoreactivity and photosensitivity. The results from this study should lead to developing applications of rutile thin films to solar energy conversion and the degradation of organics in polluted water and air under solar and interior light, along with the utilization of an anti-foggy surface derived from its hydrophilicity induced by both visible and UV light.

Acknowledgements This study was supported by the High-Tech Research Center Project for Private Universities: Matching Fund Subsidy from MEXT (Ministry of Education, Culture, Sports, Science and Technology) Japan, 2006–2010.

References

1. Weiser HB, Milligan WO (1934) J Phys Chem 38:513
2. Evans RC (1966) An introduction to crystal chemistry, 2nd edn. Cambridge University Press, New York
3. Lindsley DH (1976) Experimental studies of oxide minerals. Mineral Society of America
4. Fahmi A, Minot C, Silvi B, Causá M (1993) Phys Rev B 47:11717
5. Nishimoto S, Ohtani B, Kajiwara H, Kagiya T (1985) J Chem Soc Faraday Trans 1 81:61
6. Follis D, Pelizzetti E, Serpone N (1991) Environ Sci Technol 25:1523
7. Fox MA, Dulay MT (1993) Chem Rev 83:341

8. Fujishima A, Honda K (1972) Nature 238:37
9. Nagai H, Mochizuki C, Hara H, Takano I, Sato M (2008) Sol Energy Mater Solar Cells 92:1136
10. Nagai H, Hasegawa M, Hara H, Mochizuki C, Takano I, Sato M (2008) J Mater Sci 43(21):6902
11. Cronemeyer DC (1952) Phys Rev 87:876
12. Sato M, Hara H, Nishide T, Kuritani H, Sawada Y (1996) J Mater Chem 6:1767
13. Brinker CJ, Scherer GW (1990) Sol–gel science. Academic Press, California
14. Bruce DW, O'Hare D (1992) Inorganic materials. Wiley, Chichester
15. Tanemura S, Miao L, Jin P, Kaneko K, Terai A, Nabatova GN (2003) Appl Surf Sci 212–213:654
16. JCPDS Card 21-1276
17. JCPDS Card 21-1272
18. Ohtsuka T, Guo J, Sato N (1986) J Electrochem Soc 133:2473
19. Moses PR, Wier LM, Lennox JC, Finklea HO, Lenhard JR, Murray RW (1978) Anal Chem 50:576
20. Kwon CH, Shin H, Kim CH, Choi WS, Yoon KH (2004) Mater Chem Phys 86:78
21. Ohno T, Tsubota T, Nishizima K, Miyamoto Z (2004) Chem Lett 33:750
22. Wang R, Hashimoto K, Fujishima A et al (1997) Nature 388:431
23. Watanabe T, Nakajima A, Wang R et al (1999) Thin Solid Films 351:260
24. Machida M, Norimoto K, Watanabe T, Hashimoto K, Fujishima A (1999) J Mater Sci 34:2569. doi:10.1023/A:1004644514653
25. Gennari FC, Pasquevich DM (1998) J Mater Sci 33:1571. doi: 10.1023/A:1017515804370
26. Miao L, Jin P, Kaneko K, Terai A, Nabatova-Gabain N, Tanemura S (2003) Appl Surf Sci 212–213:255.
27. Nishide T, Hara H, Sato M (2000) J Mater Sci 35:465. 10.1023/A:1004731804075
28. Linsebigler AL, Lu G, Yates JT (1995) Chem Rev 95:735
29. Hill GJ (1968) J Appl Phys 1:1151
30. Ohmori A, Kyeung CP, Inuzuka M, Arata Y, Inoue K, Iwamoto N (1991) Thin Solid Films 201:1

J Mater Sci (2008) 43:6902–6911
DOI 10.1007/s10853-008-2993-3

An important factor for controlling the photoreactivity of titania: O-deficiency of anatase thin films

Hiroki Nagai · Moyu Hasegawa · Hiroki Hara · Chihiro Mochizuki · Ichiro Takano · Mitsunobu Sato

Received: 22 May 2008 / Accepted: 4 September 2008 / Published online: 27 September 2008

Abstract Oxygen deficient (O-deficient) anatase thin films with high photoreactivity under UV-light irradiation were fabricated by post-annealing partially nitrided anatase thin films, prepared by heat-treatment of precursor films involving a Ti complex of EDTA on an FTO glass substrate at 500 °C for 30 min in an Ar gas flow, in air at 500 °C for 5–30 min. The anatase structure of the transparent thin films was characterized by using XRD and Raman spectra. The O/Ti peak area ratio determined by using XPS of the anatase film having the highest photoreactivity, which was evaluated according to the decoloration rate of methylene blue in an aqueous solution, was 1.5. The photoreactivity of the film was 2.1 times higher than that prepared by using the sol–gel method, with an O/Ti ratio of 1.7. The thin film with the highest photoreactivity indicated the smallest refractive index, 1.99.

Introduction

Anatase, one of the three crystal forms of titania, is an attractive material as a photoreactive semiconductor that can work under ultraviolet (UV) light irradiation. The photoreactivity of anatase depends upon the chemical reactivity of the electrons and holes photo-induced in the anatase particles. Fujishima et al. reported that the electrons and holes on the surface of anatase particles recombine immediately unless redox reactions do not occur with reactants such as O_2 and H_2O near the anatase surface [1]. Porous and fine anatase particles with larger specific surface areas are more effective to photoreactions, because the number of opportunities for reactions between photo-induced electrons and holes with reactants before their recombination increases [2, 3].

The fabrication of visible-light-responsive films with enhanced UV-sensitivity was achieved in our recent study [4]. Layer-structured anatase films were prepared by using a molecular precursor method, which employs coating solutions including the alkylammonium salts of anionic Ti complex of EDTA and OX ligands in an Ar gas flow, where EDTA and OX represent ethylenediamine-*N*,*N*,*N*′,*N*′-tetraacetic acid and oxalic acid, respectively. During heat-treatment of the precursor films in the Ar gas flow, transparent anatase thin films with enhanced UV-sensitivity and even surfaces were fabricated, although the UV-sensitivities of other visible-light-responsive thin films modified by impregnating metal ions such as V^{5+} and Cr^{3+} [5, 6], N [7], C [8–10], and S [11–13] ions were decreased. It was important that the optical band edge of the layered anatase thin films did not significantly shift to a longer wavelength region and that they could function as a vis-responsive thin film in the presence of colored materials formed at the interfaces between the layers. These results suggest that anatase thin films with extremely high photoreactivity under UV-light irradiation can be prepared without increasing their specific surface areas.

In order to clarify the factors for designing anatase thin films with higher photoreactivity under UV-light

H. Nagai · M. Hasegawa · H. Hara · C. Mochizuki · M. Sato (✉)
Coordination Engineering Laboratory, Faculty of Engineering, Kogakuin University, 2665-1 Nakano, Hachioji City, Tokyo 192-0015, Japan
e-mail: ft10302@ns.kogakuin.ac.jp

I. Takano
Department of Electronic Engineering, Faculty of Engineering, Kogakuin University, 2665-1 Nakano, Hachioji City, Tokyo 192-0015, Japan

irradiation, we focused on the relationship between the photoreactivity and O-deficiency of anatase thin films fabricated by heat-treatment of precursor films, which were spin-coated on a glass substrate by applying a precursor solution involving the Ti-EDTA complex, in the Ar gas flow.

In this paper, we report the fabrication and characterization of O-deficient anatase thin films with higher photoreactivity under UV-light irradiation; these films were formed by post-annealing thin films formed in an Ar gas flow. The crystal structures and crystallite sizes of the films were characterized by means of XRD. Furthermore, the Raman spectra of the thin films were employed to determine the crystal structure. The chemical identities of the thin films were examined by means of their XPS spectra, and their surface morphologies were observed by means of FE-SEM. Optical characterization of the transparent thin films was carried out by using the absorption spectra and refractive indices. The photoreactivities of the thin films were evaluated on the basis of the pseudo-first-order rate constant of the decoloration of methylene blue dye in an aqueous solution. The formation mechanisms of highly photoreactive anatase thin films and films prepared by using a typical molecular precursor method and a sol–gel procedure in which the heat-treatment of each precursor film was performed in Ar gas flow and air, respectively, were compared.

Experimental

Materials

EDTA, methylene blue (MB), and titanium tetraisopropoxide ($Ti(O^iPr)_4$) were purchased from Kanto Chemical Co., Inc. Dibutylamine and 30% H_2O_2 were purchased from Wako Pure Chemical Industries, Ltd., and from Santoku Chemical Industries Co., Ltd., respectively. Sixty percentage HNO_3 and methanol were purchased from Taisei Chemical Co., Ltd. Ethanol was purchased from Ueno Chemical Industries, Ltd. These solvents were dried on molecular sieves 4 A before use. Other materials were used without further purification. Soda lime glass with a transparent FTO film was purchased from AGC fabritech Co., Ltd. The glass substrate of size 20 × 20 × 1.1 mm^3 for coating was washed in 2-propanol for 15 min by sonicated stirring and then dried in a drying oven at 70 °C.

Preparation of the precursor solution S_{ED} involving the Ti^{4+} complex of EDTA

The precursor solution containing the Ti^{4+} complex of EDTA was obtained by using a method previously reported [14] but slightly modified. To a mixture of 10 g of ethanol and 10 g of methanol, 3.55 g (27.4 mmol) of dibutylamine and 3.65 g (12.4 mmol) of EDTA were added. The solution was refluxed for 2 h by stirring, and then it was cooled to room temperature. After adding 3.55 g (12.4 mmol) of $Ti(O^iPr)_4$, the solution was refluxed for 4.5 h. After cooling the reacted solution to room temperature, 1.56 g (13.7 mmol) of 30% H_2O_2 was carefully added. Subsequently, the solution was refluxed for 0.5 h. The concentration of titanium was 0.4 mmol g^{-1}.

Preparation of the sol–gel solution S_{SG}

A conventional sol–gel solution was prepared by reacting 4.27 g (15.0 mmol) of $Ti(O^iPr)_4$ with 1.09 g (10.3 mmol) of 60% nitric acid and 0.82 g (45.4 mmol) of water in 25 g of ethanol [15, 16]. Thus, the as-prepared solution was obtained. The concentration of titanium was 0.5 mmol g^{-1}.

Coating and heat-treatment procedures and film thickness

Thin films were formed by heat-treatment of the precursor films spin-coated on the FTO glass substrate by applying the solutions S_{ED} and S_{SG} in an Ar gas flow or in air.

The spin-coating method at ambient temperature was used for preparing the precursor films with a double step mode: first at 500 rpm—5 s and then at 2000 rpm—30 s in all the cases. The precursor films were pre-heated in a drying oven at 70 °C for 10 min and then heat-treated at 500 °C for 30 min in an Ar gas flow of 0.1 L min^{-1}. A tubular furnace made of quartz was employed. Thus, the thin films ED and SG obtained by applying the precursor solutions S_{ED} and S_{SG}, respectively, were prepared before annealing in air. Another film ED_{air} was fabricated by firing each precursor film in air at 500 °C for 30 min.

When the concentration of titanium was adjusted to 0.4 mmol g^{-1} for S_{ED}, the film thickness was 100 nm. The sol–gel solution S_{SG} of 0.5 mmol g^{-1} was stirred for 3 days at ambient temperature in order to fabricate the anatase film of thickness 100 nm. The thickness of each film was measured by using a stylus profilometer, DEK-TAK-3 (Sloan).

Post-annealing treatment of the ED, ED_{air}, and SG thin films

The post-annealing treatments of the ED, ED_{air}, and SG thin films were carried out in air at 500 °C for 5, 10, 15, 20, and 30 min. The number in the notation of the post-annealed films indicates the annealing time (min); for example, ED-PA5 indicates that the film ED was post-annealed for 5 min.

Structural characterization of the thin films

The crystal phases of the thin films were examined by using an X-ray diffractometer, MXP-18AHF22 (Bruker AXS), with Cu-$K\alpha$ rays generated using 45 kV and 300 mA. The XRD patterns were measured in the range of 2θ, from 10° to 80° in steps of 0.05° for 2 s. Parallel beam optics with an incident angle of 0.3° was employed for each measurement.

The crystallite size of the anatase crystal formed in each film was measured by using the Scherrer and Hall methods, according to Eq. 1 [17–19], where D, B, λ, η, and θ represent the crystallite size, broadening factor FWHM of the diffraction peak of (101), wavelength of X-ray, random strain, and Bragg angle, respectively. The K value, 0.9, was used as the Scherrer constant. LaB_6 powder (NIST, USA) was employed to obtain the calibration curve.

$$\frac{B\cos\theta}{K\lambda} = \frac{1}{D} + \eta\frac{2\sin\theta}{\lambda} \quad (1)$$

The XRD measurement to determine the crystallite size was performed in the range of 2θ, from 10° to 70° in steps of 0.01° for 10 s.

The Raman spectra of the ED-PA15, ED_{air}-PA15, and SG-PA15 thin films were measured by using a micro-Raman spectrometer, NRS-2000 (JASCO), equipped with a CCD camera and 488-nm incident laser of 1.5 mW. Each spectrum in the wavelength range from 100 to 800 cm^{-1} obtained by exposing the laser beam for 30 s was accumulated 30 times.

The surface appearances of the thin films were observed by using a field-emission scanning electron microscope, FE-SEM S-4200 Hitachi, at an accelerating voltage of 5 kV.

Chemical characterization of the thin films

The thin films were characterized by means of X-ray photoelectron spectroscopy (XPS). A Phi Quantum 2000 Scanning ESCA Microprobe with a focused monochromatic Al-$K\alpha$ X-ray (1486.6 eV) source was employed to evaluate the states and amounts of the elements Ti, O, N, C, and Sn in the thin films. The chemical shift data were charge-referenced to the center of the C–C/C–H peak at 284.6 eV. The resolution was 0.2 eV in each measurement.

The depth profile in the Ar^+ etching mode was obtained by using the same instrument after Ar^+ ion beam bombardment (2 kV and 18 μA cm^{-2}) for 3 min in order to remove surface oxides. The measurements of 15 layers etched stepwise for every 3 min by bombarding Ar^+ ions with the same accelerating energy were performed over an area of 50 μm ϕ of the thin films. In order to examine the O/Ti ratios of the thin film surfaces, XPS spectra of Ti $2p$ and O $1s$ peaks were recorded without bombarding Ar^+ ion beams.

Optical characterization of the thin films

The absorption spectra of each thin film were measured in the range from 200 to 800 nm by using a double beam absorption spectrometer, and air was used as a reference in each measurement. The measurements were performed by using a Hitachi U-2800 spectrophotometer.

The optical band edge of each thin film was calculated from the difference spectrum, which was obtained by subtracting the absorption value of the FTO substrate from that of FTO substrate with the thin film at each wavelength. The optical band edge E_g of the thin films was determined by using the following Tauc expression: $\alpha = \frac{A(E-E_g)^{1/2}}{E}$, where E denotes the photon energy ($\equiv h\nu$); A, the constant; and α, the absorption coefficient at wavelength [20].

A MARY-102 (Five Lab) scanning ellipsometer was employed to measure the refractive index of each thin film by using a He–Ne laser beam with a wavelength of 632.8 nm and an incidence angle of 70.8°. The refractive index was measured thrice at eight different spots on the thin films, and each index was determined as the averaged value.

Photoreactivity measurements

The photoreactivity of each thin film of area 15 × 15 mm^2 on the substrate was examined by the decoloration rate of MB in a 10-mL aqueous solution (0.01 mmol L^{-1}). A black light, National FL10BL-B, was used for UV-light irradiation. The distances of the black light sources from the sample surfaces were adjusted to maintain the UV-light intensity at 365 nm as 1.2 mW cm^{-2}, the intensity was measured by using an ultraviolet meter, UVR-400, Iuchi Co., Ltd. The concentration of MB was determined by measuring the absorption spectra of the aqueous solution in the range from 600 to 700 nm by using a Hitachi U-2800 spectrophotometer. At intervals of 20 min during the decoloration test, ca. 3 mL of the solution was transferred into a quartz cell of dimensions 1 × 1 × 4.5 cm^3. After conducting the spectral measurements, the solution was immediately returned to the vessel and mixed with the aliquot. The mixed solution was further used until the test for each film was completed. The temperature of the MB aqueous solution was 20(±1) °C during the measurement. From the absorption spectra at 664 nm of the solutions, each concentration of MB was determined by using a method reported previously [4, 21, 22].

The pseudo-first-order kinetic constant of the decoloration of MB aqueous solutions was obtained thrice for each film, and the averaged value was obtained in terms of the rate constant k. In order to examine the effects of both adsorption and self-decoloration of MB, the same measurement was performed on the same samples without irradiation as a reference.

The k-value for each film was calculated as follows: the concentration of MB after t minutes, C(t), was determined by using formula (I), where Abs(0) and Abs(t) represent the absorption values of the solution immediately before the light irradiation and after t minutes during irradiation, respectively.

$$C(t) = 10 \times \frac{\mathrm{Abs}(t)}{\mathrm{Abs}(0)} \quad (\mu\mathrm{mol\ L^{-1}}) \qquad \text{(I)}$$

An approximate plot for the function of C(t) versus t was obtained in the range from $0 \leq t \leq 80$ min by using the method of least squares. The rate constant k for each film was estimated as the averaged gradient of the lines by using formula (II), where k_n indicates each gradient obtained thrice ($n = 1, 2, 3$), independently.

$$k = \frac{\Sigma k_n}{3} \times 10^3 \quad (\mathrm{nmol\ L^{-1}\ min^{-1}}) \qquad \text{(II)}$$

Results

Crystal structures and surface morphologies of the thin films

The XRD patterns of the post-annealed thin films ED-PAn ($n = 5$, 10, 15, 20, and 30 min), along with those of the film ED are shown in Fig. 1. The peaks at $2\theta = 25.3°$ and 53.9° observed for all films are assignable to the (101) and (105) phases of anatase [23]. The peak due to the (200) phase of anatase can be observed at $2\theta = 48.2°$ in the patterns of the post-annealed films ED-PAn ($n \geq 15$). Weak peaks at $2\theta = 27.4°$ observed in the patterns for the post-annealed films ED-PAn ($n \geq 15$) can be assigned to that of the (110) phase of rutile [24]. The peaks at $2\theta = 34.0$, 38.0, 51.9, 62.0, 66.0, and 78.8° in each pattern can be assigned to those of SnO_2 of the FTO substrate [25]. Furthermore, the peaks in the XRD patterns of the films ED_{air} and SG could be assigned to those of anatase and SnO_2 of the FTO substrate. Any additional peak assignable to rutile does not appear in the XRD patterns of the anatase films ED_{air} and SG even after they are post-annealed under the same conditions as those for the film ED.

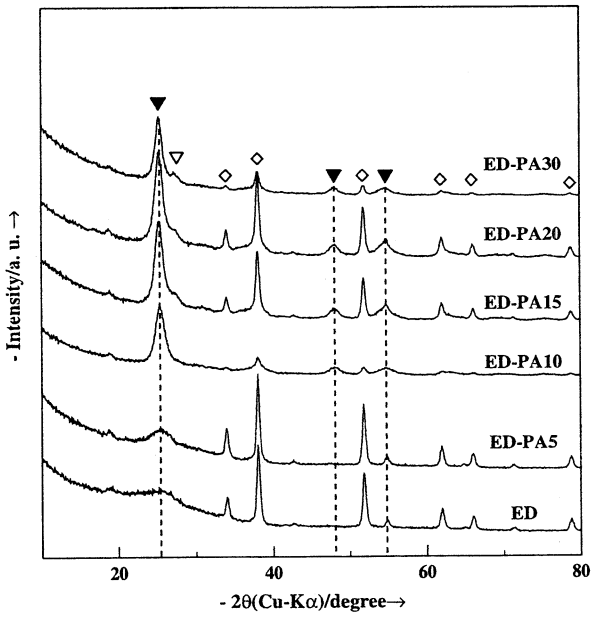

Fig. 1 XRD patterns of ED and ED-PAn thin films, $n = 5$, 10, 15, 20, and 30. The peak assignment is indicated as follows: ▼ Anatase, ▽ Rutile, and ◇ FTO

The crystallite size of each film is presented in Table 1. The thin films ED and ED-PAn have single-nano-size crystallites. The crystallite sizes of the ED_{air} and SG thin films are not significantly affected by the post-annealing treatments.

The Raman spectra of the ED-PA15, ED_{air}-PA15, and SG-PA15 thin films are shown in Fig. 2. The peaks at 144, 399, 519, and 639 cm^{-1} in each pattern are assignable to those of anatase [26].

In Fig. 3, the surface appearances of (A) ED-PA15, (B) ED_{air}-PA15, and (C) SG-PA15 are presented. The surface roughness of both (A) ED-PA15 and (B) ED_{air}-PA15 is ca. 10 nm, which is equal to the resolution of the stylus profilometer used. In comparison with the roughness (100 nm) of the FTO glass substrate, each surface without any crack or pinhole is rather smooth. The surface roughness due to the undulated surface of SG-PA15 having many fine cracks is ca. 25 nm.

Chemical characterization of the thin films by using XPS

Figure 4 shows the XPS spectra of the thin film ED. The binding energy of Ti $2p_{3/2}$ attributed to Ti–O and Ti–N has

Table 1 The crystallite size of anatase in ED, ED_{air}, SG, and post-annealed thin films

Annealing time (min)	ED	ED_{air}	SG
0	–	10	13
5	–	10	13
10	5	11	13
15	4	10	13
20	7	11	13
30	7	12	13

The crystallite size of anatase was measured with a typical Scherrer–Hall method by employing a peak assignable to only (101) of anatase, because other peak intensities due to anatase were too low to measure accurately. The crystallite size of anatase in ED and ED-PA5 could not be obtained because the (101) peak of anatase was also too weak to determine the crystallite size

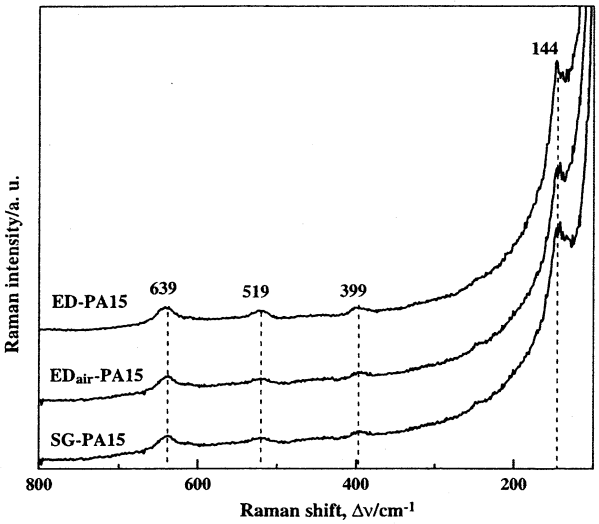

Fig. 2 Raman spectra of ED-PA15, ED_{air}-PA15, and SG-PA15 thin films which were fabricated by post-annealing of ED, ED_{air}, and SG thin films at 500 °C for 15 min in air, respectively

a typical value of 459.2 and 455.8 eV, respectively. The binding energy of O 1*s* with which the O atom bonds to the metal atom is 531.1 eV [27]. The binding energy of N 1*s* is 397.0 eV, and it exists only in the oxygen-substituted form but not in the chemisorption form [28]. These binding energies determined in the thin film ED are identical to those determined in other films fabricated during this study.

The depth profiles measured by using XPS are shown in Fig. 5. Significant amounts of C and N atoms are found, particularly in the thin film (A) ED. These C and N atoms in the thin film ED decrease due to post-annealing treatment, as shown in (B) ED-PA15 and (C) ED-PA30. The amounts of C and N atoms in the thin film (D) ED_{air} are considerably smaller than those in (A) ED. Further, the atoms of C and N atoms found in (D) ED_{air} are decreased by post-annealing treatment, as shown in (E) ED_{air}-PA15 and (F) ED_{air}-PA30. However, neither C nor N atoms are observed in the (G) SG, (H) SG-PA15, and (I) SG-PA30 thin films.

Table 2 shows the averaged O/Ti ratios determined from the XPS peak areas of O 1*s* and Ti $2p_{3/2}$ peaks of the ED, ED_{air}, SG and post-annealed thin films. The averaged values are obtained from each depth profile in the Ar^+ ion etching mode after removing the surface oxides. Extremely small values of the ratio are obtained for the ED and ED_{air} thin films. The values of the SG thin film are not affected by the post-annealing treatment.

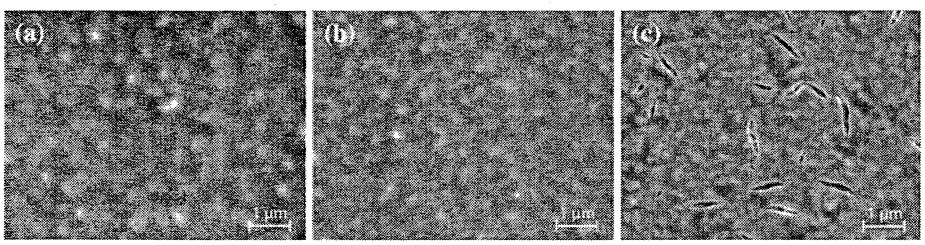

Fig. 3 SEM images of **a** ED-PA15, **b** ED_{air}-PA15, and **c** SG-PA15 thin films obtained by post-annealing the thin films ED, ED_{air}, and SG, respectively, at 500 °C for 15 min in air. Every film thickness is 100 nm

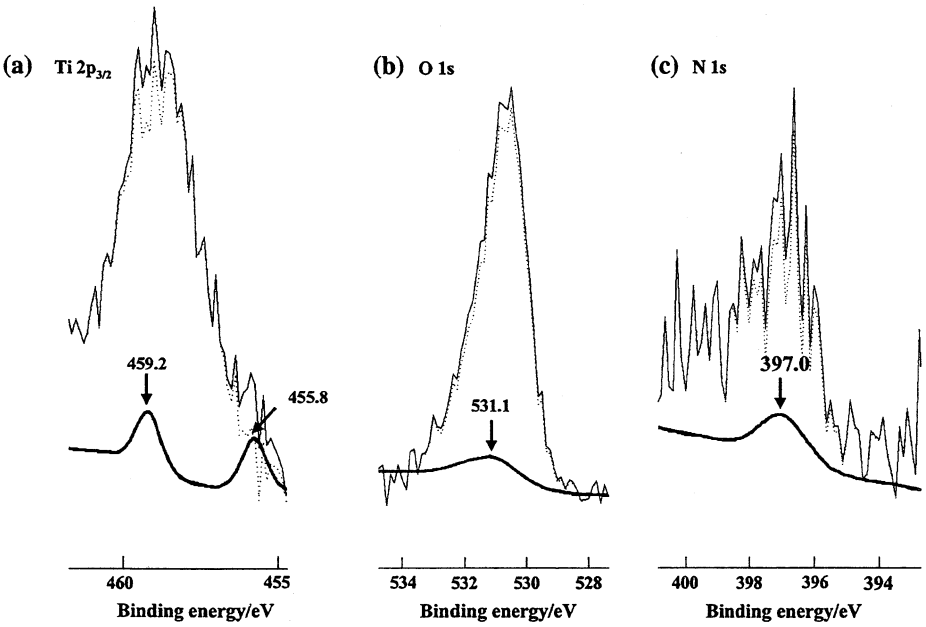

Fig. 4 XPS spectra of **a** Ti $2p_{3/2}$, **b** O 1*s*, **c** N 1*s* of the thin film ED, which was measured after Ar^+ ion beam bombardment (2 kV, 18 μA cm^{-2}) for 3 min for removal of oxides from the surface. The thin *solid lines* indicate the original data of XPS. The thick solid curves are theoretical Gaussian distribution curves. The *dashed curves* show theoretically fitted curves by assuming Gaussian distribution

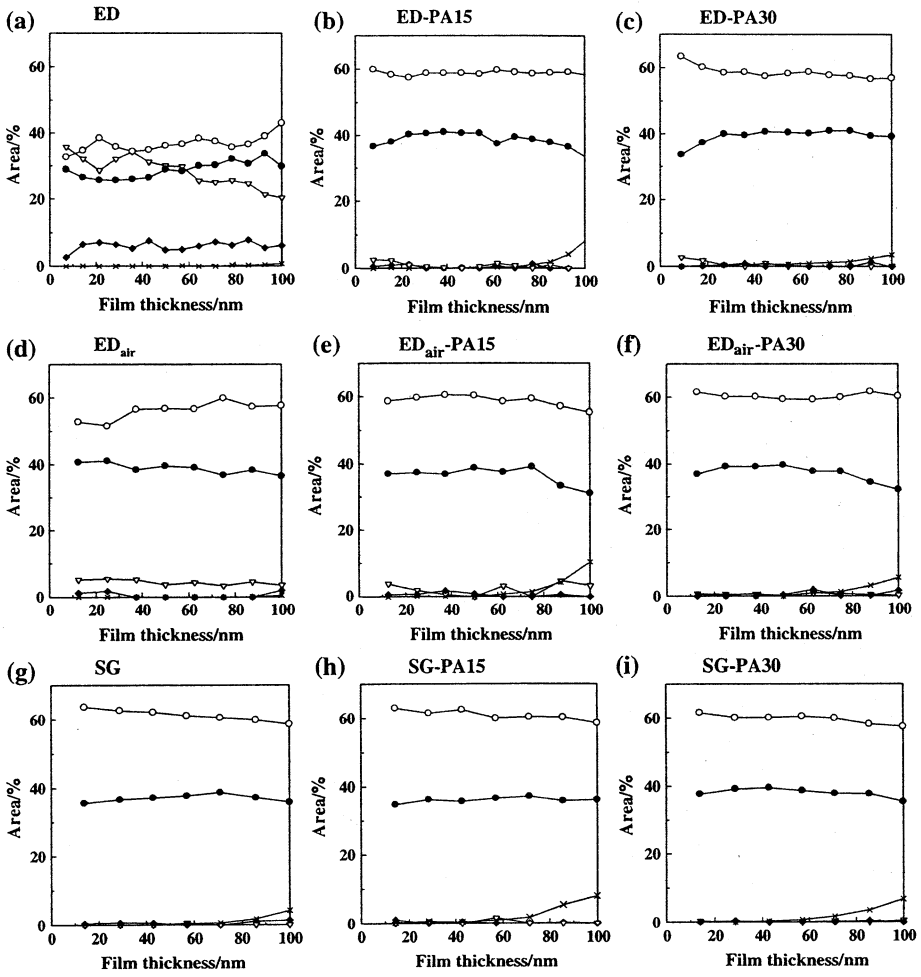

Fig. 5 Depth profile of the elements, Ti, O, N, C, and Sn in the thin films **a** ED, **b** ED-PA15, **c** ED-PA30, **d** ED$_{air}$, **e** ED$_{air}$-PA15, **f** ED$_{air}$-PA30, **g** SG, **h** SG-PA15, and **i** SG-PA30. The energy levels of the five atoms are indicated in parentheses, —●— (Ti 2*p*), —○— (O 1*s*), —◆— (N 1*s*), —▽— (C 1*s*), —×— (Sn 3*d*). Measurement of each 15 layer etched stepwise for every 3 min by bombarding Ar^+ ion with 2 kV and 18 μA cm^{-2} was performed at an area of 50 μm ϕ of the thin films

Table 2 The averaged O/Ti ratios determined by the XPS peak areas of O 1*s* and Ti $2p_{3/2}$ peaks of ED, ED$_{air}$, SG, and post-annealed thin films

Annealing time (min)	ED	ED$_{air}$	SG
0	1.37	1.49	1.65
5	1.57	1.61	1.66
10	1.53	1.58	1.66
15	1.49	1.60	1.67
20	1.50	1.60	1.67
30	1.49	1.58	1.68

The XPS peaks of thin films were measured after bombarding Ar^+ ion beam with 2 kV and 18 μA cm^{-2} for 3 min, in order to remove surface oxides. The peak area of O 1 s and Ti 2p was calculated by FWHM and peak height at the positions 531.0 and 459.0 eV, respectively, obtained from each depth profile in Ar^+ ion etching mode

Table 3 The O/Ti ratios determined by the XPS peak areas of O 1*s* and Ti $2p_{3/2}$ peaks observed from the surfaces of ED, ED$_{air}$, SG, and post-annealed thin films

Annealing time (min)	ED	ED$_{air}$	SG
0	1.60	1.67	1.92
5	1.61	1.68	1.93
10	1.62	1.68	1.95
15	1.64	1.82	1.96
20	1.72	1.90	1.96
30	1.78	1.96	1.96

The XPS peaks of the thin film surface were measured without bombarding Ar^+ ion beam. The peak area of O 1*s* and Ti 2*p* was calculated by FWHM and peak height at the positions 531.0 and 459.0 eV, respectively

Table 3 shows the O/Ti ratios for thin film surfaces. In comparison with the averaged O/Ti ratios in deep portion (Table 2), these values are considerably large. The O/Ti ratios of the ED and ED$_{air}$ thin film surfaces are remarkably smaller than those of the SG thin film. A gradual increase in the values can be observed when the films are post-annealed.

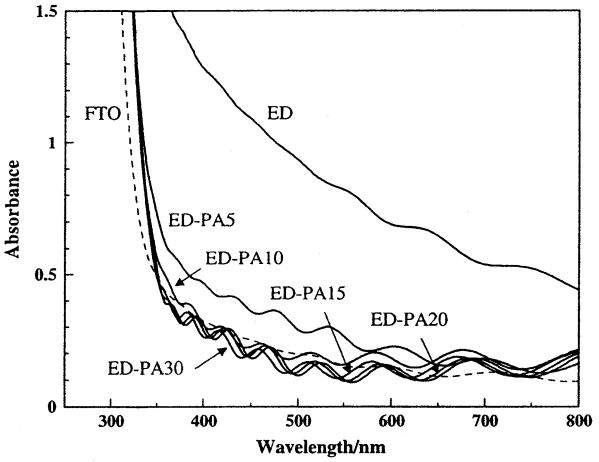

Fig. 6 Absorption spectra of ED and ED-PA*n* thin films whose thickness is 100 nm. The lines indicate each film as follows. ED and ED-PA*n*; ——, FTO substrate; - - - -

Table 4 The optical band edges of ED, ED_{air}, SG and post-annealed thin films

Annealing time (min)	ED	ED_{air}	SG
0	3.43(1)	3.68(1)	3.73(1)
5	3.72(1)	3.74(2)	3.73(1)
10	3.73(2)	3.74(2)	3.72(1)
15	3.74(2)	3.73(2)	3.69(2)
20	3.75(2)	3.73(2)	3.68(1)
30	3.75(1)	3.73(2)	3.66(2)

The edge energy was calculated from the absorption data in the range from 311 to 295 nm of the thin films by employing Tauc expression. Estimated standard deviations are presented in parentheses

Optical characterization of the anatase thin films

The UV–vis absorption spectra of the ED and ED-PA*n* thin films are shown in Fig. 6. It is shown that the absorbance of the films ED and ED-PA5 is remarkably high in the vis-light region, according to the brown color of the film.

The optical band edge shifts of the thin films are listed in Table 4. The band edge shift of the thin film ED is significantly affected by the post-annealing treatment. The optical band edge shift of the thin film SG decreases gradually according to the post-annealing duration, although those of the thin films ED and ED_{air} show a tendency to increase. In comparison with the band edge shift of 3.2 eV for the anatase single crystal, those for thin films are considerably large [29, 30].

Table 5 shows the refractive indices of the thin films. These values lie in the range reported previously for anatase thin films [30, 31]. The refractive indices of the thin films ED_{air} and SG are gradually increased by post-annealing treatment. On the other hand, the refractive index of ED decreases once from 2.17 (ED) to 1.99 (ED-PA15) with the post-annealing treatment, and then it increases with further annealing.

Table 5 The refractive index of ED, ED_{air}, SG, and post-annealed thin films

Annealing time (min)	ED	ED_{air}	SG
0	2.17	2.06	2.06
5	2.07	2.08	2.10
10	2.04	2.08	2.11
15	1.99	2.10	2.11
20	2.00	2.11	2.15
30	2.11	2.13	2.16

The refractive index was measured at eight different spot, and three measurements were performed at each spot

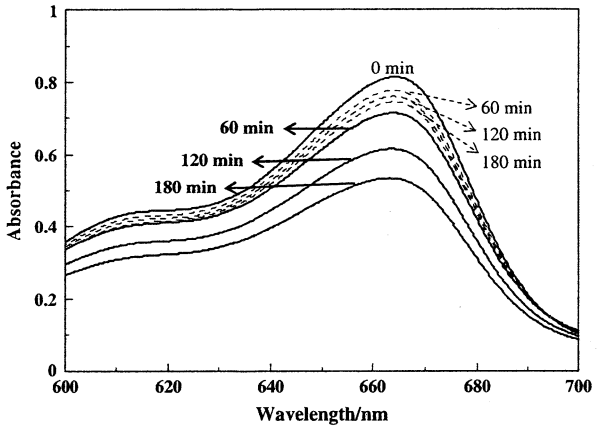

Fig. 7 Spectral changes of MB aqueous solutions during the photoreaction rate measurement by employing ED-PA15 thin film under UV-light irradiation (*solid lines*), along with those under dark (*broken lines*). The absorption value at 664 nm of the solutions was recorded in order to determine the rate constant of the decoloration

Photoreactivity of the anatase thin films

The absorption spectral changes in the MB aqueous solution during decoloration by the film ED-PA15 under UV-light irradiation are shown in Fig. 7, along with those measured under dark conditions. The pseudo-first-order kinetic constant k (nmol L^{-1} min^{-1}) of decoloration of 0.01 mol L^{-1} MB aqueous solution by photoreaction with each thin film under UV-light irradiation is summarized in Table 6, along with that measured for the thin film ED under dark conditions as the reference. The reference values ranging from 3.8 to 4.0 nmol L^{-1} min^{-1} correspond to both adsorption and self-decoloration of MB, and they are independent of the type of thin film.

The k values of the reaction reveal that every film is effective in decolorizing the MB aqueous solution by

Table 6 The pseudo-first-order kinetic constant k (nmol L^{-1} min^{-1}) of decoloration rate of 0.01 mol L^{-1} MB solution by the photoreaction with each thin film under UV-light irradiation

Annealing time (min)	k under UV-light irradiation			k under dark		
	ED	ED_{air}	SG	ED	ED_{air}	SG
0	6.4(1)	9.8(1)	9.1(1)	4.0(1)	4.1(1)	4.0(1)
5	9.1(1)	15.6(1)	10.4(1)	4.0(1)	4.0(1)	4.1(1)
10	12.9(1)	16.3(1)	11.7(1)	3.8(1)	3.9(1)	4.1(1)
15	19.8(3)	13.1(2)	10.5(1)	3.9(1)	3.9(1)	4.0(1)
20	15.0(1)	12.7(1)	11.0(1)	3.8(1)	3.9(1)	3.8(1)
30	12.0(2)	9.1(2)	8.8(1)	3.8(1)	3.8(1)	3.9(1)

The kinetic constant was measured by the decrease of absorption value at 664 nm of each test solution. Those obtained from the data measured under dark are also indicated. Calculated standard deviations are presented in parentheses

photoreaction. The thin film ED-PA15 prepared by post-annealing the ED thin film, which has the lowest photoreactivity, at 500 °C for 15 min in air showed the highest k value. In both cases of ED_{air} and SG thin films, post-annealing treatment for 10 min is mostly effective in enhancing the photoreactivity. However, the effect of post-annealing treatment on the photoreactivities of ED_{air} and SG thin films is unambiguously smaller than that on the thin film ED. In addition, it is notable that the k values of the ED_{air}-PA30 and SG-PA30 thin films are smaller than those obtained before treatment.

In Fig. 8, the photoreactivities of the thin films are presented. Each value is calculated as the difference

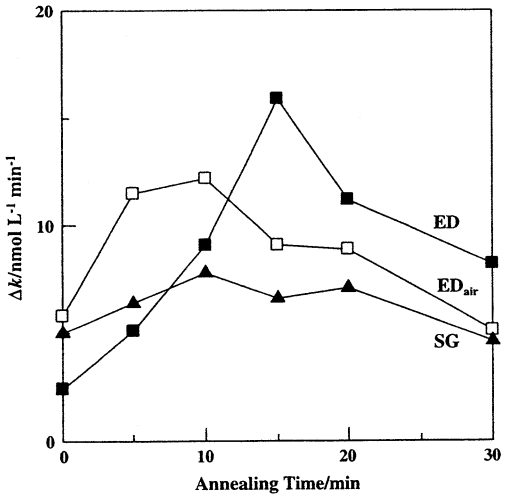

Fig. 8 Dependency of net photoreactivity of each thin film on the post-annealing time. These values were obtained as the differences between the pseudo-first-order kinetic constants (k) of decoloration of MB aqueous solution under UV-light irradiation and those under dark (Table 6). Each line indicates the thin film as follows: ED-PAn; —■—, ED_{air}-PAn; —□—, SG-PAn; —▲—

between the rate constant k under UV-light irradiation and the corresponding value measured for each thin film under dark conditions. As a result, the maximum photoreactivity of ED-PA15 prepared by using the molecular precursor method is 2.1 times higher compared with that of SG-PA10 prepared by the conventional sol–gel procedure.

Discussion

It is generally accepted that the main factors responsible for obtaining anatase with enhanced photoreactivity are (1) high crystallinity, (2) large specific surface area, and (3) low amount of impurity [32, 33]. With regard to these factors, the maximum photoreactivity obtained for the anatase thin film ED-PA15 with higher O-deficiency will be discussed, and then the formation mechanism of the O-deficient anatase by using the molecular precursor method will be discussed.

Crystallinity of the anatase thin films

Crystallite size is an indicator of crystallinity. Among the crystallite sizes of the three anatase thin films ED, ED_{air}, and SG, that of the thin film SG was the largest and that of the film ED was the smallest (Table 1). These sizes of the anatase crystallites in ED_{air} and SG thin films were not affected by post-annealing treatment in air. In contrast, the sizes of the anatase crystallites in the ED thin film were dependent on the annealing time. By means of XPS analyses, it was revealed that the amounts of C and N atoms derived from the EDTA complex in the ED thin film were significantly larger than those in the other thin films. These results suggest that the anatase crystallite in the ED thin film grew effectively with the removal of C and N atoms by annealing the film in air.

Anatase with high crystallinity is generally assumed to have high photoreactivity. However, among the thin films prepared in this study, the thin film ED-PA15, whose crystallite size of anatase is the smallest, indicated the highest photoreactivity in the decoloration of the MB aqueous solution.

Surface morphologies of the anatase thin films

Even surfaces with 10-nm roughness could be observed from the SEM images of the thin films formed by using the molecular precursor method (Fig. 3). Although the specific surface areas of the thin films are not measured quantitatively because of the difficulty involved in the procedure, it can be concluded that the degrees of adsorption of the MB molecule in the aqueous solution are almost equal among the thin films, including those formed by using the sol–gel

method (Table 6). Therefore, the differences between the photoreactivities of these thin films should be attributed to other factors, except the specific surface area.

Purity and optical properties of the anatase thin films

The purity of the transparent thin films was evaluated on the basis of the XPS spectra, and the optical properties were examined on the basis of the absorption spectra and refractive indices of the thin films.

From the XPS spectra (Fig. 5), it is observed that among the thin films, SG and SG-PA*n* show higher purity. Therefore, the highest photoreactivity of the ED-PA15 thin film cannot be attributed to its purity. Doping appropriate amounts of metal ions such as Fe^{3+} and Mg^{2+} into anatase is frequently useful in preventing photo-induced electrons and holes from recombination [34, 35]. However, it is difficult to accept that C and N atoms in ED-PA*n* and ED_{air}-PA*n* contribute toward enhancing their photoreactivities because the UV-light sensitivities of the anatase thin films simply modified by these atoms decrease [7–10]. From this point of view, the purity is not directly related to the highest photoreactivity of ED-PA15.

The strong and wide absorbance in the vis-light region observed in the spectra of the ED and ED-PA5 thin films (Fig. 6) can be attributed to the large amounts of C and N atoms observed in the XPS spectra (Fig. 5), because the absorbance disappears after post-annealing the ED thin film for longer than 10 min.

In comparison with the band edge shift of 3.2 eV for the anatase single crystal, the values of the thin films prepared in this study are larger (Table 4) but comparable with those previously reported for thin films [29, 30]. Because these larger values are mainly attributed to the stress between the thin films and substrates, the stress in the SG thin film can be effectively relaxed by post-annealing. However, it was elucidated that the thin films formed by using the molecular precursor method retain such stresses even after the post-annealing treatment. The ED thin film indicated extremely low values of stress. The result suggests that larger amounts of C and N atoms in the ED thin film produced impurity levels in the band gap, and the gap was drastically affected by eliminating the impurities with the post-annealing treatment for longer than 5 min. A similar but smaller change in the band edge shift in the ED_{air} thin film occurred, because the amounts of C and N atoms in the thin film were considerably smaller than those in ED.

The refractive indices of the thin films (Table 5) lie in the range of values reported for the anatase thin films [30, 31]. The refractive indices of the thin films ED_{air} and SG increased gradually according to the post-annealing duration. On the other hand, the refractive index of the ED thin film decreased once with the post-annealing treatment for 15 min and then increased with further annealing. The largest index, 2.17, of the ED thin film may be attributed to the strong and wide absorbance by the impurities mentioned above. Furthermore, the smallest value, 1.99, of the ED-PA15 thin film could be affected by the largest O-deficiency in the anatase thin film after removal of the impurities. It is suggested that the decrease in permittivity of the thin film was due to the low charge density derived from the O-deficiency, because the structure of anatase is rigidly maintained. The increase in the refractive index by further annealing the thin film may be due to the effects of the addition of oxygen atoms into the lattice (Table 3) and appearance of the rutile phase observed in the XRD spectra (Fig. 1).

Thin film fabrication of O-deficient anatase by using the molecular precursor method

The proposed scheme for O-deficient anatase lattice formation, which can be deduced from the XPS results, is presented in Scheme 1. This scheme indicates a skeleton involving one Ti center in parentheses on the basis that four titanium complexes should be provided to construct at least one unit cell of anatase lattice.

The coordination skeleton of (TiO_4N_2) or (TiO_5N_2) can be assumed in the EDTA complex as a precursor molecule, from the structural study on a Ti complex $[Ti(H_2O)(EDTA)] \cdot 1.5H_2O$ reported by Fackler et al. [36]. In the precursor films, two N and at least four O atoms are linked to one Ti ion.

By heat-treating the precursor complex in the Ar gas flow, neighboring complexes reacted with each other. During the process, several O atoms linked to one Ti ion could be covalently bonded by other Ti ions, and the anatase lattice was gradually structured. By eliminating large amounts of C, H, and N atoms with O atoms, oxide ion sites of the anatase lattice were partially occupied by relatively stable nitride ions derived from the coordinated N atom originally belonging to the ligand. As a result, the total negative charge of the N-substituted anatase in the ED thin film was ca. 3.6, obtained from the summation of 2.8 from the oxide ions and 0.8 from the nitride ions, toward one Ti ion. This charge oriented toward one Ti ion is larger than that, ca. 3.3, due to the oxide ions in the SG thin film (Table 2).

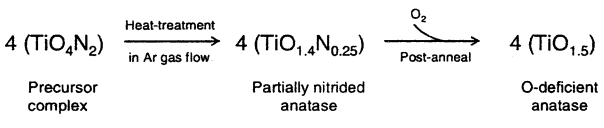

Scheme 1 Proposed scheme for O-deficient anatase lattice formation

The substitutional N atoms could be removed from the anatase lattice by post-annealing the ED thin film. Consequently, the total negative charge of the ED-PA15 thin film whose photoreactivity is highest decreased to ca. 3.0. Annealing treatment for long durations replenished oxide ions into anatase thin films from their surfaces (Table 3), and the photoreactivity was decreased (Fig. 8). Thus, it was elucidated that the O-deficiency is an important factor for controlling the photoreactivity of anatase. It is also notable that the O-deficient anatase lattice is considerably robust, because the stoichiometric Ti_2O_3 did not appear at all.

Conclusion

The molecular precursor method is useful for the fabrication of an O-deficient anatase thin film having higher photoreactivity. The chemical formula of the anatase with the highest photoreactivity under UV-light irradiation can be described as $TiO_{1.5}$, whose O/Ti ratio is quantitatively determined from the XPS spectra. The O-defect sites in anatase of fine crystallites can be generated by post-annealing anatase thin films involving Ti–N bonds derived from the molecular precursor complex. It is notable that the thin film indicates the lowest refractive index.

It was thus revealed that the O-deficiency in anatase thin films is one of the major factors involved in photoreaction by the semiconductor. This factor may be also important to synthesize the anatase powders with high photoreactivity. Therefore, we are now interested in the possibility of rutile thin film fabrication with high photoreactivity by the same principle.

Acknowledgements This study was supported by the "High-Tech Research Center" Project for Private Universities: Matching fund subsidy from Ministry of Education, Culture, Sports, Science and Technology (MEXT) Japan, 2006–2010.

References

1. Fujishima A, Rao TN, Tryk DA (2000) J Photochem Photobiol Chem 1:1. doi:10.1016/S1389-5567(00)00002-2
2. Meshmiri M, Mohseni M, Troczynski T (2004) Appl Catal B 53:209. doi:10.1016/j.apcatb.2004.05.016
3. Yu JC, Yu J, Zhao J (2002) Appl Catal B 36:31. doi:10.1016/S0926-3373(01)00277-6
4. Nagai H, Mochizuki C, Hara H, Takano I, Sato M (2008) Sol Energy Mater Sol Cell 92:1136. doi:10.1016/j.solmat.2008.04.005
5. Anpo M, Kishiguchi S, Ichihashi Y, Takeuchi M, Yamashita H, Ikeue K et al (2001) Che M Res Chem Intermed 27:459. doi:10.1163/156856701104202101
6. Anpo M (2004) Bull Chem Soc Jpn 77:1427. doi:10.1246/bcsj.77.1427
7. Asahi R, Morikawa T, Ohwaki T, Aoki K, Taga Y (2001) Science 293:269. doi:10.1126/science.1061051
8. Irie H, Watanabe Y, Hashimoto K (2003) Chem Lett 32:772. doi:10.1246/cl.2003.772
9. Sakthivel S, Kisch H (2003) Angew Chem Int Ed 42:4908. doi:10.1002/anie.200351577
10. Ohno T, Tsubota T, Toyofuku M, Inaba R (2004) Catal Lett 98:255. doi:10.1007/s10562-004-8689-7
11. Ohno T, Mitsui T, Matsumura M (2003) Chem Lett 32:364. doi:10.1246/cl.2003.364
12. Umebayashi T, Yamaki T, Itoh H, Asai K (2002) Appl Phys Lett 81:454. doi:10.1063/1.1493647
13. Umebayashi T, Yamaki T, Tanaka S, Asai K (2003) Chem Lett 32:330. doi:10.1246/cl.2003.330
14. Sato M, Hara H, Nishide T, Kuritani H, Sawada Y (1996) J Mater Chem 6:1767. doi:10.1039/jm9960601767
15. Brinker CJ, Scherer GW (1990) Sol–gel science. Academic Press, CA, USA
16. Bruce DW, O'Hare D (1992) Inoganic materials. Wiley, Chichester
17. Cullity BD (1978) Elements of X-ray diffraction. Addison-Wesley Publishing Company Inc., USA
18. Sherrer P (1918) Cottingernachr 2:98
19. Hall WH (1950) J Inst Met 75:1127
20. Tanemura S, Miao L, Jin P, Kaneko K, Terai A, Nabatova-Gabain N (2003) Appl Surf Sci 212–213:654. doi:10.1016/S0169-4332(03)00015-1
21. Kwon CH, Shin H, Kim CH, Choi WS, Yoon KH (2004) Mater Chem Phys 86:78. doi:10.1016/j.matchemphys.2004.02.024
22. Ohno T, Tsubota T (2004) Chem Lett 33:750. doi:10.1246/cl.2004.750
23. JCPDS Card 21-1272
24. JCPDS Card 21-1276
25. JCPDS Card 41-1445
26. Ohtsuka T, Guo J, Sato N (1986) J Electrochem Soc 133:2473. doi:10.1149/1.2108452
27. Moses PR, Wier LM, Lennox JC, Finklea HO, Lenhard JR, Murray RW (1978) Anal Chem 50:576. doi:10.1021/ac50026a010
28. Saha NC, Tompkins HG (1992) J Appl Phys 72:3072. doi:10.1063/1.351465
29. Miao L, Jin P, Kaneko K, Terai A, Nabatova-Gabain N, Tanemura S (2003) Appl Surf Sci 212–213:255. doi:10.1016/S0169-4332(03)00106-5
30. Wang Z, Helmerson U, Käll PO (2002) Thin Solid Films 405:50. doi:10.1016/S0040-6090(01)01767-9
31. Nishide T, Sato M, Hara H (2000) J Mater Sci 35:465. doi:10.1023/A:1004731804075
32. Yu JC, Yu J, Zhang L, Ho W (2002) J Photochem Photobiol A 148:263. doi:10.1016/S1010-6030(02)00052-7
33. Kominami H, Kato J, Murakami S, Kera Y, Inoue M, Inui T et al (1999) J Mol Catal Chem 144:165. doi:10.1016/S1381-1169(98)00350-1
34. Bandara J, Kuruppu SS, Pradeep UW (2006) Colloids Surf 276:197. doi:10.1016/j.colsurfa.2005.10.059
35. Xin B, Ren Z, Wang P, Liu J, Jing L, Fu H (2007) Appl Surf Sci 253:4390. doi:10.1016/j.apsusc.2006.09.049
36. Fackler JP Jr, Kristine FJ, Mazany AM, Moyer TJ, Shepherd RE (1985) Inorg Chem 24:1857. doi:10.1021/ic00206a032

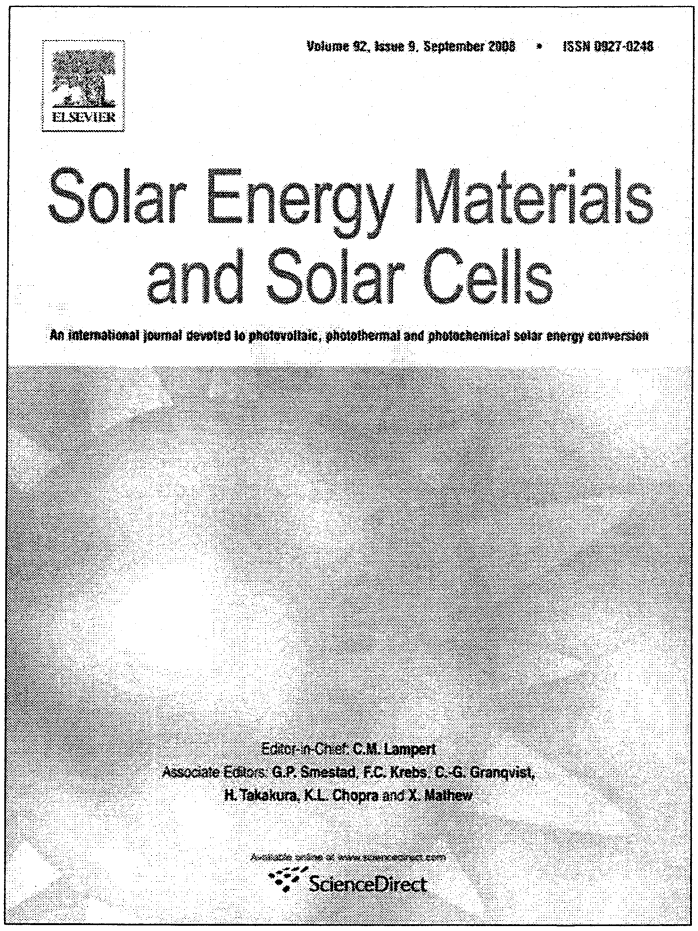

Solar Energy Materials & Solar Cells 92 (2008) 1136–1144

Contents lists available at ScienceDirect

Solar Energy Materials & Solar Cells

journal homepage: www.elsevier.com/locate/solmat

Enhanced UV-sensitivity of vis-responsive anatase thin films fabricated by using precursor solutions involving Ti complexes

Hiroki Nagai [a], Chihiro Mochizuki [a], Hiroki Hara [a], Ichiro Takano [b], Mitsunobu Sato [a,*]

[a] Coordination Engineering Laboratory, Faculty of Engineering, Kogakuin University, 2665-1 Nakano, Hachioji City, Tokyo 192-0015, Japan
[b] Department of Electrical Engineering, Kogakuin University, 2665-1 Nakano, Hachioji City, Tokyo 192-0015, Japan

ARTICLE INFO

Article history:
Received 10 September 2007
Accepted 5 April 2008
Available online 3 June 2008

Keywords:
Enhanced UV-sensitivity
Vis-responsive anatase thin films
Molecular precursor method
Photocatalytic activity
Ti complexes

ABSTRACT

Fabrication of vis-responsive anatase thin films with enhanced UV-sensitivity was attained on an ITO pre-coated glass substrate by applying two precursor solutions involving Ti complexes of oxalic acid and EDTA. The transparent and crack-free thin films were characterized by XRD, XPS, UV–vis and FE-SEM observation. The highest sensitivity to UV light of the vis-responsive film, whose photocatalytic activity was measured by the decomposition rate of methylene blue, was four times as compared with that formed by a sol–gel method under the same conditions. The vis-responsive films showed a characteristic absorption band at around 480 nm.

1. Introduction

Anatase, one of the three TiO_2 crystal forms, is an attractive material as photocatalyst because of its stable and harmless property. The photocatalytic activity of pure anatase is due to the chemical reactivity of electrons and holes that are produced by ultraviolet (UV) irradiation [1]. Fabrication and their photocatalytic activity of visible (vis) light responsive thin films by the physical and/or chemical modification of anatase films has been recently investigated by many researchers, because of the importance of photcatalysts with high reactivity under vis light. However, there is little information on the enhancement of UV-sensitivity by vis-responsive anatase films.

Implantation of transition metal ions substituted at lattice position of Ti^{4+} in anatase thin films was investigated by Anpo et al. [2,3]. The photocatalytic activity of anatase thin films chemically modified decreased fatally under UV irradiation, although those anatase thin films can work as photocatalysts under vis irradiation [4]. Since Asahi et al. reported that the non-metallic ion such as substitutional nitride ion at the oxygen sites of anatase are also effective to enable the thin film responsive to vis light [5], methods for preparing anatase with tetravalent carbon or hexavalent sulfur cations have also been investigated [6–11]. Another chemical fabrication of vis-responsive anatase thin films, which was modified under an NH_3 gas by heat-treating the resulting films formed with a sol–gel method, was attained by Miyauchi et al. [12]. However, the photocatalytic activity of those films is lower under UV irradiation as compared with those before modification in all case, although they can work as photocatalysts under vis light. Therefore, studies on chemical formation of vis-responsive anatase thin films with enhanced photocatalytic activity under UV irradiation are significant from the viewpoint of effective use of solar energy.

We previously reported the molecular precursor method which is one of the wet processes for thin film formation of several metal oxides including TiO_2 or calcium phosphate compounds [13–19]. The method is based on the design of metal complexes for appropriate precursor solutions with stability, homogeneity, miscibility, coatability, etc., which are practical advantages. In order to fabricate anatase films which can effectively respond to both UV and vis light, we recently designed two molecular precursor solutions. A coating solution was obtained by a reaction of $Ti(O^iPr)_4$ with a butylammonium salt of oxalic acid under the presence of hydrogen peroxide. Another coating solution was prepared by a reaction of $Ti(O^iPr)_4$ with ethylenediamine-*N,N,N′,N′*-tetraacetic acid (EDTA) under the presence of dibutylamine and hydrogen peroxide. By forming multi-layered thin films with alternate application of these precursor solutions, a novel type of vis-responsive anatase thin films whose photocatalytic activity under UV irradiation is extraordinary enhanced as compared with those responsive to only UV light could be fabricated.

We report here the preparation, characterization and photocatalytic activity of anatase thin films on an indium-tin-oxide (ITO) pre-coated glass substrate which is usually employed for forming effective thin film photocatalysts [20]. The mechanism of

* Corresponding author. Tel./fax: +81 42 628 4075.
E-mail address: ft10302@ns.kogakuin.ac.jp (M. Sato).

0927-0248/$ - see front matter © 2008 Elsevier B.V. All rights reserved.
doi:10.1016/j.solmat.2008.04.005

the appearance of photocatalytic activity under vis irradiation and enhanced photosensitivity to UV light will be discussed on the basis of the redox reactions between two molecular precursors during heat-treatment and the Ti–N bonds derived from a Ti complex.

2. Experimental

2.1. Materials

Oxalic acid dihydrate, EDTA, methylene blue (MB), and titanium tetraisopropoxide ($Ti(O^iPr)_4$) were purchased from Kanto Chemical Co., Inc. Amines and 30% H_2O_2 were purchased from Wako Pure Chemical Industries, Ltd., and from Santoku Chemical Industries Co., Ltd., respectively. Sixty percent HNO_3 and acetic acid were purchased from Taisei Chemical Co., Ltd. Acetaldehyde and ethanol were purchased from Sigma-Aldrich Co., Ltd., and Amakasu Chemical Industries, respectively. Ethanol was dried on molecular sieves 4 Å before use. Other materials were used without further purification. A glass substrate of $20 \times 20 \times 1.1\,mm^3$ size with transparent ITO film formed by a sputtering method was used for film fabrication. The glass substrates were washed in 2-propanol for 15 min with sonicated stirring, and then dried in a drying oven at 70 °C.

2.2. Preparation of butylammonium hydrogen oxalate hemihydrate $(C_4H_9NH_3)HC_2O_4 \cdot 0.5H_2O$

The 19.6 g (156 mmol) of oxalic acid dihydrate and 11.4 g (156 mmol) of butylamine were added to 100 mL of ethanol, and the solution was refluxed for 1 h. White powders were formed after the solution was cooled to room temperature. The powders were collected on a paper filter under reduced pressure, and air-dried.

2.3. Preparation of precursor solution S_{OX} involving Ti^{4+} complex of oxalic acid

The precursor solution S_{OX} involving Ti^{4+} complex of oxalic acid was prepared by a reaction of 4.96 g (28.8 mmol) of butylammonium oxalate hemihydrate obtained above with 4.09 g (14.4 mmol) of $Ti(O^iPr)_4$ in 20 g of ethanol. The mixed solution was refluxed for 3 h, and then cooled to room temperature. After adding 1.76 g (14.4 mmol) of 30% H_2O_2, the clear solution was refluxed for 0.5 h. The concentration of titanium was 0.5 mmol g^{-1}. The solution S_{OX} of red color kept at ambient temperature for more than 1 week could be applied to several glass substrates reproducing the film thickness once the concentration was adjusted.

2.4. Preparation of precursor solution S_{ED} involving Ti^{4+} complex of EDTA

The precursor solution S_{ED} containing Ti^{4+} complex of EDTA was obtained by a method we previously reported [14], with a modification. To a mixture of 10 g of ethanol and 10 g of methanol, 3.55 g (27.4 mmol) of dibutylamine and 3.65 g (12.4 mmol) of EDTA were added. The solution was refluxed for 2 h with stirring, and then cooled to room temperature. After adding 3.55 g (12.4 mmol) of $Ti(O^iPr)_4$, the solution was refluxed for 4.5 h. After cooling the reacted solution to room temperature, 1.56 g (13.7 mmol) of 30% H_2O_2 was carefully added. And then the solution was refluxed for 0.5 h. The concentration of titanium was 0.4 mmol g^{-1}. The coating solution S_{ED} of red color is more stable than before modification and the coating solution S_{OX}.

2.5. Preparation of sol–gel solution S_{SG} and its modified solutions added with acetaldehyde (S_{SG-AL}), or acetic acid (S_{SG-AC})

A conventional sol–gel solution was prepared by a reaction of 4.27 g (15.0 mmol) of $Ti(O^iPr)_4$ with 1.09 g (10.3 mmol) of nitric acid and 0.82 g (45.4 mmol) of water in 25 g of ethanol [21,22]. As-prepared solution was thus obtained. The concentration of titanium was 0.5 mmol g^{-1}.

Coating solutions, S_{SG-AL} and S_{SG-AC}, were prepared by adding 1.27 g (28.8 mmol) of acetaldehyde or 1.73 g (28.8 mmol) of acetic acid, respectively, to as-prepared sol–gel solutions whose amounts of solvent were reduced to 23.7 and 23.2 g in the preparation of sol–gel solution S_{SG} mentioned above. Each concentration of titanium in these solutions was thus adjusted to 0.5 mmol g^{-1}.

2.6. Coating and heat-treating procedures and film thickness

Six single-layer films were formed by heat-treating the coating solutions, S_{OX}, S_{ED} and S_{SG}, in an Ar flow or in air. The notation of thin film formed by employing these coating solutions is summarized in Table 1, along with that of modified sol–gel solutions, S_{SG-AL} and S_{SG-AC}.

Spin-coating method at ambient temperature was used for forming precursor films with a double step mode: first at 500 rpm for 5 s and next at 2000 rpm for 30 s in all case. These precursor films were pre-heated in drying oven at 70 °C for 10 min and then heat-treated for 30 min at each temperature of 475 °C for the films formed by S_{OX} and S_{SG}, or 500 °C for those by S_{ED} in an Ar gas flow with 0.1 L min^{-1}. Single-layer films OX, ED and SG were thus formed. Other single-layer films OX_{air}, ED_{air} and SG_{air} were fabricated by firing the precursor films in air at the corresponding temperature and for the same heating time as described above for OX, ED and SG. When the concentration of titanium was adjusted at 0.5 and 0.4 mmol g^{-1} for S_{OX} and S_{ED}, respectively, the film thickness was 100 nm. The sol–gel solution S_{SG} of 0.5 mmol g^{-1} was stirred for 3 days at ambient temperature in order to fabricate the anatase film of 100 nm thickness, and the resulting film of 50 nm thickness was obtained by applying as-prepared solution with stirring for 1 h at ambient temperature. Film thickness of each film was measured by a stylus profilometer, DEKTAK-3 (Sloan).

Structures of multilayered films are illustrated in Fig. 1C. In order to fabricate multilayered films, respective coating solution was applied to form each layer and the procedures for coating and heat-treatment in the Ar gas flow were repeated. The notation of

Table 1
The notation of thin films formed in an Ar gas flow and in air by employing molecular precursor solutions and sol–gel solutions

Precursor solution	Notation of film formed	
	In Ar gas flow	In air
S_{OX}	OX	OX_{air}
S_{ED}	ED	ED_{air}
S_{SG}	SG	SG_{air}
S_{SG-AL}	SG_{AL}	–
S_{SG-AC}	SG_{AC}	–

The acronyms are based on the ligand, oxalic acid (OX) and EDTA (ED), involved in the corresponding precursor solution when molecular precursor method was employed. In the case of sol–gel method, SG was used and modification with acetaldehyde (AL) and acetic acid (AC) was indicated by the subscript.

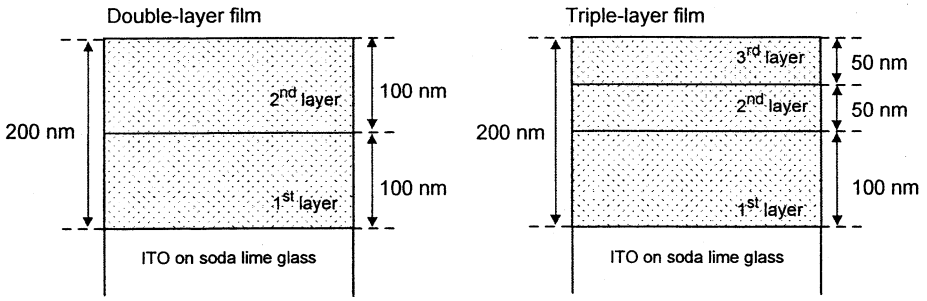

Fig. 1. Schematic structures of double-layer (left) and triple-layer (right) thin films. Double-layer structure: the first layers of OX–OX and OX–ED, and the second layers of OX and ED–OX were formed by employing S_{OX}. The first layer of ED–OX and the second one of OX–ED were fabricated by using S_{ED}. When the solution S_{OX} was applied, the precursor films were heat-treated at 475 °C for 60 min, except for OX–OX whose precursor film for second layer was heat-treated at 500 °C for 30 min. On the other hand, heat-treatment was performed at 500 °C for 30 min, when the precursor films were formed by employing S_{ED}. Triple-layer structure: each precursor film for the first layers was formed by applying S_{OX} and heat-treated at 475 °C for 30 min. The precursor film of the second layer for OX–OX–OX formed by employing the half-diluted solution of S_{OX}, and those for OX–ED–OX and OX–ED–SG formed by using the half-diluted solution of S_{ED} were heat-treated at 500 °C for 30 min. The precursor films of the third layers for OX–OX–OX and OX–ED–OX formed by employing the half-diluted solution of S_{OX}, and that for OX–ED–SG formed by using the as-prepared solution of S_{SG} with stirring for 1 h at ambient temperature were heat-treated at 475 °C for 30 min.

resulting double- and triple-layer films is indicated by the same acronyms of film by the corresponding precursor solution sequentially from left side. Each double-layer film has the first or second layer of OX or ED film with 100 nm thickness. The film OX of 100 nm thickness was formed as the first layer of all triple-layer films and then each film of 50 nm for the second and third layers of triple-layer films were formed by employing the half-diluted solutions of S_{OX} and S_{ED} with ethanol, respectively.

2.7. Chemical characterization of oxalato ligand

^1H and ^{13}C NMR spectra of the oxalate salt obtained here were measured on a JEOL JNM-270 (270 MHz) spectrometer in D_2O with tetramethylsilane (TMS = 0.0 ppm) as an external reference. IR spectra of the compound were measured on a JASCO FT-IR 620 spectrophotometer for disks diluted with KBr. Elemental analysis of the compound was performed on a Perkin-Elmer 2400 Series II CHN-analyzer.

2.8. Structural characterization of thin films

The crystal phase of the thin films was examined by an X-ray diffractometer, MXP-18AHF22 (Bruker AXS), with Cu Kα rays generated by 45 kV and 300 mA. Parallel beam optics with an incident angle in the range from 0.3° to 0.4° were employed in each measurement. Surface appearance of the thin films was observed by a field-emission scanning electron microscope, FE-SEM S-4200, Hitachi, at an accelerating voltage of 5 kV.

2.9. Chemical characterization of thin films

X-ray photoelectron spectroscopy spectra of the thin films were measured on a Physical Electronics Quantum 2000 or a Shimadzu ESCA-K1S. A Phi Quantum 2000 Scanning ESCA Microprobe with a focused monochromatic Al Kα X-ray (1486.6 eV) source evaluated the states of the nitrogen atoms in these films. Chemical shift data are charge referenced to the center of the C–C/C–H peak at 284.6 eV. A Shimadzu ESKA-K1S with Mg Kα X-rays (1253.6 eV) evaluated the amount of the titanium, oxygen, carbon, nitrogen and indium atoms in these films. The binding energies were calibrated with the $4f_{7/2}$ line of metallic gold, assumed to be 84.0 eV. The composition and chemical state of the films were determined after Ar^+ ion beam bombardment (2 kV, 18 μA cm^{-2}) for 3 min for removal of oxides from the surface.

2.10. Optical characterization of thin films

Absorption spectra of the thin films were measured in the range from 200 to 800 nm with a double beam mode and air was used as a reference in each measurement. These measurements were performed with a Hitachi U-2800 spectrophotometer.

The optical band edge of the thin films was calculated by using the difference spectra which were obtained by subtracting absorption value of ITO substrate from those at wavelength of films with ITO substrate. The optical band edge E_g of the thin films was determined using the following Tauc expression; $\alpha = A(E-E_g)^{1/2}/E$, where E is the photon energy ($\equiv h\nu$), A is the constant, α is the absorption coefficient at wavelength [23].

2.11. Photocatalytic activity measurements

The photocatalytic activity of each film whose area is 15×15 mm^2 on the substrate was examined by the decomposition reaction of MB in 10 mL aqueous solution (0.01 mmol L^{-1}). A black light, National FL10BL-B, was used for UV irradiation. Vis irradiation without UV light was obtained from a fluorescent light, Duro-Test Vita-Lite, by removing light of wavelengths shorter than 400 nm using a cut-off filter, Ishihara Window Paint α, on a soda-lime glass. The distances of the black light sources from sample surfaces were adjusted to maintain UV intensities at 365 nm of 1.2 mW cm^{-2} which was measured by an UV meter, UVR-400, Iuchi Co., Ltd. The vis light intensity after removing UV components from the fluorescent light, which was estimated by an illuminometer, LX-105, CUSTOM Co., Ltd, was 0.8 mW cm^{-2}.

The concentration of MB was determined by measuring the absorption spectra of the aqueous solution in the range from 600 to 700 nm with a Hitachi U-2800 spectrophotometer. At intervals of 20 min during decomposition test, ca. 3 mL of the solution was moved into a quartz cell of $1 \times 1 \times 4.5$ cm^3. After the spectral measurement, the solution was immediately returned to the vessel and mixed with the aliquot. The mixed solution was further used until the test for each film was completed. From the absorption value at 664 nm of the solutions, each concentration of MB was thus determined by a standardized method [24,25].

The decomposition rate of MB was examined three times for each film, and the index of photocatalytic activity (IPCA) of the film was estimated from the averaged value of the pseudo-first order kinetic constant. In order to examine the degree of adsorption on the glass substrate and self-decomposition of MB, same measurement was performed on the same samples without irradiation as a reference.

The IPCA value for each film was obtained as follows. The concentration of MB after t minutes, $C(t)$, was determined by the formula (1), where Abs(0) and Abs(t) represent the absorption values of the solution just before the light irradiation and after t minutes during irradiation, respectively:

$$C(t) = 10 \times \frac{\mathrm{Abs}(t)}{\mathrm{Abs}(0)} \quad (\mu\mathrm{mol\,L^{-1}}). \tag{1}$$

An approximate line for the function of $C(t)$ versus t was obtained in the range from $0 \leqslant t \leqslant 80$ min by a least-square method. The IPCA for each film was estimated as the averaged gradient of the lines, according to the formula (2), where a_n indicates each gradient, i.e., the pseudo-first order kinetic constant, obtained three times separately.

$$\mathrm{IPCA} = \frac{|a_1 + a_2 + a_3|}{3} \times 10^3 \quad (\mathrm{nmol\,L^{-1}\,min^{-1}}). \tag{2}$$

3. Results

3.1. Preparation of butylammonium hydrogen oxalate hemihydrate $(C_4H_9NH_3)HC_2O_4 \cdot 0.5H_2O$

The results of elemental analysis on the white powder obtained by the reaction of oxalic acid with butylamine in water was as follows: C, 42.1 (41.9); H, 8.29 (8.20); N, 8.17 (8.13) %. The calculated values for the butylammonium hydrogen oxalate hemihydrate $(C_4H_9NH_3)HC_2O_4 \cdot 0.5H_2O$, $C_6H_{14}NO_{4.5}$, are given in parentheses and well consistent to the experimental data. It was thus shown that the yield of the compound is 89% from the weight of the product, 23.9 g. In ^{1}H NMR spectra, a triplet at 2.32 ppm, two kinds of multiplets at 0.96 and 0.70 ppm, and a triplet at 0.24 ppm were observed. These peaks can be assigned to the hydrogen atoms of the methylene group linked to nitrogen atom of the butylamine, those of two methylene groups in the center of the butyl group, and those of the methyl group of the alkyl chain, in the order. In ^{13}C NMR spectra obtained by proton decoupling mode, five singlet peaks at 165.6, 39.3, 28.8, 19.0 and 12.8 ppm were observed. These peaks can be assigned to the carbon atoms of the carboxyl group in the oxalic ion, the carbon atom linked to nitrogen atom of the butylamine, those of two methylene groups in the center of the butyl group, and that of the methyl group of the alkyl chain, in the order. In the IR spectrum, characteristic bands assignable to ν_a(C=O) were observed at 1684 and 1641 cm^{-1}. It was thus elucidated by these results that the product is the butylammonium hydrogen oxalate hemihydrate.

3.2. Crystal structure and surface morphology of thin films

The XRD patterns of the single-layer films, OX, ED and SG, which were fabricated by heat treating each precursor film in an Ar gas flow, are shown in Fig. 2, along with those of OX_{Air}, ED_{Air} and SG_{Air} formed by firing in air. For the film OX, peaks at $2\theta = 25.4°$, 38.0°, 48.2°, 53.9°, 55.2° and 62.5° are assignable to (101), (004), (200), (105), (211), and (204) phases of anatase, respectively [26]. Peaks at $2\theta = 21.5°$, 30.6°, 33.1°, 35.5°, 41.8°, 45.7°, 49.3°, 51.0°, 56.0°, 59.1°, 60.7° and 63.7° can be assigned to those of In_2O_3 crystals in ITO [27]. Each peak of the film OX due to anatase can be observed in those for other five films, although the intensity of anatase is extremely low for the film ED. These results indicate that the heat-treatment of these precursor films in an Ar gas flow is effective to crystallize to anatase even though oxygen was not supplied externally.

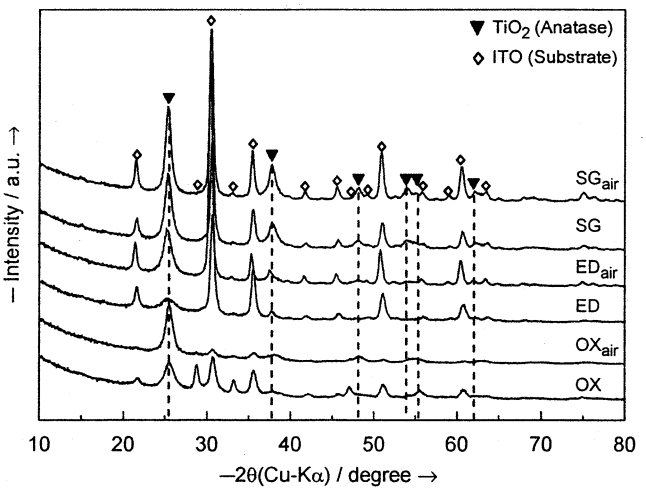

Fig. 2. XRD patterns of the single-layer films whose thickness is 100 nm.

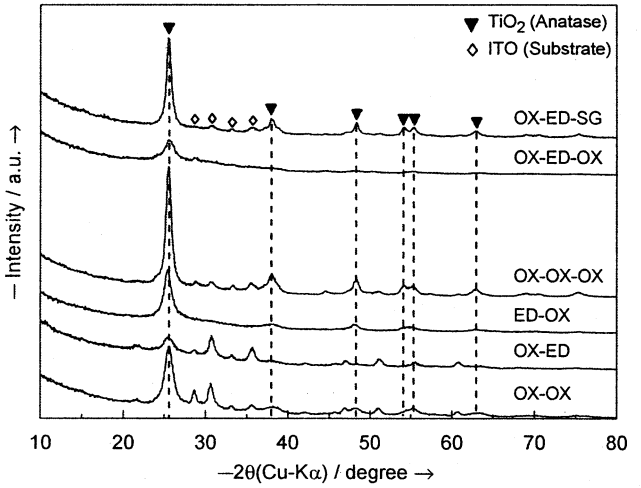

Fig. 3. XRD patterns of the double- and triple-layer films.

Fig. 3 shows the XRD patterns for the double-layer films OX–OX, OX–ED and ED–OX, and the triple-layer films OX–OX–OX, OX–ED–OX and OX–ED–SG. All peaks observed in these patterns and those for OX–ED–SG_{AL} and OX–ED–SG_{AC} by applying the modified sol–gel solutions can be also assigned to anatase and ITO.

In Fig. 4, the surface appearances of (A) a single-layer film ED and (B) a triple-layer film OX–ED–OX are presented. These SEM data show even surfaces without any crack or pinhole, and are the representative of the surface morphology of all films. These surfaces were too smooth to detect the roughness by measuring with the stylus profilometer, whose limit is ca. 10 nm.

3.3. Chemical characterization of thin films

In Fig. 5, the XPS spectra of the film ED are shown. The binding energy of Ti $2p_{3/2}$ attributed to Ti–O and Ti–N is a typical value of 459.3 and 455.4 eV, respectively. Additionally, the binding energy of N 1s is 396.9 eV and the existing nitrogen is only in the oxygen-substituted form, but not in chemisorption form [28]. These binding energies for the film ED are all identical to those for other films fabricated in the present study. Thus, direct formation of anatase thin films including substitutional nitrogen atoms was

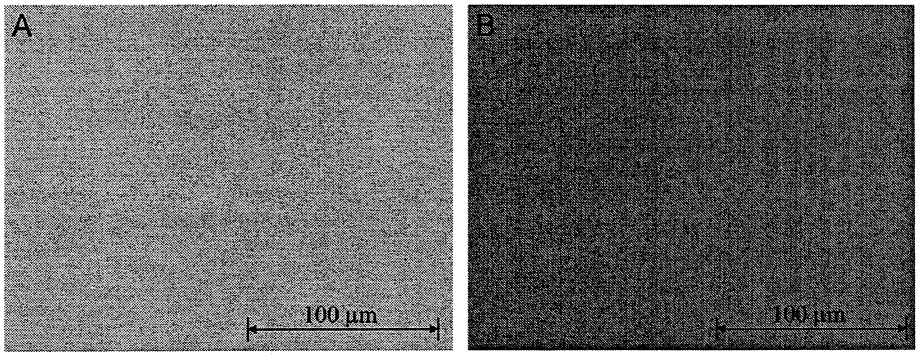

Fig. 4. SEM images of (A) ED and (B) OX–ED–OX. (A) Single-layer film of 100 nm on the ITO electrode, and (B) three-layer film of 200 nm.

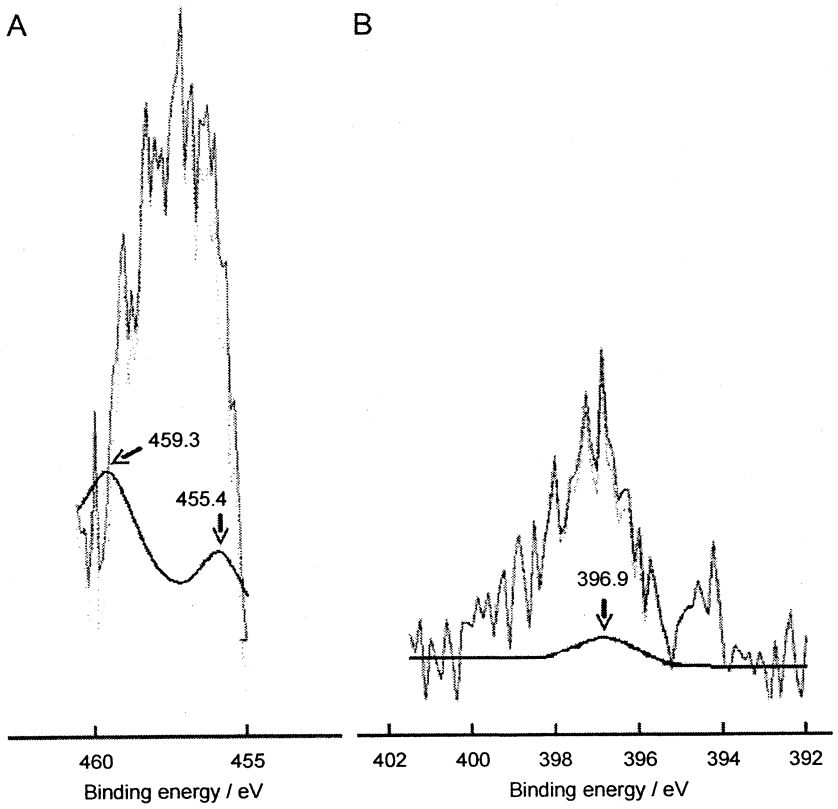

Fig. 5. XPS spectra of (A) Ti $2p_{3/2}$, (B) N 1s of the nitrogen-substituted TiO_2 thin film obtained by heat treatment of the precursor film containing the Ti complex with EDTA ligand on Na-free glass in an Ar gas flow. The thin solid lines are original data of XPS. The thick solid curves are theoretical Gaussian distribution curves. The dashed curves are theoretically fitted curves by assuming Gaussian distribution.

first attained through heat-treating the molecular precursor film fabricated by applying the solution S_{ED} in an Ar gas flow.

The averaged peak ratios of C 1s, N 1s and O 1s toward Ti 2p observed by XPS of two single-layer anatase films, OX, ED are listed along with those of three triple-layer films, OX–OX–OX, OX–ED–OX, OX–ED–SG_{AL} in Table 2. Significant amount of carbon and nitrogen atoms were found especially in the film ED. It is notable that the larger amount of nitrogen atoms in the second layer of the films OX–ED–OX and OX–ED–SG_{AL} exists comparing with other films.

The depth profile of the triple-layer film OX–ED–OX measured by XPS is shown in Fig. 6. It was thus confirmed that remarkable amounts of carbon and nitrogen atoms still remained in the second layer and the substitutional nitrogen atoms were locally distributed in the deep portion corresponding to the second layer and most of nitrogen atoms did not diffuse to other layers, although the amounts of the nitrogen and carbon atoms in the other layers cannot be neglected.

3.4. UV–vis absorption spectra and optical band edge of thin films

The UV–vis absorption spectra of single-layer films are shown in Fig. 7. It was shown that absorption intensity of the film ED in the vis region is remarkably high, according to the brown color of the film, as compared with other films of colorless.

Fig. 8 shows the UV–vis absorption spectra of the double- and triple-layer films. Absorption spectra of the films OX–ED–SG_{AL} and

Table 2
The averaged ratios of C 1s, N 1s and O 1s toward Ti 2p observed by XPS of single- and triple-layer anatase films, OX, ED, OX–OX–OX, OX–ED–OX, OX–ED–SG_{AL}

Film	Layer	C/Ti	N/Ti	O/Ti
OX		0.06	0.01	1.72
ED		2.54	0.83	2.57
OX–OX–OX	3rd	0.06	0.03	2.08
OX–ED–OX		0.19	0.06	1.43
OX–ED–SG_{AL}		0.12	0.01	1.72
OX–OX–OX	2nd	0.06	0.02	2.19
OX–ED–OX		0.19	0.11	1.37
OX–ED–SG_{AL}		0.15	0.10	1.69
OX–OX–OX	1st	0.08	0.05	2.18
OX–ED–OX		0.06	0.04	1.46
OX–ED–SG_{AL}		0.05	0.01	1.95

The values were calculated from the peak area of each element for each layer.

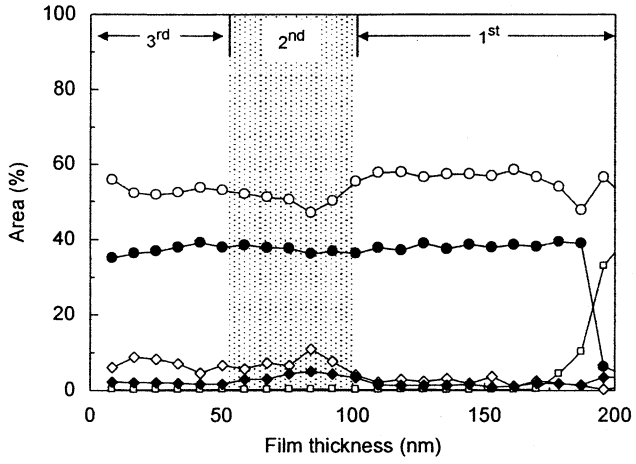

Fig. 6. Depth profile of the amount of components in the three-layer thin film OX–ED–OX. Notations indicate the energy levels of five atoms in parentheses, -●-: (Ti 2p), -○-: (O 1s), -◆-: (N 1s), -◇-: (C 1s), -□-: (In 3d). Net multiplication part is corresponding to the second layer formed by applying the solution S_{ED}.

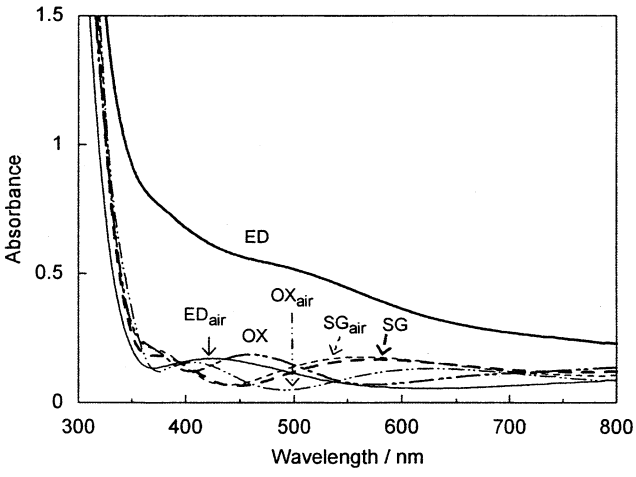

Fig. 7. Absorption spectra of six single-layer films. The lines indicate each film as follows: OX (▬ · · ▬), ED (▬▬▬), SG (▬ ▬ ▬), OX_{air} (– · · –), ED_{air} (—), SG_{air} (---).

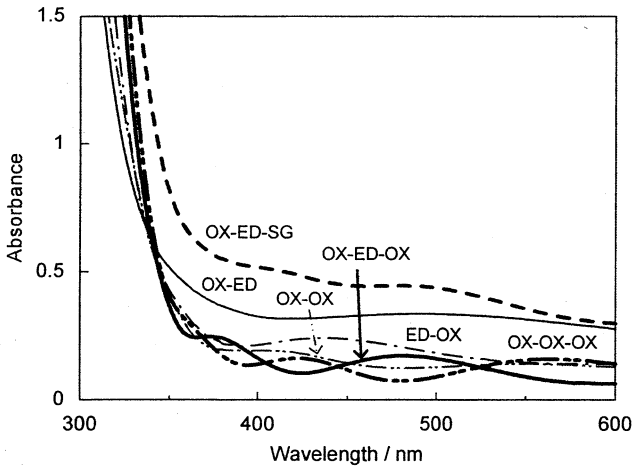

Fig. 8. Absorption spectra of double- and triple-layered films. The lines indicate each film as follows: OX–OX–OX (▬ · · ▬), OX–ED–OX (▬▬▬), OX–ED–SG (▬ ▬ ▬), OX–OX (– · · –), OX–ED (—), ED–OX (– · –).

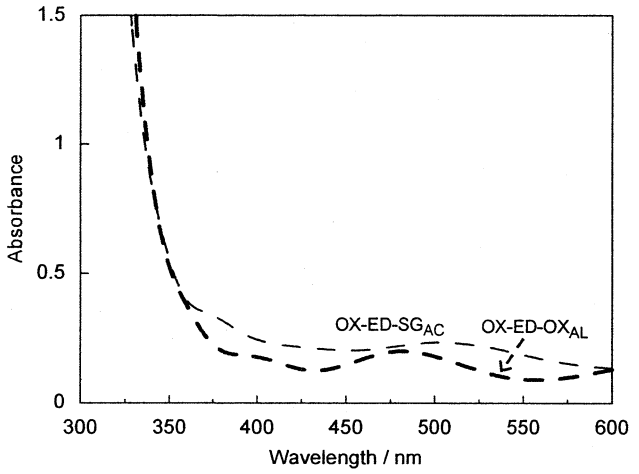

Fig. 9. Absorption spectra of multilayered films fabricated by a modified sol–gel method for their third layers. The lines indicate each film as follows: OX–ED–SG_{AL} (▬ ▬ ▬), OX–ED–SG_{AC} (---).

OX–ED–SG_{AC} by applying the modified sol–gel solutions S_{SG-AL} and S_{SG-AC} are separately shown in Fig. 9. It is notable that the absorption spectra of OX–ED–OX and OX–ED–SG_{AL} indicate characteristic absorption bands at around 480 nm, though other triple-layer films do not show such absorption band in the visible region.

The optical band edge of the thin films is listed in Table 3. The optical band edge is in the range from the lowest value 3.57 eV of the double-layer film OX–ED to 3.82 eV of the single-layer film ED_{air}.

3.5. Photocatalytic activity of thin films

The absorption spectra of the aqueous solutions containing MB during decomposition test under irradiating UV light and under dark are shown in Fig. 10, by employing the triple-layer film OX–ED–OX. In Fig. 10, the spectral changes of the same sample measured under dark are also given by the broken lines.

The IPCA of single-layer films are summarized in Table 4. The apparent IPCA value measured under dark was smaller than 4 for all thin films, as shown in Table 4. From the data obtained under dark, the contribution of the adsorption onto the sample and

Table 3
The optical band edges of single- and multi-layer anatase thin films

Film	Optical band edge[a] eV
OX	3.71 (3)
ED	3.68 (5)
SG	3.76 (3)
OX_{air}	3.78 (7)
ED_{air}	3.82 (3)
SG_{air}	3.71 (2)
OX–OX	3.63 (1)
OX–ED	3.57 (1)
ED–OX	3.71 (2)
OX–OX–OX	3.70 (1)
OX–ED–OX	3.69 (1)
OX–ED–SG	3.68 (2)
$OX–ED–SG_{AL}$	3.70 (2)
$OX–ED–SG_{AC}$	3.71 (8)

The edge energy was calculated from the absorption data in the range from 311 to 295 nm of thin films.
[a] Estimated standard deviations are presented in parentheses.

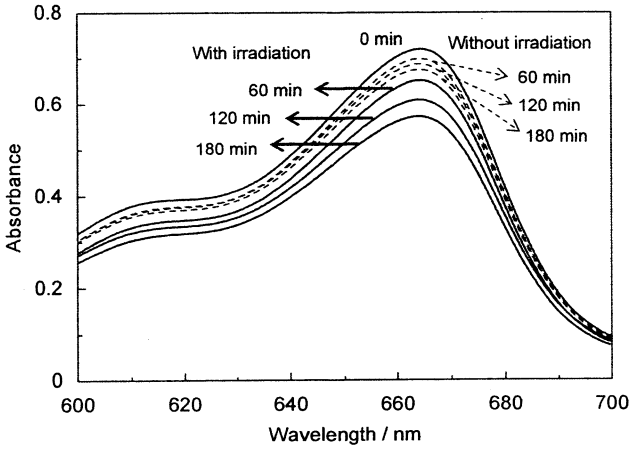

Fig. 10. The absorption spectra of MB for measurement of photocatalytic activity. The photocatalytic activity was measured by decomposition reaction of MB. The absorption of MB at 664 nm was decreased by the OX–ED–OX with UV irradiation (as photocatalyst) and without irradiation (as adsorption).

Table 4
Index of photocatalytic activity (IPCA) for single-layer film of 100 nm thickness

Single-layer film	IPCA[a]	
	Under UV irradiation	Under dark
OX	7.2 (3)	3.6 (3)
OX_{air}	8.4 (3)	3.5 (4)
ED	5.3 (4)	3.5 (4)
ED_{air}	6.4 (7)	3.6 (4)
SG	6.2 (4)	3.9 (4)
SG_{air}	6.4 (4)	3.9 (4)

IPCA values were obtained from the pseudo-first order kinetic constants of the decomposition reaction of MB in aqueous solution both under UV irradiation and under dark, which were estimated by the decrease of absorption value at 664 nm of each test solution.
[a] Estimated standard deviations are presented in parentheses.

vessel, and self-decomposition of MB was thus evaluated. Since the IPCA values under UV irradiation are larger than 4 for these films, it was revealed that they can work effectively as photocatalyst. The photocatalytic activity of the films fabricated in an Ar gas flow is slightly lower than that of those formed in air. The films OX and OX_{air} fabricated by the molecular precursor solution S_{OX} indicated higher photocatalytic activity among them, although any activity could not be observed under vis irradiation alone in any case.

Table 5
Index of photocatalytic activity (IPCA) for multilayer films of 200 nm thickness

Multilayer film	IPCA[a]	
	Under UV irradiation	Under vis irradiation
OX–OX	11.9 (3)	3.5 (3)
OX–ED	4.9 (5)	3.2 (3)
ED–OX	9.0 (10)	5.4 (6)
OX–OX–OX	19.4 (11)	3.1 (4)
OX–ED–OX	23.9 (12)	9.4 (6)
OX–ED–SG	14.3 (10)	3.7 (3)
$OX–ED–SG_{AL}$	15.8 (11)	11.4 (5)
$OX–ED–SG_{AC}$	14.3 (10)	3.6 (5)

IPCA values were obtained from the pseudo-first order kinetic constants of the decomposition reaction of MB in aqueous solution both under UV irradiation and under vis irradiation, which were estimated by the decrease of absorption value at 664 nm.
[a] Estimated standard deviations are presented in parentheses.

The IPCA values of the multilayered thin films, measured under UV or vis irradiation, are summarized in Table 5. Three multilayer films, ED–OX, OX–ED–OX and $OX–ED–SG_{AL}$, indicate effective photocatalytic activity under vis irradiation, although other films responded only to UV light. It is important that the photocatalytic activity of the vis-responsive films is extremely high under UV irradiation.

4. Discussion

4.1. Proposed structures of the precursor complexes

Two precursor solutions for anatase thin film formation were newly prepared and heat-treating the spin-coated precursor films well adhered on ITO substrates is useful to obtain transparent and crack-free thin films. The red color of these coating solutions is characteristics to Ti^{4+} complexes coordinated with peroxo ligand, as reported for several aminopolycarboxylato complexes [29]. The oxalato complexes of Ti^{4+} ion, $(NH_4)_2[TiO(C_2O_4)_2]\cdot H_2O$ and $H_2[TiO(C_2O_4)_2]$, were synthesized by Van de Velde et al. and Kolen'ko et al., respectively [30,31]. These oxo complexes prepared in aqueous solutions are, however, colorless. It was thus suggested that a peroxo complex of Ti^{4+} with oxalic acid can be formed in ethanol under the presence of butylamine. The central Ti^{4+} ion in the precursor solution may be coordinated with two oxalate ions and a peroxo group in place of an oxo ligand. By the structural study by Fackler et al., it was indicated that the central Ti^{4+} ion is linked by two nitrogen atoms of the EDTA ligand in a Ti complex $[Ti(H_2O)(EDTA)]\cdot 1.5H_2O$ [32]. Also in the Ti complex involved in the precursor solution S_{ED}, two nitrogen atoms may coordinate to the Ti^{4+} ion in the same manner.

By the stability of these coating solutions, the film thickness of the resulting anatase films can be facilely regulated by adjusting their concentrations, although those formed by sol–gel solutions are dependent on the storage term, as described in the experimental section.

4.2. Photocatalytic activity of single-layer anatase thin films

Single-layer anatase thin films formed by heat-treating with and without supplying external oxygen can work as effective photocatalysts under UV irradiation. Lowest photocatalytic activity was shown by the film ED fabricated in an Ar gas flow. This may be due to large amount of carbon and nitrogen atoms removed incompletely and found by XPS. It is generally accepted that the formation of impurity level in the band gap of anatase deactivate the photocatalyst because the impurity level affects as a recombination center of electrons and holes photoinduced [3], the organic residues being involved in the film ED may also cause the recombination between electrons and holes generated by UV-irradiated anatase.

Even though the Ti–N bonds derived from the precursor complex could be remained in the film ED, the brown film did not respond to vis light alone and no specific absorption band or shift in visible region was found for the film.

4.3. Reductants for vis-responsive multilayer thin film formation

The total energy consumption for fabricating each multilayer film was kept constant, even though the layer structure is different from each other. Therefore, the degree of photocatalytic activity of these films can be quantitatively discussed, because those conditions for fabricating thin films often affect the activity.

Three multilayer films, ED–OX, OX–ED–OX and OX–ED–SG_{AL}, indicate effective photocatalytic activity under vis irradiation. It is important that the upper layers of these films were formed by employing the precursor solution S_{OX}, on the first one of ED–OX and the second one of OX–ED–OX, respectively, where large amount of organic residues derived from the EDTA complex exist as described above for the film ED, although the organic residues significantly decreased as compared with those of the single-layer film. These suggest that the resulting species in the first layer of ED–OX and the second one of OX–ED–OX was effectively removed by redox reactions which were occurred in the Ar gas flow during heat-treating the precursor films involving the oxalato complex in the upper layer through their interfaces.

On the assumption that the reductive nature of oxalic acid in the upper layer is related to the vis-responsive film formation by reacting with the organic residues formed by the EDTA complex, film fabrication of OX–ED–SG_{AL} and OX–ED–SG_{AC} was examined in order to compare the effects of organic reductant and acid, i.e., acetaldehyde and acetic acid, respectively. As a result, the appearance of the vis-responsive property of the film is unambiguously attributable to the resulting materials produced by the reactions of acetaldehyde with the organic residues in its lower layer.

Only for the vis-responsive films, ED–OX, OX–ED–OX and OX–ED–SG_{AL}, the characteristic absorption band was observed at around 480 nm. When the absorption band of these films was disappeared by heat-treating each film at 500 °C in air for more than 20 min, the resulting films did not show the vis-responsive property. Thus, the colored materials may be composed of Ti complexes or organic components formed in the solid states.

4.4. Multilayering of anatase films

Another vis-responsive photocatalytic thin film structured by WO_3 and TiO_2 layers was chemically fabricated by Miyauchi et al. [33]. By covering with an anatase thin film on a colored WO_3 film whose absorption edge is at 460 nm, the hydrophilic property was observed on its surface by irradiating vis light alone. They suggested that the hydrophilicity may be due to the electron transfer caused from vis-irradiated WO_3 to anatase, although the multilayer film could not decompose organic compounds neither under UV or vis irradiation. Such electron transfer from colored materials to anatase enables the film to respond to vis light, like the TiO_2 electrode for dye-solar cells [34–36], although the dye molecules adsorb on the surfaces of TiO_2 particles.

These suggest that the multilayering in the present study may afford the opportunity for the reactions of the reductants like oxalic acid or acetaldehyde with the intermediates formed by the thermal decomposition of the EDTA complex in an Ar gas flow, as described above. It was revealed that the efficiency of vis-light absorption by these films and sequential electron transfer inside the anatase is too high to decompose the organic compound MB in its aqueous solution, as compared with the WO_3–TiO_2 multilayered film.

4.5. Enhancement of photosensitivity of anatase

The single and multilayer anatase thin films show larger band edge values than those reported for bulk crystals of ca. 3.2 eV. It is generally accepted for thin films that the main reason for the larger band edge might be due to an axial strain effect from lattice distortion produced by a mismatch between film and substrate lattice constant [37]. Larger absorption edge values of the anatase thin films are also observed in the present work.

It is, however, notable that the photocatalytic activity of the vis-responsive films, ED–OX, OX–ED–OX and OX–ED–SG_{AL}, is enhanced under UV light, though the energy consumption for fabricating them and film thickness are equal to those for other films sensitive to only UV light, as described above. In the case of the partially nitrided anatase film physically modified, remarkable red shift near UV region is observed as ca. 40 nm (= 0.34 eV), although the band gap energy was not reported in the literature [5]. This indicates that the physical modification did not only affect significantly the spectrum near UV region of the anatase, but also afford the vis-responsive property to the anatase. As a result, the decrease of UV-sensitivity may be occurred. On the other hand, the spectral shifts near UV region are rather small by the incorporation of Ti–N bonds into anatase films in the present vis-responsive films. In fact, the edge shifts of the triple-layer anatase films are within 0.03 eV as shown in Table 3, although the amount of Ti–N bonds in the vis-responsive film OX–ED–OX involves ca. 15 times as compared with the physically modified film. Thus, the properties of the substitutional nitrogen atoms derived from the EDTA complex are significantly different from those impregnated by the physical method with high energy or those incorporated by the reaction with NH_3 with anatase.

It is suggested that Ti–N are not directly related to the appearance of the vis-responsive property of ED–OX, OX–ED–OX and OX–ED–SG_{AL}, but significantly affect the enhancement of photosensitivity in anatase. Several studies on the enhancement of photocatalytic activity by electron-trap mechanism have been recently reported for anatase particles under UV irradiation through co-existence of several cations such as Fe^{3+} [38]. So, this is the first report on the enhancement of UV-sensitivity of vis-responsive anatase films by incorporating anionic species, i.e., nitride ions, as far as we know.

5. Conclusion

Two precursor solutions newly prepared are useful to fabricate single and multilayer anatase thin films of transparent and crack-free. It was elucidated by XPS that large amount of the substitutional nitride ions can be formed by employing the precursor solutions involving an EDTA complex. By the

quantitative evaluation of the photocatalytic activity of the resulting films, it was confirmed that three multilayered anatase thin films, ED–OX, OX–ED–OX and OX–ED–SG_{AL}, with specific layer structure indicate vis-responsive property with enhanced UV-sensitivity. The vis-responsive anatase films was formed spontaneously and significant decrease of the organic residues occurred simultaneously, during the thermal reactions of the reductants like oxalic acid or acetaldehyde in the upper layer with the organic residues formed in the lower one. From the results on the absorption spectra near UV region, it was found that the band edge energy of anatase was not affected significantly by the presence of the Ti–N bonds derived from the precursor complex of EDTA.

The photocatalytic activity of these films is independent on the surface morphology, because it was confirmed by FE-SEM observation that the surface of all films is quite even (Fig. 4). It can be concluded for these vis-responsive anatase films with the enhanced UV-sensitivity that (1) the vis-responsive property is mainly due to the novel colored materials which was formed spontaneously by chemical reactions during heat-treatment of the reductants in the upper layer with the organic residues derived from EDTA in the lower one, and (2) the large amount of Ti–N bonds derived from the metal complex can contribute to enhance the photocatalytic activity under UV irradiation. It is important that the present process can be applicable to the glass substrates of large scale from the viewpoint of utilization of solar energy. Further studies are now in progress on the chemical identification for the colored materials formed in the thin films and the possible intermediates derived from the EDTA complex, which can react with reductants in solid state.

Acknowledgment

This work was supported by "High-Tech Research Center" Project for Private Universities: Matching fund subsidy from MEXT (Ministry of Education, Culture, Sports, Science and Technology) Japan, 2006–2010.

References

[1] K. Honda, A. Fujishima, Nature 238 (1972) 37.
[2] M. Anpo, S. Kishiguchi, Y. Ichihashi, M. Takeuchi, H. Yamashita, K. Ikeue, B. Morin, A. Davidson, M. Che, Res. Chem. Intermed. 27 (2001) 459.
[3] M. Anpo, Bull. Chem. Soc. Jpn. 77 (2004) 1427.
[4] E. Borgarello, J. Kiwi, M. Gratzel, E. Pelizzetti, M. Visca, J. Am. Chem. Soc. 104 (1982) 2996.
[5] R. Asahi, T. Morikawa, T. Ohwaki, K. Aoki, Y. Taga, Science 293 (2001) 269.
[6] H. Irie, Y. Watanabe, K. Hashimoto, Chem. Lett. 32 (2003) 772.
[7] S. Sakthivel, H. Kisch, Angew. Chem. Int. Ed. 42 (2003) 4908.
[8] T. Ohno, T. Tsubota, M. Toyofuku, R. Inaba, Catal. Lett. 98 (2004) 255.
[9] T. Ohno, T. Mitsui, M. Matsumura, Chem. Lett. 32 (2003) 364.
[10] T. Umebayashi, T. Yamaki, H. Itoh, K. Asai, Appl. Phys. Lett. 81 (2002) 454.
[11] T. Umebayashi, T. Yamaki, S. Tanaka, K. Asai, Chem. Lett. 32 (2003) 330.
[12] M. Miyauchi, A. Ikezawa, H. Tobimatsu, H. Irie, K. Hashimoto, Phys. Chem. Chem. Phys. 6 (2004) 865.
[13] M. Sato, H. Hara, H. Kuritani, T. Nishide, Sol. Energy Mater. Sol. Cells 45 (1997) 43.
[14] M. Sato, H. Hara, T. Nishide, H. Kuritani, Y. Sawada, J. Mater. Chem. 6 (1996) 1767.
[15] M. Sato, T. Tanji, H. Hara, T. Nishide, Y. Sakashita, J. Mater. Chem. 6 (1999) 1539.
[16] T. Hayakawa, K. Takahashi, M. Yoshinari, H. Okada, H. Yamamoto, M. Sato, K. Nemoto, Int. J. Oral Maxillofac. Implants 21 (2006) 851.
[17] T. Hayakawa, K. Takahashi, M. Yoshinari, H. Hara, M. Sato, K. Nemoto, J. Oral Tissue Eng. 3 (2006) 139.
[18] T. Hayakawa, K. Takahashi, M. Yoshinari, H. Hara, K. Nemoto, M. Sato, J. Oral Tissue Eng. 3 (2005) 17.
[19] K. Takahashi, T. Hayakawa, M. Yoshinari, H. Hara, C. Mochizuki, M. Sato, K. Nemoto, Thin Solid Films 484 (2005) 1.
[20] J.W. Yoon, T. Sasaki, N. Koshizaki, Thin Solid Films 483 (2005) 276.
[21] C.J. Brinker, G.W. Scherer, Sol–Gel Science, Academic Press, California, 1990 (Chapter 3).
[22] D.W. Bruce, D. O'Hare, Inoganic Materials, Wiley, Chichester, 1992, pp. 519–525.
[23] S. Tanemura, L. Miao, P. Jin, K. Kaneko, A. Terai, N. Nabatova-Gabain, Appl. Surf. Sci. 212–213 (2003) 654.
[24] C.H. Kwon, H. Shin, J.H. Kim, W.S. Choi, K.H. Yoon, Mater. Chem. Phys. 86 (2004) 78.
[25] T. Ohno, T. Tsubota, Chem. Lett. 33 (2004) 750.
[26] JCPDS Card No. 21-1272.
[27] JCPDS Card No. 06-0416.
[28] N.C. Saha, H.G. Tompkins, J. Appl. Phys. 72 (1992) 3072.
[29] Y. Fujita, I. Mori, T. Matsuo, Anal. Chem. 14 (1998) 1157.
[30] M.H. Van de Velde, S. Harkema, P.J. Gellings, Inorg. Chim. Acta 11 (1974) 243.
[31] Y.V. Kolen'ko, V.D. Maximov, A.V. Garshev, P.E. Meskin, N.N. Oleynikov, B.R. Churagulov, Chem. Phys. Lett. 388 (2004) 411.
[32] J.P. Fackler Jr, F.J. Kristine, A.M. Mazany, T.J. Moyer, R.E. Shepherd, Inorg. Chem. 24 (1985) 1857.
[33] M. Miyauchi, A. Nakajima, T. Watanabe, K. Hashimoto, Chem. Mater. 14 (2002) 2812.
[34] B. O'regan, M. Graetzel, Nature 353 (1991) 737.
[35] M. Dürr, A. Shmid, H. Obermaier, S. Rosselli, A. Yasuda, G. Nelles, Nat. Mater. 4 (2005) 607.
[36] L. Matt, L. Greene, J. Johnson, R. Saykally, P. Yang, Nat. Mater. 4 (2005) 455.
[37] L. Miao, P. Jin, K. Kaneko, A. Terai, N. Nabatova-Gabain, S. Tanemura, Appl. Surf. Sci. 212–213 (2003) 255.
[38] B. Xin, Z. Ren, P. Wang, J. Liu, L. Jing, H. Fu, Appl. Surf. Sci. 253 (2007) 4390.

3. ナノ界面・粒子

表面張力を利用した水面移動ロボットの研究*

鈴木 健司[*1], 小池 裕之[*2], 髙信 英明, 三浦 宏文

Study on Water Strider Robot Utilizing Surface Tension Forces

Kenji SUZUKI[*3], Hiroyuki KOIKE,
Hideaki TAKANOBU and Hirofumi MIURA

[*3] Kogakuin University Dept. of Mechanical Systems Engineering
Nakano-machi 2665-1, Hachioji-shi, Tokyo, 192-0015 Japan

This paper describes a bio-mimetic water strider robot with microfabricated hydrophobic legs. Various kinds of supporting legs with hydrophobic microstructures on their surfaces were developed using MEMS (Microelectromechanical Systems) techniques. The lift and pull-off forces of these supporting legs were analyzed theoretically and then measured. The experimental results were in good agreement with the calculations. Water strider robot with twelve micro-fabricated legs driven by a vibration motor successfully moved on a water surface and also made left/right turns by exploiting differences in the resonant frequencies of the legs.

Key Words : MEMS, Moving Robot, Bio-Mimetics, Surface Tension Force, Resonance

1. 緒　　言

近年，半導体加工技術をマイクロ機構の製作に応用したMEMS（Micro Electro Mechanical Systems）技術が幅広い分野で利用されるようになった．マイクロ機構では体積に対する表面積の割合が増加するため，従来の機械では無視できるような静電気力，表面張力，ファンデルワールス力など表面間に働く力の影響が大きくなる．これらの力は機械要素の吸着，摩擦，摩耗の要因となり，運動の妨げになる場合が多い．このため，マイクロ機構の設計においては，これらの力の低減が重要な課題となる．しかし，一方でこれらの力をうまく利用すればマイクロスケールに特有な機能が実現できる可能性がある．自然界のマイクロ機械である昆虫の運動においても，アリの壁面歩行，アメンボの水面移動など，表面間に働く力を巧みに利用し，小さいサイズを活かした行動を行っていることが知られている．昆虫の優れた機能を工学的に解明することにより，マイクロ機構の新たな設計指針が得られる可能性がある．

以上のような背景から，本研究では，アメンボを規範とし，表面張力を利用して水面に浮上し自立的に移動する小型ロボットの開発を行った．表面張力で水面に浮くためには，支持脚の撥水性を高める必要があり，表面に微細な凹凸を施すことが有効である．このため本研究では，支持脚の表面にMEMS技術を利用して微細な構造を加工することにより撥水性を高めた．また，ロボットを小型化，自立化する上での重要な課題は，エネルギー源と，それを有効な仕事に変換するアクチュエータ，動力伝達機構の小型化である．本研究では，この問題の解決方法の一つとして，携帯電話等に利用される振動モータを用い，脚の共振を利用した駆動方法を提案した．

表面張力を利用した水面移動ロボットは，浅瀬や狭所での移動が可能であり，無線による制御，通信機能を搭載することにより，水質などの環境情報の取得や，エンタテインメントなどへの応用が期待できる．

2. アメンボの水面移動

アメンボの脚は図1に示すように多数の細かい毛に覆われており，脚表面からはロウのように水をはじく物質を分泌している(1)．表面の毛によって表面積が増加し，撥水性が高められるとともに，毛の間に空気層ができることで，より水に浮きやすくなっている．このため，支持脚が水面を破ることなく表面張力で水面上に立ち，移動することができる．

アメンボの水面移動を模倣したロボットの研究は従来にもいくつか行われている．中村ら(2)は，浮力を利用した水面移動ロボットを開発している．Hu ら(3)

*原稿受付　2008年7月28日
*1正員，工学院大学　工学部機械システム工学科
（〒192-0015　東京都八王子市中野町2665-1）
*2学生員，工学院大学大学院工学研究科
E-mail:　ksuzuki@cc.kogakuin.ac.jp

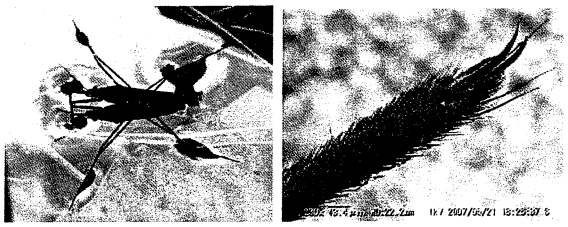

Fig.1 Water strider

は，アメンボの水面移動における運動量の伝達メカニズムを解明し，表面張力で水面に浮き弾性体に蓄えられたエネルギーで推進するRobostriderと呼ばれるロボットを開発している．Songらは，表面張力による脚の支持力を数値計算により求め[4]，表面張力で浮く1 gのロボットを開発している[5]．このロボットは圧電アクチュエータにより脚を振動させて推進するが，バッテリーは搭載していない．また，DCモータ2個とバッテリーを搭載し，推進用の脚を回転させて前進とその場回転を行う自立型ロボットも開発している[6]．また，"fisher spider"の水面移動[7]や，バシリスクの水面走行[8]のメカニズムも研究されている．

本研究では，水面上の支持脚に働く支持力と，脚を水から引き上げる際の引き離し力の理論式を解析的に導き，理論と実験により表面張力による浮上メカニズムの解明を行った．またMEMS技術を用いて円筒面上にマイクロ構造を加工した撥水性の支持脚を開発した．さらに，振動モータと脚の共振を利用した新しいロボットの駆動法を提案し，表面張力で水面に浮き，自立的に並進・旋回するロボットを実現した．

3. 水面上の支持脚に働く力

本章では，水面に浮かぶ撥水性の支持脚が水から受ける力を，2次元のモデルを用いて解析的に導く．従来の文献[4]-[6]では，本論文と同一のモデルを用いて支持力を数値的に計算していたが，解析式を導くことにより，支持脚の耐荷重性の設計が簡便に行えるようになる．また，従来の文献では考慮されていない，脚を水から引き上げる際の力（引き離し力）にも着目し，支持脚の重要な設計パラメータである直径，接触角と，支持力，引き離し力の関係を明らかにする．

3・1 支持力　図2に水面上での支持脚の2次元モデルを示す．脚を無限に長い一様な円柱と仮定し，半径をr，表面の水の接触角をθ_cとする．支持脚に作用する単位長さあたりの支持力Fは，水の表面張力による支持力F_Sと浮力F_Bの和になる．

$$F = F_S + F_B \tag{1}$$

浮力F_bは，円柱に接する水から受ける静水圧pの垂直成分の積分値であり，円柱とその上部（図2のS_1部分）の排除された水の重量に等しい．

$$F_b = \int_0^{\phi_0} p\cos\phi \cdot r d\phi = \rho g S_1$$
$$= \rho g(-2z_0 r\sin\phi_0 - r^2\sin\phi_0\cos\phi_0 + r^2\phi_0) \tag{2}$$

また，表面張力による支持力F_Sは，固体・液体・気体の接触線に働く水の表面張力γの垂直成分となる．

$$F_S = 2\gamma\sin\theta_0 \tag{3}$$

接触角θ_cと，図2に示す中心角ϕ_0，水面の傾き角θ_0の間には次の関係がある．

$$\phi_0 = \pi + \theta_0 - \theta_c \tag{4}$$

ここで，添え字0は，気，液，固の3相の接触線上での値であることを示す．水面上の任意の点(x,z)における曲率半径をRとすると，水面の圧力pは，水面の高さz，曲率$1/R$にそれぞれ比例する．

$$p = -\rho g z = \frac{\gamma}{R} \tag{5}$$

水面形状をxの関数として$z = z(x)$と表せば

$$-\rho g z = -\frac{\gamma z''}{(1+z'^2)^{3/2}} \tag{6}$$

$x = x_0$から∞まで積分し，$z' = \tan\theta$を用いると

$$\rho g S_2 = -\gamma\left[\frac{z'}{\sqrt{1+z'^2}}\right]_{x_0}^{\infty} = -\gamma\left[\sin\theta\right]_{x_0}^{\infty} = \gamma\sin\theta_0$$
$$\therefore F_S = 2\gamma\sin\theta_0 = 2\rho g S_2 \tag{7}$$

すなわち，F_sは水面のくぼみ（S_2部分）によって排除された水の重量に等しい．式(2)，式(7)を合わせると，浮力と表面張力を合計した全支持力Fは，脚により排除された水$(S_1 + 2S_2)$の重量に等しいことがわかる[9]．

一方，水面の曲線をzの関数$x = f(z)$で表せば，水面の曲率は式(8)で表される

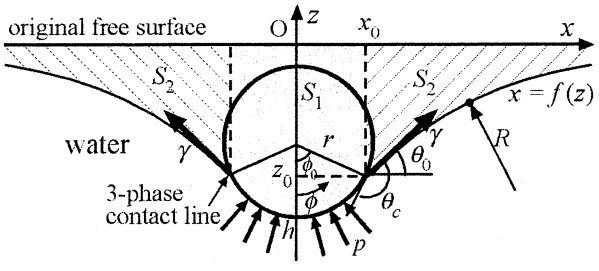

Fig. 2 Two-dimensional model of a supporting leg

$$\frac{\rho g z}{\gamma} = \mathrm{Sign}(z)\frac{f''(z)}{\left(1+f'(z)^2\right)^{3/2}} \tag{8}$$

$z=0$, $z=z_0$における境界条件は

$$f(0)=\infty, \qquad f(z_0)=x_0 \tag{9}$$

式 (8) をzで積分し，境界条件 (9) を用いると，

$$\frac{\rho g z^2}{2\gamma} = \mathrm{Sign}(z)\frac{f'(z)}{\sqrt{1+f'(z)^2}}+1 \tag{10}$$

さらに $f'(z)=\cot\theta$ の関係を用い，毛管長 κ^{-1}を

$$\kappa^{-1} = \sqrt{\frac{\gamma}{\rho g}} \tag{11}$$

と定義すると[10]，深さ z と水面の傾き角 θの関係が求められる．

$$z = \pm\kappa^{-1}\sqrt{2(1-\cos\theta)} \tag{12}$$

3 相の接触線のz 座標は式 (13) で与えられ，式 (1) ～式 (4) と組み合わせれば，脚の深さと支持力の関係が θ_0 をパラメータとして解析的に表される．

$$z_0 = \pm\kappa^{-1}\sqrt{2(1-\cos\theta_0)} \tag{13}$$

また，式 (10) を $f'(z)$ について解くと

$$f'(z) = \frac{2\kappa^{-2}-z^2}{-z\sqrt{4\kappa^{-2}-z^2}} \tag{14}$$

式 (14) を z で積分すると，水面の曲線は式 (15) のように解析的に表すことができる[10]．

$$x = f(z) = \kappa^{-1}\cosh^{-1}\left(\frac{2\kappa^{-1}}{|z|}\right)-\sqrt{4\kappa^{-2}-z^2}+C \tag{15}$$

積分定数 C は境界条件 (9) によって決定できる．式 (15) で与えられる水面形状を図 3 に示す．荷重を支持するときの水面のくぼみと，脚を引き上げるときの水面の盛り上がりは対称形となる．

脚に荷重を加えて沈めていくと，図 4 (a) のように水面の傾き角 θ_0 が $\pi/2$ のときに表面張力による支持力 F_s は最大値 2γをとる．このとき，3 相の接触線の深さは$\sqrt{2}\kappa^{-1}$ になる．25℃の水では，

$$(F_s)_{\max} = 2\gamma = 144\ \mathrm{mN/m} = 14.7\ \mathrm{gf/m} \tag{16}$$

$$z_0 = -\sqrt{2}\kappa^{-1} = -3.84\ \mathrm{mm} \tag{17}$$

となる．表面が撥水性（$\theta_c > \pi/2$）であれば接触角に関係なく$\theta_0 = \pi/2$ となり得るので,表面張力 F_s の最大値は接触角によらず 2γ である．これに対し，浮力は支持脚の直径により変化し，脚の直径が毛管長 κ^{-1} =2.71 mm より小さいとき，浮力に対して表面張力が支配的になると考えることができる．

3 相の接触線の深さが$\sqrt{2}\kappa^{-1}$ より深くなると，水面の傾き角 θ_0は $\pi/2$ より大きくなり，水面はオーバーハング形状となる．表面張力による支持力 F_s は深さの増加とともに減少する．図 4 (b) は表面が破れる直前の水面形状を示しており，$\theta_0 = \pi$ に達する前に支持脚が水没する．

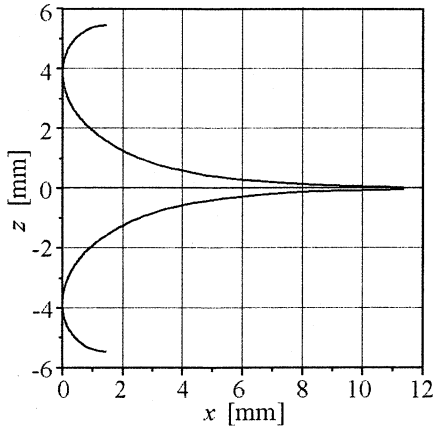

Fig. 3 Water surface profile

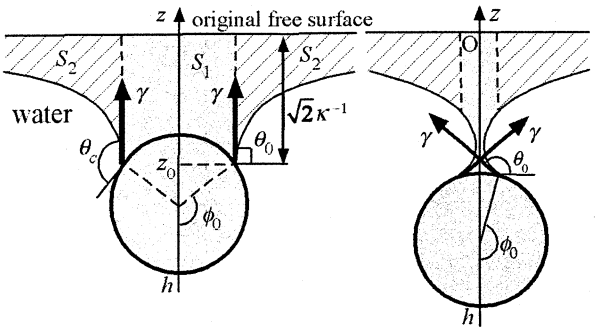

(a) Maximum surface tension (b) Maximum depth

Fig. 4 Lift force

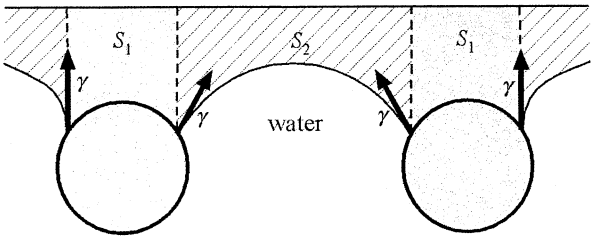

Fig. 5 Interference of two supporting legs

また，図3 より，水面にくぼみができる範囲は支持脚の左右 10 mm 程度であるため，2 本の支持脚が約 20 mm 以下に接近すると，図 5 のように水面の曲線が干渉する．2 本の脚の内側に働く表面張力は外側の表面張力より傾きが小さくなるため，垂直方向の支持力は減少し，2 本の脚の間に引力が働く．

3・2 引き離し力 支持脚を水面から引き上げる時，図 6 (a) に示すように水面は脚に引っ張られて上昇する．このとき式 (2)，式 (3) の符号は負になり，下向きの表面張力，浮力が働く．脚を引き上げるために必要な力を本論文では「引き離し力」と定義する．支持脚が完全に水面から離れるときの水面形状を図 6 (b) に示す．このとき，浮力成分は 0 になり，引き離し力の最大値は次のようになる．

$$F = 2\gamma \sin\theta_c \qquad (18)$$

式 (18) より，$\theta_c > \pi/2$ ならば接触角が大きいほど引き離し力が小さくなることがわかる．したがって，アメンボの支持脚の高い撥水性は，支持力を増加させる効果よりも引き離し力を減少させる効果が大きいと考えられる．

3・3 解析結果 図7 に単位長さ当たりの脚の支持力と引き離し力の計算値を示す．横軸は元々の水面から支持脚の最下点までの高さ h であり，縦軸は支持力を正，引き離し力を負として示している．

$$h = z_0 - r(1-\cos\phi_0) \qquad (19)$$

図 7 (a) は，支持力，引き離し力に対する脚の接触角の影響を示している．支持力は接触角にはほとんど依存しないことがわかる．脚を沈めていくと，支持力が最大値に達した後，わずかに支持力が減少して水没する．一方，脚を水面から引き上げる際には，接触角が大きいほど引き離し力は小さくなり，水面から早く離れるようになる．

図 7 (b) は，支持脚の直径が，全支持力 F_S+F_B と，浮力 F_B に与える影響を示している．直径の増加により支持力は増加するが，これは浮力 F_B が増加するためであり，表面張力成分は変化しない．ただし，脚の比重が 1 より大きい場合には，浮力の増分は脚の自重により相殺されるため，正味の支持力の増加にはつながらない．支持力の増加には，表面を撥水性の毛などで覆うことにより水を排除する空間を大きくして比重を下げることが有効である．

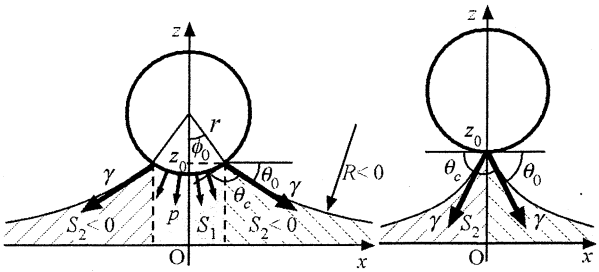

(a) (b)

Fig. 6 Pull-off force

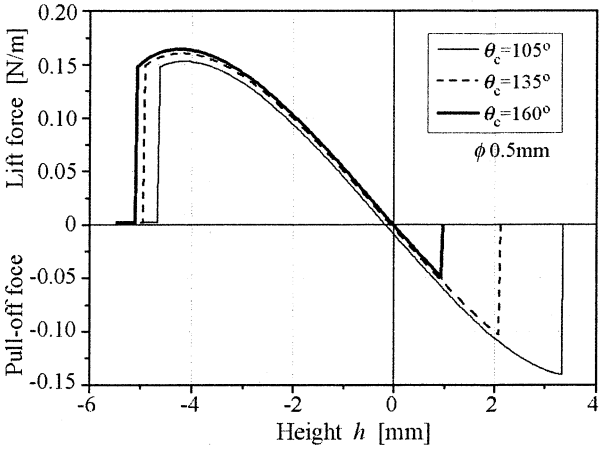

(a) Effect of contact angle

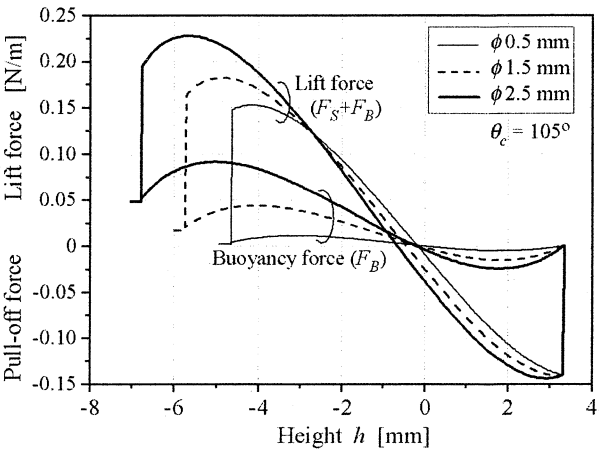

(b) Effect of diameter

Fig. 7 Lift and pull-off forces (Calculation)

4. MEMS 技術を用いた円筒面の凹凸加工

Wenzel の理論によれば，表面の微細な凹凸により平面に対して表面積が r 倍に増加した場合，接触角の余弦も r 倍に変化する．

$$\cos\theta_c' = r\cos\theta_c \qquad (20)$$

このため，$\theta_c > \pi/2$ の撥水面では，表面の凹凸により接触角が増加し撥水性が強められる．本研究では，半導体製造技術を利用して支持脚の表面に 3 種類の

方法で凹凸加工を施し，撥水性を強化した支持脚を製作した．

4・1 PDMS による細毛構造（図 8） シリコンウエハ上に厚膜ネガレジストである SU-8 を塗布し，フォトリソグラフィーにより図 8 (a) のような鋳型を作製する．次に，シリコーンゴムの一種である PDMS (Polydimethylsiloxane) を鋳型に流し込み，85 ℃で加熱して硬化させ，くし形の構造を製作する．この構造を型から剥離し，直径 0.5 mm の黄銅線に巻き付け，接着剤で固定する．最後にフッ素系撥水剤 FS1010（フロロテクノロジー社製）を浸漬により塗布する．この方法によりアメンボの支持脚と同様な撥水性の細毛構造が得られる．毛の長さは約 3mm である．

4・2 SU8 による円筒面上の凹凸加工（図 9）

厚膜のネガレジストである SU-8 を浸漬により直径 1.0 mm の黄銅線に約 80 μm の厚さで塗布する．次に黄銅線の表面を５角柱とみなし，図 9 に示すように回転させながら５回に分けてパターンの露光を行い，現像して SU8 の凹凸構造を製作する．最後に撥水剤

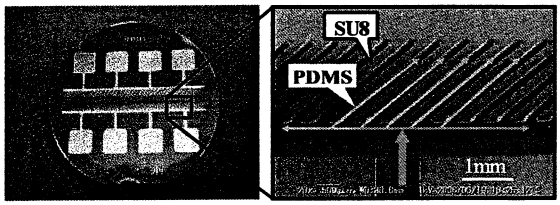

(a) SU8 mold

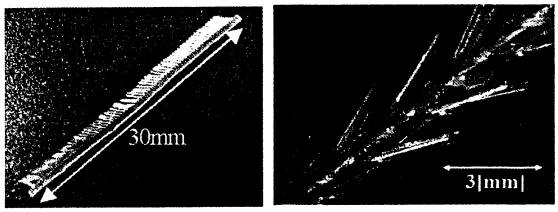

(b) Comb-shaped structure (c) Hair-like structure

Fig.8 PDMS structure

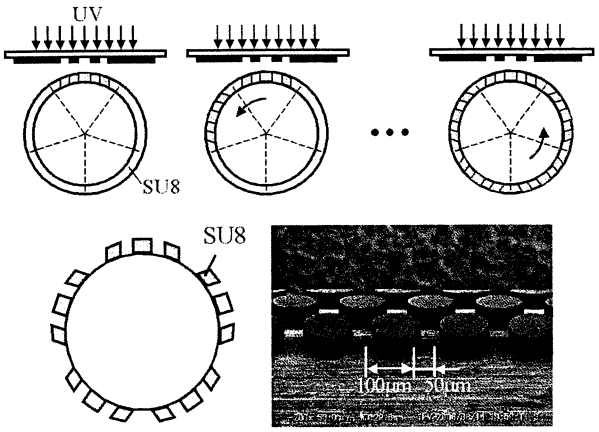

Fig. 9 SU8 structure

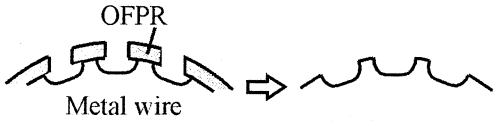

(a) Wet etching of metal wires

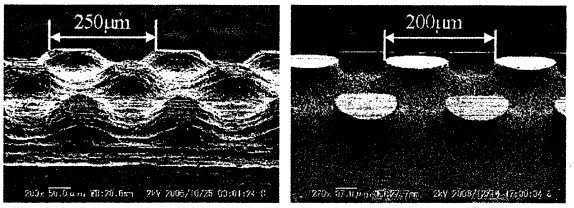

(b) Aluminum wire (c) Brass wire

Fig.10 Etched structures of metal wire

FS1010 を浸漬により塗布する．パターンの形状は直径 100 μm の円柱形で，円柱の間隔は 50 μm である．

4・3 エッチングによる凹凸加工（図 10） 紫外線ポジレジストの OFPR を金属ワイヤに浸漬によりに塗布し，図 9 と同様に円筒面を 5 回に分けてパターンの露光を行い現像する．その後，金属線の等方性ウェットエッチングを行い，凹凸面を形成し，レジストを除去する．最後に撥水剤 FS1010 を浸漬により塗布する．支持脚の材料として，直径 1.4 mm のアルミニウム線と直径 1 mm の真鍮線を用いた．マスクの形状はアルミが直径 200 μm，真鍮が直径 150 μm の円形で，パターンの間隔はいずれも 50 μm である．サイドエッチングの進行により，図 10 (b), (c) に示すような凹凸形状が得られた．真鍮線の方が形状の崩れが少なく，円形の輪郭がはっきり現われている．

5. 支持力と引き離し力の測定

5・1 実験装置 第３章の理論解析結果を実験により検証するため，撥水性の支持脚を用いて水面上での支持力と引き離し力の測定を行った．測定装置を図 11 に示す．また，本実験で用いた支持脚の寸法と形状を図 12 に，支持脚の種類を表 1 に示す．支持脚の先端部で水面を破ることを防ぐため，先端を上方に曲げた形状とした．第４章で開発したマイクロ構造を有する４種類の支持脚のほかに，マイクロ構造を加工していない直径 0.5 mm の真鍮線に接触角の異なる３種類の撥水剤を塗布したものも使用して実験を行った．

支持脚を平行平板ばねの先端に水面と平行になるように固定し，電動の z 軸ステージを用いて水面を上下に移動させる．水面を上昇させ，支持脚と水面が接触する直前の位置を支持脚の高さのゼロ点とする．さらに水面を上昇させ，支持脚が完全に水没するまでの

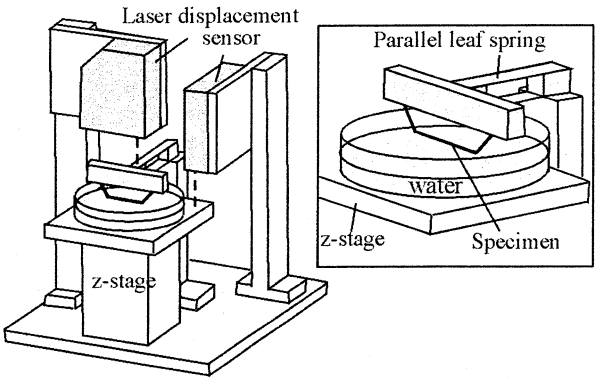

Fig. 11 Experimental setup

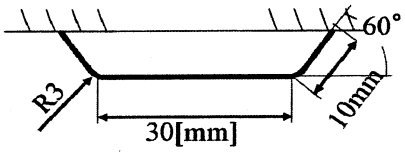

Fig. 12 Specimen's geometry

Table 1 Supporting legs

Base wire	MEMS structure	Hydrophobic coating	Outer Diameter	Contact angle
Brass ϕ0.5	—	FS6130*	0.5mm	105°
Brass ϕ0.5	—	FS1010*	0.5mm	118°
Brass ϕ0.5	—	HIREC1450**	0.62mm	138°
Brass ϕ0.5	PDMS	FS1010*	2.5mm	117°
Brass ϕ1.0	SU-8	FS1010*	1.1mm	128°
Aluminum ϕ1.4	etching	FS1010*	1.4mm	123°
Brass ϕ1.0	etching	FS1010*	1.0mm	123°

* Fluoro Technology

**NTT Advanced Technology Corporation

支持力と，脚の水面からの高さの測定を行った．支持力は板ばねの変位をレーザー変位計で測定することにより求め，脚の高さは板ばねの変位とステージの変位をそれぞれレーザー変位計で測定し，差をとることにより求めた．引き離し力は，支持脚が完全に水没した状態から水面を z ステージで下降させ，支持脚が水面から離れるまでのばねの変位から求めた．

5・2 実験結果 図 13 は直径 0.5 mm の真鍮線に 3 種類の撥水剤を塗布した支持脚の実験結果 (a) と計算結果 (b) を示している．横軸は水面から脚の最下点までの高さ h ，縦軸は脚が水から受ける力を示し，支持力を正，引き離し力を負としている．脚を水中に沈めていく際には，水面のくぼみが深くなるにつれて支持力が増加し，支持力が最大値に達した後にわずかに減少し，脚が水没する．水没すると表面張力による支持力 (F_S) は働かなくなり，浮力成分のみになる．

次にこの状態から脚を引き上げていくと，しばらく水没したままの状態が続き，脚が水面に近づいたときに急に水面のくぼみが生じ，脚が水面上に現れて表面張力による支持力が発生する．このため実験結果には図 13 (a) のようなヒステリシス特性が現れる．しかし，計算では水没後に脚を引き上げる過程は考慮されておらず，水没前の支持力のみが示されている．支持力の測定値は，脚表面の接触角にはほとんど依存せず，撥水剤が厚いために直径の大きい HIREC1450 の支持力がわずかに大きくなった．支持力の測定値は，理論値と定量的によく一致している．また，引き離し力の測定値は，接触角が大きいものほど小さく，この傾向は理論と一致した．しかし，実験値の方が理論値よりも小さい値となった．この原因については後述する．

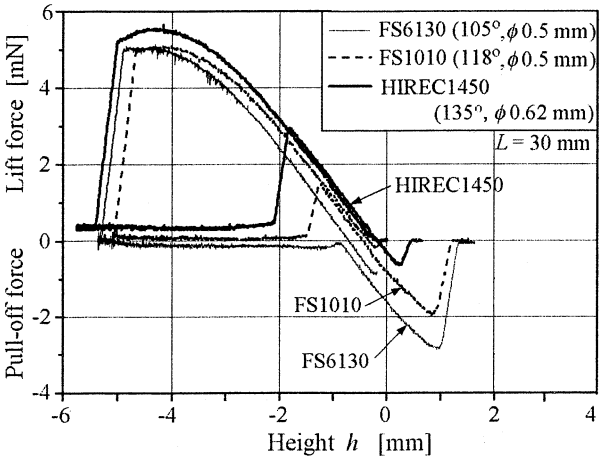

(a) Experimental results

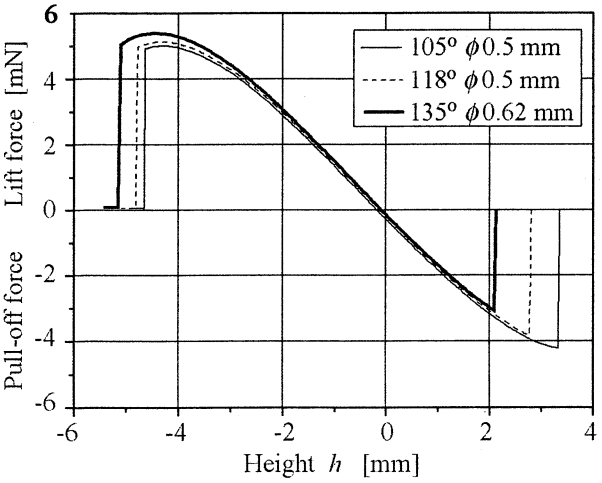

(b) Calculations

Fig. 13 Lift and pull-off forces of hydrophobic legs

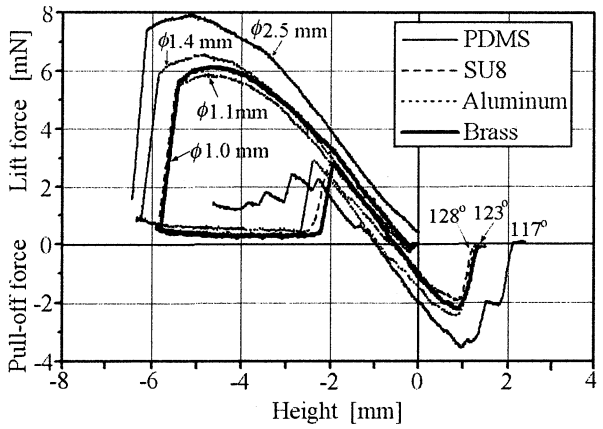

(a) Experimental Results

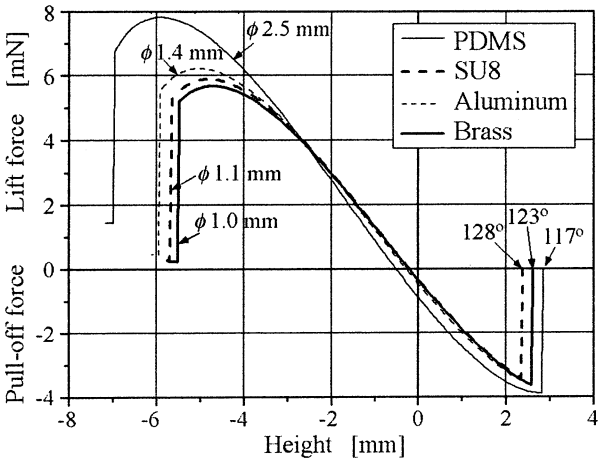

(b) Calculations

Fig. 14 Lift and pull-off forces of microstructured legs

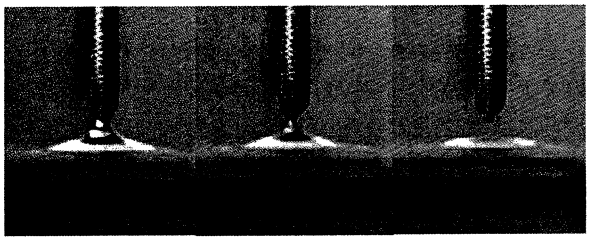

Fig. 15 Separation of the leg and water

図14 は，第４章で開発した４種類のマイクロ構造を有する支持脚の支持力と引き離し力を，実験値(a)と理論値(b) で比較したものである．支持力は，直径が大きいものほど大きくなっており，実験と理論は定量的によく一致している．PDMS の支持脚は，表1 に示すように直径 0.5 mm の真鍮線に細毛構造を加工している．撥水性の細毛の間には水が入り込まず，空気の層ができるため，みかけの直径が 2.5 mm となっており，支持力が大幅に増加している．

引き離し力は，接触角が大きいほど小さくなる傾向が見られたが，実験値は理論値より小さくなった．４種類のマイクロ構造を持つ支持脚は，いずれも接触角118° の撥水剤 FS1010を塗布しているが，PDMS 以外の３種類は，表面の微細構造の効果で接触角が増加しており，引き離し力もPDMSの支持脚に比べて小さくなった．PDMS の細毛構造は，構造のサイズが他のものに比べて大きいため，接触角を高める効果が得られなかったと考えられる．

引き離し力の実験値が理論値よりも小さくなる理由を調べるため，水面から脚が離れる瞬間を高速度カメラで観察した．水が脚から離れる際には，支持脚の端から急速に水が離れていき，最終的には図15に示すように脚の一端で円錐状のメニスカスができることが観察された．また，水が離れていく際には動的な接触角が現れ，水が離れる瞬間にはメニスカスの上部が切れて脚表面に小さな水滴が残るなど，理論では考慮していない現象が見られた．このため，引き離し力の定量的な予測には，３次元のモデルを用い，動的な要因を考慮する必要があると考えられる．しかし，２次元モデルで定性的に予測される通り，脚の接触角が大きいほど引き離し力が減少することが実験により確認され，支持脚の撥水性を高めることの有効性が示された．

以上の結果より，脚の支持力については理論値と実験値が定量的に一致し，第３章の解析式が支持脚の耐荷重性の設計に利用可能であることが確認された．また，第４章で示した微細加工技術により脚表面の撥水性を高め，接触角を増加させることは，引き離し力を減少させるために有効であり，撥水性の細毛構造を加工して脚の周囲の水を排除し見かけの直径を増加させることは，支持力の増加につながることが示された．

6. 水面移動ロボット

第４章で開発した表面にマイクロ構造を持つ撥水性の支持脚を用いて，表面張力で水面を移動する自立型ロボットの製作を行った．駆動方法として，偏心した質量を持つ振動モータを用い，支持脚を共振させることによって推進力を得ることとした．振動モータは，圧電素子などに比べ低電圧での駆動が可能であり，減速機なども不要であるため，自立化，軽量化に適している．3.7 V のリチウムポリマー電池を搭載し，PIC (Peripheral Interface Controller 12F629) を用いて回転数を PWM (Pulse Width Modulation) 制御することにより振動数を制御した．水面移動ロボットの写真を図 16 に示す．

ロボットの支持脚の耐荷重の設計には第３章の理論および第５章の実験結果を利用した．支持脚には，振動によって微細構造の剥離や損傷が生じないよう

に，真鍮線の表面にウェットエッチングで凹凸を加工したものを用いた（図 16 挿入写真参照）．表 1 より，脚表面の接触角は 123° になると予測される．また，この構造では周囲の空気層による支持力の増加は期待できないため，直径を 0.5 mm として自重による質量増加を抑えた．この場合の最大支持力は，図 7 (a) より 1 m あたり 160 mN (16.3 gf) と予測される．また，脚の全長を 1 m としたときのロボットの質量は，図 17 に示すように 7.85 g となり，安全率 2 でロボットの重量を支持することができる．

以上の考察より，ロボットの支持脚の全長を 1m と決定し，12 本の脚を放射上に配置し，支持脚 1 本あたりの長さを 70～90 mm とした．また，支持脚の端部は，水面を破ることを防ぐため図 12 と同様に両端を上方に折り曲げた形状とし，その一端をロボット本体の底面に固定した．振動モータはロボット本体の上面に固定されており，モータの振動はロボット本体を介して脚に伝達される．振動モータを回転させると，図 18 に示すように，脚は偏心質量の回転に同期して円に近い軌道を描いて共振する．振動モータの回転軸は，図 19 のようにロボットの進行方向に対して垂直に配置

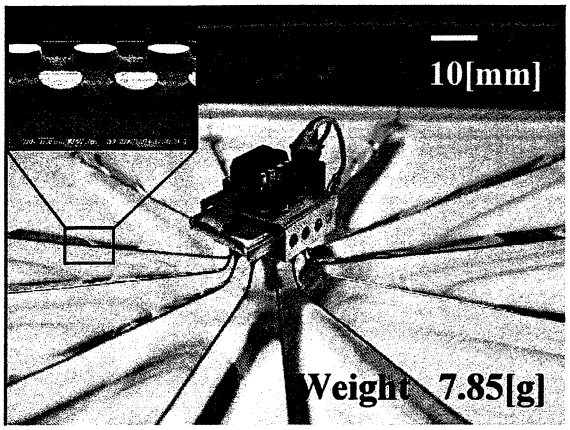

Fig. 16 Water strider robot with a vibration motor

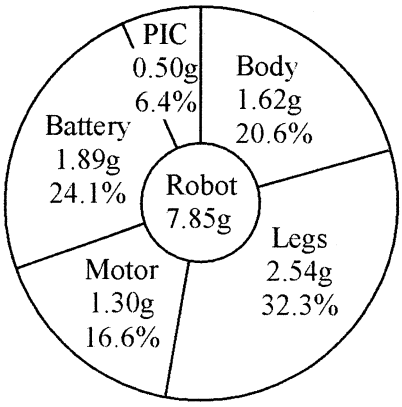

Fig. 17 Mass distribution of the water strider robot

されており，L-2～L-5, R-2～R-5 の脚が共振してモータ軸と平行な軸まわりに円運動を行い，水面を蹴ることによって推進力が得られる．L-1, L-6, R-1, R-6 の 4 本の脚はモータ軸とほぼ垂直であり，共振により発生する推進力は小さいと考えられるため荷重支持に用いた．12 本の脚は，表 2 に示すように，荷重支持（4 本），直進移動（4 本），右旋回（2 本），左旋回（2 本）の役割が与えられており，それぞれの脚の長さが異なっている．脚の長さを変えることにより固有振動数が変化するため，モータの回転数を制御するこ

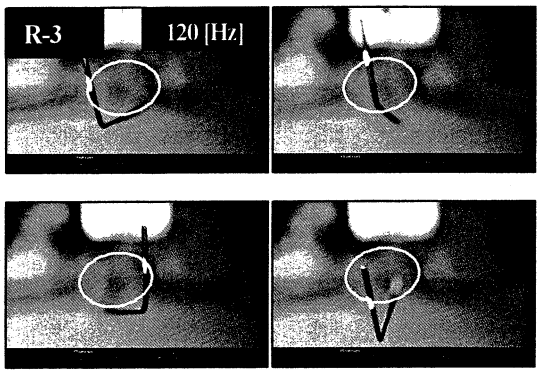

Fig. 18 Rotational vibration of the supporting leg.

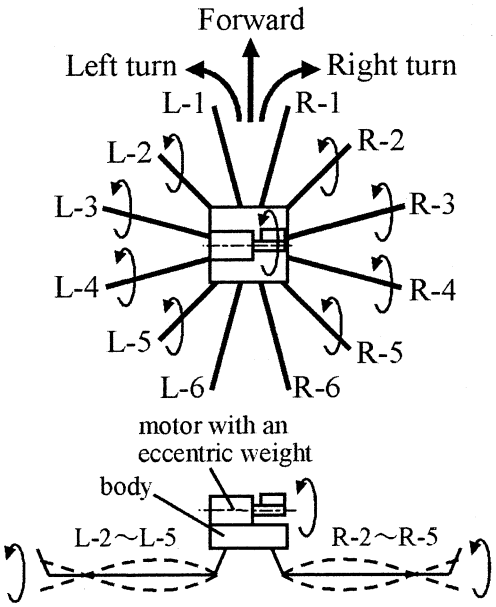

Fig. 19 Design of the supporting legs

Table 2 Lengths and resonant frequencies of the legs

Leg No	Role	Length	Resonant frequency	Duty factor
L-1,6 R-1,6	Support	85mm	—	—
L-3,4 R-3,4	Forward motion	90mm	109Hz	32%
R-2,5	Left turn	80mm	115Hz	34%
L-2,5	Right turn	70mm	132Hz	39%

とで共振する脚が変わり，一つのモータで直進，右旋回，左旋回の３種類の運動を実現することができる．3.7 V の電池を用いて PWM 制御可能な 100 Hz ～ 200 Hz の振動数では，脚は二次モードで共振する．支持脚の長さと共振周波数の関係を図 20 に示す．グラフの各点は測定値を示し，曲線は片持ち梁の固有振動数の式 (21) より求めた理論値を示す．ただし，梁の長さ L は支持脚の長さに両端部の長さ (各 10 mm) を加えたものとした．

$$f=\left(\frac{\lambda}{L}\right)^2\sqrt{\frac{EI}{\rho A}} \qquad (21)$$

ここで，E は脚の材料のヤング率，ρ は密度，$\lambda = 1.875$ (1st mode)，4.694 (2nd mode) である．脚を水面上で振動させると，脚のまわりの水が付加質量として加わり，空気中に比べて支持脚の共振周波数が減少する．

開発したロボットを用いて，屋外の池で水面移動実験を行った．その様子を図 21, 22 に示す．実験の結果，風や波などの外乱が加わっても水面を破ることなく水面上を移動し，モータの回転数を順次切り替えることにより，自立的に直進と左右の旋回移動を行うことができた．移動速度は並進移動が約 70 mm/s，旋回移動は約 50 mm/s，旋回半径は左旋回が約 700 mm，右旋回が約 800 mm となった．旋回時には，２本の脚が共振により大きく振動するが，その他の脚も振動するため，その場回転はできなかった．直進と旋回の移動速度が異なるのは，共振する脚の本数が異なるためであり，左右の旋回半径が異なるのは，旋回用の支持脚の長さが左右で異なるためと考えられる．

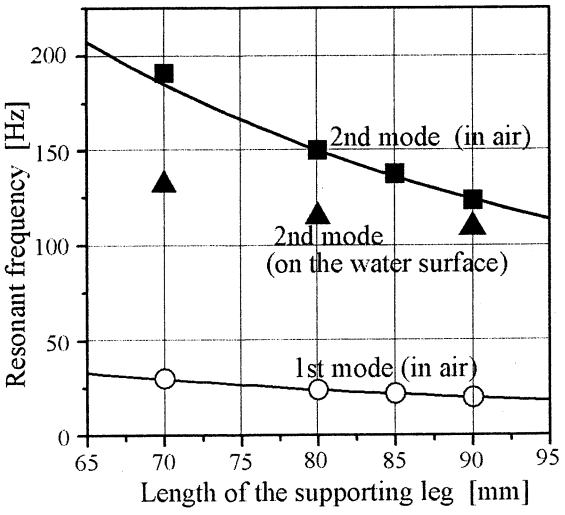

Fig. 20 Resonant frequencies of the supporting legs

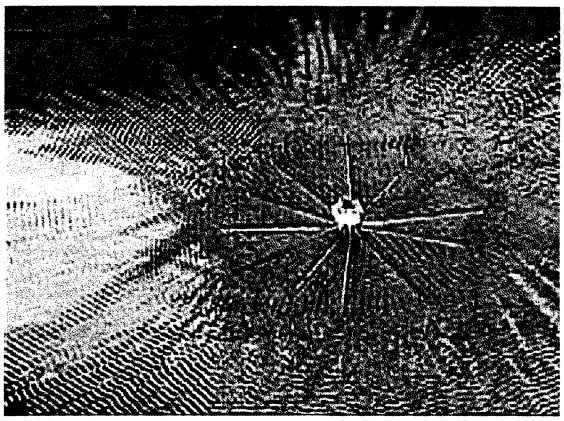

Fig. 21 Vibration of the legs on the water surface

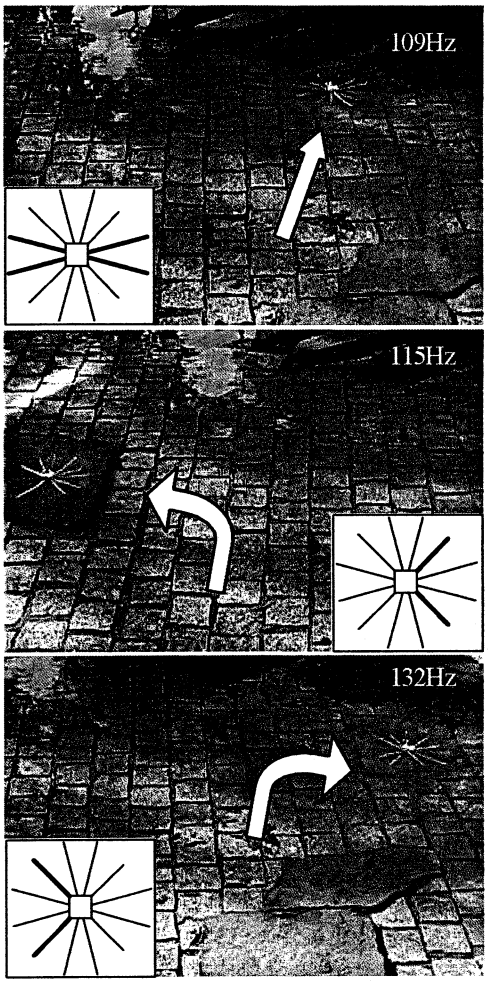

Fig. 22 Forward motion and left/right turns

7. 結　　言

1) 半導体製造技術を利用して，3 種類の方法で円筒面に微細な凹凸構造を持つ撥水性の支持脚を開発した．

2) 表面張力による水面での支持力，引き離し力の理論式を解析的に導き，支持脚の直径，接触角と支持力，引き離し力の関係を明らかにした．また，

様々な撥水性の支持脚を用いて支持力，引き離し力の測定を行った結果，支持力の理論は実験と定量的に一致し，耐荷重性の設計に利用可能であることが示された．また，支持脚の接触角が高いほど引き離し力が小さくなることが確認された．

3) MEMS技術により表面に微細構造を加工した支持脚を用いて，自立型水面移動ロボットを開発した．脚の共振を利用した駆動法を提案し，１つのモータにより並進移動と左右の旋回移動を実現した．

謝　辞

本研究は，文部科学省の私立大学学術研究高度化推進事業（ハイテクリサーチセンター整備事業）により工学院大学に整備された「マイクロ先進スマート機械，マイクロバイオシステム研究センター」の研究費、およびマイクロ加工設備を利用して行われたものである．また，本研究の一部は科学研究費補助金基盤研究 (B)（課題番号19360121）の支援を受けて行われた．

文　献

(1) Gao, X. and Jiang, L., "Water-repellent legs of water strider," *Nature*, Vol. 432 (2004), p.36.

(2) Iinuma, K., Fujii, S., and Nakamura, T., "Development of an Amphibious Robot based on a Water Strider," *Proceedings of 2007 JSME Conference on Robotics and Mechatronics* (2007-5), 1P1-C05.

(3) Hu, D. L., Xhan, B. and Bush, J. W. M., "The hydrodynamics of water strider locomotion," *Nature*, Vol.424 (2003), pp.663-666.

(4) Song, Y. S, Suhr, S. H. and Sitti, M., "Modeling of the Supporting Legs for Designing Biomimetic Water Strider Robots," *Proceedings of IEEE International Conference on Robotics and Automation* (2006-5), pp.2303-2310.

(5) Song, Y. S. and Sitti, M., "Surface-Tension- Driven Biologically Inspired Water Strider Robots: Theory and Experiments," *IEEE Transactions on Robotics*, Vol. 23, No. 3 (2007), pp.578-589.

(6) Song, Y. S. and Sitti, M., "STRIDE: A Highly Maneuverable and Non-Tethered Water Strider Robot," *Proceedings of IEEE International Conference on Robotics and Automation* (2007-4), pp.980-984

(7) Suter, R. B. and Wildman, H., "Locomotion on the Water Surface: Propulsive Mechanisms of the Fisher Spider DOLOMES TRITON," *Journal of Experimental Biology*, Vol. 200 (1997), pp. 2523-2538.

(8) J. W. Glasheen and T. A. McMahon, "A hydrodynamic model of locomotion in the Basilisk Lizard," *Nature*, Vol. 380 (1996), pp.340-342.

(9) Keller, J. B., "Surface Tension Force on a Partially Submerged Body," *Physics of Fluids*, Vol. 10 (1998), pp. 3009-3010.

(10) Gennes, P. G., Brochard-Wyart, F. and Quere, D., *Gouttes, bulles, perles et ondes (Japanese Edition)*, (2003-9), pp.44-45, Yoshioka-Shoten.

作動温度低温化を目指した固体酸化物形燃料電池の電極・電解質材料開発と界面構造の制御

Development of SOFCs Working at Lower Temperatures by Controlling Interfacial Nano-Structures

長本英俊・大友順一郎*
工学院大学工学部環境化学工学科
*東京大学大学院新領域創成科学研究科環境システム学専攻

Nagamoto Hidetoshi and Junichiro Otomo*
Department of Environmental Chemical Engineering, Kogakuin University
*Department of Environment Systems, The University of Tokyo

The development of new electrolyte and electrode materials makes it possible to advance fuel cell systems that can satisfy the requirements of higher efficiency and reliability. Lowering operation temperature is an attractive solution for constructing reliable Solid Oxide Fuel Cell (SOFC) systems, whereas it increases overpotentials resulting from ohmic loss in electrolyte as well as charge transfer reactions on electrodes. Considering the above, the enhancements of ionic conductivity and electrode reactions are of significant importance. In this report, we investigate new approaches to enhancing ionic conductivity and electrode reactions in terms of controlling the interfacial microstructures of electrolyte and electrode materials.

1. 緒言　次世代の燃料電池として期待されている固体酸化物形燃料電池（SOFC）は、高温作動に起因する構成部材の劣化が問題になっており、その信頼性の向上は極めて重要な問題である。SOFC の作動温度を低温化は、その解決方法として有効であるが、低温作動の実現には従来材料よりも高いイオン伝導率を有する電解質材料や反応過電圧の低い電極材料の開発が必要である。本研究では、電解質および電極の微構造制御に着目し、特に界面の構造制御によるイオン伝導率の向上および電極の反応過電圧の低減を目的とした。昨年度まで（平成 19 年度以前）は、特に中温域(150–300 ℃)で作動する新規固体電解質形燃料電池の開発を目的とし、電解質の微構造制御およびプロトン伝導性酸素酸塩（リン酸二水素セシウム（CsH_2PO_4）等）の評価を行ってきた[1,2]。CsH_2PO_4/SiO_2 複合体の導電率と構造相転移挙動の観測を通じて、メソ細孔を有するシリカ粒子の添加により、降温過程において CsH_2PO_4 の高伝導相（立方晶）が臨界温度より低い温度まで保持されることが明らかとなった。また、観測された現象は、メソ多孔質シリカと CsH_2PO_4 の間における界面応力によって CsH_2PO_4 の構造相転移の過冷却現象が生じたためと結論づけた[3]。

本年度（平成 20 年度）は、SOFC の作動温度の低温化のための材料開発を行った。上述の酸素酸塩に限らず、ナノスケールの界面ではイオン輸送現象に関わる特異な現象が期待される。SOFC の電解質材料や電極材料においても、界面における結晶の不規則化や酸素空孔濃度の変化によるイオン導電率への影響が予想される。以上を考慮して、本検討では SOFC の中温作動用の電解質

材料候補である Y ドープ CeO_2(YDC)の薄膜化によるイオン導電率に対する影響について検討を行った。次に、空気極材料の微構造制御による空気極反応過電圧の低減に関する検討を行った。この系では、粒界（結晶/結晶界面）特性の利用による空気極性能の向上に着目し、緻密薄膜電極の微構造を制御することによって、空気極内部の粒界部分とバルク内部分が酸素還元反応の素過程に与える影響について検証した。すなわち、現在空気極材料として検討されている $La_{1-x}Sr_xCoO_{3-\delta}$ および $La_{1-x}Sr_xMnO_{3-\delta}$ の緻密薄膜の粒径制御を行う（粒界の体積分率を変化させる）ことで空気極の高効率化の検討を行い、SOFC の更なる低温化に向けた指針を得ることを目的とした。

2. 実験方法

2.1. セリア（CeO_2）系薄膜電解質

単相膜作製に RF マグネトロンスパッタリング装置を使用した。ターゲット材料は YDC（10% Y ドープ CeO_2）粉末を用い、石英ガラスプレート上に各粉末をプレス成形した試料をターゲットとして用いた。成膜は Ar もしくは Ar:O_2= 9:1(モル比)の雰囲気で行った。RF 電力を 2.3～4.7 W/cm^2、基板とターゲットの距離を 50 mm、成膜時間を 0.25 h～5 h、Ar 圧力を 10～60 mTorr と変化させ、石英基板、シリコン基板、カーボン基板上に成膜を行った。定性分析は SEM、FE-SEM、XRD および TEM により行った。全導電率は交流インピーダンス法（2 端子法）により評価した。

2.2. 緻密薄膜空気極（$La_{1-x}Sr_xCoO_{3-\delta}$, $La_{1-x}Sr_xMnO_{3-\delta}$）

電解質として錠剤成型器でプレスして作製した $Ce_{0.9}Gd_{0.1}O_{2-\delta}$ (GDC)基板 (相対密度 93～95 %、厚さ 1.0～1.2 mm、直径 9 mm)を用いた。空気極材料としては $La_{0.9}Sr_{0.1}CoO_{3-\delta}$(LSC)粉末と $La_{0.7}Sr_{0.3}MnO_{3-\delta}$ (LSM)粉末を用いた。試料を石英シャーレ上に設置し、RF マグネトロンスパッタ装置を用いて RF 出力 100 W、Ar 圧力 35 mTorr、基板温度 400 ℃でそれぞれ 3 h 成膜し、緻密薄膜を作製した。成膜後、空気中で 600 ℃もしくは 1000 ℃の熱処理による粒径制御を行うことで、粒界の体積分率を変化させた。FE-SEM を用いて薄膜の断面及び表面構造を観察し、XRD を用いて結晶組成の評価を行った。直流法及び交流インピーダンス法を用いて 400 ℃～600 ℃の領域で三端子法により電気化学測定を行った。作用極には空気極薄膜を成膜した試料を用いた。また対極には Pt ペーストを用いた。参照極には電解質に Pt 線を巻きつけて使用した。空気極薄膜の界面導電率 σ は式(1)より算出した。

$$\sigma = \frac{1}{SR} \quad \cdots(1)$$

（σ: 界面導電率 [S cm^{-2}]、 S: 空気極面積 [cm^2]、 R: 電極抵抗 [Ω]）

3. 実験結果および考察

3.1. YDC 薄膜電解質の合成と導電率評価

3.1.1. YDC 単相膜の成膜

圧力(15～35 mTorr)、基板(シリカガラス, 結晶 Si)、基板温度の各パラメーターを変化させて成膜を試みた。XRD 測定の結果から、いずれの成膜条件においても目的物質である YDC の生成が確認された。Fig. 1 に Si 基板上に成膜した YDC 膜形態の SEM 断面写真を示す。Fig. 1(a) は基板無加熱で成膜した試料であり、Fig. 1(b) は基板加熱(600 ℃)で成膜した試料である。Fig. 1(a) の断面と比較して、Fig. 1(b) の断面はより均一で平滑な膜の形態を確認できた。また、熱処理を加えることで、(111)面方位に配向した結晶性

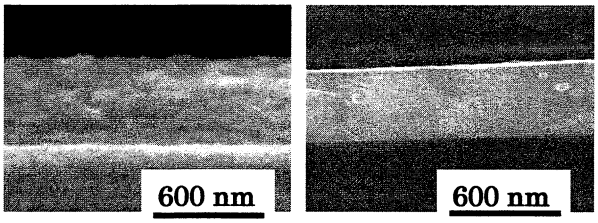

(a)基板無加熱　　(b)基板加熱(600℃)

Fig. 1 YDC 薄膜の SEM 断面写真
(Ar　35 mTorr, 出力 4.7 Wcm^{-2})

の高い薄膜の生成を確認した。したがって、YDC 単相薄膜の作製は比較的低温の処理においても容易に作製可能であることがわかった。

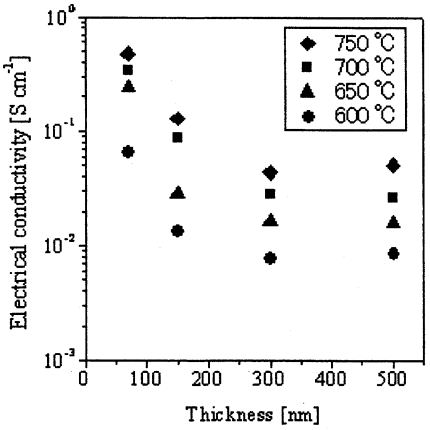

Fig. 2 YDC 薄膜における導電率の膜圧依存性

3. 1. 2. YDC のイオン導電率

基板温度 600 ℃、成膜時間 30 min、1 h、3 h で成膜した試料を用意した。膜厚はそれぞれ 70 nm、150 nm、300 nm、500 nm である。試料は 800 ℃で熱処理した後、導電率測定を行った。Fig. 2 に導電率の膜厚依存性を示す。この結果より、膜厚が薄くなるに従って導電率が上昇する現象が観測された。この傾向は 100 nm 以下の膜厚で顕著である。100 nm 以下の薄膜における導電率上昇の機構は明確ではないが、一つの可能性として、基板と YDC 薄膜の界面における YDC 結晶構造の不規則化によってもたらされた酸化物イオン伝導特性の向上による現象であることが推察される。微構造の制御によって導電率の上昇が生じることから、SOFC 低温作動の方策の一つとして有効な手段であると結果である。

3. 2. $La_{0.7}Sr_{0.3}MnO_{3-\delta}$(LSM)および $La_{0.9}Sr_{0.1}CoO_{3-\delta}$(LSC)緻密薄膜空気極の合成と導電率評価

3. 2. 1. LSM および LSC 緻密薄膜の成膜

XRD 測定結果より、GDC 基板上における LSM および LSC の合成が確認された。600℃および1000℃の熱処理を行うことにより XRD 回折パターンの半値幅が減少し、薄膜の結晶性が向上することが確認された。また、SEM 観察より、LSM および LSC の緻密薄膜が形成されていることを確認した。シェラーの式と SEM 画像から各試料の粒径を評価した結果、600℃および 1000℃の熱処理によって粒径の制御が可能であり（LSM、LSC 共に： 600℃：粒径 10 nm～20 nm の微粒子；1000℃：粒径約 500 nm)、これらの試料を用いて粒径（粒界）が空気極反応に及ぼす影響について検討した。

3. 2. 2. 電気化学測定

＜直流法＞ Fig. 3 に直流法を用いて測定した各試料の空気極分極曲線を示す。Fig. 3 より LSC 薄膜において微粒子化による界面導電率の顕著な上昇を確認し、粒界の寄与による効果である可能性が示唆された。一方、LSM 薄膜においては粒径が大きい場合に界面導電率が上昇する結果が得られた。従って、特に LSC 薄膜においては微構造の制御により粒界の特性が反応に顕著な影響を与えることが示唆された。

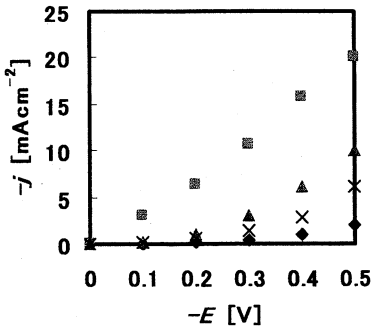

Fig. 3. 空気極分極曲線（測定温度：600℃）
■：LSC (600 ℃熱処理後)
▲：LSC (1000 ℃熱処理後)
◆：LSM (600 ℃熱処理後)
×：LSM (1000 ℃熱処理後)

＜交流インピーダンス法＞ Fig. 4 に交流インピーダンス測定から得られた Cole-Cole プロットの例を示す。Fig. 4 に示すように、3 つもしくは 2 つの半円が観測された。それぞれの半円の界面抵抗を R_H、R_M、R_L(または R_H、R_L)として、界面導電率 σ_H、σ_M、σ_L(または

σ_H、σ_L)を式(1)より算出した。時定数および電位依存性から、LSM と LSC 共に σ_L が電荷移動反応すなわち酸素還元反応に直接関与する界面導電率であると同定した。また、酸素分圧依存性の実験結果から、LSM 薄膜の場合、σ_L は酸素分圧の 0.26 次(≈1/4 次)に依存する結果が得られ、吸着酸素の電極表面拡散に由来すると考えた。一方、LSC 薄膜においての酸素分圧依存性を調べたところ、σ_L は負の依存性を示すことが確認された。Fig. 5 に粒径を変化させた場合の LSC と LSM の反応に関わる界面導電率(σ_L)の温度依存性を示す。Fig. 5 より、Fig. 3 と同様に LSC 薄膜における界面導電率の顕著な上昇が確認された。

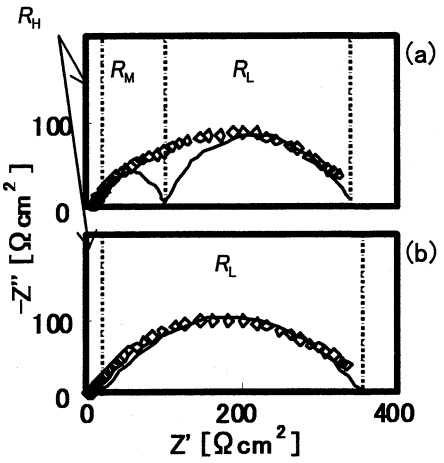

Fig. 4. Cole-Cole プロット
(a):LSM 1000 ℃熱処理後 600 ℃測定
(b):LSC 1000 ℃熱処理後 600 ℃測定

3. 2. 3. 粒界が酸素還元反応に及ぼす影響について

粒径制御が界面導電率に影響を及ぼした要因として、LSC と LSM の反応における律速過程の違いが考えられる。反応過程は、①：気相での酸素分子の拡散、②：電極表面での酸素原子の解離吸着、③：吸着酸素の電極表面拡散、もしくは③'：吸着酸素原子の電極バルク内への取り込みおよびバルク内拡散、④：空気極から電解質への酸化物イオンの移動、の 4 つの過程に分けられる。LSC 薄膜においては③'の過程の吸着酸素原子(O_{ad})が酸素空孔($V_O^{\cdot\cdot}$)に取り込まれる過程と後続のバルク内拡散が律速と考えられる。$V_O^{\cdot\cdot}$ は酸素濃度の減少に伴い増加することが予想され、$V_O^{\cdot\cdot}$ 濃度が吸着 O_{ad} の取り込み反応速度に影響を与えると考えられる。このことは、上述の LSC の σ_L が酸素分圧に対して負の依存性を示すことに矛盾しない。従って、粒界中の $V_O^{\cdot\cdot}$ 濃度がバルクのそれよりも高いことによって反応が促進されたと考えられる。一方、LSM 薄膜においては、酸素濃度依存性の結果から③の吸着酸素の表面拡散が律速であり、粒界の寄与が顕著でなかったと考えられる。

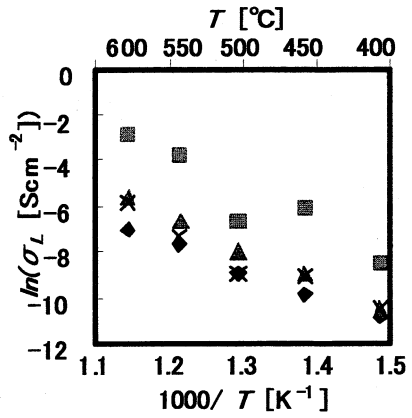

Fig. 5. 空気極分極曲線 測定温度 600℃
■：LSC (600 ℃熱処理後)
▲：LSC (1000 ℃熱処理後)
◆：LSM (600 ℃熱処理後)
×：LSM (1000 ℃熱処理後)

4. まとめ

SOFC の電解質および電極材料における微構造制御（界面構造制御）がイオン伝導および電極反応に及ぼす影響について検討し、微構造制御が SOFC の低温作動化に有効な手段であることを実験的に実証した。

引用文献

[1] J. Otomo, S. Wang, H.Takahashi and H. Nagamoto, *J. Membr Sci,* **279**(1-2), 256-265 (2006).

[2] J. Otomo, R. Kurokawa, H. Takahashi and H. Nagamoto, *Vacuum*, **81**(8), 1003-1011, (2007).

研究業績

[1] Junichiro Otomo, Takashi Ishigooka, Tomoyuki Kitano, Hiroshi Takahashi and Hidetoshi Nagamoto "Phase transition and proton transport characteristics in CsH_2PO_4/SiO_2 composites" *Electrochimica Acta* **53**(28), 8186–8195 (2008).

Electrochimica Acta 53 (2008) 8186–8195

Contents lists available at ScienceDirect

Electrochimica Acta

journal homepage: www.elsevier.com/locate/electacta

Phase transition and proton transport characteristics in CsH_2PO_4/SiO_2 composites

Junichiro Otomo[a,*], Takashi Ishigooka[b], Tomoyuki Kitano[b], Hiroshi Takahashi[b], Hidetoshi Nagamoto[b]

[a] Department of Environment Systems, Graduate School of Frontier Sciences, The University of Tokyo, 5-1-5 Kashiwanoha, Kashiwa-shi, Chiba 277-8563, Japan
[b] Department of Environmental Chemical Engineering, Faculty of Engineering, Kogakuin University, 2665-1 Nakanomachi, Hachioji-shi, Tokyo 192-0015, Japan

ARTICLE INFO

Article history:
Received 30 March 2008
Received in revised form 7 June 2008
Accepted 12 June 2008
Available online 21 June 2008

Keywords:
Cesium dihydrogen phosphate
Proton conductor
Heterogeneous composite
Phase transition
Thermal hysteresis

ABSTRACT

The stabilization of superprotonic phase in neat CsH_2PO_4 and CsH_2PO_4/SiO_2 composites as well as the anomalous phase transformation with a large hysteresis was investigated through proton conductivity, thermal analysis and Raman spectroscopy. The reversibility of the transition to the superprotonic phase and the phase transformation between monoclinic phase and cubic phase in neat CsH_2PO_4 at around $T_c = 230\,^{\circ}C$ was confirmed under humidified and sealed conditions. In CsH_2PO_4/SiO_2 composites, a large asymmetric thermal hysteresis in the conductivity appeared, i.e. significant supercooling in the superprotonic phase was induced in silica matrices. A differential thermal analysis revealed that the temperature of a reverse transition from the cubic phase (superprotonic phase) to the monoclinic phase decreased in the composites. This effect became significant with an increase in silica volume fraction. The stabilization of superprotonic phase (cubic phase) in the composites will be induced by shear elastic forces at the interface between CsH_2PO_4 and silica particles. The main origin of the anomalous asymmetric thermal hysteresis in proton conductivity is the phase stability arising from the shear elastic forces and a proton-conducting network in silica matrices.

1. Introduction

Cesium dihydrogen phosphate, CsH_2PO_4, abbreviated as CDP hereafter, is a highly proton-conducting solid electrolyte, which is classified as a hydrogen-bonded oxyacid salt crystal. CDP exhibits high proton conductivity ($>10^{-2}$ S cm^{-1}) in a superprotonic phase at a temperature above ca. 230 °C [1–5]. The superprotonic phase transition in CDP takes place at ca. 230 °C, being accompanied with a structural transformation from a monoclinic phase to a cubic phase [2–5]. Under a dry condition, however, dehydration of CDP (Eq. (1)) proceeds to form polymerization products at temperatures above 200 °C [6–9]:

$$CsH_2PO_4 \rightarrow Cs_2H_2P_2O_7 \rightarrow CsPO_3 \quad (1)$$

Since the reaction occurs in parallel with a transition to the superprotonic phase, the nature of CDP has been much discussed, from both the viewpoints of the formation of the superprotonic phase and dehydration, over the last decade [3–11]. The stabilization of the superprotonic phase in CDP without any decomposition was demonstrated under appropriate humid conditions in terms of crystallographic and electrochemical studies [3,4]. Recently, a stable fuel cell-operation using CDP as an electrolyte membrane has been demonstrated successfully in a humid atmosphere [12]. CDP has therefore attracted interest not only in fundamental aspects but also in its application to energy devices such as fuel cells [11,13]. The current status thus motivates us to further investigate specific properties in CDP. As for cesium hydrogen sulfate, $CsHSO_4$, its transition to a superprotonic phase has been extensively investigated [14–24]. The superprotonic phase transition of $CsHSO_4$ occurs with a structural transformation from a monoclinic phase to a tetragonal phase. In the superprotonic phase, it is considered that the reorientational motion of a SO_4 tetrahedron, which induces a disordering of the hydrogen bond network, facilitates proton transfer [18,19]. Similar mechanism of proton conduction is prospective in CDP. In this study, we confirmed phase transition phenomena in CDP without decomposition through the measurements of conductivity, Raman spectroscopy and thermal analysis.

On the other hand, heterogeneous doping of ionic salts with highly dispersed oxides is an effective approach to improve ionic conductivity in low and intermediate temperature regions [25–28]. Heterogeneous composites that consist of proton-conducting oxyacid salts with mesoporous silica glass particles also exhibit the enhancement of conductivity [4,29–33]. In previous work [4], we have observed the enhancement of proton conductivity in a CDP/SiO_2 composite prepared by a mechanical mixing method, but the observation of conductivity was limited in the measurement for a heating process. In this study, we employed an evaporation-to-dryness method to prepare CDP/SiO_2 composites with high dispersion of mesoporous silica grass particles [31]. Through the electrochemical measurements, we found a large asymmetric ther-

* Corresponding author. Tel.: +81 4 7136 4714; fax: +81 4 7136 4715.
E-mail address: otomo@k.u-tokyo.ac.jp (J. Otomo).

0013-4686/$ – see front matter © 2008 Elsevier Ltd. All rights reserved.
doi:10.1016/j.electacta.2008.06.018

mal hysteresis loop of conductivity in a heating–cooling cycle. New phases of ionic salts have been found in heterogeneous composite systems. In the present case of CDP/SiO_2 composites, the interfacial effect on phase stability and proton conductivity, which will be mainly induced by shear elastic forces at the interface between CDP and silica particles, is discussed. A large thermal hysteresis in a phase transition has been reported in an Ag^+ conducting composite system such as AgI/Al_2O_3 composite, which originates from an interfacial interaction [34]. To our knowledge, however, the present study is the first case demonstrating explicitly a cooperative phenomenon for proton conductivity in an oxyacid salt/insulator heterogeneous composite with the large asymmetric thermal hysteresis of phase transformation. Main concern in this study is thus the investigation of phase transition behavior in CDP/SiO_2 composites in terms of proton conductivity and structural phase transformation, based on the observation of phase transition in neat CDP. The results will provide new insight into fundamental aspects of phase transformation and the stabilization of a superprotonic phase in the oxyacid salt/insulator heterogeneous composite even below critical temperature.

2. Experimental

2.1. Sample preparations

Polycrystalline CsH_2PO_4 (CDP) was used as received (purity > 99%; Soekawa Chemical Co. Ltd., Japan). Powdered CDP sample was prepared by grinding in an agate mortar for 30 min. An XRD measurement showed all the detected peaks originated from CDP and no contaminants were observed. The powdered CDP sample was then pressed at 3 t cm^{-2} to form dense pellets (diameter: 13 mm; thickness: 1.3–1.7 mm). The resultant pellet of neat CDP was set in a glass cell, and calcined at 260 °C for 1 h. The relative density of the neat CDP pellet was over 0.94 after having calcined.

CDP/SiO_2 composite was prepared by an evaporation-to-dryness method as described below [31]. Mesoporous silica glass powder provided by Mitsubishi Chemical Corporation was used as received. The properties of the silica particle are described as follows: average particle size, 5.1 μm; specific surface area, 297 m^2 g^{-1}; average pore volume, 1.3 ml g^{-1}; and average pore size, 16 nm. First, the mesoporous silica glass particles were introduced into a CDP aqueous solution to prepare an aqueous suspension. The suspension was then stirred constantly for 60 min under a reduced pressure condition in order to remove the air in the mesopores of the silica particles and to allow the solution to easily infiltrate into the mesopores. The suspension was evaporated at 50 °C, and then dried at 90 °C for 24 h. After additional heating at 150 °C for 1 h in air to minimize the influence of adsorbed water, the resultant sample was mechanically ground for 10 min, and pressed at 3 t cm^{-2} to form pellets. Finally, the pellet of CDP/SiO_2 composite was calcined at 260 °C for 1 h in a glass cell as in the case of neat CDP. In this manner, $(1-x)$CDP/$x$$SiO_2$ composites were prepared with a variation in the volume fraction of SiO_2, x (=0–1).

2.2. Proton conductivity measurements

Silver electrodes were applied on both sides of the obtained pellets using silver paste after silver vapor deposition. The pellet samples were set in a glass tube, and then gaseous mixtures of Ar/H_2O (Ar:H_2O = 0.7:0.3; partial pressure of water vapor: 0.03 MPa) were supplied through the glass tube at atmospheric pressure. Because the dehydration of CDP (Eq. (1)) occurs at a temperature higher than 200 °C under a dry condition, the supply of water vapor is required to inhibit dehydration of CDP [4,11].

Conductivity measurements were performed by means of ac impedance spectroscopy using a Hewlett Packard 4192A impedance analyzer in the frequency range from 10 MHz to 10 Hz with an applied voltage of 50 mV or 500 mV. The conductivity as a function of temperature was measured in a cooling–heating cycle; after having maintained the samples at 250 °C, the temperature was decreased stepwise in the cooling process from 250 °C to 150 °C, and then the temperature was increased stepwise in the heating process from 150 °C to 250 °C. The samples were kept for over 30 min at each temperature so they could stabilize before the ac impedance measurement was carried out.

2.3. Characterizations

Phase transformation in neat CPD was observed by means of in situ Raman spectroscopy. The pelletized sample of neat CDP was set in a sealed glass cell. The cell was introduced into a furnace in order to observe the in situ Raman spectrum as a function of temperature that was changed stepwise from room temperature to 260 °C. After the sample was maintained for 10 min at each temperature, a spectroscopic measurement was performed to collect data in equilibrium. A continuous wave Ar^+ ion laser beam at 488 nm and 0.5 W was used as the exciting line, which was focused onto the sample through a glass window using a 2.0 cm focal length lens. The backscattered light was led inversely through the lens to a spectrometer (JASCO NRS-2000, Japan) and detected by a CCD detector. In this manner, we obtained Raman spectroscopic data on neat CDP without dehydration at temperatures above 200 °C.

Differential thermal analysis (DTA) of powdered samples of neat CDP and CDP/SiO_2 composites was performed both in the

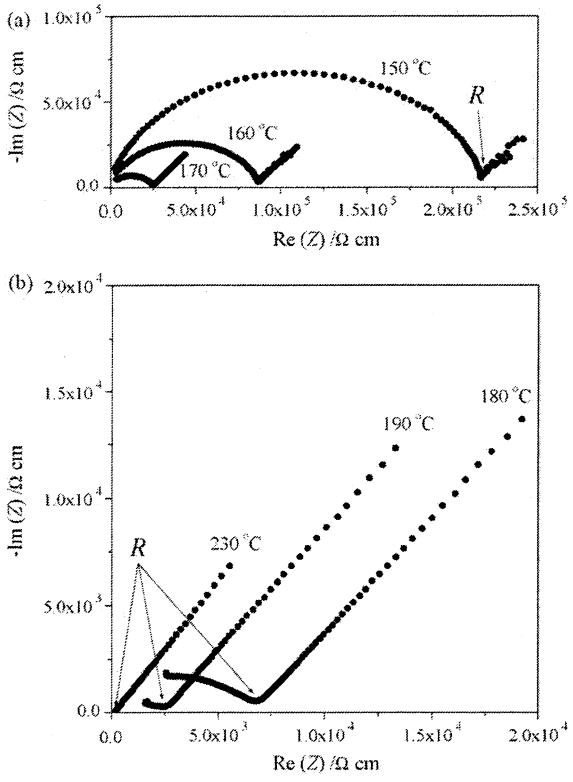

Fig. 1. Typical impedance spectra of CDP/SiO_2 composite (silica volume fraction: 0.28 vol.%).

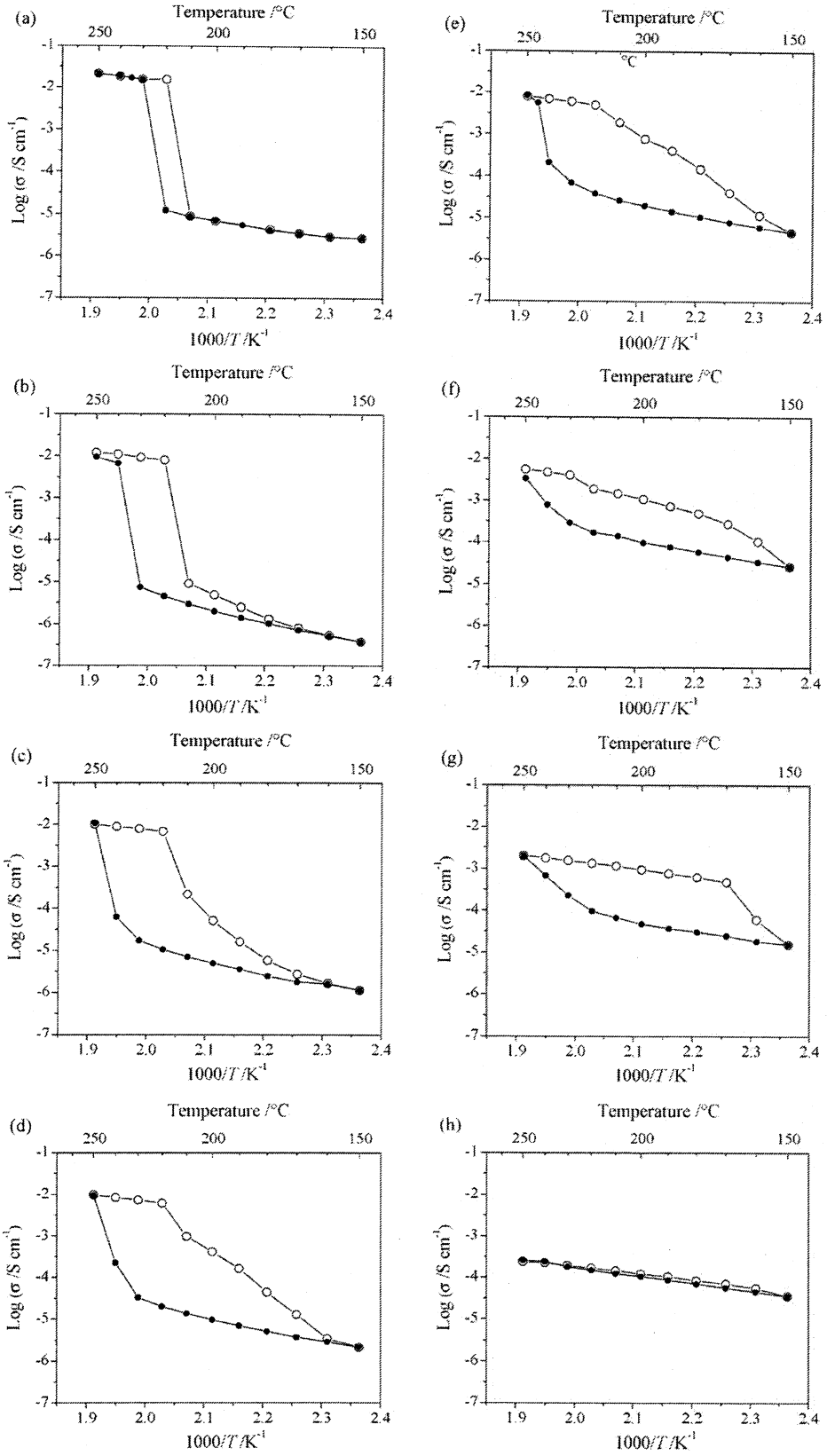

Fig. 2. Temperature dependence of conductivity in CDP/SiO_2 composites with a variety of silica volume fractions (x = 0–60 vol.%). Open circles: cooling process; filled circles: heating process. (a) x = 0 vol.% (neat CDP), (b) x = 10 vol.%, (c) x = 16 vol.%, (d) x = 22 vol.%, (e) x = 28 vol.%, (f) x = 37 vol.%, (g) x = 45 vol.% and (h) x = 60 vol.%.

heating process and cooling process between 100 °C and 270 °C (Rigaku TAS200, Japan). The heating and cooling rates were fixed at 2 K min^{-1}. Powdered samples were sealed in a steel capsule with an aluminum cover (withstand internal pressure: 5 MPa) in order to inhibit dehydration of CDP. All sealed samples were measured after having been annealed at 270 °C. In this manner, we successfully measured heat flow accompanying the phase transformation of CDP, as is stated later. In addition to the above, the X-ray diffraction (XRD) patterns of powdered samples of neat CDP and CDP/SiO_2 composites were recorded at room temperature (Rigaku Rint 2500VHF, Japan) using a Cu Kα source.

3. Results and discussion

3.1. Proton conductivity

Fig. 1 shows typical ac impedance spectra of a CDP/SiO_2 composite. In a low-temperature region, semicircles were observed (Fig. 1a). These semicircles, however, disappeared gradually with an increase in temperature and were no longer seen in a high temperature region (>230 °C), as shown in Fig. 1b, because the proton conduction process occurs too quickly to be observed with the present impedance analyzer. Instead of the semicircle, capacitance-like behavior was observed in the high temperature region, i.e. only linear impedance spectra were seen. The values of the specific resistance of proton conduction, R, were determined by extrapolating the impedance spectra to the real axis in the complex plane. Fig. 2a–h shows the temperature dependence of conductivity in neat CDP and CDP/SiO_2 composites with increasing volume fraction of SiO_2. In Fig. 2a, the conductivity in neat CDP changes abruptly at ca. 230 °C from low-conducting phase to high-conducting phase (superprotonic phase transition), and increases by over three orders of magnitude at the critical temperature, T_c. The high-conducting and low-conducting phases correspond to cubic and monoclinic phases, respectively [2–5]. The values of T_c in the heating and cooling processes differ by about 10 °C (see Fig. 2a); the neat CDP shows a small thermal hysteresis loop in the cooling–heating cycle. A remarkable result is the appearance of a large thermal hysteresis loop for conductivity in CDP/SiO_2 composites through cooling and heating processes, as described below. At 10 vol.% for the SiO_2 volume fraction, T_c in the heating process shifts to a higher temperature while T_c in the cooling process shifts to a lower temperature (Fig. 2b), i.e. superheating and supercooling in the high-conducting phase appear with an addition of SiO_2. With an increase in the SiO_2 volume fraction from 16 vol.% to 45 vol.% (Fig. 2c–g), significant supercooling in the high-conducting phase occurs; the conductivity in the cooling process retains relatively high values, and then gradually decreases with a decrease in temperature. At 45 vol.% (Fig. 2g), in particular, the high-conducting phase is retained in the cooling process from 250 °C to 170 °C. On the contrary, superheating is not significant even with an increase in the SiO_2 volume fraction from 16 vol.% to 45 vol.%; the addition of SiO_2 in the composites strongly influences the retention of the high-conducting phase. The conductivity in the CDP/SiO_2 composites (16–45 vol.% for the SiO_2 volume fractions) therefore shows large asymmetric hysteresis loops for the superprotonic phase transition in a cooling–heating cycle. With further increasing of the SiO_2 volume fraction (60 vol.%), the hysteresis loop no longer appears at temperatures between 250 °C and 150 °C (Fig. 2h), which suggests that the high-conducting phase is retained even below 150 °C. However, the conductivity at 250 °C in the CDP/SiO_2 composite (60 vol.% for the SiO_2 volume fraction) is low (2.4×10^{-4} S cm^{-1}), showing that the conductivity in the high-conducting phase is lowered by the addition of SiO_2 particles. Finally, the proton-conducting network in the composite, with a SiO_2 volume fraction higher than 80 vol.%, is broken so that the conductivity becomes around 10^{-7} S cm^{-1} to 10^{-8} S cm^{-1}.

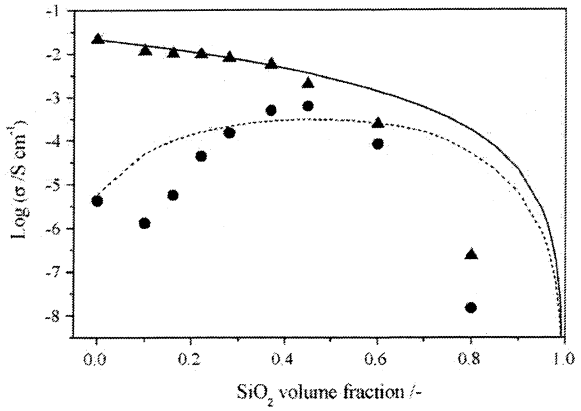

Fig. 3. Conductivity in CDP/SiO_2 composites as a function of silica volume fraction. (●) Conductivity at 180 °C (low-conducing phase), (▲) conductivity at 250 °C (high-conducing phase (superprotonic phase)). Dotted line: prediction curve at 180 °C; solid line: prediction curve at 250 °C.

Fig. 3 shows the conductivity in the CDP/SiO_2 composite versus SiO_2 volume fraction at 180 °C and 250 °C isotherms. At 180 °C, which corresponds to the temperature in the low-conducting phase in neat CDP, the highest value of conductivity is obtained at around 0.4–0.5 for the SiO_2 volume fraction in a cooling process. On the other hand, the conductivity at 250 °C, corresponding to the high-conducing phase, decreases monotonously as the SiO_2 volume fraction increases. The addition of SiO_2 powder is effective in the enhancement of proton conductivity in the low-conducting phase, while the SiO_2 powder merely plays the role of an insulator in the high-conducing phase. The behavior of conductivity as a function of SiO_2 volume fraction will be discussed in the latter part.

3.2. Structural studies: XRD and Raman spectroscopy

The XRD measurements of the powdered samples of neat CDP and CDP/SiO_2 composites were performed at room temperature. Fig. 4a shows the typical XRD patterns of CDP/SiO_2 composites (SiO_2 volume fractions of 0 vol.%, 28 vol.% and 45 vol.%). For neat CDP, a monoclinic phase (space group: $P2_1/m$) was observed (JCPDS card no. 84-0122) [35]. As is the case with neat CDP, the monoclinic phase was observed in the CDP/SiO_2 composites; all detected peaks originated from CDP and silica, and no other observable peaks were found in the composites. Miller indices for peaks observed mainly are given in Fig. 4a. In addition, the XRD main signal slightly broadens with increasing SiO_2 volume fraction, suggesting that the grain size of polycrystalline CDP partly becomes smaller or the CDP crystal structure is partly disordered in the composite. The XRD patterns of a CDP/SiO_2 composite (SiO_2 volume fraction of 60 vol.%) before a conductivity measurement is plotted with that after the conductivity measurement in Fig. 4b, which shows that the FWHM of the XRD signals becomes narrow during the conductivity measurement; the crystallization of CDP proceeds in a composite by annealing. It has been reported that the superionic phases of oxyacid salts have plasticity [24,36]. The crystallization of CDP may proceed especially in the superionic phase (> ca. 230 °C).

The Raman spectra of the internal modes of pelletized polycrystalline CDP were measured between 300 cm^{-1} and 1300 cm^{-1} in a sealed glass cell at various temperatures. All detected lines originated from CDP even at high temperatures (~260 °C), and no other lines of dehydration materials such as $Cs_2H_2P_2O_7$ were observed. Typical Raman spectra of CDP in Fig. 5a show the spectral shift

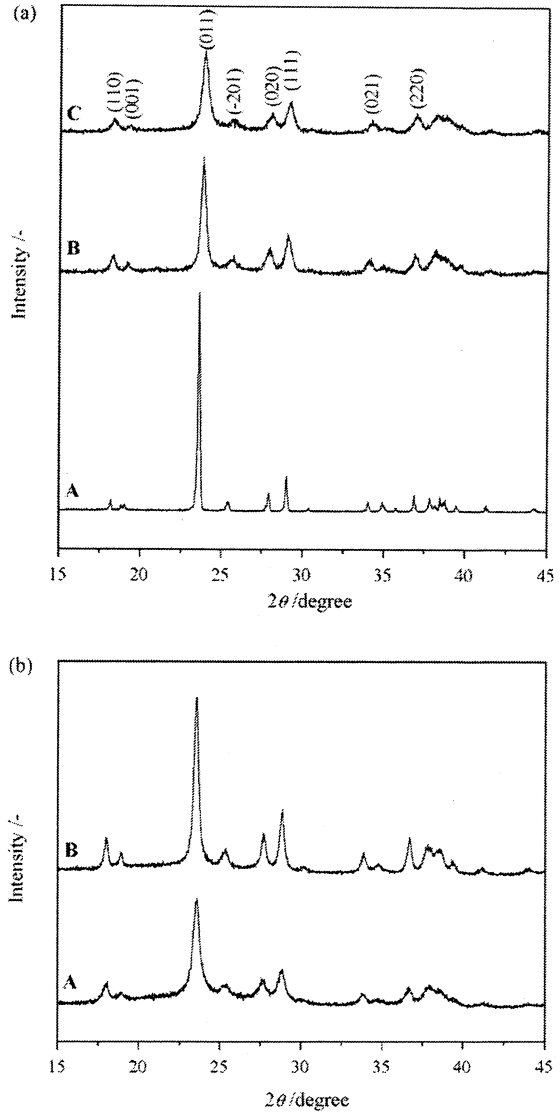

Fig. 4. XRD patterns of CDP/SiO_2 composites at room temperature (x: silica volume fraction). (a)—(A) $x = 0$ vol.% (neat CDP), (B) $x = 28$ vol.% and (C) $x = 45$ vol.%; (b) the change in the XRD pattern in CDP/SiO_2 composite with $x = 60$ vol.% from a conductivity measurement; (A) before the conductivity measurement and (B) after the conductivity measurement.

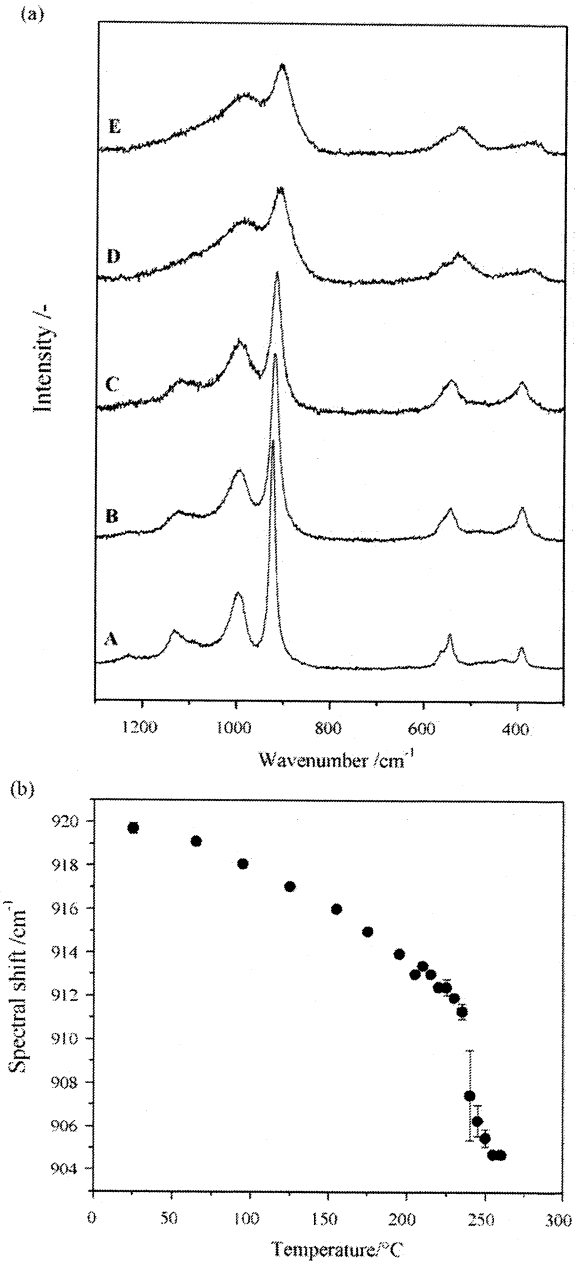

Fig. 5. (a) In situ Raman spectra for neat CDP as a function of temperature: (A) 25 °C, (B) 160 °C, (C) 220 °C, (D) 250 °C and (E) 260 °C. (b) Spectral shifts of ν(P–O) in neat CDP vs. temperature.

and broadening of linewidths for the internal modes occur as the temperature increases. Our attention was focused on the spectral shift of a symmetric stretching mode (A_g), ν(P–O), at ca. 920 cm^{-1} as a function of temperature (Fig. 5b) [37]. The red-shift of the ν(P–O) mode was observed with an increase in temperature, and besides, steep changes in the ν(P–O) mode occurred at around 230 °C. The steep change in the spectral shift corresponds to the structural phase transformation from a monoclinic phase to a cubic phase in CDP. In addition, significant line-broadening was observed at around the critical temperature (~230 °C). The line-broadening of CDP was first reported by Romain and Novak [38]. The line-broadening suggests the orientational disorder of the $H_2PO_4^-$ anion (rapid reorientational motion of $H_2PO_4^-$) will be induced [38]. The reorientational motion (libration) of anions in acid salts has been investigated in terms of the linewidths of internal modes in crystals as a function of temperature. Concerning $CsHSO_4$, Pham-Thi et al. discussed the reorientational motion of the HSO_4^- anion, based on the temperature dependence of the linewidths of the internal S–OH stretching and bending modes and the librational mode of the HSO_4^- anion [39]. This dynamic motion of the HSO_4^- anion probably accounts for fast proton diffusion in the superprotonic phase [18]. Similarly, the $H_2PO_4^-$ anion-dynamics will realize fast proton diffusion in a CDP cubic phase. Recent NMR and XRD studies have also suggested the reorientational motion of the $H_2PO_4^-$ anion in the CDP cubic phase [40,41]. An abrupt red-shift and a line-broadening at around 230 °C in Fig. 5 may be induced by weakening of hydrogen bond (P–O···HO–P) and subsequent orientational disorder of the $H_2PO_4^-$ anion in the CDP cubic phase.

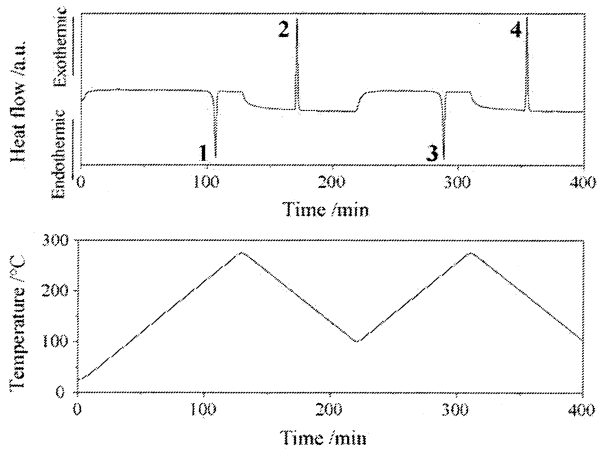

Fig. 6. DTA curve for neat CDP in heating–cooling cycles under a sealed condition. The peaks 1–4 in the figure are endothermic and exothermic heat flows that correspond to a phase transformation between a monoclinic phase (low-conducting phase) and a cubic phase (high-conducting phase).

3.3. Thermal analysis

The DTA measurements for powdered samples of neat CDP and CDP/SiO_2 composites were conducted in a heating–cooling cycle to investigate the influence of silica additive on the phase transformation of CDP in the composites. In order to suppress dehydration in CDP (Eq. (1)), the DTA measurements were performed with the powdered samples contained in sealed steel-capsules, as is the manner for in situ Raman spectroscopy. The DTA curve of neat CDP in heating–cooling cycles at the rate of 2 K min^{-1} is shown in Fig. 6. The DTA measurement in the sealed capsule demonstrates clearly a phase transformation between monoclinic phase and cubic phase in neat CDP; the endothermic heat flow associated with a phase transformation from a monoclinic phase (low-conducting phase) to a cubic phase (high-conducting phase) was observed at around 230 °C in the heating process, and then the exothermic heat flow associated with the inverse phase transformation from the cubic phase to the monoclinic phase was observed at around 200 °C in the cooling process, which repeats itself in heating–cooling cycles. A weight change during the thermal analysis was not observable because of employing the sealed steel-capsule (withstand internal pressure: 5 MPa), but no other signals in DTA resulting from dehydration of CDP were observed. Fig. 7 shows the DTA curves of the CDP/SiO_2 composite at the rate of 2 K min^{-1} in a heating–cooling cycle as a function of SiO_2 volume fraction. Each heat flow was normalized by the weight of CDP in the contents (i.e. heat flows per 1 mg of CDP in CDP/SiO_2 composites). In the CDP/SiO_2 composites, endothermic heat flows associated with a phase transformation from a monoclinic phase to a cubic phase were observed at around 230 °C in the heating process (Fig. 7a). The onset temperatures of the endothermic heat flows shifted slightly to a higher temperature with an increase in the SiO_2 volume fraction (~3 °C) but the superheating is not significant. In the cooling process, however, the addition of silica strongly influences the phase transformation in the CDP/SiO_2 composites (Fig. 7b); the onset temperatures of the exothermic heat flows were significantly lower than that for neat CDP. As shown in Fig. 7b, the exothermic heat flows can be separated approximately into three regions A, B and C, i.e. the first is peak A, appearing at the same temperature with neat CDP (ca. 200 °C), the second is peak B, which is a broad peak and appears in the temperature region between 190 °C and 160 °C, and the third is peak C, which is also a broad peak and appears in the temperature region between 160 °C and 110 °C. The area of peak A reduced abruptly even with the addition of only a small amount of silica (SiO_2 volume fraction of 10 vol.%). Instead, peak B appeared when SiO_2 powder was added (SiO_2 volume fraction ≥ 10 vol.%). The area of peak B decreased gradually with an increase in SiO_2 volume fraction, while peak C appeared and its area increased with an increase in SiO_2 volume fraction (SiO_2 volume fraction ≥ 16 vol.%). The peaks A, B and C that will correspond to a different status of CDP in a composite are designated as groups A, B and C, respectively, hereafter.

Heats of transition in the composites (total areas of the heat flows in heating process and cooling process, respectively), which were normalized with that in neat CDP, were plotted against

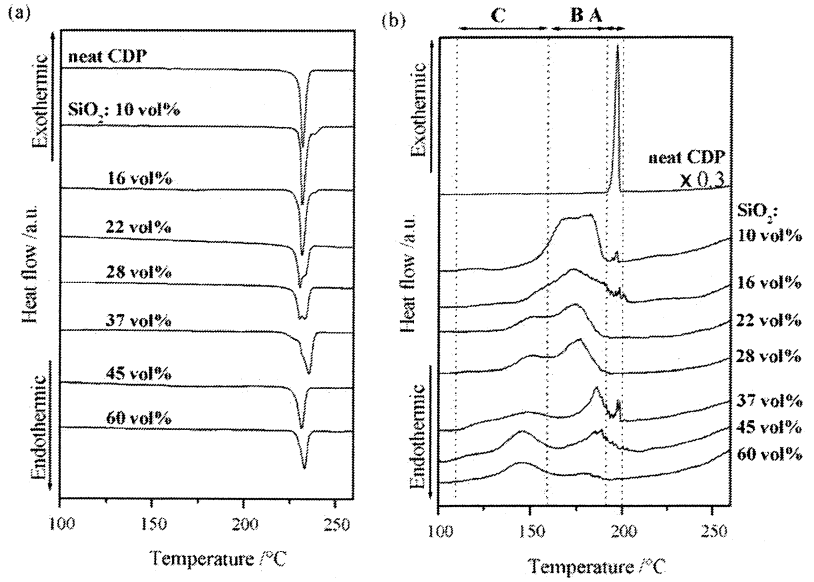

Fig. 7. DTA curves for CDP/SiO_2 composites with a variety of silica volume fractions (x = 0–60 vol.%) in a heating–cooling cycle under a sealed condition. (a) Heating process and (b) cooling process. The exothermic heat flows in figure (b) can be separated approximately into three regions, A, B and C. Note that neat CDP in figure (b) is scaled down (0.3 times).

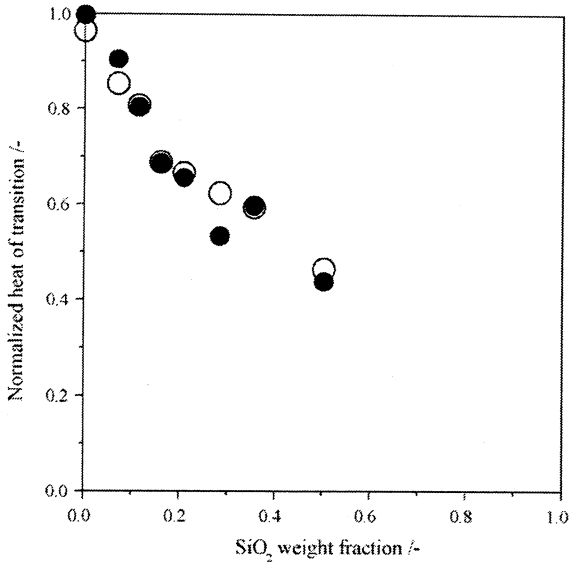

Fig. 8. Normalized heat of transition plotted against SiO_2 weight fraction. (○) Heating process and (●) cooling process.

SiO_2 weight fraction (Fig. 8), showing that the heat of transition decreased linearly with an increase in SiO_2 weight fraction. At every SiO_2 weight fraction, the heats of transition in a cooling process were mostly same as those in a heating process, which suggests that the observed transitions are reversible transitions between monoclinic phase and cubic phase in the heating–cooling cycle. In addition, we confirmed that the transition occurred reversibly during two heating–cooling cycles. CDP mole fractions of the groups A, B and C in the cooling process were evaluated as a function of SiO_2 volume fraction, assuming that the CDP mole fractions of the groups A, B and C corresponded to the heats of transition in the groups A, B and C, respectively (Fig. 9). As stated in Fig. 7, the CDP mole fraction of the group A reduces abruptly, whereas that of the group B rises with the addition of silica (SiO_2 volume fraction of 10 vol.%) instead. Then the CDP mole fraction of the group B decreases linearly and that of the group C increases linearly with an increase in SiO_2 volume fraction. The DTA measurements show clearly that a large thermal hysteresis loop for conductivity in CDP/SiO_2 composites is caused by the structural transformation of CDP affected by silica additive.

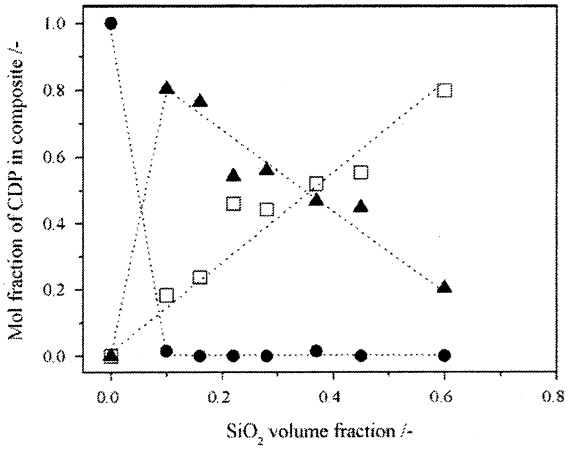

Fig. 9. CDP mole fractions of groups A, B and C in a cooling process *vs.* SiO_2 volume fraction. (●) Group A, (▲) group B and (□) group C.

3.4. Thermodynamic model for phase transformation

From the measurements of proton conductivity, Raman spectroscopy and thermal analysis (DTA) as described above, there is a clear relationship between superprotonic phase transition and monoclinic-to-cubic structural transformation in neat CDP. Additionally, it is found that a large asymmetric thermal hysteresis loop for conductivity in CDP/SiO_2 composites is associated with the thermal hysteresis of monoclinic-to-cubic structural transformation affected by silica additive in the composites, which will be induced by shear elastic forces. The present hysteretic phenomena may be typical of a martensitic transformation, which has been extensively studied in metal and alloy systems [42]. The present thermal hysteresis in the composites, i.e. the stabilization of superprotonic phase (cubic phase) in the composites, will be induced by shear elastic forces as observed in the martensitic transformation [43,44]. In this study, we attempt to explain the present asymmetric thermal hysteresis with a simple thermodynamic model. The monoclinic-to-cubic phase transformation in neat CDP is a first-order phase transition. The specific Gibbs free energy change, ΔG, for the formation of a nucleus in neat CDP can be given by

$$\Delta G = (g_m - g_c + \Delta g_e)n + \eta\sigma n^{2/3} \quad (2)$$

with the employment of a simple solid state nucleation model [45], where the specific Gibbs free energies of neat CDP in monoclinic and cubic phases are represented by g_m and g_c (the free energy per CDP structural unit); n is the number of CDP structural units; Δg_e is the elastic energy accompanying the nucleus formation; σ is the specific interfacial energy between the monoclinic phase and cubic phase; and η is the shape factor. The appearance of the thermal hysteresis ($T_c \pm \Delta T$) in neat CDP can be explained by the elastic energy term, Δg_e, and the interfacial energy term, $\eta\sigma n^{2/3}$. Assuming the temperature dependence of g_m and g_c to be linear at around T_c, Δg ($=g_m - g_c$) can be represented as $\Delta g = C\,\Delta T$, where C is a constant. When the nucleus formation becomes a critical size, i.e. $\partial\Delta G/\partial n = 0$, ΔT can be written as follows [44]:

$$\Delta T = -\frac{1}{C}\left(\Delta g_e + \frac{2}{3}\eta\sigma n^{-1/3}\right). \quad (3)$$

Thermal hysteresis in neat CDP is therefore represented by Eq. (3). Colomban et al. has suggested mechanical treatments (grinding and pressure) have an influence on structural transformation in $CsHSO_4$ [46]. Thus, even in neat oxyacid salts such as CDP and $CsHSO_4$, their structural phase transformations can be influenced by stress. The influence of stress can be emphasized in a heterogeneous system as stated below.

Next, the structural phase transformation of CDP in silica matrices is considered. According to the present thermal analysis, CDP in CDP/SiO_2 composites can be divided into three groups (groups A, B and C). Group A is assigned to the structural transformation of the bulky part of CDP in the composite, which is independent of the silica additive (n_{bulk}: the number of CDP structural units in group A). Group B is attributed to the structural transformation of CDP that is affected weakly by silica additive (n_w: the number of CDP structural units in group B). Group C, which shows significant supercooling, is attributed to the structural transformation of CDP that is affected strongly by silica additive (n_s: the number of CDP structural units in group C). Since n_{bulk} can be negligible in the composite (see the area of peak A in Figs. 7b and 9), the total number of CDP structural units in the composites is represented as $n_{total} = n_w + n_s$. Although microstructures in the regions of groups B and C are unclear, it can be estimated roughly as stated below; CDP in group C may exist in the pores of silica particles and/or at the surface on silica particles, and it adheres rigidly to silica walls, for which the structural phase transformation will be strongly prevented. CDP in group B may exist

between silica particles, and thus there is a relatively weak inhibition to the structural phase transformation. According to XRD measurement data [3,35], the difference in CDP volume between monoclinic phase and cubic phase is estimated to be ΔV = ca. 4%. The barrier in the metastable state is thus elastic stress arising in the phase transformation in the silica matrices. The condition of the phase transformation is written as

$$\Delta g n_{\text{total}} = e_{\text{w}} n_{\text{w}} + e_{\text{s}} n_{\text{s}} = E, \tag{4}$$

where e_{w} is an elastic strain energy in group B, e_{s} is an elastic strain energy in group C ($e_{\text{w}} < e_{\text{s}}$), and E is the total elastic strain energy. Hence ΔT is given by

$$\Delta T = \frac{1}{C}\left(e_{\text{w}}\frac{n_{\text{w}}}{n_{\text{total}}} + e_{\text{s}}\frac{n_{\text{s}}}{n_{\text{total}}}\right) = \frac{1}{C}(e_{\text{w}}\phi_{\text{w}} + e_{\text{s}}\phi_{\text{s}}), \tag{5}$$

where ϕ_{w} and ϕ_{s} are molar fractions for groups B and C, respectively. Fig. 10 shows a schematic diagram for the formation of an asymmetric thermal hysteresis loop. The phase transformation from monoclinic phase to cubic phase (forward transition) occurs at the temperature $T_{\text{FT}} = T_{\text{c}} + \Delta T_{\text{FT}}$, while that from cubic phase to monoclinic phase (reverse transition) occurs at the temperature $T_{\text{RT}} = T_{\text{c}} - \Delta T_{\text{RT}}$. In the present case of CDP/SiO_2 composites, an asymmetric thermal hysteresis loop ($\Delta T_{\text{RT}} > \Delta T_{\text{FT}}$) was observed. This phenomenon can be explained according to Eq. (5) if the barriers, e_{w} and e_{s}, in the forward transition are smaller than those in the reverse transition ($e_{\text{w(FT)}} < e_{\text{w(RT)}}$ and $e_{\text{s(FT)}} < e_{\text{s(RT)}}$ (i.e. $E_{\text{FT}} < E_{\text{RT}}$)). An investigation of elastic properties of CDP by Brillouin spectroscopy has been conducted between room temperature and 250 °C [47]. The results show the elastic constants, C_{el}, in CDP decrease monotonously with an increase in temperature, and the non-linear variations in the elastic constants then occur at 233 °C, i.e. the sudden drops in the elastic constants have been observed through the phase transformation from monoclinic phase to cubic phase (C_{el}(monoclinic) > C_{el}(cubic)). Hence it is probable that the barriers, e_{w} and e_{s}, change between forward transition and reverse transition in CDP. Furthermore, the asymmetric thermal hysteresis loop suggests that elastic stress relaxation such as plastic deformation (plasticity in oxyacid salts has been investigated in Refs. [24,36]) and microcracks should be involved in the forward and reverse transitions. This situation is represented by a hysteresis loop of A → B → C → D → A in Fig. 10; the forward transition (B → C) having a relatively low barrier occurs at T_{FT} accompanied by elastic stress relaxation, while the reverse transition (D → A) having a relatively high barrier occurs at T_{RT} accompanied by elastic stress relaxation (E_{FT} (process: B → C) < E_{RT} (process: D → A)). If no elastic stress relaxation occurs in the forward and reverse transitions, a hysteresis loop will track the loop of A → B′ → C′ → D → A in Fig. 10; the hysteresis loop becomes narrow and ΔT_{FT} shifts toward a temperature lower than T_{c} because of a large accumulation of elastic strain energy in the reverse transition, which cannot be supported by present results. In conclusion, elastic strain energy and its relaxation in the processes of B → C and D → A will determine the phase stability in CDP/SiO_2 composites.

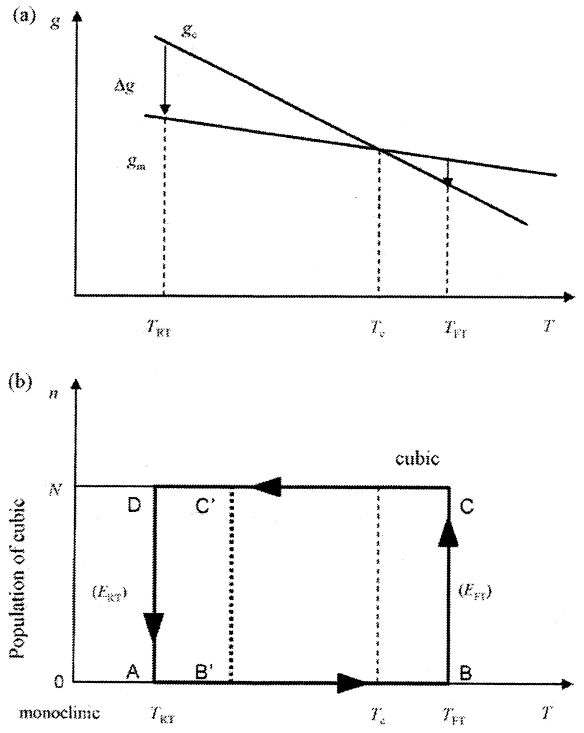

Fig. 10. Schematic diagrams for the formation of an asymmetric thermal hysteresis loop. (a) Temperature dependence of the specific Gibbs free energy in the monoclinic phase (g_m) and the cubic phase (g_c) of CDP in CDP/SiO_2 composites near the critical temperature (T_c). T_{FT} and T_{RT}: see text. (b) An asymmetric thermal hysteresis loop between a monoclinic phase (low-conducting phase) and a cubic phase (high-conducting phase).

3.5. Proton-conducting network

Finally, we mention the proton-conducting network. The SiO_2 volume fraction influences not only the phase stability but also the proton-conducting network in CDP/SiO_2 composites. The total conductivity of this system, σ_{total}, is determined by two components, CDP (proton conductor, p) and SiO_2 (insulator, i), and thus it can be represented by the sum of two terms [28]:

$$\sigma_{\text{total}}^{a} = X_{\text{p}}\sigma_{\text{p}}^{a} + X_{\text{i}}\sigma_{\text{i}}^{a}, \tag{6}$$

where X and σ denote the volume fraction and conductivity of the given components (p and i): $X_{\text{p}} + X_{\text{i}} = 1$; $\sigma_{\text{p}} \gg \sigma_{\text{i}}$. The a value in Eq. (6) ranges from −1 (consecutive connection) to 1 (parallel connection). In real systems, consecutive and parallel connections of particles, which differ in conductivity, alternate, and thus a certain intermediate variant ($-1 < a < 1$) is realized [28]. Eq. (6) indicates the σ_{total} value decreases with an increase in X_{i} if σ_{p} is independent of X_{i}. In real systems, however, σ_{p} is a function of X_{i} below the critical temperature of CDP; in a cooling process, σ_{p} increases with an increase in X_{i} because silica particles enhance the stability of cubic phase. These contradictory effects realize the appearance of a maximal value of σ_{total} as a function of X_{i}, as has already been shown in Fig. 3. In the case of conductivity at 250 °C in Fig. 3, σ_{p} has a value in a high-conducting phase and is independent of X_{i}. The σ_{total} value therefore decreases monotonously with an increase in X_{i}, according to Eq. (6). At 180 °C in Fig. 3, which corresponds to the temperature below the critical temperature of CDP, σ_{p} is strongly influenced by X_{i}; σ_{p} increases with an increase in X_{i}, whereas the second term in Eq. (6) has an effect on a decrease in the σ_{total} value with an increase in X_{i}. As a result, the maximal value of conductivity appears for the SiO_2 volume fraction, as shown in Fig. 3. The behavior of proton conduction in the composites is thus determined by the phase stability arising from shear elastic forces and proton-conducting network. According to the above, we evaluated the σ_{total} value in Fig. 3. Considering the groups A, B and C of CDP in CDP/SiO_2 composites, Eq. (6) can be rewritten as follows:

$$\sigma_{\text{total}}^{a} = \sum_{k=1}^{3} X_k \sigma_k^{a} + X_{\text{i}}\sigma_{\text{i}}^{a}, \tag{7}$$

where the given components, k ($k = 1, 2, 3$) correspond to the groups A, B, C, respectively. Conductivity, σ_k, is expressed as an Arrhenius equation:

$$\sigma = \frac{A}{T} \exp\left(-\frac{E_a}{k_B T}\right). \quad (8)$$

Activation energy, E_a, and prefactor, A, were determined from the conductivity of neat CDP in high-conducting phase (HCP) and low-conducting phase (LCP): $E_{a(HCP)} = 0.4$ eV, $A_{(HCP)} = 8.0 \times 10^4$ S K cm^{-1}, $E_{a(LCP)} = 0.5$ eV, $A_{(LCP)} = 1.0 \times 10^2$ S K cm^{-1}. In addition, the parameter values ($\sigma_i = 1.0 \times 10^{-13}$ S cm^{-1}; $a = 1/3$ [28]) were employed to evaluate the σ_{total}. A prediction curve, i.e. isothermal conductivity *vs.* silica volume fraction, for 180 °C was plotted in Fig. 3, which was calculated assuming that the groups A and B were in LCP and the group C was in HCP at 180 °C. Mole fractions of A, B and C in Fig. 9 were referred for the calculation of the prediction curve. Similarly, a prediction curve for 250 °C was calculated (Fig. 3), in which all of the groups A, B and C were in HCP. The prediction curves can explain the tendency of conductivity toward silica volume fraction, but the prediction curves deviate from the experimental data especially in a higher region of silica volume fraction (>0.5). This means that present model (Eq. (7)) cannot demonstrate breaking of a proton-conducting network exactly. Further improvement of a quantitative model should be made based on a percolation theory [27,28].

Previous studies have suggested that for $CsHSO_4/SiO_2$ composites, the structurally disordering phase of $CsHSO_4$ (interfacial amorphous phase) forms at the interface between $CsHSO_4$ and SiO_2, and proton transfer will be accelerated via the interfacial conduction-pathway in the composite [29–32]. In addition, significant thermal hysteresis in conductivity was not observed in those cases. In the present composite system, conductivity can be partly affected by adsorbed water molecules and/or structurally disordering phase at the interface between CDP and SiO_2. Our present study, however, suggests that proton transfer in CDP/SiO_2 composites prepared by the evaporation-to-dryness method is mainly governed by a crystallographic phase transition of CDP. The stabilization of a cubic phase in the composites will be induced by shear elastic forces in a cooling process, and orientational disorder of the $H_2PO_4^-$ ion (rapid reorientational motion of $H_2PO_4^-$) in the cubic phase will be maintained even below critical temperature. A structural variation among the bulky oxyacid salt, interface and insulator in heterogeneous systems thus generates complex phenomena in conductivity. In addition, from the standpoint of applications, the stabilization of the superprotonic phase by the shear elastic forces gives a hint for a strategy to use oxyacid salts as solid electrolyte in a wider temperature region.

4. Conclusion

The correlation between proton conductivity and phase transformation from a monoclinic phase to a cubic phase in neat CsH_2PO_4 (CDP) and CDP/SiO_2 composites has been investigated. Raman spectroscopy and thermal analysis under sealed conditions demonstrate clearly a reversible phase transformation between monoclinic phase and cubic phase in CDP without dehydration, which provides reliable evidence that the phase transformation is the trigger of a transition to a superionic phase in CDP. The line-broadening in the Raman spectra suggests the orientational disorder of the $H_2PO_4^-$ ion (rapid reorientational motion of $H_2PO_4^-$) occurs in the cubic phase, which induces a disordering of the hydrogen bond network to facilitate proton transfer. A large asymmetric thermal hysteresis in the conductivity of CDP/SiO_2 composites has been observed, i.e. the conductivity in the cooling process maintains relatively high values. DTA measurements suggest significant supercooling in the cubic phase of CDP is induced by the silica additive. The metastable phase (cubic phase retained below critical temperature) in the composites will be induced by shear elastic forces, and orientational disorder of the $H_2PO_4^-$ ion (rapid reorientational motion of $H_2PO_4^-$) in the cubic phase will be maintained even below critical temperature. The present complex behavior of proton conduction in the composites is mainly determined by the phase stability arising from the shear elastic forces and proton-conducting network.

Acknowledgements

The authors are very grateful to Mitsubishi Chemical Corporation for providing the mesoporous SiO_2 particles. This work was supported financially by a Grant-in-Aid for Young Scientists (B), no. 17760618, from the Ministry of Education, Culture, Sports, Science, and Technology of Japan and the "Research and Development of Polymer Electrolyte Fuel Cell" program of the New Energy and Industrial Technology Development Organization (NEDO) of Japan, which are greatly appreciated.

References

[1] A.I. Baranov, V.P. Khiznichenko, V.A. Sandler, L.A. Shuvalov, Ferroelectrics 81 (1988) 183.
[2] A.I. Baranov, V.P. Khiznichenko, L.A. Shuvalov, Ferroelectrics 100 (1989) 135.
[3] W. Bronowska, J. Chem. Phys. 114 (2001) 611.
[4] J. Otomo, N. Minagawa, C. Wen, K. Eguchi, H. Takahashi, Solid State Ionics 156 (2003) 357.
[5] D.A. Boysen, S.M. Haile, H. Liu, R.A. Secco, Chem. Mater. 15 (2003) 727.
[6] K.-S. Lee, J. Phys. Chem. Solids 57 (1996) 333.
[7] E. Ortiz, R.A. Vargas, B.-E. Mellander, J. Chem. Phys. 110 (1999) 4847.
[8] J.-H. Park, Phys. Rev. B 69 (2004) 054104.
[9] Y. Taninouchi, T. Uda, Y. Awakura, A. Ikeda, S.M. Haile, J. Mater. Chem. 17 (2007) 3182.
[10] A.I. Baranov, E.M. Kopnin, V.V. Grebenev, A. Sin, A. Zaopo, Y. Dubitsky, P. Caracino, Solid State Ionics 178 (2007) 657.
[11] J. Otomo, T. Tamaki, S. Nishida, S. Wang, M. Ogura, T. Kobayashi, C. Wen, H. Nagamoto, H. Takahashi, J. Appl. Electrochem. 35 (2005) 865.
[12] D.A. Boysen, T. Uda, C.R.I. Chisholm, S.M. Haile, Science 303 (2004) 68.
[13] T. Uda, S.M. Haile, Electrochem. Solid-State Lett. 8 (2005) A245.
[14] A.I. Baranov, B.V. Merinov, A.V. Tregubchenko, V.P. Khiznichenko, L.A. Shuvalov, N.M. Schagina, Solid State Ionics 36 (1989) 279.
[15] Ph. Colomban, M. Pham-Thi, A. Novak, Solid State Ionics 20 (1986) 125.
[16] Ph. Colomban, J.C. Badot, M. Pham-Thi, A. Novak, Phase Trans. 14 (1989) 55.
[17] T. Norby, M. Friesel, B.E. Mellander, Solid State Ionics 77 (1995) 105.
[18] W. Münch, K.D. Kreuer, U. Traub, J. Maier, Solid State Ionics 77 (1995) 10.
[19] P. Zetterström, A.V. Belushkin, R.L. McGreevy, L.A. Shuvalov, Solid State Ionics 116 (1999) 321.
[20] A. Damyanovich, M.M. Pintar, R. Blinc, J. Slak. Phys. Rev. B 56 (1997) 7942.
[21] A.R. Lim, J.H. Chang, H.J. Kim, H.M. Park, Solid State Commun. 129 (2004) 123.
[22] T. Uda, D.A. Boysen, S.M. Haile, Solid State Ionics 176 (2005) 127.
[23] K. Itoh, T. Ozaki, E. Nakamura, Acta Crystallogr. B 37 (1981) 1908.
[24] L.F. Kirpichnikova, A.A. Urusovskaya, V.V. Dolbinina, V.I. Mozgovoy, Ferroelectrics 172 (1995) 133.
[25] C.C. Liang, J. Electrochem. Soc. 120 (1973) 1289.
[26] J. Maier, J. Phys. Chem. Solids 46 (1985) 309.
[27] R.C. Agrawal, R.K. Gupta, J. Mater. Sci. 34 (1999) 1131.
[28] A.B. Yaroslavtsev, Russ. J. Inorg. Chem. 45 (2000) S249.
[29] V.G. Ponomareva, N.F. Uvarov, G.V. Lavrova, E.F. Hairetdinov, Solid State Ionics 90 (1996) 161.
[30] V.G. Ponomareva, G.V. Lavrova, L.G. Simonova, Solid State Ionics 119 (1999) 295.
[31] H. Shigeoka, J. Otomo, C. Wen, M. Ogura, H. Takahashi, J. Electrochem. Soc. 151 (2004) J76.
[32] S. Wang, J. Otomo, M. Ogura, C. Wen, H. Nagamoto, H. Takahashi, Solid State Ionics 176 (2005) 755.
[33] V.G. Ponomareva, E.S. Shutova, Solid State Ionics 178 (2007) 729.
[34] J.-S. Lee, S. Adams, J. Maier, J. Electrochem. Soc. 147 (2000) 2407.
[35] H. Matsunaga, K. Itoh, E. Nakamura, J. Phys. Soc. Jpn. 48 (1980) 2011.
[36] T. Ozaki, K. Itoh, E. Nakamura, J. Phys. Soc. Jpn. 51 (1982) 213.
[37] B. Marchon, A. Novak, J. Chem. Phys. 78 (1983) 2105.
[38] F. Romain, A. Novak, J. Mol. Struct. 263 (1991) 69.
[39] M. Pham-Thi, Ph. Colomban, A. Novak, R. Blinc, J. Raman Spectrosc. 18 (1987) 185.
[40] K. Yamada, T. Sagara, Y. Yamane, H. Ohki, T. Okuda, Solid State Ionics 175 (2004) 557.
[41] C.E. Botez, J.D. Hermosillo, J. Zhang, J. Qian, Y. Zhao, J. Majzlan, R.R. Chianelli, C. Pantea, J. Chem. Phys. 127 (2007) 194701.

[42] G.B. Olson, W.S. Owen, Martensite, ASM International, USA, 1992.
[43] J. Lajzerowicz, Ferroelectrics 35 (1981) 219.
[44] R.A. Aliev, V.N. Andreev, V.M. Kapralova, V.A. Klimov, A.I. Sobolev, E.B. Shadrin, Phys. Solid State 48 (2006) 929.
[45] J.W. Christian, The Theory of Transformation in Metals and Alloys, 3rd ed., Pergamon, Oxford, 2002 (Chapter 10).
[46] Ph. Colomban, M. Pham-Thi, A. Novak, Solid State Ionics 24 (1987) 193.
[47] Y. Luspin, Y. Vaills, G. Hauret, J. Phys. I Fr. 7 (1997) 785.

RESEARCH REPORTS OF KOGAKUIN UNIVERSITY

No. 105

October 2008

工 学 院 大 学 研 究 報 告

第 105 号

別　　刷

PLA/PBS/天然繊維複合材の機械的物性に及ぼす充填材の影響

満田　諒*，佐藤啓治**，天野智啓***，
小野充智****，佐藤貞雄*****

Effect of Fillers on Mechanical Properties of PLA/PBS/Natural Fiber Composites

Ryo MITSUTA*, Keiji SATO**, Tomohiro AMANO***,
Mitsutomo ONO**** and Sadao SATO*****

Abstract

The polymer alloying of the PLA and PBS was conducted in order to improve the brittleness in a biodegradable polymer PLA (Polylactic Acid) and the softness in PBS (Polybutylene Succinate). The PLA/PBS polymer alloy composites filled with natural fibers (NF) such as the conifer fiber (ConF), kozo fiber (KozF), and silk fiber (SilF) were produced. Various mechanical properties of the PLA/PBS polymer alloy and PLA/PBS/NF composites were investigated experimentally.

The results of examinations showed that the PLA/PBS is a compatible polymer alloy. Hence, the mechanical properties such as the tensile strength and elongation rate of the PLA/PBS polymer alloy depend on the mixture ratio which linearity, thus the additive property is consistent. The rigidity of PLA/PBS/NF polymer alloy composites increased due to NF; the tensile modulus increased and the elongation ratio decreased. These mechanical properties varied depending on the natural fibers used. Especially, the Izod impact value increased with the increase in the amount of natural fibers. It was understood that this is due to the absorption of the impact energy.

1．緒　言

埋め立てにより水と炭酸ガスに分解する生分解性ポリマーは環境負荷の低いポリマーとして注目されている．従来のポリマーは耐食性に優れる反面，その性質が廃棄物となった際に非常に自然界で分解されにくいことが問題となっていた．生分解性ポリマーは，使用後に環境中の微生物により水と二酸化炭素にまで分解されるもので，環境への負荷が低減することや，生ゴミなどとのコンポスト化により堆肥や土壌改良材として大地に還元でき循環型社会の実現に寄与する[1)-3)]といわれている．また，植物由来のポリマーは，近年地球環境を取り巻く様々な問題（地球温暖化や化石資源の枯渇など）に対して，再生可能であることやカーボンニュートラルであるという観点から原料として植物を使用した材料への関心が高まっている[2)-4)]．加えて近年では，綿糸や絹，竹繊維や麻繊維などそれ自体も自然へと還る材料を用いての複合化する研究もなされている[5)-9)]．しかし，熱に弱い，非常に脆い，または軟らかいなど硬軟両極の物性を有しているため汎用化までは至っていない．本研究では，環境負荷の低減を強く意図した硬くて脆い植物由来のポリ乳酸（PLA）系生分解性ポリマーと熱に弱く，軟らかい石油由来の生分解性ポリマー，ポリブチレンサクシネートアジペート（PBS）とのポリマーアロイ及び針葉樹繊維（Conifer fiber），楮繊維（Kozo fiber）及び絹繊維（Silk fiber）などの各種天然繊維充填ポリマーアロイ複合材の機械的物性に及ぼす混合比の影響とそのモルフォロジーについて実験的に検討した．

*機械工学専攻修士2年
**機械工学科2007年度卒業生
***機械工学科2007年度卒業生
****機械工学科2007年度卒業生
*****機械工学科准教授

2．実　験

2.1　試料

実験に供した試料は，三井化学㈱製のポリ乳酸（LACEA H-100）と昭和高分子㈱製のポリブチレンサクシネートアジペート（BIONOLLE #3020）を用いた．天然繊維充填材は，牛乳パックの原料として使用される

(A) ConF

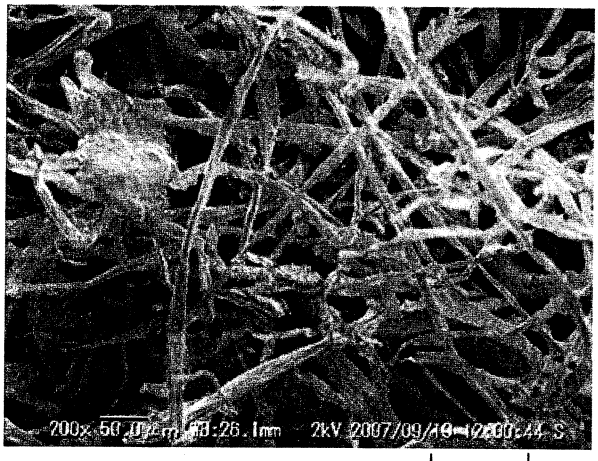

(B) KozF

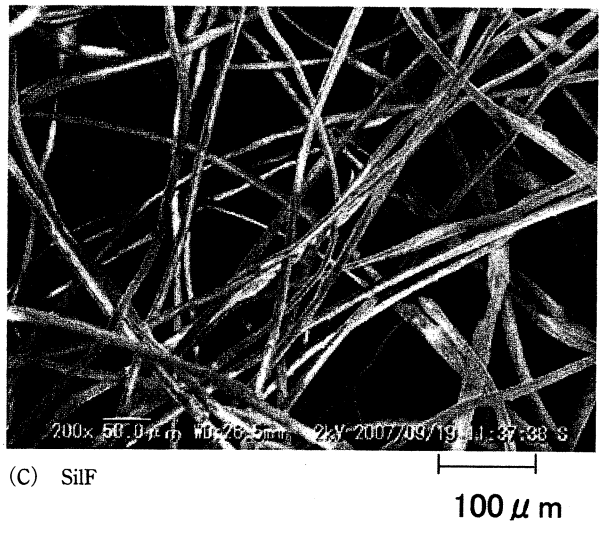

(C) SilF

Fig. 1 Morphology of natural fiber used in the experiment

針葉樹繊維（Conifer fiber），紙幣や和紙の原料として用いられる山野に自生の楮繊維（Kozo Fiber），さらに繭から取り出した絹繊維（Silk Fiber）の3種類を用いた．各天然繊維の形状は図1に示すようなもので，繊維径は15～40μm程度である．

天然繊維のうち，絹繊維を除く針葉樹繊維（牛乳パックの素材）と楮繊維は3×3cm程度の大きさに裁断して数日間水に浸漬した後，楮繊維の場合は1wt%苛性ソーダ溶液中で2時間煮沸した．水に浸漬した針葉樹繊維と2時間煮沸の楮繊維はそれぞれミキサーにより繊維をほぐして自然乾燥させた．充分乾燥させた繊維はマイクロミルを用いてさらに繊維をほぐし，図1に示すような天然繊維充填材とした．

2.2 試料の作製

物性測定試料の作製は，図2に示す東洋精機㈱社製のナノコンポジット用二軸押出機ラボプラストミルμを用いた．

任意の混合比でドライブレンドした試料を押出機を通して溶融混練させ，円形のストランド状に押し出された試料をペレタイザーによってペレットにした．それぞれの試料の略称は表1に示す．それぞれの試料は卓上射出成形機により，所定の寸法・形状の引張及び衝撃の各試験片を作製し，実験試料とした．併せて，実験試料のモルフォロジーは，試料破面を走査型電子顕微鏡（SEM）により観察し検討した．また，成形における温度条件設定は，実験に供した試料の熱重量分析（TGA）の結果により判断した．すなわち，供試したマトリックス及び天然繊維試料の熱分解温度は図3より，約290℃以上であることからポリマーアロイ化及び複合化における溶融混練温度下において，いずれの供試材も熱分解は生じないことから試料の成形温度を200℃と定めた．

3．実験結果と考察

3.1 PLA/PBSポリマーアロイの機械的物性とモルフォロジー

図4にそれぞれの混合比におけるPLA/PBSポリマーアロイの引張弾性率を示す．引張弾性率は軟質のPBSの量が増加するほど減少し，変形しやすい材料へと改質される．またPLA/PBSポリマーアロイのアイゾット衝撃値を図5に示す．同図から明らかなように，ベースとなる硬いPLAに対してPBSの混合割合が増えるほど高い衝撃値を示した．このことは，硬く脆い性質のPLAに軟らかく延性に富むPBSをアロイ化することにより，試料に柔軟性が付加されたためより高い衝撃エネルギーを吸収するためと考えられる．また，PLA50及びPLA70において軟質のPBSの衝撃値を超えるかまたは同等の結果を得た．

PLA/PBSポリマーアロイの引張強さと引張破断伸び

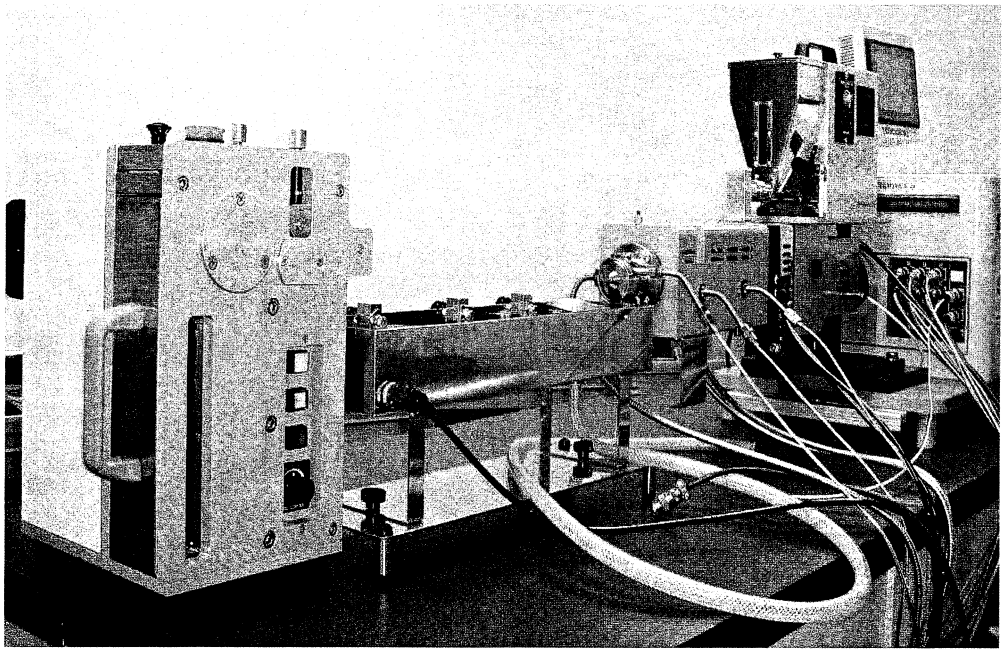

Fig. 2 Twin screw extruder for nanocomposites

Table 1 Detail of specimens used in the present experiment

Material	Ratio	Filler	Content ratio (wt. %)	Symbol
PLA	–	–	–	PLA
PBS	–	–	–	PBS
PLA/PBS	50/50	–	–	PLA50
	70/30	–	–	PLA70
	90/10	–	–	PLA90
		Conifer fiber	0.5, 5, 10	ConF
		Kozo fiber		KozF
		Silk fiber		SilF

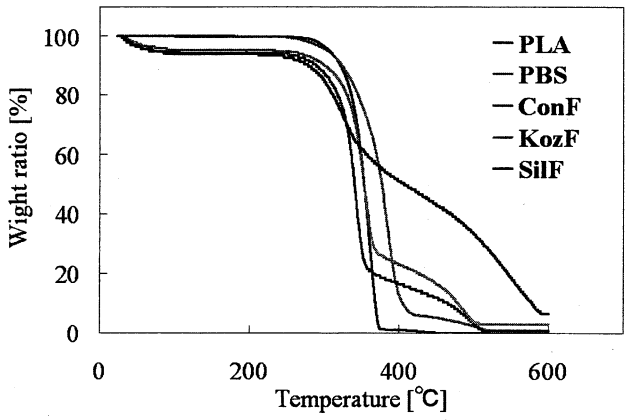

Fig. 3 TGA analysis for PLA, PBS and natural fiber

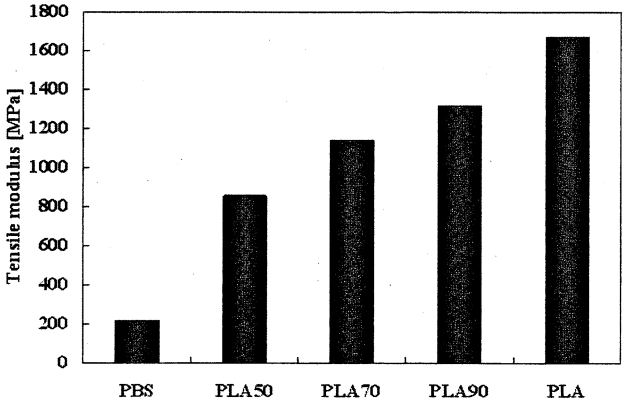

Fig. 4 Effect of content ratio on tensile modulus of PLA/PBS polymer alloys

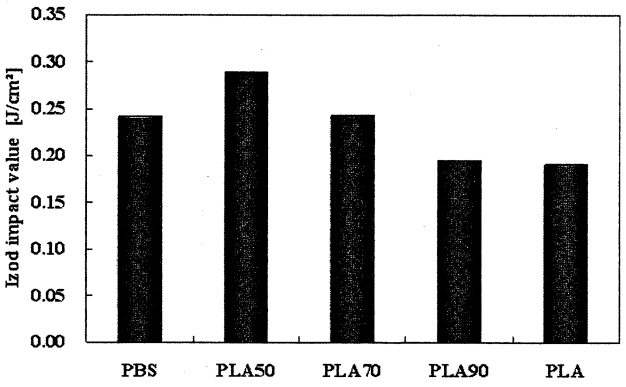

Fig. 5 Effect of content ratio on Izod impact value of PLA/PBS polymer alloys

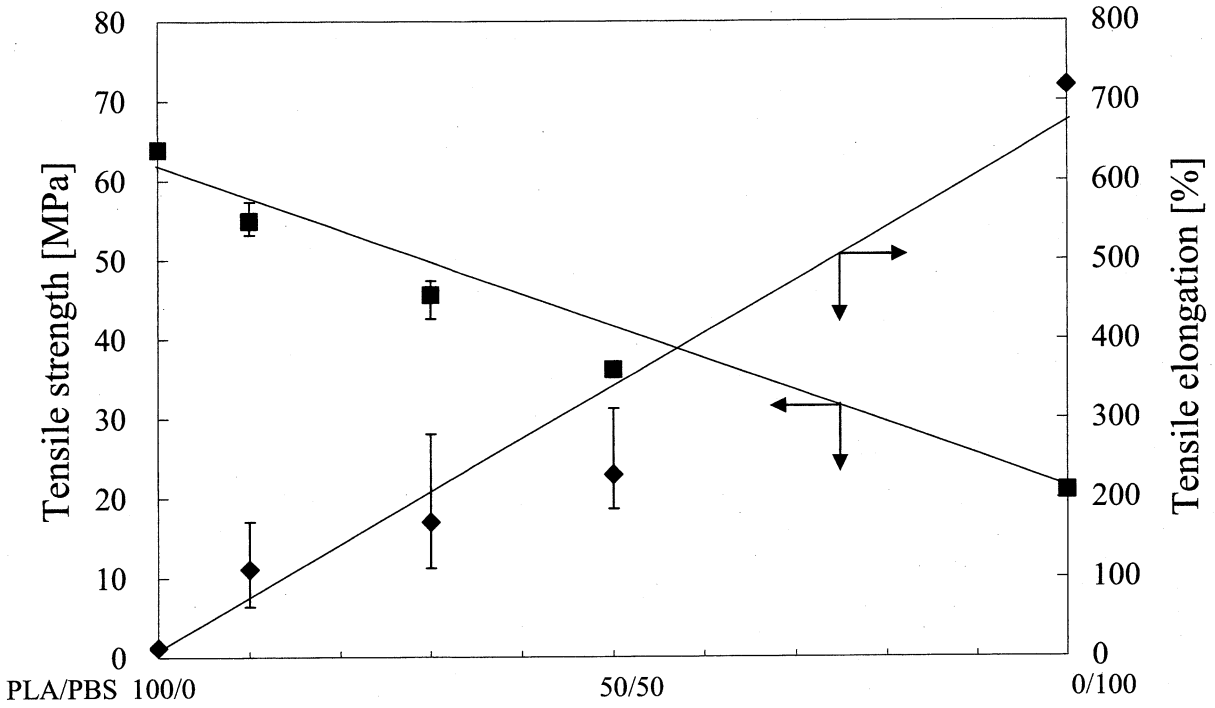

Fig. 6 Relationship between tensile strength, elongation and content ratio for PLA/PBS polymer alloy

の混合比依存性について図6に示す．これによりPBSの混合比が増加するほど引張強さは減少し，引張破断伸びは直線的に増大する．このことから今回検討したポリマーアロイには加成性が成り立ち，一般に加成性は相溶性ポリマーアロイ見られることからPLA/PBSは相溶性であると考えることができる[10]．

PLA/PBSポリマーアロイ試料の衝撃破面をSEM観察したのが図7である．PLA90では表面に亀裂が走ったような脆性的な破壊面を示しているのに対し，PLA70, PLA50とPBSの混合比が増加するほど表面が比較的平滑な凹凸が確認できるようになり，破断面に変化が生じる．この結果は，PBS割合が増加するほど向上したアイゾット衝撃値と同様の傾向と考えられる．これらのモルフォロジーから明らかなようにいずれの混合比のPLA/PBSにおいてもPLA，PBSの分別がし難いことから，先に述べたようにPLA/PBSポリマーアロイは相溶性であることがわかった．

3.2 PLA/PBS/天然繊維複合材の機械的物性とモルフォロジー

PLA/PBSポリマーアロイに天然繊維を充填することにより機械的物性の改質を図った．ここで，先述のようにポリ乳酸（PLA）はトウモロコシやジャガイモなどのでんぷんから合成される植物由来の生分解性高分子であり，石油資源を原料としているポリブチレンサクシネートアジペート（PBS）に比べて環境低負荷材料と考えられる．そこで，環境低負荷を意識し，PLA/PBS＝90/10の混合比のポリマーアロイをベースに各種天然繊維を充填した機械的物性を検討した．

PLA90に各種天然繊維を0.5，5，10wt％充填した試料の引張弾性率を図8に示す．天然繊維を充填することにより，無充填のものと比べて引張弾性率は増加した．また，充填量に依存して引張弾性率は増大する．このことから充填材の混入は複合材の引張弾性率の向上に寄与していることがわかる．

図9および10に引張破断伸びと引張強さを示す．引張破断伸びは天然繊維の充填量増加と共に剛性が増すため減少する．一方，引張強さは充填量の増加と共に13.0～27.2％程度低下する．したがって，天然繊維の充填は伸びと引張強度の向上に対しては余り寄与していない．

図11は天然繊維複合材のアイゾット衝撃値を比較したもので，これにより，PLA90に対して若干減少した複合材もあるが全体的に，天然繊維充填によりアイゾット衝撃値は向上した．また，充填量の増加に従って衝撃値は向上する．これは，試料の衝撃破壊の際に，破面に存在する繊維を断ち切ることにエネルギーが消費されたと考えられることから充填量が多くなるほど破面に存在する繊維量も増大したことがアイゾット衝撃値向上の要因と考えられる．また充填された繊維自体が衝撃に対する緩衝材の役割を果たしエネルギーを吸収したことも要因として考えられる．

(A) PLA50

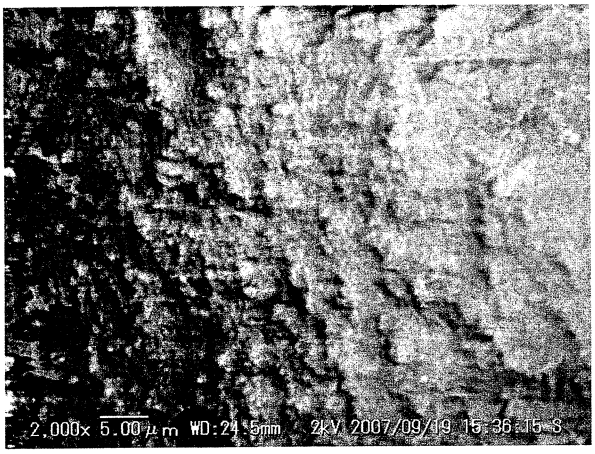

(B) PLA70

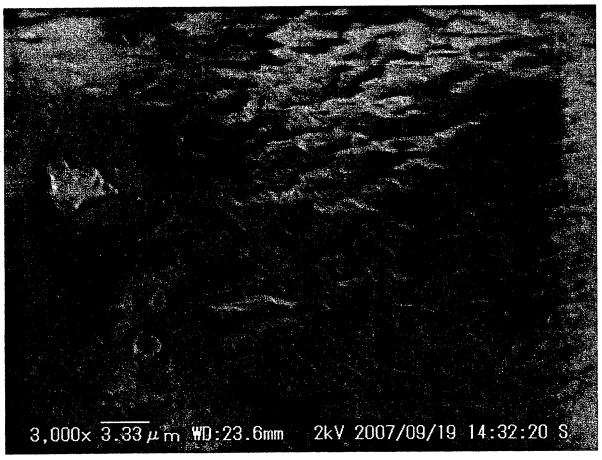

(C) PLA90

Fig. 7 Morphology for PLA/PBS polymer alloys in various content ratio.

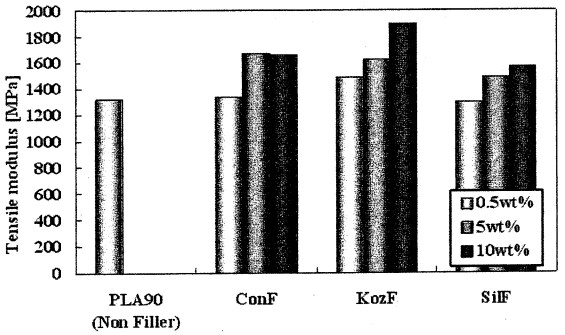

Fig. 8 Tensile modulus of non filler PLA90 and PLA/PBS polymer alloy composites

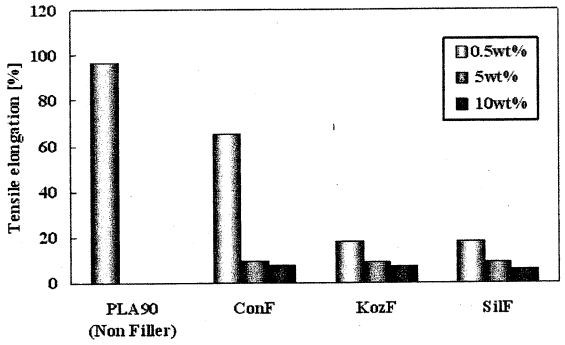

Fig. 9 Tensile elongation of non filler PLA90 and PLA/PBS polymer alloy composites

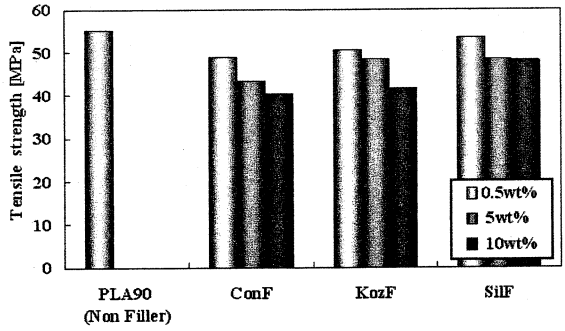

Fig. 10 Tensile strength of non filler PLA90 and PLA/PBS polymer alloy composites

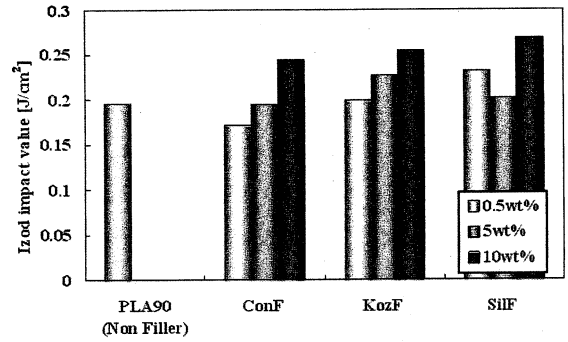

Fig. 11 Izod impact value of non filler PLA90 and PLA/PBS polymer alloy composites

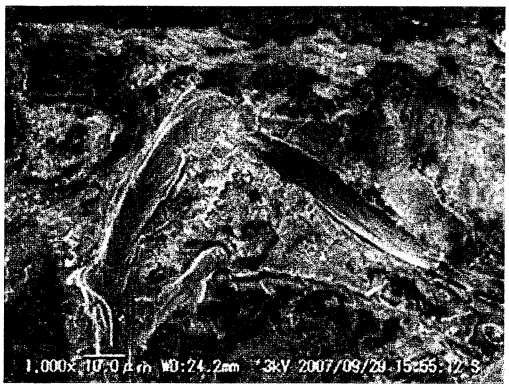

PLA90/ConF0.5

30μm

PLA90/KozF0.5

30μm

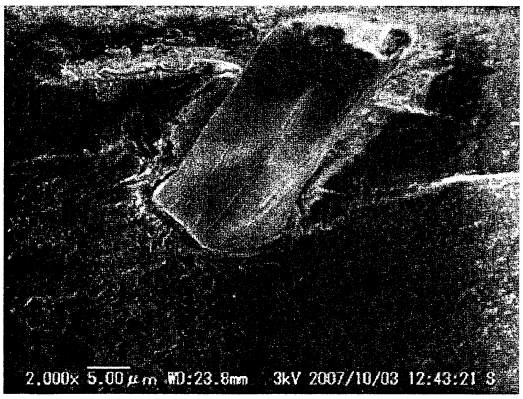

PLA90/SilF0.5

10μm

Fig. 12 Morphology of PLA/PBS/Natural fiber composites

PLA/PBSポリマーアロイ天然繊維複合材のモルフォロジー観察を行ったものが図12である．PLA90に針葉樹繊維及び楮繊維を充填したものは繊維表面に樹脂が付着していることが確認できる．また，繊維への樹脂の付着量は楮繊維のほうが針葉樹繊維よりも多く，PLA/PBSポリマーアロイには楮繊維の方が接着性は良いものと考えられる．一方，絹繊維は動物性であることから両者の濡れ性が悪く，繊維表面への樹脂の付着が確認できず，PLA/PBSポリマーアロイとは接着性が余りないものと考えられる．

4．結　論

1）硬いPLAと軟らかいPBSのポリマーアロイは相溶性であることから，機械的物性は両者の混合比に依存する．

2）PLA/PBSポリマーアロイの引張強さと伸びは混合比に依存して直線関係を示すことから明らかな加成性を示すことが分った．

3）PLA/PBSポリマーアロイのアイゾット衝撃値はPBSの混合比に依存して約2.5～51.8%増大した．

4）PLA/PBS/天然繊維複合材の引張弾性率は各天然繊維において約20～30%向上した．

5）また繊維の充填率が増加するほどアイゾット衝撃値も向上し，各天然繊維で約25～37%向上した．特に，PLA/PBS/SilF10ポリマーアロイ複合材の衝撃値は0.26 J/cm^{2}の最も高い値を示す．

5．参考文献

1）常盤　豊：バイオプロセスと生分解性プラスチック，環境バイオテクノロジー学会誌，Vol. 4，No. 1，p.6，(2004)．
2）川島信之，松尾充記，杉　正浩：循環型社会構築に向けた植物由来プラスチックの役割－ポリ乳酸“LACEA®”の事業開発を通して－，高分子論文集，Vol. 62，No. 6，pp.233，(2005)．
3）木村良晴：高分子材料One Point，5天然素材プラスチック，p.1-10，(2006)，共立出版．
4）木村浩一，端谷隆文：植物性プラスチックの環境対応製品への応用，エレクトロニクス実装学会誌，Vol. 8，No. 5，p.430，(2005)．
5）伊藤隆基，荒木敬造，木村照夫：綿糸を強化材とする生分解性プラスチックの生分解による強度特性の変化，日本機械学会論文集A，Vol. 66，No. 648，p.1555，(2000)．
6）香取重尊，木村照夫：絹/PBS生分解性複合材料の射出成形と成形品特性，成形加工，Vol. 14，No. 9，Page.592，(2002)．
7）越智真治，高木　均：竹繊維および麻繊維で強化した生分解性複合材料の力学的特性に及ぼす加熱処理の影響，材料，Vol. 53，No. 6，p.673，(2004)．
8）越智真治，庄司　彰：マニラ麻短繊維を用いた生分解性複合材の創製，日本機械学会東北支部秋季講演会講演論文集，Vol. 41，p.227-228，(2005)．
9）山田孝政，伊藤隆基，木村照夫，香取重尊：絹繊維強化生分解性プラスチックの生分解による引張強度特性変化，日本機械学会2001年度年次大会講演論文集(V)，p.111，(2001)．
10）井出文雄：実用　ポリマーアロイ設計，p.80-81，(1996)，工業調査会．

Catalysis Communications 10 (2009) 627–630

Contents lists available at ScienceDirect

Catalysis Communications

journal homepage: www.elsevier.com/locate/catcom

Low-temperature water gas shift reaction over Pt–Re/TiO_2 catalysts prepared by a sub-critical drying method

Hajime Iida *, Kenichi Yonezawa, Masaya Kosaka, Akira Igarashi *

Department of Environmental Chemical Engineering, Faculty of Engineering, Kogakuin University, 2665-1 Nakano-machi, Hachioji-shi, Tokyo, 192-0015, Japan

ARTICLE INFO

Article history:
Received 25 August 2008
Received in revised form 16 October 2008
Accepted 4 November 2008
Available online 9 November 2008

Keywords:
Water gas shift
Pt–Re/TiO_2 (rutile)
Sub-critical drying (SubCD)
Pt dispersion

ABSTRACT

In order to prepare a highly dispersed Pt–Re/TiO_2 (R: rutile) catalyst with superior catalytic activity for the low-temperature water gas shift reaction (LT-WGS), the effect of the drying conditions after impregnation on the catalytic properties and activity of Pt–Re/TiO_2(R) catalysts was examined. As a result, sub-critical drying (SubCD), where the catalyst is dried under sub-critical conditions, was effective for the enhancement of Pt dispersion and for resisting Pt loss during the drying step. The SubCD catalyst prepared with $Pt(C_5H_7O_2)_2$ exhibited superior catalytic activity for LT-WGS at 250 °C compared with that of a commercial Cu/Zn catalyst.

1. Introduction

In the hydrogen production process by steam reforming of hydrocarbons for polymer electrolyte fuel cell (PEFC) systems, the water gas shift reaction at low temperature is (LT-WGS) used for the removal of CO, which deteriorates the Pt electrode of the PEFC. The authors reported that the Pt–Re/ZrO_2 and Pt-Re/TiO_2 (R: rutile) catalysts have superior catalytic activities for LT-WGS [1], and since then, Pt-Re catalysts have been paid much attention as candidates for new LT-WGS catalysts [2–5]. However, a reduction in the use of high-priced Pt by the improvement in the Pt dispersion is demanded.

The supported metal catalysts are conventionally prepared by evaporation to dryness. However, it is known that this method causes the migration of active metals with evaporation of the solvent, and this causes the growth and broad size distribution of metal particles. Recently, super-critical drying (SCD) has been investigated as a new method to obtain highly dispersed metal particles, compared with a conventional impregnation method [6]. Natachi and Igarashi reported that low-temperature super-critical drying with CO_2 as a fluid for SCD (LT-SCD) brought about the uniformly well-dispersed Ni particles over the Ni/SiO_2 and the LT-SCD catalyst showed higher catalytic activity for the hydrogenation of benzene than the catalyst prepared by a conventional thermal drying (TD) catalyst [7]. In addition, SCD is applied at high-temperatures using organic solvents (high-temperature super-critical drying; HT-SCD) for the preparation of supported metal catalysts, because the decrease in surface tension by the increased temperature results in highly dispersed metal particles. Sugita and Igarashi et al. have reported the well-dispersed Ni/SiO_2 catalyst, prepared by HT-SCD with cyclohexane, which exhibited higher catalytic activity than the LT-SCD and TD catalysts for the hydrogenation of benzene [8].

In this study, in order to prepare a highly dispersed Pt–Re/TiO_2 (R) catalyst with superior catalytic activity for LT-WGS, the effect of the drying conditions on the catalytic properties and activities of the Pt–Re/TiO_2 (R) catalysts was examined.

2. Experimental

2.1. Catalyst preparation

The TiO_2 (R) support was obtained by calcining JRC-TIO-6 (reference catalyst of the Catalysis Society of Japan) at 500 °C for 1 h in a stream of air. The impregnation of Re on TiO_2(R) was carried out prior to the impregnation of Pt. An ethanol solution of ammonium perrhenate was then added to the support powder. The Re concentration in the solution was adjusted to a Re loading of 0.67 wt.%. The mixture was evaporated on a water bath at 60 °C, and the resultant material was dried at 100 °C for 15 h, and then calcined at 500 °C for 1 h in a stream of air.

Subsequently, a toluene solution of bis (acetyl-acetonato) platinum (II) (Pt $(C_5H_7O_2)_2$) or platinum chloride hexa-hydrate ($H_2PtCl_6 \cdot 6H_2O$) was added to the Re/TiO_2(R) powder. The ratio of the amount of toluene to the pore volume of TiO_2 (0.5 cm^3/g) (solvent/pore volume ratio; S/P) was 1.6, 2.3, or 3.5. The Pt concentration

* Corresponding authors.
E-mail addresses: iida@cc.kogakuin.ac.jp (H. Iida), igarashi@cc.kogakuin.ac.jp (A. Igarashi).

1566-7367/$ - see front matter © 2008 Elsevier B.V. All rights reserved.
doi:10.1016/j.catcom.2008.11.005

in the solution was adjusted to a Pt loading of 1wt%. The impregnated sample was dried by thermal drying (TD; 100 °C, 0.1 MPa, 15 h), HT-SCD (200, 300, 350 °C, 20 MPa, 0.5 h), or sub-critical drying (SubCD; 150 °C, 20, 15, 3.0 MPa, 0.5 h). The fluid for HT-SCD and SubCD was pentane (Tc = 196.8 °C, Pc = 3.3 MPa). The dried sample was finally calcined at 500 °C for 1 h in a stream of air.

2.2. Activity test

LT-WGS was performed using a conventional fixed bed flow reactor, as previously described [9]. The space velocity (total) was 40,000 h^{-1}, and the mole ratio of H_2O to CO was 5.0. The feed gas was a quasi-reformed gas (CO: 10%, CO_2: 15%, H_2: 75%). For comparison, a commercial Cu/Zn catalyst (MDC-7; Süd-Chemie Catalysts) was used.

2.3. Characterization

The amount of CO chemisorbed on the catalyst reduced at 500 °C was estimated using a volumetric absorption apparatus (ASAP2010, Micromeritics) with a chemisorption unit, as previously described [9].

The Pt content in the catalyst was calculated from X-ray fluorescence spectroscopy (XRF; SEA 2010, Seiko) results, as previously described [10].

The Pt dispersion of the catalyst was calculated from the amount of CO chemisorbed on the catalyst reduced at 500 °C. The Pt dispersion was calibrated on the basis of the measured Pt content. The details of this procedure have been previously described [9].

Turn over frequency (TOF) for LT-WGS was calculated from the CO conversion at 250 °C and the amount of CO chemisorbed. The details of the procedure have been previously described [9].

Diffuse reflectance infrared Fourier transform (DRIFT) was performed using an infrared spectrometer (FTIR-8600, Shimadzu) with high-temperature DRIFT attachment (Spectra Tech). The resolution was 2 cm^{-1} and the accumulation was 256 counts. KBr was used as the reference material. The catalysts dried by TD and SubCD were measured at ambient temperature in a stream of N_2.

3. Results and discussion

3.1. Effect of drying conditions on the catalytic properties

Table 1 shows the effect of the S/P ratio on the catalytic properties. The HT-SCD catalyst prepared with lower S/P ratios showed relatively higher Pt dispersion. It can be considered that the excess solvent to pore volume caused the effusion of Pt precursor from the pores during the drying step, that is, a high S/P ratio resulted in a decline in the Pt dispersion. On the other hand, the effect of the S/P ratio on the Pt dispersion for the TD catalyst is less than that for the HT-SCD catalyst. This is because the Pt dispersion of the TD catalyst is not influenced by the initial amount of solvent because Pt is fixed onto the TiO_2 surface with the evaporation of solvent. In addition, Table 1 shows that the Pt content in the HT-SCD catalysts was less than the amount of Pt loaded in the catalyst (1 wt.%). This indicates the loss of Pt during the HT-SCD. From these results, it is apparent that HT-SCD causes the loss of Pt, although an increase in the Pt dispersion is achieved by adjusting the S/P ratio.

Table 2 shows the effect of drying temperature on the catalytic properties. For the catalysts prepared from $Pt(C_5H_7O_2)_2$, the amount of CO chemisorbed on the catalyst was increased with a lowering of the drying temperature. It is thought that an increase in the drying temperature causes the thermal sintering of Pt during the drying step. Among the catalysts examined, the SubCD catalyst prepared at 150 °C, which was the temperature below critical temperature for pentane (196.8 °C), exhibited the highest Pt dispersion. This result is contrary to the increase in the Pt dispersion expected by the removal of solvent via super-critical phase that prevents the condensation and/or effusion of metal by capillary action. In addition, Table 2 shows that the Pt content approached 1 wt.% by a lowering of the drying temperature below 200 °C, although the loss of Pt was observed at temperatures over 300 °C. It is thought that the high solubility of $Pt(C_5H_7O_2)_2$ in the SCD fluid caused the effusion of Pt. This result indicates that a lowering of the drying temperature is effective for resisting the loss of Pt during the drying step.

On the other hand, the effect of drying temperature on the catalytic properties of the catalysts prepared from $H_2PtCl_6 \cdot 6H_2O$ differed significantly from that for the catalysts prepared from $Pt(C_5H_7O_2)_2$. Table 2 shows that the amounts of CO chemisorbed on the HT-SCD and SubCD catalysts prepared from $H_2PtCl_6 \cdot 6H_2O$ were significantly lower than that on the TD catalyst, and the Pt content was also decreased by the HT-SCD and SubCD. This indicates that the effects of SubCD on the Pt dispersion and Pt content were greatly affected by the Pt precursor used.

Table 1
Effect of S/P ratio on catalytic properties.[a]

Drying method	S/P ratio (–)	Pt content (%)	Amount of CO chemisorbed[b] (cm^3-STP/g-cat.)	Pt dispersion[b] (%)	Pt dispersion[b] (%)
HT-SCD	1.6	0.8	0.48	51.9	2.2
	2.3	0.8	0.43	46.3	2.4
	3.5	0.8	0.31	36.2	3.1
TD	2.3	1.0	0.51	46.8	2.4
	3.5	1.1	0.53	43.5	2.6

[a] 300 °C, 2.0 MPa.
[b] After reduction at 500 °C.

Table 2
Effect of drying temperature on catalytic properties.

Drying method	Pt precursor	Drying temperature (°C)	Pt content (%)	Amount of CO chemisorbed[b] (cm^3-STP/g-cat.)	Pt dispersion[b] (%)
TD	$Pt(C_5H_7O_2)_2$	100	1.0	0.51	46.8
	$H_2PtCl_6 \cdot 6H_2O$		1.0	0.46	38.1
HT-SCD[a]	$Pt(C_5H_7O_2)_2$	350	0.8	0.37	42.5
		300	0.8	0.43	46.3
	$H_2PtCl_6 \cdot H_2O$		0.8	0.07	7.8
SubCD[a]	$Pt(C_5H_7O_2)_2$	200	1.0	0.48	40.6
		150	1.0	0.56	49.1
	$H_2PtCl_6 \cdot 6H_2O$		0.7	0.09	10.9

[a] 20 MPa, S/P ratio = 2.3.
[b] After reduction at 500 °C.

Table 3
Effect of drying pressure on catalytic properties.[a]

Drying method	Drying pressure (MPa)	Pt content (%)	Amount of CO chemisorbed[b] (cm^3 -STP/g-cat.)	Pt dispersion[b] (%)	Pt particle size[b] (nm)
SubCD	20	1.0	0.56	49.1	2.3
	15	1.0	0.60	54.5	2.1
	3	1.0	0.61	51.1	2.2

[a] 150 °C, S/P ratio = 2.3.
[b] After reduction at 500 °C.

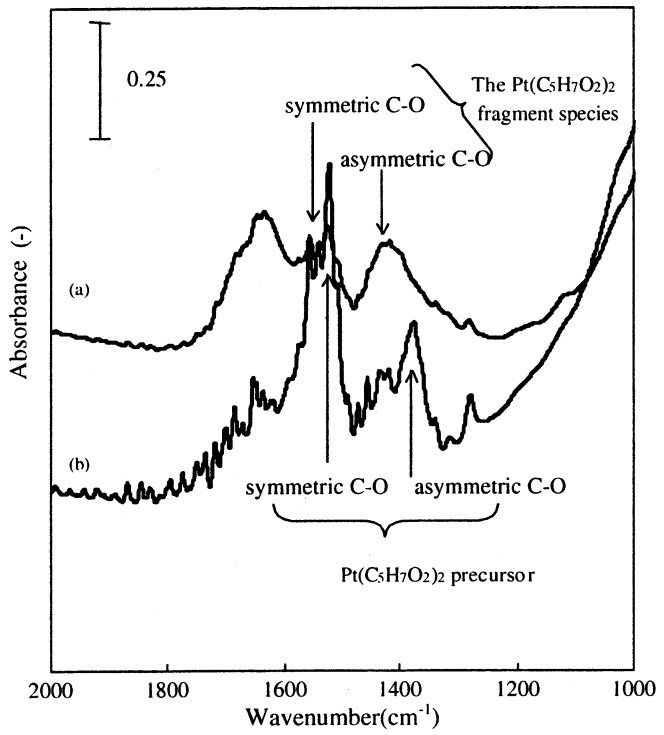

Fig. 1. Infrared spectra for the C–O stretch region of $Pt(C_5H_7O_2)_2$ on TD and SubCD catalysts: (a) SubCD (150 °C, 20 MPa), (b) TD.

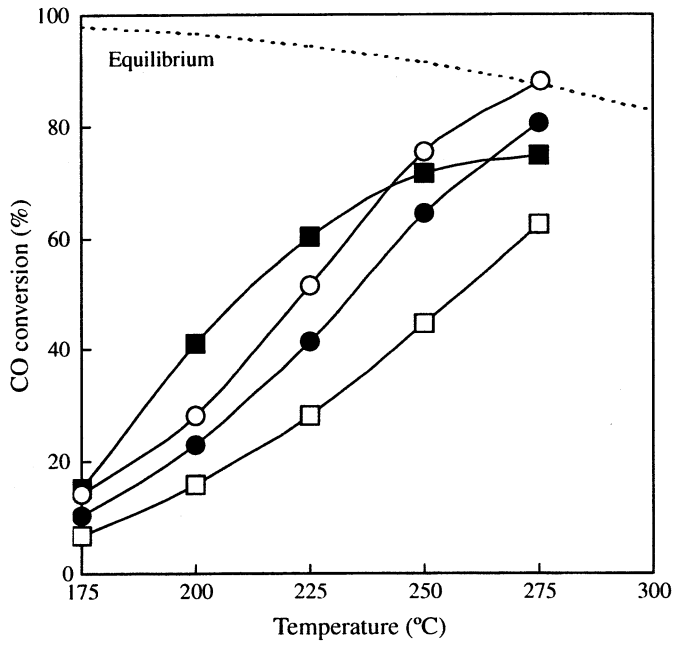

Fig. 2. Catalytic activity for LT-WGS of Pt-Re/TiO_2(R) prepared by various drying methods: (○) SubCD (150 °C, 3.0 MPa, S/P = 2.3), (□) HT-SCD (300 °C, 20 MPa, S/P = 2.3), (●) TD, (■) commercial Cu/Zn.

Table 3 shows the effect of the drying pressure on the catalytic properties. The Pt dispersion on the catalyst prepared at the low pressure is slightly higher than that of the catalyst prepared at the high pressure. This result indicates that the effect of the drying pressure on the Pt dispersion is less than that of the drying temperature.

It is therefore clarified that SubCD is an effective method for enhancement of the Pt dispersion. In addition, these results indicate that the unique adsorption property of the $Pt(C_5H_7O_2)_2$- based catalysts is related to an increase in the Pt dispersion. Therefore, in situ DRIFT spectra for the presence of $Pt(C_5H_7O_2)_2$ on the catalysts were measured. Fig. 1 shows the infrared spectra for the C–O stretch region of $Pt(C_5H_7O_2)_2$ on TD and SubCD catalysts. The peaks assigned to the C–O stretching bands of Pt $(C_5H_7O_2)_2$ fragment species on the SubCD catalyst were larger than those on the TD catalyst. This result indicates that $Pt(C_5H_7O_2)_2$ fragment

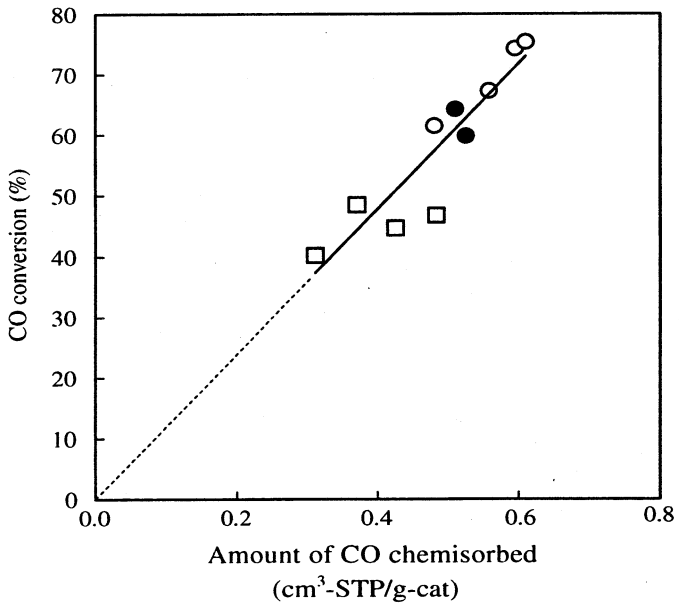

Fig. 3. Relation between the amount of CO chemisorbed and the CO conversion: (○) SubCD, (●) TD, (□) HT-SCD.

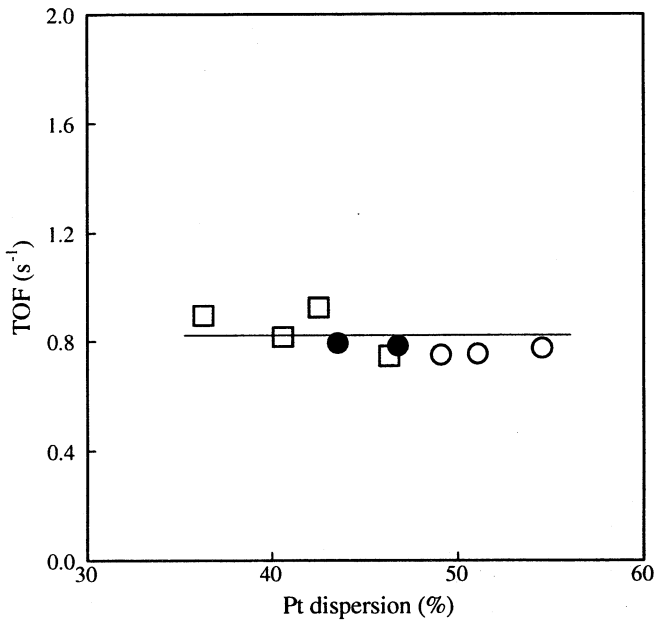

Fig. 4. Relation between the TOF and the Pt dispersion: (○) SubCD, (●) TD, (□) HT-SCD.

species are formed during SubCD. Womes et al. reported UV–Vis and IR results suggesting that the partial decomposition of the $Pt(C_5H_7O_2)_2$ complex formed a surface species of $Pt(C_5H_7O_2)_2$ fragments chemisorbed onto the surface of the supports [11]. The authors also observed that IR bands assigned to the fragment species appeared at temperatures over 120 °C in the IR spectra of Pt–Re/TiO_2 (R) prepared with Pt $(C_5H_7O_2)_2$ [12]. Consequently, the authors concluded that the fixation of Pt on the support surface due to the formation of fragment species brought about the high dispersion of Pt on the Pt/TiO_2(R) catalyst prepared with Pt $(C_5H_7O_2)_2$ [12]. Therefore, the reason why SubCD causes an increase in the Pt dispersion is the immobilization of Pt on the support, due to the formation of Pt $(C_5H_7O_2)_2$ fragment species during SubCD. It is thought that mobile Pt $(C_5H_7O_2)_2$ in the drying fluid is fixed on the support surface as a fragment species under SubCD.

In the case of TD, Pt $(C_5H_7O_2)_2$ is forcibly fixed to the support by evaporation of solvent. Therefore, it is suggested that the difference in the mechanism of Pt precursor attachment to the support for the both drying methods affects the Pt dispersion.

3.2. Effect of drying conditions on catalytic activity for LT-WGS

Fig. 2 shows a comparison of catalytic activities for LT-WGS between Pt–Re/TiO_2(R) prepared by various drying methods and a commercial Cu/Zn catalyst. The catalytic activity of HT-SCD catalyst is less than that of the TD catalyst. It is considered that the reason for this is decline in the Pt content, due to an outflow of Pt during the drying step. On the other hand, the SubCD catalyst has higher catalytic activity than the commercial Cu–Zn catalyst at temperatures over 250 °C. Consequently, it is possible that the Pt content is reduced to less than 1 wt.% by the SubCD preparation using $Pt(C_5H_7O_2)_2$ as a Pt precursor. Fig. 3 shows a linear relation between the CO conversion at 250 °C and the amount of CO chemisorbed. This indicates that the difference in the catalytic activity among the catalysts prepared is explained by the degrees of Pt dispersion on the catalysts. Especially, the SubCD catalysts with high Pt dispersion exhibit the superior catalytic activity. In addition, Fig. 4 shows that the TOF remains constant with the Pt dispersion. This indicates that LT-WGS over the Pt-Re/TiO_2 (R) prepared during various drying conditions is structure-insensitive reaction.

4. Conclusion

In order to develop a highly dispersed Pt–Re/TiO_2 (R) catalyst for LT-WGS, the effect of the drying conditions on the Pt dispersion and the LT-WGS activity was examined. Although the application of HT-SCD to prepare Pt–Re/TiO_2 was less effective for an increase in the Pt dispersion, due to the loss of Pt during the drying step, the loss of Pt was avoided by lowering of the drying temperature below the critical temperature (SubCD). Consequently, the SubCD method using the Pt $(C_5H_7O_2)_2$ precursor resulted in an increase in the Pt dispersion and catalytic activity for LT-WGS. Among the catalysts examined, the SubCD catalyst prepared at 150 °C and 3.0 MPa, exhibited higher LT-WGS activity at 250 °C than the commercial Cu/Zn catalyst. Therefore, it is possible that the Pt content is reduced to less than 1 wt.% by the SubCD preparation using Pt $(C_5H_7O_2)_2$ as a Pt precursor. The reason for the high dispersion of Pt and the superior catalytic activity of the Pt–Re/TiO_2 (R) catalyst obtained by the SubCD with Pt $(C_5H_7O_2)_2$, was considered to be that the mobile Pt $(C_5H_7O_2)_2$ in the drying fluid is fixed on the support surface as a fragment species during the SubCD. In the case of TD, Pt $(C_5H_7O_2)_2$ is forcibly fixed with the evaporation of the solvent. The differences between these drying methods affect the Pt dispersion.

References

[1] H. Iida, K. Tahara, H. Higashi, A. Igarashi, Adv. Tech. Mat. Mat. Proc. J. 4 (2002) 62.
[2] Y. Sato, K. Terada, S. Hasegawa, T. Miyao, S. Naito, Appl. Catal. A: Gen. 296 (2005) 80.
[3] S.Y. Choung, M. Ferrandon, T. Krause, Catal. Today 99 (2005) 257.
[4] R. Radhakrishnan, R.R. Willigan, Z. Dardas, T.H. Vanderspurt, Appl. Catal. B: Environ. 66 (2006) 23.
[5] K.G. Azzam, I.V. Babich, K. Seshan, L. Lefferts, J. Catal. 251 (2007) 163.
[6] A. Igarashi, Catal. Catal. 39 (1997) 275.
[7] T. Natachi, A. Igarashi, Catal. Catal. 39 (1997) 470.
[8] S. Sugita, M. Ohta, and A. Igarashi, 2000 International Chemical Congress of Pacific Basin Societies (PACIFICHEM 2000), INOR 540, 2000.
[9] H. Iida, A. Igarashi, Appl. Catal. A: Gen. 298 (2006) 152.
[10] H. Iida, K. Kondo, A. Igarashi, Catal. Commun. 7 (2006) 240.
[11] M. Womes, T. Cholley, F. Le Peltier, S. Morin, B. Didillon, N. Szydlowski-Schildknecht, Appl. Catal. A: Gen. 283 (2005) 9.
[12] H. Iida, M. Someya, K. Kondo, A. Igarashi, Stud. Surf. Sci. Catal 172 (2007) 165.

MECHANOCHEMICAL PROPERTIES OF OCTACALCIUM PHOSPHATE AND BRUSHITE

HIDEKI MONMA[1]*, TOSHINORI OKURA[1], YOSHIHIRO HARA[1], YUSUKE MORIYOSHI[2]

(*Corresponding author: monma@cc.kogakuin.ac.jp)

[1]Faculty of Engineering, Kogakuin University, 2665 Nakano-cho, Hachioji-shi, Tokyo 192-0015, Japan

[2]Faculty of Engineering, Hosei University, Kajino-cho, Koganei-shi, Tokyo 184-8584, Japan

Keywords: Octacalcium phosphate, Brushite, Calcium phosphate, Mechanochemical

Abstract: Crystalline layer-structured octacalcium phosphate ($Ca_8(HPO_4)_2(PO_4)_4 \cdot 5H_2O$, OCP) and brushite ($CaHPO_4 \cdot 2H_2O$, DCPD) were mechanochemically ground. The crystalline XRD pattern of OCP was weakened with grinding and reached almost amorphously after 72 h. However, the amorphously ground OCP possessed IR spectroscopic and thermogravimetric characteristics of OCP. On the other hand, DCPD was dehydrated to monetite ($CaHPO_4$) by grinding above 4 h. As-prepared OCP particles consisting of aggregates of fine primary thin blade crystals changed to amorphous-like sub-micron spherical particles by grinding. DCPD platy crystals changed to aggregates of very fine primary particles.

1. INTRODUCTION

Layer-structured octacalcium phosphate ($Ca_8(HPO_4)_2(PO_4)_6 \cdot 5H_2O$, hereafter referred to as OCP) is detected sometimes in bio-calcified stones and encountered experimentally as a precursor in the precipitation of hydroxyapatite ($Ca_5(OH)(PO_4)_3$, HAp). OCP with a layer structure consisting of alternate stacks of "apatitic layer" and "hydrated layer" [1] has become of interest as an applicable material for biomechanical or industrial applications similar to HAp. OCP has been thought little as a material, because OCP is thermodynamically metastable in solution. However, we have often experienced that OCP was stable in air, and not so unstable in solution. In the present study, mechanochemically ground OCP powders were investigated as a basic research on OCP for improvements in powder materials functions, comparing with the case of another layer-structured calcium phosphate, *i.e.*, brushite ($CaHPO_4 \cdot 2H_2O$, DCPD).

2. EXPERIMENTAL

OCP was prepared by stirring a dispersive solution of 20.0 g reagent grade DCPD powder in 1 dm^3 of 0.5 mol dm^{-3} $CH_3COONa \cdot 3H_2O$ kept at pH 6.0±0.1 at 50 ℃ for 24 h [2], then the powder part was separated, water-washed and dried at room temperature. The formation reaction of OCP is written stoichiometrically as follows;

$$8CaHPO_4 \cdot 2H_2O \xrightarrow{H_2O} Ca_8(HPO_4)_2(PO_4)_4 \cdot 5H_2O + H_3PO_4 + 11H_2O \quad (1)$$

Mechanochemical treatment, *i.e.*, vigorous grinding, was carried out by using an automatic agate mortar (150 mm in

diameter and 20 mm in depth) with a pestle rotation rate of 120 rpm for 3.0 g of powder sample in air at room temperature for various durations up to 72 h. The resulting ground powders were left in air for 24 h, and then characterized by X-ray powder diffraction (XRD), Fourier transform infrared (FT-IR) spectroscopy, thermogravimetry (TG) and scanning electron microscopy (SEM).

3. RESULTS AND DISCUSSION

3.1 Change in XRD pattern by grinding

FIGURE 1 shows changes in XRD patterns of OCP and DCPD with grinding. The pattern of the original crystalline OCP weakened and broadening with grinding, and reached amorphously, *i.e.*, hallow pattern, after 72 h without any intermediate new phase. DCPD was dehydrated and decomposed to $CaHPO_4$. Such mechanochemical changes in XRD patterns are generally reasonable on thinking about mechanochemical pulverization causing frictional heat and lattice distortion. The difference in mechanochemical behavior between OCP and DCPD could be explained as follows. The interlayer H_2O molecules in OCP were zeolitic [3], therefore, the OCP structure was kept even if the interlayer H_2O molecules were removed to some extent by the frictional heat. On the other hand, the interlayer H_2O molecules in DCPD were non-zeolitic, therefore, the structure of DCPD was decomposed with the dehydration by the frictional heat. FIGURE 2 shows changes in FT-IR spectra of decomposed to HAp, however specific bands at 630 and 3570 cm^{-1} assigned to OH^- in HAp were appeared during the grinding. On the other hand, DCPD was dehydrated to form $CaHPO_4$ after 4 h-grinding, and the resulting crystalline $CaHPO_4$ was kept after 72 h-grinding as well as reported in the literature [5]. Gypsum ($CaSO_4 \cdot 2H_2O$) structurally resembling DCPD is subject to a OCP and DCPD by grinding. Decreases in peak strength of the interplanar spacing (d_{100}) of the OCP structure suggested a structural degradation, probably a distortion of the hydrated layer of OCP. FT-IR spectra of OCP before and after grinding were basically the same, *i.e.*, spectroscopically the layer structure of OCP was maintained after 72h- grinding. The broad bands around 3000-3600 and 1600-1700 cm^{-1} are assigned to H_2O adsorbed on the surface and in the hydrated layer of OCP. The other 470, 570, 600, 960 and broad 1000-1200 cm^{-1} bands are assigned to PO_4^{3-} groups. Particularly a doublet at 860 and 910 cm^{-1} is characteristic of HPO_4^{2-} in OCP [4]. The doublet remained after grinding for 72 h. On dry-heating OCP is dehydrated and similar mechanochemical dehydration [6]. The layer structure of OCP seemed to be fairly strong against grinding. Such a difference between dry-grinding and furnace-heating was seemed to be characteristic of the OCP structure.

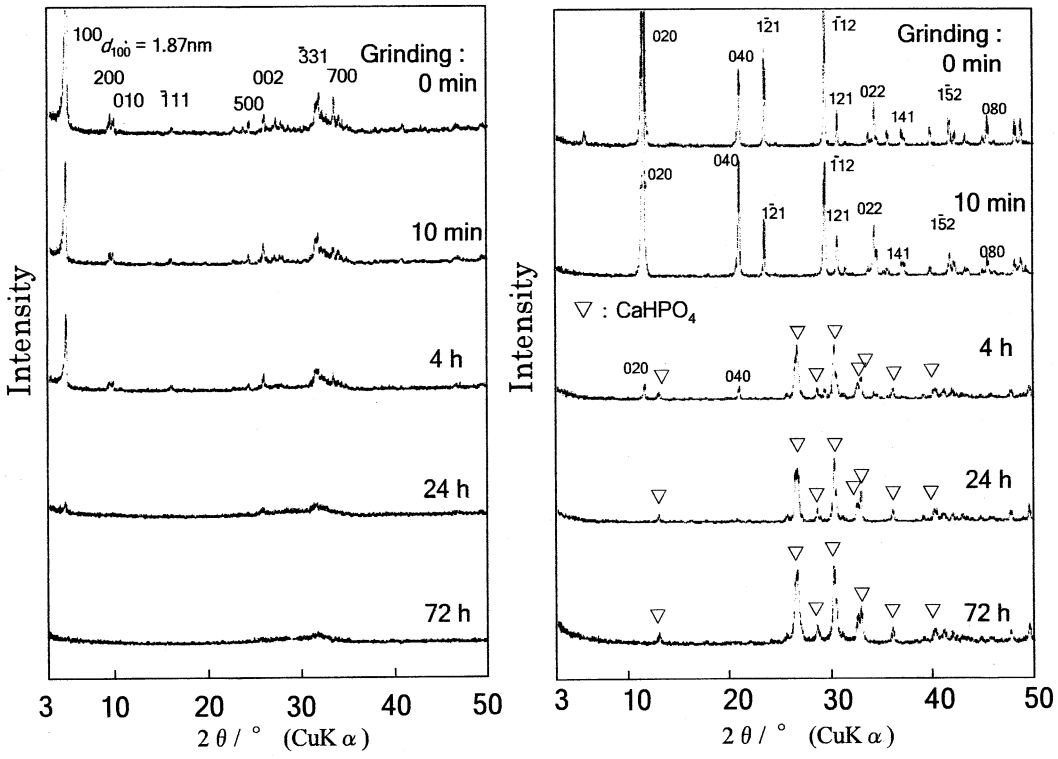

FIGURE 1 XRD patterns of ground OCP (left side) and DCPD (right side) powders.

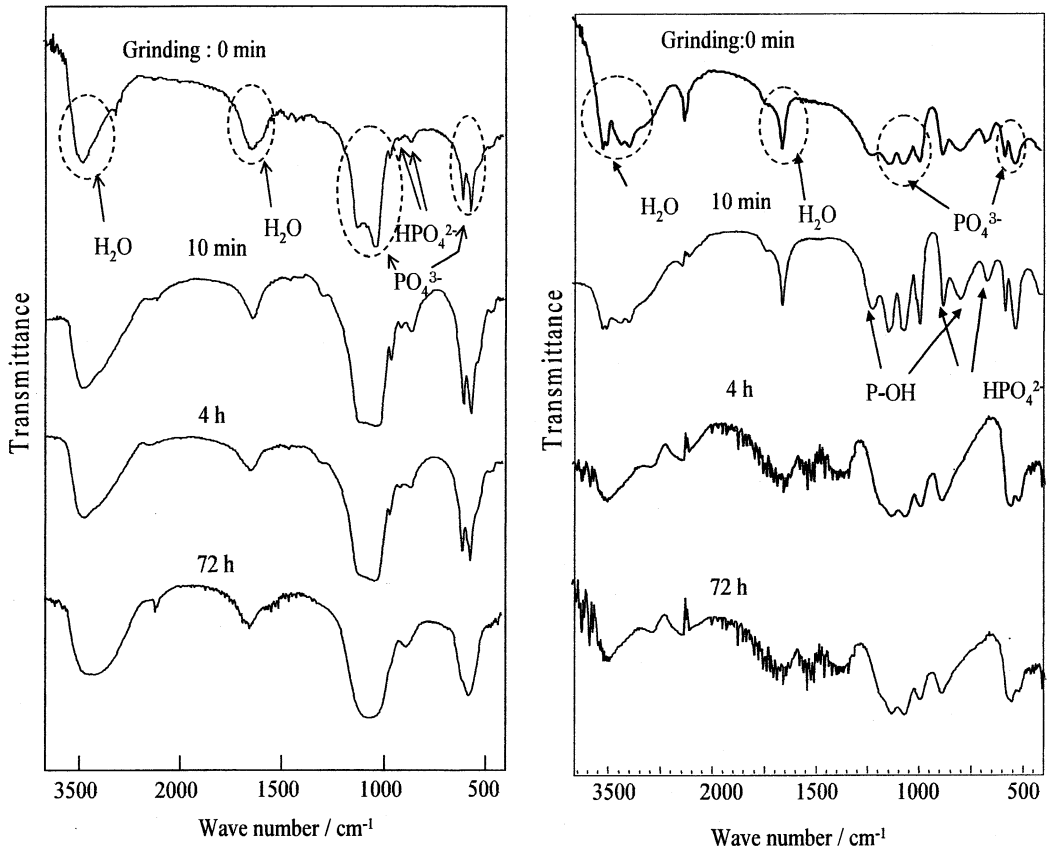

FIGURE 2 IR spectra of ground OCP (left side) and DCPD (right side)

3.2 Dehydration of interlayer H_2O in OCP by grinding

The dehydration and structural changes of OCP are already clarified as follows [7].

$$Ca_8(HPO_4)_2(PO_4)_4 \cdot 5H_2O$$

$$\sim 150\ ^\circ C \rightarrow Ca_8(HPO_4)_2(PO_4)_4 \cdot (5-m)H_2O + mH_2O\uparrow \quad (2)$$

$$150\ ^\circ C \sim \rightarrow Ca_5(OH)(PO_4)_6 + 3CaHPO_4 + 4H_2O\uparrow \quad (3)$$

$$200\ ^\circ C \sim \rightarrow Ca_5(OH)(PO_4)_3 + 3/2Ca_2P_2O_7 + 5.5H_2O\uparrow \quad (4)$$

$$600\ ^\circ C \sim \rightarrow 5/3Ca_3(PO_4)_2 + 3/2Ca_2P_2O_7 + 6H_2O\uparrow \quad (5)$$

Partially dehydrated OCP by heating below *ca.* 200 ℃ rehydrates by exposing to humid air and reverted to the original hydrated state [3]. FIGURE 3 shows TG weight losses of ground OCP and DCPD samples left in air for 24 h after grinding. The weight losses up to 150 ℃ and 800 ℃ were reasonable by considering the adsorption of H_2O on finely ground OCP particles. Approximately the same weight losses up to 4 h-grinding suggested no change in the OCP layer structure. The loss 15.5 % of the OCP after 72 h-grinding suggested partial degradation of the OCP layer structure. On the other hand, DCPD was partially dehydrated to form a mixture of DCPD and $CaHPO_4$ after 4 h-grinding, and almost $CaHPO_4$ after 72 h-grinding. The layer structure of OCP could be also said to be strong compared to that of DCPD.

3.3 Morphological changes by grinding

FIGURE 4 shows morphologies of ground OCP and DCPD particles. The particle form of as-prepared OCP powders was platy, obviously taking over the platelet form of reagent DCPD used for the preparation of OCP. OCP platy particles must be aggregates of OCP microcrystals since OCP primary particles are generally very fine and thin blade or strip. The platy OCP particles changed into spherical particles with 0.7-1.0 μm in diameter after grinding above 6 h. DCPD platy crystals changed to aggregates of very fine primary particles by grinding

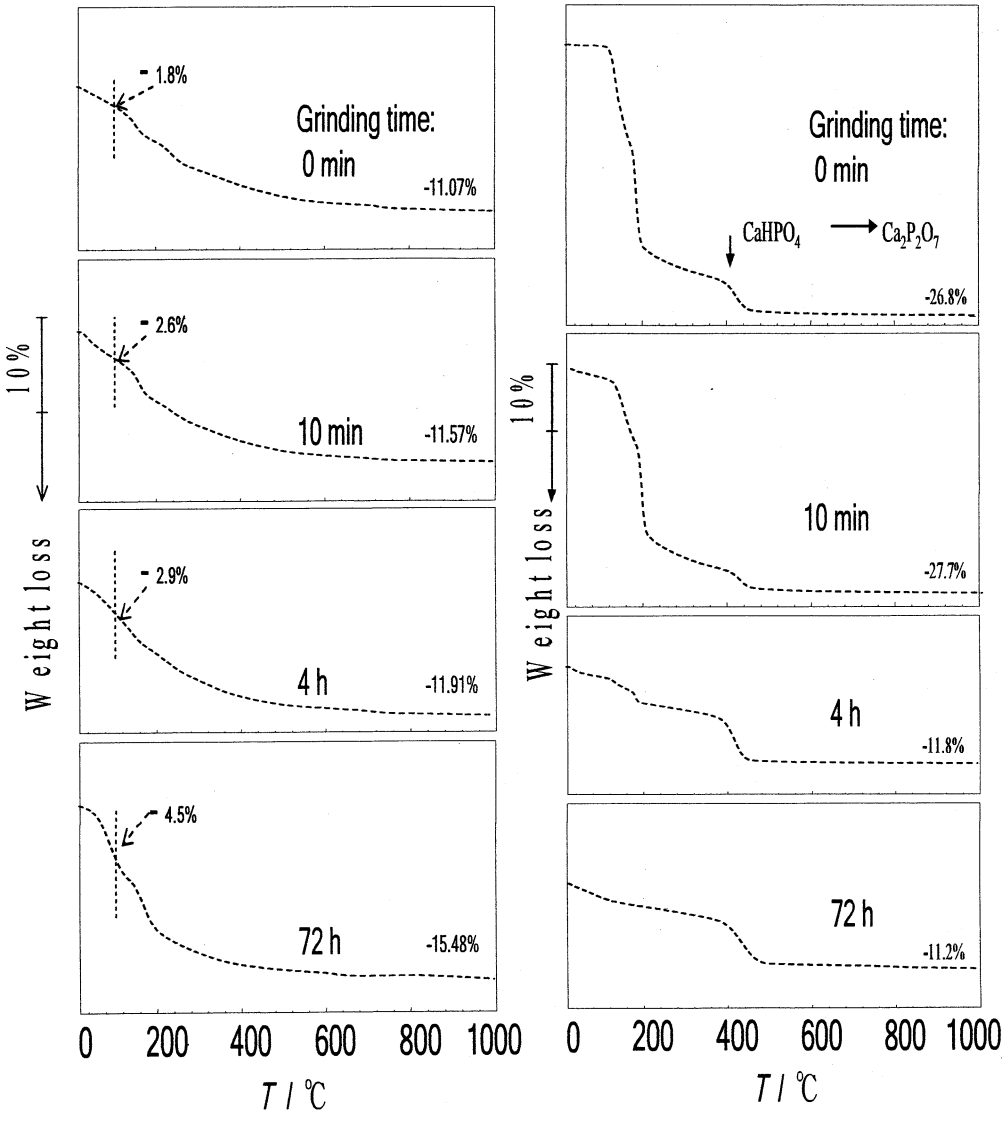

FIGURE 3 TG curves of ground OCP (left side) and DCPD (right side) powders. (Samples were exposed to air for 24 h and then supplied for measurement)

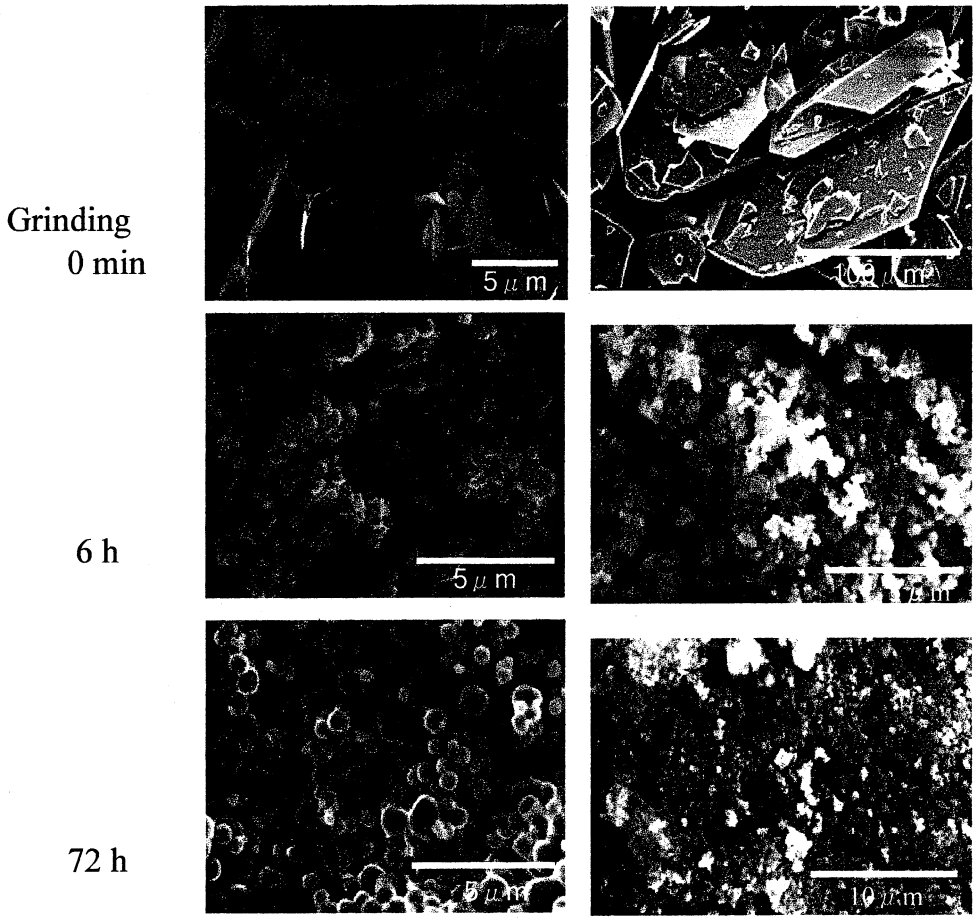

FIGURE 4 SEM microphotographs of ground OCP and DCPD powders.

4. CONCLUSIONS

Mechanochemical characteristics of layer-structured OCP ($Ca_8(HPO_4)_2$ $(PO_4)_4 \cdot 5H_2O$) and DCPD ($CaHPO_4 \cdot 2H_2O$) were investigated.

(1) The crystallinity of OCP was weakened with grinding and reached amorphously after 72 h. However, IR spectroscopic and thermogravimetric characteristics of OCP were almost maintained. On the other hand, DCPD was decomposed to $CaHPO_4$ by grinding for 4 h.

(2) The layer structure of OCP seemed to be stronger against grinding than those of DCPD.

(3) OCP platy particles consisting of aggregates of thin and blade primary microcrystals changed to homogeneous sub-micron spherical particles by grinding above 6 h, whereas DCPD platy crystals changed simply to aggregates of very fine primary particles.

REFERENCES

1. W.E.Brown, *Nature*, **196**, 1048-1055(1962).
2. J.C.Elliott, "Apatites and Other Calcium Orthophosphates (Studies in Inorganic Chemistry 18)", Elsevier(1990)p.13.
3. H.Monma, *Gypsum & Lime*, No.229, 12-17 (1990).
4. B.O.Fowler, M.Markovic, W.E.Brown, *Chem. Mater.*, **5**, 1417-1423(1993)
5. Y.Arai, T.Yasue, *Kogyo Kagaku Zasshi*, **74**(7), 1343-1348(1971).
6. Y.Arai, T.Yasue, *Kogyo Kagaku Zasshi*, **73**(12), 2603-2609(1970).
7. H.Monma, *J. Mater. Sci.*, **15**, 2428-2434 (1980).

Journal of the Society of Inorganic Materials, Japan 15, 37–41 (2008)

Note

Dry-Mechanochemical Conversion of Gypsum to Apatite

Hideki MONMA, Toshinori OKURA, Masahiro ISHIDA and Yusuke MORIYOSHI*
(Faculty of Engineering, Kogakuin University, 2665 Nakano-cho, Hachioji-shi, Tokyo 192–0015; *Faculty of Engineering, Hosei University, Kajino-cho, Koganei-shi, Tokyo 184–8584)

Dry-mechanochemical conversion of gypsum ($CaSO_4 \cdot 2H_2O$) to apatite was investigated for resource saving and materials recycling of gypsum and also as a new formation reaction for apatite. Mixtures of gypsum and Na_2HPO_4 with and without NaF or CaF_2 or $Ca(OH)_2$ were ground by using an automatic agate mortar in air up to 24 hours. No formation of apatite occurred from the mixtures without the additives. On the other hand, nearly stoichiometric fluorapatite ($Ca_5F(PO_4)_3$) formed from the mixtures added with the fluorides, and carbonated hydroxyapatite ($Ca_5(OH)(PO_4)_3$) from a mixture added with $Ca(OH)_2$.

(Received Jul. 18, 2007)
(Accepted Oct. 19, 2007)

Key words: Apatite, Hydroxyapatite, Fluorapatite, Mechanochemical reaction, Gypsum

1 Introduction

Gypsum ($CaSO_4 \cdot 2H_2O$, referred to as Gy) is a basic material in Gy board, portland cement and ceramic industries. There are two main supplies of Gy in Japan; one is the by-product in the wet-process production of phosphoric acid, and another the product by desulfurization of incineration flue gas. Recently abundantly wasted Gy has become an important subject from a viewpoint of resource saving and materials recycling. On the other hand, hydroxyapatite ($Ca_5(OH)(PO_4)_3$, HAp) has become of interest increasingly as artificial bone, carrier of photocatalyst, chromatographic absorbent, scaffold for cell culture and so forth. With the development of materials applications, various preparation methods for HAp corresponding to such applications have been developed so far. And there have been some studies on the HAp preparation or formation reaction using Gy. Each of them has been carried out in the Gy-aqueous solution systems, *e.g.*, Gy–Na_3PO_4–H_2O[1], Gy–Na_3PO_4–NaOH–H_2O[2], $CaSO_4$–NaH_2PO_4–H_2O[3] and Gy–$(NH_4)H_2PO_4$–H_2O[4,5]. The authors were interested in wet-mechanochemical preparations of HAp from Gy by Furuta *et al.*[5] In a similar way, Yokogawa *et al.*[6] studied the preparation in the system $CaHPO_4 \cdot 2H_2O$–CaO–H_2O and Boudeville *et al.*[7] studied a dry-mechanochemical preparation in the system $CaHPO_4 \cdot 2H_2O$–CaO. Mechanochemical reactions are based on mechanical energy (mainly shear stress) and frictional thermal energy given to reactants. Generally, thus prepared grinding powders are composed of very fine and chemically active particles. The present paper provides a dry-mechanochemical HAp preparation from Gy.

2 Experimental

About 1.5 g-mixtures of Gy (partly II–$CaSO_4$), Na_2HPO_4 (partly $(NH_4)_2HPO_4$), and additives (NaF, CaF_2, $Ca(OH)_2$) with the stoichiometric apatitic ratio were ground at room temperature in air for 3–24 h by using an automatic agate mortar (15 cmϕ, 250 rpm). Possible apatite formation reactions could be written stoichiometrically as follows:

$$10CaSO_4 \cdot 2H_2O + 6Na_2HPO_4 \longrightarrow 2HAp + 6Na_2SO_4 + 4H_2SO_4 + 18H_2O \quad (1)$$

$$10CaSO_4 + 6Na_2HPO_4 + 2H_2O \text{ (in air)} \longrightarrow 2HAp + 6Na_2SO_4 + 4H_2SO_4 \quad (2)$$

$$10CaSO_4\cdot 2H_2O + 6Na_2HPO_4 + 2NaF \longrightarrow 2FAp + 7Na_2SO_4 + 3H_2SO_4 + 20H_2O \quad (3)$$

$$10CaSO_4 + 6Na_2HPO_4 + 2NaF \longrightarrow 2FAp + 7Na_2SO_4 + 3H_2SO_4 \quad (4)$$

$$9CaSO_4\cdot 2H_2O + 6Na_2HPO_4 + CaF_2 \longrightarrow 2FAp + 6Na_2SO_4 + 3H_2SO_4 + 18H_2O \quad (5)$$

$$9CaSO_4\cdot 2H_2O + 6Na_2HPO_4 + Ca(OH)_2 \longrightarrow 2HAp + 6Na_2SO_4 + 3H_2SO_4 + 18H_2O \quad (6)$$

where FAp means fluorapatite ($Ca_5F(PO_4)_3$). For comparison, heating runs were also conducted by using an electric tube furnace. Ground samples were washed with water and characterized by XRD, FTIR, TG and SEM. XRD patterns were measured using an X-ray diffractometer Model M03X-HX (MAC Science) with a pyrolytic graphite monochoromator (CuKα, 40 kV-15 mA). FTIR spectra were obtained by the KBr method using an FTIR-8000PC (SHIMADZU) (resolution: 4 cm^{-1}, scanning times: 50). TG patterns were recorded using a Model TG-DTA 2000S (MAC Science) at a heating rate of 10 ℃/min (sample weight: *ca.* 20 mg). SEM observation was carried out using an SEM Model S-2380N (HITACHI) at an acceleration voltage of 15 kV.

3 Results and discussion

3·1 Dry-mechanochemical products

Table 1 summarizes dry-mechanochemical products in the different reaction systems. In the systems without additives, *i.e.*, Reactions (1) and (2), Gy was dehydrated simply into $CaSO_4\cdot 0.5H_2O$ by a grinding thermal effect as reported in the literature[8], and no formation of apatite was observed up to 24 h-grinding. The addition of the fluorides and $Ca(OH)_2$, *i.e.*, Reactions (3)–(6), was very effective for the formation of apatite. Actually, the apatites were judged to be FAp and carbonated HAp by XRD and FTIR. Such an easy formation of apatite even under dry conditions was unexpectedly.

3·2 Characterization of dry-mechanochemically formed apatite

Fig. 1 shows XRD patterns of mechanochemical products in the reaction systems (3) and (4). Crystallinities of the resulting apatitic products could be seen to correspond approximately to that of precipitated apatite prepared at 50–70 ℃. Almost the same XRD patterns from the both systems suggested that the H_2O generated by

Table 1 Dry-mechanochemical reaction products.

Starting materials			Phases of water-washed products identified by XRD and FTIR[a]	
Ca-salt	PO_4-salt	Additive	After ground for 6 h	After ground for 24 h
$CaSO_4\cdot 2H_2O$	Na_2HPO_4	—	$CaSO_4\cdot 2H_2O$, $CaSO_4\cdot 0.5H_2O$	$CaSO_4\cdot 2H_2O$, $CaSO_4\cdot 0.5H_2O$
$CaSO_4\cdot 2H_2O$	$(NH_4)_2HPO_4$	—	$CaSO_4\cdot 2H_2O$, $CaSO_4\cdot 0.5H_2O$	$CaSO_4\cdot 2H_2O$, $CaSO_4\cdot 0.5H_2O$
$CaSO_4\cdot 2H_2O$	Na_2HPO_4	NaF	FAp	FAp
$CaSO_4$	Na_2HPO_4	NaF	FAp	FAp
$CaSO_4\cdot 2H_2O$	Na_2HPO_4	CaF_2	FAp, CaF_2	FAp, CaF_2
$CaSO_4\cdot 2H_2O$	Na_2HPO_4	$Ca(OH)_2$	CO_3HAp	CO_3HAp

a) FAp : fluorapatite, CO_3HAp : carbonated hydroxyapatite.

Table 2 Reaction products using powder compacts of starting materials after heating for 3 days using electric furnace.

Starting materials			Identified phases by XRD and FTIR[a]	
Ca-salt	PO_4-salt	Additive	300℃	500℃
$CaSO_4\cdot 2H_2O$	Na_2HPO_4	—	$CaSO_4$, Na_2HPO_4	$CaSO_4$, Na_2HPO_4
$CaSO_4\cdot 2H_2O$	Na_2HPO_4	NaF	FAp, $CaSO_4$, Na_2HPO_4	FAp, $CaSO_4$, Na_2HPO_4
$CaSO_4\cdot 2H_2O$	Na_2HPO_4	CaF_2	FAp, $CaSO_4$, Na_2HPO_4	FAp, $CaSO_4$, Na_2HPO_4
$CaSO_4\cdot 2H_2O$	Na_2HPO_4	$Ca(OH)_2$	$CaSO_4$, Na_2HPO_4	CO_3HAp, $CaSO_4$, Na_2HPO_4

a) FAp : fluorapatite, CO_3HAp : carbonated hydroxyapatite

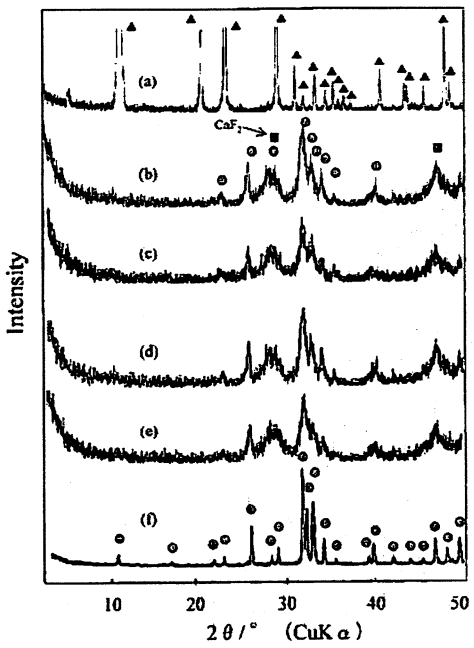

Fig. 1 XRD patterns of dry-mechanochemical products (water-washed) in the systems (3) and (4).
(a) : Reagent $CaSO_4 \cdot 2H_2O$
(b) : $CaSO_4 \cdot 2H_2O$–Na_2HPO_4–NaF, 3 h-ground
(c) : $CaSO_4 \cdot 2H_2O$–Na_2HPO_4–NaF, 24 h-ground
(d) : $CaSO_4$–Na_2HPO_4–NaF, 3 h-ground
(e) : $CaSO_4$–Na_2HPO_4–NaF, 24 h-ground
(f) : Synthetic HAp

the mechanochemical dehydration of Gy[8] did not contribute to the apatite formation.

Fig. 2 shows examples of FTIR spectra of dry-mechanochemical products. The peak at 3570 cm^{-1} and peaks at both 877 and around 1500 cm^{-1} are characteristic of OH and CO_3 in the apatite structure, respectively. The product in the system $CaSO_4 \cdot 2H_2O$–Na_2HPO_4–$Ca(OH)_2$ would be identified to be low crystalline carbonated HAp. The FAp's in the other two systems seemed to be partially hydroxylated.

The resulting products in the system (3) had no weight loss at 700–800 ℃ as shown in Fig. 3. This suggested that the chemical compositions of the apatite were nearly stoichiometric, *i.e.*, Ca /P mol ratio = 1.67, because the weight loss at 700–800℃ is an index of the non-stoichiometry of HAp[9]. Fig. 4 shows SEM micrographs of dry-mechanochemically formed apatite powders. Each powder particle was composed of aggregates of sub-micron primary grains.

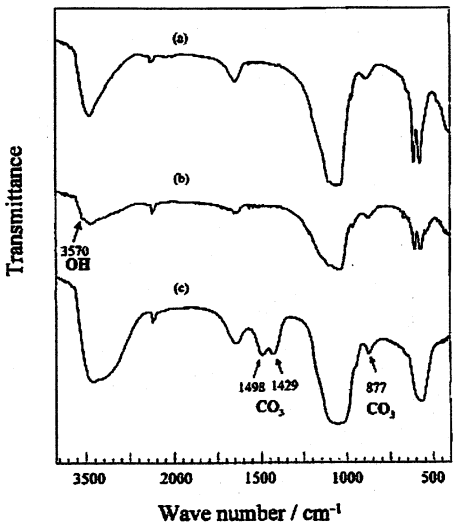

Fig. 2 FT-IR spectra of dry-mechanochemical products (24 h-ground, water-washed) in the reaction systems (3), (5) and (6).
(a) : $CaSO_4 \cdot 2H_2O$–Na_2HPO_4–NaF
(b) : $CaSO_4 \cdot 2H_2O$–Na_2HPO_4–CaF_2
(c) : $CaSO_4 \cdot 2H_2O$–Na_2HPO_4–$Ca(OH)_2$

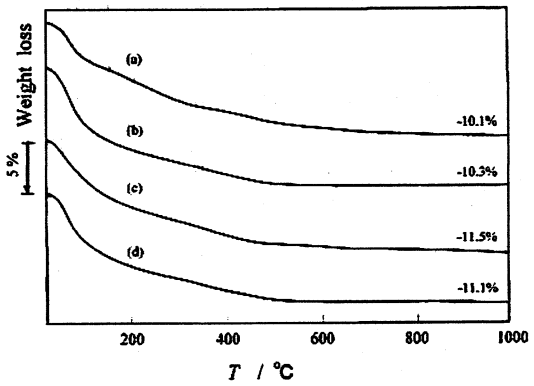

Fig. 3 TG curves of water-washed products from a mixture of $CaSO_4 \cdot 2H_2O$, Na_2HPO_4 and NaF.
(a) : 3 h-ground, (b) : 6 h-ground
(c) : 12 h-ground, (d) : 24 h-ground

3·3 Comparison of dry-mechanochemical formation and furnace-heating formation of apatite

The atomic diffusion is essential to the solid state reaction. The dry-mechanochemical formation of apatite means the occurrence of atomic diffusions among the reactants under dry conditions. As described in 3.2, mechanochemically

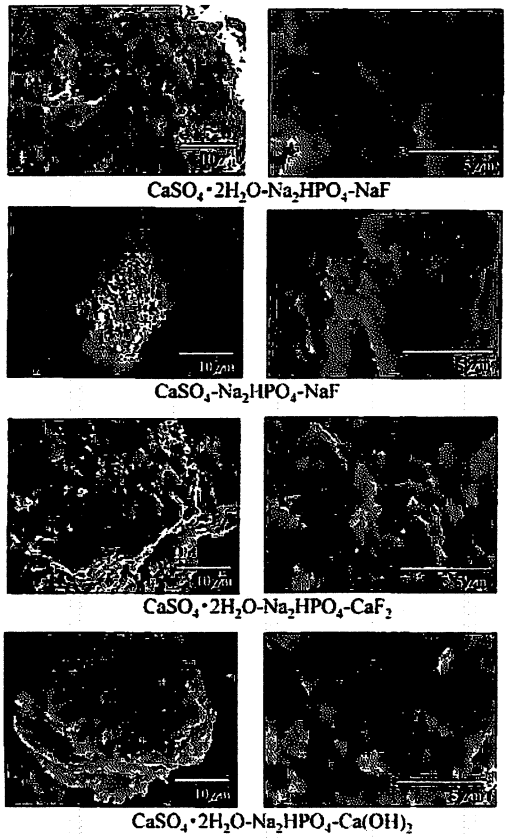

Fig. 4 SEM micrographs of apatite powders formed by dry-mechanochemical grinding for 24 h.

generated H_2O from Gy was not associated to the formation of apatite, *i.e.*, atomic diffusion. In order to get information about the apatite formation, electric furnace-heating runs were carried out. The resulting products are given in Table 2. No formation of apatite was observed in the systems without additive as well as the dry-mechanochemical runs. In the systems with the additives, FAp formed at least at 300℃, and HAp at 500℃. As it has been thought generally that the solid state formation of apatite under dry conditions occurs above 800℃, the low temperature formation of apatite was a new knowledge.

4 Conclusion

A dry-mechanochemical formation reaction for apatite was investigated by using gypsum as a new reaction system. No formation of apatite occurred from the mixtures of gypsum and phosphates; however, nearly stoichiometirc fluorapatite and hydroxyapatite were formed from mixtures of gypsum and phosphates added with NaF, CaF_2 and $Ca(OH)_2$, respectively. The H_2O in air and generated from gypsum and phosphates during dry-mechanochemical grinding was not associated to the formation of apatite.

References

1) Y. Nathan, J. Lucas, *Chem. Geology*, **9**, 99 (1972).
2) I. Mayer, S. Wahnon, S. Cohen, *Mater. Res. Bull.*, **14**, 1479 (1979).
3) K. Kandori, A. Yasukawa, T. Ishikawa, *Chem. Mater.*, **7**, 26 (1995).
4) H. Monma, S. Kobayashi, S. Takahashi, H. Kobayashi, "Proc. 3rd Int. Conf. ECOMATERIALS,", (1997) p. 71.
5) S. Furuta, H. Katsuki, *Phosphorus Lett.*, No. 36, 4 (1999).
6) Y. Yokogawa, M. Toriyama, Y. Kawamoto, T. Suzuki, K. Nishizawa, F. Nagata, R. Mucalo, *Chem. Lett.*, No. 1, 91 (1996).
7) P. Boudeville, B. Pauvert, M. P. Ginebra, E. Fernandez, J. A. Planell, *Key Eng. Mater.*, **192–195**, 115 (2001).
8) Y. Arai, T. Yasue, *Kogyo Kagaku Zashi*, **73**, 2603 (1970).
9) H. Monma, S. Ueno, T. Kanazawa, *J. Chem. Tech. Biotech.*, **31**, 15 (1981).

セッコウから水酸アパタイトへの乾式メカノケミカル転換反応

門間　英毅・大倉　利典・石田　昌寛・守吉　佑介*
（工学院大学工学部，*法政大学工学部）

セッコウを出発原料にしたアパタイト（$Ca_5X(PO_4)_3$）の新しい生成反応として，乾式メカノケミカル転換反応を検討した．カルシウム源として$CaSO_4 \cdot 2H_2O$，リン酸源としてNa_2HPO_4，X源添加物としてNaF，CaF_2および$Ca(OH)_2$を用いた種々の混合粉末を自動乳鉢で摩砕混合した（雰囲気：空気中）．X源添加無しではアパタイトは生成しなかったが，NaFおよびCaF_2添加系ではほぼ化学量論組成のフッ素アパタイトが，$Ca(OH)_2$添加系では炭酸含有水酸アパタイトを生成することがわかった．

業績リスト（大倉利典）2005年4月～2009年1月

審査付論文

1. 門間,西村,大倉, Characterization of Layer-Structured Octacalcium Phosphate/Dicarboxylate Composite, Phosphorus Research Bulletin, Vol. 18 127-134 (2005)
2. 門間,守吉,浦野,大倉, Preparation of Hydroxyapatite Porous Body and Tubular Particles from Gypsum, Phosphorus Research Bulletin, Vol. 19 166-171 (2005)
3. 古高,門間,大倉, Characteristic Reaction Processes in the System Brushite-NaOH solution, J. Eur. Ceram. Soc., 26, [4-5] 543-547 (2006)
4. 大倉,宮地,門間, Properties and Vibrational Spectra of Magnesium Phosphate Glasses for Nuclear Waste Immobilization, J. Eur. Ceram. Soc., 26, [4-5] 831-836 (2006)
5. 大倉,門間,山下, Superionic Conducting $Na_5SmSi_4O_{12}$- Type Glass-Ceramics: Crystallization Condition and Ionic Conductivity, J. Eur. Ceram. Soc., 26, [4-5] 619-622 (2006)
6. 大倉, ガラスによる高レベル放射性廃棄物の固化処理, J. Soc. Inorg. Mater. Japan, 13, 448-455 (2006)
7. 吉田,竹内,大倉,門間,若村,大崎,渡部, Super-Hydrophobic Photocatalytic Coatings Utilizing Apatite-Based Photocatalyst, Thin Solid Films, 502, 108-111 (2006)
8. 大倉,門間,山下, Na^+ Superionic Conducting Glass-Ceramics of Silicophosphates: Crystallization, Microstructure and Conduction Properties, Phosphorus Research Bulletin (Review), Vol. 20 111-118 (2006)
9. 根岸,大倉,関谷, $CaSO_4$-H_3PO_4-H_2O 系における二水セッコウの準安定性, J. Soc. Inorg. Mater. Japan, 14, 294-299 (2007)
10. 大倉,門間, ゾル - ゲル法による SiO_2-P_2O_5-GeO_2 系非晶質バルク体の合成, J. Soc. Inorg. Mater. Japan, 14, 363-368 (2007)
11. 門間,大倉,石田,守吉, Dry-Mechanochemical Conversion of Gypsum to Apatite, J. Soc. Inorg. Mater. Japan, 15, 37-41 (2008)
12. 大倉,門間, Ionic Conductivity of Na^+-Ion Implanted Na_2O-P_2O_5-SiO_2 Glass, J. Soc. Inorg. Mater. Japan, 15, 171-173 (2008)
13. 大倉,高橋,門間,山下, Effect of Substitution of Si with V and Mo on Ionic Conductivity of $Na_5YSi_4O_{12}$-Type Glass-Ceramics, Solid State Ionics, 179, 1291-1295 (2008)
14. 大倉,門間,山下, Na^+-Fast Ionic Conducting Glass-Ceramics of Silicophosphates, J. Electroceram. (Review), in press
15. 大倉,才丸,門間,山下, Ionic Conductivities of Nasicon-Type Glass-Ceramic Superionic Conductors in the System Na_2O-Y_2O_3-XO_2-SiO_2 (X=Ti, Ge, Te), Solid State Ionics, in press
16. 門間,大倉,原,守吉, Mechanochemical Properties of Octacalcium Phosphate and Brushite, Phosphorus Research Bulletin, in press

その他

著書　6
学術雑誌、研究機関への研究報告、展望、解説、論説など　10
国際学会の口頭発表　8
国内学会の口頭発表　49
特許　1

Nuclear Waste Research Advances [New magnesium phosphate glasses for high level nuclear waste immobilization]	in press	Nova Science Publishers (NY, USA)	大倉,門間

Solid State Ionics xxx (2009) xxx–xxx

Contents lists available at ScienceDirect

Solid State Ionics

journal homepage: www.elsevier.com/locate/ssi

Ionic conductivities of Nasicon-type glass-ceramic superionic conductors in the system Na_2O–Y_2O_3–XO_2–SiO_2 (X=Ti, Ge, Te)

Toshinori Okura [a,*], Mitsugu Saimaru [a], Hideki Monma [a], Kimihiro Yamasita [b]

[a] Department of Materials Science and Technology, Kogakuin University, 2665-1, Nakano, Hachioji-shi, Tokyo 192-0015, Japan
[b] Institute of Biomaterials and Bioengineering, Tokyo Medical and Dental University, 2-3-10, Kanda-Surugadai, Chiyoda-ku, Tokyo 101-0062, Japan

ARTICLE INFO

Article history:
Received 18 January 2008
Received in revised form 21 July 2008
Accepted 25 December 2008
Available online xxxx

Keywords:
Ionic conductivities
Nasicon-type
Glass-ceramics
Crystallization

ABSTRACT

Glass-ceramics of the titanium-, germanium- or tellurium-containing $Na_5RSi_4O_{12}$-type (R=rare earth; Y) Na^+-superionic conductors (N5YXS) were prepared by crystallization of glasses with the composition $Na_{3+3x}Y_{1-x}X_ySi_{3-y}O_9$ (X=Ti; NYTiS, Ge; NYGeS, X=Te; NYTeS), and the effects of X elements on the separation of the phase and the microstructural effects on the conduction properties of glass-ceramics were discussed. The combination of x and y was most varied in N5YGeS and more limited in the order of N5YTeS>N5YTiS. Their conductivities and activation energies are of the order of 10^{-2} S/cm at 300 °C and of 15 to 24 kJ/mol, respectively. The conductivity of the glass-ceramic N5YXS decreases giving the order N5YGeS>N5YTeS>N5YTiS. It is considered that this order corresponds to the N5 single phase region. Large enhancement of electrical conductivity was observed in the glass-ceramics as the grain growth was promoted with increase of heating temperature and heating time for crystallization.

1. Introduction

Glass-ceramics of the phosphorus containing $Na_5RSi_4O_{12}$-type (R=rare earth) [1,2] Na^+-superionic conductors (N5RPS) [3,4] have been developed by crystallization of glasses with the composition $Na_{3+3x-y}R_{1-x}P_ySi_{3-y}O_9$ (NRPS) [5–19]. These materials are reportedly comparable to the conventional ceramic Na^+-conductors such as Nasicon, β- and β″-aluminas (e. g., $NaAl_{11}O_{17}$ and $NaAl_5O_8$). The R elements have a significant effect on the crystallization of glasses [6], as well as on the conduction properties [1]. To date, polycrystalline N5RPS has been obtained with Sc, Y, Gd or Sm as the R element. It is currently assumed from the analogy with $Na_5RSi_4O_{12}$ that all the R ions can be octahedrally coordinated with the non-bridging oxide ions of the (SiO_4, PO_4)-tetrahedra of the 12-membered rings. The reported results on the silicate ceramics [1] show that the conductivity of N5RPS increases with increasing size of its R ions. Our phosphorus containing compositions have been confirmed superior to the mother composition of $Na_5RSi_4O_{12}$, especially in the production of the single-phase glass-ceramics. Considering the inference, our main work has recently been focused on the synthesis of various glass-ceramics with single-phase $Na_5RSi_4O_{12}$.

In the present study, the glass-ceramics of the titanium-, germanium- or tellurium-containing $Na_5RSi_4O_{12}$-type (R=Y) Na^+-superionic conductors (N5YXS) from the glasses with the composition $Na_{3+3x}Y_{1-x}X_ySi_{3-y}O_9$ (X=Ti; NYTiS, Ge; NYGeS, X=Te; NYTeS) were prepared, and the effects of X elements on the separation of the phase and the microstructural effects on the conduction properties of glass-ceramics were discussed.

2. Experimental

The glass-ceramics have been obtained under the appropriate sets of the parameters x and y of the composition formula $Na_{3+3x}Y_{1-x}X_ySi_{3-y}O_9$ ranging in x=0.1–0.55 and y=0.1–0.45. The precursor glasses were made by melting stoichiometric mixtures of reagent-grade powders of anhydrous Na_2CO_3, Y_2O_3, (TiO_2, GeO_2 or TeO_2) and SiO_2 at 1300–1400 °C for 1 h, followed by annealing for several hours at an optimum temperature (ca. 25 °C below the glass transition temperature (T_g) determined by DTA analysis). The temperatures employed for nucleation (T_n) and crystallization of glass specimens were also determined by DTA analysis. T_n was chosen in all the specimens as T_g+ca. 30 °C. The annealed specimens were heated up to 850–1000 °C for 5–24 h for crystallization. Crystalline phases were identified by the X-ray diffraction (XRD) method. Ionic conductivities of sintered disks were measured by the ac two-probe method with Au-sputtered blocking electrodes with a LF impedance analyzer. The temperature dependence of the conductivity was measured in a similar way at several temperatures ranging from room temperature to 350 °C.

3. Results and discussion

The N5YXS ionic conductors were successfully produced by crystallization of glasses. Most of the N5YXS compounds were obtained as uncracked glass-ceramics. Two other kinds of compounds are also known, and they are sometimes observed as the precursor or the impurity phase in the synthesis of $Na_5RSi_4O_{12}$-type (N5) conductors.

* Corresponding author.
E-mail address: okura@cc.kogakuin.ac.jp (T. Okura).

0167-2738/$ – see front matter © 2008 Published by Elsevier B.V.
doi:10.1016/j.ssi.2008.12.032

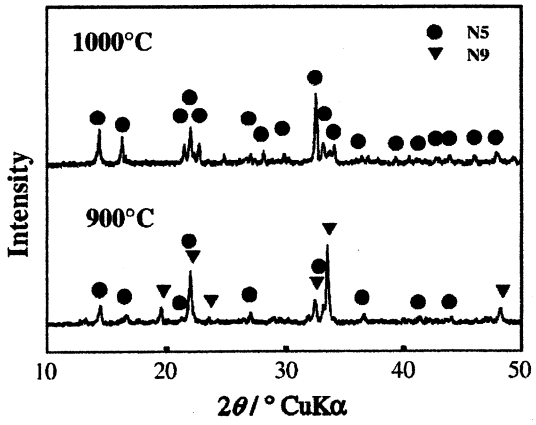

Fig. 1. X-ray diffraction patterns of $Na_{3.6}Y_{0.8}Ti_{0.2}Si_{2.8}O_9$ glass-ceramics heated at 900 °C (a) and 1000 °C (b) for 5 h. ● $Na_5RSi_4O_{12}$(N5), ▼ $Na_9RSi_6O_{18}$(N9).

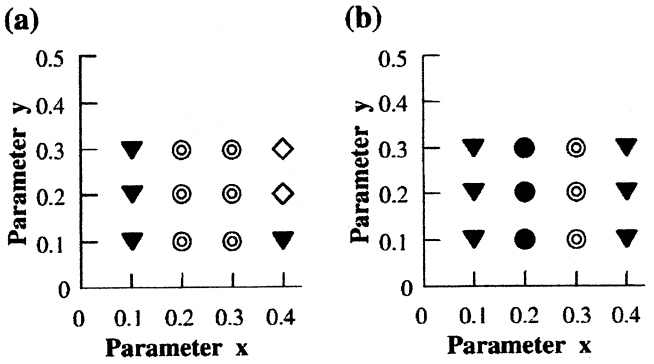

Fig. 2. The diagrams of phase-composition of NYTiS glass-ceramics heated at 900 °C (a) and 1000 °C (b) for 5 h. ● $Na_5RSi_4O_{12}$(N5), ▼ $Na_9RSi_6O_{18}$(N9), ◎ N5+N9, ◇ N3+N9.

These will be mentioned as $Na_3RSi_3O_9$-type (N3), and $Na_9RSi_6O_{18}$-type (N9) in the following. The ionic conductivity was strongly dependent upon the composition and the type of structure. Of these three kinds of compounds, N5 phase was the most conductive. Representative XRD patterns of the prepared glass-ceramics with NYTiS ($Na_{3.6}Y_{0.8}Ti_{0.2}Si_{2.8}O_9$ glass-ceramics heated at 900 °C (a) and 1000 °C (b) for 5 h) were given in Fig. 1. Figs. 2–4 show the diagrams of phase-composition-crystallization temperature of NYTiS, NYGeS and NYTeS glass-ceramics, respectively. The phase formed was dependent on composition and crystallization temperature. N5YTiS, N5YGeS and N5YTeS are obtained as a stable phase at high-temperatures. The crystallization of N5 single phase is strongly dependent both on the contents of yttrium and (titanium, germanium or tellurium) ions (or the values x and y correspond to the composition

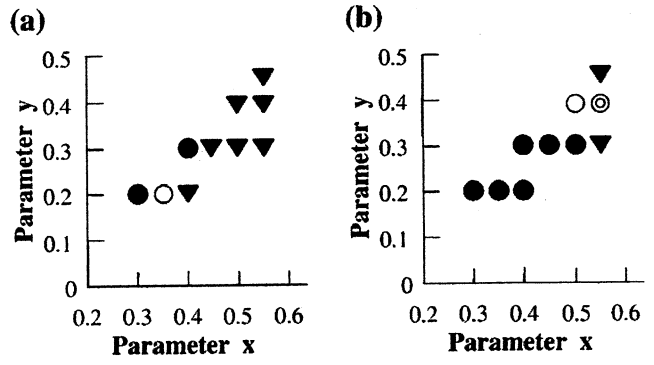

Fig. 3. The diagrams of phase-composition of NYGeS glass-ceramics heated at 900 °C (a) and 1000 °C (b) for 5 h. ● $Na_5RSi_4O_{12}$(N5), ▼ $Na_9RSi_6O_{18}$(N9), ○ N5+N3, ◎ N5+N9.

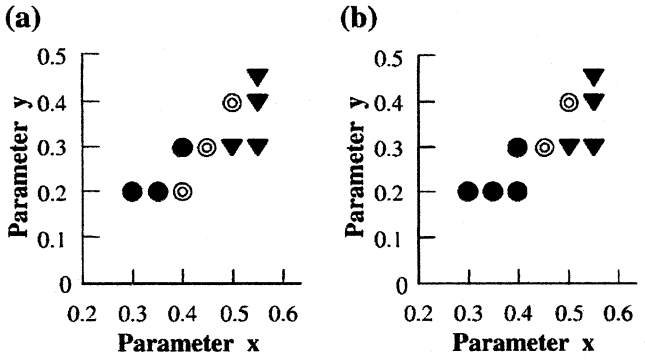

Fig. 4. The diagrams of phase-composition of NYTeS glass-ceramics heated at 900 °C (a) and 1000 °C (b) for 5 h. ● $Na_5RSi_4O_{12}$(N5), ▼ $Na_9RSi_6O_{18}$(N9), ◎ N5+N9.

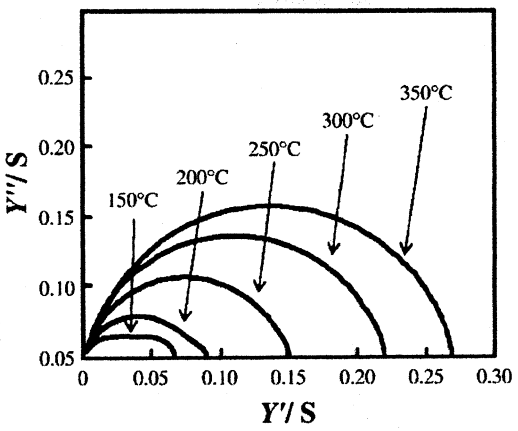

Fig. 5. Complex admittance diagram of the $Na_{3.6}Y_{0.8}Ti_{0.2}Si_{2.8}O_9$ glass-ceramics heated at 1000 °C for 5 h.

parameters in $Na_{3+3x}Y_{1-x}X_ySi_{3-y}O_9$). N3 and N9 phases can be crystallized as the high-temperature stable phases at the regions of higher [Y] and rather lower [Y], respectively. The effect of sodium content seems insignificant, because the value of [Na] is subordinately determined as [Na]=6−3[Y] (≒3+3x) depending on the content of yttrium. The combination of x and y was most varied in N5YGeS and more limited in the order of N5YTeS>N5YTiS. The complex admittance diagram of the N5 glass-ceramic specimen $Na_{3.6}Y_{0.8}Ti_{0.2}Si_{2.8}O_9$ is shown in Fig. 5 as an example. Those admittance diagrams were analyzed with the equivalent circuit shown in Fig. 6. The complex admittances of the measured glass-ceramic specimens consisted of two semicircles below 300 °C. The two intercepting points on the real axis are interpreted as the resistance of crystallized grains ($R_{G(c)}$) and the total resistance of grains and remaining glassy grain boundaries ($R_{GB(g)}$). Assume the complex admittance diagram shown in Fig. 7, where the parameters L_1 and L_2 are set here

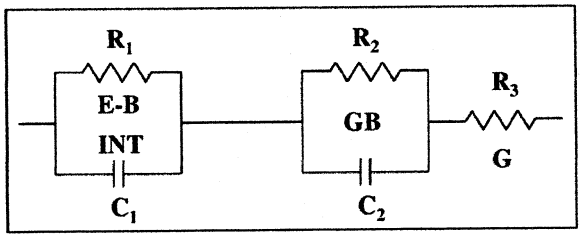

Fig. 6. Equivalent circuit employed for the admittance analysis. *E–B* INT, GB, and *G* represent the electrode–bulk interface, grain-boundaries and grains, respectively, and (R_1, C_1), (R_2, C_2), and R_3 are their resistances and capacitances.

Please cite this article as: T. Okura, et al., Solid State Ionics (2009), doi:10.1016/j.ssi.2008.12.032

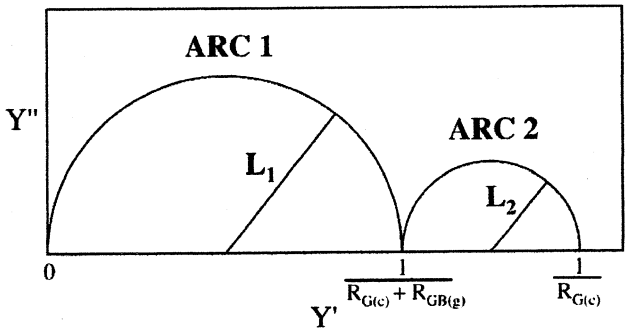

Fig. 7. An idealized diagram of complex admittance for glass-ceramics, in which arc 1 (ARC 1) and arc 2 (ARC 2) are related to the crystallized grains (G(c)) and remaining glasses (GB(g)). L_1, L_2, $R_{G(c)}$, and $R_{GB(g)}$ are, respectively, the radii of arcs 1 and 2, the resistances of G(c) and GB(g).

as the radii of the two arcs 1 and 2. Those parameters are related to one another as the following:

$$L_1 \propto 1/(R_{G(c)} + R_{GB(g)}),$$

and

$$L_2 \propto (1/R_{G(c)}) - 1/(R_{G(c)} + R_{GB(g)}).$$

Then,

$$L_2/L_1 = R_{GB(g)}/R_{G(c)}.$$

Therefore, in an ideal grass-ceramic where residual glass would have negligible influence on the total, arc 2 would be much smaller than arc 1, since $L_2/L_1 \rightarrow 0$. Fig. 8 shows examples of the temperature dependence Arrhenius plots made on the basis of the calculated conductivity values of grains and grain boundaries of the glass-ceramic specimens with the composition $Na_{3.6}Y_{0.8}Ti_{0.2}Si_{2.8}O_9$, in which the geometrical ratios of thickness to surface area for grains were also used for convenience for those of grain boundaries because of their undefinable shapes. The conductivity of the total bulk (T) is as close as to that of grains (G) at higher temperatures, while the resistance of grain boundaries (GB) dominates the whole conductance at lower temperatures. It should be noted that, concerned with the conduction properties of grain boundaries, only the activation energies are significant, since the conductivity of grain boundaries were calculated using the geometry ratio of surface area to thickness of the whole glass-ceramic bulk. Table 1 summarizes the conduction properties of the N5 glass-ceramics with $Na_{3.6}Y_{0.8}Ti_{0.2}Si_{2.8}O_9$, $Na_{4.2}Y_{0.6}Ge_{0.3}Si_{2.7}O_9$ and $Na_{4.2}Y_{0.6}Te_{0.3}Si_{2.7}O_9$ compositions. Their conductivities and activation energies are of the order of 10^{-2} S/cm at 300 °C and of 15 to 24 kJ/mol, respectively. The conductivity decreases giving the order N5YGeS>N5YTeS>N5YTiS. It is considered that this order corresponds to the N5 single phase region. Fig. 9 shows SEM photographs

Table 1
Conduction properties of the N5 glass-ceramics with $Na_{3.6}Y_{0.8}Ti_{0.2}Si_{2.8}O_9$, $Na_{4.2}Y_{0.6}Ge_{0.3}Si_{2.7}O_9$ and $Na_{4.2}Y_{0.6}Te_{0.3}Si_{2.7}O_9$ compositions

Specimen	Heat-treatment		σ_{300}	E_a/kJ mol^{-1}		
	Temperature	Time	/10^{-2} S cm^{-1}	T	G	GB
NYTiS	1000	5	2.5	15.5	19.8	10.0
NYGeS	900	5	4.0	21.1	17.3	44.0
	1000	5	4.5	24.1	19.3	56.6
	1000	24	6.7	22.9	20.6	67.2
NYTeS	900	5	3.2	19.8	18.7	43.7
	1000	5	4.6	21.8	20.5	56.6

σ_{300}: conductivity at 300 °C.
E_a: activation energy (T: total G: grain GB: grain boundary).

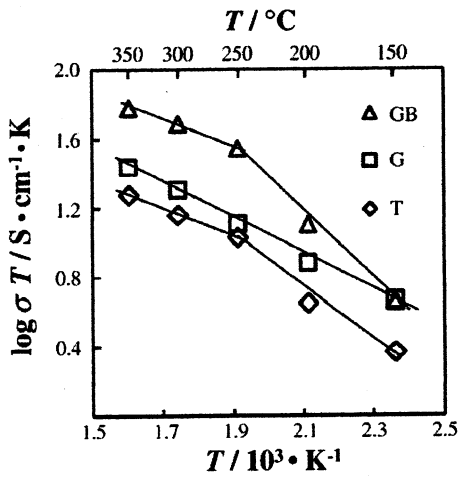

Fig. 8. Arrhenius plots of conductivities of grains (G), grain boundaries (GB) and total (T) for the $Na_{3.6}Y_{0.8}Ti_{0.2}Si_{2.8}O_9$ glass-ceramics heated at 1000 °C for 5 h.

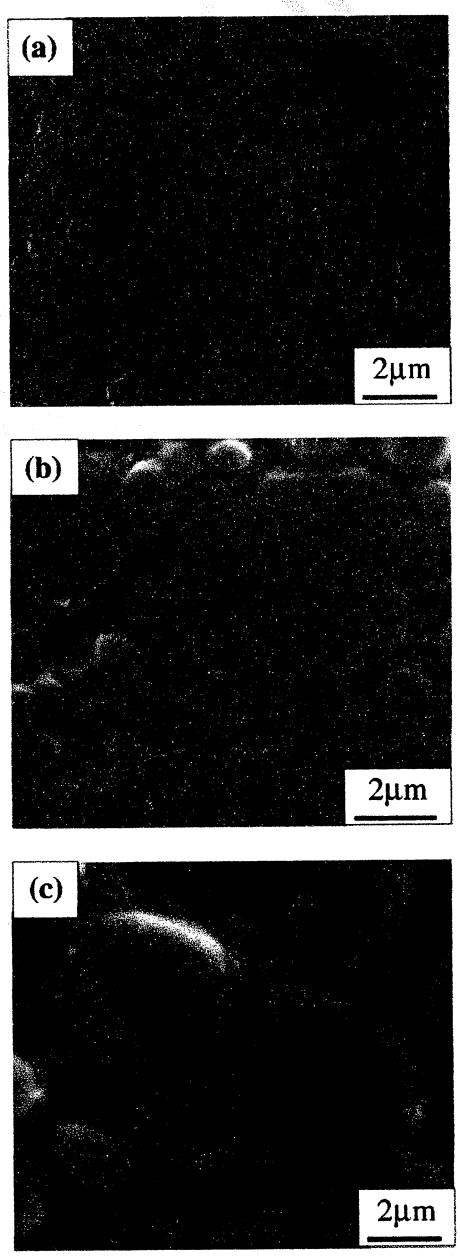

Fig. 9. SEM photographs of the $Na_{4.2}Y_{0.6}Ge_{0.3}Si_{2.7}O_9$ glass-ceramics heated at 900 °C for 5 h (a), at 1000 °C for 5 h (b) and at 1000 °C for 24 h (c).

Please cite this article as: T. Okura, et al., Solid State Ionics (2009), doi:10.1016/j.ssi.2008.12.032

of the microstructure of the $Na_{4.2}Y_{0.6}Ge_{0.3}Si_{2.7}O_9$ glass-ceramics heated at 900 °C for 5 h (a), at 1000 °C for 5 h (b) and at 1000 °C for 24 h (c), and the grain sizes of the specimens were about <1 μm (a), 4 μm (b) and 5 μm (c), respectively. Their conductivities of the specimens were 4.0×10^{-2} (a), 4.5×10^{-2} (b) and 6.7×10^{-2} (c) S/cm at 300 °C, respectively (Table 1). The grain growth is promoted with increase of heating temperature and heating time for crystallization. It was found that grain growth cause high conductivity.

4. Conclusions

We have successfully produced the glass-ceramics of the titanium-, germanium- or tellurium-containing N5 superionic conductors from the glasses with the composition $Na_{3+3x}Y_{1-x}X_ySi_{3-y}O_9$ (X=Ti, Ge, Te). The main features of this work are as follows:

1. The combination of x and y was most varied in N5YGeS and more limited in the order N5YTeS>N5YTiS.
2. Their conductivities and activation energies are of the order of 10^{-2} S/cm at 300 °C and of 15 to 24 kJ/mol, respectively.
3. The conductivity of the glass-ceramic N5YXS decreases giving the order N5YGeS>N5YTeS>N5YTiS. This order corresponds to the above result 1.
4. The grain growth is promoted with increase of heating temperature and heating time for crystallization.
5. Grain growth cause high conductivity.

References

[1] R.D. Shannon, B.E. Taylor, T.E. Gier, H.Y. Chen, T. Berzins, Inorg. Chem. 17 (1978) 958.
[2] H.U. Beyeler, T. Himba, Solid State Commun. 27 (1978) 641.
[3] Yamashita, T. Nojiri, T. Umegaki, T. Kanazawa, Solid State Ion. 35 (1989) 299.
[4] K. Yamashita, T. Nojiri, T. Umegaki, T. Kanazawa, Solid State Ion. 40/41 (1990) 48.
[5] K. Yamashita, S. Ohkura, T. Umegaki, T. Kanazawa, Solid State Ion. 26 (1988) 279.
[6] K. Yamashita, S. Ohkura, T. Umegaki, T. Kanazawa, J. Ceram. Soc. Jpn. 96 (1988) 967.
[7] K. Yamashita, T. Umegaki, M. Tanaka, T. Kakuta, T. Nojiri, J. Electrochem. Soc. 143 (1996) 2180.
[8] K. Yamashita, M. Matsuda, T. Umegaki, J. Mater. Res. 13 (1998) 3361.
[9] T. Okura, M. Tanaka, H. Kanzawa, G. Sudoh, Solid State Ion. 86 (1996) 511.
[10] K. Yamashita, M. Tanaka, T. Kakuta, M. Matsuda, T. Umegaki, J. Alloys Compd. 193 (1993) 283.
[11] T. Okura, K. Yamashita, T. Umegaki, Phosphorus Res. Bull. 6 (1996) 237.
[12] T. Okura, M. Tanaka, G. Sudoh, Mater. Res. Soc. Symp. Proc. 453 (1997) 611.
[13] T. Okura, K. Yamashita, Solid State Ion. 136–137 (2000) 1049.
[14] T. Okura, Y. Inami, H. Monma, S. Nakamura, K. Yamashita, Solid State Ion. 154 (2002) 361.
[15] T. Okura, M. Tanaka, H. Monma, K. Yamashita, G. Sudoh, J. Ceram. Soc. Jpn. 111 (2003) 257.
[16] T. Okura, H. Monma, K. Yamashita, Solid State Ion. 172 (2004) 561.
[17] T. Okura, H. Monma, K. Yamashita, Phosphorus Res. Bull. 17 (2004) 91.
[18] T. Okura, H. Monma, K. Yamashita, J. Eur. Ceram. Soc. 26 (2006) 619.
[19] T. Okura, H. Monma, K. Yamashita, Phosphorus Res. Bull. 20 (2006) 111.

Please cite this article as: T. Okura, et al., Solid State Ionics (2009), doi:10.1016/j.ssi.2008.12.032

J Electroceram
DOI 10.1007/s10832-008-9456-8

Na^+-fast ionic conducting glass-ceramics of silicophosphates

Toshinori Okura · Hideki Monma · Kimihiro Yamashita

Received: 22 November 2007 / Accepted: 13 February 2008

Abstract The Na^+-fast ionic conducting glass-ceramics with $Na_5YSi_4O_{12}$ (N5)-type structure were successfully synthesized using the composition formula of $Na_{3+3x-y}R_{1-x}P_ySi_{3-y}O_9$ for a variety of rare earth ions, R, under the appropriate composition parameters. In the crystallization of N5-type glass-ceramics, its relatives ($Na_3YSi_3O_9$ (N3)- and $Na_9YSi_6O_{18}$ (N9)-type glass-ceramics) structurally belonging to the family of $Na_{24-3x}Y_xSi_{12}O_{36}$ were found to crystallize as the precursor phase at low temperatures. In order to produce N5 single phase glass-ceramics, the concentration of both phosphorus and rare earth was found important. The meaning of the composition was evaluated by thermodynamic and kinetic studies on the phase transformation of metastable N3 or N9 phases to stable N5 phase with Na^+-fast ionic conductivity. The possible combinations of x and y became more limited for the crystallization of the fast ionic conducting phase as the ionic radius of R increased, while the Na^+ conduction properties were more enhanced in the glass-ceramics of larger R. These results are discussed in view of the structure and the conduction mechanism. Also studied were the microstructural effects on the conduction properties, which were dependent upon the heating conditions of crystallization. These effects were understood in relation to the grain boundary conduction properties as well as the transmission electron microstructural morphology of grain boundaries.

Keywords Glass-ceramics · Silicophosphate · Crystallization · Microstructure · Conduction properties

T. Okura (✉) · H. Monma
Department of Materials Science and Technology,
Faculty of Engineering, Kogakuin University,
2665-1 Nakano,
Hachioji, Tokyo 192-0015, Japan
e-mail: okura@cc.kogakuin.ac.jp

H. Monma
e-mail: monma@cc.kogakuin.ac.jp

K. Yamashita (✉)
Institute of Biomaterials and Bioengineering,
Tokyo Medical and Dental University,
2-3-10 Kanda-Surugadai,
Chiyoda, Tokyo 101-0062, Japan
e-mail: yama-k.bcr@tmd.ac.jp

1 Introduction

The use of glass-making processing is favorable for the fabrication of Na^+ conducting electrolyte tubes, which has been the key to the technological development of 1 MW Na/S secondary battery plants. However, the processing technique cannot be applied to well-known β- and β″-aluminas (e.g., $NaAl_{11}O_{17}$ and $NaAl_5O_8$) and Nasicons ($Na_{1+x}Zr_2P_{3-x}Si_xO_{12}$) because their high inclusion of Al_2O_3 or ZrO_2 brings about the inhomogeneous melting or crystallization from glasses. Alternatively, Nasicon-like glass-ceramics were synthesized using the composition with lower content of ZrO_2 ($mNa_2O{\cdot}xZrO_2{\cdot}yP_2O_5{\cdot}(100\text{-}m\text{-}x\text{-}y)SiO_2$ [m=20, 30 mol%]), however, the conductivities (σ) attained were, at most, as high as $\sigma_{300}=2\times10^{-2}$ S/cm at 300 °C with the activation energies (E_a) of approximately 30 kJ/mol [1]. These low conductivities were attributed to the crystallization of the poorly conductive rhombohedral phase in these Nasicon-like materials [1]. $Na_5YSi_4O_{12}$ (N5), which comprises 12-$(SiO_4)^{4-}$-tetrahedra membered skeleton structure (Fig. 1) [2, 3], is another Na^+-fast ionic conductor with $\sigma_{300}=1\times10^{-1}$ S/cm and E_a=25 kJ/mol [4–6]. A pioneering work on N5-type glass-ceramics has been performed by Banks et al. on the family of N5-type materials by substituting Y with Er, Gd or Sm [7].

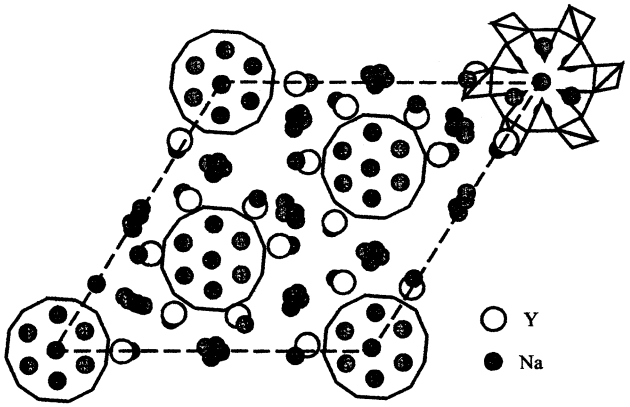

Fig. 1 Crystal structure of $Na_5YSi_4O_{12}$

However, their results were not completely satisfactory because of the relatively lower conductivities of $\sigma_{300}<2\times10^{-2}$ S/cm than the reported values of N5 [7]. This discrepancy may possibly have arisen from the occurrence of a less conductive metastable phase during crystallization [8], as is discussed below.

Contrary to the results of Banks et al., the present authors have produced glass-ceramics with $\sigma_{300}=1\times10^{-1}$ S/cm and $E_a=20$ kJ/mol [9], which were based on the phosphorus-containing N5-type materials discovered in the Na_2O–Y_2O_3–P_2O_5–SiO_2 system [9]. These N5-type materials have been obtained, as well as $Na_3YSi_3O_9$ (N3)-type [10–12] materials, with the composition formula originally derived for N3-type solid solutions and expressed as follows [13],

$$Na_{3+3x-y}Y_{1-x}P_ySi_{3-y}O_9 (x< 0.6, y< 0.5) \quad (1)$$

With the aim of searching for more conductive glass-ceramic N5-type materials, the verification of the validity of the generalized composition formula

$$Na_{3+3x-y}R_{1-x}P_ySi_{3-y}O_9 \quad (2)$$

for the synthesis of other kinds of rare earth N5-type glass-ceramics was studied first. Formula 2 is rewritten with formula 3 according to the formula N5.

$$Na_{4(3+3x-y)/3}Y_{4(1-x)/3}P_{4y/3}Si_{4(3-y)/3}O_{12} \quad (3)$$

In relation to previous works [9, 13], formula 2 was employed in this work, and formula 3 is referred to in the results. The trivalent ions employed here for R^{3+} were Sc^{3+}, In^{3+}, Er^{3+}, Gd^{3+}, Sm^{3+}, Eu^{3+}, Nd^{3+} and La^{3+} as well as Y^{3+}. These results are to be interpreted in terms of the effect of the rare earth ions on the crystallization of N5-type phase in glasses [14–19].

In the course of the fundamental studies on glass-ceramic $Na_{3+3x-y}R_{1-x}P_ySi_{3-y}O_9$, we have interestingly found the crystallization of those N3- and $Na_9YSi_6O_{18}$ (N9)-type phases as the precursors in the glasses [20]. These are the analogues to the silicates N3 and N9 [9, 21] and therefore are the same members of the family of $Na_{24-3x}Y_xSi_{12}O_{36}$ [11] as N5. Although we had also successfully synthesized those materials by the solid-state reactions of powders with the above composition of various sets of the parameters x and y [9, 21], the metastability of those precursor phases had not been noticed in the synthesis. It has been observed that such precursor phases were transformed to the Na^+-fast ionic conducting phase on specimens with appropriate sets of x and y. The present paper will deal with the thermodynamic and kinetic study on the phase transformation of metastable phases to the stable phase with Na^+-fast ionic conductivity. The superiority of our present materials to the other silicate N5 will also be detailed based on the kinetic results.

The microstructure of a glass-ceramic, including neck growth among grains as well as grain size, is generally affected by the crystallization process [22]. As the above mentioned devices utilize dc conduction properties of Na^+-fast ionic conductors, another aim was to study the microstructural effects on the conduction properties of a whole glass-ceramic [23–27]. Special attention was paid to the analysis of grain boundary properties using the Na_2O–Y_2O_3–P_2O_5–SiO_2 system. For the analysis of grain boundary properties, as will be discussed below, composition dependences of the conductivity of sodium silico-phosphate glasses containing Y_2O_3 were also studied in the Na_2O–Y_2O_3–P_2O_5–SiO_2 system. For convenience, the present materials are abbreviated as NaRPSi taken from the initials of the Na_2O–R_2O_3–P_2O_5–SiO_2 system.

2 Materials

2.1 Preparation of glasses and glass-ceramics

Precursor glasses were prepared from reagent-grade oxides of anhydrous Na_2CO_3, R_2O_3 (R=Y, Sc, In, Er, Gd, Sm, Eu, Nd, La), $NH_4H_2PO_4$ and SiO_2; the mechanically mixed powders according to formula 2 or appropriate compositions shown below were melted at 1350 °C for 1 h after calcinations at 900 °C for 1 h. The melts were quickly poured into a cylindrical graphite, then annealed at 500 °C for 3 h, giving NaRPSi glasses. The composition parameters studied were in the range of $0.2<x<0.6$ and $0<y<0.5$ of formula 2. As shown below, grain boundary conduction properties are discussed in relation to the properties of glasses. For the evaluation of the composition dependence of conductivity in Na^+ conducting glasses, various sodium yttrium silico-phosphate glass specimens with different atomic ratios of [Na]/[P+Si] and [Na]/[Y] were also prepared.

Crystallization was carried out according to the previous report [13]; bulk glasses were heated with an increasing rate

of 75 °C/h to a temperature above approximately 50 °C of the glass transition point, which had been determined in advance by differential thermal analysis (DTA). This pretreatment was done in order to obtain homogeneous nucleation [22]. After the annealing for 1 h, specimens were heated at temperatures of 800 to 1100 °C, depending on the composition, for 0.5 to 72 h, thereafter slowly cooled in a furnace with a decreasing rate of 150 °C/h to room temperature. These quenched glasses or glass-ceramic specimens were polished down with 0.5 μm diamond paste, thereafter subjected to the conductivity measurements.

2.2 Measurements and characterization

Ionic conductivities were measured by the complex impedance method on cylindrical glasses or glass-ceramics of typically 15 mm in diameter and 2 mm in thickness. Electrodes were prepared by sputtering of gold on polished surfaces. The applied ac field ranged from 5 to 10 MHz in frequency. The temperature dependence of the conductivity was measured in a similar way at several temperatures ranging from room temperature to 350 °C. The complex impedance or admittance loci of glass and glass-ceramics were analyzed by an equivalent circuit (Fig. 2), which was experimentally found to comprise one and two semicircles in NaRPSi glasses and glass-ceramics, respectively. The two intercepting points on the real axis are interpreted as the resistance of crystallized grains ($R_{G(c)}$) and the total resistance of grains and remaining grassy grain boundaries ($R_{GB(g)}$). Assume the complex admittance diagram shown in Fig. 3, where the parameters L_1 and L_2 are set here as the radii of the two arcs 1 and 2. Those parameters are related to one another as the following:

$$L_1 \propto 1/(R_{G(c)}+R_{GB(g)}) \tag{4}$$

and

$$L_2 \propto (1/R_{G(c)}) - 1/(R_{G(c)}+R_{GB(g)}) \tag{5}$$

Then,

$$L_2/L_1 = R_{GB(g)}/R_{G(c)} \tag{6}$$

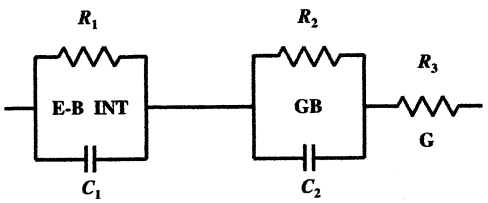

Fig. 2 Equivalent circuit employed for the admittance analysis. E-B INT, GB, and G represent the electrode-bulk interface, grain-boundaries and grains, respectively, and (R_1, C_1), (R_2, C_2), and R_3 are their resistances and capacitances

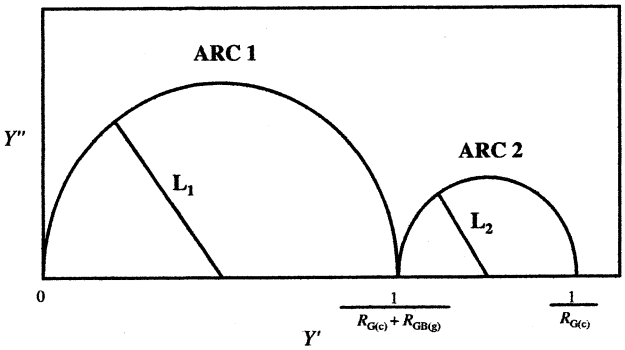

Fig. 3 An idealized diagram of complex admittance for glass-ceramics, in which arc 1 (ARC 1) and arc 2 (ARC 2) are related to the crystallized grains [G(c)] and remaining glasses [GB(g)]. L_1, L_2, $R_{G(c)}$, and $R_{GB(g)}$ are, respectively, the radii of arcs 1 and 2, the resistances of G(c) and GB(g)

Therefore, in an ideal grass-ceramic where residual grass would have negligible influence on the total, arc 2 would be much smaller than arc 1, since $L_2/L_1 \rightarrow 0$.

Crystalline phases of glass-ceramic specimens were identified by X-ray diffraction (XRD) method. The lattice parameters of the N5-type hexagonal unit cell were calculated by a least-squares method using the XRD peaks of (054), (044), (134), (440) and (024). Glass-ceramics of Y^{3+}-contained NaRPSi were subjected to scanning (SEM) and transmission electron microscope (TEM) for micro-structural analysis. Electron diffraction and compositional analyses were also performed to characterize the structure of the grain boundary.

For the description of a specific NaRPSi, R of the term will be replaced, respectively, with Y, Sc, In, Er, Gd, Sm, Eu, Nd and La as NaYPSi, NaScPSi, NaInPSi, NaErPSi, NaGdPSi, NaSmPSi, NaEuPSi, NaNdPSi and NaLaPSi for Y_2O_3, Sc_2O_3, In_2O_3, Er_2O_3, Gd_2O_3, Sm_2O_3., Eu_2O_3, Nd_2O_3 and La_2O_3.

3 Thermodynamic and kinetic study on the phase transformation

3.1 Composition dependence of precursor and high temperature stable phases

Figure 4 shows the composition dependence of both the precursor phases and the high temperature stable phases of glass-ceramic NaYPSi on the maps of phosphorus–yttrium [P–Y, Fig. 4(a)], yttrium–sodium [Y–Na, Fig. 4(b)] and phosphorus–sodium [P–Na, Fig. 4(c)], where the variables on the abscissas and ordinals are expressed with the composition parameters $1-x$, y and $3+3x-y$ for yttrium, phosphorus and sodium, respectively. As reported before [9, 20], N3- and N9-type NaYPSi glass-ceramics can be

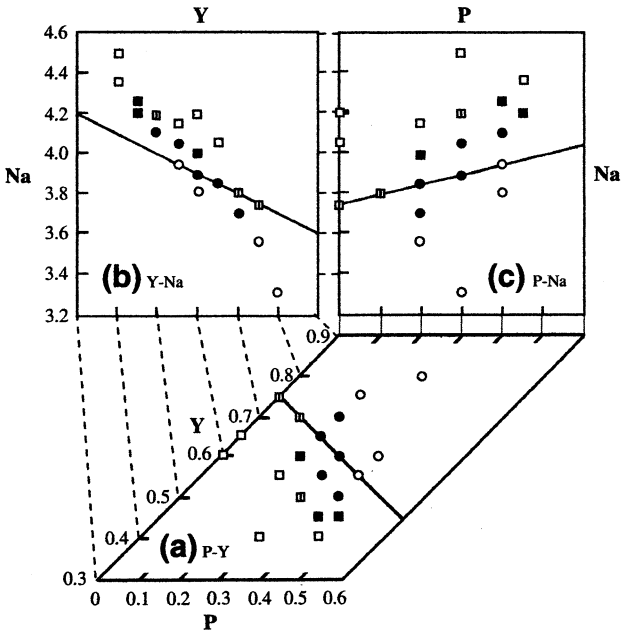

Fig. 4 Composition dependence of precursor (*pp*) and high temperature-stable phases (*sp*) of glass-ceramic NaRPSi on P–Y (**a**), Y–Na (**b**) and P–Na (**c**) maps, where precursor phases N3 and N9 are shown with *circles* and *squares*, respectively. High temperature-stable phases are shown in such a way that solid marks means that N5–NaRSi is the stable, while *open marks* indicate that the precursor phases are also stable even at high temperatures. Mixed phases are also shown: *open circle* pp = sp = N3; *filled circle* pp = N3, sp = N5; *open square* pp = sp = N9; *filled square* pp = N9, sp = N5; *open split square* pp = N9, sp = N9 + N5

crystallized as the high-temperature stable phases at the regions of higher [Y] ($1-x$>approximately 0.8) and rather lower [Y] ($1-x$<approximately 0.55), respectively, in the [Y]–[P] relation.

Concerning the precursor phases, only either N3- or N9-type NaYPSi was found in any composition, while N5-type NaYPSi was difficult to crystallize from glasses at low temperatures. It is also seen in the [P]–[Y] map [Fig. 4(a)] that, under a given phosphorus content ([P]<0.6) a composition with higher content of yttrium gives N3-type NaYPSi (open circle) as the precursor phase, while lower [Y] content results in N9-type phase (open square). The values of [Y] dividing the regions allowed for N3- and N9-type NaYPSi glass-ceramics decreased with increasing [P], and the boundary seems to locate slightly apart from the deduced line of [Y]=0.75−0.5[P] [9] shown with the solid line. Around the boundary region N5-type NaYPSi can be obtained as the stable phase at high temperatures (solid marks of circle or square). In the [Y]–[Na] or [P]–[Na] relations [Fig. 4(b) and (c)], the region where N5-type NaYPSi can be found as the high-temperature stable phase is found under approximately 3.6<[Na]<4.3. The effect of sodium content seems insignificant, because the value of [Na] is subordinately determined as [Na]=6−3[Y]–[P] (=3+3x−y) depending on the contents of both yttrium and phosphorus.

The above results may suggest that the [P]–[Y] relation dominates the region which is allowed for each NaYPSi at high temperatures. Considering this inference, we calculated the products of [P]×[Y] for all of the specimens. The values of [P]×[Y] were as follows (shown in Fig. 5); 0.16–0.25 for single phase N3-type NaYPSi, 0.14 for mixed phases of N3- and N5-type NaYPSi, 0.12–0.20 for single phase N5-type NaYPSi, 0–0.14 for the mixed phases of N5- and N9-type NaYPSi, and 0–0.17 for single phase N9-type NaYPSi, respectively. It was therefore deduced (Fig. 5) that the free energy of formation (ΔG_f) of N9-type NaYPSi would be the lowest in a lower region of [P]×[Y], N5-type NaYPSi may have the lowest ΔG_f in a medium [P]×[Y] region, and higher [P]×[Y] would lower ΔG_f of N3-type NaYPSi.

For a specimen in which N5-type NaYPSi is the stable phase at high temperatures, the aspect such as Fig. 6(a) would be illustrated in that ΔG of N3- or N9-type NaYPSi would be much smaller than that of N5-type NaYPSi near the crystallization temperature (T_c), and the value of N5-type NaYPSi would be lowered much less than of the two. Figure 6(b) indicates the aspect that ΔG or N3- or N9-type NaYPSi stable.

3.2 Kinetic effects of composition on the phase transformation

The kinetic effects of composition on the phase transformation are shown in Fig. 7, which compares the phase transformation rates of specimens $Na_{3.9}Y_{0.6}P_{0.3}Si_{2.7}O_9$ and $Na_{3.75}Y_{0.65}P_{0.3}Si_{2.7}O_9$. The transformation rate (α_v) of a

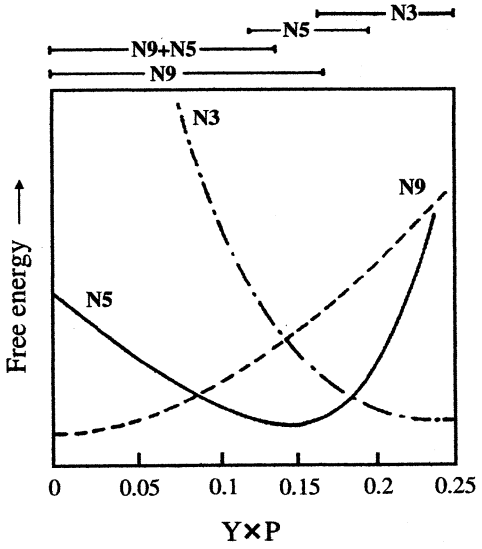

Fig. 5 Schematic figure of composition ([Y]×[P]) dependence of free energy of N5-, N3- and N9-type NaYPSi

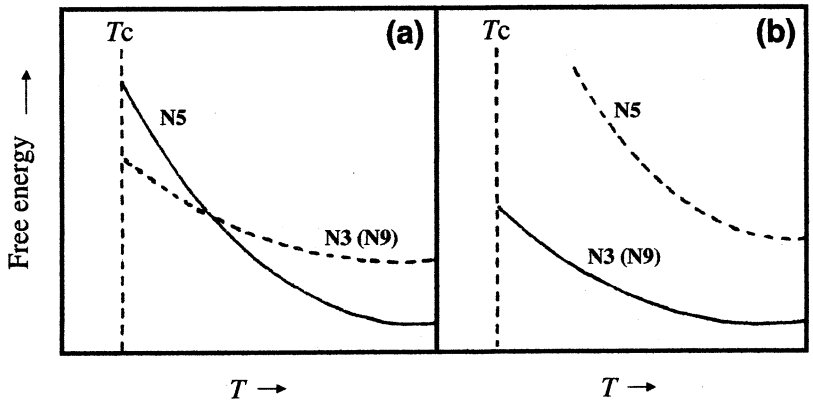

Fig. 6 Schematic figures of temperature dependence of free energy change of N5- and N3- or N9- type NaYPSi in the cases assuming N5- (**a**) and N3- (**b**) or N9-type (**b**) NaYPSi as the high temperature-stable phase, where *Tc* is the crystallization temperature

precursor phase to the stable N5 phase was determined as the weight ratio of N5-type NaYPSi in a glass-ceramic specimen. The value of α_v was experimentally obtained from the relationship of weight ratio to XRD intensity ratio, which relationship had been made previously by XRD intensity measurement on specimens with given weight ratio of N5-type NaYPSi to metastable phases. It is seen that the composition $Na_{3.9}Y_{0.6}P_{0.3}Si_{2.7}O_9$ is superior to the other, for the N5 single phase NaYPSi was difficult to obtain in the latter specimen. In specimen $Na_{3.9}Y_{0.6}P_{0.3}Si_{2.7}O_9$ a glass-ceramic of N5 single phase NaYPSi was easily obtained at a temperature higher than 900 °C for only three hours. The composition $Na_{3.75}Y_{0.75}Si_3O_9$ (or $Na_5YSi_4O_{12}$) was inferior in the same meaning.

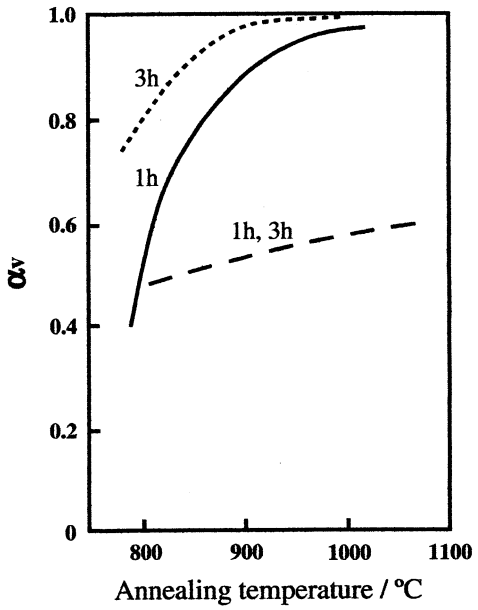

Fig. 7 Comparison of phase transformation rate (α_v) between specimens $Na_{3.9}Y_{0.6}P_{0.3}Si_{2.7}O_9$ (1-h annealing, *solid line*; 3-h annealing, *dotted line*) and $Na_{3.75}Y_{0.65}P_{0.3}Si_{2.7}O_9$ (1-h, 3-h-annealing, *dashed line*)

Figure 8 shows the kinetic characteristics of phase transformation of the metastable phase of N3- to N5-type NaYPSi of specimen $Na_{3.9}Y_{0.6}P_{0.3}Si_{2.7}O_9$ at various temperatures. The transition rates, α_v, of the silicophosphate NaYPSi were much higher than those of the $Na_{3.75}Y_{0.75}Si_3O_9$ silicate material.

The results shown were analyzed with the Avrami empirical equation, $\alpha_v=1-\exp(-kt^n)$, where k is the rate constant, and n is a constant. The data on α_v obtained at the initial and intermediate stages gave a linear relationship between $\ln(\ln(1-\alpha_v)^{-1})$ and $\ln(t)$ with a correlation coefficient of more than 0.99. The Avrami parameter and rate constants obtained are summarized in Table 1. Based on the Arrhenius relationship (Fig. 9), $k=A\exp(-E_v/RT)$ with E_v as the activation energy and constants A and R, on those k values which increased with increasing temperature, we obtained an activation energy of 1.2×10^3 kJ/mol, suggesting that the phase transformation can be rather difficult to take place. An addition of phosphorus and the excess sodium seem effective to the promotion of the phase transformation.

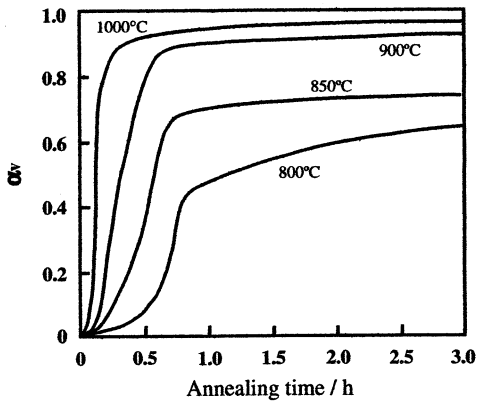

Fig. 8 Phase transformation rate (α_v) of N3- to N5-type NaYPSi on the specimen $Na_{3.9}Y_{0.6}P_{0.3}Si_{2.7}O_9$

Table 1 Kinetic parameters of phase-transformation of N3- to N5-type NaYPSi of $Na_{3.9}R_{0.6}Si_{2.7}O_9$.

Annealing temperature (K)	Avrami modulus n	ln k
1073	2.61	−20.7
1123	1.94	−14.6
1173	1.39	−9.54
1223	0.75	−4.41

4 Microstructural effects on conduction properties

4.1 Crystallization and phase diagram

As expected from the previously reported results on NaYPSi [8], the crystallization of the fast ionic conducting N5-type phase took place, depending both on the contents of [R] and [P], at temperatures of 800 °C to 1000 °C in most NaRPSi glasses of Er to Sm except for scandium and lanthanum NaRPSi glasses. The N5 single phase region was wider for NaRPSi of smaller R, but was limited at the [P]≈0 region. The effect of phosphorus substitution for Si is important in the crystallization of N5-type phase. The composition 7

$$Na_{3.9}R_{0.6}P_{0.3}Si_{2.7}O_9 \quad (7)$$

was experimentally shown as the most appropriate composition for the crystallization of N5-type phase.

The relationship between the ionic radius of R^{3+} (r_R) and the hexagonal lattice parameters of N5-type single phase is consistent with the previous report [4] on $Na_5RSi_4O_{12}$ (R=Sc−Sm) in the tendency that both lattice parameters increased with increasing r_R. The elongation of these lattice axes is attributed to the octahedral coordination of R^{3+} with the O^{2-} of SiO_4- or PO_4-tetrahedra of the 12-membered rings. The local structure around R^{3+} ions is to be further discussed below in relation to conduction properties. On the formation of N5-type single phase, the incorporation of excess sodium ions [$4(3+3x-y)/3-5=(12x-4y-3)/3$ in composition 3] and substitution of rare earth ions [$1-4(1-x)/3=(4x-1)/3$] must be accounted for in view of N5-type crystal structure.

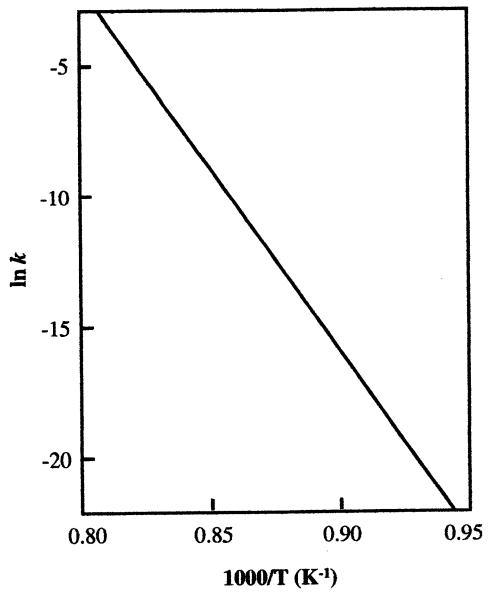

Fig. 9 Arrhenius-type plot of ln k with 1000/T of specimen $Na_{3.9}Y_{0.6}Si_{2.7}O_9$

Banks et al. [7] have reported the values of σ_{300} as 5×10^{-3} to 1×10^{-2} S/cm for glass-ceramic $Na_5RSi_4O_{12}$ (R=Er, Y, Gd, Sm), which are as low as those of the mixed phase NaRPSi specimens. The single phase N5-type glass-ceramic was not obtained in the present work. Based on the above crystallization analysis, their glass-ceramic specimens are reasonably considered to suffer from phase inhomogeneity brought about by insufficient annealing. The formation of N5-type structure from the precursor glasses is a matter of crystallization kinetics, since single-phase N5 has been synthesized in single crystal [2, 3, 28] or polycrystalline [5, 6, 10] form based on the composition of N5. It is noted here that the precursor phases identified were N3- or N9-type. Both N3 and N9 are considered to form iso-structural [11, 20, 29] with $Ca_3Al_2O_6$ [30] to be comprised of the skeleton structure of 6-membered SiO_4-tetrahedra rings [13]. It is generally known that phosphorus pentoxide acts as nucleating agent in the formation of glass-ceramics. It is therefore presumed at present that the substitution of an asymmetric PO_4-tetrahedron has the weakening effect on the bonding of the skeleton structure of 6-membered SiO_4-tetrahedra rings, resulting in the tendency to form the stable 12-membered structure.

4.2 Conduction properties of crystalline grains

The complex impedances and admittances of the measured NaRPSi glass-ceramics consisted of two semicircles below 300 °C. The two intercepting points on the real axis are interpreted as the resistance of crystallized grains (R_G) and the total resistance of grains and remaining glassy grain boundaries (R_{GB}). Shown in Fig. 10 are examples of the temperature dependence Arrhenius plots made on the basis of the calculated conductivity values of grains and grain boundaries of the glass-ceramic NaYPSi ($Na_{3.9}Y_{0.6}P_{0.3}Si_{2.7}O_9$) and NaSmPSi ($Na_{3.9}Sm_{0.6}P_{0.3}Si_{2.7}O_9$), in which the geometrical ratios of thickness to surface area for grains were also used for convenience for those of grain boundaries because of their undefinable shapes. Table 2 summarizes the measured conductivities (σ_{300}) and the calculated activation energies (E_a) assigned for grains of the glass-ceramics with composition 7 of Sc to La, regardless

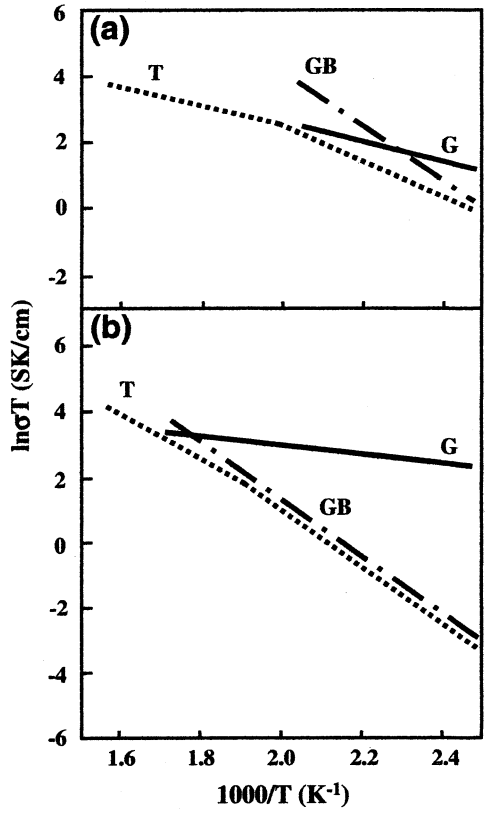

Fig. 10 The Arrhenius plots of the conductivities of grains (*G*), grain boundaries (*GB*) and the total bulk (*T*) of the glass-ceramic $Na_{3.9}Y_{0.6}P_{0.3}Si_{2.7}O_9$ (**a**) and $Na_{3.9}P_{0.3}Sm_{0.6}Si_{2.7}O_9$ (**b**)

of whether their crystalline phases are N5-type or not. The conductivities, σ_{300}, of single-phase NaRPSi specimens of Er to Sc range from 4×10^{-2} to 1×10^{-1} S/cm; in accordance the E_a falls in the range of 23 to 27 kJ/mol. In contrast, the mixed phase NaRPSi of Sc and In showed much smaller σ_{300} of 3×10^{-3} with an E_a of 35 to 40 kJ/mol, while non-NaRPSi glass-ceramics with unknown or mixed phases showed much lower conductivities of 1×10^{-5} to 1×10^{-4} S/cm with an E_a of 55 to 58 kJ/mol.

Table 2 Conduction properties of various NaRPSi glass-ceramics with composition $Na_{3.9}R_{0.6}Si_{2.7}O_9$.

R^{3+} (ions)	E_a kJ/mol	Conductivity (σ_{300})	Crystalline phase
Sc	35.3	3.2×10^{-3}	N5-type + unknown
In	39.8	3.1×10^{-3}	N5-type + unknown
Er	26.9	3.6×10^{-2}	N5-type
Y	26.6	6.6×10^{-2}	N5-type
Gd	23.0	1.3×10^{-1}	N5-type
Eu	24.4	5.2×10^{-2}	N5-type
Sm	20.9	6.3×10^{-2}	N5-type
Nd	55.1	2.2×10^{-5}	Unknown
La	57.8	1.6×10^{-4}	Unknown

The tendency of the conduction properties in single-phase NaRPSi specimens is consistent with the reported result measured on the corresponding polycrystalline $Na_5RSi_4O_{12}$ [4]; σ increased with increasing r_R. The previous works have proposed a mechanism that rare earth ions, octahedrally coordinated with the non-bridging oxide ions of the 12-membered rings of silica tetrahedra, work to expand the conduction paths for Na^+ ions along the *c*-axis [4, 28], which can explain the observed dependence of E_a on r_R in this work.

4.3 Structure and conduction properties of grain boundaries

As R_{GB} decreases rapidly with increasing temperature because of high $(E_a)_{GB}$ to a comparable value with R_G at 300 °C (Fig. 10), the total conductivities (R_G+R_{GB}) are dominated by grain boundary conductivity. The grain size-dependence of σ_{300} is therefore explained by the decrease in the number of poorly conductive grain boundaries with increasing grain size.

The conduction properties of grain boundaries were strongly dependent on the annealing conditions, although those of the grains were little changed by annealing temperature and time. Glass-ceramics are generally composites consisting of crystallized grains and small amounts of residual glass (<1%) [22]. To compare the properties of grain boundaries with those of glasses, the conduction properties of sodium yttrium silicophosphate glasses with various compositions were measured. Unlike glass-ceramics the impedance loci of glasses were comprised of one arc, which indicates that there is no polarization arising from microstructural inhomogeneity. Based on the intercepting points on the horizontal axis, the composition dependence of conduction properties of σ_{300} and E_a were evaluated. The value of σ_{300} ranged from 1×10^{-4} to 5×10^{-3} S/cm and E_a increased from 53 to 67 kJ/mol with [Na] or [Na]/[Y]. These results are also in good agreement with those reported for the glasses in the Na_2O–Y_2O_3–SiO_2 system [31]. The values of $(E_a)_{GB}$ of the specimens annealed below 950 °C for shorter times correspond to those in the range of glasses, strongly suggesting that their grain boundaries are a glassy matrix. The above mentioned dependence of $(E_a)_{GB}$ on [Na_2O] is explained by the well-known tendency that the conduction properties of glasses are improved by increasing [Na_2O], which provides the increase of carrier Na^+ ions. The ratio of [Na]/[Y] is also an important parameter for the conduction properties [31], showing an effect on the conduction properties similar to [Na_2O].

In order to identify the structure of the grain boundaries of the specimen ($Na_{3.9}Y_{0.6}P_{0.3}Si_{2.7}O_9$) annealed at 800 °C for 0.5 h, TEM analysis was performed both on grains and grain boundaries. The results show clear electron diffraction on grains, while not on grain boundaries. This fact confirms

that the grain boundaries are amorphous. Compositional analyses were also performed, however, [Na] was difficult to determine because of the evaporation by electron ablation. It was also observed that the glassy phase was condensed at triple points enclosed by grains, and that neck growth among the grains was well developed. Thus, it is reasonable to consider that the grain boundaries annealed at lower temperatures are amorphous, while those annealed at higher temperatures for longer periods of time are poorly conductive crystalline compounds in the specimens.

5 Summary

Na^+-fast ionic conducting glass-ceramics were produced using the sodium rare earth silicophosphate composition of $Na_{3+3x-y}R_{1-x}P_ySi_{3-y}O_9$, in which the rare earth elements of Sc to Sm were applicable to *R*. The meaning of the composition formula can be signified in the thermodynamic and kinetic study of crystallization and phase transformation of metastable to stable phase in the production of N5-type glass-ceramics. It was demonstrated that the medium value of content product as [P]×[R] is important in the crystallization of N5 single phase. Conduction properties of these glass-ceramics were strongly dependent upon the crystallization conditions as well as compositions. Not only complex impedance analysis but also TEM observation confirmed that this dependence was attributed to the conduction properties of grain boundaries which were glasses condensed at triple points enclosed by grains.

References

1. S. Morimoto, J. Ceram. Soc. Jpn. **97**, 1097 (1989)
2. B.A. Maksimov, Y.A. Kharitonov, A.N.V. Belov, Sov. Phys. Dokl. **18**, 763 (1974)
3. B.A. Maksimov, I.V. Petrov, A. Rabenau, H. Schulz, Solid State Ion. **6**, 195 (1982)
4. R.D. Shannon, B.E. Taylor, T.E. Gier, H.Y. Chen, T. Berzins, Inorg. Chem. **17**, 958 (1978)
5. H.U. Beyeler, T. Himba, Solid State Commun. **27**, 641 (1978)
6. H.Y.-P. Hong, J.A. Kafalas, M. Bayard, Mater. Res. Bull. **13**, 757 (1978)
7. E. Banks, C.H. Kim, J. Electrochem. Soc. **132**, 2617 (1985)
8. K. Yamashita, M. Tanaka, T. Umegaki, Solid State Ion. **58**, 231 (1992)
9. K. Yamashita, T. Nojiri, T. Umegaki, T. Kanazawa, Solid State Ion. **35**, 299 (1989)
10. R.D. Shannon, T.E. Gier, C.M. Foris, J.A. Nelen, D.E. Appleman, Phys. Chem. Miner. **5**, 245 (1980)
11. F. Cervantes, L.J. Marr, F.P. Glasser, Ceram. Int. **7**, 43 (1981)
12. C.H. Kim, B. Qiu, E. Banks, J. Electrochem. Soc. **132**, 1340 (1985)
13. K. Yamashita, S. Ohkura, T. Umegaki, T. Kanazawa, Solid State Ion. **26**, 279 (1988)
14. T. Okura, M. Tanaka, G. Sudoh, Mater. Res. Soc. Symp. Proc. **453**, 611 (1997)
15. T. Okura, K. Yamashita, T. Umegaki, Phosphorus Res. Bull. **6**, 237 (1996)
16. T. Okura, M. Tanaka, H. Monma, K. Yamashita, G. Sudoh, J. Ceram. Soc. Jpn. **111**, 257 (2003)
17. K. Yamashita, T. Umegaki, M. Tanaka, T. Kakuta, T. Nojiri, J. Electrochem. Soc. **143**, 2180 (1996)
18. T. Okura, M. Tanaka, H. Kanzawa, G. Sudoh, Solid State Ion. **86-88**, 511 (1996)
19. K. Yamashita, M. Tanaka, T. Kakuta, M. Matsuda, T. Umegaki, J. Alloys Comp. **193**, 283 (1993)
20. K. Yamashita, T. Nojiri, T. Umegaki, T. Kanazawa, Solid State Ion. **40**(41), 48 (1990)
21. K. Yamashita, S. Ohkura, T. Umegaki, T. Kanazawa, J. Ceram. Soc. Jpn. **96**, 967 (1988)
22. W.D. Kingery, H.K. Bowen, D.R. Uhlmann, *Introduction to Ceramics*, 2nd edn. (Wiley, New York, 1976), p. 368
23. T. Okura, H. Monma, K. Yamashita, J. Ceram. Soc. Jpn. **112**, S685 (2004)
24. T. Okura, H. Monma, K. Yamashita, Solid State Ion. **172**, 561 (2004)
25. T. Okura, K. Yamashita, Solid State Ion. **136**(137), 1049 (2000)
26. T. Okura, Y. Inami, H. Monma, S. Nakamura, K. Yamashita, Solid State Ion. **154**, 361 (2002)
27. T. Okura, H. Monma, K. Yamashita, J. Eur. Ceram. Soc. **26**, 619 (2006)
28. H.U. Beyler, R.D. Shannon, Appl. Phys. Lett. **37**, 934 (1980)
29. I. Maki, T. Sugimura, J. Ceram. Soc. Jpn. **78**, 129 (1970)
30. P. Mondal, J.W. Jeffery, Acta Cryst. **B31**, 689 (1975)
31. M.G. Alexander, Solid State Ion. **22**, 257 (1987)

Available online at www.sciencedirect.com
ScienceDirect
Solid State Ionics 179 (2008) 1291 – 1295
SOLID STATE IONICS
www.elsevier.com/locate/ssi

Effect of substitution of Si with V and Mo on ionic conductivity of $Na_5YSi_4O_{12}$-type glass-ceramics

Toshinori Okura [a,*], Tatsuya Takahashi [a], Hideki Monma [a], Kimihiro Yamashita [b]

[a] Department of Materials Science and Technology, Kogakuin University, 2665-1, Nakano, Hachioji-shi, Tokyo 192-0015, Japan
[b] Institute of Biomaterials and Bioengineering, Tokyo Medical and Dental University, 2-3-10, Kanda-Surugadai, Chiyoda-ku, Tokyo 101-0062, Japan

Received 6 September 2007; received in revised form 4 April 2008; accepted 10 April 2008

Abstract

Glass-ceramics of the vanadium- or molybdenum-containing $Na_5RSi_4O_{12}$-type (R = rare earth; Y) Na^+-superionic conductors were prepared by crystallization of glasses with the compositions $Na_{3+3x-y}Y_{1-x}V_ySi_{3-y}O_9$ (NYVS) or $Na_{3+3x-2y}Y_{1-x}Mo_ySi_{3-y}O_9$ (NYMS), and the effects of V or Mo elements on the separation of the phase and the microstructural effects on the conduction properties of glass-ceramics were discussed. The conductivities of the glass-ceramic NYVS and NYMS with the $Na_{3.9}Y_{0.6}V_{0.3}Si_{2.7}O_9$ and $Na_{3.7}Y_{0.7}Mo_{0.1}Si_{2.9}O_9$ compositions were 0.87×10^{-2} and 3.58×10^{-2} S/cm at 300°C, respectively, and the Na^+ ionic transport numbers of these glass-ceramics determined by Wagner polarization method were nearly 0.9 and 1 at 300°C, respectively.

Keywords: $Na_5YSi_4O_{12}$-type; Glass-ceramics; Crystallization; Conduction properties; Ionic transport number

1. Introduction

Glass-ceramics of the phosphorus containing $Na_5RSi_4O_{12}$ (N5)-type (R = rare earth) [1,2] Na^+-superionic conductors [3,4] have been developed by crystallization of glasses with the composition $Na_{3+3x-y}R_{1-x}P_ySi_{3-y}O_9$ (NRPS) [5–20]. These materials are reportedly comparable to the conventional ceramic Na^+-conductors such as NASICON, β- and β"-aluminas (e. g., $NaAl_{11}O_{17}$ and $NaAl_5O_8$). The R elements have a significant effect on the crystallization of glasses [6], as well as on the conduction properties [1]. To date, polycrystalline N5-type NRPS has been obtained with Sc, Y, Gd or Sm as the R element. It is currently assumed from the analogy with N5 that all the R ions can be octahedrally coordinated with the non-bridging oxide ions of the (SiO_4, PO_4)-tetrahedra of the 12-membered rings. The reported results on the silicate ceramics [1] show that the conductivity of N5-type NRPS increases with increasing size of its R ions. Only a limited number of works have been carried out for this type of Na^+ conductors, although the excellent ionic conduction property of the $Na_5RSi_4O_{12}$ has long been recognized for these two decades [21–29]. Our phosphorus containing compositions have been confirmed superior to the mother composition of N5, especially in the production of the single-phase glass-ceramics. Considering the inference, our main work has recently been focused on the synthesis of various glass-ceramics with N5 single-phase. In the present study, the vanadium or molybdenum with the tetrahedra configuration in the glass was substituted for the silicon. The glass-ceramics of the vanadium- or molybdenum-containing N5-type Na^+-superionic conductors were prepared by crystallization of glasses with the compositions $Na_{3+3x-y}Y_{1-x}V_ySi_{3-y}O_9$ (NYVS) or $Na_{3+3x-2y}Y_{1-x}Mo_ySi_{3-y}O_9$ (NYMS), and the effects of V or Mo elements on the separation of the phase and the microstructural effects on the conduction properties of glass-ceramics were discussed.

2. Experimental

The glass-ceramics have been obtained under the appropriate sets of the parameters x and y of the composition formulas $Na_{3+3x-y}Y_{1-x}V_ySi_{3-y}O_9$ or $Na_{3+3x-2y}Y_{1-x}Mo_ySi_{3-y}O_9$

* Corresponding author. Tel./fax: +81 426 28 4149.
E-mail address: okura@cc.kogakuin.ac.jp (T. Okura).

0167-2738/$ - see front matter © 2008 Elsevier B.V. All rights reserved.
doi:10.1016/j.ssi.2008.04.017

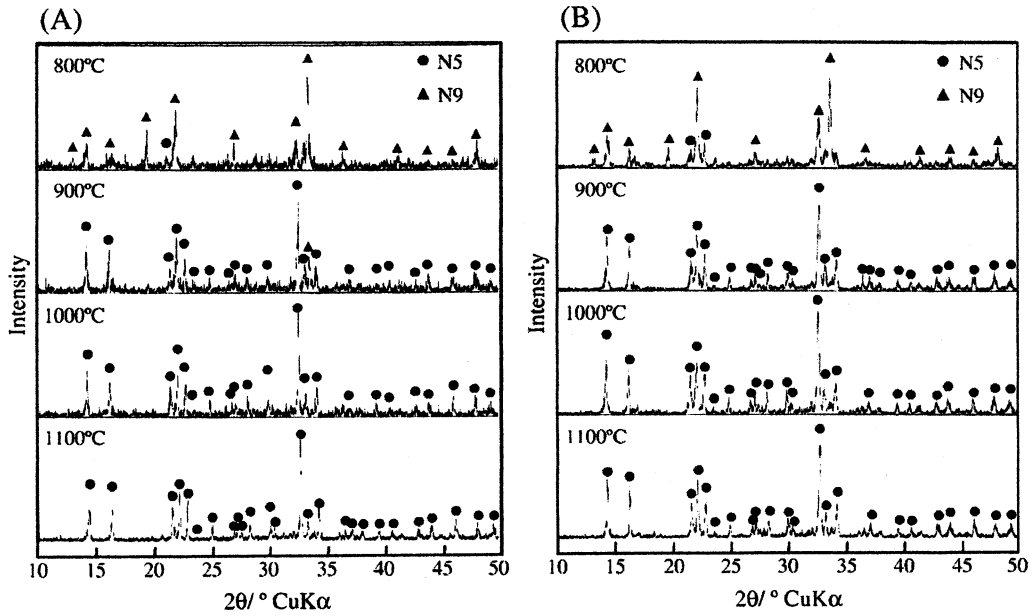

Fig. 1. X-ray diffraction patterns of the glass-ceramic specimens $Na_{3.9}Y_{0.6}V_{0.3}Si_{2.7}O_9$ (A) and $Na_{3.7}Y_{0.7}Mo_{0.1}Si_{2.9}O_9$ (B). ●$Na_5RSi_4O_{12}$(N5), ▲$Na_9RSi_6O_{18}$(N9).

ranging in $x = 0.3–0.5$ and $y = 0.1–0.4$. The precursor glasses were made by melting stoichiometric mixtures of reagent-grade powders of anhydrous Na_2CO_3, Y_2O_3, V_2O_5, MoO_3 and SiO_2 at 1400°C for 1h, followed by annealing for several hours at an optimum temperature (ca. 25°C below the glass transition temperature (Tg) determined by DTA analysis). The temperatures employed for nucleation (Tn) and crystallization of glass specimens were also determined by DTA analysis. Tn was chosen in all the specimens as Tg + ca. 30°C. The annealed specimens were heated up to 800–1100°C for 5–7h for crystallization. Crystalline phases were identified by the X-ray diffraction (XRD) method. Conduction properties of sintered disks were measured by the ac two-probe method with Au-sputtered blocking electrodes with a LF impedance analyzer. The temperature dependence of the conductivity was measured in a similar way at several temperatures ranging from room temperature to 350°C. Na^+ ionic transport numbers of these glass-ceramics were determined by Wagner polarization

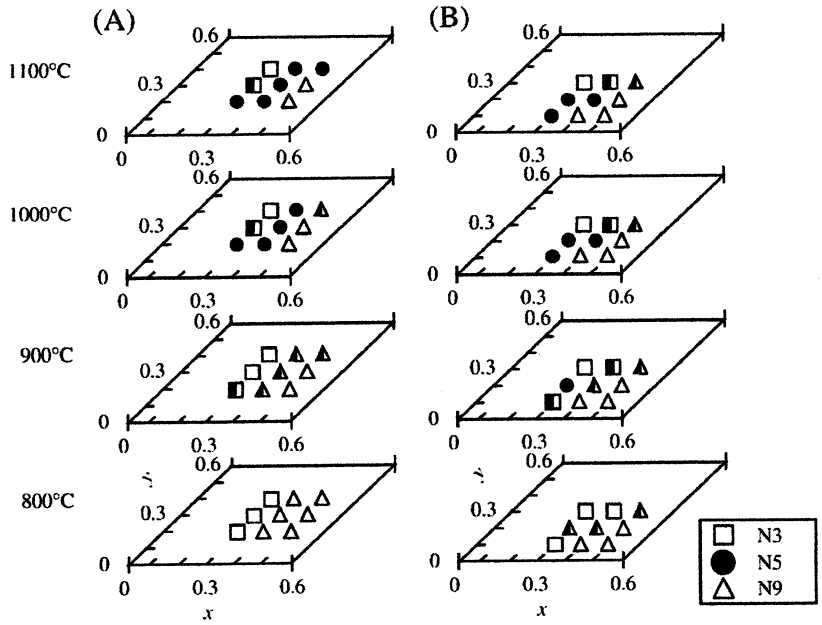

Fig. 2 The diagrams of phase-composition-crystallization temperature of NYVS (A) and NYMS (B) glass-ceramics crystallized at 800–1100 °C. ●$Na_5RSi_4O_{12}$(N5), □$Na_3RSi_3O_9$(N3), △$Na_9RSi_6O_{18}$(N9), ◧N5+N3, ▲N5+N9.

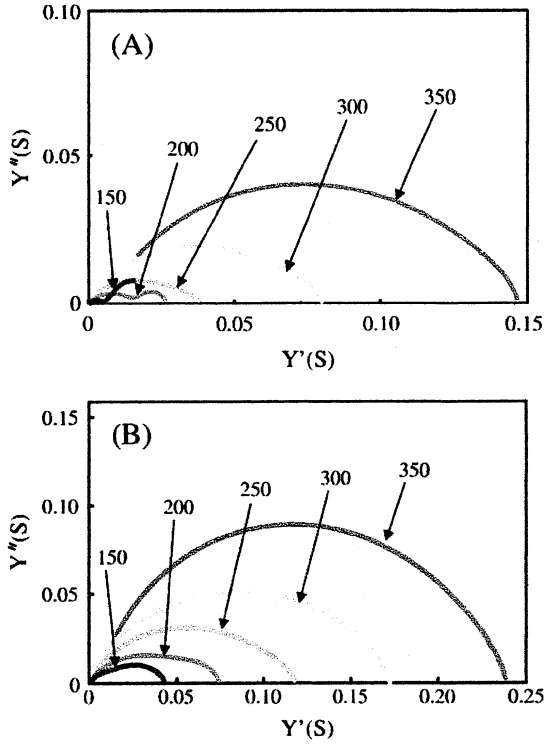

Fig. 3 Complex admittance diagrams of the glass-ceramic specimens $Na_{3.9}Y_{0.6}V_{0.3}Si_{2.7}O_9$ (A) and $Na_{3.7}Y_{0.7}Mo_{0.1}Si_{2.9}O_9$ (B).

method. The electronic conductivities of the glass-ceramic disks were measured by the dc two-probe method with Au-sputtered blocking electrodes with a potentiostat. The total conductivity minus electronic conductivity was estimated as the ionic conductivity.

3. Results and discussion

The N5-type NYVS and NYMS ionic conductors were successfully produced by crystallization of glasses. Most of compounds were obtained as uncracked glass-ceramics. Two other kinds of compounds are also known, and they are sometimes observed as the precursor or the impurity phase in the synthesis of N5-type conductors. These will be mentioned as $Na_3RSi_3O_9$ (N3)-type, and $Na_9RSi_6O_{18}$ (N9)-type in the following. Fig. 1 shows the XRD patterns of typical N5-type specimens $Na_{3.9}Y_{0.6}V_{0.3}Si_{2.7}O_9$ (A) and $Na_{3.7}Y_{0.7}Mo_{0.1}Si_{2.9}O_9$ (B). Shown in Fig. 2 are the diagrams of phase-composition-crystallization temperature of NYVS and NYMS glass-ceramics. N5-type NYVS and NYMS are obtained as a stable phase at high-temperatures. The crystallization of N5 single phase is strongly dependent both on the contents of yttrium and (vanadium or molybdenum) ions (or the values x and y correspond to the composition parameters in $Na_{3+3x-y}Y_{1-x}V_ySi_{3-y}O_9$ or $Na_{3+3x-2y}Y_{1-x}Mo_ySi_{3-y}O_9$). N3 and N9 phases can be crystallized as the high-temperature stable phases at the regions of rather lower [Y] and higher [Y], respectively. The effect of sodium content seems insignificant, because the value of [Na] is subordinately determined as [Na] = 6 − 3[Y] (= 3 + 3x) depending on the content of yttrium. It is assumed at present that the skeleton structures of N3 and N9 phases would consist of 6-(SiO_4, VO_4 or MoO_4)-tetrahedron-membered rings, while N5 phase has 12-tetrahedron-membered skeleton structure. Considering the case of the composition $Na_{2.75+3x}Y_{1-x}V_{0.25}Si_{2.75}O_9$, in which 1 of 12 SiO_4 tetrahedra are replaced by VO_4, N3 or N9 phases would consist of two kinds of rings such as 6-SiO_4-tetrahedron-membered rings and (5-SiO_4, 1-VO_4)-tetrahedron-membered rings. The skeleton of N5 phase, on the other hand, might consist of only one kind of (11-SiO_4-tetrakedron, 1-VO_4)-tetrahedron-membered rings. The inhomogeneous former structure would be thought more unstable in comparison with latter. Presently, we assume that the effect of the substitution of Si with V or Mo should be to bring about the difference of homogeneity in the ring structure between N5 and N3 or N9 phases. The complex admittance diagrams of the specimens (A) and (B) are shown in Fig. 3. The complex admittances of the measured glass-ceramic specimens consisted of two semicircles below 300°C. The two intercepting points on the real axis are interpreted as the resistance of crystallized grains and the total resistance of grains and

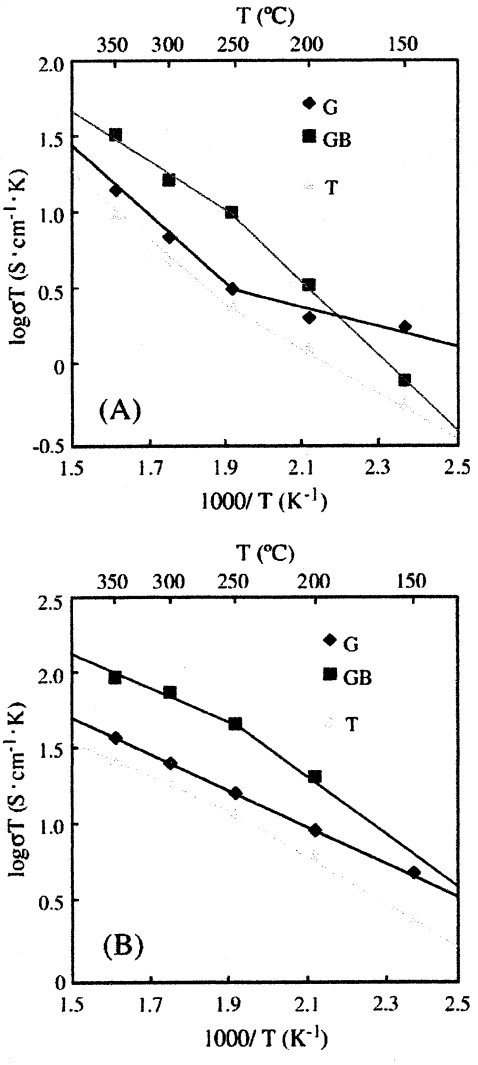

Fig. 4. Arrhenius plots of conductivities of grains (G), grain boundaries (GB) and total (T) for the glass-ceramic specimens $Na_{3.9}Y_{0.6}V_{0.3}Si_{2.7}O_9$ (A) and $Na_{3.7}Y_{0.7}Mo_{0.1}Si_{2.9}O_9$ (B).

Table 1
Total conductivities and activation energies of the glass-ceramic specimens $Na_{3.9}Y_{0.6}V_{0.3}Si_{2.7}O_9$ (A) and $Na_{3.7}Y_{0.7}Mo_{0.1}Si_{2.9}O_9$ (B)

Temperature (°C)	σ (10^{-2} S/cm)			Ea (kJ/mol)		
	G	GB	T	G	GB	T
A						
150	0.43	0.19	0.13	10.5	47.1	25.7
200	0.44	0.73	0.28			
250	0.62	1.97	0.47			
300	1.24	2.93	0.87	40.5	31.7	38.1
350	2.33	5.38	1.63			
B						
150	1.24	1.27	0.63	22.5	41.1	29.2
200	2.11	4.68	1.45			
250	3.33	9.45	2.46			
300	4.81	13.91	3.58		19.1	21.8
350	6.49	15.95	4.61			

σ: conductivity Ea: activation energy G: grain GB: grain boundary T: total.

remaining glassy grain boundaries. Fig. 4 shows examples of the temperature dependence Arrhenius plots made on the basis of the calculated conductivity values of grains and grain boundaries of the glass-ceramic specimens (A) and (B), in which the geometrical ratios of thickness to surface area for grains were also used for convenience for those of grain boundaries because of their undefinable shapes. The conductivity of the total bulk is as close as to that of grains at higher temperatures, while the resistance of grain boundaries dominates the whole conductance at lower temperatures. It should be noted that, concerned with the conduction properties of grain boundaries, only the activation energies are significant, since the conductivity of grain boundaries were calculated using the geometry ratio of surface area to thickness of the whole glass-ceramic bulk. The total conductivities and the activation energies calculated from the figures are summarizes in Table 1. The total conductivities of the specimens (A) and (B) were 0.87×10^{-2} and 3.58×10^{-2} S/cm at 300°C, respectively, and the activation energies of those specimens were 38.1 and 21.8kJ/mol, respectively. The combination of x and y was most varied in N5-type NYPS and more limited in N5-type NYVS and NYMS. The conductivity decreases giving the order NYPS > NYMS > NYVS. It is considered that this order corresponds to the N5 single phase region. We assume that the effect of the substitution of Si with V or Mo should be to bring about the difference of homogeneity in the N5 ring structure. The total and electronic conductivities and the Na^+ ionic transport numbers of the

Table 2
Total and electronic conductivities and the Na^+ ionic transport numbers of the glass-ceramic specimen $Na_{3.9}Y_{0.6}V_{0.3}Si_{2.7}O_9$ (A)

Temperature (°C)	σ_t (S/cm)	σ_e (S/cm)	t_i
150	1.312×10^{-3}	1.582×10^{-5}	0.988
200	2.752×10^{-3}	1.826×10^{-4}	0.934
250	4.728×10^{-3}	4.687×10^{-4}	0.901
300	8.715×10^{-3}	6.582×10^{-4}	0.924
350	1.627×10^{-2}	1.563×10^{-3}	0.904

σ_t: total conductivity σ_e: electoronic conductivity.
t_i: Ionic Transport Number.

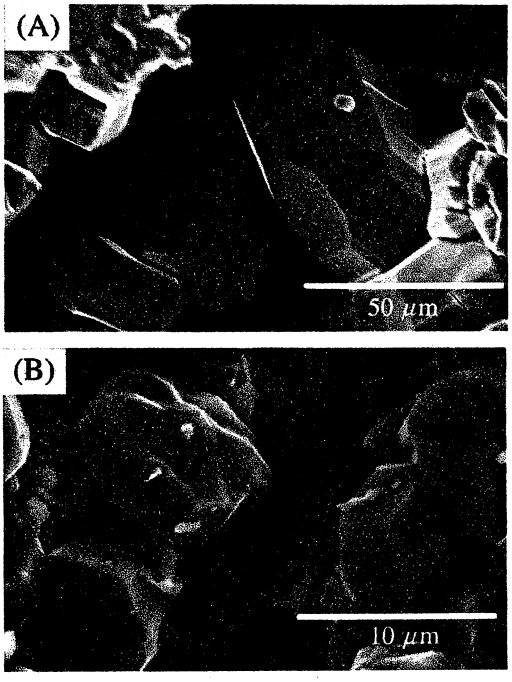

Fig. 5. SEM photographs of the glass-ceramic specimens $Na_{3.9}Y_{0.6}V_{0.3}Si_{2.7}O_9$ (A) and $Na_{3.7}Y_{0.7}Mo_{0.1}Si_{2.9}O_9$ (B).

specimen (A) determined by Wagner polarization method are summarizes in Table 2. The ionic transport numbers of the specimen (A) were nearly 0.9, while those of the specimen (B) were nearly 1. It is considered that about 10% of total conduction is electronic conduction (hopping conduction by transition metal vanadium) in the specimen (A). This result can explain following facts; the conductivity of the specimen (A) are lower than other N5 conductors [5–20], and it is seen in Fig. 4 for the specimen (A) that the lines drawn from the conductivity of grains are bending upwards. Fig. 5 shows SEM photographs of microstructure of the specimens (A) and (B). The grain sizes of the specimens were about 61 μm (A) and 10 μm (B).

4. Conclusions

We have successfully produced the glass-ceramics of the vanadium- or molybdenum-containing N5-type Na^+-superionic conductors from the glasses with the compositions $Na_{3+3x-y}Y_{1-x}V_ySi_{3-y}O_9$ or $Na_{3+3x-2y}Y_{1-x}Mo_ySi_{3-y}O_9$. The combination of x and y was most varied in N5-type NYPS and more limited in N5-type NYVS and NYMS. The conductivities of the glass-ceramic specimens with the $Na_{3.9}Y_{0.6}V_{0.3}Si_{2.7}O_9$ (A) and $Na_{3.7}Y_{0.7}Mo_{0.1}Si_{2.9}O_9$ (B) compositions were 0.87×10^{-2} and 3.58×10^{-2} S/cm at 300 °C, respectively. The conductivity decreases giving the order NYPS>NYMS>NYVS. It is considered that this order corresponds to the N5 single phase region. We assume that the effect of the substitution of Si with V or Mo should be to bring about the difference of homogeneity in the N5 ring structure. The Na^+ ionic transport numbers of these glass-ceramics determined by Wagner polarization method were nearly 0.9 for the specimen (A) and 1 for the specimen (B) at 300 °C, respectively. It is considered

that about 10% of total conduction is electronic conduction in the specimen (A). This result can explain following facts; the conductivity of the specimen (A) are lower than other N5 conductors, and it is seen in the temperature dependence Arrhenius plots for the specimen (A) that the lines drawn from the conductivity of grains are bending upwards.

References

[1] R.D. Shannon, B.E. Taylor, T.E. Gier, H.Y. Chen, T. Berzins, Inorg. Chem. 17 (1978) 958.
[2] H.U. Beyeler, T. Himba, Solid State Commun. 27 (1978) 641.
[3] K. Yamashita, T. Nojiri, T. Umegaki, T. Kanazawa, Solid State Ionics 35 (1989) 299.
[4] K. Yamashita, T. Nojiri, T. Umegaki, T. Kanazawa, Solid State Ionics 40/41 (1990) 48.
[5] K. Yamashita, S. Ohkura, T. Umegaki, T. Kanazawa, Solid State Ionics 26 (1988) 279.
[6] K. Yamashita, S. Ohkura, T. Umegaki, T. Kanazawa, J. Ceram. Soc. Jpn. 96 (1988) 967.
[7] K. Yamashita, T. Umegaki, M. Tanaka, T. Kakuta, T. Nojiri, J. Electrochem. Soc. 143 (1996) 2180.
[8] K. Yamashita, M. Matsuda, T. Umegaki, J. Mater. Res. 13 (1998) 3361.
[9] T. Okura, M. Tanaka, H. Kanzawa, G. Sudoh, Solid State Ionics 86 (1996) 511.
[10] K. Yamashita, M. Tanaka, T. Kakuta, M. Matsuda, T. Umegaki, J. Alloys Comp. 193 (1993) 283.
[11] T. Okura, K. Yamashita, T. Umegaki, Phosphorus Res. Bull. 6 (1996) 237.
[12] T. Okura, M. Tanaka, G. Sudoh, Mater. Res. Soc. Symp. Proc. 453 (1997) 611.
[13] T. Okura, K. Yamashita, Solid State Ionics 136–137 (2000) 1049.
[14] T. Okura, Y. Inami, H. Monma, S. Nakamura, K. Yamashita, Solid State Ionics 154 (2002) 361.
[15] T. Okura, M. Tanaka, H. Monma, K. Yamashita, G. Sudoh, J. Ceram. Soc. Jpn. 111 (2003) 257.
[16] T. Okura, H. Monma, K. Yamashita, J. Ceram. Soc. Jpn 112 (2004) S685.
[17] T. Okura, H. Monma, K. Yamashita, Solid State Ionics 172 (2004) 5–61.
[18] T. Okura, H. Monma, K. Yamashita, Phosphorus Res. Bull. 17 (2004) 91.
[19] T. Okura, H. Monma, K. Yamashita, J. Eur. Ceram. Soc. 26 (2006) 619.
[20] T. Okura, H. Monma, K. Yamashita, Phosphorus Res. Bull. 20 (2006) 111.
[21] B.A. Maksimov, Y.A. Kharitonov, I.V. Belov, Sov. Phys. Dokl. 18 (1974) 763.
[22] R.D. Shannon, H.Y. Chen, T. Berzin, Mater. Res. Bull. 12 (1977) 969.
[23] H.Y.-P. Hong, J.A. Kafalas, M. Bayard, Mater. Res. Bull. 13 (1978) 757.
[24] H.U. Beyeler, R.D. Shannon, H.Y. Chen, Solid State Ionics 3/4 (1981) 223.
[25] B.A. Maksimov, I.V. Petrov, A. Rabenau, H. Schulz, Solid State Ionics 6 (1982) 195.
[26] L.O. Atovmyan, O.S. Filipenko, V.I. Ponomarev, L.S. Lenova, E.A. Ukshe, Solid State Ionics 14 (1984) 137.
[27] E. Banks, C.H. Kim, J. Electrochem. Soc. 132 (1985) 2617.
[28] R.D. Shannon, T.E. Gier, C.M. Foris, J.A. Nelen, D.E. Appleman, Phys. Chem. Miner. 5 (1980) 245.
[29] J.C. Wang, M. Gaffari, S. Choi, J. Chem. Phys. 63 (1975) 772.

Journal of the Society of Inorganic Materials, Japan **15**, 171–173 (2008)

Note

Ionic Conductivity of Na^+-Ion Implanted Na_2O–P_2O_5–SiO_2 Glass

Toshinori OKURA and Hideki MONMA
(Department of Materials Science and Technology, Faculty of Engineering, Kogakuin University, 2665-1, Nakano, Hachioji, Tokyo 192-0015)

The effects of Na^+-ion implantation for the Na_2O–P_2O_5–SiO_2 glass on the conduction properties were discussed. Ionic conductivity was measured by the ac two-probe method. Large enhancement of ionic conductivity has been observed in the glass by ion implantation of Na^+ ions at 200 keV with a flux density of 10^{15} ions per cm^2. Upon this implantation the ionic conductivity of the $10Na_2O \cdot 60P_2O_5 \cdot 30SiO_2$ glass at 300℃ drastically increased from 3.4×10^{-7} S·cm^{-1} to 6.2×10^{-5} S·cm^{-1}.

(Received Aug. 20, 2007)
(Accepted Dec. 18, 2007)

Key words : Ionic conductivity, Ion implantation, Na_2O–P_2O_5–SiO_2 glass

1 Introduction

Clearly, preparing superionic material in amorphous form may have some advantages such as ease of fabrication, high volume production and good mechanical strength. Considering these advantages, sodium superionic conducting glass is a promising electrolyte material for a variety of electrochemical devices. Cation disorder is known to enhance ionic mobility and in amorphous systems cation disorder is expected to a large extent[1]. In this work, we consider that a material processing technique to introduce a large amount of mobile Na^+ ions into samples is required to realize the ionic conduction in the Na_2O–P_2O_5–SiO_2 glass system. Here, we report that a large enhancement of the electrical conductivity, probably due to Na^+ ions, has been obtained in the Na_2O–P_2O_5–SiO_2 glass by ion implantation of Na^+ ions[2),3)].

2 Experimental

Substrate glass used for Na^+-ion implantation[4)] was the $10Na_2O \cdot 60P_2O_5 \cdot 30SiO_2$ glass. The glass was prepared from reagent-grade oxides of anhydrous Na_2CO_3, $NH_4H_2PO_4$ and SiO_2; the mechanically mixed powder was melted at 1350℃ for 1 h after calcination at 900 ℃ for 1 h. The melt was quickly poured into cylindrical graphite, and then annealed at 500℃ for 3 h. The quenched glass specimens were polished down with 0.5 μm diamond paste. Approximately 5 mm thick glass disk was implanted with 200 keV Na^+ ions with flux density of 10^{15} ions·cm^{-2} at room temperature. The current density was 3 μA·cm^{-2} and the tilt angle was 0°. The depth profile of implanted Na^+ ions was calculated with the LSS theory[5)]. X-ray diffraction (XRD) measurements for the glass disks before and after Na^+-ion implantation were performed. Ionic conductivities of the glass disks before and after Na^+-ion implantation were measured by the ac two-probe method with Au-sputtered blocking electrodes with a LF impedance analyzer. The applied ac field ranged from 5 to 10 MHz in frequency. The temperature dependence of the conductivity was measured in a similar way at several temperatures ranging from room temperature to 350℃.

3 Results and discussion

Fig. 1 shows depth profile of implanted Na^+ ions calculated with the LSS theory. The Gaussian distribution was obtained in the surface layer. The calculated mean range and peak concentration were 0.38 μm and 4.7×10^{19} cm^{-3} for 200 keV Na^+ ions with flux density of 10^{15} ions·cm^{-2}, respectively.

Fig. 2 shows the XRD patterns of the specimens before and after Na^+-ion implantation. Although the glass specimen seemed to be possible to crystallize by the Na^+-ion implantation, the XRD pattern of the specimen exhibited amorphous phase. No cracking was perceived

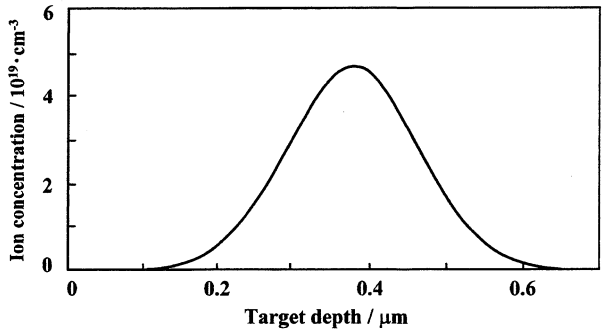

Fig. 1 Depth profile of implanted Na^+ ions calculated with the LSS theory.

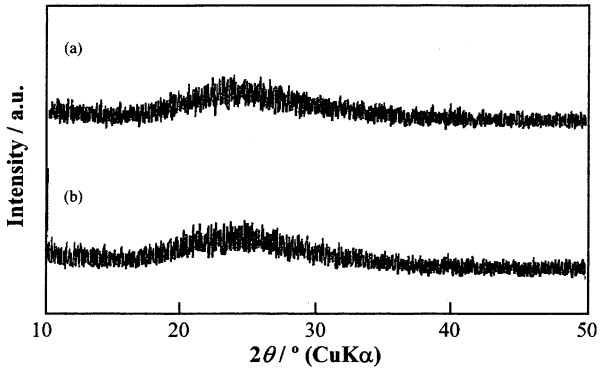

Fig. 2 X-ray diffraction patterns of $10Na_2O \cdot 60P_2O_5 \cdot 30SiO_2$ glasses before and after Na^+-ion implantation.
(a): Before Na^+-ion implantation
(b): Na^+-ion implantation

for the implanted surface.

The complex admittance diagrams were analyzed with the equivalent circuit shown in Fig. 3. I and G represent the electrode-glass interface and the whole bulk glass, respectively. R and C are their resistance and capacitance, respectively. The admittance diagrams of the specimen after Na^+-ion implantation are shown in Fig. 4 as an example, where Y' and Y'' express the real and imaginary part of the admittance, respectively. The intercepting point A on the real (Y') axis is interpreted as $1/(R_I+R_G)$ corresponding to a zero frequency, and the point B is interpreted as $1/R_G$ corresponding to an infinite frequency. The complex admittances of the measured glass specimens were analyzed by the method mentioned above. The analyzed results are shown in the form of the temperature dependence Arrhenius plots. Fig. 5 shows the Arrhenius plots made on the basis of the R_G of the glass specimens.

Table 1 summarizes the conduction properties

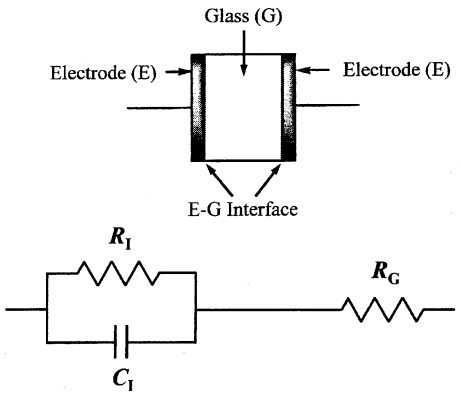

Fig. 3 Equivalent circuit employed for the admittance analysis.

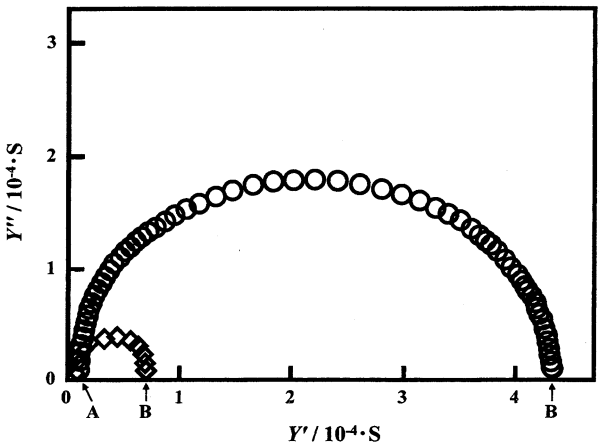

Fig. 4 Complex admittance diagrams of $10Na_2O \cdot 60P_2O_5 \cdot 30SiO_2$ glass after Na^+-ion implantation.
○ : 300℃, ◇ : 250℃

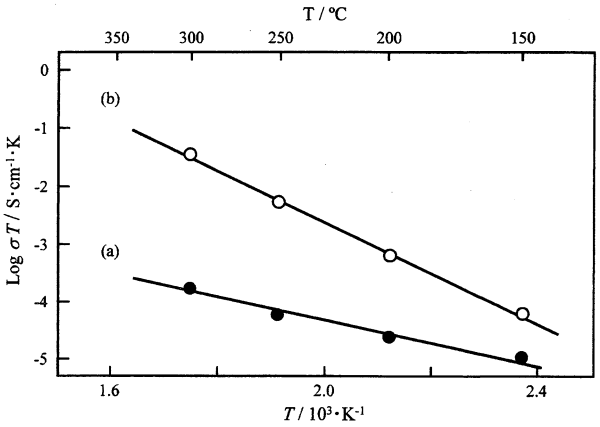

Fig. 5 Arrhenius plots of conductivities for $10Na_2O \cdot 60P_2O_5 \cdot 30SiO_2$ glasses before and after Na^+-ion implantation.
(a) : Before Na^+-ion implantation
(b) : Na^+-ion implantation

Table 1 Conduction properties of $10Na_2O \cdot 60P_2O_5 \cdot 30SiO_2$ glasses before and after Na^+-ion implantation.

Dose (ions·cm^{-2})	σ_{150} (S·cm^{-1})	σ_{300} (S·cm^{-1})	E_a (kJ·mol^{-1})
Before ion implantation	6.5×10^{-8}	3.4×10^{-7}	63.9
10^{15}	2.1×10^{-7}	6.2×10^{-5}	84.8

of the $10Na_2O \cdot 60P_2O_5 \cdot 30SiO_2$ glass samples before and after Na^+-ion implantation, where σ_{150} and σ_{300} are the conductivities at 150℃ and 300℃, respectively, and Ea is the activation energy calculated from the slope of the line in Fig. 5. The glass sample before Na^+-ion implantation showed the ionic conductivity of 3.4×10^{-7} S·cm^{-1} at 300℃. The ionic conductivity of the glass was drastically enhanced from 3.4×10^{-7} S·cm^{-1} to 5.8×10^{-5} S·cm^{-1} at 300℃ upon implantation of 200 keV Na^+ ions with a flux density of 10^{15} ions·cm^{-2}.

4 Conclusions

The Na^+-ion implanted $10Na_2O \cdot 60P_2O_5 \cdot 30SiO_2$ glass was prepared and the effects of Na^+-ion implantation were discussed with respect to the conduction properties. The main features of this work are as follows:

1) The calculated mean depth range and peak concentration with the LSS theory were, respectively, 0.38 μm and 4.7×10^{19} cm^{-3} for 200 keV Na^+ ions with flux density of 10^{15} ions·cm^{-2}.

2) The XRD pattern of the Na^+-ion implanted glass specimen exhibited amorphous phase.

3) No cracking was perceived for the implanted glass surface.

4) The $10Na_2O \cdot 60P_2O_5 \cdot 30SiO_2$ glass sample showed the ionic conductivity of 3.4×10^{-7} S·cm^{-1} at 300℃.

5) The ionic conductivity of the glass was drastically enhanced from 3.4×10^{-7} S·cm^{-1} to 6.2×10^{-5} S·cm^{-1} at 300℃ upon implantation of 200 keV Na^+ ions with a flux density of 10^{15} ions·cm^{-2}.

References

1) D. Ravaine, *J. Non-Cryst. Solids*, **73**, 287 (1985).

2) T. Okura, K. Yamashita, *Solid State Ionics*, **136–137**, 1049 (2000).

3) T. Okura, M. Tanaka, G. Sudoh, *Mat. Res. Soc. Symp. Proc.*, **453**, 611 (1997).

4) W. K. Chu, B. L. Crowder, J. W. Mayer, J. F. Ziegler, "Ion Implantation in Semiconductors and Other Materials", Ed. by B. L. Crowder, Plenum Press, New York (1973) p. 225.

5) J. Lindhard, M. Scharff, H. E. Schiott, *Kgl. Danske Videnskab Selskab, Mat. Fys. Medd.*, **33**, 14 (1963).

Na^+ イオンを注入した Na_2O–P_2O_5–SiO_2 ガラスのイオン伝導性

大倉　利典・門間　英毅

（工学院大学工学部マテリアル科学科）

Na_2O–P_2O_5–SiO_2 ガラスの導電性に対する Na^+ イオンの注入効果を検討した．原料に Na_2CO_3，$NH_4H_2PO_4$ および SiO_2 を用いて，溶融急冷法によりガラスを作製した．このガラス試料に対して，Na^+ イオンを加速電圧 200 keV で注入した．注入した量は 10^{15} ions·cm^{-2} とした．電導度測定はブロッキング電極を用いた交流二端子法により行った．$10Na_2O \cdot 60P_2O_5 \cdot 30SiO_2$ ガラスの 300℃ における電導度は，イオン注入前では 3.4×10^{-7} S·cm^{-1} であったのに対し，注入後では 6.2×10^{-5} S·cm^{-1} となり，Na^+ イオンの注入により電導度が二桁以上向上する結果を示した．

Journal of the Society of Inorganic Materials, Japan **14**, 363–368 (2007)

Paper

ゾルーゲル法による SiO_2–P_2O_5–GeO_2 系非晶質バルク体の合成

大倉　利典・門間　英毅
（工学院大学工学部マテリアル科学科）

Synthesis of Amorphous SiO_2–P_2O_5–GeO_2 Monoliths by a Sol–Gel Process

Toshinori OKURA and Hideki MONMA
(Department of Materials Science and Technology, Faculty of Engineering, Kogakuin University, 2665–1, Nakano, Hachioji-shi, Tokyo 192–0015)

Monolithic dried gels were synthesized by a sol–gel process from a mixture of $Si(OC_2H_5)_4$, $PO(OC_2H_5)_3$ and $Ge(OC_2O_5)_4$ solutions using N,N–dimethyl formamide as a drying-control chemical additive. Gelation of the solution was carried out at 60℃ and the obtained wet gel was allowed to dry by making a pinhole on the closed container at 150℃. The monolithic dried gel could be converted into an amorphous, transparent and cylindrical rod without crack and bloating by heating to 900 ～1000℃. The change of bonding state of the dried gel was investigated by Fourier transform-infrared spectroscopy. The absorption band near 1320 cm^{-1} is attributed to P＝O stretching mode. The band becomes stronger indicating an increase in the double bond character with increasing heat–treatment. It is suggested that the phosphorus component exists as a PO_4 tetrahedron in the amorphous SiO_2–P_2O_5–GeO_2. Specific surface area, average pore size and total pore volume of the gels were determined by BET method. The structure of the dried gel was porous including solvents, and the dense gel was obtained by heat-treatment. This was based on the viscous flow sintering, and it was indicated that it depended on P_2O_5 content.

(Received Mar. 20, 2007)
(Accepted Jul. 12, 2007)

Key words : Sol–gel process, SiO_2–P_2O_5–GeO_2, N,N–dimethyl formamide, Amorphous monolith Viscous flow sintering

1 はじめに

SiO_2 を骨格として P_2O_5 や GeO_2 を添加したガラスに第二高調波発生（second harmonic generation: SHG）が観測されたことから，非線形光学材料としての応用が期待されている．これまでにファイバー作製などが行われており，さらに大型の素子を得ようと様々な試みが行われている[1]．SiO_2–P_2O_5–GeO_2 系の SHG 機構は Ge の電子欠陥によるものとされ，Ge の光誘起欠陥の生成を活発にすることが重要である．従来の融液急冷法においては，Si の熱的誘起欠陥や線引き誘起欠陥が生成され，Ge の欠陥生成が抑制されてしまう．そこで本研究では，低温での合成が可能で，熱的誘起欠陥の生成が抑制できるゾルーゲル法に着目した．P_2O_5 成分を添加することで，構造の自由度が増し，Ge の欠陥生成の助長効果も期待される．また，形態をファイバーからバルク体にすることで，線引き誘起欠陥の生成を抑制できると考え，SiO_2–P_2O_5–GeO_2 系非晶質バルク体の合成を試みた．

ゾルーゲル法によるバルク体の合成は，溶液から出発するので，多成分系であっても分子レベルでの混合が可能であるので，全体の均質性が増すといった利点がある．しかしながら，溶媒を含んだ湿潤ゲル体を乾燥する過程で亀裂が発生する，乾燥ゲル体を熱処理する際に発泡や破壊が起こるなどの問題がある．山根らは $Si(OC_2O_5)_4$–CH_3OH–H_2O–NH_3 の混合液をゲル化させるときの温度について検討し，金属アルコキシドの加水分解縮重合を 60～70℃ の高温で行うと，ゲル体の細孔径が大きくなり，亀裂や破壊をともなわずにシリカゲル体が得られることを示した[2]．Wallace ら

は乾燥制御剤(Drying Control Chemical Additive: DCCA)を使用する方法を提案した．ゲル体の合成に溶媒の一部としてホルムアミドを添加すると，ゲル中の細孔径が大きくなり，均質性が向上するなどの効果がある[3]．作花らはDCCAとしてN,N-ジメチルホルムアミド(DMF)を使用することによって大きな寸法のシリカゲル体を得た[4),5]．DCCAとしてDMFを用いると，溶液全体の表面張力の影響を軽減し，ゲル体から溶媒が揮発していく際の毛管力による局部的な応力が減少するため，亀裂の発生を防ぐ効果がある．他にも様々な対策が提案されているが，すべてに共通していえることは，細孔径を大きくするということである．細孔径を大きくすれば，湿潤ゲル体から溶媒が揮発していくとき，あるいは乾燥ゲル体の熱処理過程で，表面張力の影響が少なくなるため，亀裂のない大きなバルク体が得られる[6),7]．本研究ではDCCAとしてDMFを用いる方法を採用した．DMFの添加量を変化させ，亀裂のないバルク体が得られた組成について様々な温度で熱処理を行い，その微構造変化を検討した．

2 実　　験

2・1 出発溶液の調製

出発原料として，テトラエトキシシラン($Si(OC_2H_5)_4$, TEOS)，リン酸トリエチル($PO(OC_2H_5)_3$)，およびゲルマニウムテトラエトキシド($Ge(OC_2O_5)_4$)を用いた．また，乾燥制御剤としてDMFを，触媒として塩酸を用いた．所定量のTEOSにモル比で1.6～2.4倍のDMFおよびTEOSと同量のエタノールを加え，40℃で3時間かくはんした後，TEOSに対してモル比で等倍のイオン交換水および0.003倍の塩酸を加えた塩酸水溶液を添加し，さらに2時間かくはんした．この混合溶液を室温まで冷却し，エタノールで希釈した$PO(OC_2H_5)_3$および$Ge(OC_2H_5)_4$を加え，30分間かくはんした後，イオン交換水を添加し，さらに30分間かくはんして出発溶液を調製した．

2・2 ゲル化およびゲルの熟成

調製した出発溶液をポリメチルペンテン製シリンダーに入れ，アルミニウム箔で覆い密閉し，60℃でゲル化させた．ゲル化後，48時間かけて80℃まで昇温し，ゲルを熟成させて湿潤ゲル体を得た．

2・3 ゲルの乾燥および熱処理

アルミニウム箔にピンホールを数個開け，80℃で120時間保持した後，連続的に150℃まで昇温し，24時間保持することにより乾燥ゲル体を得た．この乾燥ゲルを昇温速度20℃/hで900～1000℃まで昇温し，2時間保持することにより熱処理を行った．

2・4 ゲルのキャラクタリゼーション

乾燥ゲルの熱処理にともなう構造変化を調べるために，各試料のかさ密度を測定し，さらに粉末X線回折(XRD)測定およびフーリエ変換赤外吸収(FT-IR)スペクトル測定を行った．また，ゲルの細孔構造を評価するため，比表面積，全細孔容積および細孔径分布を窒素ガスの吸脱着により測定した．比表面積はBET法により求め，全細孔容積および細孔径分布はCranston-Inkleyの円筒型モデルを用いて算出した．

3 結果および考察

3・1 バルクゲル体の成否

P_2O_5含有量が20 mol%以上，またGeO_2含有量が10 mol%以上の組成になると，乾燥ゲル体のバルク形状維持が困難になった．これは，各アルコキシドの加水分解速度が異なるためである．バルク形状を維持できるかどうかはSiO_2骨格に強く依存すると考えられるが，$PO(OC_2H_5)_3$および$Ge(OC_2O_5)_4$は加水分解速度が速いことから3次元ネットワーク構造をそれほど発達させることができず，ダングリングボンドを多く生成し，SiO_2骨格の形成が促進されていないことが考えられる．XRD測定の結果，$Ge(OC_2O_5)_4$が10 mol%以上の組成になるとGeO_2六方晶系結晶が析出することがわかった[8]．乾燥ゲル体合成時に添加したDMFは，亀裂発生の原因となる表面張力の影響を減少させるのに有効であったと考えられるが，添加量の最適条件は組成により異なっていた．亀裂のない乾燥ゲル体は，熱処理を行ってもそのままの形状を保つことができ，無孔化することができた．しかし，昇温速度が速い場合には，細孔中の残留物の揮発による除去が十分に進まない状態で細孔の閉鎖が進行するため，また，細孔が完全に閉鎖していない状態であったとしても，温度の上昇にともなう蒸発量の急激な増大と有機成分の気化による体積膨張のため，発泡や破壊が起こることがあった．バルクの形状を保っていた試料は，XRD測定の結果から非晶質であることがわかった．

図1に$80SiO_2$-$10P_2O_5$-$10GeO_2$(DMF/TEOS=2.2)組成の乾燥ゲルおよび熱処理後の試料の写真を示す．乾燥ゲルは黄褐色で半透明であったが，300℃および500℃で熱処理した試料では，有機物の炭化により黒色あるいは濃い茶色となり，不透明になった．700℃で熱処理した試料では，ゲルの収縮が見た目でも確認できるようになり，白色で半透明になった．ゲ

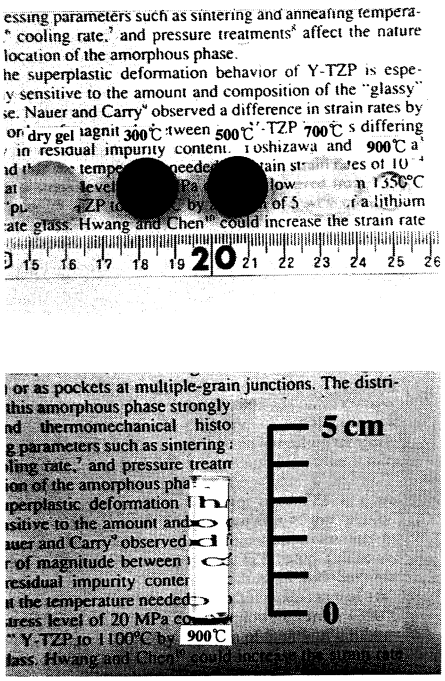

Fig. 1　Preparation of amorphous $80SiO_2$–$10P_2O_5$–$10GeO_2$ rod by sol–gel process.

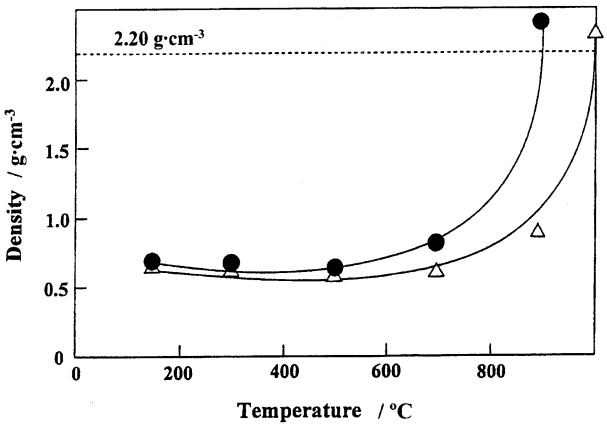

Fig. 2　Densities of gels heated at various temperatures.
●: $80SiO_2$–$10P_2O_5$–$10GeO_2$
△: $90SiO_2$–$2P_2O_5$–$8GeO_2$

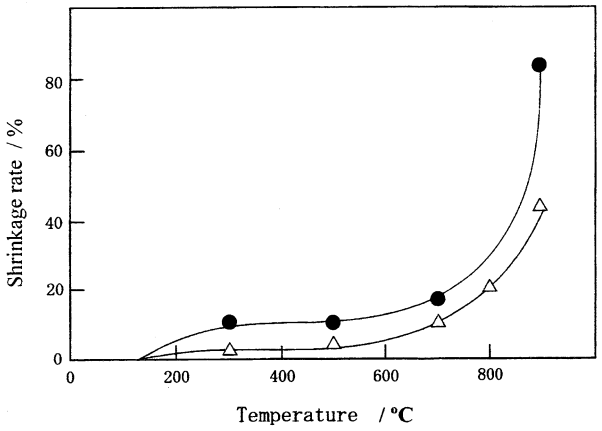

Fig. 3　Shrinkage rates of gels heated at various temperatures.
●: $80SiO_2$–$10P_2O_5$–$10GeO_2$
△: $90SiO_2$–$2P_2O_5$–$8GeO_2$

ルが白色に見えるのは，有機物の揮発により生成した細孔内に光が入り，それが散乱しているためと考えられる．900℃で熱処理した試料では，さらにゲルの収縮が進み，無色透明になった．900℃で熱処理することにより，透明で亀裂のない直径1 cm，高さ4 cm程度の円柱型非晶質バルク体を得ることができた．

3・2　熱処理によるゲルの密度変化

亀裂のないバルクゲル体が得られた $80SiO_2$–$10P_2O_5$–$10GeO_2$（DMF / TEOS = 2.2）組成および $90SiO_2$–$2P_2O_5$–$8GeO_2$（DMF/TEOS＝2.0）組成の試料について，熱処理によるゲルの密度変化を**図2**に，体積収縮率変化を**図3**に示す．$80SiO_2$–$10P_2O_5$–$10GeO_2$ 組成の試料では，密度は500℃付近までは0.6 g·cm^{-3}程度の値を示しているが，700℃付近からゲルの収縮が大きくなって密度が増加し，900℃では2.39 g·cm^{-3}となった．また $90SiO_2$–$2P_2O_5$–$8GeO_2$ 組成の試料では，700℃までは密度の値に変化がなく，それ以降にゲルの収縮が大きくなり，1000℃で2.36 g·cm^{-3}となった．

融液急冷法で作製したシリカガラスの密度が2.20 g·cm^{-3}であることから，$80SiO_2$–$10P_2O_5$–$10GeO_2$ 組成の試料では900℃，$90SiO_2$–$2P_2O_5$–$8GeO_2$ 組成の試料では1000℃で，ほぼ無孔化すると考えられる．

3・3　熱処理によるゲルのFT-IRスペクトル変化

図4に $80SiO_2$–$10P_2O_5$–$10GeO_2$（DMF / TEOS = 2.2）組成の乾燥ゲルおよび熱処理後の試料のFT-IRスペクトルを示す．乾燥ゲルでは，DCCAとして添加したDMFの＞C＝Oに起因する吸収が1660 cm^{-1}付近に大きくみられることから[4]，DMFがかなり残存していると考えられる．熱処理温度の上昇とともに吸収が次第に小さくなり，900℃以上においてはほぼ消滅した．また，乾燥ゲルでは970 cm^{-1}付近にSi–OH伸縮振動に帰属される吸収ピークが認められたが，これも熱処理温度の上昇とともに消滅した．これは，無孔化前の高温域で，細孔表面に存在するSi–OHが反応してシロキサン結合となり，細孔の閉鎖が進行したためであると考えられる．

一方，1320 cm^{-1}付近のP＝O伸縮振動に帰属される特性吸収ピークは，熱処理温度が高くなるにつれて

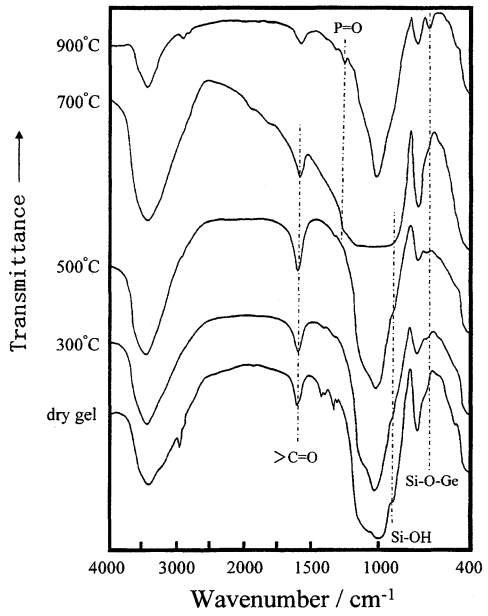

Fig. 4 FT-IR spectra of $80SiO_2$–$10P_2O_5$–$10GeO_2$ gels heated at various temperatures.

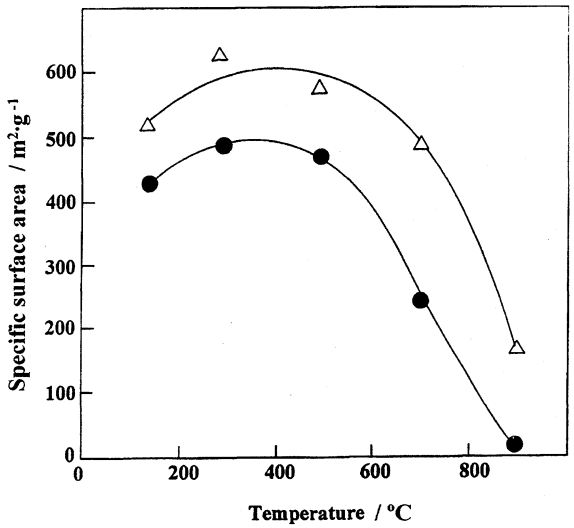

Fig. 5 Specific surface areas of gels heated at various temperatures.
●: $80SiO_2$–$10P_2O_5$–$10GeO_2$
△: $90SiO_2$–$2P_2O_5$–$8GeO_2$

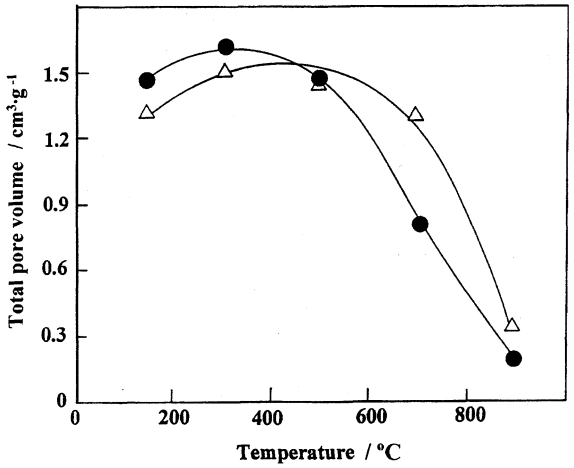

Fig. 6 Total pore volumes of gels heated at various temperatures.
●: $80SiO_2$–$10P_2O_5$–$10GeO_2$
△: $90SiO_2$–$2P_2O_5$–$8GeO_2$

増大することが観察された．このことは，リン成分は非晶質体中で PO_4 四面体として存在していることを示唆するものである[9]．乾燥ゲル体および熱処理温度が 700℃ までの非晶質体ではこの吸収が現れないのは，ゲル中に多数の水酸基が存在し，−OH と P=O の二重結合が共鳴しているためであると考えられる[9]．また 670 cm^{-1} 付近に Si-O-Ge 伸縮振動に帰属される吸収が確認された[10]．さらに SiO_2 非晶質体のスペクトルと比較してみると，1000～1200 cm^{-1} 付近の吸収ピークの幅が広くなっている．これは SiO_4, PO_4, GeO_4 四面体構造に起因する吸収が重なったためと考えられる[10]．

以上の結果より，Si, P, Ge すべてに関する吸収が確認され，この 3 成分が非晶質バルク体の骨格を形成していると判断できた．

3・4 熱処理によるゲルの微構造変化

$80SiO_2$–$10P_2O_5$–$10GeO_2$（DMF/TEOS = 2.2）組成および $90SiO_2$–$2P_2O_5$–$8GeO_2$（DMF/TEOS = 2.0）組成の試料について，熱処理によるゲルの比表面積変化を**図 5** に，全細孔容積変化を**図 6** に示す．二つの組成の乾燥ゲル体を比較すると，比表面積は $90SiO_2$–$2P_2O_5$–$8GeO_2$，全細孔容積は $80SiO_2$–$10P_2O_5$–$10GeO_2$ の方が大きいことがわかった．また，$80SiO_2$–$10P_2O_5$–$10GeO_2$ の全細孔容積は 300℃ 付近まで，$90SiO_2$–$2P_2O_5$–$8GeO_2$ では 500℃ 付近まで増加している．全細孔容積値の増加は，150℃ で揮発しなかった有機物が熱処理により分解，消失したために新たな細孔が出現したため，もしくは既存の細孔の細孔径変化によるものと考えられる．また，値の減少は粘性流動焼結により小さい細孔径のものが消失したためであり，値の大幅な減少は粘性流動焼結がさらに進んだため，大きい細孔径のものが消失したためと考えられる．さらに，FT-IR の結果から，かなりの高温まで Si-OH は存在するので，高温での熱処理により Si-OH が Si-O-Si あるいは Si-O-Ge へと変化することで体積の収縮が起こることも要因の一つであると考え

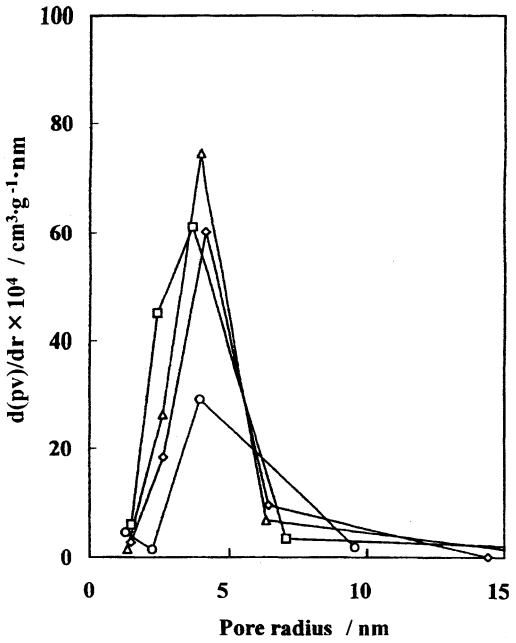

Fig. 7　Pore size distributions of $80SiO_2$–$10P_2O_5$–$10GeO_2$ gels heated at various temperatures. ◇: Dry gel, □: 300℃, △: 500℃, ○: 700℃

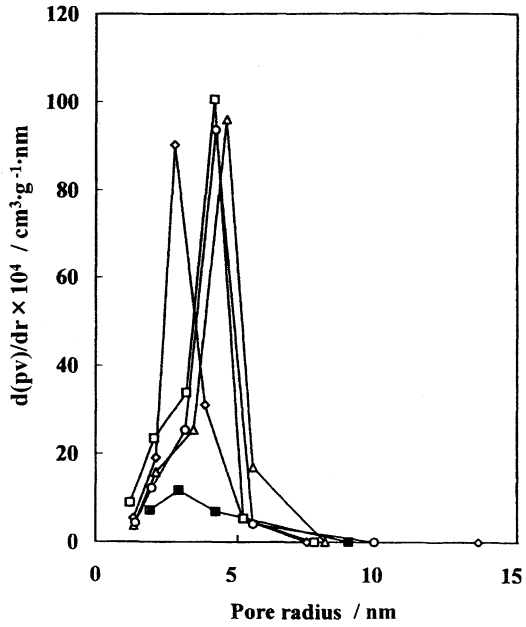

Fig. 8　Pore size distributions of $90SiO_2$–$2P_2O_5$–$8GeO_2$ gels heated at various temperatures. ◇: Dry gel, □: 300℃, △: 500℃, ○: 700℃ ■: 900℃

られる．

図 7 に $80SiO_2$–$10P_2O_5$–$10GeO_2$ 組成の試料，**図 8** に $90SiO_2$–$2P_2O_5$–$8GeO_2$ 組成の試料の細孔径分布図を示す．300℃ で熱処理した場合，有機物の揮発により新たに細孔が出現するため，細孔径の小さいものが多く存在している．500℃ では有機物の揮発により細孔径の小さいものが増加するが，それと同時に粘性流動焼結により小さい細孔の消失が起こるため，全体的には 300℃ で熱処理した場合より細孔径分布のばらつきが少なくなると考えられる．また $80SiO_2$–$10P_2O_5$–$10GeO_2$ においては 700℃, $90SiO_2$–$2P_2O_5$–$8GeO_2$ においては 900℃ で大幅な細孔の消失が起こることがわかった．さらに，熱処理温度の上昇にともない，細孔径の小さい方にシフトしていく傾向が得られた．

二つの組成を比較すると，$80SiO_2$–$10P_2O_5$–$10GeO_2$ の方が低い温度で細孔の消失が始まり，比表面積は桁違いに小さい．これは組成比より P_2O_5 成分によるものと考えられる．P_2O_5 成分は融点が低いので，P_2O_5 成分が増加することにより粘性流動焼結が促進されると考えられる．

4 まとめ

ゾル-ゲル法により SiO_2–P_2O_5–GeO_2 系非晶質バルク体の合成を試み，得られた乾燥ゲルの熱処理にともなう構造変化を検討した．得られた結果を以下に示す．

1)　ゾル-ゲル法によるバルク体の合成は，ゲルの乾燥過程で亀裂が発生することが多く，溶媒量や乾燥温度の制御が必要となる．本研究では，乾燥制御剤として DMF を用い，溶媒量や乾燥温度および熱処理温度などを検討した結果，組成によっては亀裂のない透明な円柱型の非晶質バルク体を得ることができた．

2)　乾燥ゲルの熱処理にともなう構造変化を調べるために，FT-IR スペクトル解析を行った．1320 cm^{-1} 付近の P＝O 伸縮振動に帰属される特性吸収は，熱処理温度の上昇とともに増加した．このことより，リン成分が非晶質体では PO_4 四面体として存在することが示唆された．

3)　ゲルの細孔構造を評価するため，比表面積，全細孔容積および細孔径分布を求めた．乾燥ゲルは溶媒を含んだ多孔質体であるのに対し，熱処理後のゲルは構造が緻密化していることがわかった．これは粘性流動焼結によるものであり，P_2O_5 含有量に依存していることが示唆された．

文　献

1)　渡辺裕一，高田雅介，*NEW GLASS*, **6**, 33 (1991).
2)　M. Yamane, S. Okano, *Yogyo-Kyokai-Shi*, **87**, 434 (1979).

3) S. Wallace, L. L. Hench, *Mat. Res. Soc. Symp. Proc.*, **32**, 47 (1984).
4) T. Adachi, S. Sakka, M. Okada, *Yogyo-Kyokai-Shi*, **95**, 970 (1987).
5) 作花済夫，日化，No. 3, 243 (1988).
6) M. Ohno, T. Yamada, N. Takato, *Yogyo-Kyokai-Shi*, **94**, 644 (1986).
7) K. Chou, B. I. Lee, *J. Mater. Sci.*, **27**, 520 (1992).
8) S. Shibata, K. Kitagawa, *Jpn. J. Appl. Phys.*, **25**, 323 (1986).
9) Y. S. Kim, R. E. Tressler, *J. Mater. Sci.*, **29**, 2531 (1994).
10) K. Takahashi, N. Mochida, H. Matsui, S. Takeuchi, Y. Gohshi, *Yogyo-Kyokai-shi*, **84**, 482 (1976).

Paper　　Journal of the Society of Inorganic Materials, Japan 14, 294–299 (2007)

$CaSO_4$–H_3PO_4–H_2O 系における二水セッコウの準安定性

根岸　博・大倉　利典*・関谷　道雄
(*工学院大学工学部マテリアル科学科)

Metastability of Gypsum Dihydrate in the System $CaSO_4$–H_3PO_4–H_2O

Hiroshi NEGISHI, Toshinori OKURA and Michio SEKIYA
(Department of Materials Science and Technology, Faculty of Engineering, Kogakuin University, 2665-1, Nakano-cho, Hachioji-shi, Tokyo 192-0015)

The metastability of $CaSO_4 \cdot 2H_2O$ in 24.63～49.93 (P_2O_5%) H_3PO_4 solutions was studied by a wet DTA method. On the basis of the measured values of reaction temperature and induction period for dehydration of $CaSO_4 \cdot 2H_2O$, the relation between H_3PO_4 concentration Z (P_2O_5%) and upper limit temperature Y (℃) for metastability of $CaSO_4 \cdot 2H_2O$ in the case of 1 minute induction period for dehydration was given as follows:

$$Y = -4.314e^{0.04601Z} + 112.4$$

From above results, it was confirmed that the metastable zone for $CaSO_4 \cdot 2H_2O$ in H_3PO_4 aqueous solution existed in the wide range of higher temperature than those reported by Nordengren, Zdanovskii and Murakami on metastable equilibrium for $CaSO_4 \cdot 2H_2O = \alpha$-$CaSO_4 \cdot 1/2H_2O$ in H_3PO_4 aqueous solution.

(Received Apr. 2, 2007)
(Accepted May 7, 2007)

Key words: Metastability, Gypsum dihydrate, Wet DTA, Phosphoric acid, Dehydration, Induction period

1 はじめに

$CaSO_4$–H_3PO_4–H_2O 系における硫酸カルシウムの平衡関係は，湿式リン酸の製造に関して非常に重要で，過去に多くの報告がなされている[1)~5)]．そのなかで準安定相として存在する領域での $CaSO_4 \cdot 2H_2O$ と α-$CaSO_4 \cdot 1/2H_2O$ の挙動がとくに重要であるが，それらの準安定領域については現在のところ明確にされていない．

本報は，$CaSO_4$–H_2SO_4–H_2O 系の研究において確立した湿式 DTA 法による手法[6)~9)]を用いて，H_3PO_4 溶液中における $CaSO_4 \cdot 2H_2O$ の準安定性の検討を行い，その準安定領域を明らかにすることを目的とする．

2 実　　験

2・1 試　料

用いた $CaSO_4 \cdot 2H_2O$ 試料は試薬特級（付着水 0.00%，結合水 20.68%）で，顕微鏡観察による結晶の大きさは平均で長径 16 μm，短径 5 μm である．H_3PO_4 溶液濃度は 24.63, 29.95, 35.38, 39.74, 45.45 および 49.93P_2O_5%で，試薬特級 H_3PO_4 を用いて調製した．

2・2 方　法

用いた湿式 DTA 装置[6),8),9)]は恒温槽（空気浴）とガラス製反応器からなる．恒温槽は内部容積 30×30×30 cm^3 で，二つのヒーター（350 W）を備えた恒温槽を改良したもので，槽内温度を均一にするためかくはん機を取り付け，±0.1℃ 以内に保持できるものである．反応器は媒液の蒸気圧の高い測定条件においても常圧下での等温測定を可能にするため既報[10)]の反応器を改良したもので，検出用と対照用の両器の上部に 1 mmϕ の毛細管を取り付け，それらを圧力調整びんに導き，連結し，そこで 0.7 mmϕ の毛細管によって大気圧中に開放し，両器内の蒸気圧が一定になるようにした．圧力調整びん中の媒液には反応条件と同濃度

の H_3PO_4 溶液を用いた．また，示差電圧および反応器内温度はプラチネル複熱電対を用いて検出した．

測定は，試料 3.00±0.01 g，媒液 40 cm^3 を用い，反応器内温度および示差電圧が一定になったのち試料ホルダーを破壊し，かくはん速度 500±5 rpm で行った．

2・3　H_3PO_4 溶液中における $CaSO_4 \cdot 2H_2O$ の溶解度の推定

湿式 DTA による $CaSO_4 \cdot 2H_2O$ の脱水誘導時間の測定において，測定開始直後 $CaSO_4 \cdot 2H_2O$ の溶解熱のため著しい吸熱を生じ，その影響を受けて脱水誘導時間が著しく遅れることを認めたので，あらかじめ H_3PO_4 溶液中に $CaSO_4 \cdot 2H_2O$ を溶解する方法を試みた．それには用いた H_3PO_4 濃度および温度条件における $CaSO_4 \cdot 2H_2O$ の溶解度を推定する必要があった．**図 1** に H_3PO_4 濃度 20～50P_2O_5%，温度 25～80 ℃における $CaSO_4 \cdot 2H_2O$ の溶解度の文献値[11)～15)]を示した．それらのデータを用いて，用いた H_3PO_4 濃度 Z(P_2O_5%)における $CaSO_4 \cdot 2H_2O$ の溶解度 s と温度 T の関係の実験式を求め，それを(1)～(6)に示した．

$$Z=24.63 \quad s=0.0007205 \quad T^{1.6247}+0.5260 \tag{1}$$

$$Z=29.95 \quad s=0.0004284 \quad T^{1.7429}+0.4631 \tag{2}$$

$$Z=35.38 \quad s=0.0006402 \quad T^{1.6522}+0.3500 \tag{3}$$

$$Z=39.74 \quad s=0.0010440 \quad T^{1.5377}+0.2441 \tag{4}$$

$$Z=45.45 \quad s=0.0005027 \quad T^{1.6619}+0.1957 \tag{5}$$

$$Z=49.93 \quad s=0.0001469 \quad T^{1.8848}+0.1788 \tag{6}$$

これらの実験式から求めた推定溶解度曲線を**図 2** に示した．$CaSO_4 \cdot 2H_2O$ の溶解量は，溶解度の量を用いると完全に溶解するまでに時間がかかり $CaSO_4 \cdot 1/2H_2O$ が析出する．推定溶解度の 90%溶解量では温度上昇開始から約 2 時間で溶解することを確認した．

3　結果および考察

3・1　H_3PO_4 溶液中における $CaSO_4 \cdot 2H_2O$ の脱水示差熱曲線

図 3 に 40.08P_2O_5%における脱水示差熱曲線を示した．左側は酸単味の場合，右側は $CaSO_4 \cdot 2H_2O$ をあらかじめ溶解した場合の示差熱曲線である．酸単味の

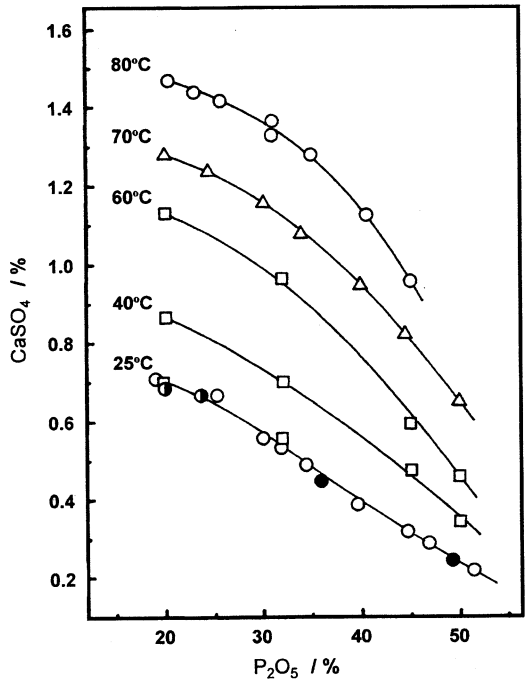

Fig. 1　Solubility of $CaSO_4 \cdot 2H_2O$ in H_3PO_4 solutions.
○ : Taperova (1940)
◑ : Pozin (1966)
● : Zdanovskii (1970)
□ : Tokarev (1969)
△ : Akajew (1976)

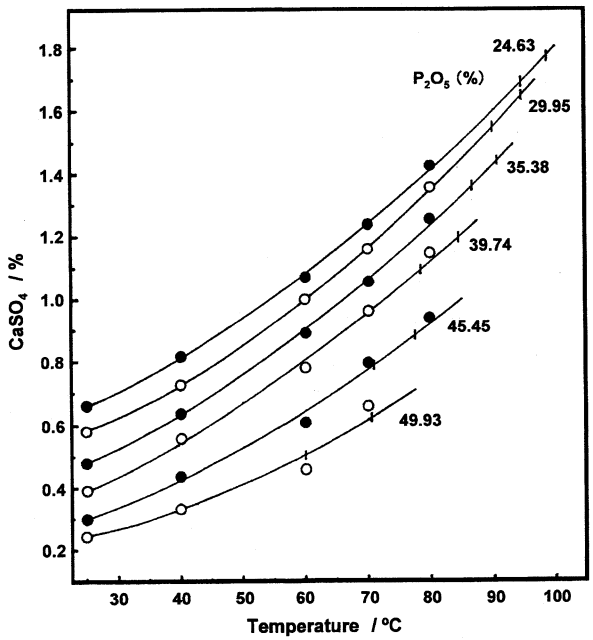

Fig. 2　Estimated solubility of $CaSO_4 \cdot 2H_2O$ in H_3PO_4 solutions.

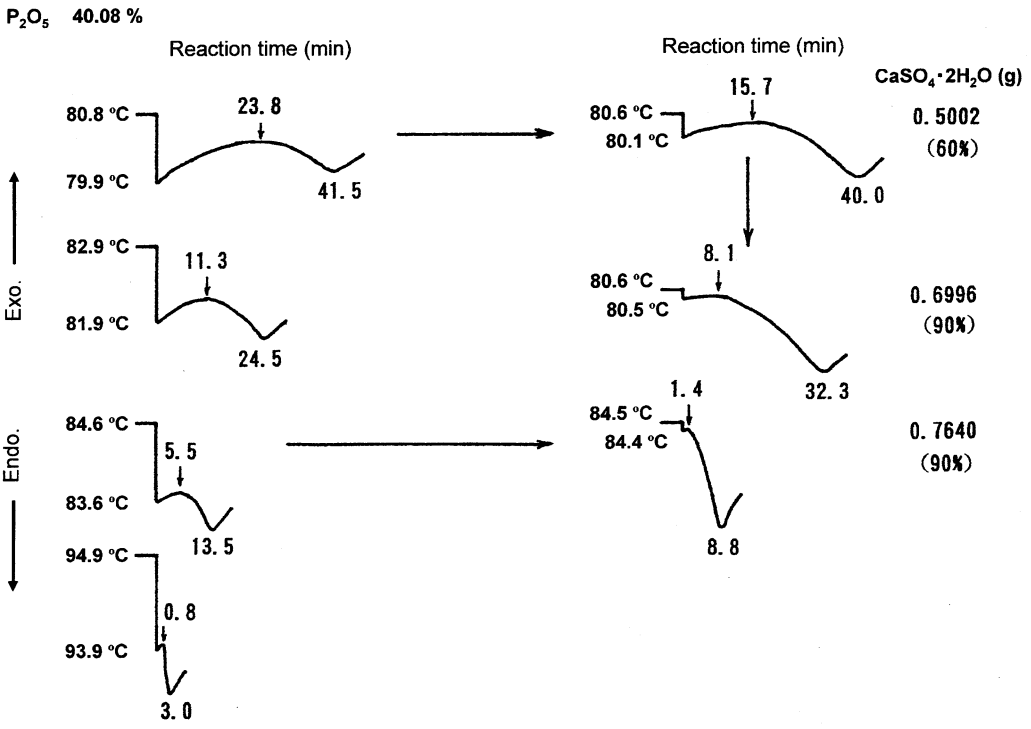

Fig. 3 Typical DTA curves obtained by dehydration of $CaSO_4 \cdot 2H_2O$ in 40.08P_2O_5% H_3PO_4 solution.

場合は試料ホルダーを破壊した直後に著しい吸熱(温度低下 1℃)を生じ，その影響を受けて脱水ピークが小さい．これに対してほぼ同一条件下で $CaSO_4 \cdot 2H_2O$ を溶解した場合は初期吸熱の減少がみられ，推定溶解度の 90%の $CaSO_4 \cdot 2H_2O$ を溶解した場合には H_2SO_4 系と同様の正常(温度低下 0.1℃)な脱水曲線が得られた．

3・2 反応温度 y と $CaSO_4 \cdot 2H_2O$ の脱水誘導時間 X の関係

図 4 に 24.63～49.93P_2O_5%H_3PO_4 溶液中における反応温度と脱水誘導時間の関係を示した．いずれの H_3PO_4 濃度においても，反応温度の低下とともに脱水誘導時間は遅延する傾向を示し，いずれの曲線も $y = aX^b$ のベキ関数のグラフに類似する．**図 5** に $\log X$ と $\log y$ の関係を示した．49.93P_2O_5%を除いて，非常によい直線関係(相関係数 $r = 0.9913 \sim 0.9991$)が得られた．49.93P_2O_5%を除いて回帰分析を行い，各パラメーターの値を求めた結果，つぎの実験式(7)～(11)が得られた．

$$Z = 24.63 \quad y = 99.05 \quad X^{-0.01510} \qquad (7)$$
$$Z = 29.95 \quad y = 94.94 \quad X^{-0.01395} \qquad (8)$$
$$Z = 35.38 \quad y = 90.97 \quad X^{-0.01449} \qquad (9)$$
$$Z = 39.74 \quad y = 85.05 \quad X^{-0.02370} \qquad (10)$$
$$Z = 45.45 \quad y = 77.62 \quad X^{-0.02654} \qquad (11)$$

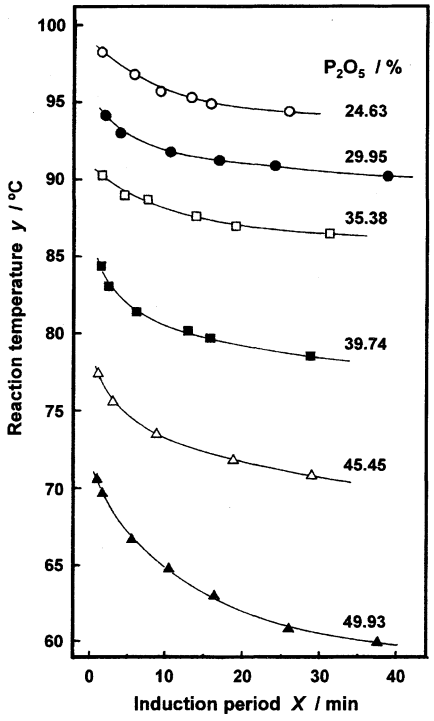

Fig. 4 Relation between reaction temperature and induction period for dehydration of $CaSO_4 \cdot 2H_2O$ in H_3PO_4 solutions.

これらの実験式から算出した誘導時間とその測定値との差(残差)を**表 1** に示した．誘導時間が 10 分以内では二つの値を除いて 1 分以内で，それ以上長い場

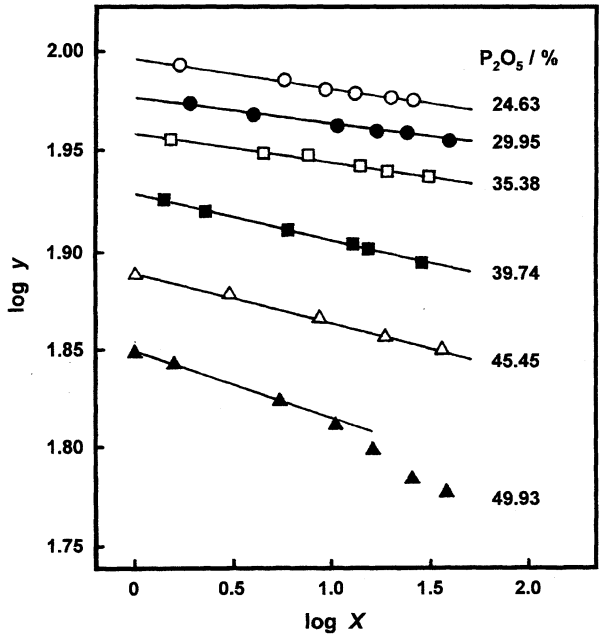

Fig. 5　Relation between log X and log y for data from Fig. 4.

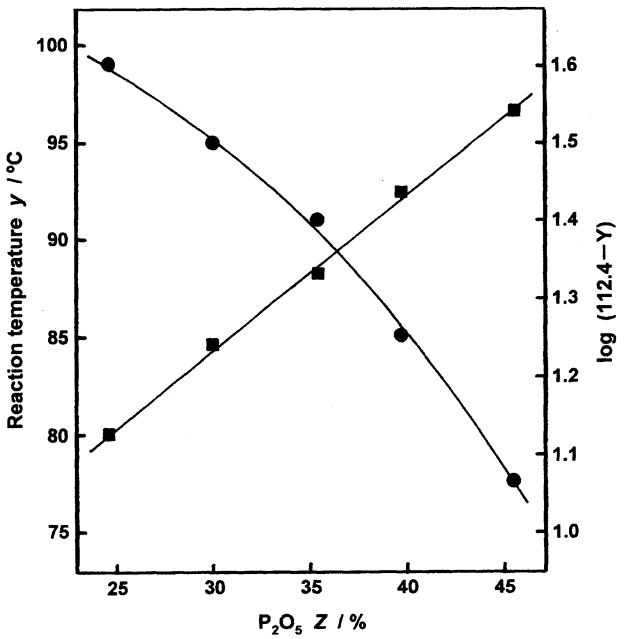

Fig. 6　Relation between H_3PO_4 concentration and upper limit temperature for metastability of $CaSO_4 \cdot 2H_2O$ at 1 minute of induction period.

合でも二つの値を除いて2分以内でよく一致した．

3・3　H_3PO_4 濃度 Z(P_2O_5%) と $CaSO_4 \cdot 2H_2O$ の脱水誘導時間1分の準安定限界温度 Y の関係

3・2で得られた Y の値が H_3PO_4 濃度が高くなるにつれて減少する傾向があることからそれらの関係をみると，**図6**に示したように Z–Y 間の曲線は $Y=-ae^{bZ}+c$ の指数関数のグラフに類似する．既報[7]と同様の手法により c を概略求めたのち，Z と log (c–Y) の間の相関係数 r が最大となるところの c を求めると，図6のように $r=0.9987$ のよい直線関係が得られた．回帰分析を行い，各パラメーターの値を求めた結果，下記の実験式が得られた．

$$Y=-4.314e^{0.04601Z}+112.4 \qquad (12)$$

式(12)から H_3PO_4 濃度0%の Y の値を推定すると108.1℃で，H_2SO_4 系で得られた106.4℃とほぼ一致した．このことから，用いた湿式DTA法とデータ解析の手法は非常に信頼性が高いものであることを確認

Table 1　Comparison between measured values and calculated values by empirical equations for induction period.

P_2O_5/%	Temp./℃	Induction period/min		
		Meas.	Calc. by eq. (7～11)	Residual
24.63	98.3	1.7	1.7	0.0
	96.8	5.8	4.6	−1.2
	95.7	9.3	9.8	+0.5
	95.3	13.3	12.9	+0.4
	94.9	15.8	17.1	+1.3
	94.4	26.0	24.2	−1.8
29.95	94.2	1.9	1.8	−0.1
	93.0	4.0	4.4	+0.4
	91.8	10.6	11.2	+0.6
	91.3	17.0	16.5	−0.5
	90.9	24.1	22.6	−1.5
	90.2	38.7	39.4	+0.7
35.38	90.3	1.5	1.7	+0.2
	89.0	4.5	4.5	0.0
	88.7	7.5	5.7	−1.8
	87.6	13.8	13.5	−0.3
	87.0	19.0	21.8	+2.8
	86.5	31.1	32.4	+1.3
39.74	84.4	1.4	1.4	0.0
	83.1	2.3	2.7	+0.4
	81.4	6.0	6.4	+0.4
	80.2	12.8	11.9	−0.9
	79.9	15.6	15.5	−0.1
	78.5	28.7	29.5	+0.8
45.45	77.4	1.0	1.1	+0.1
	75.6	3.0	2.7	−0.3
	73.5	8.8	7.8	−1.0
	71.8	18.7	18.9	+0.2
	70.8	29.0	32.1	+3.1

した．

3・4 $CaSO_4$-H_3PO_4-H_2O 系における $CaSO_4 \cdot 2H_2O$ の準安定状態図

式(12)によって求めた $CaSO_4 \cdot 2H_2O \rightarrow \alpha$-$CaSO_4 \cdot 1/2H_2O$ における $CaSO_4 \cdot 2H_2O$ の脱水誘導時間1分の等時線を Nordengren, Zdanovskii および村上の $CaSO_4 \cdot 2H_2O = \alpha$-$CaSO_4 \cdot 1/2H_2O$ の準安定平衡線とともに**図7**に示した．前報[6)~9)]でも指摘したように，それらの準安定平衡線は，溶解度法によって $CaSO_4 \cdot 2H_2O$ と α-$CaSO_4 \cdot 1/2H_2O$ の安定に近い平衡関係を推定したもので，動的因子としての誘導期間について考慮されていないため，その溶解度測定に問題がある．したがって，本実験で得られた $CaSO_4 \cdot 2H_2O$ の準安定限界線と温度差の小さい低濃度側での曲線は，より低温側に位置しなければならないと考えられる．Zdanovskii の平衡線は P_2O_5 20%までは村上の平衡線とほぼ一致するが，H_2SO_4 系と同様に P_2O_5 20%以下の濃度においては直線的に上昇し，P_2O_5 0%で本研究の準安定限界線と一致することから低濃度側に問題があると思われる．また，村上の平衡線と本研究の準安定限界線とを比較すると，P_2O_5 25%で+11℃，30%で+18℃，40%で+29℃の範囲に $CaSO_4 \cdot 2H_2O$ の準安定領域が存在し，濃度が高くなるにつれてその領域が広くなることが明らかになった．

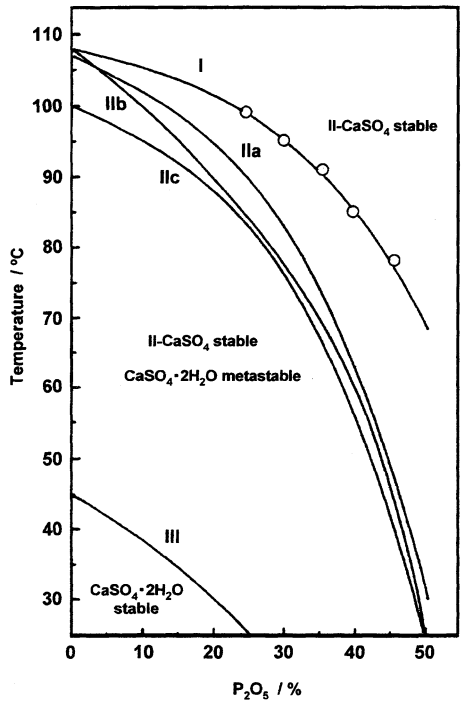

Fig. 7　Phase diagram for metastability of calcium sulfate dihydrate in the system $CaSO_4$-H_3PO_4-H_2O.
Ⅰ: Upper limit curve for metastability of $CaSO_4 \cdot 2H_2O$ at 1 minute of induction period in $CaSO_4 \cdot 2H_2O \rightarrow \alpha$-$CaSO_4 \cdot 1/2H_2O$
Ⅱ: Metastable equilibrium curves for $CaSO_4 \cdot 2H_2O \rightleftharpoons \alpha$-$CaSO_4 \cdot 1/2H_2O$ (Ⅱa: Nordengren, Ⅱb: Zdanovskii, Ⅱc: Murakami)
Ⅲ: Equilibrium curve for $CaSO_4 \cdot 2H_2O \rightleftharpoons$ Ⅱ-$CaSO_4$ (Zdanovskii)

4 まとめ

湿式DTA法を用いて，24.63~49.93P_2O_5%H_3PO_4溶液中における $CaSO_4 \cdot 2H_2O$ の準安定性の検討を行った．それらの結果をまとめるとつぎのようである．

1)　反応温度と $CaSO_4 \cdot 2H_2O$ の脱水誘導時間の測定値を用いて，H_3PO_4 濃度 Z(P_2O_5%)と脱水誘導時間1分の準安定限界温度 Y(℃)の関係を表す実験式を誘導した．

$$Y = -4.314e^{0.04601Z} + 112.4$$

2)　上記関係式によって求めた $CaSO_4 \cdot 2H_2O$ の脱水誘導時間1分の等時線を Nordengren, Zdanovskii および村上の $CaSO_4 \cdot 2H_2O = \alpha$-$CaSO_4 \cdot 1/2H_2O$ の準安定平衡線と比較した．Zdanovskii の平衡線は P_2O_5 20%までは村上の平衡線とほぼ一致するが，P_2O_5 20%以下では直線的に上昇し，P_2O_5 0%で本研究の準安定限界線と一致することから，低濃度側に問題があると思われる．また，村上の平衡線と本研究の準安定限界線を比較すると，P_2O_5 濃度が高くなるにつれて $CaSO_4 \cdot 2H_2O$ の準安定領域が広くなることが明らかになった．

文　献

1)　S. Nordengren, *U. S. 1*, **776**, 595 (1930).
2)　K. Murakami, H. Tanaka, *J. Soc. Inorg. Mater. Japan* (*Gypsum & Lime*), No. 18, 3 (1955).
3)　S. E. Dahlgreen, *J. Agr. Food Chem.*, **8**, 411 (1960).
4)　A. B. Zdanovskii, G. A. Vlasov, *Zh. Prikl. Khim.*, **44**, 15 (1971).
5)　J. Schroeder, A. Matynia, S. Zielinski, *Przem. Chem.*, **52**, 112 (1973).
6)　H. Negishi, Y. Osuga, M. Sekiya, *J. Soc. Inorg. Mater. Japan* (*Gypsum & Lime*), No. 175, 3 (1981).
7)　根岸　博，大須賀美種，関谷道雄，日化，No. 4, 507 (1983).

8) H. Negishi, M. Sekiya, *J. Soc. Inorg. Mater. Japan* (*Gypsum & Lime*), No. 184, 10 (1983).
9) H. Negishi, T. Okura, M. Sekiya, *J. Soc. Inorg. Mater. Japan*, **9**, 208 (2002).
10) K. Setoyama, K. Gotoh, M. Sekiya, *J. Soc. Inorg. Mater. Japan* (*Gypsum & Lime*), No. 72, 3 (1964).
11) A. A. Taperova, *Zh. Prikl. Khim.*, **13**, 643 (1940).
12) M. E. Pozin, B. A. Kopylev, Y. K. Yadtskaya, *Izv. Vyssh. Ucheb. Zaved. Khim. Khim. Technol.*, **9**, 171 (1966).
13) A. B. Zdanovskii, N. D. Zhukova, *Izv. Vyssh. Ucheb. Zaved. Khim. Khim. Technol.*, **13**, 729 (1970).
14) G. I. Takarev, B. A. Kopylev, V. L. Varshavskii, *J. Appl. Chem.* (*USSR*), **42**, 10 (1969).
15) O. Akajew, J. Dankiewicz, *Czas. Tech.* (*Pol.*), M (2), 44 (1976).

Available online at www.sciencedirect.com
SCIENCE DIRECT®
ELSEVIER
Journal of the European Ceramic Society 26 (2006) 619–622
www.elsevier.com/locate/jeurceramsoc

Superionic conducting $Na_5SmSi_4O_{12}$-type glass-ceramics: Crystallization condition and ionic conductivity

Toshinori Okura [a,*], Hideki Monma [a], Kimihiro Yamashita [b]

[a] *Department of Materials Science and Technology, Faculty of Engineering, Kogakuin University, 2665-1 Nakano, Hachioji, Tokyo 192-0015, Japan*

[b] *Division of Inorganic Materials, Institute of Biomaterials and Bioengineering, Tokyo Medical and Dental University, 2-3-10, Kanda-Surugadai, Chiyoda, Tokyo 101-0062, Japan*

Available online 8 August 2005

Abstract

Glass-ceramics of the phosphorus-containing $Na_5RSi_4O_{12}$ (N5)-type (R = rare earth element; Sm) Na^+-superionic conductors (NaRPSi) were prepared by crystallization of glasses with the composition $Na_{3.9}Sm_{0.6}P_{0.3}Si_{2.7}O_9$. The optimum conditions for crystallization were discussed with respect to the conduction properties and the preparation of uncracked N5-type glass-ceramics. Most of the N5-type NaSmPSi compounds were obtained as uncracked glass-ceramics when the heating time for nucleation was more than 6 h. Also studied were the microstructural effects on the conduction properties, which were dependent upon the heating conditions of crystallization. Large enhancement of electrical conductivity was observed in the glass-ceramics as the grain growth was promoted with the increase of the heating time for crystallization. The ionic conductivity of the glass-ceramic $Na_{3.9}Sm_{0.6}P_{0.3}Si_{2.7}O_9$ heated at 900 °C for 42 h was 9.07×10^{-2} S/cm at 300 °C.

Keywords: Glass; Crystallization; Glass-ceramics; Ionic conductivity

1. Introduction

Glass-ceramics are polycrystalline materials which are produced by controlled crystallization of glasses.[1] In addition to their easy fabrication into desired shapes, glass-ceramics generally have advantages over conventional sintered ceramics in mechanical properties and chemical durability because of their pore-free and small grained (<1 μm) microstructure.[1] Glass-ceramics of Na^+-superionic conductors are therefore expected to overcome the difficulties in the fabrication of practical devices such as tubes for Na/S secondary batteries. The conventional Na^+-superionic conductors, however, have not yet been produced in the form of glass-ceramics. The present authors have successfully prepared a new family of the phosphorus-containing $Na_5RSi_4O_{12}$ (N5)-type (R = rare earth element)[2,3] Na^+-superionic conductors (NaRPSi)[4] by crystallization of glasses with the composition formula, $Na_{3+3x-y}R_{1-x}P_ySi_{3-y}O_9$.[5–9] These materials are reportedly comparable to the conventional ceramic Na^+-conductors such as NASICON, β- and β″- aluminas (e. g., $NaAl_{11}O_{17}$ and $NaAl_5O_8$). The R elements have a significant effect on the crystallization of glasses, as well as on the conduction properties.[2] To date, polycrystalline N5-type NaRPSi has been obtained with Sc, Y, Gd or Sm as the R element. In the following, these NaRPSi compounds will be referred to as NaScPSi, NaYPSi, NaGdPSi and NaSmPSi, respectively. The size of the R ions has been expected to have a significant effect on the crystallization of the phase. Although the precise structural analysis of the silico-phosphate N5-type NaRPSi has not yet been completed, it is currently assumed from the analogy with $Na_5YSi_4O_{12}$[10] that all the R ions can be octahedrally coordinated with the non-bridging oxide ions of the (SiO_4, PO_4)-tetrahedra of the 12-membered rings. The reported results on the silicate ceramics[2] show that the conductivity of the N5-type NaRPSi increases with increasing size of its R ions, giving the order NaSmPSi > NaGdPSi > NaYPSi > NaScPSi.

* Corresponding author. Tel.: +81 426 28 4149; fax: +81 426 28 4149.
E-mail address: okura@cc.kogakuin.ac.jp (T. Okura).

0955-2219/$ – see front matter © 2005 Elsevier Ltd. All rights reserved.
doi:10.1016/j.jeurceramsoc.2005.07.029

It can be expected that NaSmPSi is the most conductive. However, this order was not always true in glass-ceramics.[11] Although most of the NaRPSi compounds were obtained as uncracked glass-ceramics, NaSmPSi was difficult to prevent from cracking during crystallization. It was found that uncracked NaGdPSi with larger Gd^{3+} ions was the most conductive; however, NaSmPSi with the largest Sm^{3+} ions was less conductive than NaYPSi with medium Y^{3+} ions.

In the present study, the N5-type NaSmPSi ionic conductors were prepared by crystallization of glasses. The optimum conditions for crystallization were discussed with reference to the conduction properties and the preparation of uncracked N5-type glass-ceramic NaSmPSi. The microstructure of glass-ceramics, including neck growth among grains as well as grain size, is generally affected by the crystallization process.[1] As the above mentioned devices utilize dc conduction properties of Na^+-superionic conductors, another aim was to study the microstructural effects on the conduction properties of whole glass-ceramics.

2. Experimental procedure

2.1. Preparation of glasses and glass-ceramics

The precursor glasses were prepared from reagent-grade oxides of anhydrous Na_2CO_3, Sm_2O_3, $NH_4H_2PO_4$ and SiO_2; the mechanically mixed powders according to the composition formula $Na_{3+3x-y}Sm_{1-x}P_ySi_{3-y}O_9$ with the parameters $x=0.4$ and $y=0.3$ were melted at 1350 °C for 1 h after calcinations at 900 °C for 1 h, in the air. The melts were quickly poured into cylindrical graphite, and then annealed at 500 °C for 3 h, giving NaSmPSi glasses.

Fig. 1 shows the program of temperature and time for the production of glass-ceramic NaSmPSi employed in the present work. Bulk glasses were heated with an increasing rate of 75 °C/h to 580 °C above ca. 50 °C of the glass transition point, which had been determined in advance by differential thermal analysis (DTA). This pretreatment was done in order to obtain homogeneous nucleation.[1] After the annealing for 1–10 h, specimens were heated at 900 °C for 2–42 h, thereafter slowly cooled in a furnace with a decreasing rate of 150 °C/h to room temperature. These glass-ceramic specimens were polished down with 0.5 μm diamond paste, thereafter subjected to the conductivity measurements.

2.2. Measurements and characterization

Ionic conductivities were measured by the complex impedance method on cylindrical glass-ceramics of typically 15 mm in diameter and 2 mm in thickness. Electrodes were prepared by sputtering of gold on polished surfaces. The applied ac field ranged from 5 to 10 MHz in frequency. The temperature dependence of the conductivity was measured in a similar way at several temperatures ranging from room temperature to 350 °C. The complex impedance or admittance loci of glass-ceramics were analyzed by an equivalent circuit.

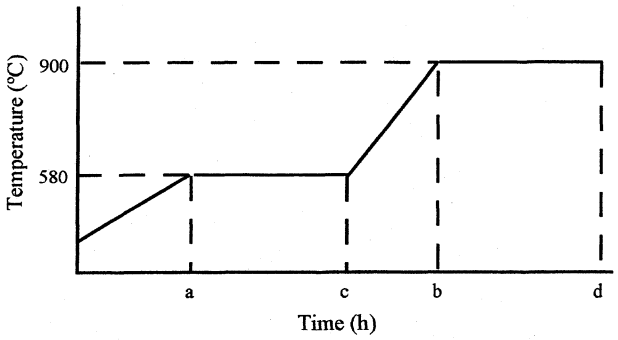

	a-b	b-c	c-d
(A)	1	7	17
(B)	3	8	10
(C)	6	8	5
(D)	6	8	8
(E)	6	8	25
(F)	6	8	42
(G)	10	8	2

a-b: nucleation c-d: crystal growth

Fig. 1. The programs of temperature and time for the production of glass-ceramics.

Crystalline phases of glass-ceramic specimens were identified by X-ray diffraction (XRD) method. Glass-ceramic NaSmPSi were subjected to scanning electron microscope (SEM) for microstructural analysis.

3. Results and discussion

3.1. Preparation of uncracked glass-ceramics: crystallization condition

The N5 single phase NaSmPSi ionic conductors with the $Na_{3.9}Sm_{0.6}P_{0.3}Si_{2.7}O_9$ composition were successfully produced by crystallization of glasses. The glass samples heated by the program pattern (A) shown in Fig. 1 broke during crystallization and the glass-ceramic NaSmPSi obtained by the pattern (B) was difficult to prevent from cracking during crystallization. Most of the NaSmPSi compounds by the patterns (C)–(G) (i.e. longer nucleation time) were obtained as uncracked glass-ceramics.

Fig. 2 shows SEM photographs of microstructure of the NaSmPSi glass-ceramics obtained by the patterns (C), (F) and (G). The grain sizes of the specimens by the patterns (C) and (F) were about 6 and 10 μm, respectively. The grain growth is promoted with increase of heating time for crystallization. The glass samples broke during crystallization when the heating time for crystallization was more than 42 h. Although grain growth may cause high conductivity, it was difficult

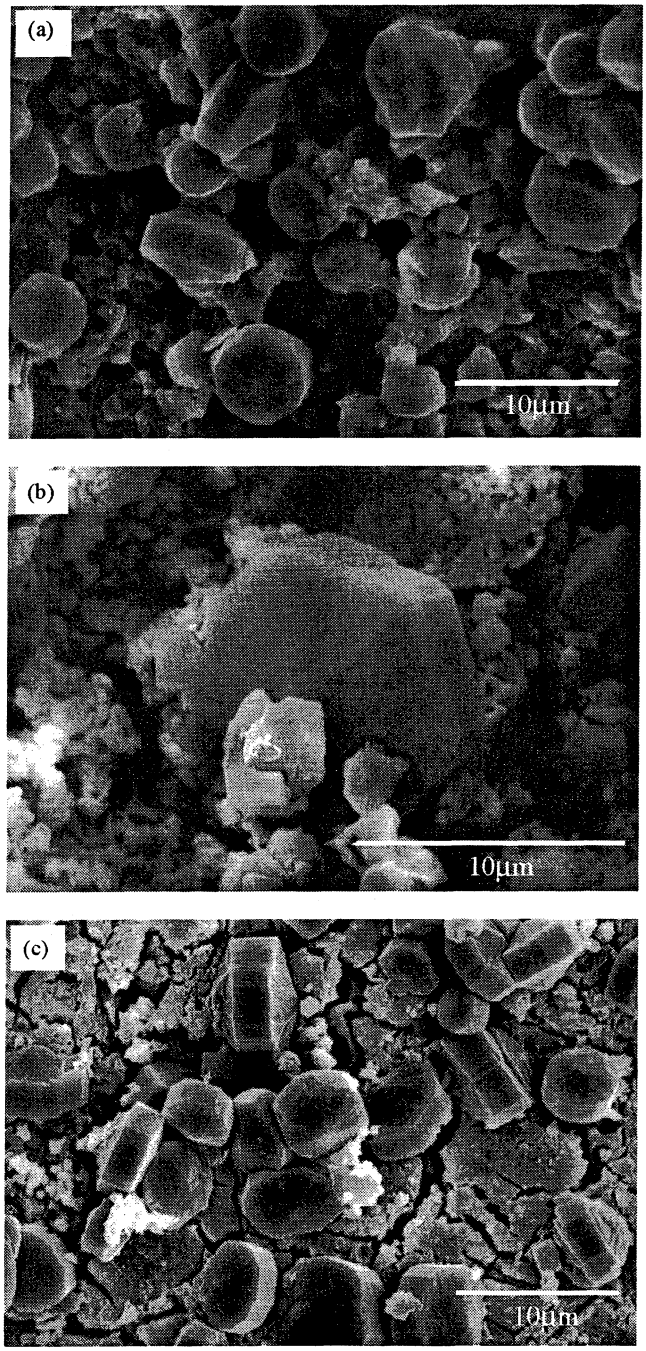

Fig. 2. SEM photographs of the glass-ceramics: (a) pattern (C); (b) pattern (F); (c) pattern (G).

to prevent the sample heated for a long time from cracking during crystallization. The microstructure of the specimen by the pattern (G) was denser and the grain size was about 5 μm. The glass samples broke during crystallization when the heating time was over 2 h.

3.2. Conduction properties of grains and grain boundaries

Fig. 3 shows the complex admittance diagrams of the glass-ceramic NaSmPSi crystallized by the program pattern (F). Those admittance diagrams were analyzed with the

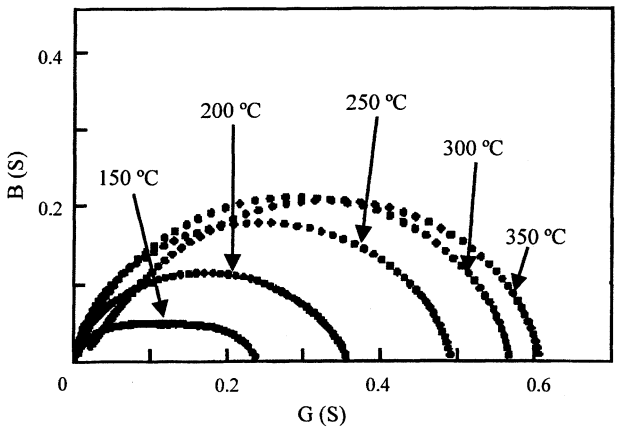

Fig. 3. Complex admittance diagrams of the glass-ceramics crystallized by the pattern (F).

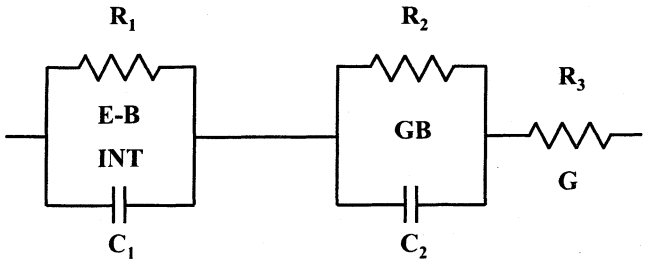

Fig. 4. Equivalent circuit employed for the admittance analysis. E-B INT, GB and *G* represent the electrode-bulk interface, grain boundaries and grains, respectively, and (R_1, C_1), (R_2, C_2) and R_3 are their resistances and capacitances.

equivalent circuit shown in Fig. 4. The complex admittances of the measured glass-ceramic specimens consisted of two semicircles below 300 °C. The two intercepting points on the real axis are interpreted as the resistance of crystallized grains (R_G) and the total resistance of grains and remaining glassy grain boundaries (R_{GB}).

Shown in Fig. 5 are examples of the temperature dependence Arrhenius plots made on the basis of the calculated

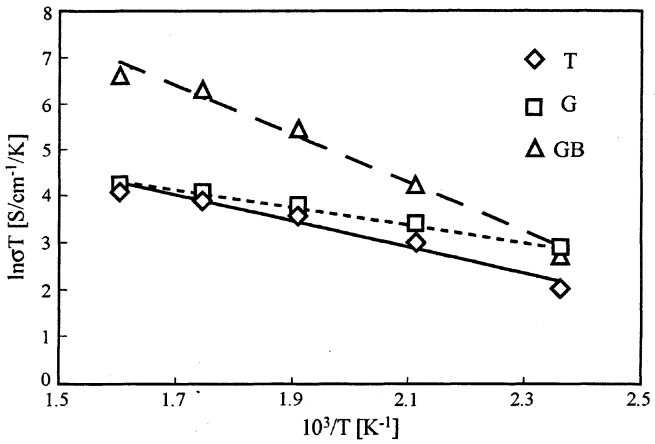

Fig. 5. Arrhenius plots of conductivities of grains (*G*), grain boundaries (GB) and total bulk (*T*) for the glass-ceramics crystallized by the pattern (F).

Table 1
Conduction properties of the glass-ceramics

Program pattern	σ_{300} (10^{-2} S/cm)	E_a (kJ/mol)		
		T	G	GB
(C)	6.59	22.77	14.36	44.65
(D)	7.39	20.78	13.57	42.02
(E)	7.57	21.56	14.92	46.61
(F)	9.07	22.34	14.75	44.22
(G)	3.10	22.43	20.77	23.88

σ_{300}: conductivity at 300 °C. E_a: activation energy (T: total; G: grain; GB: grain boundary).

conductivity values of grains and grain boundaries of the glass-ceramic NaSmPSi, in which the geometrical ratios of thickness to surface area for grains were also used for convenience for those of grain boundaries because of their indefinable shapes. The conductivity of the total bulk (T) is as close as to that of grains (G) at higher temperatures, while the resistance of grain boundaries (GB) dominates the whole conductance at lower temperatures. It should be noted that, concerned with the conduction properties of grain boundaries, only the activation energies are significant, since the conductivity of grain boundaries were calculated using the geometry ratio of surface area to thickness of the whole glass-ceramic bulk.

Table 1 summarizes the measured conductivities at 300 °C (σ_{300}) and the calculated activation energies (E_a) of the glass-ceramic NaSmPSi specimens. The samples crystallized by the program patterns (C) and (F) showed the ionic conductivities of 6.59×10^{-2} and 9.07×10^{-2} S/cm, respectively. It was found that the conductivity increased with the grain growth. The samples crystallized by the pattern (G) showed much lower conductivity of 3.10×10^{-2} S/cm.

It was found that uncracked NaSmPSi with the largest Sm^{3+} ions was more conductive than NaYPSi with medium Y^{3+} ions; however, NaSmPSi was less conductive than NaGdPSi. Further grain growth can expect the increase in the conductivity of NaSmPSi.

As R_{GB} decreases rapidly with increasing temperature because of high $(E_a)_{GB}$ to a comparable value with R_G at 300 °C (Fig. 5), the total conductivities ($R_G + R_{GB}$) are dominated by grain boundary conductivity. The grain size-dependence of σ_{300} is therefore explained by the decrease in the number of poorly conductive grain boundaries with grain size.

The conduction properties of grain boundaries were strongly dependent on the annealing conditions, although those of the grains were little changed by annealing temperature and time. Glass-ceramics are generally composites consisting of crystallized grains and small amounts of residual glass (<1%).[1]

4. Conclusions

The uncracked N5-type NaSmPSi glass-ceramics were successfully produced by crystallization of glasses with the composition $Na_{3.9}Sm_{0.6}P_{0.3}Si_{2.7}O_9$. The main features of this work are as follows:

1. Grain growth cause high conductivity.
2. The grain growth is promoted with increase of heating time for crystallization.
3. Conduction properties of these glass-ceramics were strongly dependent upon the crystallization conditions.
4. Complex admittance analysis confirmed that this dependence was attributed to the conduction properties of grain boundaries.
5. The ionic conductivity of the glass-ceramic NaSmPSi heated at 900 °C for 42 h was 9.07×10^{-2} S/cm at 300 °C.

References

1. Kingery, W. D., Bowen, H. K. and Uhlmann, D. R., *Introduction to Ceramics (2nd ed.)*. John Wiley and Sons, New York, 1976, pp. 368–369.
2. Shannon, R. D., Taylor, B. E., Gier, T. E., Chen, H. Y. and Berzins, T., Ionic conductivity in sodium yttrium silicon oxide ($Na_5YSi_4O_{12}$)-type silicates. *Inorg. Chem.*, 1978, **17**, 958–964.
3. Beyeler, H. U. and Himba, T., The sodium conductivity paths in the superionic conductors $Na_5RESi_4O_{12}$. *Solid State Commun.*, 1978, **27**, 641–643.
4. Yamashita, K., Nojiri, T., Umegaki, T. and Kanazawa, T., New fast sodium-ion conducting glass-ceramics of silicophosphates: crystallization, microstructure and conduction properties. *Solid State Ionics*, 1989, **35**, 299–306.
5. Okura, T., Yamashita, K. and Umegaki, T., Na^+-ion conduction properties of glass-ceramic Narpsio in the Y-Sm mixed system. *Phosphorus Res. Bull.*, 1996, **6**, 237–240.
6. Okura, T., Tanaka, M., Monma, H., Yamashita, K. and Sudoh, G., New superionic conducting glass-ceramics in the system Na_2O-Y_2O_3-Sm_2O_3-P_2O_5-SiO_2: crystallization and ionic conductivity. *J. Ceram. Soc. Jpn.*, 2003, **111**, 257–261.
7. Yamashita, K., Umegaki, T., Tanaka, M., Kakuta, T. and Nojiri, T., Microstructural effects on conduction properties of $Na_5YSi_4O_{12}$-type glass-ceramic Na^+-fast ionic conductors. *J. Electrochem. Soc.*, 1996, **143**, 2180–2186.
8. Okura, T., Monma, H. and Yamashita, K., Effect of substitution of Si with Ge and Te on ionic conductivity of $Na_5SmSi_4O_{12}$-type glass-ceramics. *J. Ceram. Soc. Jpn.*, 2004, **112**, S685–S689.
9. Okura, T., Monma, H. and Yamashita, K., Na^+-superionic conductors of glass-ceramics in the system Na_2O-Sm_2O_3-X_2O_3-P_2O_5-SiO_2 (X = Al, Ga). *Solid State Ionics*, 2004, **172**, 561–564.
10. Maximov, B. A., Petrov, I. V., Rabenau, A. and Schulz, H., X-ray investigations and possible mechanism for the ionic conductivity in the sodium rare earth silicate ($Na_5RESi_4O_{12}$ (RE = Y, Sc)) class of compounds. *Solid State Ionics*, 1982, **6**, 195–200.
11. Yamashita, K., Tanaka, M., Kakuta, T., Matsuda, M. and Umegaki, T., Effects of rare earth elements on the crystallization of the glass-ceramic Na^+-superionic conductor Narpsio-V. *J. Alloys Compd.*, 1993, **193**, 283–285.

では，微粒子はそれぞれ異なる方向を向くため，入射光をよく吸収する（図2.66，上図）．電圧を印加すると，針状微粒子の長軸方向が電場方向と並行に配向し，入射光の吸収断面積が減少するため，透過光が増加する（図2.66，下図）．電圧印加時の透過率は50～60％，印加しないときは数％となる．おもに可視域の入射光を吸収し，その範囲の太陽エネルギーを制御できPDLCタイプと同様，2枚のガラス板で挟んだ状態で使用される．現在，実用化に向け，多くの企業が検討している[159]．

(4) 今後の課題

市場で実用化されているのは，PDLCタイプのスマート・ウインドウ（日本板硝子[158]）とエレクトロクロミックタイプの自動車用防眩ミラー（ジェンテックス[153]）だけである．今後の課題は，前者では，透明・不透明をよりよくという性能面の改良と価格低減であり，後者では，自動車用，建築用を問わず，大面積化である．

他の開発中の材料も含め，太陽光を制御することにより，省エネルギー化が可能なスマートウィンドウの実用化は強く望まれている．それら要求を満たすには，上述の材料開発が必須であり，実用化を目指した改良がさらに進展することを期待する．　[矢野　祐一]

2.3.4 放射性廃棄物処理のためのガラス固化体

(1) 背景

原子力発電所から発生する使用済核燃料には，再び燃料として使用できるウランやプルトニウムが含まれている．これらの元素を発電用原子炉で再利用するための使用済燃料再処理工程で，高レベル放射性廃液（以下，高レベル廃液）が分離される．また，再処理工程からは，低レベルの放射性液体，固体廃棄物も発生する．高レベル放射性廃棄物とは，再処理施設で使用済燃料からウランやプルトニウムを分離・回収した後に残る，核分裂生成物を主成分とする廃棄物で，放射能濃度が高い廃棄物のことをいう．この高レベル放射性廃棄物は，低レベル放射性廃棄物に比べ，その発生量自体は少量であるが，放射線の管理に注意が必要なアクチニド元素などの半減期の長い核種も比較的多く含まれているため，長期間にわたり人間環境から隔離する必要がある．

このため，高レベル放射性廃棄物は，ガラスと混ぜて溶かし，キャニスターとよばれるステンレス鋼製の容器に注入した後，冷やして固めるという方針がとられており，この状態のものをガラス固化体という．ガラスはほかの物質に比べて化学的耐久性に優れ，機械的強度が大きく，放射性成分を多量に溶かし込むことができるので，現在，各国ともガラス固化処理方式を採用している．

(2) 指針

わが国の高レベル廃液固化については，旧動力炉・核燃料開発事業団（動燃；現在，日本原子力研究開発機構）が中心になって，国の研究機関，大学，民間企業，海外研究機関などの協力のもとに，国の方針に従って研究開発を行い，1992年4月に東海ガラス固化・貯蔵施設（TVF：Tokai Vitrification Facility；動燃東海）が完成した．研究開発が始まったのは1970年代中ごろであるが，実際の高レベル廃液を取り扱う研究は，動燃の高レベル放射性物質研究施設（CPF：Chemical Processing Facility；動燃東海）および旧日本原子力研究所（原研：現在，日本原子力研究開発機構）の廃棄物安全試験施設（WASTEF：Waste Safety Test Facility；原研東海）が稼働し始めた1980年代初めからである．

わが国の高レベル放射性廃棄物処理処分の具体的方策などは，1980年10月に原子力委員会放射性廃棄物対策専門部会で「放射性廃棄物処理処分方策について」にとりまとめられた．以下に，同報告書の主旨概要を示す．「高レベル廃液の固化処理技術開発は，ホウケイ酸ガラスによる固化に重点を置く．この技術開発の成果は，海外委託再処理にともなう返還廃棄物対策（1990年以降）および民間再処理事業者の行う固化処理（原子炉施設や再処理施設から発生する低レベルおよび高レベル廃液を

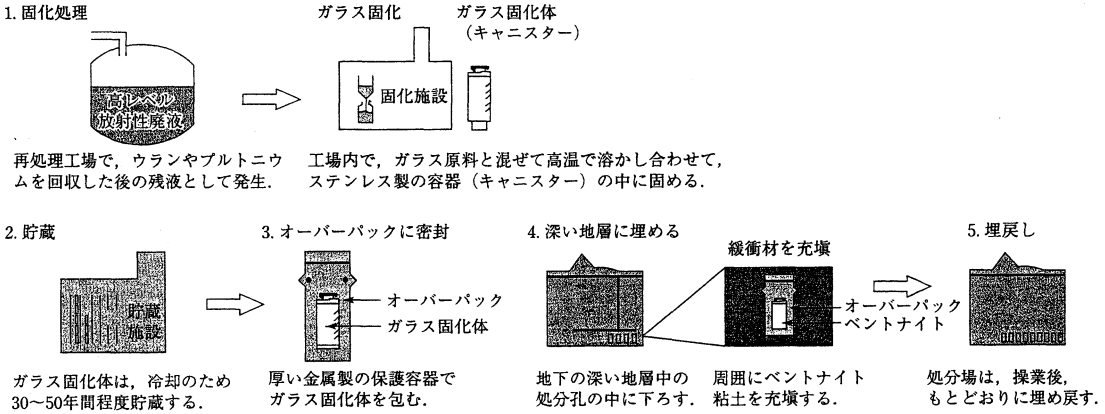

図 2.67　地層処分の概略

蒸発処理した濃縮廃液，フィルタ・脱塩基に使用された廃樹脂などをより安定な形態にするために固体状に処理すること）への活用を図る．使用済燃料として原子炉から取り出された後，再処理を経てガラス固化された固化体は，それに含まれる放射性核種の崩壊熱が深地層の岩盤に与える影響を緩和するため，深地層中に搬入されるまでの間，30～50 年間程度，冷却のため貯蔵される」というものである．

高レベル廃液のガラス固化技術は，日本を含め各国でプラント規模のガラス固化施設が廃液処理運転に入っている段階にある．ガラス固化するのには，高レベル廃液を約 600°C で加熱して酸化物粉末とし，ガラス形成剤を混入し，高温で熱溶解してガラスにする．Ru, Cs などの放射性成分の揮発を防ぐため，溶融温度は低い方が望ましい．このガラス固化体は崩壊熱を出すため，30～50 年間一時貯蔵して冷却（空冷）することにより，発熱量は約 1/3 から 1/5 に減少し，安全な処分ができるようになる．そして，最終的には，地下 300 m より深い安定な地層中に処分される．

現在は，ガラス固化体が 450°C 以下の状態になったら地層処分が可能となっている．長期間にわたっての安全性を予測・評価する場合，処分場を包むまわりの地層（天然バリア）と緩衝材（人工バリア）を組み合わせた多重バリアの機能についての検討が必要である（図 2.67）．中でも，地層処分後の地下水との接触による固化ガラスからの放射性物質の浸出がもっとも重要となり，次いでガラスの安定性および固化ガラス中の放射性物質の崩壊熱による結晶化や分相現象が問題となる．

(3) 事 例

高レベル放射性廃棄物の中には，多種類の放射性物質が含まれる．したがって，特定の放射性物質のみでなく，すべての放射性物質を化学的に安定な物質にする必要がある．ガラスの組成としては，ホウケイ酸系，アルミノケイ酸系，リン酸系が候補として検討され，固化プロセスの実現性，化学的耐久性（浸出率），廃棄物含有量，耐放射線性，熱的安定性などの比較評価の結果，現在では主としてホウケイ酸系が選択されている．その理由は，化学薬品に対する耐食性に優れていること，ガラス溶融温度を比較的低くできるため，プロセス材（溶融炉材，電極材）に対する負担が軽減できること，廃棄物成分の許容含有量が比較的高く，熱や放射線に対する抵抗も高いことなどがあげられる．

ホウケイ酸ガラスの構造は，おもにケイ酸とホウ酸が網目構造を形成するので，結晶性の物質と違い，イオン半径が異なる多種類の放射性物質が網目の中に入り，均質で安定な一種類の物質になる．放射性物質はガラス成分の一つとしてガラスそのものになる．ガラスは容積の小さい固化体にすることができ，取扱いが容易である．また，ガラスは本来水に対して非常に溶けにくい安定な物質である．古代遺跡から多くのガラス製品が出土しているが，いずれも製造当時の色彩や輝きがほとんど失われていない．

廃棄物中の成分は燃料のタイプや再処理法によりわずかに異なり，それに応じてガラスの組成も異なる．たとえば，廃棄物中に Na_2O が多い場合はガラスの溶融温度が低くなり，耐食性，放射線に対する耐久性，水に対す

キャニスター物性（例）		ガラス組成（例）	
材　　質	ステンレス鋼	SiO_2	43～47 mass%
寸　　法	直 径 43 cm	B_2O_3	14
	高 さ 104 cm	Al_2O_3	3.5～5
ガ ラ ス 量	約 110 *l*/本	Na_2O	10
ガラス重量	約 300 kg/本	その他	9～12.5
総 重 量	約 400 kg/本	廃棄物酸化物（Na_2O を除く）	15

ガラス固化体の基本特性	
密度（室温）	2.7～2.8 g cm^{-3}
熱伝導率（室温）	約 0.9 W m^{-1} $°C^{-1}$
熱膨張率	約 80～90×10^{-7} $°C^{-1}$
軟化点	600°C 前後
浸出率	2×10^{-5} g cm^{-2} d^{-1} (100°C)
（蒸留水，粒径 250～420μm）	4×10^{-3} g cm^{-2} d^{-1} (25°C)

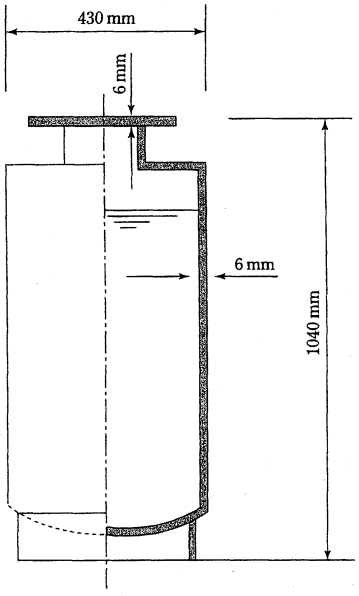

図 2.68 ガラス固化体の例

［日本原子力産業会議 編，放射性廃棄物管理ガイドブック 1994 年版，pp. 72-73 (1994)］

る耐浸出性などの低下をもたらすことになる．また，MoO_3 はガラスへの溶解度がほかの成分に比べて低く，Na_2MoO_4，Cs_2MoO_4 などのモリブデン酸アルカリとして溶融物から分離しやすい．分離析出した相はイエローソリッドとよばれ，^{90}Sr，^{137}Cs などの非常に危険な核種を固溶し，しかも水に溶けやすいため，この相の分離析出は極力避けなければならない．さらに，MoO_3 はガラスの機械的強度を弱めるので，ガラス中の廃棄物の量は制限されることになる．ガラス固化体中の放射性廃棄物の量としては，質量割合で10～20％が含まれている．

ガラス固化体の例を，図2.68に示す．これは廃棄物の含有量が酸化物（Na_2O を除く）で15％である．この場合，ガラス固化体はウラン1t当たり約110 l（約300 kg）発生する．代表的な100万kWの原子力発電所1基当たり，年間これの30倍程度のガラス固化体ができることになる．

(4)　今後の課題と展開

現在では，ホウケイ酸ガラスに対する基礎的検討はほぼ完了しており，ガラス固化体そのものが放出する放射能の影響を調べるために，γ 線や α 線などの放射線やHeなどのイオンをガラス固化体に照射させる実験が多くなってきている．

リン酸ガラスの最大の難点は溶解物が非常に腐食性であるということであるが，それにもかかわらず，多くの工学的問題を克服し，1980年代にかなりの量の廃棄物（およそ1000 m^3）がリン酸ガラスで固定された．リン酸ガラスはそのポテンシャルの高さから，現在でも米国を中心に多くの研究が行われており，様々なデータが蓄積されている．その中には，リン酸ナトリウム-アルミニウムガラスやリン酸鉄-鉛ガラス，リン酸マグネシウムガラス[160,161]などがあり，いずれもホウケイ酸ガラスに匹敵する化学的耐久性があることが報告されている．現在は，リン酸鉄-鉛ガラスの開発に焦点が当てられている[162,163]．　　［大倉　利典］

文　献

1) Baerlocher, Ch., Meier, W. M., Olson, D. H., *Atlas of Zeolite Framework Types*, Elsevier (2001).
2) Breck, D. W., *Zeolite Molecular Sieves*, Krieger Publishing Company (1984).
3) 原　伸宜，高橋　浩，ゼオライト－基礎と応用，講談社サイエンティフィク (1975).
4) 富永博夫 編，ゼオライトの科学と応用，講談社サイエンティフィク (1987).
5) 小野嘉夫，八嶋建明 編，ゼオライトの科学と工学，講談社サイエンティフィク (2000).
6) 岩本正和 監修，環境触媒ハンドブック，pp. 333-509，エヌ・ティー・エス (2001).
7) 環境影響低減化技術開発研究(e-Water)，大規模膜ろ過施設導入技術資料，pp. 2-13，水道技術研究センター (2005).
8) 佐藤常男，大久野浄水場の膜処理 — 導入の目的と技術的特徴 —，水道公論，**38**-12，80-83 (2002).
9) Hattori, K., *et al.*, Water purification systems with Monolith Type Ceramic membranes for Municipal Potable Water, *Proceedings 2004 AWWA Annual Conference*.
10) 澤田繁樹，水道における膜分離技術，化学工学，**69**-3，120-123 (2005).
11) たとえば，藤嶋　昭，瀬川浩司，光機能化学，昭晃堂 (2005).
12) 多賀康訓 監修，可視光応答型光触媒，シーエムシー (2005).
13) Nakajima, A., *et al.*, Photoinduced Amphiphilic Surface on Polycrystalline Anatase TiO_2 Thin Films, *Langmuir*, **16**-17, 7048-7050 (2000).
14) たとえば，Sakai, N., *et al.*, Quantitative Evaluation of the Photoinduced Hydrophilic Conversion Properties of TiO_2 Thin Film Surfaces by the Reciprocal of Contact Angle, *J. Phys. Chem. B*, **107**-4, 1028-1035 (2003).
15) Tatsuma, T., *J. Phys. Chem. B*, **103**, 1999 (2001).
16) Machida, M., *et al.*, The effect of SiO_2 additional in super-hydrophilic proprety of TiO_2 photocatalyst, *J. Mater. Sci.*, **34**-11, 2569-2574 (1999).
17) *Langmuir*, 2002；*J. Phys. Chem. B*, 2004.
18) Takata, Y., Enhancement of boiling and evaporation heat transfer by superhydrophilic photocatalyst, *6th UK National Conference on Heat Transfer*, 323-328 (1999).
19) NEDOプロジェクトとして実施されている．http://www.nedo.go.jp/kankyo/project/07/h15seika.html を参照のこと．
20) Yoshida, N. and Watanabe, T., Sol-Gel Processed Photocatalytic Titania Films, Handbook of Sol-gel Science and Technology, Processing, Characterization and Applications, Sakka, S., ed., Kluwer Academic Publishers (2006).
21) Teraoka, Y., Zhang, H. M., Furukawa, S., Yamazoe, N., Oxygen Permeation Through Perovskite-type Oxides, *Chem. Lett.*, **11**, 1743-1746 (1985).
22) Ishihara, T., Furutani, H., Honda, M., Yamada, T., Shibayama, T., Akbay, T., Sakai, N., Yokokawa, H., Takita, Y., Improved Oxide Ion $La_{0.8}Sr_{0.2}Ga_{0.8}Mg_{0.2}O_3$ by Doping Co, *Chem. Mater.*, **11**, 2081-2088 (1999).
23) 岩原弘育，イオン導電性酸化物による物質分離，電気化学，**63**-8，707-711 (1995).
24) 浅枝正司，無機多孔性膜による分離技術，化学装置，**27**-11，60-65 (1985).
25) 酒井清孝 監修，原谷賢治，膜分離プロセスの理論と設計，pp. 191-225，アイピーシー (1993).

4. デバイスへの応用

Proceedings of PVP2008
2008 ASME Pressure Vessels and Piping Division Conference
July 27-31, 2008, Chicago, Illinois, USA

PVP2008-61224

EFFECT OF FREE SURFACE SHAPE AT EDGE OF INTERFACE ON BONDING STRENGTH OF CERAMIC TO METAL JOINT

Masayoshi TATENO — Kogakuin University, Department of Mechanical Engineering, 2665-1 Nakano,Hachioji, Tokyo, 192-0015 Japan

Yoshiaki HAGIWARA — Graduate School, Kogakuin University, 2665-1 Nakano,Hachioji, Tokyo, 192-0015 Japan

Kunio KOKUBO — Kogakuin University, Department of Mechanical Engineering, 1-24-2 Nishi-Shinjuku,Shinjuku, Tokyo, Japan

ABSTRACT

The focus of this study is to clarify the effect of the interface edge shape on the bonding strength of ceramic to metal joint. Each silicon nitride to copper joint plate with arc-shaped free surfaces edge was produced by Electric Discharge machining (EDM). The interface edge shape was characterized by defining the edge angle as a configuration angle between the interface plane and tangential line at the arc edge of the bonded interface. Each joint was bonded at high temperature using thin braze metal under vacuum and slowly cooled. Good fit was achieved at each bonded face in this process. The dependence of the bonding strength on the edge angle was experimentally clarified in Silicon nitride to Copper joint with arc-shaped free surfaces.

The result shows that changing the edge angle from right angle improves bonding strength since it decreases residual stress near the interface edge. The highest bonding strength appears at the specific interface where the fracture pattern changes. It also shows that secondary machining, which cuts both edges into optimum geometrical conditions after bonding, can improve bonding strength.

Key Words : *Stress Relaxation, Residual Stress, Interface, Ceramic to Metal joint*

INTRODUCTION

Fine ceramics, which possess excellent mechanical properties, are increasing used for structural applications in various industries by joining them to metals. Ceramic can be used/incorporated at the required parts of engineering structures, where resistance against high temperature and/or high strength is required in optimum structural design. Use of ceramic for structures by joining to metal generates a bonded interface between the ceramic and metal. The joining of ceramic to metal comes with the serious problem of increase in residual stress near the interface edge in the cooling process when two dissimilar materials are bonded at high temperature. This residual stress considerably weakens the ceramic to metal joint.

The reliability of the bonded dissimilar materials has been studied to reduce residual stress and show the optimum geometrical shape of the interface based on theoretical and numerical analyses[1]-[11]. Studies on residual stress are advancing in the area of reliability of bonded dissimilar materials. The results[1]-[11] of past theoretical analyses show that optimum interface edge shape can improve bonding strength and reliability of ceramic to metal joint as bonded dissimilar materials. Optimum interface edge shape means that the stress singularity disappears and/or the index of the stress singularity reduces based on the theoretical elastic analysis. There are some methods for selecting interface edge shape, one of which is to machine appropriate free surface and to offset interface location.

However, the effectiveness of the optimum interface edge selection method has not been demonstrated in practical experiments. Almost all of the interface shapes used for experiments on ceramic to metal joint are plane surface, because it is very hard and complicated to machine ceramic.
It is necessary for the optimum interface to show dependence of practical bonding strength on the geometrical shape of the joint interface. This dependence enables engineers to predict the bonding strength against external load and fracture in the ceramic to metal joint with complicated interface and free surfaces. It also enables engineers to establish optimum structural design methods for geometrical interface shape to achieve maximum bonding strength and decrease residual stress near the interface edge.

This study aims to show the relationship between geometrical interface shape and practical bonding strength of silicon nitride to copper joint plate with arc-shaped free surfaces respectively (Si_3N_4 to Cu joint with arc-shaped free surfaces). It also shows the optimum interface shape for improving the bonding strength.

EXPERIMENTAL PROCEDURE

Materials and manufacturing procedure

The materials used in experiments are electro-conductive ceramic Silicon Nitride (Si_3N_4 manufactured by Sodeck New Materials LTD, and pure Copper (Cu). Copper is often applied as insert metal of ceramic to metal joint.

The specimens could be arc-machined by electric discharge machining (EDM). Good fit on the bonded face was achieved in this process. The EDM used in this experiment is a computerized numerical control machine, capable of finishing complicate shapes which engineers want to manufacture mechanically. The average roughness of the EDMed surfaces measured Rz=22.9μm in Si_3N_4 and Rz=22.9μm in Cu. Each EDMed finished surface was used for the bonding process directly.

Geometrical conditions

Fig.1 shows the configuration of Si_3N_4 to Cu joint plate with arc-shaped free surfaces. A machined free surface of the specimen viewed from the front side is defined as front-view as shown in **Fig.1**. A side view surface is perpendicular to the front view surface. The specimen possesses a straight interface and both arc free surfaces. Each interface surface is a rectangle with dimensions 8 mm in width and 5 mm in thickness.

In this study, each Si_3N_4 to Cu joint plate with arc-shaped free surfaces was produced by EDM and bonded at high temperature under vacuum conditions by brazing metal method. The geometrical conditions of the interface edge on the arc free edge were characterized by the edge angle defined as a configuration angle between the tangential line at the interface edge and straight interface on the ceramic side. The edge angles on both sides of Si_3N_4 and Cu were expressed by φ_{F1} and φ_{F2} respectively. The edge angle on ceramic side φ_{F1} was controlled by offsetting the location of the interface and set as $30° < \varphi_{F1} < 150°$, retaining the geometrical conditions of the interface edge on the arc-shaped free surface $\varphi_{F1}+\varphi_{F2}=180°$.

In order to confirm the effect of the edge angle on the bonding strength of the joint with arc-shaped free surfaces, the radius R_F of the arc free surface for evaluation was set at 5 mm based on preliminary investigations to find the effect of R_F on bonding strength. There are two major methods of producing the shape of the Si_3N_4 to Cu joint plate specimens with both arc free surfaces. With one method, each arc-shaped free surface is machined to achieve good fit of the interface by EDM and then the machined specimen is applied for the bonding process. With the other method, both edges of the bonded interface are shaped appropriately by EDM after bonding. The effect of φ_{F1} on the bonding strength in the Si_3N_4 to Cu joint plate with arc-shaped free surfaces is confirmed for both methods experimentally to find the characteristics of the bonding strength of different materials bonded together.

Bonding procedure and evaluation method

Each formed specimen was washed to remove impurities from all surfaces for the bonding process. Each joint was heated at 10 °C/min from room temperature in a furnace maintained in vacuum state, kept at T=720 °C for 10 minutes using thin braze metal/Ag-In-Cu-Ti alloy system (52.0 %Ag-12.5 %In-27.25 % Cu-1.25 %Ti) and slowly cooled. It can be seen that the effects of the twisting and bending of the bonded joint specimen on the observation results of the bonded specimen can be neglected. The bonding strength σ_B is defined by the tensile strength in the bonded state. It was evaluated at room temperature using a tensile testing machine at the crosshead speed of 0.017 mm/s. The tensile strength was obtained by dividing fracture load by the area of the interface (W 8.0 mm × t 5.0 mm). Fractured specimens were observed under the microscope (Keyence VHX-100) after the tensile test.

EFFECT OF ARC FREE SURFACE RADIUS ON BONDING STRENGTH

Preliminary examination

The stress field near the interface edge can depend on the radius of the arc free surface R_F. In cases where R_F/W approaches zero, the stress field should be of the stress singularity type at the tip of the crack along the interface. In cases where R_F/W approaches infinity, the stress field should be of the stress singularity type at the edge consisting of the straight interface and straight free surface. The stress field with

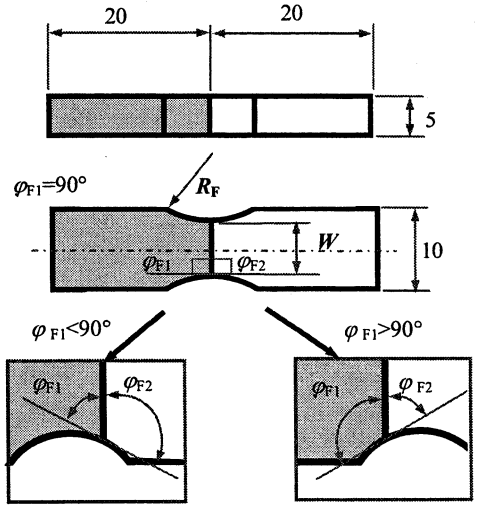

Fig.1 Configuration of specimen of Si_3N_4 to Cu joint plate with arc-shaped free surfaces

the arc free surface may be predicted by taking into account not only the geometrical edge conditions at the bonded interface but also the radius of the arc free surface of the bonded dissimilar materials. It is therefore necessary to clarify the relationship between σ_B and arc radius of the free surface.

Results of Preliminary examination

This preliminary examination evaluates the effect of R_F on σ_B under the geometrical conditions of the interface edge $\varphi_{F1}= \varphi_{F2}=90°$ when $0.2< R_F/W<3.0$ and $W= 8.0$mm.

Fig.2 shows typical fracture patterns in photographs of the joint specimens with arc-shaped free surfaces of R_F /W=0.50 in (a) and 1.25 in (b). It can be seen that fracture initially occurs at the interface edge on the ceramic side and propagates inwardly in the ceramic independent of R_F/W. It appears that each flank fracture pattern is uniform, suggesting that each fracture pattern is two-dimensional. The tensile residual stress near the interface edge dominates the bonding strength from the viewpoint that structure fractures at the weakest point where stress concentration generates.

Fig.3 shows an effect of R_F on σ_B. The dotted line in this figure expresses the average bonding strength of the joint with straight free surfaces of the Si_3N_4 to Cu joint plate. σ_B is independent of R_F in ranges over $0.2<R_F/W<3.0$ and approximates to the average of σ_B for joints with straight free surface. It is assumed that the bonding strength of a joint system depends on local geometrical conditions consisting of two dissimilar materials near the interface edge because σ_B is independent of the R_F set over $0.2 <R_F/W<3.0$.

Therefore, the free surface condition of R_F=5.0 mm (R_F/W=0.625, W=8.0 mm) is provided to easily measure the R_F of the free surface using an R gage.

EFFECT OF EDGE ANGLE ON BONDING STRENGTH

Improving effect of interface edge angle on σ_B

The effect of φ_{F1} on σ_B was experimentally clarified in the Si_3N_4 to Cu joint plate with arc-shaped free surfaces.

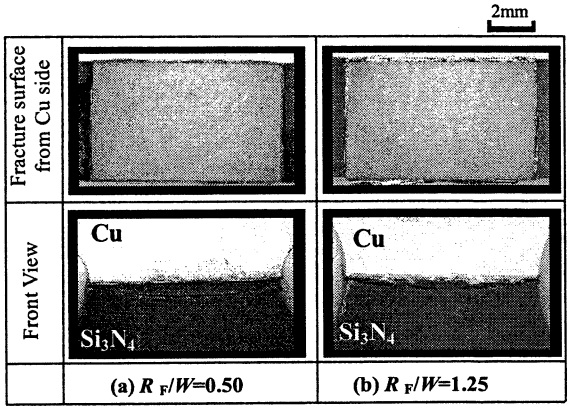

Fig.2 Fracture of Si_3N_4 to Cu joint plate with arc-shaped free surfaces after tensile test

Fig.4 shows typical fracture patterns. They appear as crack occurring near the interface edge on the ceramic side under the geometrical condition $72.1°< \varphi_{F1}<124.9°$, as shown in **Figs.4 (b)** and **(c)**. These fracture patterns are the same as the above fracture pattern in which the residual stress dominates the bonding strength. The residual stress dominates the Si_3N_4 to Cu joint with arc-shaped free surfaces.

The fracture pattern appears as a 0.5 mm long crack from the interface edge on the ceramic side under the geometrical condition $30° < \varphi_{F1}<72.1°$, as shown in **Fig.4 (a)**. This fracture pattern was similar to that of the joint fractures at the interface edge but crack occurs 0.5 tol.0 mm away from the interface edge. This suggests that stiffness of the ceramic dominates the bonding strength.

The fracture pattern shown in **Fig.4 (d)** initially appears at the interface between the ceramic and braze metal debonded. Then crack propagates along the interface and a fracture propagates towards the inside of the ceramic under the geometrical condition $124.9°<\varphi_{F1}<150.0°$. The bonding strength depends on the adhesion power of the interface between the ceramic and braze metal.

Fig.5 shows the effect of φ_{F1}on σ_B of the Si_3N_4 to Cu joint plate with arc-shaped free surfaces. Fracture patterns are classified into three categories according to the fracture origin; (i) originates at the interface edge in ceramic, (ii) originates 0.5mm long from the interface edge in the ceramic, and (iii) debonding occurs at the interface between the ceramic and braze metal. The notations Δ, •, and □ are used respectively for these categories in **Fig.5** respectively.

Decrease of φ_{F1} from the right angle increases σ_B under the geometrical condition $72.1° <\varphi_{F1}<124.9°$, in which fracture occurs at the interface edge due to decrease in residual stress. **Fig.5** shows that the maximum bonding strength appears near the condition where fracture pattern changes. The maximum bonding strength σ_{Bmax} is 33.3 MPa at $\varphi_{F1}=72.1°$ and $\varphi_{F1}<90°$, and 31.1 MPa at $\varphi_{F1}=124.9°$and $\varphi_{F1}>90°$.

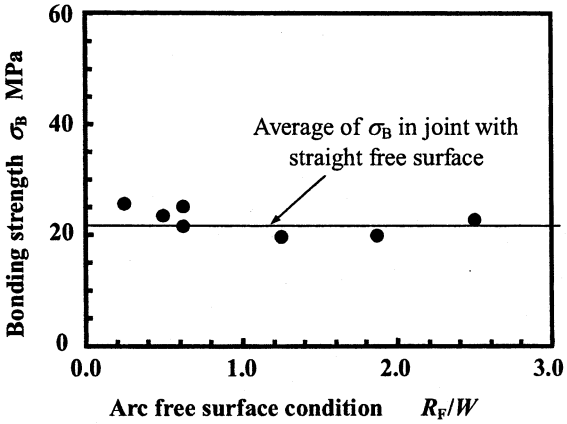

Fig.3 Relationship between bonding strength σ_B and radius of arc-shaped free surface R_F/W

Optimum interface geometrical conditions

The following describes optimum interface geometrical conditions. For $\varphi_{F1}<90°$, decrease in φ_{F1} from the right angle improves bonding strength but decreases the volume of the ceramic near the interface edge.

For $\varphi_{F1}<72.1°$, σ_B depends on the resistance of the ceramic body outside the metal against deformation of the metal because fracture occurs 0.5 to 1.0 mm away from the interface edge on the ceramic side. The stiffness of ceramic is related to its volume and elastic modulus. Even though the elastic modulus of the ceramic is considerably stiffer than that of the metal, decreasing the volume of the ceramic near the interface edge weakens the ceramic. The small volume of the ceramic follows the deformation of the inside metal, which has a large volume, causing the ceramic to fracture easily.

The main predominant factor for bonding strength changes from residual stress to stiffness of the ceramic around $\varphi_{F1}=75°$ in $\varphi_{F1}<90°$. The reason for the change in the fracture pattern is because decrease in φ_{F1} is related to not only decrease in residuals stress but also the stiffness of the ceramic side. Even though decreasing the edge angle improves the residual stress, it is not useful to increase bonding strength under the geometrical interface condition $\varphi_{F1}<72.1°$. Setting a geometrical condition whereby the ceramic volume is smaller than metal weakens the ceramic strength when $\varphi_{F1}<72.1°$. It is therefore effective to obtain high strength joints by setting $\varphi_{F1}=75°$ slightly larger than the geometrical condition where fracture pattern changes.

Increase in the φ_{F1} from the right angle improves bonding strength when $\varphi_{F1}>90°$. When the ceramic volume around the interface edge increases more than that of the metal, the stiffness of the ceramic increases in proportion with the increase of φ_{F1}.

However, the approaching of φ_{F1} to 131.8° does not improve bonding strength since the directions of both shear and normal loads change with increase in φ_{F1} from the right angle and the interface debonds easily with increase in resistance of the ceramic against the external tensile load. Increase in φ_{F1} above 131.8° is not an effective geometrical condition for producing high strength joint systems. The bonding strength is dominated by adhesion power of the interface between the ceramic and braze metal. Therefore, maximum bonding strength is obtained around the geometrical condition $\varphi_{F1}=120°$ where the fracture pattern changes. It is also effective to obtain high strength joints by setting $\varphi_{F1}=120$ ° or slightly less than the geometrical condition where fracture pattern changes.

The maximum bonding strength and optimum interface condition depend on the bonding temperature and combination of the bonded materials since the bonding strength depends on the residual stress near the interface edge and adhesion power of the interface.

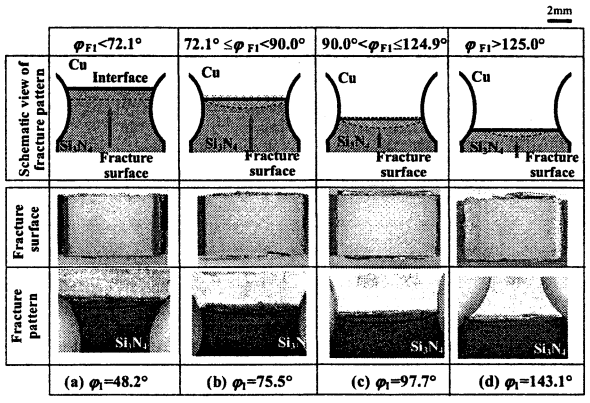

Fig.4 Fracture pattern of Si_3N_4 to Cu joint plate with arc-shaped free surface (R_F=5 mm)

MACHINING EFFECTS AFTER BONDING

It is confirmed that a possible means of improving bonding strength is secondary-machining the straight free surface at the optimum edge angle of the Si_3N_4 to Cu joint plate bonded at the high temperature of 720 °C.

Experimental procedure

The width of the interface (8.0 mm) of the Si_3N_4 to Cu joint plate with machined arc-shape free surfaces was finished after bonding. The finished interface area measured 8.0 mm in width and 5.0 mm in thickness. First, each Si_3N_4 to Cu joint plate with interface ($\varphi_{F1}=\varphi_{F2}=90°$) measuring 10mm in width was produced by brazed metal method at 720 °C. The holding time was set at 10 minutes in the vacuum state. Each 10.0 mm wide bonded interface with straight free surface includes a portion cut 1.0 mm long inwardly from each interface edge. Each bonded Si_3N_4 to Cu joint plate was slowly cooled to room temperature. They were then removed from the furnace, the bonded joint was cut with a free surface arc using EDM with a radius of 5.0 mm. Both portions cut 1.0 mm long from the

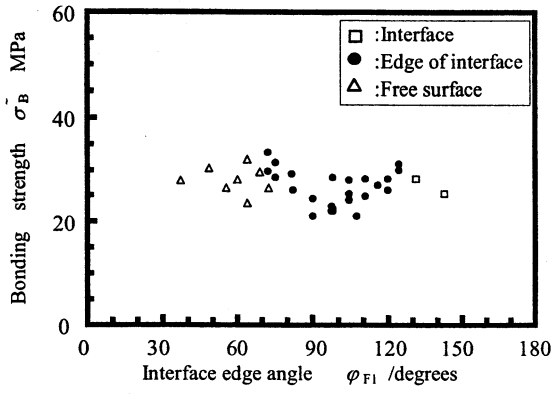

Fig.5 Effect of interface edge angle on bonding strength (Case of Si_3N_4 to Cu joint plate with arc-shaped free surface)

interface edge were machined by EDM. The edge angle φ_{F1} was machined to φ_{F1}=68.7°, 75.5° below 90° and to φ_{F1}=120.0°, 124.8° above 90° after bonding. The joint specimens were used for tensile tests, as they were finished to arc free surface.

Improvement effects

Fig.6 shows an effect of the edge angle on the bonding strength of the joint with machined arc-shape free surface to clarify improvement effects of the machining after bonding. The dotted line in this figure expresses the average bonding strength of φ_{F1}=90° in case of straight free surface.

Fig.7 shows typical fracture patterns, which indicate that residual stress is a predominant factor in the joint specimens because fracture originates at the interface edge on the ceramic side. The average bonding strength of the machined Si_3N_4 to Cu joint plate with φ_{F1}=90° was found to be 7.0 MPa larger than that of joint specimen with straight free surfaces in the bonded state.

Changing the edge angle from the right angle slightly improves bonding strength in Si_3N_4 to Cu joints machined with machined arc-shape free surfaces. The bonding strength of the joint machined with free surface arc by EDM is similar to the strength for bonded joints with arc-shaped free surfaces in the bonding state. Machining the free surface appropriately improves bonding strength because it can redistribute and reduce the residual stress near the interface edge.

Surface integrity

Fig.7 (a) shows typical the free edge of the Si_3N_4 to Cu joint with straight-shaped free surface in the bonded state from front view. In contrast in **Fig.7 (b)**, the interface edge of the joint in which free surface has been removed near the edge interface by secondary-machining is smooth, indicating that secondary-machining is also effective for improving machining conditions at edges. Gaps below 0.1 mm (0.05 to 0.07mm) are observed at the interface edge and microscopic surface machined by EDM.

Machining the free surface appropriately and arc makes the microscopic free edge even and provides smooth gap at the interface. It can be seen from these photographs that secondary machining provides good interface integrity.

Even though residual stress increases near the interface edge in the bonded joint, machining the bonded free surface according to an appropriate edge condition decreases residual stress and improves bonding strength. Consequently, secondary machining is capable of improving the bonding strength of dissimilar materials.

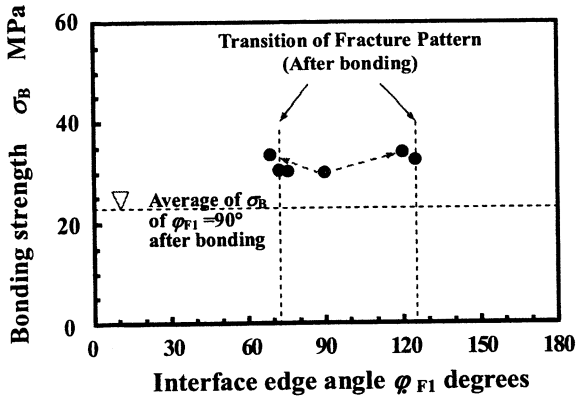

Fig.6 Effect of edge angle on tensile bonding strength after secondary machining

CONCLUSION

This study investigated the relationship between local geometrical conditions and bonding strength of the Si_3N_4 to Cu joint plate by machining free surfaces before and after bonding. The following results are obtained.

(1) σ_B is independent of R_F in the range 0.2< R_F/W<3.0 and approximates to the average of σ_B in joints with straight free surface. It is assumed that the bonding strength of a joint system comprised of dissimilar materials depends on local geometrical conditions near the interface edge because σ_B is independent of R_F when set as 0.2 < R_F/W<3.0.

(2) The stiffness of ceramic relates to its volume and elastic modulus. Even though the elastic modulus of the ceramic is considerably stiffer than that of metal, decreasing the volume of the ceramic near the interface edge weakens the ceramic. The small volume of the ceramic follows the deformation of the inside metal, which has a large volume.

(3) It is effective method to obtain high strength joints by setting φ_{F1}=75° slightly larger than geometrical conditions at which fracture pattern changes.

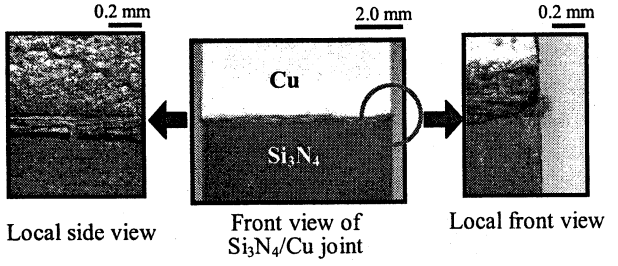

(a) Free edge of interface before EDM

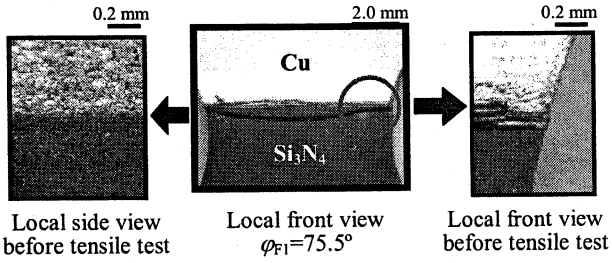

(b) Free edge of interface after EDM

Fig.7 Typical Free Edge of Si_3N_4 to Cu joint specimen with (a) straight free surface in the bonded state and (b) machined arc-shape free surface after EDM

(4) It is also effective to obtain high strength joints by setting φ_{F1}=120° slightly less than geometrical conditions at which fracture pattern changes.
(5) The maximum bonding strength and optimum interface condition depend on the bonding temperature and the combination of bonded materials, because the bonding strength depends on the residual stress near the interface edge and adhesion power of the interface.
(6) Even though the residual stress increases near the interface edge of the bonded joint, machining the bonded free surface based on appropriate edge conditions decreases residual stress and contributes to bonding strength.
(7) Appropriate secondary machining is capable of improving the bonding strength characteristics of dissimilar materials.

ACKNOWLEDGMENTS

This work was supported by "High-Tech Research Center" Project for Private Universities: matching fund subsidy from MEXT(Ministry of Education, Culture, Sports, Science and Technology),2002-2007.

REFERENCES

[1]Bogy, D. B., "Edge-Bonded Dissimilar Orthogonal Elastic Wedges Under Normal and Shear Loading", ASME JORNAL OF APPLIED MECHANICS, Vol.35, (1968), p.460-466.
[2] Bogy, D. B., "Two-Edge Bonded Elastic Wedge of Different Materials and Wedge Angles Under Surface Tractions ", ASME JORNAL OF APPLIED MECHANICS, Vol.38,(1971),p.377-386.
[3] Hein, V. L. and Erdogan, F. (1971), "Stress singularities in a two-material wedge", international Journal of Fracture echanics 7, 317-330.
[4] James P. Blanchard, Nasr M. Ghoniem, "An Eigen Function Approach to Singularity Thermal Stresses in Bonded Strips", Journal of Thermal Stress, 12, (1989), p.501-527.(1989 by Hemisphere Publishing Corporation).
[5] P.A. Kelly, D.A. Hills, D. Nowell,"The Design of Joints between Elastically Dissimilar Components (with special reference to ceramic/metal joints)", Journal of Strain Analysis, Vol.27, No.1,(1992), p.15-20.c ImechE1992.
[6] Tadanobu Inoue, Hideo Koguchi, and Yada Toshio "Solution of thermal stresses near apex in dissimilar materials by thermoelastic theory", Transactions of the Japanese Society for Mechanical Engineers (A) (in Japanese) , Vol.61,581,(1995), p.73-79.
[7]Tadanobu Inoue, Hideo Koguchi, "Characteristics of Distribution of Thermal Stresses Near Apex in Dissimilar Materials (Change of Distribution of Thermal Stresses on Variation of Singularity of Type $\log r \leftrightarrow r^{p-1}$", JSME, JORNAL OF APPLIED MECHANICS A, Vol.61,591,(1995-11), p.2461-2468.
[8]Tadanobu Inoue, Hideo Koguchi, "Influence of the intermediate material on the order of the stress singularity in three-phase bonded structure", International Journal of Solids and Structures, Journal of Applied Mechanics Vol.63,(1996), p.252-258.
[9] Tadanobu Inoue, Hideo Koguchi, "Relaxation of thermal stresses in dissimilar materials (approach based on stress intensity)", International Journal of Solids Structure, Vol.34, No.25, pp.3215-3233,1997.
[10] Y.Y.Yang and D. Munz, "Stress singularities in a dissimilar materials joint with edge tractions under mechanical and thermal loadings", International Journal Solid Structures, Vol.34, No.10, pp.1199-1216.(1997)
[11] Y.Y.Yang, "Effect of the regular term on the stress field in a joint of dissimilar materials under remote mechanical load", Applied Mechanics, Vol.69, p.364-378.(1999).

論文

マイクロサイズ材料のための疲労試験機の製作と疲労試験

21−2210

Manufacture of Fatigue Tester for Micro-sized Materials and Fatigue Tests

井口卓也* 上杉浩史* 後藤芳樹**
立野昌義** 小林光男*** 小久保邦雄**

Abstract

The size of the components used in micro-sized machine devices is considered to be in the order of microns, and the mechanical properties of such micro-sized materials are considered to be different from those of bulk (ordinary sized) materials. The evaluation of mechanical properties including static and fatigue behavior is essential issue for developing a reliable micro-sized machine in service operation. But there has been an absence of the standard test procedure for micro-sized materials. Therefore, the evaluation of mechanical properties including reliability and durability has not been performed. This is due to lack of suitable testing equipment for micro-sized materials.

In the present study, we have designed and manufactured a simple fatigue tester for micro-sized materials. Fatigue tests have been performed for aluminum bonding wire specimen with 25 μm diameter, and the S-N diagram has been obtained. The results obtained in this investigation are important information on the fatigue test method for the fine wire.

Key words: Micro-sized materials, Fine wire, Fatigue tester, Fatigue test, Aluminum bonding wire

1．はじめに

近年，電子機器の進歩にともない，機器の小型化により，集積回路の微細化・高密度化が進んでいる。従来からICチップとパッケージの接続にはボンディングワイヤーが使用されているが，電子デバイスの信頼性の向上のためには，このような極細線の機械的性質を評価する必要がある。しかし，現状では，このようなマイクロサイズ材料を評価するための標準的な試験方法は確立されておらず，信頼性の高いデータを得るためには試験方法の標準化が不可欠である。マイクロサイズ材料の引張試験については，これまでにいくつかの研究が行われ，プラスチックタブに細線を接着して引張試験を行なう方法が報告されている。我々も，前報[1]において，この方法を採用して引張試験を行い，チャッキングの難しい細線の引張試験において，プラスチックタブを用いる試験方法の有効性について報告した。また，タブを用いる疲労試験については，光ファイバー[2]，アラミド繊維[3]およびCu細線[4]についての報告があるが，まだまだデータの少ないのが現状である。そこで，本研究では，引張試験と同様に，プラスチックタブを用いた疲労試験方法を確立する目的で，一定繰返し変位を負荷できる簡単な疲労試験機を製作

※　原稿受付　2008年11月12日
*　工学院大学大学院
Takuya IGUCHI and Hiroshi UESUGI
(Graduate school of Mechanical Engineering, Kogakuin University, Tokyo)
**　工学院大学工学部機械工学科
Yoshiki GOTOH, Masayoshi TATENO and Kunio KOKUBO
(Department of Mechanical Engineering, Kogakuin University, Tokyo)
***　工学院大学工学部機械システム工学科
Mitsuo KOBAYASI
(Department of Mechanical System Engineering, Kogakuin University, Tokyo)

し，プラスチックタブを用いてアルミニウムボンディングワイヤーの疲労試験を行ってみたので，その結果について報告する。

2．試験方法

2.1　疲労試験機

Fig.1に示すように卓上に置ける小型の疲労試験機を設計・製作した。アクチュエータは容量9.8Nの電磁式加振機（㈲旭製作所，WaveMaker 01，周波数1.0～2000 Hz）を用いた。繰返し変位はレーザー変位センサー（㈱KEYENCE）で計測し，荷重の測定は容量500 mNのロードセル（㈱共和電業）を用いた。疲労試験は加振機で一定変位の正弦波を加え，片振り引張りの繰返し荷重を加えた試験を行った。疲労試験システムをFig.2に示す。この疲労試験機は，荷重制御を行っており，最大荷重が設定した値よりも低下するとロードセル上部に設置されたリニアアクチュエータ（㈱ハーモニック・ドライブ・システムズ）は，1回の作動で試験片を引張速度1.0 μ/sで1.0 μmの変位を与え，試験片に引張りの変位を加えることにより，最大荷重を一定に保つように制御している。

2.2　供試材料および試験片

試験片には，Kulicke&Soffa, Ltd.製の直径25 μmのアルミニウムボンディングワイヤー（Al：98.8－99.05%，Si：0.95－1.05%）を用いた．このAl線を所定の長さに切断して試験片とした。試験片を試験機に取り付ける際，直接チャッキングすることは困難であるため，Fig.3に示す標点間距離G. L. =1 mmのプラスチックタブを作成し，タブに試験片を接着し，タブを試験機に取り付けた後，Fig.3に示すタブの斜線部を切り離した後，試験片にのみ荷重が加わる状態で試験に供する。

タブの材料は，熱可塑性プラスチックのポリプロピレン（PP）およびポリエチレンテレフタレート（PET），熱硬化性プラスチックのポリイミド（PAI）の3種類を使用している。タブの作成は，CADで図面を描き，加工はPC制御のレーザーマーカー（㈱SUNX）を用い，レーザー加工でシートから切り出すことにより，加工精度の均一なタブを製作して加工によるタブのばらつきを少なくしている。試験片のタブへの接着にはシアノアクリレート系瞬間接着剤と，接着強度の向上を図るためにポリプロピレンの表面改質剤であるプライマーを用いた。また試験片のねじれを除くために，試験片をFig.3に示すタブの補助穴に通し，その後0.1 gの重りを試験片の両端部に取り付けた後，接着した。

2.3　試験方法

疲労試験は片振り引張り，繰り返し速度25 Hzで行った。繰返し数が10^7cycleに達しても破断しなかった場合はその時点で試験を終了した。

また，最大荷重の制御は，試験荷重が設定荷重値を下まわってある一定の時間経過したときに，リニアアクチュエータで1.0 μmの引張り変位を加える方式をとっている。そこで，最大荷重の調整のタイミングが疲労強度へ影響を及ぼしているかどうかを調べるために設定荷重値を下回った時間の長さが1 sec，5 secおよび10 secの場合について試験を行った。また，タブの材料および判定時間により，試験片の記号をPP

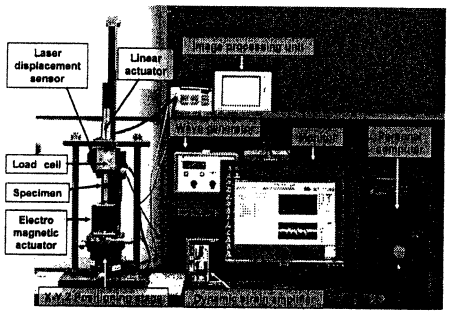

Fig. 1　Fatigue tester

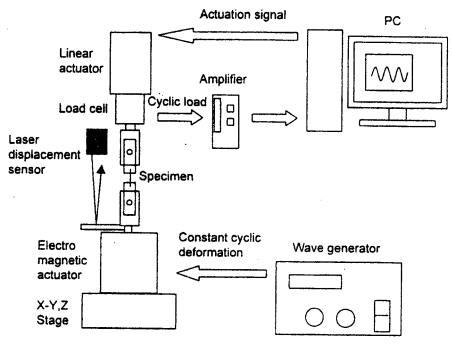

Fig. 2　Schematic diagram of fatigue testing system

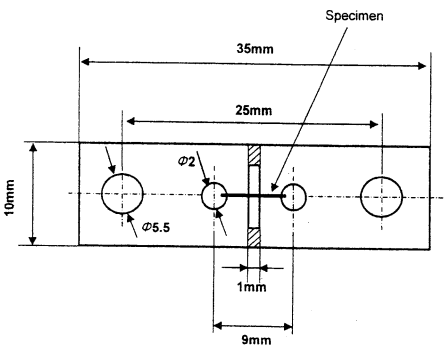

Fig. 3　Tub and specimen for fatigue test

－5，PP－10，PET－1，PAI－10 の 4 種類とした。

疲労試験終了後，走査型電子顕微鏡（KEYENCE 製 VE－8800 S）を用いて破断面の観察を行った。

3．実験結果および考察

疲労試験の結果を N－S 曲線で表すと Fig. 4 のようになる。試験はタブの材料の影響，制御の判定時間の影響の二つの要因について，疲労強度への影響を調べている段階で，異なる条件の試験結果が混在している状況であるため，これらの要因の及ぼす影響については，データが不足しており，検討することはできないが，疲労限度は 230 MPa 付近にあることが推定され，この Al ボンディングワイヤーの引張り強さは 330 MPa であることから，引っ張り強さの約 70% 程度になると思われる。

繰り返し最大応力 $\sigma_{max}=290$ MPa，破断繰返し数 $N=5.58\times10^5$ で破断した試験片の破断面を Fig. 5 に示す。この破断面から，Al ボンディングワイヤーは，破断部にくびれを生じ，ネッキングを起こして破断しており，き裂進展がほとんどないまま，不安定破断に到ったと推定される。このような，ネッキングによる破断は微小寸法材料において生じやすい[5)6)]といわれており，引張試験のときに表れる破断面によく似ていることがわかった。

試験温度の変化が，タブに与える影響，すなわち，温度によりプラスチックタブが硬化あるいは軟化することによる繰返し荷重の変動については，熱可塑性樹脂のポリプロピレンタブについて実験したところ，試験荷重が約 7 MPa/℃程度変化することが明らかとなり，温度の影響を受けにくい熱硬化性のポリイミドのタブを用いた実験を始めたところである。また，荷重制御の判定時間については，判定時間の短い 5 sec の場合，立ち上がりの荷重は設定荷重の 4.5% 増加するが，設定時間が 10 sec の場合は 2.5% と小さくなることが実験の結果明らかとなっているが，しかし，荷重制御の判定時間が疲労強度に及ぼす影響を明らかにするには，さらに多くの実験データが必要である。また，疲労試験結果のばらつきの原因には，試験機の周囲の振動の影響も考えられ，試験機の防振対策も必要と考えられる。プラスチックタブを用いた疲労試験の試験方法の確立には，まだまだ解決しなければならない問題があり，更なる実験の積み重ねが必要と考えられる。

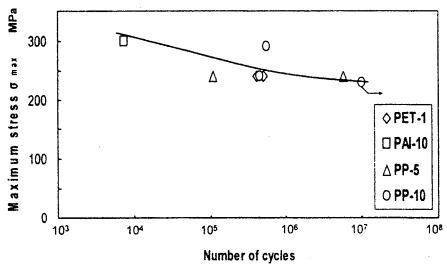

Fig. 4　S－N curves

4．結　論

プラスチックタブを用いた疲労試験方法を確立する目的で，一定繰返し変位を負荷できる簡単な疲労試験機を製作し，プラスチックタブを用いて直径 25 μm の Al ボンディングワイヤーの疲労試験を行ってみた結果，以下のことが明らかになった。

1）プラスチックタブを用いることにより，直径 25 μm の Al ボンディングワイヤーの疲労試験が可能である。

2）リニアアクチュエータを用いて試験片に微小な変位を与え，疲労試験中の試験片の伸びを補正することにより，最大荷重一定の荷重制御試験を行うことが可能である。

参考文献

1）後藤，新井，宮坂，立野，小林，小久保：材料試験技術，Vol. 53, No. 1, pp. 38－42（2008）

2）箕島，田中，石田：日本材料学会　第 269 回疲労部門委員会　第 27 回マイクロマテリアル部門委員会研究討論資料，pp. 44－45（2004－5）

3）K. Minosima, Y. Maekawa, K. Komai：日本材料学会第 269 回疲労部門委員会第 27 回マイクロマテリアル部門委員会研究討論資料，pp. 35－43（2004－5）

4）原，足立，松村，越智：第 4 回マイクロマテリアルシンポジュウム講演論文集，pp. 18－23（2008）

5）中井，橋本，竹谷：材料，Vol. 54, No. 3, pp. 284－289（2005）

6）中村，宮部，田中，中井：第 4 回マイクロマテリアルシンポジュウム講演論文集，pp. 12－17（2008）

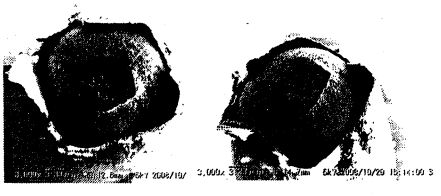

Fig. 5　Fatigue tested failure surface of aluminum bonding wire（σmax = 290 MPa, N = 5.58×10^5）

"Structure and Properties of Deep-UV AlGaN MQW Laser"

Hideo Kawanishi
Kogakuin University,
Nakano-machi 2665-1、Hachioji-shi , Tokyo 192-0015, JAPAN
kawanisi@cc.kogakuin.ac.jp

Abstract: Structure and properties of UV and deep-UV AlGaN MQW laser grown on c-plane SiC substrate are discussed. TM-mode lasing was demonstrated in deep-UV spectrum region. This is originated in band structure of AlGaN.

1. Introduction

The shortest lasing wavelengths of the AlGaN lasers were, 230nm under optical pumping [1], 342nm under current injection at room temperature [2], respectively. Stimulated emission at 210nm was also demonstrated at room temperature by single AlN layer without waveguide structure under optical pumping [3]. Recently anisotropic optical properties of the AlGaN MQW laser was also reported in the shorter wavelength region than 280-260 nm, which originated in band structure of the AlGaN semiconductor system [4-6]. TM-mode lasing was only operated in the shorter wavelength than 280nm by the AlGaN MQW laser. This paper is reviewing the recent developments of the UV and deep-UV AlGaN laser.

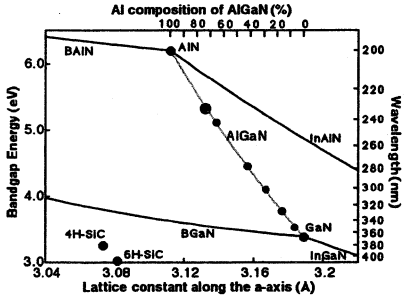

Fig.1 Band structure and a-lattice constant for BAlGaN semiconductor system ● are AlGaN MQW laser which we were demonstrated.

2. AlGaN or BAlGaN systems for UV to Deep-UV semiconductor LD

AlGaN or BAlGaN has the widest bang-gap, which covers from UV to deep-UV spectral range, as shown in Figure 1. The shortest lasing wavelength possible to lasing is around 220-230 nm of deep-UV spectral region. However, we do not find out suitable substrate for the AlGaN and BAlGaN system. Al_2O_3 and SiC were used usually for epitaxial substrate. Recently, freestanding GaN substrate is also commercially available but not AlN substrate. Therefore, epitaxialy grown AlGaN and BAlGaN include so many dislocations, such as screw, edge, and mixed dislocation. Typical dislocation density in the epitaxial layer were 10^6 -10^9 for screw dislocation and 10^9 [1/cm^2] for edge dislocation. So, optical and electrical properties of the AlGaN and BAlGaN for UV and deep-UV emitters were strongly affected by the high dislocation density.

On the other hand, AlGaN and BAlGaN include so much stress in epitaxial layers, which is caused by not only lattice mismatch but also mismatch in thermal expansion coefficient. Therefore, strain control and crack control must be important in this semiconductor system.

4. Fabrication process and structure of AlGaN MQW laser

AlGaN MQW laser was fabricated on c-plane SiC substrate by LP-MO-VPE using (AlN/GaN) Multi-Buffer Layer Structure (MBLS) at hetero-interface and thick AlN template. Laser structure was grown on the AlN template by Alternate Source-Feeding MO-VPE technique (ASF-MOVPE) as shown in Figure 2. Treading dislocations appeared on the hetero interface were mostly terminated on the (AlN/GaN) MBLS (made clear by TEM analysis) and partly on AlGaN hetero interface (for example AlGaN cladding and guide layers with different Al composition) in the laser structure, respectively. Point defects, which strongly affect to the emission efficiency and included in the active layer, were probably reduced. Therefore, threshold was decreased by about one order of magnitude. Then the shortest lasing wavelength was successfully demonstrated at 236nm at room temperature.

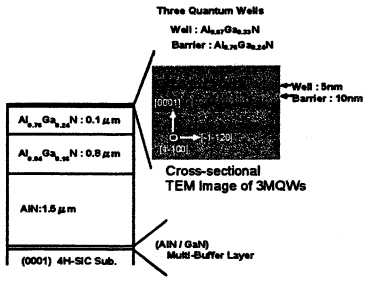

Fig. 2: UV and deep-UV AlGaN MQW laser structure grown on SiC substrate by LP-MO-VPE. High resolution TEM image of the MQW structure was interpolated.

5. Lasing and optical an-isotropic emission from AlGaN MQW laser

Spontaneous surface emission intensity was decreased as increased Al composition as shown in Figure 3. Figure 3 includes surface emission variation from AlGaN grown on m-plane SiC substrate. No dependence of surface emission from m-plane AlGaN, as indicated in Fig.3. This is originated in band structure of the AlGaN system. Isotropic surface and edge emissions were demonstrated for GaN and AlGaN with relatively small Al composition. On the other hand, surface emission decreased with increased Al composition in the AlGaN system. Then, no or extremely weak spontaneous surface emission was observed from the AlGaN with band gap wavelength shorter than about 260nm. So, lasing mode became in TM-mode in the wavelength region shorter than 260nm for AlGaN MQW laser, as shown in Figure 4.

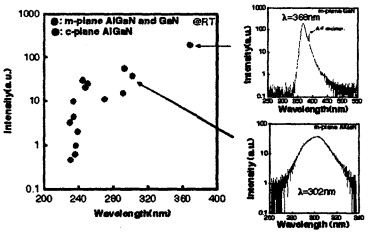

Figure 3: Surface emission intensity from c-plane and m-plane AlGaN single layers grown on c or m-plane SiC substrate.

Figure 5 shows lasing spectra that we demonstrated were summarized. As shown in this figure, we succeed in lasing from UV to deep-UV spectral region by the high quality AlGaN MQW laser grown on c-plane SiC substrate.

Temperature dependence of the lasing wavelength was extremely stable and less than 2-5 x 10^{-5} nm/degree. This temperature dependence of lasing wavelength is originated in temperature dependence of band gap. This is one of merit of the wide band gap semiconductors as AlGaN and BAlGaN.

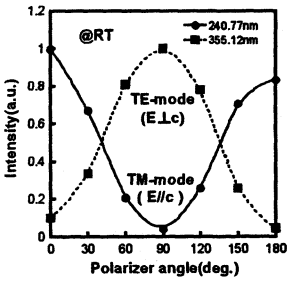

Figure 4: Lasing mode of UV and deep-UV AlGaN MQW lasers at room temperature. TM-mode lasing was obtained in the deep-UV laser.

5. Conclusions

In this paper, structure and lasing properties of the UV and deep-UV AlGaN MQW laser grown on the c-plane SiC substrate are discussed. UV to deep-UV lasing of the AlGaN MQW laser was demonstrated at room temperature from 360nm down to 364 nm at room temperature. In UV spectral region, TE-mode operation was obtained above 280 nm, but TM-mode operation was obtained shorter than 260 nm. This is fundamentally originated in the band structure of the AlGaN semiconductor system.

Temperature stability of lasing wavelength was also demonstrated by the AlGaN MQW laser and temperature dependence of lasing wavelength was as small as 2-5 x 10^{-5} nm/degree.

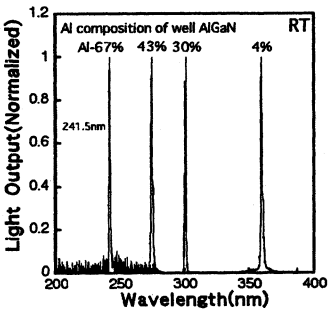

Figure 5: Lasing spectrum of GaN or AlGaN MQW lasers at room temperature. The shortest lasing wavelength that we demonstrated was 236nm.

References

1. T. Takano et al, Appl. Phys. Lett., 84(2004)3567.
2. H. Yoshida et al, Nature Photonics.
3. M. Shatalov et al., JJAP. 45(2006)L1286.
4. H. Kawanishi et al, Appl. Phys. Lett., 89(2006)041126.
5. H. Kawanishi et al, Appl. Phys. Lett., 89(2006)251107.
6 H. Kawanishi et al, Appl. Phys. Lett., 89(2006)081121.

Hideo **Kawanishi** was born in Okayama, Japan in 1946.He received his B.S. and M.S in 1971 and 1973 from Kogakuin University, and Ph. D in 1979 from Tokyo Institute of Technology. He held postdoctoral fellowship in 1979-1980 at Honeywell (Central Research Center, Minnesota, USA). He joined the Department of Physical Electronic Engineering at Tokyo Institute of Technology in 1973-1979, working in the research on GaAs/AlGaAs and GaInAsP/InP long wavelength laser diodes with Distributed Bragg Reflector (Single longitudinal mode operation laser for optical fiber communication). In 1980 he was appointed Research Associate at Kogakuin University. He became an Associate Professor in 1986 and a Full Professor in 1991 of Kogakuin University. He is a member of JSPS.

Phys. Status Solidi C 6, No. 2, 596–598 (2009) / DOI 10.1002/pssc.200880406

physica status solidi c
www.pss-c.com
current topics in solid state physics

Fabrication of MgZnO films by molecular precursor method and their application to UV-transparent electrodes

Yoshihiro Mashiyama[1], Kaori Yoshioka[1], Shigetoshi Komiyama[1], Hirohisa Nomura[2], Shunsuke Adachi[2], Mitsunobu Sato[2], and Tohru Honda[*,1]

[1] Department of Electronic Engineering, Kogakuin University, 2665-1 Nakano-machi, Hachiohji, Tokyo 192-0015, Japan
[2] Coordination Engineering Laboratory, Kogakuin University, 2665-1 Nakano-machi, Hachiohji, Tokyo 192-0015, Japan

Received 8 August 2008, revised 24 October 2008, accepted 24 October 2008
Published online 21 November 2008

PACS 61.05.cp, 72.80.Ey, 73.61.Ga, 78.60.Fi, 81.05.Dz, 81.15.Lm

* Corresponding author: e-mail ct11761@ns.kogakuin.ac.jp, Phone: +81 426 22 9291, Fax: +81 425 8982

MgZnO thin films were fabricated by the molecular precursor method (MPM) for the realization of cost-effective near-ultraviolet (UV) transparent electrodes for GaN-based UV light-emitting diodes (LEDs). The fabrication by MPM requires a common solution. It was clarified that ammonia aqueous is a common solvent for Mg, Zn and Ga precursors. MgZnO thin film was successfully fabricated on a quartz glass substrate using MgZnO precursor solution. The solid phase composition of Mg in the film is 40-50% of its molar fraction in the liquid phase. The X-ray diffraction patterns indicate the films have a hexagonal single phase, the same as in the case of ZnO. Ga doping of the MgZnO films enables their resistivity control. The possibility of applying MgZnO films for UV transparent electrodes on GaN-based UV LEDs is discussed.

1 Introduction Recently, transparent electrodes such as those of indium tin oxide (ITO), which is one of the transparent conductive oxides (TCO), are attracting much attention for the application to flat-panel displays (FPDs). UV transparent electrodes are also promising for the realizing high light-extraction efficiency in GaN-based UV light-emitting diodes (LEDs). However, the conventional indium tin oxide (ITO) is not suitable for the UV transparent use. The ZnO-based transparent electrode is one such candidate for a near UV spectral region [1]. The molecular precursor method (MPM) is a spin-coating technique [2] that is suitable for the cost-effective fabrication of those electrodes [3]. Metal-organic complexes are used for the starting materials for MPM. After the spin coating, metal nta and edta release metals at RT and those are oxidized during the annealing. This mechanism is different from the spray pyrolysis [4]. The organic parts after the metal releasing are oxidized and evaporated. The merit of MPM is the flexibility of the mixture of metal-organic materials if their common solvent is available. Although the classical absorption edge of ZnO is 3.37 eV [5], this electrode is insufficient for the GaN-based LEDs operating in UV spectral regions.

However, there are few reports concerning the fabrication of MgZnO films by MPM. In this paper, the fabrication of MgZnO films by MPM is reported. Their transparent spectra and the solid phase composition of Mg in the film are also discussed in view of transparent electrodes. The possibility of their application to UV GaN-based LEDs is also discussed

2 Experiments The base solution was prepared by the reaction of Zn-nitrilotriacetic acid (nta) complex, which was obtained from the reacted NTA aqueous solution with zinc acetate, with butylamine in ammonia aqueous. The dosed solution was prepared by the reaction of Mg-ethylenediamine-N,N,N',N'-tetraacetic acid (edta) complex. Then, the dosed solution was mixed into the base precursor solution. Here, the amount of the dosed solution (Mg-precursor) was controlled. Thus, a coating solution for MgZnO was obtained. The clear solution was spin-coated onto quartz glass (1st 3000 rpm · 3 s /2nd 4000 rpm · 5 s).

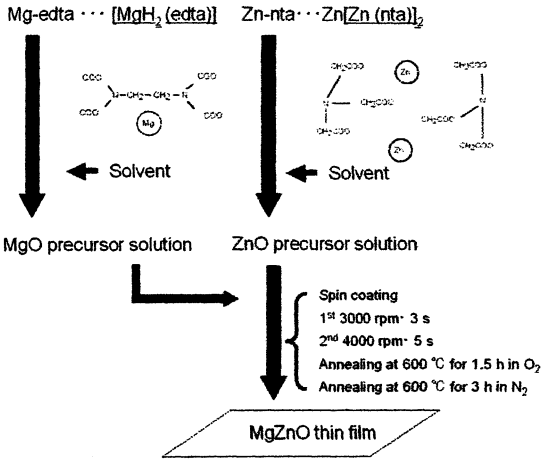

Figure 1 Schematic drawing of the fabrication process of MgZnO films by MPM.

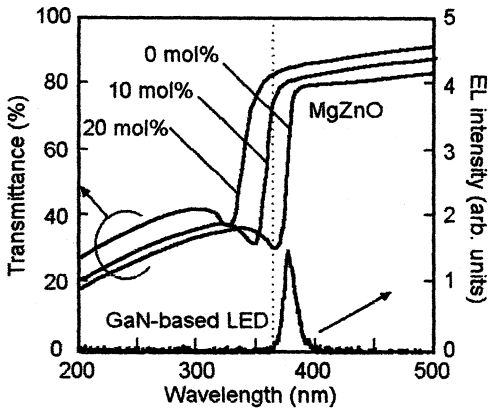

Figure 2 Transparent spectra of MgZnO films observed at RT. An electroluminescent spectrum of the GaN-based light-emitting diode [8] is also shown in the figure.

The precursor films were dried at 70 °C for 10 min and then fired at 600 °C for 90 min. The 3rd annealing atmosphere was N_2 (3rd 600 °C · 3 h). These procedures are summarized in Fig. 1.

The films were characterized using X-ray diffraction (XRD), X-ray photoelectron spectroscopy (XPS), and transparent spectra. The resistivity was measured using a conventional four-probe method. Tungsten needles were used as the probes.

3 Results

3.1 Fabrication of MgZnO films A common solvent for Zn-nta and Mg-edta was required for the fabrication of MgZnO films by MPM. Some solvents such as ethanol, methanol and ammonia aqueous were tested and we found that ammonia solution is suitable. The transparent spectra of MgZnO films fabricated by MPM are shown in Fig. 2. With increasing molar fraction of Mg sources, the excitonic absorption peak shifted towards the higher energy side. This indicates that the deposited films were MgZnO alloys. The XRD spectra of MgZnO films fabricated by MPM are shown in Fig. 3. The XRD patterns show that the structure of the deposited films is hexagonal and polycrystalline. No diffraction peaks from MgO and other materials are observed. The Mg concentration and Mg composition of MgZnO films observed by XPS spectra are shown in Fig. 4. The solid phase composition of Mg in the film is 40-50% of its molar fraction in the liquid phase. Thus, these results indicate that the MPM is suitable for the cost-effective fabrication of MgZnO alloy films.

3.2 Ga doping to MgZnO films The realization of low resistivity was required for the application of transparent electrodes. It is reported that Ga or Al doping in ZnO is effective for the realization of low resistivity [6-8] in the case of pulsed laser deposition (PLD) and sputtering fabrications. Thus, Ga doping in the MgZnO films was performed. Ga-nitrilotriacetic acid (nta) complex was used for doping. It was mixed into the Mg-EDTA and Zn-NTA solutions and spin-coated onto the glass substrates. The annealing conditions were the same as a case of the fabrication of undoped MgZnO films.

The resistivity of the fabricated Ga-doped ZnO and MgZnO films is shown in Fig. 5. Here, their thickness is approximately 0.1 μm. With an increasing amount of the Ga source, the resistivity of ZnO decreased. The MgZnO films also showed low resistivity. The I-V plotting with the outside probes of the MgZnO (Mg 20 mol%, Ga 5 mol%) film is also shown in the inset of Fig. 5. Ohmic-like contact between the tungsten probe and the MgZnO film was realized. These indicate that the doping technique is effective for the fabrication of ZnO-based UV transparent electrodes by MPM.

4 Discussion It is found that the ammonia aqueous can be used as a common solution. The fabrications of MgZnO films and Ga-doping to them were achieved using it. Although carbon contaminations were not investigated, no disadvantages originated from carbon contaminations were observed at present.

Generally, the composition of transparent electrodes based on multinary compound semiconductors is determined on the basis of their fundamental absorption edge. However, the transparent spectra, as shown in Fig. 2, indicate that the composition of $Mg_xZn_{1-x}O$ should be determined in accordance with its excitonic absorption shape. For example, the Mg composition will be over 10% for the fabrication of MgZnO-based transparent electrodes on GaN-based LED operating in the spectral range of approximately 370 nm [9]. The MgZnO films whose Mg compositions over 10% could be fabricated by MPM.

The resistivity control of MgZnO films is possible by the Ga-doping technique in the case of MPM fabrication. This indicates the future possibility of the fabrication of cost-effective UV transparent electrodes, although their re-

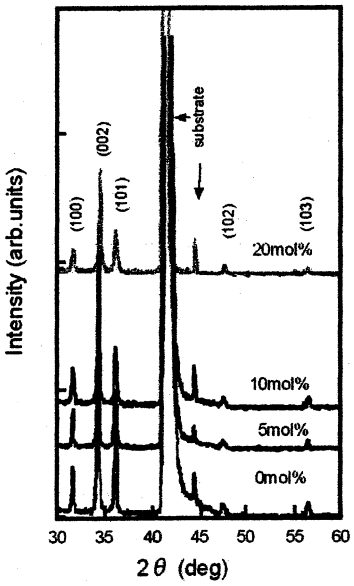

Figure 3 X-ray diffraction patterns of MgZnO films fabricated on glass substrates.

sistivities are still higher than those of reported ZnO films fabricated by sputtering [8] at present. Because the MgZnO films were polycrystalline, the control of their grain size is one of the future technical issues for the realization of the low resistivity. We consider that the annealing conditions are an important factor to control the grain size. We consider that the annealing conditions are important factor to control the grain size. The Ga-doping enables to the resistivity control from 10^4 to 10^0 Ω·cm, as shown in Fig. 5.The contact property, as shown in the inset of the figure, indicates that the crystallites in the films have a low resistivity. We consider that the control of grain size will reduce the resistivity. Nevertheless the roles of generated defects and of the impurities still need to be addressed, aiming to reach highly transparent and conductive films.

5 Summary MgZnO fabrication by MPM requires a common solvent for both Zn and Mg precursor solutions. We found that ammonia solution is a common solvent. MgZnO thin film was fabricated on a quartz glass substrate using the MgZnO precursor solution. The Mg composition in the films was estimated by X-ray photoelectron spectroscopy (XPS). The solid phase composition of Mg in the film was 40-50% of its molar fraction in the liquid phase. The resistivity control of MgZnO films was possible by the Ga-doping technique. The results indicated that the MPM is suitable for the cost-effective fabrication of MgZnO alloy films.

Acknowledgments The authors thank Professors Emeriti Y. Suematsu and K. Iga of Tokyo Institute of Technology for encouragement and Professor H. Kawanishi of Kogakuin University for support. This work was supported by a Grant-in-Aid (No. 18560344) from the Ministry of Education, Culture, Sports, Science and Technology.

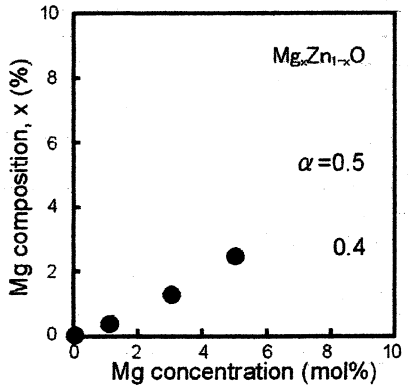

Figure 4 Solid phase composition of Mg in the film as a function of molar fraction in the liquid phase.

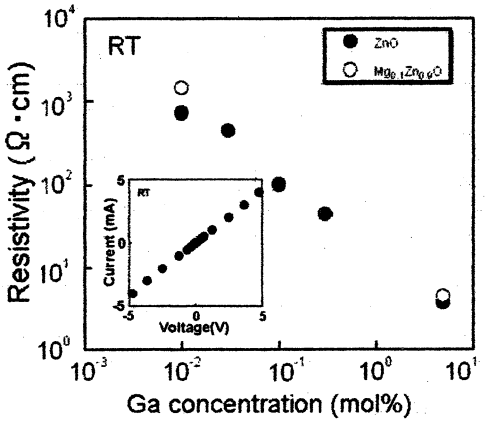

Figure 5 Resistivity of ZnO and MgZnO films (Mg: 20 mol%) as a function of Ga molar fraction in the liquid phase. Inset of the figure, I-V characteristics of Ga-doped (5 mol%) MgZnO films are shown.

References

[1] T. Minami, MRS Bull. **25**, 38 (2000).
[2] M. Sato, H. Hara, H. Kuritani, T. Nishide, and Y. Sawada, J. Mater. Chem. **6**, 1767 (1996).
[3] K. Yoshioka, S. Egawa, T. Kobayashi, T. Baba, K. Sugimoto, M. Arai, H. Nomura, M. Sato, and T. Honda, Phys. Status Solidi C **4**, 162 (2007).
[4] T. Y. Ma, S. H. Kim, H. Y. Moon, G. C. Park, Y. J. Kim, and K. W. Kim, Jpn. J. Appl. Phys. **35**, 6208 (1996).
[5] D. C. Look, Sci. Eng. B **80**, 383 (2001).
[6] V. Bhosle and J. Narayan, J. Appl. Phys. **100**, 093519 (2006).
[7] Z. Q. Li, D. X. Zhang, and J. J. Lin, J. Appl. Phys. **99**, 124906 (2006).
[8] T. Minami, T. Miyata, Y. Ohtani, and Y. Mochizuki, Jpn. J. Appl. Phys. **45**, L409 (2006).
[9] T. Honda, T. Kobayashi, S. Komiyama, and Y. Mashiyama, J. Vac. Sci. Technol. B **25**, 1529 (2007).

Journal of Crystal Growth ▮ (▮▮▮▮) ▮▮▮–▮▮▮

Contents lists available at ScienceDirect

Journal of Crystal Growth

journal homepage: www.elsevier.com/locate/jcrysgro

Formation of AlN layer on (111)Al substrate by ammonia nitridation

Tohru Honda *, Hiromi Yamamoto, Masashi Sawadaishi, Satoshi Taguchi, Kouki Sasaya

Department of Electronic Engineering, Kogakuin University, 2665-1 Nakano-machi, Hachiohji, Tokyo 192-0015, Japan

ARTICLE INFO

PACS:
61.05.Jh
68.37.Ps
82.80.Pv
81.15.Hi

Keywords:
A1. RHEED
A1. XPS
A3. Molecular beam epitaxy
B1. Nitrides

ABSTRACT

AlN layers were formed on (111)Al substrates at a temperature below the melting point of Al using preheated ammonia in vacuum. The effect of the removal of the surface oxides on the substrate in the process was investigated. It was found that treatment using a buffered HF solution and subsequent annealing in vacuum was effective for obtaining a clean Al substrate surface. It was clarified that the removal of the surface oxides is required for the nitridation of Al substrates at a low temperature below the melting point of Al.

1. Introduction

The deposition of III-N materials on a metal substrate has led to the cost-effective and large-scale fabrication of nitride-based light-emitting devices. Aluminum is a cost-effective substrate and its thermal conductivity is high compared with semiconductors, resulting in an improvement in the lifetime of optical devices such as GaN-based electroluminescent devices [1]. On the other hand, there is a large lattice mismatch between aluminum and III-N materials. A large difference in thermal expansion coefficients also exists between them. However, the fabrication of III-N materials on Al substrates is still desirable. For the realization of III-N materials on Al substrates, the nitridation of Al substrates was investigated as a possible first step of the fabrication of III-N materials on Al substrates.

The reduction of the process temperature is a crucial issue for the nitridation of Al substrates. This is due to the low melting point of aluminum (660 °C). On the other hand, the existence of surface oxide layers on the Al substrates must also be considered for the nitridation.

In this paper, the formation of AlN layers on (111)Al substrates using ammonia is reported. In particular, the necessity of removing the surface oxide on the Al substrates is discussed. Although polycrystalline Al substrates are conventionally used, single-crystalline Al substrates were used to clarify the deposition conditions of III–V nitrides on Al substrates.

2. Experiments

The (111)Al and (0001) sapphire substrates were used in this study. First, the nitridation of sapphire substrates was performed to investigate the nitridation temperature. After that the removal of the surface oxides on the Al substrates and their subsequent nitridation were investigated.

To remove the surface oxides, buffered hydrogen fluoride (BHF) [2], which is a mixture of hydrogen fluoride (HF) and ammonium fluoride (NH_4F) solutions, was used. After the cleaning, the substrates were introduced into a vacuum chamber for thermal cleaning below the melting point of aluminum (~660 °C) for 15 m. Note that before the introduction of the substrate into the vacuum chamber and after the BHF treatment, the substrate was handled in air. Ammonia preheated to 700 °C [3] was used as the source in the nitridation. The ammonia flow rate was 6 ccm and the background pressure during the nitridation is 1×10^{-6} Torr. For the nitridation of the substrate without the removal of surface oxides, thermal cleaning was performed under the same conditions before the nitridation.

Reflection high-energy electron diffraction (RHEED) patterns of the samples were observed. The surface conditions were also observed by X-ray photoelectron spectroscopy (XPS) and by using X-ray diffraction (XRD) patterns.

3. Results

3.1. Surface nitridation of oxides

The melting point of aluminum limited the process temperature of the nitridation. The surface oxide layer on the aluminum

*Corresponding author. Tel.: +81 426 22 9291; fax: +81 426 25 8982.
E-mail address: ct11761@ns.kogakuin.ac.jp (T. Honda).

0022-0248/$ - see front matter © 2009 Elsevier B.V. All rights reserved.
doi:10.1016/j.jcrysgro.2009.01.026

substrates could not be perfectly nitrided below the melting point, although nitride-related peaks were observed in the XPS spectra. We also attempted the nitridation of sapphire substrates using ammonia, but their RHEED patterns did not change below a substrate temperature of 660 °C. Although nitride-related patterns were observed from the substrates that underwent the nitridation at a high temperature of 850 °C, as shown in Fig. 1, the nitridation of aluminum oxide was difficult to achieve at the low temperature of approximately 660 °C. The results mean that the removal of the surface oxide layer is crucial for the nitridation of Al.

3.2. Removal of surface oxides

RHEED patterns of an as-received (111)Al single-crystal substrate and of the substrate after the BHF treatment are shown in Fig. 2. The results indicated that the surface oxides were etched and the reoxidation of the substrates was suppressed. The XPS spectra of Al substrates with the BHF treatment are shown in Fig. 3. F atoms were observed from the surface before thermal cleaning. No hydrogen-related peak such as a chemical shift of an Al2p peak was observed. This indicates that the F atoms were terminated on the Al surface. On the other hand, the F-related peak disappeared in the XPS spectrum of the substrate after thermal cleaning.

3.3. Nitridation

The surface oxide layer on the Al substrate was chemically removed and its clean surface was confirmed from its RHEED pattern. The XRD and RHEED patterns of the Al substrate after surface nitridation are shown in Fig. 4. The diffraction peaks of polycrystalline hexagonal AlN were observed. The XPS results for the nitridated substrate after Ar ion beam etching indicate that the thickness of the AlN layer is approximately 20 nm. On the other hand, in the case of the nitridation of Al substrates with surface oxides, no reduction of oxygen-related peaks was observed in the XPS spectra although a weak nitrogen peak was observed. This indicates that the small amount of the surface oxides was replaced by nitrides. The results are consistent with those of sapphire nitridation.

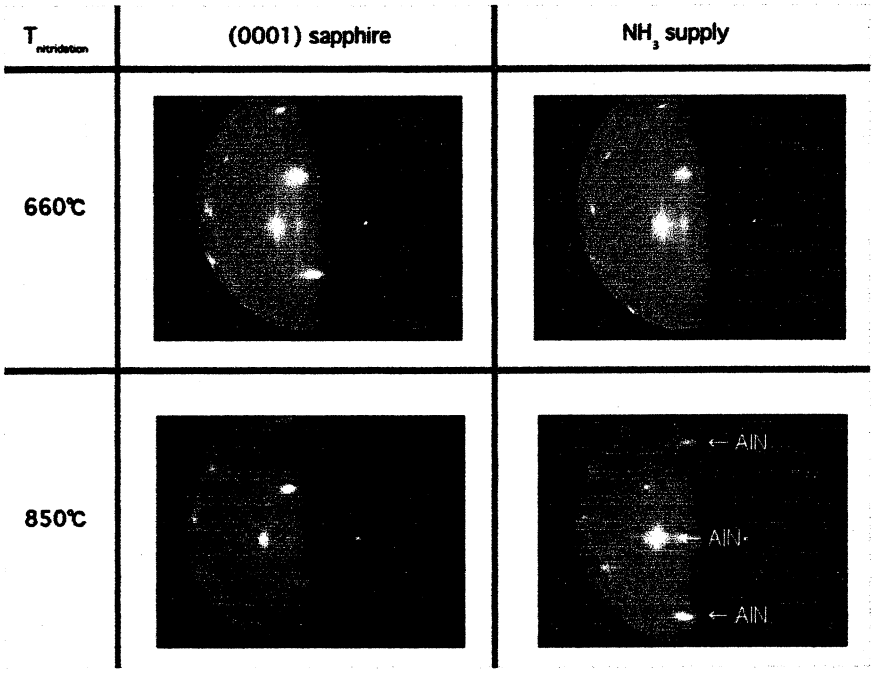

Fig. 1. RHEED patterns of (0001) sapphire substrates with and without nitridation.

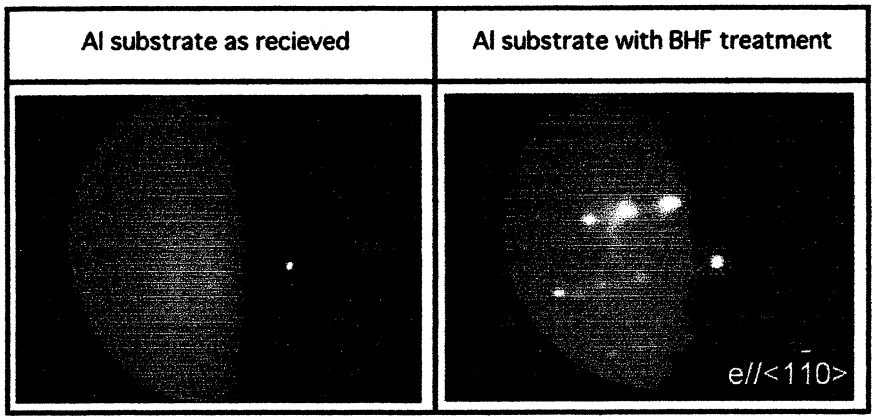

Fig. 2. RHEED patterns of as-received (111)Al substrates and the substrate after BHF treatment.

Please cite this article as: T. Honda, et al., J. Crystal Growth (2009), doi:10.1016/j.jcrysgro.2009.01.026

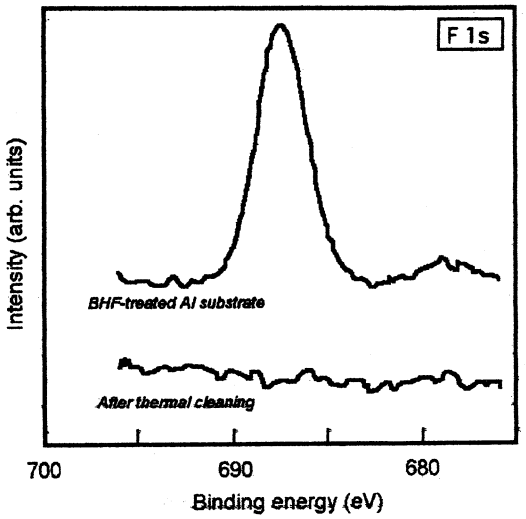

Fig. 3. XPS spectra of Al substrates after BHF treatment around the F1s binding energy.

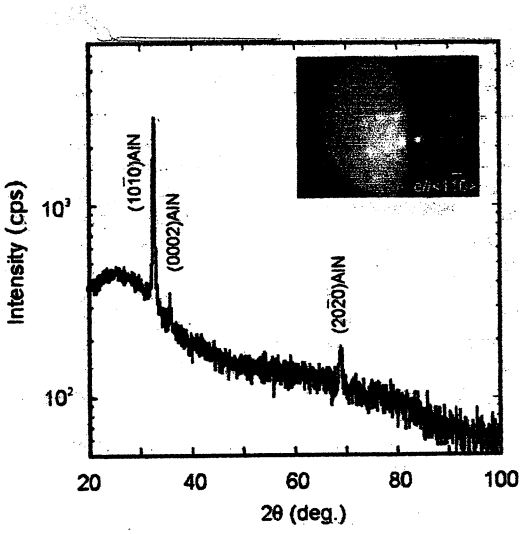

Fig. 4. XRD pattern of Al substrate after nitridation. The RHEED pattern is also shown in the inset of the figure.

4. Discussion

Al substrates have surface oxides on them. Thus, the necessity of their removal must be investigated for nitridation. The surface nitridation of sapphire substrates in the molecular beam epitaxy (MBE) growth has been reported [4]. The surface of sapphire is composed of oxides. This means that the nitridation can be achieved without the removal of the oxides. However, the reported nitridation temperature was higher than the melting point of Al. The results in this study show that the nitridation of surface oxides on Al substrates is difficult to achieve at low temperatures below the melting point of Al. Thus, the removal of the surface oxides is necessary for the nitridation.

The wet etching of surface oxides on the Al substrates was performed using BHF solution. BHF solution can also be used for the removal of surface oxides on Si substrates [2]. Hydrogen termination on the Si substrates after the treatment was reported, which suppresses the reoxidation of the surface. In case of Al substrates, the suppression of oxidation in air was also observed for the wet-etched substrates, although F atoms were terminated on their surface. This indicates that the termination of F atoms is effective for the reduction of surface reoxidation.

The nitridation of the substrates with and without BHF treatment was performed using preheated ammonia. The diffraction peaks related to AlN, as shown in Fig. 4, were observed from the surface-cleaned substrates after the nitridation. On the other hand, no diffraction peaks were observed from the untreated substrates. This means that the nitridation of Al using preheated ammonia is possible, although the nitridation of the surface oxides is difficult at the low temperature below the Al melting point. These results show that the removal of surface oxides on Al substrates is necessary for their nitridation using preheated ammonia.

5. Summary

An AlN layer was formed on a (111)Al substrate by using preheated ammonia in vacuum. In the process, it was clarified that the removal of the surface oxides was required for the nitridation at a low temperature below the melting point of aluminum. The chemical cleaning process using BHF solution and the thermal cleaning effectively removed the surface oxides.

Acknowledgments

The authors thank Professors Emeriti Y. Suematsu and K. Iga of Tokyo Institute of Technology for encouragement and Professor H. Kawanishi of Kogakuin University for the support. They also thank Professors A. Koukitu and Y. Kumagai and Dr. H. Murakami of Tokyo University of Agriculture and Technology for the help in the XRD measurements. This work was supported by a Grant-in-Aid (no. 18560344) from the Ministry of Education, Culture, Sports, Science and Technology.

References

[1] T. Honda, S. Egawa, K. Sugimoto, M. Arai, J. Cryst. Growth 301–302 (2007) 424.
[2] For example G.S. Higashi, R.S. Becker, Y.J. Chabal, A.J. Becker, Appl. Phys. Lett. 58 (1991) 1656.
[3] T. Honda, M. Sawadaishi, H. Yamamoto, M. Arai, K. Yoshioka, T. Okuhata J. Cryst. Growth 310 (2008) 1781.
[4] N. Grandjean, J. Massies, M. Leroux, Appl. Phys. Lett. 69 (1996) 2071 For example.

Please cite this article as: T. Honda, et al., J. Crystal Growth (2009), doi:10.1016/j.jcrysgro.2009.01.026

Journal of Crystal Growth ▮ (▮▮▮▮) ▮▮▮–▮▮▮

Contents lists available at ScienceDirect

Journal of Crystal Growth

journal homepage: www.elsevier.com/locate/jcrysgro

Nitridation of (111)Al substrates for GaN growth by molecular beam epitaxy

Masashi Sawadaishi, Satoshi Taguchi, Kouki Sasaya, Tohru Honda *

Department of Electronic Engineering, Kogakuin University, 2665-1 Nakano-machi, Hachiohji, Tokyo 192-0015, Japan

ARTICLE INFO

PACS:
61.05.jh
68.37.Ps
82.80.Pv
81.15.Hi

Keywords:
A1. RHEED
A1. XPS
A3. Molecular beam epitaxy
B1. Nitrides

ABSTRACT

The GaN layers were grown by compound-source molecular beam epitaxy (CS-MBE) on (111) aluminum (Al) substrates with and without nitridation. The melting point of Al substrates limits the growth temperature. The layers were grown at 650 °C. Reflection high-energy electron diffraction (RHEED) patterns of the layers indicate that the nitridation is effective for GaN growth by CS-MBE on aluminum substrates. Photoluminescence was observed from the layer grown on the Al substrate with nitridation at RT.

1. Introduction

GaN-based high-power light-emitting diodes (LEDs) have been developed [1] and applied to large-scale flat-panel displays (FPDs). For future application to small FPDs, the integration of LEDs on flexible or metal substrates is attractive [2]. In particular, aluminum (Al) substrates are suitable for cost-effective GaN-based light-emitting devices, although its melting point is lower (660 °C) than the conventional growth temperature of GaN by metal-organic vapor phase epitaxy (MOVPE) [3]. Molecular beam epitaxy (MBE) is suitable for low-temperature growth at less than 660 °C. Compound-source MBE (CS-MBE) of GaN has been proposed and demonstrated as a method of low-temperature growth [4]. However, the initial conditions of the Al substrate are unclear at present in the case of GaN grown on an Al substrate. In this study, the surface nitridation of (111)Al substrates and GaN growth on these substrates are reported. Here, the requirements of the surface treatments, including the nitridation for GaN growth, are discussed.

2. Experiments

Single-crystalline (111)Al substrates were used in this study. The thickness and size of the substrates are approximately 500 μm and 1 cm^2, respectively. Although polycrystalline Al substrates are suitable for the cost-effective fabrication of GaN films on Al substrates, we consider that the use of the single-crystalline Al substrate for GaN fabrication is required to clarify the initial growth conditions. For the removal of the surface oxide, buffered hydrogen fluoride (BHF) [5], which is a mixture of hydrogen fluoride (HF) and ammonia fluoride (NH_4F) solutions, was used. The concentration of ammonium monohydrogen difluoride (NH_4HF_2) in the solution was 20.8 wt%. The etching time and temperature are 10 min and RT, respectively. After the cleaning, the substrates were introduced into the vacuum chamber and thermally cleaned below the melting point of Al (~660 °C) for 15 min. Here, before the introduction of the substrate into the vacuum chamber, it is exposed to air after the BHF treatment. However, a clean Al surface was obtained after thermal cleaning because of the termination by fluorine on the Al surface after the BHF treatment [6].

The chemically cleaned Al substrates described above were used for the nitridation. Preheated ammonia (700 °C, 6 ccm) was used for the nitridation. After the nitridation for 1 h, reflection high-energy electron diffraction (RHEED) analysis, X-ray photoelectron spectroscopy (XPS) of a sample subjected to Ar^+ ion beam etching (IBE) and transmission electron microscope (TEM) observation were carried out.

The GaN layers were grown by CS-MBE on Al substrates with and without nitridation. GaN powders and ammonia were used as the sources in CS-MBE growth [7]. Here, the ammonia was introduced into the growth chamber after preheating at 700 °C. The substrate temperature during the growth was kept at 650 °C. The GaN powder used as a source was maintained at 850 °C in a Knudsen cell (K-cell). The ammonia was supplied at a

*Corresponding author. Tel.: +81 42 622 9291; fax: +81 42 625 8982.
E-mail address: ct11761@ns.kogakuin.ac.jp (T. Honda).

0022-0248/$ - see front matter © 2008 Elsevier B.V. All rights reserved.
doi:10.1016/j.jcrysgro.2008.11.007

flow rate of 6 ccm, which is the same as in the case of nitridation. The thicknesses and growth rate of GaN layers were approximately 0.5 μm and 50 nm/h, respectively.

3. Results

3.1. Nitridation of Al substrates

The surface oxide layer on the Al substrate was chemically removed and a clean substrate surface was confirmed from the RHEED pattern, as shown in Fig. 1. After the nitridation, ring RHEED patterns were observed. XRD diffraction patterns clarified that polycrystalline AlN was formed after nitridation [6]. XPS results for the nitridated substrate after Ar ion-beam etching indicate that the thickness of the AlN layer is approximately 20 nm. This was consistent with the thickness of the AlN layer observed in the cross-sectional TEM image shown in Fig. 2. On the other hand, in the case of the nitridation of Al substrates with surface oxide, no reduction of oxygen-related peaks was observed in the XPS spectra, although a weak nitrogen peak was observed. This indicates that a small amount of the surface oxide was replaced by the nitrides. These results are consistent with those of sapphire nitridation [6].

3.2. GaN growth on Al substrates

The GaN layers were grown on surface-cleaned (111)Al substrates with and without nitridation. Their RHEED patterns are shown in Fig. 3. In the case of GaN growth on Al substrates without nitridation, ring RHEED patterns were observed. On the other hand, additional spotty RHEED patterns were observed from the GaN layer on the Al substrate with nitridation. These patterns indicate that the crystalline quality of the GaN layers on the Al substrates with nitridation is better than that on the Al substrate without nitridation. The surface morphology is hypothesized to affect the crystalline qualities. This is currently under investigation.

Photoluminescence (PL) spectra of GaN layers grown on Al substrates with and without nitridation were observed at RT. The 325 nm light of the He–Cd laser (1 mW) was used for excitation. The laser beam with a diameter of approximately 1 mm was focused on the sample. Although the intensity of the PL spectra of the layers on Al substrates without nitridation was very weak and those spectra were not detected, those of the layers grown on Al substrates with nitridation were relatively strong, as shown in Fig. 4. The emission spectra started from the band edge of hexagonal GaN. The assignment of the peaks is under way.

4. Discussion

The atomic orderings of GaN, AlN and Al are important in the consideration of the crystalline quality of the GaN layers, although the layers are not single crystals at present. The crystalline structure of single-crystalline Al substrates is a face-centered cubic, its atomic ordering on the (111)Al surface is hexagonal, and its duration at RT is 2.862 Å [8]. The lattice constant of AlN along the a-axis is 3.11 Å at RT [9]. There is a large lattice mismatch of 8.7% between the AlN and Al substrates. On the other hand, the lattice mismatch between GaN and Al is 11.4% [10]. The lattice constants indicate that the AlN layer formed upon nitridation acts as a buffer layer during GaN growth, which leads to the high crystalline quality. This is consistent with the results shown in Fig. 3. However, the large mismatch leads to a high dislocation density in the GaN layers. A strain reduction strategy, such as the introduction of multi-buffer layers [11], will be required.

It was observed that the PL intensity of the GaN layer grown on the Al substrate with nitridation is higher than that in the case without nitridation. This is due to the following: (1) the improvement of crystalline quality and (2) the blocking of excited carriers, which prevents their diffusion to the substrate. At present, the main reason is under investigation. Two peaks were observed in the spectrum. The peak observed at the higher energy in the PL spectrum is due to the near-band-edge emission of hexagonal GaN [12]. Although the origin of the other peak is unknown at present, we hypothesize that it is due to the cubic GaN [13] that formed around the stacking faults [14]. The PL intensity will also be improved by introducing strain reduction systems.

We have already reported the electroluminescent devices based on a GaN layer deposited on oxide insulators fabricated on Al substrates [4]. The observation of the PL spectrum with a near-band-edge emission indicates that the layer has potential application in light-emitting devices.

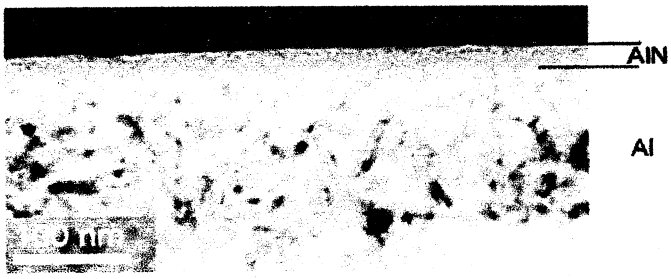

Fig. 2. Cross-sectional TEM image of (111)Al substrate with nitridation. AlN layer thickness is approximately 20 nm.

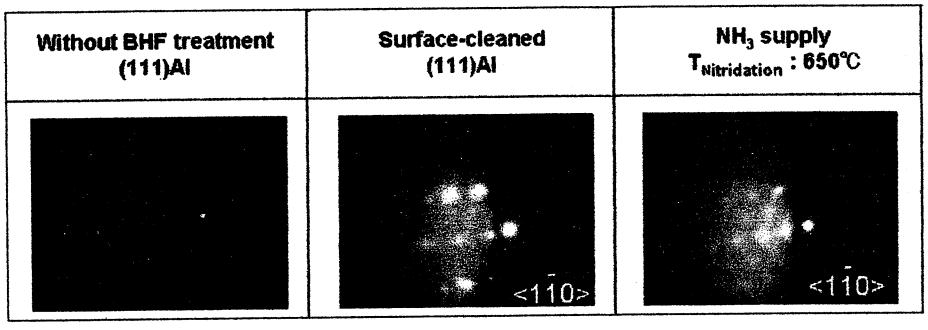

Fig. 1. RHEED patterns of as-received (111)Al and (111)Al surface-cleaned by BHF with and without nitridation.

Please cite this article as: M. Sawadaishi, et al., J. Crystal Growth (2009), doi:10.1016/j.jcrysgro.2008.11.007

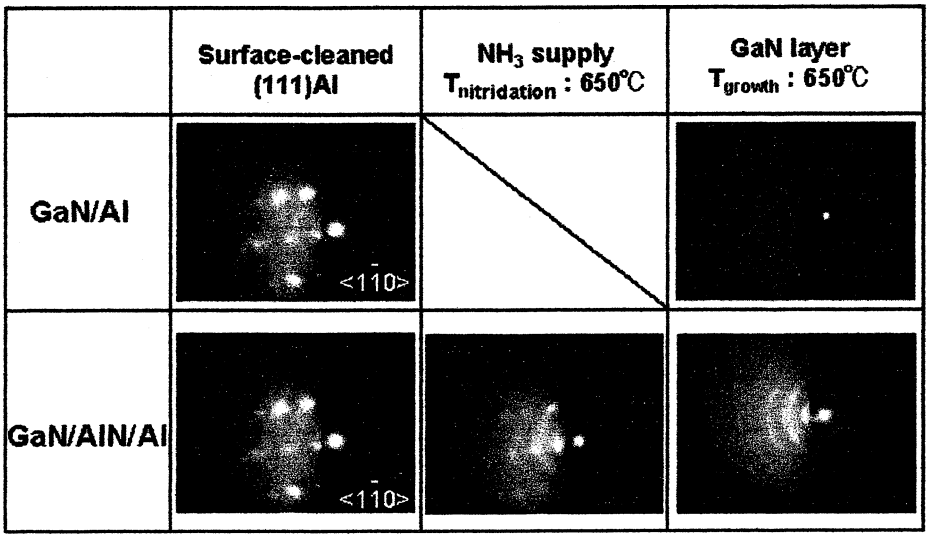

Fig. 3. RHEED patterns of GaN layer on Al substrates with and without nitridation.

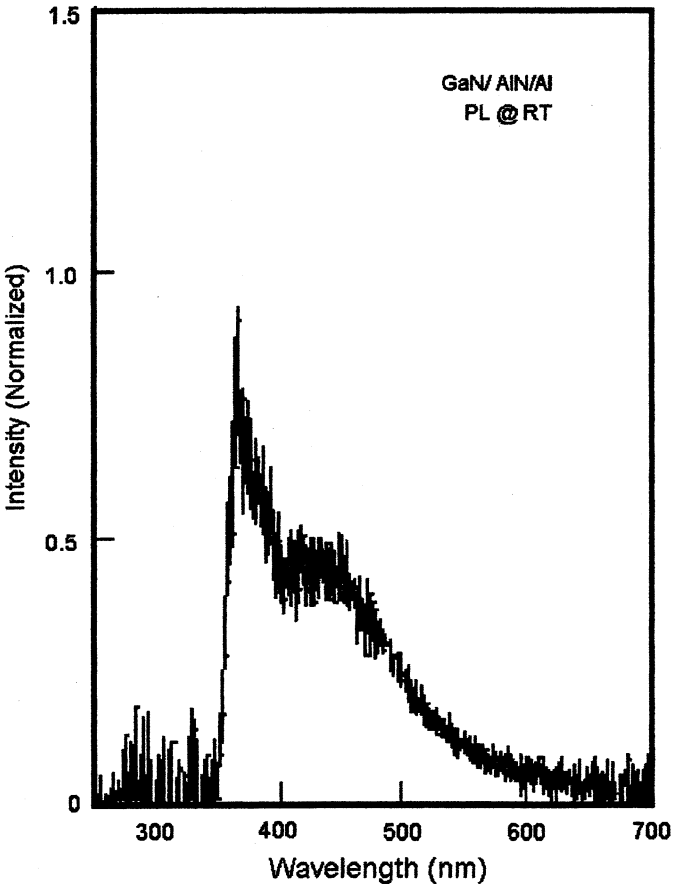

Fig. 4. PL spectrum of GaN layer grown on (111)Al with nitridation at RT.

5. Summary

GaN layers were grown by compound-source molecular beam epitaxy (CS-MBE) on (111)Al substrates with and without nitridation. Reflection high-energy electron diffraction (RHEED) patterns of the layers indicated that nitridation improves the crystalline quality of the layers. The photoluminescence (PL) spectrum of the layer on (111)Al with nitridation was observed. The spectrum includes the near-band-edge emission of hexagonal GaN. The GaN layer on the Al substrate has potential for application to light-emitting devices.

Acknowledgments

The authors thank Professors Emeriti Y. Suematsu and K. Iga of Tokyo Institute of Technology for encouragement and Professor H. Kawanishi of Kogakuin University for support. They also thank the Japan Light Metal Co. for carrying out the TEM measurements. This work was supported by a Grant-in-Aid (No. 18560344) from the Ministry of Education, Culture, Sports, Science and Technology.

References

[1] T. Mukai, D. Morita, S. Nakamura, J. Crystal Growth 189/190 (1998) 778.
[2] S. Guha, N. Bojarczuk, Appl. Phys. Lett. 73 (1998) 1487.
[3] I. Akasaki, H. Amano, Jpn. J. Appl. Phys. 36 (1997) 5393.
[4] T. Honda, S. Egawa, K. Sugimoto, M. Arai, J. Crystal Growth 301–302 (2007) 424.
[5] G.S. Higashi, R.S. Becker, Y.J. Chabal, A.J. Becker, Appl. Phys. Lett. 58 (1991) 1656.
[6] T. Honda, H. Yamamoto, M. Sawadaishi, S. Taguchi, K. Sasaya, J. Crystal Growth, in print.
[7] M. Sawada, M. Sawadaishi, H. Yamamoto, M. Arai, T. Honda, J. Crystal Growth 301–302 (2007) 67.
[8] A.G. Jackson, M.P. Hooker, J. Appl. Phys. 38 (1967) 4998.
[9] S. Iwama, K. Hayakawa, T. Arizumi, J. Crystal Growth 56 (1982) 265.
[10] M. Leszczynski, T. Suski, H. Teisseyre, P. Perlin, I. Grzegory, J. Jun, S. Porowski, T.D. Moustakas, J. Appl. Phys. 76 (1994) 4909.
[11] M. Kurimoto, T. Nakada, Y. Ishihara, M. Shibata, T. Honda, H. Kawanishi, Jpn. J. Appl. Phys. 38 (1999) L551.
[12] O. Lagerstedt, B. Monemar, J. Appl. Phys. 45 (1974) 2266.
[13] J. Wu, H. Yaguchi, K. Onabe, R. Ito, Y. Shiraki, J. Crystal Growth 189/190 (1998) 415.
[14] S. Strauf, P. Michler, J. Gutowski, H. Selke, U. Birkle, S. Einfeldt, D. Hommel, J. Crystal Growth 189/1900 (1998) 682.

Please cite this article as: M. Sawadaishi, et al., J. Crystal Growth (2009), doi:10.1016/j.jcrysgro.2008.11.007

phys. stat. sol. (c) 5, No. 6, 2176–2178 (2008) / DOI 10.1002/pssc.200778522

physica status solidi c
www.pss-c.com
current topics in solid state physics

Fabrication of GaN-based UV TF-ELDs by CS-MBE technique and their application to RGB light-emitting pixels

M. Arai, K. Sugimoto, S. Egawa, and T. Honda*

Department of Electronic Engineering, Kogakuin University, 2665-1 Nakano-machi, Hachiohji, Tokyo 192-0015, Japan

Received 7 September 2007, accepted 12 January 2008
Published online 3 April 2008

PACS 78.60.Fi, 81.05.Ea, 81.15.Hi, 85.60.Jb

* Corresponding author: e-mail ct11761@ns.kogakuin.ac.jp, Phone: +81 426 22 9291, Fax: +81 426 25 8982

GaN-based thin-film electroluminescence devices (TF-ELDs) operating in the UV spectral region were fabricated on Al substrates. GaN films were deposited by compound-source molecular beam epitaxy (CS-MBE) technique. Red, green and blue (RGB) light-emitting pixels were fabricated using the GaN-based TF-ELDs as excitation sources. The emission efficiencies of such TF-ELDs were reported. The estimated luminances of the RGB emitters based on the GaN films were 0.2-7 kcd/m^2, which indicate that the GaN-based TF-ELDs have a potential for application in flat-panel displays (FPDs).

1 Introduction III-V nitrides such as gallium nitride (GaN) have been attracting much attention for optoelectronic devices such as light-emitting diodes (LEDs) or laser diodes (LDs) operating in the visible and ultraviolet (UV) spectral regions [1, 2]. GaN-based light emitting devices have promising applications in flat-panel displays (FPDs). Outdoor-type large FPDs have been achieved using GaN-based LEDs [3]. However, the fabrication of outdoor-type small (personal-use) FPDs using III-V nitrides is still under investigation. Such FPDs require the low-cost fabrication of light-emitting pixels. The low-temperature process and large-scale integration of GaN-based light-emitting devices are one of the crucial issues in the development of such pixels [4].

Compound-source molecular beam epitaxy (CS-MBE), which is useful for the low-temperature deposition of GaN films, is effective for the low-cost fabrication of light-emitting devices [5, 6]. GaN-based thin-film electroluminescent devices (TF-ELDs) are one of the most suitable light-emitting devices for application in FPDs because of their simple structure. Low-cost GaN light-emitting devices using Mg-doped GaN combined with indium-tin oxide (ITO) electrodes [7] and rare-earth-doped GaN diodes [8] have already been proposed. We consider that the use of TF-ELDs using low-temperature GaN films by CS-MBE technique is one of the technical routes to realizing cost-effective FPDs. The advantage using TF-ELDs in a full-color system is that it is easy to integrate them. Their pixel is composed of UV-light-emitting devices and red, green and blue (RGB) phosphors. We can separate the integration of UV-light-emitting devices, instead of RGB self-emitting devices, and RGB phosphors. This leads to cost-effective fabrication.

In this study, GaN-based TF-ELDs operating in the UV spectral region were fabricated on Al substrates. GaN films were deposited by CS-MBE technique. RGB light-emitting pixels were fabricated using GaN-based TF-ELDs combined with RGB phosphors. The emission efficiencies of RGB phosphors during excitation by UV TF-ELDs are discussed.

2 Experimental GaN films were deposited on Al substrates by CS-MBE technique. GaN powder (4Nup), which was synthesized using the reaction between gallium and ammonia, was used as a source material. The typical GaN cell temperature was 860°C. The substrate temperature of the emission layer was kept constant at 500 °C for 5 hours. A GaN buffer layer was deposited at RT for 15 minutes before the emission layer deposition [4]. During the deposition, no additional nitrogen source such as ammonia was introduced. For the fabrication of GaN-

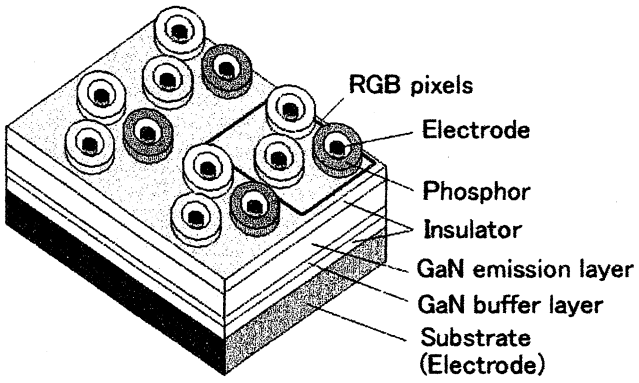

Figure 1 RGB light-emission system excited by UV GaN-based TF-ELD.

based TF-ELDs, a bottom insulator (Ta_2O_5) was formed by spin coating prior to GaN deposition. After the deposition, a top insulator (cyanoethylpullulan) was formed by spin coating on the GaN film. Finally, an Al top electrode was deposited by evaporation onto the surface. RGB phosphors, which were dispersed in cyanoethylpullulan, were positioned around the electrodes. The phosphors Y_2O_2S:Eu, $BaMgAl_{10}O_{17}$:Eu+Mn, $BaMgAl_{10}O_{17}$:Eu (NP-2310-57, NP-108-62, NP-107-58, respectively, Nichia Chemical Industries) were used in this study.

The photoluminescence excitation (PLE) of RGB phosphors was measured using a deuterium/tungsten halogen lamp. The excitation light source was selected by monochrometer.

3 Results The GaN-based TF-ELDs were operated at an AC voltage of 350 V at 200 Hz. UV light emission, whose peak located at 370 nm, was observed. The average optical power of GaN-based TF-ELDs, which was estimated by comparison with that of InGaN-based LEDs, was approximately 1.1 μW. We considered that some power that flowed into the GaN TF-ELDs did not contribute to the emission. This is because the GaN-ELDs were operated using pulsed voltage and the emission time was approximately 4 μs. Thus, the peak output power of the GaN-based TF-ELDs was approximately 700 μW. We consider that the physical origin of emission is same as the case of the conventional ELDs [9], although the detailed mechanism is under investigation.

A schematic of the RGB pixels fabricated on a GaN-based TF-ELD is shown in Fig. 1. The RGB pixels are composed of RGB emitters, each of which has UV light emitter. The RGB light emission peaks located at 626, 517 and 457 nm, respectively. The spectra of these peaks are shown in Fig. 2. The RGB phosphors were excited by UV emissions from the GaN-based ELDs. These phosphors are used for the fabrication of cathode ray tubes (CRTs). The results clarified that UV light radiated from GaN-based TF-ELDs is sufficient to excite RGB phosphors.

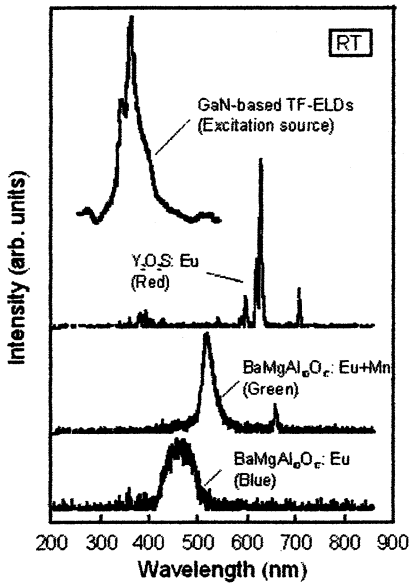

Figure 2 EL spectrum of UV GaN-based TF-ELD and PL spectra of RGB light-emission system excited by UV GaN-based TF-ELD.

The photoluminescence (PL) spectra and excitation efficiency of the RGB light-emission system excited by UV GaN-based TF-ELDs are shown in Fig. 3. Excitation efficiency was estimated by the PLE measurement of the RGB phosphors.

The excitation efficiencies of the RGB phosphors at 370 nm were 8.3, 6.0 and 2.5 %, respectively.

4 Discussion The optical output power of the RGB light-emission system was estimated from the excitation efficiency of the RGB phosphors and the estimated average optical output power of GaN-based TF-ELDs. As a result, the optical output powers of this system were 270, 660 and 910 nW, respectively. Table 1 shows the luminescences of the RGB pixels on GaN-based ELDs computed using Eqs. (1)-(4) [10].

$$\Phi = \iint_s \phi(\lambda) ds \,. \tag{1}$$

$$\phi(\lambda) = K_m \times \mathrm{W}_\lambda \times V(\lambda) \,. \tag{2}$$

$$I = \frac{d\Phi}{d\Omega} \,, \tag{3}$$

$$L = \frac{dI}{dA} \,. \tag{4}$$

Here, η is the excitation efficiencies of the RGB phosphors, K_m is the maximum luminous efficiency (which is

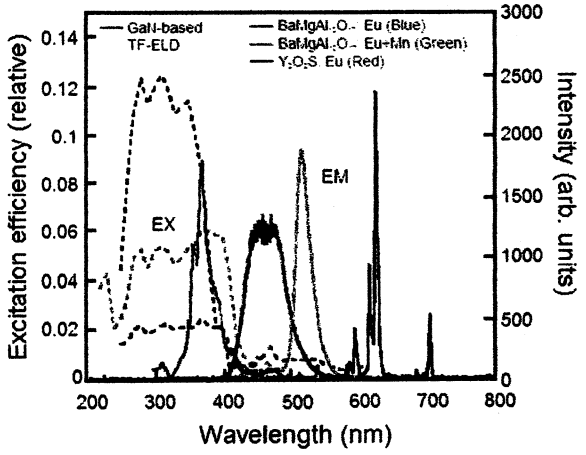

Figure 3 PLE (dashed lines) and PL (solid lines) spectra of GaN-based TF-ELDs with RGB phosphors.

683 lm/W under photopic conditions), V(λ) is the photopic luminous efficiency function, W is the optical output power of the RGB light-emission system, Φ is the total luminous flux, $\phi(\lambda)$ is the luminous intensity, and L is the luminance. A is the surface area of the receiving element ($A = 4\pi r^2$ with lens radius r = 0.002 m).

We assumed that the RGB radiances were only spectral radiances, at 626, 517 and 457 nm, respectively. The photopic luminous efficiency functions V(λ) of the RGB spectral region were 0.30, 0.66 and 0.05, respectively. The luminances of the RGB light-emitting system were 26, 41 and 1.2 cd/m^2, respectively, which are summarized in Table 1.

The RGB pixels were integrated approximately 90 thousand times for each 1 m^2, because approximately 270 emitters in each 1 m^2 were integrated into the Al substrates. We also considered the distance are what between the display and the observer as d = 0.3 m, because out-door-type small (personal-use) FPDs. Thus, the estimated luminances of the integrated RGB light-emitting system are 3, 7 and 0.2 kcd/m^2, respectively. Here, we assume that the emission time of each pixel is 1/60 second. The estimated luminance of RGB emitters based on GaN films indicate that GaN-based TF-ELDs have potential for application in FPDs in comparison with luminance of typical FPDs (Organic EL displays:0.2 kcd/m^2 [11]).

4 Conclusion UV GaN-based TF-ELDs were fabricated using GaN films deposited by CS-MBE technique at low temperature. RGB light-emitting pixels were fabricated using the GaN-based TF-ELDs as excitation sources. The estimated luminances of the RGB emitters based on the GaN films were 0.2-7 kcd/m^2, which indicate that GaN-based TF-ELDs have potential for application in FPDs.

Table 1 Estimated luminances of RGB pixels on GaN-based ELDs.

	W [nW]	φ(λ) [μ lm]	I [mcd]	L [cd/m^2]	L for FPDs [kcd/m^2]
Red	910	186	0.33	26	3
Green	660	297	0.52	41	7
Blue	270	9.2	0.02	1.2	0.2

Acknowledgements The authors thank Professors Emeriti Y. Suematsu and K. Iga of Tokyo Institute of Technology for encouragement and Professor H. Kawanishi of Kogakuin University for support. This work was supported by a Grant-in-Aid (No. 18560344) from the Ministry of Education, Culture, Sports, Science and Technology.

References

[1] I. Akasaki and H. Amano, Jpn. J. Appl. Phys. **36**, 5393 (1997).
[2] S. Nakamura, T. Mukai, and M. Senoh, Appl. Phys. Lett. **64**, 1687 (1994).
[3] A. A. Bergh, phys. stat. sol. (a) **201**, 2740 (2004).
[4] T. Honda, S. Egawa, K. Sugimoto, and M. Arai, J. Cryst. Growth **301**, 424 (2007).
[5] K. Ohkawa, A. Tujimura, T. Nishikawa, S. Yoshii, T. Yokogawa, M. Kubo, and Y. Sasai, J. Cryst. Growth **159**, 632 (1996).
[6] T. Honda, K. Sato, T. Hashimoto, M. Shinohara, and H. Kawanishi, J. Cryst. Growth **237**, 1008 (2002).
[7] S. Yagi, S. Suzuki, and T. Iwanaga, Jpn. J. Appl. Phys. **40**, L1349 (2001).
[8] A. J. Steckl and J. M. Zavada, MRS Bull. **24**, 33 (1999).
[9] R. Kimura and K. Takahashi, Jpn. J. Appl. Phys. **39**, 1039 (2000).
[10] R. S. Berns, Billmeyer and Saltzman's Principles of Color Technology (John Wiley & Sons, Inc. USA, 2000), p. 62.
[11] T. Gohda, Y. Kobayashi, K. Okano, S. Inoue, K. Okamoto, S. Hashimoto, E. Yamamoto, H. Morita, S. Mitsui, and M. Koden, SID 06 Digest **58**, 3 (2006).

phys. stat. sol. (c) 5, No. 9, 3026–3028 (2008) / DOI 10.1002/pssc.200779262

physica status solidi c
www.pss-c.com
current topics in solid state physics

Fabrication of AlN films at low temperature by CS-MBE technique

Tohru Honda*, Kenji Watanabe, Koichi Sugimoto, Masatoshi Arai, and Kazuhisa Takeda

Kogakuin University, Department of Electronic Engineering, 2665-1 Nakano-machi, Hachiohji, Tokyo 192-0015, Japan

Received 5 October 2007, revised 25 December 2007, accepted 9 January 2008
Published online 5 June 2008

PACS 68.55.–a, 81.05.Ea, 81.15.Hi, 82.80.Pv

* Corresponding author: e-mail ct11761@ns.kogakuin.ac.jp, Phone: +81 42 622 9291, Fax: +81 42 625 8982

The low-temperature deposition of AlN films by compound-source molecular-beam epitaxy (CS-MBE) technique was studied. AlN powder was used as the source and no additional nitrogen source was introduced during the deposition. X-ray photoelectron spectroscopy (XPS) results show that Al-N bonds were formed in the deposited films. It was clarified that the nitrogen atoms were supplied to the substrate from the AlN source and that the oxygen concentration in the deposited AlN films depended on the residual oxygen concentration in the AlN powder used as the source. The breakdown electric field of the AlN film was over 4.2 MV/cm, which indicates that the films deposited at a low temperature of less than 300 °C can be applied as the insulator in GaN-based electroluminescent devices.

1 Introduction Aluminum nitride (AlN) is an attractive material for the application to deep-UV light-emitting devices such as light-emitting diodes (LEDs). Recently, AlN-based LEDs were realized by metal-organic vapor phase epitaxy (MOVPE) [1]. On the other hand, an AlN layer is used as an insulator in conventional semiconductor devices based on Si [2]. Indeed, for the fabrication of GaN-based UV light-emitting devices, AlN films can be considered as insulators, because of their large band-gap energy compared with that of GaN.

AlN growth by molecular-beam epitaxy (MBE) has been investigated [3]. The results in previous reports showed that low temperature growth is one of the advantages of MBE growth, which is in contrast to the MOVPE growth, for which high temperature is required. From the view point of the thermal expansion coefficient of the grown materials, the low-temperature deposition and/or growth is effective for nitride growth on substrates other than III-V nitrides. The low-temperature growth of GaN layers by compound-source MBE (CS-MBE) has also been reported [4]. CS-MBE has been used for the fabrication of ZnSe-based green laser diodes [5]. Here, GaN powder was used as the source material and no additional nitrogen source was introduced during the growth. Part of the GaN powder was sublimated although part of it was decomposed [6]. The possibility of AlN growth by CS-MBE is a very attractive proposition for the fabrication of GaN-based light-emitting devices with low process temperatures. However, there are few reports concerning AlN growth by CS-MBE. It is crucial to determine whether nitrogen atoms are supplied from the AlN compound source in the case of CS-MBE growth.

In this study, the low-temperature deposition of AlN films by CS-MBE technique is reported. Here, AlN was used as the source material and no additional nitrogen source was introduced, as for the case of GaN deposition by CS-MBE [4]. The conditions required for AlN deposition by CS-MBE technique are also discussed. In particular, the supply of nitrogen atoms during CS-MBE technique is focused on.

2 Experiments Two different AlN powders (99.9% and 99.0%, Tokuyama Corporation) with different oxygen concentrations were used as the source for the deposition. The x-ray photoelectron spectroscopy (XPS) spectra of the AlN powders are shown in Fig. 1. The AlN with the lower oxygen concentration was named "source A" and the other was named "source B." An AlN beam was supplied onto the substrate using a K-cell whose temperature was 1300 °C. The deposition was performed for 3 hours. The substrate temperature was less than 300 °C, which was due to the thermal radiation from the K-cell. No additional

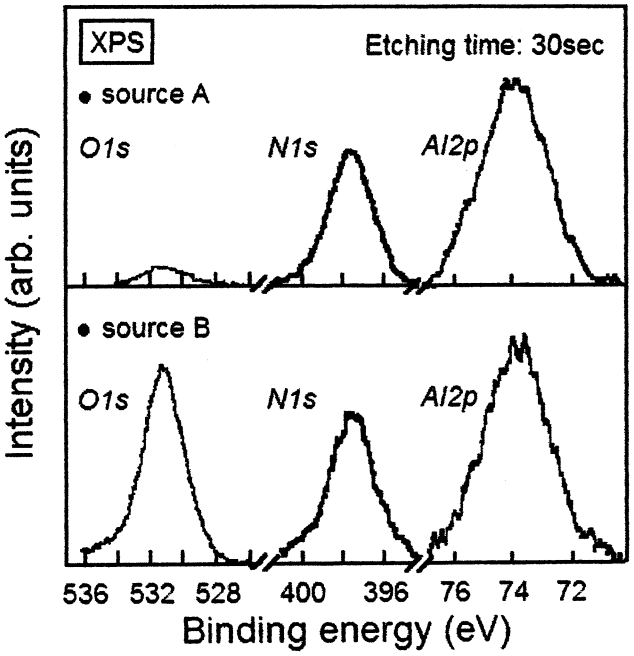

Figure 1 XPS spectra of two kinds of AlN powders used for the depositions.

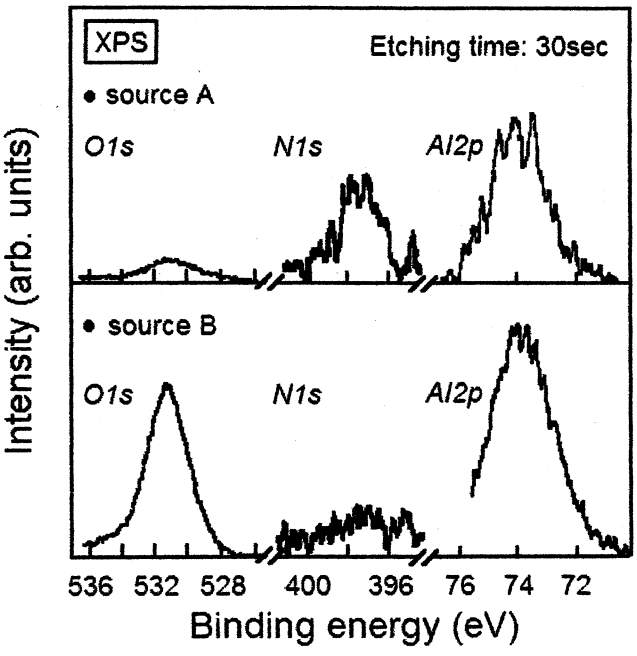

Figure 2 XPS spectra of AlN films deposited by CS-MBE technique using different AlN powders.

nitrogen sources were introduced during the deposition. The films were deposited on (111)Si and polycrystalline Al substrates. The deposited films were characterized by XPS subjected to Ar^+ ion beam etching (IBE). The thickness of the deposited film was measured by atomic force microscopy (AFM). The reflection high-energy electron diffraction (RHEED) patterns of the deposited film were also observed.

3 Results The XPS spectra of AlN films deposited by CS-MBE technique using the different powders are shown in Fig. 2. The formation of Al-N bonds was confirmed from the spectra [7, 8]. The RHEED patterns of the deposited films are indistinct, which indicates that there was no long-range ordering in the film. However, the short-range ordering of Al-N bonds was observed in the XPS spectra, indicating that the films were amorphous.

It was clarified that the nitrogen atoms in the deposited films were supplied from the AlN powder due to its sublimation. However, part of the AlN was decomposed. The Al beam generated from the decomposed AlN was also supplied to the substrate. This leads to the formation of Al-rich AlN films. Furthermore, the results suggest that the oxygen concentration in the AlN films depends on that in the AlN powder source. Also, the nitrogen concentration of the AlN film deposited using source A was higher than that deposited using the conventional AlN powder (source B).

The breakdown electric fields of both AlN films were estimated by measuring the I-V characteristics, as shown in Fig. 3. By taking into account the thicknesses of the AlN films, the breakdown electric fields of the AlN films using sources A and B are 4.2 MV/cm and 0.6 MV/cm, respectively. The results indicate that oxygen impurities affect the breakdown voltage of AlN films. Since GaN-based electroluminescent devices (ELDs) operating in the UV spectral region [9] require insulators whose breakdown electric field is larger than 1 MV/cm, AlN films can be used as an insulator in the GaN-based ELDs.

4 Discussion In the case of GaN growth by CS-MBE, excess Ga, which is due to the decomposition of GaN powder, was oxidized in air and converted to gallium oxide [6]. In this study, the deposited films were Al-rich AlN films. Although part of the AlN powder was sublimated, part of it decomposed. The excess Al appears to have been converted to aluminum oxide.

Here, there is a relationship between the breakdown electric field and oxygen concentration in the deposited film. Thus, the reduction of excess Al in the AlN film is crucial for realizing a high breakdown electric field. In the case of GaN, the excess Ga was reevaporated from the substrate because of the thermal energy of the substrate. On the other hand, the partial pressure of Al is lower than that of Ga at the same substrate temperature. This means that the reevaporation of the excess Al in AlN films requires a higher substrate temperature than that of Ga in GaN films. Thus, it is thought that the substrate temperature required for the deposition of AlN films by CS-MBE technique must be higher than that for GaN films.

The results in Figs. 1 and 2 suggest that the oxygen concentration in the AlN films depends on that of the source AlN powder. Furthermore, the nitrogen concentration of the AlN film deposited using source A was higher than that using source B. This means that the oxygen con-

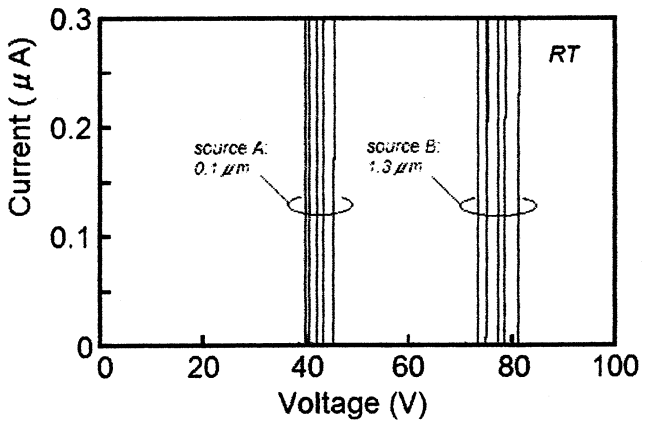

Figure 3 I-V characteristics of AlN films deposited by CS-MBE technique different AlN powders. In figure, thicknesses of the films are shown.

centration in the AlN films is connected with the amount of excess Al in the films. In other words, part of the excess Al is not supplied as aluminum metal, but as aluminum oxide. In the case of GaN deposition by CS-MBE, the residual oxygen concentration also affects the amount of oxygen impurity in the GaN films [10].

5 Summary AlN films were deposited on (111)Si and Al substrates at a low temperature of less than 300 °C by CS-MBE technique. The XPS results show the existence of Al-N bonds in the deposited films. This means that part of the AlN powder used as the source was sublimated. It was clarified that the oxygen concentration of the AlN powder strongly affects the residual oxygen concentration in the deposited AlN films. A low oxygen concentration in the AlN powder leads to a low oxygen concentration and high nitrogen concentration in the AlN films. It was clarified that AlN films fabricated from AlN powder with a low oxygen impurity concentration have a high breakdown electric field.

Acknowledgements The authors thank Professors Emeriti Y. Suematsu and K. Iga of Tokyo Institute of Technology for their encouragement and Professor H. Kawanishi of Kogakuin University for his support. We also thank Tokuyama Corporation for providing AlN powder. This work was supported by a Grant-in-Aid (No. #18560344) from the Ministry of Education, Culture, Sports, Science and Technology.

References

[1] Y. Taniyasu, M. Kasu, and T. Makimoto, Nature **441**, 325 (2006).
[2] G. A. Slack, R. A. Tanzilli, R. O. Pohl, and J. W. Vandersande, J. Phys. Chem. Solids **48**, 641 (1987).
[3] S. Yoshida, S. Misawa, and A. Itoh, Appl. Phys. Lett. **26**, 461 (1975).
[4] T. Honda, K. Sato, T. Hashimoto, M. Shinohara, and H. Kawanishi, J. Cryst. Growth **237-239**, 1008 (2002).
[5] K. Ohkawa, A. Tsujimura, T. Nishikawa, T. Yokogawa, M. Kubo, and Y. Sasai, J. Cryst. Growth **159**, 632 (1996).
[6] N. Obinata, K. Sugimoto, K. Ijima, M. Ishibiki. S. Egawa, T. Honda, and H. Kawanishi, Jpn. J. Appl. Phys. **44**, 8432 (2005).
[7] Y. Cho, Y. Kim E. R. Weber, S. Ruvimov, and Z. Liliental-Weber, J. Appl. Phys. **85**, 7909 (1999).
[8] M. Losurdo, P. Capezzuto, and G. Bruno, J. Appl. Phys. **88**, 2138 (2000).
[9] T. Honda, S. Egawa, K. Sugimoto, and M. Arai, J. Cryst. Growth **301/302**, 424 (2007).
[10] M. Arai, K. Sugimoto, S. Egawa, T. Baba, and T. Honda, phys. stat. sol. (c) **4**, 1719 (2007).

phys. stat. sol. (c) 5, No. 6, 2225–2227 (2008) / DOI 10.1002/pssc.200778592

physica status solidi c
www.pss-c.com
current topics in solid state physics

Fabrication of GaN-based Schottky-type light-emitting diodes for micropixels in flat-panel displays

T. Honda*, T. Kobayashi, S. Komiyama, Y. Mashiyama, M. Arai, and K. Yoshioka

Department of Electronic Engineering, Kogakuin University, 2665-1 Nakano-machi, Hachiohji, Tokyo 192-0015, Japan

Received 7 September 2007, accepted 17 December 2007
Published online 21 April 2008

PACS 73.30.+y, 73.40.Ei, 78.55.Cr, 78.60.Fi, 85.60.Jb

* Corresponding author: e-mail ct11761@ns.kogakuin.ac.jp, Phone: +81 42 622 9291, Fax: +81 42 625 8982

Microsize integrated light-emitting diodes (LEDs) that operate in the UV spectral region were fabricated using GaN layers grown on sapphire substrates by metal-organic vapor phase epitaxy (MOVPE). Schottky-type (ST) and metal-oxide-semiconductor (MOS) LEDs were realized. The near-band-edge emission of GaN was observed in the electroluminescent spectra with reversed bias under pulsed-voltage conditions. The insertion of an aluminum oxide layer in the GaN-based LED led to an increase in electroluminescent intensity. The internal optical absorption in the GaN layer of the GaN-based ST-LEDs was also estimated to be 75% of the emission light power.

1 Introduction GaN-based light-emitting diodes (LEDs) have been applied for outdoor-use large-scale flat-panel displays (FPDs) [1]. LED-based FPDs also show potential for home use. Although discrete LEDs are applied for large-scale FPDs, cost-effective micro-LEDs and their integration are required for the fabrication of home-use small FPDs based on LEDs. In the case of large-scale FPDs, discrete LEDs are applied for them. The high external quantum efficiency of p-n-junction-type LEDs has been achieved by the introduction of carrier confinement structures such as quantum wells and a double heterostructure. However, carrier confinement structures also act as waveguides. Although such structures are suitable for the operation of semiconductor lasers, they are unsuitable for application to integrated LEDs for small FPDs, because the optical waveguide causes interference in each pixel. Thus, discrete LED chips with optical reflection cups, which change the optical direction of the waveguided light, are adopted in LED-based large FPDs. These discrete LED chips are not suitable for the fabrication of micropixels in small FPDs because of their cost. We have proposed the integration of Schottky-type (ST) LEDs for the fabrication of the micropixels [2]. In this study, we consider small LED-based FPDs that are composed of GaN-based UV light emitters and RGB phosphors. This means that one pixel is composed of three UV light emitters covered with RGB phosphors. The schematic drawing of our proposed pixel is shown in Fig. 1(a). In this structure, ST-LEDs with a simple structure are adopted for the UV light source. In the case of ST-LEDs, the interference of emission light in each pixel is suppressed compared with that in conventional double-heterostructure (DH) LEDs. The main technical issue for LEDs is the optical absorption in electrodes, as shown in Figs. 1(b) and 1(c). The optical absorption leads to a reduction of the quantum efficiency of ST-LEDs. For example, GaN-based metal-insulator-semiconductor (MIS) LEDs have been reported [3], whose quantum efficiency was still low. Thus, increasing the quantum efficiency of GaN-based ST-LEDs is one of the crucial issues for their application.

In this paper, the insertion of an oxide layer into the metal-semiconductor contact in GaN-based ST-LEDs is reported. Here, we name these LEDs metal-oxide-semiconductor (MOS) LEDs. The optical absorption of GaN in the ST-LEDs is also discussed.

2 Experiments The GaN-based ST-LED has Schottky and ohmic electrodes, as shown in Fig. 1(a). Both contacts absorb the LED emission light. However, the light absorption in the Schottky electrode is undesirable, al-

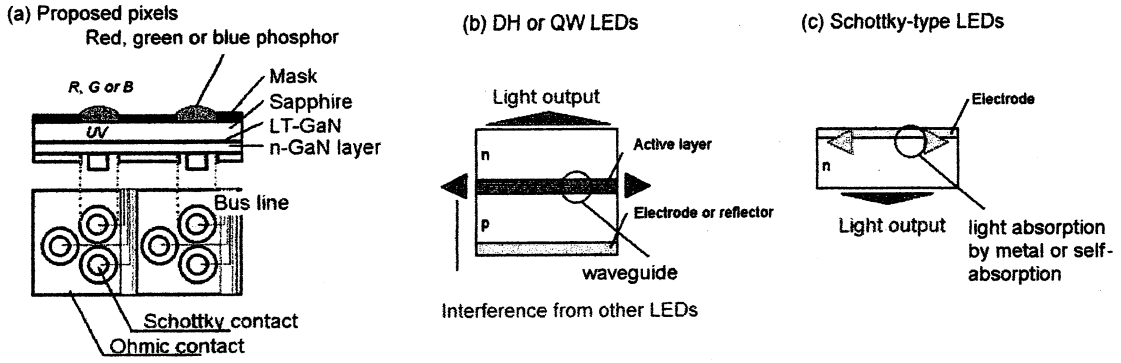

Figure 1 Schematic drawings of (a) proposed pixels, (b) double-heterostructure LED and (c) Schottky-type LED.

though that in the ohmic electrode suppresses the interference of emission light in each pixel. Thus, the insertion of aluminum oxide under the Schottky electrode was investigated because the distance between the Schottky electrode and the emission point determines the amount of optical absorption.

GaN layers were grown on (0001) sapphire substrates by metal-organic vapor phase epitaxy (MOVPE). A low-temperature GaN buffer layer deposited at 500 °C was introduced during the GaN growth at a substrate temperature of 1050 °C. The growth pressure was 760 Torr. A horizontal nickel reactor was used [4]. Trimethylgallium (TMGa) and ammonia were used as precursors. The thickness of GaN layers used for the diodes was 1 μm. The layers were n-type and their carrier density was approximately middle of 10^{17} cm^{-3}.

ST-LEDs operating in the UV spectral region were fabricated using an Al/Au large electrode and Au small electrodes. Their patterns were formed by screen printing and the lift-off technique [5]. The lift-off was performed in acetone. The emission light was observed from the sapphire-substrate side at the time of electrical operation. In the fabrication of MOS-LEDs, an aluminum oxide (AlO_x) layer was inserted in the interface between the Schottky contact and the GaN layer. The aluminum oxide layer was obtained from a vacuum-evaporated aluminum film, which was patterned on the GaN layer, then oxidized in air at 450 °C. X-ray photoelectron spectroscopy (XPS) spectra indicate that the layer was oxidized to Al_2O_3 [5]. The thickness of the Al film was 20 nm, and its resistivity was 13 nΩ·cm, which became 1.2 kΩ·cm upon oxidation.

The devices were characterized using photoluminescence (PL) and electroluminescence (EL). Light of 325 nm wavelength (3.81 eV) from a He-Cd laser was used as an excitation source for PL. EL from the LED was observed under pulsed operation (typically ~ -26 V, 70 mA, width 25 ms).

3 Results and discussion

3.1 Effects of inserting aluminum oxide The EL spectra of GaN-based ST and MOS-LEDs at RT are shown in Fig. 2. Both devices were driven at same input power of 1.44 W. The EL intensity of the MOS-LED is higher than that of the ST-LED. In the case of the GaN-based MOS-LED, the output powder detected using an optical fiber was approximately 0.1 mW. The increase of the output power is due to the reduction of light absorption in the Schottky electrode.

We consider that the light-emission mechanism is based on impact ionization caused by hot electrons [5, 6]. In the GaN layers, no emission centers, such as rare-earth atoms, were introduced. Thus, the light emission occurred in the flat-band position near the depletion layer [5]. The wave packets of the emitted light are generated near the electrode. The distance between the flat-band area and the electrode strongly affects the amount of light absorption in the electrodes. In the case of the ST-LED, the depletion layer width determines the distance. On the other hand, the distance in the MOS-LEDs is greater than that in the ST-LEDs, because the MOS-LED includes an oxide layer. This leads to a reduction of light absorption in the electrodes. However, the average output power of the MOS-LED detected using an optical fiber was approximately 0.1 mW. Another optical loss factor such as a self-absorption of the GaN layer in the ST-LED must be reduced.

3.2 Internal absorption in GaN The internal absorption loss due to GaN in GaN-based ST-LEDs is a crucial issue. A pseudo-heterostructure formed by thermal en-

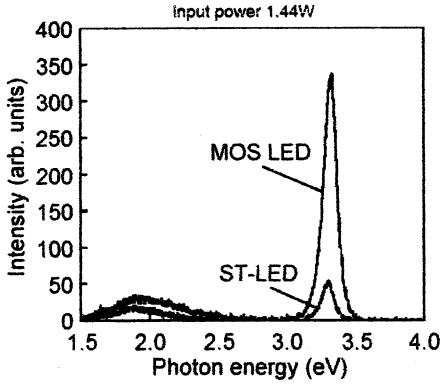

Figure 2 EL spectra of GaN-based Schottky and MOS-LEDs. Both emissions were detected from the substrate side using an optical fiber.

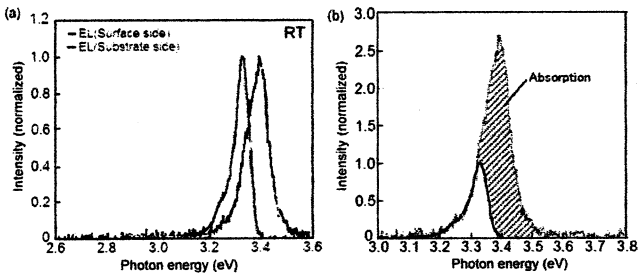

Figure 3 EL spectra of GaN-based Schottky-type LED. The spectra are observed from the surface side and the sapphire-substrate side. The PL spectrum of the GaN layer used for the device fabrication is also shown in (a). Normalized EL spectra of the GaN-based Schottky-type LED are shown in (b).

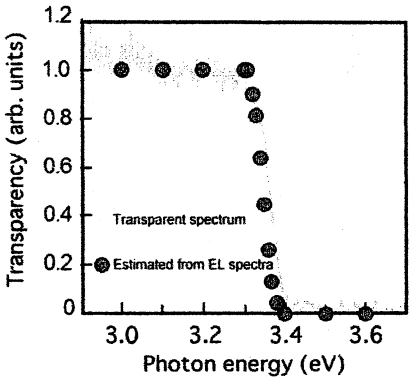

Figure 4 Transparent spectra of the GaN layer and the GaN-based Schottky-type LED. The spectrum of the LED is estimated using the EL spectra shown in Fig. 3(b).

ergy in the ST-LEDs has been reported [7]. However, internal absorption loss still occurs in such a structure. Thus, the EL spectra were observed from the surface side and the substrate side. The PL and transparent spectra of the GaN layers at RT were also observed. The EL spectra of the GaN-based ST-LED observed from the surface and substrate sides are shown in Fig. 3(a).

The peak energy of EL spectra observed from the surface side was shifted towards the lower-energy side compared with the PL spectrum observed from the surface side at RT. This is due to the thermal energy generated around the emission area. The energy offset, ΔE, of the pseudo-heterostructure between the emission point and the other GaN area is approximately 20 meV, which is due to band-gap narrowing by thermal energy. Here, we assume that the internal loss did not affect the EL spectrum as shown in Fig. 3(a), because the emission was located near the surface. The emission peak of the EL spectrum observed from the substrate side was considerably shifted towards the low-energy side compared with that from the surface side. Although the stokes shift due to thermal energy enables to observe the light emission from the substrate side, a large internal loss due to the self-absorption of GaN will still remain.

To estimate the amount of internal loss in the GaN-based ST-LED, we normalized the EL spectra. Here, we assume that (1) the peak shift is due to the internal loss by self-absorption and (2) the emission spectra in the lower-energy side (3.20–3.25 eV) are not affected by the self-absorption. The normalized EL spectra are shown in Fig. 3(b). To confirm these assumptions, a transparent spectrum (SP1) is estimated from the normalized EL spectra, and is shown in Fig. 4. The transparent spectrum (SP2) of the GaN layer using white light emitted from a D_2 lamp is also shown in Fig. 4. SP1 and SP2 are consistent, indicating that the assumptions are correct. Thus, the amount of internal loss was estimated from Fig. 3(b). It is clarified that 75% of the light emission power was lost by the self-absorption in the GaN layer.

For the realization of high output power, the reduction of the self-absorption is a crucial issue. One of the methods of realizing this is to improve the GaN crystal quality, which leads to an abrupt change in an absorption coefficient of the GaN layer around the absorption edge. Another method is to increase the band offset, ΔE, in the pseudo-heterostructure. The offset created by thermal energy depends on the carrier density of the GaN layer. Thus, carrier density control is required to achieve a high output power.

4 Summary The insertion of an aluminum oxide layer in Schottky-type LEDs based on GaN layers grown by MOVPE was effective for increasing the light output power. The internal absorption in the Schottky-type LEDs was also estimated using electroluminescent and transparent spectra. At present, 75% of the emission light power was self-absorbed in the GaN layer. This indicates that a high band offset in the pseudo-heterostructure is insufficient for the reduction of self-absorption in a GaN layer, although it enables light detection from the substrate side.

Acknowledgements The authors thank Emeritus Professors Y. Suematsu and K. Iga of the Tokyo Institute of Technology for their encouragement. We also thank Professor H. Kawanishi of Kogakuin University for his support. This work was supported by a Grant-in-Aid (No. #18560344) from the Ministry of Education, Culture, Sports, Science and Technology.

References

[1] For example, A. A. Bergh, phys. stat. sol. (a) **201**, 2740 (2004).
[2] T. Kobayashi, S. Egawa, M. Sawada, and T. Honda, phys. stat. sol. (c) **4**, 61 (2007).
[3] I. Akasaki and H. Amano, Jpn. J. Appl. Phys. **36**, 5393 (1997).
[4] T. Honda, T. Kobayashi, S. Egawa, M. Sawada, K. Sugimoto, and T. Baba, J. Cryst. Growth **298**, 736 (2007).
[5] T. Honda, T. Kobayashi, S. Komiyama, and Y. Mashiyama, Vac. Sci. Technol. B **26**, 1596 (2007).
[6] S. Yamaga, Jpn. J. Appl. Phys. **30**, 437 (1991).
[7] T. Honda, T. Kobayashi, S. Egawa, M. Sawada, K. Sugimoto, and T. Baba, J. Cryst. Growth **300**, 90 (2007).

Available online at www.sciencedirect.com
ScienceDirect
Journal of Crystal Growth 310 (2008) 1781–1784
JOURNAL OF CRYSTAL GROWTH
www.elsevier.com/locate/jcrysgro

Introduction of preheated ammonia during GaN growth on Si by compound-source MBE at low temperature

Tohru Honda*, Masashi Sawadaishi, Hiromi Yamamoto, Masatoshi Arai, Kaori Yoshioka, Takashi Okuhata

Department of Electronic Engineering, Kogakuin University, 2665-1 Nakano-machi, Hachiohji, Tokyo 192-0015, Japan

Available online 14 December 2007

Abstract

Preheated ammonia was introduced during GaN growth on Si by compound-source molecular-beam epitaxy (CS-MBE) at a low temperature. The use of preheated ammonia increased the surface smoothness and the intensity of cathodoluminescence (CL). Although the introduction of ammonia leads to the limited migration of the Ga surface atoms during the growth, the thermal energy supplied by the preheated ammonia assisted the surface migration. Furthermore, it was demonstrated that the introduction of preheated ammonia during the growth was effective for improving the CL intensity of the GaN layers at low temperatures. This is due to the reduction of the hydrogen concentration in the layers.

PACS: 81.15.Hi; 78.55.Cr; 78.60.Fi

Keywords: A3. Molecular-beam epitaxy; B1. Gallium compounds; B1. Nitrides; B3. Light-emitting devices

1. Introduction

Hexagonal GaN and related III-nitride compounds are very attractive for application of light-emitting devices operating in the blue to UV spectral region [1]. The fabrication of cost-effective light-emitting devices requires large-scale and low-cost substrates, for which silicon substrates are the possible candidates. Generally, GaN and related materials have been grown by metal-organic vapor-phase epitaxy (MOVPE) for the fabrication of light-emitting diodes (LEDs). However, MOVPE growth requires a high growth temperature of approximately 1000 °C. Such a high temperature (HT) is not suitable for application of LEDs because of the residual strain generated in the heteroepitaxial layers. Moreover, it has been reported that Si atoms on the surface of the substrate were diffused into the surface Ga wetting layer during the MOVPE growth at a HT [2]. Thus, the low-temperature growth of GaN on Si is very desirable.

The low-temperature growth of GaN by compound-source molecular-beam epitaxy (CS-MBE) has been reported [3]. In our previous report, GaN powder used as the source with no additional nitrogen source such as ammonia was introduced during the growth. Although the epitaxial growth of GaN was possible at the low temperature of 450 °C, its photoluminescence intensity was lower than that of GaN grown by MOVPE. It is partly because of the Ga-rich growth conditions of GaN fabrication by CS-MBE. To improve the growth conditions, ammonia was introduced during the GaN growth by CS-MBE [4], which increased the growth rate of GaN. However, the reflection high-energy electron diffraction (RHEED) patterns of the GaN layers became spotty because of the resulting limited surface migration.

In this paper, the introduction of preheated ammonia during the CS-MBE growth is presented. Moreover, the advantages and disadvantages of the introduction of ammonia during the growth are summarized.

*Corresponding author. Tel.: +81 42 622 9291; fax: +81 42 625 8982.
E-mail address: ct11761@ns.kogakuin.ac.jp (T. Honda).

0022-0248/$ - see front matter © 2007 Elsevier B.V. All rights reserved.
doi:10.1016/j.jcrysgro.2007.11.223

2. Experiments

GaN powder and ammonia were used as the source materials for GaN growth by CS-MBE, a schematic diagram of which is shown in Fig. 1. The GaN powder was synthesized from Ga metal and ammonia. It was annealed in vacuum at 800 °C for up to 20 h. The chemically cleaned (1 1 1)Si substrates underwent thermal cleaning for 30 min at 1000 °C prior to the growth. A GaN buffer layer deposited for 1 h at RT was adopted for the growth. GaN layers were grown for 5–13 h at the low substrate temperatures of 400–650 °C. During the growth, GaN powder was kept at 850 °C in a Knudsen cell (K-cell) and ammonia was supplied at a rate of 1–6 ccm. After the growth, RHEED patterns of the GaN layers were observed. X-ray photoelectron spectroscopy (XPS) spectra of the GaN layers were observed to confirm the amount of residual oxygen in the layers. The XPS spectra of layers subjected to Ar^+ ion beam etching (IBE) were also observed. Cathodoluminescence (CL) spectra of the GaN layers were observed at 20 K and the acceleration voltage used for their measurements was 20 kV. We also observed the Fourier-transform infrared spectrometer (FTIR) absorption spectra of the layers at RT.

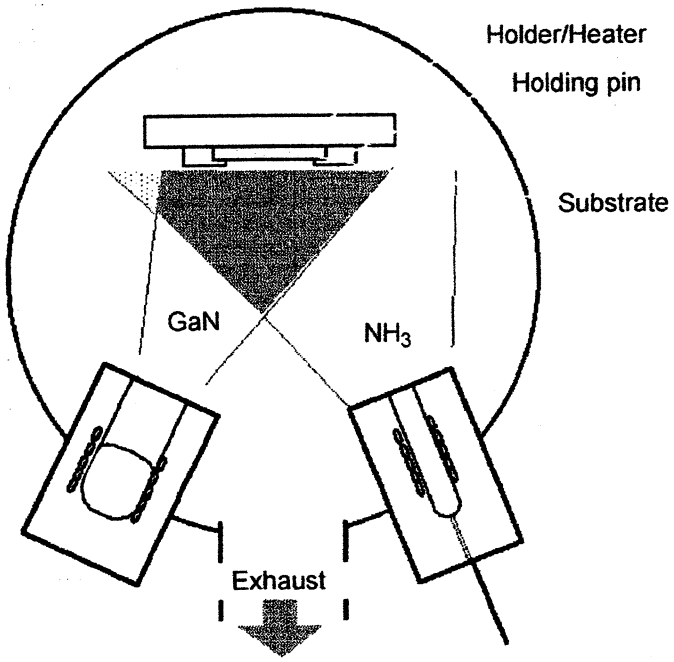

Fig. 1. Schematic drawing of compound-source MBE system.

3. Results

Fig. 2(a–c) shows RHEED patterns of the GaN layers grown on (1 1 1)Si by CS-MBE (a) without ammonia, (b) with ammonia and (c) with preheated (700 °C) ammonia. Here, an electron beam was introduced onto the layers along the $\langle 1\bar{1}0 \rangle$ direction of the (1 1 1)Si substrates. Although streaky patterns were observed from the layers grown without an ammonia flow, as shown in Fig. 2(a), spotty patterns were observed from the layers grown with an ammonia flow (2 ccm), when the gas was at RT, as shown in Fig. 2(b). The results shown in Fig. 2(a) and (b) indicate that growth conditions such as the V/III ratio were affected by the ammonia flow. On the other hand, streaky patterns were observed from the layers grown with a preheated ammonia flow (2 ccm) as shown in Fig. 2(c). This is discussed below in more detail.

In GaN growth by CS-MBE, it has been reported that excess Ga in the layers is changed to gallium oxide in air [5]. Thus, the oxygen concentration in the GaN layers is an important factor when considering the growth conditions. The relative oxygen concentration in the GaN layers as a function of the ammonia flow rate during the growth is shown in Fig. 3. Here, the relative oxygen concentration represents the Ga–O/Ga–N ratio estimated from the XPS spectra of Ga2p signals [6]. It is clear that increasing the ammonia flow rate reduces the residual oxygen concentration, which results in the reduction of excess Ga in the layers. The growth rate also depends on the ammonia flow rate as shown in Fig. 3. In the case of an ammonia flow rate less than 2 ccm, the growth rate linearly increases with increasing flow rate. This means that the growth rate under such a condition is limited by the flow rate. In the case of an ammonia flow rate, over 2 ccm the growth rate is saturated. This means that the growth conditions change

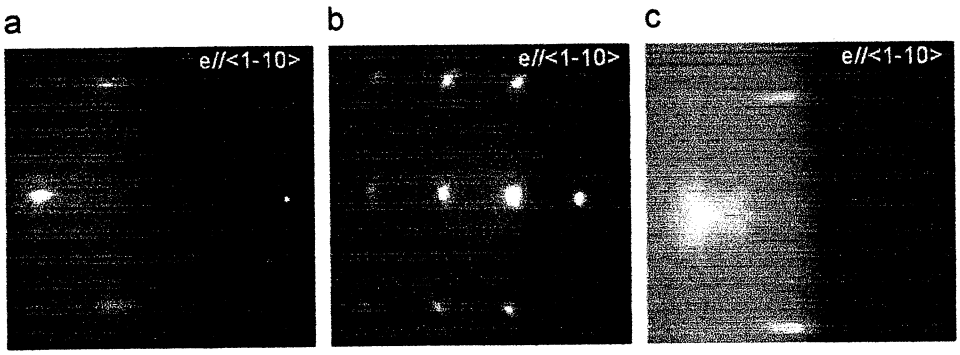

Fig. 2. RHEED patterns of GaN layers grown on (1 1 1)Si by CS-MBE. The growth temperature was kept at 600 °C. (a) Without ammonia, (b) with ammonia (2 ccm) and (c) with preheated ammonia (2 ccm at 750 °C).

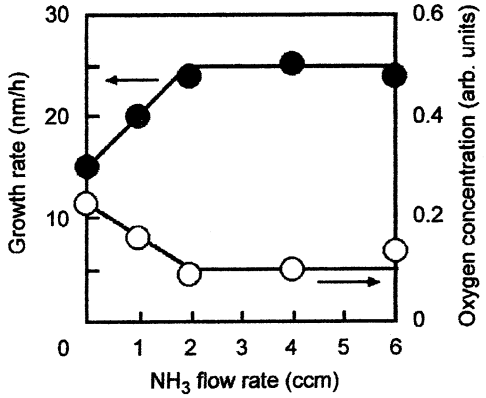

Fig. 3. Growth rate and relative oxygen concentration of GaN layers as functions of ammonia flow rate.

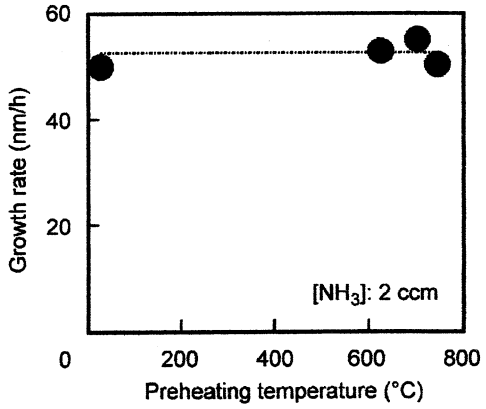

Fig. 4. Growth rate as a function of NH_3 preheating temperature. The ammonia flow rate is fixed at 2 ccm.

from Ga-rich to N-rich with an increasing ammonia flow rate. Here, the cell temperature of GaN powder was kept at 850 °C, although its beam-equivalent pressure is unknown at present. The results indicate that the V/III ratio during the growth with an ammonia flow rate of 2 ccm was almost unity.

The growth rate of GaN layers grown with preheated ammonia is shown in Fig. 4. The growth rate is almost constant as a function of the preheating temperature of the ammonia. Here, the ammonia flow rate was fixed at 2 ccm, for which the V/III ratio was almost unity. We were concerned that the preheating energy would decompose the ammonia, leading to a change in the V/III ratio. However, the growth rate remained unchanged upon changing the preheating temperature of the ammonia. This confirmed that the V/III ratio was independent of the preheating temperature. HT preheating leads to the decomposition of ammonia. However, chemical species such as NH and NH_2 generated by thermal cracking are unstable and they immediately become ammonia or nitrogen and hydrogen gases [7]. This means that the preheating temperature in this study was insufficient to decompose all the supplied ammonia.

Although the preheating temperature does not affect the growth rate, it affects the CL intensity of the GaN layers.

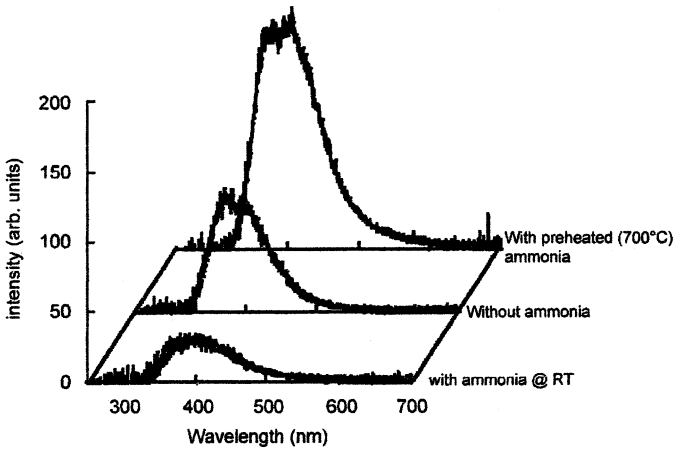

Fig. 5. CL spectra of GaN layers grown (a) with ammonia supplied at RT, (b) without ammonia, and (c) with ammonia preheated to 700 °C. The spectra were observed at 20 K.

The CL spectra of GaN layers grown at the low temperature of 600 °C are summarized in Fig. 5. The spectra were observed at 20 K. The emission intensity of the GaN layers decreased upon increasing ammonia at RT. On the other hand, it increased upon the added preheated ammonia (700 °C).

4. Discussion

During the low-temperature growth of GaN on Si, the migration of atoms is crucial for the realization of a flat surface. A spotty RHEED pattern was observed for the GaN layer grown on a (1 1 1)Si substrate with an ammonia flow at RT, as shown in Fig. 2(b). This indicates that the migration length of Ga metal atoms during the growth was strongly limited [8]. The limitation is due to the energy loss during the reaction between excess Ga metal and ammonia to form GaN, which requires thermal energy [9]. On the other hand, the ammonia flow reduces the residual oxygen concentration in the GaN layers, as shown in Fig. 3. Here, the vertical axis showing relative oxygen concentration is in arbitrary units and is defined relative to the oxygen concentration in a GaN layer on a (0 0 0 1) sapphire grown by the MOVPE. Introducing ammonia flow is also effective in increasing the growth rate because the re-evaporated Ga metal is changed to GaN by the supplied ammonia. Thus, the introduction of ammonia is advantageous for GaN growth by CS-MBE, but the limitation of migration, which leads to a rough surface, is a disadvantage. To overcome this advantage, the introduction of preheated ammonia is proposed. The RHEED pattern of the GaN layers grown with a preheated ammonia flow was streaky, as shown in Fig. 2(c). The additional thermal energy provided by the preheated ammonia leads to the enhancement of surface migration.

The preheating of ammonia also increases the CL intensity, as shown in Fig. 5. The change in CL intensity is due to the additional thermal energy. Because the

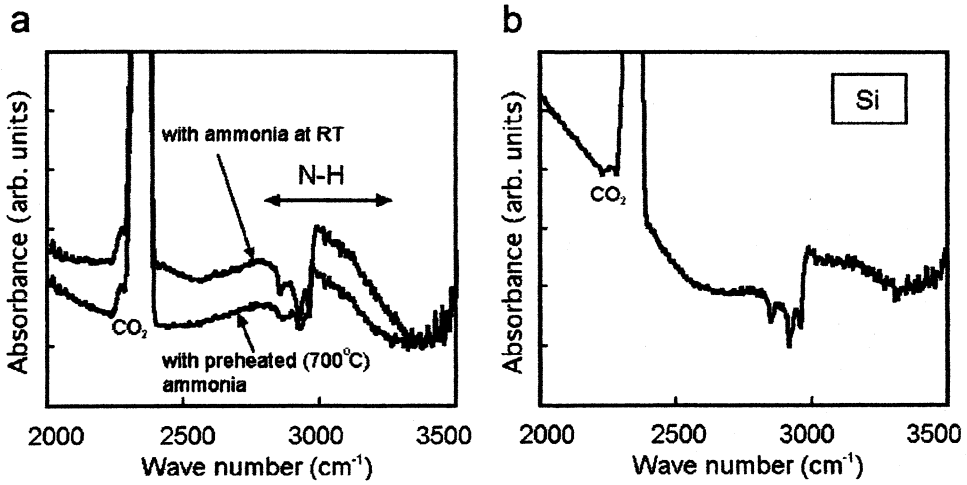

Fig. 6. FTIR absorption spectra of (a) GaN layers grown on Si and (b) Si substrate.

formation of GaN requires thermal energy, some hydrogen atoms will remain in the grown layers as N–H bonds. The additional thermal energy also breaks the N–H bonds in the layers. Thus, the hydrogen concentration in the GaN layers grown with preheated ammonia (700 °C) will be lower than that in layers grown with an ammonia flow at RT. To confirm this, the FTIR spectra of the GaN layers were observed. The results are shown in Fig. 6. We observed (a) GaN layers grown on (1 1 1)Si and (b) a Si substrate as a reference. A N–H absorption band of 2800–3500 cm^{-1} has been reported for GaN films [10]. In reference [10], a N–H band in IR spectra was observed from sputtered GaN films on Si in the presence of hydrogen. No band was observed from the films without hydrogen and it was concluded that the band was originated from the N H bond in GaN films. We now focus upon this spectral region. A broad absorption peak at 3050 cm^{-1} was observed from the layer grown with an RT ammonia flow. The intensity of this peak was decreased upon using a preheated ammonia flow. Such an intensity change was also observed for GaN films deposited on fused-glass substrates. At present, we consider that the peak is due to the N–H bonds in the GaN layer [10]. The reduction of the peak intensity means that preheating the ammonia is effective for reducing the amount of residual hydrogen in the GaN layers.

In the case of Mg doping of the GaN layers grown by MOVPE, residual hydrogen affects the CL intensity. The reduction of hydrogen leads to an increase in the CL intensity [11,12]. Thus, residual hydrogen in GaN layers will form nonradiative centers.

5. Summary

GaN growth by the CS-MBE with an ammonia flow was investigated. The introduction of ammonia is effective for enhancing the growth rate and reducing the excess Ga in the GaN layers. However, the ammonia flow limits the migration of the Ga metal atoms, which adversely affects the surface smoothness. The use of preheated ammonia during the growth enhances the surface migration. The preheated ammonia flow also increases CL intensity.

Acknowledgments

The authors thank Professors Emeriti Y. Suematsu and K. Iga of the Tokyo Institute of Technology for encouragement and Professor H. Kawanishi of Kogakuin University for support. The work was supported by a Grant-in-Aid (No. #18560344) from the Ministry of Education, Culture, Sports, Science and Technology.

References

[1] I. Akasaki, H. Amano, Jpn. J. Appl. Phys. 36 (1997) 5393.
[2] H. Ishikawa, K. Yamamoto, T. Egawa, T. Soga, T. Jimbo, M. Umeno, J. Crystal Growth 189 (190) (1998) 178.
[3] T. Honda, K. Sato, T. Hashimoto, M. Shinohara, H. Kawanishi, J. Crystal Growth 237 (2002) 1008.
[4] M. Sawada, M. Sawadaishi, H. Yamamoto, M. Arai, T. Honda, J. Crystal Growth 301–302 (2007) 67.
[5] N. Obinata, K. Sugimoto, M. Shinohara, S. Egawa, T. Honda, H. Kawanishi, Jpn. J. Appl. Phys. 44 (2005) 8432.
[6] S.D. Wolter, B.P. Luttther, D.L. Waltemyer, C. Onneby, S.E. Mohney, R.J. Molnar, Appl. Phys. Lett. 70 (1997) 2156.
[7] M. Kamp, M. Mayer, A. Pelzmann, K.J. Ebeling, MRS Internet J. Nitride Semicond. Res. 2 (1997) 26.
[8] S. Strite, H. Morkoc, J. Vac. Sci. Technol. B 10 (1992) 1237.
[9] A. Koukitu, H. Seki, Jpn. J. Appl. Phys. 36 (1997) 750.
[10] T. Miyazaki, K. Takada, S. Adachi, J. Appl. Phys. 97 (2005) 093516.
[11] H. Amano, M. Kito, K. Hiramatsu, I. Akasaki, Jpn. J. Appl. Phys. 28 (1989) L2112.
[12] S. Nakamura, M. Senoh, T. Mukai, Jpn. J. Appl. Phys. 30 (1991) L1708.

Journal of Crystal Growth 310 (2008) 5214–5216

Contents lists available at ScienceDirect

Journal of Crystal Growth

journal homepage: www.elsevier.com/locate/jcrysgro

Excitonic absorption in GaN layers of GaN-based UV Schottky-type light-emitting diodes grown by metal–organic vapor phase epitaxy

Shigetoshi Komiyama, Kazuyuki Noguchi, Shota Suzuki, Tohru Honda *

Department of Electronic Engineering, Kogakuin University, 2665-1 Nakano-machi, Hachiohji, Tokyo 192-0015, Japan

ARTICLE INFO

Available online 16 September 2008

PACS:
85.60.Jb
81.15.Gh
81.05.Ea

Keywords:
A1. Absorption
A3. MOVPE
B1. Nitrides
B2. Semiconducting III–V materials
B3. Light-emitting diodes

ABSTRACT

Internal absorption loss in GaN layers was investigated for GaN-based Schottky-type light-emitting diodes (ST-LEDs) operating in the UV spectral region. The peak energy of electroluminescence (EL) spectra of the device observed from its substrate side was shifted towards energy lower than those observed from its surface side. This is due to the internal absorption loss in the GaN layer. In particular, the large excitonic absorption in the GaN layer is one of the obstacles for light extraction from the ST-LEDs. Thus, light extraction from the surface side is effective for reduction of the internal absorption loss.

1. Introduction

Integration of light-emitting diodes (LEDs) is one of the important issues in the fabrication of flat panel displays (FPDs) using red, green, and blue (RGB) light emitters. Although discrete LEDs are applied for large FPDs, cost-effective LEDs are required for the fabrication of small FPDs. For the realization of cost-effective LEDs, a simple structure is required. Schottky-type light-emitting diodes (ST-LEDs) are one of the cost-effective LEDs [1]. We have previously proposed multipixel arrays composed of UV light emitters and RGB phosphors [2]. Thus, the realization of UV ST-LEDs is a technical issue at present.

Conventional GaN-based LEDs with a quantum well or a double heterostructure have a waveguide, which leads to a crosstalk at the time of their integration. This means that the waveguided light is scattered by its interface roughness and the scattered light is observed everywhere. On the other hand, ST-LEDs can reduce crosstalk because of their waveguide-less structure. It has been reported that a pseudo-heterostructure was realized in GaN-based UV ST-LEDs by using thermal energy [3]. The thermal energy generation, which is observed as an increase of temperature, was confirmed using a thermocouple on the Schottky contact. Here, band-gap narrowing due to thermal effects also leads to an increase in the refractive index. Thus, carriers and light are three-dimensionally confined in the pseudo-heterostructure by thermal effects. Experimental results support the possible use of GaN-based integrated ST-LEDs in the fabrication of FPDs. However, the ST-LEDs or metal–insulator–semiconductors (MISs) suffer from a low external quantum efficiency [4]. There are three explanations for the low quantum efficiency: (1) internal absorption in the semiconductors, (2) absorption within the electrodes, and (3) low internal quantum efficiency in the light-emitting areas. The second explanation has been discussed elsewhere [5]. A schematic drawing of the device structure is shown in Fig. 1. It was clarified that light absorption in large-size electrodes (ohmic contact) is effective in reducing crosstalk [5], while absorption in small electrodes (Schottky contact) is a crucial issue in the external quantum efficiency. The insertion of an aluminum oxide layer at the interface between the Schottky contact metal and GaN layer in the LED (MOS LED) reduces light absorption in the electrodes [5]. The third explanation is a major issue. That will be discussed elsewhere.

In this paper, internal absorption in ST-LEDs is discussed. The structural issue of devices that must be resolved to enable integration is "waveguide-less," which means that the band-gap offset between the light-emission area and other parts is negligible or a three-dimensional heterostructure is formed. Here, a three-dimensional pseudo-heterostructure is formed through the use of thermal energy, which is generated around the emission area beneath the Schottky electrode (Au, 300 μm in diameter). Electroluminescence (EL) spectra were recorded from the surface and substrate sides of the sample.

2. Experiments

GaN layers were grown on sapphire substrates using atmospheric pressure metal–organic vapor phase epitaxy (MOVPE).

* Corresponding author. Tel.: +81 42 622 9291; fax: +81 42 625 8982.
E-mail address: ct11761@ns.kogakuin.ac.jp (T. Honda).

0022-0248/$ - see front matter © 2008 Elsevier B.V. All rights reserved.
doi:10.1016/j.jcrysgro.2008.08.061

A horizontal nickel chamber was used for GaN growth. A low-temperature buffer layer was first grown at 500 °C. Then the substrate temperature was raised to 1050 °C to grow a 1 μm-thick epilayer. Trimethylgallium (TMGa) and ammonia were used as precursors.

A He–Cd laser operating at 325 nm was used as the excitation source for photoluminescence measurements. The excitation power density was approximately 26 mW/cm^2. The PL results were then used to estimate the temperature of emission layer in ST-LEDs [3].

ST-LEDs operating in the UV spectral region were fabricated using a large Al/Au ohmic electrode and a small Schottky Au electrode. The as-grown samples were processed using screen printing and lift-off techniques. A schematic of the structure is shown in Fig. 1. Output light emitted from the LEDs was detected under pulsed operation, from the sapphire substrate side. The thickness of the sapphire substrate was approximately 330 μm.

The EL spectra were measured using a reversed bias (100 mA). A pulsed voltage was applied to the ST-LED to reduce and control heat generation in the emission area. Here, the pulse width was fixed at 25 ms and its frequency was changed to control the duty ratio.

3. Results and discussion

3.1. EL spectra of ST-LEDs

The EL spectra observed from substrate and surface sides are shown in Fig. 2(a). The spectra are normalized using the peak intensity at 3.3 eV. Here, we assume that the internal absorption due to the deep levels is negligible and that the total emission power obtained from the surface side is the same as the one obtained from the substrate side. Although the EL intensities were normalized at 3.3 eV, the intensity of the deep-level emission region (3.2–3.3 eV) observed from the substrate side was equal to that from the surface side. This means that the assumptions are correct. A large optical absorption occurs when the light is collected from the substrate side. The transmission spectrum of the GaN layer used for fabrication of the ST-LEDs is also shown in Fig. 2(b). Here, we assume that the emission area is located beneath the Schottky electrode. The transmission spectrum was obtained by dividing the substrate-side emission spectrum by the surface-side emission spectrum shown in Fig. 2(a). The EL transparency is very similar to that of the GaN layer when using a D_2 lamp. This indicates that the optical absorption is due to internal absorption in the GaN layer, except for the emission area.

To allow a detailed discussion, absorption coefficients are plotted, as shown in Fig. 3. The plot of $(\alpha E)^2$ indicates that the "classical" absorption edge of the GaN layer in the ST-LED is consistent with that reported previously [6]. Absorption tailing is also observed in Fig. 2(a). The absorption around the classical absorption edge in the spectral region includes the excitonic absorption in the GaN layer [7]. Moreover, the absorption spectrum obtained from the EL spectra includes a Gaussian peak absorption that was not observed when using the D_2 lamp, as shown in Figs. 2(b). This is due to absorption

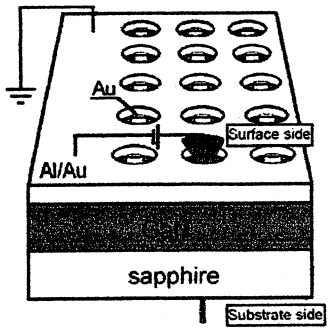

Fig. 1. Schematic drawing of GaN-based Schottky-type light-emitting diode structure.

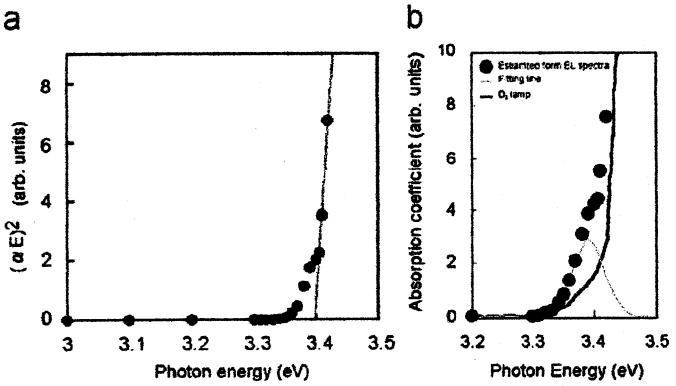

Fig. 3. (a) Plot of $(\alpha E)^2$ data. The absorption spectra are also shown in (b).

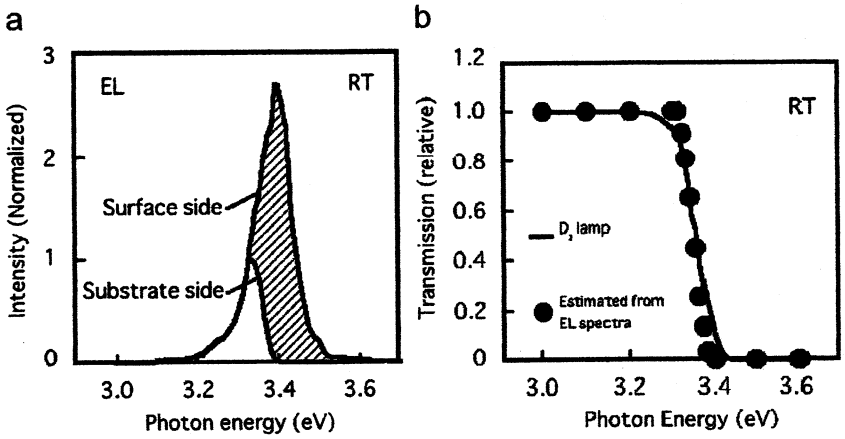

Fig. 2. (a) Electroluminescence spectra of GaN-based ST-LEDs observed from surface and substrate sides. The transmission spectra estimated from EL spectra and using D_2 lamp are also shown in (b).

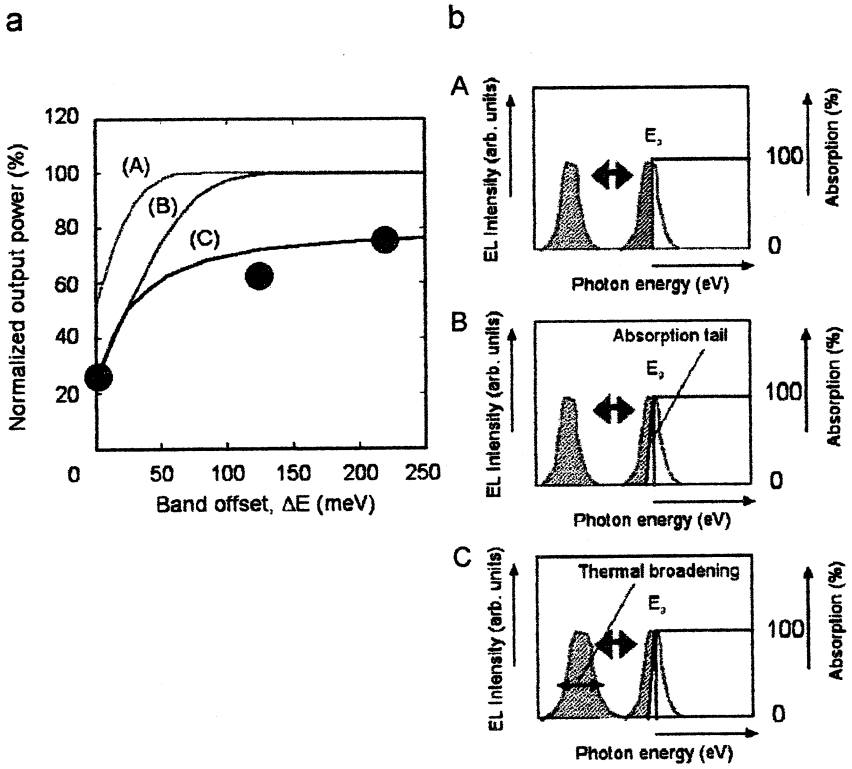

Fig. 4. (a) Output power of a GaN-based ST-LED as a function of band offset (solid circles). Here, the power observed from the substrate side was normalized by the power from the surface side. Those models are schematically shown in (b). The "classical" direct-band-gap absorption was considered in model (A). The additional absorption due to excitonic absorption was considered in model (B). In model (C), thermal broadening of the emission peak was considered.

of the transition area in the interface of the pseudo-heterostructure.

3.2. Relationship between output power and band offset

Operation of ST-LEDs requires electron and hole generation. However, ST-LEDs with n-type GaN films are operated using major carrier (electron) flow. Thus, impact ionization caused by a reversed bias was used to obtain electron and hole pairs in the devices [8]. Because the emission area is located near the surface, the excitonic absorption affects the EL spectra observed from the substrate side. To confirm the effects, the normalized output power of the LED observed from the substrate side was estimated as a function of band offset in the pseudo-heterostructure, as shown in Fig. 4. The band offset was a result of thermal energy generated in the emission area. The band offsets were estimated using the thermocouple temperature on the Schottky contact and PL emission peaks observed above RT [3]. The three solid lines (A)–(C) shown in Fig. 4 were obtained using absorption models. Model (A) is the consideration of thermal narrowing of the band gap. In the case of model (B), the absorption tailing due to excitonic absorption was additionally considered. Furthermore, thermal broadening of emission spectra by thermal energy was considered in model (C). The results indicate that excitonic absorption affects optical loss in the EL spectra observed from the substrate side.

The above results indicate that light extraction from the surface side has an advantage compared to that from the substrate side. However, light emission occurs under the Schottky electrode. Thus, a UV transparent electrode is required for the Schottky electrode in the devices.

4. Summary

Internal absorption loss in GaN layers was investigated for GaN-based Schottky-type light-emitting diodes (ST-LEDs). The internal absorption loss in the GaN layer was estimated using the EL spectra observed from substrate and surface sides. In particular, the large excitonic absorption in the GaN layer affects light extraction from the ST-LEDs. Thus, light extraction from the surface side is effective for reduction of internal absorption loss.

Acknowledgments

The authors thank Professors Emeriti Y. Suematsu and K. Iga of the Tokyo Institute of Technology for their encouragement. They also thank Professor H. Kawanishi of Kogakuin University for his support. This work was supported by a Grant-in-Aid (no. 18560344) from the Ministry of Education, Culture, Sports, Science, and Technology.

References

[1] A.J. Stekl, J.M. Zavada, Mater. Res. Soc. Bull. 24 (1999) 22.
[2] T. Honda, T. Kobayashi, S. Egawa, M. Sawada, K. Sugimoto, T. Baba, J. Crystal Growth 298 (2007) 736.
[3] T. Honda, T. Kobayashi, S. Egawa, M. Sawada, K. Sugimoto, T. Baba, J. Crystal Growth 300 (2007) 90.
[4] I. Akasaki, H. Amano, Jpn. J. Appl. Phys. 36 (1997) 5393.
[5] T. Honda, T. Kobayashi, S. Komiyama, Y. Mashiyama, J. Vac. Sci. Technol. B 25 (2007) 1529.
[6] H.P. Maruska, J.J. Tietjen, Appl. Phys. Lett. 15 (1969) 327.
[7] S. Chichibu, T. Mizutani, T. Shioda, H. Nakanishi, T. Deguchi, T. Azuhata, T. Soda, S. Nakamura, Appl. Phys. Lett. 70 (1997) 3440.
[8] S. Yamaga, Jpn. J. Appl. Phys. 30 (1991) 437.

Mol. Cryst. Liq. Cryst.に投稿中

Alignment Characteristics of Nematic Liquid Crystal on UV Curable Resin Film with Periodical Groove Structure

Shiina TETSUYA, Susumu SAITO and Taiju TAKAHASHI

Department of Electronic Engineering, Kogakuin University,

2665-1 Nakano-cho Hachioji, Tokyo 192-0015, Japan

Periodical groove structure was formed on the substrate surface by copying the structure on the grating film on the market to the photo curable resin coated on the substrate surface. And then, the substrate surface with groove structure was rubbed along the direction perpendicular to the groove. Alignment of LC on such substrate surface was experimentally investigated. In a cell constructed using such substrate and the substrate treated by a vertival alignment material, distinctive domains with different orientation direction were observed. This suggests us that the bistable alignment property can be adapted on the substrate surfaces by the method above mentioned. A new type of the bistable LCD is proposed utilizing the substrate with bistable anchoring property.

KEYWORDS: nematic liquid crystal, groove structure, bistable LCD

1. INTRODUCTION

With the surge of the environmental awareness, the electronic (E) paper has attracted attention since they have both superior properties of paper and an electronic display device. A thin thickness, a light weight, a low power consumption and a rewrite-ability etc are required for the electronic paper. For the electronic paper in which a liquid crystal is used, the adaptation of memory effect on the LC alignment results on the low power consumption.

So far, some types of the E paper have been proposed. Foe example, the electro-phoretic display and some new types of LCD such as the Bi-Nem (Bistable Nematic) LCD and the ZBD (Zenithal Bistable Display) were proposed with the intention of applying to the E paper. Among them, in the ZBD proposed by Bryan-Brown and others in 1997 (1), the groove (grating) structure is constructed on the one side substrate surface and a vertical alignment treatment is conducted on the groove surface to adapt the bi-stable anchoring properties. On the other substrate surface, a vertical alignment treatment or a parallel alignment treatment is conducted.

When a dc field perpendicular to the substrate surface is applied, either one of a homeotropic alignment or a parallel alignment perpendicular to the grooves is obtained at the interface on the substrate with a groove structure, according to the polarity of the applied dc voltage.

In this study, a new method to adapt the bistable anchoring properties on the surface with a groove structure is proposed. In our method, a periodical groove structure was formed on the substrate surface by copying the structure on the grating film on the market to the photo curable resin coated on the substrate surface. And then, the substrate surface with groove structure was rubbed along the direction perpendicular to the groove. Alignment of LC on such substrate surface was experimentally investigated.

2. EXPERIMENTALS

2..1 Sample preparation

As a UV curable resin, the Technovit 2000LC (Heraeus Kulzer GmbH&Co.KG) was coated on the substrate on which an inter-digit in-plane electrode (the pectinate electrode) has been constructed as shown in Fig. 3.1. The diffraction grating film was stacked on the resin under an appropriate uniform pressure. Then, a UV light was irradiated on the UV curable resin through the diffraction grating film set on the resin

film.

The UV light irradiation energy was 7 J/cm^2. The pitch of the diffraction grating film was 1μm. After removing the diffraction grating film resin, which was not cured, the UV light was irradiated again for 30 min to be completely cured.

Two types of cell were prepared. One of them was constructed using a substrate on which the groove structure was constructed and the substrate on which a kind of polyimide SE1211 (Nissan Chemical Ind.) was coated to obtain a vertical alignment. Hereafter, this type of cell is called as the cell-A

For the other one of cells, the surface of groove structure was rubbed three times along the direction perpendicular to the groove direction using a rubbing roller. The cell was constructed using the substrate treated by the method mentioned above and the substrate on which a kind of polyimide SE1211 (Nissan Chemical Ind.) was coated to obtain a vertical alignment. Hereafter, this type of cell is called as the cell-B.

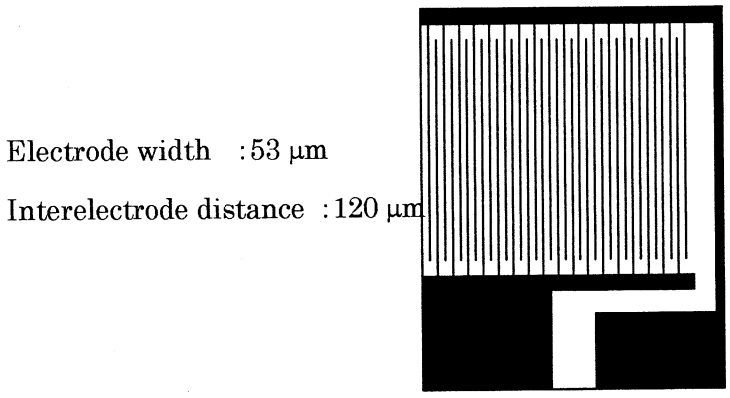

Fig. 3.1 Electrode pattern

The sample cell was fabricated by using the substrate on which the groove structure was formed and the other substrate treated by the SE1211. As the LC material, a single compound nematic LC, 5CB (Merck) was used. The spacer material with a diameter of 6 μm was used.

3. EXPERIMENTAL RESULTS AND DISCUSSIONS

3..1 Observation of the groove structure formed by UV Curable resin film

The diffraction grating film and the transferred groove structure on the substrate was

observed by a laser beam microscope. The observed results are shown in figure 4.1(a), (b). A laser micrograph after the rubbing treatment conducted along the direction perpendicular to the groove structure is shown in figure 4.1(c). It can be confirmed that the groove structure of the diffraction grating film was copied neatly to the UV curable resin film from Figs. 4.1(a) and (b). Comparing Fig.4.1(c) with Fig. 4.1(a) and Fig.4.1(B), it is known that the resin was shaved off by rubbing, and the height of the groove structure was lowered by rubbing processing.

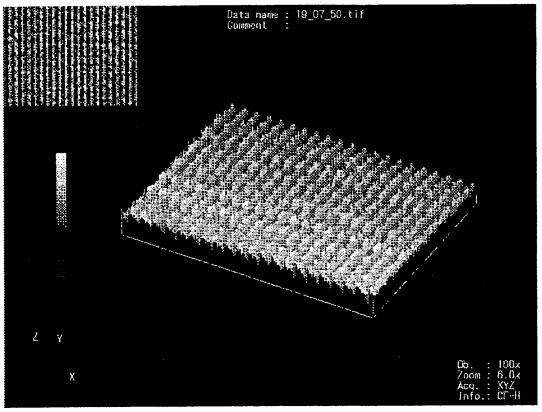

Fig. 4.1(a) Diffraction grating film original

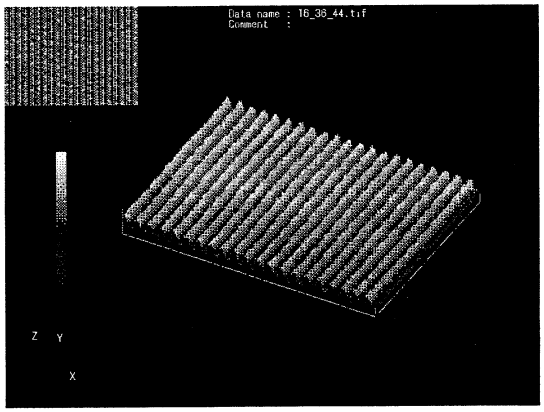

Fig. 4.1(b) Copy-printing groove structure on the glass substrate

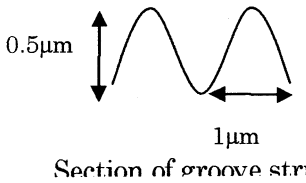

Section of groove structure

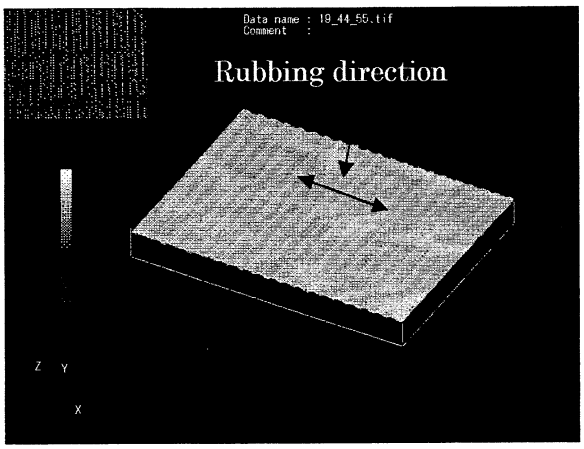

Fig. 4.1(c) After processing rubbing treatment

3.2 The alignment of the liquid crystal molecule by the groove structure

The molecular alignment in the cell-A was investigated under the cross Nicho condition in which the direction of the polarizer was set at an angle of 45 deg. with respect to the direction of the grooves. It was confirmed that the LC molecules in the

cell-A is in the configuration of the hybrid alignment and they aligned along the grooves on the substrate with the groove structure. The direction of molecular orientation was determined by inserting a compensation plate together with the sample cell between the cross Nichol and searching the extinction position by rotating the compensation plate.

3.3 *Alignment of the liquid crystal molecule in the cell-B.*

The molecular alignment in the cell-B was investigated with a polarizing optical microscope under the cross Nichol condition in which the direction of the polarizer was set at an angle of 45 deg. with respect to the direction of the grooves. Figures 4.3 (a) to (c) show the photographs of the observed domains with distinctive alignments. It was confirmed that the angle of the directions of molecular alignment with respect to the rubbing direction were -59 degree and +56 degree in those two domains. Those angles were obtained by searching the optical extinction position by rotating the compensation plate as shown in Fig. 4.3(b) and Fig. 4.3(c).

Next, the change of molecular alignment with the application of an in-plane electric field was investigated. A rectangular wave voltage with the amplitude of 20 V and a frequency of 1 Hz was applied between the inter-digit electrodes. The observed results are shown in Figs. 4.3 (d) to Fig. 4.3(f). Figure 4.3(d) is the initial state before applying the voltage. Figure 4.3 (e) is the state during the voltage application. Figure 4.3 (f) is the state after removing the applied voltage. It should be noted that the one domain marked by the circle changed to the extinction state by the voltage application. This change means that the transition of molecular orientation from the direction of one easy axis denoted as n_1 in Fig. 4.3 (g) to the direction of the other easy axis denoted as n_2 in Fig.4.3 (g) occurred by the applied in-plane field.

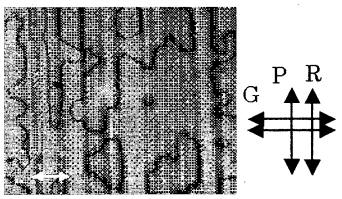

Fig. 4.3 (a) P is parallel to the Rubbing direction (Initial state)

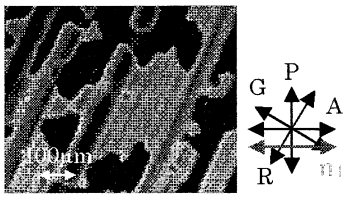

Fig. 4.3 (b) One of the optical extinction state: the cell was rotated by 31 deg. in the clockwise (CW) from the initial state

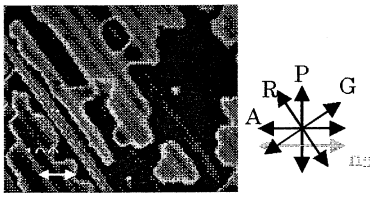

Fig. 4.3 (c) Another of the optical extinction state: the cell was rotated by 34 deg. in the counter clockwise (CCW) from the initial state

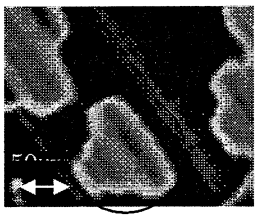

Fig. 4.3 (d) Before applying the voltage (0V)

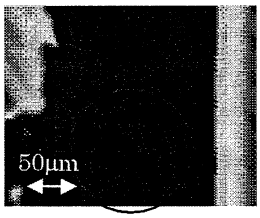

Fig. 4.3 (e) During the application of the voltage (1Hz,±20V)

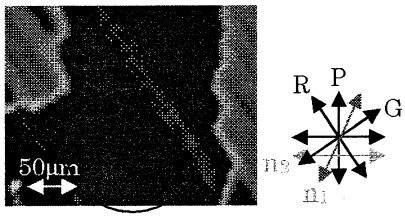

Fig. 4.3 (f) After removing the applied voltage (0V)

A : analyzer G : groove structure
P : polarizer n_1,n_2 : director

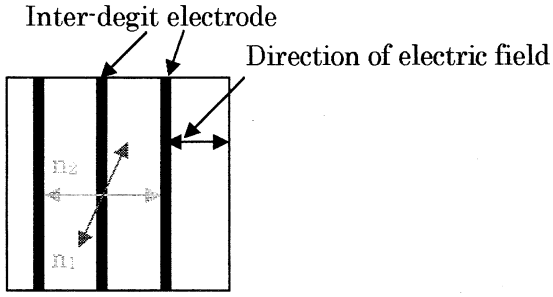

Fig. 4.3 (g) Schematic of electrode pattern

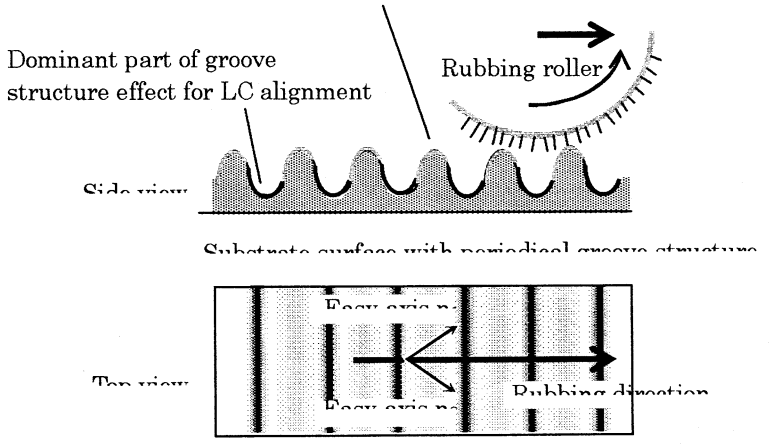

Fig. 4.3(h) Two orientation easy axes with groove structure

4. CONCLUSIONS

In this report, we proposed a new type bistable LCD. On one of substrate surfaces, the periodical groove structure was formed by copying the structure on the diffraction grating film to the photo curable resin coated on the substrate surface. The surface of groove structure was rubbed three times along the direction perpendicular to the groove direction using a rubbing roller. The cell was constructed using the substrate treated by the method mentioned above and the substrate on which a kind of polyimide SE1211 (Nissan Chemical Ind.) was coated to obtain a vertical alignment. It was confirmed that the substrate treated by the method above mentioned have two orientation easy axes. Furthermore, the transition of the molecular orientation from the one easy axis to the other easy axis was confirmed by the application of in-plane field. However, in the present stage, only one directional switching was succeeded. It will be necessary to examine the method in the future for the bidirectional switching.

Acknowledgements

The authors would like to thank Merck Co. Ltd and Nissan Chemical Industry for supplying LC materials and alignment materials, respectively. This work was supported by a "High-Tech Research Center" Project for Private Universities: matching fund subsidies from MEXT (Ministry of Education, Culture, Sports, Science and Technology), 2006-2010.

REFERENCES

[1]G.P.Bryan,C.V.Brown,J.C.Jones,E.L.Wood,I.C.Sage,P.Brett and J.Rudin:SID'97 Digest,37 (1997)

[2]D.W.Berreman:Phys.LEtt.,28,1683(1972)

[3]N.Kimura,M.Akabane「Japanese liquid crystal society magazine」EKISHO Vol.8,No.3,2004.pp.166-175

Mol. Cryst. Liq. Cryst.に投稿中

Orientation on Periodical Micro Pattern with Vertical and Homogeneous Alignments using Anodic Porous Alumina for Bi-stable Surface

Keiji IMAI, Atsushi YOKOYAMA, Susumu SAITO, and Taiju TAKAHASHI

Department of Electric Engineering and Electronics, Graduate School of Kogakuin Univ
2665-1 Nakano-cho Hachioji, Tokyo 192-0015, Japan

Abstract

In order to obtain the bistable surface, a new method is proposed to fabricate the micro-patterned substrate surface formed by stripes of alternating vertical and planer anchorings. In this method, aluminum film evaporated in vacuum on substrate surfaces was etched in stripe pattern using the photolithography techniques. And then, stripes of aluminum were anodized. Coexistence of the vertical alignment on stripes of porous alumina and the planer alignment along stripes due to grooves between stripes of alumina is experimentally confirmed. However, the bistable property has not been observed yet.

KEYWORD: Vertical alignment, Porous alumina, Anodization, Bistable LCD

1. Introduction

Recently, portable devices equipped with LCD have rapidly, spread and the demand for the low power consumption display has increased. The research and development the bistable nematic LCD with permanent memory characteristics have actively proceeded from the aim of realizing low power consumption display.

In recent years, a variety of bi-stable liquid crystal displays have been proposed. The bi-stable LCDs are classified into two types according to whether the bi-stability is based on bi-stable anchoring properties of the alignment layer, or only on the bi-stability of molecular orientation configurations. Some techniques have been proposed for the adaptation of bi-stable anchoring properties within the alignment layer. B. Jerome et al have demonstrated an in-plane bi-stability which uses approximately 20 nm thick SiO films obliquely evaporated in a narrow range of incidence angles between 60° and 72°. G. P. Bryan-Brown et al proposed the zenithal bi-stable device (ZBD) in which a grating surface treated with a homeotropic surfactant was found to support two stable pre-tilt configurations when at an optimal groove depth pitch. J. H. Kim et al have demonstrated a robust liquid crystal alignment in-plane bistability based on tailored submicrometer-sized surface domains in a frustrated alignment. An atomic force microscope (AFM) was used to prepare a checkerboard pattern orientation on a polyimide layer which consists of a square-unit domain in which the alignment is locally constrained to be planar yet orthogonal between the neighboring domains. T. N. Oo et al have proposed a micro-patterned liquid crystal device in which the patterns are formed by alternating planar and homeotropic stripes. A micro-patterned surface provides the bi-stable anchoring.

Additionally, as the alignment material, some inorganic materials with higher reliabilities than organic materials have been required for the use in a high temperature environment.

In this study, as a vertical alignment layer for the nematic liquid crystal, a porous alumina film obtained by anodizing aluminum.are investigated. Furthermore, as a method for the adaptation of bi-stable anchoring properties within the alignment layer, the micro-striped porous alumina is investigated. It is thought that the bistable anchoring property is resulted from the combination of the parallel alignment due to the groove structure formed by the micro-striped alumina and the vertical alignment due to the porous alumina.

2. Vertical alignment of LC molecules on anodized aluminum film and new method to obtain a bistable anchoring property

The anodization develops the oxide film on the surface with engender the oxidation reaction coercively by oxygen of hydroxide ion in the electrolytic solution react with material of the anodic by flow the current as the target material is anodic in electrolytic solution. The oxide film has high corrosion resistance. Consequently, it is used as the high reliability material.

The oxide film is obtained by anodization of aluminum is porous structure as shown in Fig. 1(a). It is honeycomb structure orderly arranged in hexagonal cylinder with porosity of columnar in center of the cell, and the diameter of porosity is about several 10 to several 100 nm, and the depth becomes deep while lengthening anodization time. The bottom of the porosity is in contact with aluminum substrate on both sides of the alumina layer with high purity called a hemispherical barrier layer. Additionally, the size of a liquid crystal molecule is small at about 5 to 10nm compared with the size of this porosity. Thus, it is thought that the liquid crystal molecule goes into the porosity when liquid crystal is injected into this porous film.

The vertical alignment of the nematic liquid crystal using this porous film is shown in Fig.1 (b). How the vertical alignment due to this mechanism above mentioned, and planer alignment due to the shape effect of the groove affect the occurrence of bistable alignment is shown in Fig. 2(a) and Fig.2 (b).

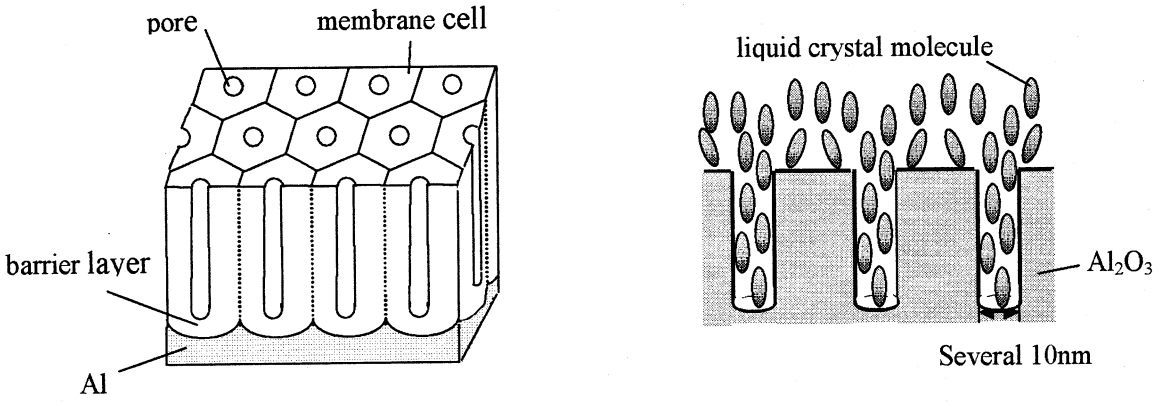

(a) Model of the porous film structure (b) Principle of the vertical alignment

Fig.1 Anodization of the aluminum

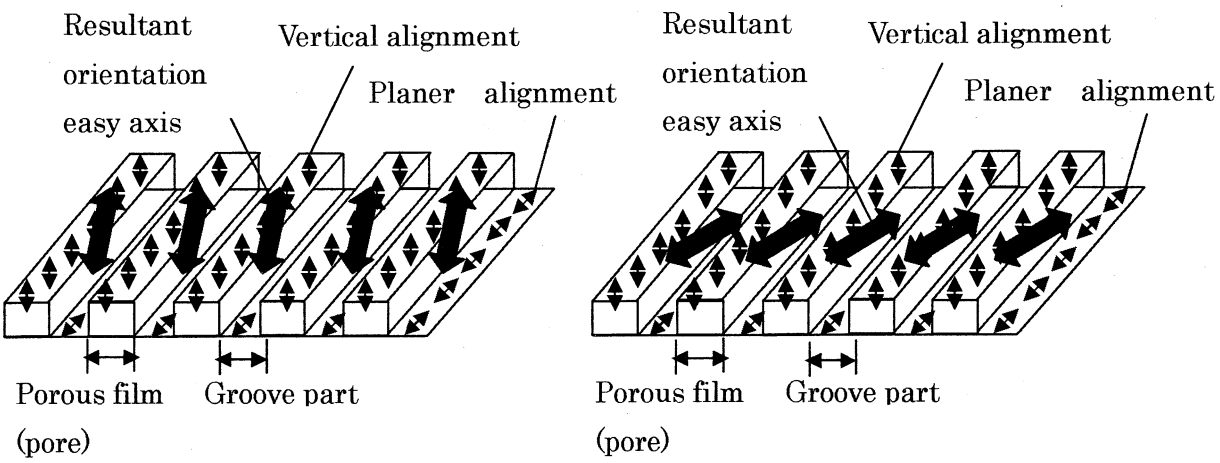

(a) Alignment pattern 1 (b) Alignment pattern 2

Fig.2 Schematic explanation for the LC molecules alignment on anodized Al film with groove structure

3. Preparation of the sample cell

Aluminum was evaporated on the metal Cr coated ITO glass substrate under 3×10^{-4}. Pas.. The thickness of evaporated Al was about 1μm. A periodical micro stripe structure with 5μm pitch was fabricated on the Al film by the photolithography technique. After that, the anodizing treatment was done under the constant current 12.5 μA/cm^2 in a 0.5 mol/l oxalic acid solution. A polyimide alignment material for vertical alignment was coated on another one of substrates. The sample cell with a 6μm cell gap was fabricated by assembling these substrates. The nematic LC having negative dielectric constant was injected within isotropic phase into the cell, then cooled down to LC phase.

4. Result and Discussion

The V-t curve in the process of constant current anodization is shown in Fig.3. The change in the V-t curve gives us the information about the situation of anodization. Anodization was done for about 100 second when the voltage saturates to about 1.6V.

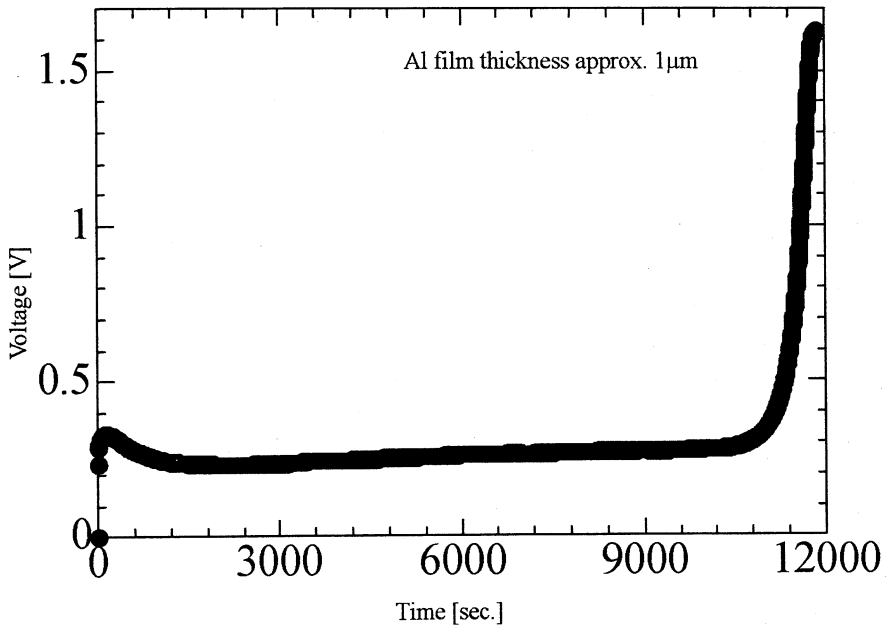

Fig.3 V-t curve in constant current anodization (example)

The situation of surface of the anodized aluminum film with groove structure observed by the laser beam microscope is shown in Fig. 4. It can be confirmed that the groove structure has been constructed.

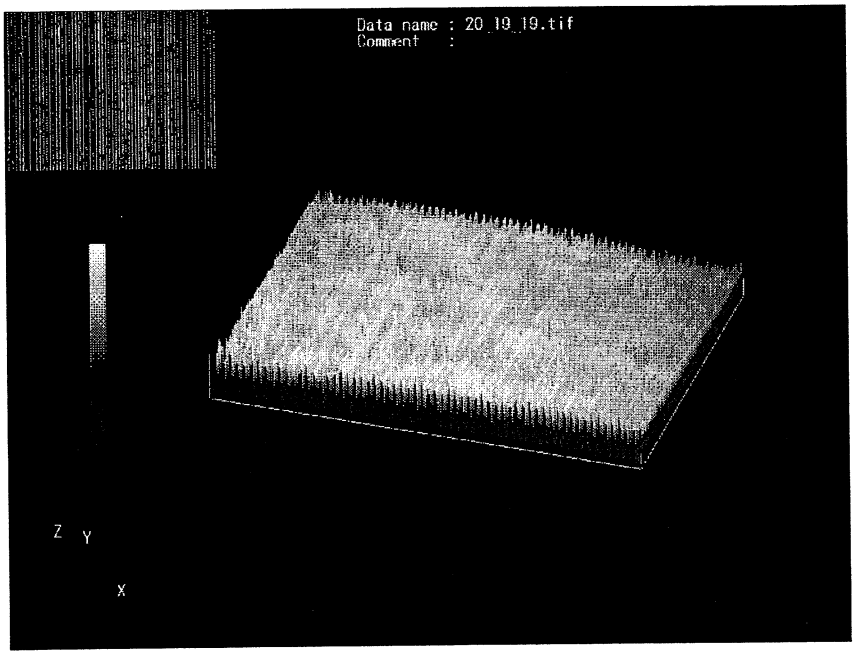

Fig.4 Surface structure after the anodization of the Al film by the laser microscope

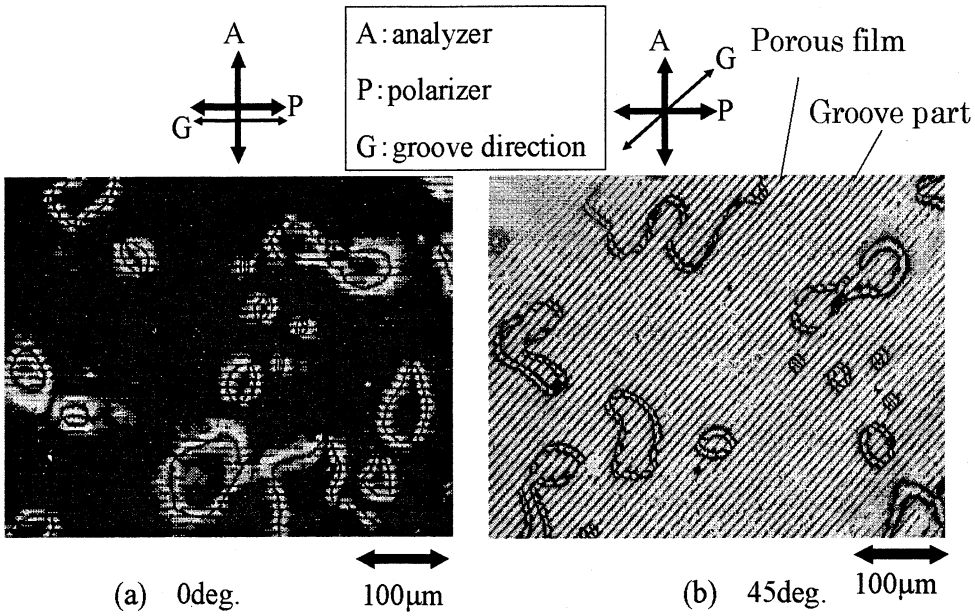

Fig.5 Al anodization film with the groove structure was used as an alignment film (Cell gap 6.0μm)

Next, the situation of LC molecular alignment in the cell was observed using the polarizing optical microscope. The result when a cell was rotated is shown in Fig. 5.

Since in the part of the anodized aluminum, only the extinction state was observed even if the cell was rotated, it is confirmed that LC molecules are vertically aligned on the anodized aluminum On the other hand, in the part of the groove, it can be confirmed that LC molecules align parallel along the grooves, since the extinction was observed when the direction of grooves coincided with the direction of transmission axis of polarizer and the brightest state was observed when the direction of groove becomes 45deg. with respect to the transmission axis of polarizer. Coexistence of the vertical alignment and the planer alignment is experimentally confirmed. However, the bistable property has not been observed yet. It is thought that the width of aluminum and the space of the groove were too large.

Furthemore, the defect was partially confirmed in the liquid crystal cell. This defect was not confirmed in cell using the aluminum anodization film without groove structure. Therefore, the groove structure made of the striped alumina is thought as one of the causes of the appearance of the defects.

5. Conclusions

In order to obtain the bistable surface, a new method is proposed to fabricate the micro-patterned substrate surface formed by stripes of alternating vertical and planer anchorings. In this method, aluminum film evaporated in vacuum on substrate surfaces was etched in stripe pattern using the photolithography techniques. And then, stripes of aluminum were anodized. Coexistence of the vertical alignment on stripes of porous alumina and the planer alignment along stripes due to grooves between stripes of alumina is experimentally confirmed. However, the bistable property has not been observed yet.

Acknowledgements

The authors would like to thank Merck Co. Ltd and Nissan Chemical Industry for supplying LC materials and alignment materials, respectively. This work was supported by a "High-Tech Research Center" Project for Private Universities: matching fund subsidies from MEXT (Ministry of Education, Culture, Sports, Science and Technology), 2006-2010.

REFERENCES

1) G.P.Bryan-Brown, C.V.Brown, J.C.Jones, et al: SID 97 Digest, (1997) 37

2) I.Dozov, M.Nobili and G.Durand: Appl.Phys.Lett, 70, (1997) 1179

3) M.Yoneya, J.H.Kim and H.Yokoyama: Appl.Phys.Lett, 80, 374 (2002)

4) T.Maeda and K.Hiroshima: Jpn.J.Appl.Phys.43,8A,(2004)L1004-L1006

5) T.N.Oo, R. Bansho, N. Tanaka, M. Kimura, T. Akahane: Jpn.J.Appl.Phys.45, (2006) 4176.

IDW'08

Electro-Optical Properties of Optically Compensated No-Bias-Bend LCD

H. Shidara, T. Takahashi, and S. Saito

Kogakuin Univ., 2665-1 Nakano, Hachioji, Tokyo 192-0015, Japan

ABSTRACT

In this report, electro-optical characteristics and transient response properties of the no-bias-bend (NBB) cell are investigated and are compared with those of the conventional bias-bend (BB) cell keeping the application to optically compensated cell in mind. As a result, it is shown that comparing the NBB cell with the BB cell both of which have a cell thickness giving a phase difference larger than π, the NBB is not always superior to the BB.

1. INTRODUCTION

The optically compensated bend (OCB) nematic liquid crystal display (LCD) has attracted considerable attention due to its superior characteristics such as a fast response time and a wide viewing angle[1-4]. In the OCB-type LCD, the pi-cell[5,6] is used with an optical compensation film for improved viewing angles and contrast ratio[7]. The pi-cell is constructed using a pair of substrates rubbed in parallel directions. When the pretilt angle is lower than the critical angle, the pi-cell takes the splay state as the stable state as shown in Fig.1. Thus, the OCB-type LCD needs the initial transition operation from the splay state to the bend state by applying high voltage at start up, and always need an operation voltage higher than its critical voltage to maintain the bend state. This is one serious drawback of the OCB-type LCD.

Recently, high pretilt angles of near 45 deg. were achieved reliably by using nano-textured alignment surfaces. One application of such high pretilt angles is in making pi-cell with no bias voltage as shown in Fig.2 (b). Such pi-cell is called the no-bias bend (NBB) cell[8].

F.S.Y. Yeng et al. reported that the NBB cell has very fast transient response characteristics. However, in their comparison, they did not necessarily bear the application to the optically compensation LCD in mind. In this paper, electro-optical properties and transient response characteristics of the NBB cell are investigated and those properties are compared with that of conventional BB cell keeping the application to an optically compensated LCD in mind.

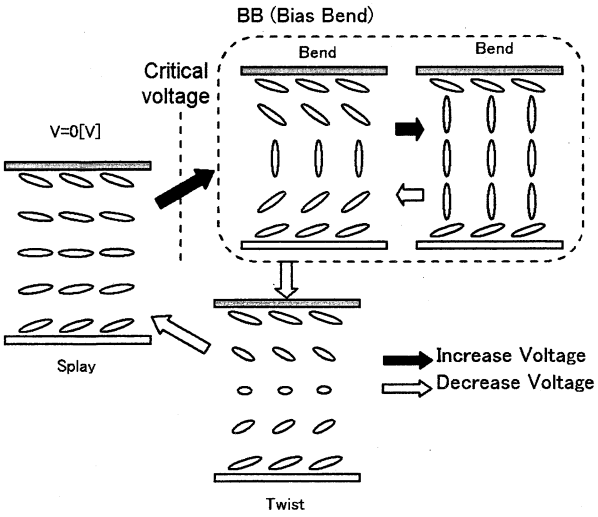

Fig.1 Transition operation of bias-bend cell.

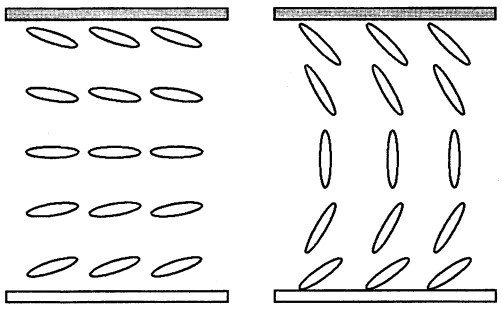

(a) Splay cell (b) No-bias-bend cell

Fig.2 Initial alignment.

2. THE CELL THICKNESS REQUIRED FOR THE OPTICALLY COMPENSATED BEND (OCB) CELL

As is well known, the transmittance of the bend cell is given by following equation under the crossed Nicole condition, when the angle between the transmission axis and the projection of the input director onto the substrate surface is 45 deg.

$$T_\lambda = T_{p\lambda} \sin^2 \frac{\delta_\lambda}{2} \qquad (1)$$

$T_{p\lambda}$ represents the total transmittance of the paral-

lel polarizer and two substrates coated by ITO and alignment materials. δ_λ is the phase difference caused between the ordinal ray and the extra-ordinal ray when they transmit through the LC layer.

When $(n_e^2-n_o^2)/n_e^2<<1$ is assumed, δ_λ is approximately given by

$$\delta_\lambda = \frac{2\pi}{\lambda}\Delta n\int_0^d \cos^2\theta dz \qquad (2)$$

Where λ is the wave length, θ the tilt angle of director and d cell thickness. The refractive anisotropy $\Delta n=n_e-n_0$, where n_e and n_o are the refractive indices of extra-ordinary ray and ordinary ray, respectively.

When no voltage is applied, the director profile in the bend cell is approximated as follows;

$$\theta = \frac{2\left(\frac{\pi}{2}-\theta_0\right)}{d}z+\theta_0 \qquad (0\le z\le\frac{d}{2}), \quad (3)$$

$$\theta = \frac{2\left(\frac{\pi}{2}-\theta_0\right)}{d}(z-\frac{d}{2})-\frac{\pi}{2} \quad (\frac{d}{2}\le z\le d) \quad (4)$$

where θ_0 is pretilt angle.

Then, eq. (3) is given by

$$\delta_\lambda = \frac{\pi}{\lambda}\Delta nd\left\{1-\frac{1}{(\pi-2\theta_0)}\sin 2\theta_0\right\}, \qquad (5)$$

$$d = \frac{\lambda\delta_\lambda}{\pi\Delta n}\left\{1-\frac{1}{(\pi-2\theta_0)}\sin 2\theta_0\right\}^{-1}. \qquad (6)$$

By adapting an optically compensation film on the BB cell or NBB cell, one can construct an OC-BB cell or an OC-NBB. To obtain a high contrast ratio and high brightness due to the OCBB or the OC-NBB, it is required that δ_λ is higher than π when no voltage is applied. We assumed that δ_λ =1.3π is most appropriate. Then the optimum cell thickness is evaluated by substituting δ_λ =1.3π rad. into eq. 6.

3. EXPERIMENT

3-1 Sample Preparation

To obtain high pletilt angles of near 45 deg., a mixed solution of PI-A and SE-1211 (Nissan Chem. Ind.) was used as an alignment material[9]. The PI-A and SE-1211 are polyimide compounds which were composed to obtain parallel alignment and perpendicular alignment, respectively. The alignment material was coated on the substrate surface by a spin coater and was baked at 220 ℃ for 60 min. And then, the substrate surfaces were rubbed by using a rubbing roller. By assembling a pair of substrates in such a way that those rubbing directions become parallel, sample cells were fabricated.

As LC materials, ZLI-2293 (Merck) and 5CB (Merck) were used. The refractive anisotropy of ZLI-2293 is Δn=0.13, and that of 5CB is Δn=0.20. Using those LCD materials, four kinds of sample cells were prepared.

The first one was the BB cell. This type of cell is used in conventional OCB-type LC cells. As an LC material, ZLI-2293 was used. The cell thickness was designed to be 6 μm at which the variation width of the phase different of 1.3π rad. is obtained for a wavelength of 589.3 nm, that is, the maximum transmittance is obtained when optical compensation film is added.

The second one was the NBB cell (named as NBB-1) of ZLI-2293 with a thickness of 6 μm which is the same as the BB cell above mentioned.

The third one is the NBB cell (named as NBB-2) of ZLI-2293. The cell thickness was designed to be 18 μm at which the variation width of the phase different of 1.3π rad. is obtained for a wavelength of 589.3 nm, that is, the maximum transmittance is obtained when optical compensation film is added.

The fourth one was the NBB cell (named as NBB-3) of 5CB with a larger refractive anisotropy than ZLI-2293 was used. The cell thickness was designed to be 13 μm. It should be noted that this cell thickness is thinner considerably than the NBB cell of ZLI-2293. The thickness of 13 μm is sufficient to obtain the variation width of the phase difference of 1.3π rad., that is, the maximum transmittance is obtained when an optical compensation film is added.

3-2 Measurements

The relationships between an applied voltage and transmittance were measured for continuously increasing and decreasing the applied voltage. As an applied voltage, a sinusoidal wave voltage with a frequency of 20 kHz was used. The variation speed of applied voltage was 5 V/min. As a light source, He-Ne laser was used. The cell was set between a crossed Nicole and the direction of the transmission axis of polarizer was set at an angle of 45 deg. with respect to the projection of the input director onto the substrate. Transient response times were measured for the sample cells. The applied voltage was changed from 4 V to any

voltage higher than 4 V and vice versa since the BB cell needs an operation voltage higher than its critical voltage to maintain the bend state.

4. EXPERIMENTAL RESULTS

4-1 Applied voltage vs. transmittance relations

Figure 3 shows the applied voltage vs. transmittance characteristics of the conventional BB cell. The V-T curves for an increased voltage and a decreased voltage don't coincide. The BB cell takes a splay state as the initial molecular state. When applied voltage is increased, the V-T curve in a voltage range from 0 V to about 3.5 V corresponds to the characteristics of the splay state. Above about 3.5 V, the transition from the splay state to the bend state occurs. When applied voltage is continuously decreased from 10 V, the V-T curve (dashed line) corresponds to the characteristics of the bend state in a range of voltage higher than about 1.5 V. Below 1.5 V, the transition from the bend state to the twisted state occurs. When applied voltage is remained at 0 V, the twisted state relaxed naturally to the splay state. This means that the initial transition operation from the splay state to the bend state by applying high voltage is needed at start up, and always need an application of bias voltage higher than its critical voltage to maintain the bend state.

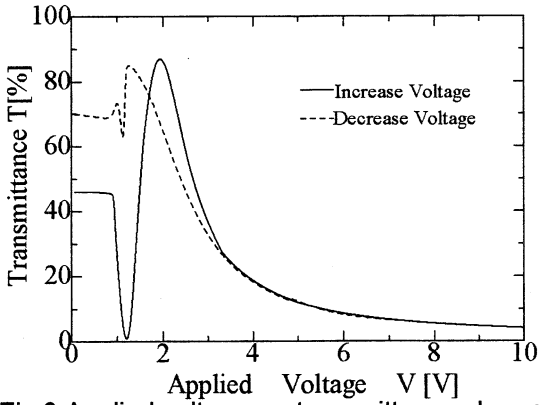

Fig.3 Applied voltage vs. transmittance characteristics of BB cell.

Figure 4 shows the applied voltage vs. transmittance characteristics of cell NBB-1 with the same cell thickness as the conventional BB cell. The V-T curves for an increased voltage and a decreased voltage coincide. This means that in this NBB-1 cell, the bend state has been realized as the stable state. In this BB-1 cell, the maximum transmittance is considerably lower than that of BB cell and the other NBB cell. This is due to the high pretilt angle and thin cell thickness.

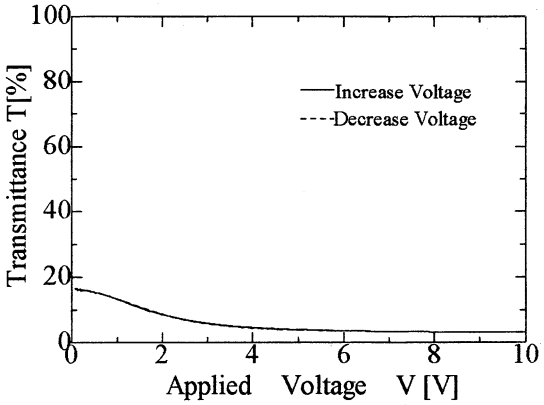

Fig.4 Applied voltage vs. transmittance characteristics of NBB cell of same cell thickness as conventional OCB-type LC cell.

Figure 5 shows the applied voltage vs. transmittance characteristics of the cell NBB-2 with a thickness of 18 μm. In this cell、 ZLI-2293 was used. Similarly to the cell NBB-1, the V-T curves for an increased voltage and a decreased voltage coincide. Comparing with the V-T curve of NBB-1 cell, the transmittance of the NBB-2 cell with the cell thickness of 18 μm is higher than that of NBB-1 cell.

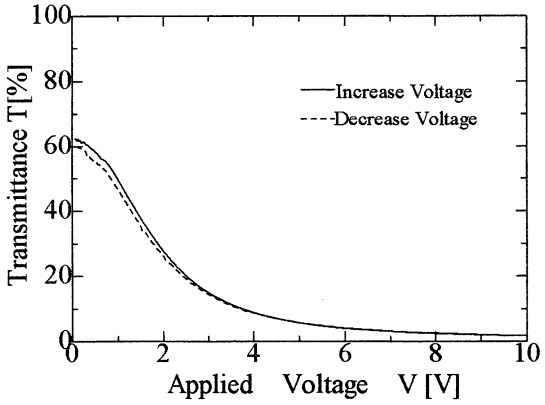

Fig.5 Applied voltage vs. transmittance characteristics of NBB cell with 18 μm-thickness, and LC material ZLI-2293 is used.

Figure 6 shows the applied voltage vs. transmittance characteristics of NBB-3 cell with 13μm-thickness, in which 5CB is used. In the same way with NBB-1 and NBB-2 cells, the V-T curves for an increased voltage and a decreased voltage coincide. The maximum transmittance of this NBB-4 cell is high similarly to the NBB-2 cell.

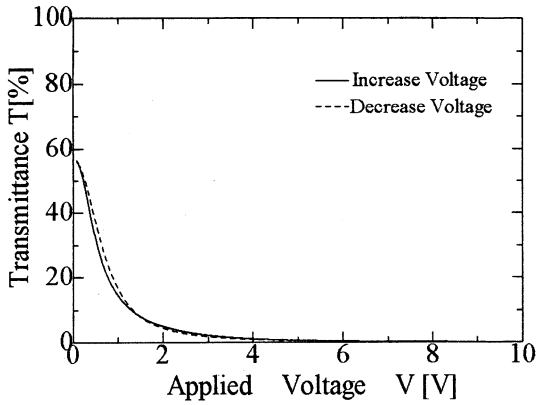

Fig.6 Applied voltage vs. transmittance characteristics of NBB cell with 13 μm-thickness, and LC material 5CB is used.

4-2 Transient response characteristics

Figure 7 shows transient response characteristics as a function of the applied voltage. Figure 7 (a) shows the rise time, and Fig.7 (b) shows the decay time.

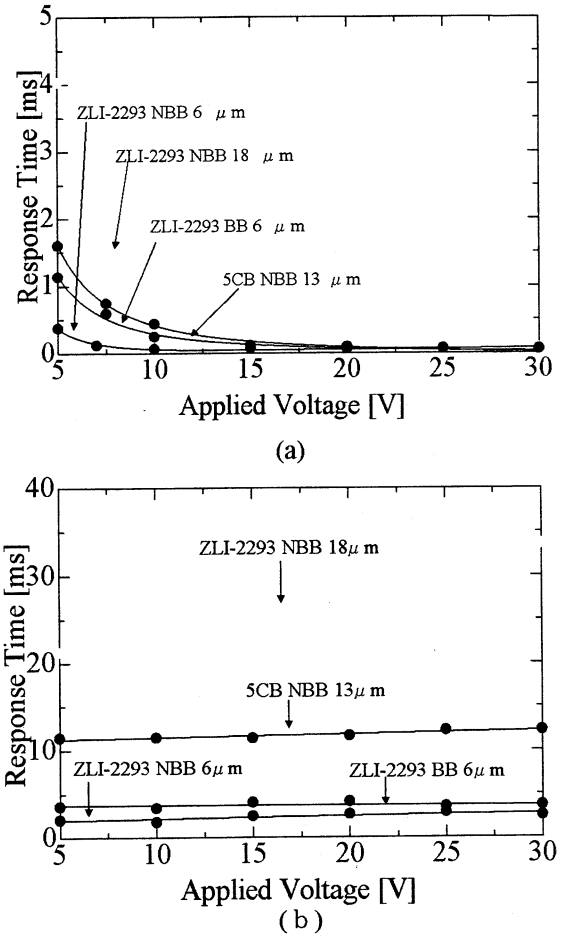

Fig.7 Transient response characteristics as a function of the applied voltage (a) rise time, and (b) decay time.

As is known from these figures, the NBB cell with the same cell thickness as the conventional BB cell shows the fastest response speed of four sample cells. This means that if the thickness is the same, the response time of the NBB cell exhibits faster response speed than that of the BB cell. The NBB cell with the cell thickness of 18 μm in which ZLI-2293 was used shows the slowest transient response. And the response time of the NBB cell of 5CB is faster than the NBB cell of ZLI-2293.

5. CONCLUSIONS

In this report, we examined the optical properties of NBB cell which was proposed as a potential candidate to improve the characteristics of conventional BB cell. If it is the same cell thickness, the response time of the NBB cell is faster than that of the BB cell. However, the maximum transmittance of this NBB cell becomes considerably low. In addition, when the cell thickness is increased to restrict the deterioration of transmittance, the response speed becomes slow. As a result, we pointed out that the NBB cell is not necessarily superior as the LCD for which bright images are required.

Furthermore, from our experimental result that response speed of the NBB-2 cell of 5CB with the optimized cell thickness became faster than that of NBB-2 cell of ZLI-2293, we thought that an NBB cell exhibiting faster response may be obtained by examining LC materials in the NBB cell.

6. REFERENCES

[1] Mi Jun Jung, Chul Gyu Jhun, Jae Chang Kim, and Tae-Hoon Yoon: IDW'04, pp.121-124.

[2] P. J. Bos and J. A. Rahman: 1993 SID int. Symp. Dig. Tech. Pap. (1993)273.

[3] Y. Yamaguchi, T. Miyashita and T. Uchida: 1993 SID int. Symp. Dig. Tech. Pap. (1993)277.

[4] Chen-Lung Kuo, Tetsuya Miyashita, Makoto Suzuki and Tatsuo Uchida: Jpn. J. Appl. Phys, pp. L1362-L1364, Vol. 34, No. 10 (1995).

[5] P. J. Bos and K. R. Koehler / Beran: Mol. Cryst. Liq. Cryst. 113(1984)329.

[6] Hajime Nakamura and Michikazu Noguchi: Jpn. J. Appl. Phys, pp. 6368-6375, Vol. 39, No. 11 (2000).

[7] Seng-Huei Chang, Chien-Lin Pan: IDW'04, pp.137-139.

[8] F.S.Y. Yeung, Y.W.Li and H. S. Kwok: IDW/AD'05, pp.41-44.

[9] F. Sze-Yan Yeung, F.-C. Xie, H.-S. Kwok: SID 05 DIGEST, pp. 1080-1083 (2005).

Transition from the U-State to the T-State through an Over-Twisted State in Bi-Nem LC Cell

Y. Uchiyama, H. Terashi, T. Takahashi and S. Saito
Kogakuin Univ., 2665-1 Nakano, Hachioji, Tokyo 192-0015, Japan

Abstract

Transition from the U state to the T state through an over twisted process in the Bi-Nem cell was experimentally observed for the first time. It is theoretically shown that such transition through the over twisted process occurs in the case of relatively large surface dissipation coefficient.

1. Introduction

The bistable twisted nematic liquid crystal (LC) cell (Bi-Nem) has received considerable attention since the proposal by Dozov et al[1]. The Bi-Nem LC cell has many superior properties, such as a simple structure, a fast response, a high contrast ratio and a wide viewing angle in addition to a permanent memory effect. The theoretical investigation on the switching mechanism has been carried out by Dozov et al[1]. Takahashi et al[2)3)]. and Jy-Shan Hsu et al[4)] independently used computer to simulate the dynamic behaviors of the Bi-Nem cells, they showed possibilities that the director configuration switched from the uniform state (U state) to the twisted state (T state) takes a 270 degree twist first and then gradually changes to the T state. These behaviors are different from the model proposed by Dozov, in which the directors go directly to the T state.

The transition from the U state to the T state through an over twisted state has not been experimentally confirmed yet. Thus, in this study, we try to confirm experimentally such transition of director configuration in the Bi-Nem LC cell.

2. Experiments

2-1 Sample Preparation

Two types of Bi-Nem cell, called the cell A and the cell B were prepared and those optical transient response to the applied voltage pulse were compared. On the slave substrate of the cell A, SiO was obliquely evaporated at an evaporation angle of 60 degree as an alignment layer. On the slave substrate of the cell B, the optical alignment treatment was carried out. A kind of polyimide RN-1650 (Nissan Chemical Industry) was used as an optical alignment material. On the master substrate of both types of cell, the cell A and the cell B, the rubbing treatment was carried out.

As the LC materials, the nematic single compound 5CB (Merck) was used. A chiral material CB15 (Merck) was added in 5CB by an appropriate quantity. In the Table 1, the samples prepared are listed with the sample name and the alignment treatments.

Table 1: Sample lists

Sample name	Thickness [μm]	Alignment treatment on the slave substrate
Cell A	1.9	Oblique evaporation of SiO
Cell B	1.8	Optical alignment for RN-1650

For master plate of all cells, the rubbing treatment was carried out.

2-2 Measurements

The sample was set on the stage of a polarizing optical microscope under the crossed Nicole condition. The transmission axis of polarizer sets at an angle of 45 degree with respect to the direction of input director. Since the transition from the U state to the T state starts to occur not over entire region but from many small domains, the light intensity transmitted through only one of domains was detected by a photo diode which was set through the ocular and the transient variation of the transmitted light intensity associated with the voltage

pulse application was observed by a digital storage oscilloscope.

3. Experimental Results and Considerations

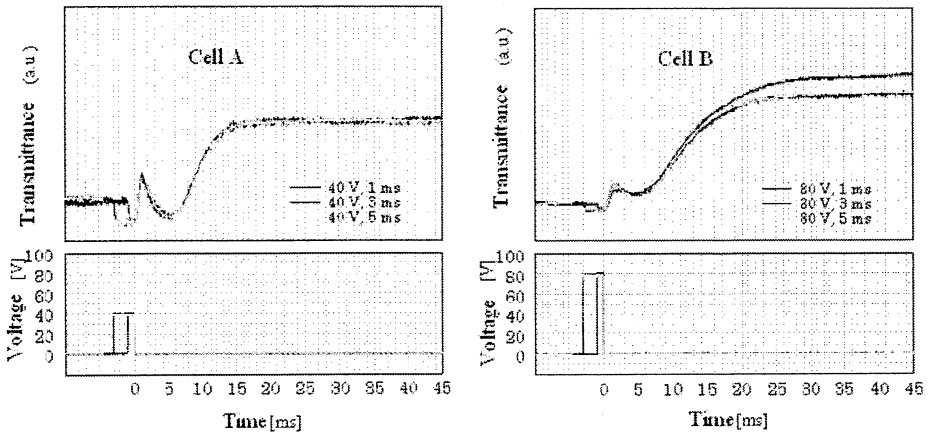

Fig.1 Experimental results on the dependence of optical response with on duration time of applied voltage pulse.

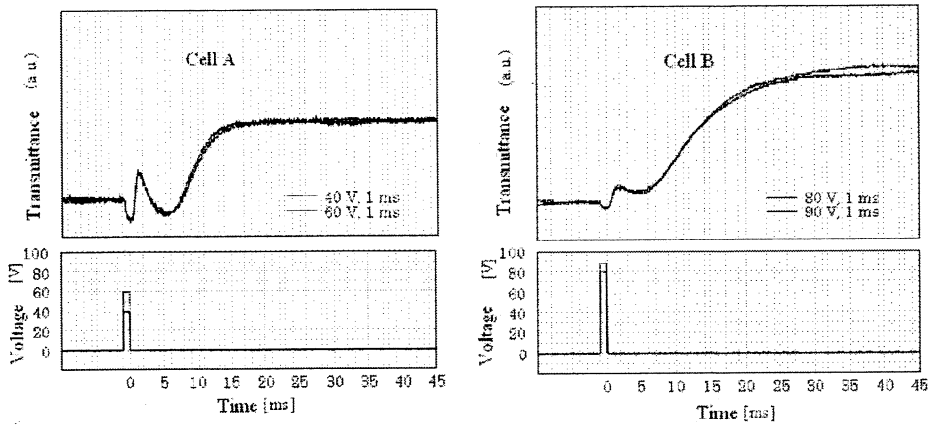

Fig.2 Experimental results on the dependence of optical response on the amplitude of applied voltage pulse.

Observed transient variations of transmitted light intensity occurred by the voltage pulse application for the cell A and the cell B are shown in Fig.1 and Fig.2 as a parameter of the duration time and the amplitude, respectively. The optical response curves were almost independent of the duration and amplitude of applied voltage pulse. The cell A could be transformed from the U state to the T state by the application of voltage pulse with lower amplitude and shorter duration than the cell B.

The transmitted light intensity takes a maximal value just after the application of voltage pulse and then increases and saturates gradually. As has been pointed out

by Jy-Shan Hsu et al[4], this first maximal is reflected by the transition from the U state to the T state through the over twisted process. The first maximal value in the cell A is higher than that in the cell B. As will be shown in the next, this means that the transition from the U state to the T state in the cell A through an over twisted angle higher than that in the cell B.

Theoretical calculations on the optical response associated with the U-T transition to investigate what does affect the first maximal value in the optical response. As a result, it can be known that the surface dissipation coefficients affect most remarkably the first maximal in the optical response, as shown in Fig.3.

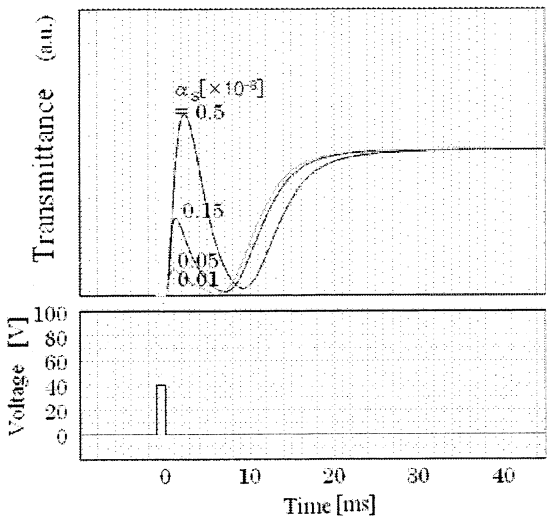

Fig.3 Calculated results on optical response as a parameter of surface dissipation coefficient.

As is known from Fig.3, the first maximal in the optical response become the larger for the larger surface dissipation coefficient. Comparing the experimental results shown in Fig.1 and Fig.2 with the calculated result shown in Fig.3, the surface dissipation coefficients are estimated as $\alpha s=0.15\times10^{-8}Ns^2/m$ and $\alpha s=0.05\times10^{-8}$ Ns^2/m for the surfaces of slave substrates in the cell A and the cell B, respectively.

In Fig.4, the changes of the director configuration in the U-T transition process are shown by using a polar coordinate system and the optical response are shown for a surface dissipation coefficient of $\alpha s=0.15\times10^{-8}Ns^2/m$ which corresponds to the cell A.

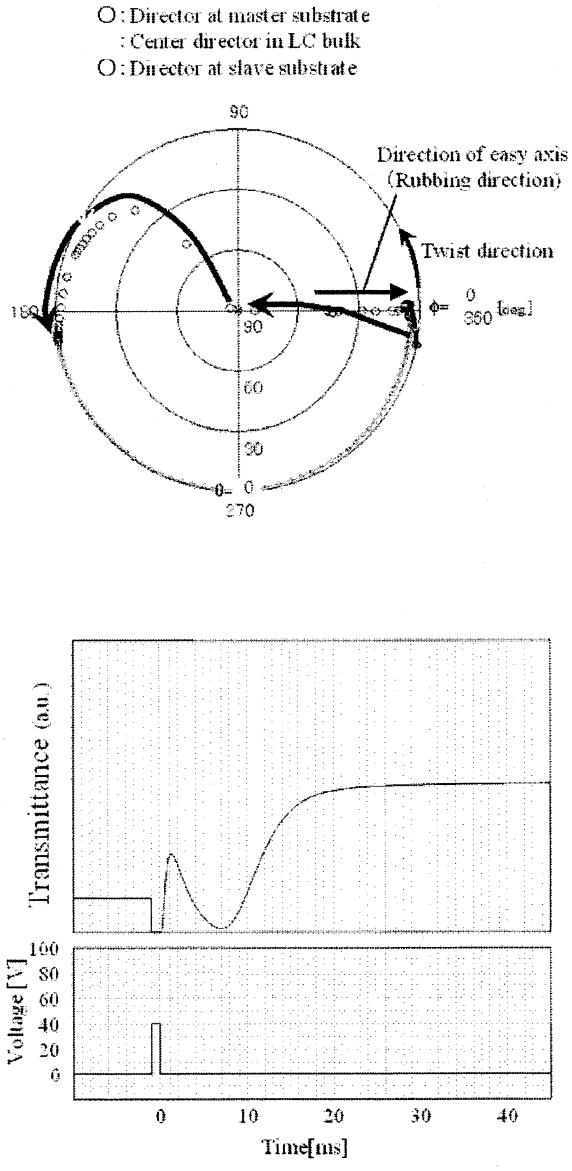

Fig.4 Transient variation of director profile plotted in a polar coordinate system and the optical response for the case of $\alpha s=0.15\times10^{-8}$ Ns^2/m.

In Fig.5, the changes of the director configuration and the changes of the direction of flow velocity in the vicinity of the slave plate (at z=d/8) in the U-T transition process for three cases of surface dissipation coefficient of $\alpha s=0.5 \times 10^{-8} Ns^2/m$, $\alpha s=0.15 \times 10^{-8} Ns^2/m$, and $\alpha s=0.05 \times 10^{-8} Ns^2/m$.

It should be noted that the direction of flow velocity coincides with the direction of displacement of surface director toward the over twist on the slave plate. These behaviors are different from the model proposed by Dozov, in which the directors go directly to the T state.

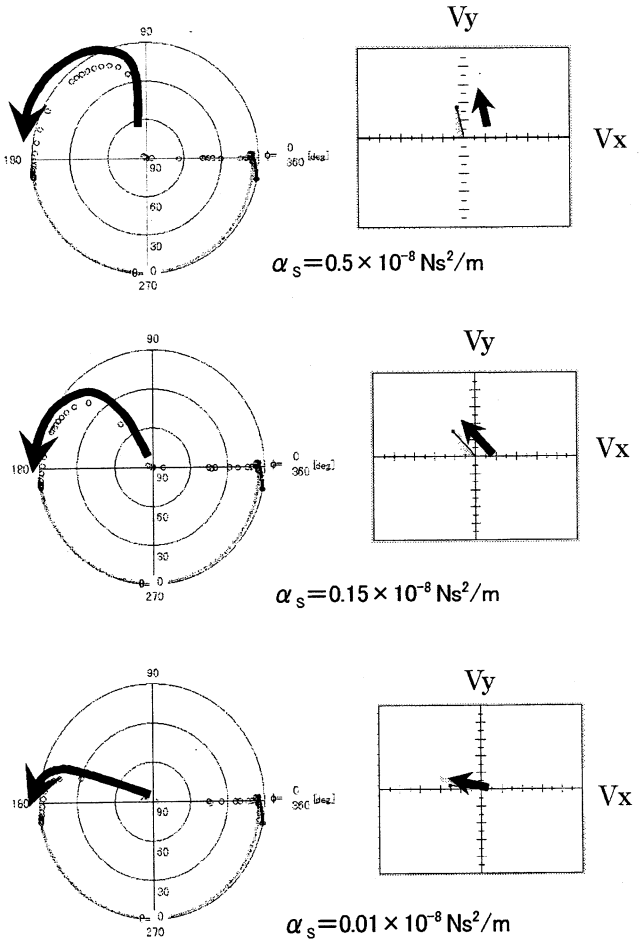

Fig.5 Calculated results on the changes of director profiles in a polar coordinate system and the flow velocity at z=d/8 in the transition process from the U state to the T state for different three surface dissipation coefficients.

4. Conclusions

Transition from the U state to the T state through an over twisted process in the Bi-Nem cell was experimentally observed for the first time. It has been theoretically shown that the twist angle of over twist greatly depends on the surface dissipation coefficients, and such transition through the over twisted process occurs in the case of relatively large surface dissipation coefficient.

Furthermore, it has been shown that the direction of flow velocity coincides with the direction of displacement of surface director toward over twist on the slave plate. These behaviors are different from the model proposed by Dozov, in which the directors go directly to the T state.

5. References

[1] I.Dozov, Ph. Martinot-Lagarde, E. Polossat, I.Lelidis, M. Giocondo and G. Durand.: Proc. SPIE 3015(1997) p.61

[2] S. Saito, T. Takahashi, T. Chiba and S. Tsuchida.:Jpn. J. Appl. Phys. 41(2002) p.3841

[3] T. Takahashi, S. Tsuchida, M. Udagawa and S. Saito: Jpn. J. Appl. Phys. 43 (2004) p. 1469

[4] Jy-Shan Hsum Bau-Jy Liang and Shu-Hsia Chen: Jpn. J. Appl. Phys. 44 (2005) p.6170.

IDW08

Improvement of Transient Response Characteristics of Polymer Stabilized Bend Alignment Liquid Crystal Cell

T. Kobayashi, Y. Asakawa, T. Takahashi and S. Saito

Kogakuin Univ., 2665-1 Nakano, Hachioji, Tokyo 192-0015, Japan

Abstract

Influences of LC and UV curable LC monomer materials on the transient response characteristics of a polymer stabilized bend (PSB) cell are investigated. It is shown that the decay time of the PSB cell can be improved by using a fluorinate nematic mixture, ZLI-4792 (Merck) and RMM-34 (Merck) as the LC material and the UV curable LC monomer, respectively.

1. Introduction

The optically compensated bend (OCB) nematic liquid crystal display (LCD) has attracted considerable attention due to its superior characteristics such as a fast response time and wide viewing angle[1)8)]. In the OCB-type LCD, the bend alignment state in the pi-cell[2)] is used with an optical compensation film. Since the pi-cell with pretilt angle lower than the critical angle takes the splay configuration as the stable state[2)], the OCB-type LCD needs the initial transition operation from the splay alignment to the bend alignment by applying high voltage at start-up and always need an operating voltage higher than its critical voltage to maintain the bend alignment. This is one serious drawback of OCB-type LCD.

To mitigate this problem, some methods have been proposed[3)-7)]. As one of potential methods, the polymer stabilization method has been proposed[3)6)10)], in which the bend alignment stabilized by forming a polymer network using the optical polymerization of UV curable liquid crystalline monomers. However, in our previous paper[13)], we reported that the both the rise and decay times in the transient responses of the bend cell are deteriorated by the polymer stabilization treatment. In this study, how the LC material and UV curable LC monomer material affect the transient response characteristics of the polymer stabilized bend alignment LC cell is investigated.

2. Experiments on Transient Response Characteristics of Pi-Cell

2.1 Sample preparation

Typical nematic mixtures, ZLI-4792 (Merck) and ZLI-2293 (Merck), in which RMM-34 (Merck) or UCL-001 (DIC) was doped by 5 wt% as the UV curable LC monomers were used. It is well known that the ZLI-4792 is a fluorinate compound. As the alignment material, a kind of polyimide, PI-A (Nissan Chemical Industry) was coated by a spinner on the ITO coated substrates and was baked at 250 °C for 60 min. Then those substrates were rubbed by a rubbing roller and assembled so as the rubbing directions become parallel. The cell thickness was 6 μm. The UV light was irradiated by 10 J/cm^2 under the voltage application of 4 V. From the measured V-T curve, it was confirmed that the bend alignment was stabilized in the cell.

2.2 Experiments

The rise and decay times were measured as a function of applied voltage. The rise and decay times were evaluated as the time interval in which the transmittance changes by 90 percent of the change width in transmittance. These transient response times were measured before and after the UV light irradiation for the cells in which the mixture of LC and UV curable LC monomers was injected.

Before the UV light irradiation the molecular orientation in the cell takes the splay state, the application of bias voltage of 4 V was necessary to maintain the bend state. Thus, the rise time was measured for the change in applied voltage from 4 V to a voltage higher than 4 V, and decay time was measured for the reverse change of applied voltage.

After the UV light irradiation, the molecular orientation in the cell takes the bent state as the equilibrium state. The transient response times of those PSB cells were measured at the same conditions mentioned above for the comparison.

The applied voltage was a sinusoidal wave voltage of 10 kHz. The ambient temperature of the cell was maintained at 20 °C.

2.3 Experimental results on transient response characteristics

In Fig.1, the experimental results on the rise and decay times are shown as a function of applied voltage for the cells in which ZLI-2293 + RMM-34 was used. For comparison, the corresponding characteristics are shown in Fig.2, Fig.3, and Fig.4 for ZLI-4792 + RMM-34, ZLI-2293 + UCL-001, and ZLI-4792 + UCL-001, respectively. In these figures,

the solid line indicates the applied voltage dependence of response time before the UV light irradiation, and the dotted line after the UV light irradiation. As can be seen from these results, how the polymer stabilization affects on the transient response characteristics of the bend cell depends on both of the LC material and the UV curable LC monomers. When RMM-34 is used as the UV curable LC monomers, the decay time of cell of ZLI-2293 is deteriorated by the polymer stabilization treatment. Then, however, the decay time of the cell of ZLI-4792 is drastically improved by the polymer stabilization treatment, though the rise time is slightly deteriorated. When UCL-001 is used as the UV curable LC monomer, the polymer stabilization treatment has only a little influence on the rise and decay times in both cells of ZLI-2293 and ZLI-4792.

To clarify the origin of these tendencies, the

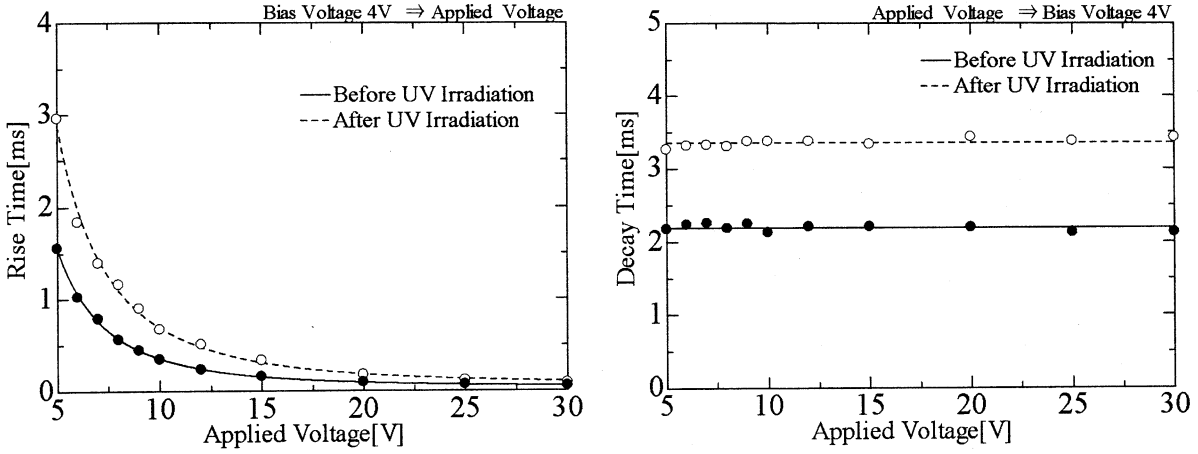

(a) rise (b) decay

Fig.1 Transient response characteristics of the bend aligned LC cell.
N-LC: ZLI-2293 in which RMM-34 was doped by 5 wt%.
Irradiation of UV light: 10 J/cm^2.

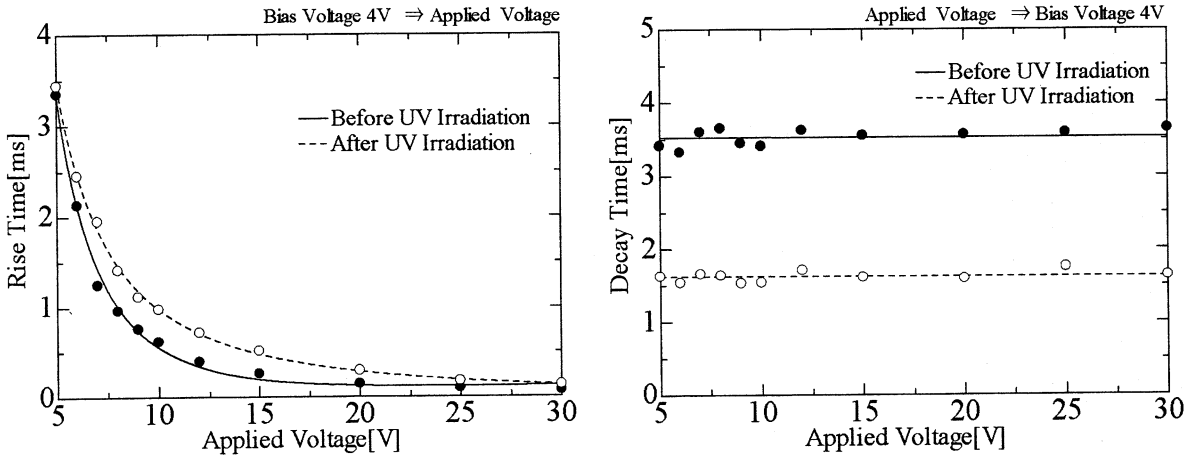

(a) rise (b) decay

Fig.2 Transient response characteristics of the bend aligned LC cell.
N-LC: ZLI-4792 in which RMM-34 was doped by 5 wt%.
Irradiation of UV light: 10 J/cm^2.

influence of polymer stabilization on the rotational viscosity were investigated.

Using ZLI-4792 and ZLI-2293 in which RMM-34 or UCL-001 were doped by different concentrations,

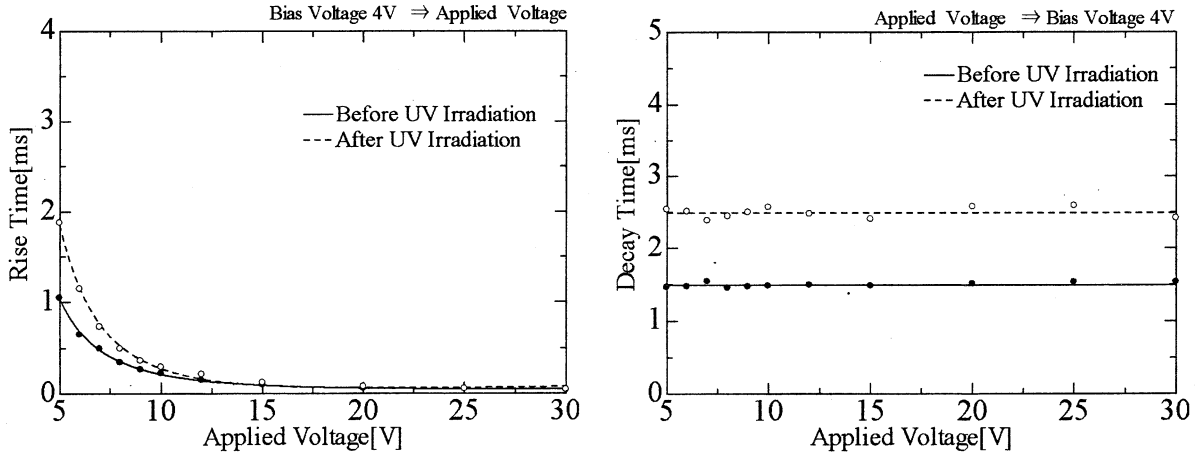

(a) rise (b) decay

Fig.3 Transient response characteristics of the bend aligned LC cell.
N-LC: ZLI-2293 in which UCL-001 was doped by 5wt%.
Irradiation of UV light: 10 J/cm^2.

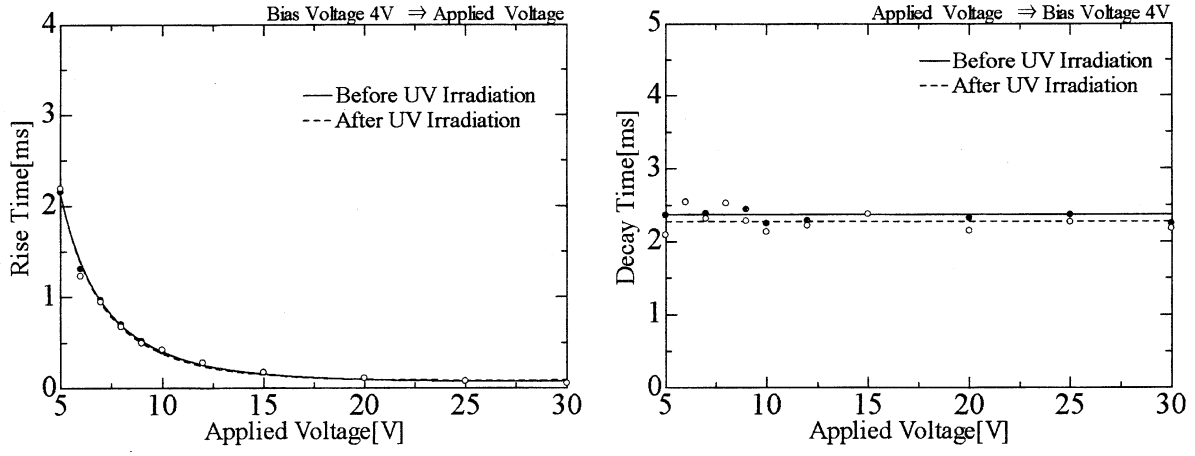

(a) rise (b) decay

Fig.4 Transient response characteristics of the bend aligned LC cell.
N-LC: ZLI-4792 in which UCL-001 was doped by 5wt%.
Irradiation of UV light: 10 J/cm^2.

3. Dependence of Rotational Viscosity on Monomer Concentration

3.1 Sample preparation and measurements

To investigate the influence of polymer stabilization on the transient response of the bend cell, the rotational viscosity was measured as a function of the concentration of UV curable LC monomer. We used the transient displacement current method previously proposed by Imai et al.[11] at first. Recently, Y. Asakawa el al.[12] represented that the applicability of the transient displacement current method for the case taking account of the polymer stabilization.

homogeneous cells were prepared and the polymer stabilization treatment carried out for those cells by irradiating the UV light by 10 J/cm^2.

3.2 Experimental results

Experimental results for the monomer concentration dependencies of the rotational viscosity are shown in Fig.5. The rotational viscosity was increased with the increase of the concentration of UV curable LC monomer for all of four combinations of the LC and the UV curable LC monomer. Such increment of rotational viscosity was most remarkable in the cases which ZLI-2293 was used as the LC material.

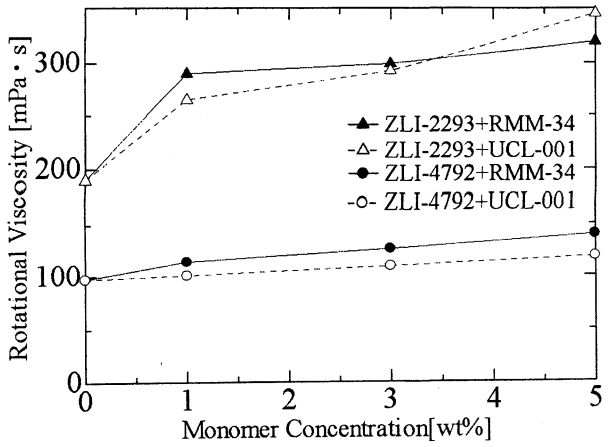

Fig.5 Monomer concentration dependence of rotational viscosity.

4. Discussion

As shown in a previous section, the influence of the polymer stabilization treatment depends on both the kind of LC and the kind of the UV curable LC monomer.

In our previous paper[9)10)], we introduced an additional term F as shown in eq.(1), which represents the contribution of polymer stabilization to free energy density F_{stab} of the LC bulk, to calculate theoretically the behaviors of polymer-stabilized LC cells.

$$F_{stab} = \frac{1}{2} A_{stab} \left[1 - (\mathbf{n}_{stab} \bullet \mathbf{n})^2 \right] \qquad (1)$$

A_{stab} is the polymer stabilization coefficient. It can be thought that $\mathbf{n}_{stab}$ is an interaction field. The profile of the interaction field $\mathbf{n}_{stab}$ coincides with the profile of the director field when UV light is irradiated and it is memorized as the conformation of the polymer network formed by UV light irradiation. The A_{stab} contributes equivalently to the change of elastic constants of LC material. The value of A_{stab} may be influenced by the kind of LC material and the kind of the UV curable LC monomer. The effects of polymer stabilization can not completely explain by the A_{stab}. The values of various Leslie's viscosities including the rotational viscosity and dielectric constants may be changed by polymer stabilization. Furthermore, it is well known that the flow of LC caused by the abrupt change in applied voltage affects considerably the transient behaviors of the bend aligned LC cell.

In the cell in which ZLI-2293 and RMM-34 were used, both rise and decay times are deteriorated by the polymer stabilization. This is thought that the influence of the increase in rotational viscosity was stronger than the influence of changes in the flow velocity pattern and the equivalent increase in elastic constants due to polymer stabilization.

On the other hand, in the cell in which ZLI-4792 and RMM-34 were used, the decay time is drastically improved due to the polymer stabilization treatment, though the rise time is slightly deteriorated. These tendencies are thought that the rise time deteriorated by the increase in rotational viscosity and the decay time was more strongly affected by the change of flow velocity pattern and the equivalent increase in elastic constant than the increase in the rotational viscosity.

In the cell in which ZLI-2293 and UCL-001 were used, both rise and decay times deteriorated by the polymer stabilization treatment. This tendency was similar to the cell in which ZLI-2293 and RMM34 were used.

In the cell in which ZLI-4792 and UCL-001 were used, the polymer stabilization treatment had little influence on rise and decay times. This is thought that the deterioration of transient response time by rotational viscosity was completely compensated by the effects of the changes in the flow velocity pattern and the equivalent increase of elastic constants.

5. Conclusions

It was clarified that by selecting the kind of the LC material and the UV curable LC monomer, the transient response characteristics of the bend cell does not necessarily deteriorate and can be improved due to the polymer stabilization treatment.

Reference

1) T. Miyashita, Y. Yamaguchi and T. Uchida: Jpn.J.Appl.Phys. 34 (1995) 177.
2) S. Saito, Y. Shirakura and M. Kamihara: Trans. IEICE Electron. E63-C (1980) 32 (in Japanese).
3) M. Xu, D.-K. Yang, J. Bos, X. Jim, F. W. Harris, and S. Z. D. Cheng: SID Int. Symp. Dig. Tech. Pap. 29 (1998) 139.
4) X.-D. Mi, M. Xu, D.-K. Yang, and P. J. Bos: SID Int. Symp. Dig. Tech. Pap. 30 (1999) 24.
5) T. Konno, T. Miyashita, and T. Uchida: Asia Display'95, (1995) 581.
6) S. H. Kim, and L. C. Chien: Jpn. J. Appl. Phys. 43 (2004) 7643.
7) H.Kikuchi, H. Yamamoto, H. Sato, M. Kawakita, K. Takizawa, and H. Hujikake: Jpn. J. Appl. Phys. 44 (2005) 981.
8) P. J. Bos and J. A. Rahman: SID Int. Symp. Dig. Thech. Pap., (1993) 273.
9) T. Takahashi, T. Umeda, H. Furue, and S. Kobayashi: Jpn. J. Appl. Phys. 38 (1999) 5991.
10) Y. Asakawa, K. Yokota, M. Nanaumi, N. Takatuka, T. Takahashi, and S. Saito: Jpn. J. Appl. Phys. 45 (2006) 5878.
11) M. Imai, H. Naito, M. Okuda, and A. Sugimura: Jpn. J. Appl. Phys. (1994) L119.
12) Y. Asakawa, T. Takahashi, and S. Saito: Jpn. J. Appl. Phys. 46 (2007) 7774.